SSC-SR-2020

Conceptual Design of the Superconducting Super Collider

SSC Central Design Group*

March 1986

*Operated by Universities Research Association under contract with the U.S. Department of Energy

A publication of the SSC Central Design Group
c/o LBL, 90/4040, 1 Cyclotron Road, Berkeley,
CA 94720 (415) 486-4772.

Corrected second printing, September 1986

Editor:	J.D. Jackson
Art Editor:	R.G. Barton
Production Editor:	R. Donaldson
Typesetting:	D.K. Savage

U.S. Department of Energy
Contract DE-AC02-76CH03000/3001

Universities Research Association, 1111 19th
Street, N.W. Suite 400, Washington, DC 20036

Acknowledgements

It is impossible to thank individually all of the skilled and dedicated persons whose efforts were essential to successful completion of this report. Some groups and individuals stand out. The clerical staff of the Central Design Group coordinated by Glenda J. Fish have made extraordinary efforts in helping us accomplish this immense task. The superb support of Richard A. Bailey and the word processing, editorial and illustration groups of the LBL Technical Information Division is most gratefully acknowledged. In particular, the skill and professionalism of Ralph C. Dennis, Valerie Y. Kelly, Alice S. Ramirez, and Jean A. Wolslegel made possible our impossible schedule. Finally, profound thanks are due LBL Director David A. Shirley for his support and hospitality.

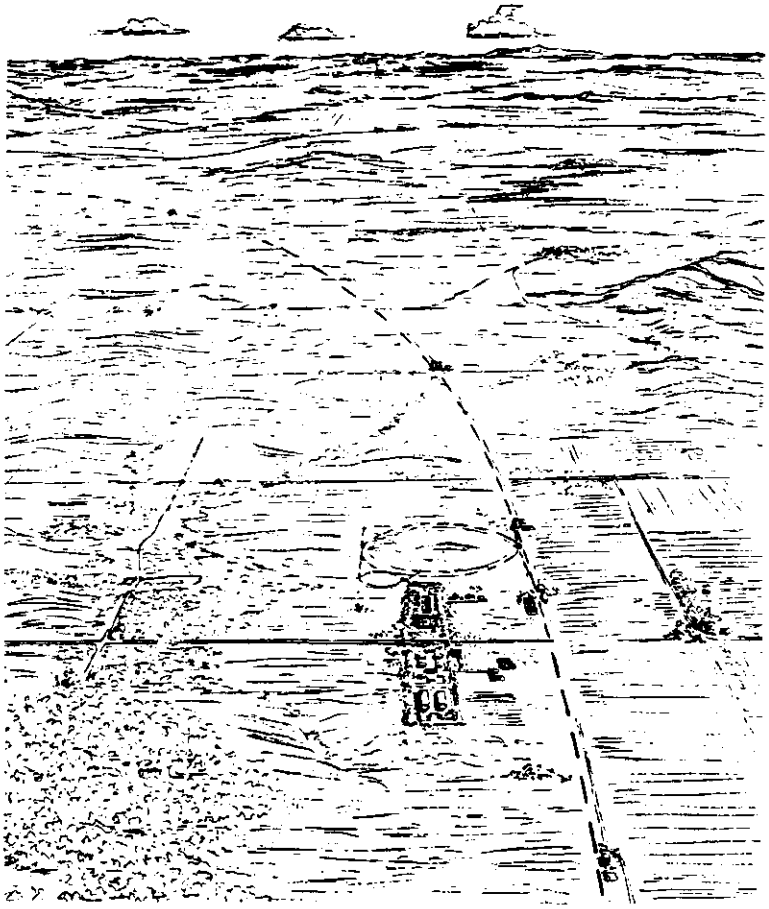

Artist's sketch of an aerial view of the SSC from an altitude of 30,000 feet. The main campus and injector complex are apparent in the foreground. Very little of the collider ring is visible from the air. The dashed line indicates its underground path.

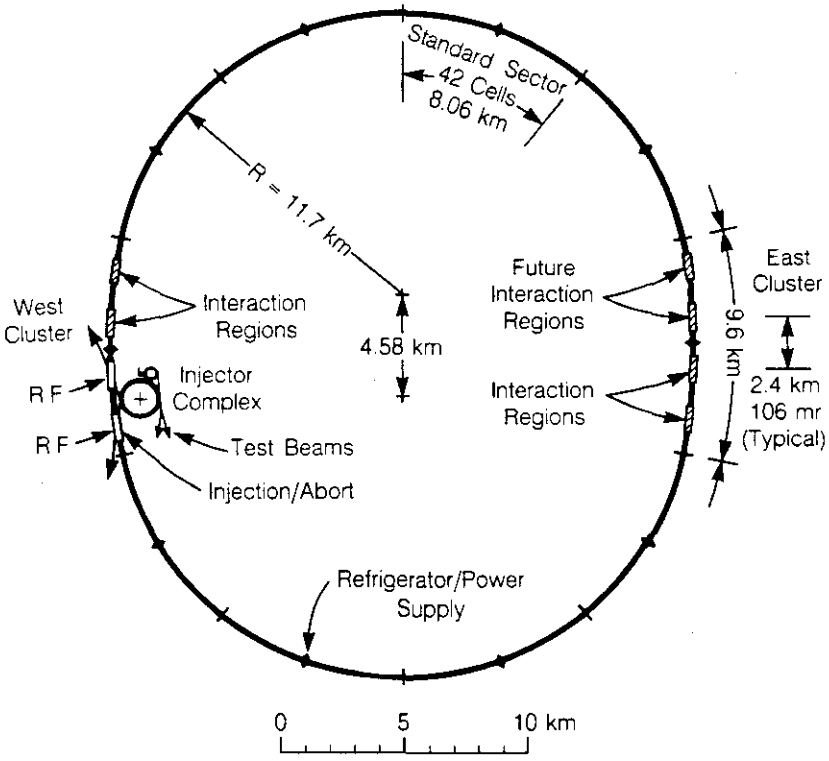

SSC collider ring layout. The clusters form the concentrations of activity, with interaction regions and utility sections having the injection and rf acceleration equipment. Ten refrigerator and power supply units are distributed around the arcs at 8 km intervals. The total circumference is 83 km (52 miles).

Executive Summary

In recent years it has become clear that the need to understand the most basic structure of matter and energy requires a major advance in the energy frontier of particle accelerators. This report describes a powerful instrument, the Superconducting Super Collider (SSC), that fills this need.

Its purpose is to accelerate and guide oppositely directed and tightly focused streams of ultra high energy protons into collision, thereby releasing enormous energy in a volume of subnuclear size and creating there conditions such as are believed to have occurred during the first moments of our universe. The subnuclear interactions made possible by the SSC will reveal a level of detail heretofore unachievable. Direct evidence about the most fundamental physical forces and entities is carried by the emergent collision products and captured in sophisticated detectors which surround the interaction region.

In the SSC, six of these interaction regions are clustered along the straightaways of its fifty-two mile racetrack-like course. This multiplicity of interaction regions is required so that detectors specialized to observe various aspects of the particle interactions, all of which are needed to obtain a complete picture, can be operated simultaneously. The buildings that house the detectors, together with a campus and small auxiliary buildings, are the visible signs of the SSC Laboratory. Most of the accelerator's fifty-two mile circumference lies unseen beneath the ground while normal daily life goes on overhead, undisturbed. The campus, comprised of laboratories, shops, offices and other support buildings is joined to the injector complex which supplies beams to the main collider. An artist's perspective view is shown at the top of the accompanying figure, while a schematic diagram showing the main technical elements of the entire facility is at the bottom. It is envisioned that about three thousand persons will normally be present at the Laboratory of whom at least five hundred will be visiting scientists from across the country and around the world, engaged in high energy particle physics research at the SSC.

Research and development leading directly to the SSC conceptual design had its origin in a unanimous recommendation of HEPAP, the High Energy Physics Advisory Panel of the Department of Energy (DOE) in July 1983. It urged "immediate initiation of a multi-TeV, high luminosity, proton-proton collider with the goal of physics experiments at this facility at the earliest possible date." Subsequent to this recommendation the DOE launched an R&D program aimed at establishing a sound technical base for a conceptual design of the Superconducting Super Collider (SSC), a 20 TeV on 20 TeV proton-proton

collider with a luminosity of 10^{33} $cm^{-2}sec^{-1}$. These primary parameters derive from an extensive study of the scientific needs that can be addressed with the SSC. The particle beam energy of 20 trillion electron volts (TeV) is sufficient to probe into domains where markedly new phenomena are expected. At 20 TeV each proton in the beams would have a kinetic energy more than twenty thousand times the total energy it possesses at rest. The luminosity is a parameter that characterizes the rate at which the wanted collision events take place. The most revealing of the subnuclear interactions generated by the SSC are expected to be relatively rare. The design luminosity is chosen to assure that a sufficient number are available for study.

This conceptual design report, requested by the DOE, incorporates the results of the SSC R&D program to date. It presents a discussion of scientific needs, a technically feasible design based on extensive accelerator physics studies, and a detailed cost estimate and construction schedule based on the design.

Our studies show that the basic principles of design used for existing accelerators can conservatively be extended to a proton collider having the SSC specifications of energy and luminosity. Our confidence rests on the current successful operation of colliders fully as complex as the SSC, albeit on a smaller scale. The economical construction and operation of the SSC is made possible by recent developments in the technology of superconductivity, used for the magnets that guide and focus the SSC beams. The U.S. has recently put into operation the Fermilab Tevatron, which pioneered in the use of superconducting accelerator magnets. The SSC magnets, while different from the Tevatron magnets in detail, represent a natural evolution of its design, incorporating recent technological advances.

In the design we focused on creating the SSC Laboratory of scope sufficient to support a comprehensive research program by U.S. physicists and physicists from throughout the world. Considerations of the experimental use of the SSC are presented in separate reports. The conceptual design presented here is not specific to a particular site, but rather treats the design and cost of creating the facility in a variety of realistic settings for which efficient construction methods exist. Sites permitting open cut and fill techniques were considered, as were sites requiring tunneling through mixed soil and rock and sites deep underground, bored through hard rock. A construction schedule based on detailed industrial manufacturing plans and detailed consideration of a range of site settings was derived. It shows that the facility could be constructed in a six and one-half year period.

On the basis of the detailed results of this study, the estimated construction cost for the SSC as defined above is three billion (FY 1986) dollars. This number includes a prudent contingency intended to be adequate to make the total an upper bound. The cost figure does not include research equipment, pre-construction R&D, or site acquisition. Selection by the DOE of a particularly favorable site and further development of superconductor technology could effect a modest but worthwhile reduction in cost.

The SSC has immense potential for major advances in understanding the fundamental nature of matter and energy. Its timely completion will ensure a forefront U.S. role in this important basic science for the mid-1990s and into the next century.

Contents

1. Introduction 1
   1.1 Search for Fundamental Laws 1
   1.2 Supercollider Facility and Its Discovery Potential 3
      1.2.1 SSC Facility 3
      1.2.2 Discovery Potential 4
   1.3 Origins of the SSC and Status of the R&D Program 7
      1.3.1 HEPAP Recommendation 1983 7
      1.3.2 Earlier Actions 7
      1.3.3 Preliminary R&D and Reference Designs Study 7
      1.3.4 Major R&D Efforts and Conceptual Design 8
   1.4 Conceptual Design Report 8
      1.4.1 Panels, Task Forces, Workshops 10
      1.4.2 Structure of the Report 13

2. Scientific and Technical Basis for SSC 15
   2.1 High Energy Physics Today 15
      2.1.1 History of Particle Physics 15
      2.1.2 Standard Model 19
      2.1.3 Outstanding Problems 21
      2.1.4 Existing and Proposed Collider-Accelerators 23
   2.2 Scientific Need For The SSC 26
      2.2.1 Physics at SSC Energies 26
      2.2.2 Connections to Other Scientific Fields 30
   2.3 Discovery Potential of a Multi-TeV Collider 31
      2.3.1 Concepts of Very High Energy Collisions 32
      2.3.2 Discovery Potential of a Multi-TeV Collider 34
   2.4 Recent Advances in Accelerator Technology 39
      2.4.1 Introduction 39
      2.4.2 Magnet Development 40
      2.4.3 Superconductor Development 47
      2.4.4 Beam Dynamics and Aperture 51
      2.4.5 Synchrotron Radiation and Vacuum 52
      2.4.6 Conclusion 54
   References 54

3. Collider Concepts 55
   3.1 Accelerator Physics of Synchrotron Colliders 55
      3.1.1 Synchrotron Components 56
      3.1.2 Basic Collider Definitions 61
      3.1.3 Magnet Field Quality and Aperture 63
      3.1.4 Lattice 65
      3.1.5 Luminosity Lifetime 66
   3.2 Review of Tevatron Parameters and Components 67
      3.2.1 Design Outline 67

3.2.2 Components 70
3.2.3 Performance 75
3.3 Supercollider Facility 76
3.3.1 Overview 76
3.3.2 Principal Parameters of the SSC 79
3.3.3 Layout and Beam Optics of the SSC 79
3.3.4 Conventional Systems 83
3.4 Reliability 84
3.4.1 Historical Examples 85
3.4.2 Approach to System Reliability 85
3.4.3 System Availability Goals for the SSC 87
3.5 Setting, Environment and Radiation 90
3.5.1 Environmentally Benign Nature of the Facility 90
3.5.2 Environmental Modifications from Construction 91
3.5.3 Environmental Consequences of Operations 92
References 92

4. SSC Accelerator Physics Parameters 93
4.1 Primary Parameters 93
4.1.1 Luminosity 94
4.1.2 Other Primary Parameters 97
4.1.3 Effects of Variation of Parameters 99
4.1.4 Primary Lattice Features 105
4.2 Lattices 106
4.2.1 Lattice Considerations 106
4.2.2 Clustered Interaction Regions 108
4.2.3 Arc Module 112
4.2.4 Interaction Region Modules 114
4.2.5 Utility Module 118
4.2.6 Optical Properties 118
4.2.7 Tilted Plane and Nonplanar Possibilities 122
4.3 Magnet Aperture and Field Quality 124
4.3.1 Magnet Field Errors 124
4.3.2 Aperture Requirements 128
4.3.3 Magnet Coil Size and Cell Length 132
4.3.4 Effect of Linear Coupling and Orbit Distortion 136
4.3.5 Tune Variation 137
4.3.6 Momentum Aperture 137
4.4 Tolerances and Correction Systems Specifications 140
4.4.1 Spool Elements 140
4.4.2 Magnet Misalignment and Orbit Correction 141
4.4.3 Linear Corrections 144
4.4.4 Sextupole Corrections 148
4.4.5 Analysis of Effects of Multipole Field Errors 149
4.4.6 Multipole Feeddown Due to Orbit Errors 155
4.4.7 Multipole Corrections 157

4.4.8 Interaction Region Magnet Error Tolerances 159
4.4.9 Ground Motion 159
4.4.10 Noise in the Radio-frequency System 162
4.5 Beam Current Limitations 164
4.5.1 Space Charge Tune Shift 164
4.5.2 Impedance Estimates 165
4.5.3 Parasitic Heating 177
4.5.4 Longitudinal Instabilities 179
4.5.5 Transverse Instabilities 182
4.5.6 Intrabeam Scattering 184
4.5.7 Synchro-betatron Resonances Due to Crossing Angle 188
4.5.8 Head-on Beam-Beam Effects 189
4.5.9 Long-range Beam-Beam Effects 195
4.5.10 Pacman Effect 202
4.6 Collider Operational Considerations 203
4.6.1 Injection and Acceleration Cycle 203
4.6.2 Beam and Luminosity Lifetimes 209
4.6.3 Radio-Frequency Systems Requirements 211
4.7 Synchrotron Radiation 216
4.7.1 Description of Synchrotron Radiation 216
4.7.2 Consequences of Synchrotron Radiation 218
4.7.3 Conclusions 219
4.8 Beam Losses 219
4.8.1 Scattering Models 220
4.8.2 Magnet Heating 222
4.8.3 Long-Range Lost Particles 226
4.8.4 Radiation Effects 228
4.9 Cryogenic System Requirements 231
4.10 Injector System 233
4.10.1 Injector Parameters 233
4.10.2 600 MeV H^- Linac 237
4.10.3 Low Energy Booster 239
4.10.4 Medium Energy Booster 243
4.10.5 High Energy Booster 248
4.10.6 Test Beams for HEB 253
References 256

5. Technical Systems: Engineering Design 261
5.1 General Description of Needed Technical Systems 261
5.1.1 Magnets 261
5.1.2 Cryogenics 262
5.1.3 Vacuum 263
5.1.4 Main Power Supplies 263
5.1.5 Quench Protection 264
5.1.6 Radio-Frequency System 264
5.1.7 Injection and Abort Systems 265

5.1.8 Control and Instrumentation Systems 265
5.1.9 Injector Complex 266
5.1.10 R&D Needs and Opportunities 267
5.2 Magnets 267
5.2.1 Introduction 267
5.2.2 Performance Requirements, Magnetic Design 270
5.2.3 Superconductor 277
5.2.4 Coils 283
5.2.5 Beam Tube Assembly 285
5.2.6 Yoke and Helium Containment 288
5.2.7 Correction Coils 290
5.2.8 Quench Protection Features 292
5.2.9 Cryostat 293
5.2.10 Assembly 300
5.2.11 Magnet Testing and Measurements 301
5.2.12 Quadrupoles 304
5.2.13 Correction Magnets, Spool Pieces 307
5.2.14 Special Magnets 316
5.2.15 Magnet Installation 322
5.3 Cryogenic System 326
5.3.1 Cryogenic System Description 327
5.3.2 Description of the Arc Region Cryogenics 329
5.3.3 Description of IR Region Cryogenics 332
5.3.4 Refrigeration Station Description 336
5.3.5 Liquid Nitrogen Supply 344
5.3.6 Design Operating Conditions 346
5.3.7 Failure Mode Operation 351
5.3.8 Cooldown and Warmup Operation 354
5.3.9 Quench and Quench Recovery 355
5.3.10 Utilities Interruption 356
5.3.11 System Maintenance and Repair 358
5.3.12 Ring Cryogenic Instrumentation 362
5.4 Vacuum 362
5.4.1 Cold Beam Tube Vacuum Considerations 363
5.4.2 Cold Beam Tube Design 368
5.4.3 Warm Beam Tube Vacuum Considerations 369
5.4.4 Warm Beam Tube Vacuum Design 369
5.4.5 Insulating Vacuum 371
5.5 Magnet Power Supplies and Quench Protection 372
5.5.1 Magnet Power Supplies 372
5.5.2 Quench Detection and Protection 379
5.6 Correction Element Power Supplies 387
5.6.1 Main Arc Correction Elements 388
5.6.2 Cluster Region Correction Elements 391
5.6.3 Special Cluster Region Corrections 394
5.6.4 Power Supplies and Quench Protection 394

5.6.5 Reliability 395
5.7 Radio-Frequency Accelerating System 396
5.7.1 Choice of RF Frequency 396
5.7.2 Description of System 396
5.7.3 Accelerating Structure 397
5.7.4 Layout of the System 400
5.7.5 Cavity Coupling 400
5.7.6 RF Monitoring, Phasing, and Controls 402
5.7.7 Klystrons 402
5.7.8 Power Supplies 402
5.7.9 System Reliability 404
5.8 Beam Stabilization 404
5.8.1 Low Level Feedback in the Main RF System 404
5.8.2 Longitudinal Feedback System 406
5.8.3 Transverse Feedback Systems 408
5.8.4 Collision Assurance System 410
5.9 Collider Injection System 410
5.9.1 Overall Description 413
5.9.2 Injection Process 413
5.9.3 HEB Extraction Channel 415
5.9.4 Beam Transfer Line 415
5.9.5 Collider Ring Injection Channel 416
5.9.6 Major Elements of the Injection System 416
5.9.7 Diagnostics and Tuning 425
5.9.8 Failure Modes 425
5.10 Beam Abort System 426
5.10.1 Overall Description 426
5.10.2 Required Aperture in the Abort System 429
5.10.3 Elements in the Ring 429
5.10.4 External Beam Line and Beam Dump 435
5.10.5 Abort Generation 440
5.10.6 Diagnostics and Tuning 443
5.10.7 Failure Modes 443
5.11 Interaction Regions 444
5.11.1 Variable Strength Quadrupoles 444
5.11.2 Vertical Beam Separation 448
5.11.3 Orbit Control 448
5.11.4 Dispersion Suppressors 450
5.11.5 Medium Luminosity Interaction Region 451
5.11.6 Scattered Beams 453
5.11.7 Collimators 453
5.11.8 Beam Monitoring With IR Collisions 455
5.12 Beam Instrumentation 456
5.12.1 General 456
5.12.2 Beam Position Monitoring System 458
5.12.3 Beam Loss Monitoring System 463

5.12.4 Beam Profile Monitoring System 464
5.12.5 Beam Intensity Monitoring System 465
5.12.6 Beam Schottky Monitoring System 465
5.12.7 Other Beam Diagnostic Systems 466
5.13 Control System 466
5.13.1 Overall Description 466
5.13.2 Host Computer 472
5.13.3 Sector Computers 473
5.13.4 Accelerator Interface Crates in the Tunnel 474
5.13.5 Ring Information Network 475
5.13.6 Software Development Effort 476
5.13.7 Installation Effort 477
5.13.8 Reliability 477
5.14 Personnel Safety Interlock System and Communications 486
5.14.1 System Description 488
5.14.2 Modes of Entry 488
5.14.3 System Operation 489
5.15 Injector Complex 491
5.15.1 600 MeV H^- Linac 491
5.15.2 Magnets 499
5.15.3 Cryogenics 506
5.15.4 Vacuum Systems 510
5.15.5 Power Supplies 514
5.15.6 Radio-Frequency Systems 519
5.15.7 Beam Transfers and Aborts 521
5.15.8 Diagnostics 525
5.15.9 Controls 526
5.15.10 Layout of the HEB Test Beams 527
5.16 Survey and Alignment 527
5.16.1 Introduction 527
5.16.2 Survey Above Ground 529
5.16.3 Transfer from Surface to Tunnel 530
5.16.4 Establishing the Tunnel Net 530
5.16.5 Installation Alignment 531
5.16.6 Smoothing Alignment 531
5.16.7 Smoothing Algorithms 531
References 534

6. Conventional Systems 537
6.1 General Description of Requirements 537
6.2 Example SSC Sites 539
6.2.1 Example Site Concepts 539
6.2.2 Geotechnical Data Base 539
6.2.3 Generic Rock and Soil Models 547
6.2.4 Generic Topography and Geological Materials Distributions 547
6.2.5 Facility Site-Orientation Models 551

6.3 Tunneling and Collider Enclosures 551
6.3.1 Introduction 551
6.3.2 Site A Tunnel 553
6.3.3 Site B Tunnel 555
6.3.4 Site C Tunnel 555
6.4 Central Laboratory Facilities 557
6.4.1 General Features 557
6.4.2 Site Arrangement and Plan 559
6.4.3 Central Laboratory Building 561
6.4.4 Heavy Works Buildings 563
6.4.5 Shop Buildings 565
6.4.6 Ancillary Buildings 567
6.5 Injector Facilities 569
6.5.1 Introduction 569
6.5.2 Linac 569
6.5.3 Low Energy Booster 570
6.5.4 Medium Energy Booster 574
6.5.5 High Energy Booster 576
6.5.6 Test Beam Facilities 578
6.6 Collider Ring Facilities 581
6.6.1 Tunnel Configuration 581
6.6.2 Collider Service Areas 585
6.6.3 Injection, Extraction and RF Areas 590
6.7 Experimental Facilities 594
6.7.1 Features of Experimental Areas 594
6.7.2 Clustered Interaction Regions 595
6.7.3 Collision Halls 595
6.7.4 Access Halls and Assembly Areas 597
6.7.5 Detector Staging Buildings 600
6.8 Utilities 600
6.8.1 Electrical 600
6.8.2 Water 604
6.8.3 Fuel 605
6.8.4 Telecommunications 606
6.9 Environment and Safety 606
6.9.1 Introduction and General Policy 606
6.9.2 Radiation Shielding and Radioactivity 606
6.9.3 Collider Ring and Tunnel Shielding 608
6.9.4 Injector Shielding 610
6.9.5 Other Environmental Issues 610
6.9.6 Site Safety 611
6.9.7 Site Security 615
6.9.8 Waste Disposal 616
6.9.9 Decommissioning 616
References 616

7. Project Plan 617
7.1 Laboratory Organization 617
7.1.1 Overall Structure 619
7.1.2 Project Management 619
7.1.3 Laboratory Support Services 621
7.1.4 Research and Development, Pre-Operations, and Physics Support 621
7.2 Technical Systems 623
7.2.1 General Plan for Design and Fabrication 623
7.2.2 Superconducting Magnet Production 624
7.2.3 Technical Systems Fabrication and Procurement 624
7.2.4 Quality Assurance for Technical Systems 627
7.3 Conventional Systems 628
7.3.1 General Plan 628
7.3.2 Site Acquisition 629
7.3.3 Mobilization 629
7.3.4 Design and Construction Approach 630
7.4 Construction Plan 631
7.4.1 Overall Schedule and Milestones 631
7.4.2 Conventional Systems 635
7.4.3 Technical Systems Schedule 635
7.4.4 Schedule Analysis 642
7.4.5 Manpower Analysis 654
References 656

8. Cost Estimate 657
8.1 Introduction 657
8.1.1 General Methodology 657
8.1.2 Conventional Systems Analysis 660
8.1.3 Work Breakdown Structure 661
8.1.4 Labor Rates 662
8.1.5 Data Format and Procedures 670
8.1.6 Data Assembly and Presentation 671
8.1.7 Project Cost Summary 671
8.2 Technical Systems Cost 672
8.2.1 Injector Systems 673
8.2.2 Collider Systems 676
8.3 Conventional Systems Cost 678
8.4 Systems Engineering and Design Costs 680
8.4.1 EDI for Technical Systems 680
8.4.2 AE/CM for Conventional Systems 682
8.5 Management and Support Costs 685
8.5.1 Project Management 685
8.5.2 Project Support Equipment 686
8.5.3 Project Support Facilities 687
8.6 Project Contingency 689
8.6.1 Technical Components 689

8.6.2 Contingency – Conventional Systems 691
8.6.3 Contingency – Systems Engineering and Design 693
8.6.4 Contingency – Management and Support 694
8.7 Total Project Cost 695
8.7.1 Total SSC Systems Cost Roll-up 695
8.7.2 Cost Profile 695

9. Conclusions 703
9.1 Physics Opportunities 703
9.2 Design Parameters 703
9.3 Technical Feasibility 704
9.3.1 Accelerator Physics 704
9.3.2 Accelerator Engineering 707
9.4 Cost 709
9.5 Construction Schedule 711
9.6 Summary 712

1. Introduction

1.1 Search for Fundamental Laws

Since the earliest times mankind has sought to understand the marvelous complexity of the physical world in basic terms. In recent years powerful strides towards that goal have been made. The frontier of our knowledge today encompasses material structures one thousand times smaller than the smallest atomic nucleus and gives order to them. This report describes the conceptual design of a new instrument that will allow us to strike deep into new territory far beyond today's frontier.

Our quest is the continuation of the work of those who, in the decades around the turn of the century, discovered the oneness of light, electricity and magnetism, and first discerned and explored the atom. As exploration has progressed to smaller and smaller reaches within the atom (indicated schematically in Fig. 1.1-1), larger and larger facilities have been required. The sealing wax and string of Rutherford's time have been replaced by the impressive accelerators and detectors of today. The investigations with these machines, carried out primarily by physicists in the United States and Canada, Europe, Japan, and the Soviet Union, have produced a remarkable picture of the microcosm. Within the past twenty years, a new sublevel of matter (quarks) smaller than the proton has become known. Within the past few years there has been experimental confirmation that the phenomena of radioactivity and ordinary light are intimately related. These advances, and others, are not only striking in themselves but have far reaching consequences. They enable us to ask deeper questions than ever before. What is the origin of matter? How did the fundamental particles and forces work together to produce the world around us today?

The domain of high energy or particle physics seems far from our everyday experience. High energy accelerators and detectors are the light sources and microscopes used to look inside the proton and neutron which are themselves a hundred thousand times smaller than an atom. They produce and analyze collisions of fundamental particles producing in turn new particles traveling at velocities near the speed of light. In this domain times are measured in billion billionths of a second. As remote as these conditions seem to us, there was a time at the beginning of the universe, according to current thinking, when such conditions prevailed. The expanding universe was filled with the myriad exotic particles now

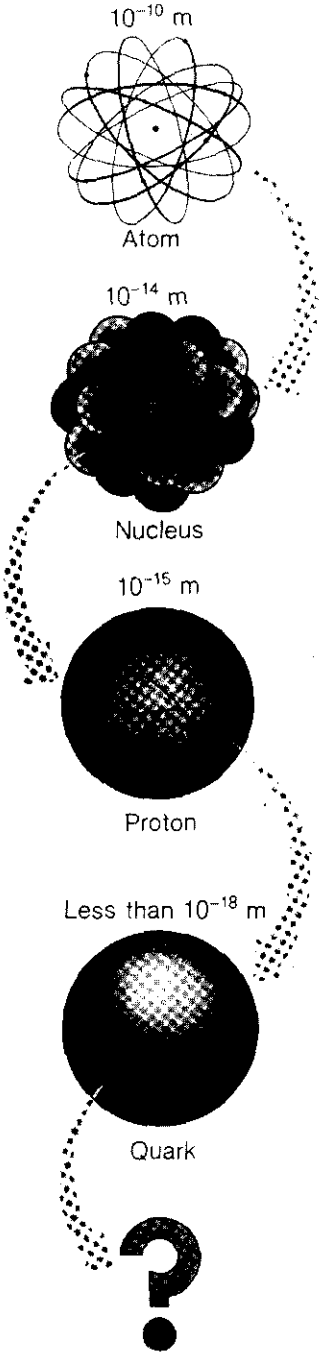

Figure 1.1-1. The progression of investigations at smaller and smaller scales requires accelerators of larger and larger size. The SSC will probe to distances of 10^{-19} m and less.

investigated by high energy physicists. The interactions of these particles shaped the development of the universe to the state which we marvel at today.

The explosion of new knowledge gleaned from the search for the fundamental over the past century has profoundly deepened and broadened our understanding of the natural world. At the same time, the practical consequences of this knowledge have been universally felt. In addition to the intellectual and cultural wealth generated by these most basic scientific pursuits, enormous economic wealth has accrued to society by turning the new knowledge to practical ends. The drive to elucidate the nature of electricity provided the foundations upon which scientists and engineers built the electrical industry. This, together with the discovery of quantum mechanics which flowed from the exploration of the atom, provided the foundation for all of chemistry and for our modern electronics industry and has illuminated the development of many other engineering sciences. The exploration of the atomic nucleus taught us to win energy from the transmutation of the elements through controlling the fission process and has brought us tantalizingly close to controlling the even more efficient fusion process.

The developments of the past 100 years have shown that the pursuit of the fundamental laws of nature leads to practical as well as intellectual benefits in directions and magnitudes inconceivable before the fact. If history is any guide, unexpected discoveries waiting to be made will have at least as profound an impact on our understanding and ability to make use of the world around us.

1.2 Supercollider Facility and Its Discovery Potential

High energy physics is both a theoretical and an experimental science, but its progress is largely paced by the technology of its accelerator and detectors. Accelerators called colliders are now the instruments of choice for producing the reactions that reveal the basic material entities and their interactions. In colliders, beams of energetic particles from opposite directions collide, producing in abundance new forms of matter with the beam energies fully available for the purpose.

1.2.1 SSC Facility

The proposed Superconducting Super Collider (SSC) is such an accelerator, unique in the world, providing access to particle collisional energies at least an order of magnitude greater than are available at existing facilities. The major design objectives for the SSC are given in Table 1.2-1.

Table 1.2-1
Primary SSC Design Objectives

Proton beam energy	20 TeV
Luminosity	$10^{33}\ cm^{-2}s^{-1}$
Number of interaction regions	6

Oppositely directed bunches of protons, each with an energy of 20 TeV (20 trillion electron volts), are caused to collide, almost head-on, making available a total of 40 TeV of energy in each proton-proton collision. As the protons collide, their constituents can interact. Since the probability of interaction is comparatively low, the beams can be recirculated to collide repetitively for many hours without significant attenuation. Thus the SSC is constructed as a pair of storage rings capable of holding tightly confined proton beams on closed paths for a day or more without replenishment. The rings are made to cross at six locations where the collisional reactions take place and where detectors that count and measure the reaction products for physics study are located. This arrangement is shown schematically in Fig. 1.2-1.

The rings confining the proton beams are housed one above another in an underground tunnel that includes the interaction regions. The beams are guided around the desired path or orbit through an evacuated tube by a system of electromagnets. This magnetic confinement system consists of a periodic array of bending and focusing magnets, the bending magnets serving to establish the curvature of the orbit and the focusing magnets to confine the protons to a narrow region about the desired orbit. The circumference of the rings is 83 km (52 miles), a size governed by the maximum design magnetic field of 6.6 tesla (66,000 gauss) and the energy of 20 TeV. Also depicted in the figure are an injector system and an accelerating system. The operating cycle of the SSC begins with the collider magnets maintained at low current for about forty minutes while the proton beams are loaded into both collider rings. With injection complete, the acceleration system is activated. The slow increase in the beam energy is accompanied by a corresponding increase in the confining magnet strength thus keeping fixed the position of the beam orbit. This final synchronous acceleration is complete in about fifteen minutes when the beams reach their collision energy of 20 TeV, twenty times the injection energy. Then the accelerating system is turned down and the beams are steered into collision. The resulting reactions can be studied for a day or more before the beams are depleted sufficiently so that the cycle must be repeated. The design luminosity, a measure of the effectiveness of a collider in producing useful collisions, is $10^{33}\ cm^{-2}s^{-1}$.

The injector systems consist of a source and linear accelerator, followed by three booster synchrotrons in cascade, similar to previous large accelerator complexes. The final booster is a synchrotron with superconducting magnets; the others have conventional copper and iron magnets to permit rapid cycling. In addition to providing protons for the two main rings, the final booster synchrotron produces external beams for testing the response of detector components before their installation in the interaction regions of the SSC.

It is anticipated that about 3000 persons will be present at the facility at any given time. Of these about 2500 will be staff and 500 will be visiting scientists from across the nation and around the world who are participating in experimental and theoretical work at the facility.

1.2.2 Discovery Potential

The scientific work of the laboratory will be focused on the study of reactions among the elementary constituents of matter at the highest possible energies at the six interaction points (four developed initially) where the proton beams are brought into collision. For

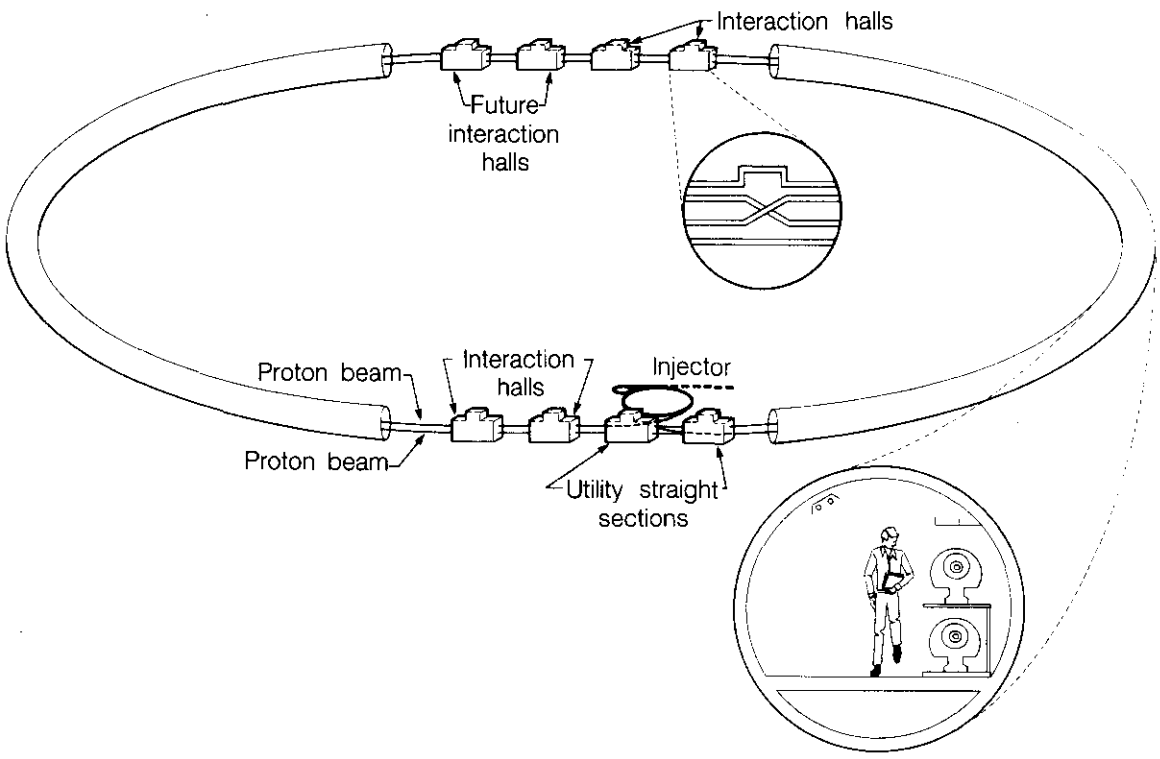

Figure 1.2-1. Schematic layout of the SSC. The large ring represents the underground tunnel that houses the two collider rings and is 83 km in circumference. The clusters of facilities provide for injection and acceleration of the proton beams, and for physics experiments in the six interaction halls (four to be developed initially). The tunnel cross section (lower right) shows the magnet rings, one above the other. The enlargement inside the collider rings indicates how the oppositely moving beams of protons are made to collide. The distance between centers of interaction halls is 2.4 km.

this purpose large detectors surround the interaction regions, each capable of recording the signature of a reaction by measuring the charged particles and energy flow emerging from the interaction points. Analysis of these data permits the experimenter to infer the happenings at distances of the order of 10^{-19} m or less, or equivalently at constituent energies of 2 TeV or more. Our capabilities over the next several years will be in the 0.2–0.3 TeV range.

As mentioned briefly in Section 1.1, the recent progress of particle physics has brought astounding results. A distinct level of matter below the proton has been identified. Three generations of that matter have been found. The basic forces between these particles have been identified. Moreover, the weak and electromagnetic forces have been united into a single theory which has passed every experimental test so far. The theory correctly predicted the approximate mass of the previously undiscovered charm quark and the precise masses of the carriers of the weak force, the W and the Z particles. This description of the strong, electromagnetic, and weak forces is extraordinarily successful, but still is not complete. Undiscovered is the mechanism of giving mass to some particles, but not to all. Unclear is the reason for the duplication of the generations of particles and the pattern of their masses. Are there still more quarks and leptons? Are there additional forces and new forms of matter beyond those we have observed so far? Are there additional levels of matter beneath the quarks and leptons? These are some of the challenges in particle physics today.

Facilities in operation, or soon to be, will explore the near frontier—the domain of our current knowledge and its edges—but they will be unable to extend the energy frontier as far as we know is necessary to address many of the important questions. The energies of interest are constituent energies of 1 TeV or more. These can only be reached with present and foreseeable technology by a high-luminosity, multi-TeV proton collider.

While the energy range of interest is known, what we shall find there is not certain. There are many theoretical speculations that extend our present picture to higher energies in different ways. Our current understanding and these extensions are summarized in Chapter 2. At the risk of oversimplification, we note that the SSC will have impressive potential for discovery:

New quarks and leptons

The SSC will extend the mass range of known quarks and leptons by a factor of 40, from the present 0.05 TeV to 2 TeV.

New force particles

The SSC will search for new force particles, like the W and Z of the weak force, up to masses of 7 TeV, a factor of 20 beyond the present 0.3 TeV.

New hypothetical particles

The SSC will search for hypothetical new "supersymmetric" particles up to masses of 1.5 TeV, a factor of 30 beyond today's limits.

Mass generation

The SSC will explore the mass-generating phenomenon at energies up to 1 TeV, more than an order of magnitude beyond current capabilities.

Internal structure

The SSC will search for internal structure (even more basic building blocks) in quarks and leptons to distances 40 times smaller than the present limits.

These examples serve only to illustrate the power of the SSC relative to existing facilities or ones nearing completion. Nature is often more subtle and intricate than the projections of the human mind. Surprises will surely occur and a rich and diverse research program will develop in directions perhaps not now contemplated. The basic strength of the SSC is its long reach up in energy and its accompanying high luminosity.

1.3 Origins of the SSC and Status of the R&D Program

1.3.1 HEPAP Recommendation 1983

In July, 1983, the High Energy Physics Advisory Panel (HEPAP) transmitted to the Office of Energy Research of the Department of Energy (DOE) a unanimous recommendation for the "immediate initiation of a multi-TeV high-luminosity proton-proton collider project with the goal of physics experiments at this facility at the earliest possible date." This proposed facility was designated the Superconducting Super Collider (SSC). In his letter transmitting this recommendation, the chairman of HEPAP commented that the SSC "would be the forefront high energy facility of the world and is essential for a strong and creative United States high energy physics program into the next century." Recently this recommendation has been reiterated by the U.S. National Academy of Sciences Survey of all physics in the United States.

1.3.2 Earlier Actions

The concept of a multi-TeV accelerator was first publicly discussed more than ten years ago. Two workshops sponsored by the International Committee on Future Accelerators (ICFA), one at Fermilab in 1978 and one at CERN in 1979, examined various possibilities for very high energy machines, including proton-proton colliders in the 20 TeV per beam range. The SSC itself can be said to have its origins in a 1982 Snowmass Summer Study, sponsored by the Division of Particles and Fields (DPF) of the American Physical Society. This and other workshops on detectors and accelerators held in 1983 at Lawrence Berkeley Laboratory and Cornell University, respectively, led to the HEPAP recommendation.

1.3.3 Preliminary R&D and Reference Designs Study

As a result of that recommendation, in the fall of 1983, the DOE initiated preliminary R&D for the SSC. Hearings were held before the House Science and Technology Committee of the U.S. Congress concerning redirection of resources towards this R&D. In December of 1983 the DOE and the Directors of the U.S. high energy accelerator laboratories chartered a Reference Designs Study (RDS) with beam energy and luminosity goals specified. That study, which was completed in April 1984, drew upon the expertise of about 150 accelerator physicists and engineers from across the nation. Three different

approaches to an SSC were studied and it was concluded that each of them could form the foundation of a technically feasible 20 TeV beam energy collider. The report of that study with its detailed cost estimates was reviewed extensively by the DOE and its consultants. In March 1984 the DOE assigned responsibility for oversight of the national SSC effort during the R&D and preconstruction phase to the Universities Research Association (URA). In June and July a second DPF Summer Study at Snowmass examined the reference designs and SSC utilization for physics experiments. The Summer Study reaffirmed the primary parameters of the RDS, 20 TeV per beam at 10^{33} $cm^{-2}s^{-1}$ luminosity, as important for meeting the physics goals. By the summer of 1984 extensive work on model magnets for the SSC was already underway at Brookhaven National Laboratory (BNL), Fermi National Laboratory (FNAL), Lawrence Berkeley Laboratory (LBL), and the Texas Accelerator Center (TAC).

1.3.4 Major R&D Efforts and Conceptual Design

By the fall of 1984, URA had formed the SSC Central Design Group (CDG) to carry out its responsibilities of directing and coordinating the national R&D work and put its headquarters at LBL, with Dr. Maury Tigner of Cornell University as Director. The CDG technical staff members were drawn from high energy physics and accelerator and technical groups across the country, representing both universities and national laboratories. The organizational structure through which the work of the many contributing institutions, firms, and individuals has been focused on the R&D effort leading to the Conceptual Design Report and beyond is displayed in Fig. 1.3-1(a) and (b).

The principal activities for FY 1985 were conducting a diversified effort on model magnet and cryostat R&D in order to provide the technical basis for selection of one of the five superconducting magnet designs then under study as the basis of the SSC design, and beginning the conceptual design based on that selection. Also important was the preparation of a siting parameters document which could provide a technical basis for eventual DOE site selection. These goals were accomplished, and magnet selection was made in September 1985. Early FY 1986 has focused on engineering developments to improve the cost effectiveness of the selected magnet style and to flesh out the conceptual design and cost estimate displayed in this report. Our purpose in so doing is to help the DOE and the scientific community decide how to proceed with a vigorous and effective program of High Energy Physics research in the 1990s and on into the next century.

1.4 Conceptual Design Report

This Conceptual Design Report rests on the R&D efforts and the many earlier studies previously noted. In all, about 250 individual scientists and engineers participated in R&D and design studies that led directly to the Conceptual Design Report through the organizational structure shown in Fig. 1.3-1(b). The scientific and academic institutions involved in the R&D or from which individuals were drawn are shown in Table 1.4-1.

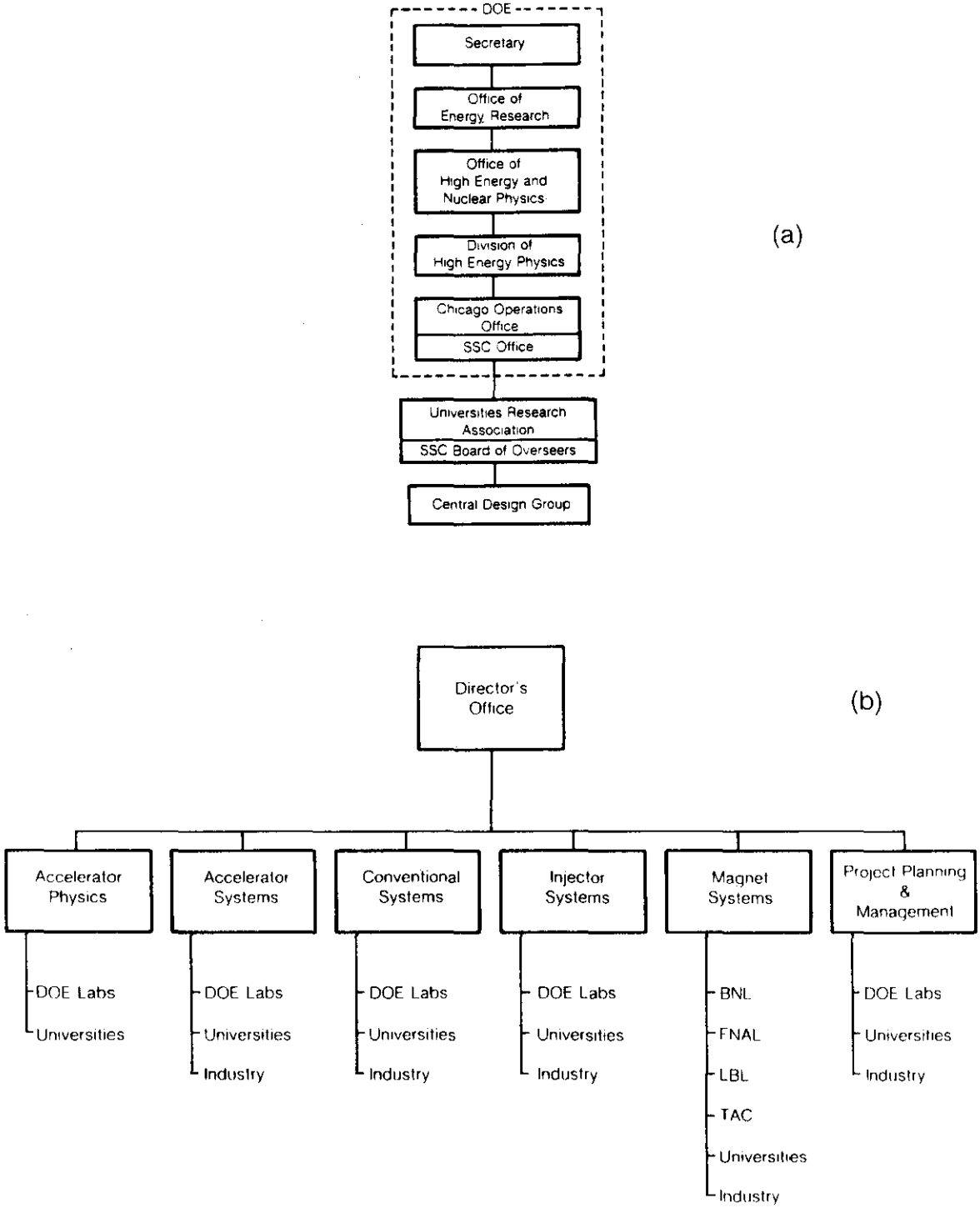

Figure 1.3-1. Organizational framework for the SSC R&D effort. (a) Responsible DOE and URA offices. (b) Organization of the Central Design Group and its relationships to other institutions.

Table 1.4-1
Institutional Participation in the SSC R&D
and Conceptual Design Report

Brookhaven National Laboratory
Fermi National Accelerator Laboratory
Lawrence Berkeley Laboratory
Los Alamos National Laboratory
Stanford Linear Accelerator Center
Texas Accelerator Center
University of California, Berkeley
University of California, Los Angeles
Cornell University
University of Houston
University of Maryland
University of Michigan
Ohio State University
Rice University
Stanford University
Texas A&M University
University of Utah
Washington University
University of Wisconsin
CERN, European Laboratory for Particle Physics (Europe)
Deutsches Elektronen-Synchrotron DESY (Germany)
National Laboratory for High Energy Physics, KEK (Japan).

1.4.1 Panels, Task Forces, Workshops

An additional 280 technical and managerial experts participated in the many CDG task forces, workshops, and panels that supplied key advice and technical information. Table 1.4-2 contains a list of these task forces, workshops, and panels.

Table 1.4-2
SSC Central Design Group Panels, Task Forces, or Workshops
(Period of Activity)

Photo Desorption Task Force (8/84-12/84)
11 participants

Magnet System Test Site Task Force (9/84-10/84)
14 participants

Technical Magnet Review Panel (10/84-12/84, 7/85)
10 participants

Magnet Fiscal and Management Review Panel (10/84-11/84)
4 participants

Aperture Workshop and Task Force (11/84-8/85)
49 participants

SSC Impedance Workshop (12/84-10/85)
16 participants

Tunneling Technology Review Panel (12/84)
9 participants

Task Force on Commissioning and Operation of the SSC (1/85-7/85)
11 participants

DOE Workshop on Fine Filament NbTi Strand (1/85-)
13 participants

Siting Parameters Document Review Panel (2/85-3/85)
13 participants

Business Affairs and Management Advisory Panel (3/85-12/85)
6 participants

Task Force on Quench Protection and Power Supply Operation (4/85-7/85)
10 participants

Task Force on Low Temperature Operation (4/85-6/85)
7 participants

Clustered Interaction Region Study Group (4/85-9/85)
16 participants

Task Force on Detector R&D for the SSC (5/85)
12 participants

Realistic Lattice Workshop (5/85-10/85)
16 participants

Cost Estimating Task Force (7/85-8/85)
11 participants

Magnet Selection Advisory Panel (6/85-9/85)
11 participants

Magnet Length Workshop (10/85)
15 participants

Workshop on Environmental Radiation Considerations (10/85)
17 participants

Workshop on Cryogenic Design (10/85)
16 participants

Magnet Systems Integration Meetings (10/85-)
17 participants

Magnet Program Advisory Panel (10/85-)
12 participants

Underground Technology Advisory Panel (11/85-)
11 participants

Injector Workshop (11/85)
29 participants

Those academic, scientific, and governmental institutions from which individuals were drawn to participate in workshops, panels, and task forces are listed in Table 1.4-3.

Table 1.4-3
Institutional Affiliations of Individuals who Participated in CDG Panels, Task Forces, and Workshops*

Argonne National Laboratory	Lawrence Berkeley Laboratory
University of British Columbia	Los Alamos National Laboratory
Brookhaven National Laboratory	University of Maryland
California Institute of Technology	University of Michigan
University of California, Berkeley	National Laboratory for High Energy Physics (KEK)
University of California, Santa Barbara	Oak Ridge National Laboratory
University of California, Santa Cruz	University of Pennsylvania
Centre d'Etudes Nucleaires de Saclay	Rutherford Appleton Laboratory
CERN European Laboratory for Particle Physics	Stanford Linear Accelerator Center
University of Chicago	Stanford University
University of Colorado	State University of New York at Stony Brook
Columbia University	SSC Central Design Group
Cornell University	Swiss Federal Institute of Technology (ETH)
Deutsches Elektronen Synchrotron	Texas Accelerator Center
DOE, Chicago Operations	University of Tokyo
Fermi National Accelerator Laboratory	TRIUMF
Harvard University	Tsukuba University
University of Heidelberg	University of Victoria, British Columbia
Huazhong Normal University	University of Wisconsin
Karl Marx Institute, Leipzig	

*There was also important participation by individuals from private industry and business.

Responsibility for the many technical judgments that went into the parameters and designs displayed herein lies with the CDG and its Board of Overseers. Credit for the enormous amount of R&D, analysis, and synthesis that underlie this report belongs to the many individuals and their generously supporting institutions mentioned above. Work on the Conceptual Design Report itself was carried out during the months of November 1985 through March 1986. To assist the CDG in carrying out its duties with respect to the needed conventional facilities, the Department of Energy contracted with the architectural and engineering joint venture, RTK, for the necessary design and cost estimation.

1.4.2 Structure of the Report

As can be seen from the table of contents, this report is structured in a layered fashion, proceeding from general overview through successively increasing levels of detail. Our purpose is to describe the scientific justification for the SSC and the technical underpinnings upon which the design is built. It is intended that the overview sections can be understood by generally informed readers, while sufficient detail is also given to allow the technically expert reader to form an independent opinion as to the technical feasibility of the proposed scheme.

This volume on the Conceptual Design is supplemented by four accompanying volumes—Attachment A, the detailed SSC Parameters List; Attachment B, the technical details of the magnet design; Attachment C, the RTK report on the conventional facilities, and Attachment D, the detailed cost estimate. Because a cost estimate of the facility is an essential part of this work, the present volume contains sufficient engineering detail to serve as a guide to the detailed cost estimate attachment. The other attachments provide the detailed information needed to follow the cost estimate line by line.

In Chapter 2 we review the history of our search for the fundamental structure of the physical world and detail the motivation for yet deeper inquiry. The discovery potential of the SSC is then described, as is the recent historical basis for the needed accelerator technology.

Chapter 3 contains an introduction to modern accelerator and collider concepts and an expansion on the immediately underlying technology through the example of the Tevatron, the first operating synchrotron to employ superconducting magnet technology extensively. An overview of the current SSC design and its operational requirements and impact leads into the presentation in Chapter 4 of the detailed accelerator physics basis for the design and principal technical systems.

With the system requirements thus derived, we proceed in Chapters 5 and 6 to describe the technical and conventional systems that meet these requirements and which comprise the complete facility. Chapter 7 then presents a hypothetical but technically feasible plan for component manufacture and system assembly into the whole with in situ subsystem testing complete.

The eighth chapter describes the methods and presents the summary results of the cost estimate based on this plan and on the technical materials displayed in Chapters 5 and 6. Completing the main body of the Conceptual Design Report is a summary chapter reiterating the main conclusion of the scientific, technical, planning, and cost estimate aspects of the report.

2. Scientific and Technical Basis for SSC

The field of physics and within it, the field of elementary particle physics, is the scientific discipline concerned with the most fundamental laws of nature. As the successive layer of the subatomic would have been uncovered, particle physics has, by definition, been the frontier of investigation of the most basic known constituents and the forces among them. Successively, the atom, the nucleus, the nucleon, and now the nucleon's substructure, the quark, have defined that frontier. The study of smaller and smaller constituents has required ever more powerful "microscopes"—progressively, visible light, x rays, alpha particles and gamma rays, electron beams, and increasingly more energetic particle beams produced by large accelerators.

The state of high energy physics today is reviewed in Section 2.1, with a brief synopsis of the history of particle physics, a summary of our present description of the fundamental entities and laws, and a discussion of outstanding problems and questions that the SSC would address. The types of phenomena that would be manifest at SSC energies are next described (Section 2.2). A somewhat more technical, but still accessible, discussion follows on the discovery potential of the SSC (Section 2.3).

Some recent achievements in accelerator technology are described in Section 2.4. These advances are illustrative of the progress in accelerator building and supporting fields that makes the SSC technically feasible.

2.1 High Energy Physics Today

2.1.1 History of Particle Physics

To understand the goals of particle physics, it is important to recollect its early history. The experimental achievements of J.J. Thomson, the Curies, Rutherford, and their contemporaries led to the picture of matter as composed of atoms, each having a heavy, small nucleus surrounded by a much larger cloud of light electrons. This work was the basis for the discovery in the 1920s of quantum mechanics which provides the foundation for our understanding of the behavior of all matter.

The modern picture of the atom was first developed by Niels Bohr in 1913, but was not really completed until the discovery of the neutron in 1932. The protons and neutrons

are bound together in the nucleus by the "strong" force. Particles experiencing the strong force are called hadrons. Those, like the electron, that do not experience this force, are called leptons. The negative electrons are bound to the positive nucleus by the electromagnetic force. This can be viewed as resulting from the emission and absorption of light in discrete quanta called photons. Although the constituents of everyday matter had been found, there remained unexplained phenomena. Radioactivity, first discovered in the 1890's, could be described only partially. There was little understanding of the forces holding the nucleus together. Moreover, observations of cosmic rays soon produced startling results, the observation of new particles never encountered in ordinary matter — antiparticles, muons, pions, and kaons. Starting in about 1950, advances were made rapidly as the introduction of high energy particle accelerators superseded cosmic ray studies. It became possible to control the experimental conditions by providing beams of particles with intensities far in excess of the cosmic radiation to a specified location and with a specified energy, rather than relying on random events occurring beyond experimental control. The high energy beams made possible the copious creation of new particles according to Einstein's relation, $E = mc^2$.

Major technical advances contributed to the experimental progress. Measurements had to be made of particles moving nearly at the speed of light, living only fractions of a billionth of a second. Enormous quantities of data strained the capacities of existing computers. The recording of collisions of high energy particles required new techniques in optics and electronics. These demands were met increasingly with ideas and designs for advanced instrumentation.

Soon patterns began to emerge in the data. The new particles could be grouped into a table like the periodic table of elements. Each particle could be characterized by its mass and its electric charge. Other characteristics emerged. Particles came in sets — a pair like the proton and neutron, a triplet of pions of different electric charges, π^+, π^0, π^-. Each particle in a set had nearly the same mass. Another characteristic was identified and dubbed "strangeness." Strangeness is akin to electric charge. Electric charges are made in pairs: an atom can lose an electron (charge -1) and become a positive ion (charge $+1$). Strange particles were produced in pairs, one with positive strangeness, one with negative strangeness. Unlike electric charge, strangeness could be lost altogether through relatively slow processes called weak interactions. Thus a K^+ particle (strangeness $+1$) can turn into a π^+ and π^0, neither of which has strangeness.

Further discoveries disclosed that larger groupings could be made, joining several sets of particles together. These theoretical structures were soon confirmed by experiments revealing predicted, but hitherto unseen, particles. These larger groupings organized the enormous number of new particles into a striking order. What was the reason for this ordering?

It was proposed in 1963 that all these subnuclear particles could be understood as being composed of still smaller entities — quarks. A hundred or more particles could suddenly be understood in simple terms. There were then three quarks imagined: u, d, and s. Three of these put together made a "baryon," a particle like the neutron (2 d's and a u) or proton (2 u's and a d). One quark and one antiquark could combine to make a meson — the pion, kaon etc. Simple counting could predict new particles — and they were found.

At first, the quarks seemed like artificial constructs. No quarks had ever been seen, so many thought they were simply a convenient mathematical fiction. Such was the attitude

at first, but a series of important experiments over the next ten years provided convincing evidence that the quarks were real.

The construction of the Stanford Linear Accelerator Center (SLAC) provided an extremely powerful tool for exploration inside the proton. The accelerator produced electrons with unprecedented energy, nearly 20 billion electron volts (20 GeV). When the electrons collided with protons, characteristics of these collisions gave evidence for the internal construction of the proton, just as Rutherford's alpha particles had sixty years earlier for the atom. Moreover, just as Rutherford had been surprised to find a hard nucleus inside a soft atom, the SLAC results showed that there were hard constituents — dubbed partons — inside the proton.

Similar experiments were done at the Fermi National Accelerator Laboratory (Fermilab) in Illinois and at CERN, the European facility in Geneva, Switzerland. Some of the experiments were done using neutrinos in place of electrons. Neutrinos are massless particles that are produced in radioactive decay of nuclei and in the decay of particles like muons and pions. They interact only feebly with matter. Since they have no strong interactions, they are classed as leptons. Indeed, they can pass right through the earth undeflected. Occasionally a neutrino does collide with a proton or neutron, and those rare collisions can be studied. Once again, these collisions revealed point-like constituents within the proton. Moreover, when these collisions were compared with electron collisions at SLAC, the ratio of the two was just what would be expected if the hard objects inside the proton were quarks.

The reality of quarks was established convincingly with the simultaneous discovery in 1974 at the Brookhaven National Laboratory and at SLAC of an astonishing particle: J/ψ. A series of remarkable results from SLAC and the West German laboratory, DESY, established that the J/ψ was the first of a series of atom-like states, composed of a new quark, the c or charmed quark, and its antiquark. Similar states of a subsequent, fifth quark, denoted b, were discovered at Fermilab in 1977. Its properties have been extensively studied at Cornell and at DESY. A sixth quark, partner of the b, is expected, but there are no convincing data to support its existence as yet.

The most powerful forces we know of are those that bind the quarks together to form protons and neutrons. These are termed "strong" forces. The other forces are gravity, electromagnetism, and weak forces. The weak forces are responsible for beta-decay (a form of radioactivity discovered by Rutherford and Soddy at the turn of the century) and the interactions of neutrinos. In 1934, Enrico Fermi wrote down a theory that, with only minor modifications, still describes weak interactions at low energies. A major achievement occurred in 1956 when T.D. Lee and C.N. Yang noted that the weak interactions might violate parity, that is, they might distinguish between left and right in a fundamental way. It had previously been thought that if an experiment were done and at the same time was viewed both directly and in a mirror, both views would appear to be physically sensible. Lee and Yang proposed that this might not be so for the weak interaction and they were proved correct in experiments conducted soon after. The results were incorporated in an improved version of the Fermi theory adequate to describe the experiments that had been done at Fermilab and CERN exploring the structure of the proton using neutrino beams.

In 1973, a group working with a bubble chamber at CERN announced a startling result. Previously, all scattering events with a neutrino incident, resulted in a charged electron or

muon going out. Such events were called charged current events since charge had to be transferred to the neutrino, a neutral lepton, to make it into a charged lepton. The CERN group had convincing evidence of events in which the neutrino emerged, still uncharged. These were called neutral current events. They were analogous to the electron scattering at SLAC where the incident electron interacted electromagnetically (via photon exchange) with the proton, but still emerged as an electron. Since the electron was viewed there as emitting a neutral particle — the photon — during the scattering process, the neutrino in the CERN experiment had to be viewed as emitting a neutral particle. This neutral particle could not be the photon, since the photon sees only charged particles and the neutrino is chargeless. There had to be another neutral particle in addition to the photon.

In the Fermi theory, charged particles, the W^+ and W^-, could account for the weak force the way the photon accounted for the electromagnetic force. While the photon was massless, the W would be quite massive. Its great mass would account for the feebleness of the weak force. The discovery of neutral currents at CERN, subsequently confirmed at Fermilab and Argonne National Laboratory, indicated that an additional heavy particle was called for. It was denoted by Z. Such a particle had been hypothesized independently by Glashow, Salam, and Weinberg some years earlier, and work in the early 70's showed that the theories containing the Z were renormalizable — a technical word which might be translated as "calculable."

The theories containing the W and the Z were all the more remarkable because they united the weak and electromagnetic interactions, an accomplishment reminiscent of the unification of electricity and magnetism by James Clerk Maxwell in the middle of the last century. They contained four force carrying particles: W^+, W^-, Z, and the photon. These fitted together in an essential way. Neutral currents provided strong circumstantial evidence for the theory. Stronger evidence came from an experiment at SLAC on the scattering of polarized electrons which showed parity violation, the signature of exchange of both a photon and a Z with the target proton. The unified electroweak theory looked convincing. A key prediction stood out. The extensive neutral current experiments performed in the 1970s made it possible to predict the masses of the W and Z.

The predicted masses were between 80 and 100 GeV, too heavy to be produced at existing machines. CERN responded by developing an innovative way to use its 400 GeV machine (similar to the one at Fermilab at the time), which could normally produce particles with a mass no more than about 10 GeV. The inefficiency is due to a simple fact: conservation of momentum. When a 400 GeV proton strikes a stationary target, the resulting products must have 400 GeV of momentum. Thus much of the initial energy of the collision goes into the kinetic energy of the products, rather than into making new mass. CERN had previously built the Intersecting Storage Rings (ISR) to collide protons with protons at a beam energy of 30 GeV. That required two separate rings, with protons circulating clockwise in one and counter-clockwise in the other. To exploit the existing much larger 400 GeV accelerator (SPS) without building another ring, CERN decided to send antiprotons around the SPS same ring, going the opposite way. This had already been done for electrons and positrons, but that was enormously simpler. The problem with antiprotons was to make enough of them, and confine them into a small beam.

In 1982, CERN succeeded in this enterprise. It was thus able to reach a useful energy of 540 GeV, whereas the SPS alone or Fermilab machine using a stationary target could

reach only about 30 GeV. The project paid off handsomely. Both the W and the Z were discovered at the predicted masses.

The investigation of the W and Z has just begun. SLAC is pursuing an ingenious plan to study the Z, using a modification of its existing accelerator. Meanwhile, CERN is constructing a new accelerator, 27 kilometers in circumference, to study first the Z and then the W. Fermilab has completed and tested a large collider similar to CERN's, but at several times the energy. The results of these new accelerators are sure to enrich our understanding of these new fundamental particles.

Although these new facilities are just coming into operation now or in the near future, it is not too early to envision the next step. As mentioned briefly in Chapter 1, a significant increase in energy is needed. To understand the need it is necessary first to comprehend the depth and breadth, as well as the limitations, of our present picture of the fundamental particles.

2.1.2 Standard Model

What are the basic building blocks of matter? The answer to this question has changed as we have learned more and more. In the 19th century, chemists established the existence of atoms as the fundamental units of matter. As mentioned earlier, the inner structure of the atom was determined starting in the 1890s and culminating in the early 1930s. The atom is composed of electrons surrounding a much tinier and more massive nucleus, which is itself composed of protons and neutrons.

So far as has been determined, the electron still appears elementary, that is, it does not seem to have an inner structure. As discussed in the previous section, the situation is different for the proton and neutron. They are composed of quarks — two u-quarks and one d-quark for a proton and two d-quarks and one u-quark for a neutron. A neutron, because it is a bit more massive than a proton, is not stable but instead decays to a proton, an electron and an electrically neutral particle called a neutrino (actually, an antineutrino). This decay can be viewed as the change of a d-quark to a u-quark, an electron, and an antineutrino through the action of the weak force.

The four particles, the u-quark, the d-quark, the electron, and the neutrino form a set we refer to as a "generation". All but the neutrino have electric charge and thus participate in electromagnetic interactions. The two quarks experience the "strong force" that binds quarks together to form protons and neutrons. This force is analogous to the electromagnetic force except that it depends not on electric charge, but on the so-called "color-charge". The electron and neutrino do not experience the strong force; they have no color-charge.

The first generation — the u-quark, the d-quark, the electron, and the neutrino — is enough to make all the ordinary matter of atoms. However, two other generations have been discovered. This is displayed in Fig. 2.1-1. The second generation consists of the c-quark (charmed-quark), the s-quark (strange-quark), the muon, and another neutrino (called the muon-neutrino). Why there should be more than one generation is a puzzle. The third generation consists of the b-quark (bottom-quark), the yet-to-be-confirmed t-quark (top-quark), the tau, and a third neutrino (tau-neutrino).

Each generation parallels the first. All the quarks have color and participate in the strong interactions. The particles like the electron and neutrino that do not have color are called leptons. All but the neutrinos have electric charge and experience electromagnetic

Constituent Particles in the Standard Model

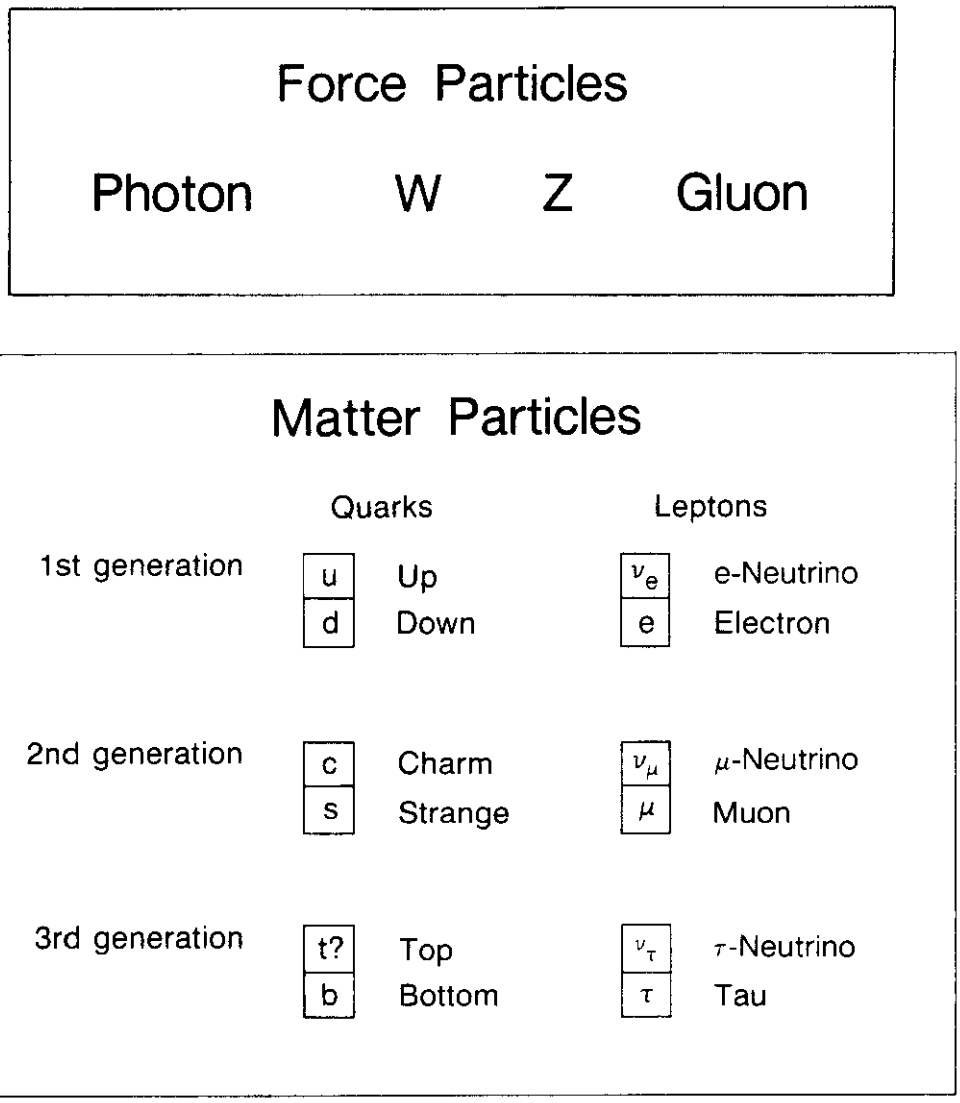

Figure 2.1-1.

forces. The weak interactions can change s-quarks to c-quarks, and vice versa, just as they change d-quarks into u-quarks, and also, with reduced probability, cause transitions between generations.

The standard model stipulates that there are two basic categories of particles: the matter particles which comprise the three generations of quarks and leptons, and the force particles (technically called "gauge" particles).

Figure 2.1-1 also displays the force particles. As already mentioned, the electromagnetic force is transmitted from one charged particle to another by a quantum of electromagnetic energy — a photon. Similarly, the strong force is transmitted from one colored particle to another by a quantum called the gluon (since it "glues" the quarks together to form the protons and neutrons). The gluon is more complex than the photon because, while the photon is itself neutral, the gluon carries color charge. Thus gluons can interact with each other in a way in which photons cannot. The consequences of this are dramatic. Two electrically charged objects can be pulled apart far enough that the force between them becomes negligible. The same is not true for a quark and an antiquark. No matter how far apart they are pulled, the force between them does not decrease. For this reason, no quark has ever been seen in isolation.

The weak force is similarly transmitted by the exchange of the W^+, W^-, and Z particles. We saw in the previous section that the weak and electromagnetic forces have a common origin, with the photon, and W and the Z being very similar particles in certain ways. For example, just as light (photons) can be polarized, so can the W and Z. Unlike the photon, the W and Z are very massive particles, a difference that needs explanation.

The model shown in Fig. 2.1-1 is a remarkably successful one. There are no data that contradict the model at present, even though vigorous efforts have been made to find failings that would hint at what lies beyond it. Nevertheless, it is almost certainly not the last word for there are many questions for which it provides no answer.

2.1.3 Outstanding Problems

The photon seems most unlike the W and Z. Photons surround us and are ultimately the source of our contact with the physical world. The W and Z were never observed directly before 1983. How can they be so analogous as to warrant being included in a single family, the force particles?

The interaction of light and matter was the first subject of investigation after the invention of quantum mechanics. P.A.M. Dirac found a way to incorporate special relativity and his theory was immediately successful in describing many physical phenomena. Unfortunately, his theory was only an approximation, albeit an excellent one. When the corrections to the theory were calculated, they turned out to be infinite! This puzzle was solved shortly after World War II, and the resulting theory, quantum electrodynamics (QED), has proved the most complete and successful physical theory ever developed, with agreement between theory and experiment to nine digits in some cases.

Since QED works so well, it is natural to pattern a theory of the weak interactions after it. Difficulties arise because the weak force particles (W and Z) are massive — the success of QED seems to depend on the photon being massless. The conceptual way out of this predicament is to augment the simple theory, in which the W and Z are initially massless, by the addition of a "field" pervading all space uniformly and interacting with the W and Z

to give them their masses. The theory turns out to be like QED in that its corrections can be calculated and are finite, while the W and Z acquire masses. In fact, all the particles, the quarks and leptons included, start out being massless and only obtain mass from this mysterious "field," which might be thought of as a ubiquitous molasses, slowing down all the particles, since without it, they would all be massless and move at the speed of light. The idea of the mass-generating field is central to the development of the unified theory of weak and electromagnetic interactions discussed earlier, even though there is as yet no experimental evidence that it is right.

Is there any way to verify that this mass-generating field is really there? Actually, there are several ways that this field can arise and each has its characteristic signals. In all cases, there must be new particles or a new interaction, so far undiscovered, that are the vestige of the mechanism that gives masses to most particles. We cannot say precisely where these new particles or interactions will be found, but there are general, persuasive arguments that some evidence must lie within the range of the SSC.

The simplest model for the mass-generating process requires that there be one more particle besides the matter and force particles described above. This particle is called the Higgs particle. It is a remnant of the omnipresent "field" giving mass to all other particles. Paradoxically, its own mass is unknown to us although its other properties can be predicted.

In another model, there are many particles analogous to the Higgs particle, but they are not fundamental. Instead they are composites of new particles rather like the known quarks or leptons. A more comprehensive theory called supersymmetry incorporates the mass-generating mechanism in a framework of twice as many basic constituents as are now known, each force and matter particle having a symmetry partner (See Section 2.2.1).

The search for new particles that are linked to the ultimate source of mass is a primary goal of the SSC, as is discussed in more detail in Sections 2.2 and 2.3.

The standard model is incomplete in other ways. There is no understanding of why there are three generations; in fact, there may be more. There is no understanding of why the quarks and leptons have the masses they do. Even if these masses arise from interaction with the mass-generating field, the actual values of the masses seem to be arbitrary.

Our lack of understanding of the masses of the various particles is a very deep problem. Not only are we unable to predict the masses of the quarks and leptons exactly, we cannot even provide a crude estimate. The masses of the W and Z were predicted before their discovery by comparison with the Fermi coupling constant, G_F, which is measured in beta-decay. However, we have no understanding of this number. It sets the scale for the W and Z masses to be about 100 GeV. No one can explain why the number was not a million times larger or a million times smaller. Another unexplained energy scale is related to gravity. Gravitational interactions between elementary particles are important only at energies of about 10^{19} GeV. This stupendous energy, nearly a billion billion times higher than the energies associated with the W and Z, is called the Planck scale. There is a great disparity between the Planck scale and the masses of the W and Z. Why this is so is a mystery.

Between the 100 GeV energy scale explored by the CERN and Fermilab Colliders and the Planck scale is an enormous terra incognita. The SSC would be the first machine to begin to explore this region of which we are so ignorant.

It has been suggested that the unification of weak and electromagnetic interactions is only the beginning. Perhaps the strong interactions are in some way united with the

electroweak. This is a very attractive possibility. There could be extra force particles that could turn quarks into leptons. In that case the proton itself could decay, albeit very slowly, for example permitting $p \rightarrow \pi^0 e^+$. Unfortunately, despite a major experimental effort, no evidence has been found for such processes.

There are reasons for suspecting that the electroweak and strong interactions should be unified. A powerful one is that the proton and electron have electric charges which are precisely equal and opposite. If there are force particles that permit the proton to decay into a positron and a neutral pion, the proton and positron must have precisely the same electric charge, and the proton and the electron precisely opposite charges.

While the possibility of uniting the strong interactions with the electroweak interactions has a strong esthetic appeal, there is a serious lack of pertinent experimental information. New discoveries at the SSC might provide a clue to the validity of this exciting hypothesis. For example, still heavier leptons of other generations may begin to manifest some internal structure, rather than being merely heavier point-like electrons.

2.1.4 Existing and Proposed Collider-Accelerators

The progress of the last thirty-five years in particle physics has been dependent on the development of a series of ever more powerful accelerators. These are of two sorts: proton accelerators and electron accelerators. The beam of particles produced by the accelerator may then be directed at a stationary target. Some of the energy carried by each electron or proton is transformed into new matter according to Einstein's relation $E = mc^2$. The incident particle carries a great deal of momentum which has to be shared among the produced final particles. As a result, only a small fraction of the energy is actually available for production of new particles. To circumvent this problem, a new type of accelerator called a collider was developed. In a collider, the collisions occur between two beams moving in opposite directions. The momentum in one of the beams is just opposite the momentum in the other. Since the sum of the momenta is zero, none needs to be carried away after the collision and all the energy is available for particle production.

The first proton-proton collider (1971) was the Intersecting Storage Rings (ISR) at CERN. It had two rings with particles circulating in opposite directions. The proton beams collided with each other at several locations where the rings crossed. With 30 GeV beams, it was equivalent to a machine with a single beam of energy 2000 GeV bombarding a stationary target, an energy still not achieved to this day by a single-beam facility.

The effectiveness of a collider of a given energy is judged by its luminosity, a measure of the number of collision partners each proton encounters as the beams collide. The collision rate is proportional to the luminosity. Each process studied has an effective area or "cross section." If two protons approach each other, the likelihood they will collide depends on how large the protons appear, that is, their total cross section. This was measured to be about 45×10^{-27} cm^2 at the ISR. The rate of proton-proton collisions is given by the product of the cross section and the luminosity. The ISR reached a peak luminosity of about 10^{32} cm^{-2}s^{-1} corresponding to a rate of proton-proton collisions of about 4 million per second. Of course, only a very small fraction of these events will be of interest; only part of the total cross section needs to be studied. In fact, a process in which a large mass, M, is created has a cross section that varies roughly as $1/M^2$. If M is very large, the

cross section is very small. For this reason, it is important for a high-energy machine like the SSC to have a high luminosity.

Colliding beam machines have also been made with electrons and positrons (anti-electrons). Two such machines are operating at the Stanford Linear Accelerator Center, SPEAR, with a beam energy of 1.5 to 4 GeV and PEP, with a beam energy of about 15 GeV. Similar machines have operated at the West German laboratory DESY, in Hamburg. A very successful electron-positron colliding beam accelerator, CESR, is located at Cornell University. The existing and planned high-energy colliding beam machines are listed in Table 2.1-1.

Table 2.1-1(a)
Hadron-Hadron Colliders

Name	Energy (GeV)	Particle Types	Luminosity ($cm^{-2}s^{-1}$)	Status
ISR (CERN, Geneva)	30+30	pp	10^{31}–10^{32}	completed 1971 decommissioned 1984
	30+30	$p\bar{p}$	$\sim 10^{28}$	1981–1982
$Sp\bar{p}S$ (CERN, Geneva)	310+310	$p\bar{p}$	$> 10^{29}$	completed 1982
Tevatron (FNAL, USA)	1000+1000	$p\bar{p}$	$\geqslant 10^{30}$ (design)	first test 1985 operational in late 1986
UNK (Serpukhov, USSR)	400+3000	pp	10^{32} (design)	completion projected for 1990s
LHC* (CERN, Geneva)	6000+6000 ?	$p\bar{p}$	$\leqslant 10^{32}$?	1990s ?
SSC	20000+20000	pp	10^{33}	proposed for completion in 1994

*Currently under discussion as one possible future option at CERN.

Table 2.1-1(b)
Electron-Positron Colliders

Name	Energy (GeV)	Luminosity ($cm^{-2}s^{-1}$)	Status
SPEAR (SLAC, USA)	4+4	$\sim 10^{31}$	operating since 1972
DORIS (DESY, Hamburg)	5+5	$\sim 10^{31}$	operating since 1974
VEPP-4 (Novosibirsk, USSR)	6+6	$\sim 10^{30}$	initial operation in 1979 (at lower energies)
CESR (Cornell, USA)	8+8	$\sim 3 \times 10^{31}$	operating since 1979
PEP (SLAC, USA)	18+18	$\sim 3 \times 10^{31}$	operating since 1980
PETRA (DESY, Hamburg)	22+22	$\sim 3 \times 10^{31}$	operating since 1978
TRISTAN (KEK, Japan)	30+30	$\sim 10^{31}$ (design)	scheduled for completion in 1986
SLC (SLAC, USA)	50+50	$> 10^{30}$ (design)	scheduled for completion in early 1987
LEP (CERN, Geneva)	50+50	$\sim 10^{31}$ (design)	scheduled for completion late 1988
	100+100		energy upgrade of the facility planned for early 1990s

Hadron colliders and electron-positron colliders have important similarities, but also important differences. Both are effective ways of producing very high useful energies. Electron-positron colliders can be tuned to produce a precise collision energy. This makes them ideal for studying a particle like the Z which can be produced when an electron and positron of the right energy annihilate. In contrast to electrons and positrons, the proton is not elementary, but contains quarks and gluons which share the energy of the proton. As a result, a collision of one quark (or gluon) from each of the colliding protons uses only a fraction of the total proton-proton energy. This suggests that at the same particle collinear energy electron-positron machines would give higher effective collision energies since the colliding particles are not composed of smaller pieces. However, the hadron-hadron machines more than make up for this disadvantage because it is far easier to increase the beam energy of hadron machines. The reason is that the very light-weight electrons (but

not protons) in a circular machine radiate enormous amounts of energy which must then be pumped back into the beam. To avoid this loss of energy by radiation, the accelerator at SLAC was built not as a circular machine, but as a straight one. Electron-positron machines with energies much greater than those at LEP (whose circumference will be 27 km) will have to be linear colliders. The Stanford Linear Collider, SLC, is a first step in that direction, but years of effort are still needed to bring linear electron colliders to the same state of development as circular proton colliders.

One machine is being constructed that lies between the categories discussed above. The DESY laboratory in Hamburg has just begun construction of an electron-proton collider called HERA. It will have 820 GeV protons colliding with 30 GeV electrons with a luminosity of about $5 \times 10^{31}\ \mathrm{cm}^{-2}\mathrm{s}^{-1}$.

The SSC will build on the experience of earlier hadron-hadron colliders, especially the Tevatron Collider, just now coming into operation with its high energy and its superconducting magnets. The SSC represents an enormous step in both energy and luminosity over existing machines. In the energy regime of interest only a proton-proton machine is today capable of the high luminosity necessary to gather information on the rarest and possibly most interesting phenomena. The very high energy of the SSC will take it to a completely unexplored domain, providing answers to some of the fundamental questions posed above and undoubtedly uncovering new, unanticipated phenomena.

2.2 Scientific Need For The SSC

The results of the experiments conducted thus far at the CERN SPS Collider confirm a simple picture of high energy proton collisions. The protons are composed of three fundamental quarks, plus a mixture of quarks, antiquarks, and gluons. The most interesting collisions of protons occur when a single parton (quark, antiquark, or gluon) from one proton collides with a single parton from the other. Thus the total energy in the basic collision is considerably less than that apparently available from the two beams. It is the fundamental interactions of the partons that we wish to study.

At the CERN Collider, clear signals have been seen for the scattering of partons through large angles. One process of this sort is illustrated in Fig. 2.2-1. It shows one quark from each proton interacting by exchanging a gluon. The exiting quarks carry a large energy transverse to the direction of the beams. These quarks turn into observable pions, kaons, protons, etc. If a quark from one proton and an antiquark from the other collide, they might produce a W or a Z. It is this sort of event that provided the evidence for these particles.

2.2.1 Physics at SSC Energies

At the SSC, the same basic mechanisms would be at work. The energy available in the collision of the partons would be enormously greater, however, than in the collisions observed in any earlier machine. These collisions could thus produce new particles, never before observed. What might these particles be? Based on our understanding of fundamental interactions to date, we can make some speculations. The list provides some guideline for possible phenomena at the SSC:

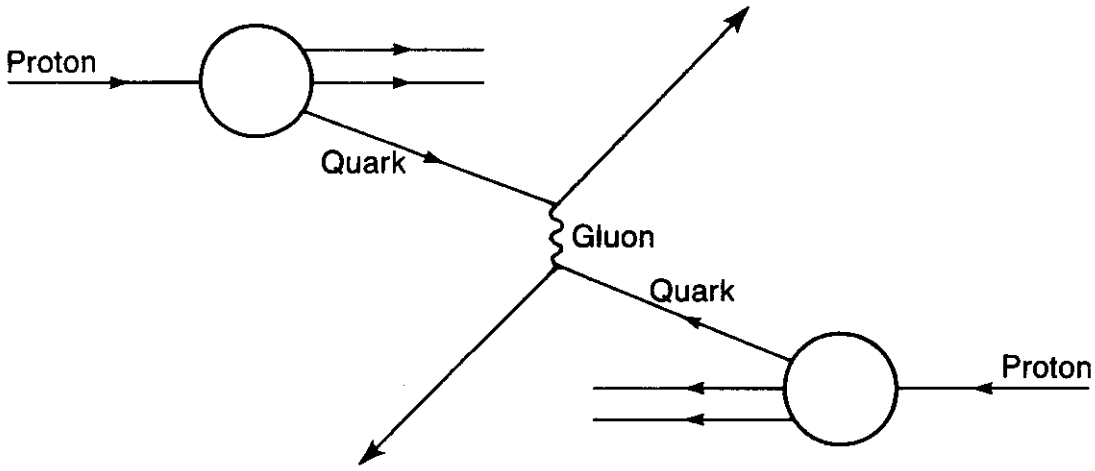

Figure 2.2-1. Parton-parton scattering. The constituents inside the proton (called partons) share the proton's momentum. In a high-energy collision between protons, it is actually the partons that collide. The example shown is quark-quark scattering by gluon exchange.

1. Higgs particle(s)
2. Supersymmetric particles
3. Technicolor particles
4. New quarks and leptons
5. New force (gauge) particles
6. Constituents of quarks and leptons

The first three items on the list are related to the origin of the masses of particles. As mentioned in Section 2.1.3, the standard model begins as a theory of massless particles. The quarks, charged leptons, W, and Z get masses through their interaction with an omnipresent field. The first and simplest version of the model contains a single additional particle, the Higgs particle, that is intimately connected with this mass-generating field. Assuming it exists, we can predict reliably all its properties except one, its mass. If it is light enough (less than about 35 GeV), it should be observed in Z decays studied at SLC or LEP. The SSC is suited to finding it should the mass of the Higgs particle lie above 200 GeV.

Higgs Particle

The Higgs particle is not stable, but decays into other particles. Because it is related to the origin of masses, it turns out that it is most likely to decay into very massive particles. If the Higgs mass is greater than twice the mass of the W or Z, it will decay into two Ws or two Zs. Some of these decays could be detected. If enough events of this sort are accumulated, the Higgs particle could be identified.

Although the mass of the Higgs particle cannot be predicted, there are powerful general arguments that demonstrate that the phenomena associated with the Higgs particle must manifest themselves at an energy less than about 1 TeV. A similar argument was used some years ago to show that some new phenomenon had to occur below about 300 GeV for the case of weak interactions. That new phenomenon turned out to be the W particle found at a mass of 83 GeV. The argument comes simply from calculating predictions in a theory without the Higgs particle (or in the earlier instance, without the W particle). At some high energy, here 1 TeV, the calculations predict that some process must occur with a probability greater than 100%. This absurd result shows that something has been omitted from the calculation. There must be some additional phenomenon that enters before this energy is reached.

This argument is quite general. It applies even if the simplest model, which has a single Higgs particle, is not correct and instead there are some other particles that play the role of the Higgs particle. Therefore, the scale of 1 TeV is one that is singled out as a target for the SSC, just as a lower energy scale was singled out in the search for the W. The task here is much more difficult than it was for finding the W and Z. There it was possible to make precise predictions for the masses. That is not possible at present for the Higgs particle.

The Higgs particle may be difficult to find because most of its decays are into many particles, some neutral and some very weakly interacting. However, a number of extensions of the standard model have alternative mechanisms to give rise to particle masses. In these extensions there are other particles besides the Higgs particle that would reveal themselves. Most of these particles would be much easier to find.

Supersymmetry

One extension is called supersymmetry. In this model there are several Higgs particles to look for. This makes the task easier. There are, besides, many other new particles that would be produced at the SSC if supersymmetry plays a role in the generation of the masses of the known particles.

Supersymmetry proposes that there are connections between particles with angular momentum one-half (e.g., the quarks and leptons), particles with angular momentum one (e.g., the force particles), and particles with zero angular momentum (e.g., the Higgs particle). For every quark or lepton there must be a "supersymmetric" partner with spin zero, called squarks and sleptons. For every force particle, there should be a partner with angular momentum one-half — for the photon a photino, for the gluon a gluino, for the W a Wino, and for the Z a Zino.

Where are these particles? None has been found to date, but if supersymmetry is connected to mass generation, these particles cannot be too much heavier than the known particles, surely less than a few TeV. If they exist, many of them should be produced at the SSC.

While no experimental evidence of supersymmetry has been found, the theory has great attractiveness. It provides a partial answer to the hierarchy problem. In most theories, it is hard to prevent the mass of the Higgs particle from increasing up to the highest mass scale available, the Planck mass. In supersymmetric models, the mass of the angular momentum zero particles is not so pathological. The reason is that when one calculates the mass, for every contribution pushing the mass up, there is one of equal strength, pushing down.

Supersymmetry has other virtues. It is possible to incorporate gravity into the model and unify all four forces. Indeed, recent theoretical advances have produced models that incorporate all the forces and avoid the devastating problems that have previously plagued theories of quantum gravity. These new models are based on "superstrings". The basic units in the theory are not point particles, but strings of fantastically small dimensions. Superstring theories look very promising and enormously challenging. Efforts are being made to derive predictions that could be tested with accelerators including the SSC.

Technicolor

The term technicolor was coined to describe models in which there are forces analogous to the color forces carried by the gluon, but which are characterized by a mass scale (1 TeV) set by the W and Z masses, rather than the 1 GeV mass scale of ordinary hadrons. These hypothetical forces would act between techniquarks, particles analogous to ordinary quarks. States of techniquarks and anti-techniquarks bound together by the technicolor force could play the role of the Higgs particle in the simple theory described above. Because such Higgs particles are not fundamental, but are composed of other particles, some of the technical difficulties of the simple model can be avoided. Technicolor models predict a great variety of new particles that could be observed at the SSC.

New Quarks and Leptons

In addition to new particles associated with the problem of mass, there may be new quarks and leptons that can be discovered at the SSC. So far, three generations of quarks and leptons have been discovered (see Fig. 2.1-1.), but there is no assurance that there are

not more. Important evidence will come from the study of Z decays at the SLC and LEP. By measuring Z decays, it is possible to infer how many neutrinos there are, assuming, as is so far the case, that all neutrinos are massless (or at least very light). It is possible that quarks and leptons come in more complex arrangements than the families we have seen thus far. Perhaps there are additional quarks even with charges in a different pattern than those observed up to now. Another possibility is that there are additional leptons and that both the charged and neutral ones are very massive. Such particles could be observed at the SSC.

New Force (Gauge) Particle

Perhaps more dramatic than the discovery of a new quark or lepton would be the discovery of a new force particle. Each force particle represents a specific force: the photon, the electromagnetic force; the gluon, the strong force; the W and Z, the weak force. Thus a new force particle would indicate a new force, or at least a complication of an existing law of force. This would be quite startling because the four known forces were already apparent early in this century. A new force particle would be observed just as the W and Z were at CERN. In a high energy collision a quark and an antiquark could annihilate to form the force particle which would subsequently decay. Its decay into a pair of light leptons would be an especially clean signature.

Quark and Lepton Sub-Structure

So far as we know at present, the quarks and leptons are fundamental particles in the sense that they do not appear to be made of more fundamental constituents. Of course, we may have failed to find the constituents inside them only because we have not probed deeply enough. The constituents of the proton only revealed themselves when SLAC was able to direct its high energy electron beam on protons. Previous experiments at lower energy were incapable of resolving the details inside the protons and neutrons. The SSC will provide the means to probe more deeply than ever before inside matter and may reveal a new layer beneath the quarks and leptons.

This partial list of possible discoveries — Higgs particles, supersymmetric particles, technicolor particles, etc. — cannot be more than a guess. Past experience suggests that a new accelerator opening up a vast new energy range will make discoveries that could not be anticipated in advance. It is these discoveries that are often the most important ones. Still, the tentative list demonstrates that the reach of the SSC will encompass issues fundamental to our understanding of the basic constituents and forces of matter, and especially important to the understanding of the origin of mass.

2.2.2 Connections to Other Scientific Fields

While particle physics continues to probe more and more deeply into matter and deals with higher and higher energy, the issues at stake have not become narrower. On the contrary, the concerns of particle physics are becoming more and more entwined with those of neighboring fields. This is especially true of astrophysics, condensed matter physics, and nuclear physics.

Cosmology and particle physics share a common frontier: interactions at very high energy. At the beginning of the universe, according to our current picture, the energies of the existing particles were extremely high. The exotic particles studied in high energy accelerators existed in great numbers. By studying the highest energy reactions, we are studying the conditions that prevailed in the earliest fraction of a second of the universe. Moreover, some of these exotic particles may have persisted to this day. There is evidence that much of the mass of the universe is not present in the stars or ordinary matter between them. It may be that it is in the form of yet unobserved fundamental particles. These particles could be related to supersymmetry or some other theory that could be tested at the SSC.

In studying the phenomenon that confines the quarks inside observed particles and prevents the quarks from being seen individually, particle physicists have had to confront phase transitions. In the generation of particle masses in the electroweak theory, there is also a phase transition, this one analogous to that occurring inside a superconductor. The field of phase transitions has been an area of fruitful interaction between particle physics and condensed matter physics. Phase transitions also play an essential role in our understanding of the early moments of the universe.

Study of the phase transition that causes quarks to be confined inside observed hadrons may be possible in nuclear collisions between relativistic heavy ions. Collisions between such large aggregates have the potential of occasionally providing enough energy density over a large enough region to cause momentary creation of a quark-gluon plasma, rather than a collection of very energetic, but ordinary, particles. This rare deconfined phase should exhibit properties different from the usual collisions, thereby throwing light on collective aspects of the strong force not accessible in elementary particle collisions.

The SSC, through its investigation of fundamental physical processes, will provide new insights into these questions of great significance to other sciences as well as particle physics, and to our general appreciation of the world in which we live. It will be a powerful tool for extending those investigations of matter that have led us to an understanding of the atom, the nucleus, and on to their smallest components.

2.3 Discovery Potential of a Multi-TeV Collider

The physics motivation for the SSC, as seen from our present vantage point, has been argued in the previous section. The broad unknown of the multi-TeV energy frontier has many salients of potentially new physical phenomena. The present section describes, at a somewhat more technical level, the extent of exploration possible with the SSC in the various directions suggested by our current understanding.

It needs emphasis that these considerations are indicative at best. Experience has shown that, whenever a new energy domain or major new technique is opened up, unexpected discoveries are made — discoveries not anticipated at the planning stage, discoveries that alter and focus our thinking in productive new directions. Whichever of the theoretically possible particles are found, physics with the SSC will surely yield a bountiful harvest of surprises.

2.3.1 Concepts of Very High Energy Collisions

The energy range that can be explored by the SSC cannot be defined in a single statement. The range depends on the particular physics being explored. Each incoming proton is composed of partons (quarks, antiquarks, and gluons) that share the proton's momentum. The fundamental processes are the collisions of partons.

Figure 2.3-1 illustrates the production of a pair of new particles Y and $\overline{Y}$. The process is described by the following equation for the interaction cross section,

$$\sigma = \int dx_1 dx_2 f_i(x_1) f_j(x_2) \hat{\sigma} \tag{2.3-1}$$

The elemental collision is that of two partons of types i and j, which could be quarks or gluons depending upon the particular process. These partons have energies x_1 and x_2 times the energy of the incident proton beams. The quantity $f_i(x_1)dx_1$ is the probability that there is a parton of type i with energy fraction between x_1 and $x_1 + dx_1$ within a proton, and similarly for $f_j(x_2)dx_2$. These probabilities differ in detail, depending on parton type, but are largest when x is small. The integral in the equation corresponds to summing over all the combinations of parton energies, weighted with the probability of occurrence.

The equivalent parton beam energy $\hat{E}$ flowing into the interesting process is related to the energy of the proton beam E by

$$\hat{E} = \sqrt{x_1 x_2}\, E \tag{2.3-2}$$

The probability of having a collision with useful total energy $2\hat{E}$ in a collider of total energy $2E$ is a rapidly falling function of $\hat{E}/E$, since $f_i(x_1)$ and $f_j(x_2)$ decrease as x_1 and x_2 increase.

The quantity $\hat{\sigma}$ is the cross section for the process of pair production of $Y\overline{Y}$ from incident partons i and j. This cross section is easy to estimate. Incoming partons with energy $\hat{E}$ probe distances of order $1/\hat{E}$; as the energy is increased, shorter distances are probed. The typical probed area or cross section is approximately $1/\hat{E}^2$. The exact value depends, of course, on the particular process. Nevertheless, this simple behavior illustrates the increasing importance of luminosity in high energy colliders. (Recall that the event rate is equal to the cross section times the luminosity).

The event rate for some new process can be written as the product of three factors, the actual luminosity of the collider, the effective luminosity for the type of collision (quark-quark, gluon-quark, etc) and the cross section for the parton process. The form of this effective luminosity can be deduced from the Eq. (2.3-1),

$$\text{effective luminosity} = \int \frac{dx}{x} f_i(x) f_j(\hat{E}^2/E^2 x) \ . \tag{2.3-3}$$

The effective luminosity depends upon the energy of the beams of the parton process and upon the types of partons. It can be used to discuss the relative merits of different combination of beam energy and luminosity without recourse to specific theoretical models.

Figure 2.3-2 shows the behavior of this effective luminosity for gluon-gluon collisions for a variety of proton energies. A simple example will illustrate the utility of this figure.

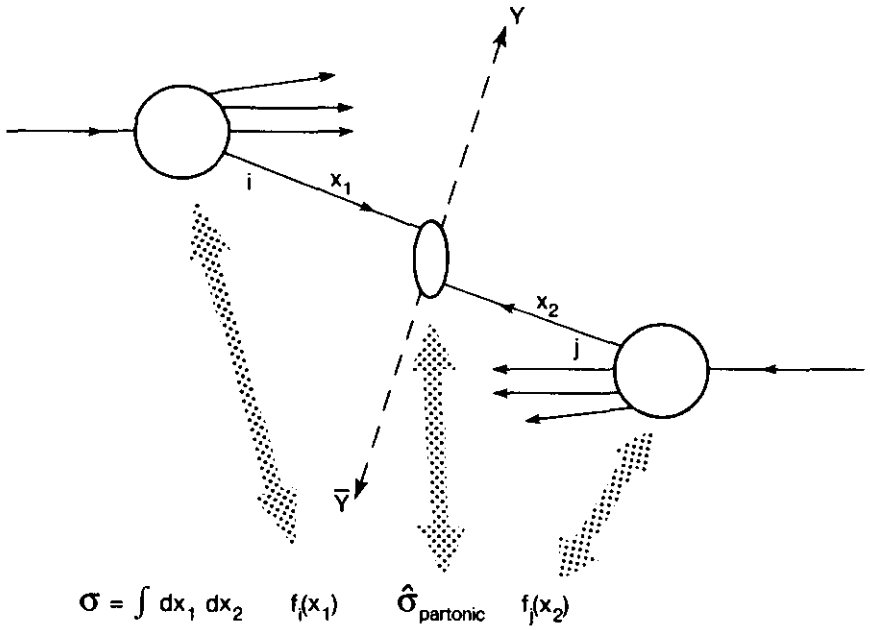

Figure 2.3-1. General parton-parton interaction. A parton of energy x_1E in one proton collides with a parton of energy x_2E from the other proton to produce a particle-antiparticle pair $Y\bar{Y}$ at large angles. The observed cross section is formed from the partonic cross section, folded with the respective probabilities of finding the specific partons of energies x_1E and x_2E within the two protons.

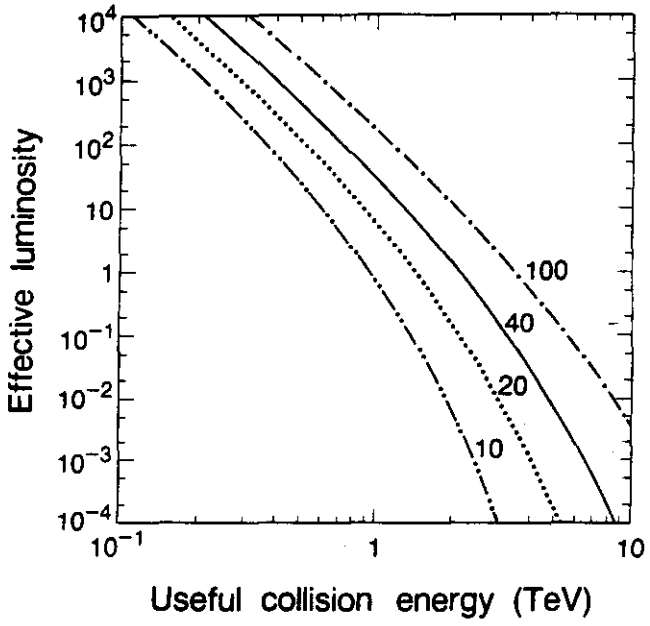

Figure 2.3-2. The effective luminosity (see text) for gluon-gluon interactions as a function of $2E$, the useful energy available in a gluon-gluon collision. The numbers on the curves are *twice* the proton beam energy in a collider. The solid curve corresponds to the SSC.

Suppose that we wish to investigate the production of a new quark of mass 1 TeV. Since this new quark must be produced in pairs the useful energy required is 2 TeV at least. We can see that the effective luminosity at this energy is approximately a factor of 10 smaller in a collider with 10 + 10 TeV beams than it is in one with 20 + 20 TeV beams. We can therefore produce the same number of events in these machines only if the lower energy one has 10 times more luminosity. Such a rule of thumb is useful but should not be abused; there are cases where the lower energy machine is less effective even at higher luminosity because there are relatively more uninteresting events to obscure the sought-for signal.

It is interesting to note that at multi-TeV beam energies the parton contents of protons and antiprotons are very similar. Thus, except for minor details, multi-TeV collisions of $\bar{p} + \bar{p}$, $p + \bar{p}$ or $p + p$ all produce the elementary reactions we seek to study. Said another way: At equal luminosities and equal beam energies, $p\bar{p}$ and pp colliders are essentially equivalent. Considerable success has been registered at current energies with $p\bar{p}$ collisions which have the advantage that, at least at low beam intensities, only one ring of magnets is needed. Two of the three hadron colliders built to date are $p\bar{p}$ machines. Note that the luminosity of the pp machine (ISR, see Table 2.1-1(a)) was 100 times that which is expected to be achieved with the $p\bar{p}$ colliders currently operating. Note also, as was observed above, the luminosity required rises roughly as the square of the interaction energy being studied. For this reason, while future technological developments may make high luminosity $p\bar{p}$ colliders feasible, the current SSC design utilizes colliding proton beams, counter circulating in separate rings.

2.3.2 Discovery Potential of a Multi-TeV Collider

The need to probe mass scales of order 1 TeV is discussed in Section 2.2.1. We must ensure that the SSC has sufficient energy and luminosity to carry out this search effectively. Thus, all of the theoretical options must be considered in order to ensure that the SSC is capable of exploring each and every one of them. This task was undertaken in detail by a number of researchers [2.3-1, 2, 3].

Higgs Particle

The simplest possibility is that there are no additional particles beyond those present in the standard model. As discussed in Section 2.2.1, this circumstance implies that either there will exist a well-defined scalar Higgs particle with mass considerably less than 1 TeV or there will be some structure in the final state of 2 Ws or 2 Zs when the sum of the transverse energies of the Ws or Zs is of order the Higgs particle mass. As this mass increases the cross section for such events will fall since the fraction of the total energy going into the subprocess is increased.

A Higgs particle of mass, say, 600 GeV will decay predominantly into either a pair of W or a pair of Z particles. An experimental search will therefore consist of looking for structure in the W or Z pair production cross section. This is illustrated in Fig. 2.3-3. Enough events must be produced so that we can clearly see the peak and so be certain of a discovery. It is not clear how efficiently one can detect W or Z particles. The most pessimistic scenario assumes that only the leptonic decay modes of the particles are observable. If this is true, then the observation of final states of four isolated electrons or muons

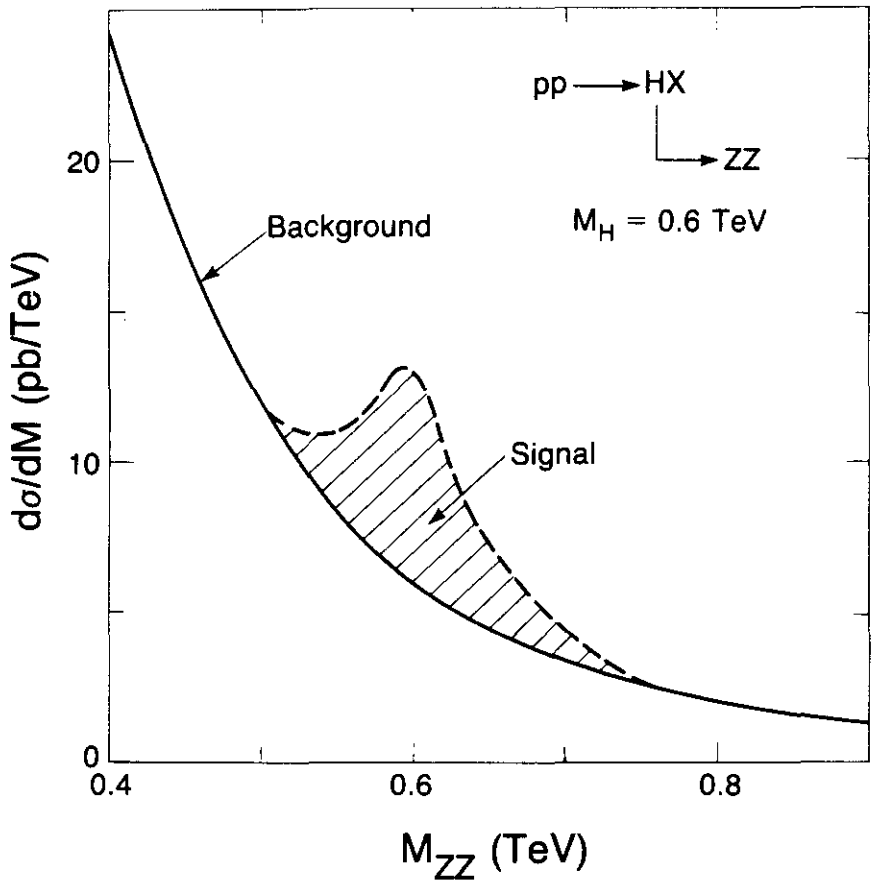

Figure 2.3-3. Cross section for production of two Z particles as a function of the invariant mass of the pair. The falling curve represents the "background" (from dynamically uncorrelated Z pairs). The shaded "signal" represents production of a Higgs particle of mass 0.6 TeV and its decay into a pair of Z particles. Other sources of background are assumed negligible — the selection of four-lepton events making a pair of Z particles is a very powerful constraint.

originating from the decays $Z \rightarrow \mu^+\mu^-$ and $Z \rightarrow e^+e^-$, will enable the Higgs to be detected. Requiring that a year of running produce 20 events in these channels implies that a beam energy of at least 14 TeV and luminosity of 10^{33} $cm^{-2}s^{-1}$ is necessary for a Higgs mass of 600 GeV.

Figure 2.3-4 illustrates the maximum Higgs mass that can be reached for different choices of the energy and luminosity using the same criterion. Notice that the luminosity is critical. A machine with 20 TeV beams and a luminosity of 10^{32} $cm^{-2}s^{-1}$ has only a small window (180 GeV $< M_H <$ 270 GeV) of discovery, and one with a luminosity of 10^{31} $cm^{-2}s^{-1}$, none at all.

Supersymmetric Particles

One other theoretical option involves the existence of supersymmetric particles. Again, as discussed above, their masses must be less than a few TeV if supersymmetry is to be relevant to the problems of electroweak mass generation. One supersymmetric particle of particular interest is the gluino, which is the spin 1/2 partner of the gluon and will be produced in pairs and decay to give final states with jets (collimated groups of particles) and neutrino-like particles, e.g. photinos. In principle, photinos can be detected by absorption or scattering, but in fact are almost impossible to detect. Absorption or scattering can occur only with the real or virtual creation of the supersymmetric partner of some ordinary particle. Such particles are evidently very massive and therefore energetically impossible to create, or, if created virtually, make the probability of photino scattering exceedingly small. The escaping photinos will cause the detected jets to appear in violation of energy and/or momentum conservation.

There are serious backgrounds to gluino production, arising for example from the decay of top quarks where neutrinos are emitted. Consequently, a large number of events will be required to ensure a discovery. A detailed calculation indicates that we may need to produce 10,000 pairs to be sure of a discovery. Figure 2.3-5 shows the gluino mass range that can be searched in a year's running at various collider energies and luminosities. Again, it can be seen that high energy and luminosity are required in order to probe the TeV region. For example, a 20 TeV collider operating at a luminosity of 10^{33} $cm^{-2}s^{-1}$ will be able to find a gluino if its mass is less than 1.6 TeV, whereas if the luminosity is reduced by a factor of 100, the mass must be less than 600 GeV if a gluino is to be found. There is no appreciable difference in the production rate at proton-proton and proton-antiproton colliders with the same energy and luminosity.

New Force (Gauge) Particle

The presence of additional massive force particles (similar to the W and the Z) is required by theories in which parity becomes a good symmetry at high energy, or in some superstring theories. Present knowledge provides no estimate for the masses of these particles, if they exist, so it is important to be able to search as large a range as possible. Figure 2.3-6 shows the accessible masses of new W particles if 1000 are to be produced in a year of running, a reasonable criterion if they are only observable via their decays into electrons or muons with branching ratios of a few per cent.

This is one of the few cases where antiprotons may provide an advantage, since the initial state consists of a quark and an antiquark. It will be noted from the figure that this advantage is not present significantly in colliders with luminosity of 10^{32} $cm^{-2}s^{-1}$, where

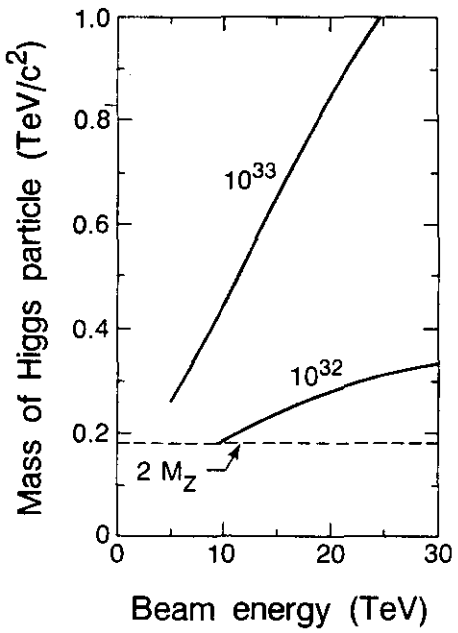

Figure 2.3-4. Upper and lower limits on the masses of Higgs particles that can be discovered with a hadron collider as a function of beam energy and luminosity. The effective lower limit of $2M_Z$ is set by the difficulty of finding a decay signal if the Higgs particle is unable to decay into Z pairs because its mass is less than $2M_Z$.

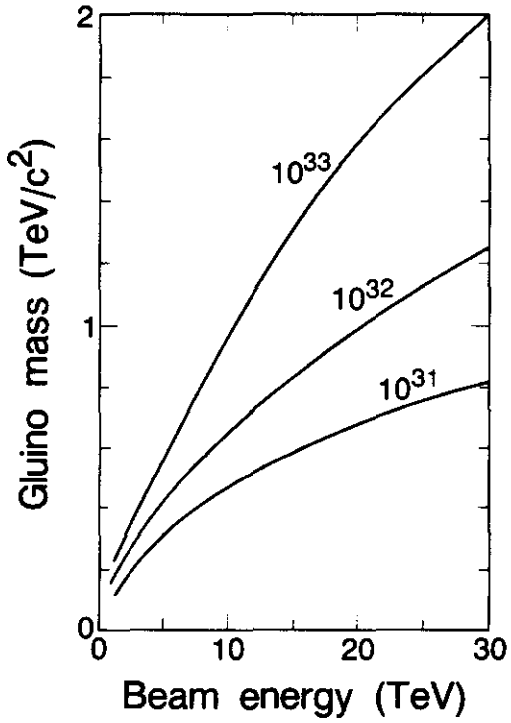

Figure 2.3-5. Discovery limits on masses for gluinos (supersymmetric partners of gluons) as a function of beam energy and luminosity for hadron colliders.

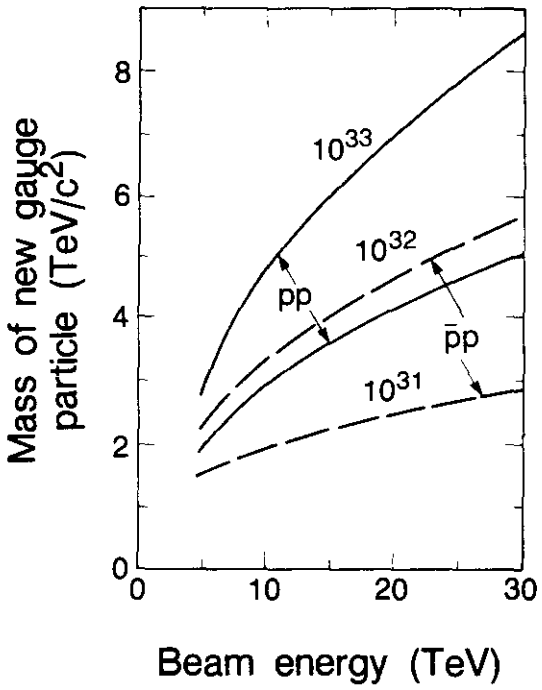

Figure 2.3-6. Discovery limits on masses of additional force (gauge) particles as a function of beam energy and luminosity for proton-proton colliders (solid lines) and proton-antiproton colliders (dashed lines).

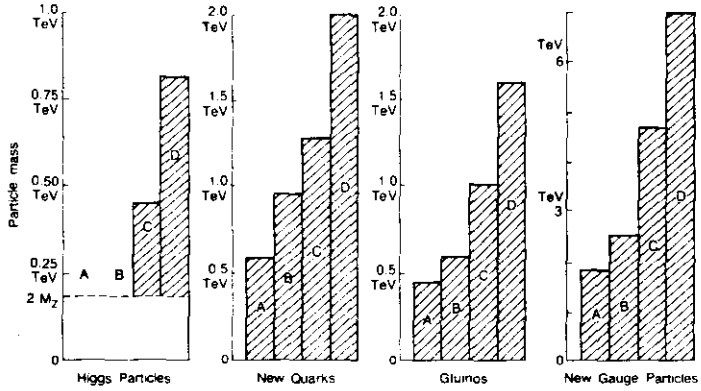

Figure 2.3-7. Histograms showing the discovery reach (maximum observable mass) of different hadron colliders for four possible types of new particles. The colliders are

Designation	Beam Energy (TeV)	Luminosity ($cm^{-2}s^{-1}$)
A	10	10^{31}
B	20	10^{31}
C	10	10^{33}
D	20	10^{33}

"Discovery" is defined as 20 events per year in the mode $H \rightarrow ZZ$, both $Z \rightarrow \ell^+\ell^-$, 500 events per year for new quarks, 10^4 events per year for gluinos, and 10^3 events per year for new gauge particles.

the lines on the figure corresponding to proton-proton (solid) and proton-antiproton (dashed) collisions are not far apart. A proton-proton collider operating at 10^{33} $cm^{-2}s^{-1}$ is certainly more effective than a proton-antiproton collider at one tenth of the luminosity.

Summary

Figure 2.3-7 provides a summary of the capabilities of different colliders. This figure emphasizes that the power of the colliders increases dramatically as their energies and luminosities are increased. The increase in capability is almost independent of the particular search being conducted as can be seen by comparing the relative heights of the histograms on the figure. For example, a 20 TeV collider operating at 10^{33} $cm^{-2}s^{-1}$ (case D) is sensitive to gluino masses 4 times larger than those which can be discovered at a 10 TeV machine operating at 10^{31} $cm^{-2}s^{-1}$ (case A). It is to be noticed that in one of the most critical areas, that of searching for a Higgs particle, colliders with luminosities of 10^{31} $cm^{-2}s^{-1}$ (cases A and B) are ineffective. This is the one particle whose mass is limited by theory and only the 20 TeV collider operating at 10^{33} $cm^{-2}s^{-1}$ is capable of searching the entire range above 200 GeV.

2.4 Recent Advances in Accelerator Technology

2.4.1 Introduction

The technical basis for the SSC is rooted in the experience and expertise gained in the construction and operation of large nuclear and high energy accelerator facilities throughout the world. The intricate and complex system of components of a large accelerator has been created and operated routinely in a number of locations, in ever increasing size. All of these facilities except the Tevatron utilize conventional iron and copper magnets in their confinement systems. In principle, the extension of this technology to a machine of the capabilities of the SSC is straightforward, but its practical realization depends on the use of superconductivity on a large scale.

Superconductivity is the property of conduction of electricity with absolutely no resistance whatsoever, a property exhibited by some elements, compounds, and alloys at temperatures very near absolute zero. Discovered by a Dutch scientist, Kamerlingh Onnes in 1911, superconductivity was a laboratory curiosity until recent times, when a combination of scientific and technological developments led to its practical application.

The advantages of a ring of superconducting magnets are two-fold: (a) The magnetic field strength can be greatly increased over that attainable with conventional copper and iron magnets, increasing proportionately the maximum energy possible for a given sized ring; (b) the power consumption in resistive heat loss can be eliminated, with relatively modest need of power to provide the needed refrigeration. Quantitatively, magnetic field strengths can be tripled with superconducting magnets, while power consumption in the magnet system can be reduced by factors of 10 or more. The conventional main ring of magnets at Fermilab dissipates approximately 130 MW at full energy. In the SSC, an instrument with a particle energy capability of 40 times the Fermilab main ring (20 TeV vs. 0.5 TeV), the losses in the magnets themselves are negligible, although there is roughly 30 MW needed for the refrigerator system to maintain the magnets in their cold

superconducting state. Without superconductivity the SSC would need at least 4000 MW for its main rings!

The development of a large synchrotron with superconducting bending and focusing magnets was pioneered by Fermilab. The successful operation of the Saver/Doubler ring in 1983 and the Tevatron Collider complex, which had its first operational test of proton-antiproton collisions at a total energy of 1.6 TeV in October 1985, provides a firm technological foundation and proof that a SSC-like accelerator is feasible.

The success at Fermilab is being exploited in Hamburg, West Germany, where the Hadron-Electron-Ring Anlage (HERA), a proton-electron collider, is currently under construction, as mentioned in Section 2.1.4. The maximum proton energy will be 0.8 TeV, comparable to the Tevatron, with 4.7 tesla superconducting magnets patterned closely on the Fermilab design. This facility is expected to be operational in 1990.

While the technical basis for the SSC is well established, it was realized early that R&D effort was desirable to optimize the design for a cost-effective and reliable facility. The following sections describe briefly some of the issues and the associated R&D. A more detailed discussion of many of the subjects is given in the SSC Interim Report [2.4-1], and also in Attachment B to this report.

2.4.2 Magnet Development

Our understanding of superconducting accelerator magnets has matured in the last few years; the Tevatron is operating, HERA is under construction in Europe. Many model magnets have operated successfully and superconducting materials are much better understood. To produce a minimum cost SSC, the magnet-bore diameter must be reduced to the limits allowed by beam dynamics (See Section 2.4.4), and long magnets must be built using mass-production techniques. The R&D efforts of the past two years have clarified the issues of field strength, field uniformity, predictability and reproducibility of performance, and have led to a clear choice of magnet type for the conceptual design of the SSC.

Magnetic Components

Because reproducible, reliable, and long lasting bending magnets with good field characteristics are essential and are the single most costly technical component of the SSC, the magnet R&D effort has been considerable [2.4-2]. Initially, parallel efforts were pursued to explore a number of alternative styles of magnet. The various ideas (two magnetically coupled beam tubes and coils in a single thermally insulating cryostat; an iron-dominated, low field design; an improved design based on the Tevatron magnets) were explored to determine whether potential cost savings in construction and/or in operation of the accelerator were indeed realizable.

In the course of these efforts at the national laboratories (Brookhaven National Laboratory, Fermilab, Lawrence Berkeley Laboratory) and the Texas Accelerator Center, many short (1 meter) and long (4.5 meters and more) model magnets were built and tested. Figure 2.4-1 shows a sampling of test results on the peak field for six 4.5 m bending (dipole) magnets built at Brookhaven National Laboratory and eight 1.0 m dipoles from Lawrence Berkeley Laboratory. The data show that all the R&D magnets repeatedly achieved peak magnetic fields in excess of 6 tesla at 4.2 K after only a few cycles of bringing the magnet up to full power. Some small variation from magnet to magnet can be seen as a

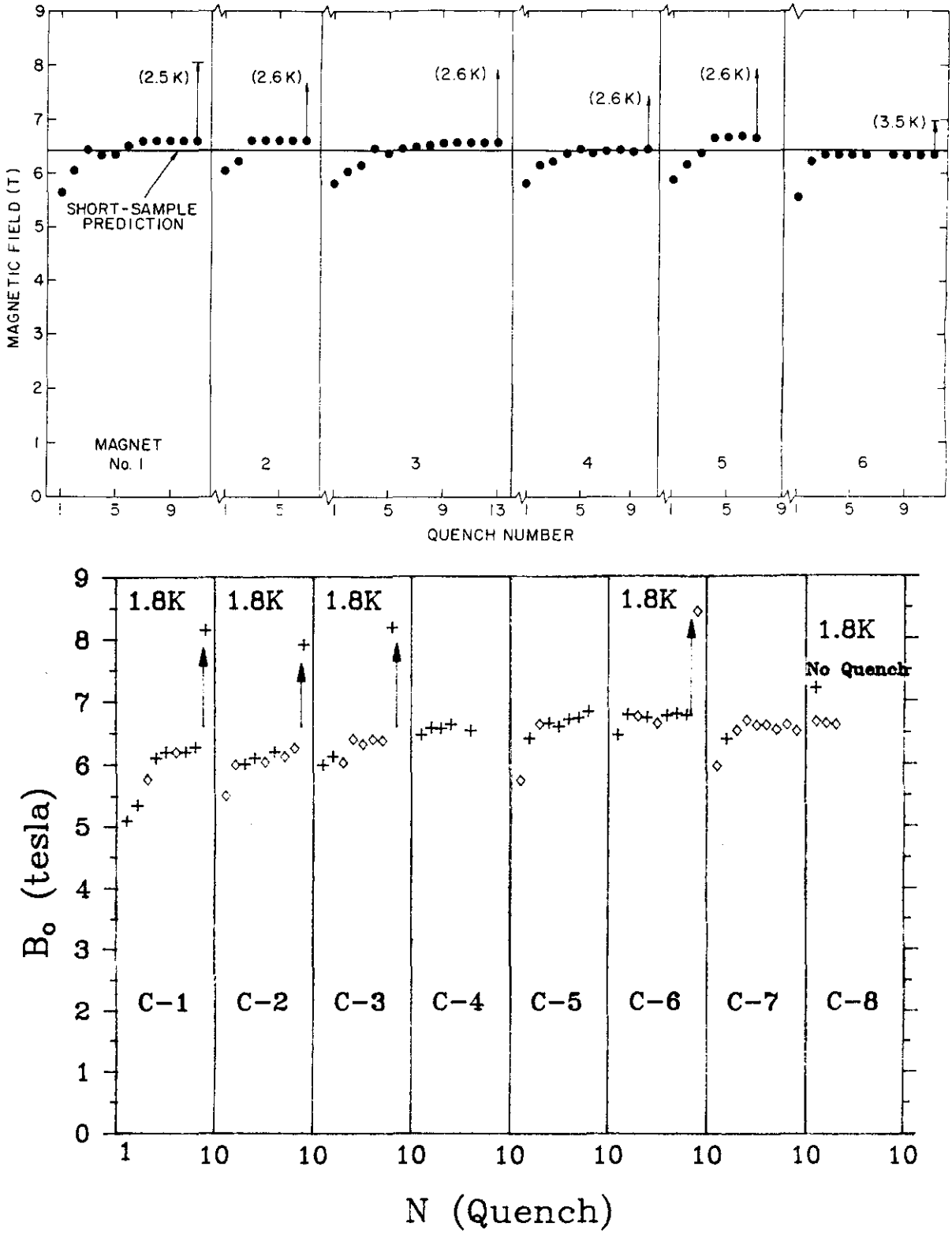

Figure 2.4-1. Peak magnetic fields attained at 4.2 K in model magnets upon successive slow rampings up in current. At top are data from six 4.5 meter "type D" model magnets made at Brookhaven National Laboratory. Below are the results for eight 1.0 meter "type D" models built at Lawrence Berkeley Laboratory.

consequence of different superconducting cables being used. The trend towards higher peak field with successive LBL models is a reflection of the improvement of the quality of the superconductor, as is discussed in Section 2.4.3.

A significant feature of these results is the evidence for higher peak fields at lower operating temperatures. The BNL models achieved fields close to 8 tesla when operated at 2.5 K rather than 4.2 K, while the LBL models exceeded 8 tesla at 1.8 K. Lower operating temperatures would permit an increase in the maximum possible field and energy of the protons for the same sized ring and the same magnets, although such operation would require increased refrigeration capacity.

The uniformity of the field in the bending magnets is important, as is the maximum attainable field strength. Small systematic departures from uniformity can be compensated by correction coils, but random departures because of inevitable small errors in fabrication cause nonuniformity of the field that varies randomly from one magnet to the next. Such variations must be kept within acceptable limits to have a successful accelerator.

The departures from the ideal of a uniform field are described in terms of multipole coefficients (a_n, b_n) which give the relative contributions of successive multipole fields (quadrupole, sextupole, etc.). A convenient unit of measurement of the multipole coefficients is $10^{-4}B_0$, that is, one part in 10,000 of the main dipole field at a radius of 1 cm. If multipole coefficients are kept to the order of magnitude of a few or less, in these units, the proton beams can be successfully guided through the confinement system without loss. See Section 4.3.

Data from a sample of six model magnets (type D, 4 cm aperture, 4.5 m long, built at Brookhaven National Laboratory) are shown in Fig. 2.4-2. The particular design has certain relatively small systematic multipoles that need not concern us here (since they are easily corrected for). The important question is reproducibility, in other words, the random errors or deviations found in a set of actual magnets. On the basis of the details of the magnet fabrication process and its various tolerances, a number of models were developed to permit estimation of the random errors. Model parameters were adjusted to fit the measured random errors of the Tevatron and CBA magnets and then make predictions for the SSC magnets. The rms deviations of the various multipole coefficients expected from this analysis are shown by the open circles and triangles in Fig. 2.4-2. The actual rms deviations measured for the integral field in the six BNL models are given by the solid circles and triangles. For the lowest 12 coefficients the measured random errors are all less than the predictions. (See Table 4.3-1.) For the highest order multipoles studied, the coefficients are zero within measurement errors.

Since the expectations of the models were the basis of the aperture studies described in Section 2.4-4, and the measurements indicate even smaller random errors, one can conclude that the manufacturing techniques are capable of producing many identical magnets of completely acceptable field quality, within tight tolerances.

The conclusions of the extensive R&D effort on model magnets are that the magnet performance can be predicted reliably, that model SSC magnets achieve the necessary peak field strengths and have adequate field quality for accelerator operation, that the magnet fabrication techniques assure reproducibility from magnet to magnet, and that these techniques are ready to be transferred to industry. On the latter point, it should be noted that, although the six Brookhaven 4.5 m model magnets were produced as prototypes in the

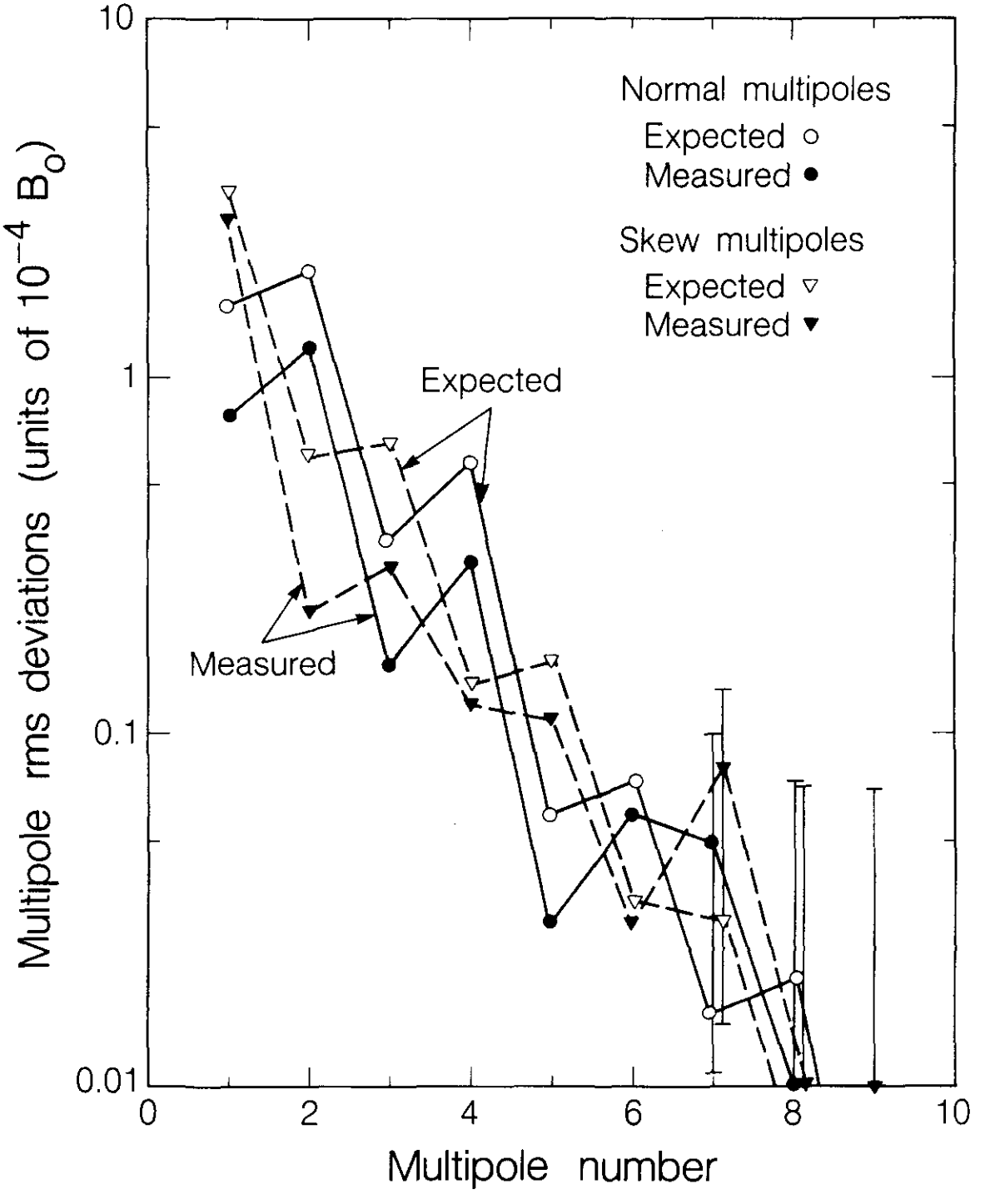

Figure 2.4-2. Expected and measured rms deviations of multipole coefficients b_n and a_n for the six BNL 4.5 m model dipole magnets of the style selected for the SSC. Within measurement accuracy, the actual multipoles are less than expected for all n.

laboratory, the fabrication methods and tooling were designed with large-scale industrial production in mind.

Detailed consideration of model magnet performance, commissioning and operation of the accelerator, and cost comparisons of the magnets and magnet-dependent systems led to the conclusion in September 1985 [2.4-3] that a high-field, 1-in-1 (one beam tube and coil assembly in one thermally insulating cryostat), collared-coil, cold-iron design (called type D) was preferred as the basis for the SSC conceptual design and for further development into the actual SSC magnet. A perspective drawing of the so-called single-phase package or cold mass, the parts of the assembly kept at liquid helium temperature, is shown in Fig. 2.4-3. The diameter of the assembly is 26 cm (~10 in.). The inner diameter of the inner layer coil is 4 cm (1.57 in.) and the inner diameter of the beam tube is 3.3 cm (1.3 in.). The design length of the magnet is approximately 17.3 m (57 ft). Roughly 7700 of these bending magnets and nearly 1800 focusing (quadrupole) magnets are needed for the two rings of the SSC collider. An important aspect of the continuing R&D effort, now that a specific magnet configuration has been chosen, is the optimization of the design for ease of manufacture and long life. For a detailed discussion, see Section 5.2 and Attachment B.

Cryostat Development

A superconducting magnet for an accelerator consists of a cold mass (beam tube, superconducting coils, stainless steel collars, and iron yoke), as shown in Fig. 2.4-3, installed in a cryostat or thermally insulating vessel. A cross section of the type D magnet is shown in Fig. 2.4-4. The cold mass has passages in it for the flow of the supercritical liquid helium that maintains the superconducting coils near 4 K. Nearby are liquid and gaseous helium return tubes. Outside an insulating jacket of aluminum and mylar layers that marks the 20 K boundary is the intermediate region of liquid nitrogen flow at 80 K. Beyond that are thick layers of insulation surrounded by the outer vacuum-tight jacket at room temperature (293 K). The weight of each cold mass, roughly 8 tons, must be supported by posts that extend into the warm outside world, but prohibit as much as possible the leakage of heat into the cold regions.

The Tevatron cryostats (of a different design, because the iron in those magnets is on the outside) have a heat leakage of approximately 1.5 W/m to the 4 K helium region. This heat must be conducted away from the coils by the circulating helium and so puts a load on the refrigeration system that must recool the heated helium for recirculation. Because of its greater size, a heat leakage of 1.5 W/m in the SSC would be unacceptable. In the Reference Designs Study it was calculated that the cryostat heat leak to the 4 K and 20 K regions could be reduced to an acceptable 0.2 – 0.3 W/m. Comparable amounts of heat are generated by synchrotron radiation (see Sections 4.7 and 5.3).

The R&D effort on cryostats has focused on the thermal and mechanical properties of the cryostat, with the aims of reducing the heat leak per unit length and of studying the cryostat behavior during thermal cycles. Careful attention to the properties of the multilayer insulation and its installation, as well as the design of posts with low thermal conduction, are essential to reduction of the heat leak. A successful program at Fermilab has demonstrated a thorough understanding of the behavior of the cryostat during warm up and cool down and also shown that heat leaks of the order of 0.25 W/m or less are achievable by careful design of the support posts and fabrication. A support post being readied for testing and the complete heat-leak cryostat test assembly are shown in Fig. 2.4-5.

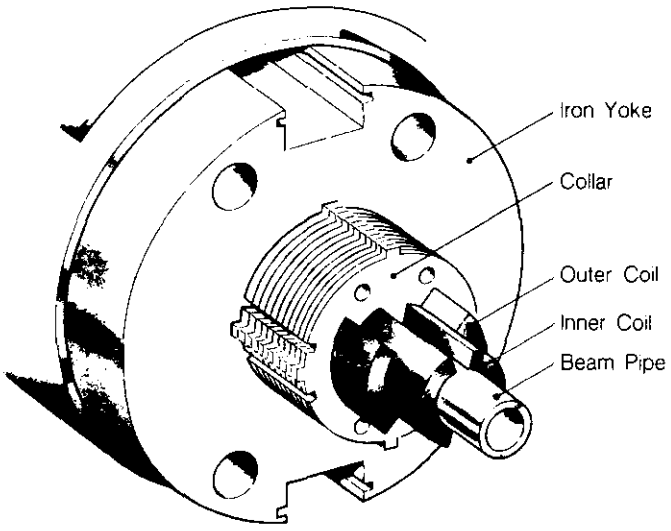

Figure 2.4-3. Perspective drawing of the inner (magnetic) components of the SSC dipole magnet. The iron yoke is 0.264 m (10.4 in.) in diameter.

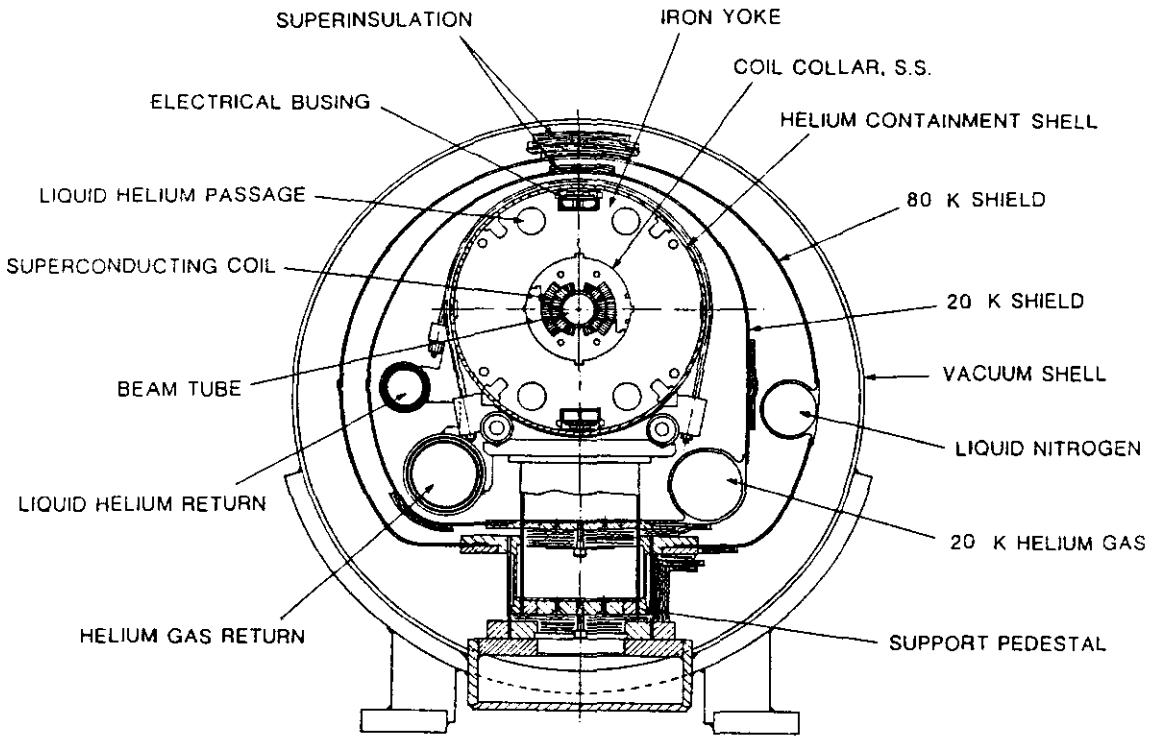

Figure 2.4-4. Cross section of the SSC dipole magnet assembly at a support post. The magnetic components are in a stainless steel helium containment vessel, surrounded by helium liquid and gas tubes, an insulating layer, a liquid nitrogen region, more insulation, and finally an outer vacuum shell of steel. The outer shell is approximately 0.61 meter (24 in.) in diameter.

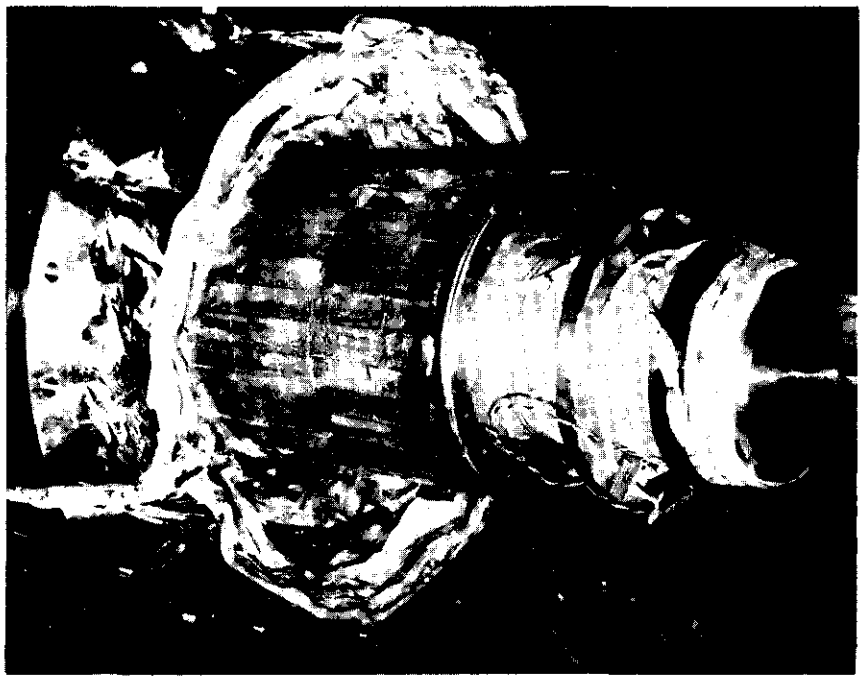

(a)

(b)

Figure 2.4-5. (a) Installation of a support post in the suspension heat leak measurement dewar. At this phase of the installation, the post is horizontal and the connection to the 20 K shield has been completed. (b) Heat leak model cryostat during final preparation for connection of the center section to the end vessels.

Further Development Efforts

The magnet R&D program, having established the primary goal of selection of a preferred type for further development, is now focusing on the optimization of detailed magnetic and cryogenic features of the design and on the building of a series of full-length models. The model magnets are to be tested as a combined system, as well as individually, to test quench protection devices, the vacuum system, connections between magnets, and other aspects of the cryogenics. It is envisioned that the systems test will evolve into an accelerator systems test facility for the engineering development of other technical components. A separate life test will provide data on magnet lifetimes under extreme conditions, not ever anticipated in accelerator operation. The model magnet fabrication and test program is aimed at optimization and engineering development of the magnets, now that the most important questions have been answered.

2.4.3 Superconductor Development

The exploitation of superconductivity on a large scale in accelerators like the Tevatron depended up on long-term, productive interaction among the accelerator building community, the scientific experts on superconductivity, the commercial suppliers of the basic materials, and the wire and cable manufacturers. The employment of superconducting magnets in accelerators, except for special purposes, has been slow in maturing because of the novelty and the intrinsic difficulties with the physical and magnetic properties of the materials. For a number of technical reasons, superconducting alloys are preferred for the winding of coils for magnets. Two alloys in particular were singled out for development, niobium-titanium (NbTi) in a 46%/54% ratio, and niobium-tin (Nb_3Sn). The Nb_3Sn compound has the advantages of higher maximum magnetic field at a given temperature and higher current carrying capacity at high field (and so requiring less superconductor for a given field), but is a brittle material, difficult to fabricate into wire and flexible cable. While R&D continues on Nb_3Sn and other materials, the superior mechanical properties of NbTi have made it the center of development.

The superconducting state of a sample in a magnetic field can be destroyed in a number of ways, one of which is a change of the magnetic field with time. To enhance stability of the superconducting state against the inevitable changes of the magnetic fields of an accelerator, it was found necessary to develop multi-filament strand. Such strand typically consists of thousands of NbTi filaments embedded in a copper matrix, with a ratio of one or two parts by weight of copper to one of superconductor. An enlargement of the cross section of a representative strand is shown in Fig. 2.4.-6.

A figure of merit of superconducting strand is the maximum possible current density J_c (in amperes per square millimeter, or A/mm^2) of the superconductor itself at 4.2 K and in a magnetic field of 5 tesla. The higher is J_c, the less is the amount of superconducting material needed for a given peak magnetic field. Since superconductor is expensive, there is a premium on increasing the current-carrying capacity of the NbTi alloy, provided the cost of the improvement does not cancel the savings from use of less superconductor. At the time of construction of the magnets for the Tevatron (1980–83), commercial strand had J_c in the range of 1800–1900 A/mm^2. In the Reference Designs Study (Spring of 1984) it was assumed that improvements in J_c would occur without significant cost increases to values of at least 2400 A/mm^2. This value was taken as the nominal SSC specification.

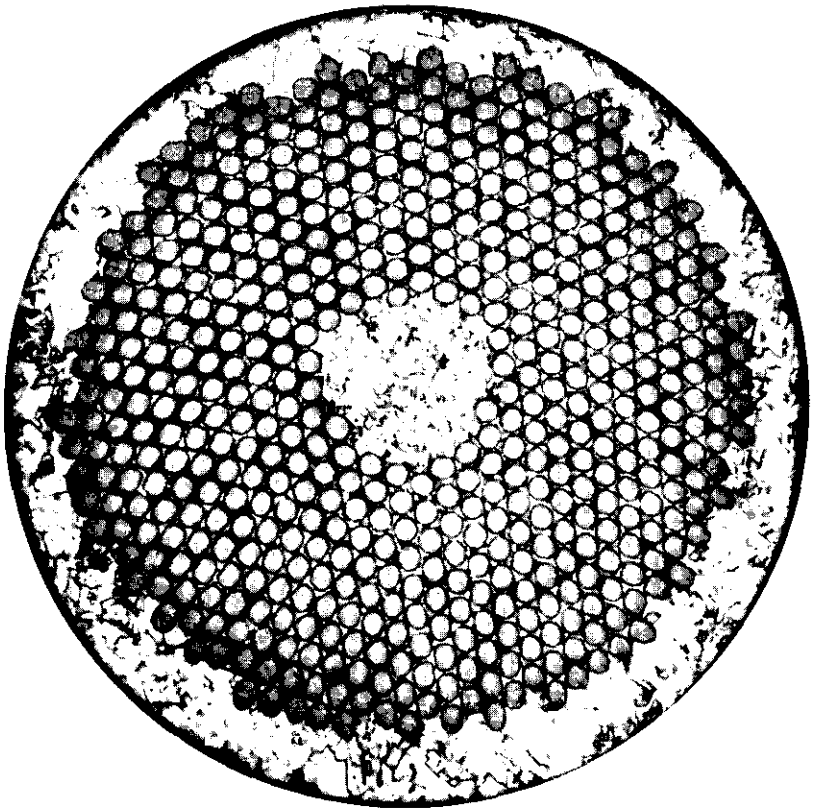

Figure 2.4-6. Microphotograph of multi-filamentary superconducting strand for SSC magnets. Overall diameter is 0.81 mm. The filament diameter is 20 μm, and the copper-to-superconductor ratio is 1.3:1. (Courtesy of Intermagnetics General Corporation)

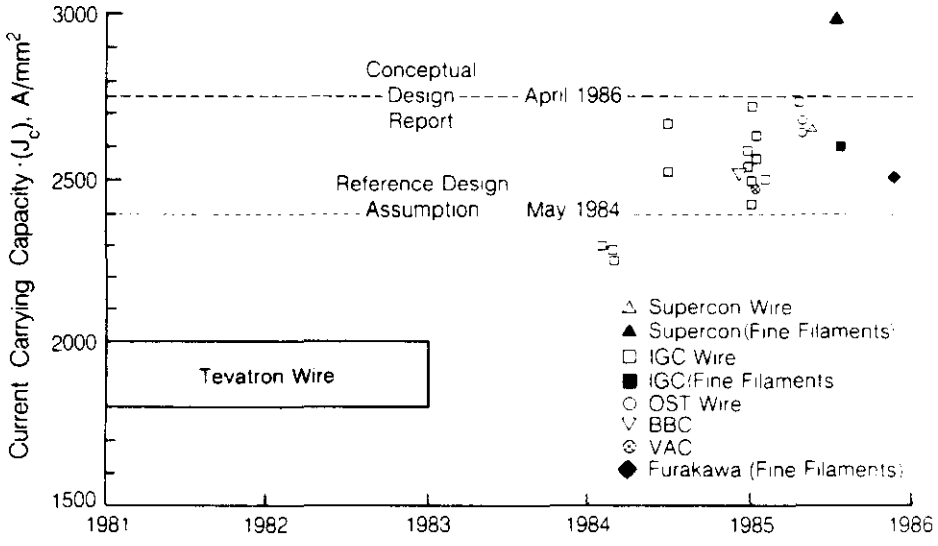

Figure 2.4-7. Achievable critical current density J_c of superconducting NbTi strand (in A/mm^2 at a temperature of 4.2 K and a magnetic field of 5 tesla) as a function of time. The lower rectangle represents the spectrum of values for the strand used in Tevatron magnets. The improvement in the past two years is striking.

Improvements in J_c

In the past two and one half years a DOE-funded R&D program aimed at superconductor improvements has been carried out jointly by national laboratories (Brookhaven National Laboratory and Lawrence Berkeley Laboratory), universities (University of Wisconsin), and industry. The program has been remarkably successful. Crucial areas for improvement were identified — reduction of the small ($\pm 5\%$) fine-scale fluctuations in the homogeneity of the NbTi alloy, greater care in the heat treatment and drawing processes, coating the NbTi rods with a thin barrier layer of Nb — then developed in the laboratory, largely at Wisconsin, and successfully transferred to industry.

A measure of the dramatic success of the program is shown in Fig. 2.4-7. The joint effort has produced a 50% increase in J_c, from the 1800–1900 A/mm^2 of the Tevatron strand to 2500–3000 A/mm^2, in the past two or three years. The nominal RDS value of 2400 A/mm^2 has been surpassed. Present SSC magnet design is based on 2750 A/mm^2.

Finer Filaments and Cabling

The SSC magnets must have a spatially very uniform field over a range of field strengths from 5% of full field to full field. Eddy currents that do not decay are induced in superconducting filaments when the field is changed. These persistent currents cause a distortion in the field that, for a given conductor, is roughly proportional to filament size. Such field distortions, which are most important at low field (injection), must be corrected if they are above some minimum level. While it is possible to put small coils along the length of the magnet on the outside of the beam tube to provide the correction, it is desirable to work towards finer filaments in the strand to make such coils minimal or unnecessary. Filaments sizes of 15–25 μm are now typical of regular strand; with it, persistent current effects need correction at injection. The R&D program for improvement of the superconductor therefore has as a goal the production of strand with fine filaments (as small as 2 or 3 μm in diameter), as well as higher maximum current-carrying capacity. The present design is based on 5 μm filaments.

Proper processing and quality control, as well as use of the thin barrier of niobium, has led to the production by several manufacturers of samples with fine filaments (2 to 4 μm in diameter) and excellent current-carrying capabilities. A U.S. company has achieved a sample strand with 3 μm diameter filaments and J_c of 3000 A/mm^2. See Fig. 2.4-7.

For use in the fabrication of magnets, strands must be wound into a cable of precisely controlled dimensions. The cable, typically 0.1 – 0.2 cm thick and 1 cm wide, is made up of 20 to 40 strands, wound in a spiral pattern, as shown in top half of Fig. 2.4-8. An enlarged cross section of a 23-strand cable for the model SSC magnets is shown in the bottom half of the figure.

R&D on cabling techniques has occurred at Lawrence Berkeley Laboratory as part of the SSC effort, with results transferred to industry. Production speeds of the order of 10 ft/min are presently attainable in the laboratory and in industry. Continuous lengths of cable up to 5000 ft are possible. Problems associated with winding cable having 30 or more strands by industry have been solved by mutual efforts.

The fine filaments strand presents a cabling problem. Practical limitations of how many NbTi rods can be put in a copper matrix and drawn down leads to very small strand (a few tenths of a millimeter in diameter). Even then there may be 4000 filaments inside. To make a cable of the desired dimensions, a two-step cabling process has been developed.

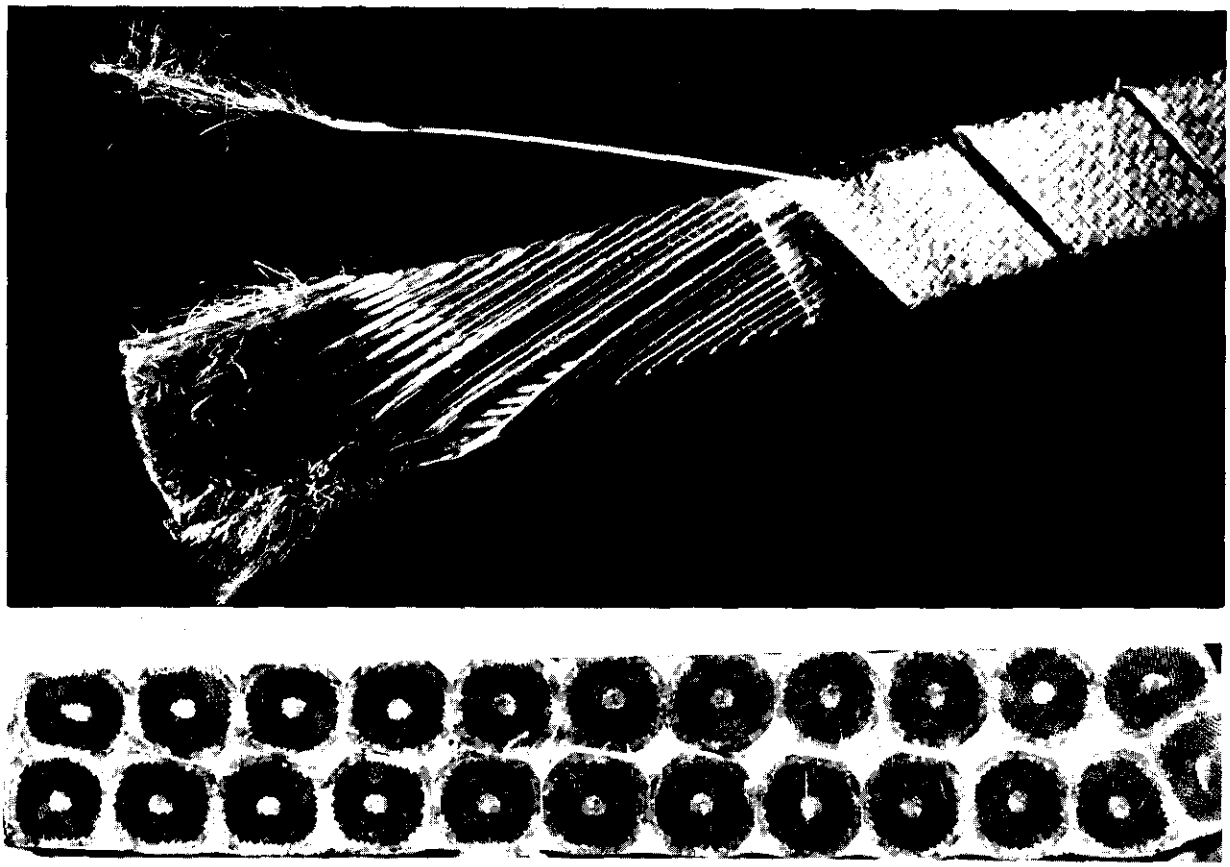

Figure 2.4-8. Enlargements of SSC superconducting cable. (Upper) Spiral wound cable of 30 strands, approximately 1 cm wide, wrapped with insulating tape. The ends of the strands have been etched in acid to remove the copper and reveal the NbTi filaments. (Lower) Cross sectional view of a 23 strand cable (enlarged approximately 16 times). The "keystone" shape conforms to the arch-like configuration of the cable in the dipole coils.

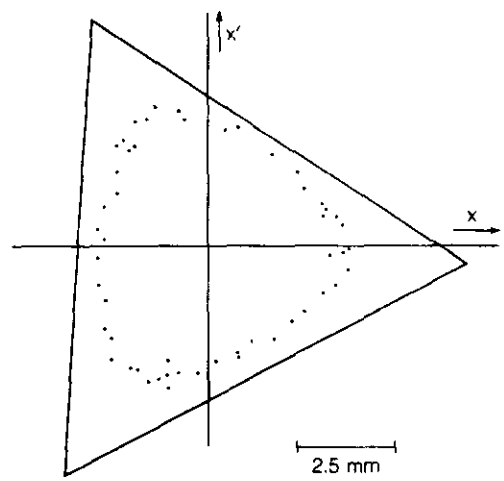

Figure 2.4-9. Horizontal position-velocity (x, x') diagram for displaced bunch motion in a Tevatron experiment. The dots represent the "positions" of the bunch on successive revolutions past the detector. The triangle shows the expected domain of stable operation for the conditions of the experiment.

An initial seven-strand cable of the fine filament wires with a copper core becomes the "strand" for a 23-element cable of the final SSC dimensions. The cable developments in the laboratory are transferred regularly to the industrial cabling firms by means of workshops.

Remarkable progress in raising the maximum current-carrying capacity of the strand and in creating strand with fine filaments has occurred in the past few years through the cooperative efforts of government, industry and the universities. This progress benefits the SSC directly in lower costs and greater simplicity. The increased current-carrying capacity also benefits other users of superconducting wire and cable, for example, the manufacturers of NMR medical imaging devices with superconducting magnets.

2.4.4 Beam Dynamics and Aperture

Successful operation of the SSC depends on the detailed understanding of the motion of thousands of bunches of protons accelerated in the cascaded accelerators of the injector and then accelerated and stored in the collider rings. The protons in the bunches make small excursions transversely and back and forth from the ideal position (in orbit and phase). Some of these deviations would be present in a perfect machine; others are induced by various initial conditions, perturbations and imperfections. If the departures from the ideal position are too great, the beam is lost.

The detailed study of beam motions is the domain of accelerator physics, the subject of Chapter 4. A central issue is the definition of the "aperture," the cross-sectional area within which the particle motion is stable. If the available area is large enough, the accelerator will operate without rapid loss of beam. If it is too small (relative to, say, the needs of the beam emerging from the injector), the beam will be unstable and will be lost by striking the walls of its vacuum chamber. Clearly, one wants a comfortably large aperture. This can be achieved in many ways — injecting a very high quality beam needing a small aperture, or having a large region of very uniform magnetic field transverse to the beam, etc. Such solutions cost money. Injection of a very high quality beam presumes an elaborate and expensive injector complex. Larger diameter magnets mean more cost in materials, more stored energy, more elaborate quench protection and cryogenic capabilities, etc. The aperture issue is thus a compromise. One wishes the smallest possible physical aperture (inside dimension of the evacuated beam pipe), consistent with adequate space for stable motion of the particles in the beam (dynamic aperture) both at full energy and at injection. Relevant are the random imperfections in the magnets, as well as the systematic departure of the magnetic field inside the beam pipe from its ideal form because of limitations in magnet design, and also errors in injection.

Detailed analytic and numerical methods have been used to study beam dynamics in the SSC and to determine appropriate physical dimensions for the beam tube under realistic assumptions about the magnet quality and reproducibility. Experiments have been undertaken at the Tevatron and at SPEAR to supplement and verify the numerical calculations. A sample of the results from one such experiment is shown in Fig. 2.4-9. The accelerator conditions were adjusted to enhance a particular type of beam motion having a three-fold symmetry in transverse velocity-position space. The beam was then displaced and its subsequent motion followed. The data show that the motion possesses the expected three-fold symmetry and is consistent with the predictions of theory.

The conclusion of the aperture studies and associated cost comparisons [2.4-4] is that a beam tube within a coil of approximately 4 cm (1.5 inches) inside diameter is adequate from the point of view of beam dynamics. The actual envelope of expected motion of the protons is approximately half as large. A detailed discussion of the aperture question and other accelerator physics issues can be found in Chapter 4.

2.4.5 Synchrotron Radiation and Vacuum

A charged particle moving at high speeds and bending in a magnetic field emits electromagnetic radiation, called synchrotron radiation. The energy radiated in each revolution must be replaced by the radio-frequency accelerating system. In electron accelerators, the synchrotron radiation loss is significant and is the ultimate factor that makes circular electron accelerators beyond a certain energy uneconomical (roughly 100 GeV beams, the ultimate energy of LEP). For proton accelerators, the situation is much less severe — for fixed radius of ring, the energy loss per turn is proportional to $(E/mc^2)^4$, where E is the particle energy and mc^2 is its rest energy. For the 50 GeV electrons in LEP, the ratio is $E/mc^2 = 10^5$. Because of their much larger mass, the 20 TeV protons of the SSC give a ratio only 1/5 as large, even though their energies are 400 times larger. In fact, the SSC will be the first proton accelerator in which the synchrotron radiation is at all significant.

Making up the radiated energy is no problem for the rf system, but the radiation does have an impact on the cryogenic system and the vacuum. A 70 mA beam of 20 TeV protons circulating in the SSC will radiate about 9 kW in synchrotron radiation. The power (approximately 0.13 W/m) is dumped directly onto the wall of the cold beam tube. The helium flow must carry this heat away from the 4 K region, placing another burden on the refrigeration system. A total of 18 kW from the two beams necessitates about 10 MW of refrigerator capacity, roughly 60% of the total cryogenic load at 4 K.

In addition to the added heat load, the synchrotron radiation, whose broad spectrum consists mainly of soft x rays in the 100–300 eV range, causes gas molecules (H_2, CO, CO_2) present in the metal of the beam tube to be ejected into the vacuum. If sufficient gas is knocked out, the quality of the vacuum can be affected and the lifetime of the stored beam reduced because of collisions with the gas molecules.

This photon-induced desorption of gases from metallic surfaces at liquid helium temperatures has previously been studied very little. It presented a potential expense of unknown magnitude and complexity, if severe. The solution in electron synchrotrons, where the phenomenon is severe, is straightforward — distributed pumping around the room-temperature beam tube. At liquid helium temperatures, the beam tube is a priori a superb "pumping" device because gas molecules strike the wall and attach themselves. But in the presence of the synchrotron light the molecules get knocked off again and drift slowly about, intercepting the beam.

To assess the seriousness of the effect, it was necessary to mount a series of experiments at the National Synchrotron Light Source (NSLS) at Brookhaven National Laboratory. Warm and cold tubes were evacuated and exposed to a beam of synchrotron radiation from the NSLS vacuum ultraviolet ring, adjusted in impinging angle to simulate the radiation in the SSC. (See Fig. 2.4-10.) Two mass spectrometers coupled to the dummy beam tube, as shown in the bottom half of Fig. 2.4-10 were used to analyze the gases desorbed by the radiation. Preliminary results indicate that some desorption of gases does

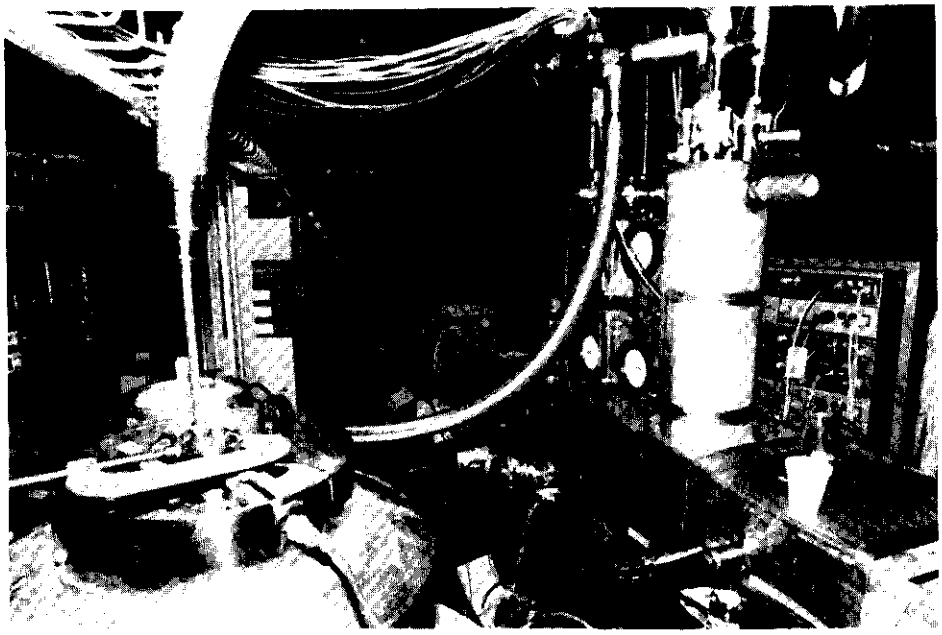

(a)

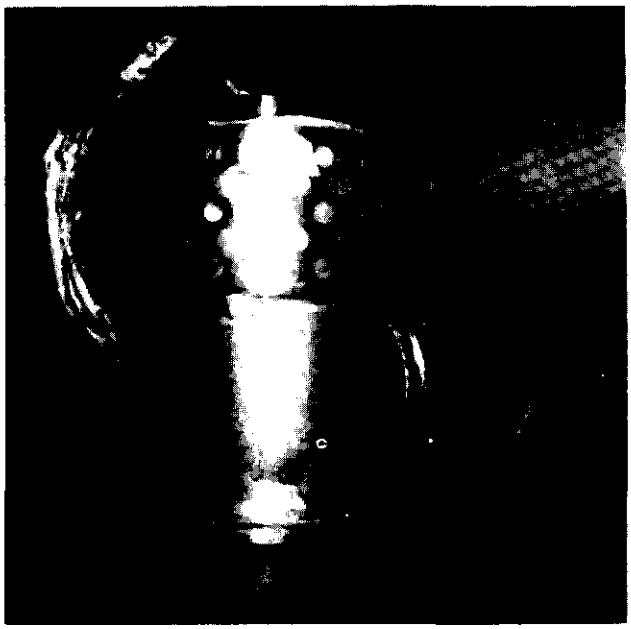

(b)

Figure 2.4-10. (a) Photodesorption experiment. Beam of synchrotron radiation comes from the rear into the rectangular box holding the cold beam tube and its cryostat. (b) Close up of the two mass spectrometers attached to the beam tube. These devices measure the amount and mass composition of the molecules knocked out of the wall of the beam tube by the synchrotron radiation.

occur, but that the effect will not cause difficulty. For example, based on these measurements, the lifetime of the beam from scattering by desorbed hydrogen gas (the most abundant of the various species) is estimated to be in excess of 300 hours. Since beam lifetimes from other causes are expected to be in the range of 24–48 hours, the contribution to beam decay from desorbed hydrogen is of little consequence. Other gases contribute negligibly.

Further experiments at Brookhaven and a parallel series in Japan with different beam pipe materials will provide additional data. It is clear already that photodesorption by the synchrotron radiation is not a vacuum problem requiring major attention.

2.4.6 Conclusion

The technical base for the SSC is provided by the successful operation of large accelerator complexes around the world. The SSC system is a cascade of accelerators of the type for which extensive operational experience exists. It differs from its predecessors only in scale and numbers, but not kind, of its technical components. In its use of superconducting magnets it builds on the experience of the Tevatron at Fermilab. The chosen magnet style, while different in some features from the Tevatron magnets, is a natural evolution of that magnet in its most important part, the high-field collared-coil assembly.

While much detailed engineering design and development remains to be done for the SSC, the ten year R&D program in the U.S. and abroad that led to the Tevatron, as well as intensified efforts of the recent past, have established the technical basis for a practical conceptual design and accurate cost estimate.

References

2.3-1. Working Groups on Testing the Standard Model and Beyond the Standard Model, in Proc. 1982 DPF Summer Study on Elementary Particle Physics and Future Facilities, June 28–July 16, 1982, Snowmass, Colorado, eds. R. Donaldson, R. Gustafson, and F. Paige, Division of Particles and Fields, American Physical Society, p. 1–49, 155–297.

2.3-2. E.J. Eichten, I. Hinchliffe, K.D. Lane, and C. Quigg, Reviews of Modern Physics **56**, 579 (1984).

2.3-3. Physics Section of Proc. 1984 DPF Summer Study on the Design and Utilization of the Superconducting Super Collider, June 23–July 11, 1984, Snowmass, Colorado, eds, R. Donaldson and J.G. Morfin, Division of Particles and Fields, American Physical Society, p. 1–303.

2.4-1. SSC Central Design Group, "Interim Report," SSC-SR-1011 (June 1985).

2.4-2. "Supercollider R&D: The First Two Years," URA booklet (December 1985).

2.4-3. F. Sciulli et al., Report to the Director of the SSC Central Design Group, SSC Magnet Selection Advisory Panel, September 9, 1985.

2.4-4. Aperture Task Force, SSC Central Design Group Report No. SSC-SR-1013 (August 1985).

3. Collider Concepts

As the energy needed for experiments has grown, the increasingly wasteful technique of bombarding a stationary target has been supplanted by the more effective method of collisions between oppositely directed beams of high energy particles. Such devices are known variously as accelerator-colliders, accelerator-storage rings, or just colliders. They embody the same general components as any modern accelerator complex, but have the capability of bringing into collision oppositely moving beams of particles. Existing and planned high-energy colliders are listed in Table 2.1-1. These facilities are now the focal points of research in high energy physics. The recent history of the field has been dominated and paced by their ability to open up new energy domains for experimentation.

The present chapter is intended to give an introduction to collider concepts and the SSC. The first section describes in elementary terms the major components of a modern synchrotron and their workings. It then presents ideas and basic definitions providing an introduction to the accelerator physics of colliders described in more detail in Chapters 4 and 5.

The second section (3.2) is a review of the Tevatron accelerator at Fermilab. In its collider aspects the Tevatron is similar to the earlier $Sp\bar{p}S$ at CERN. It is an essential example for the present discussion because the Tevatron is the first accelerator-collider to make extensive use of superconducting magnet technology, an example the SSC is to follow.

The SSC itself is described broadly in Section 3.3, both in terms of the technical components of the accelerator and how they are brought to bear on the task of providing high-luminosity collisions and in terms of the physical layout and conventional systems. The last two sections treat questions of reliability and projected availability of the SSC for physics research and the setting, environment and radiation.

3.1 Accelerator Physics of Synchrotron Colliders

To understand the nature of the SSC it is useful to describe in elementary terms the workings of the various components of any modern accelerator-storage ring complex. At the SSC experimenters will study the collisions of oppositely directed bunches of protons. As discussed in Section 2.1.4, such collisions are much more efficient in utilizing the energy of the beam particles than the bombardment of a stationary target in the laboratory. The

bunches are slim cylinders 5 micrometers or less in radius and about 15 centimeters in length along the line of collision. Each bunch contains about 10^{10} protons. Because of the small probability for proton loss during the collision, these bunches can pass through each other repeatedly for many hours without need for replenishment. This is accomplished in a storage-ring collider by causing streams of bunches to counter-circulate on closed paths which intersect head-on, or at a small angle, at the desired interaction points. Several such colliders, based on the synchrotron principle, have been built. While it will attain a beam energy 20 times the highest achieved so far, the design of the SSC follows the principles established by previous machines.

3.1.1 Synchrotron Components

The synchrotron accelerator is a direct descendant of the cyclotron, using magnetic fields to guide the charged particles in a closed path and repetitive acceleration to increase their energy, but incorporating essential discoveries made in the 1940s and 1950s. A synchrotron has three basic sub-systems: (1) A source of the charged particles, which usually includes some early acceleration before injection into the synchrotron, (2) a magnetic confinement system, and (3) an accelerating system. These are shown schematically in Figs. 3.1-1 and 3.1-2.

Source

The basic source of protons to be accelerated is a small volume of ionized hydrogen gas from which the charged nuclei (protons) are extracted by suitably arranged electrodes and emerge with kinetic energies of a few keV (Fig. 3.1-2, top left). Such a beam is slow moving and quite divergent. For these reasons it is common practice to preaccelerate the beam from the ion source before introducing it into the synchrotron. This is accomplished initially by static electric fields and then by one or more linear accelerators whose radio-frequency electric fields cause the accelerated particles to cluster in bunches as they gain energy (Fig. 3.1-2, top center and top right). Typically the beam is carried to an energy of several hundred million electron volts (MeV) before transfer to a synchrotron.

Confinement System

The deflection of a charged particle by a magnetic field provides the mechanism for steering and confining a beam as its energy is increased or as it is stored at fixed energy. The bending radius of a magnetic guide field is related to the energy of the particle and the field strength according to

$$R(\text{km}) = \frac{10\,E(\text{TeV})}{3\,B(\text{tesla})} \qquad (3.1\text{-}1)$$

When allowance is made for the spaces between bending magnets for focusing magnets and other equipment, the average physical radius of an accelerator can be up to 50% larger.

The language of optics is used to describe the deflection and focusing of particle beams. The dipole bending magnets are the prisms, while the quadrupole focusing magnets are the lenses of the beam-optical system. The dipoles have a uniform magnetic field perpendicular to the plane of the synchrotron ring and produce a constant deflection of the beam in

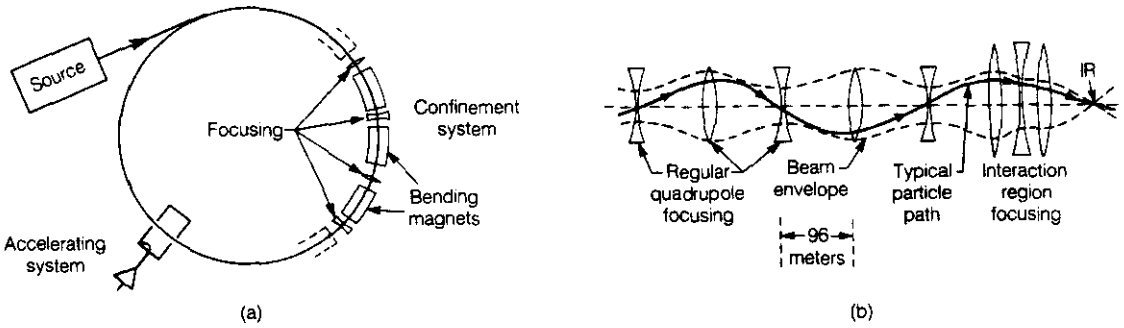

Figure 3.1-1. (a) Schematic diagram of the major components of a modern synchrotron. (b) Diagram of the focusing parts of the magnetic confinement system. Optical lens symbols are used for the magnetic elements. In the SSC, each "lens" is actually a quadrupole magnet over 3 meters long. Not shown between successive quadrupoles are the dipole bending magnets. For the SSC, the quadrupole separation is 96 meters (315 ft), with room for 5 bending magnets.

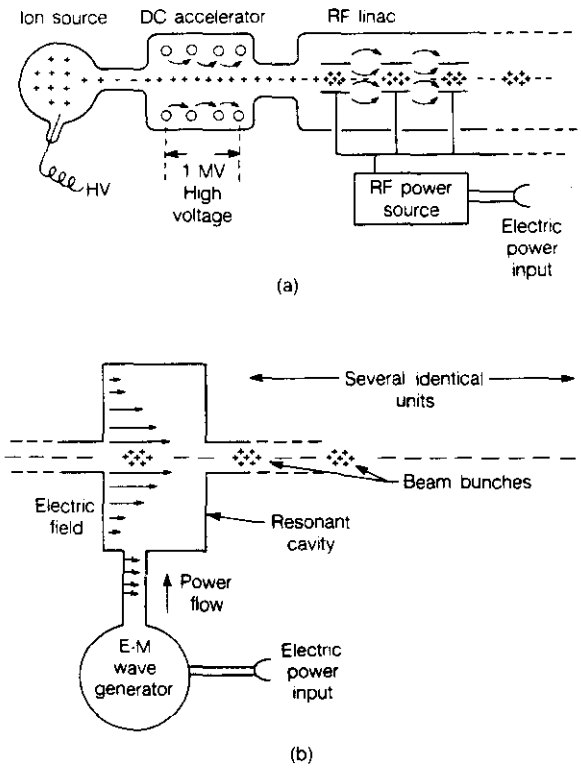

Figure 3.1-2. (a) Schematic diagram of the proton source and early stages of acceleration. Ions are accelerated electrostatically through approximately 1 million volts, and then by radio-frequency fields in one or more linear accelerators. (b) Sketch of one of the main ring radio-frequency accelerating cavities. The proton bunches pass through the cavity at the right time to be accelerated by the oscillating electric field.

the plane. The stronger the field, the smaller is the radius of curvature, for a fixed particle energy. The focusing quadrupole magnets are so constructed that the magnetic field strength is zero at the very center line and grows in proportion to the distance from the axis. Particles passing exactly along the equilibrium orbit then are undeflected in traversing the focusing magnet. Particles traversing it off axis are deflected in proportion to how far off center they are. By this proportionality of deflection to displacement, the particles are focused into a beam of the needed size.

As indicated with the use of convex and concave lens symbols in Fig. 3.1-1, the focusing magnets are alternately focusing and defocusing. (Actually, things are a bit more complicated. A "focusing" magnet (convex lens symbol) focuses particles in, say, the horizontal direction and defocuses them in the vertical direction, while a "defocusing" magnet (concave lens symbol) does the opposite.) By alternating the sense of the focusing magnets, beams can be focused simultaneously in both directions This scheme was discovered in the 1950s to produce much smaller excursions or oscillations of the particles away from the equilibrium orbit and permit smaller beam tubes and smaller magnets than in the weaker focusing scheme then in use. Near the points where the beams are to collide, extra strong lenses are used to focus the beam to a very high density thereby enhancing the luminosity and reaction rate, as indicated schematically in Fig. 3.1-1, bottom right.

This scheme of separate bending and focusing magnets is remarkably tolerant to alignment errors as the equilibrium orbit tends to follow the centers of the focusing magnets. Over a length of about 1 km along the orbit, alignment errors of individual focusing magnets centers need be better only than about 0.5 to 1 mm. On a larger scale, drifts in the average position of the centers can be considerably more, subject, of course, to the condition that the ring close on itself.

If the focal lengths and positions along the orbit of the quadrupoles are chosen correctly, a particle with the same momentum as one on the designed orbit will perform a stable oscillation about that orbit. This situation is depicted in Fig. 3.1-1(b). For historic reasons, this motion is called a betatron oscillation. Its frequency and other characteristics are governed by the strengths and separations of the quadrupoles. The prescription for stable oscillation is surprisingly simple: the distance between quadrupoles along the orbit must be less than twice their focal length. The design for the SSC collider rings that is described in Chapter 4 has the quadrupoles of the long arcs placed at intervals equal to their focal length.

The magnet arrangement is called the lattice of the synchrotron; the state of motion of the oscillations is described by the "tune." The tune is actually a pair of numbers, like 82.42 and 82.38, that indicates the number of cycles of oscillation in the horizontal and vertical directions the particles undergo in one turn around the machine. It is a feature of the alternating scheme of focusing that the tune must be picked carefully so that the powerful focusing features of the scheme are not spoiled by resonant blow-up of the beam.

Accelerating System

Acceleration, or increase of the beam's energy along the orbit, is accomplished by transformer action, indicated schematically in the bottom of Fig. 3.1-2. The beam particles typically gain an energy of several MeV each time they pass through the acceleration system. The electric current of the beam flows in the secondary circuit of the transformer while the primary is driven by a radio-frequency cavity whose dimensions are adjusted so

that it resonates electrically at the driving frequency. The frequency must be a multiple of the rotation frequency of particles in the ring in order that they receive the proper acceleration each time they come around. Particles in the beam pass through the accelerating system at slightly different times and so receive greater or lesser energy gain than the mean. If their departures from the mean are not too great, on successive passages they oscillate back and forth around the mean. This is the principle of phase stability that is the defining characteristics of the synchrotron. Such oscillations in energy and phase of passage through the accelerating system are called synchrotron oscillations. It is a consequence of the acceleration scheme that the circulating beam consists of a series of short bunches some distance apart.

An acceleration arrangement appropriate for the SSC has component parts quite similar to those used in electron colliders. (See Fig. 3.1-3.) Modern acceleration systems are so efficient that the entire cavity array for the SSC main rings will occupy a length of only 25 m along the orbit, one such system for each ring.

Cascade of Accelerators

Given the basic sub-systems, how does a modern synchrotron accelerator function? Particles from the source, after acceleration to several hundred MeV kinetic energy in a linear accelerator, are transferred to a synchrotron. During this injection phase the magnetic field of the synchrotron's confinement system is held constant at the value corresponding to the injection energy and the radius of the ring. When the requisite number of protons have been transferred, the magnetic field is increased and the beam energy grows in proportion through the action of the acceleration system. If the synchrotron is to be used as a collider, the magnetic field is increased to a value corresponding to the desired beam energy and then held constant for many hours, even days, while the beams collide and slowly attenuate. When the reaction rate has become too small to be optimal, the beam is extracted from the ring and the acceleration and storage process is repeated.

The protons that make up the beam inevitably have some natural divergence, that is, they have some small component of momentum transverse to the direction of the desired orbit and require focusing. The ratio of this small transverse component to the momentum along the orbit is the angle which the particle trajectory makes with the wanted path. As the momentum along the equilibrium orbit is increased by the acceleration system, this angle decreases, which, together with the increasing magnetic field, results in a decrease in the transverse beam size compared to that at injection. Because an important part of the cost of the confinement system is proportional to the volume occupied by magnetic field, for high energy synchrotrons it is economically advantageous to use a series of synchrotrons with successively increasing top energies and decreasing apertures, rather than a single synchrotron to accomplish the full span of acceleration required. For this and other technical reasons the ratio of top energy to injection energy of a synchrotron is usually designed to be somewhere between 10 and 100, although higher ratios have been used successfully. The large proton accelerators at Fermilab and at CERN, Geneva each consist of a cascade of accelerators, and so will the SSC.

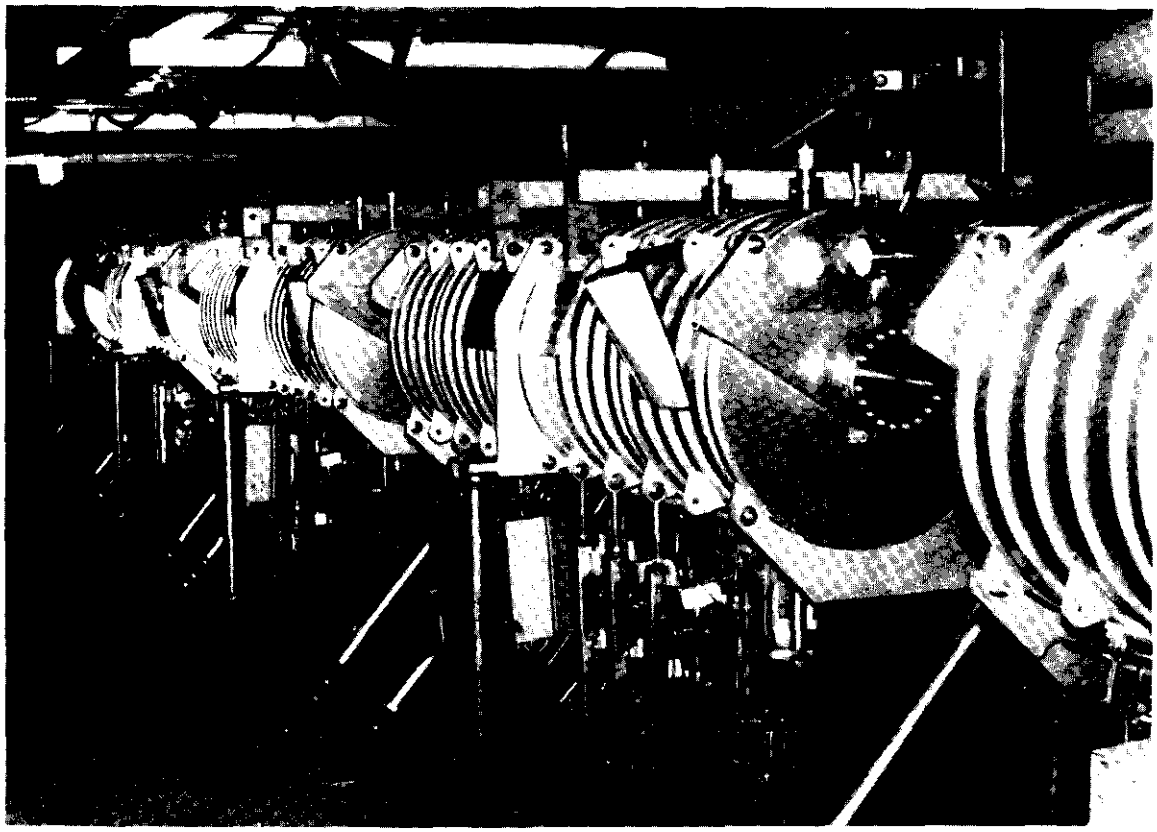

Figure 3.1-3. One of the rf accelerating units of the PEP electron-positron accelerator-storage ring at Stanford University. The SSC main ring unit will be essentially the same.

3.1.2 Basic Collider Definitions

Luminosity

In a discussion of colliders, it is appropriate to set down a reasonably precise definition of luminosity and show how it is related to some of the other principal parameters. Suppose two bunches of particles collide head on. Each bunch contains N_B protons and presents the same transverse area A to the other. For the moment, assume that the particles are uniformly distributed within the area A. Then, any particle in one bunch will "see" a fraction $N_B\Sigma/A$ of the area of the other bunch obscured by the interaction cross section* Σ of the N_B particles in the other bunch. The number of interactions per bunch-bunch passage is $N_B^2\Sigma/A$. If the frequency of collisions is f, then the interaction rate is

$$R = f\ N_B^2\Sigma/A \tag{3.1-2}$$

The luminosity $\mathscr{L}$ is defined as the interaction rate per unit cross section and is a characteristic of the collider,

$$\mathscr{L} = f\ N_B^2/A \tag{3.1-3}$$

The transverse density distribution of a real bunch is not uniform; depending on the form of the distribution, the effective area A will change. For the SSC, the distribution at an interaction point is that of a cylindrical Gaussian beam. The particle density horizontally (x) or vertically (y) from the beam center is described by the product of two Gaussians having the same standard deviation, σ.

$$dN(x,y) = \frac{N}{2\pi\sigma^2}\, e^{-x^2/2\sigma^2}\, e^{-y^2/2\sigma^2}\, dxdy \tag{3.1-4}$$

The summing of the contributions to the luminosity over x and y yields an effective area of $4\pi\sigma^2$. If we also express the frequency of bunch-bunch encounter, f, as the ratio of the bunch spacing, S_B, to their speed, which for these calculations is indistinguishable from the speed of light c, then Eq. (3.1-3) becomes

$$\mathscr{L} = N_B^2 c/4\pi\sigma^2 S_B \tag{3.1-5}$$

and it is with this form that the detailed discussion of Chapter 4 begins.

Emittance

The luminosity expression must be evolved one more step to exhibit its dependence on the basic parameters. The quantity σ characterizing the beam size depends both on intrinsic features of the beam and on the optical environment in which the beam is placed. That relationship is discussed in Section 4.1.2; here we only state the result,

*The unconventional usage of Σ for cross section here and subsequently is to avoid confusion with the many uses of σ for rms properties of the beam.

$$\sigma = (\epsilon_N \beta^* / \gamma)^{1/2} \tag{3.1-6}$$

where ϵ_N is the normalized beam emittance and $\gamma = E/mc^2$, the ratio of the particle's total energy to its rest energy. These two quantities are beam characteristics. The other factor, β^*, expresses the ability of the beam optical system to minimize the beam size at the interaction point. The smaller the value of β^*, the closer the beam approaches the (unattainable) limit of a true focus.

With the use of Eq. (3.1-6), the luminosity becomes

$$\mathscr{L} = \frac{\gamma N_B^2 c}{4\pi\beta^* \epsilon_N S_B} \tag{3.1-7}$$

What one might loosely call the quality of the beam is expressed by the single parameter ϵ_N. This emittance is the rms area (divided by π) in a one-degree-of-freedom phase space for one of the transverse coordinates. If there were no coupling to the other two degrees of freedom and there were no perturbations at work to increase the emittance, then ϵ_N would be an invariant of the motion. Neither of the conditions of the last sentence is true, of course. The benefits of a small emittance for luminosity can only be realized if that small emittance is achieved and preserved in the face of processes that seek to increase it. This preservation is a major concern of accelerator physics and engineering.

Intensity Dependent Effects

A variety of dynamical effects that are negligible or nonexistent at low beam intensities require attention in any present day synchrotron. The production of luminosity is itself an intensity dependent effect, and indeed impacts the beam lifetime in a way that is nearly unavoidable. Particles leaving the interaction region that have undergone elastic or inelastic interactions can deposit their energy in the superconducting magnets; protective measures similar in spirit to those used in the Tevatron will be necessary in the SSC. But additional phenomena deserve introduction in this subsection.

Intensity dependent effects arise because the particles interact with each other, mostly through electromagnetic fields. Often the electromagnetic interaction occurs through the intermediary of the vacuum chamber through which the beam propagates. In a collider, there are single beam effects and beam-beam effects.

One single beam effect is the space charge repulsion of the protons traveling together within a single bunch. This repulsion adds a defocusing gradient to the focusing forces of the quadrupoles. The gradient is strongest for particles traveling near the center of a bunch. As a consequence, the betatron oscillation frequencies of individual particles are shifted by varying amounts depending on the location of a particle within a bunch. An excessive spread in frequencies can lead to beam loss or emittance dilution from magnetic field imperfections, as discussed in Section 3.1.3. But for the parameters of the SSC collider rings, the effect is small. Space charge is an important consideration in the injector design, as is shown in Section 4.10.

The most celebrated of the beam-beam phenomena arises from the same space charge repulsion considered in the preceding paragraph, but now it is the space charge due to the particles in one bunch acting on particles of another bunch during a bunch-bunch collision.

In effect, a bunch presents a nonlinear lens to the particles of another. The consequent spread in betatron oscillation frequencies is a fundamental consideration in the design of electron storage rings, with their intense bunches, but is of less concern for the SSC.

The passage of a bunch through the vacuum chamber will set charges in motion in the chamber walls. The fields created by these wall charges can in turn act back on the particles of the bunch that created them, or on particles of subsequent beam bunches. These interactions can cause a rich set of so-called coherent instabilities in which bunches display a variety of oscillatory modes that grow in amplitude until either beam loss occurs or sufficient emittance growth stabilizes the oscillation. The accelerator physics design of Chapter 4 includes provisions for rendering these instabilities innocuous, by suitable design of the vacuum chamber, by adjustment of such beam characteristics as momentum spread, and by the use of beam feedback systems.

The statistical effects of scattering of particles within a single dense bunch can also be a source of emittance growth. This intrabeam scattering makes an important contribution to the decay of luminosity with time in the $S\bar{p}pS$ collider at CERN.

3.1.3 Magnet Field Quality and Aperture

The bending magnets of a proton collider represent a significant fraction of the total project cost. The magnet cost grows with the size of the aperture provided for the beam, so while it is essential that the aperture be large enough to permit the performance specifications of the collider to be achieved it is also important that it not be excessively large. Some of the considerations that play a role in the aperture decision are outlined here.

Fields in Superconducting Magnets

A bending magnet is supposed to produce a uniform magnetic field throughout the beam pipe and if the diameter of the coil of the magnet shown in Fig. 2.4-3 could be made arbitrarily large, the field quality would approach that ideal. For realistic magnets, one must accommodate to the circumstance that there will be field nonuniformities or "errors."

Field errors in superconducting magnets can arise for several reasons. First, the individual conductors in the coil are not quite where they are designed to be. This leads to field errors that differ from one magnet to another — so-called random errors. Field nonuniformities at the level of a part in a hundred thousand are dynamically significant. It is remarkable that the conductors of superconducting magnets can be positioned with the exacting tolerances needed to attain this level of uniformity.

Second, even if the fabrication of a magnet were done to perfection, it can still exhibit field nonuniformity due a peculiar property of superconducting materials. Once a superconducting filament (see Fig. 2.4-6) has been penetrated by a magnetic field, current will still flow after the field has been removed. Since no net current is required of the coil (the magnet is "off"), current in one portion of the filament will be balanced by an oppositely directed current in another portion. Current densities are high, at the critical value. These persistent currents are exactly that — they will remain indefinitely so long as the coil is superconducting. The resulting field is reminiscent of the remanent magnetization of a conventional magnet. As discussed in Section 2.4.3, the use of finer filaments can reduce the distortions caused by persistent currents.

Broadly speaking, a field imperfection produces a steering or a focusing error — of course, the second could be considered to be a special case of the first, but the distinction is useful. Steering errors deflect the centroid of the beam. Focusing errors perturb the beam size, and if sufficiently severe, can lead to beam instability. Because a beam particle will sense a given field imperfection on each turn around the collider ring, instability from a resonance between the focusing and imperfection forces is a major (and standard) concern.

Correction Magnet System

Modern synchrotrons contain large numbers of auxiliary magnets that act in conjunction with the main magnets to provide the requisite effective field uniformity. They are also used to make adjustments in accelerator parameters as operational conditions change.

Since today's synchrotrons depend upon their correction systems, an analysis of the magnet aperture problem must take the auxiliary magnets into account. Just as there is a cost penalty for making the main magnet aperture too large, so also there is a penalty for making the correction system too complex. The greater burden placed on correction magnets leads to more effort in main magnet measurement, increased capability of the beam diagnostic system, an expanded control system, and so on. One of the tasks of the accelerator physics design effort is to identify the proper balance between field uniformity requirements for the main magnets and the functions to be demanded of the correctors.

Physical, Dynamic, and Linear Aperture

In the accelerator context, the word aperture has several meanings, and for clarity, is often preceded by an adjective. For a bending magnet, the physical aperture is the inside of the beam pipe. The dynamic aperture is the region through which particles may propagate and remain in stable motion; this is the aperture as described in Section 2.4.4. The dynamic aperture depends only on the magnetic fields, and, in principle, could be larger than the physical aperture. It depends on the fields throughout the entire ring and is not necessarily related in a straightforward way to the properties of a single magnet.

Within the dynamic aperture, there is a smaller region in which the motion of particles approximates the behavior of a beam in a ring of perfect bending magnets and achromatic lenses. This region is referred to as the linear aperture, and is the space in which the beam is intended to be normally found. The simplicity of particle trajectories in this regime makes for easy analysis of beam conditions in an operating accelerator.

The dynamic and linear apertures are explored, during the design stage, by extensive computer simulations. A model of the synchrotron is developed, in which every main magnet is endowed with unique field imperfections. Particles are then followed by the computer through the thousands of magnets in the accelerator for turn after turn. In the case of the dynamic aperture, one is looking for the limiting amplitude of oscillation beyond which the motion becomes unstable, with the particles quickly diverging from the central orbit. In the case of the linear aperture, motion approaching that of a simple harmonic oscillator is the goal.

Aperture requirements — physical, dynamic, and linear — are based on calculations and on observations and experience with existing synchrotrons. Input on anticipated field imperfections is derived from measurement data on superconducting magnets. The numerical simulations are then used to develop insight into the dependence of the dynamic and linear aperture on the magnet coil diameter, on the functions performed by the correction

system, and on such key parameters as quadrupole spacing and focal length. These matters are the subject of much of Chapter 4.

3.1.4 Lattice

The detailed description of the way in which magnets of various sorts and strengths are placed to form the ring of a synchrotron is conventionally called the lattice. The lattice of all but the simplest of accelerators generally is built from a number of pieces with more or less identifiable separate functions. In order that the ring have reasonable optical properties, the pieces are fitted to each other by a process called matching.

The standard cell is the primary bending and focusing unit of a ring. For all large synchrotrons, it consists of a quadrupole, an interval containing mainly bending magnets, a quadrupole of opposite focusing character from the first, and a second set of bending magnets equal in length to the first. This pattern of so-called FODO cells would form a complete lattice if replicated until it closed on itself.

The interaction region contains the optics necessary for producing the near-focus at the crossing point and the bending magnets to bring the beams together, or sketched schematically in Fig. 3.1-1(b). The purpose of matching can perhaps be clarified at this point. The limiting excursions of a betatron oscillation are described by a function of position around the ring called the amplitude or beta function, β. The separation between orbits of differing momenta is given by another function of position, called the dispersion function, η. Both the standard cell and the interaction region have, at their boundaries, values of the amplitude and dispersion functions intrinsic to the structure of each. Matching consists of ensuring that at the point where the two units join, the value and slope of the two functions for each unit are the same. When that condition is satisfied (in both transverse dimensions) the betatron amplitude and dispersion functions of the combined system are the same throughout as those for the individual units. When the condition is not met, a mismatch is said to occur, and in general the functions will oscillate about their matched values as one proceeds through the lattice and so periodically become larger than would otherwise be the case.

The interaction regions are located in the experimental areas of the collider. The purpose of the standard bending cells is just to return the beam time after time to the interaction regions. There need be only one variety of standard cell, but there may well be a demand for several types of interaction regions, adapted to particular experimental situations. One of the interesting lattice design challenges for a high luminosity collider is the devising of flexible interaction region layouts to meet changing needs with a fixed set of components.

The third distinct lattice element is the utility module. The utility modules contain those accelerator systems that are too extensive or demanding in terms of special requirements to fit into other spaces in the lattice. Injection and beam abort are the two main examples. Both processes are associated with at least occasional beam loss and so protection of superconducting magnets is needed in the neighborhood of these systems.

3.1.5 Luminosity Lifetime

Storage Cycle

The first readily identifiable step in the storage cycle is the filling of the collider rings with protons from the injector. Before this step, however, there will be a period devoted to systems tests and checkouts. Its duration depends on operational experience, but as a practical matter, it must be short in comparison to the time length of the operational cycle.

The last synchrotron in the injector chain to the SSC rings is another superconducting accelerator, with a circumference more than a factor of ten less than that of one of the two collider rings. If the acceleration cycle of the injector is a minute, it may require three quarters of an hour to fill the two collider rings.

For rings on the scale of the SSC, a leisurely acceleration period of 20 or 30 minutes will not impose excessive demands on the radio-frequency or cryogenic systems, nor place too great a tax on the overall cycle. After acceleration, a similar time may be needed to establish colliding beam conditions at the several interaction regions.

Collider operation will need a storage time on the scale of a day to be efficient. The short term instability questions have received commentary above; the slow processes with a long time scale must now be addressed.

Factors Affecting the Lifetime

From Eq. (3.1-7) it can be deduced that a reduction in luminosity can only be due to loss of particles or an increase in emittance. The two effects are related. For instance, in the collision of two bunches, a pair of protons may interact so strongly that they vanish from the beam or so weakly that their amplitudes of betatron oscillation grow by a small amount.

Two other collision processes are at play. Protons may strike residual gas molecules in the vacuum chamber, or they may encounter their neighbors in the same beam bunch. These encounters can lead to particle loss or emittance growth. In the case of collisions within members of the same bunch, the relative energy of the particles is so low that the interaction is one of simple Coulomb scattering.

The last significant factor is synchrotron radiation. If a charge is accelerated, whether its energy is being changed or not, it radiates energy in the form of electromagnetic waves. At very high energies, where the speed of the particles approach that of light, the rate of energy loss to radiation is enhanced, especially in circular motion. This synchrotron radiation process is unimportant in the Tevatron, but the situation changes at the higher energy and magnetic field of the SSC. It has a significant impact on the cryogenic system. Detailed discussion is given in Sections 4.7 and 5.3.

The emission of energy via synchrotron radiation has the remarkable consequence of damping betatron and synchrotron oscillations. In electron storage rings, the rate of damping is fast, with oscillation amplitudes halved in ten milliseconds or so. The SSC will be the first proton accelerator to be impacted by this damping effect. Oddly enough, the shrinkage of emittance caused by the synchrotron radiation in the SSC can lead to an increase of luminosity with time. The luminosity versus time curve that is shown in Fig. 4.6-3(a) rises for a time comparable with a day, reflecting the dominance of the synchrotron radiation. Eventually, a combination of the other processes conspire to produce luminosity

reduction. After a total time of about two days the luminosity is back down to its value at the beginning of the storage cycle.

3.2 Review of Tevatron Parameters and Components

3.2.1 Design Outline

Context and Initial Decisions

When the Fermi National Accelerator Laboratory and its accelerators were designed in the late 1960s, it was too early to give serious consideration to the use of superconducting magnets in the main proton synchrotron, for the necessary technology was in its infancy. But space was reserved in the Main Ring enclosure and in the service buildings for the eventual addition of a superconducting synchrotron. Because the "supermagnets" might be expected to reach twice the field of their room-temperature counterparts, the superconducting ring was called the Energy Doubler.

After high energy physics experiments were underway in 1972, it became possible to devote some attention to the Doubler idea. A major factor in the design context was already settled: the superconducting synchrotron would occupy the same tunnel as the Main Ring. A number of other design principles were established at the very outset, a few of which are relevant to the SSC and deserve mention here. The decision to use a cold beam tube was controversial at the time; today it is the natural choice. A warm iron magnet design was chosen, but the debate over the relative virtues of cold or warm iron still continues and successful magnets have been constructed with both approaches. The decision to use NbTi was (and remains) a recognition of the state of technology.

The superconducting magnet designs of that time were quite unsuited to the needs of a large synchrotron. Nor was there an established production base for filamentary NbTi in the volume or quality required. A substantial research and development program was necessary, focused almost exclusively on the magnets and their cryogenic system. The evolution and verification of a successful magnet design for a mass production environment led to the construction of over 200 full scale prototypes.

In 1978, after six years of concentration on magnet development, it became possible to expand the Doubler effort to include the design of the entire accelerator-collider synchrotron. The research and development program terminated in 1979 with the publication of a design report that served as the basis for the accelerator construction project. A detailed account of the Energy Doubler, the first synchrotron to use large-scale superconducting accelerator magnet technology [3.2-1], has recently been published [3.2-2]. The synchrotron was eventually designated the "Tevatron". Both the older and newer names are used here.

Development of the Fixed Target Design

For Fermilab, one concern dominated all others. Could beam extraction be performed so efficiently that beam particles striking the magnets would not cause a superconducting-to-normal transition?

For use in high energy physics experiments with stationary targets, the beam is removed from the synchrotron by a process called resonant extraction. After the beam of

over 10^{13} protons has been accelerated, the particles are gradually spilled from the ring at a rate of about 10^7 per turn. The delicate control needed to coax such a small fraction of the protons out on each orbit is provided by nonlinear magnetic fields that excite a resonance in their motion. The particles leaving the circulating beam encounter the entrance to an extraction channel and are separated from those that will remain within the ring by a material boundary. Inevitably, some particles strike this boundary (septum), producing secondary particles that can deposit their energy in superconducting magnets downstream.

The fact that the Energy Doubler would occupy the same enclosure as the Main Ring implied that the magnet disposition of the Doubler would be a near-replica of the resident synchrotron. An exact reproduction of the Main Ring optics would lead to energy deposition exceeding permitted bounds above by a factor of fifty to a hundred. Fortunately, it was not necessary that the superconducting ring duplicate its predecessor exactly bend-for-bend and lens-for-lens. By introducing conventional bending magnets in the neighborhood of the extraction septa, local orbit modifications were made that reduced losses from inelastic interactions by an order of magnitude. Similarly, a modification in the focusing order of the quadrupole lenses spread the beam out as it approached the extraction septa and so improved the extraction efficiency. Finally, collimation was introduced within the arcs to intercept particles that had undergone elastic scattering in the primary septum.

Thus, the ring as constructed was a hybrid: mainly composed of superconducting magnets, but with a vital admixture of traditional steel and copper hardware.

Transformation to a Collider

In the mid-1970s, the growing appreciation of the potential of hadron colliders added an additional function to the requirements for the superconducting ring. It should perform as a storage ring as well. Though there was a period during which proton-proton collisions involving the Main Ring and the Doubler was contemplated, the decision finally fell in favor of proton-antiproton collisions in the Doubler.

Interestingly enough, the potentially vexing question of magnet aperture had been settled by the slow extraction requirement. The 7.5 cm inner diameter of the coil was fixed in 1975 following an analysis of the aperture and field quality needed for resonant extraction. It was judged that magnets of the resulting design would be adequate for single particle stability during beam storage.

Rather, the main issue raised by the additional application was a good deal less subtle; namely, where yet another set of functions was to be put within the existing tunnel. A major colliding beam experiment needs space surrounding the beam tube for a detector some 20 meters in length, and on either side there must be strong quadrupole lenses to reduce the beam area at the interaction point. In short, at least one or two of the six long straight sections permitted by the tunnel geometry would have to be reserved exclusively for colliding beam physics, with the accelerator and fixed-target physics systems compressed into the other regions in both the Main Ring and the Energy Doubler.

The layout of the Main Ring and Energy Doubler is shown schematically in Fig. 3.2-1. and a short summary of the principle design parameters is given in Table 3.2-1. The ratio between peak beam energy and injection energy may look surprisingly low, but this is simply a consequence of the Doubler sharing the tunnel with the Main Ring and so having a high energy injector available. Some of the other parameters are discussed in Section 3.2.3, when we compare performance to date with expectations.

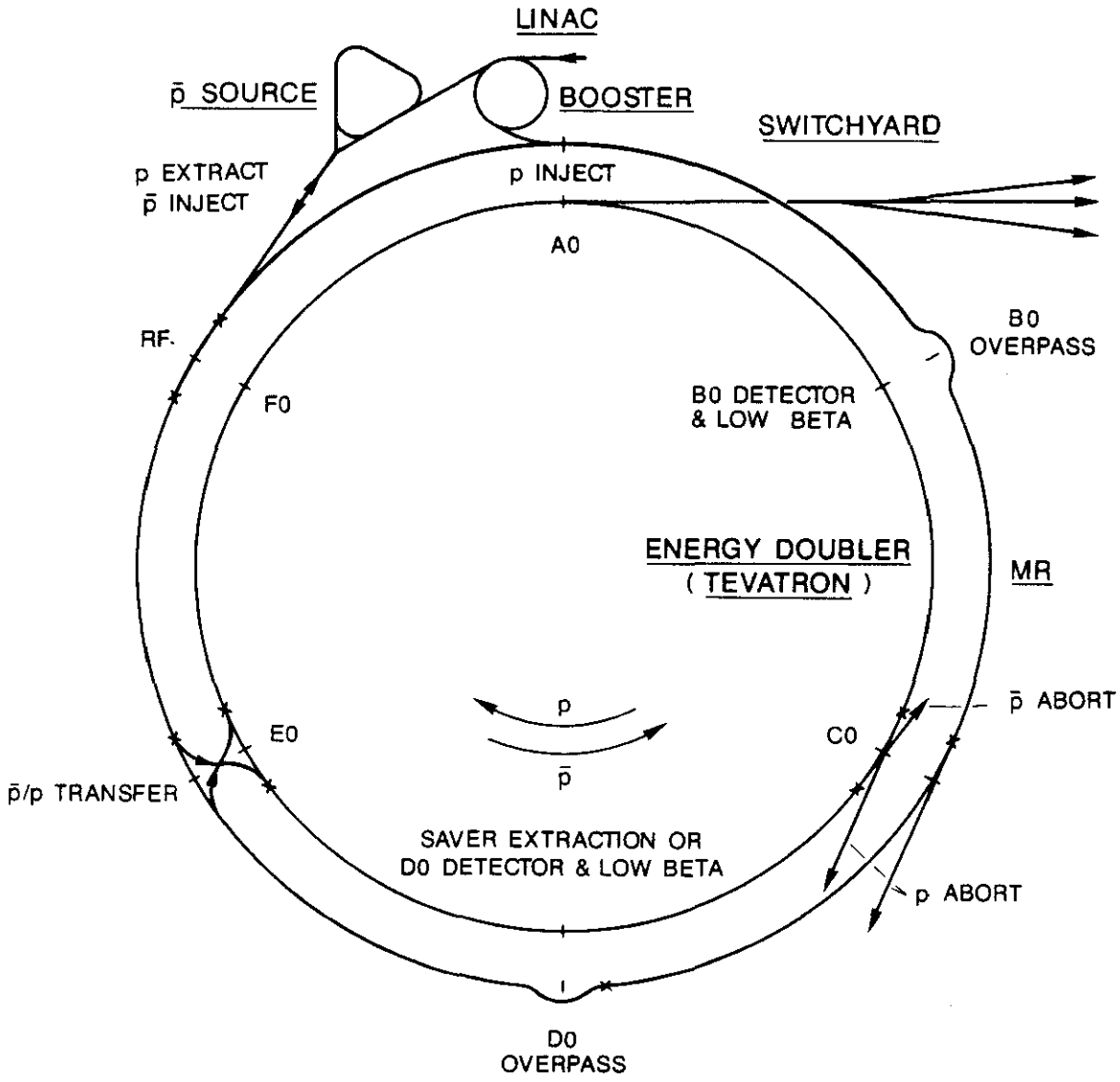

Figure 3.2-1. Tevatron accelerator including the new antiproton source rings and the Energy Doubler. The straight sections are labeled A0 through F0. A0 and D0 are needed for extraction, with D0 as a colliding beam area as well. B0 is the other dedicated colliding beam area. Injection occurs at E0; rf acceleration at F0. Beam abort is at C0.

Table 3.2-1
Tevatron Parameters

General	
Accelerator radius	1 km
Peak beam energy	800–1000 GeV
Injection energy	150 GeV
Bend magnetic field at 1000 GeV	4.4 tesla at 4400 Amperes
Beam emittance ϵ_N (rms)	4 mm mrad
Fixed target	
Intensity	$\sim 2 \times 10^{13}$ protons/cycle
Acceleration rate	50 GeV s^{-1}
Cycle time	60 s
Slow spill duration	20 s
Fast spill	5 pulses at 2×10^{12} protons
Collider	
Intensity per bunch	6×10^{10} expected
Number of bunches	3p, $3\overline{p}$
Luminosity	10^{30} $cm^{-2}s^{-1}$
Storage time between fills	$\sim$ 4 h
Amplitude function β^*	1 m (x,y)

3.2.2 Components

The main special design features of a superconducting accelerator are, of course, the magnets themselves and the cryogenic system to cool them. But other systems are required to assume new roles in the superconducting ring. For example, the magnet power system must take on the primary burden of protecting the magnets if they quench. The vacuum system must provide thermal insulation for the cryostats in addition to establishing the empty space in which the beam circulates. Finally, a higher standard of reliability is demanded of the conventional accelerator systems, in order to compensate for the inevitable maintenance demands of the the components at the frontier of technology. For details, see [3.2-2].

Superconducting Magnets

The potential benefits of superconductivity for synchrotron magnets are high field in a compact package with low power consumption. As the Energy Doubler design effort began, high field meant 4.4 tesla, a figure twice that of the Main Ring.

At present, the superconducting magnet complement of the Energy Doubler includes 774 bending magnets (dipoles), 210 quadrupoles, and 720 small correction and adjustment elements. The main bending magnets are the dominant magnetic element. The standard dipole is 6.4 m long and 38 cm by 25 cm in cross section. The evacuated beam pipe runs

the length of the magnet through its center, and the vertically-oriented magnetic field deflects the protons and antiprotons by an angle of 8.1 mrad.

A transverse section of the magnet is shown in Fig. 3.2-2 (compare Fig. 2.4-4). Just outside the square beam tube, there is space for the liquid helium that cools the inner edge of the coil. Each of the many small rectangles in the coil represents the cross section of the cable. The coil is clamped by stainless steel collars in a highly reproducible, accurate configuration that does not distort during magnet excitation. There are additional spaces for liquid helium flow between the outer surfaces of the collared coil assembly and the enclosing tube. The next annular region contains two-phase (liquid and gas) helium flowing in the direction opposite to that of the single-phase fluid and extracting heat from the interior. Successive annular regions consist of an insulating vacuum, a path for liquid nitrogen, and a second insulating vacuum with aluminized Mylar insulation. The whole magnet-cryostat assembly is vacuum tight. It is held in a laminated iron yoke that contributes some 18% to the total magnetic field. The cryostat is precisely adjusted relative to center with suspension blocks of epoxy-fiberglass laminate and preloaded suspension cartridges that allow for contraction and expansion during the thermal cycle.

Measurements on superconducting cable for the Doubler magnets gave an average critical current density in the NbTi of 1800 A/mm^2 at 5 T and 4.2 K. Taking into account the magnet geometry, field, and operating temperature of 4.6 K, one finds that this critical current density should permit the magnets to achieve 4.6 T. All magnets prior to their installation in the ring were measured under two different excitation conditions, "quench" and "cycle". In the first test, magnets were ramped at 200 A/s until a quench occurred. In the second test, repetitive ramps approximating the accelerator cycle were used and the peak current was gradually increased until the quench limit was found. The results [3.2-2] indicate that excitation of the ring in the 900–950 GeV range should be possible with only a few magnet replacements, whereas to reach 1 TeV will probably require either very slow ramps or cryogenic modifications.

Cryogenics

The helium refrigeration system is the world's largest. It consists of a large helium liquefier, a nitrogen reliquefier, a distribution system for the cryogens around the ring, and 24 satellite refrigerators spaced around the ring. These components can provide a total of 24 kW of cooling at 4.7 K for the magnets as well as liquid helium for power lead cooling and liquid nitrogen for the cryostat heat shields.

The satellite refrigerators are located directly above the tunnel and feed helium and nitrogen directly into the magnet string below. The flow is split and goes upstream and downstream (with respect to the proton beam) through typically 16 dipoles and associated components in each direction. Throughout this outward flow, the helium is in a single subcooled liquid phase; it is this helium that is in direct contact with the magnet coil. At the end of the string, the helium passes through an expansion valve which lowers its temperature and pressure. These new conditions are adjusted so that the helium is a boiling liquid at a temperature of about 4.5 K, one or two tenths of a degree lower than the temperature of the single-phase fluid. The two phase fluid is directed back through the string of magnets and absorbs heat from the outgoing stream. Thus each magnet is a counterflow heat exchanger. The ratio of gas to liquid in the two phase path increases as the distance to the refrigerator feed point decreases, but the temperature remains nearly constant. Energy

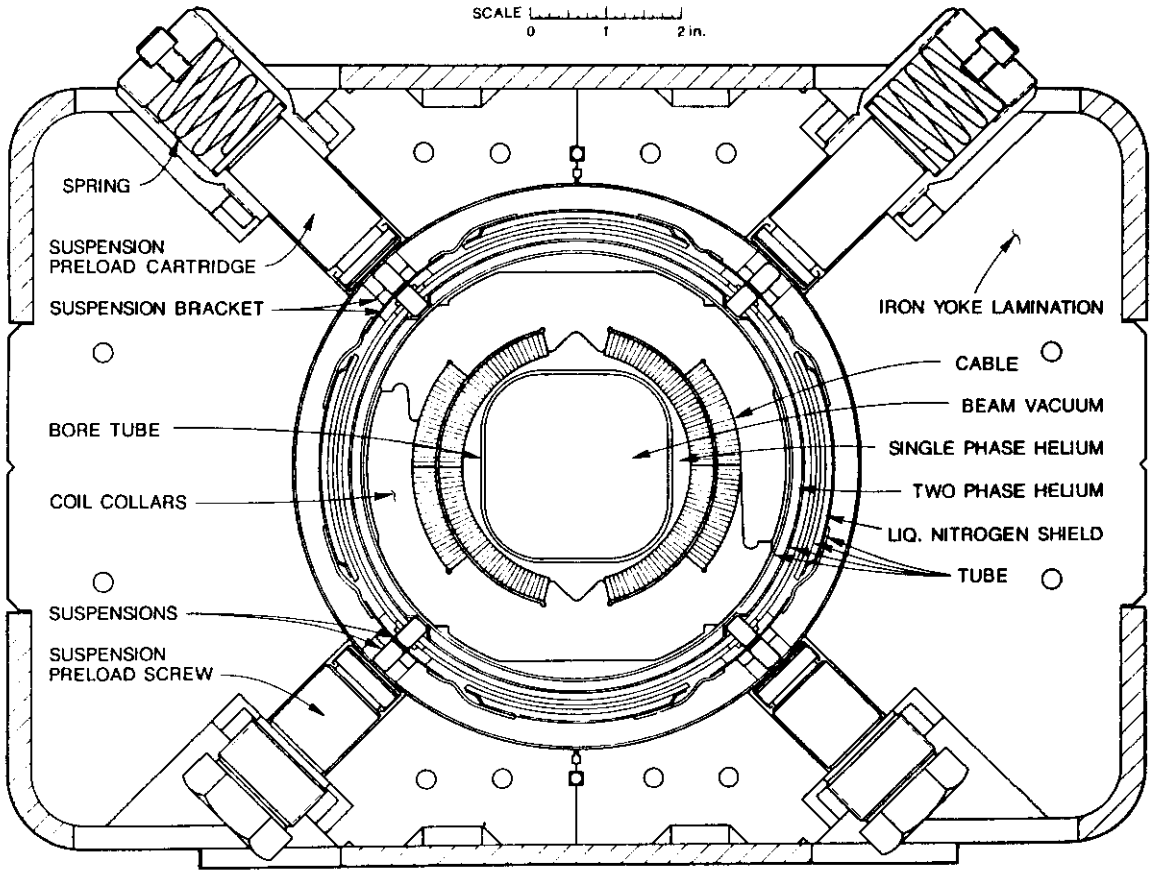

Figure 3.2-2. Cross section of the Energy Doubler dipole magnet showing the collared coil assembly, the cryostat, and the warm iron yoke.

generated in the coil is thereby removed efficiently by the single-phase liquid and absorbed as heat of vaporization in the two-phase region. Nitrogen for the magnet shields makes a single pass to the ends of each string, where it is discharged into a nitrogen header as 92 K gas.

The central plant plus satellites arrangement offers a wide variety of operating conditions, and provides the redundancy necessary to the continuous operation of the synchrotron. In "satellite mode," the central plant supplies large amounts of cold helium to the magnet strings and thus to the return side of the satellite heat exchangers. The excess flow in the satellite heat exchangers results in 1 kW of refrigeration from the satellites without use of their gas expansion engines. At the other end of the spectrum is the "stand-alone mode". Here, without the availability of helium from the central plant, each satellite is able to deliver 450–500 W of refrigeration plus 25 liters per hour of liquid helium. This capability is adequate to compensate the static heat load of the magnets. A variety of intermediate cases are possible depending on the availability of helium from the central plant.

Power System and Quench Protection

The magnet power system plays the dual roles of powering the main dipole and quadrupole magnet string and protecting these same magnets from the stored energy in the magnetic field should any fraction of the superconductor in the whole ring become normal (resistive) for any reason. Because this system requires quick detection of quenches and consequent action of electrical components in order to save the magnets from self-destruction, it is called "active" as opposed to one that might require little or no external action, that is, a "passive" system.

The main dipole and quadrupole magnets form a single series circuit, in which the 12 power supplies are uniformly distributed. Each power supply is capable of ramping to 4500 A at 1 kV. Since the resistance of the circuit is small (but not zero, for there are conventional magnets in the circuit), a single well-regulated unit is able to handle the load during particle injection, flattop, or storage conditions.

Our main interest here lies in the quench protection aspect of the system. Consider what happens in the cable of a magnet coil when a "normal zone" appears during operations as a result of a number of causes, and current transfers from the NbTi to the copper in which the superconductor filaments are embedded. The copper, which now conducts most of the current, has too high a resistivity to prevent further heating, and the cable will melt unless some means is found to remove the current expeditiously. A peak allowable temperature of 460 K is specified in order to protect the numerous soft-solder splices and the silver-tin coating on cable strands. At the maximum operating current, there is less than one-half second available for removing the magnet current to prevent permanent damage.

The magnets and their interconnections are divided into 24 quench protection units and continuously monitored for a resistive voltage component. Once the onset of a quench is detected, the power supplies are turned off, and the current is shunted through dump resistors at the supply locations. The resulting exponential current decay has a 12 second time constant that is too slow to protect the normal zone in the particular magnet that has quenched, so locally the current must be reduced much more quickly. A safety lead circuit is activated by the closing of thysister switches to convey the decaying magnet current rapidly around the quench protection unit that contains the quenching magnet. The

process of diminishing the current in the magnet coils is aided by the use of heaters energized in the dipoles of the protection unit to quench a large quantity of superconductor (in addition to the magnet that initially quenched). The resulting rapid resistance growth drives the current down with a time constant appropriate to an in-bounds temperature rise.

Vacuum System

The vacuum system consists of three separate subsystems with different characteristics and requirements. The cryostat insulating vacuum system is the most complex and is completely isolated from the high-vacuum cold beam tube system inside the magnets. The straight sections and other noncryogenic regions have warm beam tube, bakeable, conventional vacuum systems.

All in all there are about 1300 cryogenic interfaces between magnets or between magnets and other components. A magnet-to-magnet interface includes a beam tube seal, two liquid helium connections, one liquid nitrogen connection, and a large external room temperature insulating vacuum seal. Each of the cryogenic seals must be able to be verified at room temperature with sufficient sensitivity to assure that it will not leak liquid helium. During initial installation each interface took on the average one man-week to check; subsequent work has been done in about half this time.

The static heat leak of the cryostat-magnet system is due to thermal radiation and heat conduction through magnet supports and other structural elements as well as through residual gas in the insulating space of the cryostat. For the Energy Doubler geometry, the static heat load doubles at a pressure of 2×10^{-5} Torr of helium. An upper limit of 10^{-5} Torr is set for operation. The insulating vacuum is pumped with turbo molecular pumps.

The pressure in the cold beam tube is very low if helium leaks are absent. Pressures of 5×10^{-11} Torr cold (5×10^{-10} Torr as measured warm) are normal. The cold beam tube provides an economical practical way of obtaining the high vacuum required for beam storage over the major fraction of the ring circumference. The main concern in adopting the cold bore approach was the potential of helium leakage to the beam tube. Because of this worry, the cryostat was designed so that the beam tube seam weld is the only weld between the helium spaces and the bore tube vacuum.

The Tevatron vacuum systems, with their many flanges, seals, pumps, valves, and gauges, have been remarkably trouble free and reliable. This is, to a large extent, because of the cryo-pumping ability of the refrigerated surfaces. The fact that most of the circumference of the ring (93%) is cold means that the pressure in the warm regions need not be particularly low. With 5×10^{-11} Torr where cold and 10^{-8} in the warm regions, the reduction in luminosity during storage from interactions in the residual gas is expected to be 23% after 20 hours.

Other Systems

Correction magnets are used to compensate for field imperfections or alignment errors of the main magnets, and to tune the optics of the ring to desired operating conditions. With a few exceptions, these are superconducting magnets configured in circuits suitable for specific functions. The correction magnet power supplies can be programmed to produce virtually any waveform throughout the accelerator cycle. The strengths of the superconducting elements are sufficient for use at full excitation, a design feature that has proved particularly valuable for steering corrections.

Beam diagnostics using the position and loss monitoring systems are essential to the operation of the synchrotron. The fact that recovery from a quench can take an hour or more makes it imperative that the reasons for erratic beam behavior be sorted out with as few beam pulses as possible. The position monitoring system can measure the deviation of the beam horizontally or vertically from center at 200 locations around the ring. The system has a wide dynamic range to permit start-up of operations with a beam so low in intensity that a quench is unlikely. A similar number of loss monitors are distributed around the ring. These are radiation detectors placed outside of but close to the magnets. The electronics for each detector is designed so that the output signal is related to the probability of quenching the magnets. Outputs of the loss monitors are continuously checked and used to abort the beam automatically (within 200 microseconds) if the signal is larger than tolerances derived from experience.

The radio-frequency accelerating system consists of eight 53 MHz resonant cavities, each of which can produce 0.33 MV. The frequency must be changed by only 2 kHz from 150 GeV to 1000 GeV to compensate for the change in the proton's speed, since the proton is already moving at 99.998% of the speed of light at injection. All eight cavities are used for acceleration of protons during fixed-target operation. The cavities have been positioned relative to one another so that, by appropriate phasing of their radio-frequency excitation, they will function as one set of four for acceleration of protons and the second set of four for independent acceleration of antiprotons. The colliding point of the two beams can be moved circumferentially around the accelerator and frozen at a particular point by frequency and phase adjustment of the two sets.

3.2.3 Performance

The Energy Doubler was commissioned in the summer of 1983. On July 3, protons were accelerated to 512 GeV, and the Doubler became the highest energy accelerator in the world. Operation for fixed target physics began in October of that year at an energy of 400 GeV. The following February the energy was raised to 800 GeV and the goal of doubling the energy of the Main Ring had been reached.

To date, there have been three fixed target runs and one brief period of storage and colliding beam operation in connection with the commissioning of the antiproton source in October 1985. The Main Ring and the Energy Doubler have been off during late 1985 and the first half of 1986 because of civil construction and ring modifications required by the colliding beams program. Operation is scheduled to resume in the fall of 1986 with a continuation of the collider activity. Since operation as a storage ring leads to far less beam loss in the magnets than the fixed target regime, it is intended to run the Doubler at still higher energy — perhaps 900 GeV.

Generally speaking, the beam dynamics behavior of the Doubler has been excellent. Of course, a small beam size at injection and an extensive correction magnet system are a big help. But, more to the point, some of the weaknesses that had been attributed to the new magnet technology failed to materialize. For instance, there had been concern that the coils of magnets would gradually move as many ramps accumulated or suddenly move as a result of quenches. Such has not been the case; operating conditions are more stable and reproducible from day to day than for the older synchrotrons in the accelerator chain.

Reliability is of concern as the facility becomes more complex. There are now four accelerators in the chain for fixed target physics; for colliding beam physics, there are six. Actual up-time for high energy physics is about 65% of scheduled time, as opposed to 80% for Main Ring operation prior to the Doubler era. About 50% of the down time is attributable to the Energy Doubler, with the cryogenic system, the magnet power supply and quench protection, and quenches the leading causes. It is obvious that the long term success of the Tevatron, as well as the credibility of larger, higher energy proton accelerators, lies in the ability to attain high operational reliability. The question of reliability for the SSC is discussed in Section 3.4.

3.3 Supercollider Facility

3.3.1 Overview

As already described in Section 1.2 and Chapter 2, the central purpose of the SSC is to produce reactions among the elementary constituents of matter at the highest possible energies. Its primary design parameters (Table 1.2-1) are proton beams of 20 TeV, which are brought into collision at six interaction points in such a way as to produce a luminosity of 10^{33} $cm^{-2}s^{-1}$. At the interaction points (four to be operational initially) detectors are placed to record and analyze the reaction products. The overall configuration of the facility is indicated in the artist's view of Fig. 1.2-1.

The SSC is made up of the various components already described in Section 3.1. The injector system consists of a source and linear accelerator, followed by three booster synchrotrons. The linear accelerator brings the protons up to 600 MeV kinetic energy. The cascade of boosters then accelerate the protons successively to 7.1 GeV, 100 GeV, and 1 TeV kinetic energy. The final booster is a synchrotron with superconducting magnets; the others have conventional copper and iron magnets to permit rapid cycling. In addition to providing 1 TeV protons for the two main rings, the final booster synchrotron produces external beams for testing the response of detector components before their installation in the interaction regions of the SSC.

The largest synchrotron of the injector system is comparable in size, complexity, and number of components to the Fermilab Tevatron. The SSC main collider rings are much larger. Because of the choice of a higher magnetic field for the bending magnets (6.6 tesla compared with 4.4) the circumference of the SSC is about 13 times that of the Tevatron, even though the energy is 22 times larger. The general nature of the technical components of the collider rings is the same in both machines. There are just an order of magnitude more of them in the SSC. The dipole bending magnets, for example, are 6.4 m long in the Tevatron, with an inner coil diameter of 7.5 cm, while in the SSC design they are 16.5 m in length, with an inner coil diameter of 4 cm. Despite the factor of 2.5 greater length and 50% higher field, the stored energy per magnet is only a factor of two greater than for a Tevatron dipole because of the smaller coil diameter. Similar correspondences can be made for other technical components. The Tevatron, with its successful proof of the technology of superconducting magnets in a modern accelerator, provides a bench mark for the extension to SSC energies.

The SSC collider ring is 83 kilometers in circumference. In the curved parts, 86 percent of the orbit length is occupied by the bending magnets. An isometric cutaway view of a bending magnet is shown in Fig. 3.3-1. (Compare Figs. 2.4-3, 2.4-4, and 3.2-2.) The inner body of the magnet is thermally isolated from its outer casing so that it can be maintained at its operating temperature of 4.35 K (269 Celsius degrees below zero) without undue refrigeration power being required. Design calculations and measurements of the SSC magnets show that the electric power required to operate the refrigerators of the SSC will be about 30 megawatts, comparable to or less than that being used to operate the largest existing accelerators.

As with the Tevatron magnets, the working fluid of the refrigeration system is liquid helium, as that is the only substance which maintains its fluid properties at the needed operating temperature. Cold liquid is introduced from refrigerators into the arrays of magnets at ten locations around the ring, cooling the superconducting coils as it flows through. At the end of an array it is withdrawn and sent back through the magnet cryostats to the refrigerators for recooling. About two million liters of liquid helium are stored in the refrigeration system during operation. This impressive amount of liquid helium is still only about 1/30 of recent U.S. annual usage.

In addition to the bending magnets, the continuous cryogenic envelope surrounding the beam vacuum chambers contains a focusing (quadrupole) magnet about every 100 meters and special orbit and focusing correctors at the same interval, along with various pressure, thermal and electrical measurement and control devices. At less frequent intervals the cryogenic envelope contains valves and heat exchangers needed for the vacuum and refrigeration systems. Linking these all together with the injectors and refrigeration equipment and permitting the monitoring and control of the entire system is a network of computers connected by a broadband communication network and forming the collider control system.

The collider magnet system, its refrigerator and the attendant injector system, form the principal technical components of the SSC. Of them, the collider magnet system is dominant in bulk and in cost.

As previously noted, the rings and beam collision areas are housed underground. This provides a stable environment for the technical systems while at the same time containing the radiation associated with the operation of the beams. As discussed in Section 3.5, twenty feet of soil above the top of the tunnel is adequate radiation shielding even for a loss of a full intensity beam. Paradoxically, although the SSC is a much higher energy device than any existing accelerator, because of its very long cycle time, the radiation problems associated with it are generally less than those routinely and safely dealt with at existing accelerators.

Surface buildings are needed to house the equipment used for the high energy physics experiments and the support functions such as shops and warehouses. In addition there must be housing for the injector complex and for the auxiliary equipment of the collider such as cooling and refrigeration equipment, power supplies and other utilities. While the experimental halls, injector, and general support buildings will be clustered together near the beam collision zones, eight above-ground utility buildings will be distributed uniformly around the periphery of the arcs.

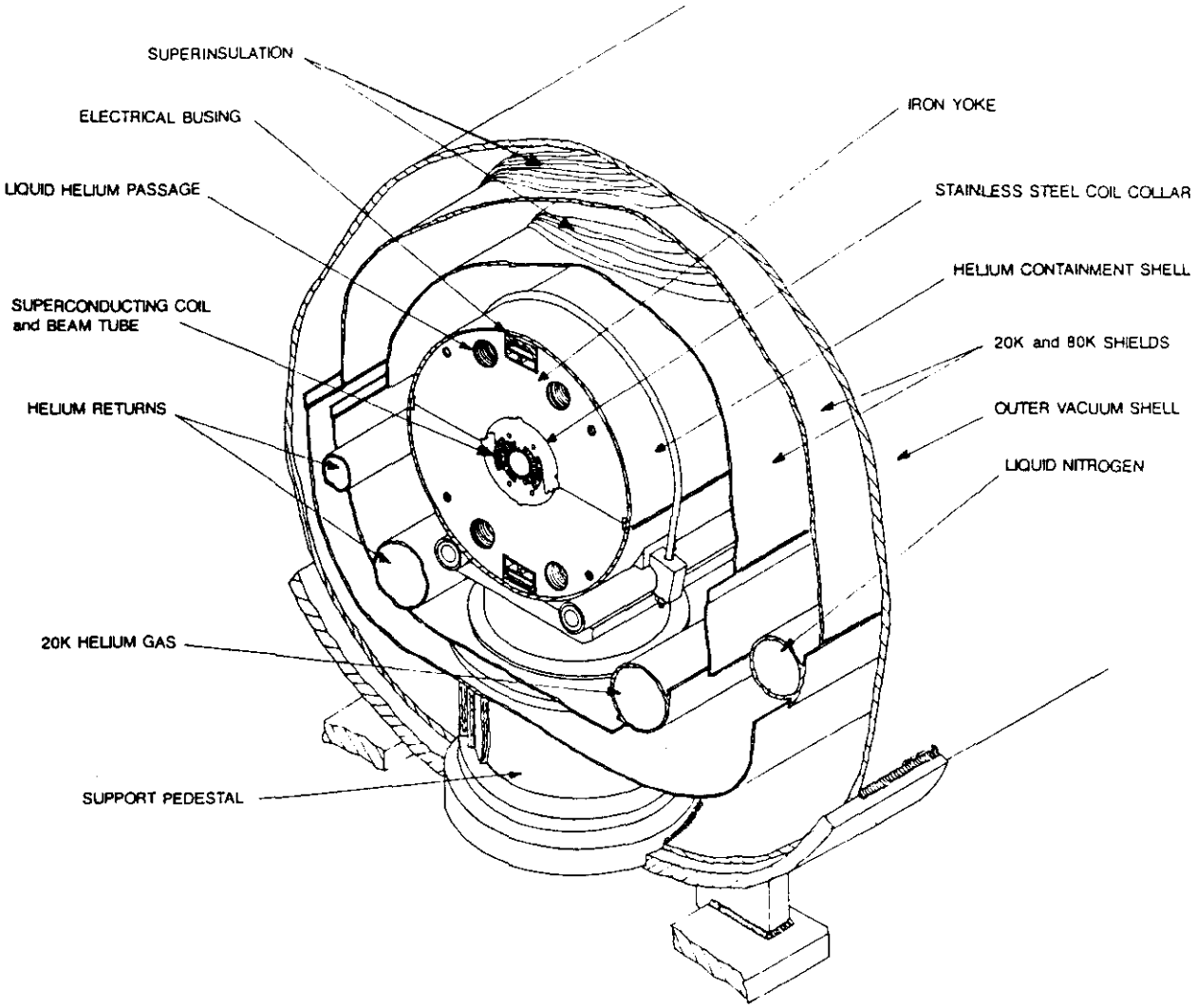

Figure 3.3-1. Isometric cutaway perspective drawing of the 6.6 tesla SSC dipole magnet.

3.3.2 Principal Parameters of the SSC

In Section 2.3 the discovery potential at the TeV mass scale is discussed and the need for high luminosity is emphasized. The primary parameters of the SSC as a proton-proton collider with 20 TeV per beam and a maximum operating luminosity of 10^{33} $cm^{-2}s^{-1}$ per collision point have been chosen to assure an extensive "discovery reach" into the region characterized by that mass and the expected cross sections. To accommodate a wide variety of experimental techniques and detectors, provision is made in the design for six separate collision regions that can operate simultaneously under a variety of conditions.

Based upon economic studies and availability of advanced superconducting materials, an initial operating magnet field of 6.6 tesla has been chosen. The bunch spacing of 4.8 m and, to a lesser extent, a beam-beam tune shift of 10^{-3} per collision region (conservatively chosen, based on experience at the $Sp\bar{p}S$ collider) serve as a basis for deriving the other technical parameters of the accelerator. Detailed arguments for the choices of specific parameters of the accelerator are presented in Chapter 4 and the conceptual design of the systems to meet these requirements in Chapter 5. Table 4.1-1 is a summary of the major accelerator parameters.

3.3.3 Layout and Beam Optics of the SSC

As the result of a number of studies involving accelerator physics, economics and operating efficiency considerations, it appears advantageous to cluster the beam crossing regions into two groups incorporating both physics experimental areas and major supporting equipment. A plan view of the facility laid out in this fashion is presented schematically in Fig. 3.3-2. As indicated in the figure, refrigeration support buildings and tunnel access points are located at regular intervals in the ring arcs. Expanded plan diagrams of the cluster regions are shown in Fig. 3.3-3. The inclusion of bending in the spaces between collision points is done in order to prevent particles produced in one region from interfering with the study of collisions in another.

High and intermediate luminosity collision zones are being designed as part of the initial conceptual design study. It is possible to structure the ring optics in such a way that a wide variety of crossing zones can be accommodated. This flexibility will permit modification of the crossing zones to optimize experimental usage over the life of the facility. Here we present some details of a high luminosity crossing zone which meets the need for crossing the beams at a very tight focus, separating the beams, adjusting the focusing of the confinement system between injection and storage conditions, and optimizing the matching of the crossing regions to the regular lattice. A vertical section at a crossing region, showing the optical components and the beam orbits, is presented in Fig. 3.3.-4.

The lattice of Fig. 3.3-2 is made of three types of modules: arcs, interaction regions (IR) and the utility modules. The IR and the utility modules are interchangeable from the lattice design point of view. They both have length of 2400 m and both match at their ends to the arcs in the same way.

The IRs are arranged in two clusters, 4 IRs in one of the clusters, called the East cluster, and 2 IRs and 2 utilities in the other (West) cluster. The clustered IRs are adopted for the SSC because it is more cost effective to have experimental and utility regions sharing the same nearby support facilities.

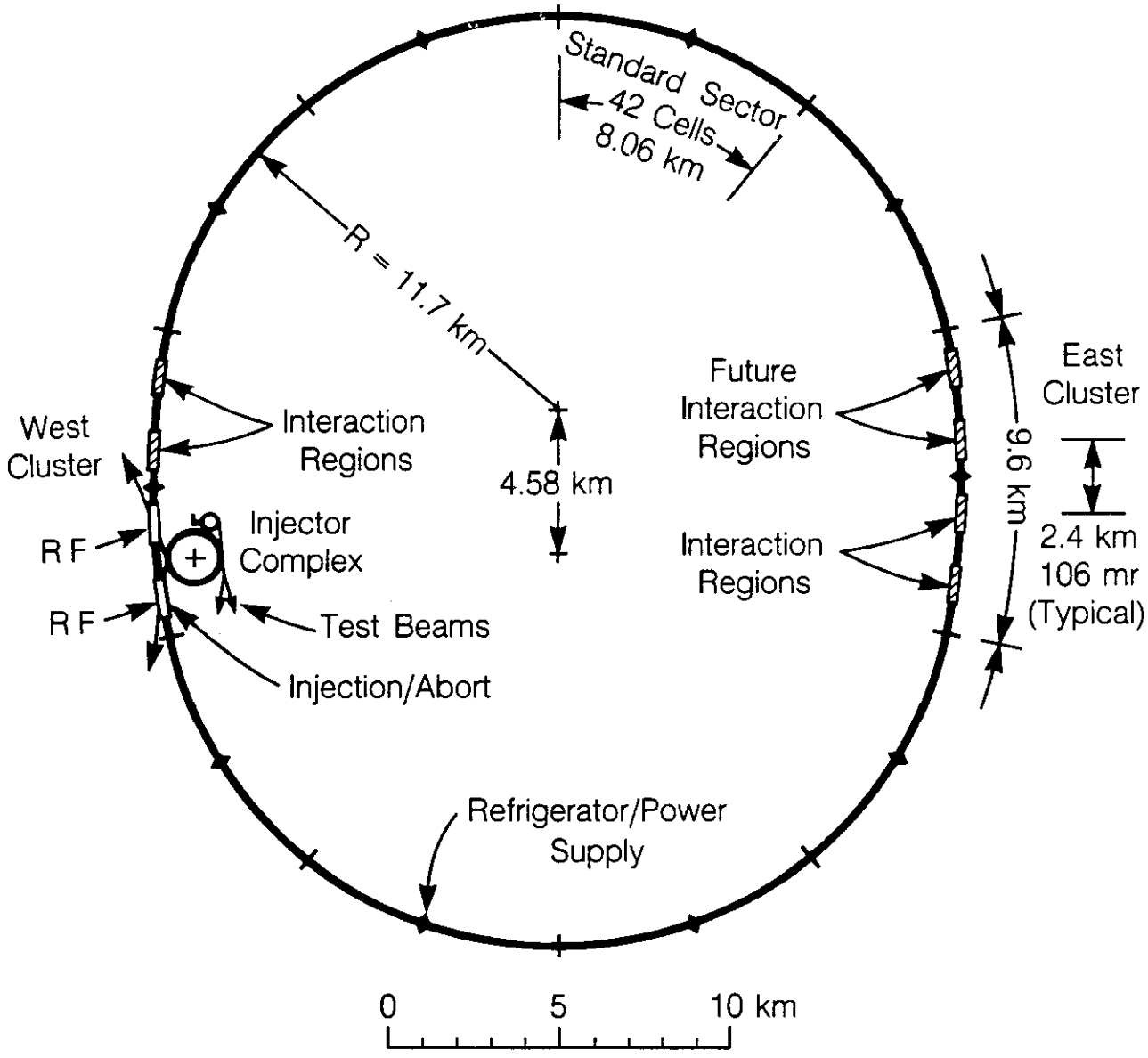

Figure 3.3-2. SSC collider ring layout. East and west clusters are joined by arcs of 11.7 km radius. The east cluster consists of four interaction regions separated by 2.4 km. The west cluster has two interaction regions and two utility straight sections (open rectangles) for injection and abort and for acceleration (rf). The cascade of synchrotrons that form the injector is inside the main ring at the utility straight sections. There are 10 refrigeration and power units around the ring (black diamonds).

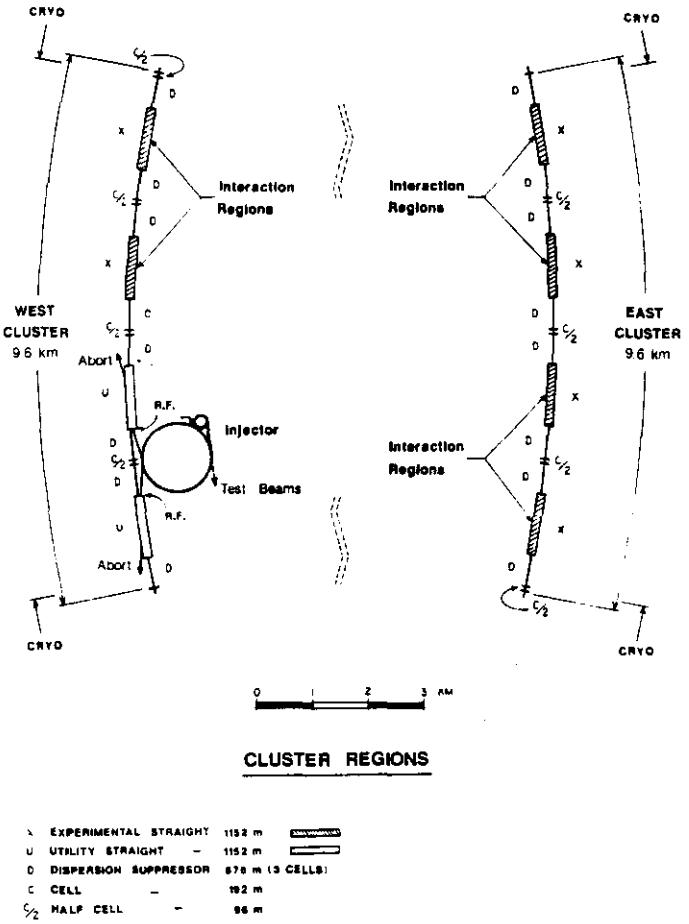

Figure 3.3-3. Enlargement of the layout of the east and west clusters.

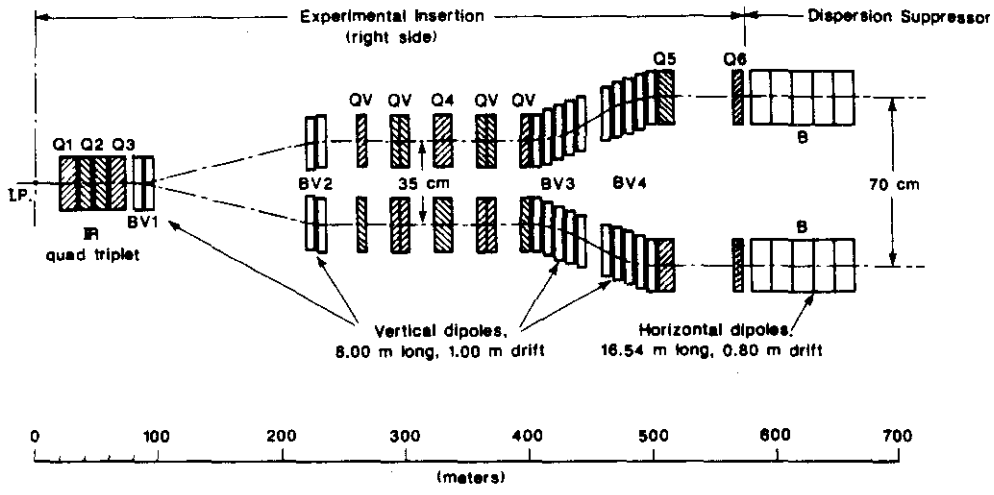

Figure 3.3-4. Geometry of the vertical beam crossing at a high-luminosity interaction point. Open rectangles represent bending magnets (horizontal or vertical); cross-hatched rectangles represent quadrupole focusing elements. The inner triplet of quadrupoles provides the final focus at the interaction point (IP).

On each side of an interaction region a triplet of quadrupoles is used to provide the strong focusing needed at the interaction point. Two interaction area designs employing the same optical scheme are included as examples in the conceptual design. The matching sections employed are flexible enough that many variants, with details arranged to accommodate particular physics experiments, are possible. The highest luminosity region has $\beta^*_x = \beta^*_y = 0.5$ m with $L^* = 20$ m, the distance from the interaction point (IP) to the face of the first quadrupole. The maximum beta is 8 km. In the other example IR, $L^* = 100$ m $\beta^*_x = \beta^*_y = 10$ m.

The beams cross each other at a very small angle at the interaction points. The full angle is typically 75 μrad, but is variable from 0 to 150 μrad. As shown in Fig. 3.3-4, after the triplet (at the extreme left of the figure), the beams are separated vertically in two stages to a separation of 70 cm. The optical elements are such that the properties of the beam are matched to the arc (or cluster) parts of the confinement system away from the interaction region.

The clusters are connected by arc modules or cells, periodic arrays of bending and focusing magnets. Each cell of the array consists of 10 bending magnets and two focusing quadrupole magnets each focusing (defocusing) in a separate plane. The cell length of 2×96 meters and cell focusing phase advance of 60 degrees were chosen to give minimum cost of the magnet system for the needed aperture. (See Section 4.3.) In addition to the bending and quadrupole magnets, each half cell contains a beam position monitor attached to the quadrupole and a correction magnet and cryogenic device unit, referred to as the spool piece. There are 332 cells per ring in the regular arcs.

To secure proper functioning of the accelerator, a number of magnetic correction elements must be introduced: (a) Stability of the beams against the collective head-tail effect must be ensured by chromatic corrections effected with sextupole magnets placed in each spool piece. Most of these sextupoles are powered together in two families, although possible advantages of multiple family schemes are still being investigated. (b) Random manufacturing, powering, and installation survey errors of the dipoles and quadrupoles result in a requirement for independently powered dipole correction magnets to be housed in each spool piece. (c) Random departures from perfect uniformity of the dipole bending field also require a correction scheme to maximize the useful aperture and reduce resonance widths. To this end groups of normal and skew quadrupole, sextupole and octupole correctors are housed in certain of the spool pieces. (d) In others, skew quadrupoles are arranged to minimize error coupling of horizontal and vertical betatron motion. (e) Other groups of quadrupole corrections are provided for correction of cumulative focusing function and dispersion errors and adjustment of the tune. Tune adjustment capability of ± 2 units is provided so that the optimum operating point can be explored experimentally. (f) Finally, distributed correctors for the sextupole and decapole components of the persistent currents in the dipole windings are provided. They consist of an array of wires, 200 μm in diameter, attached to the beam tube itself within each of the dipole magnets.

3.3.4 Conventional Systems

The major feature of the SSC is the collider ring that is buried underground, and invisible. The shape of the ring is determined by the results of detailed physics calculations incorporating the capabilities of the required technical systems. For the current SSC design the two proton beams are contained within a tunnel having an overall circumference of 83 km (52 miles).

The tunnel is composed of arc sections of uniform periodicity, interrupted by special sections called clusters. Within these clustered areas are found the experimental facilities as well as the utility sections needed for specialized accelerator functions such as injection, rf acceleration, and the beam abort/dump facilities.

Connecting to the below-ground systems are a whole array of electrical cables and mechanical pipes. At the surface and distributed around the ring are ten refrigerator facilities with large helium compressors. In the associated control rooms are found the power supplies that provide the current needed to energize the superconducting magnets, as well as one of the nodes of the accelerator control system. There will be a number of transformers and heat exchangers in the area to provide the services required by the technical systems. At two locations around the large ring are located major electrical substations connecting the accelerator complex to the power grid. Here power derived from overhead transmission lines is transformed to a lower voltage appropriate for the magnet power supplies and for distribution to sub-station locations in the acceleration complex. Other utilities such as water and sources of fuel will be provided as needed at the cluster areas and at the service areas around the ring.

Allowance has been made for the construction of six collision halls surrounding the proton-proton beam interaction regions. Only four such areas are proposed to be constructed as part of the initial development of the SSC. A typical collision hall with a height of 15 m (50 ft) is envisioned to provide a central gallery 21 m (70 ft) by 21 m, with smaller galleries at each end. At the side, behind a massive shield door, is an underground assembly area where detectors can be partially assembled before being introduced into the collision hall.

In one of the cluster areas will be found a research campus for the SSC. The campus complex may consist of fifteen or more buildings arranged in four major groups — laboratory, industrial, warehouses, and support buildings. The laboratory buildings will provide office and work space for the administrative and technical personnel. The buildings will contain the electronics development laboratories, control rooms, computing facilities, a cafeteria, meeting rooms, an auditorium, and other space for the purposes of the staff. Industrial buildings will house limited component assembly activities and associated offices. Warehouses serve as receiving and storage facilities. The support buildings — fire, site patrol, rescue and maintenance provides services to the entire SSC.

The site must accommodate the accelerators and experimental facilities [3.3-1]. The collider is conceived of as a planar ring 52 miles in circumference with the possibility of a slight tilt (up to 0.5 degrees) or perhaps a fold (± 0.5 degrees maximum) to reflect the profile of the land. Up to 8,000 acres of land appropriately distributed around the ring are required. Other important attributes include:

(a) The site should be such that the SSC facility can be positioned, constructed, and operated in an environmentally acceptable way.

(b) The geology of the site must be such as to allow efficient tunneling or cut and cover construction with resulting structural stability and without encountering significant problems from the presence of ground-water.
(c) The site should provide year-round access by road, have a major airport nearby, and have adequate housing and educational facilities potentially available for the staff and visitors. Adequate industrial and construction resources are needed in the vicinity.
(d) The proposed site should have a source of adequate and reliable water (up to 2000 gal/min) and electrical power (up to 250 MW).
(e) Accelerator operation requires avoidance of excessive very low frequency noise and vibration adjacent to the tunnels.
(f) Ease of construction and the cost and reliability of operation of the facility make desirable the avoidance of extremes of temperature and humidity.

Several geological settings have been studied as part of the conceptual design effort. Topographies and profiles representative of generic sites that exist at numerous locations in the United States have been assembled. One generic site consists of various layers of soil overlaying soft to hard rock. The plane of the tunnel has been sloped slightly to fit the surface topography. The depth of the collider ring has been set to provide a minimum of 20 feet of ground cover over the tunnel. Two additional geologic configurations were carried through to completion for the purposes of estimating the costs for the underground facilities. These called for a deep tunnel in hard rock and a relatively shallow cut-and-cover tunnel in soft ground.

The conventional facilities are described in detail in Chapter 6.

3.4 Reliability

One of the design goals of the SSC is to aim for high operational availability of the machine for physics experiments. The SSC is comparable in complexity to recently constructed and operated particle accelerators even though it is an order of magnitude larger in size. Only a moderate extrapolation of existing data is required to predict its availability. Furthermore, engineering techniques are now available (perfected in the aircraft industry) that can be used to identify critical items and increase the reliability of components and systems of the SSC at reasonable cost.

Reliability is determined largely by the quality of design and is intimately linked with quality assurance (QA) and quality control (QC). Quality assurance begins with the detailed engineering designs and prototype testing which show whether the design is capable of meeting its reliability goals. Quality control is then required to see that the actual production meets the design standards. Although the bulk of QA/QC work properly belongs to the detailed engineering design and construction phase, we have already begun to address these issues in the conceptual design. This permits us to include cost and schedule implications properly.

3.4.1 Historical Examples

A large number of accelerators have been constructed and successfully operated for high energy physics experiments. These accelerators have varied in type from electron and proton linacs, to proton and electron synchrotrons supplying beams for fixed target experiments, to electron-positron, proton-proton, and proton-antiproton colliders. The colliders are all comprised of several accelerators linked together to form a complete system as is the case for the SSC. Some of the more recent colliders are as complex in the number and variety of their subsystems as the SSC. The most relevant examples for the SSC are CERN proton-antiproton collider ($Sp\bar{p}S$) and the Tevatron at Fermilab.

The CERN $Sp\bar{p}S$ provides collisions at 630 GeV center-of-mass energy by storing counter-rotating beams of protons and antiprotons in the main ring of the machine. This is an achievement involving unusual beam manipulations and high reliability of systems. The antiprotons obtained from secondary beam production from another proton accelerator (PS) are collected, deaccelerated, stacked, cooled, and stored in yet another machine (AA) for many hours before being injected back into the PS and into the $Sp\bar{p}S$ ring. In addition, protons must traverse the linac, the booster synchrotron, and the PS before being injected into the $Sp\bar{p}S$ containing the antiprotons. Failure in any of the many subsystems or operations can cause loss of the antiprotons, resulting in a 24 hour restart time. Even though this system is far more complex than the SSC, the $Sp\bar{p}S$ has successfully operated at a 60% to 80% availability and made what many consider to be the major physics discoveries of the 1980s.

The Tevatron is the first machine constructed with superconducting magnet technology and is a demonstration that large systems of superconducting magnets can be operated at high reliability. The Fermilab magnets have already run through more cycles than the number required for SSC operation over a twenty-year period. This gives confidence that superconducting magnets are capable of the reliability needed for the SSC.

3.4.2 Approach to System Reliability

The reliability of the SSC depends on its component systems. It is therefore advantageous to specify explicitly a set of goals for the reliability and availability of the various systems of the SSC. It is important to set realistic goals, to view the accelerator as a complete entity in order to avoid setting unattainable goals for particular systems, and to avoid unprofitable investment of manpower and time. Historical data from accelerators can be used in conjunction with accelerated life tests and quality control programs to validate designs and indicate areas where it would be useful to concentrate more than the ordinary effort. A system reliability analysis resting on the data base of existing accelerators can be used to understand how various problems scale to the size of the SSC. The data show that some failure rates scale with size, while others do not.

From the achieved availability of existing accelerators, performance standards for a viable experimental program can be established. For the purposes of this discussion we define the availability as

$$\text{Availability} = \frac{\text{(Scheduled up-time)} - \text{(Unscheduled down-time)}}{\text{(Scheduled up-time)}}$$

where scheduled up-time is the total time scheduled for accelerator operations, including machine studies as well as use for experiments. System availability includes the effects of repair time and the re-establishment of usable beam.

Table 3.4-1 shows the percentage of unscheduled down-time relative to scheduled up-time of the major systems of various machines for recent extended running periods. In compiling these data, all unscheduled down-time is taken into account in each of the entries. Thus, for example, although CESR does not report its power supply failures separately, they are included in the other systems, such as magnets. We note here that the entries are not exactly compatible from machine to machine, so comparisons are sometimes difficult but trends are clear. Subsystem reliabilities above 95% have been achieved for complex systems. The more involved injector systems of the Tevatron are a greater cause of down-time than the less complex systems of CESR and PETRA, but it should be noted that the failure rates of many of these systems do not scale with size. Thus the CESR vacuum system has the same failure rate as the Fermilab system.

Some of the entries are anomalous. The large percentage down-time of the PEP injector is unusual, as the SLAC linac has operated reliably for many years. It probably contains a large contribution from the modifications that were taking place in preparation for operation of the SLAC Linear Collider (SLC). A thorough analysis of the collected down-time data will form an invaluable data-base for detailed engineering of SSC systems.

Table 3.4-1
System Down-Times as a Percentage of Scheduled Up-Time

System*	CESR	PEP	PETRA	Tevatron 800 GeV	CERN Fixed Target
Power Supplies	–	3.0	4.2	4.1	1.0
Cryogenics	–	–	–	4.2	–
Vacuum	0.4	0.6	1.7	0.4	0.2
Control/Instr	1.1	1.6	0.6	0.7	0.8
RF	12.2	0.9	4.2	0.6	1.4
Injector Complex	2.3	25.0	7.1	14.6	6.0
Injection/Abort	–	–	–	0.7	–
Utilities	0.9	1.8	1.0	3.0	3.4
Interlocks	0.4	0.8	–	–	–
Magnets	3.3	–	–	6.2	1.8
Miscellaneous	1.7	6.0	4.0	1.1	3.0
System Availability	77.7%	60.3%	77.2%	64.4%	82.4%

*Data extracted from recent annual reports of the indicated institutions and from supplemental operation logs supplied by D. Rice, CESR, J. Paterson, PEP, H. Kumpfert, PETRA, R. Mau, Tevatron, G. Brianti, CERN.

In addition, Table 3.4-1 shows the total availability for each accelerator. From these data, a realistic standard of performance of an accelerator to produce physics is a 60 to 80% availability. It seems appropriate to aim for an availability of 80% for the SSC.

3.4.3 System Availability Goals for the SSC

Where data and understood procedures exist, modeling was performed to estimate system availability. This procedure yields realistic results for large systems. Where no detailed data exist, or where procedures are not well understood, scaling by size from the data of Table 3.4-1 was attempted. Where necessary, redundancy or other design changes are proposed to increase availability, and the additional cost was added to the cost estimate. It has been assumed that the running schedule will involve cyclic periods of ten days of high energy physics, followed by a four day period of maintenance and machine studies.

The resulting availability goals for the various systems of the SSC are shown in Table 3.4-2. The estimates are made for a mature machine. Table 3.4-2 represents a set of *goals* for the SSC systems, and in that sense they are set at a somewhat higher level than existing machine reliabilities, taking advantage of potential progress in technology.

Table 3.4-2
SSC Goals for System Availability

System	Availability Goal
Magnet System	0.96
Power Supplies and Quench Protection	0.96
Cryogenics	0.98
Vacuum	0.995
Control and Instrumentation	0.98
RF	0.98
Injector Complex	0.95
Injection/Abort	0.985
Utilities	0.99
Safety and Interlocks	0.995
Overall SSC Availability	0.80

In the following paragraphs the reasons for the establishment of the goal figure for each system are described briefly. Scaling from existing machines is done where possible. Other specific studies contribute, as noted below.

Magnet System

The SSC magnet system containing approximately 9600 magnets represents a critical element in determining operational availability of the collider. The operation of the Tevatron and other HEP facilities provides a large data base for SSC magnets. The reliability and performance of superconducting components are now being accumulated and analyzed. As a measure of the significance of the Tevatron as an engineering data base, we note that in its operation it has already been through more ramping cycles that the SSC will have in its whole lifetime as a collider.

The detailed analysis of the Tevatron and other available data, with respect to initial component failures and production problems, will aid significantly in attainment of reliable magnet design. At the present time extrapolation of the available data, evaluation of current design, and experience with laboratory models indicate that the availability goal of 96% for the magnet system is achievable. This availability corresponds to approximately three magnet failures per year.

Power Supply and Quench Protection System

The power supply and quench protection system was modeled on the Tevatron system. The SSC has a total of 30 high current supplies compared with 12 at the Tevatron, so that extrapolation is not great. The quench protection system is much larger, however, and the design requires redundancy to avoid significant down time. With the proposed redundancy, the quench protection system is expected to have less than a 50% failure probability in a 240 hour running period. Assuming a five hour recovery time (repair fault and reload beams), the down time from quench protection failures would be 1%. For the design of the system, see Section 5.5; for the proposed model for redundancy, Section 5.13.

Scaling the main power supply system is more difficult. The down time because of power supply failure at CESR is assigned to the magnet system; from Table 3.4-1 it cannot be more than 3.3%. CESR has over 200 power supplies, albeit each considerably smaller than the SSC power supplies. The Tevatron experienced about 1% down time due to the main power supply system, not including the quench protection. Doubling that results in 2% for the SSC.

The correction element power supply system for the SSC has about 2500 supplies. In this case, it is necessary to double up on each supply for redundancy, and the expected down time due to correction power supplies is 1%, provided that each failed half power supply is repaired during the regular maintenance period (see Section 5.6).

The aggregate availability of the complete power supply system thus estimated is 96%.

Cryogenic System

The cryogenic system design rests on existing systems in industry and at laboratories. The number of large refrigerators (11) forced redundancy. Each refrigerator is sufficiently oversized that the entire system can be operational with one and sometimes even two refrigerators not functioning. The redundancy scheme is described in Section 5.3, and the reliability, based on data from the Central Liquefier at Fermilab, is calculated in detail in [3.4-1]. The result is that the availability is expected to be 98%.

Control and Instrumentation

The control and instrumentation systems were based on a similar system at Fermilab, with redundancy added and extrapolated to the SSC size using a realistic model for the electronic components (see Section 5.13). The major sensitive items in the control system are crate power supplies and the quench protection system, already mentioned. The crate power supplies are designed to be redundant in the same way that the correction element supplies are. There are also two complete collider-ring data links, since the failure of a data link could prevent prompt diagnosis of the cause of failure and thereby significantly increase the time to repair. The total down time is dominated by the quench protection system, which is included in the power supply system. A 98% availability is assigned to the rest of the control system.

RF System

The rf system is derived from the PEP system. The scaling is by cavity length and power for the high power parts of the system, and directly for the low level parts (see Section 5.7). The resulting availability is 98%.

Injector Complex

Perhaps the hardest system to scale is the injector. The FNAL Tevatron system is the likely candidate for analysis since it is approximately the same size and complexity as the SSC injector. The scaling is not obvious, however, because the SSC injector has to be available only a small percentage of the time. The remaining time it is used as a source of protons for test beams. It is assumed in our model that the injector priority will always be such as to allow repair and tune-up for injection into the collider, with its function as a source of test beams falling to a lower priority. On occasion, there will be need to inject the beam at unexpected times, because of premature loss of the collider beams. Because of the long luminosity lifetime in the SSC, there is considerable flexibility about when the injector complex is needed. The collider can be operated with an existing fill a bit longer until the injector is ready. In these circumstances, only very long repair times for the injector or unexpected fill requests need to be considered, and it is expected that the injector complex will be available 95% of the time, in the sense that it will be the cause of 5% of the down time of the collider rings.

Other Systems

The other systems of the SSC each account for a small amount of down time. The vacuum system for the SSC is taken directly from the Tevatron. Table 3.4-1 indicates that down time due to malfunctions of the vacuum system are independent of the size and complexity of the machine. The injection and abort systems are roughly twice the complexity of the Tevatron systems, although the number of modules are considerably larger. The down time is scaled to be a factor of two more than the Tevatron. The safety interlock system is of equal complexity to the Fermilab system, with roughly the same number of entrances, and even fewer service buildings, so it is not scaled. The down time because of utilities is assumed to be 1%.

Summary

Meeting the availability desiderata clearly represents a significant challenge. Fortunately, there are widely available today engineering tools and organizational schemes whereby reliability criteria can be incorporated into designs and the design standards maintained during construction. At this conceptual design stage we believe we have shown that none of the goals are inconsistent with physical law or engineering principle. We have tried at this conceptual level to include reliability considerations and incorporate them into the cost estimate. In estimating contingencies, we have attempted to include the possibility that reliability-enhancing design changes may be indicated during the detailed engineering phase.

3.5 Setting, Environment and Radiation

3.5.1 Environmentally Benign Nature of the Facility

As described in Section 3.3.4, the SSC facility consists in a campus/injector area and a very large collider ring tunnel. The collider ring tunnel houses the accelerator rings, with eight auxiliary installations at eight kilometer intervals along the major arcs (see Fig. 3.3-2). Two experimental areas are adjacent to the campus/injector and four are diametrically across the ring (see also Fig. 3.3-3). In spite of the collider ring dimensions the surface area required for the facility amounts to only approximately 8000 acres. Easements required for the underground tunnel could bring the total impacted area to a somewhat higher total of 11,000 acres as discussed in the Siting Parameters Document [3.3-1].

As a radiation source the SSC is similar to the projection tube of a television set consisting in a beam of particles that can be steered by electric or magnetic fields and turned on and off. For normal operation the design of the machine includes sensors to turn the beam off in case of malfunction and to inhibit operation if any potentially unsafe condition exists. The characteristics of the produced radiation are well understood from numerous experiments and extensive calculations [3.5-1]. Based on this understanding, the ring tunnel will have a minimum earth cover of 6 meters (20 feet). With this much cover people in the vicinity are shielded to well below levels set by applicable federal regulations [3.5-1]. The beams extracted from the ring, either at the end of a routine run or by the safety system, will be steered into isolated, massive abort dumps which will be sufficiently large to absorb the resultant radiation. The dumps are designed to prevent radiation from interacting with any ground water sources. For a more detailed discussion see Section 6.9.

The tunnels to house the collider ring and injector may be constructed by tunneling or by cut-and-cover methods depending on the characteristics of the site that is selected. In the case of tunneling the land above the tunnel will be left undisturbed except for the surface installations at 8 km intervals on the collider ring. For a cut-and-cover operation the surface will be restored to its prior condition and, as far as possible, to its prior use except for the occasional surface installations. The auxiliary installations on the surface will be sited to minimize their effect on the local environment. For the most part the operation of these facilities will be monitored and controlled from the main control room at the campus, so there will be very little traffic and movement associated with them.

The campus/injector area will be very similar to the existing Fermi National Accelerator Laboratory in Illinois. That facility has been operating continuously since 1972 at operating levels above those required for the SSC injector. All of the environmentally sensitive aspects of their operations have been carefully monitored, with detailed annual reports submitted to the Department of Energy. These Fermilab operations have never posed any radiological problem, in spite of the fact that the Laboratory is unfenced and open to the general public [3.5-2]. The SSC laboratory will follow similar monitoring and reporting procedures.

3.5.2 Environmental Modifications from Construction

The beginning of construction of the SSC will bring a fairly substantial increase of transient population in the areas around the site. The work sites will be spread along a distance of some 80 km (50 miles), which will mitigate the impact, especially for any site near a sizable metropolitan area. Nonetheless, the amount of activity in and around the work sites will place added burdens on both the load and traffic capacity of roads in the vicinity.

For a tunneled site this activity for the collider ring will be concentrated at the eight locations around the ring that are the access points for the completed ring. There will be no disturbance of existing surface facilities above the ring, and the ring will be sited to minimize the impact of necessary surface installations. The tunnels will be excavated for a distance of 8 km (5 miles) in either direction from alternate access points. Since the excavated cross section of the tunnel will be only 11 m^2 (120 sq. ft.) the total volume removed per day from a given access will be approximately 900 m^3 (1200 cu. yd.), extended over a period of 9 months. This spoil will be disposed of as close to the access as possible to minimize the traffic dust and noise.

For a cut-and-cover site the activity will be around the entire periphery of the collider ring, though it will affect only the periphery and not the region interior to the ring. The ring will be sited to minimize the interference with existing surface features, such as roads, utilities and streams. Where interferences do exist it will be necessary to make temporary cuts or diversions and restore following completion of that section of tunnel. Upon completion of the construction the surface will be restored to its original condition as far as possible, with only the surface installations at 8 km intervals (and small tunnel exit and fan units halfway between) evidencing the presence of the machine below.

Additional construction activities will take place at the east and west cluster regions of the site. At the west cluster, besides the tunnels for the collider ring and the various tunnels and support facilities required for the injector, there will be substantial construction for the laboratory, shop and administrative buildings required to maintain and operate the SSC facility. As far as possible these will be designed and configured to blend with the environment in a campus-like setting. At the north end of the cluster will be two of the large experimental areas where the scientific research work of the laboratory will be focussed. During the construction and installation period there will be major activity here involving the assembly of massive detector components. The four remaining experimental areas will be located in the east cluster area. Like the west cluster these will be places of intense activity during the construction period. Unlike the west cluster the campus-like support facilities here will be minimal, sized to support only the experimental activities within this cluster.

Following the completion of construction, as noted above, the site will be restored as far as possible to its original condition. For a tunneled site only the presence of the occasional surface installations around the collider ring, and the presence of and activities in the east and west clusters will remain. Road patterns and capacities may have had to be altered to accommodate the facilities and equipment to be transported. For a cut-and-cover site there may have been some permanent rerouting of watercourses. For all sites the use of water to provide cooling for the technical systems and the removal of water by sumps to maintain the integrity of the tunnel must be carefully studied. Evaporative cooling towers could produce vapor plumes in the vicinity of the remote collider ring installations. The noise produced by the screw compressors at these locators will be controlled by soundproofing and underground installation.

3.5.3 Environmental Consequences of Operations

As noted in 3.5.1 above, production of radiation is attendant upon operation of the SSC. The characteristics and intensities of this radiation are well understood from the operation of existing accelerators and from studies of the very high energy radiation in the natural background of cosmic radiation. When a site for the SSC has been selected a comprehensive environmental monitoring system will be initiated to determine the baseline levels of naturally occurring radiation on the site. The design of the facility will draw on this information to provide safeguards against even remotely possible adverse consequences of the laboratory's operation. The professional staff of the laboratory will include a section charged with responsibility for environmental health and safety. This group will monitor the levels of prompt radiation from beam operation, radiation levels in ground water and in air on and near the site, and noxious gases in the air to guard against any increments above the baseline levels. As at existing Department of Energy laboratories, detailed annual reports of their findings must be submitted to the Department.

References

3.2-1. R. Palmer and A.V. Tollestrup, Annual Review of Nuclear and Particle Science, **34**, 247(1984).

3.2-2. H.T. Edwards, Annual Review of Nuclear and Particle Science, **35**, 605(1985).

3.3-1. Siting Parameters Document, SSC Central Design Group Report No. SSC-15 (1985).

3.4-1. E. Shrauner, SSC Central Design Group Internal Report No. SSC-N-60 (1985).

3.5-1. Workshop on Environmental Radiation, SSC Central Design Group Report No. SSC-SR-1016 (1986).

3.5-2. S.I. Baker, Fermilab Report No. 85/32 (1985).

4. SSC Accelerator Physics Parameters

The SSC accelerator physics issues are considered in this chapter. As in the Reference Designs Study [4.1-1], no qualitatively new accelerator physics issues are discovered. However, in the past two years studies on several critical parameters have been carried out in much more detail than before. For example, the important parameter of the magnet aperture has been studied in detail together with the lattice design to minimize the overall construction cost. Various arrangements of the six interaction regions were studied and a particular clustered arrangement has been selected for the non-site-specific Conceptual Design. Various designs of the lattice cell and the interaction straight sections have been compared in detail and a particular modular design has been chosen. Tolerances on the various magnet alignment and construction errors, together with the correction schemes, have been specified. Impedances contributing to collective beam instabilities and cryogenic heating were reviewed, itemized, and budgeted. The coherent and incoherent beam-beam effects were also studied in detail taking into account long-range interactions.

The operating cycle, as influenced by beam loss and luminosity lifetime, the requirements of the rf accelerating system, and the needs of the cryogenic system have all been examined in depth. The injector, a major accelerator complex in its own right, has had its components specified in response to the emittance, intensity, and other requirements of the main rings. The features of the synchrotron radiation from the multi-TeV protons and its consequences on the vacuum quality have been studied, both theoretically and experimentally (as described in Section 2.4.5). Issues of energy deposition and experimental backgrounds around the interaction regions, beam loss, and shielding requirements have been addressed in some detail.

The results of these studies are presented in this chapter.

4.1 Primary Parameters

The performance of the SSC can be specified by a relatively small number of primary parameters. To optimize the SSC performance it is necessary first to optimize among these parameters. The design goal is a 20 TeV pp collider storage ring that can achieve a peak luminosity of 10^{33} cm^{-2} s^{-1} with a small number of interactions per bunch-bunch

collision. The basis for these parameters is discussed in Chapter 2, especially Section 2.3. Table 4.1-1 is a summary of the SSC primary parameters.

4.1.1 Luminosity

The counter-rotating beams in the two collider rings consist of trains of proton bunches, spaced S_B apart, with N_B protons per bunch. The beams are bunched in order to attain the desired luminosity with minimum total beam current and to provide the gaps necessary for aborting the beams. Low current is desirable to minimize beam-gas scattering background, beam stored energy, activation in the dumps and scrapers, irradiation of the electronics, refrigeration power, and stability control requirements.

The luminosity at an interaction region is given for head-on collisions by Eq. (3.1-5),

$$\mathscr{L} = N_B^2 c / 4\pi\sigma^2 S_B \tag{4.1-1}$$

where c is the speed of the beam, taken to be the speed of light, and σ is the rms transverse beam spread (assumed equal in both dimensions) at the interaction point. Note that, with the beam current $I = ec\, N_B/S_B$, the luminosity is proportional to $I^2\, S_B$, other parameters held fixed. For a given $\mathscr{L}$, the beam current can be reduced by increasing the bunch spacing. Unfortunately, N_B increases as $\sqrt{S_B}$, causing an increase in the number of interactions per bunch crossing.

The average number of interactions per bunch crossing is

$$\langle n \rangle = \mathscr{L}\, S_B\, \Sigma_{\text{inel}}/c \tag{4.1-2}$$

where Σ_{inel} is the inelastic proton-proton cross section, which we take to be 90 mb at 20 TeV [4.1-2], ignoring the elastic events, as they are not detected. The probability that exactly k interactions occur per bunch crossing is given by a Poisson distribution. The corresponding effective luminosity is

$$\mathscr{L}_k = \mathscr{L} \frac{\langle n \rangle^k}{k!} \exp(-\langle n \rangle) \tag{4.1-3}$$

Some experiments may prefer to have one and only one interaction per bunch crossing. The effective luminosity for those experiments is

$$\mathscr{L}_1 = \mathscr{L} \langle n \rangle \exp(-\langle n \rangle) \tag{4.1-4}$$

With $\mathscr{L} = 10^{33}\ \text{cm}^{-2}\ \text{s}^{-1}$ and $\Sigma_{\text{inel}} = 90$ mb given, $\langle n \rangle$ and $\mathscr{L}_1$ are directly related to S_B, as shown in Fig. 4.1-1. For a given $\mathscr{L}$, maximum $\mathscr{L}_1$ occurs when $\langle n \rangle = 1$, which corresponds to $S_B = 3.3$ m. The conceptual design has a bunch spacing of 4.8 m, corresponding to $\langle n \rangle \simeq 1.4$ and $\mathscr{L}_1 = 0.33 \times 10^{33}\ \text{cm}^{-2}\ \text{s}^{-1}$. The loss in $\mathscr{L}_1$ from choosing $\langle n \rangle = 1.4$ rather than $\langle n \rangle \simeq 1$ is about 10%. The reasons that S_B is chosen to be 4.8 m are given in Section 4.1.3.

Table 4.1-1
SSC Parameter Summary

type of machine	proton-proton collider
beam energy, max	20 TeV
circumference (revolution frequency)	82.944 km (f_0 = 3614 Hz)
straight-section configuration, initial	West cluster: 2U + 2XL (β^* = 0.5 m) East cluster: 2U + 2XM (β^* = 10 m)
luminosity at β^* = 0.5 m/10 m	$10^{33}/cm^2s/5.6 \times 10^{31}/cm^2s$
bunch separation, no. bunches per ring	4.8 m (min), 1.71×10^4 (max)
avg. no. reactions/bunch crossing at $10^{33}/cm^2s$	1.4 (90 mb cross section)
no. protons	7.3×10^9 per bunch, 1.27×10^{14} per ring
beam current	2.0 A (pk), 73 mA (avg)
beam energy per ring	405 MJ
normalized transverse emittance	1.0×10^{-6} rad-m
luminosity lifetime	~1 day
synch. rad. power	9.1 kW per ring
synch. rad. energy damping time	12.5 h
beam-beam tune shift, linear/long-range, XL	0.84×10^{-3}max/2.1×10^{-3} per IR
rms energy spread, inj/20 TeV	$1.75/0.5\times10^{-4}$
long emittance, inj/20 TeV (rms area/π)	0.035/0.233 eV-s
arc lattice/total no. long-arc cells	FODO, 60°, 192-m cells/332
betatron tune, x,y	78.27, 78.28
momentum compaction factor	0.000223
natural chromaticity	−204
nominal IP space betw. magn. quad ends	±20 m (± 101 m)
beta max, min in arc	332, 111 m
horiz dispersion, max, min in arc	3.92, 2.36 m
crossing angle	75 μrad (typ),150 μrad (max)
distance between adjacent IPs	2.40 km
angle between adjacent IPs	106 mrad
superconducting magnet type	collared, cold iron, 1-in-1
magnet configuration	over/under, 0.7 m separation
magnetic field, dipole	6.6 T (max)
magnetic radius of curvature	10.1 km
magnetic gradient, arc quad	212 T/m
dipole length (magnetic/slot)	16.54/17.34 m
arc quad length (magnetic/slot)	3.32/4.32 m
no. regular SC dipoles/quads (both rings)	7680 horiz. dipoles/1776 quads
excitation current (dipole and cell quad)	6504 A (nominal)
vacuum chamber ID, normal	3.226 cm
rf: frequency/wavelength/harmonic	374.74 MHz/0.80 m/103,680
acceleration period	1000 s
energy gain per turn per proton	5.26 MeV
peak rf voltage/total rf power per ring	20 MV, 2 MW
rf system slot length (per ring)	25 m
rms bunch length	6.0–7.3 cm
synchrotron tune (inj/20 TeV)	$8.2/1.9\times10^{-3}$
Injector system	0.6 GeV linac, 8 GeV/c LEB, 100 GeV MEB, 1 TeV HEB

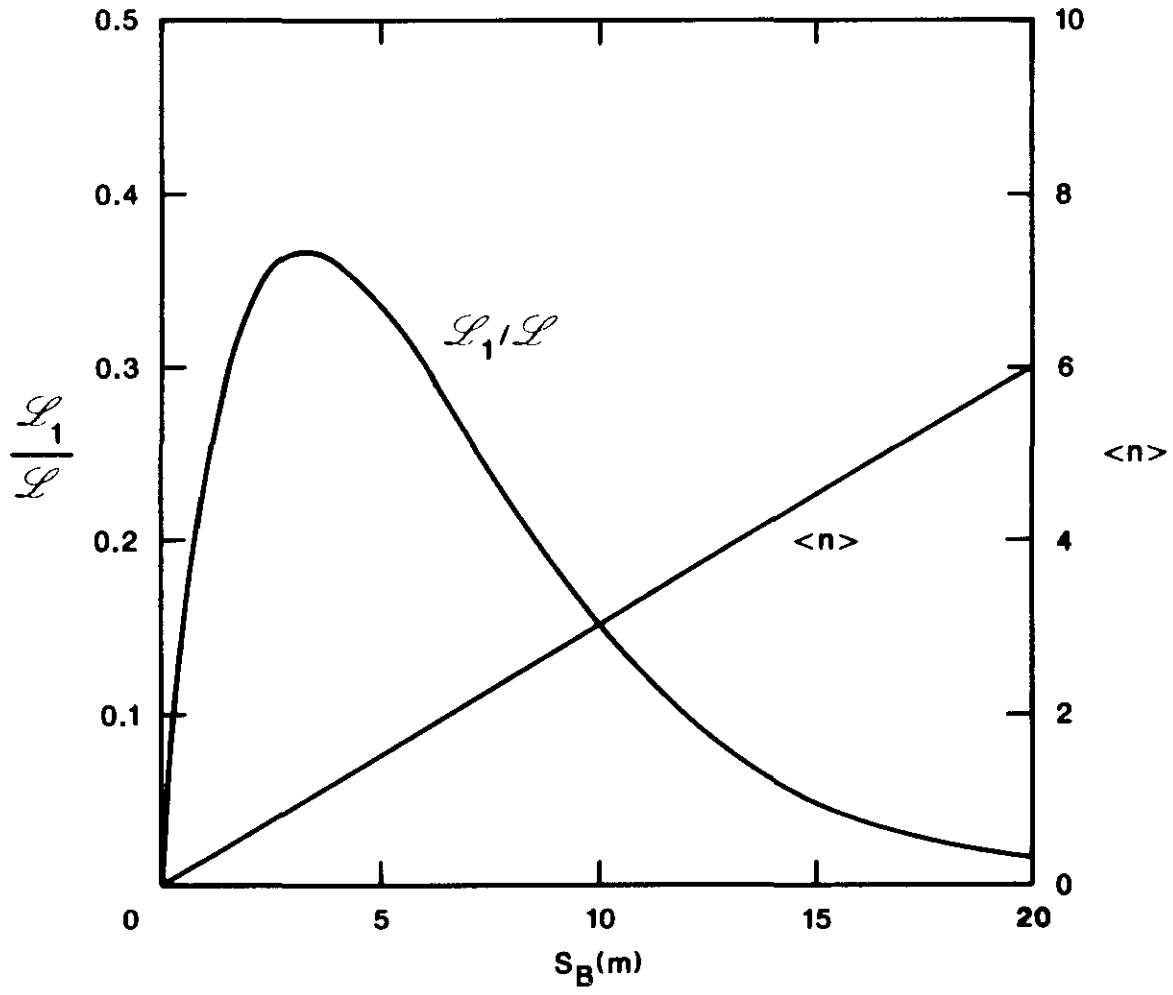

Figure 4.1-1. The average number of interactions per bunch crossing, $\langle n \rangle$, and the single-event luminosity relative to the total luminosity, $\mathscr{L}_1/\mathscr{L}$, as functions of bunch spacing S_B in meters.

4.1.2 Other Primary Parameters

The bunch spacing S_B, the number of protons per bunch N_B, and the rms transverse radius of the beam at the interaction point σ have already been introduced. Together they define the luminosity $\mathscr{L}$, Eq. (4.1-1). Other primary parameters are the betatron amplitude function at the interaction point β^*, the normalized beam emittance ϵ_N, the total number of protons in each ring N_T, the synchrotron radiation power P, the beam-beam tune shift (head-on, $\Delta\nu_{HO}$, and long-range $\Delta\nu_{LR}$), and the partial beam lifetime from proton-proton collisions τ_{pp}. For a given choice of maximum proton energy, luminosity, ring circumference, and bending radius, all the parameters can be expressed in terms of a few, chosen here to be ϵ_N, β^*, and S_B. These parameters are then set through an optimization constrained by accelerator physics and detector and accelerator technology. The bending radius (10.1 km) and the circumference (83 km) are set by technological and economic considerations.

Betatron Amplitude Function

The transverse particle motion through the bending and focusing magnets of the confinement system, described in Sections 2.4.4 and 3.1, is conveniently described in terms of the so-called betatron amplitude function or beta function $\beta(s)$, where s is the longitudinal distance around the ring. The envelope of transverse oscillations of the protons about the equilibrium closed orbit is proportional to $\sqrt{\beta(s)}$ — see Fig. 3.1-1(b). To maximize the specific luminosity the beams must be focused to a small transverse size at the interaction points. Thus the confinement system must make β(s) small there. The special value of $\beta(s)$ at an interaction point is denoted by β^*.

Normalized Beam Emittance

The normalized transverse emittance ϵ_N is a measure of the phase space area of the beam in either of the two transverse degrees of freedom. A particle undergoing betatron oscillations with amplitude a has a canonically conjugate momentum amplitude $a\gamma mc/\beta(s)$ where m is the particle's rest mass and $\gamma = E/mc^2$. Assuming independent motion in the two transverse dimensions, the particle will be confined to an area $\pi a^2 \gamma mc/\beta$(s) in phase space in one transverse dimension. A real beam contains particles with many different amplitudes and phases. At a given position around the ring, the particles in the beam have a transverse spread with an rms value σ in one dimension. We define the normalized emittance ϵ_N to be the phase space area for $a = \sigma$, divided by πmc. Thus, we have

$$\epsilon_N = \gamma \sigma^2/\beta^* \tag{4.1-5}$$

where σ and β^* are chosen for convenience to be the values at an interaction point. The dimensions of ϵ_N are length; the common unit is μm or μm-rad (or mm-mrad). By virtue of Liouville's theorem and the adiabatic invariance of phase space, ϵ_N is an invariant quantity for one-dimensional motion unless there are spatially non-uniform fields or sudden changes in the environment of the beam as it moves through the sequence of accelerators of the SSC. Since the beta function is a property of the lattice, it follows that specification of the luminosity, and hence σ, determines the requirement for the normalized beam emittance. This in turn sets requirements on the injector system.

Experience shows that the beam particles are distributed in an approximately Gaussian fashion. The phase space area $\pi\epsilon_N$, with ϵ_N given by (4.1-5), then corresponds to a radius $R = \sigma$ in coordinate space that contains approximately 39% of the beam inside it. Another definition of emittance multiplies ϵ_N by six (95% of the beam inside $R = \sqrt{6}\sigma$).

Total Number of Particles

The bunched beam has N_B protons per bunch with spacing S_B. If the circumference of the ring is C and we assume no gaps in the bunch train, there are C/S_B bunches present and the total number of protons is

$$N_T = CN_B/S_B \tag{4.1-6}$$

The total number of protons and the circumference determine the time-averaged beam current according to $I = ec\ N_T/C$, where e is the proton's electric charge. N_T also enters linearly in the amount of synchrotron power that must be removed by the refrigeration system. The conceptual design has C = 82.944 km and S_B = 4.8 m, corresponding to 17,280 bunches per ring, if we ignore the injection and abort gaps.

Synchrotron Radiation Power

A single relativistic particle moving along a path with instantaneous radius of curvature ρ radiates electromagnetic energy (so-called synchrotron radiation) at a rate, in SI units,

$$P = \frac{Z_0}{6\pi}\frac{e^2c^2\gamma^4}{\rho^2} \tag{4.1-7a}$$

where $Z_0 = \sqrt{\mu_0/\epsilon_0}$ = 377 ohms is the impedance of free space. In the SSC, the bending is not continuous, but is interrupted by gaps between magnets, drift spaces, etc. The average power per particle is therefore diminished by a factor $(2\pi\rho/C)$. The assumption of incoherent emission by all the protons leads to an expression for the total synchrotron radiation power per ring

$$P = \frac{Z_0}{3}\frac{e^2c^2\gamma^4}{C\rho}N_T \tag{4.1-7b}$$

At 20 TeV, the bending radius corresponding to 6.6 T is 10.1 km. Numerically, the power is P (kW) $\simeq 7 \times 10^{-14} N_T$.

Beam-Beam Tune Shift

As the two beams collide head-on the particles in one beam are defocused by the collective electromagnetic field of the other. This highly nonlinear focusing is characterized by a tune spread [4.1-3] given explicitly by

$$\Delta\nu_{HO} = N_B r_p/4\pi\epsilon_N \tag{4.1-8}$$

where r_p is the classical proton radius (see Ref. 4.1-1, p. 78–9). Too large a value of $\Delta\nu_{HO}$

causes the motion of individual beam particles to become unstable. A $\Delta\nu_{HO}$ per crossing point of about 0.004 (cumulative total tune spread of 0.024 for six crossing points) is the experimentally determined limit in the Sp$\bar{p}$S operating in the colliding mode [4.1-4]. Similar figures should be achievable in the SSC, if need be. The current design, however, results in a tune spread of less than 0.001 per crossing point.

In addition, because the bunch spacing is short compared with the field-free space on either side of the crossing point, bunches in one beam are subjected to several close encounters with bunches in the counter-streaming beam while traversing the field free region. This interaction, which is inversely proportional to the center-to-center distance of the bunches as they pass, results in an equilibrium orbit distortion and a shift in single particle tune called the long range beam-beam tune shift. The value of this tune shift for particles executing small-amplitude betatron oscillations is [4.1-5]

$$\Delta\nu_{LR} = \Delta\nu_{HO}\, 2n(\sigma/\beta^*\alpha)^2 = N_B r_p n/2\pi\gamma\beta^*\alpha^2 \tag{4.1-9}$$

where n is the number of long-range encounters in the interaction region and α is the crossing angle between the two beam trajectories. Typically we may have α = 75 μrad, and n = 70 with S_B = 4.8 meters. For high luminosity operations in the SSC, the linear tune shift from the long-range beam-beam interactions is about twice that caused by the head-on interactions. The tune spread and its associated nonlinear effects are, however, not as strong as their head-on counterparts. Discussion of these aspects is found in Section 4.5.9.

Partial Beam Lifetime from Proton-Proton Collisions

As the beams collide to produce physically interesting interactions, particles are lost from the bunches. The corresponding beam lifetime, referred to as the partial beam lifetime from proton-proton collisions, is

$$\tau_{pp} = N_T/n_{\mathscr{L}}\mathscr{L}\,\Sigma_{\text{inel}} \tag{4.1-10}$$

where $n_{\mathscr{L}}$ is the effective number of interaction regions that utilize the full luminosity of $\mathscr{L}$. We take $n_{\mathscr{L}}$ = 2.1 and Σ_{inel} = 90 mb as representative values.

4.1.3 Effects of Variation of Parameters

The design requirements of the SSC set limits on the various accelerator physics parameters of the machine or, conversely, the choice of a few basic parameters largely determines the overall characteristics of the accelerator. We explore the inter-relationships among the primary parameters, assuming that E = 20 TeV, $\mathscr{L}$ = 10^{33} cm^{-2} s^{-1} at 20 TeV per beam, circumference C = 83 km and ρ = 10.1 km.

Basic Equations

We express σ, N_B, N_T, P, τ_{pp}, $\Delta\nu_{HO}$ and $\Delta\nu_{LR}$, as functions of β^*, ϵ_N and S_B using the above relations. The numerical expressions, at 20 TeV, are

$$\sigma[\mu\text{m}] = 6.85\,(\epsilon_N\beta^*)^{1/2}$$

$$N_B\,[10^{10}] = 0.44\,(\epsilon_N\beta^*)^{1/2}\,S_B^{1/2}$$

$$N_T\,[10^{14}] = 3.68\,(\epsilon_N\beta^*)^{1/2}\,S_B^{-1/2}$$

$$I\ (\text{mA}) = 213\,(\epsilon_N\beta^*)^{1/2}\,S_B^{-1/2}$$

$$P\ [\text{kW}] = 26\,(\epsilon_N\beta^*)^{1/2}\,S_B^{-1/2} \qquad (4.1\text{-}11)$$

$$\tau_{pp}\ [\text{h}] = 324\,(\epsilon_N\beta^*)^{1/2}\,S_B^{-1/2}$$

$$\Delta\nu_{HO}\,[10^{-3}] = 0.54\,(\beta^*/\epsilon_N)^{1/2}\,S_B^{1/2}$$

where ϵ_N is in units of μm-rad, β^* and S_B are in meters. The units of the dependent quantities are indicated in the square brackets on the left. Strictly speaking, the expressions are valid only for head-on collisions, but the changes for finite crossing angle are known and small (see below Eq. (4.1-13)).

The long-range beam-beam tune shift depends on additional quantities, i.e., the crossing angle α and the number of long range encounters per interaction region, n. Taking the values of $\alpha = 75$ μrad and $n = 70$ (4.8 m/S_B), we obtain

$$\Delta\nu_{LR}\,[10^{-3}] = 3.0\,(\beta^*/\epsilon_N)^{-1/2}\,S_B^{-1/2} \qquad (4.1\text{-}12)$$

The first six quantities in Eq. (4.1-11) are functions of the product $\epsilon_N\beta^*$ through the beam size at the interaction point. The two beam-beam tune shifts $\Delta\nu_{HO}$ and $\Delta\nu_{LR}$ are functions of β^*/ϵ_N.

Variation of β^* and ϵ_N

Reducing the product $\epsilon_N\beta^*$ reduces the needed beam current for a given luminosity. Although reduced $\epsilon_N\beta^*$ results in a smaller τ_{pp} and a smaller beam size and thus tighter position tolerances, most of the effects of reduced beam current are advantageous. Thus the smallest values of ϵ_N and β^* commensurate with the conservative application of current technology are chosen: $\epsilon_N = 1$ μm and $\beta^* = 0.5$ m. The minimum possible value of ϵ_N is set by achievable ion source brightness. Sources capable of current adequate for SSC purposes have $\epsilon_N \simeq 0.1$ μm, sufficiently bright to permit the design emittance in the collider (see Section 4.10). The minimum practical value of β^* is set in this instance by the maximum quadrupole gradient and aperture considerations. Use of special materials or lower temperatures in the final-focus quadrupoles or shortening the experimental free space may

make lower values of β^* possible. The choices of ϵ_N and β^* also affect the beam-beam tune shifts. In the present case, however, the tune shifts are well below the projected limits and changes of a factor of two in ϵ_N or β^* result in only a 5% change in total tune shift.

Variation of S_B

Having fixed the design values of $\beta^* = 0.5$ m and $\epsilon_N = 1$ μm, we must select S_B through optimization among conflicting essentials. The important considerations are shown graphically in Fig. 4.1-1 and 4.1-2(a) and (b). The rf frequency and relative lengths of the arcs and straight sections have been chosen so that many different bunch spacings are possible. For specificity we have chosen a design consistent with operation close to the peak of $\mathscr{L}_1$, the effective luminosity for one event per crossing. By moving slightly off the peak at $S_B = 3.3$ m to 4.8 m we gain about 50% in the repetition time for the detectors (from 11 to 16 ns) and make a significant saving in synchrotron radiation power and in bandwidth required for the bunch-by-bunch feedback system, while losing only 10% in $\mathscr{L}_1$. At $S_B = 4.8$ meters and an rf frequency of 375 MHz, every sixth bucket is filled.

Energy Dependences

Luminosity at energies other than 20 TeV depends on whether it is limited by the beam-beam tune shift or by the average number of interactions per bunch crossing. Since the head-on beam-beam tune shift at 20 TeV is 0.84×10^{-3}, smaller than the value 4×10^{-3} estimated to be the beam-beam stability limit, the operation at high energies is not beam-beam instability-limited. At 20 TeV, the beam intensity is also limited by the cryogenic system capacity to absorb synchrotron radiation. As we lower the beam energy from 20 TeV and keep the synchrotron radiation power constant, the beam intensity can increase like $N_B \propto E^{-4}$, leading to a luminosity increase like $\mathscr{L} \propto E^{-7}$, and $\langle n \rangle \propto E^{-7}$. However, growth of N_B is limited by the capabilities of the injector system and the sharp increase in $\langle n \rangle$ is presumably not acceptable for the detectors. A more realistic scenario is to keep $\mathscr{L}$ and $\langle n \rangle$ constant as E is lowered from 20 TeV. Then, we have $N_B \propto E^{-1/2}$, $\Delta\nu_{HO} \propto E^{-1/2}$, and $\Delta\nu_{LR} \propto E^{-3/2}$. Figure 4.1-3 shows the energy dependence of these parameters in this scenario of operation.

As the beam energy is reduced the head-on beam-beam tune shift does not reach 4×10^{-3} until the beam energy is lowered to 1 TeV. The long-range beam-beam tune shift, however, increases rapidly as the energy is lowered. In the scenario shown in Fig. 4.1-3 we thus make the assumption that the beam-beam limit is reached when the *total* tune shift per crossing $\Delta\nu_t$ is 5×10^{-3}. This occurs at 11.2 TeV. As the beam energy is further reduced, it is possible to keep the long-range beam-beam tune shift constant by increasing the crossing angle with the scaling $\alpha \propto E^{-1/2}$. Below 11.2 TeV, we have $\Delta\nu_t$ = constant, N_B = constant, $\mathscr{L} \propto E$ and $\langle n \rangle \propto E$. These behaviors are also shown in Fig. 4.1-3. At the lowest energies (below about 2 TeV), there might be practical restrictions on the crossing angle. If so, the luminosity will be somewhat reduced from that shown in Fig. 4.1-3.

Crossing Angle

To enjoy the benefits of relatively small S_B, the beams must cross at an angle to avoid having more than one collision in each experimental straight section. A small reduction in luminosity results [4.1-6]

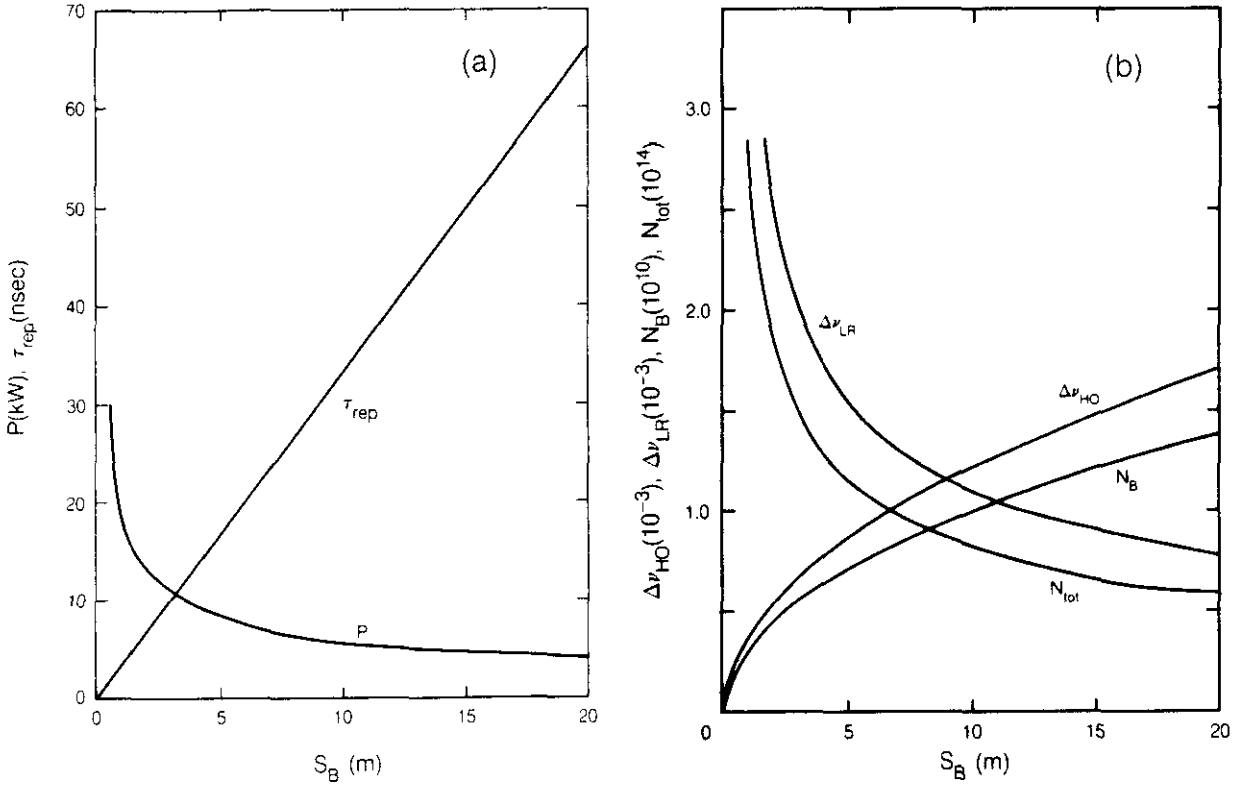

Figure 4.1-2. Dependence of various primary parameters on the bunch spacing S_B. (a) the synchrotron radiation power P and the detector repetition time τ_{rep} versus S_B. (b) the head-on and long-range beam-beam tune shifts $\Delta\nu_{HO}$ and $\Delta\nu_{LR}$, number of particles per bunch N_B, and total number of particles per beam N_T versus S_B.

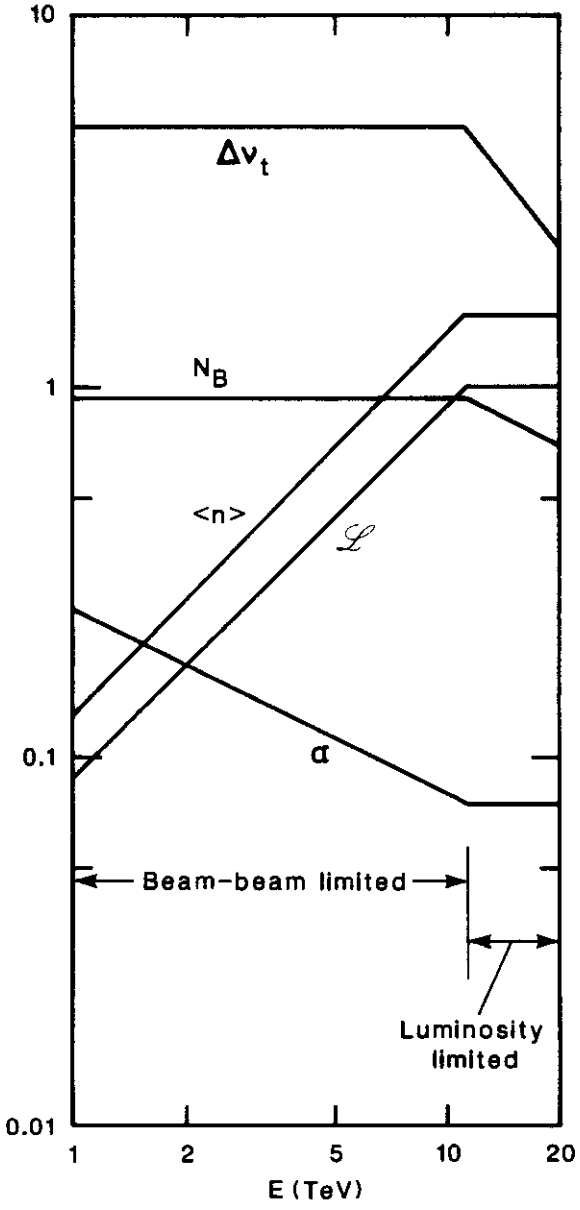

Figure 4.1-3. Dependence of a few primary parameters on the beam energy. In this scenario, the operation is luminosity limited above 11.2 TeV and beam-beam limited below 11.2 TeV. The units for the parameters are $[\mathscr{L}] = 10^{33}$ cm^{-2} s^{-1}, $[\alpha]$ = mrad, $[\Delta\nu_t] = 10^{-3}$ and $[N_B] = 10^{10}$.

$$R \equiv \frac{\mathscr{L}}{\mathscr{L}_o} = \frac{1}{\sqrt{1 + (\alpha\sigma_z/2\sigma)^2}} \tag{4.1-13}$$

where σ_z is the longitudinal rms bunch dimension. The effect is small even in the high luminosity interaction regions where it is most pronounced. To maintain a given $\mathscr{L}$, the quantity N_B (and consequently N_T, I, P, τ_{pp}, and $\Delta\nu_{LR}$) must be increased by a factor $R^{-1/2}$. With $\alpha = 75$ μrad, $\sigma_z = 7$ cm, and $\sigma = 4.8$ μm, the increase in N_B is 7%. The needed increase for the intermediate luminosity case is hardly noticeable.

A finite crossing angle also slightly affects the head-on beam-beam tune shift. The tune shift in the crossing plane is [4.1-6]

$$(\Delta\nu_{HO})_{\text{crossing plane}} = \frac{N_B r_p}{4\pi\epsilon_N}\left(\frac{2R^2}{1+R}\right), \tag{4.1-14a}$$

while in the non-crossing plane, it is

$$(\Delta\nu_{HO})_{\text{noncrossing plane}} = \frac{N_B r_p}{4\pi\epsilon_N}\left(\frac{2R}{1+R}\right). \tag{4.1-14b}$$

The values of quantities listed in Eq. (4.1-11) are given below, taking into account the crossing angle effects ($\beta^* = 0.5$ m, $\epsilon_N = 1$ μm-rad, $\alpha = 75$ μrad and $\sigma_z = 7$ cm)

$$\begin{aligned}
&R = 0.88\\
&\sigma = 4.8\ \mu\text{m}\\
&N_B = 7.3 \times 10^9\\
&N_T = 1.27 \times 10^{14}\\
&I = 73\ \text{mA}\\
&P = 9.14\ \text{kW}\\
&\tau_{pp} = 187\ \text{h}\\
&(\Delta\nu_{HO})_{\text{crossing plane}} = 0.74 \times 10^{-3}\\
&(\Delta\nu_{HO})_{\text{noncrossing plane}} = 0.84 \times 10^{-3}\\
&\Delta\nu_{LR} = 2.1 \times 10^{-3}
\end{aligned} \tag{4.1-15}$$

The synchrotron radiation power listed includes the additional 0.09 kW contribution from the beam separation dipoles on each side of the interaction points.

It should be stressed that the values of Eq. (4.1-15) are nominal, chosen for this conceptual design. There is considerable flexibility in crossing angle, bunch spacing, and other parameters to provide optimal conditions in actual operation.

4.1.4 Primary Lattice Features

The lattice is made of three types of modules: arcs, interaction regions (IR), and the utility modules. Designating these three modules by A, X, and U, respectively, the SSC lattice consists of the following sequence: *F, F, X, X, A, U, U, X, X, A*, where F indicates a future interaction region that at present has the lattice structure of a utility section. See Fig. 3.3-2. The IR and the utility modules are interchangeable from the lattice design point of view. They both have lengths of 2400 m and both match to the same optical functions of the basic arc cells at their ends.

The IRs are arranged in two clusters, 4 IRs in one of the clusters, called the East cluster, and 2 IRs and 2 utility modules in the other (West) cluster, as described in Section 3.3. The clustered IRs are adopted for the SSC to permit extensive sharing of support facilities. A comparison between evenly distributed and clustered IRs is included in Section 4.2.2.

As shown in Fig. 3.3-4, on each side of an interaction region, a triplet of quadrupoles provides the strong focusing needed at the interaction point (IP). In the high luminosity operation, the interaction point has $\beta^*_x = \beta^*_y = 0.5$ m and the distance between the IP and the face of the first IR quadrupole is $L^* = 20$ m. The last 3 m of this 20 m space contains also parts of cryogenic systems and scrapers for the secondary beams to protect the triplet quadrupoles. The maximum beta function in the triplet is about 8000 m. The conceptual design also describes a different interaction region that provides intermediate luminosities. The interaction point has $\beta^* = 10$ m; the free space around the interaction point is ± 102 m; the luminosity is 0.56×10^{32} cm^{-2} s^{-1}. The flexibility of the lattice design permits continuous evolution of the interaction region layout to optimize experimental usage over the life of the facility. In the present lattice design, the two east IRs have intermediate luminosities, while the west IRs have high luminosities. During colliding beam operations, the luminosity of an individual low-beta IR can be controlled by adjusting β^* in the range between 0.5 m and 6 m, the latter being the value at injection.

The choice of $\beta^* = 0.5$ m for high luminosity operations depends on the value of $L^* = 20$ m. The possibility of shortening L^* to allow a lower value of β^*, and thus higher luminosity without increasing the beam intensity, is being studied [4.1-7]. Tentative results indicate that reducing L^* to 15 m would allow β^* to be lowered to about 0.4 m with an increase of the maximum beta function or an increase in the maximum strength in the triplet quadrupoles. With $\alpha = 75$ μrad and $\sigma_z = 7$ cm, this allows the luminosity to increase by 25%. Increasing L^* to 25 m, on the other hand, would cause β^* to increase to 0.65 m, thus reducing the luminosity by about 20%.

The beams cross each other with a small angle at the interaction points. The angle is typically 75 μrad but is variable from 0 to 150 μrad or higher. The triplets are shared by both beams. After the triplet the beams are separated vertically in two stages to a separation of 70 cm. The section that provides the beam separation also matches and removes vertical dispersion. The horizontal dispersion is then matched to the regular arc cell values by another section that also matches the betatron functions.

The utility module is shown in Fig. 4.2-6. Free spaces are available for the beam injection and abort systems. The rf cavities, occupying a total space of 25 meters, are also located in the utility sections.

The clusters are connected by arc modules, periodic arrays of 192-meter cells, each consisting of 10 bending magnets and two focusing quadrupole magnets, as shown in Fig. 4.2-3.

The particular cell length and the focusing phase advance of 60 degrees are chosen to give minimum cost of the magnet system taking the needed aperture into account. There are 166 cells in each of the arcs. The bending magnet field at 20 TeV is 6.6 T. The quadrupole gradient is 212 T/m.

In each cell, two spaces are reserved for so-called spool pieces where various correction coil packages, as well as cryogenic connections, are located. Orbit distortions, for example, are corrected by dipole correctors, while the phase advance per cell can be varied by trim quadrupoles in the spool pieces. The range of variation of phase corresponds to a tune variation of ± 2 units. Two families of chromaticity sextupoles are also included in the spool pieces. In addition, several multipole correctors are available in the spool pieces to stabilize particle motion in the presence of the nonlinear magnet field errors.

4.2 Lattices

The lattice design of the SSC is critical because of the variety of experimental and operational needs it must accommodate while minimizing intrinsic nonlinearities in the designed ideal structure, sensitivity of particle motion to various errors, and cost.

The primary lattice parameters have been described in Section 4.1.4. In Section 4.2.1, we describe in detail the beam optics considerations that led to the design of the SSC lattice. One issue, namely the distribution of the interaction regions, involves a more extensive study and is described separately in Section 4.2.2. The lattice chosen on the basis of these considerations is described in Sections 4.2.3, 4.2.4, and 4.2.5. In Section 4.2.4, tuning of the IR optics to accommodate injection is also described. The optical properties of the ideal lattice without magnet field errors are given in Section 4.2.6. Effects of the magnet errors are treated in Section 4.3. An example of a non-planar design is described briefly in Section 4.2.7.

4.2.1 Lattice Considerations

For high luminosity operation and assumed equal horizontal and vertical emittances, the beam at the interaction point (IP) is round, with $\beta^*_x = \beta^*_y = 0.5$ m. On each side of an IP, a triplet of quadrupoles rather than a doublet is used to provide the strong focusing needed at the IP [4.2-1, 4.2-2]. This has the advantage that the maximum beta function in the interaction region (IR) quadrupoles is minimized. The magnet polarities are antisymmetric about the IPs. This simplifies the IR design since a symmetric design necessarily requires two types of IRs. Moreover, the cancellation of chromatic aberrations between the triplets in adjacent IRs in a cluster, as described in Section 4.2.2, is not feasible in the symmetric situation.

The distance between the IP and the face of the first IR quadrupole is $L^* = 20$ m. This gives maximum beta function values in the triplet of about 8 km in the colliding mode with $\beta^* = 0.5$ m. The nonlinear chromatic effects introduced by this IR insertion are relatively small compared with those introduced by the arc dipole magnets (with their field errors), and the beam energy spread is small ($\sigma_\delta = 0.5 \times 10^{-4}$). Thus the major consequences of the relatively large maximum beta are tightened alignment tolerances. A beam-steering

feedback system based on a scanned luminosity measurement as its input signal will secure the needed alignment.

The beams are separated vertically by 70 cm in the arcs. The magnets in the arcs are arranged in an over-under configuration rather than side by side. The 70 cm separation allows the magnets of the two rings to be decoupled cryogenically as well as magnetically. The over-under arrangement has the advantages that the tunnel space can be utilized more effectively and that the path lengths between collision points in the two rings can be more easily equalized. The decoupled magnets allow separate operation of the two rings. This makes it possible to perform accelerator physics studies on one ring when the other ring is not available [4.2-3].

In a side-by-side arrangement, the horizontal dispersion introduced by the separation section can be removed by the horizontal dispersion suppressor already incorporated in the lattice. In an over-under arrangement, the vertical dispersion caused by the vertical separation section has to be compensated by an additional vertical dispersion suppressor. This can be done in two ways, depending on whether the beam separation starts immediately after the IR triplets (the early separation scheme) [4.2-2] or about 200 m after the triplet (the late separation scheme) [4.2-4]. The former allows more flexibility for operating and making corrections on the two rings separately and it minimizes the long range beam-beam perturbations. Early separation also makes it easier to remove the forward secondary particles that are generated by beam collisions. The latter has the advantage that the beta functions are more easily controlled, giving smaller beta function values in the matching quadrupoles beyond the main triplets.

The present conceptual design adopts the early separation scheme. The vertical dispersion suppression is accomplished by dividing the 70 cm separation into two steps and then introducing a FODO section which has 180 degree phase advance between the two steps. The vertical dispersion contributions from the two steps cancel outside the separation region.

Chromatic correction is performed by two families of sextupoles located in the spool pieces of the arc cells. This is common in proton accelerators, but is quite different from the multi-family designs typically used in high energy electron storage rings. This suffices because the rms beam energy spread is 1.5×10^{-4} at injection and 0.5×10^{-4} during storage and the expected maximum energy error at injection is 10^{-3}. These values are small compared with those of the electron storage rings. The demand for chromatic uniformity is therefore much less severe. On the other hand, the introduction of multiple sextupole families or octupole families as future improvements is left open at this stage.

The arc cells have a length of 192 m, a result from cost minimization, given the aperture needed for stability of particle motion. (This subject is discussed in Section 4.3.) The betatron phase advance per cell has been chosen to be 60 degrees. In the presence of magnet field errors, the 90 degrees case is clearly better optically for a given cell length [4.2-5]. However, the stronger quadrupoles of the 90-degree cells require additional cost. A comparison was therefore made between a 60 degree phase advance with 100 m cells and 90 degrees with 120 m cells. It was found [4.2-5] that the two alternatives are quite comparable in performance. More specifically, the 60 degree phase advance gives better on-momentum behavior, but worse off-momentum behavior, than does the 90 degree case. Both choices provide acceptable aperture for stable particle motion, although the better on-momentum behavior of the 60 degree choice is slightly preferred.

Tune variations are obtained by varying the two families of trim quadrupole coils in the corrector spool packages. The range of the tune variation is ± 2 units in each plane. The phase advance per cell then deviates slightly from 60 degrees, but this deviation does not cause reduction in beam aperture (see Section 4.3.5). In addition, the optimum phase advance between IRs can be maintained by the quadrupoles in the IR regions over a considerable range of optical parameters. For example, it is possible to keep the tune advance between adjacent IPs in a cluster fixed when β^* is varied from 6 m to 0.5 m. Moreover, the insertion clusters are designed with unit matrix transformations, so that phase changes in their cells cause no mismatch in the arcs and virtually none at the IPs.

4.2.2 Clustered Interaction Regions

An example of clustered IRs is shown in Fig. 3.3-2. The two IRs in the West cluster, adjacent to the two utility sections, are the high luminosity IRs with low β^*. The two IRs opposite the two utility sections are regarded in this example to be future IRs, undeveloped at the startup of the SSC, and optically identical to the two utility sections. The remaining pair of IRs are similar in structure to the low-β^* ones, but they have intermediate luminosity with a modest value of β^* and extended free space about the interaction points.

In this section, we discuss the various issues associated with clustering the IRs. Figure 3.3-2 is just one of several possible clustering configurations. Other configurations are sketched in Fig. 4.2-1. The layout of Fig. 3.3-2, the one selected for the conceptual design, is designated by $(2,4)_b$.

The beam optics, beam-beam effects, and background radiation are some of the accelerator physics issues to be considered when discussing clustered interaction regions. The results of a study of these questions [4.2-7] are summarized in the present section. More information on the beam-beam effect can be found in Section 4.5 and more on the backgrounds in Section 4.8. The main conclusion of the study is that both distributed and clustered IRs are acceptable for the SSC design from the accelerator physics point of view. However, the clustered scheme is more cost effective because of considerations concerning the conventional facilities and so was recommended for the SSC conceptual design.

Generally speaking, evenly distributed IRs permit a higher superperiodicity and thus fewer resonances in the tune space. For the case of SSC, this means a superperiodicity of 6, if the utility sections and crossings are ignored. Realization of the consequences of high superperiodicity requires correlation of particle motion in magnets that are separated by 1/6 of the ring circumference, i.e., about 14 km. Because of various magnet field and alignment errors, correlation over this long distance is not likely to be maintained. The superperiodicity is thus broken in reality and all low-order resonances, systematic and accidental, need to be avoided.

The fact that a high superperiodicity is not very important for the SSC is demonstrated by particle tracking using the programs PATRICIA [4.2-8] and RACETRACK [4.2-9] on various lattices [4.2-10]. The maximum amplitude of stable motion (referred to as the dynamic aperture in Sections 3.2 and 4.3) is plotted in Fig. 4.2-2 as a function of momentum deviation $\delta = \Delta E/E$. Random magnet multipole errors (Table 4.3-1) are included in these simulations. For each case, the same tunes are used, away from systematic resonances. The dependence of dynamic aperture on the IR layout, and thus the superperiodicity, is not significant.

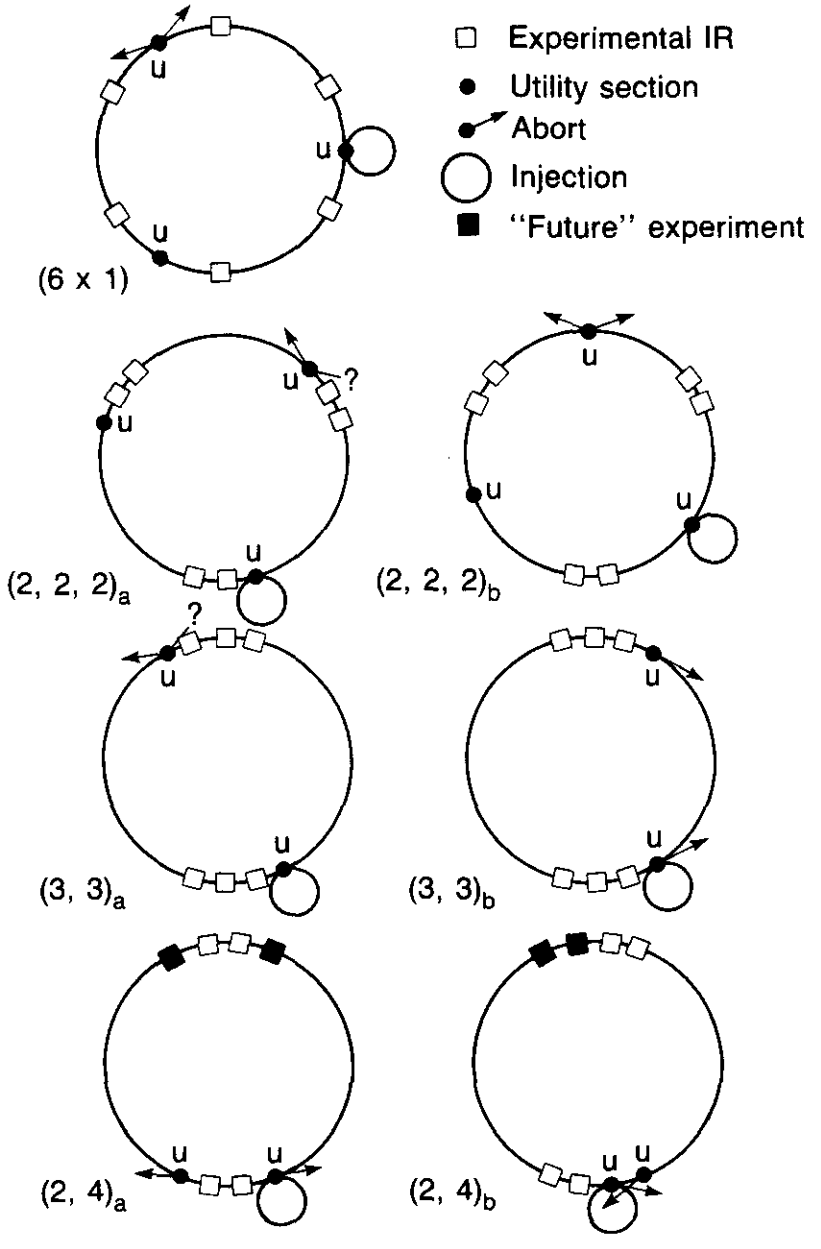

Figure 4.2-1. Various possible IR clustering arrangements for the SSC.

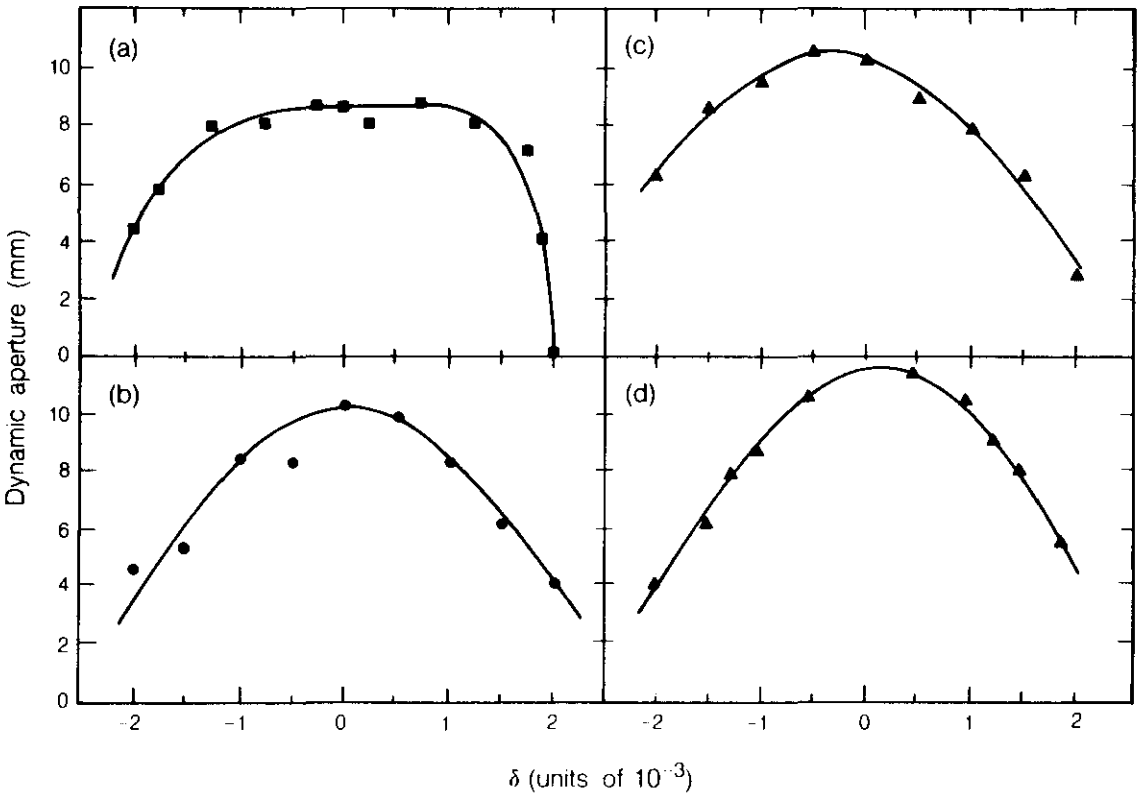

Figure 4.2-2. Comparison of dynamic aperture for three different IR arrangements. (a), (b), (c) and (d) are examples 1, 2, 4 and 6 of Table 4.2-1, corresponding to the (6×1), (3,3), $(2,4)_a$ and $(2,4)_b$ designs, respectively.

The betatron phase advance per cell in general depends on the momentum deviation δ. This dependence of the phase advance is specified by the chromaticity, i.e., the derivative of the phase advance with respect to δ, divided by 2π. In a storage ring with IRs, chromaticity accumulates over an interaction region, but is reset to zero by properly setting the two families of chromaticity sextupoles in the adjacent arcs. This is done for all IR layouts. However, for the clustered layout, the chromaticity accumulates over a few IRs before it is corrected in the arcs. A possible undesirable effect of this is a betatron phase modulation of the beam-beam kicks because of synchrotron oscillation. The amplitude of the phase modulation, however, is only about 0.6 degrees for a particle executing a synchrotron oscillation with amplitude of $\delta = 10^{-4}$. Such a phase modulation is negligible compared with that considered in Sections 4.5.7 and 4.5.8 for the beam-beam effects. The possibility of having multiple sextupole families rather than two to control the chromaticities locally has been studied for various clustering arrangements [4.2-10]. The chromatic behavior in general was found to deteriorate as compared with the two family scheme.

There is a potential optical advantage of IR clustering. Compared with distributed IRs, clustered IR lattices have one more variable to control the optical quality, namely, the betatron phase advance μ between adjacent IPs in a cluster. The optimum value of μ is found to be an odd multiple of $\pi/2$ [4.2-7, -11, -12]. By pairing IRs in a cluster and setting μ to the optimum value, one minimizes the chromatic aberrations of particle motion. This optimum phase also helps to reduce the orbit effect from long-range beam-beam interactions and to suppress some of the incoherent beam-beam resonances.

To be more specific, the tune dependence on momentum is described to first order by the chromaticity. As mentioned, the chromaticity is set to zero by properly setting the two families of chromaticity sextupoles in the arcs. The second order dependence of the tune on momentum could be removed by introducing multiple sextupole families, but it is also substantially reduced if adjacent IRs are paired with $\mu = (2n+1)\pi/2$. Table 4.2-1 gives the tune deviation at $|\delta| = 10^{-3}$ for a few examples of test-lattice designs [4.2-10]. The adopted SSC lattice design has an IR clustering that is close to example 6 of Table 4.2-1, although the numerical values differ in detail. The value of μ is not listed for examples 1 and 2 since pairing does not apply. The condition of $\mu = (2n+1)\ \pi/2$ also minimizes the energy dependence of β^* and the beta function in the triplets, which in turn minimizes the spurious dispersion at the interaction point from misalignment of the IR quadrupoles [4.2-7].

The phase advance between clusters, accumulated through the long arcs, also has an effect on the chromatic behavior. Some of the examples in Table 4.2-1 have advantageous phase advances between clusters. Strictly speaking, to minimize further the chromatic aberrations, it is necessary to choose this phase advance to be also close to an odd multiple of $\pi/2$ [4.2-11]. This is not adopted in the conceptual design because it implies restricting the overall tune to values close to a low order resonance. Furthermore, the field errors along the long arc are likely to distort the optimum phase condition. We thus leave the phase advance between clusters open in the design and let the actual operation determine the optimum phase between clusters.

Table 4.2-1
Tune deviation for $\delta = 10^{-3}$ for six examples of test lattices. Each example has acceptable chromatic behavior.

Example	Lattice	ν_x	ν_y	$\mu/2\pi$	$\Delta\nu_x$	$\Delta\nu_y$
1	(6×1)	85.285	85.265	—	0.0025	0.0025
2	(3,3)	85.26	85.28	—	0.0028	0.0029
3	(2,2,2)	85.255	85.275	0.75	0.0018	0.0017
4	$(2,4)_a$	89.264	89.285	0.71	0.0019	0.0017
5	$(2,4)_b$	89.264	89.285	0.71	0.0035	0.0036
6	$(2,4)_b$	89.264	89.285	0.75	0.0015	0.0014

The beam-beam effects are discussed in detail in Section 4.5. Suffice it to say here that [4.2-7]

(a) The coherent beam-beam effect is quite similar between the distributed and the (3,3) design, even when long-range interactions are taken into account. The density of resonances doubles for the (2,4) arrangement or for the distributed and (3,3) designs if all IRs are not identical, but the strengths of these coherent beam-beam resonances are weak.

(b) The incoherent beam-beam effect favors the IR pairing. With paired IRs and an odd multiple of $\pi/2$ phase advance between them, the beam-beam resonances are maximally suppressed. The (2,4) arrangement thus is preferred as compared with the distributed or the (3,3) arrangement.

It is important to realize that choosing the proper phase advance between adjacent IRs is not absolutely necessary since the chromatic aberration is not intolerably large without cancellation. The (6×1) and the (3,3) designs without pairing can work acceptably within the interesting range of δ. Pairing between adjacent IRs, however, is desirable, when possible, and is done in the conceptual design. Note also that chromatic aberrations are inversely related to β^*. Thus the best chromatic cancellations are obtained by pairing identical IRs, especially those with low β^*.

Background effects, are discussed in detail in Section 4.8. Scraping of the beam amplitude tail and energy tail is needed on each side of an interaction region to prevent particles from entering the detectors located in the adjacent IRs. This beam scraping will be needed whether the IRs are clustered or not [4.2-7].

4.2.3 Arc Module

There are two arc modules in the SSC, each consisting of 166 cells. With a 60 degree phase advance and 192 m length per cell, an arc module has a tune contribution of 27 2/3 and a length of 31872 m. Figure 4.2-3 shows the magnet arrangement and lattice functions of a unit cell [4.2-2]. Five bending magnets, each with magnetic length of 16.54 m, are

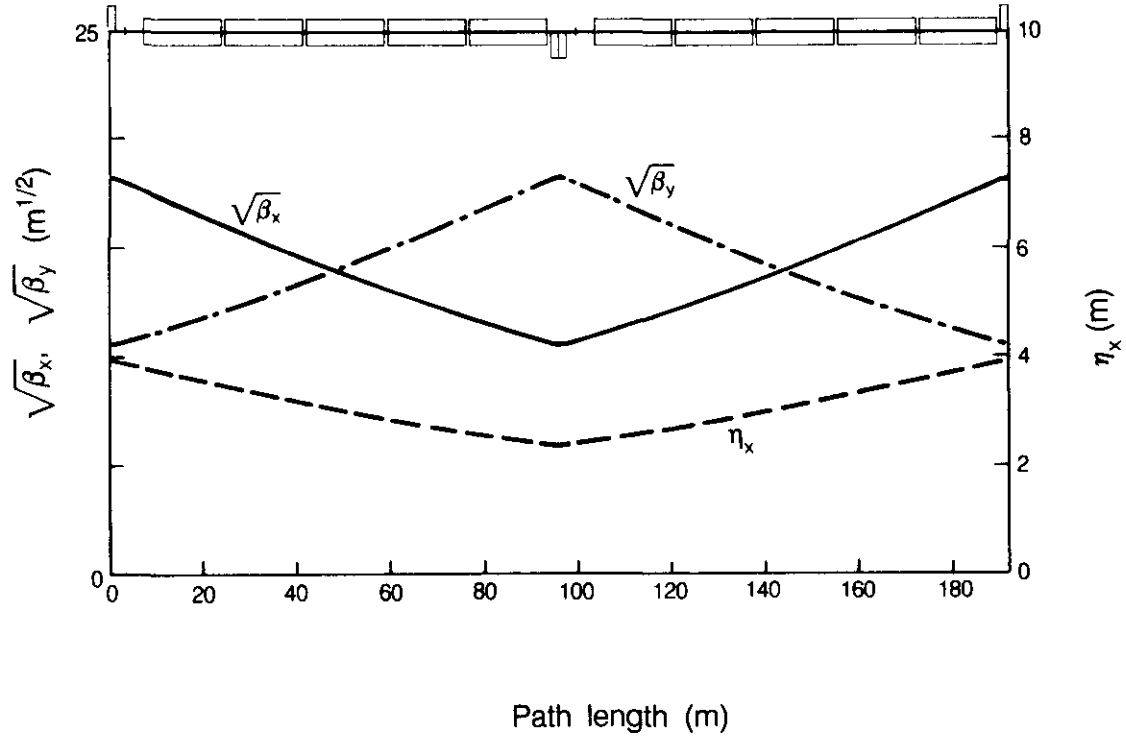

Figure 4.2-3. Magnet arrangement and lattice functions of a unit cell in the arc module.

placed between adjacent quadrupoles. The corresponding magnets of the two rings are placed exactly above and below each other, separated by 70 cm. The two quadrupoles at a given longitudinal position have the same gradient but opposite focusing effect on the two beams.

In order to make room for the correction spool pieces, the group of five bending magnets is shifted (in the same direction in all cells) by 2.59 m away from the center of the drift space. This shift does not affect the beta functions but slightly alters the dispersion function, giving rise to a finite slope $\eta_x' = 0.00022$ at the centers of the focusing and defocusing quadrupoles. To the extent that this perturbed dispersion needs to be corrected, it can be matched into the utility and IR modules by their dispersion suppressor quadrupoles, although these might have to be slightly different in the two rings. An alternative way to deal with this dispersion mismatch by slightly perturbing the design trajectory in the arc has been studied as a future possibility [4.2-13].

4.2.4 Interaction Region Modules

It is envisioned that the SSC will eventually have six IRs. Initially, however, only four will be used. An attractive possibility, adopted for the conceptual design, is to have two IRs with high luminosities (10^{33} cm^{-2}s^{-1}) and two with intermediate luminosities (0.57×10^{32} cm^{2}s^{1}). The high-luminosity module has $\beta^* = 0.5$ m and a free space $L^* = \pm 20$ m about the IP, while the intermediate-luminosity module has $\beta^* = 10$ m and a much longer free space $L^* = \pm 101$ m. The value of $\beta^* = 0.5$ m for the high-luminosity module is believed to be close to the tightest focusing allowed by the presently conceived system. On the other hand, $\beta^* = 10$ m for the intermediate-luminosity module is somewhat flexible. The two initially unused IRs are simply represented by utility sections in this conceptual design.

Except for an added half cell at one end, an IR module is centered about the interaction point (IP) and is optically matched to link to the arc or to other modules. The quadrupole polarities are antisymmetric about the IP. Both modules have the same length and horizontal beam geometry as the utility module. The betatron phase advances are $3.75 \times 2\pi$ for the $\beta^* = 0.5$ m module and $3.25 \times 2\pi$ for the $\beta^* = 10$ m modules. These phase advances are chosen to minimize some of the nonlinear chromatic effects, as discussed in Section 4.2.2. Figure 4.2-4 shows the magnet arrangement and lattice functions for the two modules. The two beams are separated vertically by 70 cm when entering the IRs. They are brought into collision by translating the beam trajectories toward the median plane. This is done in two steps which, combined with the 180 degree section between them, cancel each other's vertical dispersion. The two beams exchange their vertical positions after crossing the IP.

Except for the extra half cell at one end, the horizontal bending is essentially symmetric about the IP. The symmetry is slightly broken by the fact that, within the strictly symmetric geometric pattern of the quadrupoles, all bending magnets are unidirectionally shifted by 2.59 m as in the cells.

The quadrupole focusing in the IR module is strictly antisymmetric about the IP. This antisymmetry is needed to produce essentially the same optics in both rings, since the triplet quadrupoles around the IP are shared by both beams. The antisymmetry is also the reason for including the extra half cell in the definition of the IR modules.

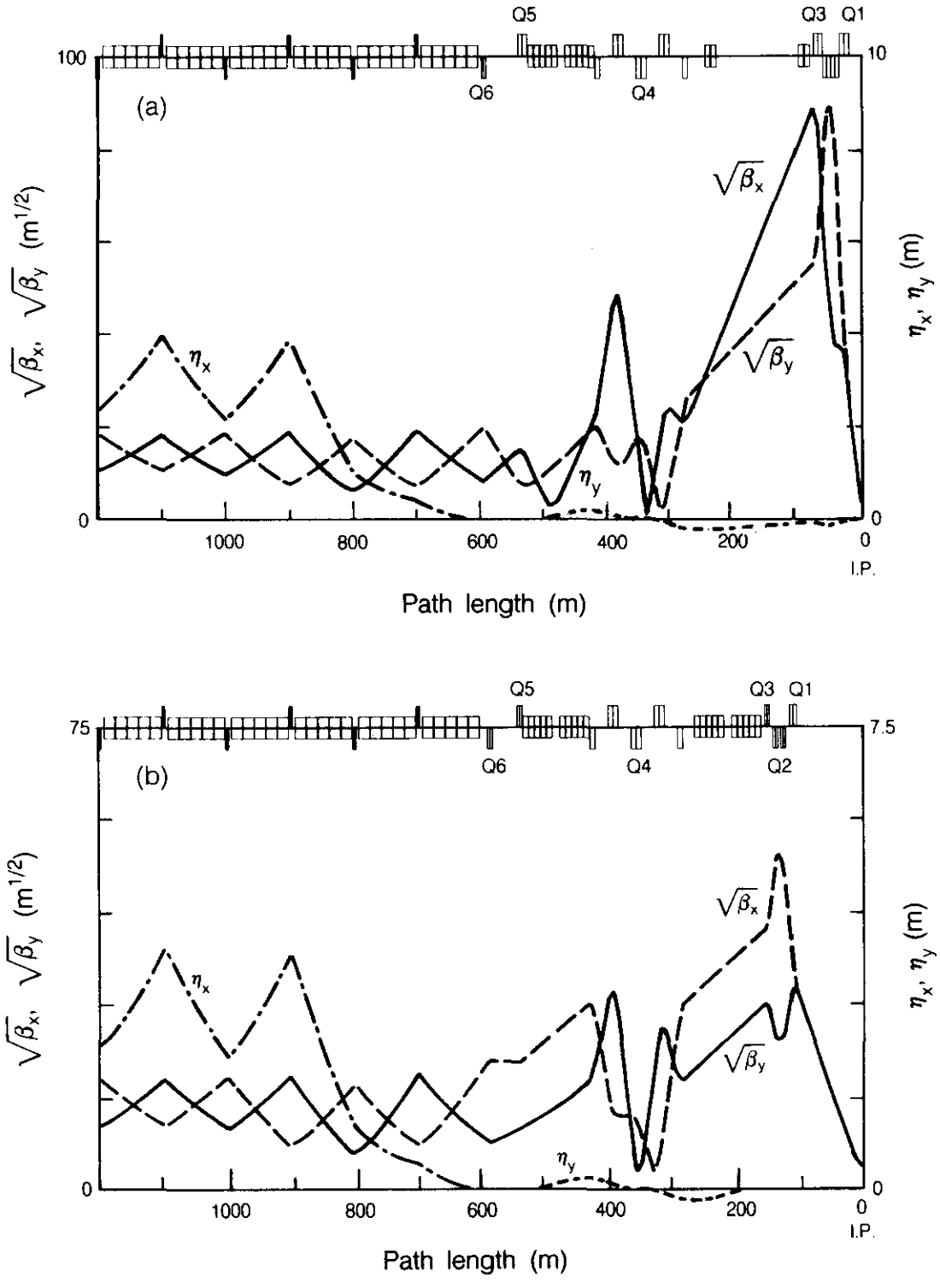

Figure 4.2-4. Magnet arrangement and lattice functions of (a) the high-luminosity module with $\beta^* = 0.5$ m and $L^* = \pm 20$ m, and (b) the intermediate-luminosity module with $\beta^* = 10$ m and $L^* = \pm 101$ m. Only half modules are shown. Magnets Q1 through Q6 are indicated. Quadrupole polarities are reversed in the other half of the modules, so that the β_x and β_y functions are interchanged.

The IR module is, in the order proceeding toward the IP, composed of the following subsections [4.2-14, 4.2-15].

Dispersion Suppressor

The dispersion suppressor has the same magnet geometry and bending magnet strengths as three normal arc cells, but the quadrupole lengths are different. Four of the five quadrupole lengths are adjusted so that the dispersion is suppressed, including the small slope $\eta_x' = 0.00022$ introduced by the shifting of bending magnets in the arc cells. A fifth variable is introduced to minimize the beating of the beta function within the suppressor. To the extent that η_x' needs to be matched, the five quadrupole settings will be slightly different between the top and the bottom rings. This is because in one ring the matching across the module is from η_x' to η_x' while the other ring has $-\eta_x'$ to $-\eta_x'$ matching.

Matching Quadrupole Doublet

The matching quadrupole doublet (Q5 and Q6), in conjunction with Q4, which is discussed next, match the beta functions and the betatron phase advance from the dispersion suppressor to the IR triplet.

Vertical Translation

The vertical translation of each beam is done in two steps of 17.5 cm each. The two pairs of vertical bending magnets are located in two rather long drift spaces that have between them a section consisting of two 90-degree cells. When fully periodic, the section has a transformation matrix $M = -1$. The vertical dispersion from the two translational steps thus cancel each other, while the beta functions outside the $M = -1$ section are unperturbed by the insert. Since the vertical dispersion goes through zero at quadrupole Q4, which is located at the center of the section, the strength of Q4 can be varied to control the beta functions without appreciably affecting the vertical dispersion cancellation. This is particularly useful in producing the injection optics, as is described below.

Quadrupole Triplet

The quadrupole triplets (Q1, Q2, Q3) around the IP match the beta functions into the desired values at the IP. The conditions matched to are $\beta_x^* = \beta_y^* = \beta^*$ and $\alpha_x^* = \alpha_y^* = 0$, where $d\beta(s)/ds = -2\alpha(s)$. The maximum gradient of these triplet quadrupoles is 231 T/m.

The small beam diameter required at the IP for collisions is obtained by having a small β^*, which in turn implies a large beta function in the adjacent triplets. For the $\beta^* = 0.5$ m module, for example, the maximum beta function in the triplet is about 8000 m. This represents a severe aperture restriction. Although believed to be acceptable for colliding beams, this aperture is too small for beam injection. We have thus provided for each IR module an accompanying injection optics, which has much smaller maximum beta functions. The lattice functions of the injection lattices are shown in Fig. 4.2-5 [4.2-14, 4.2-15]. The beams are injected and accelerated in the detuned optics. At the end of acceleration

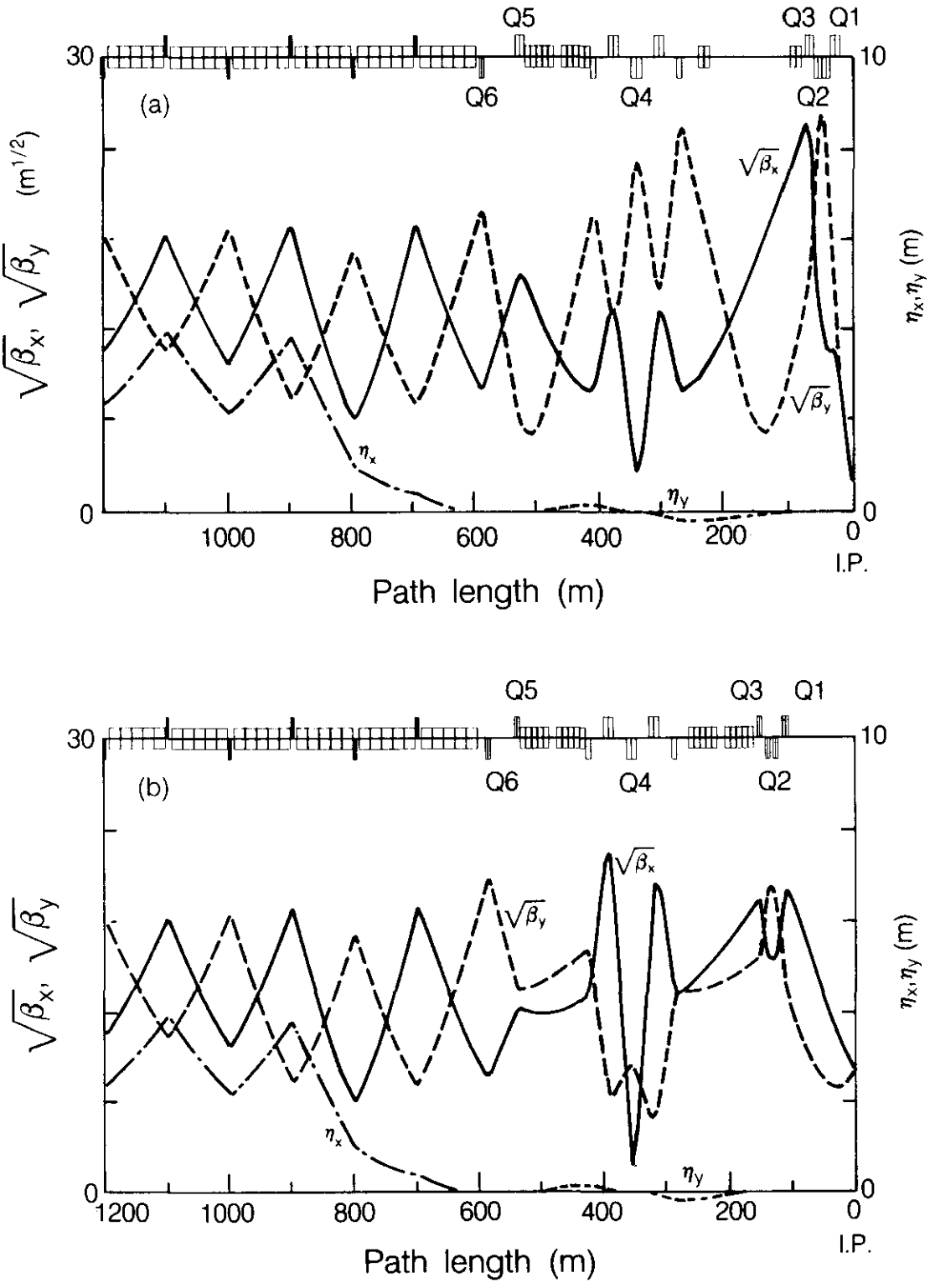

Figure 4.2-5. Optics for the two IR modules when detuned for injection. The beta functions at the IP are $\beta^* = 6$ m and 64 m, respectively.

and necessary orbit and tune adjustments, the injection optics is gradually transformed to the low-β^* optics along a well-defined path [4.2-14,4.2-16]. During the change, the betatron phase advance across the module is kept fixed.

4.2.5 Utility Module

The two utility sections located side by side in the west cluster provide space for beam injection, abort, and rf cavities. These sections are straightforward from an optics point of view. The magnet arrangement and the lattice functions are displayed in Fig. 4.2-6. The phase constraint of an IR module is applied here also; each utility module has a phase advance of $2.25 \times 2\pi$.

At each end of the utility section, there is a dispersion suppressor of the same design as that in the interaction region modules. The long non-dispersive region is convenient for beam injection. Four quadrupole doublets, antisymmetrically located about the center of the section, provide the focusing. The beta functions have a peak value of about 1100 m. The aperture of these quadrupoles is larger than that of the arc quadrupoles so that there is sufficient room for the beam during injection. A 1 cm oscillation in the arcs, for example, requires 1.8 cm beam-stay-clear radius at the beta function peaks. The inner coil diameter of these quadrupoles is thus taken to be 5 cm, the same as that of the High Energy Booster quadrupoles, rather than the 4 cm used for the arc quadrupoles. The radio-frequency cavities are located in regions with lower beta functions to reduce their effects on transverse instabilities. The average beta functions in the 25 meter space for the rf cavities are β_x = 220 m and β_y = 70 m.

4.2.6 Optical Properties

The chromatic behavior of the colliding beam lattice (two IRs with β^* = 0.5 m and two with β^* = 10 m) is shown in Fig. 4.2-7. The variation of betatron tunes ν_x and ν_y, the lattice functions β^* and α^* at the interaction points, and the closed orbit Δx^* and Δy^* at the interaction points are shown as functions of the relative energy deviation $\delta = \Delta E/E$. This behavior is quite acceptable within the range $|\delta < 10^{-3}$.

The program MARYLIE [4.2-17] has been used to analyze the tune dependence on the betatron emittances ϵ_x and ϵ_y (related to the normalized ϵ_N by $\epsilon = \epsilon_N/\gamma$). The result can be expressed as

$$\Delta\nu_x = a\ \epsilon_x + b\ \epsilon_y \quad \text{and} \quad \Delta\nu_y = b\ \epsilon_x + c\ \epsilon_y \tag{4.2-1}$$

A third order map is used to extract the values of coefficients a, b and c. The map contains tune shift information up to second order in sextupole strengths and first order in octupole strengths (coming from fringing fields). The results of the analysis are given in Table 4.2-2. The tune shifts in the table correspond to maximum betatron amplitudes of 1 cm in the arc cells, or equivalently $\epsilon_x = \epsilon_y = 0.3\ \mu$m.

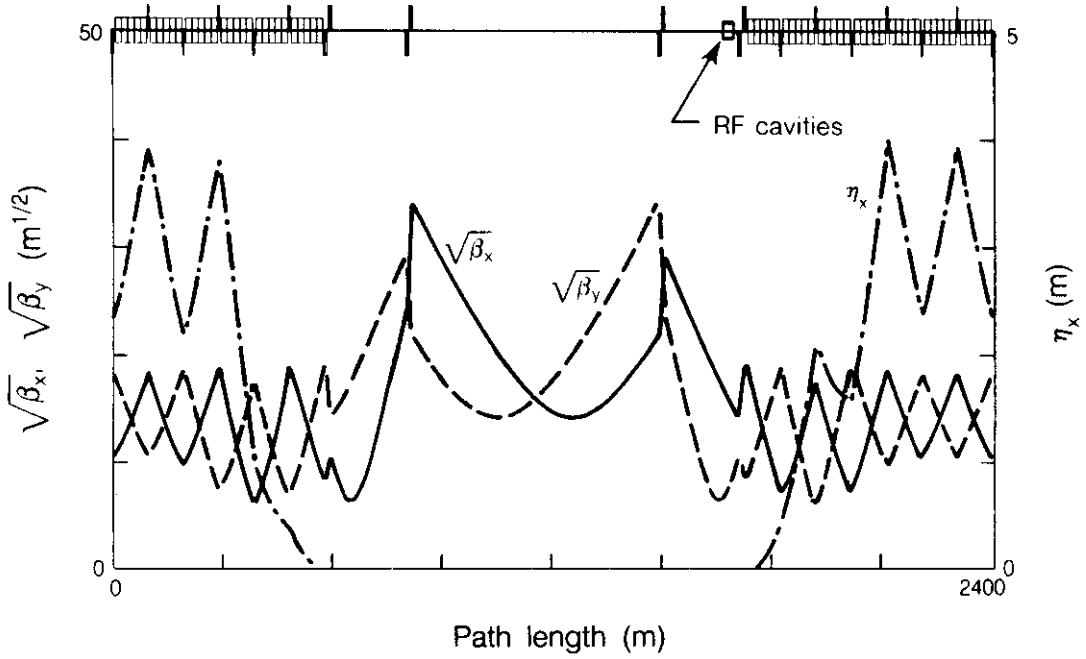

Figure 4.2-6. Magnet arrangement and lattice functions of the utility module. Locations of the rf cavities are indicated.

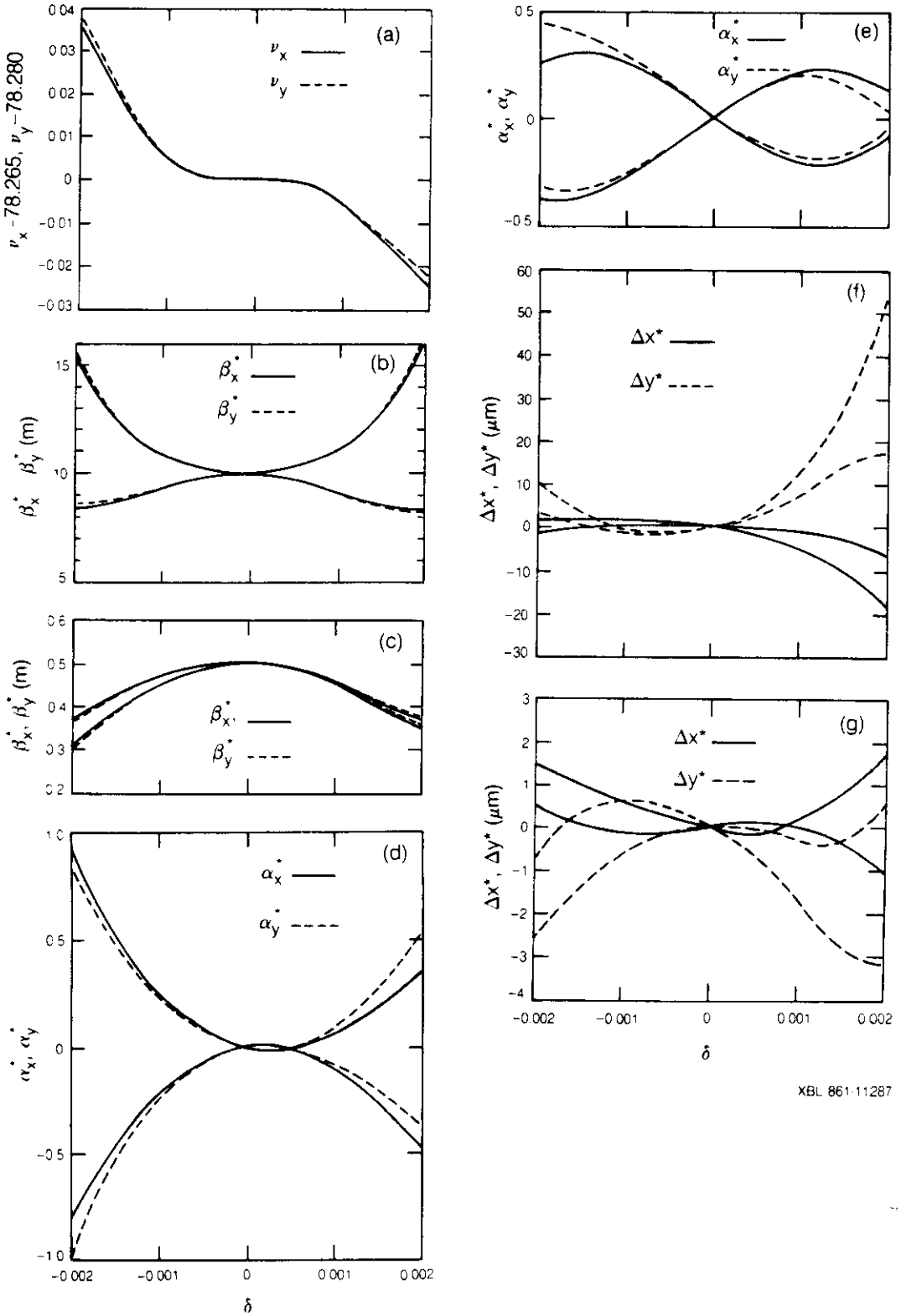

Figure 4.2-7. Chromatic behavior of various lattice quantities for the nominal colliding beam lattice. (a) Horizontal and vertical tunes ν_x and ν_y. (b) Beta functions β_x* and β_y* for the two intermediate-luminosity IRs. (c) β_x* and β_y* for the two high-luminosity IRs. (d) and (e) Negative half slopes of the beta functions α_x* and α_y* for the two types of IRs. (f) and (g) Orbit dispersions Δx* and Δy* for the two types of IRs.

Table 4.2-2
Betatron tune shifts as function of emittances
for the injection and collision optics.

Lattice	a (m^{-1})	b (m^{-1})	c (m^{-1})	$\Delta\nu_x$	$\Delta\nu_y$
Injection	−645	−2350	−409	−0.0009	−0.0008
Collision	−2258	−10080	−1182	−0.0037	−0.0034

The momentum dependence of the beta function and its slope ($\beta' = -2\alpha$) at the interaction point will make the minimum beta function $\beta_{\min}$ and its location $s_{\min}$ momentum dependent [4.2-18]

$$s_{\min}(\delta) = \beta^*(\delta)\,\alpha^*(\delta)/[1 + \alpha^*(\delta)^2] \tag{4.2-2}$$

Over the range of beam energy spread of $\sigma_\delta = 0.5 \times 10^{-4}$ at collision energy, the value of $\alpha^*(\delta)$ is less than 0.01, as shown in Fig. 4.2-7. The shift in the location of minimum beta function is therefore less than 0.5 cm, small compared with the rms bunch longitudinal spread of 7 cm.

The SSC is the first proton collider in which synchrotron radiation makes a noticeable impact on particle motion. The radiation damping times for the three degrees of freedom of motion are given by [4.1-6]

$$\tau_{x,y,s} = 2\,ET_0/UJ_{x,y,s} \tag{4.2-3}$$

where T_0 is the revolution time, U is the energy loss of a particle per revolution from synchrotron radiation, and $J_{x,y,s}$ are the partition numbers satisfying the sum rule $J_x+J_y+J_s = 4$. For the SSC lattice and for on-momentum particles, the partition numbers are $J_x = 1\text{-}D$, $J_y = 1$, and $J_s = 2+D$, where D is of the order of $1/\nu_x^2$, or about 10^{-4}. All three damping times are thus positive, meaning particle motion is damped in all dimensions. In Section 4.7 the energy loss per turn at 20 TeV is calculated to be $U = 0.123$ MeV. Since $T_0 = 1/3600$ s, the damping time in the vertical direction is $\tau_y = 10^5$ s = 25 h.

The partition numbers are different for off-momentum particles. For the SSC lattice, the value of D changes with $\delta = \Delta E/E$ according to $dD/d\delta = 1028$. In order for both J_x and J_s to be positive, the value of D has to be between 1 and −2. This condition leads to an energy window of [4.2-19]

$$-1.94 \times 10^{-3} < \delta < 0.97 \times 10^{-3}. \tag{4.2-4}$$

When the energy of a particle exceeds this window, the synchrotron radiation antidamping still does not cause immediate loss of the particle since the antidamping times are very long. The partition numbers also vary, but negligibly, in the presence of orbit or dispersion errors.

4.2.7 Tilted Plane and Nonplanar Possibilities

A horizontal planar ring for the SSC is preferred for a number of reasons. The planar aspect simplifies the beam dynamics. Dispersion in the arcs exists only in the plane and the transverse (betatron) motions of the particles are decoupled to a great extent. The beam behavior is then easier to understand, to measure and correct, helping to maintain the high beam quality needed for SSC operation. The horizontal orientation of a planar ring is not of importance for beam dynamics, but it tends to simplify surveying alignment, and avoids complexities and additional costs in the water, cryogenic, and safety systems.

Despite these considerable advantages, for some potential sites there may be major savings in having a more complex tunnel configuration that conforms more closely to the local geology. These savings can then be weighed against the consequences of compromising some of the advantages of the horizontal plane layout. The simplest alternative to the horizontal plane is a tilted plane, as selected for the e+e- storage ring LEP. The next possibility is to fold the ring along a diameter so that it lies in two planes at a small angle to each other. It is believed that the engineering complications of the tilted plane or engineering and beam dynamics complications of the folded configuration are manageable if the ring plane is tilted by not more than 0.5 degrees or folded symmetrically by not more than one degree [4.2-3].

An example of a folded ring design has been studied [4.2-20]. The folding is made around two lattice hinges diametrically opposed to each other. Each folding hinge consists of six regular 60-degree-cells around the arc center and is thus a section with unity transformation. The folding angle is taken to be 1 degree, allowing the two IR clusters to be elevated by about 100 m. The geometry of the example design is sketched in Fig. 4.2-8. The long arcs lie in planes that are tilted upwards by an angle ω about axes AA' and BB' shown in Fig. 4.2-8. The six-cell hinge sections are tilted downwards about CC' and DD' by an angle ω'. All magnets are oriented normally with respect to their local planes.

The angles ω and ω' are related to each other in such a way that the long and short arcs have a common tangent line at the joining points so that the relative rotation is about the beam axis by an angle $(\omega^2+\omega'^2)^{1/2}$. This condition links ω,ω' and the bend angles ϕ,ϕ' of the large and small arcs by [4.2-20]

$$\cos\omega = \cos\phi'/\sin\phi$$
$$\cos\omega' = \cos\phi/\sin\phi' \qquad (4.2\text{-}5)$$

The ratio ϕ/ϕ' must be kept fixed at 31, the same value for a plane ring design, because the same bending magnets are used in the long and short arcs. The angle ω is set to be 0.5 degrees. The solution of Eq. (4.2-5) is found to be $\phi = 87.23$ degrees, $\phi' = 2.814$ degrees and the tilt of the small arc is $\omega' = 10.23$ degrees.

The IR clusters are raised by a height of H and the arc centers are lowered by a height H', where

$$H = R(1-\cos\phi)\sin\omega = 97.452 \text{ m}$$
$$H' = -R(1-\cos\phi')\sin\omega' = -2.512 \text{ m} \qquad (4.2\text{-}6)$$

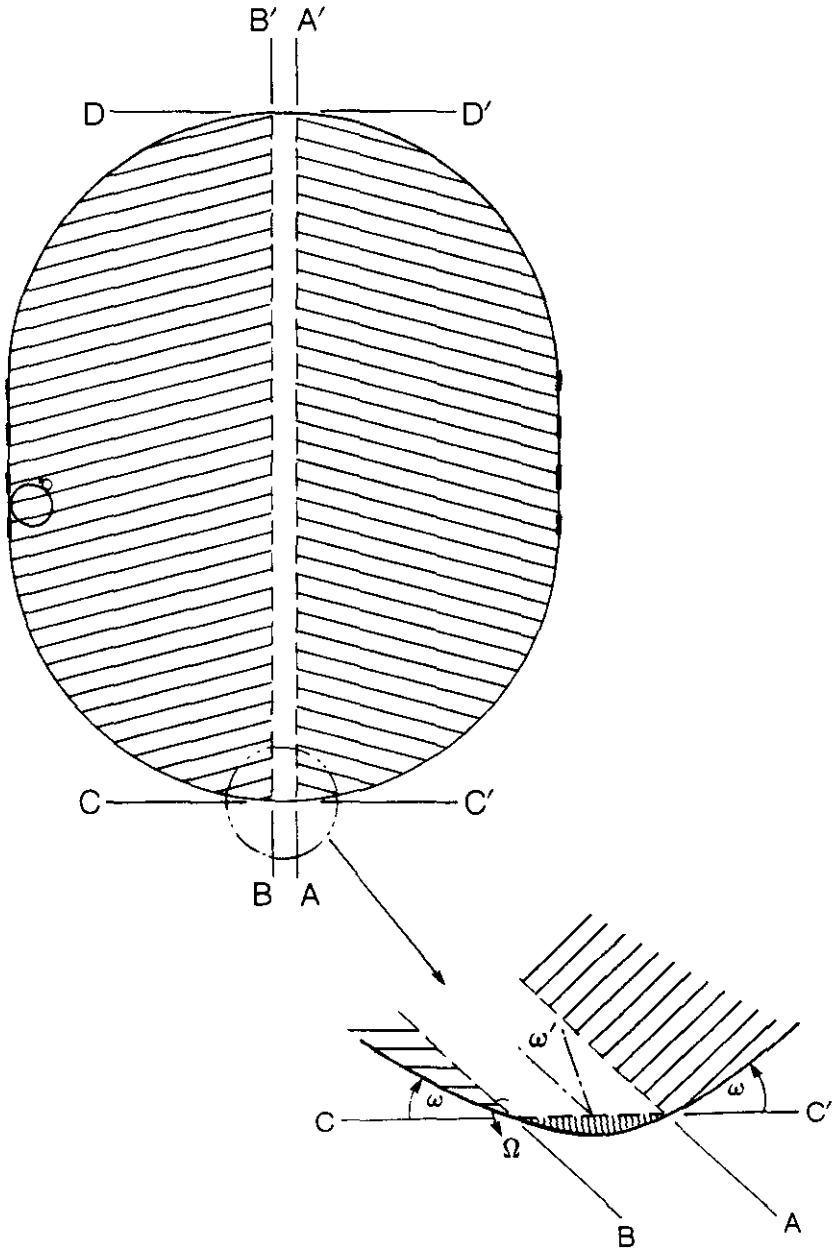

Figure 4.2-8. Geometry of an example of a folded lattice.

The bending angles ϕ and ϕ' are larger than the planar design by 0.0497%. This increase can be obtained by either raising the magnetic field or by lengthening the dipoles in the cells by the same percentage. In the latter case, the ring circumference increases by 35.5 m.

The rotation angle of the hinge section about the beam axis is 10.24 degrees. Since the hinge section is a unit transformation, this rotation does not cause mismatch of dispersion and beta functions outside the section. The rotation, however, does cause a mismatch inside the six-cell section. The nominally horizontal dispersion, for example, will be coupled to give a vertical dispersion. The maximum dispersion function distortions in the section are $\Delta\eta_x \approx 6$ cm and $\Delta\eta_y \approx 70$ cm. The coupling between horizontal and vertical betatron oscillations increases the maximum oscillation amplitudes in either dimension by 10.6%. These effects are not expected significantly to influence the aperture requirements.

4.3 Magnet Aperture and Field Quality

The critical parameter that governs the magnet aperture and field quality is the inner diameter of the superconducting coil package, designated by d_c. The magnet cost, including the costs of the superconducting material and the cryogenic system, depends sensitively on this parameter. To minimize the total magnet cost, it is desirable to have d_c as small as possible. On the other hand, the coil diameter has to be large enough to allow good field quality so that there is sufficient room for stable motion of the beam particles. In addition, the vacuum chamber pipe must fit inside the coil package with its wall sufficiently far away from the beam to avoid collective instability effects. The collective effects are discussed in Section 4.5. It turns out that single particle dynamics impose the more stringent requirement and therefore set d_c. Here we concentrate on field quality specifications for the arc magnets. Those for the interaction region magnets are discussed separately in Section 4.4.8. For the present purposes, the interaction regions can be regarded as perfect in the sense that all IR magnets are without errors. They are included in the lattices employed in these aperture studies because they do contribute to chromatic aberrations and thus have an impact on the strengths of the chromaticity sextupoles in the arcs.

Magnet field quality specifications have been arrived at by an iterative procedure taking demonstrated magnet technology, magnetic field calculations, accelerator physics, and cost factors into consideration. Here we give only the results and indicate that the aperture requirements and field quality specifications are self consistent.

4.3.1 Magnet Field Errors

The magnetic field components B_x and B_y produced by a bending magnet can be specified by a multipole expansion according to

$$B_y + iB_x = B_o \sum_{n=0}^{\infty} (b_n + ia_n)(x + iy)^n \tag{4.3-1}$$

where B_o is the design bending field, x and y are the horizontal and vertical coordinates measured from the magnet center. The field errors of a magnet are specified by the

multipole coefficients a_n and b_n. For a pure bending dipole magnet, a_n and b_n vanish, except for $b_o = 1$. The b_n coefficients give the normal multipole components with mid-plane symmetry while the a_n coefficients give the skewed field components. The correspondence of multipole order with the index n is that the order equals $2(n + 1)$. Thus b_2 is called the normal sextupole coefficient, a_3 the skew octupole, etc. The dimensions of a_n and b_n are (length)$^{-n}$. It is customary to express them in units of 10^{-4} cm^{-n}, as this is the order of magnitude of the lower order coefficients in a dipole magnet of good quality. A higher order multipole coefficient of order unity in these units is potentially dangerous for particle stability. Thus one desires a magnet to have multipole coefficients that decrease reasonably rapidly with increasing n.

There are two contributions to each of the relative multipole coefficients a_n and b_n, a systematic contribution and a random contribution. The former stems from persistent-current magnetization in the superconductor, from saturation in the iron, and from conductor placement within the coil and coil placement within the iron. Persistent current effects dominate at low magnet excitation while geometric and saturation effects dominate at high excitation. The random component stems from conductor placement errors and the distribution of filament sizes and critical currents.

These various errors influence the aperture in different ways. The so-called dynamic aperture is mainly determined by the random errors. The so-called linear aperture is influenced by both; the phase or tune part by the systematic, the amplitude part by random errors.

The systematic field errors from persistent currents have been calculated [4.3-1, 4.3-2] and checked by measurement, as discussed at the end of Section 5.2.2, where references are cited. Errors caused by iron saturation have been calculated using the Poisson program [4.3-3] (see Table 5.2-2) as well as measured in models [4.3-4].

Dipole Tolerances

The resulting specifications or tolerances for the random multipole errors of the SSC arc dipole magnets are given in Table 4.3-1, along with some results on the random errors of two sets of model magnets of the basic SSC design. The setting of these specifications has been predicated on several assumptions:

Systematic Error Assumptions

(a) Systematic quadrupole distortions (a_1 and b_1) are corrected by a combination of shimming the collared coil package in the yoke and lumped correctors.
(b) Systematic sextupole (b_2) and decapole (b_4) errors from all sources are corrected by distributed windings mounted on the beam pipe inside the dipoles. Skew sextupole errors are compensated by lumped correctors.
(c) Other systematic multipoles are controlled to tolerable levels in manufacture.

Random Error Assumptions

(d) Random errors caused by inaccuracies in conductor placement during construction scale approximately with coil diameter d_c as [4.3-2]

$$a_n, b_n \propto d_c^{-n-\frac{1}{2}} \tag{4.3-2}$$

This scaling law follows from assuming that the azimuthal cable placement error scales as $r^{-1/2}$, where r is the radial position of the conductor. This scaling behavior is consistent with data from the Tevatron (700 magnets), CBA (20 magnets) and 5 cm aperture SSC prototypes (10 magnets), which have different coil diameters.

(e) The experience of manufacturing the Tevatron and CBA dipole magnets is applicable to the SSC dipoles in the estimation of reasonable tolerances on the random errors, provided the above scaling law is used to convert the earlier experience.

(f) The Tevatron experience, discussed at the end of Section 5.2.2, is applicable for the estimation of the random error part of the persistent current distortions (caused by magnet-to-magnet variation in the critical current density of the superconductor and in the operating temperature).

The random error tolerances given in Table 4.3-1 are the result of three separate models of the manufacturing and component quality control tolerances, normalized to data on Tevatron and CBA magnets, and scaled according to Eq. (4.3-2) to d_c = 4 cm [4.3-5,6,7]. The three models, while differing in detail, yield essentially the same results for random errors expected under manufacturing and material procurement conditions achieved in the past. They are therefore a reasonable choice for the design tolerances for the arc dipoles. The random errors at low fields from persistent currents can be inferred from Tevatron data to be approximately 10% of the systematic errors from conductor variations and about 1% from temperature variations. (See Section 5.2.2.)

The model magnet program has produced enough magnets of the same types to begin to assess the degree of success in achieving the random error tolerances. (Detailed changes in design from magnet to magnet and differences in superconductor make analysis of systematic errors less significant at this stage.) The rms deviations of various multipole coefficients for a series of six 4.5 m models made at Brookhaven National Laboratory and a series of four 1.0 m models built at Lawrence Berkeley Laboratory are given in Table 4.3-1. The BNL data are presented graphically in Fig. 2.4-2. Comparison with the specifications shows that, apart from a_1 and b_1 (which were not corrected during assembly in these models), and some of the higher order multipoles (where measurement errors dominate the values), the measured values meet or exceed specifications. These are preliminary and sparse data on short magnets, but they indicate that the specifications are not unreasonable and are not impossible to meet. Further consideration is deferred to Section 5.2.

The specifications of Table 4.3-1 can be extended to any size of coil through the use of Eq. (4.3-2). In the calculations discussed below, these random errors are used, and it is assumed that the persistent current systematic sextupole and decapole errors at low field and the iron saturation effects at high field are corrected with distributed correction coils or lumped correctors. It is expected that the correction of systematic errors by correctors will be roughly 90% effective, but that operational adjustment using test beams will remove the remaining 10%. There remain the random errors in the persistent current distortions (roughly 10% of the systematic). These are added in quadrature to random field errors of Table 4.3-1.

Table 4.3-1

Specifications for the rms random multipole errors in the SSC dipole magnet with $d_c = 4$ cm and 5 μm filament size. Also tabulated are rms values of the random multipole coefficients measured on some 4.5 m BNL and 1.0 m LBL models. The units of a_n and b_n are 10^{-4}cm^{-n}.

Multipole coefficient	Specified tolerances	Measured random errors	
		BNL (6 models)	LBL (4 models)
a_1	0.7	2.77*	0.41*
a_2	0.6	0.22	0.36
a_3	0.7	0.29	0.15
a_4	0.2	0.12	0.13
a_5	0.2	0.11	0.04
a_6	0.03	0.03	0.02
a_7	0.2	0.08	0.15
a_8	0.05	0.01	0.03
b_1	0.7	0.79*	1.96*
b_2	2.0	1.24	4.27
b_3	0.3	0.15	0.27
b_4	0.7	0.30	0.68
b_5	0.1	0.03	0.08
b_6	0.2	0.06	0.14
b_7	0.2	0.05	0.16
b_8	0.1	0.01	0.10

*Coil position in yoke not adjusted to compensate.

Quadrupole Errors

We have so far concentrated on the dipole magnet errors. A preliminary estimate of the rms quadrupole field error coefficients based on a scaling similar to Eq. (4.3-2) is given in Table 4.3-2. The effect of field errors in the normal arc quadrupoles on particle motion is small compared with that of the dipoles. On the other hand, errors of the interaction region quadrupoles do require special attention and are discussed in Section 4.4.8. The random error in the a_1 coefficient in Table 4.3-2 corresponds to a roll angle rms alignment error of 0.5 mrad, while that of the b_1 coefficient corresponds to rms integrated quadrupole strength error of $\Delta q/q = 5 \times 10^{-4}$. These values are used in Section 4.4.3.

Table 4.3-2

Estimated rms random multipole tolerances in the SSC quadrupole magnets with $d_c = 4$ cm. The units of a_n and b_n are 10^{-4} cm^{-n} with the quadrupole field evaluated at 1 cm radius.

n	1	2	3	4	5
a_n	—	2.6	1.2	0.3	0.14
b_n	—	2.9	0.5	0.3	0.56

Fringe field effects are not very important for the SSC because of the relatively great length of individual magnets. The ends of the dipole magnets are designed to minimize the multipole errors. The main effective multipole content for a dipole end is second order in the particle coordinates and is therefore equivalent to a sextupole. Its strength is found to be small compared with that of the chromaticity sextupoles. The horizontal and vertical chromaticity contributions from modeled wedge dipole fringe fields, for example, are 0 and -1.2×10^{-3}, compared with the natural chromaticities of -204.

Quadrupole fringe fields act like an octupole. Fringe fields of the interaction region quadrupoles which are strong and are located at high beta-function locations, for example, can be characterized by the horizontal and vertical tune shifts with betatron amplitudes. Referring to Eq. (4.2-1), the coefficients a, b and c contributed from the IR quadrupole fringe fields for the collision lattice are -1066 m^{-1}, -1301 m^{-1} and -1027 m^{-1}, respectively. These values are smaller than the contribution from the rest of the unperturbed storage ring, which are in any case small.

4.3.2 Aperture Requirements

As mentioned before, the magnet coil size is a critical parameter for the SSC and is specified by the inner diameter of the coil package d_c. To minimize the magnet cost, d_c has to be chosen to be the minimum value allowed by particle stability considerations. To obtain the minimum d_c, it is necessary first to specify how much room is needed for the beam stability and operational purposes. This information can then be translated to the

minimum value of d_c for a given cell length. In this section, the optimization of d_c, together with the choice of the lattice cell length, is described.

Room for particle motion in the SSC is characterized by three quantities: the linear aperture, the dynamic aperture, and the momentum aperture. We first discuss the linear and the dynamic apertures. The momentum aperture is discussed at the end of this section.

Linear and Dynamic Aperture

The linear aperture is a region around the axis of the magnets within which particle motion is basically linear. It represents the high quality aperture needed for routine beam operations. Within the linear aperture, not only are particle motions stable but also predictable within the approximation of linear uncoupled motion, at least for on-momentum particles. It is regarded of importance for the SSC to have sufficient linear aperture to allow for stable and efficient beam operations.

The dynamic aperture is a region larger than the linear aperture, within which particle motion is stable but not necessarily linear. If the beam is exploring the full dynamic aperture, its detailed behavior may not be easy to understand and the beam emittance may not be suitable for high luminosity runs, but it still permits valuable diagnosis, trouble shooting, and safe abort.

The linear and dynamic apertures depend differently on the magnet multipole errors. The former depends mostly on the lower order multipoles, primarily the a_2 and the b_2 errors, while the latter depends mostly on higher random multipoles. It is important that the achieved dynamic aperture be sufficiently larger than the linear aperture. It is still the linear aperture, however, that is regarded as the prime requirement in choosing the value of d_c. Figure 4.3-1 is an illustration of the relative position and sizes of the superconducting coils, the vacuum chamber pipe, and the linear and dynamic apertures.

Numerous particle tracking simulations have been performed, typically by tracking particles for several hundred to a few thousand revolutions. Little attempt has yet been made to study the intricate long term stability behavior of the single particle motion. This is based on the expectations that

(a) The linear aperture can be determined by a relatively small number of tracking turns. Past accelerator experience has shown that, once motion is shown to be linear, long term stability is expected.

(b) The dynamic aperture is needed for beam diagnosis and abort purposes. For these purposes, the beam need last only for several synchrotron oscillation periods, or a few thousand turns. Whether the beam has long term stability is not of prime importance.

In linear motion, the particle trajectory in phase space is a perfect ellipse and the Courant-Snyder amplitude [4.3-8] is a true invariant. When nonlinearities are present, the ellipse smears and the value of the "invariant" fluctuates from turn to turn. The rms fractional value of this fluctuation is referred to as the smear. To define the linear aperture quantitatively, we use the criteria that the smear does not exceed 10% and that the on-momentum tune shift with amplitude does not exceed 0.005. The linear aperture is given by the amplitude beyond which either one of the two criteria is violated. This definition is based on past accelerator experience [4.3-9]. It is expected that further accelerator studies, at the Tevatron or Sp$\bar{p}$S, will improve the accuracy of these criteria.

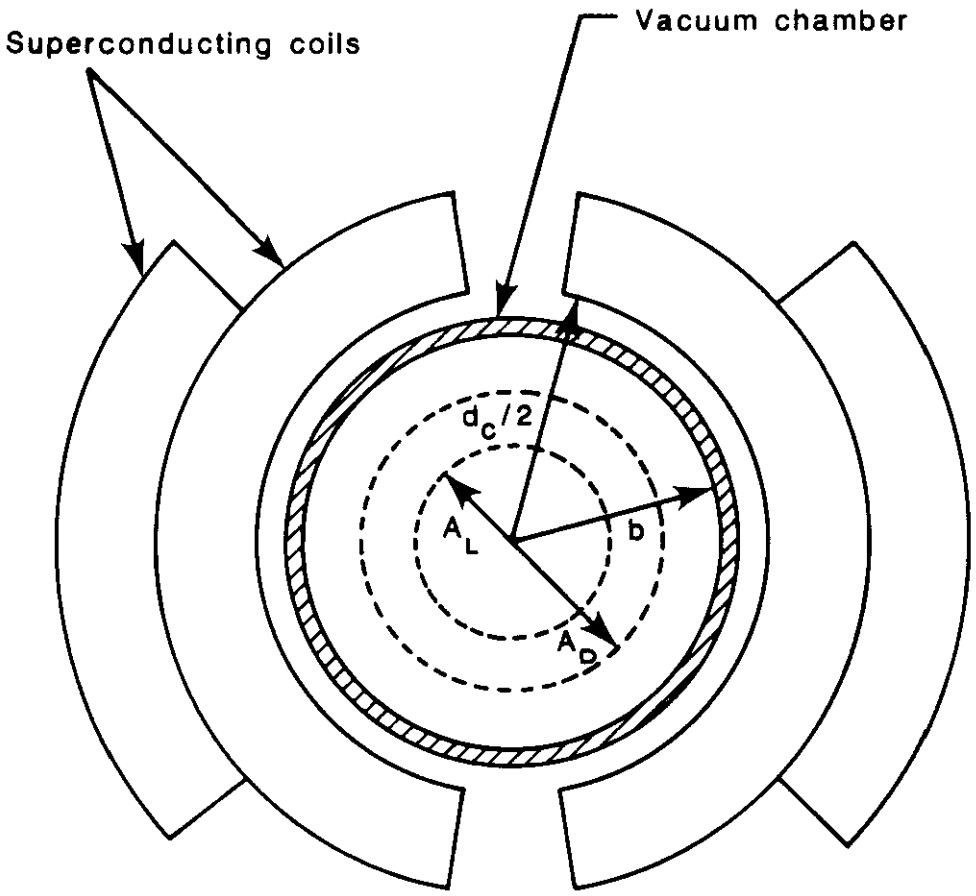

Figure 4.3-1. The relative position and sizes of the superconducting coil packages, the vacuum chamber pipe, and the linear and dynamic apertures. The SSC design has $d_c/2 = 2$ cm, $b = 1.65$ cm. The exact values of the linear and dynamic apertures depend on the exact values and arrangement of the random magnet field errors. The dotted curves represent their mean expected values, after magnet sorting, with $A_{\text{linear}} = 0.89$ cm and $A_{\text{dynamic}} = 1.2$ cm. (See the end of Section 4.3.3.)

Needed Linear Aperture

The needed linear aperture is a function of lattice cell design, particularly the half-cell length L and the betatron phase advance per cell μ. In Section 4.2.1, we have discussed the choice of μ. In the following, μ is considered fixed to be 60 degrees while the aperture dependence on L is studied.

The aperture required is largest at injection and is composed of several components. For a location with a typical beta function of 300 m, these requirements are [4.3-10]

(a) Beam size — for a typical half-cell length L = 100 m, the beam size is $\sqrt{6}\sigma$ = 1.3 mm at 1 TeV and 0.29 mm at 20 TeV.
(b) Beam position fluctuation at injection — up to 1.5 mm.
(c) Orbit distortions — up to 1.25 mm.
(d) Miscellaneous effects (power supply ripple, lattice mismatch, etc.) — up to 0.5 mm.

These aperture requirements can be scaled to different half-cell lengths. An empirical expression for the needed linear aperture (expressed as a transverse amplitude), valid approximately in the range L = 50 m to 150 m, is [4.3-11]

$$A_{\text{linear}}\,(\text{mm}) = 0.934\,[L\,(\text{m})]^{0.36} \tag{4.3-3}$$

For example, with L = 100 m, Eq. (4.4-3) gives a linear aperture requirement of 4.9 mm. The aperture requirements relax substantially after injection. The needed aperture does not depend sensitively on the injection energy because the beam size is not a dominating contribution to the aperture need.

The aperture required because of injection errors can be reduced substantially by applying a feedback system to damp the betatron and energy oscillations rapidly. In the aperture requirement, Eq. (4.3-3), however, this is not taken into account. The effects of a feedback system to counter injection errors are discussed in Section 4.6.1.

Momentum Aperture

In addition to the on-momentum linear and dynamic apertures, we must consider their momentum dependences. For beam stability and operation, it is necessary to provide sufficient room for not only the on-momentum particles but also the off-momentum particles. The momentum aperture refers to the range of energy deviation within which the linear and the dynamic apertures are substantially maintained. The momentum aperture requirements should cover the injection energy errors ($<1.5 \times 10^{-4}$) and the fractional beam energy spread at injection of $\sqrt{6}\,\sigma_\delta = 3.7 \times 10^{-4}$. It is suggested that, for the SSC, an aperture of $\Delta E/E = \pm 10^{-3}$ should be sufficient to accommodate these requirements. The energy spread of the beam and consequent rf specification are determined by the need to counteract certain collective instabilities, as is discussed in Section 4.5.

Experiments

It is important to compare theoretical predictions with experiments performed under realistic operating conditions. Experiments have been undertaken at the Tevatron and at SPEAR to supplement and verify the theoretical calculations. A sample of the results from one such experiment is shown in Fig. 2.4-9. A family of sextupoles are powered while the

horizontal tune is made to approach the resonance value of 19 1/3. The beam was then displaced and its subsequent motion in the (x, x') space followed turn by turn to show the expected triangular behavior. The result agrees well with what is expected from a first order resonance theory.

Continuation of these experiments is expected to sharpen the understanding of the needed linear and dynamic apertures and to confirm the theoretical predictions to a more detailed level. Such efforts are of great importance to the SSC design and will most certainly be pursued as the SSC design proceeds.

4.3.3 Magnet Coil Size and Cell Length

Having defined the required aperture for beam stability and operation, it is necessary to specify the field quality that achieves this requirement. The field quality, as mentioned before, is governed mainly by the magnet coil size d_c. For $d_c = 4$ cm, the magnet field errors are given by Table 4.3-1 while for other values of d_c, the random field errors are obtained by the scaling of Eq. (4.3-2). The random error coefficients a_1 and b_1, not included here, produce linear distortions that must be controlled by quadrupole and skew quadrupole correction elements. The effects of a_1 and b_1 are shown in Section 4.3.4 to be unimportant in the considerations of coil size versus cell length.

For given d_c and L, analytical and numerical techniques can be applied to calculate the achieved linear aperture. Analytic results are discussed in Section 4.4.5. Tools used in the numerical studies consists of several particle tracking programs including DIMAT [4.3-12], PATRICIA [4.2-8], MARYLIE [4.2-17], RACETRACK [4.2-9] and TEAPOT [4.3-13]. The motions of single particles with various betatron amplitudes and momentum offsets are tracked in the presence of magnet field errors (omitting a_1 and b_1) to determine the smear and the tune shifts. The linear aperture is then determined according to the criteria mentioned in Section 4.3.2.

Test Lattices

Most of the numerical studies of the arc magnet aperture have been made on test lattices, which are simplified versions of the SSC lattice designed for purposes of efficient studies. For example, these test lattices do not have utility sections, since they are not believed to be an important feature in determining the aperture. Interaction regions are included, but for studying the arc magnet aperture, the interaction region magnets are assumed to be without errors. Nonlinearity in the test lattices comes mainly from arc dipole magnet field errors. Chromatic aberrations from the perfect IR quadrupoles and the aberrations from the chromaticity sextupoles are also included, although they are found to be relatively small. Tracking results for more realistic lattices can be found in Section 4.4.8.

Unless specified otherwise, these test lattices have six evenly distributed IRs with $\beta_x^* = \beta_y^* = 1$ m. This represents a somewhat conservative choice — the aperture requirement is mainly for injection purposes; the injection lattice has a larger value of β^* and consequently the (relatively unimportant) nonlinear aberrations from the IR quadrupoles and the chromaticity sextupoles are correspondingly smaller. Only when we discuss the field errors in the IR quadrupoles in Section 4.4.8 does the higher value of β^* in the injection lattice become essential. The difference between evenly distributed IRs and the clustered arrangements is shown to be small in Section 4.2.2.

Tracking Results

The tracking results on linear aperture, evaluated at β = 330 m, can be summarized by the expression [4.3-11]

$$A_{\text{linear}}(\text{mm}) = (13 \pm 3)[L(\text{m})]^{-0.76}[d_c(\text{cm})]^{1.89} \tag{4.3-4}$$

The region of applicability for Eq. (4.3-4) is approximately L = 50 to 150 m and d_c = 2.5 to 5 cm. The actual numerical results from several tracking programs for d_c = 4 cm and different half-cell lengths are shown in Fig. 4.3-2, together with the predictions of Eq. (4.3-4) for d_c = 3, 4, and 5 cm, and the needed aperture, Eq. (4.3-3). The achieved aperture depends on the specific values and distribution of the random field errors. The rms deviation in Eq. (4.3-4) reflects the rms spreads in the random magnet errors. For L = 100 m and d_c = 4 cm, the achieved aperture is (5.5 ± 1.3) mm, compared with the needed aperture of 4.9 mm.

Sorting

It is possible to improve the linear aperture substantially by sorting the magnets. The multipoles of all magnets will be measured. The magnets can then be ordered to minimize the nonlinear effects. In one simple sorting scheme, the measured magnets arrive for installation in batches of 60; the number of magnets per batch corresponds to 2π betatron phase advance. The magnets are sorted so that their b_2 coefficients are arranged according to Table 4.3-3. This is then repeated for the next batch of magnets (second half of the table) until all magnets in the ring are sorted. Sorting is performed only on b_2, ignoring a_2, since the rms random value of b_2 is much larger than that of a_2, according to Table 4.3-1. More sophisticated sorting schemes are of course not ruled out at this stage. In some of the studies mentioned in Section 4.3.6, sorting is applied to both a_1 and b_2 with lesser weight on a_1. When the simple sorting of Table 4.3-3 is applied, the achieved linear aperture is found to change from (5.5 ± 1.3) mm to (8.9 ± 2.0) mm for L = 100 m and d_c = 4 cm. Sorting is clearly an effective means to improve the aperture.

Table 4.3-3

A simple sorting scheme. The index +1 means the magnet that has the most positive b_2 among the group being sorted, −1 means the most negative, etc. Magnets in the 5th π advance will be ordered the same way as the first π.

1st π phase advance:	3rd π phase advance:
+1, −1, +3, −3, +5, −5	−1, +1, −3, +3, −5, +5 ....
2nd π phase advance:	4th π phase advance:
+2, −2, +4, −4, +6, −6	−2, +2, −4, +4, −6, +6 ....

In obtaining Eq. (4.3-4), we have ignored the linear distortions due to quadrupole and skew quadrupole field errors (a_1 and b_1). Orbit distortions are also ignored, other than the

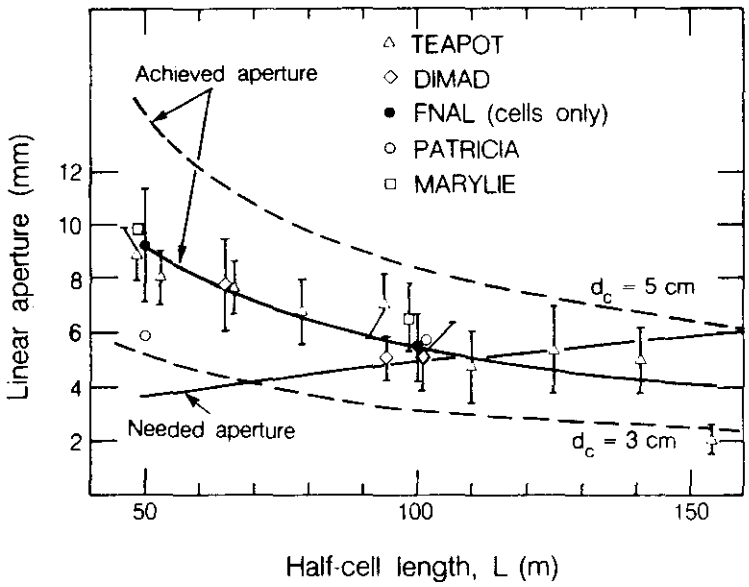

Figure 4.3-2. Compiled tracking results using several programs. The linear aperture is shown by the solid curve as a function of half-cell length L for fixed $d_c = 4$ cm. The curve is a fit using Eq. (4.3-4), A_{linear} (mm) = 180 $[L(\text{m})]^{-0.76}$. The dashed curves on either side show the behavior for $d_c = 3$ and 5 cm. The needed aperture Eq. (4.3-3) is also shown.

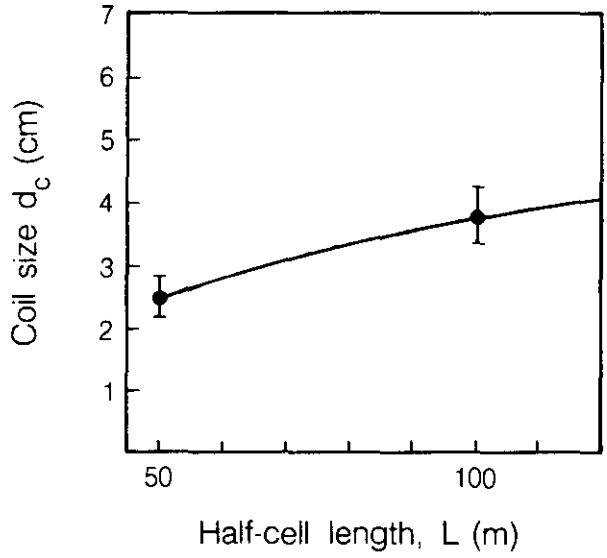

Figure 4.3-3. Relationship between the minimum acceptable magnet coil size d_c and the half-cell length L on the basis of linear aperture.

fact that the orbit contribution has been included in the aperture requirements. Tracking results with linear distortions and orbit errors are discussed in Section 4.3.4. More discussions on these effects from the analytical point of view can be found in Sections 4.4.2 to 4.4.6. Quadrupole errors in the arcs are also not included, but, as is shown in Section 4.4.8, they do not noticeably affect the aperture achieved.

Coil Size and Half-cell Length

When the needed aperture, Eq. (4.3-3), and the achieved aperture, Eq. (4.3-4), are equal, we obtain a relationship between the half-cell length L and the coil size d_c (without magnet sorting),

$$d_c\,(\text{cm}) = (0.25 \pm 0.03)[L(\text{m})]^{0.59} \tag{4.3-5}$$

Figure 4.3-3 shows this relationship. Points below the curve are not acceptable since the needed aperture is not achieved. Points above the curve are acceptable in terms of linear aperture, but the magnet cost is then unnecessarily expensive. The curve thus indicates the optimum choice of d_c for a given L. For L = 100 m, the needed d_c is (3.8 ± 0.4) cm.

As shown in Fig. 4.3-3, a long half-cell length requires a large coil size while a short half-cell length allows the coil size to be reduced. Since longer cell and smaller coil size are preferred for cost minimization, the constant-cost curves are almost parallel to the optimal d_c vs. L curve, leading to a rather broad optimum of cost minimization [4.3-11]. If we take the mean value of Eq. (4.3-5) without sorting, for example, the minimum cost occurs anywhere on the d_c vs. L curve between (L = 85 m, d_c = 3.4 ± 0.4 cm) and (L = 105 m, d_c = 3.9 ± 0.5 cm).

The central value in Eq. (4.3-5) represents a 50% confidence level that the needed linear aperture will be achieved with that coil size. It is advisable that the size be chosen so that there is a much higher level of confidence. If a 95% confidence level is adopted, the value of d_c has to be above the mean value by 1.66 times the rms deviation, assuming the sample distribution is gaussian. Without sorting, this leads to a needed coil size of d_c = 4.6 cm for L = 100 m. However, since at least a rudimentary sorting scheme is been planned during the magnet installation, we adopt a coil size of d_c = 4 cm. With sorting, and with this coil size, the achieved linear aperture of (8.9 ± 2.0) mm is two standard deviations above the needed aperture of 4.9 mm, corresponding to a 98% confidence level. To establish whether the samples do obey a gaussian distribution and therefore validate these confidence level estimates requires more statistics, but the choice of d_c = 4 cm is believed to be close to optimum at the present stage of SSC design.

Dynamic Aperture

Dynamic aperture, like the linear aperture, is obtained by tracking particles with various starting betatron amplitudes. The maximum amplitude that allows stable motion for typically 400 revolutions is identified as the dynamic aperture. Instability is identified when the particle amplitude exceeds a cut-off which is typically taken to be 1 m. Tests are made to show that the dynamic aperture so obtained does not change appreciably with the number of revolutions tracked and the amplitude cut-off.

Assuming L = 100 m and d_c = 4 cm and without sorting, tracking studies show that the dynamic aperture achieved is (9.1 ± 1.5) mm. This is about 70% larger than the achieved

linear aperture. When sorting is applied, the dynamic aperture becomes (12 ± 1.5) mm. A summary is given below:

	Linear aperture	Dynamic aperture
Without sorting	5.5 ± 1.3 mm	9.1 ± 1.5 mm
With sorting	8.9 ± 2.0 mm	12 ± 1.5 mm

The percentage improvement of the dynamic aperture by sorting is smaller than that of the linear aperture. This is expected since higher multipoles are not sorted. The sorted values have been used in Fig. 4.3-1.

We emphasize here that the aperture evaluations depend on three assumptions. First, the needed aperture is that given by Eq. (4.3-3). Second, magnet errors are those shown in Table 4.3-1. Finally, at least a simple sorting, as shown in Table 4.3-3, is made on the SSC magnets. Changes on these assumptions will necessarily change the aperture evaluation and the choice of the optimum cell length and magnet coil size.

4.3.4 Effect of Linear Coupling and Orbit Distortion

So far the tracking results do not include the random field error components a_1 and b_1. They also do not include effects of orbit distortion. In this section, these effects are included. It is shown that with proper compensation, these error effects do not cause significant reduction in the linear and dynamic apertures achieved.

We will first discuss the a_1 and b_1 effects without orbit errors. In the presence of linear coupling, the usual horizontal and vertical invariants lose their meaning and are replaced by two invariants in the coupled coordinates. A generalization of the previous definition of the linear aperture is the betatron amplitude for which these invariants are smeared by 10%. Alternatively, we can use the TEAPOT program to introduce four skew quadrupole correction packages that remove the $x-y$ coupling elements in the linear transformation matrix that describes one revolution in the tracking simulation.

Both approaches have been used to evaluate the linear and dynamic apertures when all random field error coefficients in Table 4.3-1, including a_1 and b_1, are employed in the simulation. In the TEAPOT simulation, the four correction skew quadrupole families are located near the Q2 and Q5 quadrupoles on both sides of each interaction region. The needed strength of these skew quadrupoles is about 1/30 of an arc quadrupole. The two approaches give very similar results; the criterion based on the generalized invariants gives a linear aperture of (5.2 ± 1.1) mm without sorting and (9.4 ± 2.0) mm with sorting, while the diagonalization scheme gives a linear aperture of (5.7 ± 0.5) mm without sorting and (9.9 ± 0.8) mm with sorting. The latter approach also yields a dynamic aperture of (10.1 ± 1.3) mm without sorting and (13.5 ± 2.4) mm with sorting. These results agree quite well with those obtained without the random a_1 and b_1 field errors.

In the presence of orbit distortion, there are additional contributions to linear field errors from the feeddown of higher multipole errors. In this case, the closed orbit distortion, as well as the linear distortions such as tune shifts and $x-y$ coupling, is to be

corrected before the aperture is determined. This procedure was simulated using TEAPOT [4.3-14]. Using the specifications of Section 4.4.2, the rms orbit distortion after correction was found to be 0.35 mm and 0.36 mm in the horizontal and vertical planes. The rms corrector strengths in the two planes are 7 μrad and 8 μrad, respectively. In the simulation, magnet sorting was applied. After the linear corrections, the on-momentum dynamic aperture was found to be 12.8 mm and the linear aperture was 9.6 mm, relative to the closed orbit. These apertures are basically the same as those found without orbit errors. When the errors are doubled in the simulation, the dynamic aperture shrinks by 10% to 11.5 mm.

4.3.5 Tune Variation

To optimize the performance of the SSC, it is necessary to have sufficient flexibility during operation in choosing the horizontal and vertical betatron tunes, two of the most critical quantities in terms of storage ring performance. For this purpose, it is important that the betatron tunes can be varied within a certain range. Tune variation is accomplished by varying the cell trim quadrupole strengths. For a nominal setting of phase advance per cell of $\mu = 60$ degrees, the range of variation in μ is shown in Fig. 4.3-4. With 332 cells capable of quadrupole strength variations for this purpose, the range of variation in tune units is at least ± 2. If needed, more tune variation range can be obtained by tuning the IR optics.

A phase advance of 60 degrees minimizes the nonlinear effect of the chromaticity sextupoles in the bare lattice without magnet field errors. It is necessary to demonstrate in the presence of magnet field errors that the achieved linear aperture does not deteriorate appreciably as the tune departs from the chosen value. The aperture studies described in the previous sub-section assume fixed betatron tunes of $\nu_x = 85.29$ and $\nu_y = 85.28$. To make a meaningful demonstration, the fractional part of ν_x and ν_y is kept the same; only the integral part is varied. A tracking study using RACETRACK has been performed with $\Delta\nu_x = \Delta\nu_y = \pm 2$. The linear aperture for the cases of $\Delta\nu = -2$ and $+2$ are found to be 8.9 mm and 9.0 mm, respectively, essentially the same as the aperture achieved by $\mu = 60$ degrees. Although 60 degree cells are regarded as beneficial for the bare lattice, strict adherence to 60 degrees is not essential when the magnet field errors are included in the consideration.

After the working point is more or less chosen, it is still necessary to explore the (ν_x, ν_y) plane to make sure there is enough operating space around the working point. It is also important to check tracking results to see if the results are distorted by a strong nonlinear resonance in the neighborhood. Although tune variation is done often in our tracking studies, we show only one example, in Table 4.4-6 of Section 4.4.8.

4.3.6 The Momentum Aperture

The discussion so far has been restricted to on-momentum particles. Aperture studies must also be done for off-momentum particles, as well as those with the correct momentum for the bending field. The momentum aperture was defined above in Section 4.3.2 as the fractional range of momentum or energy over which the linear and dynamic apertures are substantially maintained. Operating considerations led to a specification of $\delta = \Delta E/E = \pm 10^{-3}$ as the needed aperture at injection. It is necessary to show that the lattice design and the coil size of $d_c = 4$ cm indeed meet this momentum aperture requirement.

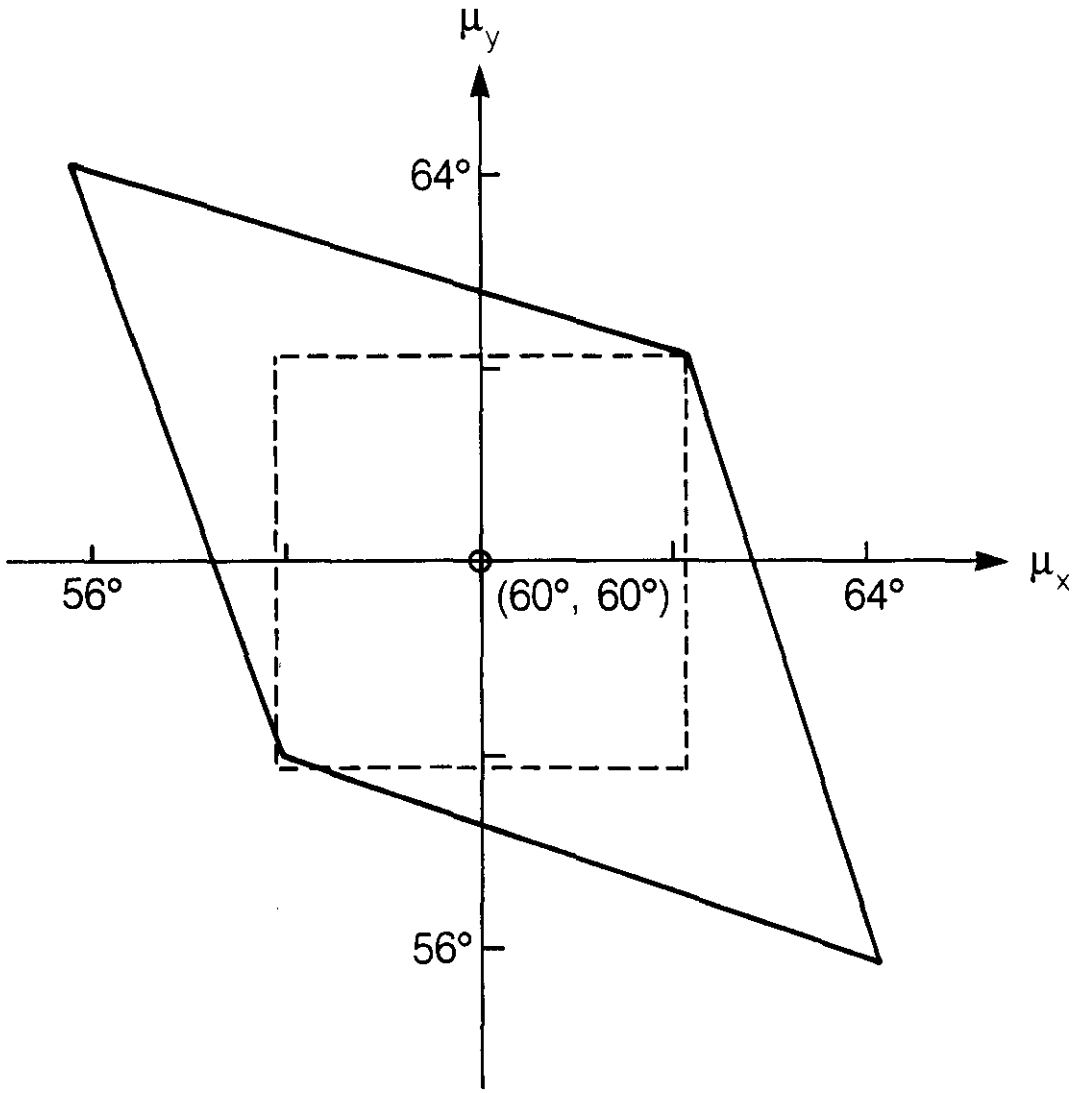

Figure 4.3-4. The diamond shaped region is the range of variation in the horizontal and vertical phase advances per cell covered by varying the trim quadrupole coil strengths in the arc spool pieces. The dotted square corresponds to total tune variation of ± 2 units.

To explore the momentum aperture, off-momentum particles with given $\Delta E/E$ are tracked for typically 400 revolutions and the dynamic aperture is obtained for each momentum. The momentum aperture is then indicated by the momentum deviation beyond which the dynamic aperture is substantially reduced from the on-momentum value. For the bare lattices without magnet field errors, the momentum aperture far exceeds the needed 10^{-3} value [4.2-10, 4.3-15]. When magnet field errors are included, the dynamic aperture at $\delta = \pm 10^{-3}$ for all cases does not decrease substantially from the on-momentum value. In particular, as discussed in Section 4.2.2 and shown in Fig. 4.2-2, the dynamic aperture and the momentum aperture do not depend sensitively on the IR arrangements.

Off-momentum dynamic aperture has also been evaluated when the random linear field errors a_1 and b_1 are included. Using TEAPOT, the results with five sets of random numbers are

δ	Without sorting	With sorting
−0.001	7.7 ± 1.6 mm	11.1 ± 0.5 mm
0.0	10.1 ± 1.3	13.5 ± 2.4
+0.001	9.8 ± 2.7	13.0 ± 0.5

The linear distortions have been corrected by four families of skew quadrupoles. Sorting here was made mainly on the b_2 coefficients but also on a_1. These results agree with Fig. 4.2-2 without the linear field errors and their corrections. The off-momentum dynamic aperture has not decreased because of the linear field errors. Tracking studies are also used to find the off-momentum linear aperture. The results show a decrease of a factor of two from the on-momentum value at $\delta = \pm 10^{-3}$. The reduction of linear aperture off-momentum is somewhat more than that of the dynamic aperture because of the feeddown of higher multipoles, but the factor of two reduction at $\delta = \pm 10^{-3}$ is believed acceptable [4.3-16].

Synchrotron Oscillation

An error of beam energy at injection causes a synchrotron oscillation of the beam which can be damped by a feedback system. The requirement on the off-momentum linear aperture therefore depends on the feedback system. If the feedback damping is sufficiently fast, the condition of having a large linear aperture at $\delta = \pm 10^{-3}$ may be relaxed. In the conceptual design, however, we impose the condition that the linear aperture be maintained at the full $\pm 10^{-3}$, except that the linear distortions for off-momentum particles coming from the feed-down of the nonlinear multipoles are removed from the evaluation of the smear.

Particle tracking with synchrotron oscillations is being studied. Results are not yet available. The need of having to perform tracking with synchrotron oscillations is alleviated by the fact that (1) the synchrotron oscillations will be damped by a feedback system; (2) the linear aperture does have enough energy window to allow energy oscillations of up to 10^{-3}, as long as the betatron amplitude is not too large at the same time; (3) need of

dynamic aperture does not require the beam to maintain a high quality when it is executing large synchrotron oscillations; (4) analytic estimation — including the synchro-betatron resonance effects — has been done in Section 4.4.5; (5) previous accelerator experience shows long-term stability with synchrotron oscillations, provided the motion is very linear.

4.4 Tolerances and Correction Systems Specifications

Departures from the ideal occur in any technical system, partly from the limitations of the design, partly from errors in fabrication, and partly from flaws in operating. Such departures mean greater or lesser degradation in performance and, if severe, failure to meet specifications. Identification of errors and the allowed tolerances is particularly important for the SSC, in part because of its large size and the associated possibility of accumulation of errors from a large number of components. To make the design as cost effective as possible, error tolerances and the required correction systems must be specified carefully. Trade offs between tight tolerances with simple correction systems and loose tolerances with sophisticated correction systems need to be examined. The subject of tolerances is an on-going effort in the SSC design study. The present tolerances and design specifications of the correction elements are described in this section. The emphasis is on the tolerances for the magnetic confinement system, but corrections for ground motion and also rf noise in the accelerating system are discussed briefly. One of the most important tolerance specifications concerns the random multipole errors of the arc dipole magnets, already discussed in Section 4.3.

The types of correction elements needed become apparent if operation of the SSC is considered. First, the beam must be steered to complete one turn. As the beam positions can be measured, the orbit distortion—which can be regarded as the zeroth order optical distortion—must be minimized by an orbit correction scheme. Following the orbit correction, the first-order optical distortions must be corrected. This involves corrections of the betatron tunes, the beta-function distortions and the $x-y$ coupling. Chromaticity (tune change with energy) corrections by sextupoles then immediately follow the linear corrections. Higher order (multipole) correctors are also present in the design.

Section 4.4.1 summarizes the specifications for the correction elements to be installed in the spool pieces. Section 4.4.2 describes the orbit correction scheme and its specifications. The linear corrections are described in Section 4.4.3, while sextupole corrections are discussed in Section 4.4.4. Sections 4.4.5 and 4.4.6 describe analytical estimates of the multipole field error tolerances. The corrections of the multipoles are then discussed in Section 4.4.7. The IR corrections deserve special attention and are discussed in Section 4.4.8. Ground motion and rf system noise are also special subjects of concern to the SSC; they are discussed in Sections 4.4.9 and 4.4.10. Effects of power supply fluctuations and specifications of the various feedback systems are summarized in Sections 5.5 and 5.8.

4.4.1 Spool Elements

Magnetic correction elements are located as packages in the spool pieces. Design of the spools is discussed in Section 5.2.13. There are two types of correction packages, primary

and secondary. Adjacent to each focusing quadrupole in the arcs, there is a primary package equipped with horizontal dipole, focusing quadrupole and focusing sextupole windings. Adjacent to each defocusing quadrupole, there is a primary package equipped with vertical dipole, defocusing quadrupole and defocusing sextupole windings.

The two arcs are each divided into four sectors with a total of 166 cells per arc. The dipole windings in the primary packages have individual power supplies, totaling 332 for the horizontal and 332 for the vertical dipoles. All focusing quadrupole circuits in a sector are ganged together with one power supply, yielding a total of eight power supplies in the arcs. The defocusing quadrupoles, the focusing sextupoles and the defocusing sextupoles are arranged similarly.

Adjacent to each primary package, there is space for a secondary package if needed. The secondary packages are inserted in the lattice in 20 spool pieces that are located in the vicinities of the cryogenic feed points of each arc sector. At present, the secondary packages are four each of either normal quadrupole and skew quadrupole correctors, or normal or skew sextupole or octupole correctors. These special circuits have individual power supplies, but in operation it is envisioned that they often will be ganged into software-defined families. It is conceivable that some of the octupole circuits may be traded for decapole circuits at a later stage.

The arc correction schemes are indicated in Table 4.4-1, which lists the physical quantities to be measured and the elements to be adjusted to improve them. The items are arranged according to the priorities envisioned during operation. The strengths of the correction elements are discussed in the following sections and are summarized in Table 4.4-2. In general, when correcting effects caused by random errors, the maximum corrector strengths are capable of compensating three times the rms effect. This is true except in the case of orbit correction, where the maximum dipole corrector strength can correct six times the rms orbit distortion. The strengths given in Table 4.4-2 correspond to the maximum values at 20 TeV. Note that some corrections, such as the higher multipole corrections, are needed mostly for injection. For these, the strengths needed may be substantially reduced from those listed (presently under investigation).

4.4.2 Magnet Misalignment and Orbit Correction

Two of the main sources of errors are the misalignment of magnet positions and incorrect magnet strengths. As a result, the closed orbit of the beam deviates from the ideal trajectory. If uncorrected, this closed orbit easily exceeds the vacuum chamber of a large storage ring like the SSC. The uncorrected rms orbit distortion in the arcs from quadrupole magnet misalignments alone, for example, is given by [4.1-1]

$$x_{\mathrm{rms}} = \frac{N^{1/2}\beta_{\max}^{1/2}\,(\beta_{\max}+\beta_{\min})^{1/2}}{2\sqrt{2}\,\sin\pi\nu} \cdot \frac{\delta x}{f} \tag{4.4-1}$$

Table 4.4-1
Correction of optics in the arcs. Items ordered approximately according to priority during operation.

Effect	Observation	Adjustments
Orbit steering (a) first turn (b) global	664 BPM readings x_i, y_i	Orbit correctors (332 in x, 332 in y) (a) piecewise corrections (b) all correctors
Tune correction	ν_x, ν_y	Two primary quadrupole families
Chromaticity	$d\nu_x/d\delta$, $d\nu_y/d\delta$	Distributed sextupole and decapole windings at the dipoles and two primary chromaticity sextupole families
Linear $x-y$ coupling (global)	$\nu_x-\nu_y$	Secondary skew quadrupoles in spools and IRs in two software-defined families
Beta-function distortion	$d\nu_{x,y}/dq$	32 secondary quadrupoles, q = their strengths
Horizontal & vertical dispersion distortion	$dy_i/d\delta$ and $dx_i/d\delta$ at BPMs	32 secondary skew quads, primary orbit correctors
Linear x-y coupling (local)	Resonance widths, Fourier tune spectrum, beam response to kick	32 secondary skew quads
Sextupoles	Resonance widths, Fourier tune spectrum, beam response to kick	Primary and secondary normal and skew sextupoles
Octupoles	Resonance widths, Fourier tune spectrum, beam response to kick	Secondary normal and skew octupoles

Table 4.4-2
Suggested maximum strengths of the correction elements in the spools. The strengths are given as the integrated field strength at 1 cm radius.

Primary correction packages	
Dipole	3.10 T-m
Quadrupole	0.28 T-m
Sextupole	0.11 T-m
Secondary correction packages	
Quadrupole	0.49 T-m
Skew quadrupole	0.88 T-m
Sextupole	0.50 T-m
Skew sextupole	0.46 T-m
Octupole	0.26 T-m
Skew octupole	0.52 T-m

where N is the total number of cells in the storage ring, β_{max} and β_{min} are the maximum and minimum beta functions in the cells, f is the quadrupole focal length and δx is the rms misalignment. With β_{max} = 332 m, β_{min} = 111 m, N = 332, ν = 78.3, f = 95 m and δx = 0.5 mm, the rms orbit distortion is x_{rms} = 16 mm. The peak orbit deviation clearly will exceed the vacuum pipe radius of 16.5 mm. It is therefore envisioned that the beam at injection is first guided piecewise to complete one revolution. After the beam begins to circulate, its closed orbit will be measured and corrected, by orbit correction systems described below.

In the SSC arcs, the orbit correction system consists of a horizontal orbit corrector near each focusing quadrupole (QF), a vertical orbit corrector near each defocusing quadrupole (QD) and a beam position monitor (BPM) near each QF and each QD. For each plane, there are one corrector and two BPMs per cell. There are 850 BPMs (664 in the arcs) and 768 orbit correctors of both horizontal and vertical types (664 in the arcs) per ring. The orbit deviations are measured by the BPMs. The information is then used to determine the orbit corrector strengths needed to minimize the orbit distortion.

The orbit correction algorithm used is one that minimizes the rms orbit deviations using a beam-bump technique [4.4-1]. Simulations of this technique applied to the SSC arcs have been made using the following assumed errors:

(a) The quadrupole magnet misalignments in x (horizontal) and y (vertical) are 0.5 mm. The misalignment in x is mainly from surveying errors. The initial alignment in y will presumably be more accurate, but the 0.5 mm value also includes contributions from ground settlements.

(b) The BPMs are attached to, and therefore misaligned together with, the quadrupoles. The relative misalignment between the center of a quadrupole and its attached BPM is 0.1 mm.
(c) The rms dipole strength error due to construction errors is $\Delta B/B = 3 \times 10^{-4}$. This contributes to horizontal orbit distortion only.
(d) The rms dipole roll angle due to misalignment as well as construction errors is 0.6 mrad. This contributes to vertical orbit distortion only.

It is found [4.4-2] that the rms bend-angle corrector strength needed is 7.5 μrad (or 0.50 T-m for 20 TeV operation) and 7.74 μrad (0.52 T-m) to perform the horizontal and vertical orbit corrections, respectively. The strength is needed mainly to correct for the misalignment of the QFs in the horizontal plane and by the QDs in the vertical plane. The rms values of the horizontal and vertical deviations for the corrected orbits are 0.38 mm. The programs TEAPOT [4.3-13] and PATPET [4.4-3, 4.4-4] have been used to simulate the orbit correction process. The TEAPOT results are described in Section 4.3.4. Results such as the rms orbit distortion after correction and the needed rms corrector strengths from both programs agree well with the analytic estimates. The dipole correction coils in the spool pieces have a maximum strength of 3.1 T-m, corresponding to six times the rms value. The correction scheme can be compared with that used in the Tevatron, for which the maximum corrector strength is four times the rms value [4.4-5].

Survey and orbit errors contribute to a difference in the circumference between the two rings. To assure that the collision points do not drift, the rf systems must have their frequencies locked to each other so that the two beams travel equal distance per revolution by having the two beam energies slightly different. Assuming the magnetic field strengths are the same, a circumference difference of ΔC translates into a fractional difference between the mean energies of the two beams of

$$\Delta E/E = (\Delta C/C)/\alpha \tag{4.4-2}$$

where α is the momentum compaction factor of the lattice. It is necessary that this energy difference is well within the energy aperture (10^{-3} at maximum). If we take a permitted $\Delta E/E = 10^{-4}$ and $\alpha = 0.00022$, the tolerable circumference difference is found to be $\Delta C/C = 2.2 \times 10^{-8}$. With $C = 83$ km, we have $\Delta C = 1.8$ mm [4.4-6]. This seemingly tight tolerance is acceptable since it represents the tolerance on the difference between the two circumferences and not on their absolute errors. The contribution from horizontal orbit distortion to ΔC is estimated to be about 0.2 mm after orbit correction.

4.4.3 Linear Corrections

One of the main effects of orbit distortion is that higher order field errors feed down to lower orders. Sextupole field errors, for example, will contribute to quadrupole and skew quadrupole field errors, causing linear optical distortions similar to those from a_1 and b_1. In this section, we describe how these linear distortions are to be corrected in the SSC. We assume that the horizontal and vertical orbits have been corrected.

The random rms values of a_1 and b_1 are listed in Table 4.3-1 to be 0.7×10^{-4} cm^{-1}. This is the expected value after the superconducting coil packages of individual magnets

have been carefully centered. Before coil centering, the uncompensated rms values are $a_1 = 3.3 \times 10^{-4}\ \mathrm{cm}^{-1}$ and $b_1 = 1.6 \times 10^{-4}\ \mathrm{cm}^{-1}$. The centering is performed at 1 TeV. At 20 TeV, iron saturation makes centering less effective in canceling the field errors. It is estimated that 30% of the uncompensated a_1 and 10% of the uncompensated b_1 will then reappear, leading to effective field errors of $a_1 = 1.21 \times 10^{-4}\ \mathrm{cm}^{-1}$ and $b_1 = 0.72 \times 10^{-4}\ \mathrm{cm}^{-1}$.

Linear optical distortions appear as tune shifts, errors in the beta functions, errors in the dispersion functions, and in $x-y$ coupling. The sources of these errors come mainly from the field errors a_1 and b_1 in the bending magnets, quadrupole magnet roll-angle misalignments and closed orbit errors in sextupole magnets.

Quadrupole Errors

Designating the effective rms quadrupole field errors per cell as σ_q and letting N be the number of cells in the arcs, the order of magnitude of the rms tune shifts is given by

$$\Delta\nu_{x,y} = N^{1/2}\,(\beta_{x,y})_{\mathrm{ave}}\,\sigma_q/4\pi \tag{4.4-3}$$

where $(\beta_{x,y})_{\mathrm{ave}}$ is the average value of the $\beta_{x,y}$-function in the cells. The effective quadrupole error per cell is given by the quadratic sum of contributions from dipoles, quadrupoles and sextupoles in the cell, i.e.,

$$\sigma_q = [\sigma_q(D)^2 + \sigma_q(Q)^2 + \sigma_q(S)^2]^{1/2} \tag{4.4-4}$$

where

$$\sigma_q(D) = b_1\,\theta\,n^{-1/2} = 3.7 \times 10^{-5}\ \mathrm{m}^{-1}$$

$$\sigma_q(Q) = \sqrt{2}\,\sigma_{\Delta q/q}\,f^{-1} = 0.73 \times 10^{-5}\ \mathrm{m}^{-1}$$

$$\sigma_q(S) = \sqrt{2}\,\sigma_{\Delta x} r\ /\ f\,\eta_{\mathrm{ave}} = 1.0 \times 10^{-5}\ \mathrm{m}^{-1}$$

The bending angle per cell is $\theta = 16.4$ mrad, the number of dipole magnets per cell, $n = 10$, the arc quadrupole focal length, $f = 95$ m, the ratio between the total chromaticity and its cell contribution, $r = 2$, the average dispersion function in the arcs, $\eta_{\mathrm{ave}} = 3$ m. For the errors, we have taken $b_1 = 0.72 \times 10^{-2}\ \mathrm{m}^{-1}$, the rms quadrupole strength error $\sigma_{\Delta q/q} = 5 \times 10^{-4}$ and the rms horizontal orbit deviation $\sigma_{\Delta x} = 1$ mm. Equation (4.4-4) then yields $\sigma_q = 3.9 \times 10^{-5}\ \mathrm{m}^{-1}$, with a dominating contribution from the dipole field errors. With $\beta_{\mathrm{ave}} = 220$ m, and N = 332 the expected tune shift, Eq. (4.4-3), is about 0.012.

The tune correction is straightforward with the primary trim quadrupole coils in the spools. The same coils are needed to provide tune variations of ± 2 units for operation optimization and to compensate for differential saturation of $\pm 1\%$ between dipoles and quadrupoles. (Dipoles saturate by about 2%, which can be split with the quadrupole strength.) Tune corrections in the ± 0.012 range require a coil strength that is much smaller

than that for tune variation of ± 2 units. Tune variation of ± 2 units requires a strength of 3.1×10^{-4} m^{-1}. Compensating for differential saturation requires a strength of 1.1×10^{-4} m^{-1}. The total required primary quadrupole strength in the spools is therefore 4.2×10^{-4} m^{-1}, or equivalently, an integrated field of ± 0.28 T-m at a radius of 1 cm, as indicated in Table 4.4-2.

In addition to tune shifts, the quadrupole field errors also contribute to distortion in the beta functions and the dispersion functions. Before correction, the rms fractional variation in the beta functions is

$$(\Delta\beta/\beta)_{\text{rms}} = (N/2)^{1/2}\, \beta_{\text{ave}}\, \sigma_q/(2 \sin 2\pi\nu) \tag{4.4-6}$$

With $\nu = 78.3$, we obtain $\Delta\beta/\beta = 5.8\%$. The beta-function distortions are to be corrected by secondary quadrupole coils in the 8 spool systems located near the refrigerators. Since each location needs to correct for errors from approximately 42 cells, the rms strength needed to perform the beta-function correction is $\sqrt{42}\,\sigma_q = 2.5 \times 10^{-4}$ m^{-1}. The maximum strength required of these secondary quadrupole coils is taken to be 3 times the rms expected values, i.e., 7.5×10^{-4} m^{-1}, or an integrated field of 0.49 T-m at 1 cm radius.

The distortion of the horizontal dispersion function η_x from quadrupole errors is given by

$$(\Delta\eta_x/\eta_x)_{\text{rms}} = (N/2)^{1/2}\, \beta_{x,\text{ave}}\, \sigma_q/(2 \sin\pi\nu_x) \tag{4.4-7}$$

which resembles the $\Delta\beta/\beta$ expression except for the argument of the sine function. The numerical value, using $N = 332$, $\beta = 220$ m, $\sigma_q = 3.9 \times 10^{-5}$ m^{-1}, $\eta = 3$ m, and $\nu = 78.3$ is about 20 cm. The dispersion distortion is not expected to cause severe problems. Nevertheless, if desired, it can be corrected by the secondary quadrupole correctors or by the primary dipole orbit correctors. Attention will be given to the dispersion distortions at the interaction points and also at the rf cavities.

Skew Quadrupole Errors

We now consider the effects of the skew quadrupole errors. Designating the effective rms skew quadrupole field error per cell as σ_{sq}, the $x-y$ coupling coefficient has an rms order of magnitude given by

$$|C|_{\text{rms}} = N^{1/2}\, (\beta_x \beta_y)_{\text{ave}}^{1/2}\, \sigma_{sq}/4\pi \tag{4.4-8}$$

which resembles the tune shift formula, Eq. (4.4-3), for quadrupole field errors. Particle motion will be strongly coupled if the unperturbed tunes are close to the linear coupling resonance $\nu_x = \nu_y$, i.e., if they are separated by less than about $2|C|$. In the strongly coupled region, the minimum separation between the perturbed tunes of the two betatron normal modes is given by $2|C|$. Away from the coupling resonance, the beam orientation tilts relative to the $x-y$ coordinates by an angle approximately given by $2|C|/(\nu_x - \nu_y)$.

Like the quadrupole error, the effective skew quadrupole error per cell is given by the quadratic sum of three contributions,

$$\sigma_{sq} = [\sigma_{sq}(D)^2 + \sigma_{sq}(Q)^2 + \sigma_{sq}(S)^2]^{1/2} \tag{4.4-9}$$

where

$$\sigma_{sq}(D) = a_1\,\theta\,n^{-1/2} = 6.4 \times 10^{-5}\ \mathrm{m}^{-1}$$

$$\sigma_{sq}(Q) = 2\sqrt{2}\,\sigma_{\Delta\phi}/f = 1.5 \times 10^{-5}\ \mathrm{m}^{-1}$$

$$\sigma_{sq}(S) = \sqrt{2}\,\sigma_{\Delta y}\,r\,/\,f\eta_{\mathrm{ave}} = 1.0 \times 10^{-5}\ \mathrm{m}^{-1} \tag{4.4-10}$$

We have taken the field error coefficient to be $a_1 = 1.21 \times 10^{-2}\ \mathrm{m}^{-1}$, the rms roll-angle alignment error to be $\sigma_{\Delta\phi} = 0.5$ mrad and the rms vertical orbit deviation to be $\sigma_{\Delta y} = 1$ mm. Equation (4.4-9) then yields $\sigma_{sq} = 6.7 \times 10^{-5}\ \mathrm{m}^{-1}$. The estimate is somewhat pessimistic because it is dominated by the dipole field errors whose effect may be reduced to an extent by sorting the magnet locations. With $\beta_{\mathrm{ave}} = 220$ m and $N = 332$, the uncorrected coupling coefficient, Eq. (4.4-8), is about 0.021, which is unacceptably large.

In addition to the coupling coefficient, skew quadrupole field errors also cause distortion in the vertical dispersion function. The expression for the rms distortion is the same as Eq. (4.4-7), with x replaced by y and σ_q replaced by σ_{sq}. Using $\sigma_{sq} = 6.7 \times 10^{-5}\ \mathrm{m}^{-1}$ leads to $\Delta\eta_y = 35$ cm. Scaled to the interaction point with $\beta^* = 0.5$ m, $\Delta\eta_y = 1.7$ cm. With $\sigma_\delta = 0.5 \times 10^{-4}$ at 20 TeV, this contributes 0.8 μm to the rms beam spot size of 4.8 μm. Again, magnet sorting is expected to help reducing this distortion. In addition, corrections can be provided by secondary skew quadrupoles, as well as the vertical orbit correctors.

The maximum strength of the skew quadrupole correction coils in the secondary spools is $3\sqrt{42}\,\sigma_{sq} = 1.3 \times 10^{-3}\ \mathrm{m}^{-1}$, corresponding to an integrated field of 0.88 T-m at 1 cm radius. To correct for the coupling constant, it is envisioned to use not only the skew quadrupole coils in the arcs but also those in the interaction regions since they are more effective and have better phase locations. The coupling constant after correction is expected to be less than 0.005, perhaps as small as 0.001.

Measurements of β and η

The secondary quadrupoles in the spools near the refrigerators, as well as quadrupole trims in the interaction region and utility sections, can be used to measure the local beta functions. This amounts to a total of 32 locations in the arcs and 32 more in the IRs where local beta functions can be measured. We believe this is important for the monitoring and correction of the SSC optics. Measuring a beta function at the location of a quadrupole is done by recording the tune change as the quadrupole strength is varied. For example, if a full swing in the secondary quadrupole coil is available and if the tune measurement accuracy is 0.0001, the beta functions can in principle be measured to an accuracy of about 1 m, with 10 m accuracy regarded as adequate.

To measure the dispersion functions, the beam positions at the orbit monitors are measured as a function of beam energy. By varying the rf frequency by ± 36 Hz, the beam energy changes by $\Delta E/E = \pm 0.5 \times 10^{-3}$. The corresponding orbit change at a location of 3 m dispersion is ± 1.5 mm. If the orbit monitors can measure the orbit to a relative accuracy of 0.03 mm, the dispersion functions at the orbit monitors can be measured to an accuracy of 3 cm. With the same rf frequency swing and the capability of measuring the betatron tunes to accuracy of 0.0001, the chromaticities can be measured to accuracy of 0.1 unit, although such high accuracy is not necessary during normal operations. The dispersion and chromaticity measurements are two useful diagnostic tools. The needed rf frequency range is easily achievable. The associated energy swing is within the momentum aperture allowed by the magnet field quality.

4.4.4 Sextupole Corrections

Primary Sextupole Correctors

Primary sextupole coils are provided in each spool. Their purpose is to make chromaticity corrections. In the ideal case, they compensate for the natural chromaticities of $\xi_x = \xi_y = -204$. The nominal settings of these coils are $B''\ell/B\rho = 0.0098\ \mathrm{m}^{-2}$ and $-0.0159\ \mathrm{m}^{-2}$ for the focusing and defocusing families, respectively. In the presence of dipole magnet field errors, the chromaticities are shifted. The chromaticity shifts due to a systematic field error of b_2 are given by

$$\Delta\xi_{x,y} = \pm\, b_2 \langle \eta_x \beta_{x,y} \rangle \tag{4.4-11}$$

where the + and − signs apply to $\Delta\xi_x$ and $\Delta\xi_y$, respectively, and $\langle \eta_x \beta_x \rangle = 650\ \mathrm{m}^2$, $\langle \eta_x \beta_y \rangle = 600\ \mathrm{m}^2$. The systematic field errors are to be corrected by distributed coil windings around the vacuum chamber pipe inside the dipole magnets. If uncorrected, the systematic field error at injection due to the persistent current effect is about $b_2 = -4.7\ \mathrm{m}^{-2}$, yielding $\Delta\xi_x$ of magnitude 3100, which is excessively large. The distributed compensation is expected to be able to correct this sextupole error to the 10% level (less than $\pm 0.5\ \mathrm{m}^{-2}$ in b_2).

The order of magnitude of the chromaticity shifts due to random field errors is given by Eq. (4.4-11), but reduced by a factor of $\sqrt{N_b}$ where N_b is the total number of bending magnets and b_2 is interpreted as the rms random error coefficient. With $b_2 = 2.01\ \mathrm{m}^{-2}$ from Table 4.3-1 and $N_b = 3840$, the rms b_2 error is $0.03\ \mathrm{m}^{-2}$ and the chromaticity errors have a rms value of about 21 units. (Magnet sorting will reduce this value.)

The chromaticity errors are to be corrected by the primary sextupole coils. Their maximum strength is set so that they can provide the chromaticity correction due to both systematic and 3 times the rms random errors. This amounts to a range in b_2 of $0.6\ \mathrm{m}^{-2}$ or in chromaticity of $\pm$ 390 units. The strengths of the two sextupole families to remove the chromaticities caused by a b_2 of $0.6\ \mathrm{m}^{-2}$ are $0.0093\ \mathrm{m}^{-2}$ and $0.013\ \mathrm{m}^{-2}$, which are approximately equal to the nominal settings. The maximum strength of the sextupole coils is therefore twice the nominal setting of the defocusing sextupole family, corresponding to 0.11 T-m at 1 cm radius, as stated in Table 4.4-2.

Secondary Sextupole Correctors

In addition to the primary sextupoles, there are secondary coils to correct for potential resonances. Since there are 420 dipole magnets between adjacent secondary sextupole correctors, the rms effective b_2 field error is $\sqrt{420}$ times the rms value per magnet. To correct for these errors, the maximum strength of the secondary sextupole coils is set to be 3 times the rms value, yielding an integrated field at 1 cm radius of 1.5 T-m at 20 TeV and 0.075 T-m at 1 TeV. Since sorting on sextupole field errors is expected to reduce the resonance driving strength by an order of magnitude, the suggested strength of 0.5 T-m for the secondary sextupole coils should be sufficient. Note that even without sorting the strength is more than sufficient at 1 TeV. Additional control of resonances can be obtained by allowing the eight circuits of each primary sextupole family to carry different currents.

Alignment of Distributed Sextupole Windings

The distributed sextupole windings that correct for the persistent current contributions need to be aligned relative to the magnet centers [4.4-7]. The alignment accuracy required is such that the feeddown from the persistent current $b_2 = -4.7\ \mathrm{m}^{-2}$ to a_1 and b_1 be much less than the rms values themselves ($a_1 = 1.21 \times 10^2\ \mathrm{m}^{-1}$, $b_1 = 0.72 \times 10^{-2}\ \mathrm{m}^{-1}$). This requires the horizontal and vertical misalignments to be less then $b_1/2b_2$ and $a_1/2b_2$, respectively. With the above numerical values, an alignment tolerance of 0.2 mm satisfies the criterion.

4.4.5 Analysis of Effects of Multipole Field Errors

Before discussing the multipole corrections, it is worthwhile to provide an analysis of the nonlinear effects expected from the multipoles. Recent studies in the Sp$\bar{\text{p}}$S, the CERN Antiproton Accumulator, and the Tevatron have identified high order nonlinear resonances as a source of instability in particle motion. A resonance occurs when the betatron tunes ν_x and ν_y nearly satisfy the condition

$$n\,\nu_x + m\,\nu_y = p \tag{4.4-12}$$

where n, m and p are integers. The order of the resonance is $|n| + |m|$. Near a resonance, particle motion is strongly perturbed by the nonlinear multipole field of the corresponding order. In addition, tune modulation from synchrotron motion and power supply ripple introduce sidebands to the resonances. Overlap of these sidebands causes stochastic motion that leads to diffusional blow-up of the beam. The nonlinear resonance effects also apply to the beam-beam interaction, as is discussed in Sections 4.5.7 and 4.5.8.

Two quantities enter the nonlinear resonance considerations, the tune shift $\Delta\nu$ and the resonance width $\pm\delta\nu$. Tune shift refers here to the variation of the betatron tune as a function of the betatron amplitude and energy deviation $\delta = \Delta E/E$. Resonance width is the distance in tune units from the resonance condition (4.4-12) within which the resonance has a significant effect on particle motion. To assure reasonably linear particle motion, both tune shift and resonance width need to be controlled.

Tune Shift

(a) Bending Magnets

In one-dimensional horizontal motion, the tune shift caused by a systematic multipole b_n in the dipole bending magnets is given by

$$\Delta\nu = \beta b_n \langle \cos\phi(\eta\delta + A_\beta \cos\phi)^n \rangle / A_\beta \tag{4.4-13}$$

where A_β is the betatron oscillation amplitude, η is the dispersion at the location of the multipoles and the brackets imply an average over the betatron phase angle ϕ. For the first six n values the expressions are

n	Multipole	$\Delta\nu$
1	Quadrupole	$\beta b_1/2$
2	Sextupole	$\beta b_2\,\eta\delta$
3	Octupole	$3\beta b_3(\eta^2\delta^2/2+A_\beta^2/8)$
4	Decapole	$\beta b_4(2\eta^2\delta^2 + 3A_\beta^2/2)\eta\delta$
5	12th pole	$5\beta b_5(\eta^4\delta^4/2+3A_\beta^2\eta^2\delta^2/4+A_\beta^4/16)$
6	14th pole	$3\beta b_6(\eta^4\delta^4+5A_\beta^2\eta^2\delta^2/2+5A_\beta^4/8)\eta\delta$

To assure reasonable operation of the SSC at injection, a condition of sufficient linear aperture has been imposed in Section 4.3.2. For the systematic field errors, we suggest that (1) the tune shift $\Delta\nu$ caused by each multipole component be less than 0.005 for betatron amplitudes $A_\beta < 0.5$ cm at $\beta_{max} = 330$ m and $|\delta < 10^{-3}$, and (2) $\Delta\nu < 0.005$ for $A_\beta < 0.7$ cm at $\beta_{max} = 330$ m and $\delta = 0$. The dotted lines in Fig. 4.4-1 indicate the phase space region in which the $\Delta\nu < 0.005$ criterion applies. Such a stringent linear aperture requirement will be advantageous for injection operations. During beam storage and collision at 20 TeV, the requirements can be relaxed because of the smaller beam dimensions, smaller energy spread and better orbit controls. For collision operations, the range in A_β and δ for $\Delta\nu < 0.005$ are reduced by a factor of 2 in the above criteria (1) and (2).

Systematic field errors in dipole magnets are given by the b_n coefficients with even n. The tune shift thus vanishes for on-momentum particles ($\delta = 0$) and only criterion (1) applies. Table 4.4-3 gives the maximum tolerable systematic multipole coefficients in the absence of any corrections, according to the tune shift criterion [4.4-8]. The tolerance on b_n for colliding beam operations is a factor of 2^{n-1} times that for injection.

Table 4.4-3

Tolerances of systematic and random multipole field errors in the dipole magnets (in units of 10^{-4} cm^{-n}) in the absence of lumped correctors outside the dipoles, according to the criteria that $\Delta\nu < 0.005$ for $A_\beta < 0.5$ cm, $\delta < 0.001$ for injection and that $\Delta\nu = 0.005$ for $A_\beta < 0.25$ cm, $\delta < 0.0005$ for colliding beam operations. Lattice functions are taken to be β_{max} =330 m and η_{max} = 4 m.

Multipole Coefficient (b_n)	Tolerance at Injection		Tolerance at Collision	
	Systematic	Random	Systematic	Random
b_1	—	0.28	—	0.28
b_2	0.0076	0.47	0.015	0.94
b_3	—	0.71	—	2.8
b_4	0.018	1.08	0.14	8.6
b_5	—	1.64	—	26
b_6	0.040	2.5	1.3	80
b_7	—	3.7	—	
b_8	0.089	5.4	11	
b_9	—	8.2	—	
b_{10}	0.19	12	97	

The systematic sextupole (b_2), and decapole (b_4) errors from persistent currents exceed the tolerances listed in Table 4.4-3 and thus need to be compensated. As discussed in the previous section, distributed coils are provided to compensate the systematic sextupole and decapole distortions. For injection operations, the distributed b_2 coil is expected to reduce the net b_2 from -4.7×10^{-4} cm^{-2} to less than $\pm 0.5 \times 10^{-4}$ cm^{-2} thereby meeting the dynamic aperture requirement and permitting low-intensity test beams to be injected to measure the chromaticities. The distributed b_2 circuit and the two lumped sextupole coils in the spool pieces are then empirically adjusted to make the chromaticities vanish. A similar procedure can be applied to the decapole component. The sensitivity of tune to these field components allows their accurate empirical compensation. The tune shift from the 14-pole, although larger than the calculated tolerance, is rather weak in the sense that, as shown in Fig. 4.4-1(a), the tune shift exceeds 0.005 only in a narrow region in the desired phase space [4.4-9]. It is not regarded as a serious deficiency and is not considered further in the conceptual design.

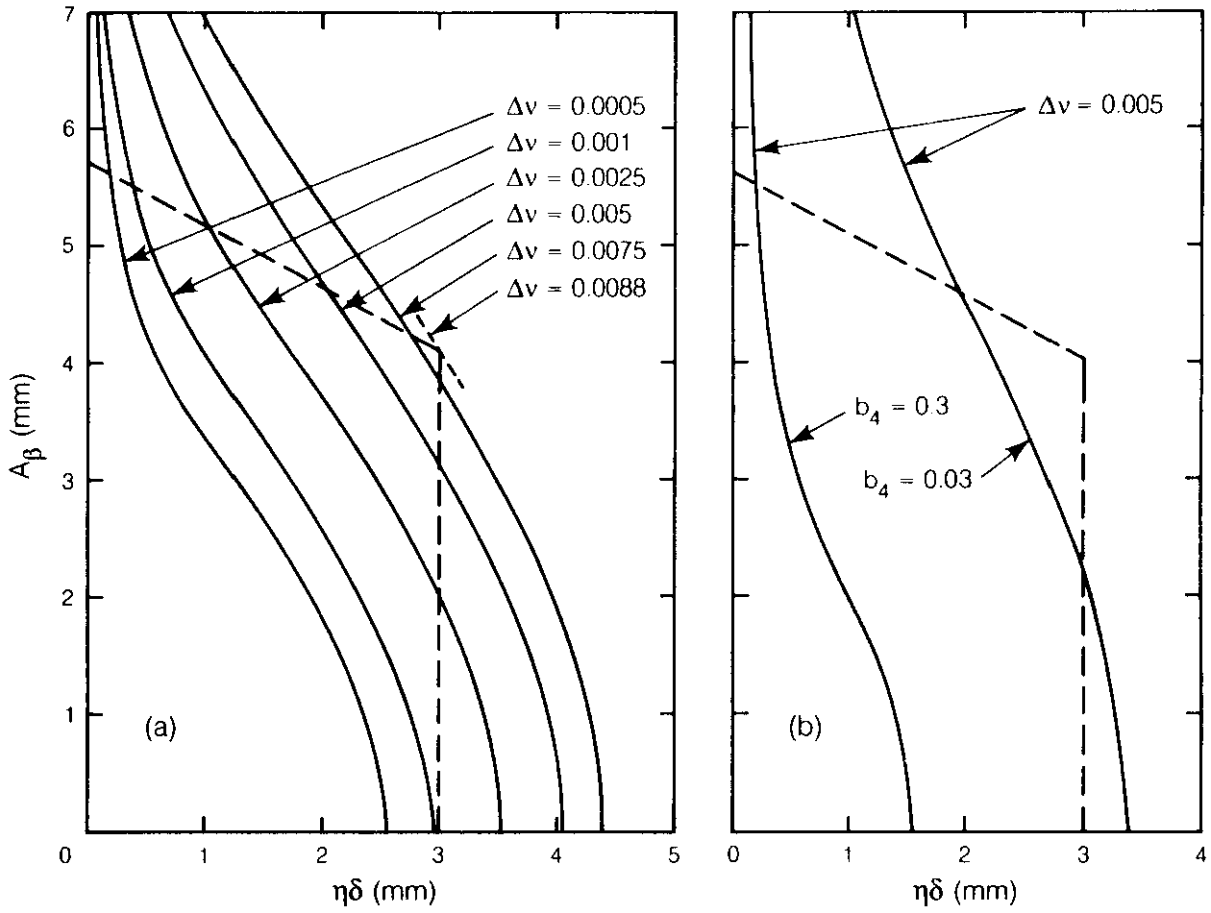

Figure 4.4-1. Tune shift in the (A_β $\eta\delta$) phase space. (a) Tune shift due to systematic $b_6 = 0.07 \times 10^{-4}\text{cm}^{-6}$. (b) Tune shift due to systematic $b_4 = 0.3 \times 10^{-4}$ cm^{-4} and 0.03×10^{-4} cm^{-4}, corresponding to the uncorrected and the 90% corrected cases.

It may be useful to emphasize that the tolerances listed in Table 4.4-3 assume no lumped corrections. Lumped corrections are most effective to remove the tune shift due to the systematic b_2 error. Although not adopted in the conceptual design, two families of lumped sextupoles are capable of handling the tune shifts caused by a systematic b_2 error up to 3×10^{-4} cm^{-2} [4.4-10]. It may also be useful to point out that the tolerances can be relaxed by going to 90 degree cells of approximately the same length, by adjusting the dipole magnet design, or by using finer superconducting filaments. The possibility of eliminating the distributed multipole correction coils by a combination of these efforts is being studied. The conceptual design, however, has included these distributed coils in the cost estimate. Figure 4.4-1(b) shows the phase space region in which the tune shift exceeds 0.005 due to the systematic decapole field. As mentioned, the linearity of this phase space region can be recovered by lumped corrections and empirical adjustment of the distributed decapole current.

(b) Focusing Magnets

Systematic multipole errors that appear in the focusing quadrupoles are b_n with $n = 4k+1$. Unlike the case of dipoles, the tune shift does not vanish for on-momentum particles, but the requirement that $\Delta\nu < 0.005$ for $|\delta| < 10^{-3}$ and $A_\beta < 0.5$ *cm* at injection, still leads to the most stringent condition. The tolerable systematic multipole coefficients in the arc quadrupoles are $b_1 = 0.33 \times 10^{-4}$ cm^{-1}, $b_5 = 2.0 \times 10^{-4}$ cm^{-5} and $b_9 = 9.8 \times 10^{-4}$ cm^{-9}, where these b_n coefficients are relative to the quadrupole field strength at 1 cm radius. The b_1 systematic error can be compensated by the quadrupole coils in the primary correction packages. The tolerances on the systematic b_5 and b_9 coefficients of the arc quadrupoles are readily achievable.

(c) Random Multipole Errors

For random multipole errors in the dipole magnets, the tune shift expression (4.4-13) is to be divided by $\sqrt{N_b}$, where $N_b = 3840$ is the total number of bending magnets, and $\Delta\nu$ and b_n are to be interpreted as rms values. The rms values of the tolerable multipole coefficients are listed in Table 4.4-3. Comparison with the values listed in Table 4.3-1 for the SSC magnets shows that the tune shift criterion does not impose a significant constraint of the random multipoles except for the b_1 and b_2, which are controlled by the correction coils in the spools. Constraints on the random skew multipoles a_n are the same as on the corresponding normal multipoles.

Tune shifts to lowest nonvanishing order in the betatron amplitudes can be described in terms of Eq. (4.2-1). In the presence of random sextupole and octupole components, the coefficients a, b and c can be evaluated by the program MARYLIE. Simulations give results that agree reasonably well with Table 4.4-3.

Resonance Width

Tolerance criteria on the random multipoles are also imposed by considerations of the resonance width. For example, the resonance width for one-dimensional betatron motion around $\nu = p/n$ caused by the rms multipole of b_{n-1} is given by [4.4-11]

$$\delta\nu = 2^{-n+1} N_b^{-1/2} b_{n-1} \beta A_\beta^{n-2} \tag{4.4-14}$$

The resonance widths for particles executing betatron oscillations with amplitudes 10 times the rms value for the beam are given in Table 4.4-4, assuming the calculated rms multipole coefficients of Table 4e of Attachment A.

According to Table 4.4-4, the third order resonances driven by sextupole field errors are the only potential concern. This suggests that one gains by sorting magnet positions on the sextupole field components. In addition, the possibility of correcting these resonances is provided by the secondary sextupole coils. On the other hand, as mentioned below Eq. (4.4-12), synchrotron oscillations can cause a betatron tune modulation of the form

$$\nu = \nu_0 + q \cos \nu_s \theta \tag{4.4-15}$$

where θ is the azimuthal angle around the ring, and q and ν_s are the modulation amplitude and synchrotron tune, respectively. The tune modulation splits the betatron resonance into a series of synchro-betatron sideband resonances, ν_s/n apart in tune space. If these sideband resonances are wide enough to overlap, particles will execute stochastic motion across the resonances. The effective resonance width will become of the order of q even if the betatron resonance is narrower. This overlapping can be avoided when ν_s is large enough. A conservative estimate of the minimum ν_s to avoid overlapping for particles with betatron amplitude of 10σ is shown in Table 4.4-4 [4.4-11]. The results indicate that it is advisable to avoid resonances up to the seventh order within the tune spread of the beam since the synchrotron tune is about 0.0082 at injection and 0.0019 during storage.

Table 4.4-4
Resonance widths from random multipoles in the dipoles.

Resonance order n	$b_{n-1} \times 10^4$ (cm^{-n+1})	Resonance width $\delta\nu$	Minimum ν_s
3	2.01	0.0080	0.12
4	0.35	0.00032	0.027
5	0.59	0.00012	0.018
6	0.059	2.6×10^{-6}	0.003
7	0.075	7.6×10^{-7}	0.0017
8	0.016	3.6×10^{-8}	0.0004
9	0.021	1.1×10^{-8}	0.00023
10	0.003	3.4×10^{-10}	0.000044
11	0.007	1.8×10^{-10}	0.000034

Linear Aperture

One more analytic estimation of the linear aperture can be obtained by integrating the perturbation of a particle's motion from the random multipole errors over one revolution. This contribution to the betatron amplitude is then compared with the unperturbed value. The maximum betatron amplitude for which the perturbation is less than 10% of the unperturbed amplitude is a rough estimate of the linear aperture achieved [4.4-12]. With the random multipoles from Table 4e of Attachment A, the linear aperture calculated this way is

found to be 0.51 cm for $\delta = 0$, consistent with the tracking results obtained in Section 4.3-3 before sorting is applied.

4.4.6 Multipole Feeddown Due to Orbit Errors

The multipole coefficients listed in Table 4.3-1 refer to the center of the magnets. In case there is an orbit distortion, the beam traverses a magnet off center. The distorted orbit passes through fields with a different multipole expansion (relative to the orbit) from the on-center orbit. We speak of this as the higher multipoles feeding down to the lower ones. In Section 4.3.4, we have shown by tracking that a corrected orbit does not significantly reduce the stability aperture of particle motion. In this section, we evaluate the effect of orbit distortion through an estimate of this feeddown process.

The multipole coefficients in the presence of orbit distortion Δx and Δy can be written as

$$\Sigma\,(b_n + ia_n)\,(z + \Delta z)^n = \Sigma\,(B_n + iA_n)\,z^n \tag{4.4-16}$$

where $z = x + iy$ and $\Delta z = \Delta x + \mathrm{i}\Delta y$. We assume that all multipole coefficients are uncorrelated, that Δx and Δy are uncorrelated, and that the orbit distortion has a round parabolic distribution in Δx and Δy with rms deviation of $\langle \Delta x^2 \rangle^{1/2} = \langle \Delta y^2 \rangle^{1/2} = d$. The first few rms coefficients with feeddown from orbit distortion are

$$\langle A_0^2 \rangle = \langle B_0^2 \rangle = d^2 \left(\langle a_1^2 \rangle + \langle b_1^2 \rangle \right) + 3\,d^4 \left(\langle a_2^2 \rangle + \langle b_2^2 \rangle \right) + \cdots$$

$$\langle A_1^2 \rangle - \langle a_1^2 \rangle = \langle B_1^2 \rangle - \langle b_1^2 \rangle$$

$$= 4\,d^2 \left(\langle a_2^2 \rangle + \langle b_2^2 \rangle \right) + 27\,d^4 \left(\langle a_3^2 \rangle + \langle b_3^2 \rangle \right) + \cdots \tag{4.4-17}$$

$$\langle A_2^2 \rangle - \langle a_2^2 \rangle = \langle B_2^2 \rangle - \langle b_2^2 \rangle$$

$$= 9\,d^2 \left(\langle a_3^2 \rangle + \langle b_3^2 \rangle \right) + 108\,d^4 \left(\langle a_4^2 \rangle + \langle b_4^2 \rangle \right) + \cdots$$

Figure 4.4-2 shows the effective rms multipole coefficients as functions of d up to $n = 4$. The feeddown effect becomes appreciable when the rms orbit deviation reaches about 2 mm or more. The most affected multipoles are the normal and skew quadrupole components (B_1, A_1), from the b_2 coefficient. The A_0 and B_0 coefficients contribute to closed orbit distortions which are handled by the orbit correction scheme. With an alignment tolerance of 1 mm for the dipole magnets and an expected orbit deviation of 0.4 mm after correction, the feeddown effect is not serious.

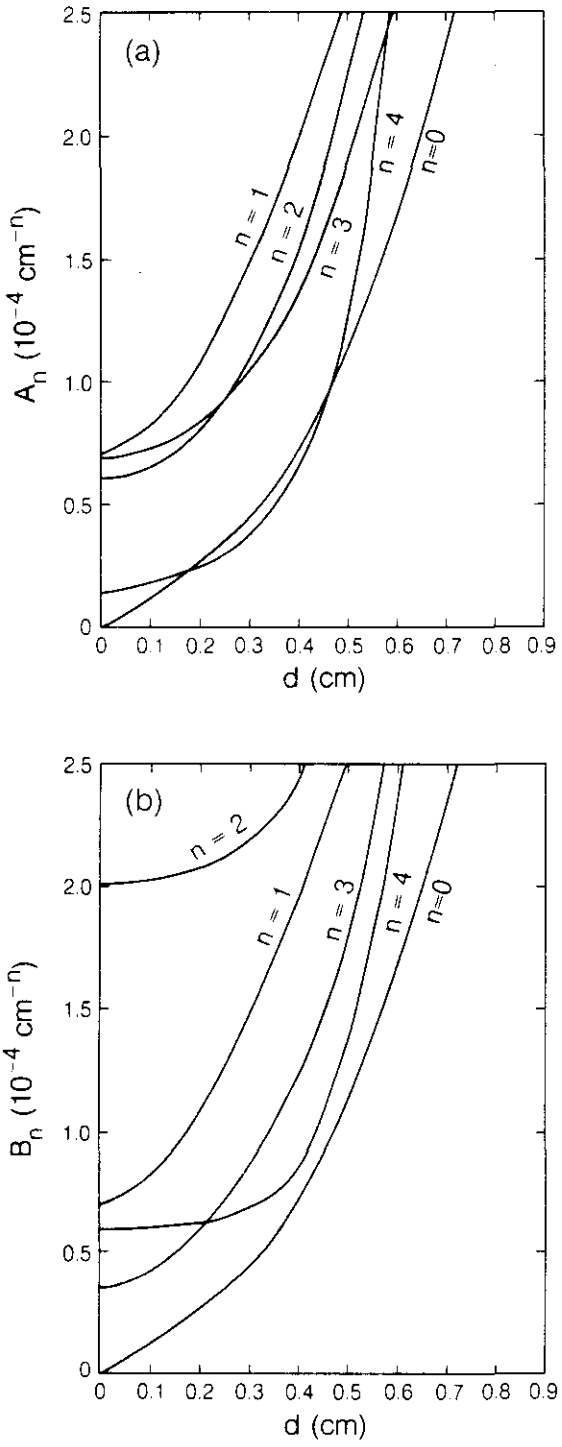

Figure 4.4-2. Effective multipole error coefficients as functions of the rms orbit deviation due to the feeddown effect for (a) the skew multipoles, (b) the normal multipoles.

4.4.7 Multipole Corrections

The secondary spools, as presently envisioned, contain coils for quadrupole, sextupole, octupole fields and their skew counterparts. Their maximum strengths are set to compensate for 3 times the rms contribution from the corresponding magnet field errors. The quadrupole, skew quadrupole and sextupole strengths have already been discussed. Taking the rms field error to be $a_2 = 0.61\ m^{-2}$, $a_3 = 69\ m^{-3}$ and $b_3 = 35\ m^{-3}$ from Table 4.3-1, the secondary correction element strengths at 20 TeV are those given in Table 4.4-2, i.e., skew sextupole = 0.46 T-m, octupole = 0.26 T-m, skew octupole = 0.52 T-m. The octupole and skew octupole correctors are used mainly during injection. The strengths listed correspond, however, to 20 TeV.

The multipole elements are provided for use during operation. For example, the beam trajectory may be perturbed by either a kicker magnet or a corrector and its displacement measured at the BPMs (time domain analysis) or Fourier analyzed (frequency domain analysis). The signals are then used to set the correctors. Alternatively, one can compensate empirically for a resonance while having the tune close to it. Simulations of these operational procedures and optimization of the multipole correction scheme are presently being studied. However, the conceptual design specifications do not claim any potential benefits from these corrections, although they are included in the cost estimate.

4.4.8 Interaction Region Magnet Error Tolerances

The field quality of the interaction region magnets is critical to the performance of the SSC. Because of their large beta functions, IRs represent bottlenecks as far as aperture is concerned. For example, for a high-luminosity IR with $\beta^* = 0.5$ m, the maximum beta function is about 8000 m in the triplet neighboring the interaction point. To maintain a high gradient, these quadrupoles have an inner coil diameter of 40 mm. Extra room is needed to provide multipole coils for local field error compensation, so that the physically available room for particles in the triplets is within a pipe of inner radius 15.5 mm. Part of the 15.5 mm is needed to allow for the finite beam crossing angle, reducing the accessible radius to 12.8 mm. With $\beta = 8000$ m, this 12.8 mm radius is equivalent to a 2.6 mm amplitude in the arcs where the maximum beta function is 330 m. This 2.6 mm is small compared to the achieved dynamic aperture in the arcs of (9.1 $\pm$ 1.5) mm without sorting and (12 $\pm$ 1.5) mm with sorting (Section 4.3.3). Note that 15.5 mm is over 75% of the inner coil radius of 20 mm, indicating that field errors in the triplet magnets need to be compensated locally, as is discussed below.

Ample dynamic aperture is critical at beam injection. The low-beta optics for colliding beams does not provide sufficient aperture. The IR optics has to be detuned to accommodate injection needs. On the other hand, it is not necessary to maintain a 12 mm dynamic aperture during collisions. With proper control of closed orbits, linear distortions, chromaticities, and the leading nonlinear effects, a 2.6 mm aperture is believed to be sufficient for colliding beams at 20 TeV. We have thus set $\beta^* = 0.5$ m as the design goal of the SSC for the high-luminosity IRs.

We now investigate the effects of IR magnetic errors on the dynamic aperture for the colliding beam optics (2 IRs with $\beta^* = 0.5$ m and 2 IRs with $\beta^* = 10$ m) by means of particle tracking [4.4-13] using the program PATRICIA. Five sets of random number seeds are used and particles are tracked for 400 revolutions. For simplicity, no magnet sorting has

been applied and only on-momentum particles are considered. Table 4.4-5 gives the results of the study. Case 1 is when all field errors are ignored except for the dipole magnets in the arcs. The dynamic aperture obtained agrees with the value (9.1 ± 1.5) mm which represents an average over all previous studies. Case 2 is when the arc quadrupole field errors, given by Table 4.3-2, are also included. The arc quadrupole field errors are clearly not very important. Case 3 is when field errors of all IR quadrupoles, excluding those in the $M = -1$ section and in the triplet (see Section 4.2.4) but including those in the utility sections, are added. When the $M = -1$ section quadrupoles are included, case 4 shows a noticeable reduction of the dynamic aperture.

Table 4.4-5
Dynamic aperture behavior as various sources of magnet field errors are included successively [4.4-13].

Case	Sources	Dynamic Aperture (mm)
1	Arc dipoles	8.8 ± 1.3
2	Arc quadrupoles	8.9 ± 1.2
3	IR quadrupoles except those in $M = -1$ section and triplet	8.3 ± 1.1
4	$M = -1$ quadrupoles	6.2 ± 1.0
5	Beam separation dipoles	5.5 ± 0.42
6	Triplet quadrupoles × 1.0	2.5 ± 0.32
7	Triplet quadrupoles × 0.1	4.9 ± 0.45

It has been pointed out that the vertical separation dipoles in the IRs cause significant aperture reduction if they have the same coil diameter as the arc dipoles [4.4-14.]. Since these dipoles are weaker, a coil diameter of 7.5 cm is chosen for them. The study of Table 4.4-5 assumed, however, a coil diameter of 5 cm, leading to a slight further reduction of aperture, as shown by case 5.

The IR triplets represent by far the most significant aperture bottleneck. Assuming a inner coil diameter of 4 cm, inclusion of their field errors (Table 4.3-2) makes the dynamic aperture drop to (2.5 ± 0.32) mm. This is not acceptable for three reasons. First, in order to assure that the full extent of 2.6 mm is available for colliding beams with 98% confidence level (to the extent that the error distribution is gaussian), the mean expectation value of dynamic aperture obtained by simulation needs to be 2 standard deviations above 2.6 mm. Second, it is advisable that particle motion in the 2.6 mm aperture is as linear as possible, while the linearity is not guaranteed by a dynamic aperture. Third, it is envisioned that the design goal of $\beta^* = 0.5$ m is achieved in steps of decreasing values of β^*. A larger aperture has to be available in order that the design goal can be reached through these operational steps.

We thus suggest that the triplet quadrupoles be measured individually and their field errors compensated locally by multipole coils up to the a_5 and b_5 components. To model the effectiveness of the compensation, we study the effect on the dynamic aperture of scaling the IR triplet field errors by a factor, as is shown in Fig. 4.4-3. The dynamic aperture is acceptable only when the compensation is better than 80%. With 90% compensation, the aperture is (4.9 ± 0.45) mm (case 7 of Table 4.4-5).

Field error compensation in the IR triplets is not as critical for the injection optics. Assuming a 90% compensation, tracking with five sets of random numbers give a dynamic aperture of (8.0 ± 0.6) mm. Field errors in the IR magnets thus cause about 10% reduction in dynamic aperture for the injection optics. Figure 4.4-4 shows the momentum dependence of the dynamic aperture for the injection optics. Sorting on the IR quadrupoles as well as the arc dipoles will improve the dynamic aperture.

In tracking studies, we have often checked to assure that the results are not misleading because of an unnoticed strong resonance nearby. Table 4.4-6 is such an example showing dynamic aperture dependence on the betatron tunes for colliding beam optics with 90% compensation of the triplet quadrupole errors. No appreciable aperture deterioration is noted within the tune range of ±0.01 units in both tunes.

Table 4.4-6
Dynamic aperture (mm) in the neighborhood of a typical working point [4.4-13]. (Tunes are quoted as differences from an integer, in this case 78)

	$\nu_x = 0.265$	$\nu_x = 0.275$	$\nu_x = 0.285$
$\nu_y = 0.285$	4.9 ± 0.4	4.9 ± 0.5	5.0 ± 0.5
$\nu_y = 0.275$	5.0 ± 0.4	5.0 ± 0.8	5.0 ± 0.5
$\nu_y = 0.265$	4.5 ± 0.4	4.8 ± 0.5	5.0 ± 0.5

4.4.9 Ground Motion

For a pp collider such as the SSC, there are two rings, one for each beam. The lattice is such that, at a given quadrupole location, one ring has a focusing quadrupole and the other ring has a defocusing quadrupole. The beta functions are different for the two rings. If the quadrupoles move, each beam still follows its own equilibrium orbit, but the two equilibrium orbits are different, causing the beams to move relative to each other at the interaction points [4.4-15].

Ground motion is coupled to the magnets through the magnet supports. In this section, effects that concern beam motion due to magnet motions are described and an estimated tolerance on magnet motion is given. The tolerance specifications are given independent of the sources of ground motion or the magnet support design. For simplicity, we assume the magnet supports are rigid so that the magnet motion is the same as the ground motion.

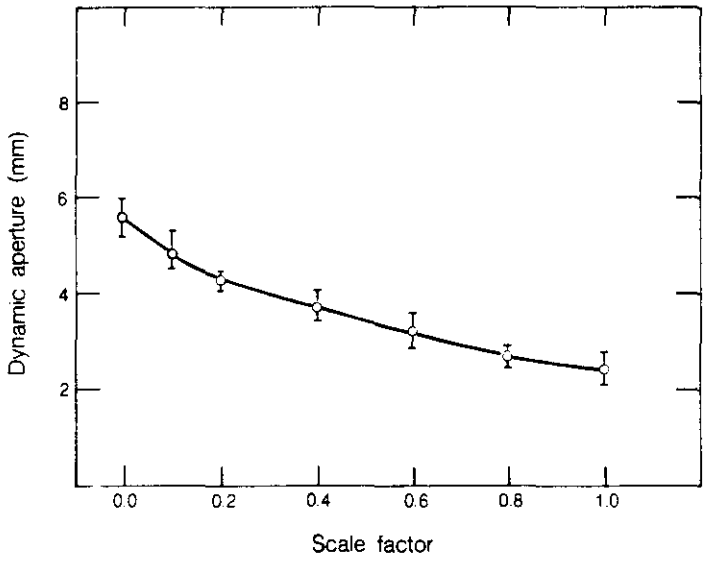

Figure 4.4-3. Dynamic aperture as function of scale factor introduced to model the compensation of field errors in the IR triplet magnets [4.4-13]. The lattice is that for colliding beams with two IRs having $\beta^* = 0.5$ m and two IRs having $\beta^* = 10$ m. Betatron tunes are $\nu_x = 78.266$, $\nu_y = 78.283$.

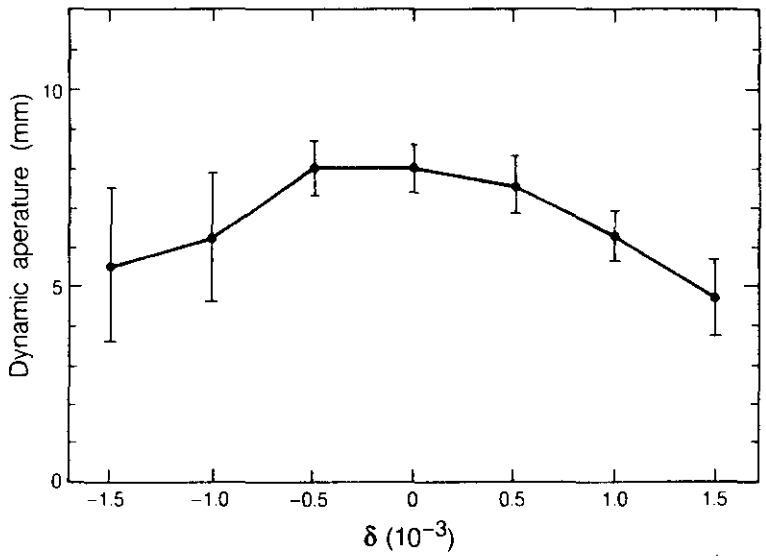

Figure 4.4-4. Dynamic aperture as a function of energy deviation $\delta = \Delta E/E$ for the injection optics [4.4-13].

The effect of ground motion on the beams depends on its frequency. Ground motion due to natural sources tends to have low frequencies (period of years to fractions of seconds). Relevant man-made noise tends to have higher frequencies (a few to 50 Hz). The lowest frequency concerns ground settlement, which causes either horizontal or vertical distortions of the ring geometry, especially with cut-and-cover tunnels. The cure is to power the orbit correctors to make the beams follow the geometry. An rms settlement of 1 mm over a distance of 192 m (the spacing between dipole correctors) requires an rms dipole strength of 5 μrad. This is to be compared with the rms orbit corrector strength of 7.5 μrad. We assume that the ground settlement will be a fraction of 1 mm over 192 m distance over the time between ring re-alignments, so that all the corrector strength is not used to compensate for ground settlement. Sites with substantial tectonic motion must be avoided. On the other hand, earth tides are not of much concern.

Assuming a ground motion speed of 2.5 km/s, the lowest frequency that will influence beam motion is approximately 0.02 Hz, corresponding to a wavelength of the order of the SSC diameter of 30 km. At higher frequencies, the effect of ground motion on the beam becomes enhanced until the wavelength of ground motion is of the order of the betatron wavelength of the beam. This happens at a ground motion frequency of about 2.5 Hz. At still higher frequencies, the effect becomes weaker again.

Let Δd be the displacement of a quadrupole (focusing for one beam and defocusing for the other beam) of strength K. The separation between the two beams at an interaction point because of this quadrupole displacement is given by

$$\Delta y^* = \beta^{*1/2} K \Delta d \, |\beta_F^{1/2} \cos(\pi\nu - \phi_F) - \beta_D^{1/2} \cos(\pi\nu - \phi_D)|/\sin 2\pi\nu \qquad (4.4\text{-}18)$$

where β^* is the beta function at the interaction point, β_F and ϕ_F are the beta function and betatron phase of the moved quadrupole in one ring, β_D and ϕ_D are the same quantities for the other ring.

The contributions from all quadrupole locations are added to give the total beam separation due to ground motion. In the range between 0.02 Hz and 3 Hz, motions of individual quadrupoles can be assumed to be correlated (according to a sinusoidal wave). Then the total beam separation is related to the ground motion amplitude by $\Delta y^* = 4.7\, \Delta d$. For frequencies higher than 3 Hz, quadrupoles move more or less uncorrelated to one another and the effect is less pronounced, with $\Delta y^* = 1.3\, \Delta d$.

To set the tolerance on ground motion, we propose the somewhat conservative criterion that the beam separation Δy^* at the interaction points does not exceed 0.1 times the rms beam spread σ, which for the high luminosity interaction point is 4.8 μm. We thus require the magnet movement be less than 0.1 μm in the 0.02 to 3 Hz range and 0.4 μm beyond 3 Hz in the absence of feedback control. These values are summarized in Table 4.4-7 [4.4-15].

A feedback system can be used to assure beam collisions. A magnetic bump located at a position with $\beta = 4000$ m near an interaction region quadrupole can be used for this purpose. A bandwidth of a few tens of hertz and a strength of 100 gauss-meters would be sufficient. Such a feedback system is also useful for damping noise from power supply ripple. The signal for the feedback can be derived from a luminosity monitor using the Jöstlein technique [4.4-16], as is discussed in Sections 5.8.4 and 5.11.8. The technique is effective for frequencies lower than about 20 Hz. Assuming the feedback system is capable of

suppressing the effect of noise by a factor of 10 below 20 Hz and ineffective above 20 Hz, the tolerable magnet motion is given in Table 4.4-7. These specifications can be met by paying appropriate attention to siting, control of man-made noise and design of magnet supports. The compromises necessary among site and technical parameters are not studied here.

Table 4.4-7
Estimate of magnet motion tolerances [4.4-15]

Frequency	Without Feedback	With Feedback
0.02 Hz $< f <$ 3 Hz	0.1 μm	1 μm
3 Hz $< f <$ 20 Hz	0.4	4
20 Hz $< f$	0.4	0.4

Longitudinal motion and rolling motion of the dipole magnets also cause beam separation. The effect is found to be small. Uncorrelated motion of the interaction region quadrupoles, which is unlikely for the strong triplet quadrupoles, has an effect comparable to that due to the arc quadrupoles. The tune shift is about 4×10^{-7} per μm of orbit distortion [4.4-15], which is very small.

Quadrupole displacements also cause changes in path length, which drive synchrotron motion of the beams. Since the synchrotron frequency is about 7 Hz during storage, the beam follows adiabatically only the lowest frequency components of the ground motion. However, even assuming the ground motion is correlated so as to maximize the path length modulation, the resulting modulation on the rf phase is only 10^{-3} degrees per 1 μm of magnet motion. Such a phase oscillation is easily controlled by the phase lock system for rf magnet noise feedback discussed next.

4.4.10 Noise in the Radio-frequency System

The rf voltage and phase need to be locked to constant values. In case these parameters contain noise, the beam particles will diffuse in longitudinal phase space, leading to emittance growth and eventually particle loss. Particle loss due to rf phase noise has been observed in the Sp$\bar{p}$S and was cured by a phase feedback system [4.4-17]. In order to avoid excessive particle loss due to rf noise, it was found in the Sp$\bar{p}$S that the bunch area $\pi\epsilon_E\epsilon_t$ in synchrotron phase space should not be larger than about 1/18 of the bucket area. The ratio planned in the SSC conceptual design is 1/15.5 (see Section 4.6.3). In the following, we provide the noise tolerance specifications and discuss the necessary feedback systems.

The rf voltage can be written as

$$V = V_{rf}\,(1 + a)\,\sin(\psi + \phi), \tag{4.4-19}$$

where a and ϕ are noise in the relative voltage and phase, respectively. The phase noise

drives the synchrotron dipole motion of a bunch while the amplitude noise drives the quadrupole motion. The strength of the noise is specified by the phase and amplitude noise power spectra $P_\phi(f)$ and $P_a(f)$. The bunch motion is especially sensitive to the phase noise power at frequencies $nf_0 + f_s$ and the amplitude noise power at $nf_0 + 2f_s$, where f_0 and f_s are the revolution and synchrotron frequencies. The quantities of interest are

$$S_\phi = \sum_{n=-\infty}^{\infty} P_\phi (nf_0 + f_s) \quad \text{and} \quad S_a = \sum_{n=-\infty}^{\infty} P_a (nf_0 + 2f_s) \tag{4.4-20}$$

Since the rf noise is sharply peaked around the carrier frequency $f_{rf} = hf_0$, where h is the harmonic number, the dominant terms in the summations come from $n = \pm h$. The units of S_ϕ and S_a are rad^2 Hz^{-1} and Hz^{-1}, respectively.

In the absence of a feedback system, a coherent dipole or quadrupole motion will eventually filament into incoherent motion, leading to an effective increase in the longitudinal emittance of the beam. Incoherent motion can also result from a noise spectrum at frequencies higher than that corresponding to the bunch length. Defining X to be the longitudinal emittance, related to the rms bunch longitudinal spread through $X = (2\pi\sigma_z/\lambda_{rf})^2$, the diffusion effect can be described by [4.4-18, 4.4-19]

$$dX/dt = 2\pi^2 f_s^2 (S_\phi + X S_a) \tag{4.4-21}$$

The noise tolerance in the absence of feedback is set by requiring the initial emittance doubling time be longer than 50 hours at 20 TeV. Using $f_s = 7$ Hz, $\sigma_z = 7$ cm and $\lambda_{rf} = 0.8$ m, one finds $X = 0.30$ and the specifications $S_\phi < 1.7 \times 10^{-9}$ rad^2 Hz^{-1} and $S_a < 6 \times 10^{-9}$ Hz^{-1}.

With the low synchrotron frequency of the SSC, these rf noise tolerances are not easily achieved. Feedback systems are therefore necessary. The possibility of using a superconducting rf cavity that has a frequency band width much less than the synchrotron frequency has not been studied in this conceptual design. With a phase loop feedback, it is the noise in the loop that determines the bunch diffusion. Let the noise power of the phase feedback loop at f_s be P_u, the diffusion due to phase noise is given by making the replacement $f_s^2 S_\phi \rightarrow m(\delta f_s)^2 P_u$ in Eq. (4.4-21), where δf_s is the synchrotron frequency spread caused by the nonlinearity of the rf bucket [4.4-18]. The factor m, the number of f_0 sidebands covered in the rf bandwidth, is present because the P_u noise is not sharply peaked around hf_0 (as is P_ϕ). With $f_{rf} = 375$ MHz, $Q_{rf} = 4.3 \times 10^4$ and $f_0 = 3.6$ kHz, we have $m = 2.3$.

In a perfectly linear bucket without filamentation, there will be no diffusion when a feedback system is turned on. This is reflected by the fact that the diffusion disappears when $\delta f_s = 0$. For a sinusoidal bucket of the SSC, $\delta f_s = f_s X/8$. An initial emittance doubling time of more than 50 hours gives the tolerance $P_u < 0.6 \times 10^{-6}$ rad^2/Hz. Such a tolerance is within the capability of current technology [4.4-20].

In the presence of phase feedback noise, it is possible to reduce the noise diffusion by linearizing the bucket using a higher harmonic rf cavity. The disadvantage is that it reduces the Landau damping that is useful for counteracting the longitudinal collective instabilities. This possibility has not been studied in this conceptual design.

4.5 Beam Current Limitations

This section deals with effects that are important only for high intensity beams. The most pronounced examples of such effects are the various collective instabilities that occur as the beam distribution executes coherent oscillations.

The SSC beam intensity per bunch is relatively low in order to maintain a small average number of collisions per bunch crossing. The single bunch instabilities typically encountered in bunched beam storage rings are therefore not serious in the SSC. On the other hand, with a relatively small number of particles per bunch, a large number of bunches are needed to maintain the high luminosity. Potentially, multi-bunch instabilities are of much greater significance. In particular, feedback systems are required to damp the transverse and longitudinal bunch-to-bunch dipole motions.

There are several other collective or current-dependent effects to consider. One example is the space charge effect that causes a tune shift in single-particle betatron motion. Another is the parasitic beam energy loss that heats up the vacuum chamber, some of which occurs at liquid helium temperature and thus contributes to the cryogenic load. Coulomb scattering of particles in a bunch is still another example. It causes emittance growths (intrabeam scattering) and particle losses (the Touschek effect). Still one more important example discussed in this section is the beam-beam effect.

In Section 4.5.1 the space-charge tune shift of single-particle motion is calculated. Coherent instabilities and the parasitic energy loss, on the other hand, are described in terms of the impedances of the storage ring. An estimate of the various longitudinal and transverse impedances for the SSC is given in Section 4.5.2. From the estimated longitudinal impedance, parasitic heating in the SSC vacuum chamber environment is calculated in Section 4.5.3. The longitudinal and transverse instabilities are discussed in Sections 4.5.4 and 4.5.5, while intrabeam scattering and Touschek effects are treated in Section 4.5.6.

One of the beam-beam interaction effects important for the SSC is that of the synchro-betatron resonances driven by beams crossing at an angle. Section 4.5.7 is devoted to this particular issue.

Other beam-beam effects can be categorized either by whether they result from head-on or long-range encounters, or whether they involve coherent or single-particle motion. The first categorization is adopted in this report; the head-on and long-range beam-beam effects are thus discussed separately in Sections 4.5.8 and 4.5.9. As is shown there, the beam-beam effects are not serious in the SSC for two reasons: (a) the total head-on tune shift for four interaction regions is only 0.0034 and (b) the long-range interaction is mainly a linear perturbation for particles with modest betatron amplitudes and thus is not potentially as damaging as its head-on counterpart.

4.5.1 Space Charge Tune Shift

The space-charge tune shift does not involve coherent beam motion. In calculating it, the beam distribution as a whole is assumed to be static in time. The electromagnetic field carried by the beam, including the modification caused by the vacuum chamber environment, perturbs single particle motion without causing the overall beam distribution to oscillate in time. This effect is characterized by the single-particle incoherent tune shift

$$\Delta\nu = -N_B M \beta r_p F/(2\pi a^2 \gamma^3 B_f) \tag{4.5-1}$$

where N_B is the number of particles per bunch, M is the number of bunches per beam, β is the average beta function of the storage ring, r_p is the classical radius of the proton, and a is the transverse beam radius (taken to be its rms spread value). The form factor F and the filling factor B_f are given by [4.5-1]

$$F \approx 1 + 2B_f(\gamma a x_{co}/b^2)^2 \quad \text{and} \quad B_f = \sqrt{2\pi}\sigma_z/S_B \tag{4.5-2}$$

with x_{co} the beam closed orbit deviation from the pipe center, b the vacuum chamber radius, σ_z the rms longitudinal spread of a bunch, and S_B the spacing between bunches. We have ignored the effect of a magnetic image current in the above expressions, since the iron in the magnets is sufficiently far from the beam.

Taking the numerical values of $N_B = 7.3 \times 10^9$, $M = 17280$, $\beta = 220$ m, $S_B = 4.8$ m, $\sigma_z = 7$ cm, $b = 1.65$ cm, $x_{co} = 1$ mm and a normalized emittance of 1 μm, we obtain a tune shift of -0.9×10^{-3} at 1 TeV and -1.0×10^{-5} at 20 TeV. Since this tune shift is experienced only by particles with small betatron amplitudes, it represents a tune spread across the beam distribution. Its magnitude is small and considerably less than that caused by beam-beam interactions.

4.5.2 Impedance Estimates

The interaction between the beam and its vacuum chamber environment can be described in terms of two frequency dependent quantities, the transverse impedance $Z_\perp(\omega)$ and the longitudinal impedance $Z_\parallel(\omega)$. A relativistic particle moving in the vacuum chamber leaves behind it an electromagnetic wake field that influences the motion of the following particles. The electromagnetic force associated with the wake field can be decomposed into longitudinal and transverse components. The longitudinal and transverse impedances are related to the Fourier transforms of the wake force components in the frequency domain. The units of $Z_\parallel$ are ohms. Since the transverse wake force is given for unit transverse beam displacement (the transverse wake force vanishes when the beam is centered), the units of $Z_\perp$ are ohms/meter.

The longitudinal and transverse impedances can be defined explicitly in the following way. Consider a beam current of a given frequency, $I(z,t) = I_0\, e^{i(kz-\omega t)}$. This current generates a longitudinal retarding wake field $E_z(z,t)$. The voltage $V(z,t) = -E_z(z,t)\,L$ across an accelerator section of length L is related to the beam current through $V(z,t) = I(z,t)Z_\parallel(\omega)$. If the beam current is displaced from the center of the beam pipe by $\mathbf{x}$, the transverse deflecting wake field gives rise to a perpendicular force $\mathbf{F}_\perp(z,t) = e(\mathbf{E} + \mathbf{v} \times \mathbf{B})_\perp = ieI(z,t)Z_\perp(\omega)\mathbf{x}/L$. It should be noted that the convention for the imaginary parts of impedances is the physicist's (going with $e^{-i\omega t}$). Equations are, however, in SI units.

There are very many different wake fields seen by the beams as they circulate, because of the presence of rf cavities, beam instrumentation, etc. For the coherent motion, it is the sum of the impedances, weighted by the beta function in the transverse case, around the ring that governs the motion and the instabilities. To assure beam stability, it is necessary to limit the total impedance to be below a certain threshold value.

The impedances are complex quantities, whose real and imaginary parts have different effects on beam motion. The parasitic energy loss is determined by the real part of $Z_{\|}$. The real parts of the impedances also give the instability growth rates. The imaginary parts are associated with frequency shifts of the coherent oscillation modes. The imaginary part of the longitudinal impedance also causes distortion of the rf bucket and consequently bunch shape distortion.

A smooth, infinitely conducting pipe does not perturb particle motion other than a space charge contribution. The impedance therefore comes mainly either from discontinuities in the vacuum chamber pipe or from finite resistivity on the pipe wall. For the SSC, the total impedance can be broken down into contributions from the following elements:

(a) rf cavities
(b) resistive wall of the vacuum chamber
(c) space charge
(d) bellows
(e) beam collimators
(f) beam position monitor pick-ups
(g) beam injection and abort kickers
(h) coherent synchrotron radiation

These impedance contributions are separately discussed and estimated below.

RF Cavities

In the present design, the SSC rf system consists of eight five-cell 374.7 MHz structures, similar to that of the PEP storage ring at SLAC (see Fig. 3.1-3). The rf cavity impedance consists mainly of sharp peaks at frequencies corresponding to cavity modes. Besides the accelerating mode at the fundamental frequency, there are a number of parasitic modes at higher frequencies up to the cut-off frequency of about 2.9 GHz determined by a pipe radius of 5 cm at the rf cavity noses. These narrow impedance peaks correspond to wake fields that ring in the cavity for a large number of rf oscillations, causing a bunch to interact with other bunches, and, if the beam intensity is large enough, leading to coupled-bunch instabilities.

Each longitudinal parasitic mode of the rf cavity contributes a resonant impedance of the form

$$Z_{\|}(\omega) = \frac{R_s}{1 - iQ[(\omega_R/\omega) - (\omega/\omega_R)]} \tag{4.5-3}$$

where R_s, Q and $f_R = \omega_R/2\pi$ are the shunt impedance, the quality factor and the resonant frequency of the mode. Each mode is described by its own set of values for R_s, Q and ω_R. Similarly, each transverse parasitic mode of the cavity contributes an impedance

$$Z_{\perp}(\omega) = \frac{R_t(\omega_R/\omega)}{1 - iQ[(\omega_R/\omega) - (\omega/\omega_R)]} \quad . \tag{4.5-4}$$

The PEP cavity cell provides a typical example of the mode structure for the rf system to be used for the SSC. Its shape and dimensions are shown in Fig. 4.5-1 [4.5-2]. The parasitic mode parameters were computed using the program URMEL [4.5-3]. Table 4.5-1

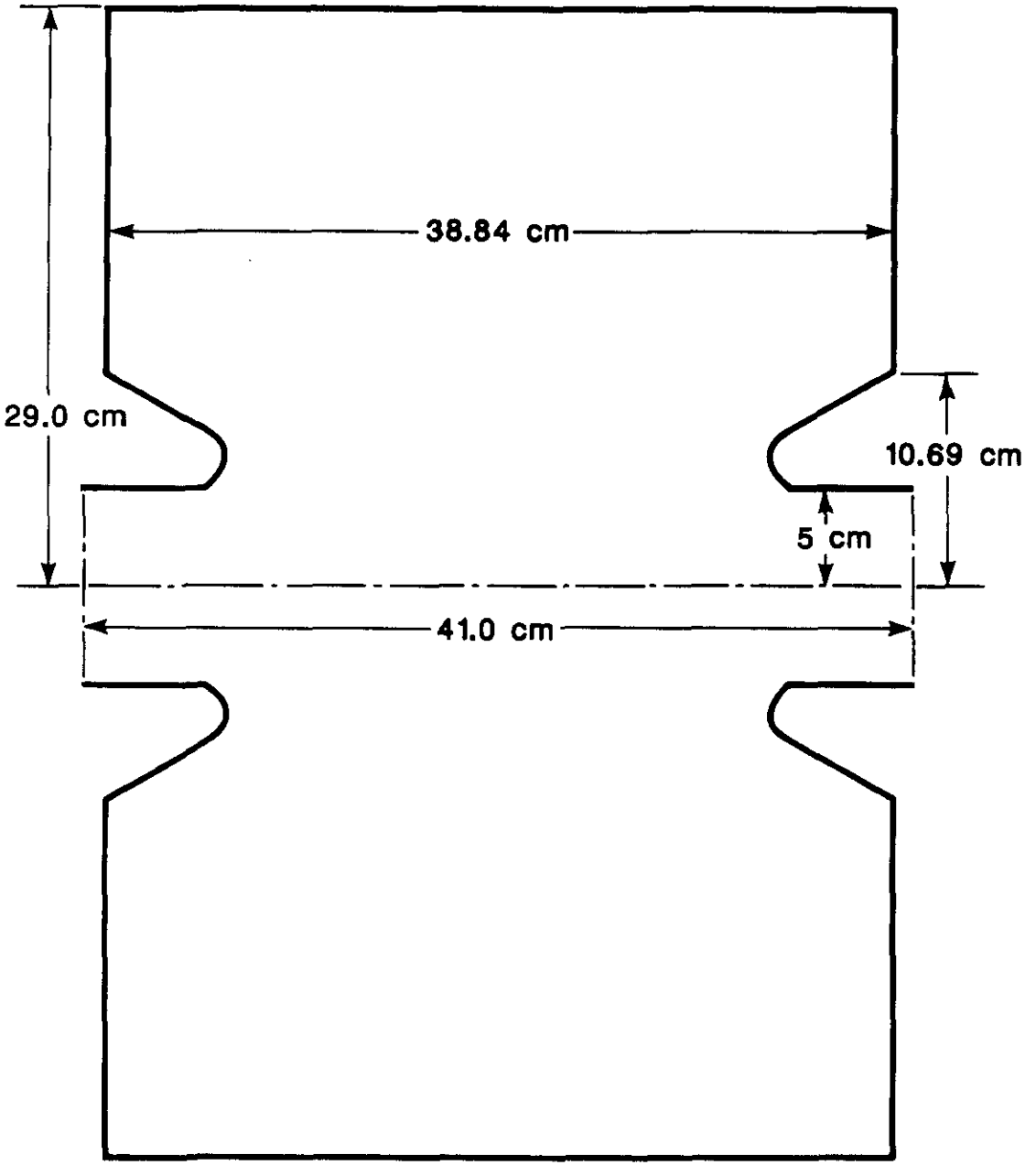

Figure 4.5-1. Plan view and dimensions of the cylindrical PEP rf cavity cell with fundamental accelerating frequency 358.8 MHz.

gives the properties of some prominent longitudinal and transverse modes up to the cut-off frequency. Note that the cut-off at 2.9 GHz implies that there is a smooth transition of pipe dimension from 1.65 cm radius in the normal arc to 5 cm radius in the rf section. The values of R_s and R_t in Table 4.5-1 are for a single rf cell. There are 40 rf cells in the SSC for each ring. If all cells are identical, the total impedances will have R_s and R_t 40 times the values tabulated. However, due to cavity construction errors and temperature variations, the resonance frequencies will differ slightly among the cavity cells, effectively broadening each resonance peak. When calculating the instability effects caused by the rf cavity impedance, it is necessary to know the exact values of the mode frequencies of each individual cell, or to perform a statistical calculation by taking several ensembles of frequency distributions. A crude estimate of the average value of the instability growth rates can be obtained by decreasing the quality factors to represent the spread of resonant frequencies. In the parasitic heating and instability described below, the impedance of 40 cells is obtained from Table 4.5-1 with Q values that are 20 times smaller and R_s and R_t that are 2 times larger than the tabulated values.

Table 4.5-1
Prominent Longitudinal and Transverse Modes for a PEP rf Cavity Cell [4.5-1]

Longitudinal			
Mode	f_R (MHz)	R_s (M Ω)	Q
1	358.9	11.84	42.9×10^3
2	507.2	2.03	36.5
4	883.4	0.532	54.5
5	926.1	1.482	35.8
6	1167.1	0.622	50.6
8	1440.1	0.434	91.5
9	1447.4	0.555	60.7
16	2065	0.794	71.5
Transverse			
Mode	f_R(MHz)	R_t (MΩ/m)	Q
1	506.0	1.57	47.1×10^3
2	633.8	1.81	62.7
3	774.4	17.32	48.5
5	967.4	2.30	98.4
7	1091	5.78	62.8
8	1094	12.28	41.5
10	1243	2.50	59.3
11	1367	13.37	67.3
16	1606	3.41	62.8
18	1697	6.71	63.5

Resistive Wall of Vacuum Chamber

The vacuum chamber can be made of stainless steel or aluminum. When a stainless steel pipe is used, as is discussed below, it is necessary to coat the inside with a thin layer of high conductivity material (e.g., copper). This reduces the resistive wall impedance and in particular the parasitic heating. It also shields the beam from any possible high frequency variations in external magnetic fields. If the thickness of the coating is comparable to or larger than its skin depth, the resistive wall impedances are given by

$$Z_{\parallel}(\omega) = (1 - \mathrm{i})R/(b\sigma_1\delta_1) \tag{4.5-5}$$

and

$$Z_{\perp}(\omega) = (2c/\omega b^2)\, Z_{\parallel}(\omega) \tag{4.5-6}$$

where R is the circumference of the ring divided by 2π, σ_1 is the conductivity and $\delta_1 = (2/\mu_0\sigma_1\omega)^{1/2}$ the skin depth of the high conductivity layer.

The conductivity of copper or aluminum at liquid helium temperature is higher than that at room temperature by a large factor, the residual resistance ratio (RRR). For laboratory samples of pure copper, RRR can be 10^4 or higher. Preliminary measurements of RRR of a copper-coated vacuum chamber in a high magnetic field give an RRR of about 30 to 300. In this report, as in the Reference Design Study, we take RRR = 30 for copper at 4 K and 6.6 T [4.5-4], yielding a conductivity of $\sigma_1 = 1.8 \times 10^9\ (\Omega\text{-m})^{-1}$. The conductivity of stainless steel at 4 K is $\sigma_2 = 2.0 \times 10^6\ (\Omega\text{-m})^{-1}$.

For a two-layer beam pipe, when ω is low enough that the thickness of the high-conductivity layer is smaller than its skin depth, the impedances are modified by a multiplicative factor [4.5-5]

$$\zeta = [1 + (\sigma_2/\sigma_1)^{1/2} Z_1 Z_2]/[Z_1 + (\sigma_2/\sigma_1)^{1/2}\, Z_2] \tag{4.5-7}$$

where

$$Z_k = \{1 - \exp[-2(1 - \mathrm{i})\, t_k/\delta_k]\}/\{1 + \exp[-2(1 - \mathrm{i})t_k/\delta_k]\}$$

with t_k the thickness of the kth layer and $k = 1,2$ for the copper and stainless steel, respectively. For high frequencies with $t_1 \gg \delta_1$, the modifying factor is $\zeta = 1$.

The lowest frequency of interest is $(\nu\text{-}n)$ times the revolution frequency $\omega_0 = 2.27 \times 10^4\ \mathrm{s}^{-1}$, where n is the nearest integer to the betatron tune ν. Without much constraint on the tune choice, we take $\nu\text{-}n$ to be 0.1, for which the cold copper and stainless steel skin depths are 0.63 mm and 19 mm, respectively. The present pipe design has $t_1 = 0.1$ mm (4 mils) and $t_2 = 1$ mm. Figure 4.5-2 shows the transverse and longitudinal resistive wall impedances given by Eqs.(4.5-5) to (4.5-7). The copper layer thickness corresponds to a shielding frequency (where $t = \delta$) of $\omega/2\pi = 14$ kHz. Above 14 kHz, the impedance is basically determined by the copper layer, while below it, the impedance is influenced by the stainless steel.

Note that the copper coating is needed to prevent excessive parasitic heating, as is discussed in Section 4.5.3. Note also that a thin copper coating is preferred in order to

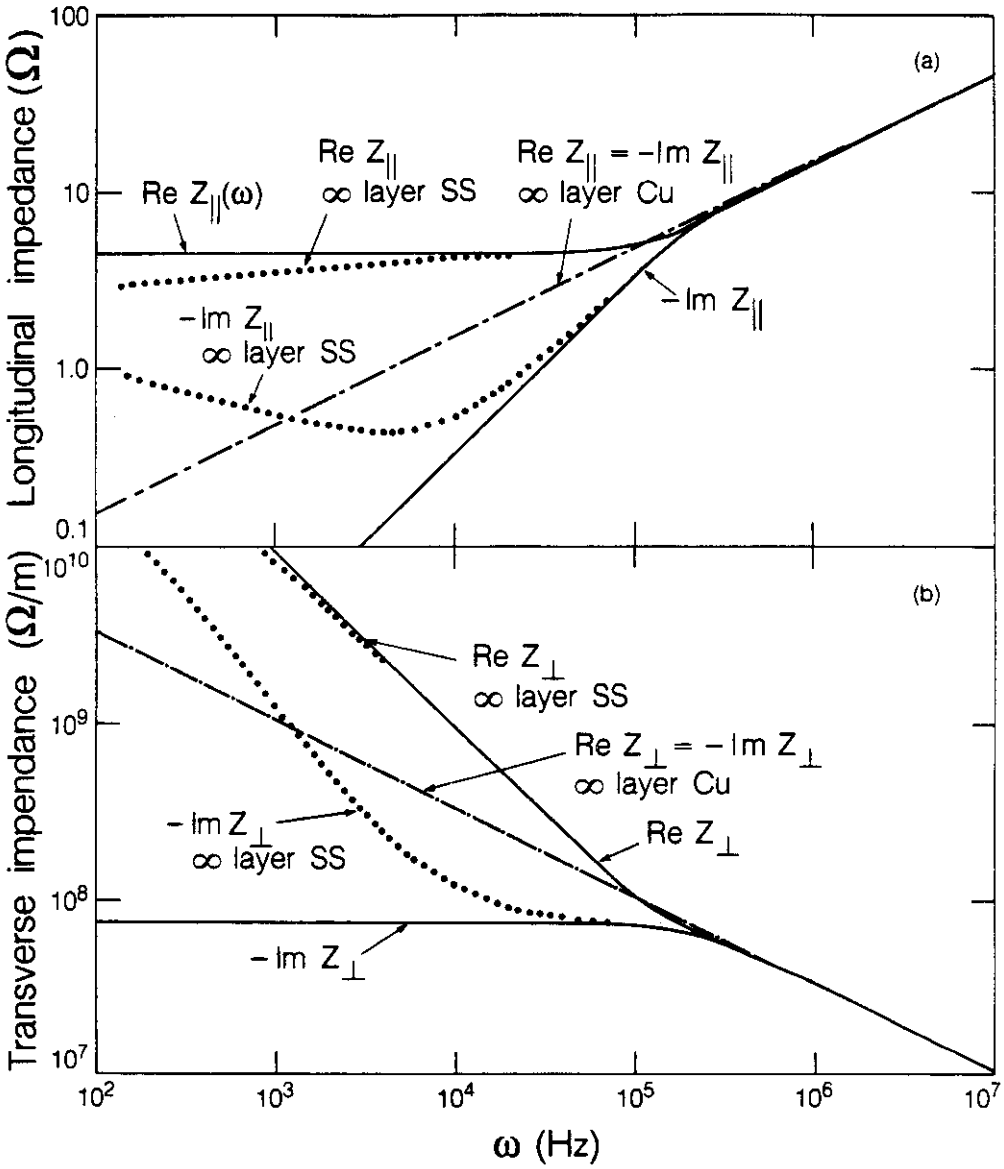

Figure 4.5-2. The solid curves are the SSC resistive wall impedance with t_1 = 0.1 mm, t_2 = 1 mm, $\sigma_1 = 1.8 \times 10^9$ $(\Omega\text{-m})^{-1}$ and $\sigma_2 = 2.0 \times 10^6$ $(\Omega\text{-m})^{-1}$. (a) real and imaginary parts of $Z_{||}$. (b) real and imaginary parts of $Z_{\perp}$. For comparison, the dotted (dashed) curves are for the stainless steel (copper) layer infinitely thick. The differences between the dotted, the dashed and the solid curves are significant only at the lowest frequencies.

minimize the eddy current effects during a magnet quench. More discussion on eddy current effects can be found in Section 4.6.1.

Space Charge

To analyze the collective space charge effects, we assume a perfectly conducting pipe wall with radius b and a round beam of radius a. The low frequency ($\omega \ll \gamma c/b$) longitudinal impedance is

$$Z_{\|}(\omega) = \frac{i\omega R}{2c} \cdot \frac{Z_0}{\gamma^2} [1 + 2 \ln(b/a)] \tag{4.5-8}$$

where the factor of γ^2 in the denominator comes from the cancellation between the electric and the magnetic forces. To understand the phase and frequency dependence we note that the longitudinal wake field is local and is proportional to $d\lambda(s)/ds$, where s is the position coordinate around the ring and $\lambda(s)$ is the longitudinal line density of electric charge. The impedance, given by the Fourier transform of the wake force, is then linearly proportional to $ik = i\omega/c$.

In dealing with the longitudinal coherent instabilities, it is often convenient to express the longitudinal impedance by dividing $Z_{\|}$ by n, where $n = \omega/\omega_0 = \omega R/c$. For SSC space charge, taking a to be the rms beam size in the arcs, we have $Z_{\|}/n = i\ 1.4 \times 10^{-3}\ \Omega$ at 1 TeV and $i\ 0.46 \times 10^{-5}\ \Omega$ at 20 TeV.

The space charge transverse impedance for low frequencies is

$$Z_{\perp}(\omega) = i(Z_0 R/\gamma^2)[a^{-2} - b^{-2}] \tag{4.5-9}$$

The values are $Z_{\perp} = i\ 21\ M\Omega/m$ at 1 TeV and $i\ 1.1\ M\Omega/m$ at 20 TeV.

Bellows

Sections of the vacuum chamber are mechanically joined by bellows. During cool down, the bellows absorb the length change from thermal contraction. For a stainless steel pipe with an expansion coefficient of 1.3×10^{-5}/C, a temperature variation of 316 C and 31% compressibility for the bellows, the bellows occupy 1.3% of the 76 km cold length around the storage ring circumference, or about 1 km [4.5-6]. Bellows are the largest contributors to the impedance that causes the transverse single-bunch instability. If unshielded, they will restrict the beam intensity below the desired value. We consider two ways to shield them, either by an inner bellows of the type used in PEP or by a sliding contact.

The bellows wake fields are obtained using the time-domain code TBCI [4.5-7]. The impedances are calculated by fast Fourier transforms. For shielding inner bellows, the pipe geometry is sketched in Fig. 4.5-3(a). The impedances per inner bellows corrugation have been calculated for several sets of dimensions [4.5-8]. One example with $b = 1.65$ cm, $p = 2.2$ mm and $\Delta = 3.5$ mm is shown in Fig. 4.5-3(b) and (c). The impedances resemble the resonant impedances of the form (4.5-3) and (4.5-4). The longitudinal impedance shown in Fig. 4.5-3(b) can be approximated by two resonant contributions with $R_s = 13.5\ \Omega$, and $3.5\ \Omega$ at frequencies $f_R = \omega_R/2\pi = 12.3$ GHz and 49 GHz, and with quality factors of $Q = 4$ and 20, respectively. The 49 GHz peak is not very significant as far as parasitic heating is concerned since the bunch has an rms length of $\sigma_z = 7$ cm, corresponding to a spectrum

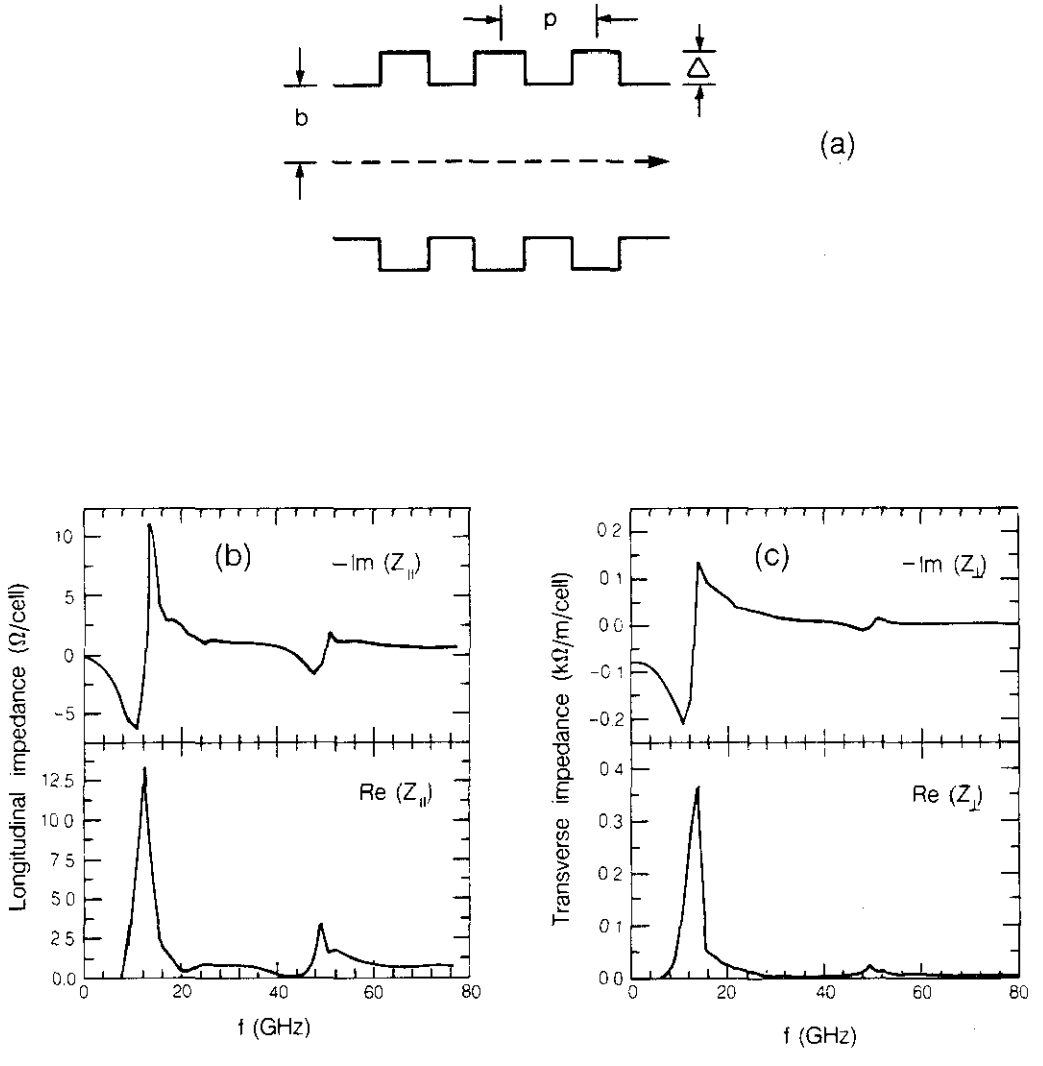

Figure 4.5-3. (a) Model of inner bellows geometry used in impedance estimates. (b) Longitudinal and (c) transverse impedance per inner bellows corrugation for b = 1.65 cm, p = 2.2 mm and Δ = 3.5 mm.

that extends to about $f = c/2\pi\sigma_z = 0.7$ GHz. The impedance at low frequencies estimated from the two resonant contributions is purely capacitive with $Z_{\|} = i0.31f(\text{GHz})\Omega$, which agrees with Fig. 4.5-3(b).

The transverse impedance per corrugation shown in Fig. 4.5-3(c) consists of two resonant contributions with $R_t = 370\ \Omega/\text{m}$ and $27\ \Omega/\text{m}$ at $f_R = 13.5$ GHz and 50 GHz with $Q = 5$ and 20, respectively. The impedance at low frequencies is $Z_{\perp} = i\ 79\ \Omega/\text{m}$, agreeing with that estimated for the resonators.

With 1 km total length and 2.2 mm per corrugation, there are 4.54×10^5 corrugations in total. As an order of magnitude estimate of the importance of the bellows impedance, we take the low frequency values to obtain $Z_{\|}/n = 0.50\ \Omega$ and $Z_{\perp} = 36\ \text{M}\Omega/\text{m}$ for the entire ring. Evaluated at the dominating impedance peaks, we obtain the more pessimistic values of $Z_{\|}/n = 1.8\ \Omega$ and $Z_{\perp} = 168\ \text{M}\Omega/\text{m}$.

A second bellows shielding method uses a sliding contact. The bellows geometry is sketched in Fig. 4.5-4(a) [4.5-9]. A gap is left between the two cylindrical shields to represent a possible mechanical defect. Its width has been exaggerated at $\Delta = 2$ mm. Each bellows package is assumed capable of absorbing a length contraction of 10 cm during cool down. There are 5000 such bellows packages in the entire ring, with a maximum contraction length of 500 m. Impedance calculations were performed using the program TBCI and neglecting the corrugations behind the shield. The results are shown in Fig. 4.5-4(b) and (c).

The longitudinal impedance from the bellows is similar to that of a cavity formed by closing the gap between the two shields. The gap contributes a nonzero impedance at $f = 0$, effectively because electromagnetic energy is leaking through the gap. In fact, the gap can be viewed as a coaxial transmission line of infinite length and inner and outer radii 1.7 and 1.9 mm [4.5-9]. Such a line has an impedance $(377\ \Omega/2\pi)\ln(1.9/1.7) = 6.7\ \Omega$, in agreement with Fig. 4.5-4(b). This impedance contributes at low frequencies to parasitic beam energy loss, as is discussed in Section 4.5.3.

The cavity formed by closing the gap between the two shields can be approximated by two resonators with $R_s = 20\ \Omega$ and $30\ \Omega$ at $f_R = 6.2$ GHz and 16 GHz and $Q = 6$ and 1, respectively. At low frequencies, the resonator part of the impedance gives $Z_{\|} = i2.4f(\text{GHz})$ ohms, agreeing with Fig. 4.5-4(b). The impedance is insensitive to the choice of $g = 10$ cm. The transverse impedance shows structure with several resonances, the first of which occurs at 2.8 GHz with $R_t = 1.9\ \text{k}\Omega/\text{m}$ and $Q = 3.5$. At low frequencies, the impedance is approximately $Z_{\perp} = i1.4\ \text{k}\Omega/\text{m}$.

With 5000 bellows packages, the total impedances at low frequencies are $\text{Re}(Z_{\|}) = 34\ \text{k}\Omega$, $\text{Im}(Z_{\|}/n) = 0.043\ \Omega$ and $Z_{\perp} = i\ 7\ \text{M}\Omega/\text{m}$. Except for the parasitic energy loss consideration, the impedance of the sliding contacts is an order of magnitude less than that of the inner bellows. With care taken to limit the gap ($\Delta < 0.1$ mm), the sliding contacts are acceptable for the conceptual design.

Beam Collimators

To protect the superconducting quadrupoles from the spray of secondary particles from collisions at the interaction points, a collimator is inserted along the beam line before the first triplet quadrupole. To model its geometry, we assume a circular collimator with an aperture radius of 0.55 cm in an otherwise 1.65 cm radius pipe. The collimator length is taken to be 1 meter. TBCI was used to calculate the wake fields and the impedances

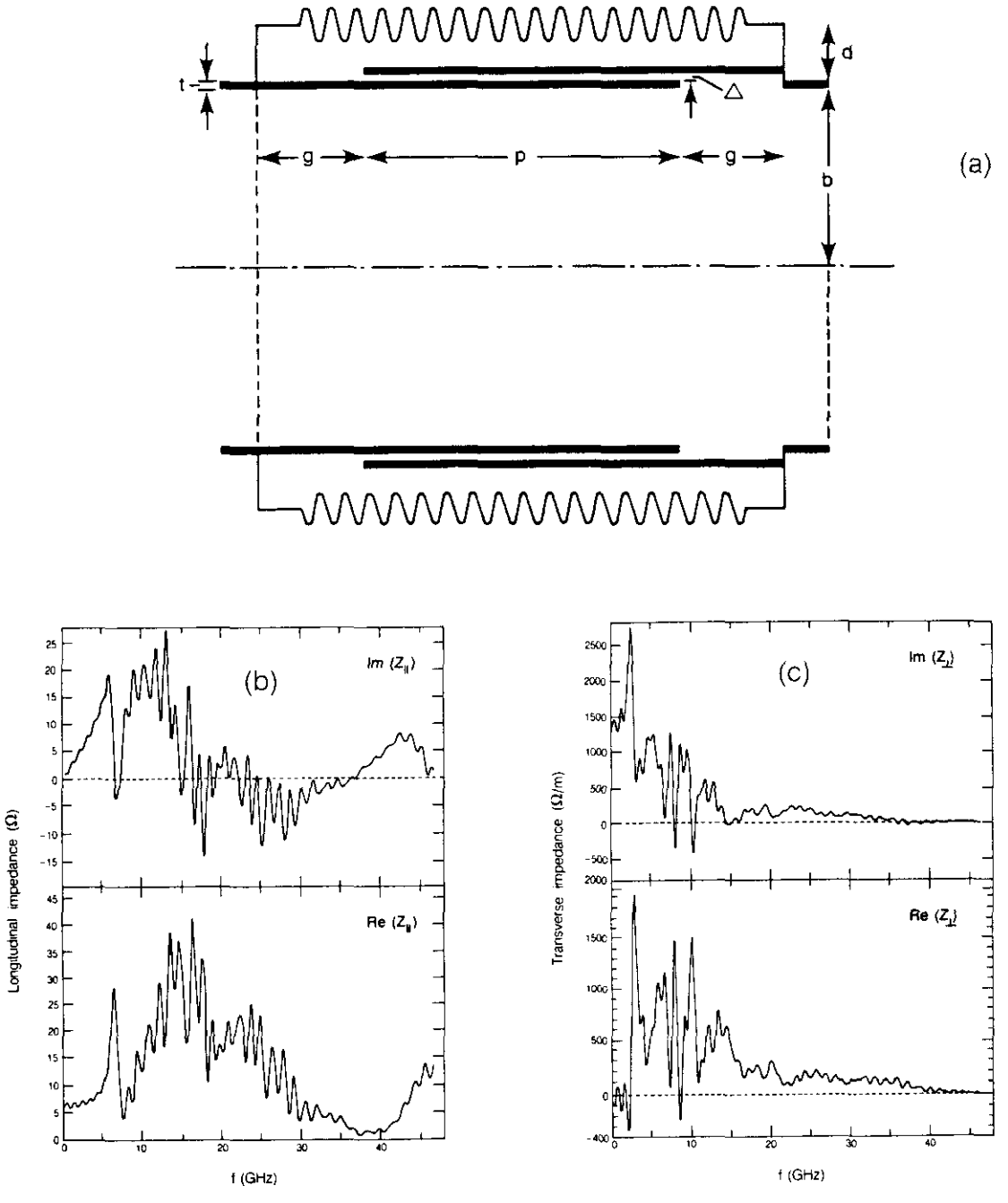

Figure 4.5-4. (a) The bellows geometry with sliding contact shielding in the expanded position. Parameters used for impedance calculations are b = 1.5 cm, g = 10 cm, d = 5 mm, p = 30 cm, shield thickness t = 2 mm, gap between shields Δ = 2 mm. (b) Longitudinal and (c) Transverse impedance per bellows package.

[4.5-11]. It was found that, for our purposes, the collimator-generated wake can be regarded as local. The impedances per collimator are given by

$$Z_{\parallel}(\omega) = -\mathrm{i}\,13.2\,f(\mathrm{GHz})\ \Omega$$

$$Z_{\perp}(\omega) = -\mathrm{i}\,12.5\ \mathrm{k}\Omega/\mathrm{m} \tag{4.5-10}$$

With 8 collimators in the ring, the total impedances are $Z_{\parallel}/n = -i\,3.7 \times 10^{-4}\ \Omega$ and $Z_{\perp} = -i\,0.10$ MΩ/m. These values are small compared with the bellows and the space charge impedances. This is true even when the fact that the collimators are located at positions with relatively high beta functions is taken into account. The collimator impedances are neglected in the subsequent discussions.

Beam Position Monitors

A beam position monitor is provided at each quadrupole to measure the horizontal and vertical beam positions. We consider stripline beam position monitors as described in Section 5.12. Each monitor is $d = 20$ cm long and consists of four strip electrodes, each subtending $\phi = 55$ degrees in azimuth. The impedances per monitor at low frequencies are given by [4.5-12]

$$Z_{\parallel}(\omega) = -\mathrm{i}(\phi/\pi)^2\, Z_s \omega d/c \tag{4.5-11}$$

$$Z_{\perp}(\omega) = -\mathrm{i}Z_s d[4\,\sin(\phi/2)/\pi b]^2$$

where $Z_s = 50\ \Omega$ is the characteristic impedance of the stripline, and $b = 1.65$ cm is the radial position of the striplines. With 850 monitors in each ring, the impedances above give $Z_{\parallel}/n = -i\,0.06\ \Omega$ and $Z_{\perp} = -\mathrm{i}11$ MΩ/m. Equation (4.5-11) is valid for frequencies lower than $\omega < \pi c/2d = 375$ MHz. The higher frequency behavior depends on details of the monitor design. In later calculations, we approximate the impedances of the beam position monitors by $Q = 1$ broad-band resonances with $f_R = 2.9$ GHz. The longitudinal and transverse peak values are taken to be $R_s = 0.050$ MΩ and $R_t = 11$ MΩ/m.

Injection and Abort Kickers

We consider injection and abort kickers as described in Sections 5.9 and 5.10. Calculations [4.5-13] were performed assuming no attempt is made to shield the beam from the kicker impedance. The injection kickers are ferrite with a single-turn design (Table 5.9-1 and Fig. 5.9-7) and the abort kickers are of a window-frame design with tape wound cores (Table 5.10-1).

The total impedances are shown in Figs. 4.5-5 and 4.5-6 for the injection and abort kickers, respectively [4.5-13]. We find that $Z_{\parallel}/n$ is about 0.09 Ω for the injection kickers and about $1.5 \times 10^{-3}\ \Omega$ for the abort kickers. The peak transverse impedances are 0.6 MΩ/m and 0.8 MΩ/m for the injection and abort kickers. These impedances are modest compared with other impedance sources. In later calculations, we approximate the total longitudinal impedance of both types of kickers by that of a single $Q = 1$ resonance with R_s

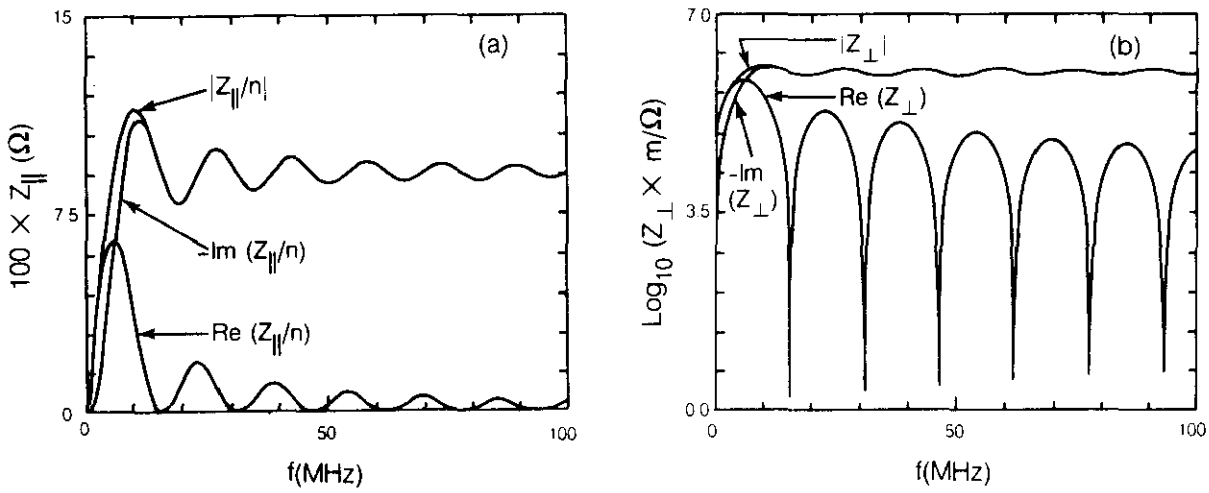

Figure 4.5-5. (a) Longitudinal and (b) transverse impedances of the injection kickers.

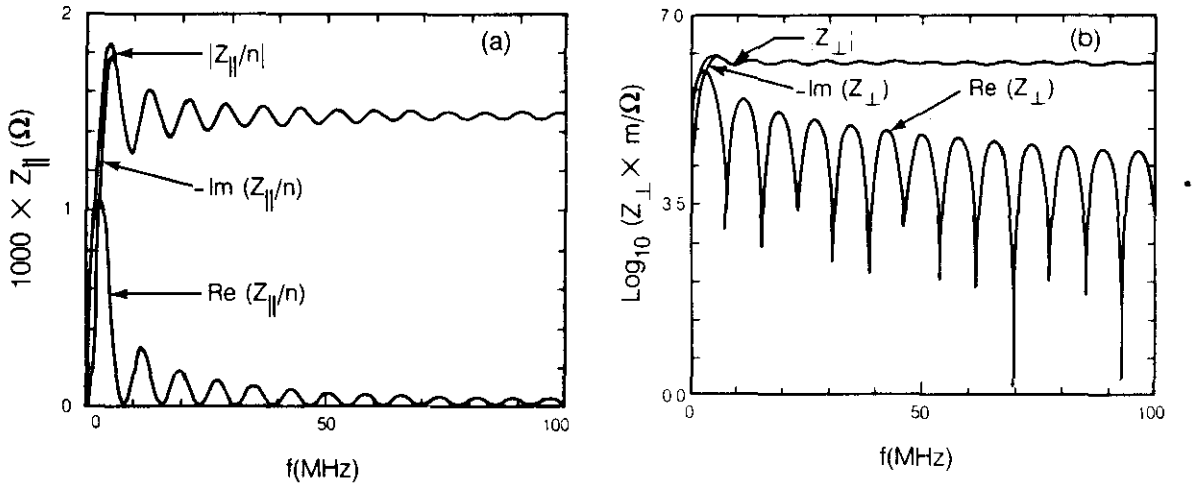

Figure 4.5-6. (a) Longitudinal and (b) transverse impedances of the abort kickers.

= 0.072 MΩ and f_R = 2.9 GHz. The total transverse impedance is approximated as a resonance with $Q = 1$, f_R = 2.9 GHz and R_t = 1.4 MΩ/m.

Coherent Synchrotron Radiation

Synchrotron radiation can be described in terms of an impedance

$$Z_{\|}(\omega) = (24)^{-1/3}\,\Gamma(2/3)(\omega/\omega_0)^{1/3}(\sqrt{3} - i)\,Z_0 \tag{4.5-12}$$

valid for frequencies far beyond the GHz range, up to the critical frequency $\omega_c = 3\gamma^3\omega_0/2$. Equation (4.5-12) fails at higher frequencies and also at frequencies below the cutoff of the beam pipe. Equation (4.5-12) can be used to treat the incoherent synchrotron radiation, but it is most useful in describing the coherent synchrotron radiation. The coherent radiation power is discussed in Section 4.5.3 as a special case of parasitic energy losses.

4.5.3 Parasitic Heating

As the beam circulates around in the vacuum chamber, it loses energy continuously because of the retarding longitudinal wake fields. This power loss from the beam is related to the real part of the longitudinal impedance by

$$P = (M\ N_B^2 e^2 \omega_0^2/2\pi^2) \sum_{p=0}^{\infty} \mathrm{Re}[Z_{\|}(p\omega_0)]\exp(-p^2\omega_0^2\sigma_z^2/c^2) \tag{4.5-13}$$

where M is the number of bunches per beam, N_B is the number of particles per bunch, ω_0 is the angular revolution frequency, p is the harmonic number index, and σ_z is the rms bunch longitudinal spread. For an impedance that does not contain sharp peaks, the summation over p can be replaced by an integral.

The parasitic losses from the beam heat the vacuum chamber pipe. Impedances that are located in the cryogenic environment are of particular concern since they contribute to the cryogenic load. The dependence of this cryogenic load on the bunch length, as shown in Fig. 4.6-4, has an impact on the choice of rf frequency, as is discussed in Section 4.6.3.

The space charge wake field does not cause parasitic energy losses. The parasitic energy loss due to the resistive wall can be approximated by taking the impedance (4.5-5) without taking into account the modification (4.5-7) from the stainless steel layer (relevant only at very low frequencies). Substitution of Eq. (4.5-5) into Eq. (4.5-13) gives the resistive wall contribution to parasitic heating,

$$P = \Gamma(3/4)\,M(N_B ec/2\pi)^2\,(Z_0/2\sigma)^{1/2}\sigma_z^{-3/2}\,b^{-1} \tag{4.5-14}$$

where $\sigma = 1.8 \times 10^9\ (\Omega\text{-m})^{-1}$ is the conductivity of the copper layer and $\Gamma(3/4) = 1.23$. Taking b = 1.65 cm, $N_B = 7.3 \times 10^9$, $M = 17280$, σ_z = 7 cm, we find P = 71 watts. With two rings operating, the total resistive wall heating load on the cryogenic system is 142 watts.

A copper coating is needed on a stainless steel pipe since otherwise the parasitic heating will be a factor of $(\sigma_1/\sigma_2)^{1/2}$ = 30 times larger, i.e., 4.3 kW for two beams. For an aluminum pipe with $\sigma = 2.2 \times 10^8\ (\Omega\text{-m})^{-1}$ without coating, the cryogenic load is 401 watts for

two beams. Furthermore, with a copper-coated stainless steel pipe, the heating will be 246 watts for two beams if the residual resistance ratio RRR is 10 instead of the assumed value of 30.

The longitudinal impedance is often approximated as a superposition of resonant contributions. Each resonant impedance (4.5-3) gives [4.5-14].

$$P = M(N_B ec)^2 \,\mathrm{Re}[z\ w(z)](4Q^2 - 1)^{-1/2} R_s/(2\pi\sigma_z R) \tag{4.5-15}$$

where $w(z)$ is the complex error function and $z = \sigma_z\omega_R[(4Q^2 - 1)^{1/2} + \mathrm{i}]/2Qc$. For relatively high-$Q$ resonances (e.g., rf cavity impedance), Eq. (4.5-15) reduces to

$$P \approx M(N_B e)^2(R_s/Q)(\omega_0\omega_R/4\pi)\exp(-\omega_R^2\sigma_z^2/c^2) \tag{4.5-16}$$

These expressions are used to compute the parasitic heating from the various resonant impedances discussed in the previous section. The rf cavities, the inner bellows, the sliding bellows (without gap), the beam position monitors and the kickers contribute parasitic heating of 270 W, 62 W, 16 W, 154 W and 220 W, respectively. Note that the fundamental accelerating mode has been excluded in the rf impedance and that Eq. (4.5-16) breaks down for superconducting rf cavities.

If sliding contacts are used for bellows shielding, and if there is a gap Δ between the shields due to mechanical error, as mentioned in the previous section, the gap allows electromagnetic field energy to leak through. Such gaps can be important contributors to parasitic heating [4.5-8]. The real part of the longitudinal impedance therefore contains an extra term at low frequencies,

$$\mathrm{Re}\ Z_\parallel = (Z_0/2\pi)\ln[(b + \Delta)/b] \approx (377\ \Omega/2\pi)(\Delta/b) \tag{4.5-17}$$

that is proportional to the gap size Δ and is independent of frequency. Substitution of Eq. (4.5-17) into (4.5-13) yields the parasitic loss per bellows as

$$P = M(N_B e)^2\omega_0\Delta c Z_0/(8\pi^{5/2}\sigma_z b) \tag{4.5-18}$$

Equation (4.5-18) can also be derived in the time domain by calculating the electromagnetic field energy scraped away by the gap. The extra heating predicted by Eq. (4.5-18) agrees well with the numerical results predicted by TBCI. We suggest a maximum tolerable gap size of 0.1 mm. The parasitic heating for 5000 bellows packages is then 190 W per beam. In the absence of the gap, the shielded bellows contribute only 0.6 W of heating per beam [4.5-10].

Beam energy loss from coherent synchrotron radiation can naively be obtained by substituting Eq. (4.5-12) into Eq. (4.5-13). If one integrates over all frequencies this gives the power as

$$P \approx 2.8 \times 10^{-2}\, M\, N_B^2 e^2 c^2 \rho^{-2/3}\sigma_z^{-4/3}(\rho/R)\, Z_0 \tag{4.5-19}$$

where ρ is the bending radius of the dipole magnets. Expression (4.5-19) is independent of the beam energy. Since the bunch frequency spectrum falls far short of the critical frequency of synchrotron radiation, use of Eq. (4.5-12) introduces little error at the high fre-

quency end. With ρ = 10.1 km, the coherent radiation power loss given by Eq. (4.5-19) is 1.3 kW per beam, which is not negligible. However, the low frequency cut-off of the vacuum chamber reduces the power to negligible values. If we approximate the chamber by two infinite conducting planes a distance b apart with the beam between, the radiation power has to be multiplied by a factor of the order of $b\rho^{-1/3}\sigma_z^{-2/3}$ [4.5-15], which is about 0.0045, leading to a radiation power of 6 watts.

Table 4.5-2 summarizes the parasitic heating due to various impedance sources. Excluding the rf cavities and the kickers that are located in room temperature sections, the others contribute a total of 0.9 kW of cryogenic load for two beams, assuming sliding contact bellows.

Table 4.5-2
Parasitic Heating of Various Impedance Sources

Impedance source	Power loss/beam (watts)
rf cavities	270
Resistive wall	71
Bellows	
– inner bellows	61
– sliding contact	16 + 190
Position monitors	154
Kickers	220
Coherent synchrotron radiation	6

4.5.4 Longitudinal Instabilities

A collective instability in the SSC can be categorized by whether it is transverse or longitudinal, or whether it involves a single bunch or multiple bunches. In this section, we discuss first the coupled-bunch longitudinal instabilities and then the single-bunch longitudinal effects .

Multi-bunch Effects

Two mode numbers are needed to describe a longitudinal coupled-bunch mode. For a beam consisting of M equal bunches, there are M coupled-bunch modes with mode number m = 0,1,...(M − 1). In addition, an index n is required to describe the motion of individual bunches in synchrotron phase space. For example, n = 1 means a dipole mode in which bunches move rigidly as they execute the longitudinal oscillations; n = 2 means a quadrupole mode in which bunch head and bunch tail oscillate longitudinally out of phase, etc.

In the unperturbed case, the frequency of mode (m,n) is $n\nu_s\omega_0$, where ν_s is the unperturbed synchrotron tune. The complex frequency shift of the mode (m,n) caused by longitudinal impedance $Z_\parallel(\omega)$ is [4.5-16]

$$\Delta\Omega^{(m,n)} = \mathrm{i}\left(\frac{n}{n+1}\right)\left(\frac{8\pi^2 N_B r_p c^2 \alpha}{3\gamma\sigma_z^3\nu_s Z_0}\right)\sum_p [Z_\parallel(\omega_p)/\omega_p]h_n(\omega_p)/\sum_p h_n(\omega_p) \qquad (4.5\text{-}20)$$

where α is the momentum compaction factor, $\omega_p = \omega_0 (pM + m + n\nu_s)$ and $h_n(\omega)$ are the mode spectra, depending on the unperturbed bunch length and shape. The summations are over p from $-\infty$ to ∞. Note that the longitudinal instability is driven not by the impedance $Z_{\|}$, like the parasitic heating, but by $Z_{\|}/\omega$, or equivalently by $Z_{\|}/n$. The real part of $\Delta\Omega$ gives the mode frequency shift; the imaginary part gives the instability growth rate.

In the SSC, the multi-bunch instabilities are driven mainly by the narrow-band rf cavity impedance. Table 4.5-3 lists the growth times for the most unstable longitudinal coupled-bunch modes driven by the rf cavity impedance [4.5-17]. These are calculated using the program ZAP [4.5-18] and assuming a parabolic bunch shape.

Table 4.5-3
Growth Times at 1 TeV and 20 TeV of the Most Unstable Longitudinal Coupled-Bunch Modes Caused by the rf Cavity Impedance

Mode Numbers		Growth Time (seconds)	Growth Time (seconds)
n	m	1 TeV	20 TeV
1	7382	0.63	4.2
	7381	0.63	4.2
2	6325	2.49	16.5
	6324	2.49	16.5

The collective instabilities are counteracted by Landau damping from the synchrotron frequency spread within the bunch caused by the nonlinearity of the rf bucket. Landau damping is obtained if the shifted mode frequency lies inside the frequency spread of the bunch. The modes listed in Table 4.5-3 are in fact all Landau damped, except for the $n = 1$ modes at 1 TeV.

Inclusion of the space charge, the resistive wall and the low-Q resonant impedances (bellows, monitors, and kickers) does not change the instability growth rates noticeably. Although the mode frequency shifts caused by the low-Q resonant impedances are much larger than those due to the rf cavity impedance, they are not large enough to change the Landau damping characteristics [4.5-17]. A feedback system, described in Section 5.8, is required to damp the $n = 1$ modes at 1 TeV.

Note that although $Z_{\|}/\omega$ for the resistive wall behaves like $\omega^{-1/2}$, it does not contribute as a narrow-band impedance at low frequencies as far as multi-bunch instability is concerned. This is because the $n = 1$ mode spectrum vanishes sufficiently rapidly at $\omega = 0$ to outweigh the divergence of the impedance. The same is not true for the resistive-wall transverse multi-bunch instabilities, as discussed in Section 4.5.5.

Single Bunch Effects

The low-Q resonant and space charge impedances contribute to single bunch coherent effects. The broad-band impedances excite wake fields that damp out rapidly before subsequent bunches arrive. Equation (4.5-20) for the complex frequency shift still applies, although it is easy to show that the result does not depend on the mode number m for broad-band impedances and Eq. (4.5-20) can be slightly simplified accordingly.

The space charge effects described by the impedances (4.5-8) and (4.5-9) are strictly local phenomena. The frequency shift from the longitudinal space charge impedance is therefore real and given by

$$\Delta\Omega^{(n)} = -[n/(n+1)][4\pi^2 N_B r_p cR\alpha/(3\gamma^3\sigma_z^3\nu_s)][1 + 2\ln(b/a)] \tag{4.5-21}$$

For the longitudinal dipole mode ($n = 1$), the coherent tune shift ($\Delta\Omega/\omega_0$) is found to be -6×10^{-6}. Since the mode frequency shifts are purely real, the space charge effect does not directly cause instability growth and, as already mentioned, the frequency shift does not affect the Landau damping characteristics of the multi-bunch instabilities.

The most pronounced longitudinal single-bunch instability is the microwave instability, also known as turbulent bunch lengthening [4.5-19]. For a given longitudinal broad-band impedance, microwave instability occurs when the peak beam current exceeds a certain threshold value. Beyond the threshold, the bunch lengthens turbulently with a growth time much shorter than the synchrotron period until the peak current is just below the threshold value. This longitudinal microwave instability threshold occurs when the impedance exceeds the value [4.5-8]

$$|Z_\parallel/n| = (\pi/2)^{1/2}\alpha\gamma\sigma_\delta^2\sigma_z Z_0/N_B r_p \tag{4.5-22}$$

The value of $Z_\parallel/n$ in Eq. (4.5-22) is the effective value averaged over the bunch spectrum, which extends to about 0.7 GHz for a 7 cm rms bunch longitudinal spread. Table 4.5-4 gives numerical values of the threshold impedances based on Eq. (4.5-22).

Another single-bunch longitudinal instability is the mode-coupling instability, which occurs when the coherent frequencies of two neighboring low-order modes shift to become equal. The degenerate modes are unstable with a growth time smaller than the synchrotron period near the threshold. Since the mode frequency shifts are related to the imaginary part of the impedance, the instability limit is given by a threshold value of $\mathrm{Im}(Z_\parallel/n)$, namely [4.5-8]

$$\mathrm{Im}(Z_\parallel/n) = 4\pi^{1/2}\alpha\gamma\sigma_\delta^2\,\sigma_z Z_0/N_B r_p \tag{4.5-23}$$

The numerical value of this threshold impedance is given in Table 4.5-4. The transverse thresholds are discussed in Section 4.5.5. With precautions in budgeting the impedances as described in the previous section, these thresholds are easily met. The longitudinal broad-band impedances also cause bunch shape distortion. For the SSC, this is a negligible effect.

Table 4.5-4
Impedance Thresholds for Microwave and Mode-Coupling Instabilities at 1 TeV

Instability	Longitudinal Threshold	Transverse Threshold
Microwave	$\lvert Z_\parallel/n\rvert = 15.5\ \Omega$	$\lvert Z_\perp\rvert = 590\ \mathrm{M\Omega/m}$
Mode-coupling	$\mathrm{Im}(Z_\parallel/n) = 87\ \Omega$	$\mathrm{Im}(Z_\perp) = 250\ \mathrm{M\Omega/m}$

The threshold impedances listed in Table 4.5-4 are to be compared with the calculated values of $Z_{\parallel}/n \approx 0.2\ \Omega$ and $Z_{\perp} \approx 40\ \mathrm{M}\Omega/\mathrm{m}$ for broad-band contributions. The single-bunch instabilities are not serious for the SSC.

4.5.5 Transverse Instabilities

Multi-bunch Effects

As in the longitudinal case, two mode numbers m and n describe a transverse coupled-bunch mode. One difference is that the index n can assume the value $n = 0$, meaning bunches move rigidly as they execute the transverse oscillations; n = 1 means the bunch head and tail oscillate transversely out of phase, etc. In the unperturbed case, the frequency of mode (m,n) is $(\nu + n\nu_s)\omega_0$, where ν is the unperturbed betatron tune. Again one can describe the bunch motion in terms of mode spectra $h_n(\omega)$, that depend on the unperturbed bunch length and shape. The complex frequency shift of the mode caused by the impedances can be written as [4.5-16]

$$\Delta\Omega^{(m,n)} = -\mathrm{i}\, N_B r_p \beta_{\mathrm{ave}} \omega_0 [Z_0 \gamma \sigma_z (n+1)]^{-1} \sum_p Z_{\perp}(\omega_p) h_n(\omega_p) / \sum_p h_n(\omega_p) \qquad (4.5\text{-}24)$$

where β_{ave} is the average beta function at the location of the impedance, $\omega_p = \omega_0(pM + m + \nu + n\nu_s)$ and we have ignored the chromaticity effect. Table 4.5-5 lists the growth times at 1 TeV and 20 TeV for the most unstable transverse coupled-bunch modes driven by the rf cavity impedance for $\beta_{\mathrm{ave}} = 220$ m [4.5-17]. The growth time at 20 TeV is simply 20 times that at 1 TeV because of the beam rigidity.

Table 4.5-5
Growth Times at 1 TeV and 20 TeV of the Most Unstable Transverse Coupled-Bunch Modes Resulting From the rf Cavity Impedance

Mode Numbers		Growth Time (seconds)	Growth Time (seconds)
n	m	1 TeV	20 TeV
0	1684	2.3	46
	1683	2.3	46
1	8713	4.9	98
	8712	4.9	98
2	8713	21	420
	8712	21	420
3	1683	79	1570
	1684	79	1570

Table 4.5-5 shows that the rigid dipole modes ($n = 0$) have the fastest growth rates. The higher modes ($n > 0$) are stablized by Landau damping because of the spread in the betatron and synchrotron frequencies within the bunch. The spread in synchrotron frequency is

caused by the nonlinearity of the rf bucket. The spread in betatron frequency comes mainly from nonlinear magnetic fields and the beam-beam interaction.

As in the longitudinal case, inclusion of the space charge and the low-Q resonator impedances does not change the instability growth rates appreciably and, although it does make large mode-frequency shifts, a small betatron tune spread of about 1×10^{-4} at injection is sufficient to suppress the instability of all modes with $n > 1$. Such a tune spread is well within the range provided by the octupoles in the spool pieces. The unstable rigid bunch ($n = 0$) motions are damped by a feedback system. The feedback strength required is much weaker than that needed to damp the betatron oscillations of the beam due to injection errors.

Unlike the longitudinal case, the resistive wall impedance also contributes to multi-bunch growth rates of the $n = 0$ modes because of its narrow-band nature at low frequencies. The coherent mode frequency is, in the limit of short bunch length,

$$\Delta\Omega^{(m,0)} = -\mathrm{i}\, M\, N_B r_p \beta_{\mathrm{ave}} \omega_0^2 \sum_p Z_\perp(\omega_p)/(2\pi\gamma c Z_0) \tag{4.5-25}$$

where $\omega_p = \omega_0(pM + m + \nu)$. The resistive wall impedance is sharply peaked at the origin as $\omega^{-1/2}$. With $M = 17280$ and $\nu \approx 78$, the most unstable mode has $m = -78$ and the summation over p is dominated by the term with $p = 0$. The growth rate is given by

$$\begin{aligned} \tau^{-1} &= \mathrm{Im}\, \Delta\Omega^{(-78,0)} \\ &= \pm M\, N_B r_p \beta_{\mathrm{ave}} \omega_0 c (2\pi\sigma_1\omega_0\Delta\nu)^{-1/2} (2\pi\gamma b^3)^{-1}\, \mathrm{Im}[(1 + \mathrm{i})\zeta] \end{aligned} \tag{4.5-26}$$

where $\Delta\nu$ is the deviation of ν from 78 and ζ is the modifying factor (4.5-7) for a two-layer vacuum chamber, evaluated at frequency $\omega_0\Delta\nu$. The + and - signs, corresponding to unstable and stable cases, apply when the tune is below and above the nearest integer, respectively.

To avoid significant restriction on tune choice, we require the feedback system to be able to damp the instability when the tune is below an integer by 0.1. Setting $\Delta\nu = 0.1$, we obtain $\zeta = (2.98 + \mathrm{i}2.87)$ for the beam pipe described below Eq. (4.5-7), and a growth time of 8.5 ms for 1 TeV, to be cured by the feedback system. The growth rate would be 100 times faster if the 1 mm stainless steel pipe were not copper coated. Since adjacent bunches move very similarly in the $m = -78$ mode, the bandwidth for this feedback system is narrow, corresponding to a response time of about one revolution time. The largest band-width is required to damp a mode with m about equal to $M/2$, for which the instability growth time is about 14 s. This requirement is already met by the feedback system to damp the multi-bunch instability caused by the rf impedance.

Single Bunch Effects

Substituting Eq. (4.5-9) into Eq. (4.5-24) gives the coherent frequency shifts caused by the space charge impedance,

$$\Delta\Omega^{(n)} = -N_B r_p \beta c [2\pi\gamma^3\sigma_z(n + 1)]^{-1}(1/a^2 - 1/b^2) \tag{4.5-27}$$

The coherent dipole tune shift, with $n = 0$, for example, is -0.3×10^{-3} at 1 TeV. This is to be compared with the incoherent tune shift of -0.9×10^{-3} calculated in Section 4.5.1. As far as tune shifts are concerned, the space charge effect is small but not ignorable.

The threshold of transverse single-bunch microwave instability is given by [4.5-8]

$$|Z_\perp = 2Z_0\alpha\gamma n_R\sigma_\delta\sigma_z/N_B r_p\beta_{\text{ave}} \tag{4.5-28}$$

where $n_R = f_R/f_0$ with f_R the resonator frequency of the broad-band impedance and f_0 the revolution frequency. The value of $Z_\perp$ is an effective value averaged over the bunch spectrum. Taking $f_R = 2.9$ GHz, the pipe cut-off frequency, and $\beta_{\text{ave}} = 220$ m, the threshold impedance for 1 TeV is given in Table 4.5-4.

The threshold for transverse single-bunch mode-coupling instability (or the fast head-tail instability) is given by [4.5-8]

$$\text{Im}Z_\perp = (4/3\pi^{1/2})\alpha\gamma\sigma_\delta cZ_0/N_B r_p\beta_{\text{ave}}f_0 \tag{4.5-29}$$

At the threshold, the $n = 0$ mode frequency has shifted by the synchrotron frequency. Unlike the longitudinal case, the transverse mode-coupling instability sets a tighter limit on impedance than the microwave instability. The numerical value of the threshold according to Eq. (4.5-29) is given in Table 4.5-4. The impedances calculated for the SSC are well within the limit.

4.5.6 Intrabeam Scattering

Coulomb scattering of particles within a bunch leads to excitation of the betatron and synchrotron oscillations of the scattered particles. Multiple small-angle Coulomb scattering causes redistribution of beam emittances in both transverse and longitudinal spaces. In the beam rest frame, the rms momentum spreads in the three dimensions are $\sigma_{x'}p_0$, $\sigma_{y'}p_0$ and $\sigma_\delta p_0/\gamma$, respectively, where $\sigma_{x'}$ and $\sigma_{y'}$ are the local rms values of dx/ds and dy/ds. At 1 TeV, they are 2 MeV/c, 2 MeV/c and 0.14 MeV/c while at 20 TeV they are 9 MeV/c, 9 MeV/c and 0.05 MeV/c. Motion is thus nonrelativistic in the beam rest frame. These numerical values also indicate that Coulomb scattering will predominantly transfer momentum from the betatron dimensions to the synchrotron dimension, nominally leading to damping of transverse betatron beam emittances and growth in the longitudinal emittance. On the other hand, the excitation of synchrotron motion is coupled to horizontal betatron motion through the dispersion function in the lattice. For large enough dispersion, the excitation of horizontal betatron oscillations by coupling to the synchrotron motion more than compensates the damping effect. Nominally, one therefore expects the vertical motion to be slowly damped and both horizontal and synchrotron motions to grow.

Assuming a smooth lattice, the invariant during the intrabeam scattering process is [4.5-20]

$$-\eta\sigma_\delta^2 + \sigma_{x'}^2 + \sigma_{y'}^2 = \text{invariant} \tag{4.5-30}$$

where $\eta = \alpha - 1/\gamma^2$ with α the momentum compaction factor. If we ignore the damping in the vertical dimension, the invariant gives a relationship between the emittance growth rates, τ_x and τ_s, of horizontal and synchrotron dimensions

$$\tau_x/\tau_s = \sigma_{x'}^2/\eta\sigma_\delta^2 \tag{4.5-31}$$

With $\sigma_{x'} = 0.46$ μrad, $\alpha = 0.00022$ and $\sigma_\delta = 5 \times 10^{-5}$ at 20 TeV, the ratio of τ_x to τ_s is about 0.38. At 1 TeV, the ratio is 0.85.

A numerical calculation of the growth rates, taking into account of variation of lattice functions with azimuth, has been performed using the program ZAP [4.5-17,18]. The emittance growth rates can be expressed in the following form [4.5-20,21]

$$\tau_{x,y,s}^{-1} = N_B f_{x,y,s}(\gamma,\epsilon_{xN},\epsilon_{yN},\sigma_\delta)/(\epsilon_{xN}\,\epsilon_{yN}\,\sigma_\delta\sigma_z) \tag{4.5-32}$$

where N_B is the number of particles per bunch, ϵ_{xN} and ϵ_{yN} are the normalized emittances and $f_{x,y,s}$ are functions that involve averages of lattice functions over the storage ring circumference. The growth times for the nominal set of SSC parameters are given in Table 4.5-6.

Table 4.5-6
Growth Times from Coulomb Scattering

Beam Energy (TeV)	τ_x(h)	τ_s(h)	τ_y(h)
1	26	27	-1.2×10^4
20	126	277	-1.9×10^7

The ratio τ_x/τ_s obtained by the detailed calculation agrees reasonably well with that obtained by Eq. (4.5-31). Negative growth time for the vertical emittance indicates that it is slightly damped, but a spurious vertical dispersion function can make the damping into a net growth as well.

The dependence of the growth rates on N_B and σ_z is straightforward with $\tau \propto \sigma_z/N_B$. Over the range of interest, the functions $f_{x,y}$ are almost independent of the normalized emittances (say, from $\epsilon_N = \epsilon_{xN} = \epsilon_{yN} = 0.2$ μm to 2 μm) and the function f_s is proportional to ϵ_N. Therefore we have $\tau_{x,y} \propto \epsilon_N^2$ and $\tau_s \propto \epsilon_N$. The dependences on the two remaining parameters γ and σ_δ are more complicated. Figure 4.5-7 gives the growth times as functions of σ_δ at the injection and storage energies. The times are much longer than the beam lifetime at 20 TeV. In addition, the emittance growth will be more than compensated by the synchrotron radiation damping. If there is need to collide beams at 1 TeV, the synchrotron radiation damping is too weak to help and intrabeam scattering will degrade the beam performance somewhat. Figure 4.5-8 gives the dependence of the growth times on the beam energy E.

Coulomb interactions within a beam bunch occasionally cause a large angle scattering in the bunch rest frame and produce a phenomenon called the Touschek effect [4.5-22]. The scattering most probably occurs between particles with large transverse momentum in the rest frame. If the scattering angle is large enough, both particles will acquire a large longitudinal momentum after the collision. If the acquired longitudinal momentum exceeds the acceptance, these particles will be lost. The acceptance is set by the rf bucket height or by the momentum aperture of the storage ring. The Touschek lifetime is calculated by averaging the instantaneous loss rate over the ring circumference using ZAP.

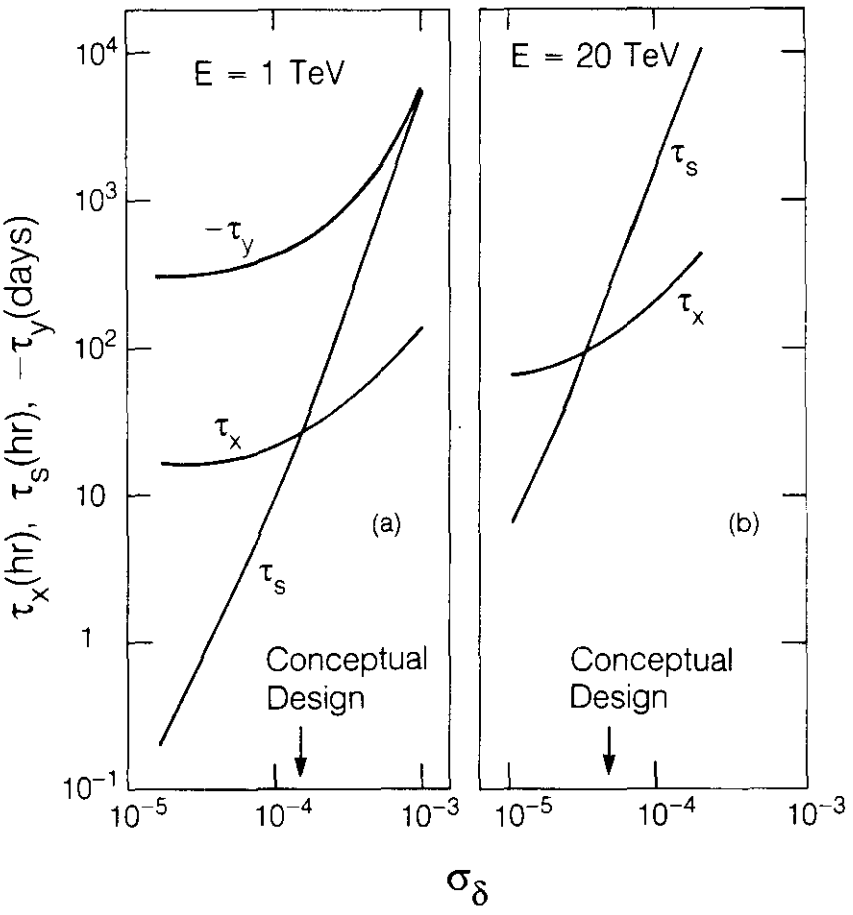

Figure 4.5-7. Intrabeam scattering growth times $\tau_{x,y,s}$ as functions of beam rms relative energy spread σ_δ for (a) 1 TeV and (b) 20 TeV. The curve for τ_y is omitted from (b) because it is in the irrelevant range of 10^4 years.

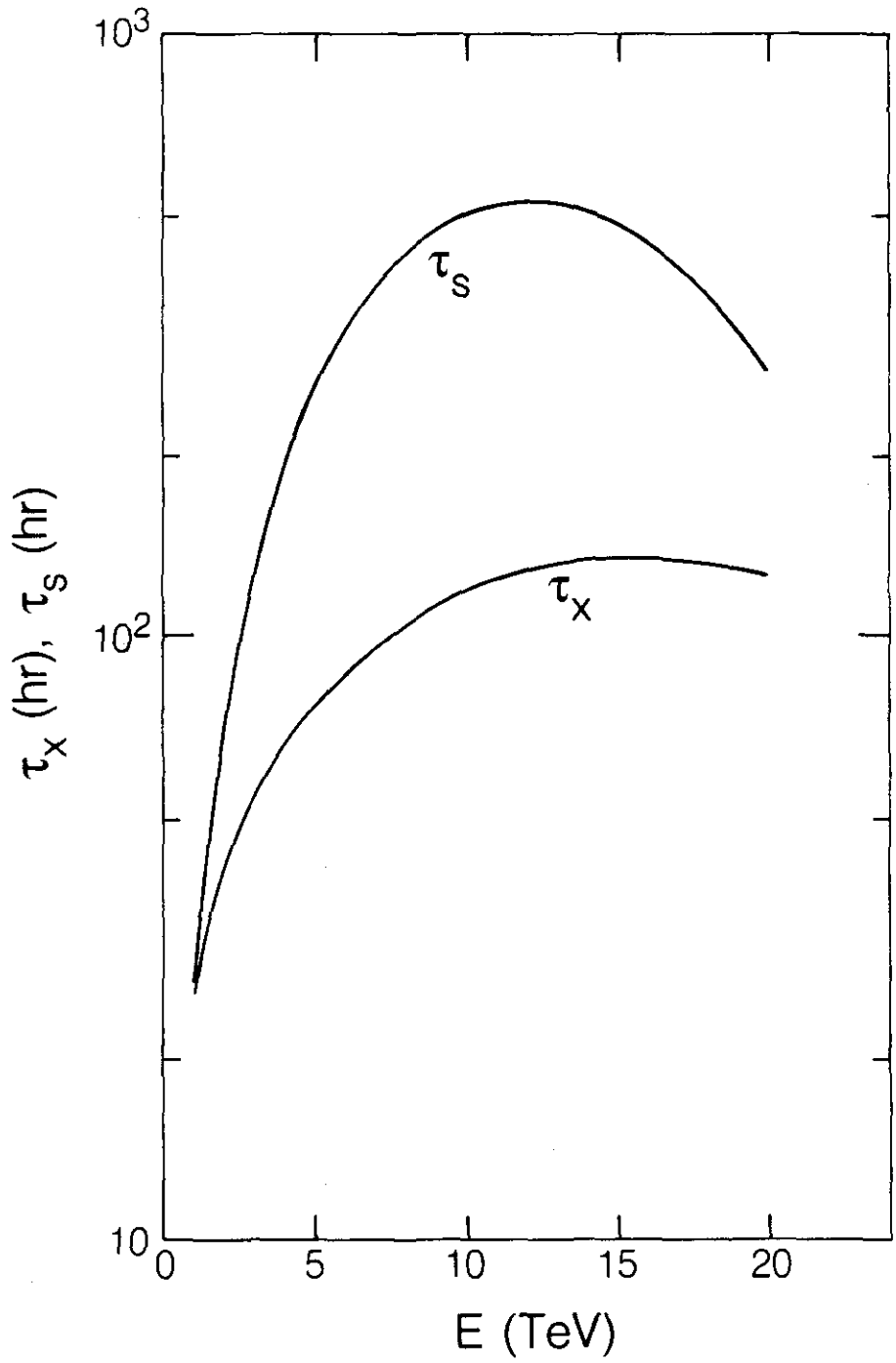

Figure 4.5-8. Intrabeam scattering growth times $\tau_{x,s}$ as functions of beam energy E.

Assuming an rf voltage of 20 MV, the beam lifetime is found to be 4.5×10^4 h at 1 TeV and 3.9×10^4 h at 20 TeV. The Touschek effect is not important for beam lifetime considerations.

4.5.7 Synchro-betatron Resonances Due to Crossing Angle

In the SSC, the beams cross at a small angle α at the interaction points to avoid multiple head-on collisions with the short bunch spacing of $S_B = 4.8$ m. Because of a smaller overlapping of the beam distributions, the luminosity is reduced by a factor $(1 + r^2)^{1/2}$, where $r = \alpha\sigma_z/2\sigma$, as described in Section 4.1.3. Here we describe another consequence of a nonzero crossing angle, also related to the parameter r, namely the effect of the beam-beam driven synchro-betatron resonances. Long-range beam-beam interactions are ignored for the present.

Synchro-betatron resonances driven by the beam-beam interaction with a crossing angle have limited the luminosity in the e^+e^- storage ring DORIS [4.5-23]. Their potential effect has also caused the ep storage ring HERA to be designed with head-on collisions. It is therefore important for the SSC to establish that a nonzero crossing angle is indeed acceptable from this point of view.

Besides the parameter r, two additional parameters are of importance: the beam-beam strength parameter ξ, which is taken to be $1/(1 + r^2)$ times $\Delta\nu_{HO}$ of Eq. (4.1-8), and the synchrotron tune ν_s. Roughly speaking, ξ specifies the overall strength of the beam-beam force, while r specifies the relative importance of the nonlinearities that drive the higher order resonances. Small values of ξ and r are thus preferred. A small synchrotron tune ν_s is also preferred since it means the synchro-betatron resonances will cluster around a betatron resonance, leaving more space for choice of a working point. For the low-beta IRs, the SSC has $r = 0.55$, comparable to the value for DORIS, but has ξ and ν_s values an order of magnitude or more smaller ($\xi = 0.0009$, $\nu_s = 0.0019$).

In general, the beam-beam interaction with a crossing angle excites resonances of the form

$$n_x\nu_x + n_y\nu_y + n_s\nu_s = m \quad , \tag{4.5-33}$$

where n_x, n_y, n_s and m are integers. Because of the symmetry of the beam-beam force, only resonances with even values of $n_x + n_y + n_s$ are excited in first approximation. The synchrotron term results from the non-zero crossing angle. The linear synchro-betatron resonances $\nu_y \pm \nu_s = m$, for example, are driven when beams cross vertically. Because of the beam-beam interaction with a crossing angle, the beam orientation in the (y,s) plane is tilted relative to the direction of motion of the beam by an angle $\theta \approx \xi\alpha/\Delta$, where Δ is the distance from the resonance condition in tune units [4.5-24]. Taking $\xi = 8 \times 10^{-4}$, $\alpha = 75$ μrad and $\Delta = 0.1$ gives $\theta \approx 0.6$ μrad. This tilt does not cause noticeable reduction in luminosity because the rms transverse spread of 5 μm is much larger than $\theta\sigma_z \approx 0.04$ μm.

The resonances (4.5-33) are driven in general by the nonlinear beam-beam interaction. The strengths of the resonances were obtained by a simulation performed by Piwinski [4.5-25]. It is found that the relevant resonances for the SSC are sidebands of the third order betatron resonances, i.e.

$$3\nu_y + n_s\nu_s = m\ , \quad \nu_x + 2\nu_y + n_s\nu_s = m\ ,$$
$$2\nu_x + \nu_y + n_s\nu_s = m\ , \quad 3\nu_x + n_s\nu_s = m\ . \tag{4.5-34}$$

The largest increase in amplitude occurs for the $n_s = \pm 1$ sidebands, with a factor of about 5. The $n_s = \pm 2$ sidebands give an amplitude increase of about a factor of 2. The $n_s = \pm 3$ sidebands are suppressed but still visible. Sidebands of the fourth and fifth order betatron resonances are not observed for the SSC parameters.

Figure 4.5-9 is an example of the simulation results showing some of the resonances. Since the synchrotron tune is small, the synchro-betatron resonances driven by crossing beams are concentrated in small regions. Between these regions are large working spaces for the betatron tunes.

A finite crossing angle is not the only mechanism that causes a beam-beam perturbation to be modulated by synchrotron motion of a particle and thus drives is synchro-betatron resonances. Other mechanisms include various modulations given below:

(a) Even with head-on collisions, finite bunch length introduces a modulation of a beam-beam perturbation of relative magnitude of the order of $(\sigma_z/\beta^*)^2$. With $\sigma_z = 7$ cm and $\beta^* = 0.5$ m, the amplitude of this modulation is only 2%.

(b) The chromaticity accumulated through the low-beta interaction regions also drives synchro-betatron resonances through phase modulation of the beam-beam perturbation. This effect is most relevant for clustered interaction region designs. If the chromaticity accumulated between adjacent interaction points within a cluster is denoted by ξ, the phase modulation has an amplitude of $2\pi\xi\delta$ for a particle with energy deviation of $\delta = \Delta E/E$. Taking $\xi = 20$ and $\delta = 10^{-4}$, the phase modulation is only about 0.01 radians.

(c) The interaction regions are dispersion free. However, spurious dispersion may be generated by errors. The effect of a synchro-betatron resonance on a particle with relative energy error δ due to a dispersion of η^* at the interaction point is approximately equivalent to that on a particle with longitudinal deviation z due to a crossing angle α if $\alpha \approx \eta^*\delta/z$. Taking $\eta^* = 1$ cm, $\delta = 0.5 \times 10^{-4}$, $z = 7$ cm and $\alpha = 75$ μrad as typical values, we find that the crossing angle effects are stronger than the dispersion effects by a factor of 10.

(d) Finite chromaticity in the storage ring causes betatron tunes to be modulated by synchrotron oscillation, thus allowing the synchro-betatron resonances to be driven by the beam-beam interaction. These effects are potentially much more serious because a betatron modulation of $\Delta\nu$ is equivalent to a phase modulation of magnitude $\Delta\nu/\nu_s$, where ν_s is the synchrotron tune. A small tune modulation is thus equivalent to a large phase modulation. This effect is discussed in more detail in the next section. Note that the tune modulation does not have to be caused by chromaticity. Power supply ripples that modulate betatron tunes have similar effects.

4.5.8 Head-on Beam-Beam Effects

Head-on beam-beam effects can be categorized by whether they involve incoherent motion of single particles or coherent motion of the bunch distribution. In the incoherent limit, a single test particle interacts with the nonlinear electromagnetic field generated by

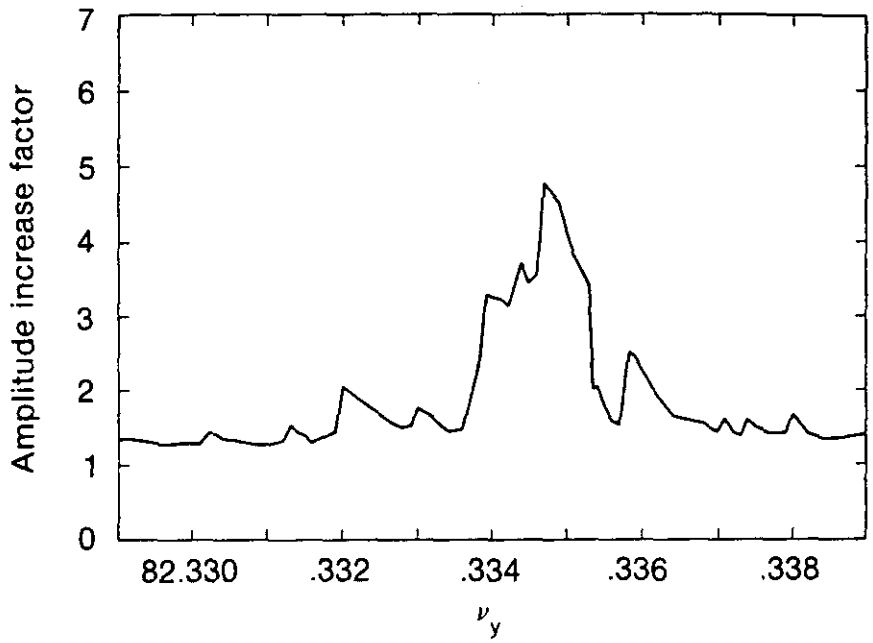

Figure 4.5-9. Maximum amplitude reached in 50000 revolutions for particles with initial amplitudes $\sqrt{2\sigma_x}$, $\sqrt{2\sigma_y}$ and $\sqrt{2\sigma_\delta}$ so that their rms values are σ_x, σ_y and σ_δ. The maximum amplitude is normalized to the rms transverse beam size at the interaction points given by $(\sigma_x^2 + \alpha^2\sigma_z^2/4)^{1/2}$. Vertical tune ν_y is varied while ν_x is held constant at 82.34. The crossing angle is $\alpha = 80$ μrad; beam-beam strength parameter is $\xi = 0.0009$; synchrotron tune is $\nu_s = 0.0019$.

bunches in the other beam that are taken to have rigid distributions. In a coherent beam-beam effect, bunches interact with one another as oscillating distributions in one or more possible multipole modes.

Incoherent Effects

In the incoherent limit, motion of a test charge is described by kicks at the interaction points

$$\Delta x'/x = \Delta y'/y = -[2N_B r_p/\gamma(x^2+y^2)]\{1 - \exp[-(x^2+y^2)/2\sigma^2]\}$$

$$= -(N_B r_p/\gamma\sigma^2)[1 - (x^2+y^2)/4\sigma^2 + (x^2+y^2)^2/24\sigma^4 \cdots] \qquad (4.5\text{-}35)$$

The leading term in the power series expansion gives rise to the head-on tune shift $\Delta\nu_{HO}$, Eq. (4.1-8). The most prominent effect caused by the higher order nonlinear terms is that of a tune spread. Particles with small betatron amplitudes see only the linear part of the beam-beam force and experience a tune shift of $\Delta\nu_{HO}$ per crossing. In the SSC, the four IRs contribute approximately the same values of $\Delta\nu_{HO} = -0.84 \times 10^{-3}$, leading to total shifts of -0.0034 in both horizontal and vertical tunes.

Particles with large betatron amplitudes, however, do not experience appreciable tune shifts. Head-on tune shifts are therefore functions of α_x and α_y defined to be $(A_x/2\sigma)^2$ and $(A_y/2\sigma)^2$, where $A_{x,y}$ are the betatron amplitudes and σ is the rms beam spread at the interaction point. The expressions are

$$\Delta\nu_x = -\Delta\nu_{HO} \int_0^1 du \exp[-(\alpha_x+\alpha_y)u]\, I_0(\alpha_y u)[I_0(\alpha_x u) - I_1(\alpha_x u)]$$

$$= -\Delta\nu_{HO}[1 - (3\alpha_x+2\alpha_y)/4 + (5\alpha_x^2+6\alpha_x\alpha_y+3\alpha_y^2)/12 - \cdots] \qquad (4.5\text{-}36)$$

and one for $\Delta\nu_y$ similar to Eq. (4.5-36) with x and y exchanged, where I_0 and I_1 are modified Bessel functions. A particle with oscillation amplitudes $A_x = A_y = \sqrt{2}\sigma$ for example, has a net tune shift of about $0.6\Delta\nu_{HO}$, substantially smaller than that of a small amplitude particle. The dependence of tune shifts on betatron amplitudes thus leads to a total tune spread of 0.0034 across the beam distribution from head-on collisions.

Figure 4.5-10(a) shows the tune spreads induced by the head-on beam-beam interactions using the full expression for the beam-beam force [4.5-26]. The unperturbed working point (taken to be the origin in Fig. 4.5-10) is extended into a working area because of the head-on interaction. It is necessary to provide sufficient space in the (ν_x,ν_y) tune space, free of low order resonances, to accommodate the tune spread. Since the total tune spread is rather low in the SSC, this requirement is easy to meet. The remaining parts of Fig. 4.5-10 are discussed in the next section.

To estimate the effect of low order resonances driven by head-on beam-beam interactions, we apply a resonance overlap criterion [4.5-27]. Consider a one-dimensional motion in which the betatron tune is close to a rational number n/p and is being modulated by synchrotron oscillations:

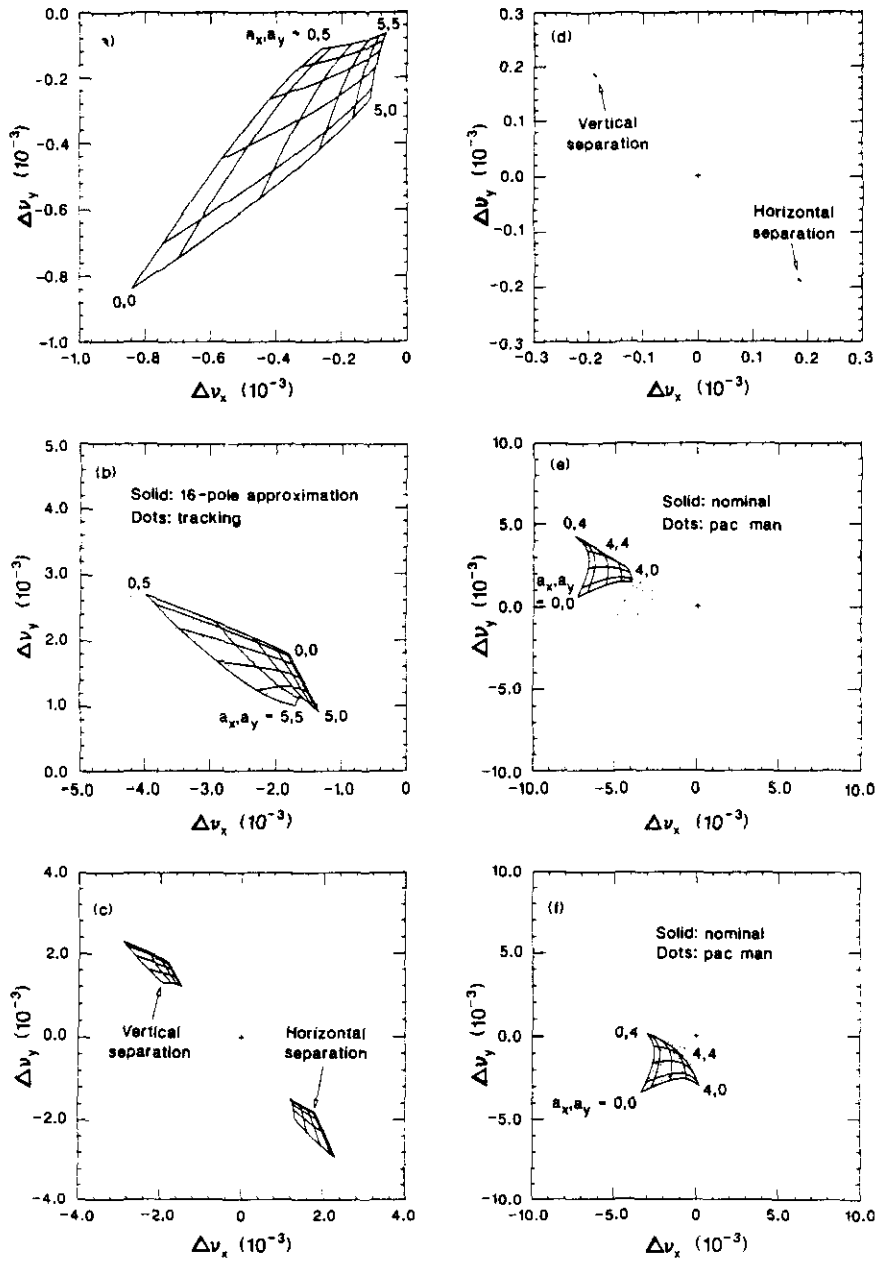

Figure 4.5-10. (a) Tune shifts and spreads per crossing due to head-on interactions. The unperturbed working point is at the origin. The contours are for constant values of $a_x = A_x/\sigma$ and $a_y = A_y/\sigma$. Small amplitude particles have tune shifts of $\Delta\nu_x = \Delta\nu_y = -0.00082$. (b) Tune shifts and spread per vertical crossing due to long-range interactions. Solid curves are obtained using an 16-pole expansion equivalent to Eq. (4.5-44). The dotted curves are obtained by particle tracking. (c) Shows the long-range effect for vertical and horizontal beam crossings. The IR has $\beta^* = 0.5$ m. Contours are drawn up to $a_x = a_y = 4$. (d) is the same as (c) but for the $\beta^* = 10$ m IRs. Note that both the tune shifts and the tune spreads are much smaller than those for the $\beta = 0.5$ m IRs. (e) shows the case for the nominal lattice with two $\beta^* = 0.5$ m IRs and two $\beta^* = 10$ m IRs. All crossings are vertical. Both long-range and head-on contributions are included. The unperturbed working point is indicated by a cross. The dotted curves are for one of the pacman bunches. (f) is the same as (e) but for alternately horizontal and vertical crossings. The needed total working space is smaller than is shown in (e).

$$\nu = \nu_0 + q \cos \nu_s \theta \tag{4.5-37}$$

where q is the magnitude of the tune modulation, ν_s is the synchrotron tune and θ is the azimuth. In one dimension, tune modulation of Eq. (4.5-37) causes synchro-betatron sideband resonances at

$$\nu = n/p + m\nu_s/p \tag{4.5-38}$$

where $m = \pm 1, \pm 2$, etc. In the following analysis, we assume $\nu_s = 0.002$ and $q = 0.001$, corresponding to a particle with $\Delta E/E = 2 \times 10^{-4}$ and chromaticity of 5. Note that another important source of tune modulation is the magnet power supply ripple, in which case ν_s is the ripple tune. However, power supply ripple is at multiples of 60 Hz, which corresponds to a modulation tune of $\nu_s = 0.017\ n$, at least 10 times greater than the synchrotron tune. This implies a looser tolerance for stochastic beam blow-up than that associated with synchrotron motion. The tune tolerance for ripple has been taken to be less than ± 0.001.

Each sideband resonance in Eq. (4.5-38) has a width, which can be expressed in tune units. When these resonances are wide enough that they overlap, a stochastic particle motion occurs, leading to apparent emittance growth and possibly loss of the particle. There are two conditions for stochastic motion to occur: (a) The unperturbed tune has to be within $\pm q$ from the resonant value of n/p. (b) For a given head-on beam-beam tune shift $\Delta\nu_{HO}$ and a particular betatron resonance n/p, overlapping of sidebands occurs only when the particle amplitude is larger than a certain critical value.

Figure 4.5-11(a) shows the stability region in (ν, a) space for $\Delta\nu_{HO} = 0.0034$, where a is the betatron amplitude normalized by the rms beam spread. Stochastic regions are represented by the heavy lines, which are centered around resonant tune values and have total width of $2q = 0.002$. To assure a good beam lifetime, the tune spread of the beam should fit between the stochastic regions up to $a \approx 5$. The only important resonances excited by the weak beam-beam interaction are those lower than the 6th order. There should be little difficulty in finding an acceptable working point for the SSC.

Figure 4.5-11(b) shows the stability domain when the total head-on tune shift is increased to 0.0051, corresponding to the situation when the two future IRs are commissioned. The resonance features are more pronounced. Resonances up to the 10th order become relevant. However, there should still be sufficient room for the colliding beams. The results shown in Fig. 4.5-11 require a few more remarks:

(a) Figures 4.5-11(a) and (b) assume the worst case, with the resonance strengths from the four IRs adding coherently for all resonances considered. In reality, the four contributions are to be added with proper phase factors, leading to a net suppression factor for each resonance. In particular, when betatron phase advance between adjacent interaction points within an IR cluster is an odd multiple of $\pi/2$, like the (2,4) IR arrangement adopted in the conceptual design, resonances with $p = 2$, 6 and 10 are suppressed to first order in the beam-beam strength. Figure 4.5-11(c) is a repetition of Fig.4.5-11(b) but taking full account of the suppression factor.

(b) The effects of beams crossing at an angle are treated in Section 4.5.7. In the presence of errors, bunches may collide slightly off-center. As is discussed in Section

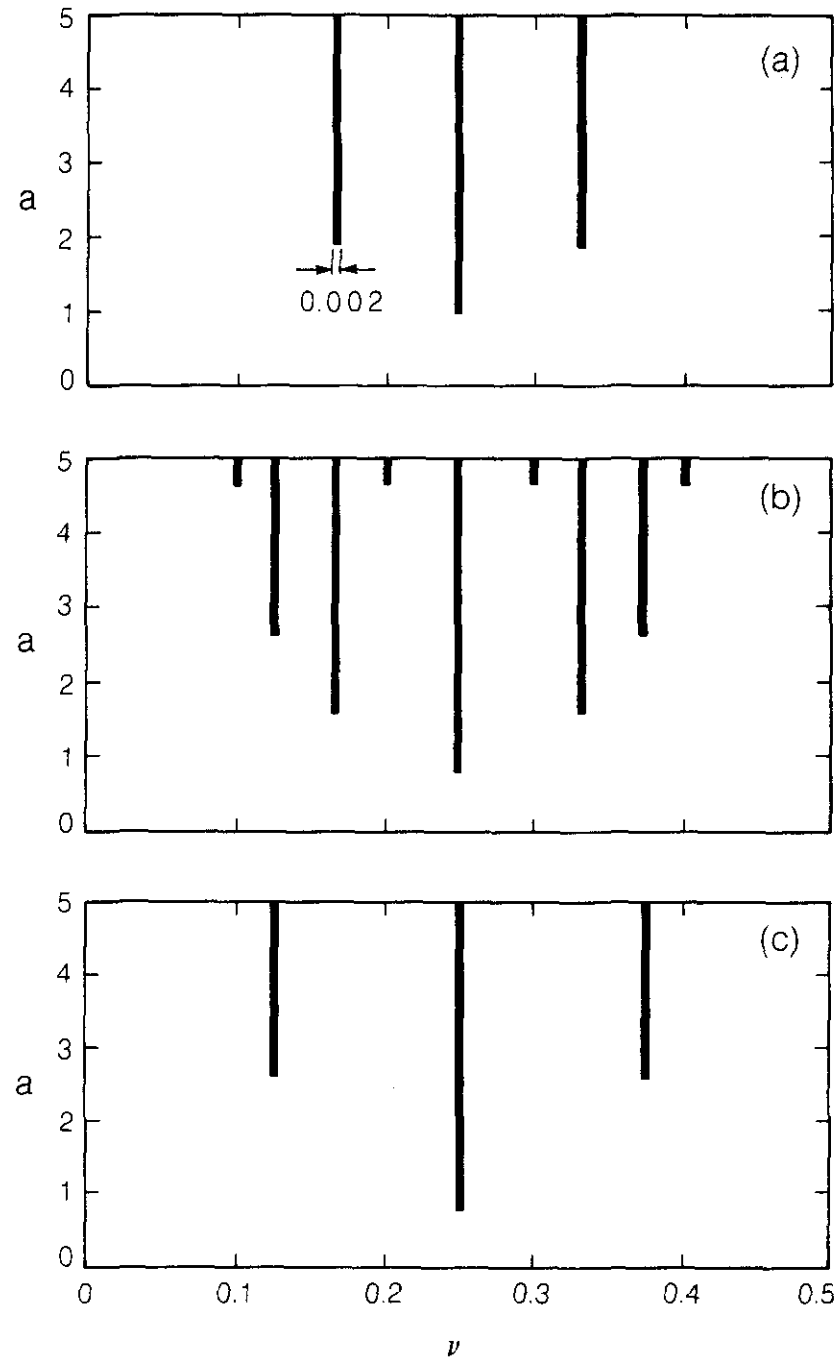

Figure 4.5-11. Stability region against head-on beam-beam incoherent effects in the (ν, a) space. The tune spread of the beam has to fit between the stochastic regions indicated by the heavy lines. (a) is when $\Delta\nu_{HO} = 0.0034$. (b) is when $\Delta\nu_{HO} = 0.0051$. (c) is the same as (b) but taking full account of resonance suppressions for resonances with p = 2,6 and 10.

4.5.10, there are some irregular bunches that collide off-center even when all other bunches do not. Because of these effects, odd order resonances are excited by the beam-beam collisions. However, these resonances are much weaker than the corresponding even order resonances and thus do not impose strong restriction on working point choices.

(c) Higher order resonances are also excited by magnetic field errors. Even though the beam-beam resonances are weak, it is still desirable to avoid having resonances of order 10 or lower trespassing the beam tune spread region. (Analysis of resonance widths in Section 4.4.5 indicates that resonances of 7th order or less are to be avoided.) With a total tune spread of 0.0034, this is not difficult to do.

Coherent Effects

The simplest coherent beam-beam modes involve dipole motion of M bunches per beam, each executing rigid motion as macro-particles and interacting with the M bunches in the other beam. The beam-beam force is a function of x_1-x_2 where $x_{1,2}$ are the transverse displacements of two bunch distribution centers as they collide at the interaction point. Dipole motion of bunches is excited by the leading term in this beam-beam force (linear in x_1-x_2). For a ring in which all diametrically opposite IPs are optically identical, these dipole modes become unstable if ν is close to an integer. For a ring without this symmetry, like the conceptual design, instability occurs when ν is close to an integer or a half-integer.

Figure 4.5-12(a) shows the stability region in ($\Delta\nu_{HO}$, ν) space. It is obtained by a simulation program [4.5-28,29,30] for the nominal case, i.e. two IRs with $\beta^* = 0.5$ m and two IRs with $\beta^* = 10$ m. The areas under the saw-tooth curve indicate regions stable against the coherent dipole beam-beam effect. One sees that the tolerable value of $\Delta\nu_{HO}$ per IR is zero when ν is a half-integer, but away from these resonances, the tolerable head-on tune shift easily exceeds the SSC value of 0.84×10^{-4}. The remainder of Figure 4.5-12(b) is discussed in Section 4.5.9.

The bunch distribution can oscillate not only in the rigid dipole modes but also in multipole modes. An analysis of the stability condition for these multipole modes using a Vlasov equation technique has been developed in [4.5-29, 4.5-31]. The treatment assumes evenly distributed IRs with diametrical symmetry. The dipole, quadrupole, sextupole modes are therefore unstable for ν close to integers, 1/2-integers, 1/3-integers, etc. Results of analysis for four evenly distributed IRs with $\beta^* = 0.5$ m are shown in Fig. 4.5-13(a). One sees that the higher multipole resonances are narrow. Instabilities of low order multipole modes do not occupy too much tune space while the higher order ones are narrower than the natural tune spread of the beam and are therefore expected to be damped by the Landau mechanism.

4.5.9 Long-range Beam-Beam Effects

With beams crossing at an angle α, there are unavoidable long-range beam-beam interactions at locations evenly spaced by a distance of $S_B/2 = 2.4$ m (nominal value) on both sides of the interaction point until the two beams are separated by the vertical separation dipoles. A large number of long-range beam-beam interactions (60 in the high-luminosity IRs and 125 in the intermediate-luminosity IRs) is special to the SSC.

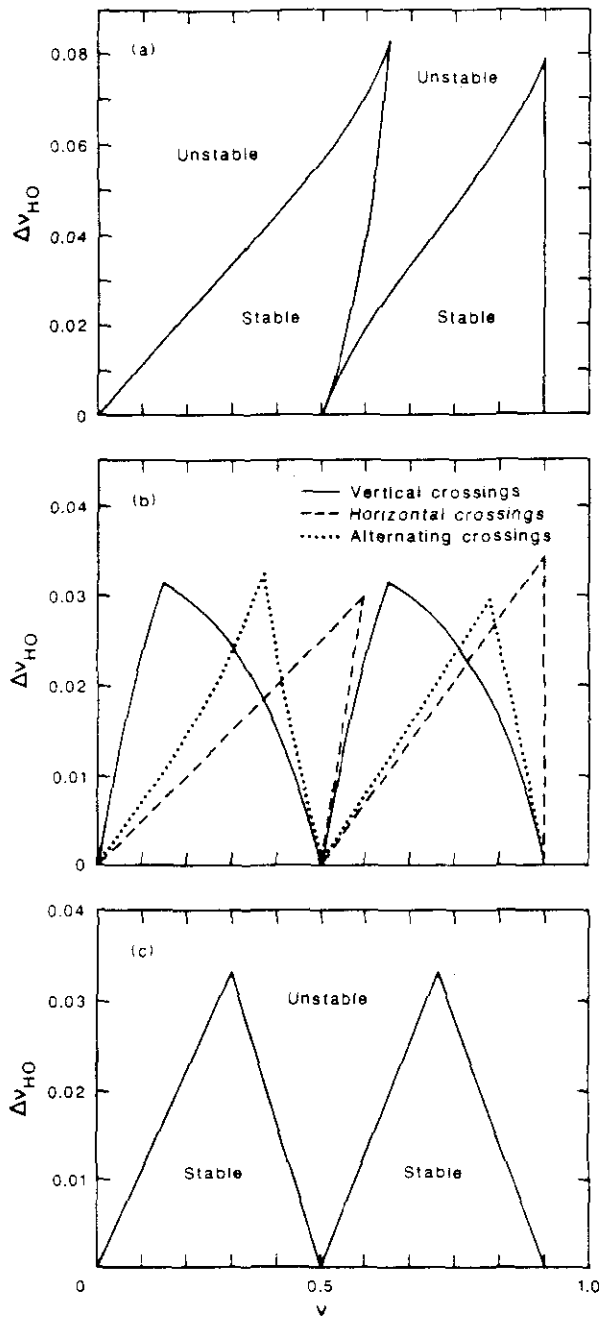

Figure 4.5-12. Stability region of the coherent dipole model in the ($\Delta\nu_{HO}$, ν) space. $\Delta\nu_{HO}$ is the head-on beam-beam tune shift per crossing and ν is the betatron tune. For the conceptual design, instabilities occur when ν is close to any half-integer. (a) is when only head-on interactions are included. (b) also includes the long-range interactions with purely vertical, purely horizontal, and alternately vertical and horizontal crossings in the IRs. The $\Delta\nu_{HO}$ shown in (b) is the vertical head-on tune shift. For the stability diagram of the horizontal tune shift, the solid and the dashed curves are simply reversed. (a) and (b) are for the nominal conceptual design. (c) is for the circumstance when the two future IRs are commissioned with intermediate luminosities with $\beta^* = 10$ m. It applies to the vertical tune shift for purely vertical crossings. Figures are periodic in ν with period of unity.

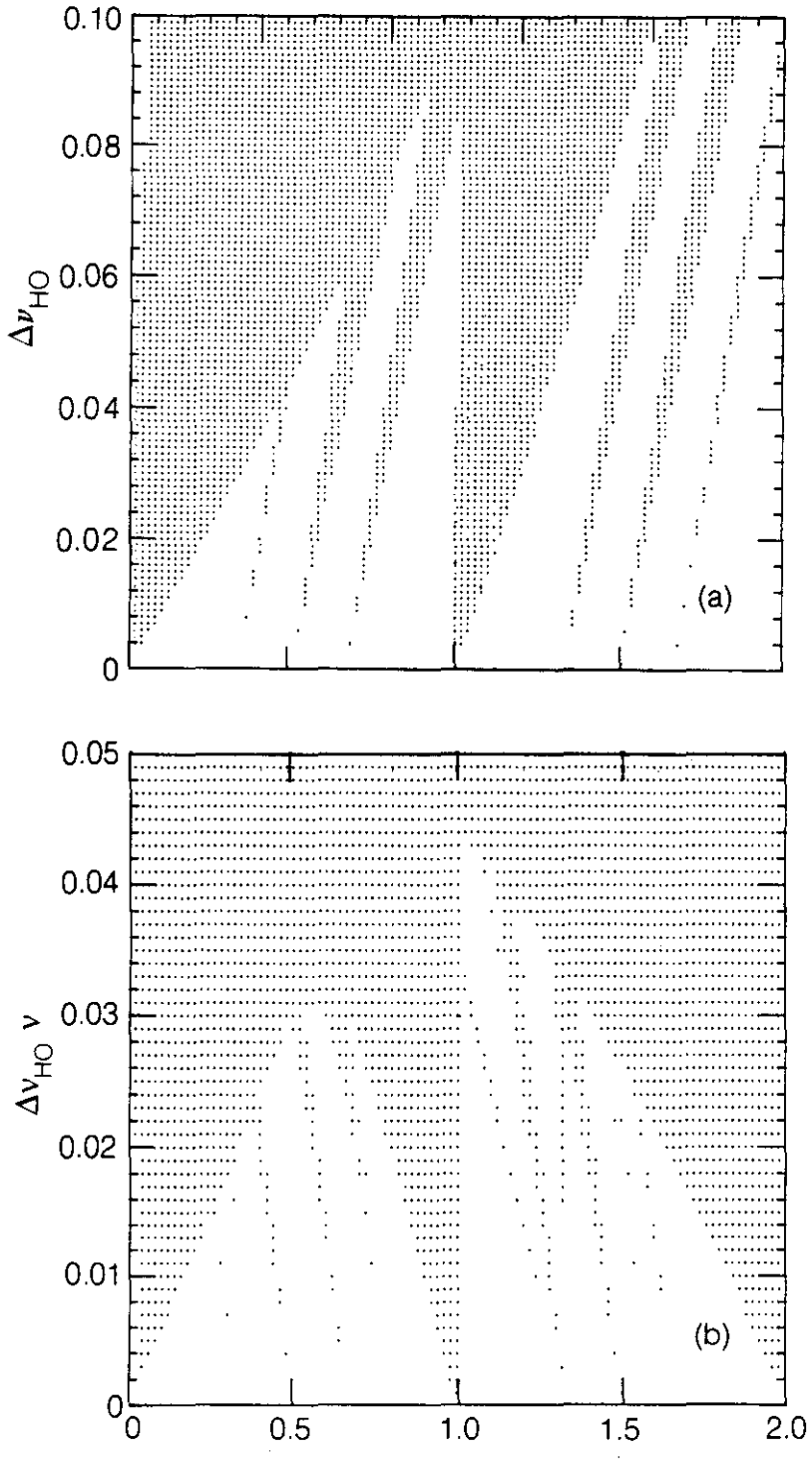

Figure 4.5-13. Stability diagram of coherent multipole beam-beam motion in the vertical dimension. (a) is with head-on interactions only. (b) includes also long-range interactions. The example studied is for four evenly distributed IRs with $\beta^* = 0.5$ m and vertical crossings. Figures are periodic in ν with period 2.

Incoherent Effects

The long-range beam-beam effects depend on whether the beams cross at a horizontal or vertical angle. When two bunches interact with a vertical separation d much larger than the beam dimensions, the long-range beam-beam force causes kicks in the orbital trajectory by the amounts,

$$\begin{aligned}\Delta x' &= (2N_B r_p/\gamma)\, x/[(d+y)^2 + x^2] \\ &= (2N_B r_p/\gamma d)\,[x/d - 2xy/d^2 + (3xy^2 - x^3)/d^3 + \cdots] \\ \Delta y' &= (2N_B r_p/\gamma)\,(d+y)/[(d+y)^2 + x^2] \\ &= (2N_B r_p/\gamma d)\,[1 - y/d - (x^2 - y^2)/d^2 + (3x^2 y - y^3)/d^3 + \cdots]\end{aligned} \tag{4.5-39}$$

These kicks have been expanded into vertical dipole, quadrupole, skew sextupole and octupole contributions. If the separation d is in the horizontal dimension, the kicks are given by Eq. (4.5-39) with x and y interchanged everywhere on both sides of the equation. The kicks are then equivalent to a horizontal dipole, a quadrupole, a normal sextupole and an octupole, etc.

Comparing Eqs. (4.5-35) and (4.5-39), the long-range beam-beam interaction is seen to be qualitatively different from its head-on counterpart. The long-range interaction causes closed orbit distortion through the dipole terms, while the head-on interaction does not cause orbit distortions. Both interactions contribute to tune shifts. The horizontal and vertical tune shifts are of the same sign for head-on interactions and of opposite signs for long-range interactions. For the SSC, the long-range tune shifts per crossing ($\beta^* = 0.5$ m) are about twice the head-on values. The long-range encounters take place mainly in the $1/r$ tail of the beam-beam force. As the nonlinear terms are compared, the long-range contributions rapidly become smaller by powers of σ/d. As a result, for particles with modest amplitudes, the long-range interaction does not cause as much nonlinear effect, such as tune spreads, as does the head-on interaction. This leads to the following table:

	orbit distortion	tune shift	tune spread
head-on	no	yes	yes
long-range	yes	yes	small for moderate betatron amplitudes

In the following, we discuss in sequence the orbit distortions, the tune shifts and the nonlinear effects of the long-range beam-beam interaction.

Orbit Distortion

We assume that the long-range beam-beam interaction takes place in a drift space $\pm L$ around the interaction point at locations with $s \gg \beta^*$. In the conceptual design, there are

four beam crossings, designated by A, B, C and D. Table 4.5-7 gives one possible crossing arrangement. Alternating the horizontal and vertical crossings, although not necessary, helps reduce the long-range beam-beam tune shifts.

Table 4.5-7.
An Example of Beam-beam Crossing Pattern

Interaction region	β^* (m)	L (m)	Crossing angle (μrad)	D (μm)
A	0.5	72	75, horizontal	0.42
B	0.5	72	75, vertical	0.42
C	10.	150	75, horizontal	0.88
D	10.	150	75, vertical	0.88

The orbit distortion at an interaction point consists of contributions from the crossings at all interaction regions. The orbit distortion from one crossing, outside the interaction region where the crossing takes place, is given by (same expression for horizontal or vertical crossing) [4.1-5].

$$\Delta x(s) = -\mathrm{D}[\beta(s)/\beta^*]^{1/2}\sin[\pi\nu - \Psi(s)]/\sin(\pi\nu) \tag{4.5-40}$$

where $\mathrm{D} = 4N_B r_p L/(\alpha\gamma S_B)$ and $\Psi(s)$ is the betatron phase at position s. For the interaction point in the interaction region where the crossing takes place, the orbit distortion vanishes because of the symmetry assumed. With $\alpha = 75$ μrad, $N_B = 7.3 \times 10^9$, values of D for 20 TeV beam are given in Table 4.5-7. The phase advances between interaction points A and B and between C and D are chosen to be odd multiples of $\pi/2$ ($3.75 \times 2\pi$ and $3.25 \times 2\pi$, respectively) for chromatic optimizations, as described in Section 4.2.2. The phase advances between B and C and between D and A are equal and are determined by the overall tune, which is taken to be $\nu = 78.3$. The horizontal and vertical orbit distortions at the four interaction points, including the contributions from all crossings [4.5-32], are shown in Table 4.5-8. These orbit distortions are small compared with the beam sizes at the interaction points (4.8 μm at A and B, 22 μm at C and D). On the other hand, capacity of fine tuning the orbits at interaction points is desirable.

Tune Shifts

The quadrupole terms of the long-range beam-beam force cause tune shifts per crossing [4.1-5]

$$\Delta\nu_x = -\Delta\nu_y = \pm 2N_B r_p L/(\pi\gamma\alpha^2\beta^* S_B) \tag{4.5-41}$$

where the +(−) sign is for a horizontal (vertical) crossing. Equation (4.5-41) is the same as Eq. (4.1-9). The magnitudes of the tune shift contributions from the four crossings are given in Table 4.5-8.

Table 4.5-8
Orbit Distortions and Tune Shifts from Beam-Beam Crossings

Interaction Region	$\Delta x(\mu m)$	$\Delta y(\mu m)$	$\Delta\nu_x$	$\Delta\nu_y$
A	−0.24	0.31	0.0018	−0.0018
B	−0.31	0.24	−0.0018	0.0018
C	2.3	−0.64	0.00019	−0.00019
D	0.64	−2.3	−0.00019	0.00019

The long-range tune shift in the IRs with $\beta^* = 10$ m (C and D) is small, in contrast with the head-on case, where all four IRs contribute equally to the tune shift. If beam crossings are all horizontal or all vertical, the total long-range tune shifts are ± 0.004. Although not believed to be a serious limitation, these tune shifts require compensation during storage ring operation. For example, the tunes change as beams are brought into collision. In addition, as discussed in Section 4.5.10, bunches near the abort gap in the bunch-train have different tune shifts from the normal bunches and require special attention. By crossing the beams horizontally and vertically in alternation, the net tune shifts vanish, thus reducing the operational complications correspondingly.

Nonlinear Effects

Sextupole terms in Eq. (4.5-39) do not contribute to the chromaticity because the interaction takes place in a dispersion-free region. The strengths of these terms are equivalent to sextupoles with $B''L = Z_0 N_B e/\pi d^3$. For example, the strongest encounter takes place closest to the interaction point with $d = \alpha S_B/2$. With $\alpha = 75$ μrad, $S_B = 4.8$ m and $N_B = 7.3 \times 10^9$, we find $B''L = 2 \times 10^4$ T/m, which is about twice the strength of a chromaticity sextupole at 20 TeV. The effects of these beam-beam sextupoles, however, are to be weighted by $\beta^{3/2}$, which is about 140 times smaller than typical values in the arc. In addition, there is a cancellation between contributions on each side of crossing. The net effect is thus negligible.

The octupole terms in Eq. (4.5-39) contribute to the tune shift that depends on betatron amplitudes. In general, the tune shift is given by

$$\Delta\nu_x = -(\beta_x/2\pi A_x)\,\langle \cos\phi_x \Delta x' \rangle \tag{4.5-42}$$

with a similar expression for $\Delta\nu_y$, where $\beta_{x,y}$ are the beta functions at the position of long-range encounter, $\langle \cdots \rangle$ means averaging over ϕ_x and ϕ_y with $x = A_x\cos\phi_x$, $y = A_y\cos\phi_y$ in the expression for $\Delta x'$ and $\Delta y'$. Substitution of the expressions (4.5-39) into (4.5-42) gives the tune shifts per long-range encounter with vertical crossing

$$\begin{aligned}
\Delta\nu_x &= (\beta_x N_B r_p/2\pi\gamma d^2)\left[-1 + 3(A_x^2 - 2A_y^2)/4d^2 - \cdots\right] \\
\Delta\nu_y &= (\beta_y N_B r_p/2\pi\gamma d^2)\left[1 + 3(A_y^2 - 2A_x^2)/4d^2 + \cdots\right]
\end{aligned} \tag{4.5-43}$$

For horizontal crossings, the tune shifts are obtained by interchanging x and y.

The tune shift per crossing is obtained by adding the contributions from all encounters. For the crossing with vertical crossing angle α, this gives per crossing [4.5-26]

$$\Delta\nu_x = \Delta\nu_{LR}\,[-1 + 3(\alpha_x - 2\alpha_y)(\sigma/\alpha\beta^*)^2 - \cdots]$$
$$\Delta\nu_y = \Delta\nu_{LR}\,[1 + 3(\alpha_y - 2\alpha_x)(\sigma/\alpha\beta^*)^2 + \cdots] \qquad (4.5\text{-}44)$$

where $\Delta\nu_{LR}$ is given by Eq. (4.5-41), σ is the beam spread at the interaction point and $\alpha_{x,y}$ are defined in Eq. (4.5-36). Note that, for $\beta^* = 0.5$ m and $\alpha = 75$ μrad, $(\sigma/\alpha\beta^*)^2 = 0.0164$ is a small quantity, reflecting the fact that, in all long-range encounters, bunches are separated by distance d which is much larger than the local beam spread. A particle with moderate amplitudes $A_x = A_y = \sqrt{2}\sigma$ at the IP, for example, has a long-range tune shift that differs from that of a small amplitude particle by only $0.06\Delta\nu_{LR}$, which is much smaller than the head-on effect. The nonlinearities of the long-range interaction for particles with moderate amplitudes are thus not significant compared with those coming from the head-on interaction. On the other hand, with 4σ oscillations, the long-range tune shifts become comparable to the head-on values and must be taken into consideration.

Figures 4.5-10(b)-(f) show the long-range beam-beam tune spread. Curves indicated by $n\sigma$ represent contours generated along $(A_x = n\sigma,\ 0 < A_y < n\sigma)$ and $(0 < A_x < n\sigma,\ A_y = n\sigma)$. Expansion (4.5-44) is extended to the 16-pole terms in the calculation. The figures show the results for $\beta^* = 0.5$ m and $\beta^* = 10$ m, and for horizontal and vertical crossings, respectively. One sees that the long-range beam-beam tune shift and spread are much reduced for the $\beta^* = 10$ m crossings. Figure 4.5-10(b) also shows the agreement between the analytic results with a particle tracking result [4.5-26]. The conceptual design with two IRs with $\beta^* = 0.5$ m and two IRs with $\beta^* = 10$ m is shown in Fig. 4.5-10(e) and (f), corresponding to purely vertical crossings and alternately horizontal and vertical crossings, respectively. One sees that the long-range tune shifts for large amplitude particles interfere with head-on tune shifts, producing a substantially different tune shift versus amplitude relationship. The overall tune spread, however, is not increased at SSC parameters. The dashed areas in Figs. 4.5-10(e) and (f) are discussed in Section 4.5.10.

Coherent Effects

Figure 4.5-12(b) shows the situation when the long-range interaction is taken into account in the stability of the coherent dipole modes [4.5-30]. Comparing with Fig.4.5-12(a), one sees that the dipole long-range interaction substantially reduces the stability region. The results shown are for the nominal conceptual design. When the long-range interaction is introduced, the horizontal and vertical motions become different, giving different regions of stability (solid and dashed curves in Fig. 4.5-12(b)). A slight further reduction of the region of stability against coherent dipole motions occurs when the two future IRs are commissioned. Figure 4.5-12(c) shows the change for all vertical crossings when two $\beta^* = 10$ m IRs are added. In these studies, the orbit distortion caused by the long-range interactions is assumed to be compensated at the interaction points by external means.

Extension to coherent multipole modes is shown in Fig.4.5-13(b). Like the study leading to Fig.4.5-13(a), only the situation with evenly distributed IRs with $\beta^* = 0.5$ m has been analysed. One concludes from comparing Figs. 4.5-13(a) and 4.5-13(b) that the influence of the long-range interaction on the dipole modes is substantial, but the effects on the higher multipole modes become progressively less significant as the order of the multipole is increased. The long-range interaction thus does not cause significant loss of stable operating region.

4.5.10 Pacman Effect

In the SSC, each of the two colliding beams consists of a train of bunches. In each bunch train is a 3.1-microsecond abort gap corresponding to about 200 missing bunches. Normally, a bunch in one beam meets filled buckets of the other beam at all head-on and long-range interaction points, but bunches near the edge of the abort gap will meet the abort gap in the oncoming beam in some of the encounters. Bunches with an irregular sequence of collisions are potentially less stable than those bunches with a normal collision sequence. The tune spread and the nonlinear effects due to head-on and long-range beam-beam interactions are different for the two types of bunches. The orbit distortion caused by long-range interactions are also different. For the normal bunches, the tune spread and nonlinear effects can be handled by carefully choosing a resonance-free region for the working point of the tunes. The orbit distortion can be cured by proper corrections. These tune choices and orbit corrections should be made such that they are acceptable to the irregular bunches as well. Otherwise, these irregular bunches will have a poor beam lifetime, causing loss of bunches leading or trailing the abort gaps, much like what appears in the early video game "pacman". This potential effect of losing bunches near the abort gaps is thus referred to as the "pacman" effect [4.1-5,4.5-33]. Two possible mechanisms for the pacman effect are (a) the pacman bunches collide off-center with bunches of the other beam even if the regular bunches do not, and (b) the chosen working point is not optimized for the tune shift and spread of the pacman bunches.

The direct loss of luminosity due to the slightly off-center collisions is negligible. On the other hand, the off-center beam-beam collisions make particle motion vulnerable to odd-order resonances. To avoid losing the pacman bunches, it is necessary to take into account the richer resonance structure when choosing the working point. With the small total tune spread in the SSC, it is not difficult to accommodate this constraint. Figures 4.5-10(e) and (f) show the tune spread of a pacman bunch that sees only half the tune shifts and tune spreads. Different pacman bunches have different working areas. The total area thus covered stretches between the regular area and the pacman area shown in the figures. The working area for beam operation has to be chosen so that the pacman area is free of low-order resonances. One sees that purely vertical crossings require a total tune space of about 0.007, which should be achievable, while alternate crossings require a smaller total tune space of about 0.004.

Possible ways to cure the pacman effect, if necessary in the operation of the SSC, include orbit and tune controls that are different for the pacman bunches, crossing beams horizontally and vertically in alternation, and developing fast kickers or using conventional magnets in the vicinity of the abort system so that the abort gap can be eliminated (although the injection gaps will remain).

4.6 Collider Operational Considerations

Proton beams are prepared in the High Energy Booster and injected into the collider rings at 1 TeV. The booster and the injection lines are discussed in Sections 4.10 and 5.9 respectively. Section 4.6.1 describes injection and the acceleration cycle in the collider rings. During this stage, beams are separated at the interaction points to avoid beam-beam effects. A beam executes betatron or synchrotron oscillations when injected with error. These oscillations need to be damped by feedback systems.

The magnet strengths, the rf voltage and rf frequency are controlled in synchronism during the 1000 seconds of acceleration. Several beam parameters, such as beam size, bunch length, energy spread and synchrotron tune, vary accordingly in synchronism along the path. These variations are discussed in Section 4.6.1, as are the effects of eddy currents induced in the vacuum chamber pipe by the changing magnetic field during acceleration or magnet quenching.

In the SSC, several processes contribute to particle loss and phase-space dilution. It is customary to describe the particle loss rate by a beam lifetime. Similarly, particle loss and phase-space dilution contribute to a luminosity lifetime. In detail, however, the behaviors of both the beam intensity and the luminosity with time during storage are not simple exponentials. In particular, synchrotron radiation damping makes the beam emittance shrink. Shrinking emittance in turn makes the luminosity increase, which causes a higher rate of particle loss. Shrinking emittance also makes the intrabeam scattering stronger, retarding further emittance shrinking. The interplay among the beam intensity, the luminosity, the emittance and other parameters is described in Section 4.6.2.

The rf requirements — choice of rf frequency, range of frequency variation and peak rf voltage — are summarized in Section 4.6.3. An additional requirement is that the rf system be reasonably free of noise in order to maintain the beam quality over long storage time. The specification on rf noise in the presence of a phase feedback system is discussed in Section 4.4.10.

4.6.1 Injection and Acceleration Cycle

Each collider ring is filled with fifteen beam batches from the 1-TeV High Energy Booster (HEB), as described in Section 4.10.5. Each batch is 18.1 μs in length (1130 bunches) and is loaded 0.16 μs behind its predecessor batch. With the revolution time of 276.7 μs, this arrangement produces a 3.0-μs abort gap between the first and the last batches. The injection-kicker rise time must be less than 0.16 μs, but its fall time can be as long as 3.0 μs. The 60-second cycle time of the HEB allows the 15 batches to be loaded in 15 minutes.

After one collider ring is filled, the polarity of the HEB is reversed and its injection and extraction systems switched so as to be able to load the second collider ring in the opposite direction. The polarity change may take a few minutes. Both rings may thus be loaded in approximately 35 to 40 minutes, allowing for several low-intensity test pulses to be made prior to the actual loading process.

Beam Injection

Beam-beam collisions are avoided by separating the beams near the crossing regions during injection and the acceleration ramp. Figure 4.6-1 shows the beam separation during injection for the high and the intermediate luminosity interaction regions. In both cases, the beams are separated horizontally by 4 mm at the interaction point and injected with a vertical opening angle (40 μrad for the intermediate-luminosity case and 90 μrad for the high-luminosity case) in order to maintain a beam-beam separation of at least 10 local beam-size standard deviations throughout the region between the vertical splitting magnets (308 m and 159 m in the two cases). After acceleration to 20 TeV, the beams are moved horizontally into collision and the crossing angle is set to 75 μrad. The crossings can be either horizontal or vertical. As the beams are brought into collision, a slight orbit adjustment at the interaction point can be performed to compensate for the orbit distortion caused by the long-range beam-beam interaction. These corrector settings can be predetermined.

For injection, the optics of the four interaction regions are modified so as to require less aperture in the high-β regions and to be more tolerant of small injection errors. (Details of the injection optics are given in Section 4.2.4. The effect of field errors in the interaction region magnets on aperture are discussed in Section 4.4.8.) After injection and acceleration, the optics are gradually transformed into the collision optics along a carefully chosen path [4.2-16].

To ensure beam stability at injection against single-bunch transverse effects, the longitudinal emittance $\epsilon_s = \sigma_E \sigma_t$ will be increased from 0.0016 eV-s to 0.035 eV-s in the HEB before injection into the collider.

Feedback Systems for Injection Errors

Collective betatron oscillations result from inevitable injection errors. Feedback systems of strength sufficient to damp them before significant emittance growth occurs are provided. This feedback process, taking into account the random magnetic field errors obtained from Table 4.3-1 and the magnet sorting according to Table 4.3-3, has been simulated by particle tracking [4.6-1]. The results using 500 particles are summarized in Table 4.6-1. The strengths of the horizontal and vertical damping systems are capable of giving a ± 2 μrad kick per cm of displacement, if located at points of normal beta. At 1 TeV, this corresponds to a damping time of 45 revolutions. The injected beam has normalized emittances of $\epsilon_x = \epsilon_y = 1$ μm-rad, and an rms relative energy spread of $\sigma_\delta = 1.5 \times 10^{-4}$. In the simulation it was assumed that the chromaticities from random sextupoles have been corrected by adjusting the chromaticity sextupoles. Injection jitter tolerances have been set to be ± 1.5 mm in x and y and $\pm 1.5 \times 10^{-4}$ in δ [4.3-10]. Without feedback, the beam size would double by filamentation, but the feedback system is capable of preserving the beam sizes under these injection errors. Beams injected with much larger errors (for example, because of failure of one of the injector kicker modules) will suffer significant beam size growth, and have to be aborted for colliding beam operations.

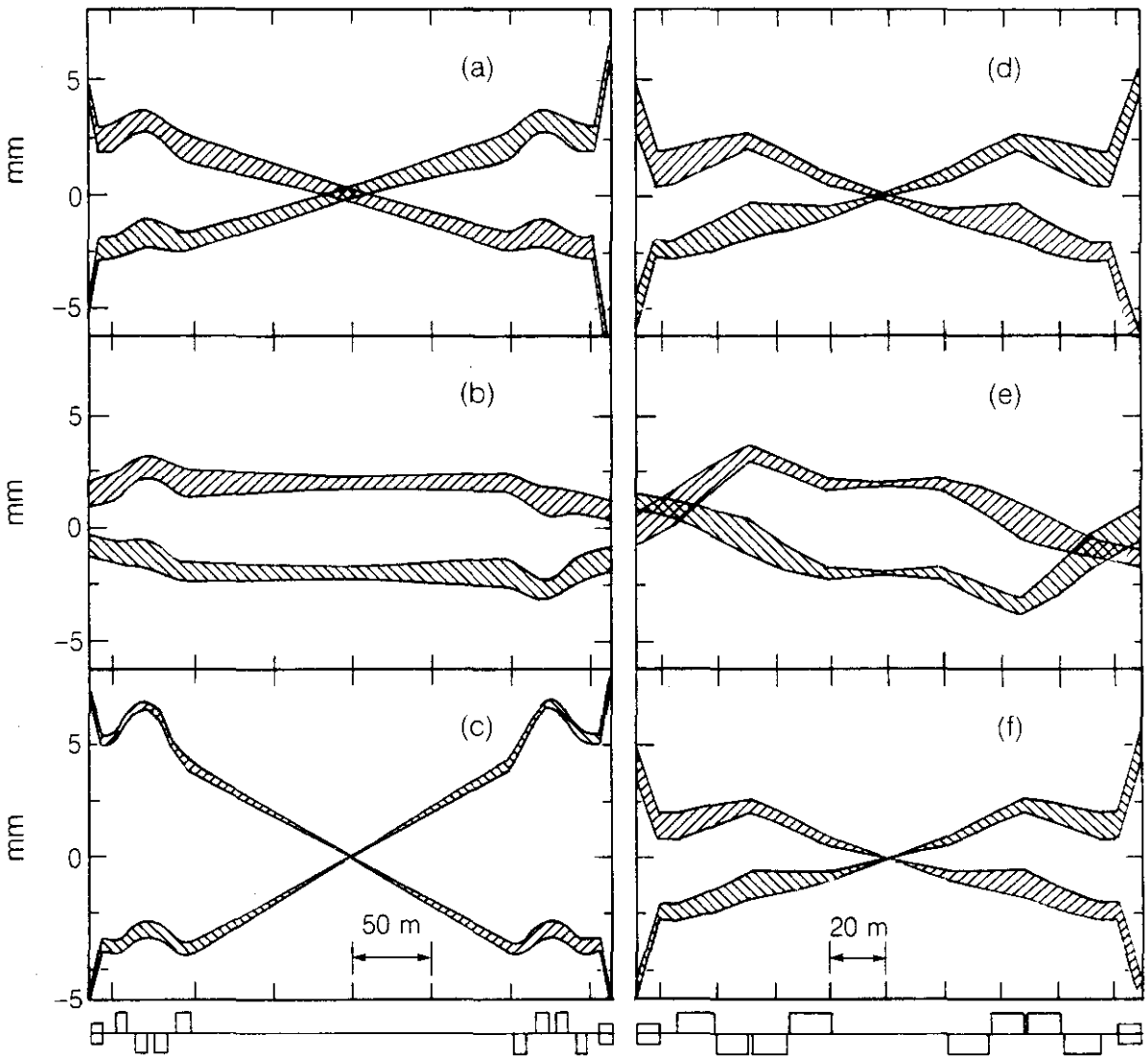

Figure 4.6-1. Beam crossing geometry around the interaction points. (a) and (b): Vertical and horizontal beam profiles for the intermediate-luminosity IR during injection and acceleration. Shaded regions indicate ± one rms beam spread. (c): Beam profiles during beam collisions at 20 TeV. (d), (e) and (f) are the same as (a), (b) and (c) but for the high-luminosity IRs.

Table 4.6-1

Percentage increases in the rms beam spread $\Delta\sigma_x$ and $\Delta\sigma_y$ after damping for various injection conditions, given by a particle tracking simulation [4.6-1]. The beam is injected with offsets x_0 and y_0 (at β = 330 m) and δ_0. The feedback damping time is 45 revolutions (12.5 ms).

x_0 (mm)	y_0 (mm)	δ_0 (10^{-4})	$\frac{100\,\Delta\sigma_x}{\sigma_x}$	$\frac{100\,\Delta\sigma_y}{\sigma_y}$
0	0	0	0.7	0.4
1.5	1.5	0	2.4	7.4
1.5	1.5	1.5	1.7	14.3
2.5	0	0	2.8	2.4
2.5	2.5	0	5.6	17.3
0	0	4.5	2.1	14.2
1.5	6.0*	1.5	8.6	102.3

*One kicker module fails.

It is envisioned that the feedback system also serves to control the collective instabilities discussed in Sections 4.5.4 and 4.5.5.

Orbit, Chromaticity, and Persistent Current Correctors

Two other correction systems are normally active throughout the operating cycle. Dipole coils in the correction spools serve to correct the horizontal and vertical closed orbits and sextupole coils in the spools reduce the normal chromaticity to approximately zero. These correction systems track the ring magnets. A separate correction system will be used to compensate the magnetic field perturbations due to the persistent currents in the superconducting filaments and saturation in the iron. The sextupole and decapole components of these known field errors are corrected by coils distributed on the dipole bore tubes. These corrections are maintained during injection and acceleration.

Acceleration Cycle

The two beams are accelerated from 1 to 20 TeV in 1000 seconds. It is necessary that several collider parameters be changed in a programmed manner during acceleration. The magnets are ramped linearly in time, requiring an energy gain of 5.26 MeV per turn. To stablize transverse and longitudinal emittance growth from intrabeam scattering during the storage cycle, the longitudinal emittance is increased approximately linearly with time during the acceleration cycle from 0.035 to 0.233 eV-s by controlled injection of rf noise into the 375 MHz acceleration system. A constant peak rf voltage of 20 MV is satisfactory for this acceleration cycle. Figure 4.6-2 gives the values of several parameters during the 1000-

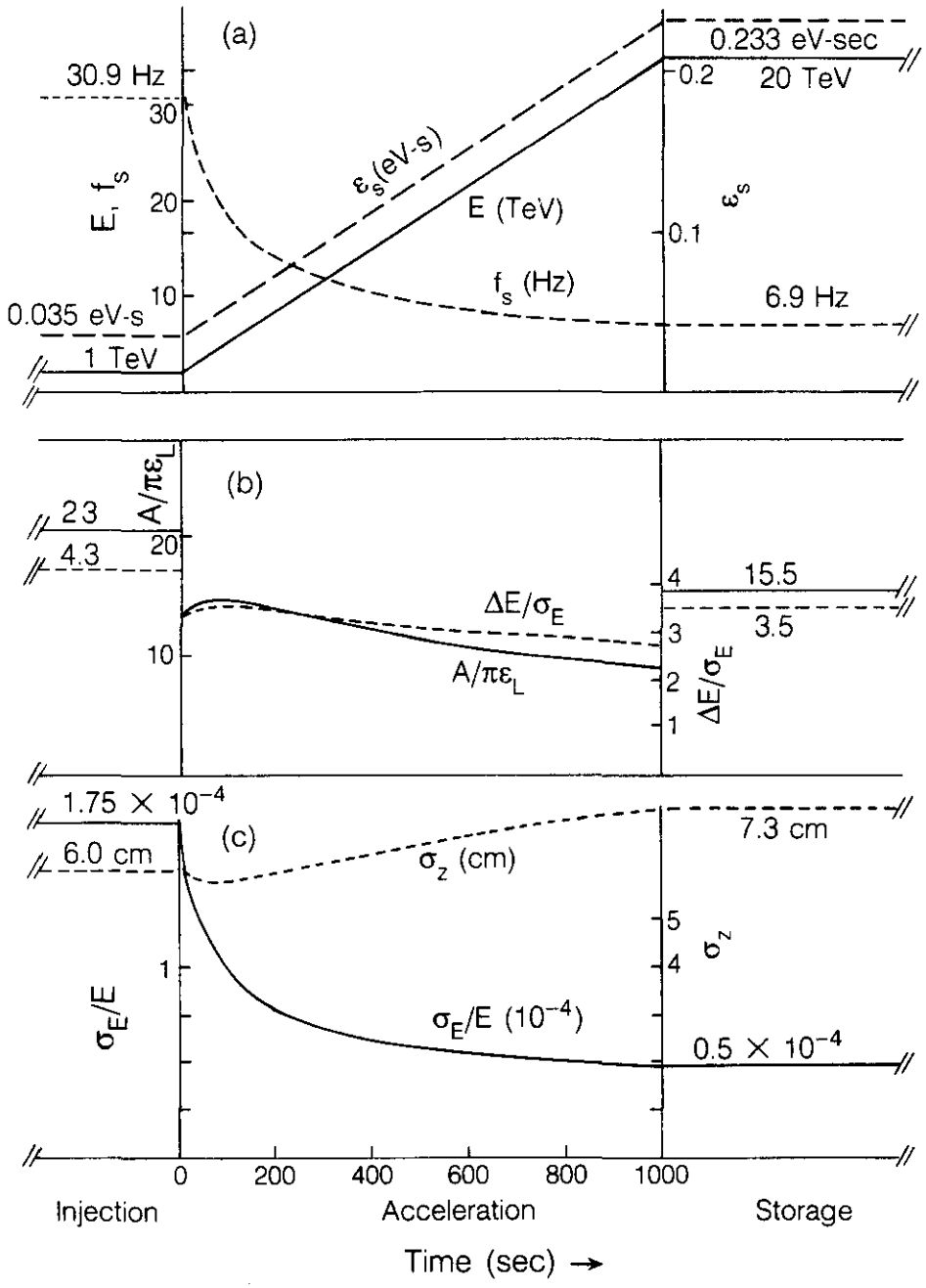

Figure 4.6-2. Variation of rf and beam parameters during the 1000-second acceleration ramp. The peak 375 MHz rf voltage is kept constant at 20 MV. (a) beam energy E, longitudinal emittance $\epsilon_s = \sigma_E \sigma_t$, synchrotron frequency f_s. (b) the ratio of bucket area A to beam area $\pi\epsilon_s$ and ratio of bucket half-height ΔE to rms energy spread σ_E. The discontinuities at the end of acceleration are caused by a shift in the rf phase. (c) rms longitudinal spread σ_z and rms fractional energy spread σ_E/E.

second acceleration time. Feedback control of beam stability along the path has been verified using the program ZAP [4.5-17,-18].

Eddy Currents

During acceleration, the changing magnetic field induces an eddy current in the vacuum chamber pipe that flows longitudinally along the pipe wall. There are two consequences — an induced magnetic dipole field contribution and ohmic heating. Because of the slow ramping, such eddy current effects are weak in the SSC.

The eddy current induces a dipole magnetic field that opposes the applied field,

$$\Delta B_y = -\mu_o \dot{B}\, b\, \sigma \Delta/2 \tag{4.6-1}$$

where σ is the conductivity of the pipe material, b is the pipe radius, Δ is the pipe thickness. Taking the ramping rate to be $\dot{B}$ = 6.6 tesla/1000 s, $\sigma\Delta = 1.8 \times 10^9\,(\Omega\text{-m})^{-1} \times 0.1$ mm for the copper coating at 4 K (corresponding to RRR $\simeq$ 30 and a thickness of about half of the skin depth at 3600 Hz [4.6-2]; the stainless steel contribution is negligible), b = 16.5 mm, we obtain $\Delta B_y = -0.12$ gauss, or $\Delta B_y/B = -0.36 \times 10^{-4}$ at 1 TeV. This small field change can easily be compensated by the dipole orbit correctors, if necessary. The ohmic power loss created by the eddy current is given by

$$P = \pi \dot{B}^2 b^3 \sigma \Delta (2\pi\rho) \tag{4.6-2}$$

where ρ = 10.1 km is the bending radius. The loss is 7 watts per ring. The current in the two halves of the pipe wall flow in opposite directions, each carrying a current of magnitude

$$I = 2\dot{B}\, b^2 \sigma \Delta \tag{4.6-3}$$

which is about 0.64 amperes. The corresponding equatorial pressure on the beam pipe is $BI/2b$, or 0.02 psi at the end of acceleration, an insignificant value.

For the more rapidly cycling HEB, the eddy current effects are for the most part ignorable because there is no copper layer on the stainless steel beam pipe. Even with a ramping rate 30 times faster than the main ring, the incremental field only is $\Delta B_y \simeq -0.03$ gauss. The total ohmic power loss during ramping is approximately 3 W, or 0.15 kJ/cycle, a completely negligible amount.

The rapid time variation of field during a magnet quench — with a change of 6.6 tesla in a fraction of a second — causes much larger transient eddy currents and mechanical forces than from ramping. Pressures exceeding the yield strength of beam pipe materials can occur if care is not taken to keep the current, Eq. (4.6-3), within bounds [4.6-3]. Too thick an inner layer of very high conductivity material can be dangerous. A balance must be reached between the desire for low surface impedance of the inside of the beam pipe at low frequencies (see Sections 4.5.3 and 4.5.5) and mechanical integrity during a quench [4.6-4].

4.6.2 Beam and Luminosity Lifetimes

Table 4.6-2 lists several processes of particle loss and emittance change, together with their underlying causes. In this section, we discuss the effect of these processes on the beam intensity and the luminosity. Collective effects, effects of magnet field nonlinearities and beam-beam effects are not treated. Proper choices of operating conditions and corrections make these latter effects unimportant in the present considerations.

Table 4.6-2
Leading Causes of Particle Loss and Emittance Change in the SSC

Causes	Particle Loss	Emittance Change
beam collisions at interaction points	inelastic interactions	elastic scattering
residual gas	nuclear interaction	multiple scattering
Coulomb scattering within bunch	Touschek lifetime (single scattering)	intrabeam scattering (multiple scattering)
synchrotron radiation	quantum lifetime (effect negligible)	radiation damping

Ignoring the small modification introduced by a finite crossing angle, the rate of change of luminosity $\mathscr{L}$ is related to the rates of change of the number of particles per bunch N_B and the emittance ϵ through

$$\frac{1}{\mathscr{L}}\frac{d\mathscr{L}}{dt} = \frac{2}{N_B}\frac{dN_B}{dt} - \frac{1}{\epsilon}\frac{d\epsilon}{dt} \tag{4.6-4}$$

The particle loss rate per bunch from proton-proton collisions is given by

$$(dN_B/dt)_{pp} = -\mathscr{L}_t \Sigma_{inel}/M \tag{4.6-5}$$

where $\mathscr{L}_t$ is the total luminosity at two IRs with $\beta^* = 0.5$ m and two IRs with $\beta^* = 10$ m, $\Sigma_{inel} = 90$ mb is the cross section for inelastic collisions, $M = 17280$ is the number of bunches per beam. The initial loss rate, Eq. (4.6-5), is 1.1×10^4 particles/s per bunch. Another possible contribution to particle loss collisions is bremsstrahlung. It is estimated that, for the SSC with two high-luminosity IRs, the loss rate is only about 40 protons/s [4.6-5].

Although the main particle loss is from collisions in the IRs, other processes contribute. The second particle loss mechanism listed in Table 4.6-2, residual gas nuclear scattering, is given by

$$\frac{1}{N_B}\frac{dN_B}{dt} = -c\sum_i N_i\sigma_i$$

$$= -\sum_i \frac{(P_i/10^{-9}\ \text{Torr})(\sigma_i/52\text{mb})}{5030\ \text{h}} \tag{4.6-6}$$

where N_i is the number density of the ith molecular species in the gas, σ_i the cross section for a 20 TeV proton incident on the ith kind of molecule, and P_i is the room-temperature-equivalent partial pressure of the ith species. The partial pressures estimated on the basis of desorption measurements made at the National Synchrotron Light Source [4.6-6] are given in Table 5.4-1. From them we obtain a residual gas nuclear scattering lifetime of greater than 300 h, or an initial particle loss rate of 7000 s^{-1} per bunch. This particle loss contributes a cryogenic load of 380 watts per beam.

The third mechanism is the Touschek effect [4.5-22]. The loss rate is

$$(dN_B/dt)_{\text{Touschek}} = -(9.4\times10^{-19}\ \text{s}^{-1})\,N_B^2 \tag{4.6-7}$$

which gives a negligible initial loss rate of 53 particles per second per bunch.

Similarly, the emittance change has contributions from the four mechanisms listed in Table 4.6-2. The first contribution from elastic collision events can be written as

$$(d\epsilon/dt)_{\text{pp}} = (\beta_1^*\mathscr{L}_1 + \beta_2^*\mathscr{L}_2)\sigma_{\text{el}}\langle\theta^2\rangle/MN_B \tag{4.6-8}$$

where $\langle\theta^2\rangle^{1/2} = 9\ \mu$rad is the estimated rms projected scattering angle at 20 TeV [4.6-7], $\sigma_{\text{el}} = 30$ mb is the estimated elastic scattering cross section, $\beta_{1,2}^*$ and $\mathscr{L}_{1,2}$ are the beta-functions and luminosities of the two high-luminosity and two intermediate-luminosity interaction points, respectively. Taking $\beta_1^* = 0.5$ m, $\beta_2^* = 10$ m and initial values of $\mathscr{L}_1 = 10^{33}\ \text{cm}^{-2}\text{s}^{-1}$ and $\mathscr{L}_2 = 5.6\times10^{31}\ \text{cm}^{-2}\text{s}^{-1}$, we obtain an initial rate of $(d\epsilon/dt)_{\text{pp}} = 2.0\times10^{-17}$ m/s.

Multiple scattering from the residual gas contributes

$$(d\epsilon/dt)_{\text{RG}} = c\beta_{\text{ave}}d\langle\theta^2\rangle/ds \tag{4.6-9}$$

This can be rewritten as

$$(d\epsilon/dt)_{\text{RG}} = (1.76\times10^3\ \text{m s}^{-1})\,\beta_{\text{ave}}\left(\frac{14.1\ \text{MeV/c}}{p_o}\right)^2\sum_i\frac{P_i\mu_i}{X_i} \tag{4.6-10}$$

where p_o is the beam momentum and P_i, μ_i, and X_i are, respectively, the partial pressure (in Torr), molecular weight (in g/mole), and the radiation length (in g cm^{-2}) for the ith molecular species in the residual gas. Using the composition and limits given in Table 5.4-1, one obtains $(d\epsilon/dt)_{\text{RG}} < 7\times10^{-17}\ \text{m s}^{-1}$.

The remaining two effects on emittance changes are the most important for the SSC. The intrabeam scattering contribution is discussed in Section 4.5.6. The result at 20 TeV

can be summarized by the approximate expression

$$(d\epsilon/dt)_{\mathrm{IBS}} = 3.3 \times 10^{-37} N_B/\epsilon \tag{4.6-11}$$

With $N_B = 7.3 \times 10^9$ and $\epsilon = 4.7 \times 10^{-11}$ m, the initial emittance growth rate is $(d\epsilon/dt)_{\mathrm{IBS}} = 5.1 \times 10^{-17}$ m/s. Although this initial rate is only comparable to the two previous effects, the intrabeam scattering contribution becomes more important as the emittance shrinks by synchrotron radiation damping.

Synchrotron radiation damping times, as given in Section 4.7.2, are 12.5 hours and 25 hours for the longitudinal and transverse amplitudes respectively. The transverse emittance damping time is half that of the amplitude damping time, or 12.5 hours. This gives

$$(d\epsilon/dt)_{\mathrm{SR}} = -(2.2\times10^{-5}\mathrm{s}^{-1})\,\epsilon \quad . \tag{4.6-12}$$

The initial rates of change of N_B and ϵ produce an increasing luminosity; however, they are not sufficient to determine the long-term behavior of the beam intensity and the luminosity. The interplay among the parameters N_B, $\mathscr{L}_t$ and ϵ are obtained by numerically integrating the rate equations. With these parameters given, the head-on and long-range beam-beam tune shifts, $\Delta\nu_{HO}$ and $\Delta\nu_{LR}$, can be obtained as functions of time. These results are shown in Fig. 4.6-3.

Because of synchrotron radiation damping, the luminosity increases initially as the emittance decreases with time. For small emittances, intrabeam scattering becomes more important, slowing the emittance damping process. In the meantime, the beam intensity decreases sufficiently that the luminosity reaches a maximum and then decreases with time. After 50 hours of colliding beams, the luminosity is still roughly 10^{33} cm^{-2}s^{-1}. In this scenario, we have not restricted the number of events per collision. In case this constitutes a problem for the detectors, it is conceivable that β^* can be increased by small steps to compensate for the increasing luminosity. It is possible that, in steady state of operation, the beams can be kept colliding for a few days before a refill is needed.

4.6.3 Radio-Frequency Systems Requirements

The rf system is needed for maintaining the bunched nature of the injected beam at 1 TeV, for accelerating the beam from 1 to 20 TeV and for storing the beam at 20 TeV. In the SSC, the rf system is small; a total of eight 5-cell-cavities per ring is sufficient to provide the beam needs. The rf cavities are located in the utility sections, as shown in Fig. 4.2-6. The rf frequency is chosen to be 374.741 MHz, corresponding to a wavelength of exactly 0.8 meters. Various accelerator physics considerations give a broad optimum in choosing this parameter. Final selection is then made by choosing a proper harmonic number, given the lattice design.

The accelerator physics considerations are as follows:

(a) The bunch spacing was chosen to be 4.8 m in Section 4.1.2. This spacing must be an integral multiple of the rf wavelength. This gives a lower limit of rf frequency of 62.5 MHz.

(b) The luminosity reduction factor due to crossing angle α, Eq. (4.1-12), is given by $(1+r^2)^{-1/2}$, where $r = \alpha\sigma_z/2\sigma$. Lower rf frequencies give longer rms bunch longitudinal

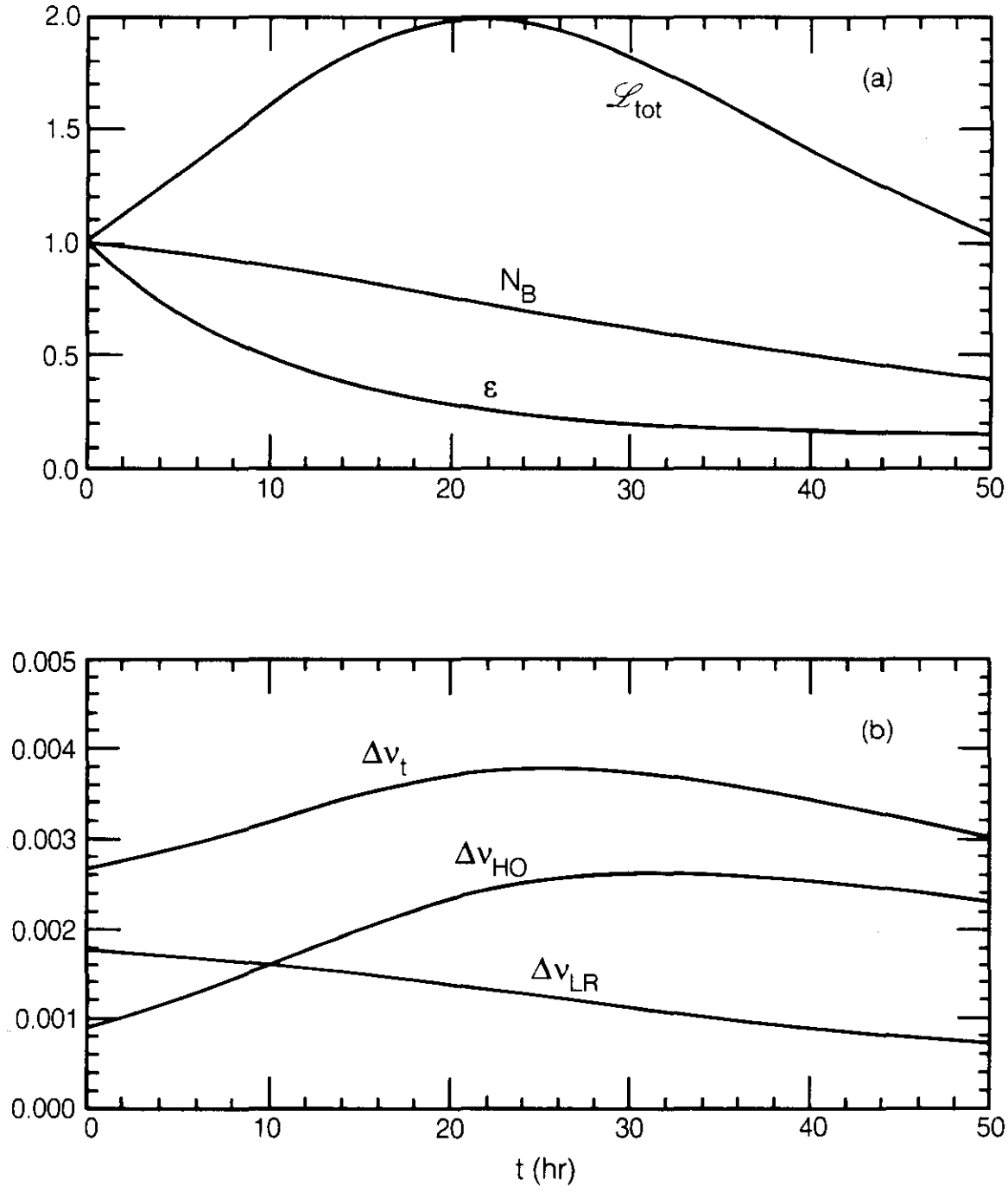

Figure 4.6-3. Time dependence of various quantities during collision. (a) N_B, $\mathscr{L}_t$ and ϵ, normalized by their initial values. (b) $\Delta\nu_{HO}$, $\Delta\nu_{LR}$ and their sum $\Delta\nu_t$ for the high luminosity interaction points.

spread σ_z, producing a larger reduction factor. For a given ratio of bucket to beam area in synchrotron phase space, σ_z is inversely proportional to the rf frequency, as is shown below in Eq. (4.6-13). With a crossing angle of 75 μrad, the reduction factor for the high-luminosity operation for several rf frequencies are given in Table 4.6-3. To maintain the design luminosity goal, the reduction factor has to be compensated by increasing the number of particles per bunch N_B by the inverse square root of the reduction factor. This in turn increases the cryogenic load from synchrotron radiation heating. To limit this effect, the rf frequency should be 200 MHz or higher.

Table 4.6-3
Dependence of a Few Parameters on the rf Frequency

f_{rf} (MHz)	σ_z (cm)	r	Luminosity reduction factor	N_B (10^9)	Synchrotron radiation power/beam (kW)
60	42	3.3	0.29	12.8	15.7
120	21	1.6	0.52	9.5	11.7
180	14	1.1	0.68	8.3	10.2
240	10.5	0.81	0.78	7.8	9.5
300	8.4	0.65	0.84	7.5	9.2
360	7.0	0.55	0.88	7.3	9.0
420	6.0	0.46	0.91	7.2	8.9
480	5.3	0.41	0.92	7.1	8.8
600	4.2	0.33	0.95	7.0	8.7

(c) The parameter r also characterizes the crossing-angle-induced beam-beam synchro-betatron resonances, as described in Section 4.5.7. For the SSC, it is desirable to keep the value of r less than 1. Again, this indicates the rf frequency should be higher than about 200 MHz.

(d) Parasitic heating becomes more serious as the bunch length becomes shorter. The load on the cryogenic system per beam as a function of the rms longitudinal spread σ_z is shown in Fig. 4.6-4 [4.6-8]. Limiting the load to 1 kW requires $\sigma_z > 5$ cm or $f_{rf} < 500$ MHz.

(e) The multi-bunch collective instability growth rates depend on the bunch length. The growth time of the most unstable transverse dipole mode decreases from 2.3 s for σ_z = 7 cm to 1.8 s for σ_z = 5 cm, and 1.5 s for σ_z = 3 cm at 1 TeV. More importantly, both the transverse and longitudinal quadrupole modes are no longer Landau-damped if $\sigma_z < 4$ cm [4.5-17]. Without feedback systems for these modes in the present design, f_{rf} needs to be less than 600 MHz.

(f) Single-bunch collective instabilities become more pronounced for shorter bunches. The leading transverse mode-coupling instability is cured by fixed energy spread σ_δ, but the transverse and longitudinal microwave instabilities also become limiting factors if $\sigma_z < 4$ cm.

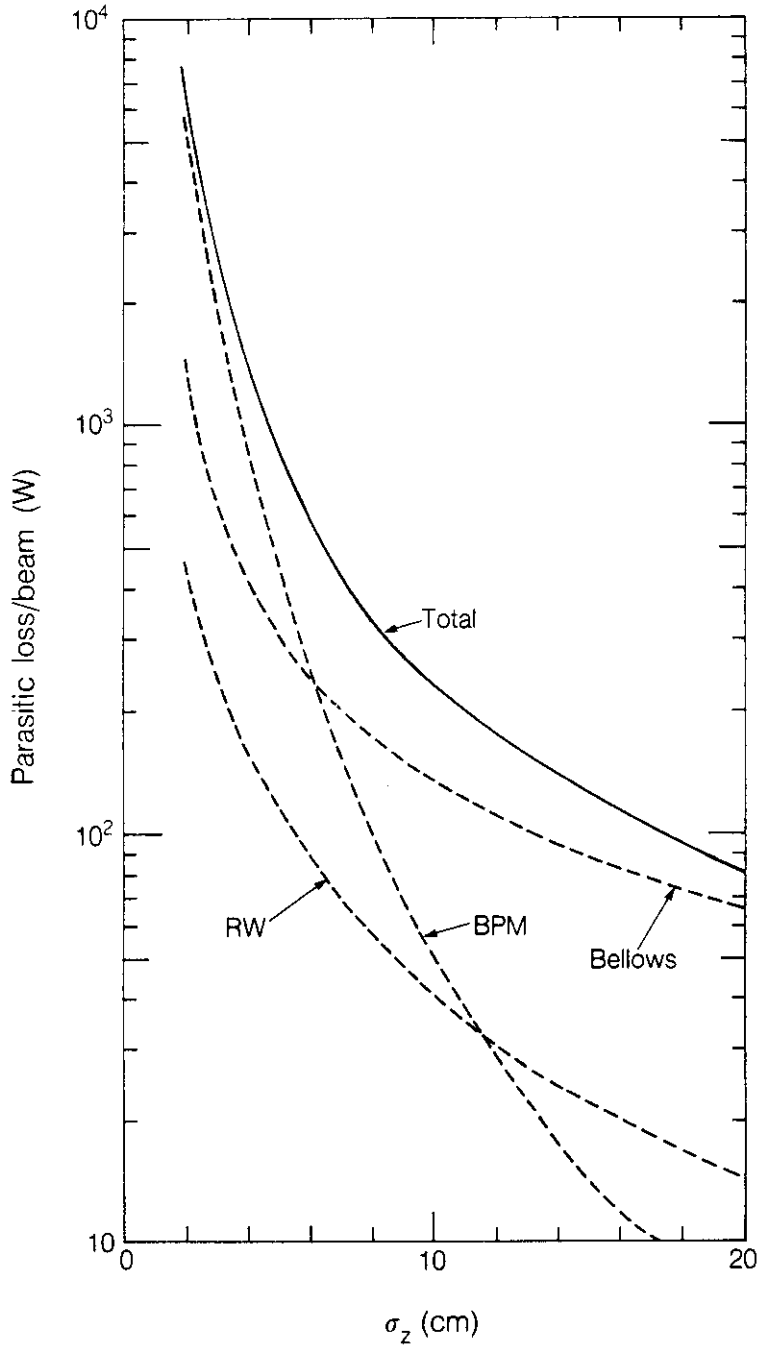

Figure 4.6-4. Parasitic heating contributions to the cryogenic load from resistive wall of beam pipe, beam position monitors, and bellows.

(g) The emittance growth rate from intrabeam scattering is inversely proportional to the bunch length. In order to benefit from the luminosity increase caused by synchrotron radiation damping, the intrabeam emittance growth time should be longer than 60 hrs. A growth time of 120 hrs at 360 MHz implies an upper limit of roughly double that, or 700 MHz, for the frequency.

The above considerations indicate that the choice of the rf frequency has a broad optimum in the 200 to 500 MHz range. To fine tune this parameter, we have to consider the choice of a harmonic number h, given the lattice design.

The distance between interaction points within a cluster is exactly $L_x = 2400$ m and the distance around the arc is exactly $L_a = 31872$ m. The total circumference is $L = 8L_x + 2L_a$. The rf wavelength λ_{rf} is chosen so that L, L_x and L_a are integer multiples of λ_{rf} and that there are many common factors among these integers to provide a wide range of choices of possible bunch spacing S_B. The procedure gives the following choice [4.6-9],

$$f_{rf} = 374.741 \text{ MHz}, \quad \lambda_{rf} = 0.8 \text{ m exactly},$$

$$L_x/\lambda_{rf} = 3000, \quad L_a/\lambda_{rf} = 39840, \quad h = 103680.$$

Possible choices of S_B are any combination of integer factors of $2^4 \times 3 \times 5$ times the rf wavelength. The design bunch spacing is 4.8 m, which means every sixth rf bucket is occupied and there are nominally 17280 filled buckets, discounting the injection and abort gaps.

The rf voltage must be sufficient to supply the necessary energy gain per particle of 5.26 MeV per turn, determined by the 1000-second accelerating ramp, and 0.123 MeV per turn at 20 TeV to compensate for synchrotron radiation. The rf voltage also has to provide a bucket compatible with the beam energy spread and bunch length requirements. To control emittance growth at 20 TeV from intrabeam scattering, the longitudinal emittance $\epsilon_s = \sigma_E \sigma_l$ has to be increased by a factor of 6.6 from 0.035 eV-s at 1 TeV to 0.233 eV-s at 20 TeV. By keeping a constant rf voltage, the bucket area increases by a factor of $\sqrt{20}$ from 1 to 20 TeV. A constant rf voltage of 20 MV allows the longitudinal emittance to be deliberately increased linearly with time during the acceleration ramp, while maintaining a reasonable ratio of bucket to beam area and without requiring additional aperture because of momentum width. This acceleration cycle is illustrated in Fig. 4.6-2.

In order to control the emittance growth from rf noise, we have maintained a bucket-to-beam area ratio R of the order of 15.5 for the SSC (see Section 4.4.10). Given R, the rms bunch longitudinal spread σ_z is simply related to the rf wavelength by

$$\sigma_z = (2\lambda_{rf}/\pi)\,|\alpha(\phi_s)/R\pi|^{1/2}(\cos\phi_s)^{-1/4} \tag{4.6-13}$$

where ϕ_s is the synchronous phase and $\alpha(\phi_s)$ is the normalized rf bucket area [4.5-1] (1.0 for $\phi_s = 0$ and 0.582 for $\phi_s = 15.24°$ during ramping). With $R = 15.5$ at 20 TeV, we have $\sigma_z = 0.091\ \lambda_{rf}$. During ramping, R is typically about 12, which gives $\sigma_z = 0.080\ \lambda_{rf}$. The small variation in bunch length during the ramp follows from the similarly small variation in R produced by the acceleration scheme. At 20 TeV, R is 15.5, sufficient to prevent undesired long-term emittance growth from noise in the rf system.

The rf cavities contribute to high-Q beam impedances that can potentially drive multi-bunch instabilities, as described in Sections 4.5.4 and 4.5.5. To minimize this effect, it is necessary to locate the cavities where beta functions are not excessively large. For the present location in the utility section, the average beta functions over its 25 meters are β_x = 70 m and β_y = 220 m, which are quite acceptable. Additionally, the rf cavities are located in a region of zero dispersion to avoid coupling between synchrotron and betatron degrees of freedom.

There are two common circumstances when the rf frequency needs to be slightly adjusted. The first is during injection and acceleration; the second is when the chromaticities and dispersion functions are to be measured during operation. The rf frequency is 374,740,568.8 Hz at 20 TeV. Because of the slightly slower initial speed of the protons at injection, it is decreased by 161.2 Hz and is linearly interpolated during the acceleration time of 1000 seconds. As mentioned in Section 4.4.3, an rf frequency swing range of ± 36 Hz is sufficient, in principle, to measure the chromaticities to an accuracy of 0.1 and the dispersion functions to an accuracy of 3 cm. This frequency change is easily accommodated.

4.7 Synchrotron Radiation

It is well known from the operation of electron accelerators that high energy electrons moving in a magnetic field radiate energy in the form of light. The existence of high power synchrotron radiation, so called because it was first observed in an electron synchrotron, has had a major influence on the design of electron accelerators and storage rings, but until the SSC, it has had a totally negligible effect on proton ring designs. Although the power radiated in the SSC is much less than in large electron storage rings, it is sufficient to have a major impact on the cryogenic system and the vacuum system. It has very little influence on the rf design. The damping associated with the radiated photons, though small, does have important implications for the luminosity lifetime.

4.7.1 Description of Synchrotron Radiation

The energy loss per turn for a proton of mass m_p, total energy E, traveling at constant speed v in a circle of radius, ρ, is

$$U = \frac{e^2 c Z_0}{3\rho} \left(\frac{v}{c}\right)^3 \left(\frac{E}{m_p c^2}\right)^4 \tag{4.7-1}$$

The result is also valid for a proton moving in a closed path of circumference C with magnets of bending radius ρ. Numerically,

$$U(\text{MeV}) = 7.78 \times 10^{-6} \frac{[E(\text{TeV})]^4}{\rho(\text{km})} \tag{4.7-2}$$

The synchrotron light has a power spectrum as a function of photon energy, u, given by

$$\frac{dP(u)}{du} = \frac{P_\gamma}{u_c} S(u/u_c) \tag{4.7-3}$$

where $u_c = (3\hbar c/2\rho)\,(E/m_p c^2)^3$ is the characteristic photon energy above which half the power is radiated, P_γ is the total radiated power, and S is a universal function of the dimensionless ratio u/u_c [4.7-1]. Numerically, the characteristic energy for protons is

$$u_c(\text{eV}) = 0.358\,\frac{[E(\text{TeV})]^3}{\rho(\text{km})} \tag{4.7-4}$$

Because the function S peaks near $u = u_c$ and falls off rapidly above it, the power spectrum can be very qualitatively described as being composed of photons of energy near the characteristic energy, u_c, with relatively little power at frequencies very much less than or greater than this characteristic energy. The photon distribution, that is, the number of quanta emitted per unit time per unit energy interval at energy u, is

$$\frac{dn(u)}{du} = \frac{P_\gamma}{u_c u} S(u/u_c). \tag{4.7-5}$$

This diverges like $u^{-2/3}$ at low photon energy, although the integral is finite. The effect of the synchrotron radiation on the vacuum system most probably depends on the power radiated per unit length. The effect on the cryogenic system, of course, depends on the total radiated power, because that power must be taken out of the cooling stream at low temperature—a very inefficient process.

With a bending radius of 10.1 km, at 20 TeV the characteristic energy is $u_c = 284$ eV. The energy loss per turn, Eq. (4.7-2), is $U = 0.123$ MeV. The average power radiated per particle is $P_\gamma = cU/C$, where C is the circumference of the ring (82.944 km). With a total of 1.27×10^{14} protons per ring ($I \simeq 73$ mA), the total synchrotron power loss per beam is 9 kW. The number of photons per second radiated by each beam is approximately 6×10^{20}.

The estimate of 9 kW is based only on the radiation caused by bending magnets. Orbit distortion contributes a small correction because of radiation in the quadrupole magnets. The power radiated in the quadrupole magnets can be estimated assuming an rms orbit deviation in the quadrupoles. Taking 0.5 mm as the rms orbit deviation after correction, the radiation in the arc quadrupoles is about 0.1 W per ring. Allowing for an rms orbit distortion of 3 mm, the radiation power per ring becomes 3.1 W. The interaction region quadrupoles may require a larger orbit allowance for comfortable operation. Taking it to be 1 cm, the radiated power may reach 2.0 W per interaction region per beam. In addition to radiation in the quadrupoles, there is radiation in the dipole orbit correctors, which have an rms strength of 7.7 μrad. Allowing for the possibility of 3 times the rms strength, they contribute up to 2.7 W per ring. The additional requirement on the cryogenic system due to orbit distortion and correction is therefore not in excess of $3.1 + 6 \times 2.0 + 2.7 = 17.8$ W per beam.

4.7.2 Consequences of Synchrotron Radiation

Cryogenic Considerations

Under normal circumstances the few kilowatts of radiated power would be no problem, because it corresponds to only a tenth of a watt per meter. With superconducting magnets, however, it is difficult and expensive to remove heat at temperatures near 4 K and the impact is significant. Heat loads for the SSC magnet design are purposely very low, in order to make the operating cost of the machine low. The synchrotron radiation heat load for both beams of 18 kW represents about half the total 4 K cryogenic load. Each kilowatt of power that has to be removed at 4 K takes about 0.5 MW of compressor power at room temperature. A synchrotron radiation heat load of 18 kW, then, implies an operating demand of about 10 MW. Considerable thought has been given to providing a liner for the beam tube that intercepts the radiation at temperatures higher than 4 K, and therefore saves compressor power in proportion to the higher temperature. At this time, however, it does not appear that the additional complications would be worthwhile for the magnetic field level considered.

Vacuum Considerations

The large number of photons hitting the beam tube desorb gas molecules that are dissolved in the wall material. This is a well known problem in electron storage rings, and will also be a factor in the operation of the SSC. An experiment to determine the gas pressure in the cold beam tube due to the desorbed gases was performed at the National Synchrotron Light Source (NSLS) at Brookhaven National Laboratory. The characteristic energy and radiated power of the vacuum ultraviolet storage ring at NSLS are very close to those parameters for the SSC. A description of and the results from that experiment are discussed briefly in Section 2.4.5 and in detail in Section 5.4. Here we will simply state the results. The predominant gas desorbed is hydrogen. An upper limit of hydrogen gas pressure in the cold beam tube has been determined to be 8×10^{-9} Torr, room temperature equivalent. The beam lifetime from the amount of hydrogen and lesser amounts of other gases, mainly CO and CO_2, is estimated to be in excess of 300 hours, considerably greater than design specifications.

Additionally, the desorbed gases contribute to possible instabilities because of electron neutralization of the beam, and increase the possibility of pressure avalanches. These phenomena are due to the ionization of residual gas and the trapping of the produced electrons, or the acceleration of the positive ions to the wall by the electrostatic potential of the beam. Because the cold beam tube is such an effective pump, the pressure avalanches are not a problem, even at much higher beam intensities than presently envisioned. The bunched nature of the beam considerably ameliorates beam neutralization by trapped electrons, so this effect also appears not to be serious. If the beams were continuous instead of bunched, or if the stored beams were antiprotons instead of protons (antiprotons trap slowly moving positive ions, instead of fast electrons, so the bunch structure does not help in clearing them from the beam), the above conclusions might have to be reconsidered. Details on the phenomena of electron beam neutralization, pressure avalanche, and multifactoring are given in Section 5.4.

Acceleration Systems

Because the energy loss per turn is very small compared with the rf voltage, the effect on the rf system is small. The energy loss does have the consequence, however, of making it nontrivial to run with debunched beams. Running with continuous beams would require a special acceleration system and a method for handling the abort gap.

Radiation Damping

There are two other effects of the synchrotron radiation upon the beam. Because of the radiation of energy, the longitudinally and transverse emittance of the stored beam are not constant, and in fact decrease exponentially with a time constant that, in the longitudinal dimension, is just the time it would take a particle to radiate away all its energy. The explicit formula is [4.1-6]

$$\tau_{\parallel} \simeq E/Uf_0 \tag{4.7-6}$$

where $f_0 = 3614$ Hz is the revolution frequency and U is given by Eq. (4.7-2). For the transverse directions, $\tau_{\perp} \simeq 2\tau_{\parallel}$. This phenomenon, which decreases the beam size, does not go on forever, for there is a competing process arising from the statistical fluctuations due to the quantum nature of the discretely emitted radiation. These two processes result in an equilibrium transverse beam size and energy spread. In any case, because the radiation levels are so small, the damping time constants are very long, approximately 12.5 hours for the longitudinal amplitude, and twice that for the transverse amplitude. Likewise, the equilibrium beam size and energy spread due to synchrotron fluctuations are much smaller than effects due to other causes. This is in contrast to the situation in electron storage rings, where these phenomena are the major factors determining beam size.

4.7.3 Conclusions

The fact that protons at 20 TeV produce significant synchrotron radiation has an important impact on the cryogenic system, approximately doubling the heat load at 4 K. It also creates a measurable gas pressure in the cryogenic beam tube. This pressure has been experimentally determined and implies a beam lifetime lower limit of 300 hours. This lifetime limit exceeds design requirements. The effects of quantum fluctuations are insignificant. Implications of damping for the luminosity lifetime are covered in Section 4.6.2.

4.8 Beam Losses

Beam losses occur through p-p collisions at each interaction point, through beam-gas scattering which occurs uniformly around the rings, as well as through instabilities and beam manipulation errors. To deal with the resulting radiation, materials and components must be carefully selected, and designs must accommodate dissipation of the radiation heat load, shielding against background in the experimental facilities, protection of tunnel electronics, and radiation safety. Radiation safety is discussed in Section 6.9; the other considerations are the subject of this Section.

In an interaction region (IR) operating with 20 TeV beams at a luminosity of 10^{33} cm^{-2}s^{-1}, an effective p-p cross section of 120 mb results in approximately 800 W of

secondary and scattered particles. Most of the energy flux is highly collimated along the beam directions. Low-energy charged particles leave the beam pipe in the IR triplets, resulting in a substantial cryogenic heat load. Neutrals continue forward, to a dump provided to absorb them. Quasi-elastic scattering products remain within the machine aperture for some distance; their fate is controlled by collimation to prevent excessive backgrounds in other IRs.

Beam loss from scattering by residual gas in the beam pipe can be characterized by its contribution to the beam lifetime. For a vacuum of 8×10^{-9} Torr and an effective beam-gas cross section per atom of 50 mb, the beam lifetime is 300 hours. An average of 4.6 mW m^{-1} of scattered particles will strike the vacuum pipe in each ring. This ubiquitous process produces low-energy neutrons and other radiation whose effect on electronics in the tunnel (ranging from microprocessors to quench protection diodes) must be controlled. While the ionizing radiation dose will be quite small, the annual neutron fluence may approach 10^{11} cm^{-2}.

4.8.1 Scattering Models

Although the measured total cross section for p-p collisions rises only gradually with energy, it is uncertain at SSC energies because of the large extrapolation to 40 TeV. Phenomenological theories applied to ISR and early SPS measurements used expressions for the total cross section growing as $\ln^2 s$ (Froissart bound behavior) and extrapolating to nearly 200 mb at SSC energies [4.8-1]. However, a recent review of new $S\bar{p}pS$ data suggests a less rapid rise, with an extrapolated cross section as low as 100 mb [4.8-2]. A total cross section of 120 ± 15 mb at $\sqrt{s} \simeq 30$ TeV has been derived from data obtained with the "Fly's Eye" air shower detector, where the inelastic proton-air cross section was measured [4.8-3]. We choose $\sigma_{tot} = 120$ mb for beam loss analysis. For $\mathscr{L} = 10^{33}$ cm, $\sigma_{tot}\mathscr{L} = 1.2\times10^{8}$ interactions per second, and $\sigma_{tot}\mathscr{L}\sqrt{s} \approx 800$ W. The uncertainty in the actual cross section at 40 TeV is allowed for by conservative use of the numbers derived.

The total cross section results from elastic and inelastic scattering, the latter further divided into diffractive dissociation and central inelastic collisions. The diffractive process can be single, with a quasielastic proton continuing in one direction and hadronic debris going in the other, or double, with the diffractive process leading to a breakup of both protons into hadronic debris. Again, the cross section extrapolation to 40 TeV is uncertain. We choose as plausible extrapolations the fractions 0.25, 0.25, and 0.50 for elastic, diffraction, and central or non-diffractive inelastic scattering.

The p-p elastic cross section at 40 TeV is dominated by a forward elastic peak of the form $\exp(bt)$, where $-t$ is the invariant momentum transfer squared and the slope parameter b is estimated to be about 14.5 GeV^{-2}. The corresponding distribution in θ has a projected gaussian width of $\sigma_{\theta_x} \simeq 9$ μrad. Since the machine emittance produces a corresponding beam angular divergence of about 10 μrad at $\beta^* = 0.5$ m, most of the elastically scattered protons remain well within the machine aperture.

Numerical integrations have been performed to estimate heating effects in the IR optics, caused by the showering of secondary products from inelastic collisions and from hadronic breakup in diffractive scattering. We treat their effects by combining 15 mb of the diffractive process with the full 60 mb of non-diffractive inelastic scattering. For this purpose we follow the Reference Designs Study in taking

$$x_R \frac{d^3 N}{dx_R dp_\perp^2} = \frac{C_m}{(1 + p_\perp/p_{\perp 0})^m} \sum_i A_i (1 - x_R)^{n_i} \tag{4.8-1}$$

for the charged meson distribution, summed over mesons of type i, in the normalized radial energy variable $x_R = E_{CM}/E_{CM\,max}$ and in the transverse momentum $p_\perp$. The parameters are based upon FNAL, ISR, and Sp$\bar{p}$S measurements [4.8-5, 4.8-6, 4.8-7]. The exponent m varies between 6.5 and 9.0, depending upon angle, $p_{\perp 0}$ is 1.3 GeV/c, and C_m is chosen to normalize the integral of $C_m/(1 + p_\perp/p_{\perp 0})^m$ over $p_\perp$. For π^+, π^-, K^+, and K^-, the exponents n_i are taken as 3.5, 4.2, 2.8, and 5.2, respectively, and the A_i as 1.12, 1.12, 0.125, and 0.125.

Equation (4.8-1) describes the average number distribution in an inelastic event. The distribution is narrowly peaked along the beam in either direction, and clearly the energies of all the particles in either direction should sum to the beam energy. Integration over $p_\perp$ and x_R yields 0.52 for the fraction of the beam energy carried by charged mesons in one direction. This fraction is somewhat high, since another half of this amount (0.26) is carried by neutral mesons, and a leading baryon will also carry perhaps 0.4 of the total. Similarly, we obtain $N = 24.2$ for the average charged meson multiplicity in each direction. Although the charged multiplicity at 40 TeV is expected to be considerably higher than this, the energy flow, which determines the beam loss effects of interest here, is less sensitive to the way it is distributed among particles. (The energy integral does not contain the low-x_R divergence of the number integral, and it matters little if the energy is carried by a few hard mesons or a large number of soft ones.)

Backgrounds caused by IR collisions elsewhere around the ring have been studied by Monte Carlo techniques. We are particularly concerned with the inter-IR backgrounds for the clustered IRs. Features of both ISAJET [4.8-8], which treats hadronization by independent fragmentation, and LUNDJET [4.8-9], with its color-string fragmentation, have been used for this study. While these and similar models show differences in their predictions at SSC energies (particle multiplicities vary by factors of two), they represent the best information available and are being continually refined as improved data and techniques become available.

ISAJET has been chosen for the treatment of the inelastic collisions. Inelastic events are generated on a unit weight basis and the secondary-particle four-vectors are provided to the user. The ISAJET non-diffractive inelastic cross section for the SSC design energy is 137 mb and an average of 109 stable particles are produced for each collision. We scale the effects to our standard 60 millibarn non-diffractive inelastic cross section. The particles are highly collimated along the beam line. Pions and protons carry the preponderance of the charged secondary energy flux and are tracked through the machine elements with the program DIMAT [4.8-10].

LUNDJET was used for the study of elastic scattering and for single and double diffractive scattering, since these processes are not included in ISAJET. LUNDJET incorporates essentially the same analytical cross sections that are found in the Reference Designs Study, and applies its color-string fragmentation for proton breakup to the Monte Carlo simulation. The cross sections are 25.7 mb for single and 3.1 mb for double diffraction scattering, with mean particle multiplicities of 25 and 30 respectively.

4.8.2 Magnet Heating

Common Elements in the IR

A detailed study of the energy deposition rate of IR collision secondary particles in the final focus triplet, vertical separation dipoles, and associated collimators has been made. Trajectories were computed for each meson type for a range of energies and forward angles. If the particle struck the beam pipe or a collimator, its energy was assigned to that position, appropriately weighting by the cross section. Scaling by the design luminosity then gives the deposited power. Hadronic shower development was not followed, but since the hadronic cascade distance is small compared with the bin size, the broadening due to shower development is minor. Transverse distributions of the energy distribution would be useful, but are not yet available.

The dimensions, positions, and strengths of the magnets chosen for the study, together with the results, are given in Table 4.8-1. Circular "collimators" (zero thickness) were located just in front of the triplet (C1), in front of the separation dipoles (C2), and at the end of the drift space after the separation dipoles (C3).

Table 4.8-1
IR optics and collimators. Much of the power listed for the final collimator is actually deposited in shielding along the beam pipe in the drift space (see Fig. 5.11-5).

Object		Bore Radius (cm)	Gradient (T/m) or Field (T)	Start (m)	Length (m)	Power (W)
Collimator	C1	0.50		20.00	0.0	39.9
Quadrupole	Q1	1.65	223.	20.00	14.50	15.2
Quadrupole	Q2-1	1.65	−213.	35.30	11.79	8.9
Quadrupole	Q2-2	1.65	−213.	47.89	11.79	16.0
Quadrupole	Q3	1.65	216.	60.48	13.04	13.5
Collimator	C2	1.65		79.50	0.0	6.4
Dipole	BV1-1	3.30	5.2	79.50	8.00	5.8
Dipole	BV1-2	3.30	5.2	88.50	8.00	
Collimator	C3	1.00		218.0	0.0	19.3

With the assumptions given above, inelastic processes produce a total of 480 W at each standard IR. Charged mesons carry 52% of this power, 125 W in each direction. We can also expect two neutral beams carrying 62 W each.

The power absorbed by the first collimator and front triplet element are shown in Fig. 4.8-1 as a function of collimator radius. A representative power distribution through the inner optics is shown in Fig. 4.8-2, in this case for an 0.5 cm (250 μrad) collimator in front of the triplet. The first half of Q1 is shadowed by C1, but in the second half low energy defocused particles strike the cryogenic beam tube with $dP/dz \approx 2.2$ W m^{-1}. (With a

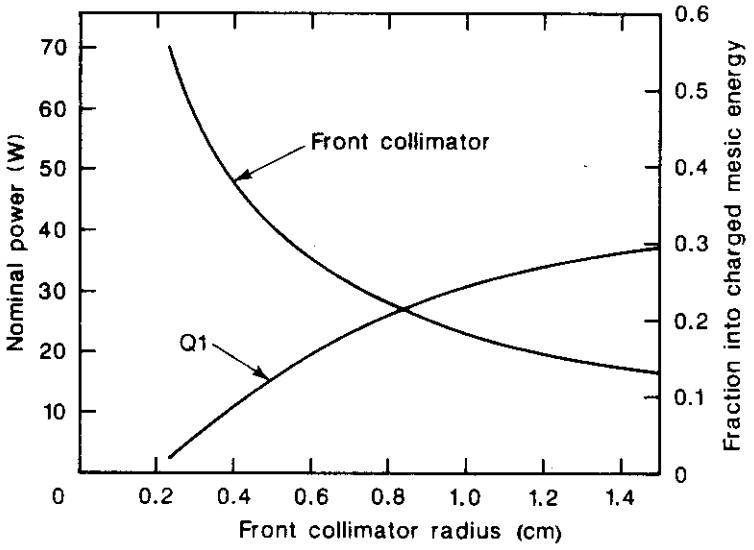

Figure 4.8-1. Power deposition in the collimator just in front of the first triplet element (Q1) and in Q1 as a function of collimator radius. Beam spreading in the drifts between magnets leads to the spikes at magnet entrances.

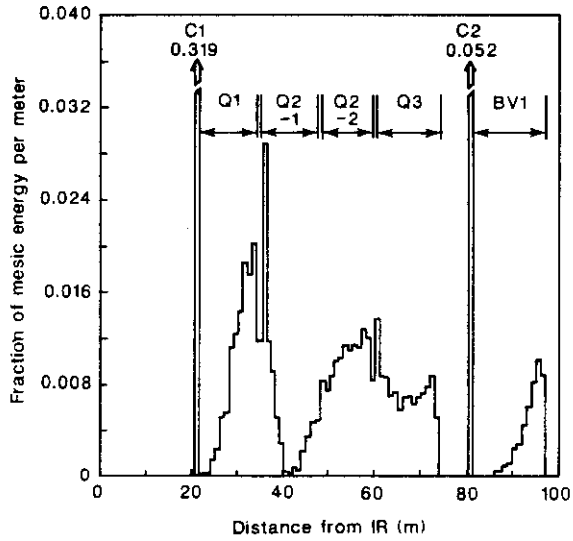

Figure 4.8-2. Power deposited by charged mesons in initial IR optics, for a front collimator radius of 0.5 cm. Bore radii are as given in Table 4.8-1.

beam-tube diameter, front collimator, 3.3 W m^{-1} would be deposited.) Although more total power is deposited in Q2-2, the maximum dP/dz reaches only about 2/3 of these values.

Since the most severe power deposition occurs in the second half of Q1, a collimator in the center of Q1 was also modeled in an attempt to decrease the cryogenic load further. A significant fraction of the power hit this collimator only if C1 had a fairly large radius. Because of this and the difficulty of splitting Q1, we prefer to use C1 only. While it is advantageous to make its radius as small as possible, incoming halo particles will produce prohibitive "splash" in the detector if the collimator is too small. The optimum radius appears to be about 0.5 cm.

As expected, power deposition in Q2-1, Q2-2, and Q3 is insensitive to the radius of C1. It could be reduced by additional collimators between these elements, but only by introducing long (~3 m) gaps in the triplet.

Figure 4.8-3 shows the charged meson energy x_R-distribution surviving to various points in the system. If we define a cutoff at the point where dN/dx_R has decreased by a factor of five, then only particles with $x_R > 0.21$ survive the triplet, and only those with $x_R > 0.29$, representing 20% of the charged mesonic energy, survive to the second vertical bend dipole. At C3 the beta function is large, the beams are separated, the dispersion is large, and there is abundant free space, making it an optimal point for beam scraping during colliding beam conditions.

Power absorption rates in each common element are given in Table 4.8-1 for a C1 radius of 0.5 cm. Under nominal conditions, the total cryogenic load in each direction is 60 W. At least two IRs will contribute similar loads, while the loads from intermediate-beta IRs will be lower by a factor of at least twenty.

In the absence of a detailed Monte Carlo shower simulation, we estimate the power density in the superconductor as follows: A hadron is incident on the beam pipe at grazing incidence, and the first few hadronic collisions in the shower occur in or close to the beam pipe. In each collision about one third of the hadronic energy is transferred to electromagnetic showers via π^0 production, so that an estimated 80% of the total energy shows up in electromagnetic showers near the inner wall. Such showers develop with a typical transverse dimension of about a radiation length, which for copper is about 1.4 cm. Focusing in the quadrupoles produces four nearly identical "hot spots", so a cross sectional area of about 8 cm^2 is involved. The estimated 2.2 W m^{-1} then implies 2 mW cm^{-3}, or ~0.2 mW g^{-1}. Quench thresholds for the IR quadrupoles are not yet known, but are expected to be about 10 mW g^{-1}. The scattered particle heat load thus poses no apparent problem for magnet quenches.

Neutral Scattered-particle Beam

Neutral secondaries from collisions in the high-luminosity IRs carry 62 W in the form of a tightly-collimated forward beam in each direction. These are predominantly γ rays from π^0 decay which traverse the front collimator and triplet quadrupoles without hitting, and leave the bore when the beams separate. Tails of the angular distribution are cut off at about 0.25 mrad by the front collimator, creating a fairly clean beam spot. The neutrals exit the machine vacuum through a specially designed thin low-Z window (larger than the beam spot) when the beam separation is about 10 cm (130 m from the IR). They immediately re-enter a long vacuum pipe and travel to a neutral beam dump just before the next

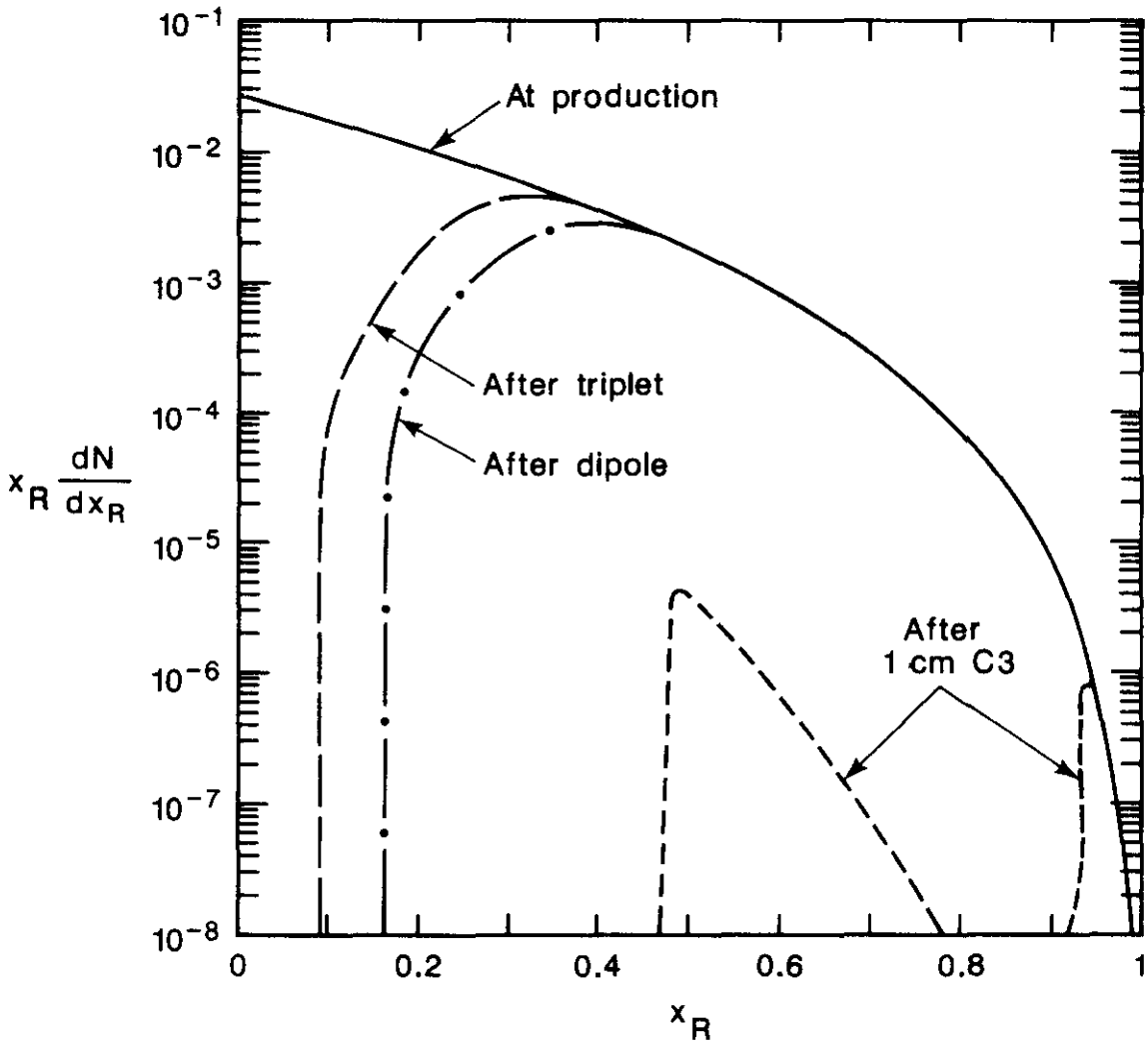

Figure 4.8-3. Charged meson energy x_R-distribution (a) at production, (b) surviving after the final focus triplet, (c) after the separation dipole, and (d) after C3, with positions and radii as given in Table 4.8-1. Only 10^{-4} of the energy survives C3, mostly carried by intermediate-energy mesons with unusual orbits in the dipole.

vertical bend. A detector imbedded in this dump provides the feedback signal to keep the beams centered, as discussed in Section 5.8.3, and serves as a secondary luminosity monitor for the IR. This arrangement is discussed further in Sections 5.11.6 and 5.11.8.

Arcs

Beam-gas interactions produce 370 W of hadronic debris distributed around each ring if the beam-gas lifetime is 300 h. Since the synchrotron heat load is 9 kW/ring at the same beam current, this heat load represents only a 4% increment. The associated radiation damage effects are considered in Section 4.8.4.

4.8.3 Long-Range Lost Particles

Elastic and Quasi-Elastic Particles that Remain In-Aperture

An issue of particular concern for the clustered IR format is the background generated at one IR by p-p collisions at another. Particle secondaries of highest energy are tightly collimated in the beam direction. Some are carried by the machine bending and focusing elements from one IR to the next where their further interaction could present a problem in the form of unwanted background triggers to the experiments or background clutter in interesting events. To assess the potential problem, quasielastic protons from inelastic interactions and from single and double diffraction scattering have been generated by the ISAJET and LUNDJET programs and tracked through the inter-IR machine elements by means of the program DIMAT.

Low-momentum secondaries are swept out by the IR quadrupoles. The vertical magnets for the two-step beam separation and the initial horizontal-bend magnets in the dispersion-suppression section form a momentum-selecting spectrometer of increasing refinement. Protons that survive these elements may be captured by the lattice with negligible interaction in the elements immediately upstream of the following IRs. Some are subsequently lost in regions of high dispersion and the remainder form a beam halo that builds up with time. If there were no losses and no recovery through synchrotron radiation damping, the halo would reach a level of about 0.1% in one day. Elastically scattered protons differ little from the stored beam; the dominant contribution to the halo is from diffraction scattering, as is shown in the momentum and radial distributions in Fig. 4.8-4.

Loss occurs primarily at positions of high dispersion, well away from the IRs. We conclude that inter-IR background will cause negligible problem for the experimental facilities.

Muons

Penetrating muons arise from direct production (i.e., the decay of unstable particles with short lifetime), from the decay of pions, and from electromagnetic pair production. In the absence of magnetic bending the resulting muon beam would constitute a radiation hazard even after penetrating 2 km of soil. However, the softer muons ($x \lesssim 0.2$) are dispersed in all directions by the triplet, and the separation dipole spreads the remainder into a narrow vertical fan.

The return flux path of the separation dipole acts as a "mirror" for muons penetrating the magnet. If it were a "C" magnet with the return yoke on top, then all muons bent downward would be harmlessly lost below ground. The remaining muons with trajectories

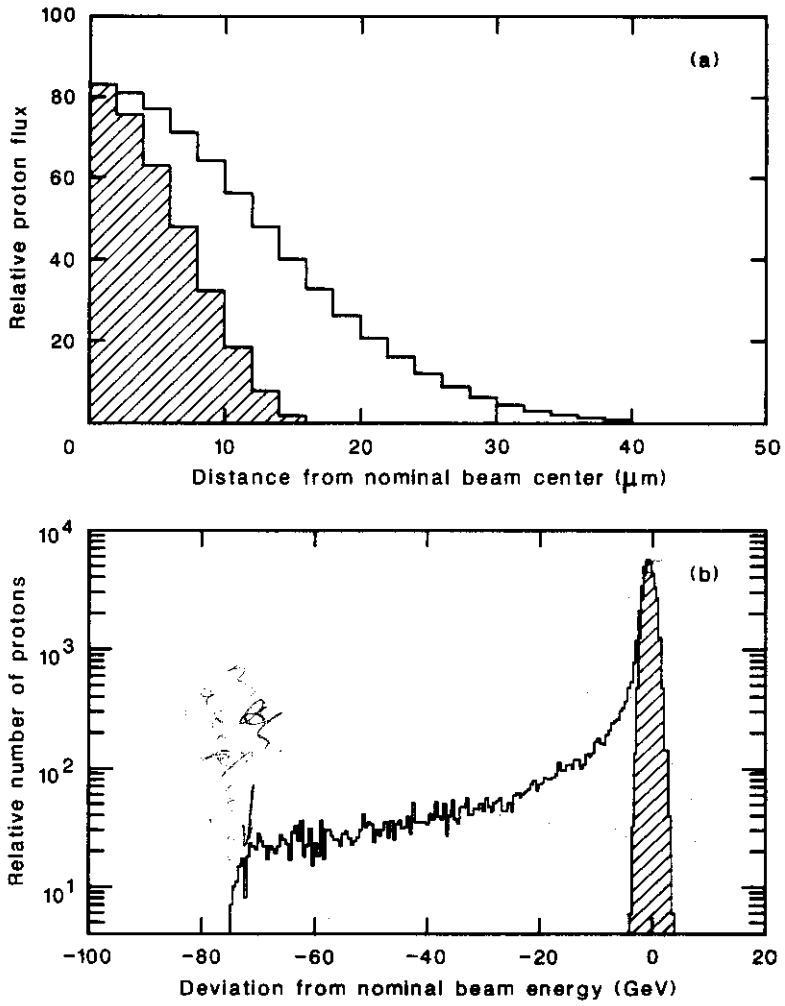

Figure 4.8-4. Distributions (a) in the radial position and (b) in the differences between proton energy and nominal beam energy for secondary protons at an interaction point compared to those for the stored beam (shaded distributions). The proton secondaries are those produced at the previous IR in the cluster.

above the exiting beam would all have the same charge and could also be reflected downward, by an additional solid iron magnet above the beam. It is not yet clear that these special magnets provide worthwhile advantages.

The muon flux is decreased by ensuring that decaying mesons enter degrader material as soon as possible. However, with drift spaces averaging 50 m, meson decay is not the main muon source; a combination of prompt production and electromagnetic muon pair production in showers dominate. Meson decay muon spectra for the standard IR have been calculated, and are given elsewhere [4.8-11].

4.8.4 Radiation Effects

Radiation Intensity in the IR Common Elements

As noted above, the power deposition in the second half of Q1 reaches about 0.2 mW g^{-1} at four symmetric "hot spots". This translates to 0.2 Gy/s.* For a standard 10^7 second SSC "year", the radiation dose would be 2×10^6 Gy. In present designs the most vulnerable part of an SSC magnet is believed to be the polyimide (Kapton) insulation. According to CERN data, room-temperature Kapton becomes unusable after doses in excess of 10^7 Gy (in air) to 10^8 Gy (in vacuum) [4.8-12]. Its tolerance at cryogenic temperatures is expected to be better still. On this basis we conclude that radiation lifetimes of the triplet magnets are sufficiently long. At the same time, prudent design will include careful collimation and careful magnet design, in part to minimize activation of these components.

Radiation Intensity in Arc Dipoles

A large fraction of the 380 W lost through beam-gas collisions ends up in electromagnetic showers, concentrated in a "hot spot" on the outside of the ring with typical transverse dimensions of a radiation length in copper, 1.4 cm. The conservative assumption that all 380 W is deposited in this 2 cm^2 region leads to 2.5×10^{-3} W kg^{-1} (or 2.5×10^{-3} Gy s^{-1}) of ionizing radiation in the copper, and about 3.3×10^{-3} Gy s^{-1} in the adjacent polyimide insulation. The resulting annual dose rate, 3×10^4 Gy yr^{-1}, is well under 1% of the dose which would seriously damage even warm polyimide. The dose rate outside the magnet assembly, e.g., in the cryostat, is lower by more than an order of magnitude and poses no threat to insulation or supports.

Tunnel Electronics

The normal operation of electronic components can be disrupted by (a) ionizing radiation, which by producing electron-hole pairs upsets normal currents and voltages, and (b) radiation that produces dislocations in the semiconductor lattice. The conditions in the SSC tunnel will be such that γ rays are responsible for most of the ionizing radiation, while fairly low-energy neutrons cause most of the lattice damage. There is no sharp failure threshold, and the critical dose for a given circuit depends on in its design. Reasonable assumptions lead to the rough damage thresholds given in Table 4.8-2 [4.8-13]. It is clear from these data that electronics containing typical components will fail soon after receiving a neutron fluence of 10^{11} cm^{-2} or an ionizing radiation dose of 10 Gy(Si). What is less clear

*Ionizing radiation dose is usually quoted in rads (1 rad = 100 ergs/g) or Grays (1 Gy = 100 rad, or 1 J/kg). For assessment of possible damage to solid state electronics, it is convenient to convert doses to a standard reference material, usually silicon.

is the way in which the mean time between failures (MTBF) decreases as the lethal fluence is approached. This decrease apparently becomes significant at an order of magnitude below the lethal neutron fluence [4.8-14]. A preliminary reliability model analysis of the SSC control system indicates that after a neutron fluence of 10^{11} cm^{-2} the board failure rate due to radiation damage dominates over other failure causes, whereas at 10^{9} cm^{-2} "normal" board failures dominate. Conservatively, the tunnel electronics should be protected from a fluence greater than about 10^{10} cm^{-2} over the lifetime of the machine, and in any case careful component choices must be made.

Table 4.8-2
Threshold for Radiation Damage in
Various Semiconductor Devices [4.8-13]

Device		Neutron fluence (n/cm^2)	Total Ionizing Dose (Gy(Si))
Transistor	High power	10^{11}	10^2–10^3
	Low power	10^{12}	
Diode	High power	5×10^{11}	
	Low power	10^{13}	
Digital IC	TTL	10^{13}	10^4
	LS, ECL	10^{14}	
Linear IC	Op Amp	5×10^{11}	10^2
	Comparator	5×10^{12}	
	Voltage regulator	10^{12}	
Memory	Normal feature size	10^{13}	20–10^3
	Small feature size	10^{9}	
μ-Processors	8080B		15
	68000	5×10^{12}	50
	9900	10^{13}	10^4

Measurements

Measurements at existing accelerators may be reasonably extrapolated to estimate SSC tunnel dose rates. A neutron fluence of 5.5×10^{-2} cm^{-2} has been measured at the wall of an accelerator tunnel (radius 2.3 m) where the loss rate of the 3 GeV proton beam was normalized to 1 cm^{-1} s^{-1} along the beam [4.8-15]. At Fermilab, an LBL/FNAL group measured neutron fluence (ϕ) and spectra ($d\phi/dE$), photon dose/neutron fluence, and charged particle dose/neutron fluence, using a Bonner sphere spectrometer 2.0 m from the 800 GeV beam line [4.8-16]. Their results are summarized in Table 4.8-3. It is of particular interest that the distribution $E(d\phi/dE)$ has a prominent peak centered at 200 keV. About 60% of the flux lies between 1 eV and 1 MeV, and about 25%, including thermal neutrons, has energies below 1 eV.

Interpretation of the FNAL results is somewhat clouded by lack of knowledge of the loss rate of protons from the beam. An effective beam lifetime of 350 h has been assumed on the basis of pressure measurements in a warm section immediately upstream of the apparatus, but the number is quite uncertain.

Scaling with energy can be done in a straightforward manner. Detailed calculations have been made at CERN using the cascade program FLUKA82, which scales both cross section and multiplicity [4.8-17]. As might be expected, the neutron yield is roughly proportional to incident proton energy, but with deviations because of the changing cross section and, with increasing energy, a larger fraction of the cascade energy going into the electromagnetic part of the shower.

Table 4.8-3
Summary of Radiation Measurements at 800 GeV [4.8-16]

Neutron flux @ 2.0 m	3.6 $cm^{-2}s^{-1}/10^{11}$ protons
Photon dose/neutron fluence	$<2\times10^{-11}$ Gy cm^2
Minimum ionizing dose/neutron fluence	$<2\times10^{-12}$ Gy cm^2
Fraction of neutrons with E > 1 eV	0.75
Fraction of neutrons with E > 1 keV	0.65
Peak in $Ed\phi/dE$ distribution	100 keV–1 MeV

The agreement between the 3 GeV and 800 GeV measurements is surprisingly good. At the Tevatron, 10^{11} protons lost with a 350 h lifetime implies a loss rate of 0.13 $cm^{-1}s^{-1}$. Scaling the 3 GeV data in energy and by this loss rate, one obtains a predicted flux of 1.1 $cm^{-2}s^{-1}$ for the FNAL conditions, as compared with the measured 3.6 $cm^{-2}s^{-1}$. Further extrapolation of both numbers to SSC conditions yields fluences of 0.24×10^{11} cm^{-2} and 0.84×10^{11} cm^{-2} for a nominal 10^7 second "year". Similarly, if the same ratio of photon plus ionizing dose to neutron fluence holds, the total ionizing dose rate will be less than 1 Gy/yr, which is comparatively unimportant.

If electronics in this environment were not protected, the "lethal fluence" of neutrons for some components would be reached in less than five years. The MTBF would decrease substantially within several months. It therefore appears necessary to house major electronic devices in such a way as to shield them from beam-associated neutrons. The design proposed has each electronics rack recessed in a ceiling hole, from which the counterweighted rack could be pulled for maintenance purposes. A shielding "plug" on the bottom of the rack reduces the neutron fluence by a factor of ten. In addition, increasing the distance of the electronics from the neutron source effectively reduces the size of the source, leading to an additional tenfold neutron fluence reduction.

The quench-protection diodes present a similar problem. It had been proposed that they be located inside the cryostats, and of necessity quite close to the beam. Radiation hardness usually means the ability of a device to self-anneal its radiation-induced defects, and this self-annealing is inhibited at low temperatures. Although the sensitivity of cooled

high-power diodes to radiation damage has yet to be assessed, the above numbers, together with known diode thresholds at room temperature, argue for placing the diodes outside the cryostats, in a lower-dose environment, pending the completion of research in progress.

4.9 Cryogenic System Requirements

The SSC requires an extensive cryogenic system that not only must provide for the operating requirements of the superconducting magnets, but also must provide for transient conditions such as cooldown and magnet quench, and for magnet maintenance. In addition, it must run on a schedule set by the use of the beam and a schedule consistent with the high beam availability that is necessary to the success of the collider facility as a whole.

One of the features of the SSC operating realm that is new, at least for proton colliders, is the presence of synchrotron radiation in significant amounts. The total power in synchrotron radiation varies for a fixed beam energy inversely as the ring radius, and for a fixed radius directly as the fourth power of the beam energy. Thus it "turns on" at about 15 TeV as the beam energy is ramped to the 20 TeV operating level. For the SSC the synchrotron radiation power is 9 kW in each ring and has an intensity of 0.14 W/m of dipole. This 18 kW, together with other types of beam losses amounting to a few kilowatts, sets the scale of the heat load for the SSC cryogenic system. This "unit" of refrigeration plant is the equivalent of 22 kW at 4.2 K. The cost-optimized total cryogenic heat load is about three times this amount.

A fundamental parameter of a superconducting magnet and its cryogenic system is the operating temperature. The choice for the SSC that is consistent with the performance of the niobium-titanium superconductor at the 6.6 T operating field is 4.35 K maximum. In addition to the temperature itself, two important system parameters are the temperature uniformity and the temperature stability required for proper operation. Temperature gradients from one part of the system to another are necessary for heat transport. Because of the large synchrotron radiation heat load that varies strongly with beam energy, temperature gradients change with time as the rings are ramped. In the SSC the allowed gradients are limited mainly by the systematic sextupole field in the dipoles from temperature dependent persistent currents in the superconducting coils. The non-uniformities that are tolerable from the limits on sextupole moment depend on their periodicity relative to the periodicity of the lattice, on the energy of the beam, and on the filament size of the superconductor. The fine-filament superconductor has a smaller temperature dependent magnetization. The worst situation arises at injection where the sextupole has the largest effect. Here the limit on temperature gradient has been calculated to be a minimum of 0.56 K for the 5 micron filament size selected for the SSC [4.9-1]. This is not a very severe constraint, and in practice the temperature gradient is limited more by system efficiency considerations than by the need to maintain uniformity.

The ancestor of the SSC is, of course, the Tevatron, and this heredity is reflected in the cryogenic system requirements. The Tevatron has produced a body of successful superconducting magnet operating experience with beam and beam-loss heating. The Tevatron magnets are cooled by immersion in supercritical helium, the so-called single-phase flow, that is cooled in turn by heat exchange with boiling helium. Although other systems are possible and may have attractive features, any fundamental change in the single-phase cooling

concept requires development and demonstration under realistic operating conditions. This is a complex and expensive task; unless some very strong reasons can be adduced for the superiority of some alternative system, the Tevatron model must be used for the SSC.

The SSC is some fourteen times the circumference of the Tevatron and consists of two rings. Such a large scale system, if it is to be constructed and brought into operation in a comparable length of time, requires a parallel plan for tunnel construction and for phased installation and commissioning of the magnets. Thus a highly centralized cryogenic system is not appropriate. Instead, a system of units capable of independent operation, but interconnected for redundancy, more nearly matches the requirements. The choice of the number of units is a trade-off between the economy of scale in the refrigeration plants and the costs of transporting the heat load. Longer cryogenic loops require larger cryostats with larger inventory of helium. Larger cryostats require more room for handling and installation and most important, greater spacing between the rings. The present design of the SSC has ten cryogenic sectors.

With these overall constraints in mind, the cryogenic features of the SSC are summarized in Table 4.9-1 below. In addition to the specifications, important issues that must be confronted in the design of the system are refrigeration capacity adjustment to match the variable load, tolerance to contaminants, repairability, and high availability. The operating schedule must support the operation of the collider facility and provide for in particular cooldown, magnet maintenance and quench recovery. Efficient collider commissioning also is of importance and suitable provision for magnet training or conditioning must be made.

Table 4.9-1
Summary of SSC Cryogenic System Features

Operating temperature, coils	4.35 K max
Operating temperature, refrigerator	4.15 K nominal 4.05 K minimum
Number of refrigerators	10
Number of air separation plants	2
Total heat load (both rings)	
4.15 K refrigeration	
synchrotron radiation	18.2 kW
other beam-related loss	3.8
static heat leak	9.5
Total	31.5 kW
4.15 K liquefaction	135 g/s
20 K	48.2 kW
84 K	390 kW
Total magnet mass	5×10^7 kg
Total helium inventory	2.1×10^6 liters

The conceptual design of the SSC cryogenic system is described in Section 5.3.

4.10 Injector System

A series of accelerators are needed to present a high quality beam to the collider rings of the SSC for acceleration to 20 TeV. The use of cascaded accelerators is a now standard method of raising the energy of protons by many orders of magnitude while preserving fundamental beam parameters such as intensity and emittance. The choice of injection energy into the collider is influenced by many elements which include collider magnet field quality and aperture, correction systems, and the cost of the injector system. As discussed in Section 4.10.1 the consideration of these elements leads to the choice of 1 TeV as the final energy of the injector string. It is pointed out in Section 4.1 that achieving the design luminosity of the SSC requires the injector system to have a high brightness source. In this Chapter we describe the four particle accelerators constituting the injector chain that preserves this brightness. The injector system described below includes a 600 MeV (kinetic energy) linear accelerator, an 8 GeV/c low energy booster, a 100 GeV medium energy booster, and a 1 TeV superconducting high energy booster. The layout of the injector complex is shown in Fig. 4.10-1.

4.10.1 Injector Parameters

The SSC injection system has been designed to satisfy the following criteria for collider operation:

Injection Energy of 1 TeV

As discussed in Section 4.3.2 the required aperture in the SSC is only weakly dependent upon the transverse emittance of the injected beam. As a result, the choice of injection energy is dictated primarily not by the beam size at injection but rather by the field quality of the collider magnets at low field. The sextupole component of the magnetic field in the dipoles due to persistent currents becomes very large at low fields. Figure 4.10-2 shows the calculated persistent-current multipole components b_2 and b_4 as a function of field in the SSC dipole [4.3-1]. A distributed correction system that is capable of compensating for this effect in the collider has been described in Section 4.4.4. Raising the injection (i.e., minimum) energy of the collider would reduce the requirements placed upon this system. However, it would be necessary to raise the injection energy into the 2–3 TeV range ($B \simeq 0.7$–1.0 T) before the system could be replaced by a lumped corrector system. The cost of this alternative in terms of the injection system is prohibitive and precludes serious consideration of such an option. Further examination of Fig. 4.10-2 reveals that the operating point of the magnet at injection is on that portion of the curve where the effect grows rapidly with decreasing field. Lowering the injection energy by only 25% would greatly increase the requirements placed on the correction system with modest associated savings in cost in the injector.

Normalized transverse emittance of less than 1 mm-mrad (rms)

This requirement is imposed in order to produce the design luminosity while keeping the total number of circulating protons low and is discussed in Section 4.1.

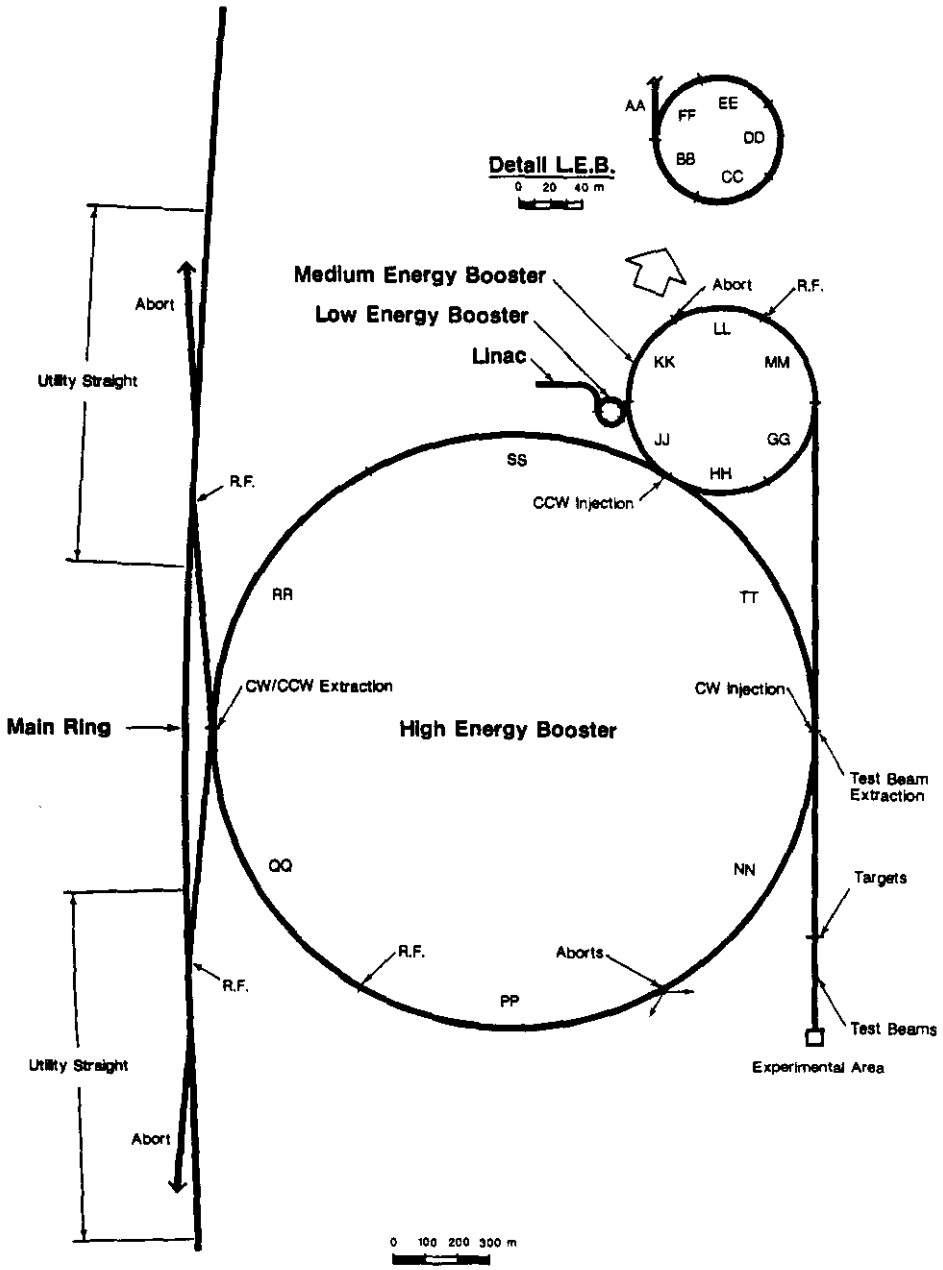

Figure 4.10-1. Layout of the SSC injector complex.

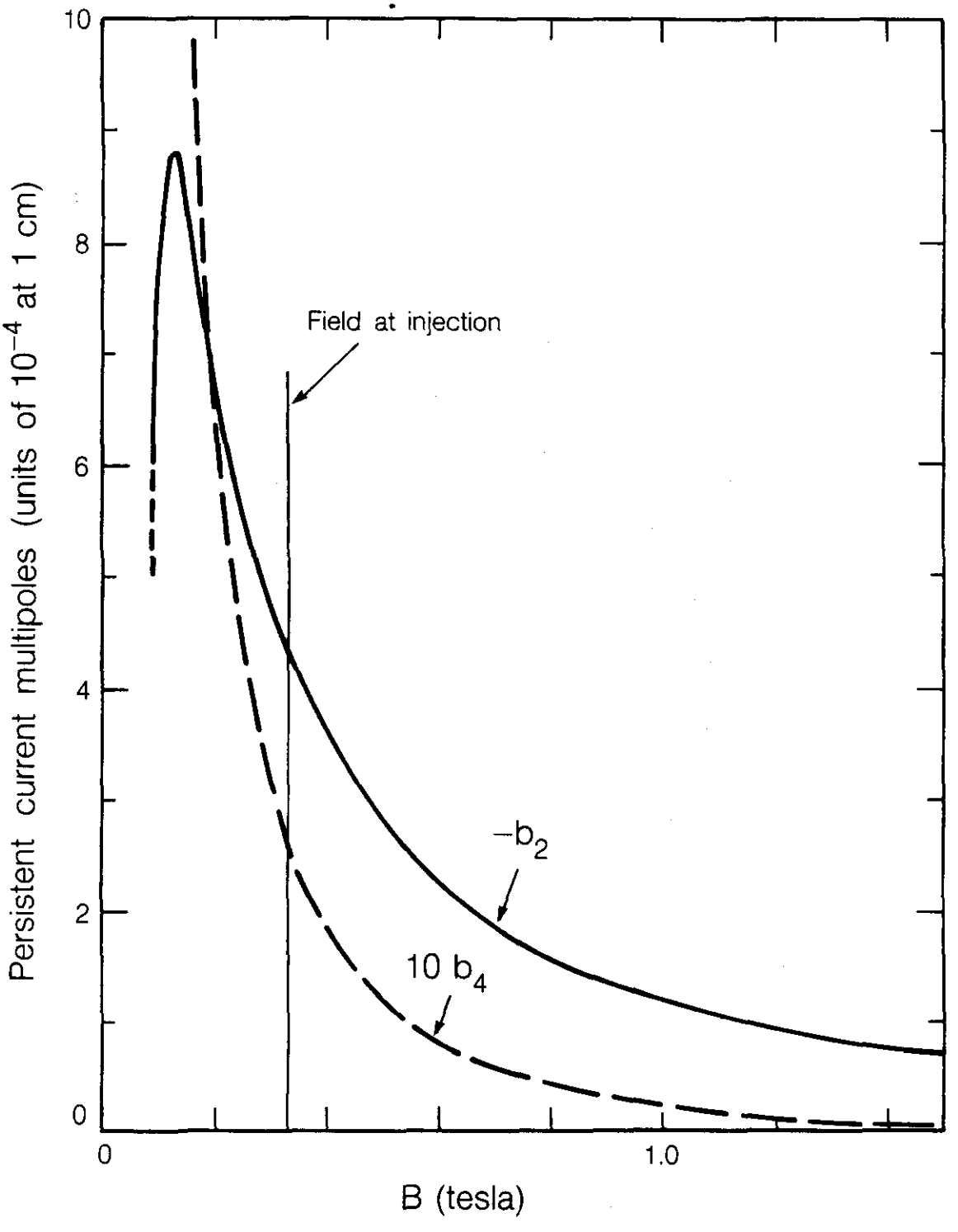

Figure 4.10-2. Sextupole (b_2) and decapole (b_4) multipole coefficients from persistent currents in 5 μm superconducting filaments as a function of main ring magnetic field for the SSC bending magnet. For 1 TeV injection the field is 0.33 tesla. Only the relevant (increasing field) side of the hysterisis loop is shown. Computations from [4.3-1,-2].

Momentum Spread of at Least 1.5×10^{-4} (rms)

This requirement arises from the beam stability requirements discussed in Section 4.5.

Bunch Spacing of 4.8 Meters

The choice of bunch spacing is described in Section 4.1.2. The injector as designed also affords the option of operation with bunch spacings of 9.6 and 19.2 meters, if desired.

1.0×10^{10} Protons/Collider Bunch

The bunch intensity requirements have been described in Section 4.1.

Filling Time of Less than 60 Minutes

The filling time of the two collider rings should clearly be small compared to both the colliding beam lifetime at 20 TeV and the single beam lifetime at injection. Since both of these lifetimes are expected to be a day or more, a filling time for the collider of a few hours would be sufficient during normal operating periods. A maximum of one hour (<30 minutes per ring) has been chosen in order to facilitate both the commissioning and diagnostic/study periods that are a necessary part of on-going operations. Shortening the filling time significantly would require a more powerful refrigeration system. (See Section 4.10.5).

Slow Extracted Test Beams of Energy 1 TeV

Requirements for testing and calibration of experimental detector components are described in Section 4.10.6.

The design of the injector described here has been driven by two concerns, (a) the desire to guarantee preservation of transverse emittance in the presence of space charge effects at injection into the lowest energy ring (see, for example, [4.10-1]), and (b) the desire to avoid transition energy crossing (with the inevitable degradation of beam quality) anywhere in the system. Accommodating these two concerns restricts the injector design to be close to that described here. A parametric description of the injector elements is contained in Table 4.10-1. The injector consists of a 600 MeV (kinetic energy) linear accelerator (linac) followed by three circular accelerators. H^- ions are accelerated through a three-stage linac consisting of a radio-frequency-quadrupole front end followed by drift tube and side-coupled linac structures. The H^- ions are stripped at injection into a small Low Energy Booster (LEB). The LEB accelerates the protons to 8 GeV/c. The protons are transferred to the Medium Energy Booster (MEB) where they are accelerated to 100 GeV/c, and then into the High Energy Booster (HEB) where they reach the SSC injection energy of 1 TeV. The LEB and MEB are both constructed with conventional magnets, while the HEB is made superconducting in order to limit its physical size. Injection into either of the two collider rings in a reasonable manner requires that the HEB be bipolar. The optics of the three rings are arranged such that the protons never cross through the transition energy of any of the rings—acceleration in the LEB occurs below transition, while acceleration in the MEB and HEB occurs above transition. As shown in the table, 10% emittance dilution during each beam transfer is allowed. Fast transverse dampers are used in all rings to minimize emittance dilution arising from injection orbit errors. All beam transfers take place in

Table 4.10-1
SSC Injector Parameters

	Linac	LEB	MEB	HEB
Injected particle	H^-	H^-	H^+	H^+
Injection momentum	0.0	1.21	8.0	100.0 GeV/c
Extraction momentum	1.22	8.0	100.0	1000.0 GeV/c
Circumference	125.0	249.6	1900.8	6000.0 meters
rf frequency (at extraction)	1336.0	62.0	62.5	62.5 MHz
Bunch spacing	4.8	4.8	4.8	4.8 meters
Average current (at extraction)	3.9	99.	92.	87. mA
Normalized transverse emittance (rms)	0.45	0.75	0.83	0.91 mm-mrad
Longitudinal emittance (rms area/π)	0.012*	1.8	1.8	35 meV-s
Cycle time	0.1	0.1	4.0	60.0 s

*At 1336 MHz.

the horizontal plane and, with the exception of LEB injection, are accomplished through single turn extraction and injection.

4.10.2 600 MeV H^- Linac

A chain of linear accelerators is utilized as the source of the particles that feed the Low Energy Booster (LEB). This chain consists of an H^- ion source, a radio-frequency quadrupole (RFQ) structure, a beam chopper, a drift tube linac (DTL), and a side-coupled linac (SCL), collectively called the "linac". This linac provides a beam of 600 MeV H^- particles through a transfer line to the LEB. The choice of linac energy is determined by the design of the LEB and is discussed in Section 4.10.3. H^- ions are used because, through the use of multiturn injection, they allow the creation of large circulating currents in the LEB without requiring a large peak current in the linac.

Beam

A scheme proposed by Colton and Thiessen [4.10-2] involves injection from the linac into pre-existing rf buckets in the LEB. This scheme sets the linac beam parameters.

The SSC main ring utilizes beams with 4.8 m bunch spacing and containing 10^{10} protons per bunch. The transfer energy between the linac and the LEB is 600 MeV (v/c = 0.792). The rf frequency at v/c = 1 is 62.457 MHz; therefore, the LEB frequency at injection is 0.792 × 62.457 = 49.46 MHz. The DTL frequency is chosen to be nine times this value or 445.2 MHz, and the SCL frequency is another three times, or 1336 MHz. The

LEB circumference is 249.6 m, corresponding to a revolution frequency of 0.951 MHz (1.051 μs/turn) at injection. The harmonic number is 52, which for a final bunch spacing of 4.8 m, requires filling all 52 buckets. For bunch spacings of 9.6 m, every other bucket would be filled.

The LEB bucket-filling scenario utilizes a linac beam in which 2 of 9 DTL buckets are filled and laid in sequence into each of the 52 LEB buckets. The LEB is filled in 20 turns. Twenty turns require that beam be delivered for 21.0 μs. With 2.5×10^8 H^- per bucket the instantaneous peak current is 17.6 mA, and the average current over the pulse is 3.9 mA. The instantaneous current (17.6 mA) sets the linac design and determines the beam properties, such as emittance. Some of the relevant beam structure parameters are given in Table 4.10-2. Calculated properties are for a peak current of 17.6 mA. The LAMPF linac at Los Alamos routinely delivers a proton beam having this peak current at a duty factor 150 times that needed for the SSC.

The exact method of chopping the beam to provide the 2 in 9 filled 445.2 MHz rf buckets requires additional study. One possibility is to insert a beam deflecting system into the accelerator structures. Another is to operate the RFQ at 49.5 MHz. A study of the various possibilities led to the fortuitous result that the simplest system appears to work best. The use of a single 49.5 MHz RFQ is proposed and costed for the SSC.

Table 4.10-2
Linac Beam Structure

445.2 MHz buckets	
full	1 and 2
empty	3 thru 9
Number LEB turns to fill	20
Time to fill LEB	21.0 μs
Number H^- per 445.2 MHz bucket	2.5×10^8
Instantaneous current	17.6 mA
Current over macropulse	3.9 mA
LEB cycle rate	10 Hz
Beam duty factor	0.021%
Time averaged current	0.82 μA
H^- delivered per second	5.2×10^{12}
Normalized Transverse Emittance (rms)	0.45 mm-mrad
Longitudinal Emittance (rms area/π)	1.2×10^{-5} eV-s*
Energy Spread (rms)	0.25 MeV

*At 1336 MHz

4.10.3 Low Energy Booster

Introduction and Primary Parameters

The Low Energy Booster (LEB), the first of three cascaded separate-function alternating-gradient synchrotrons in the SSC injector system, accelerates protons from a momentum of 1.219 GeV/c (corresponding to the linac kinetic energy of 600 MeV) to 8 GeV/c at a repetition rate of 10 Hz. Its primary parameters are listed in Table 4.10-3. The choice of LEB parameters and, indeed, the decision to use three rings, are strongly influenced by the need to reduce the effects of space-charge tune shifts in the LEB in order to minimize beam loss and the dilution of transverse emittances. In the limit of small tune shifts, the incoherent Laslett tune shift [4.10-3] for protons undergoing small oscillations near the center of the beam is given approximately by

$$\Delta\nu = \frac{r_p N_T}{4\pi B \beta\gamma^2 \epsilon_N} \tag{4.10-1}$$

where $r_p = 1.535 \times 10^{-18}$ m is the classical radius of the proton, N_T is the total number of protons in the ring, B is the bunching factor, i.e., the ratio of average beam current to peak current in a bunch, beta and gamma are the usual Lorentz relativistic factors, and ϵ_N is the normalized rms emittance. Two form factors which contribute less than 3% in this case have been dropped in order to simplify Eq. 4.10-1. According to this formula, the tune shift can be reduced by increasing the injection energy and, for a given bunch spacing and number of particles per bunch, by reducing the number of bunches, i.e., the radius of the machine. A small radius requires a ring efficiently filled with dipoles of high magnetic field. At 8 GeV/c, the lattice design and ring circumference of 250 meters require a dipole field of 1.24 tesla, as high as practical for a rapid-cycling machine that must avoid iron saturation. Creating variable bunch spacing (4.8, 9.6, or 19.2 meters) upstream of the LEB requires that the rf harmonic number be a multiple of four. For a circumference of 249.6 meters, the fundamental bucket spacing of 4.8 meters implies a harmonic number of 52. For these parameters and for 10^{10} protons per bunch, a bunching factor of 0.25 gives a tune shift of 0.16 at the injection energy.

The use of three rings also makes it possible to avoid passing through transition in all rings in order to minimize beam loss and the dilution of longitudinal emittance. This decision requires for the LEB a high transition energy, which strongly influences the choice of lattice, and implies a peak energy comfortably above the transition energy of the next ring, the Medium Energy Booster (MEB).

LEB Lattice

A separated-function lattice with dipoles and quadrupoles electrically in parallel is chosen for simplicity of construction, operation, and analysis. The lattice consists of 20 cells with ten straight sections provided by leaving out dipoles in a pattern that creates five superperiods; thus there are 40 quadrupole magnets and 30 dipoles. Figure 4.10-3(a) shows the LEB layout, including the allocation of functions to straight sections. One straight section is used for injection, two adjacent ones for extraction, five for rf cavities, and one for transverse superdampers. Space for beam diagnostics and for correction elements is

Table 4.10-3
Low Energy Booster Parameters

Injection momentum	1.22 GeV/c
Extraction momentum	8.0 GeV/c
Circumference	249.6 m
Number of bunches	52
Protons/bunch	1.0×10^{10}
Circulating current	99 mA
Normalized transverse emittance (rms)	0.75 mm-mrad
Longitudinal emittance rms area/π)	0.0018 eV-s
Horizontal tune	4.39
Vertical tune	4.41
Transition gamma	10.5
Natural chromaticity	
(H)	−5.2
(V)	−4.9
Lattice type	Separated function FODO
Superperiodicity	5
Maximum beta (arcs)	21.5 m
Maximum dispersion	10.1 m
Number of dipoles	30
Dipole length	4.5 m
Dipole field (max)	1.24 T
Full good field aperture (Hor)	80 mm
Number of standard quadrupoles	40
Standard quad length	0.3 m
Standard quad strength (max)	18.4 T/m
Full good field aperture	80 mm
Number of special quadrupoles	0
Number of sextupoles	10
Number of families	2
Sextupole strength ($B''\ell$)	5.6 T/m
rf frequency (injection)	49.5 MHz
rf frequency (extraction)	62.0 MHz
Cycle time	0.1 s
rf voltage	350. kV
Synchronous phase angle	30 degrees

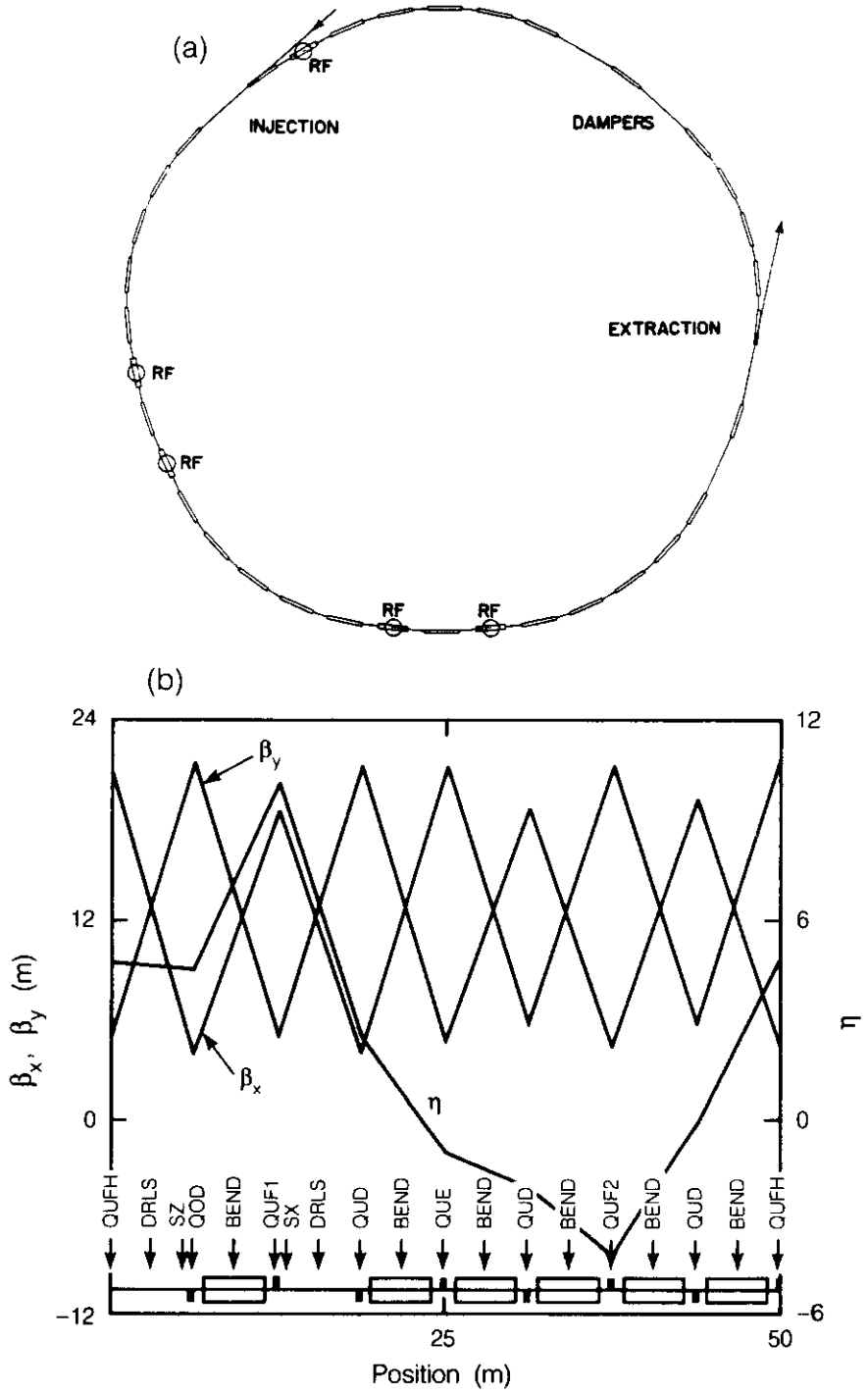

Figure 4.10-3. (a) Layout of the low energy booster. (b) The LEB lattice. One of five superperiods is shown.

allotted adjacent to the quadrupoles. (Space for other apparatus is available in the one empty straight section and in the rf straight sections.)

It is well known [4.10-4] that a lattice with the horizontal tune slightly below the number of superperiods can have a high transition energy. The tunes should be chosen just below an integer or half-integer so that a large space charge tune depression can be accommodated without crossing half-integral or integral resonance lines. Tunes are chosen near 4.4 rather than 4.9 because the $\nu = 5$ lines will be strong structural resonances. It can easily be shown that no systematic sum resonances of order less than or equal to the superperiodicity S enter the square region of tune space defined by $S - 1 < \nu_x, \nu_y < S$. The working point is chosen to be $\nu_x = 4.39$, $\nu_y = 4.41$.

Figure 4.10-3(b) shows the lattice structure and the lattice functions resulting from the above design choices for one superperiod of the LEB. Table 4.10-3 also lists the major lattice parameters. The average phase advance per cell of 79 degrees is close to the optimum value to minimize the peak lattice envelope function and hence reduce aperture requirements. The strength of the horizontally focusing quadrupole labeled QUF1 in the figure is 8% higher, and that of QUF2 9% lower, than the others. This, together with the pattern of missing dipoles, causes a fifth-harmonic dispersion wave that reduces the average dispersion in the dipoles, thereby increasing the transition gamma to ten with relatively small variations in the beta functions amongst the cells. It is worth noting that the price paid for raising the transition energy is a high maximum dispersion, 10 meters. In a detailed engineering design, the horizontal apertures of the magnets adjacent to the high-dispersion region could be made larger than the rest, but that nicety is ignored here.

LEB Injection

H^- are stripped at injection by passing through a thin foil. The injection apparatus is all contained in a single straight section. A set of four pulsed dipoles bumps the closed orbit vertically (and with it, the previously injected circulating beam) onto the stripping foil during the time that beam is injected. The dipole length of 0.5 m and strength of 0.4 T produce a closed-orbit displacement of 3 cm, about twice the full size of a beam having an rms invariant emittance equal to 1 mm-mrad. The incoming H^- ions are inflected through a pulsed-current septum magnet adjacent to the first orbit-bump dipole, which must therefore be a "C" magnet. For symmetry, then, the first and fourth magnets are identical "C" magnets whereas the second and third are identical "H" magnets of larger aperture. Circulating protons and H^- ions bend with opposite curvature in the second orbit-bump magnet, allowing the phase spaces of the two beams to merge at the stripping foil. After the desired number of turns have been injected, the field in the orbit-bump dipoles decays rapidly, moving the circulating beam off the foil.

To fill each bucket with 10^{10} protons using the filling scheme described earlier requires injection of about 20 turns. If it takes ten more turns for the orbit-bump dipoles to move the beam off the foil after injection is complete, the invariant rms emittance will grow by about 0.1 mm-mrad due to Coulomb scattering on the foil during the injection process.

Emittance growth can be caused not only by foil scattering but also by injection errors, resonances, and instabilities. Injection errors must be controlled by very good regulation of magnetic injection elements and by slow software feedback loops using beam pickups to correct successive injection cycles. Although the previous discussion of the tune diagram suggests that resonances are not a major problem, if necessary they can be corrected by

correction elements of the appropriate multipolarity and harmonic distribution. Single-bunch instabilities are not a problem at these moderate intensities provided that reasonable care is taken to reduce the wall impedances. Nevertheless, bunch-by-bunch transverse dampers are planned; they also aid in the correction of injection errors.

The limited energy range of the LEB leads to fairly strong magnetic fields at injection energy, reducing remnant field effects. The resulting good field quality at injection time should reduce particle losses and emittance dilution.

Acceleration Cycle

It is assumed for design purposes that the central beam momentum varies with time as a 10 Hz harmonic function with a constant offset

$$p = \frac{1}{2}(p_{max} + p_{min}) - \frac{1}{2}(p_{max} - p_{min})\cos\omega t \qquad (4.10\text{-}2)$$

This neglects small effects such as magnet saturation. As the beam momentum varies from p_{min} = 1.219 GeV/c to p_{max} = 8 GeV/c, its speed rises from 0.792 c to 0.993 c. Figure 4.10-4(a) shows the time dependences of the total beam energy and the rf frequency, during one LEB acceleration cycle. The rf frequency, tracking the beam velocity, varies from 49.5 MHz to 62.0 MHz during the cycle.

The incoming linac beam will be injected into small stationary buckets according to the filling scheme described previously. The rf requirements for acceleration follow from the time dependence of the central momentum and from the bucket area necessary to contain the longitudinal emittance. Figure 4.10-4(b) shows the time dependence of the bucket area, the synchrotron frequency, and the synchronous phase angle for a reasonable ring voltage program, which never exceeds 350 kV. The synchronous phase angle rises from zero degrees to 31 degrees and is small early in the cycle, leading to long bunches and a favorable bunching factor.

4.10.4 Medium Energy Booster

Introduction and Primary Parameters

The Medium Energy Booster (MEB) is designed to accept the 8 GeV/c beam extracted from the LEB and accelerate it to 100 GeV/c for injection into the High Energy Booster (HEB). The MEB is a conventional accelerator with a circumference of 1900 meters. Parameters describing this ring are found in Table 4.10-4. The design chosen has sixfold symmetry with a regular arrangement of cells. There are a total of 48 cells in the lattice. Of the eight in each superperiod, two have missing magnets which create straight sections to be used for injection, extraction, rf, and aborts. Since the LEB circumference is 250 m, an abort gap of 500 ns is created in the MEB following the injection of seven LEB batches. The functional allocation of the six straight sections may be found in Fig. 4.10-1.

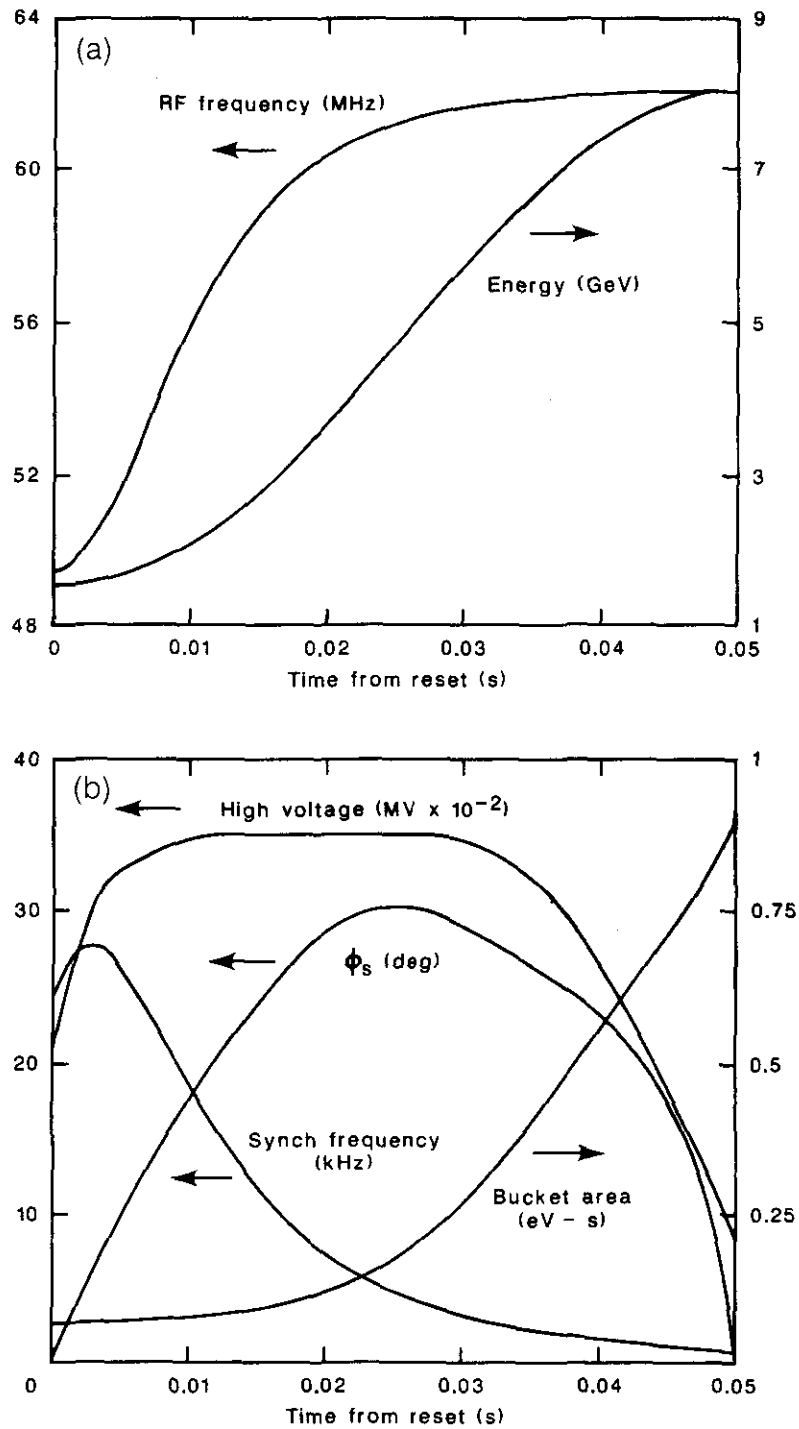

Figure 4.10-4. (a) Energy and rf frequency during the LEB acceleration cycle. (b) Variation of the rf voltage, synchronous phase, bucket area, and synchrotron frequency through the LEB acceleration cycle.

Table 4.10-4
Medium Energy Booster Parameters

Injection momentum	8.0 GeV/c
Extraction momentum	100.0 GeV/c
Circumference	1900.8 m
Number of bunches	364
Protons/bunch	1.0×10^{10}
Circulating current	92 mA
Normalized transverse emittance (rms)	0.83 mm-mrad
Longitudinal emittance (rms area/π)	0.0018 eV-s
Horizontal tune	8.41
Vertical tune	8.41
Transition gamma	7.2
Natural chromaticity	
(H)	−9.4
(V)	−9.3
Lattice type	Separated function FODO
Superperiodicity	6
Maximum beta (arcs)	67.2 m
Maximum beta (straight section)	67.2 m
Maximum dispersion	14.2 m
Number of dipoles	216
Dipole length	5.4 m
Dipole field (max)	1.8 T
Full good field aperture (Hor)	80 m
Number of standard quadrupoles	96
Standard quad length	0.75 m
Standard quad strength (max)	22.8 T/m
Full good field aperture	80 mm
Number of special quadrupoles	0
Number of sextupoles	72
Number of families	2
Sextupole strength ($B''\ell$)	4.4 T/m
rf frequency	62.5 MHz
Cycle time	4 s
rf voltage	600 kV
Synchronous phase angle	30 degrees

Lattice

The lattice functions and arrangement of magnets in the MEB is shown in Fig. 4.10-5(a). The figure extends from the center of one straight section to the midpoint of one arc. The MEB lattice is mirror symmetric around each of these points so the figure represents one twelfth of the ring. As described earlier it is deemed desirable to avoid crossing transition at any point during acceleration through the injector. For the MEB it is easier to set the transition energy below the injection energy of 8.06 GeV than to raise it above the extraction energy of 100 GeV. Since $\gamma_t^2 = C/2\pi\langle\eta\rangle$, where C is the circumference of the accelerator and $\langle\eta\rangle$ is the average dispersion function, a small γ_t requires a large average (and hence maximum) dispersion. The large dispersion is obtained by using a long FODO cell and results in a low tune. The phase advance per cell is about 63 degrees. In addition, the average η is increased by arranging the FODO cells so that each arc contains six cells. This arrangement produces a very large η at the center of the superperiod and little dispersion in the straight sections. (In fact the dispersion in the straight sections would be exactly zero if the phase advance per cell were exactly 60 degrees in the arcs.) The maximum dispersion in the arcs is about 14 meters. Even so, the momentum aperture of the MEB is designed to be $\pm 0.3\%$ — comfortably larger than the $\pm 0.1\%$ it is expected to be asked to accelerate.

Acceleration

The MEB runs on a 4 second cycle. In contrast to the LEB it does not use a resonant power supply but is simply ramped in the same manner as the 400 GeV Main Ring at Fermilab.

The desire for a 4.8 m bunch spacing in the SSC requires that the accelerating frequency in the MEB be a harmonic of 62.5 Hz. An rf frequency of 62.5 MHz is chosen for the MEB, as for the LEB. For a cycle time of 4 seconds the voltage requirements are modest — 600 kV for a synchronous phase of 30 degrees. For the longitudinal emittance expected in the MEB the maximum momentum spread produced during the acceleration cycle (95%) is $\pm 0.1\%$.

Correction Systems

The MEB does not have correction quadrupoles for adjusting the tune. Instead, the dipole and two quadrupole buses are independently powered. This allows maximal flexibility in selecting the operating point in the tune diagram.

There is a trim dipole and a sextupole associated with each quadrupole in the ring for controlling the orbit and chromaticity. The trim dipoles are each independently powered, while the sextupoles are arranged into two families. A beam position monitor located at each quadrupole provides the primary information to be used in correcting the orbits.

Beam Stability

Beam stability is not expected to be a problem in the MEB. An estimate of the longitudinal and transverse impedances has been made which includes beam pipe resistivity, beam position monitors, bellows, and kickers. For a longitudinal emittance of 0.0018 eV-s and a normalized transverse emittance of 0.75 mm-mrad, the longitudinal and transverse stability limits occur at 20 times and 2.5 times the required beam intensity, respectively.

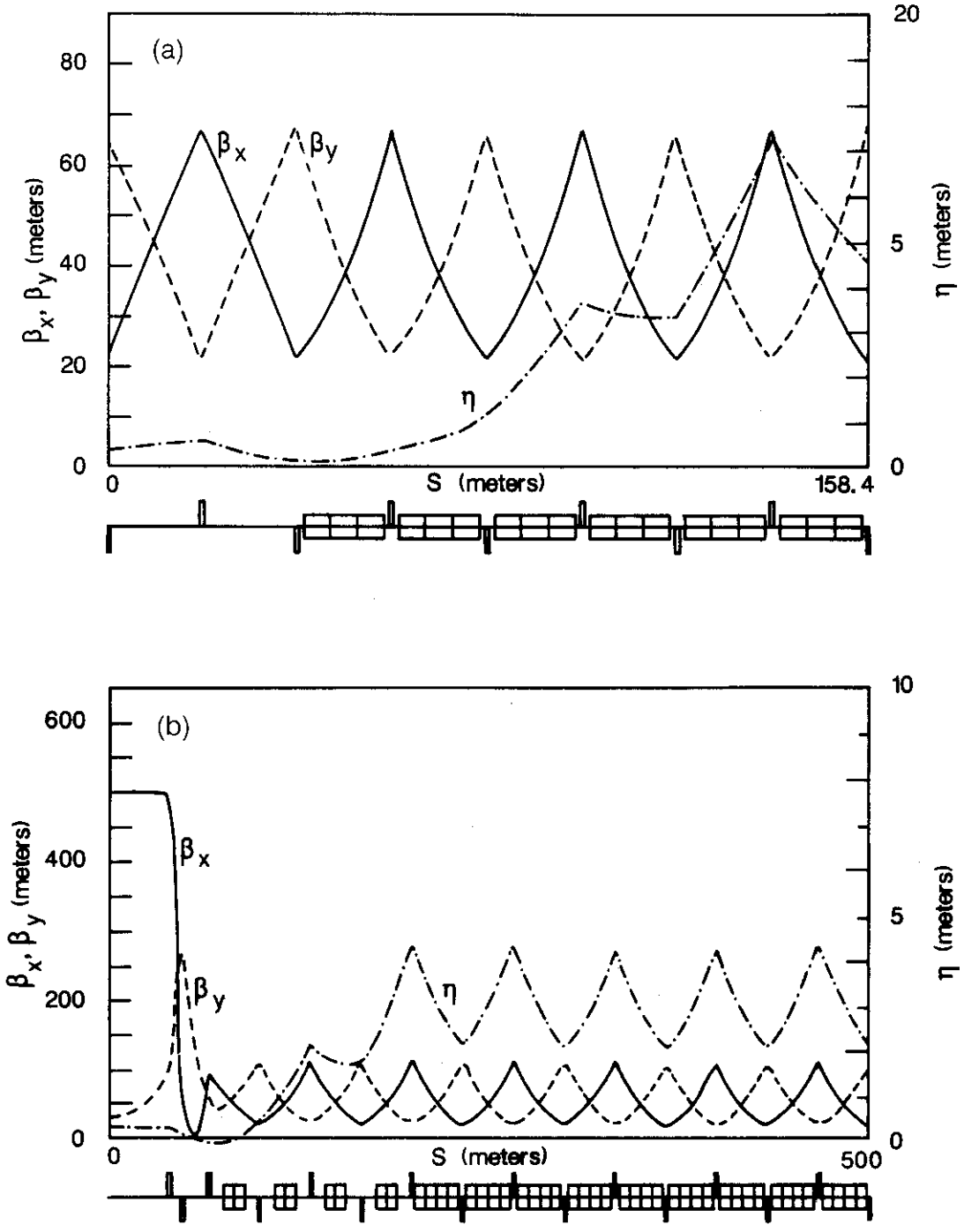

Figure 4.10-5. (a) The MEB lattice. One half of one of six superperiods is shown. (b) The HEB lattice. One half of one of six superperiods is shown.

4.10.5 High Energy Booster

Introduction and Primary Parameters

The high energy booster is a superconducting accelerator similar in scope to the Fermilab Tevatron. Table 4.10-5 contains a listing of some of the parameters describing the HEB. Protons are injected into the HEB at 100 GeV/c and are extracted at 1000 GeV/c. The ring has a circumference of 6000 m and contains six long (133 m) straight sections. Filling the HEB with three MEB batches produces a 2.5 μs abort gap. The circulating current in the HEB is the same as in the SSC itself except for missing bunches in the abort gap. The total number of particles circulating in the HEB is 1.1×10^{13}. The utilization of the six straight sections is as follows (see Fig. 4.10-1):

- NN0 Clockwise injection from the MEB and the slow extraction for test beams (Lambertson magnet).
- PP0 Beam aborts (both directions).
- QQ0 Location of the rf cavities.
- RR0 Extraction to the SSC.
- SS0 Open.
- TT0 Counter-clockwise injection from the MEB, and the electrostatic septum used for slow extraction.

The magnetic field in the dipole magnets varies between 0.57 T at injection and 5.7 T at extraction. The linear aperture required is ± 13 mm, which translates into a coil-to-coil diameter of 50 mm. The HEB has been designed so that the aperture required for slow extraction is the same as that required for injection. While the magnet aperture requirement precludes the use of the SSC superconducting magnet, the magnet of choice is a scaled version of this magnet with a 5 cm aperture. The cryostat is modified in order to accommodate the larger heat load generated because the HEB is relatively rapid cycling. The refrigeration system is similar to that required for the collider magnets and consists of a single additional refrigerator. The rf frequency is chosen to be 62.5 MHz. This frequency is dictated by the smallest bunch spacing (4.8 m) required. For an acceleration time of 24 seconds and a synchronous phase angle of 30 degrees, a peak rf voltage of 1.5 MV is required. Emittance dilution and bunch rotation are performed immediately prior to extraction in order to provide the required momentum spread at injection into the collider and to shorten the bunches so that they fit into single 375 MHz buckets.

Lattice

The HEB lattice is shown in Fig. 4.10-5(b). The figure extends from the center of one straight section on the left, to the midpoint of one of the arcs on the right. The lattice is mirror symmetric about each of the end points on the figure. Since the HEB has six superperiods the figure represents 1/12 of the total circumference. The lattice is based on a 90 degree standard cell. Each cell contains eight dipole magnets of length 7.0 m, and two 1.0 m quadrupoles. Fifty-four such cells constitute the arcs of the ring. In addition two cells at either end of the arcs (24 total cells) have one-half of the bending removed in order to suppress the dispersion through the straight sections. Following the dispersion suppressor a quadrupole triplet is used to produce the high beta straight section. The entire straight section is 133 m long with 80 m of free space. The beta in the straight section is chosen so

Table 4.10-5
High Energy Booster Parameters

Injection momentum	100.0 GeV/c
Extraction momentum	1000.0 GeV/c
Circumference	6000.0 m
Number of bunches	1092
Protons/bunch	1.0×10^{10}
Circulating current	87. mA
Normalized transverse emittance (rms)	0.91 mm-mrad
Longitudinal emittance (rms)	0.035 eV-s
Horizontal tune	25.415
Vertical tune	21.415
Transition gamma	18.7
Natural chromaticity	
(H)	−66.5
(V)	−39.6
Lattice type	Separated function FODO
Superperiodicity	6
Maximum beta (arcs)	117 m
Maximum beta (straight section)	500. m
Maximum dispersion	4.2 m
Number of dipoles	528
Dipole length	7.0 m
Dipole field (max)	5.66 T
Full good field aperture (Hor)	26 mm
Number of standard quadrupoles	150
Standard quad length	1.0 m
Standard quad strength (max)	144.0 T/m
Full good field aperture	26 mm
Number of special quadrupoles	36
Special quad length	2.0–3.0 m
Special quad strength	144.0 T/m
Full good field aperture	40 mm
Number of sextupoles	138
Number of families	2
Sextupole strength ($B''\ell$)	138.0 T/m
rf frequency	62.5 MHz
Cycle time	60. s
rf voltage	1500. kV
Synchronous phase angle	30 degrees

that the aperture requirements arising from injection and from slow extraction are the same. The length of the straight section is sufficient for allowing the two extraction systems required for injection into the two rings of the SSC to co-exist in a single straight section.

The tune of the HEB is 25.415 horizontally and 21.415 vertically. The tunes are located in a region of the tune space that is free of resonances through eleventh order. Trim quadrupoles are available for adjusting the tune, if necessary. The horizontal tune is chosen to provide an odd number of quarter wavelengths between adjacent straight sections. This feature greatly facilitates the slow extraction. The chromaticity is high because of the large beta straight sections. It is however easily corrected with two families of sextupoles of modest strength. Tracking studies indicate that the sextupoles in no way compromise the dynamic aperture of the HEB.

Magnet Design Considerations

The HEB superconducting magnets are patterned after the collider magnets. The coils have been enlarged to give a 5 cm aperture, and the dipole magnets have been shortened to 7 m in length. Estimates of the good field region are consistent with the 26 mm required for injection, ramping, and extraction. The conductor placement is different from that of the collider dipoles and is shown in Fig. 4.10-6. Based on this arrangement of conductor and steel, the calculated higher order components of the field are given in the left-hand column of Table 4.10-6. The multipole variations caused by inaccuracy of conductor placement have been estimated and are shown in the right-hand column of Table 4.10-6. Persistent current effects are not included in the table. The only observable contribution is expected to be to the b_2 (sextupole) component at injection. For a 5 μm superconducting filament size this contribution is expected to be -1.2 in the units given.

Correction Systems and Diagnostics

There is a correction element spool piece associated with each standard quadrupole in the HEB lattice. The 150 spool pieces contain 1) trim dipoles, 2) trim quadrupoles, 3) sextupoles, and 4) octupoles. The trim dipoles are used to correct the effects of magnet misalignment errors and magnetic field errors. Each trim dipole is powered independently. The trim quadrupoles are used to adjust the tune of the machine, while the skew elements control the coupling between the horizontal and vertical planes. The sextupoles are used to remove the chromatic variation of the tunes. The trim quadrupoles, sextupoles, and octupoles are each organized into two independently powered families.

The primary diagnostic devices in the HEB are the beam position monitor (BPM) system and the beam loss monitor (BLM) system. A beam position pickup and a BLM are placed at every quadrupole in the ring. The beam position pickups are deployed with horizontally sensing devices at horizontally focusing quadrupoles, and vertically sensing devices at horizontally defocusing quadrupoles. These systems are identical to those used in the collider itself, except for the larger aperture of the beam position pickups. (See Section 5.12.)

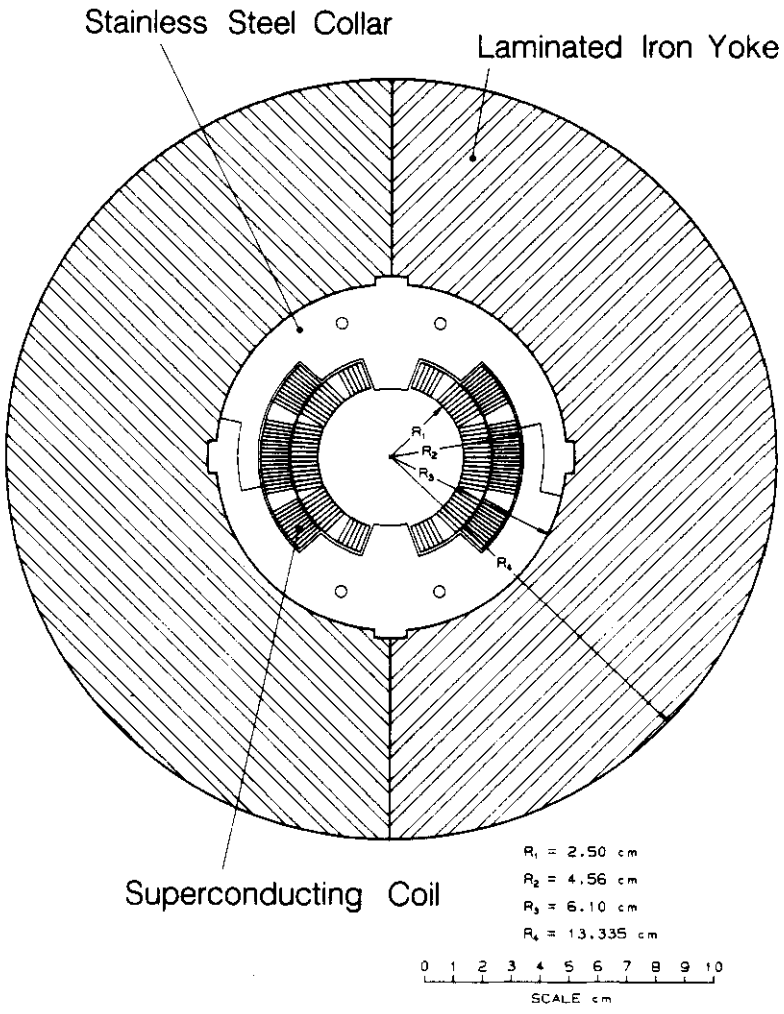

Figure 4.10-6. Coil arrangement of the HEB dipole.

Table 4.10-6
Design and Random Multipole
Coefficients for the HEB Dipole

		Coefficients are in units of 10^{-4} cm^{-n}	
Multipole		Design	Random (rms)
Quadrupole	a_1	0.0	0.56
	b_1	0.0	0.56
Sextupole	a_2	0.0	0.41
	b_2	0.0084	1.40
Octupole	a_3	0.0	0.40
	b_3	0.0	0.20
Decapole	a_4	0.0	0.07
	b_4	0.0006	0.29
12 Pole	a_5	0.0	0.069
	b_5	0.0	0.025
14 Pole	a_6	0.0	0.012
	b_6	0.0006	0.028
16 Pole	a_7	0.0	0.0094
	b_7	0.0	0.0050
18 Pole	a_8	0.0	0.0017
	b_8	0.034	0.0057

Beam Current Limitations

The maximum number of protons per bunch in the HEB is roughly half of what has been accelerated successfully in the Fermilab Tevatron. However, before dilution, prior to injection into the collider, the nominal longitudinal emittance is much smaller. It is calculated that prior to dilution, when the bunch area is 0.0018 eV-s, the beam is close to or above the microwave instability threshold at 1 TeV. It is expected that the longitudinal emittance will dilute by a factor of two at this point. Since it is required in any case that the emittance be diluted by a factor of 20 prior to injection into the collider, this is not a major concern.

Cryogenic System Requirements

Since the HEB incorporates superconducting magnets, a cryogenic system that provides the necessary liquid helium temperature refrigeration is needed. The system has to be sized for the 60 s cycle used for filling the collider rings, but, equally important, must accommodate transient operations such as cooldown, quench recovery, and emergency magnet replacement. The HEB magnets have, like the collider magnets, very low static heat leak. Because of the 60 second repetition time, the energy loss per cycle is an important consideration. Five sources of heat are superconductor hysteresis, eddy current losses in the copper matrix surrounding the NbTi, hysteresis and eddy current losses in the iron, eddy current losses in the copper wedges used for field shaping, and eddy current losses in the beam pipe.

The superconductor losses per magnet are about 440 J/cycle (dB/dt = 0.2 T/s and filament diameter = 5 μm) and the iron loss is 300 J/cycle. Thus, the total loss for a 60 second cycle will be about 0.74 kJ per magnet. This heat load has implications for the cryostat design, especially for the gaseous helium return path, and for the operating temperature of the magnet. In order to use a cryostat design as similar to the collider magnet cryostat as possible, a 60 second cycle is assumed and an operating temperature of 4.8 K.

4.10.6 Test Beams for HEB

Summary of Test Beam Requirements

Test beam needs for the SSC have been extrapolated from current test beam use by the major colliding beam detectors at CERN and Fermilab. Current experience indicates that test beam use varies from detector to detector, but never goes to zero. Figure 4.10-7 from [4.10-6] shows the number of test beams required by each of four major detectors during the past few years, and the projected needs for the next few years. One is led to the conclusion that approximately one test beam is needed per detector even after the detector has begun data taking.

The need for test beams cannot be discussed without defining the specific requirements placed on the beams by the users. Table 4.10-7 is a compilation of requirements that was produced at Snowmass 84 [4.10-5]. It is worthwhile to note that apparently experimenters do not foresee a strong need for beams with energies greater than 1 TeV. This may be because they feel constrained by the energy of the HEB, but there are some who claim that it is relatively easy to calculate the high energy response of their detectors from the data obtained at 1 TeV.

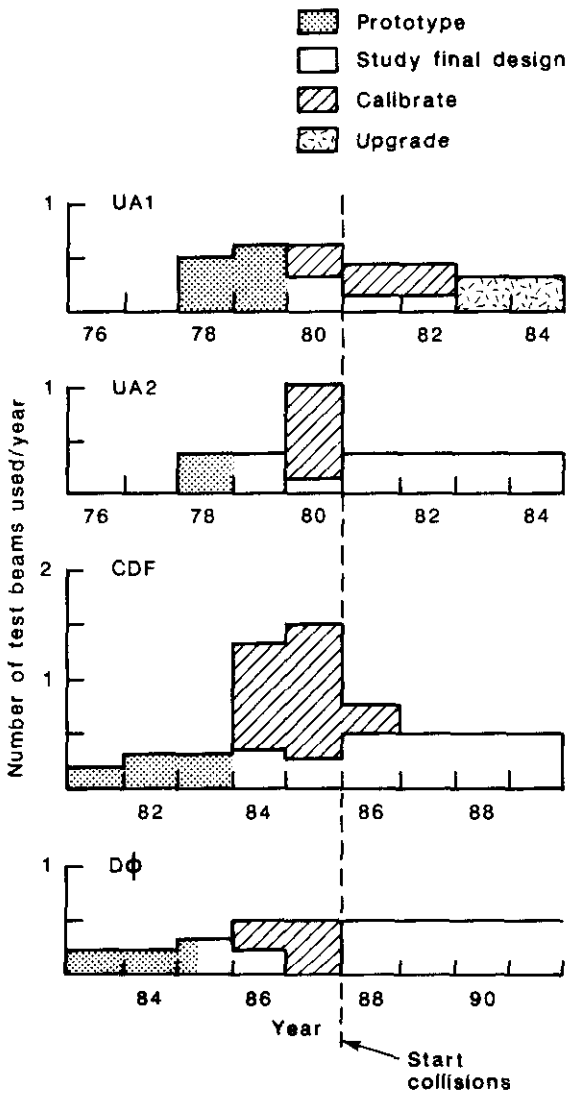

Figure 4.10-7. Test beam requirements of major detectors before and after first operation for experiments.

Another feature of the requirements is the relatively low demand for intensity. The highest rates foreseen are the order of 10^7 Hz. This would allow construction of modest beam lines with modest targeting stations. It will also simplify extraction since large quantities of beam will not have to be extracted. It is important to note that all experimenters require slow spill. It is difficult to imagine any use for single turn or other types of fast extraction.

Uses of Test Beams

Test beams serve a variety of purposes for the major colliding beam detectors. The uses can be categorized as follows:

1. Prototyping detectors.
2. Measurement of tracking chamber resolutions.
3. Measurement of calorimeter resolutions.
4. Measurement of π/e separations in calorimeters or other devices.
5. Study of the response of the various detectors across cracks and other geometric anomalies, as well as magnetic fields.
6. Measurement of hadron punch through for muon detectors.
7. Calibration of the calorimetry.
8. Check of the calibration over time.

For example, the CDF collaboration at Fermilab plans to keep one of their central calorimeter wedges in a test beam for the duration of their run to measure the change in calibration over time. UA1 has taken a similar approach. The D0 collaboration on the other hand uses liquid argon/uranium calorimetry, which they believe will not change over time. Moreover, each individual component of the D0 calorimeter will not be calibrated in a test beam because it is believed that calibrating one module automatically gives the calibration for all of the modules.

Table 4.10-7
Anticipated Test Beam Requirements

	Tracking	Electron identification	Muon identification	Calorimetry
Energy range	0.1–1 TeV	10–800 GeV	2–100 GeV	$\leqslant$1 TeV
Momentum resolution	10%	0.5%	5–10%	1%
Particle types	—	electron, pion	pion, muon	electron, pion, muon proton, photon
Rates (Hz)	$\leqslant 10^7$	$\leqslant 10^2$	$\leqslant 10^3$	10^3–10^7

References

4.1-1. Report of the Reference Designs Study Group on the Superconducting Super Collider, U.S. Department of Energy (May 8, 1984).

4.1-2. M. Block and R.N. Cahn, Rev. Mod. Phys. **57**, 563 (1985), Section V.

4.1-3. F. Amman and D. Ritson, *Proc. Int. Conf. on High Energy Accelerators*, Brookhaven National Laboratory (1961), p. 262.

4.1-4. L. Evans and J. Gareyte, IEEE Trans. Nucl. Sci. **NS-32**, 2234 (1985).

4.1-5. P.L. Morton and J.F. Schonfeld, in Proc. Workshop on Accelerator Physics Issues for a Superconducting Super Collider, Ann Arbor, Michigan, ed. M. Tigner, University of Michigan report UM HE 84-1 (1984), p. 54–5.

4.1-6. M. Sands, in *Physics with Intersecting Storage Rings*, Proc. Int. School of Phys. "Enrico Fermi", Varenna, Course 46, ed. B. Touschek, Academic Press, NY (1971), p. 257.

4.1-7. D.E. Johnson, SSC Central Design Group Internal Report No. SSC-N-151 (1986).

4.2-1. Reference 4.1-1, Section 4.4.

4.2-2. Realistic Lattices Group, SSC Central Design Group Report No. SSC-SR-1015 (1985).

4.2-3. Task Force on Commissioning and Operations, SSC Central Design Group Report No. SSC-SR-1005 (1985).

4.2-4. S. Peggs, SSC Central Design Group Internal Report No. SSC-N-87 and SSC Central Design Group Internal Report No. SSC-N-88 (1985).

4.2-5. A. Chao and E. Forest, SSC Central Design Group Internal Report No. SSC-N-81 (1985).

4.2-6. E.D. Courant, D.R. Douglas, A.A. Garren and D.E. Johnson, IEEE Trans. Nucl. Sci. **NS-32,** 1669 (1985).

4.2-7. Clustered IR Study Group, SSC Central Design Group Report No. SSC-SR-1014 (1985).

4.2-8. H. Wiedemann, Stanford Linear Accelerator Center Internal Report No. PEP-220 (1976).

4.2-9. A. Wrulich, DESY Report No. DESY 84/26 (1984).

4.2-10. B. Leemann and A. Wrulich, SSC Central Design Group Internal Report No. SSC-N-133 (1986).

4.2-11. D. Neuffer, Appendix, SSC Central Design Group Report No. SSC-2 (1984), submitted to Part. Accel., 1985.

4.2-12. B. Montague, private communication (1986). For an example of clustered IR design with a (3,3) arrangement, see D. Blechschmidt et al., Nucl. Inst. Methods **156**, 375 (1978). IR pairing was considered for LEP. Note that the range of δ for LEP is 10 times that of the SSC.

4.2-13. A. Garren and K. Steffen, SSC Central Design Group Internal Report No. SSC-N-125 (1986).

4.2-14. K. Steffen, SSC Central Design Group Internal Report No. SSC-N-126 (1986).

4.2-15. E. Courant, A. Garren, D.E. Johnson, and K. Steffen, SSC Central Design Group Internal Report No. SSC-N-139 (1986).

4.2-16. A. Garren and D.E. Johnson, SSC Central Design Group Internal Report No. SSC-N-140 (1986).

4.2-17. A. Dragt, in *Physics of High Energy Particle Accelerators*, A.I.P. Conf. Proc. No. 87, ed. R.A. Carrigan, F.R. Huson, and M. Month, American Institute of Physics, NY (1982), p. 147.
4.2-18. D. Neuffer, SSC Central Design Group Internal Report No. SSC-N-115 (1986).
4.2-19. S. Peggs, SSC Central Design Group Internal Report No. SSC-N-130 (1986).
4.2-20. A. Garren, SSC Central Design Group Report No. SSC-65 (1986).
4.3-1. M.A. Green, in *Workshop on Accelerator Physics Issues for a Superconducting Super Collider*, Ann Arbor, Michigan, December 1983, ed. M. Tigner, University of Michigan Report No. UM HE 84-1, p. 126.
4.3-2. H.E. Fisk et al., SSC Central Design Group Report No. SSC-7 (1985).
4.3-3. POISSON, developed by K. Halbach and R. Holsinger, is a descendant of the TRIM program, A. Winslow, J. Comp. Phys. **1**, 149 (1967).
4.3-4. See, for example, P. Dahl et al., Brookhaven National Laboratory Report No. BNL-37011 (1985), in Proc. 9th Int. Conf. on Magnet Technology, Zurich, September 1985 (to be published).
4.3-5. H.E. Fisk, Ref. 4.3-2, p. 44.
4.3-6. R. Meuser, Ref. 4.3-2, p. 50
4.3-7. J. Herrara and P. Wanderer, Ref. 4.3-2, p. 58.
4.3-8. E.D. Courant and H.S. Snyder, Ann. Phys. **3**, 1 (1958).
4.3-9. D. Edwards, SSC Central Design Group Report No. SSC-22 (1985). T.L. Collins, SSC Central Design Group Report No. SSC-26 (1985).
4.3-10. M. Harrison, SSC Central Design Group Report No. SSC-27 (1985).
4.3-11. Aperture Task Force, SSC Central Design Group Report No. SSC-SR-1013 (1985).
4.3-12. R.V. Servranckx and K.L. Brown, Stanford Linear Accelerator Center Report No. SLAC-270 (1984).
4.3-13. L. Schachinger and R. Talman, SSC Central Design Group Report No. SSC-52 (1985).
4.3-14. L. Schachinger and S. Peggs, SSC Central Design Group Internal Report No. SSC-N-149 (1986).
4.3-15. B. Leemann, D. Douglas, and E. Forest, IEEE Trans. Nucl. Sci. **NS-32**, 2300 (1985), SSC Central Design Group Report No. SSC-24 (1985).
4.3-16. E. Forest and A. Wrulich, SSC Central Design Group Internal Report No. SSC-N-44 (1985).
4.4-1. S. Peggs, Ph.D. thesis, Physics Department, Cornell University, 1981.
4.4-2. A. Chao and S. Peggs, SSC Central Design Group Report No. SSC-48 (1985) and SSC Central Design Group Internal Report No. SSC-N-96 (1985).
4.4-3. H. Wiedemann and L. Emery, Stanford Synchrotron Radiation Laboratory Internal Report No. ACD-Note-36 (1985).
4.4-4. K. Lau, University of Houston Report No. UH-IBPD-006-86 (1986).
4.4-5. M.J. Syphers, IEEE Trans. Nucl. Sci. **NS-32**, 2362 (1985).
4.4-6. J. Peterson and A. Chao, SSC Central Design Group Internal Report No. SSC-N-7 (1985).
4.4-7. A. Wrulich, SSC Central Design Group Internal Report No. SSC-N-59 (1985).
4.4-8. D. Neuffer, SSC Central Design Group Internal Report No. SSC-N-113 (1986).
4.4-9. D. Neuffer and J. Peterson, SSC Central Design Group Internal Report No. SSC-N-135 (1986).

4.4-10. A Chao, E. Forest, and J. Peterson, SSC Central Design Internal Report No. SSC-N-145 (1986).
4.4-11. D. Neuffer, SSC Central Design Group Internal Report No. SSC-N-112 (1986).
4.4-12. S. Peggs, M. Furman and A. Chao, SSC Central Design Group Report No. SSC-20 (1985).
4.4-13. F. Dell, SSC Central Design Group Internal Report No. SSC-N-132 (1986).
4.4-14. F. Dell, IEEE Trans. Nucl. Sci. **NS-32**, 1623 (1985).
4.4-15. G.E. Fischer and P. Morton, Stanford Linear Accelerator Center/SSC Central Design Group Report No. SLAC-PUB-3870/SSC-55 (1986).
4.4-16. H. Jöstlein, Fermilab Internal Report No. TM-1253 (1984).
4.4-17. D. Boussard, CERN Report No. 84-15, Accelerator School on Antiprotons for Colliding Beam Facilities, 1984, page 261.
4.4-18. G. Dôme, Ref. 4.4-17, page 215.
4.4-19. S. Chattopadhyay, SSC Central Design Group Internal Report No. SSC-N-150 (1986).
4.4-20. L. Cutler, Hewlett-Packard Corporation, private communication, January 1986.
4.5-1. C. Bovet, R. Gouiran, I. Gumowski, and K.H. Reich, CERN Report No. CERN/MPS-SI/Int. DL/70/4 (1970).
4.5-2. Z. Farkas, K. Bane, P. Wilson, SSC Central Design Group Internal Report No. SSC-N-124 (1986).
4.5-3. C. Palm, U. Van Rienen and T. Weiland, DESY Report No. M-85-11 (1985).
4.5-4. B. Abraham-Shrauner, SSC Central Design Group Internal Report No. SSC-N-121 (1985).
4.5-5. J.D. Jackson, SSC Central Design Group Internal Report No. SSC-N-110 (1986); E.D. Courant and M. Month, Brookhaven National Laboratory Report No. BNL-50875 (1978).
4.5-6. M. Tigner, SSC Central Design Group Internal Report No. SSC-N-136 (1986).
4.5-7. T. Weiland, DESY Report No. DESY 82-015 (1982).
4.5-8. K. Bane and R. Ruth, in SSC Central Design Group Report No. SSC-SR-1017 (1985), p. 10.; J. Bisognano and K.Y. Ng, ibid., p. 45; R. Ruth, in *Accelerator Physics Issues for a Superconducting Super Collider*, Ann Arbor, December 1983, ed. M. Tigner, University of Michigan Report No. UM HE 84-1, p. 151; J.M. Wang and C. Pellegrini, Proc. XI Int. Conf. on High Energy Accelerators, Geneva, CERN (1980), p. 554; R.D. Ruth and J.M. Wang, IEEE Trans. Nucl. Sci. **NS-28**, 2405 (1981).
4.5-9. K.Y. Ng, in SSC Central Design Group Report No., SSC-SR-1017 (1985), p. 61.
4.5-10. K. Bane, 1985, private communication.
4.5-11. H. Lee, SSC Central Design Group Internal Report No. SSC-N-146 (1986).
4.5-12. R. Shafer, in SSC Central Design Group Report No. SSC-SR-1017 (1985), p. 127.
4.5-13. E. Colton and T.S. Wang, ibid, p. 119; SSC Central Design Group Internal Report SSC-N-144 (1986).
4.5-14. M. Furman, SSC Central Design Group Internal Report No. SSC-N-142 (1986).
4.5-15. J.S. Nodvick and D.S. Saxon, Phys. Rev. **96**, 180 (1954).
4.5-16. F. Sacherer, CERN Divisional Report No. CERN/SI-BR/72-5 (1972); F. Sacherer, IEEE Trans. Nucl. Sci. **NS-24**, 1393 (1977).

4.5-17. S. Chattopadhyay, SSC Central Design Group Internal Report No. SSC-N-152 (1986).
4.5-18. M. Zisman, S. Chattopadhyay, and J.J. Bisognano, Lawrence Berkeley Laboratory Report No. LBL-21270 (1986).
4.5-19. L.J. Laslett, K.V. Neil and A.M. Sessler, Rev. Sci. Inst. **32**, 279 (1961); A. Hofmann, CERN Report No. 77-13, Int. Accel. School, Erice (1976), p. 405.
4.5-20. A. Piwinski, Proc. 9th Int. Conf. High Energy Part. Accel. (1974), p. 405.
4.5-21. J.D. Bjorken and S.K. Mtingwa, Part. Accel. **13**, 115 (1983).
4.5-22. C. Bernardini et al., Phys. Rev. Lett. **10**, 407 (1963).
4.5-23. A. Piwinski and A. Wrulich, DESY Report No. DESY 76/07 (1976).
4.5-24. B. Richter and D. Ritson, Int. Conf. High Energy Accelerator, Dubna (1963), p. 461.
4.5-25. A. Piwinski, SSC Central Design Group Report No. SSC-57 (1986).
4.5-26. D. Neuffer and S. Peggs, SSC Central Design Group Report No. SSC-63 (1986); S. Heifets, SSC Central Design Group Internal Report No. SSC-N-129 (1986); S. Heifets, University of Houston Report No. UH-IBPD-007-86 (1986).
4.5-27. L. Evans and J. Gareyte, IEEE Trans. Nucl. Sci. **NS-30**, 2436 (1983).
4.5-28. M. Furman and A. Chao, IEEE Trans. Nucl. Sci. **NS-32**, 2297 (1985).
4.5-29. E. Forest and M. Furman, SSC Central Design Group Report No. SSC-32 (1985).
4.5-30. M. Furman, SSC Central Design Group Report No. SSC-62 (1986).
4.5-31. E. Forest, SSC Central Design Group Report No. SSC-51 (1985).
4.5-32. A. Chao and S. Peggs, SSC Central Design Group Internal Report No. SSC-N-80 (1985).
4.5-33. R. Diebold, in *Accelerator Physics Issues for a Superconducting Super Collider*, ed. M. Tigner, U. Michigan Report No. UM HE 84-1, 1983, p. 5.
4.6-1. D.E. Johnson, SSC Central Design Group Report No. SSC-60 (1986).
4.6-2. J.D. Jackson, SSC Central Design Group Internal Report No. SSC-N-110 (1986).
4.6-3. R.P. Shutt, Brookhaven National Laboratory Internal Report No. 141–20, SSC-MD-107, 10 p. (1985).
4.6-4. J.D. Jackson, SSC Central Design Group Internal Report No. SSC-N-199 (1986).
4.6-5. A. Chao and J.D. Jackson, SSC Central Design Group Internal Report No. SSC-N-86 (1985).
4.6-6. H. Jöstlein et al., submitted to J. Vac. Sci. Technol. (1986).
4.6-7. Clustered Interaction Study Group, SSC Central Design Group Report No. SSC-SR-1014 (September 1985), p. 30.
4.6-8. M. Furman, SSC Central Design Group Internal Report No. SSC-N-143 (1986).
4.6-9. D.E. Johnson, J. Peterson, and M. Tigner, SSC Central Design Group Internal Report No. SSC-N-117 (1986).
4.7-1. M. Sands, Ref. 4.1-6, p. 359, Eq. (5.4).
4.8-1. R. Castaldi and G. Sanguinetti, Ann. Rev. of Nuc. Sci. **35**, 351 (1985).
4.8-2. M.M. Block and R.N. Cahn, Lawrence Berkeley Laboratory Report No. 20159 (1985).
4.8-3. R.M. Baltrusaitis, et al., Phys. Rev. Lett. **52**, 1380 (1984).
4.8-4. SSC Reference Designs Study, p. 154 (1984).
4.8-5. G. Arnison, et al., Phys. Lett. **118B**, 167 (1982).

4.8-6. J.R. Johnson, et al., Phys. Rev. **D17**, 1292 (1978).
4.8-7. A.E. Brenner, et al., Phys. Rev. **D26**, 1497 (1982).
4.8-8. F.E. Paige and S.D. Protopopescu, BNL-37271 (1985).
4.8-9. H.-U. Bengtsson and G. Ingelman, CERN Report No. TH.3820-CERN (1984).
4.8-10. R.V. Sevranckx, K.L. Brown, L. Schachinger, and D. Douglas, Stanford Linear Accelerator Center Report No. 285 (1985).
4.8-11. D.E. Groom, SSC Central Design Group Internal Report No. SSC-N-153 (1986).
4.8-12. R.L. Keizer and M. Mottier, CERN Report No. 82-05 (1982).
4.8-13. M.A. Rose, et al., Harry Diamond Laboratory Report No. HDL-CR-81-015 (U.S. Army ERDACOM, July 1981); M.G. Knoll, Air Force Weapons Laboratory Report No. AFWL-TR-78-5 (Kirtland AFB, NM, 1978); M.E. Daniel and F.N. Coppage, IEEE Trans. Nuc. Sci. NS-26, 2600 (1979); G.L. Dinger and M.G. Knoll, Air Force Weapons Laboratory Report No. AFWL-TR-79-118 (Kirtland AFB, NM, 1980); E.E. King and G.J. Manzo, IEEE Trans. Nuc. Sci. **NS-27**, 1449 (1980); R. Polimadie, H. Eisen, K. Pinero, Harry Diamond Laboratory Report No. HDL-D5-80-1 (U.S. Army ERDACOM, July 1980).
4.8-14. J. Kalinowski, in *Transient Radiation Effects in Electronics,* p. E12–E30, Defense Dept. Doc. Center (Sept. 1969).
4.8-15. T.W. Armstrong and J. Barish, Nuc. Sci. and Engineering **38**, 265 (1969).
4.8-16. J.B. McCaslin, R-K. S. Sun, and W.P. Swanson, A.J. Elwyn, W.S. Freeman, and P.M. Yurista, SSC Central Design Group Report No. SSC-58 (1986).
4.8-17. P.W. Arnio, et al., CERN Divisional Report No. TIS-RP/106 (1983).
4.9-1. A.W. Chao and J.M. Peterson, SSC Central Design Group Internal Report No. SSC-N-62 (1985).
4.10-1. J. Simpson et al., in Proc. 1984 Summer Study on the Design and Utilization of the SSC, eds. R. Donaldson and J.G. Morfin, DPF, American Physical Society, NY (1984), p. 313.
4.10-2. E.P. Colton and H.A. Thiessen, Los Alamos National Laboratory Report No. LAMPF2-85-012 (1985).
4.10-3. L.J. Laslett, in Brookhaven National Laboratory Report No. BNL-7534, p. 324 (1963)
4.10-4. L.C. Teng, Fermilab Internal Report No. FN-207 (1970)
4.10-5. J.W. Cooper, Ref. 4.10-1, p. 462.

5. Technical Systems: Engineering Design

5.1 General Description of Needed Technical Systems

The SSC concept, technical basis, and accelerator physics parameters have been discussed globally in the preceding chapters. Realization of these goals in the form of technical systems is constrained by the available technology, by likely scenarios of commissioning and operation, by the interrelations of the subsystems, and by the requirement that the total cost be minimized. The present chapter describes the major technical components of the SSC and sketches the conceptual design of each.

The general framework has already been discussed in Section 3.3, and is shown in Figs. 1.2-1 and 3.3-2. Two independent rings of superconducting magnets bend and focus the particles through nearly 156 degrees in each of two opposite arcs. Joining the arcs on either side are clusters containing interaction regions (IRs) and utility sections separated by short bending sections. The arcs are repetitions of the standard cell shown in Fig. 4.2-3, whereas the cluster areas are more complex and less regular in their arrangement of components. Near one of the clusters is a complex containing the control center and the cascade of injection accelerators.

5.1.1 Magnets

By far the largest of the SSC technical systems consists of the main ring magnets — some 7680 dipoles, nearly 1800 quadrupoles, and an almost equal number of "spool pieces" which contain correction windings and other instrumentation.

A perspective drawing of the magnetic components of the SSC dipole is shown in Fig. 2.4-3. At its center is the beam tube, whose a high-conductivity liner minimizes beam image current losses. Two correction coils are wound on the outside of the tube to compensate for systematic distortion of the magnetic field from iron saturation and persistent currents in the main windings. Around it is placed a two-layer main coil of superconducting cable, with interspersed copper wedges to adjust the current density for a uniform dipole field inside. This coil, subjected to magnetic forces of about 7×10^5 N m^{-1} at full current (6500 A), is held in place by laminated stainless steel or aluminum collars. The collars are keyed together after compression. Because the coil and collars shrink different

amounts during cooldown, the room temperature preload is about 2.5 times greater than the remnant preload at 4 K needed to prevent coil movement caused by the magnetic forces. A yoke of laminated low-carbon steel, surrounded by a stainless steel skin which also serves as a pressure vessel, completes the inner assembly. Passages through the iron are provided for the liquid helium coolant, as well as for buses carrying current to adjacent magnets.

This yoked assembly is supported inside a cryostat, as is shown schematically in Fig. 5.2-10(a). It is supported by pedestals consisting of concentric fiberglass-epoxy tubes, chosen for their low thermal conductivity and high strength. Intermediate thermal shields concentric with the assembly insulating blankets are at nearly 20 K and 80 K. A cost optimization study of manufacturing, transportation, and accelerator operation led to the selection of a dipole length of 17 m, with 5 dipoles per half cell [5.1-1]. A completed dipole weighs 9 tons.

Quadrupoles are similarly constructed, except with the coil arrangement shown in Fig. 5.2-14(a). An arc quadrupole with its cryostat and beam position monitor is 4.3 m long. Associated with each quadrupole is a drift space filled with a cryogenic device called a spool piece, containing correction magnets and elements of the cryogenic, power supply, and control systems. A spool piece in the arcs is about 5 m long; a schematic diagram is presented in Fig. 5.2-16. As shown in Fig. 5.2-17, separate windings provide dipole, quadrupole, and sextupole corrections, permitting corrections to the closed orbit, tune, and chromaticity of the beam.

Interaction region magnets are of necessity somewhat different. Wherever possible, their structure is the same as that of arc magnets, to minimize special tooling. Lengths have been adjusted to permit the use of common power supplies to as great an extent as practical. The vertical bend dipole in which the beams are brought together is special in that the beam separation at one end exceeds the good-field region of standard dipoles; for this application larger aperture dipoles are used. As shown in Fig. 3.3-4, the beam separation occurs in two steps. Between the two steps the beam separation is only 35 cm, and so magnets in this region must occupy common cryostats.

5.1.2 Cryogenics

An extensive cryogenic system is required to maintain the magnets at the design temperature of 4.35 K or less. From a cryogenic point of view the machine is divided into 10 sectors, four in each arc and one in each cluster. The arc sectors are 7.7 km long. An eleventh refrigerator cools the high energy booster. Each has about the same cryogenic load (3 kW at 4.15 K), requiring 2.6 MW to power its helium refrigerator, which supplies 400 g s^{-1} at 4.15 K and four atmospheres pressure.

Each of the ten sectors is divided into four cryogenic loops, with loops going both ways in each ring from the refrigerator at the sector midpoint. The helium stream in each loop warms as it removes heat from the magnets. At every cell (more specifically, at alternate spool pieces), the high pressure helium stream passes through a heat exchanger (recooler), where it is cooled by a pool of boiling helium supplied from the return lines. The temperature rise of the high pressure helium depends upon the heat input and the flow rate, but is calculated to be less than 0.15 K between recoolers. The returning boiloff gas absorbs further heat in the refrigerator heat exchanger.

Each cryogenic loop in the arcs is sub-divided into four sections, each about 960 m long. A section is the smallest part of the machine that can be independently warmed to room temperature. It terminates at either end with a special spool piece that contains U-tubes, for cryogenic connection from one section to the next, and a short piece of warm beam tube with a vacuum gate valve. Warmup is accomplished by isolating a section by removing the U-tubes at each end, then turning on electric heaters inside the cryostat. The entire operation of warming up a section, removing and replacing a magnet, and cooling down again is estimated to take about six days.

The cryogenic systems of each sector are independent, but are connected one to the next through the magnets. In this way, neighboring refrigerators can be used to assist one another during cooldown, or to take over for a malfunctioning refrigerator. In the interest of reliability, the high energy booster refrigerator is cryogenically connected to the main ring so that it can also participate in the redundancy. Each refrigerator is oversized by 50% for this purpose. Except in the cluster regions, all of the cryogenic transport is contained within the magnet cryostats. A single six-inch pipe external to the magnets returns the warm helium gas from boiloff at the power leads and from cooldown operations. In the cluster regions there are also transfer lines to route cryogens around warm parts of the ring.

The magnet cryostats have two thermal shields, one cooled by helium gas at 20 K, supplied directly from the helium refrigerator heat exchanger, and the other cooled by liquid nitrogen at about 80 K. The nitrogen is supplied from two 180 metric ton/day air separation plants (requiring 5.6 MW each) and storage dewars at the helium refrigerators.

5.1.3 Vacuum

There are two independent vacuum systems in each of the collider rings. A very low residual pressure is required within the beam tube to permit a long beam life. A comparatively modest insulating vacuum is required in the magnet cryostats. In both cases, initial pump-down is accomplished with the use of portable carts that contain turbo-molecular pumps and diagnostic instruments. Once pump-out and cooldown are complete, hand valves are closed, and the carts taken away. Since both systems contain surfaces near 4 K, they are primarily cryo-pumped — i.e., gas molecules eventually hit cold surfaces and are frozen there.

Vacuum gauges are permanently installed at each spool piece, and are read through the control system. Ion pumps installed on the beam tube at every other spool piece are turned on during cooldown before cryo-pumping becomes effective, and during operation function as vacuum gauges.

Unlike previous proton machines, synchrotron radiation from the 20 TeV protons in the SSC desorbs gas molecules from the beam tube walls. As discussed in Section 5.4.1 (and 2.4.5), detailed studies of this process at a synchrotron light source have shown that the pressure rise will not significantly degrade the lifetime of the SSC beams.

5.1.4 Main Power Supplies

Power distribution makes use of the same sector division as does the cryogenics, so that main power supplies for the arcs are located with the refrigerators. The dipoles and quadrupoles of a sector of each ring are connected in series to a single 6500 A, 300 V power

supply. Hence, each ring is independently powered, and has eight power supplies in the arcs. Since the beams pass through common magnets in the IRs, the rings are coupled together during normal two-beam operation. The 300 V requirement permits ramping the ring to full current in 500 s, which will be particularly useful during testing and commissioning. Regulation between sectors is done with the aid of differential transductors at the ends of each sector.

The power supply arrangement in the clusters has additional features. The current in many of the quadrupoles used in the IRs must be varied (e.g. when changing β^*); elements with the same excitation program are often a kilometer or so apart; the number of power leads and expensive high-current power supplies must be minimized. The mini-arcs between interaction regions are powered with the same program as the main arcs, along with the vertical bends and some of the IR quadrupoles. The same supply provides current for the triplet quadrupoles nearest the interaction points (Q1, Q2, and Q3 in Fig. 3.3-4) as well as for Q6, but connected to each of these elements is also a shunt supply capable of 10% of the current of the main supply. Two of the quadrupoles used to vary β^* have individual 6500 A supplies because of the large current variation required. They are run together with the matching set on the other ring to reduce the number of supplies. A total of 30 high-current supplies are needed for the SSC collider rings.

5.1.5 Quench Protection

An active quench protection system is used. A microprocessor at each cell measures the voltage across the cell and across each magnet in the cell. Hence, 12 voltages are used to compute dI/dt. If the microprocessor determines that a quench is occurring, heaters are fired in the offending half-cell, the sector power supply is turned off, and dump resistors are switched into the power supply circuit. The decay time constant for the sector is 20 seconds. For radiation protection reasons the bypass diodes are external to the cryostat, in holes in the tunnel wall, and are connected to the magnets with pairs of leads (safety leads) at every spool piece.

5.1.6 Radio-Frequency System

The acceleration system is relatively small. It must accelerate the beams from 1 TeV at injection to the final storage and collision value, 20 TeV, and must also maintain the tight bunch structure of the beam during collision while replenishing the 9 kW lost to synchrotron radiation in each ring. Systems recently developed at electron accelerators can in fact be used directly for the SSC, and the cavities, power amplifiers, and major controls developed for the PEP collider at the Stanford Linear Accelerator Center (SLAC) have been adopted.

A peak accelerating voltage of 20 MV per ring at an operating frequency of 375 MHz meets the requirements. This voltage can readily be produced with the PEP cavity units driven by two 1 MW klystrons. The cavities occupy only 25 m along each beam line. Unless the tunnel is very deep, the total of four klystrons needed to drive both rings will be located above ground over the cavities, as is done at PEP and at the SLAC linac. The accelerating unit layout is shown schematically in Fig. 5.7-1, and a photograph of a PEP cavity in Fig. 3.1-3 (An isometric cut-away appears in Fig. 5.7-2).

5.1.7 Injection and Abort Systems

The abort system for one of the rings is immediately downstream of the injection line for that ring, in one of the utility regions. Injection and abort for the other ring are similarly arranged in the other utility straight section. The high energy booster (HEB) accelerates beams in either direction, and is centered between the two utility straight sections, but out of the plane of the collider by seven meters. Proton beams are extracted tangentially from the same HEB straight section in opposite directions, and bent down to the plane of the collider. Putting the two machines on different levels allows personnel access to one while the other is operating.

Since the abort is downstream of injection, the beam can be steered directly into the collider ring abort dump, allowing complete tuning of the injection line before any beam is actually injected into the collider.

The beam is extracted from the HEB in a single turn and injected into the collider. This process is repeated 15 times, filling the collider completely except for a gap to accommodate the abort system rise time. For a one-minute HEB cycle time it takes about 40 minutes to fill both rings, including the time to changed the HEB polarity.

5.1.8 Control and Instrumentation Systems

With its long time constants (perhaps a day between cycles), precisely sequenced operations, and large energies stored in its beams, the SSC requires extensive beam instrumentation. Over 800 beam position monitors per ring, for example, are needed to provide the information necessary for orbit control. Other parameters, such as beam profile, loss rate, and intensity must also be monitored.

Because of the large size of the collider rings, the controls system must be distributed so that modules are close to the devices to be monitored and controlled. In practice this means modules in every cell, close to the quadrupoles. As has been discussed in Section 4.8, the neutron flux in the tunnel necessitates recessing the modules into the tunnel ceiling.

Intelligent modules are used locally, in order to hold the communications load on the network to a minimum. Two ringwide networks are used for redundancy. For the same reason, microprocessors in the tunnel are capable of sharing each other's work load.

As shown in Fig. 5.13-1, the control system consists of a large central multi-processor computer that contains the complete data base, and which communicates in one direction to the ring network, and in the other to control consoles. The next level of computer is located at the ten sector service buildings around the ring, and in the control computers for other major systems, such as the injector complex accelerators. Since these computers have their own copies of the relevant data base, the system is not loaded down with data base transmissions. The function of the sector and similar computers is to communicate with the distributed microprocessors in the tunnel, and, if necessary, control the refrigerators, main power supplies, and a local control console.

5.1.9 Injector Complex

Linear Accelerator

Negative hydrogen ions are accelerated by three linac stages, each optimized for the average velocity of the particles being accelerated. The first, a radio-frequency quadrupole stage, accelerates to about 2.5 MeV. A drift tube linac then accelerates to 125 MeV, and a side-coupled linac finally accelerates to 600 MeV. The total length is about 125 m. H^- ions are accelerated so that multi-turn, charge exchange injection into the low energy booster can be used to minimize brightness dilution. Each section of the linac is patterned after devices already in operation, primarily at Los Alamos National Laboratory.

Low Energy and Medium Energy Boosters

These relatively rapid-cycling synchrotrons are of conventional design, utilizing laminated iron magnets. Particular attention is paid to smoothness of the beam vacuum envelope to avoid emittance-diluting instabilities. Their injection transfer energies are selected to serve the dual purpose of controlling space-charge tune shift and avoiding transition energy. At low momentum, the self-repulsion of beam particles works together with the focusing properties of the ring to lower the beam brightness. This effect can be avoided by limiting the so-called space charge induced tune shift to 1/4 or less. Similarly, while the additional momentum spread incurred in crossing transition energy would not be harmful, the transient state of high beam density that occurs during the crossing can lead to brightness dilution through other instabilities.

In the Low Energy Booster (LEB) the 600 MeV injection (kinetic) energy is sufficient to hold $\Delta\nu \approx 1/4$ for the lowest emittances and highest currents expected. Its 7.12 GeV top kinetic energy is selected to be below transition energy for this ring. In the Medium Energy Booster (MEB), the lattice design is selected so that the beam energy is always above transition. As it turns out, this configuration also meets the space charge criterion. The LEB and HEB need to cycle relatively rapidly in order not to add significantly to the cycle time of the High Energy Booster (HEB), which for reasons of cryogenic load must cycle rather slowly. The resulting 10 Hz repetition rate for the linac and LEB and 1/4 Hz rate for the MEB are well within the state of the art. The peak energy of 100 GeV for the MEB is chosen to keep the ratio of peak energy to injection energy relatively low.

High Energy Booster

Injection energy into the collider ring is set by a number of economic and practical considerations. Among these is field distortion at low energies, caused by persistent currents in the superconductor. This effect can be ameliorated by using very fine filaments in the superconducting cable of the magnets, as is discussed in Sections 2.4.3 and 5.2.3. Whatever the filament size, the field dependence of the multipole coefficients b_2 and b_4 is such that 1 TeV appears appropriate for injection into the collider — at lower energies, the correction system must be more powerful; yet it is still needed up to several TeV, where the cost of the HEB would be prohibitive. (See Section 4.10.1.) At 1 TeV, economical operation of the HEB requires the use of superconducting technology for that synchrotron as well as for the collider.

5.1.10 R&D Needs and Opportunities

Most of the detailed engineering development for standard SSC technical components and subsystems can be carried out during the early phases of construction. However, the expense and criticality of the superconducting magnet system warrant continuing R&D effort prior to the production phase. Two aspects stand out. First, it is important to verify through extensive and exhaustive tests that the basic magnet design fully meets the reliability requirements over the long lifetime of the collider and that the system behavior is as expected. A series of full scale dipole models now under construction will be used for these tests [5.1-2]. Second, continuing advances in component development, particularly the performance of the NbTi superconductor, are being registered in the laboratory. Efforts to incorporate these advances into collider magnet designs as well a streamlining the designs further for easier manufacturing could, if successful, result in further cost savings. For example, the superconductor critical current performance used in this report is 2750 A/mm^2 at 4.2 K and 5 T. Through the university-DOE Laboratory-industry collaboration [5.1-3], some manufacturers are delivering materials with 3000 A/mm^2 capability. In the laboratory, critical current densities in excess of 3500 A/mm^2 are being achieved. If proved practical in large-scale production, these advances could be used to reduce the amount of superconductor needed or to increase the operating field of the magnets, in both cases resulting in lowered collider cost.

In the following sections, the conceptual design of each of the technical systems is discussed in detail.

5.2 Magnets

5.2.1 Introduction

The magnet system for the SSC must bend and focus the protons as they circulate in the rings and are brought to collision in the experimental areas. The strength of the dipole field determines the size of the rings and is chosen as high as practicable consistent with minimum total accelerator cost. The uniformity of the magnetic fields must be high in order to assure a long lifetime for the stored beams. Finally, the magnet reliability must be high over the lifetime of the machine in order to provide high availability. During a projected twenty year lifetime, an individual magnet is required to survive 10^4 acceleration cycles, $\sim$20 thermal (warmup, cooldown) cycles, up to 50 quenches, and a radiation dose of 10^6 Gys. To meet these fundamental requirements, the dipole magnet emerges as by far the most expensive single component in the machine, due to the large numbers required, and it is for this reason that the early R&D effort has focused on this device.

Early studies indicated that it would be possible to build the dipole magnets for the SSC with several possible designs. The magnet R&D program for the SSC [5.2-1] developed a number of these proposed designs to the point where accurate cost estimates and an evaluation of their performance characteristics could be made [5.2-2]. The choice that emerged is a high field magnet using a two-layer cos theta NbTi coil configuration. The coil is clamped with stainless steel collars and the collared subassembly is held in a cold

iron yoke. This cold mass, approximately 17 m in length, is mounted in a cryostat using a folded post support system. The rings of magnets are magnetically, electrically, and cryogenically independent of one another for operational reasons [5.2-3]. The physical aperture of the magnet is chosen to minimize the cost, but consistent with the field quality required for stable particle motion (see Section 4.3.2).

The technical aspects of the various magnet subsystems are described in greater detail in the sections that follow. Some more general characteristics of the magnet design and construction and the reasons for making particular choices, are given first, however.

The high operating field of the dipole magnet, 6.6 T at 4.35 K, is made possible by the availability of high current density superconducting NbTi alloy. Further improvements in this parameter can be used to reduce costs, either by reducing the amount of NbTi in the magnets at constant magnetic field or increasing the magnetic field at a constant amount of superconductor. The latter possibility is bounded by the need to provide an increasing amount of copper as the current in the superconductor increases. Potential for increased B in the current design must be assessed by measurement.

The superior superconductor planned for the SSC has been made possible by the very successful R&D program carried out through a collaboration between university, industry and the national laboratories. The high J_c of the present material (2700–3000 A/mm^2 at 4.2 K, 5 T) is due to new heat treatments made possible by the high homogeneity NbTi alloy currently being produced. In addition, incorporation of barriers to prevent CuTi intermetallic compound formation during heat treatment has promoted filament diameter uniformity during the drawing of the wire. This last advance has made possible the fabrication of high current density material with filaments in the 2–3 μm range, resulting in a reduction in superconductor persistent currents (magnetization) at low field levels. The conceptual design is based on 5 μm filament size.

The coils of the magnets are wound on automated winding machinery and then formed to a precise size in a molding operation where the epoxy in the epoxy-impregnated cable wrap is cured, thus forming a rigid, precise structure, guaranteeing coil-to-coil reproducibility and lending itself particularly well to industrial fabrication. The random magnet-to-magnet errors, which are largely determined by the variation in coil sizes, can be held within the required tolerances through this technique.

The molded coils, including the beam tube, are assembled and held in place at the required prestress through the use of stainless steel collars. This technique, used for the Tevatron magnets, provides an intermediate assembly step where the electrical integrity of the Kapton insulation and the harmonic content of the field produced by this subassembly can be checked.

Final assembly of the magnet cold mass involves the insertion of the collared coil into the iron yoke laminations and the closure of the helium containment by the welding together of two half shells of stainless steel around the iron yoke. Through the use of alignment keys and slots, the position of the coils is accurately fixed relative to the outside of this assembly and can thus be precisely aligned through the cryostat suspension system to the outside of the vacuum enclosure. The need for precision surveying during the assembly of a magnet is thus minimized. The iron yoke, in addition to giving substantial field enhancement, acts to hold the coils rigidly in place and makes possible a low heat-leak suspension system for the cold mass. There is some magnetic saturation of the iron at high field levels, but this nonlinear perturbation of the dipole field can easily be compensated by

the power supplies and correction elements designed into the machine. The need to cool the great mass of iron lengthens somewhat the cooldown time of the machine, but the price is not severe [5.2-3].

The cryostat is designed to provide stable yet simple and low heat leak support of the cold mass in a way that can be reliably implemented in an industrial production setting. Support posts, constructed as a nested pair of thin-walled fiberglass-epoxy tubes loaded in compression, provide the required support for the vertical and horizontal loads. The support posts are located and fastened to the cold mass using precision fixturing such that the magnet location, including the required slight sagitta, is determined as the cold mass is assembled into the cryostat and later installed onto the tunnel supports. The folded posts, located at five points along the length of the magnet, minimize the number of penetrations through the insulating shields and barriers. This reduces the chance of introducing heat leaks by thermal radiation through imperfect application of the insulation. By minimizing the number of support points, the danger of introducing unequal stresses into the support system and into the cold mass is reduced.

During and after assembly of the magnets, electrical tests are performed to guarantee the absence of shorts and the required high voltage stand-off capability of the coils. Warm-magnet field measurements are made after collaring of the coil and again after assembly and closure of the iron yoke. Cold testing is also performed, as discussed in Section 5.2.11. Because of the rigorous testing during assembly, it is anticipated that very few assembled magnets will have to be rejected.

The magnets are quench-protected by active heaters built into each magnet. These heaters are activated when a quench is detected and serve to spread the quench quickly throughout the entire magnet, thereby avoiding local hotspots or unacceptably high voltages. The use of active heaters represents a conservative approach. As discussed in Section 5.2.8, a passive system may be adequate. The chosen design avoids the need for quench protection diodes in each magnet; such diodes may be vulnerable to the neutron radiation caused by beam-gas interaction during operation.

The quadrupole design features many of the same parameters as the dipole design: same bore, same cable (outer), same suspension system, and current in series with that of the dipole magnets. The coils are wound and cured in a fashion similar to that used for the dipoles. The quadrupole magnet iron does not saturate as much as the dipole iron (0.5% vs 2.2%, respectively). This difference, reproducible from cycle to cycle, is compensated by the correction quadrupole magnets in the spool pieces.

In summary, the magnet design for the SSC makes use of the technological base that has been developed in the construction of the Tevatron and in the R&D program at BNL and LBL. Where applicable, it incorporates advances, such as in the quality and performance of the NbTi superconductor, that enhance the performance and reduce the cost of the SSC. The techniques developed for the construction of the magnets lend themselves well to industrial production [5.2-2]. Most importantly, the design is conservative throughout so that these magnets can be expected to perform reliably for the lifetime of the SSC.

5.2.2 Performance Requirements, Magnetic Design

A quadrant of the dipole coil cross section is shown in Fig. 5.2-1(a) depicting the conductor distribution in the two coil layers with spaces for pole pieces and intervening wedges. Figure 5.2-2 shows a cross section of the magnet, including the iron yoke, emphasizing elements and features essential to the magnet design. The main design parameters are listed in Table 5.2-1.

Both coil layers are wound from partially keystoned, flat NbTi cable. The cable and its constituent wires are discussed in some detail in Section 5.2.3. The departure from radial stacking because of the partial keystone of the cable, evident in Fig. 5.2-1, is compensated by the inclusion of insulated copper wedges in the coil cross section. The wedges are also required to maximize the field uniformity. The field in the outer coil is lower than in the inner coil: B_{max}(outer) = 0.844 B_0 vs. B_{max}(inner) = 1.055 B_0. Therefore, the cable is graded to adjust current density with the inner layer (16 turns distributed in 4 blocks in each coil section) wound from a 23-strand cable of Cu:SC ratio 1.3:1 and the outer layer (20 turns in 2 blocks) from a 30-strand cable (1.8:1). The current density in the superconductor of the outer layer is 1.19 times that in the inner layer. The two layers are powered in series, with approximately 6.5 kA producing a central field of 6.6 T.

The coils are surrounded by a nearly circular, split and laminated iron yoke of low carbon steel, separated from it by non-magnetic stainless steel collars which provide the necessary restraint to maintain the coils under a compressive stress (approximately 3.5 kpsi at operating field). The iron yoke contributes approximately 1.7 T to the magnetic field. The relatively thin radial width of the collars (15 mm) minimizes the loss in this contribution. Conversely, a magnetic benefit from collars is a sharp decrease in the effect of iron saturation on the allowed field harmonics (e.g., the change in the sextupole term is 1.2×10^{-4} of the dipole field, at 1 cm). If necessary, these could be made smaller by shaping the iron.

The coil end windings are of the usual saddle-shaped winding configuration. To ensure proper "lay" of the relatively wide cable and to minimize field enhancement as well as field harmonics in the coil ends, the end turns are spaced out by interleaving molded spacers and wedge extensions. The iron yoke extends over the coil ends, but with an inside diameter larger than in the magnet "straight section". This further minimizes the field enhancement in the magnet end, yet retains the advantages of providing good local mechanical coil support and minimizes the external fringe field.

Magnet Load Line, Central Field, and Saturation

As noted, the two coil layers are powered in series. Field calculations agree reasonably well with magnet measurements [5.2-4]. The operating (central) field B_0 of 6.6 T (at 4.35 K) corresponds to a current of approximately 6.5 kA, or a transfer function of 1.015 T/kA. The drop in B_0/I at 6.6 T relative to its low field value, because of iron saturation, is about 2%. At B_0 = 6.6 T, the calculated (two-dimensional) peak field in the inner coil layer is 7.0 T; in the outer layer it is about 5.6 T. The approximate location of the respective peak fields is indicated in Fig. 5.2-1(b), which shows the distribution of magnetic lines of force in a somewhat simplified model of a dipole quadrant. (As noted earlier, the central field end enhancement normally found in race track or saddle coil-wound dipole magnets is largely eliminated by spacing the end turns and enlarging the iron inner radius in the end region.)

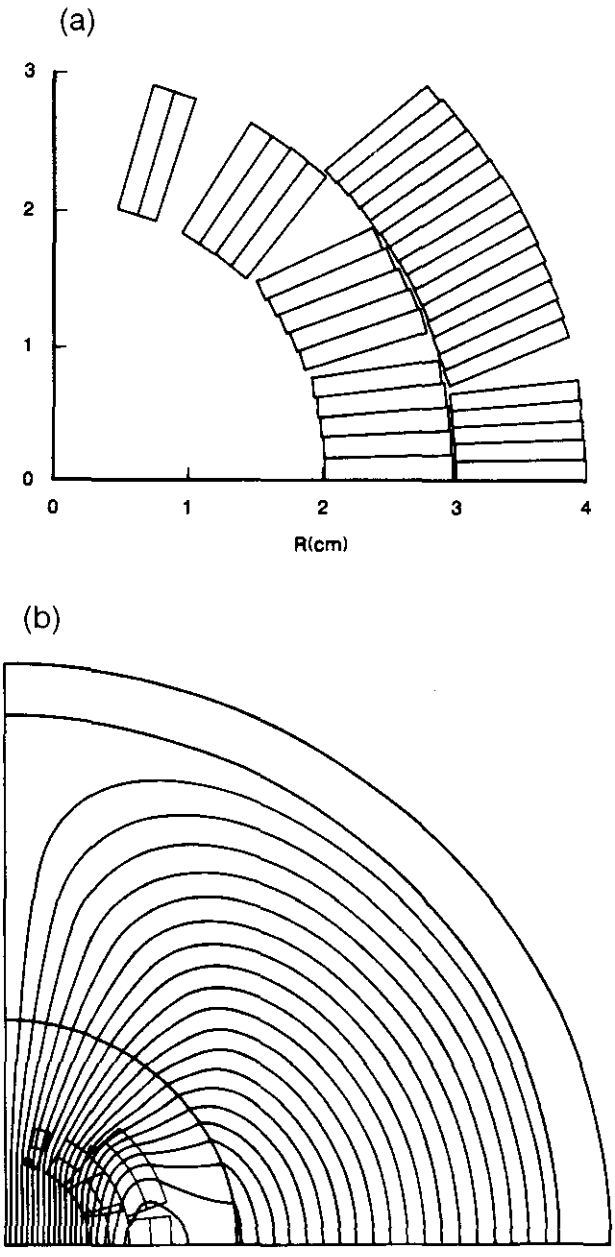

Figure 5.2-1. (a) Quadrant of dipole coil cross section, showing distribution of partially keystoned superconducting cable. (b) Quadrant of dipole, showing magnetic field lines. The peak field locations in the inner and outer coils are also indicated.

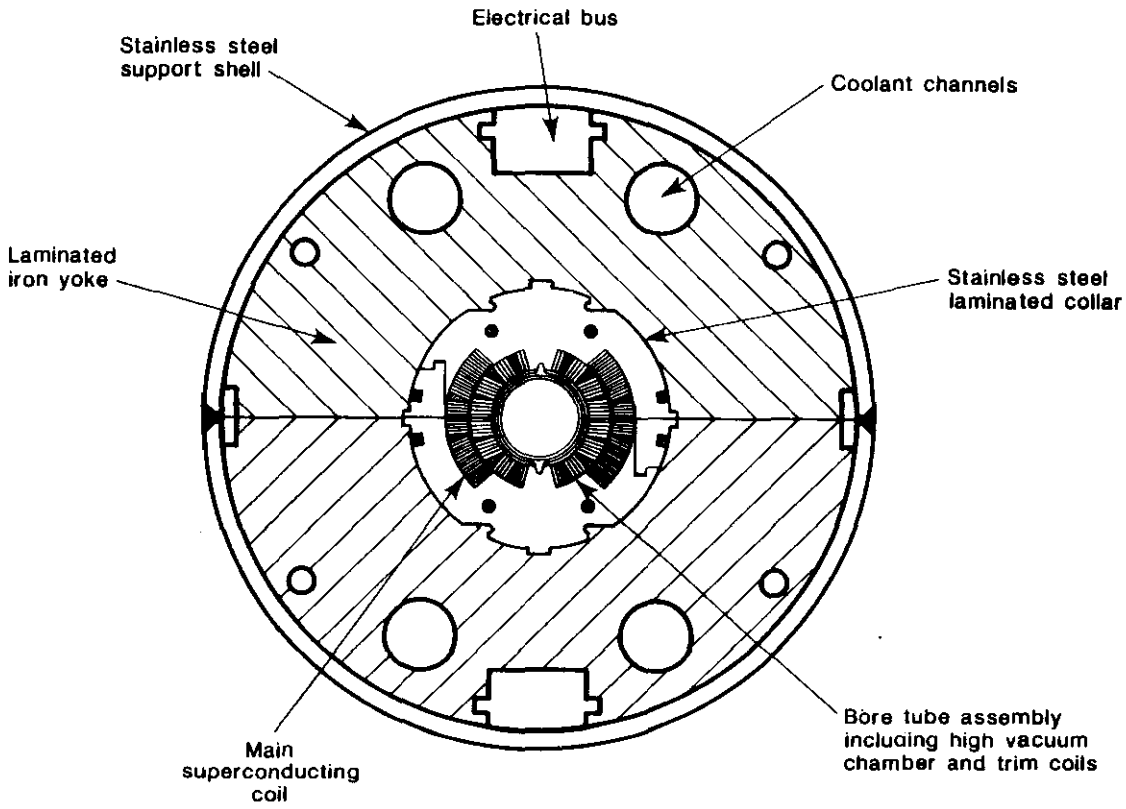

Figure 5.2-2. Overall cross section of dipole showing coil, collars, iron yoke, and yoke support tube.

Table 5.2-1
Dipole Magnet Parameters

General	
No. of dipoles per ring	3840
Overall length/interface length [m]	17.35/0.8
Magnetic length [m]	16.54
Bore tube inner diameter [cm]	3.226
Mass of conductor [kg]	208
Cold mass [kg]	6759
Central field [T]	6.6
Current [A]	6500
Inductance [mH]	53
Stored energy [MJ]	1.12
Bore Tube Assembly	
Bore tube, material	stainless steel
Outer diameter [cm]	3.45
Wall thickness [cm]	0.10
Copper coating [mm]	0.13
Trim coil, type	sextupole/decapole
Mean diameter [cm]	3.515/3.58
No. of turns per pole	15/9
Max. current [A]	5/5
Winding	
Inner layer	
No. of turns (per coil section)	16
Inner diameter [cm]	4.000
Outer diameter [cm]	5.923
Cable length [m] (for 2 coil sections)	1076
Cable mass [kg] (for 2 coil sections)	100
Maximum field [T]	7.0
Outer layer	
No. of turns (per coil section)	20
Inner diameter [cm]	5.974
Outer diameter [cm]	7.986
Cable length [m] (for 2 coil sections)	1341
Cable mass [kg] (for 2 coil sections)	108
Maximum field [T]	5.6
Conductor	
Inner layer	
Cross section, bare [mm]	9.30×(1.59–1.33)
Keystone [deg.]	1.61
Strand diameter [mm]	0.808
No. of strands	23
Strand twist pitch [per cm]	0.4
Cable twist pitch [per cm]	0.126
Copper-to-superconductor ratio	1.3:1
No. of superconductor filaments	11000
Filament diameter [μm]	5

Outer layer	
Cross section, bare [mm]	9.73×(1.27–1.07)
Keystone [deg.]	1.21
Strand diameter [mm]	0.648
No. of strands	30
Strand twist pitch [per cm]	0.4
Cable twist pitch [per cm]	0.136
Copper-to-superconductor ratio	1.8:1
No. of superconducting filaments	6000
Filament diameter [μm]	5
Collars	
Material	stainless steel, nitrogen hardened
Lamination thickness [mm/in.]	1.52/0.060
Outer diameter [cm]	11.09
Radial thickness, nominal [cm]	1.5
Iron Yoke	
Material	low carbon steel
Inner diameter [cm]	11.14
Inner diameter, magnet ends [cm]	17.51
Outer diameter [cm/in.]	26.67/10.5
Lamination thickness [mm/in.]	1.5/0.060
Weight of iron [kg]	5171
Yoke Containment Structure	
Material	stainless steel
Outer diameter [cm/in.]	27.62/10.878
Thickness [cm]	0.47
Weight of shell [kg]	540
Cryostat	
Vacuum vessel material	steel
Vacuum vessel outer diameter [cm/in.]	60.96/24.00
Wall thickness [cm]	0.635
Heat shield material	aluminum
80 K heat shield, outer diameter [cm/in.]	45.72/18.00
20 K heat shield, outer diameter [cm/in.]	40.64/16.00
Superinsulation layers, outside 80 K shield	52
Superinsulation layers, outside 20 K shield	13
Cold mass support type	reentrant post
Support materials	F.R.P. unidirectional
Number of supports	5
Support interval [m]	3.5
Load per support [kg]	1352

The margin in critical current at operating field, J_c/J_o, where J_c is the minimum critical current density of the strands before cabling, is 1.25, as discussed in Section 5.2.3.

Multipoles: Low and High Field

The description of the magnetic field within the magnets has been discussed in Section 4.3.1. The various multipole coefficients b_n and a_n are measures of the field quality. The coil design shown in Fig. 5.2-1 gives a very uniform magnetic field; expressed in terms of a multipole analysis, the calculated field quality is shown in Table 5.2-2.

Table 5.2-2
Calculated Systematic Multipoles at Low and High Field from the Presence of the Iron Yoke
(units are $10^{-4}\, B_0\, \text{cm}^{-n}$)

Multipole	Low Field ($\mu = \infty$)	High Field (6.6 T)
Quadrupole (b_1)	not allowed	—
Sextupole (b_2)	0.00	1.18
Octupole (b_3)	not allowed	—
Decapole (b_4)	0.00	−0.05
Dodecapole (b_5)	not allowed	—
14-Pole (b_6)	0.00	−0.01
16-Pole (b_7)	not allowed	—
18-Pole (b_8)	0.00	0.02

Low field values (typically 1 T) are calculated for infinite permeability iron; high field calculations (6.6 T) include the effect of iron saturation.

Table 5.2-2 not only shows that all low field harmonics are less than 0.01 units or 10^{-6} of the main dipole field, but, because of the presence of the collars, the effect of iron saturation is acceptably small as well. The only harmonic of note at high field, the sextupole term, can be easily canceled with a distributed sextupole correction coil mounted inside the main dipole winding. (The main function of the correction coil is to compensate for expected magnetization effects in the injection field region, 0.33 T, discussed below.)

Inductance and Stored Energy

The inductance at a current of 6.5 kA is computed to be 3.2 mH/m, giving a stored energy of 1.12 MJ for a magnetic length of 16.6 m at a central field of 6.6 T.

Leakage Field

At 6.4 kA, the mean flux density on the median plane in the iron is computed to be 2.13 T, just equal to the saturation flux density. The fringe field at the iron surface (at a radius of 13.33 cm) is about 640 gauss. It falls off rapidly as a function of radius, as shown in Table 5.2-3.

Table 5.2-3
Field Outside Iron Median Plane

Distance from[a] Iron Surface (cm)	Field (T)
0	0.064
2	0.030
4	0.020
6	0.014
8	0.012
10	0.010

[a)]Outer radius of iron yoke ~13.33 cm.

Expected Multipole Errors

Multipole fields in an actual magnet will, in fact, differ from the design values. Their systematic variation with iron saturation has already been discussed. There are also small errors in construction.

The dominant sources of random construction errors are expected to be variations in coil and conductor placement. The rms widths of the multipole distributions arising from these construction errors have been estimated in three independent ways for SSC magnets from measurements made on Tevatron and CBA dipoles [5.2-5]. The three estimates are in general agreement with one another and have been chosen to define the specifications of the random error tolerances for the SSC dipoles as discussed in Section 4.3.1. Results from the model magnet program show that these tolerances can be met or exceeded — see Table 4.3-1 and Fig. 2.4-2.

Superconductor Magnetization

Superconductors subjected to changing magnetic fields exhibit an inherent magnetic hysteresis, or magnetization. This is caused by local persistent, diamagnetic current loops induced within the individual filaments of the twisted composite superconducting wire. The effect has been studied experimentally for well over a decade [5.2-6], and is amenable to analytical treatment on the basis of various models of the superconducting state [5.2-7, 5.2-8]. The induced magnetization currents constitute elementary dipoles whose strength and orientation depends on the magnetic history of the superconductor, the local magnetic field in the magnet winding, and the superconducting properties. In terms of the so-called

critical state model, i.e., assuming full field penetration, the field-dependent magnetization $M(H)$ can be expressed in terms of the critical current density J_c and superconducting filament diameter d as follows

$$-M(H) = \frac{1}{3\pi} \lambda J_c(H) d \quad , \tag{5.2-1}$$

where λ is the fraction of superconductor in the composite. By summing the contributions of the elementary current dipoles over the coil winding, the magnetization can be formulated in terms of residual, systematic multipole fields whose contributions diminish rapidly with increasing field, because of the field dependence of J_c. These multipoles, primarily a sextupole, dominate the systematic error fields near injection (0.33 T in case of the SSC) and are compensated locally by a distributed correction winding, if necessary.

Figure 5.2-3 illustrates the typical magnetization behavior exhibited in measured sextupole harmonics for increasing and decreasing currents in several recent 4.5 m SSC model dipoles. About 25 units of sextupole are evident at the injection field, or at a current of about 300 A. These magnets, however, utilized a conductor with relatively large filaments — approximately 20 μm in diameter. The linear dependence on filament size [5.2-9] has prompted a vigorous R&D effort over the past several years to develop commercially available materials with substantially finer filaments without sacrificing current density. The present dipole design is predicated on a filament size of 5 μm, a reasonable expectation based on R&D progress to date. See Sections 2.4.3 and 5.2.3. Scaling the measured value, we can expect a systematic magnetization sextupole of about 6 units for 5 μm filaments. As a result, the demands on the correction coil system (Section 5.2.7) are quite modest.

In addition to the mean sextupole contribution to be expected from superconductor magnetization, its variation must also be considered since, at low fields, this may increase the variation already present from errors in construction. Based on experience with the Tevatron (800 dipoles or 400 billets of conductor), a 10% variation, or about 0.5 units in b_2 at 0.33 T, can be expected. Temperature variation adds another 0.1 unit (through the temperature dependence of J_c). The total is of the same order as the random errors (Table 4.3-1).

5.2.3 Superconductor

The superconductor used in accelerator magnets is typically combined with a normal conductor that can carry current for short periods of time to "stabilize" the superconducting cable and to provide protection against burnout during a quench. In most magnets, the normal conductor material is copper of moderate purity, having a resistance at 4.2 K of about 1 per cent of its room-temperature value. A conductor billet is formed by coating rods of NbTi with copper and stacking a number of these elements in a copper container. The entire assembly is then extruded at a temperature high enough to ensure a good metallurgical bond between the NbTi and the copper. A microphotograph of a multifilamentary superconducting strand is shown in Fig. 2.4-6.

The particular superconductor selected for the main dipole and quadrupole designs is the result of a collaboration over the past several years between the national laboratories,

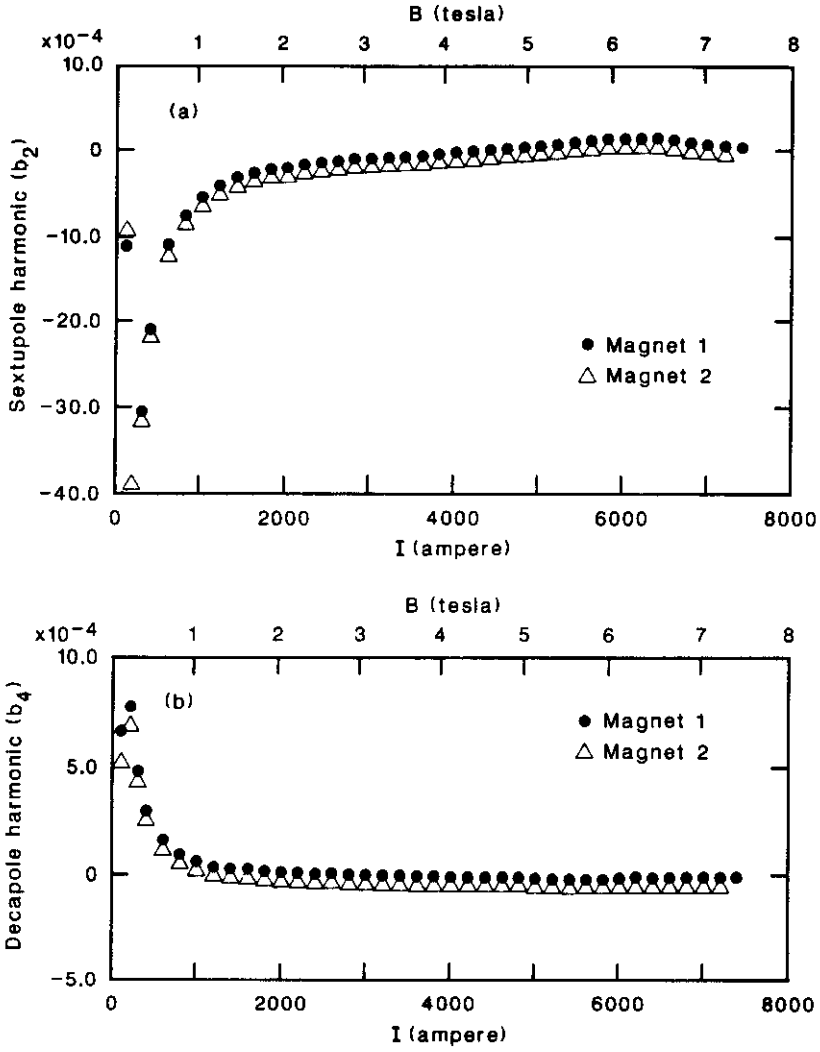

Figure 5.2-3. Variation of measured sextupole (top) and decapole (bottom) harmonics with field in two SSC model dipoles.

universities, and industry, as noted in Section 2.4.3. The goals of this (still ongoing) development have been to obtain a high current density, fine filament material in a commercially available product capable of operating at the SSC design fields with low magnetization effects. The resulting material, including detailed wire and cable parameters, are discussed in the appendix to this report. A group of reports outlining the substantial progress and status in the areas of metallurgy of the basic NbTi superconducting alloy, methods of processing the composite conductor to achieve the necessary filament size and critical current density, and improved techniques for the measurement of short sample characteristics and magnetization effects, may be found in a recent technical note [5.1-3].

Critical Current Density and Filament Size

The superconductor represents a large fraction (approximately 30%) of the total cost of the magnet system for the machine. Therefore, the choice of those superconductor parameters that most strongly impact on superconductor costs must be analyzed carefully. The parameter of primary importance in selecting a superconductor is the critical current density (J_c) at the appropriate operating temperature and field. A key feature in obtaining a high J_c in NbTi alloys is the uniform precipitation of Ti rich material. Such a material, produced from a high homogeneity NbTi alloy by heat treatments, has been available commercially since 1985. It possesses critical currents well in excess of the RDS (1984) target specification of 2400 A/mm^2 (at 5 T, 4.2 K). (For comparison, the specification for the Tevatron conductor was 1800 A/mm^2.) Another favorable development is the ability to produce much longer lengths of conductor without wire breakage than was possible with earlier material; this greatly facilitates cabling, and simplifies testing and quality control.

In addition to the requirement of a high current density, it is imperative to use conductors with a fine filament size in order to reduce field distortions at low fields due to the magnetization effect discussed in Section 5.2.2. The SSC target specification is a filament diameter of 5μm, chosen to minimize the requirements on the distributed sextupole correction winding in the main ring dipoles, and a critical current density of 2750 A/mm^2 at 5 T and 4.2 K. Conductors with filament diameters of 2.5 μm and current densities exceeding 3000 A/mm^2 have been produced commercially and are under active development; such conductors would greatly ameliorate the correction problem.

Several recent developments in the production of NbTi superconductor have aided the achievement of small filament size without breakage in production quantities. One technique consists of enclosing the NbTi rods at extrusion size in a barrier material (Nb or Ta, typically 0.1 mm thick), to prevent titanium-copper intermetallic formation — a problem previously resulting in extensive filament breakage and sometimes strand breakage. Careful selection of raw materials and clean room practice in billet assembly can minimize the introduction of foreign particles during billet preparation. Finally, non-uniform reduction in the extrusion step is avoided by compacting the billet, or rod stack, before extrusion.

Superconducting Cable

As noted earlier, the SSC conductor is a flat, spiral cable of multi-filamentary superconducting strands. No electrical insulation is needed between strands of the cable to suppress eddy currents because the cycle time of the machine is quite long (1000 s). Since the fields are different in the two dipole coil layers (higher in the inner layer) the conductor is graded with strand and cable parameters adjusted to achieve higher overall current density in the

outer layer. This results in a significant reduction in outer conductor costs. The parameters for the two multi-filamentary strand types are given in Table 5.2-4.

Table 5.2-4
Parameters for NbTi Superconducting Wire

	Inner Layer	Outer Layer
Nb-Ti composition (by weight)[a]	46.5% Ti	46.5% Ti
Critical current,[b] [A]	613	323
Critical current density (non-Cu) [A/mm^2]	2750	2750
Copper-to-superconductor ratio	1.3:1	1.8:1
Filament diameter [μm]	5	5
Strand diameter [mm/in.]	0.808/0.0318	0.648/0.0255
No. of filaments	11,000	6,000
Strand twist pitch [per cm]	0.4	0.4
Copper residual resistance ratio, R_{295}/R_{10}	>80	>90

[a]High-homogeneity material (see text)
[b]At 5 T, 4.2 K, and a resistivity of 10^{-14} Ω-m

The most important cable parameters are: copper-to-superconductor ratio, number and size of strands, keystone angle, amount of compaction, and allowable dimensional tolerances. These parameters were established with reference to a particular dipole magnet design — in this case the SSC dipole at 40 mm aperture (inner coil diameter). The aperture has been chosed on the basis of accelerator physics analysis of the needed room for beam and the interplay of magnetic field errors, coil diameter, and magnet cost, as discussed in Section 4.3.3. Emphasis was placed on obtaining high current density NbTi superconductor and on minimizing the amount of copper in the cable. The copper-to-superconductor ratio is chosen to assure approximately equal quench protection behavior in the inner and outer coil layers. The number of strands in each cable are chosen so that the inner and outer layers could be energized in series at the maximum efficiency. The "partial keystone" cable design is chosen in order to reach an optimum between achieving the maximum number of turns, and to have a self-supporting winding ("Roman arch") without excessive space occupied by wedges. The keystone angle is the maximum possible for each cable without incurring severe wire distortions that can damage the strands. As a result of these considerations, the parameters listed in Table 5.2-5 have been established for the cables in the inner and outer coil layers, respectively. Cross sections of the two cables are shown in Fig. 5.2-4.

23 STRAND KEYSTONED CABLE

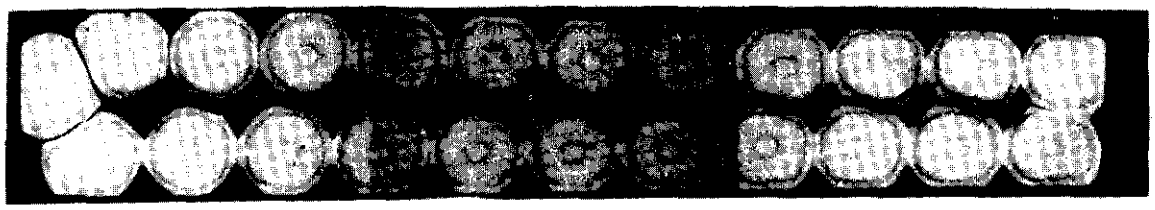

30 STRAND KEYSTONED CABLE

Figure 5.2-4. Cross sections of 23 strand ("inner") and 30 strand ("outer") keystoned cable.

Table 5.2-5
Parameters for Superconducting Cable

	Inner Layer	Outer Layer
Critical current density[a] (non-Cu) [A/mm^2]	2750	2750
Number of strands	23	30
Strand diameter [mm/in.]	0.808/0.0318	0.648/0.0255
Cable width (bare) [mm/in.]	9.30/0.366	9.73/0.383
Cable thickness (bare)		
Wide side [mm/in.]	1.59/0.0625	1.27/0.050
Narrow side [mm/in.]	1.33/0.0522	1.07/0.042
Keystone angle [deg.]	1.61	1.21
Cable twist pitch [per cm]	0.126	0.136
Residual resistance ratio, R_{295}/R_{10}	>70	>70

[a]At 5 T, 4.2 K, and a resistivity of 10^{-14} Ω-m

Operating Current Density

The minimum critical current of the strands, Table 5.2-5, is specified to be 2750 A/mm^2 at 4.2 K, 5 T, and $\rho = 10^{-14}$ Ω-m. The critical current of most NbTi conductors decreases linearly with field; in boiling liquid helium at atmospheric pressure, it vanishes at a field of about 10 T. For fields greater than 5 T, the critical current at a given field is linearly dependent on the difference between the bath temperature and the critical temperature. This behavior allows scaling of $J(T,B)$ with temperature and field to the SSC operating conditions at 4.35 K and 6.6 T, as shown in Table 5.2-6. Here J_o is the operating current density, and J_c, the strand critical current density. A minimum design value of 1.25 has been chosen for J_c/J_o to allow an "operating margin". This margin is needed to allow for possible degradation of J_c during cable manufacture, small temperature excursions caused by radiation heating during beam abort (see Attachment B), and other small effects that can reduce J_c. Comparison of actual peak fields with predicted performances (based on strand J_c) for the 1.0 m and 4.5 m model magnets built to date shows that 1.25 is a reasonable margin to permit 6.6 tesla operation with confidence. Note that the inner and outer cables are reasonably well balanced, with the outer coil having slightly more operating margin (J_c/J_o) than the inner coil.

Table 5.2-6
Dipole Operating Conditions

	Inner Coil	Outer Coil
T [K]	4.35	
B_0 [T]	6.595	
I [A]	6497	
B_{max} [T]	6.961	5.566
J_o [A/mm^2]	1265	1837
J_c [A/mm^2]	1581	2347
J_c/J_o	1.250	1.278

5.2.4 Coils

Figure 5.2-5 shows a cross section of the collared dipole coil assembly. The specifications of the two-layer coils are given in Table 5.2-1. The complete two-layer coil assembly is actually manufactured in four sections. The inner and outer coils are wound separately, and each are made in two (upper and lower) halves. The cable is insulated with a wrap of overlapping 0.025 mm thick Kapton tape, followed by one layer of 0.10 mm thick fiberglass tape impregnated with B-stage epoxy, wrapped with nominally zero spacing between turns. The latter serves to hold the coil section together during handling until the magnet is fully assembled. Fabrication of a magnet coil consists of two operations. First, the coil is wound on a winding mandrel, and then this mandrel, with coil attached, is placed in a curing press where the coil is heated to mold the individual turns into monolithic conductor blocks.

Coil Fabrication

Model magnets are presently being fabricated using methods similar to the mass production methods envisaged for the SSC. The individual coil sections are wound on a precision laminated convex mandrel in a microprocessor-controlled winding machine, depicted in Fig. 5.2-6. The cable is fed from a quasi-stationary supply spool onto the mandrel which acts as a shuttle. A turn is initiated by winding the cable around one coil end with the mandrel rocking in unison to ensure a proper lay. Next, one side of a straight section is wound as the mandrel travels the requisite distance with the stationary reel paying out cable. The supply spool retraces its steps, laying cable around the other end of the racetrack-shaped path, and the turn is completed with the mandrel returning shuttle-fashion to its starting position. When all turns of a coil have been wound, molded end spacers are mounted; these are used to square off the ends of the coils and serve as a bearing surface for the end restraints. Finally, the entire coil-mandrel package is wrapped with half-lapped Tedlar, 0.025 mm thick and 10 cm wide, tensioned at approximately 20 pounds. In addition to securing the coil firmly to the mandrel for the next operation, the Tedlar will also perform the subsequent role of mold-release agent.

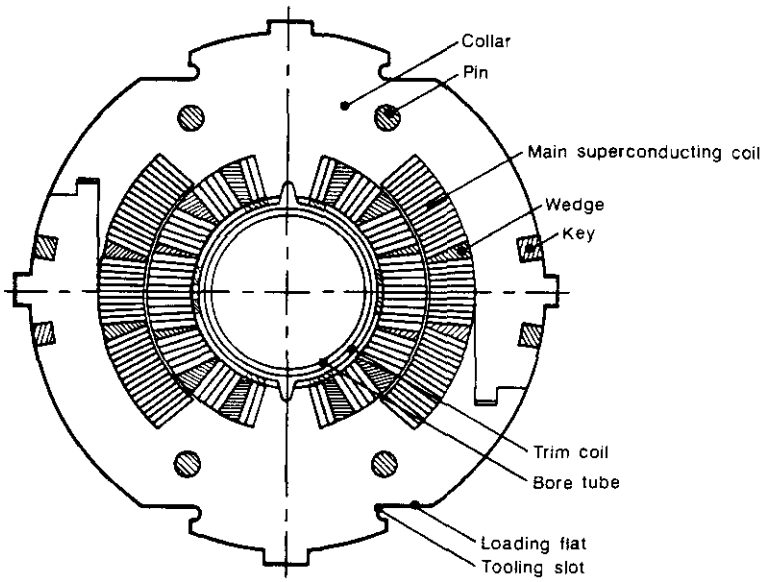

Figure 5.2-5. Cross section of collared coil assembly, showing bore tube, main coils and stainless steel collar.

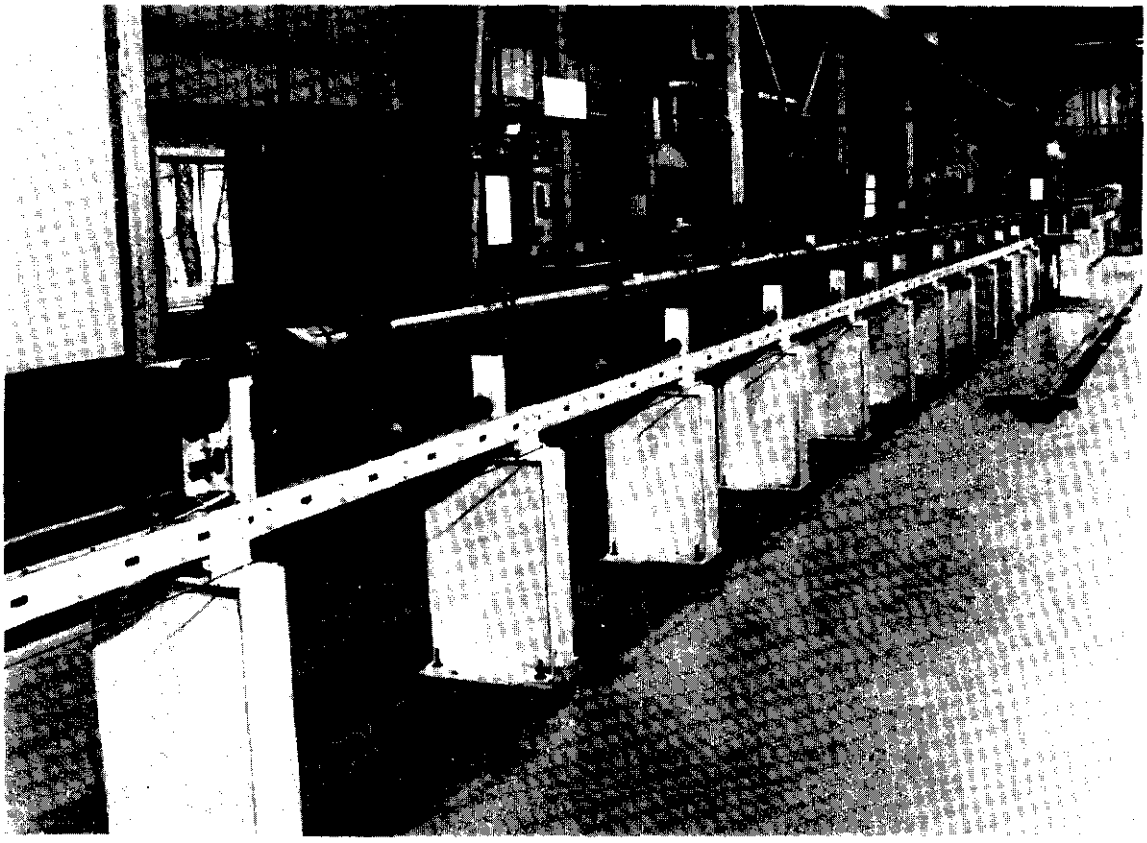

Figure 5.2-6. Coil winding fixture for full-length prototype dipoles. The fixture is designed to accommodate dipole coil segments of arbitrary length up to a maximum length of 16.7 m.

A hydraulically operated, oil heated coil curing fixture is shown in Fig. 5.2-7. It is assembled from 11 module sections, each approximately 1.5 m long. The coil and mandrel are lowered into the curing fixture, previously prepared with additional mold-release and various tooling components in place. The coil is cycled through a heating sequence with both side and end pressure applied in a particular order. The curing portion of the cycle takes place at 135° C for a period of 90–105 minutes.

Coil Collaring

The interlocking collars provide the basis for accurate positioning of the coil sections and the concomitant ability to perform "warm" field measurements early in the magnet production line, prior to final coil-in-yoke assembly. They must also counteract the substantial Lorentz forces generated when the magnet is energized to operating field. Detailed analysis and experience with model magnets has shown that the minimum azimuthal prestress necessary to restrain the conductors from moving at the magnet poles at full field is approximately 3.5 kpsi. In order to achieve this load when the magnet is at operating temperature and energized, a somewhat greater load needs to be applied during room temperature assembly. This load, estimated to be 5 kpsi for inner as well as outer coils, takes into account the loss of prestress due to subsequent thermal contraction and stress relaxation.

The shape of the collars is similar to those of the Tevatron magnets. Fabrication and assembly of the collar packs, 15 cm long, is also similar except there is no welding involved; pins and keys are used instead, as shown in Fig. 5.2-5. The pins hold the collar packs together, and the dual, square keys lock mating collar packs around the compressed coil assembly. The external key tabs on the midplane and the vertical center line register the collared coil assembly in the yoke (to an angular tolerance $\pm$ 0.5 mrad), while the key slots in the inner coil post register the bore tube relative to the collared coil. The diameters of the collar and yoke are dimensioned so that the collars do not bear against the yoke and are therefore self-supporting.

5.2.5 Beam Tube Assembly

The beam tube separates the helium-cooled portion of the magnet structure from the beam high vacuum chamber and is thus the inner wall of the cylindrical helium containment vessel. On its outside surface this tube supports the distributed correction coils. The correction coils are described in detail in Section 5.2.7. They are supported and electrically insulated from the main coil by plastic spacers bonded to its outer surface; these spacers also define longitudinal helium cooling passages between the two coils. Figure 5.2-8 shows a cross section of the bore tube assembly.

The beam tube is fabricated from stainless steel tubing of 1.0 mm thickness that is copper coated inside to reduce the electrical resistance of the wall to image currents. The inside diameter of the beam tube is 3.25 cm. Its outer surface is covered with Kapton-Teflon insulation, followed by the correction coil layer consisting of superconducting wires embedded in a Kapton-epoxy sheet. The coil pattern is produced by embedding high-purity copper wire containing NbTi filaments in the epoxy substrate by an automatic process. G-10 spacer strips, as well as the locating pins and keys for aligning the bore tube assembly with respect to the main dipole winding, are also shown in the figure.

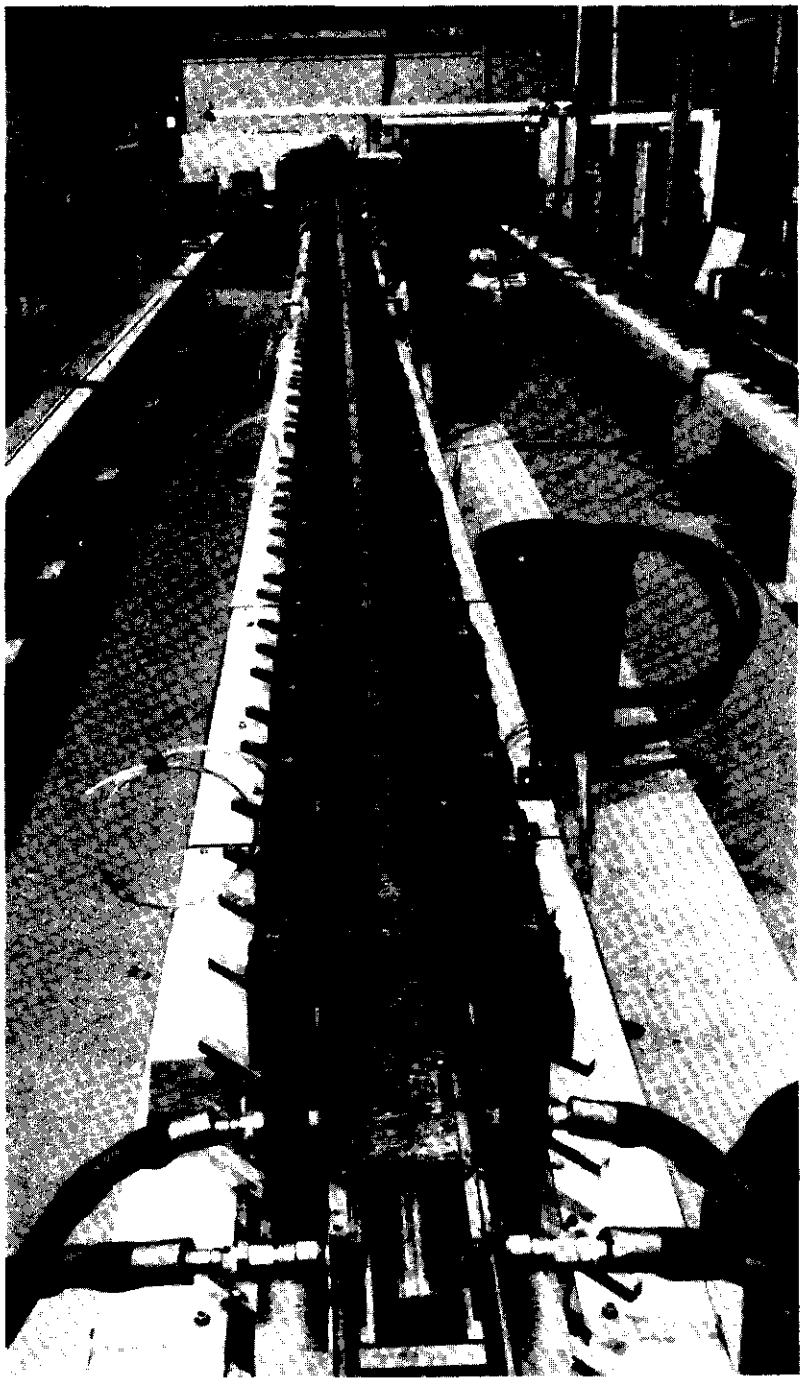

Figure 5.2-7. Coil curing fixture for full-length prototype dipoles. The fixture is assembled from eleven 1.5 m module sections.

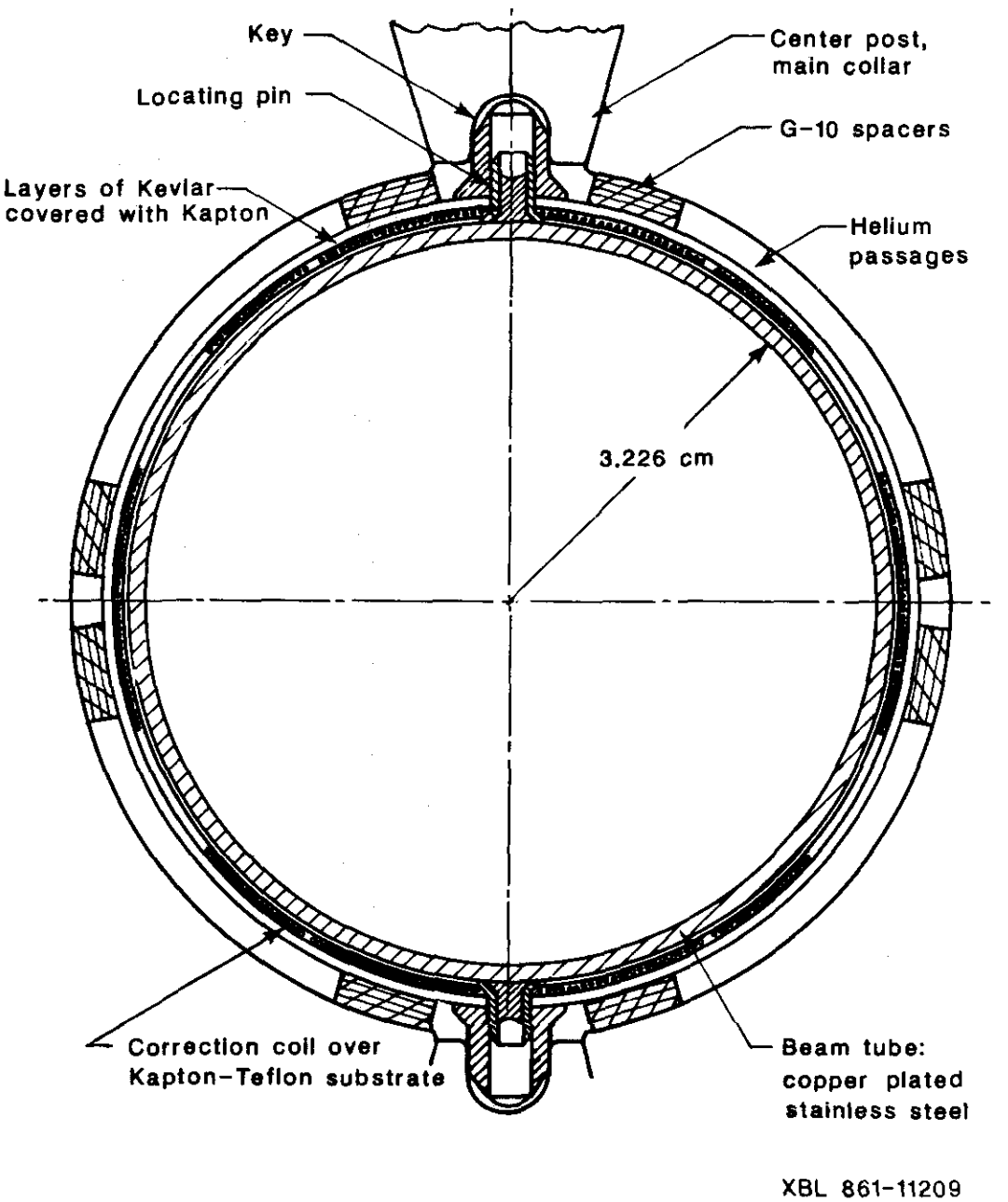

Figure 5.2-8. Cross section of bore tube assembly, including beam tube (high vacuum chamber), superconducting correction coil winding, and spacers bearing against the inner surface of the main dipole coil.

5.2.6 Yoke and Helium Containment

Figure 5.2-2 shows an overall cross section of the cold mass, that portion of the magnet assembly maintained at liquid helium temperatures. The yoke is contained within a cylindrical, welded stainless steel support shell which also serves as the outer wall of the helium containment vessel. Longitudinal slots in the yoke provide conduits for the electrical bus between magnets; longitudinal holes act as the primary magnet coolant channels. Fiducial marking plugs extend through the helium containment shell. These provide accurate alignment references for relating the position of the magnet to the external vacuum vessel.

Iron Yoke

The magnet yoke consists of stacked iron laminations, split on the midplane, mounted in the helium containment shell, as shown in Fig. 5.2-2. They are accurately die-punched from 1.5 mm thick sheets of low carbon, cold-rolled electrical steel possessing magnetic properties typical of those required for accelerators; e.g., low coercive force, high permeability at both low and high induction, and high saturation induction. The laminations are 26.67 cm in diameter. They are punched with keyways to provide accurate positioning of the collared coil assembly when mounted in the yoke. Two rectangular slots are provided in the laminations, located at top and bottom in a low-field region of the yoke. The top slot provides conduit space for the main electrical bus which carries current from one magnet to the next; the bottom slot provides similar space for the correction coil leads. The main helium flow passes through the four large symmetrically placed "bypass" holes. Four small holes are provided for accommodation of full-length electrical heating elements, used when necessary to warm the magnet to room temperature in about 24 hours.

Helium Containment Vessel

The helium containment vessel consists of yoke support shell, "bonnets," end plates, and the beam tube described earlier. The shell, which fits closely around the yoke, is formed initially as two half shells that are welded with automatic equipment to produce the finished assembly. The bonnets are short, thicker circular cylinders which are circumferentially welded to the ends of the shell. They provide a way of retaining the end plates which complete the helium vessel or "single phase" assembly, and also present a smooth cylindrical surface to which the interconnection bellows can be welded. The end plates help to retain the yoke within the shell, and provide a solid end for the coil to bear against during operation.

Heat Generation, Cooling, and Temperature Distribution in the Magnets

As the magnetic field is raised, heat is generated in the conductors by magnetization of the superconducting material, by induced currents in the conductor cables and, in the beam tube, by induced currents in the copper used for plating the inside of the tube; finally, heat is generated by synchrotron radiation impinging on the inside surface of the tube. Near full energy, for the anticipated beam intensity, and for a ramp-up time of 1000 s, the total amount of power to be dissipated increases to 2.8 W/dipole, 80% of which is from the synchrotron radiation. The static heat from magnet support, and radiation and conduction

from the inner heat shield, kept at 20 K, amounts to 0.3 W. When a steady field is reached, only the static heat and the synchrotron radiation, amounting to 2.3 W/dipole, are left.

The magnets are cooled by supercritical helium flowing longitudinally through the magnets at a rate of 100 grams per second. Only 1 g/s of this amount flows through a passage between the correction coil located around the beam tube and the inner surface of the inner main coil. Here the annular gap width is 1.3 mm, partially blocked at the locations of the spacers between trim and main coils. Because of the great length of the magnet and the small pressure drop, the flow is only 1 g/s. The bulk of the helium flows through the 4 circular bypass holes in the magnet yoke, each 29 mm in diameter.

Some of the heat generated in coils or beam tube is carried off by the helium flowing through the coil passage. However, most of the heat diffuses radially toward the bypass holes. From the inner surface of the beam tube heat must pass through tube wall, correction coil assembly and insulation, helium in the coil passage, more insulation and main coil assemblies, coil-prestressing collars, a 0.25 to 0.5 mm annular gap filled with helium, and finally through the yoke laminations into the helium flowing in the bypass holes. If the narrow gap of the coil passage were blocked due to accumulation of frozen gases or for other reasons, it would be stagnant, but could still pass the required amount of heat due to the large surface for heat exchange. Since synchrotron radiation preponderantly impinges on the outer side of the curved beam tube, a small temperature gradient is established during machine operation which causes the helium in the coil passage also to circulate around the beam tube due to convection, thus promoting heat exchange.

For the described cooling method, a magnet temperature increase of only 0.016 K is expected during field ramp-up. This increase is small because of the large amount of helium contained in magnets and interconnection regions. Within limits, the increase does not depend on the helium mass flow.

Table 5.2-7 shows calculated distributions during operation of maximum temperatures at the helium outlet ends of the dipoles for both turbulent flow (1 g/s) and stagnant helium in the coil passage.

Table 5.2-7
Calculated Temperature Distributions

	T_p	T_t	T_o	T	T_a
Turbulent helium flow (1 g/s)	4.43	4.38	4.36	4.35	4.30 K
Stagnant helium	4.52	4.44	4.39	4.36	4.30 K

T_p = Temperature at inside of beam tube wall.
T_t = Temperature in trim coil.
T_o = Helium temperature in coil passage.
T = Average temperature in main coils.
T_a = Helium temperature in bypass.

These temperatures are based on an input helium temperature of 4.3 K. After exiting from the passages, the helium flows mix, giving a resulting temperature increase of 0.089 K per cell, or an average of 0.0074 K per dipole. There is to be one recooler available per cell. Half of the temperature difference between T and T_a is due to the collars. The pressure drop per refrigerator loop (21 cells) is calculated to be 0.35 atm.

5.2.7 Correction Coils

The main function of the distributed correction coils (or trim coils) located between the main dipole winding and the beam tube is to compensate for field distortions due to (diamagnetic) superconductor magnetization currents induced in the main winding during field ramping — a predominantly low-field effect discussed in Section 5.2.2. Although the field component affected is mainly the sextupole, the decapole term is also affected to a lesser extent (Fig. 5.2-3). Therefore, a decapole correction winding is included as well. Such a winding can be readily accommodated with simple adjustments in the bore tube assembly.

Figure 5.2-9 illustrates the winding geometry of the single-layer sextupole coil embedded in the bore tube package of Fig. 5.2-8. Its parameters, with those of a matching decapole coil, are listed in Table 5.2-8. The sextupole (decapole) coil consists of 15 (9) turns wound with a 0.3 mm diameter (bare) superconducting wire. Designed for an operating current of ~ 5 A, they provide 4 (1.2) units of sextupole (decapole) correction at full field. Since the critical current at 6.6 T is approximately 22 A, the operating margin exceeds a factor of 4 — substantially more at injection.

Table 5.2-8
Parameters of Correction Coils

	Sextupole	Decapole
Overall length [m]	16.9	16.7
Magnetic length [m]	16.9	16.7
Mean diameter [cm]	3.515	3.58
Number of turns	15	9
Wire diameter, bare [mm/in.]	0.30/0.012	0.30/0.012
Wire diameter, insulated [mm/in.]	0.38/0.015	0.38/0.015
Copper-to-Superconductor ratio	1.6	1.6
Filament diameter [μm]	~20	~20
Strength (at 1 cm radius)		
gauss/ampere	5.5	1.61
b_n/A (10^{-4} units/amperes @ 6.6 T)	0.83	0.25

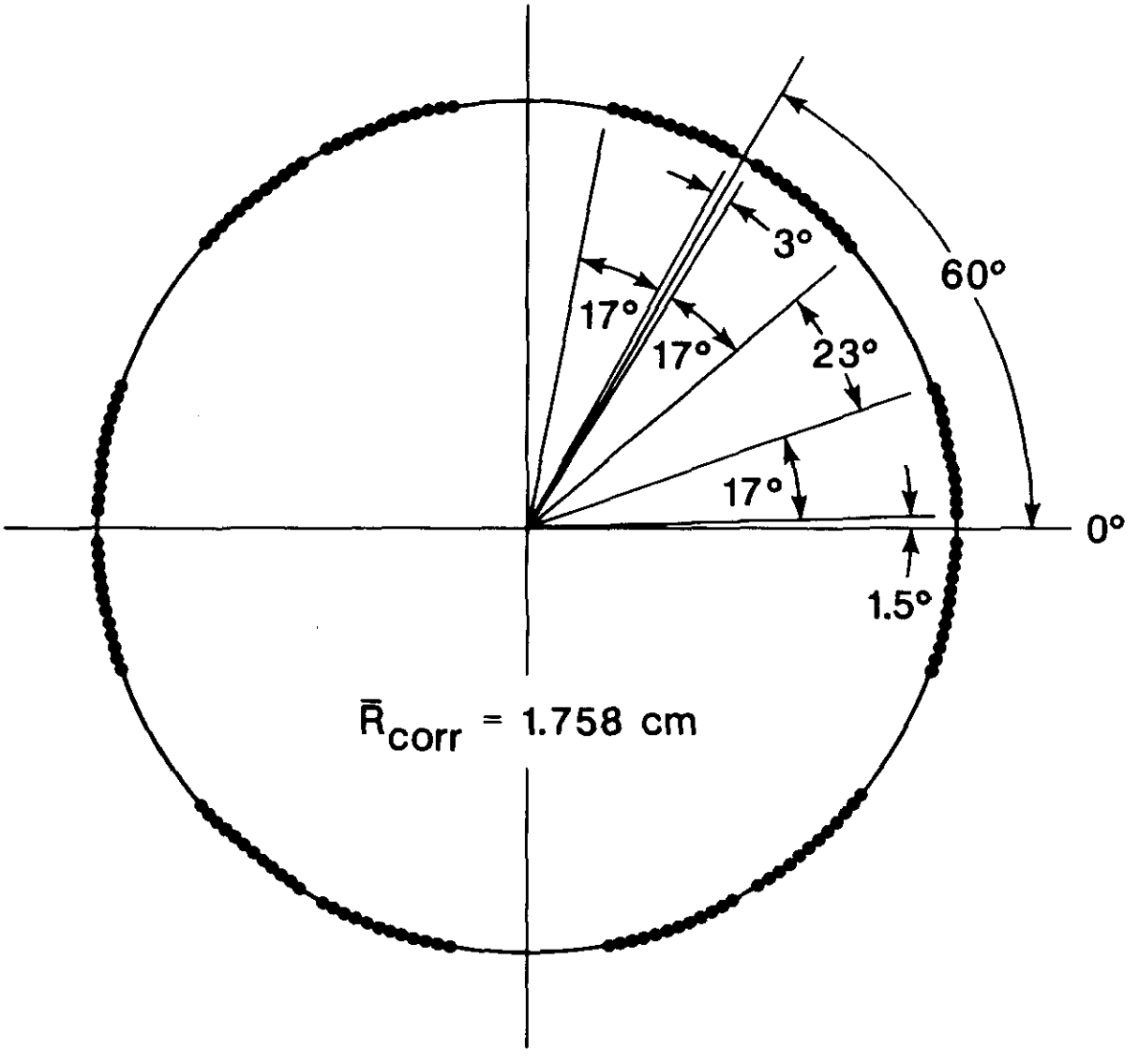

Figure 5.2-9. Winding scheme for correction ("trim") coil mounted inside main dipole coil. The correction coil compensates for the sextupole magnetization effect at low field.

The effects of systematic and random multipole contributions from the sextupole correction coil have been estimated [5.2-10]. The first allowed (systematic) term is the 18-pole. Random harmonics will be generated from imperfect wire placement and imperfect trim coil placement with respect to the main dipole coil. The analysis shows that the only multipoles of significance will be the skew sextupole and the skew and normal quadrupole terms, as a result of which the respective random errors are increased by approximately 5% over those from construction errors in the dipole alone.

In the SSC R&D program, the 4.5 m model magnets had two different types of correction coils, one conventionally wound and fastened in place with spacers and epoxied insulation and the other laid down and bonded to an insulating substrate by a high-speed, computer-controlled machine. The latter technique promises high precision, as well as simple, automated fabrication.

5.2.8 Quench Protection Features

Quenches can be initiated in the SSC magnets by a variety of events including beam loss, vacuum failure, and possibly conductor motion associated with training. The magnet quench protection system is described in Section 5.5. It is designed to reduce the current fast enough to hold coil temperature below the damage level. The part of the magnet that initially quenches will reach a slightly higher temperature than the rest of the system, because of the extra 20 to 50 ms of heating. The peak temperature will not exceed 550 K (see Section 5.5.2).

Unbalanced voltages occur during quenching of superconducting magnets because the entire coil volume of the magnet may not revert to the normal state. With the design protection system, the outer layer of the dipole is driven normal by heaters, and the inner layer follows a short time later. In the extreme case where the inner layer does not revert to the normal state, the peak internal voltage will reach about 1 kV. The insulation in the magnets is designed and tested for over 2 kV.

Essential elements of the active protection system are the heater strips located within each dipole. In case of a quench they are activated electronically by discharging a capacitor bank into them, thereby inducing additional quenches and accelerating the normal resistive zone, ensuring that the magnetic energy is distributed rapidly over a large coil volume to prevent local overheating of the conductor.

There are four heaters in each dipole, one per magnet quadrant, embedded in the Kapton ground insulation on the outer surface of each outer coil segment. They are fabricated from copper-plated stainless steel strips with bare spots serving as the heating elements at 12 equidistant locations along the strips. The speed of the induced quench is weakly dependent on the duration of the heater pulse, but pulse lengths longer than 15 ms do not appreciably reduce $\int I^2 dt$. The details of the circuits and power supplies are described in Section 5.5.

As mentioned in the introduction, the use of active heaters avoids the need for quench protection diodes in each magnet. Quench propagation measurements have shown, however, that the natural quench propagation velocities are considerably higher than previously calculated in these magnets, from the warming up of the yet unquenched superconductor ahead of the quench front. The Cu/SC ratios chosen for the wires in the coils are clearly adequate and the magnet is safe from burnout, due to absorption of its own energy, by a

larger margin than had been anticipated. A passive protection system consisting of one or two diodes to bypass the current around a quenching magnet would then be adequate for a 17 m dipole. Further R&D is being pursued to study voltage transients and radiation damage to the diodes in this passive scheme. For the conceptual design, the known, conservative choice has been made of the active system described above.

5.2.9 Cryostat

Introduction

The cryostat must facilitate proper magnetic functioning of the magnet housed within it, provide low refrigeration loads, be highly reliable and be mass producible at low cost. Conditions that control and affect the cryostat design include magnet assembly, transportation and installation; transient, steady-state, and upset operating conditions are also important factors. Component design considerations include fluid flow, material performance, structural integrity, positional stability, and thermal performance. Functional design tradeoffs were used to optimize the effectiveness of each component as it relates to the overall, long-term performance of the integrated magnet system.

General Cryostat Arrangement

The general cryostat arrangement is shown in Fig. 5.2-10. The major elements are the cryogenic piping, cold mass assembly, suspension system, thermal shields, insulation, vacuum vessel, and the interconnection region.

Cryogenic Piping

The cryostat assembly contains all piping that interconnects the magnet refrigeration system throughout the circumference of the ring. A system consisting of five pipes has been selected for cryogenic and magnet safety reasons.

Pipe 1: The complete cold mass helium containment assembly that contains the supply of single-phase helium fluid flowing through the magnet's iron and collared coil assembly.

Pipe 2: The 4.35 K fluid helium return and recooler supply pipe.

Pipe 3: The 4.35 K helium gas return pipe. The gas is generated in the helium recooler assemblies spaced around the accelerator ring to regulate the temperature of the single-phase helium fluid.

Pipe 4: The 20 K thermal shield cooling pipe. This pipe connects to the helium relief header during system cooldown, or to the return or supply headers during operation. The 20 K line provides quench buffering.

Pipe 5: The 80 K thermal shield cooling pipe. This pipe connects to the liquid nitrogen return or supply header.

Cold Mass Assembly

The cold mass assembly consists of the beam tube (Section 5.2.5), collared coils (Section 5.2.4), stacked iron yoke laminations and outer helium containment shell with alignment fiducials (Section 5.2.6); all are joined together to provide a leak-tight and structurally rigid welded assembly. The helium containment shell is the principal structural element of

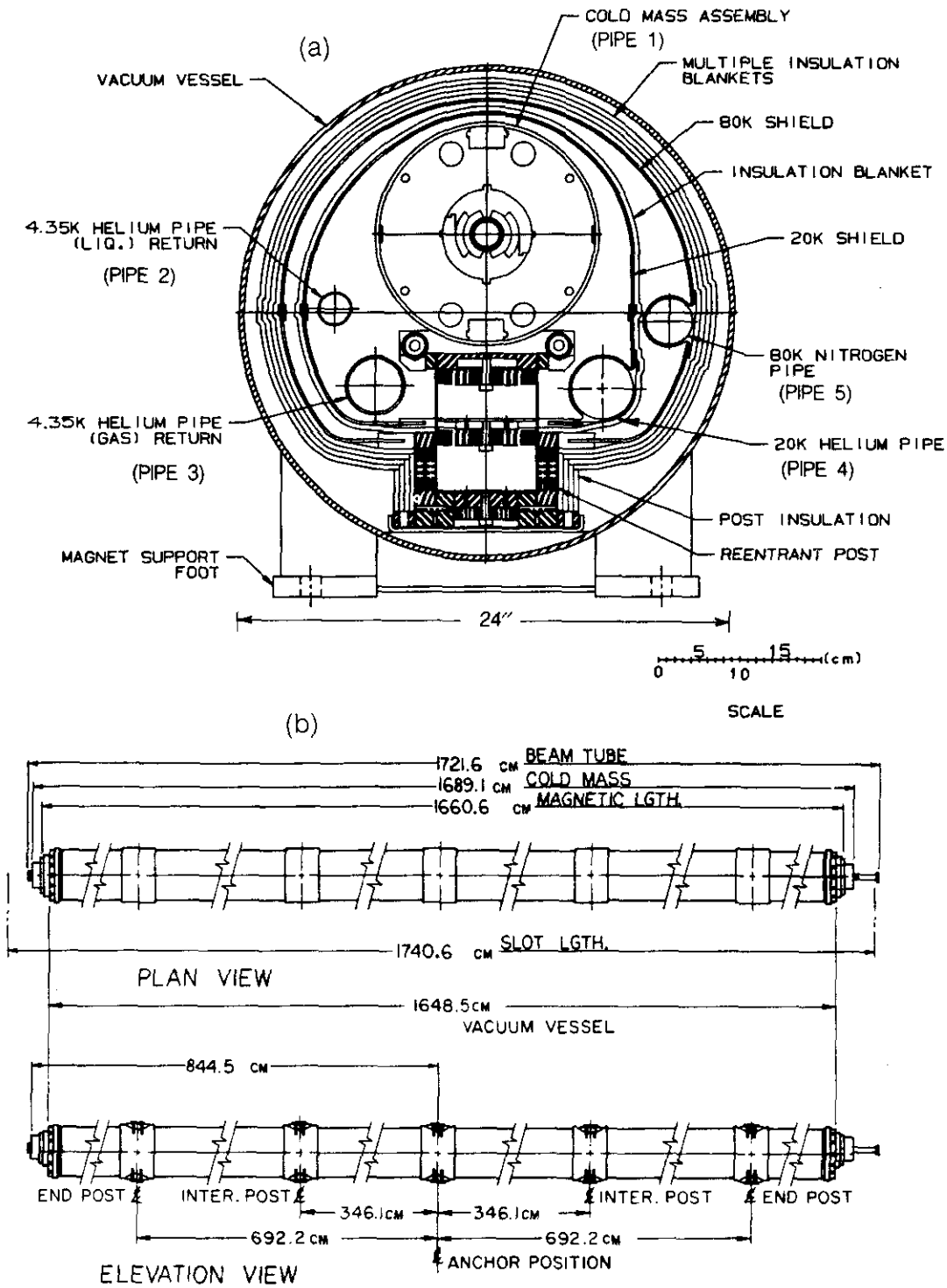

Figure 5.2-10. (a) Dipole cryostat cross section. The vacuum-vessel support-foot arrangement shown here is that used in prototype units. The arrangement of the conceptual design is shown schematically in Fig. 5.2-22(a). (b) Longitudinal sections of dipole cryostat, indicating support points and associated parameters.

the cold mass assembly, and provides the required flexural rigidity between suspension points.

Suspension System

The cold mass assembly and thermal shields with their distributed static and dynamic loads are supported relative to the vacuum vessel by the suspension system. The system functions under conditions that include cryostat assembly, transportation and installation, magnet cooldown and warmup, and magnet steady-state operation and transient conditions. Its requirements include: low heat leak, high reliability, dimensional stability, installation and adjustment ease, and low cost. The cold mass and shields are supported at five points along their length. The number and location of the support points were determined by analysis of the deflection of the cold mass assembly as a beam, limited to 1 mm between supports, and by the need to minimize the number of support points for reasons of magnet fabrication ease and low heat leak. After consideration of tension member, compression member, elliptical arch and post type suspension systems, a cylindrical post type support [5.2.9-11, 5.2-12] was selected. The significant features of such a support are:

(a) Load Carrying Versatility — The cylindrical section results in a versatile support member that can carry tension, compression, bending and torsional loads.
(b) Thermal Contraction Structural Insensitivity — The post configuration connections to the cold mass and thermal shield assemblies allow them to move axially relative to the post as they expand or contract, thus eliminating changes in post loading due to thermal transients.
(c) Low Heat Leak — The use of fiber-reinforced plastic (FRP) materials with effective heat intercepts result in predictably low heat leaks. A minimum number of penetrations through the shields and their insulation are required, which reduces the potential thermal radiation heat flux.
(d) Integral Restraint — The hollow, central region of the post permits the installation of an integral restraint member that connects the warm and cold ends. The restraint is employed during transportation and handling and is removed prior to operation.
(e) Installation and Adjustment Ease — The post, involving a single support member at a suspension point, simplifies installation and adjustment.

The details of the reentrant post support are indicated in Fig. 5.2-11. The insulating sections are of fiber-reinforced plastic tubing with metallic interconnections and heat intercepts. The junctions between the FRP tubing and the metallic connections, which must be able effectively to transmit tension, compression, bending and torsional loads, are made by shrink fitting. In order to ascertain the long-term stability (and thus reliability) of shrink-fit junctions, creep tests of junctions were made. The creep extrapolated over a 20 year machine lifetime indicates there will be no significant loss in joint strength. A post support is subject to internal axial and radial thermal radiation that can significantly affect thermal performance. Control of such radiation is achieved by the use of multilayer insulation. Proper design of the thermal connections between the 20 K and 80 K intercepts of the supports and the thermal shields is essential to minimize the heat leak. A 5 K temperature rise at 80 K and a 1 K temperature rise at 20 K are budgeted. The support post is fixed at its 300 K end and incorporates a slide at the 4.35 K end to accommodate the axial differential

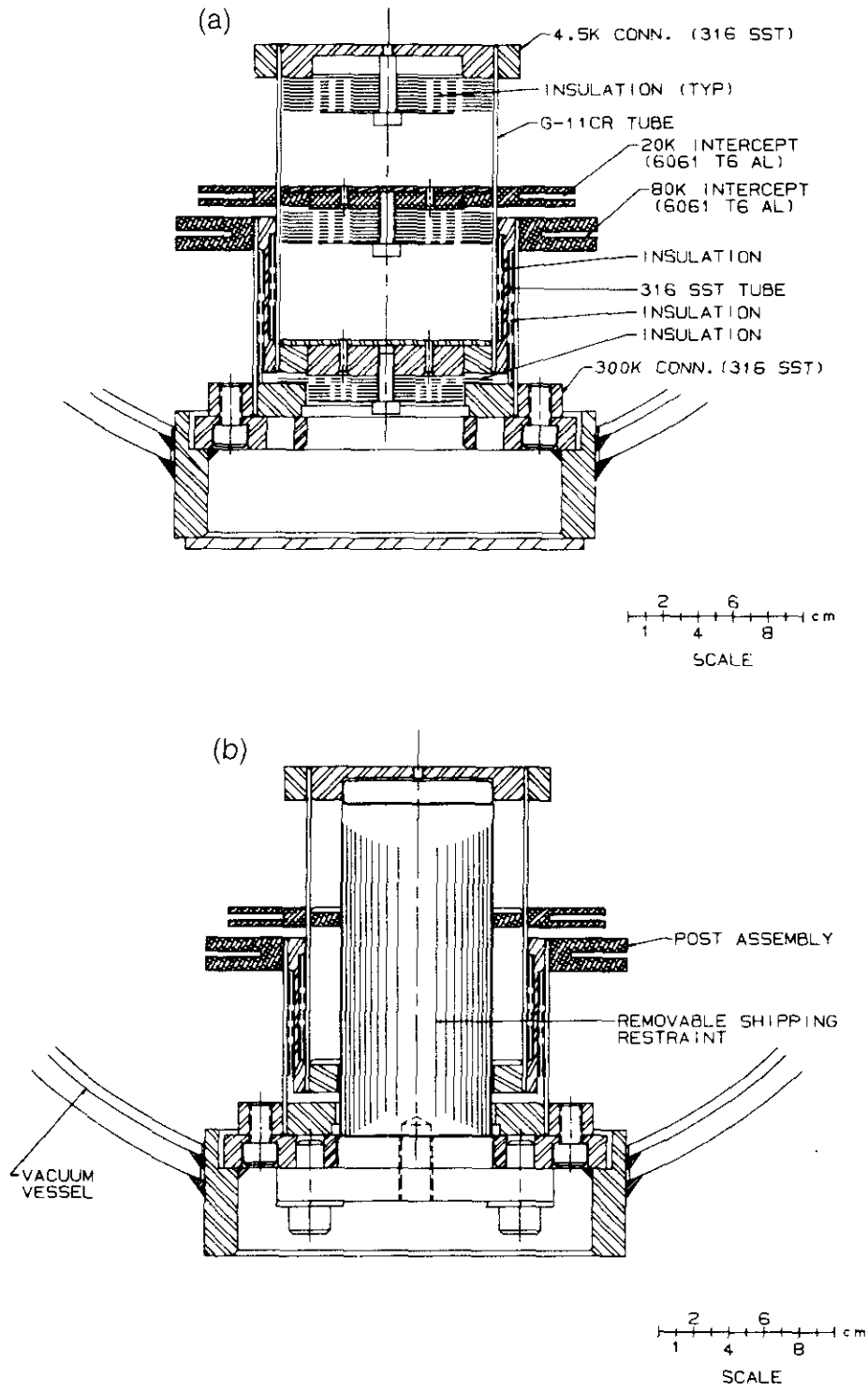

Figure 5.2-11. (a) Reentrant support post cross section. (b) Reentrant post support assembly with removable shipping restraint.

contraction between the mid-span anchored cold mass assembly and the vacuum vessel. Analysis of transient conditions indicates that significant transient bowing of the cold mass assembly is not expected. The 20 K and 80 K shields will undergo transient bowing, so the shield-post interfaces are designed to allow relative motions while providing support.

Post type supports performed as expected, both structurally and thermally, in several test assemblies in the R&D program [5.2-13, 5.2-14]. A reentrant tube post support, instrumented with temperature sensors, was installed and evaluated in a specially configured heat leak measurement dewar [5.2-15]. The measured vs. predicted temperature profiles and heat leaks are in good agreement; the actual cryostat for the SSC is expected to match closely this performance.

In order to permit the post support to withstand the lateral handling loads without incurring a severe operational heat leak penalty, the design incorporates an integral, coaxial, removable shipping restraint, as shown in Fig. 5.2-11(b). The restraint is installed at the time of magnet assembly and is removed at the site. The cryostat incorporates a similarly removable axial shipping restraint. This restraint provides a strong structural axial connection between the cold mass assembly and the vacuum vessel shell. It is installed during magnet assembly and is also removed before cryogenic operation.

Thermal Shields

Thermal shields, maintained independently at 20 K and 80 K, surround the cold mass assembly. They absorb the radiant heat flux, and provide heat sink stations for the suspension system intercepts. The shields are constructed of aluminum and are fabricated from a combination of extruded flow channels and rolled shapes. The 4.35 K liquid and gaseous helium return pipes are supported from the cold mass assembly by hangers. The 20 K and 80 K shields are supported by, and are thermally anchored to, the cold mass assembly post support system.

The thermal and structural response of the inner shield, when subjected to a 100 K temperature differential across the section, was measured and was also modeled and predicted by finite element methods [5.2-16]. The observed thermal bowing was within acceptable limits. Based on this analysis of shield behavior, the refrigeration system design limits the transient shield thermal excursions to 100 K. During steady state operation, the temperature difference across the shield is only 1 K.

Insulation

Thermal insulation is installed between the 300 K and 80 K surfaces and between the 80 K and 20 K surfaces. The insulation system consists of flat, reflective radiation shields of aluminized Mylar film with randomly oriented fiberglass mat spacers (commonly called superinsulation). The system is prefabricated in blankets of 13 Mylar and 12 fiberglass layers. Four blankets are installed on the 80 K surface and one is installed on the 20 K surface. Prefabricated transition pieces and well defined installation procedures are utilized to eliminate voids in the insulation system, either incurred during assembly or from differential thermal contraction. The plastic substrate of the insulation system and the fiberglass mat should not suffer performance degradation when subjected to the estimated radiation environment of less than 10^6 Gy over the 20 year machine life. A vacuum pumpout space equal to the thickness of each insulation blanket is provided around one boundary of each insulated assembly.

The insulation system has been successfully employed in two, full-section model cryostats (i.e., 6 m Magnetic Effects Model and 12 m Heat Leak Model). The radiation heat transfer factors employed for the design were 6.1×10^{-1} Wm^{-2} to 80 K, 7.5×10^{-2} Wm^{-2} to 20 K and 2.7×10^{-4} Wm^{-2} to 4.35 K. The insulation system was readily manufactured and performed well during heat leak measurements both in a good (10^{-6} Torr) and poor (10^{-2} Torr) vacuum.

Vacuum Vessel

The vacuum vessel provides the insulating vacuum space as well as the connection for the support system of the magnet to the tunnel floor. Since the vessel has no magnetic requirements, candidate materials were carbon steel, stainless steel, 9% nickel steel, and aluminum. Carbon steel was selected on the basis of cost. The composition of the steel will be a compromise between the material's mechanical properties and fabrication cost.

Interconnections

Mechanical and electrical interconnections are required at the magnet ends. It is essential that the connections be straightforward to assemble and disassemble, compact, reliable and economical. The dipole-to-dipole mechanical connections are between beam tube sections, helium containment vessel sections, helium lines, liquid nitrogen shield lines, insulating vacuum vessel sections, thermal radiation shield bridges and insulation. The dipole-to-dipole electrical connections include magnet current bus bars, quench bypass bus bars, quench protection diodes (if used), instrumentation leads, quench detection voltage taps, correction coil leads, etc. The interconnection design has stressed ease of assembly and disassembly operations in the SSC tunnel. The resulting geometry permits the use of automated welding and cutting equipment that is essential for installation efficiency and interconnection reliability. To reduce costs, straight pipe connections are used between magnets. All vacuum-tight connections are circular. Bellows, needed for axial thermal contractions, are also able to accommodate minor misalignments. For the pipes, two bellows are employed in series better to accommodate offsets. The interconnection region incorporates 20 K and 80 K heat shield bridges to maintain radiation heat transfer barriers. The bridges are attached to the magnet shields by riveting, with thermal connections provided by conductive braids. A single blanket of multilayer insulation is installed on the 20 K shield bridge. Four blankets of multilayer insulation surround the 80 K shield bridge.

The details of the interconnection region are as shown in Fig. 5.2-12.

Heat Leak

The cryostat heat leak consists of two major elements, thermal radiation and conduction. Table 5.2-9 shows the estimated center section heat leak in these categories for the cryostat model that is now under construction. Testing of this full-scale model is scheduled to begin early in April, 1986, and will provide final measurements on which to base the heat leak allowances for the dipole cryostat.

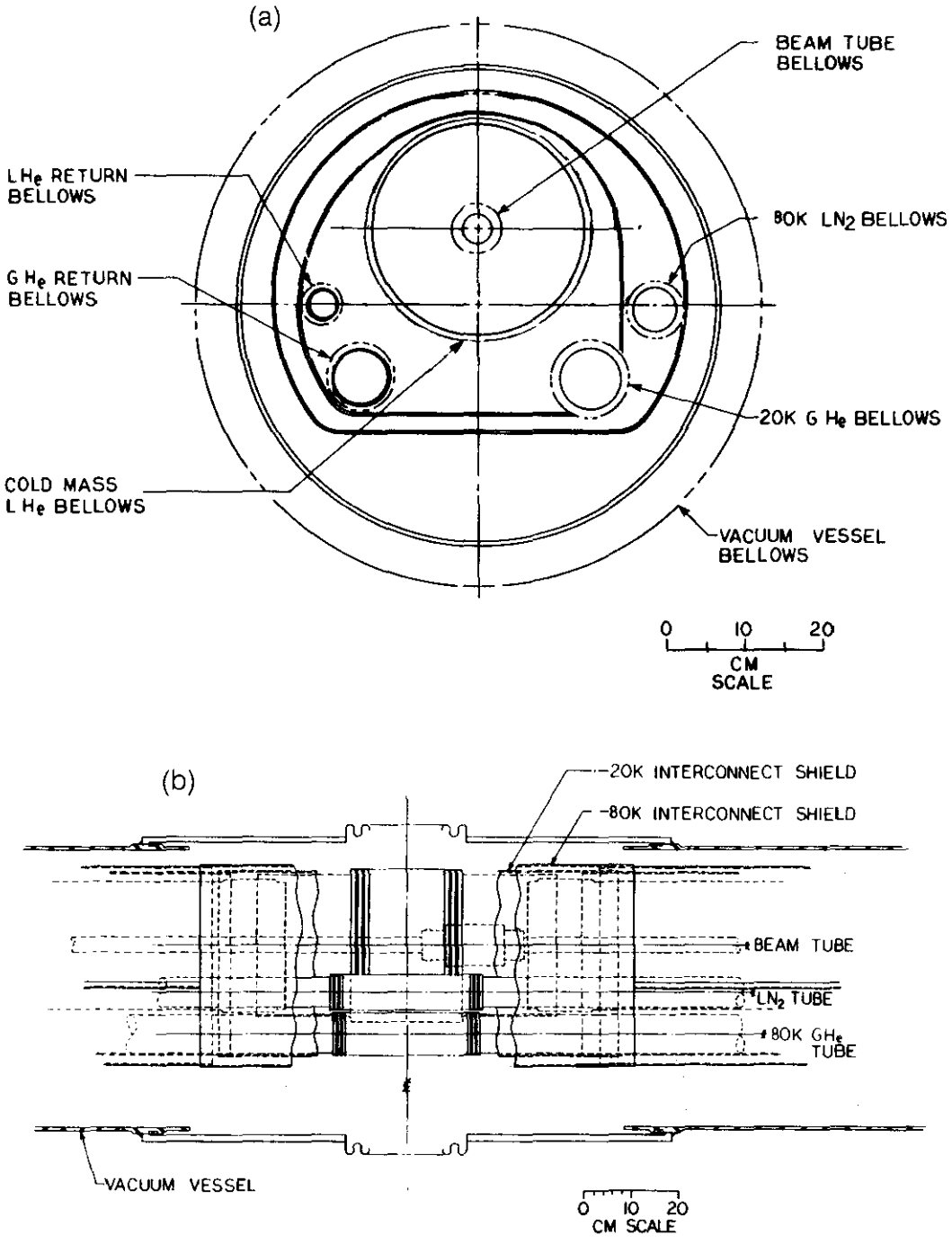

Figure 5.2-12. (a) Details of the interconnection region, indicating the various bellows. (b) Elevation view of the interconnection region.

Table 5.2-9
Dipole Cryostat Heat Leak Model
Center Section Heat Leak Prediction (watts)

	80 K	20 K	4.35 K
Thermal Radiation	17.68	1.778	0.002
Cold Mass Supports[1-3]	6.53	0.695	0.172
Cold Mass Anchor[2,3,4]	0.66	0.047	0.017
Total	24.87	2.52	0.191
Design Budget	25	2.5	0.3

Notes

1. For five 5 in. × 7 in. × 1/16 in. G11 CR reentrant posts.
2. Corrected for predicted intercept temperatures of 85 K and 21 K.
3. Corrected for calculated *vs* measured Suspension Heat Leak Dewar experience factor.
4. For 2 × 0.050 in. G11 CR strut pair.

For the particular choices that have been made in the design of the cryogenic system as a whole, the magnet cryostats will operate with temperatures ranging from 78 to 89 K for the outer shield and from 17 to 21.5 K for the inner shield. The magnet will have a maximum operating temperature of 4.35 K with a nominal refrigerator operating temperature of 4.15 K. The heat leak totals for the installed cryostat that have been used in estimating the refrigeration capacity needed for the SSC are 27 watts to an average temperature of 84 K, 3.3 watts to an average temperature of 20 K, and 0.32 watts to the average magnet temperature of 4.25 K.

Other contributions to the total heat leak at 4.25 K include 0.1 watt/magnet due to conductor splice ohmic heating and 2.34 watt/dipole due to synchrotron radiation. A heat leak budget for a complete arc sector is given in Table 5.3-2.

5.2.10 Assembly

The major components of the dipole cryostat (Section 5.2.9), i.e., the magnet proper in its helium containment vessel (cold mass), cryogenic piping, heat shields, insulation, and alignment fiducials, are located and supported by reentrant post supports connected to the vacuum vessels as shown in Fig. 5.2-10(a). This major subassembly, complete with the anchor system and heat intercepts, is inserted into an outer vacuum vessel. Figure 5.2-10(b) shows longitudinal views of the finished assembly, and indicates various pertinent length parameters and the location of the magnet supports relative to the central anchor position.

Cold Mass Subassembly

As a first step in final magnet assembly, the pre-manufactured magnet cold mass is located on an assembly station, and slide cradles with their supporting subassembly, and alignment fiducial targets, are installed. The cold mass passes to another assembly station, where the axial anchor subassembly, as well as helium return lines, are attached (Fig. 5.2-13). Next, the five assembled support posts are installed on a locating fixture. The support post heat intercepts are attached, and the 20 K and 80 K heat shields are installed quadrant by quadrant, attached to the support post intercepts. Thermal insulation blankets come next (one blanket on the 20 K heat shield, four on the 80 K shield), followed by heat conduction straps also connected to the intercepts. These steps complete the preparation of the entire cold mass subassembly for insertion into the vacuum vessel.

Vacuum Vessel

The vacuum vessel is fabricated from cylindrical sections of welded steel pipe, with precision machined mounting feet attached. The machined surfaces of the feet are perpendicular and parallel to related surfaces of the support posts. This arrangement assures alignment of the center of the beam tube in the cold mass with respect to the outside of the vacuum vessel. End rings to hold shipping restraints and reinforcing segments to the support points are attached, and all welding is completed using automated equipment. The inspected assembly is then transferred to the final assembly station where the alignment and support tray (used for the final operation, below) is installed.

Final Assembly

The cold mass subassembly and the vacuum vessel are lined up, and a slide and pulley system draws the cold mass into the vacuum vessel. Precision fixture points, together with the position location of the support post feet, allow the cold mass to be located properly relative to the vacuum vessel. A system of optical fiducials is checked to assure the correct alignment. The towing plate is removed, and the assembly is clamped and welded together. All external vacuum vessel alignment fiducials are set. The magnet is then inspected, given a final leak check, painted, and the post and vessel shipping restraints are installed. It is now ready for final testing and measurements.

Cryostat Alignment Reference

The alignment of the magnetic centerline of the magnets depends on the transfer from the iron yoke to reference marks on the outside of the cryostat. Optical tooling techniques are normally used for these transfers, but the special circumstances of tunnel installation and alignment of large numbers of magnets suggests the use of other methods, such as photogrammetry (stereo photographs, digitized and analyzed by computer, with photographs providing a permanent record of quality control).

5.2.11 Magnet Testing and Measurements

A thorough program of quality assurance and quality control must be carried out during all stages of design and manufacture. All completed magnets will be tested at room temperature to meet electrical and field quality specifications. Approximately the first 100 magnets will undergo a complete warm and cold measurement program to evaluate fully

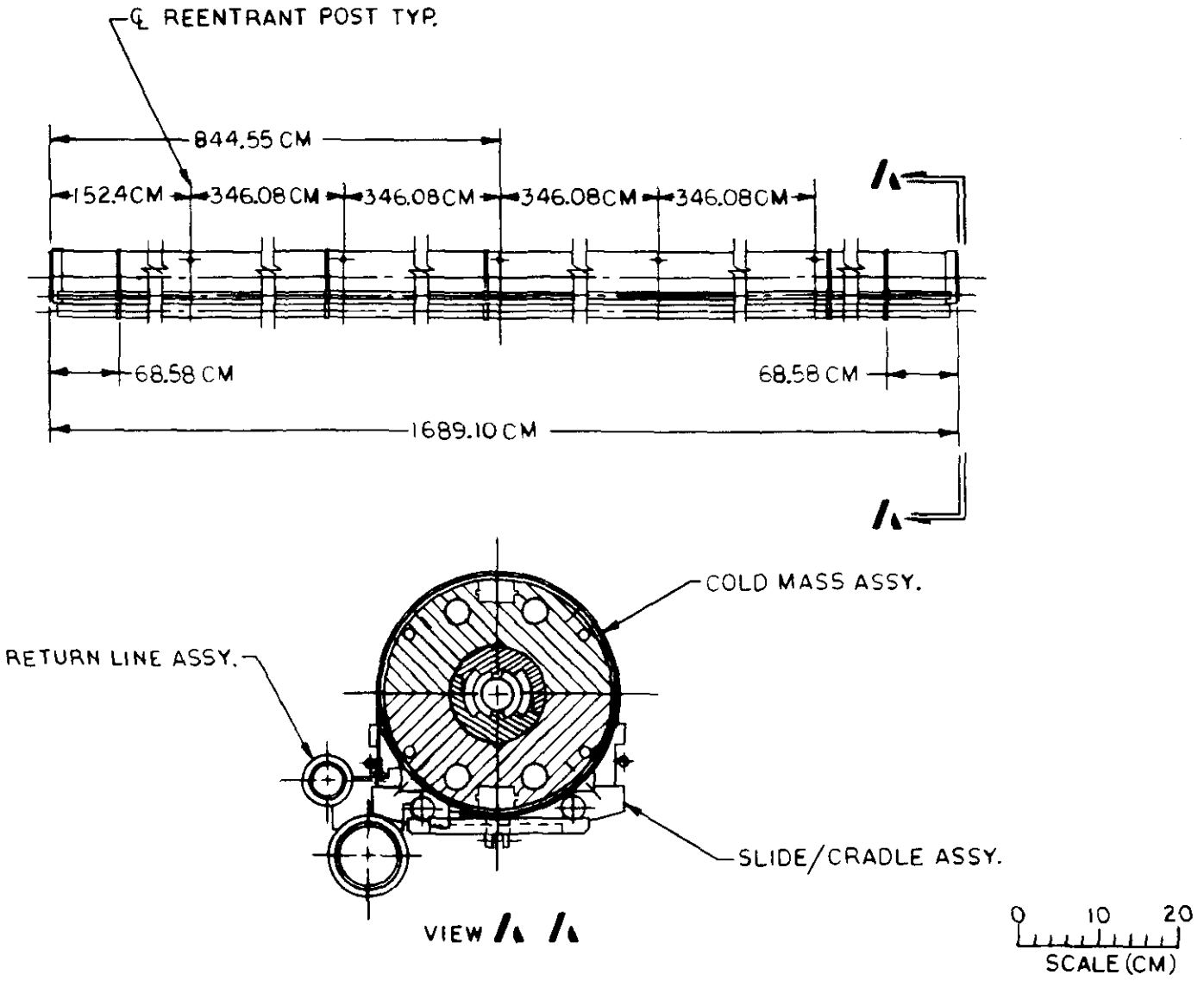

Figure 5.2-13. Cold mass subassembly, including dipole magnet in helium containment shell, helium return pipes, and slide assembly.

field quality and training characteristics of production units. As experience is gained, a sampling method will be employed, keyed to production quality, time, and number of assembly lines. A sampling rate of 10% is anticipated.

Selection of a final test procedure sequence will be based on the observed magnet performance.

Factory Certification Tests

The tests required to certify each dipole for SSC acceptance, before it leaves the factory or factories, include several types and are performed at various stages of the fabrication and assembly process. These tests, conducted at room temperature, are summarized below.

(a) Electrical Measurements and Tests
   1. Resistance, inductance, and Q of each of the four windings and of the complete magnet.
   2. Hi-pot between windings, between windings and collars, and between coil and bore tubes to 2–3 kV.

(b) Magnetic Measurements
   All magnets will have field measurements made at room temperature. The current will be limited to ± 15 A, and the following quantities will be measured: B_0, a_n and b_n, n = 1 to 6. The field at 15 A is about 150 G.

Initial Production Units: Cold Test

As indicated above, approximately one hundred units of initial production will be cold tested. This has to be accomplished promptly so that production quality can be verified and fabrication procedures can be modified, if necessary. These tests are planned to be performed at BNL or Fermilab. Five magnet assemblies could be tested in parallel. Five to seven magnets could be tested per week.

Cold Tests

The tests summarized below shall be performed with the magnet cooled to 4.35 K:

(a) Repeat electrical tests above
(b) Calibrate quench protection circuits
(c) Measure field harmonics at several field levels
(d) Measure integral field strength
(e) Operate to design current (train if necessary)

Training

The large number of SSC magnets requires that their testing and training must be accomplished as efficiently as possible. The training curves for the 8 model magnets fabricated by BNL and for 10 model magnets fabricated by LBL were examined. (See Fig. 2.4-1.) Statistical analysis indicates that 3 training quenches are desirable to reduce the probability of subsequent quenches in the tunnel to an acceptably low number during 6.6 tesla operation. Although it may be possible to improve the magnet design sufficiently to eliminate training quenches, it is prudent to plan for training or preconditioning.

One possible method for eliminating training is to pre-condition the magnet at a reduced temperature. At reduced temperatures, below the 4.35 K operating temperature,

the higher critical current allows the magnet to be driven well above the normal operating current, field, and forces, yet remain below its critical field. At reduced temperatures the first quench is likely to occur well above 6.6 T. Therefore, it is possible that at such a temperature the magnet can be energized to, say, 7 T or 7.5 T without quenching. Subsequently at 4.35 K the magnet will not train. This low temperature conditioning can be done on individual magnets or on a string of magnets. Results with R&D models make the method appear promising. However, it needs to be statistically proven over a wider range of operating conditions. An R&D program is planned to provide the necessary data base for a timely decision.

Identification of the methods and sequence of magnet training has implication in reliability, operating levels, and both time and dollar costs. The following options have been examined:

(a) Testing and training magnets in a fabrication facility
(b) Testing and training magnets at the national laboratories
(c) Testing and training magnets on site
(d) Testing and training magnets in the tunnel

Each of the above options can be implemented either at 4.35 K or at 2 K. Option (a) embodies the possibility of returning a defective magnet to the factory floor for immediate correction and feedback on production quality. It does, however, require duplication in cryogenic and measuring equipment and additional trained staff. Option (b) requires the least equipment investment, but costs of additional transportation offset the reduced on-site equipment requirement. Option (c) requires early occupancy at the site and prompt installation of one of the planned SSC refrigerators. This option appears to be one of minimum risk. The cost of refrigerator and additional production testing equipment should be less than $20M. Option (d) requires interfacing with tunnel construction and early installation of one of the corresponding SSC cryogenic systems. It presents more complex installation logistics, and the magnet system will experience more training quenches because of the interaction of the magnets under test. It is, however, the least costly method, particularly if accomplished at 2 K.

In summary, there are several viable alternatives within cost and schedule constraints to test and train magnets either at 4.35 K or 2 K.

5.2.12 Quadrupoles

There are 678 standard arc quadrupole magnets per ring, or a total of 1356 such magnets. (Special quadrupoles in the interaction regions are described in Section 5.2.14.) The quadrupoles have the same bore tube diameter and the same inner coil diameter as the dipoles. To maximize the operating gradient, the coil winding has 19 turns distributed in two layers as shown in Fig. 5.2-14(a). The inner layer has 8 turns with a wedge inserted in each octant to maximize uniformity of the gradient. Four such double coil layers are arranged in the usual way to generate the quadrupole field.

The cable is identical to the cable used in the outer coil layer of the dipole: 30 strands of 0.65 mm diameter each, with a copper-to-superconductor ratio of 1.8:1 and partially keystoned. The quadrupoles are designed to operate in series with the dipoles. At I = 6500 A, the operating margin is somewhat higher than that of the dipole (J_c/J_o = 1.35 vs. 1.25).

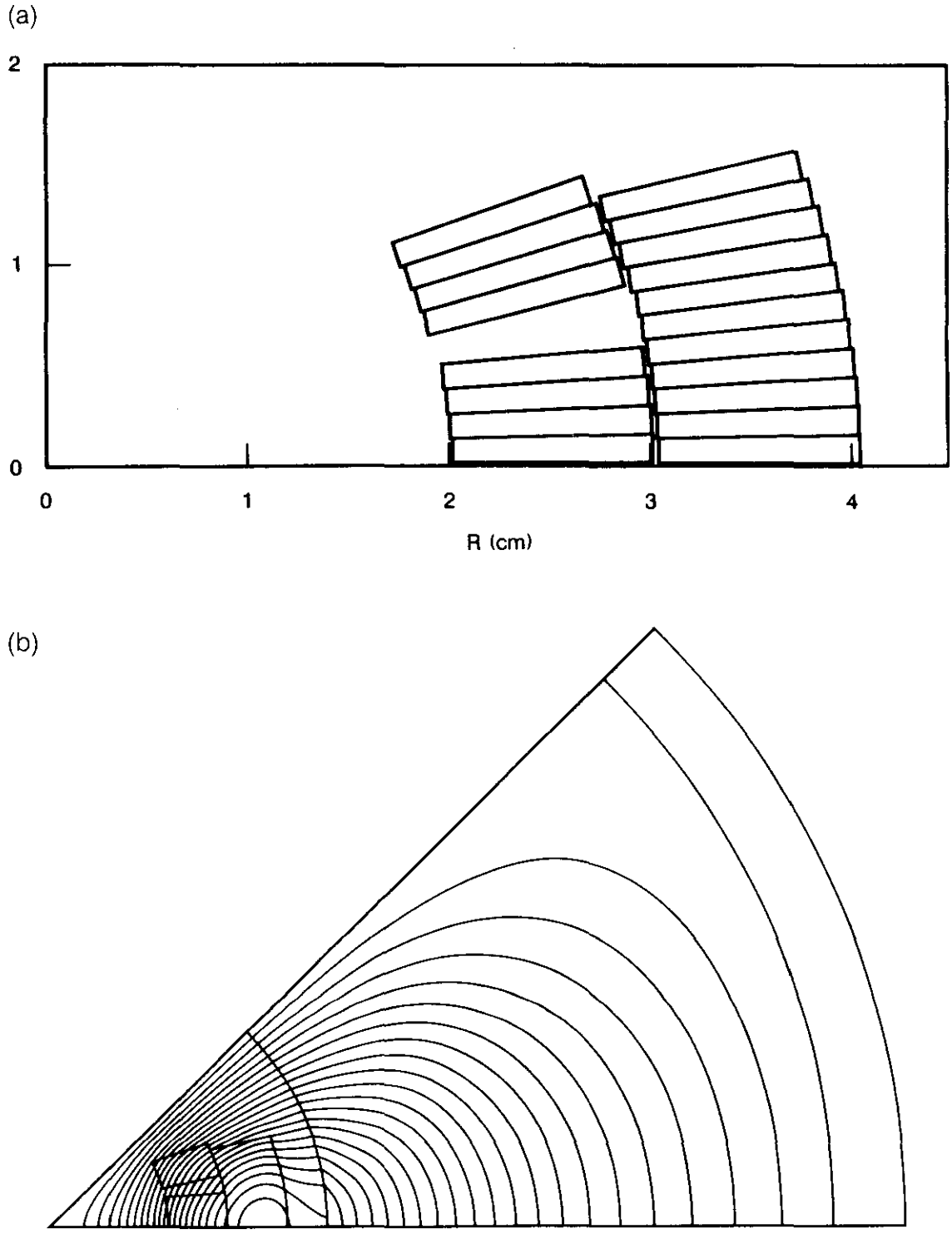

Figure 5.2-14. (a) Octant of quadrupole cross section, showing distribution of partially keystoned superconducting cable. (b) Octant of quadrupole showing calculated magnetic field lines.

Table 5.2-10
Regular Cell Quadrupole Magnet Parameters

General	
No. of quadrupoles per ring	678
Overall length [m]	4.32
Magnetic length [m]	3.32
Bore tube inner diameter [cm]	3.226
Mass of conductor [kg]	83
Cold mass [kg]	1114
Central field gradient [T/m]	212
Current [A]	6500
Inductance [mH]	0.57
Stored energy [kJ]	12.0
Winding	
Inner layer	
No. of turns (one coil per pole tip)	8
Inner diameter [cm]	4.000
Outer diameter [cm]	5.966
Cable length [m] (for 4 coils)	219
Cable mass [kg] (for 4 coils)	17.5
Maximum field [T]	5.2
Outer Layer	
No. of turns (one coil per pole tip)	11
Inner diameter [cm]	5.986
Outer diameter [cm]	7.952
Cable length [m] (for 4 coils)	300
Cable mass [kg] (for 4 coils)	24
Maximum field [T]	~4.0
Conductor	
Cross section, bare [mm]	9.73×(1.27–1.06)
Keystone [deg.]	1.21
Strand diameter [mm/in.]	0.648/0.0255
No. of strands	30
Strand twist pitch [per cm]	0.4
Cable twist pitch [per cm]	0.136
Copper-to-superconductor ratio	1.8:1
No. of superconducting filaments	6000
Filament diameter [μm]	5
Iron Yoke	
Material	Low carbon steel
Inner diameter [cm]	10.31
Outer diameter [cm]	22.86
Lamination thickness [mm/in.]	1.5/0.060
Weight of iron [kg]	1005
Yoke Containment Structure	
Material	Stainless steel
Outer diameter [cm]	27.62
Thickness [cm]	0.47
Weight of shell [kg]	109

The quadrupole gradient is 212 T/m at 6500 A. (The dipole field is 6.6 T at this current.) There is an overall 0.5% decrease in gradient per ampere between injection and maximum current because of saturation effects in the iron. This can be compared to a saturation drop of about 2% in B_0/I in the dipole. To maintain proper focusing, there are trim quadrupoles in the correction package. Table 5.2-10 lists the principal quadrupole parameters.

The coils are constructed by techniques developed for the Tevatron and are very similar to those used for dipole fabrication and described in Section 5.2.4 — basically, precision molded after winding, using an identical insulation scheme. Field uniformity of a theoretically perfect winding is shown in Table 5.2-11, expressed in terms of the multipoles b_n. The $n = 1$ term is the quadrupole, $n = 2$ the sextupole, etc. Symmetry insures that only the $n = 1, 5, 9, 13$, etc., terms are allowed. Terms above $n = 17$ are smaller than 10^{-7}. The listed terms do not change significantly as current varies from zero to maximum value. Figure 5.2-14(b) shows calculated field lines in a simplified rendering of a magnet octant. Calculated rms random multipole errors for the arc quadrupoles are given in Table 4.3-2.

Table 5.2-11
Calculated Systematic Multipoles[a]

n	b_n
1	10^4
5	0.00023
9	0.06345
13	0.076
17	−0.0016

[a]The multipoles are in units of 10^{-4} cm^{-n}.

Mechanical coil support and accurate alignment are provided by a system of collars, as in the dipoles. The arrangement is shown in Fig. 5.2-15, which depicts an overall cross section of the quadrupole. The collaring arrangement is nearly identical to the system used at Fermilab to construct the quadrupoles for the Tevatron. The collared coil assembly is installed in a split iron yoke similar to the dipole yoke, and held together by a welded stainless steel shell that is also the helium containment vessel.

The cryostat is also shown in Fig. 5.2-15. It is identical in cross section to that of the dipole, with the minor exception that the two support posts will have a reduced cross-sectional area to minimize the heat leak. End connections are nearly identical to those for the dipole.

5.2.13 Correction Magnets, Spool Pieces

There is a need in the collider ring to have correction magnets and a large variety of other equipment that cannot be integrated into the dipoles or quadrupoles of the lattice. These devices are located in the drift spaces adjacent to every quadrupole in the rings, and are incorporated in a cryogenic enclosure called a spool piece.

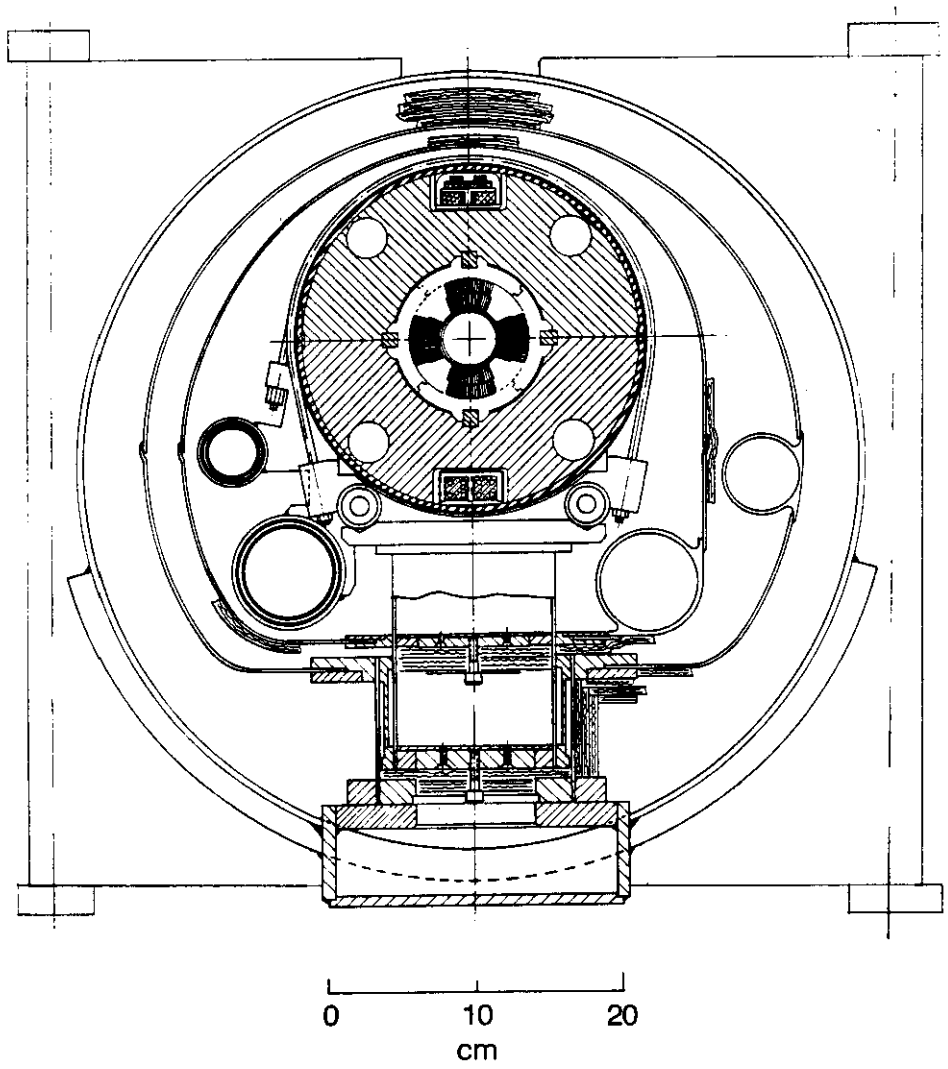

Figure 5.2-15. Overall cross section of quadrupole magnet. The vacuum-vessel support-foot arrangement shown here is that used in prototype units. The arrangement of the conceptual design is shown schematically in Fig. 5.2-22(a).

There are two different lengths of spool pieces. Those in the main bending arcs and adjacent to the quadrupoles in the interaction regions and utility regions have an alloted (slot) length of 4.98 m. The spool pieces in the short bending arcs in the cluster regions have a slot length of 3.35 m. There are no spool pieces within the inner triplets of the interaction regions.

The longer spool pieces are of eight basic types, characterized by whether they have heat exchangers (recoolers) or not, whether they have one or two correction packages, and whether they are designed to serve a special cryogenic function (which could be a cryogenic feed point, a cryogenic termination point, a cryogenic isolation point) and whether they are contained in a two-in-one cryostat. The spool pieces with two correction packages are distinguished further by the type of correction element in the second package. This could be a quadrupole (normal or skew), or normal or skew sextupole, or octupole. The shorter spool pieces have one correction package, do not have special cryogenic functions, and are characterized only by whether they contain recoolers or not. All of the spool pieces are subcategorized by the orientation of the dipole in the primary package. Table 5.2-12 lists the different types and number of spool pieces. The major equipment that is contained in the spool pieces can be categorized by function and by frequency of occurrence in the lattice.

Standard Spool Pieces

The large majority of the spool pieces in the ring, are of one of the four following types:

1. Minimal spool piece (SPA1)
   Every spool piece in the collider rings contains at least the following equipment:
   (a) A magnetic correction package for the adjustment of tune (quadrupole) and chromaticity (sextupole) and dipole correctors to compensate for the effects of random errors in the bending field or alignment of the main dipoles and quadrupoles. This correction-element package, described in more detail below, is 1.5 m long and is referred to as the primary correction package.
   (b) Current bypass leads (safety leads) that are used to protect the main magnets in the event that they quench.
   (c) Pumping ports, gauges, pumps, and valves for the beam-tube and cryostat vacuum, and barriers that isolate the cryostat vacuum space of each half-cell from its neighbors.
   (d) Electrical lead pairs for the correction elements, pulsed quench heater strips, and magnet warmup heaters.
   (e) Pressure relief valves for the supercritical helium circuit.
   Figure 5.2-16 shows a regular spool piece with one correction package, type SPA1.
2. Minimal spool piece with recooler (SPR1)
   In addition to the above, every second spool piece contains:
   (a) Heat exchangers (recoolers), monitoring and control devices for the cryogenic system.
   (b) Feed-throughs for sensing leads that are used to measure the voltage across each magnet for the detection of quenches.

Table 5.2-12
Types of Spool Pieces

Name	Type	Slot Length (m)	Recooler	Corrector Packages	6.6 kA Leads	Number in SSC Arcs	Clusters
SPA1	Standard	4.98	No	1	No	504	0
SPR1	Standard	4.98	Yes	1	No	376	0
SPA2i	Standard	4.98	No	2	No	160	32
SPR2i	Standard	4.98	Yes	2	No	160	0
SPAS	Short	3.35	No	1	No	0	96
SPRS	Short	3.35	Yes	1	No	0	96
SPAD1	Dual	4.98	No	1	No	0	40
SPRI	Isolation	4.98	Yes	1	No	96	56
SPF	Feed	4.98	No	1	Yes	16	4
SPE	End	4.98	Yes	1	Yes	16	4
				Totals		1328	328
				Grand Total		1656	

3. Spool piece with two correction packages (SPA2 or SPR2)
   In each main bending sector of each ring there are 20 spool pieces that have two correction element packages, one as described above (the primary package), and the other being a 2 m long higher order corrector (secondary package) of a type that depends on the location of the spool. These types of spool pieces may (SPR2) or may not (SPA2) contain recoolers, depending on their location. In the cluster regions there are spools with secondary packages that consist of dipoles only.
4. Short spool piece (SPAS or SPRS)
   In the bending arcs of the cluster regions the spool pieces are shorter, because the adjacent quadrupoles are longer. These spool pieces only have the primary correction package, and every other one contains a recooler (SPRS).

Special Spool Pieces

There are a small number of spool pieces in the collider rings serving special functions associated with the cryogenic system or the power supply system. Since the special functions require extra space, none of these spools have a secondary correction package. The equipment related to the special function is constrained to fit in the 2 m that is gained by eliminating the secondary package.

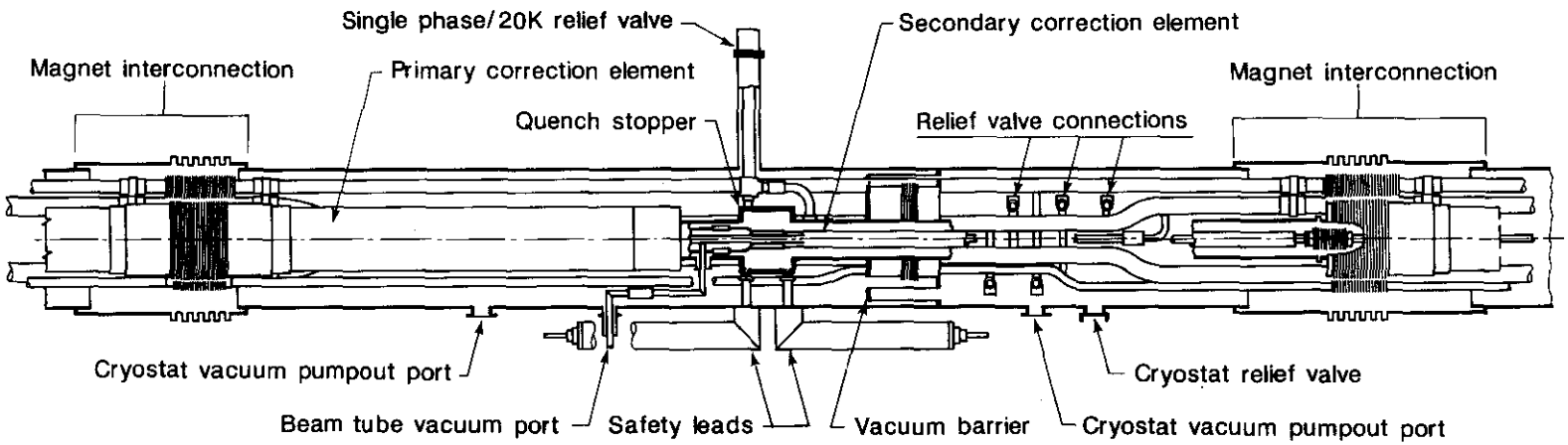

Figure 5.2-16. Regular spool piece with correction package.

1. Dual spool piece (SPAD1)
   The spool pieces in the vertical bend sections near each interaction region are not separated sufficiently to be placed in separate cryostats. These spools are identical internally to two regular spools without recoolers (SPA1), except that they are both in one cryostat.
2. Isolation spool piece (SPRI)
   Every tenth spool piece in the main bending arcs is an "isolation spool", which contains a transition from 4.5 K to room temperature and back to 4.5 K, leaving a short section of warm beam tube with a gate valve. The cryogens are conducted across the transition with a set of U-tubes that can be removed to interrupt the cooling to any one kilometer length (a section) of the rings. The high current bus is continuous through the isolation spool through a special cryogenic feed-through. These spools are also used near the interaction and utility regions to connect to transfer lines that span those areas. A drawing of an isolation spool with a recooler is shown in Fig. 5.3-4.
3. Feed spool piece (SPF)
   At the center of each sector of the main bending arcs, and near the center of the cluster regions, there are "feed spools", the purpose of which is to permit the refrigerator to be connected to the magnet strings. These spool pieces are similar to the isolation spools, except that they also have two pairs of high current leads for the main power supplies.
4. End spool piece (SPE)
   At either end of each sector and at the ends of the cluster regions there are "end spools", the purpose of which is to provide for the termination of cryogenic flow, and to connect to the adjacent region. These spools contain two pairs of high current power leads.

Description of Major Components of Spools

Primary Correction Coils

Each primary correction package consists of a correction dipole, quadrupole, and sextupole in the same 1.5 meter circumferential space shown in Fig 5.2-17(a). The dipole is strong enough to correct six times the predicted rms closed orbit error. The quadrupoles are capable of a tune change of ± 2 units and the sextupoles can adjust chromaticity by plus or minus twice the natural chromaticity. The parameters are listed in Table 5.2-13. To implement the cos θ distribution in the correction coils a keystoned, flat ribbon conductor is used.

Secondary Correction Coils

Specific design requirements and conceptual design dimensions for the secondary correction coils are shown in Table 5.2-13. Figure 5.2-17 shows their cross-section configurations. Each of the secondary coils is 2 m in length. The quadrupole and skew quadrupole are nested within the same assembly. The sextupole and octupole are in separate units in order to allow the required high fields. The same conductor is employed in the secondary coil package as for the primary correction coils. The skew sextupole and octupole are made by inserting secondary sextupole and octupole coils into the spool piece at the appropriate angle.

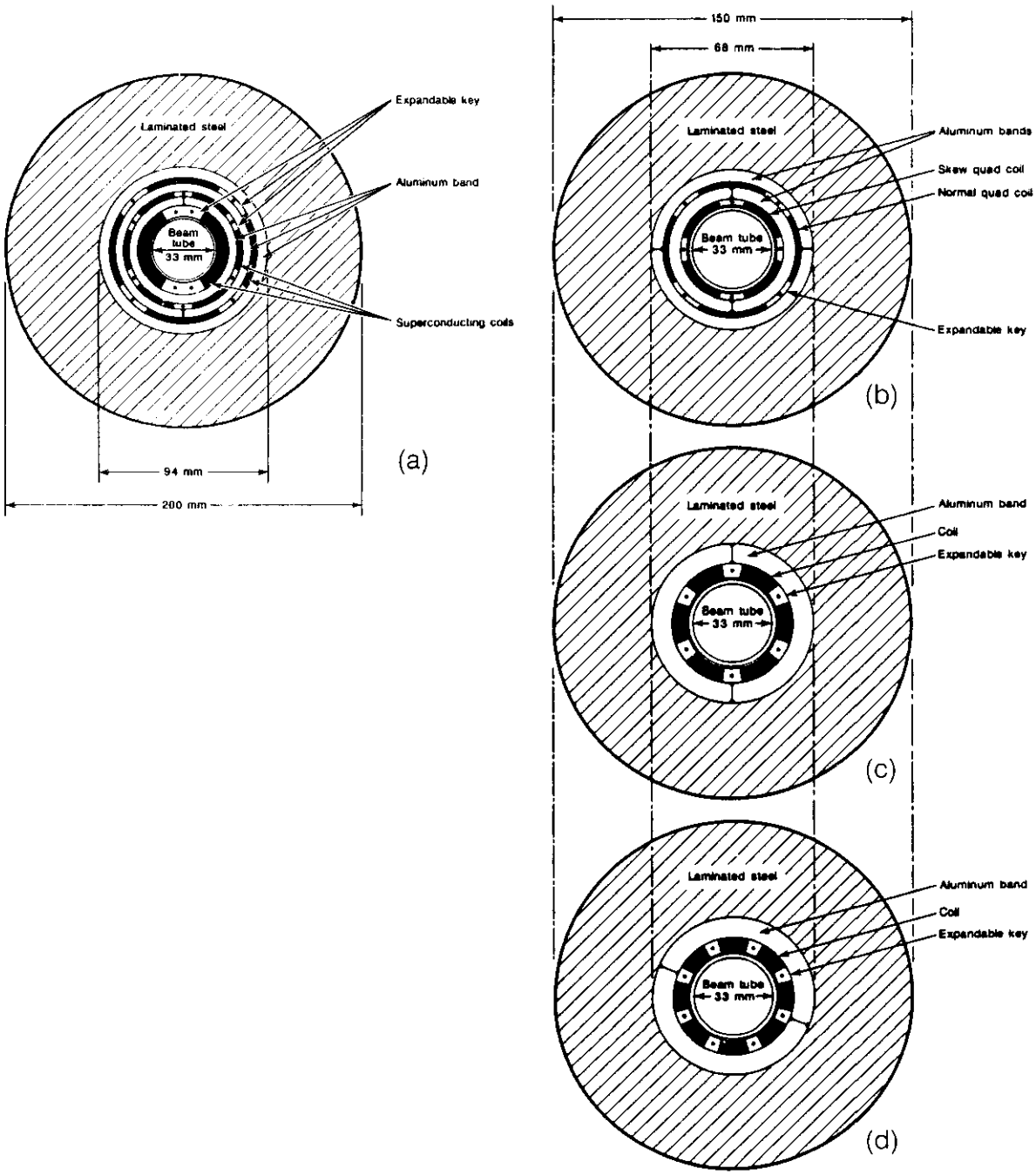

Figure 5.2-17. (a) Primary corrector package. (b,c,d) Secondary correction coils.

Table 5.2-13
Spool Piece Correction Coils

Type	Length (m)	Inner Radius (mm)	Outer Radius (mm)	Strands per Cable Layer	Cable Layers per Pole	Turns per Pole	B (1 cm) no Iron @ 100 A (T)	B (1 cm) with Iron @ 100 A (T)	BL (1 cm) @ 100 A (T-m)	Inductance (H)
PRIMARY										
Beam Tube		16.5	18.0							
Dipole	1.5	18.5	25.0	14	36	504	1.75	2.12	3.16	1.40
Sextupole	1.5	30.0	33.0	6	20	120	0.08	0.09	0.13	0.21
Quadrupole	1.5	38.0	41.0	6	38	228	0.27	0.40	0.60	0.85
Steel	1.5	47.0	100.0							
SECONDARY										
Quadrupoles										
Beam Tube		16.5	18.0							
Skew Shell	2.0	18.5	21.5	6	18	108	0.40	0.45	0.90	0.16
Norm. Shell	2.0	26.5	28.5	4	26	104	0.20	0.28	0.56	0.18
Steel		34.0	75.0							
Sextupole										
Beam Tube		16.5	18.0							
Coil	2.0	18.5	25.0	14	12	168	0.38	0.40	0.80	0.55
Steel	2.0	34.0	75.0							
Octopole										
Beam Tube		16.5	18.0							
Coil	2.0	18.5	25.0	14	9	126	0.18	0.18	0.36	0.41
Steel	2.0	34.0	75.0							

The superconductor diameter = 0.406 mm wire (1.8 to 1, Cu to SC) + 0.025 mm thick Formvar insulation.

The cable is made of parallel strands 0.528 mm thick, and slightly keystoned on 0.07 mm thick Kapton. Hence, J_{sc} = 2160 A/mm^2 @ 100 A and J_{ave} = 340 A/mm^2 @ 100 A.

Other Components

A detailed description of the major utility components of the spools follows. Most of these features, except the recooler, have been utilized at the Tevatron.

1. The *cooldown valve line* is used during the changing conditions prevailing during cooldown of the magnet string, as described in Section 5.3.8. The cooldown valve operates at ambient or near ambient temperature. The line from the single-phase flow is provided with bellows and thermal intercepts at 20 K and 80 K to limit the heat leak.
2. The *recooler* heat exchanger removes heat by providing boiling liquid at lower temperature than the magnet coolant flow, which passes through the other side of the exchanger. The heat is removed from the coolant by evaporating the helium into a gas return line.
3. *Safety Leads and Quench Stopper.* The safety leads carry current only when a magnet in that half cell quenches. Because of the large number of such leads, they are made as simple as possible, compatible with a small heat leak. They are constructed from stainless steel bar, wrapped with electrical insulation and sheathed in flexible tubing as a close-fitting vacuum jacket. The room temperature end passes through a high-voltage electrical feed-through. A small flow of helium is established in the lead to reduce the heat leak.

   The quench stopper [5.2-17] is made of brazed copper strips soldered to the magnet bus on one end, and brazed to the safety lead on the other end. The stopper has sufficient cross section and surface area to dissipate the heat generated in the safety lead during current bypass. This limits the temperature rise on the other side of the stopper, allowing the magnet bus to remain superconducting and preventing the quench from passing to the next magnet.
4. *The isolation box* permits the separation of all fluid and vacuum channels from one sector (containing 12 half cells) to another. This is accomplished for the cryogenic fluid streams by short lengths of jacketed transfer lines called U-tubes. These can be withdrawn from bayonet joint sockets in the isolation boxes located at the end of each sector. Room temperature ball valves at the top of the sockets are closed after the U-tube is withdrawn. This method of isolation avoids the unreliability of cryogenic valves operating in a large system that may contain contamination or debris preventing proper valve operation. Special U-tubes can be installed to permit reconnecting the fluid lines to maintain low temperature readiness in adjacent sectors during a magnet installation or replacement.

   A riser length in the magnet coolant flow, like an inverted U, permits the magnet bus to be continuous as needed during operation, while the helium flow is isolated when needed for magnet replacement. At the top of the inverted U there is a flow-blocking plate with electrical feed-throughs for the magnet bus.
5. *Vacuum barriers* in the insulating vacuum are needed to subdivide the vacuum chamber into reasonable lengths for installation and leak hunting. They are installed in every regular spool and are implicit in the isolation and end spools. Each barrier is a set of three nested cylinders with alternately closed ends. The inner end plate is maintained at 4.5 K and is welded to the magnet coolant flow tube. The next one is at 20 K, the one beyond that at 80 K, and the outer one at

ambient temperature. The design is optimized in wall thickness and length to withstand a 5 atm pressure differential from either side with a minimum heat leak. The vacuum barrier is shown on the drawing of the regular spool, Fig. 5.2-16.

5.2.14 Special Magnets

Introduction

In addition to the magnets described so far, several types of special magnets are needed in the interaction regions and for the abort system. This section addresses only the special superconducting magnets; conventional magnets are described in Section 5.10 on beam abort.

The special dipoles and quadrupoles differ from the arc magnets in some combination of length, aperture and field, as demanded by the special requirements of the beam transport in the insertion regions. The list of these special magnets is given in Table 4d of Attachment A, the SSC Parameter List. Though relatively small in number, these 500 or so special magnets are crucial to the proper functioning of the interaction regions and must at the same time preserve the beam quality to assure long beam storage times. All special dipoles are used to bend the beams in the vertical plane. The special quadrupoles, on the other hand, serve a variety of purposes from dispersion suppression to the final, strong focusing at the interaction point in the low-beta IRs.

Vertical Bending Magnets

There are two types of IRs, as shown in Figs. 5.11-1 and 5.11-4. Near the low-beta regions the beams are fairly large and their separation varies. To accommodate the large beam size and, in the case of dipoles BV1A and BV1B, two beams, a coil inner diameter (i.d.) of 7.50 cm was selected for the majority of the dipoles. The coil design is similar to that of the Tevatron dipoles, but the use of improved superconductor permits a peak field of 5.2 T. Cold iron is used, just as for the arc dipoles. With BV1A/B the beams are separated vertically by 2 cm. The next vertical bending magnets away from the IRs are BV2C and BV2D. Because beams are separated by about 35 cm in this region it is necessary to place two of the BV1A/B dipole iron assemblies in a single cryostat, as shown in Fig. 5.2-18. This figure is also representative of the BV3 magnets except that the separation between the beams varies from 35 to 47 cm. The walls of the vacuum enclosure of the cryostat are vertical between the two beam regions to maintain about the same horizontal envelope as the rest of the accelerator. Horizontal cross members are used to withstand some of the external pressure without increase of the vacuum wall thickness. The next set of dipoles in both the low-beta and medium-beta interaction regions are the BV4A-E. The beams in this region are separated by between 60 and 70 cm. Two of the BV1A/B vertical bending magnets in individual cryostats, stacked one on top of another, with the appropriate separations, satisfy the requirements for these dipoles. Special fixtures may be required to provide the appropriate alignment for the BV4 dipoles.

All the vertical bending magnets in the low-beta insertion regions are constructed of similar 7.5 cm i.d. coils, packaged appropriately for the local beam separation. The medium-beta IRs require additional special dipoles (BV1C and BV1D) to accommodate the two beams when they are widely separated but converging near the interaction point. At

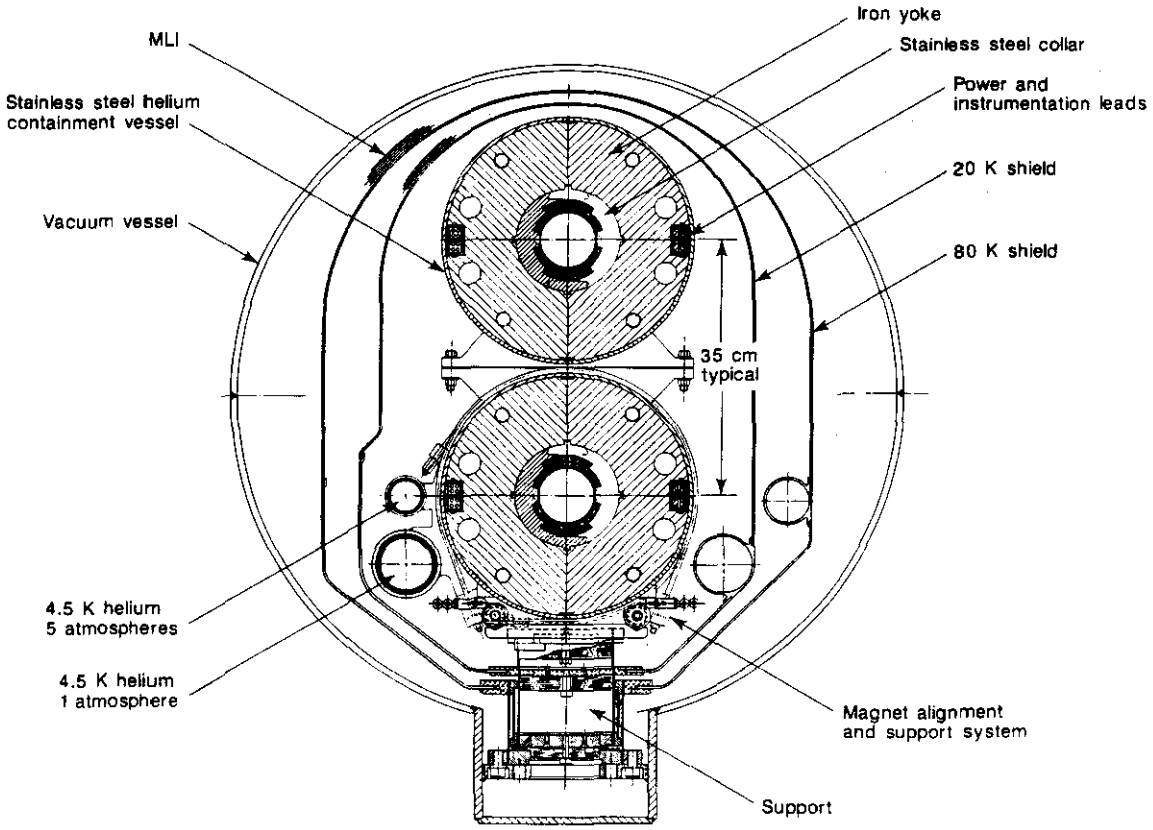

Figure 5.2-18. Two bending magnets in common cryostat — part of the vertical separation system in the low-beta insertion region. The individual magnets have 7.5 cm apertures.

the widest point in BV1D the beams are about 8.4 cm apart. A coil aperture of 16 cm is selected to give a good field region around each beam. At present there are no 5-T, 16-cm bore accelerator dipoles; however, the CBA magnets were only slightly smaller than this dimension and reached the 5.25 T operating field with the NbTi conductor of 1980. The coil configuration chosen for BV1D is thus a modified two-layer CBA design with SSC dipole-quality conductors. The size requirements on BV1C are slightly less than those on BV1D. However, as there are only 4 of them in the entire accelerator, they will be made identical to the BV1D dipoles.

The next set of magnets in the medium-beta IR, BV2A and BV2B, will be constructed with dipole coil packages similar to those of BV1A/B etc., but the two dipoles will be inside a single iron yoke, as shown in Fig. 5.2-19. The cryostat in this case is circular, with a slightly larger i.d. than the rest of the machine. Because the iron return will not be symmetric in these elements, the coils or perhaps a correction package may have to be made specially for each of the magnets.

All of the special vertical bending magnets are listed in Table 5.2-14, including the total number required in the different IRs. In all cases the peak field is 5.212 T and the effective length is 8.0 m. The large apertures of the BV magnets are chosen in part to provide good field quality in the IR regions. Correction packages are used in the bore tubes in the arc dipoles to correct the magnetization effects and small systematic offsets, if needed. A similar correction package could be used in the BV magnets. The expected fields to be corrected would again be sextupole and decapole.

Table 5.2-14
Characteristics of Vertical Bending Magnets

Designation	Bore (cm)	Type	Separation (cm)	Total No. of Packages in low-beta IR	medium-beta IR
BV1A/B	7.5	1 in 1	—	8	8
BV1C	16.0	1 in 1	—	0	4
BV1D	16.0	1 in 1	—	0	4
BV2A[a]	7.5	2 in 1 yoke	26	0	4
BV2B	7.5	2 in 1 yoke	30	0	4
BV2C/D	7.5	2 in 1 cryostat	35	8	8
BV3A/B	7.5	2 in 1 cryostat	35	8	8
BV3C	7.5	2 in 1 cryostat	38	4	4
BV3D	7.5	2 in 1 cryostat	41	4	4
BV3E	7.5	2 in 1 cryostat	44	4	4
BV4A	7.5	1 in 1	60	4×2	4×2
BV4B	7.5	1 in 1	63	4×2	4×2
BV4C	7.5	1 in 1	67	4×2	4×2
BV4D/E	7.5	1 in 1	70	8×2	8×2

[a]There are 8 dipoles in the 4 BV2A magnet packages.

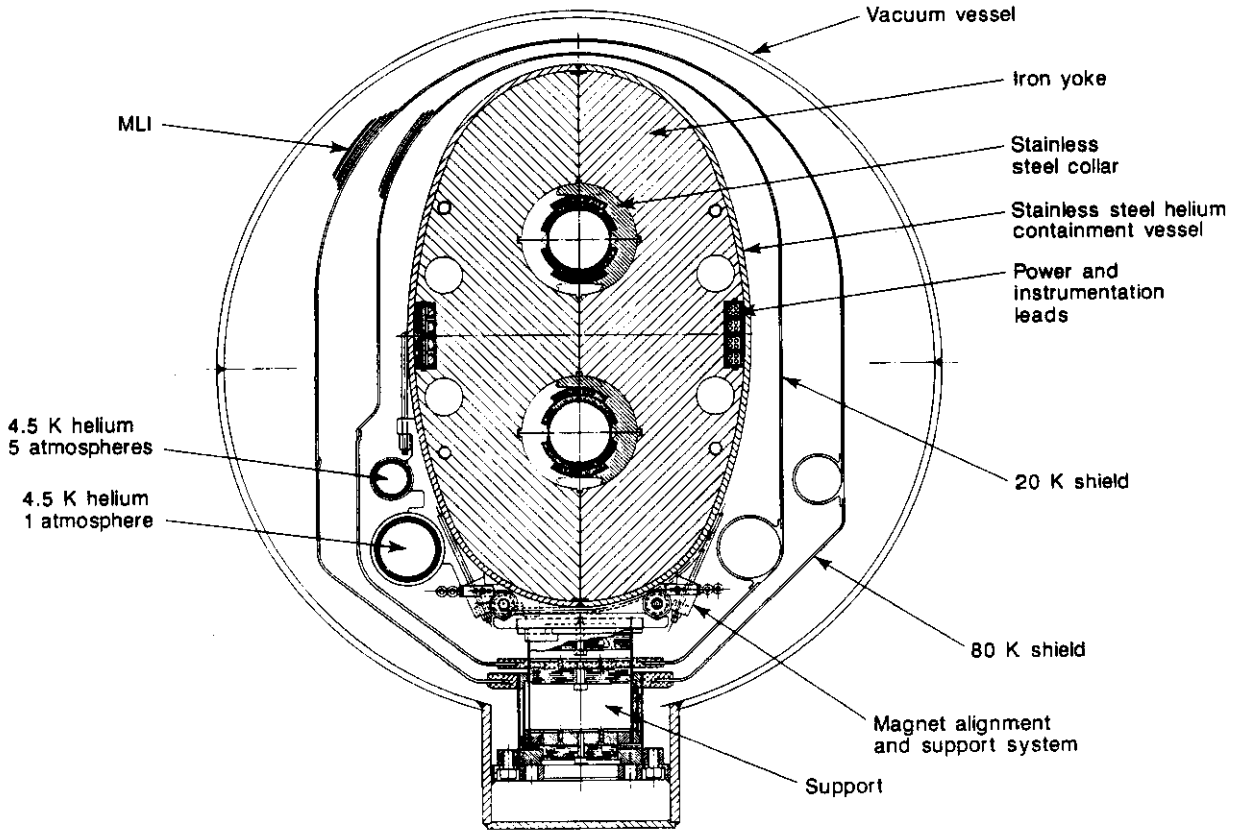

Figure 5.2-19. Two-in-one dipole for medium-beta insertion region.

IR Quadrupoles

At each interaction region special quadrupole magnets are required to maximize the collision rate. A list of these magnets is given in Table 4d of Attachment A. The focal length, and therefore the overall distance required for the IR regions, is directly affected by the achievable gradient. For the low-beta IRs, we have designed for a gradient of 230 T/m, corresponding to a 40 mm magnet aperture and the SSC conductor. The design consists of a 21 turn, two layer coil, with close-in iron as shown in Fig. 5.2-20. Saturation has an insignificant effect on field multipoles although it does affect the peak gradient. The transfer function decreases about 7% over the operating range.

The IR quadrupoles are connected to the main 6500 A bus. Because of the saturation and also the necessary gradient variation when β^* is changed at an IP, there is a $\pm 10\%$ (± 650 A) shunt supply across each IR quadrupole.

The conductor used in the low-beta quadrupoles is very similar to the outer dipole cable used in the arc quadrupoles. For a maximum field at the conductor of 6.5 T, the operating margin (ratio of strand critical current density to operating current density) is 1.25 at 4.45 K. This operating temperature is 0.1 K higher than for the dipoles to allow for the effects of additional radiation heating.

Each of the two low-beta IRs requires 8 high-gradient quadrupoles with 230 T/m and lengths between 13 m and 14.5 m. Construction is similar to that of the dipoles and arc quadrupoles. Instead of the collars used in the arc quadrupoles, a magnetic iron yoke provides pre-compression of the coils and containment of magnetic forces. A stainless-steel shell is welded around the finished yoke as in the dipole, as shown in Fig. 5.2-20. All other 40 mm bore quadrupoles have a gradient of 212 T/m and are identical in cross section to the arc quads although with varying lengths up to 15 m.

Uniformity requirements are stringent in the final focus quadrupoles. Distortions will be corrected locally by a nested set of windings mounted directly on the bore tube and designed to correct both normal and skew distortions. These windings are very similar to those for the dipoles, except that smaller wire can be used. A quadrupole "roll" correction winding is also provided to compensate for any small error in mechanical azimuthal alignment of the quadrupoles in their final installation.

Because the beam separation varies in the IR regions, it is necessary to package some of the quadrupoles in 2-in-1 cryostats. The 96-QV and 32-Q4 quadrupoles (see Figs. 5.11-1 and 5.11-4), have the regular gradient of 212 T/m, but, because they are in the region where the beams are separated by 35 cm, will all be in 2-in-1 cryostats. Figure 5.2-18, showing the 2-in-1 BV dipoles, is representative of the quadrupole configuration though not the coil or iron cross section. The associated spool pieces will be in common cryostats.

Utility Insertion Quadrupoles

The beam size will be large in the utility insertion regions, requiring some of the quadrupoles to have a bore larger than the standard 4 cm. The 8 quadrupoles of each of the four designations QFT, QDT, QFU, QDU, or a total of 32, will have a bore diameter of 5.0 cm. Accordingly, the gradient will have to decrease to 4/5 of the 212 T/m of the main quadrupoles, or 170 T/m. The focusing power is maintained by increasing the magnet length to 11.6 m for the QDT and QFTs and to 11.9 m for the QFU and QDUs. The other quadrupoles in the utility insertion regions can be standard arc quads, in terms of cross section and gradient (212 T/m), but will have effective lengths of 10.08 and 10.78 m, respectively.

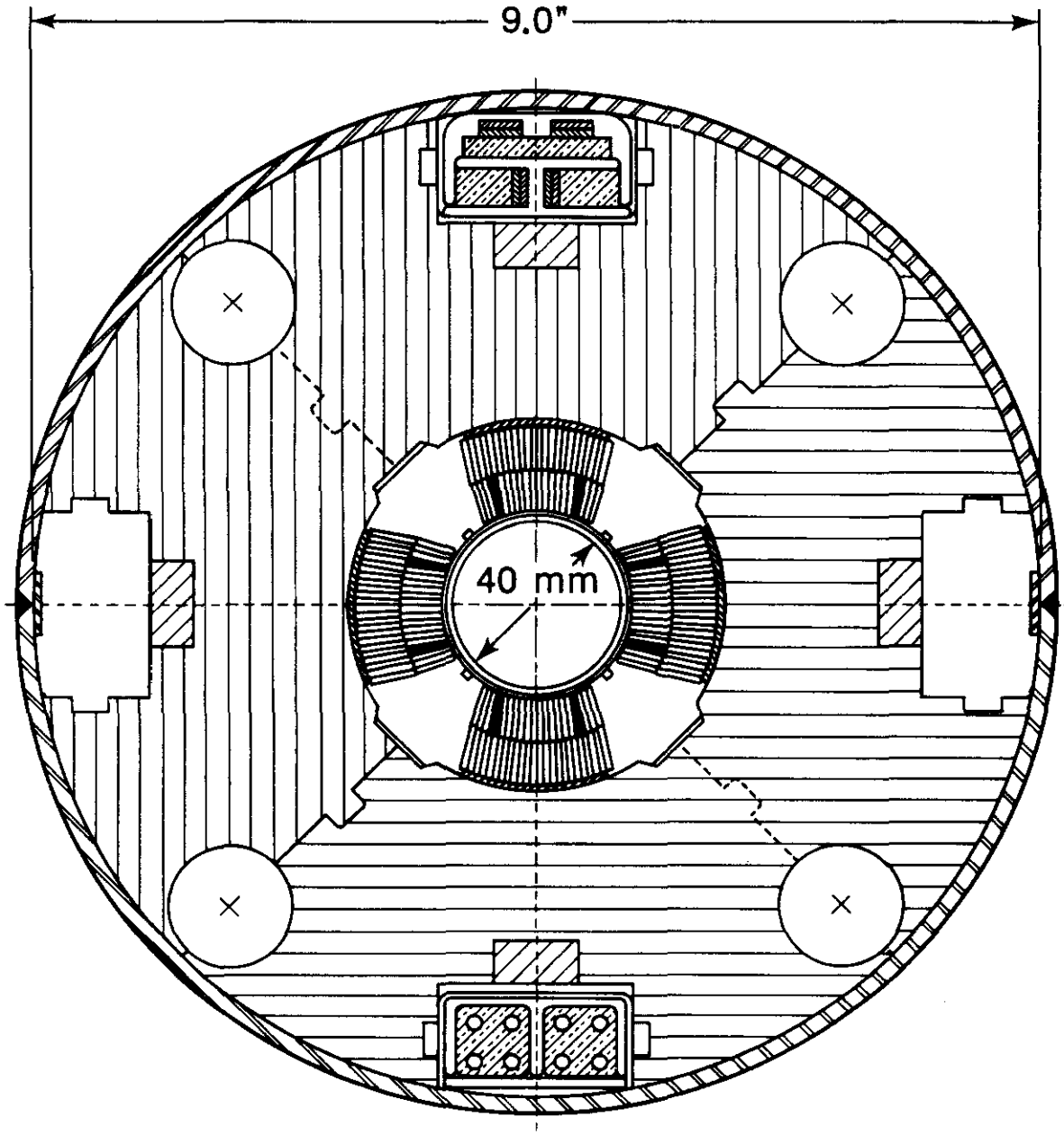

Figure 5.2-20. Special high gradient quadrupole for the interaction regions.

The 5 cm bore quadrupole uses standard SSC dipole cable and is collared with the iron yoke spaced about 0.5 cm from the conductor, so that good field quality can be expected.

Horizontal Dispersion Suppressor Quads

There are 160 horizontal dispersion suppressor quadrupoles in the 8 insertion regions. These magnets are identical to the arc quadrupoles in all respects except for length, which varies from 3.48 to 4.88 m. Their lengths are individually selected specifically for the desired focusing characteristics when all quads in one IR are powered in series. To reduce other fabrication details and avoid a host of cryostat designs, they will all be placed in 5.88 m long cryostats.

5.2.15 Magnet Installation

Installation of the large quantity of devices envisioned in the SSC main ring will require systems and techniques that minimize cost and labor while preserving the required high quality and reliability. This section considers installation to encompass accurate placement and alignment as well as the systems interconnection of device to device. Also considered is the removal of devices. Survey methods are not discussed here.

Magnet Placement

The magnet assembly in its shipping configuration, placed in a cradle designed to facilitate lowering the assembly from the surface to the tunnel level through the 10 m diameter vertical shaft, is shown schematically in Fig. 5.2-21. The assembly is then removed from the cradle, placed in the transporter, and conveyed to the designated location in the collider ring. The magnets must be aligned horizontally and vertically to within ± 1 mm and in azimuth to within ± 1 mrad.

To minimize cost and add simplicity to the installation procedure, the magnet's vacuum vessel incorporates its own mounting stand at each cold mass support location. The position of the beam centerline is referenced by means of datum features incorporated in each stand. Figure 5.2-22(a) shows a dipole cross section defining these reference features. Figure 5.2-22(b) shows the relationship of each of the five stands.

With the stands as integral parts of the magnets, the upper magnet can be installed directly atop the lower. The stand's datum features are used to ensure alignment of beam center lines with respect to one another. Shims of uniform and nominal thickness are provided between the lower magnet and its base plate and between the lower and upper magnets. These allow for minor corrections after installation due to slab settling or other perturbations. Figure 5.2-23 shows this arrangement in the tunnel.

The base plates onto which the lower magnets are fitted must be installed to predetermined accuracies. It is the base plates, and not the magnets, that are surveyed into position. To accomplish this requires precision fixturing which can relate to a survey base line. The base plate mounting is a two-part operation. Part one encompasses installation and grouting of primary base plates. These plates are installed to a rough tolerance and provide a solid sub-base for precision installation of the secondary plate, which is used to position the magnets via their datum features. Figure 5.2-24 depicts the primary and secondary plates.

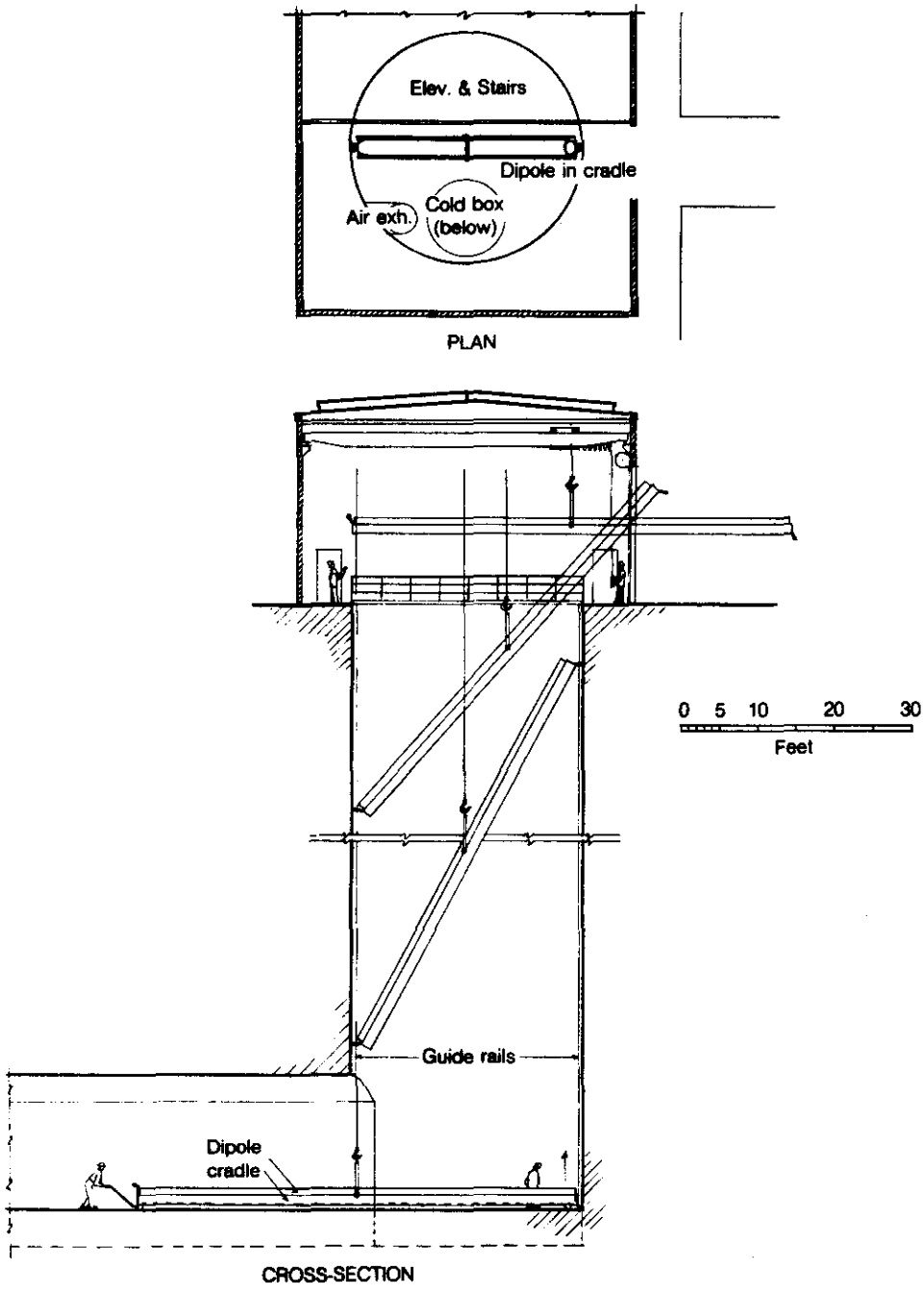

Figure 5.2-21. Magnet assembly being lowered to tunnel level.

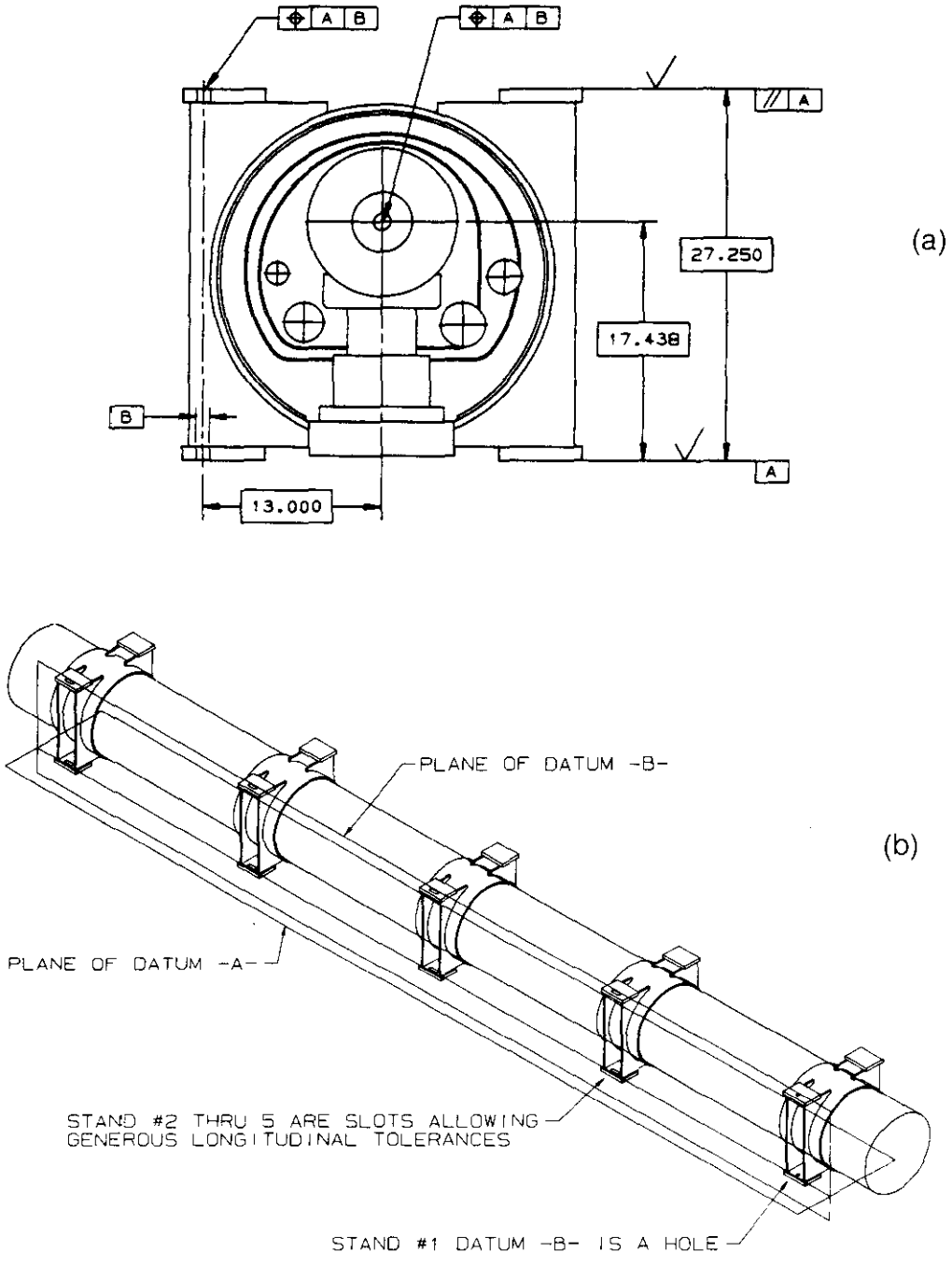

Figure 5.2-22. (a) Magnet cross section with reference datums. (b) Magnet longitudinal view.

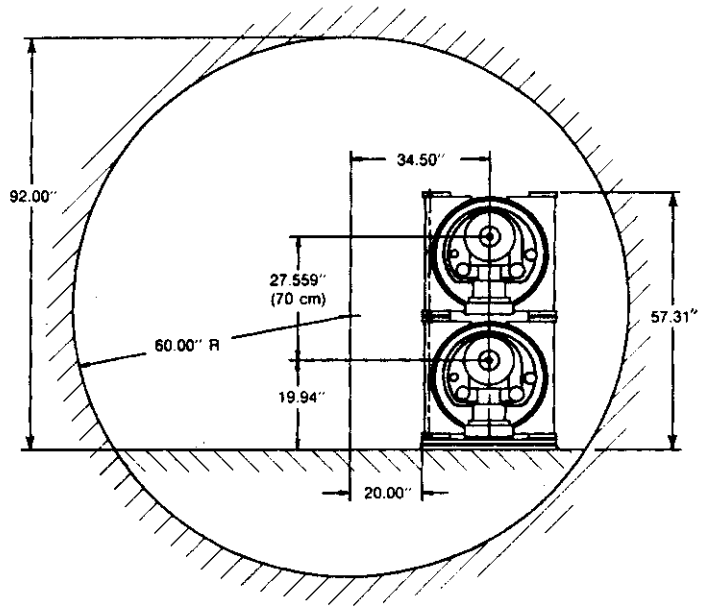

Figure 5.2-23. Magnet cross sections in tunnel.

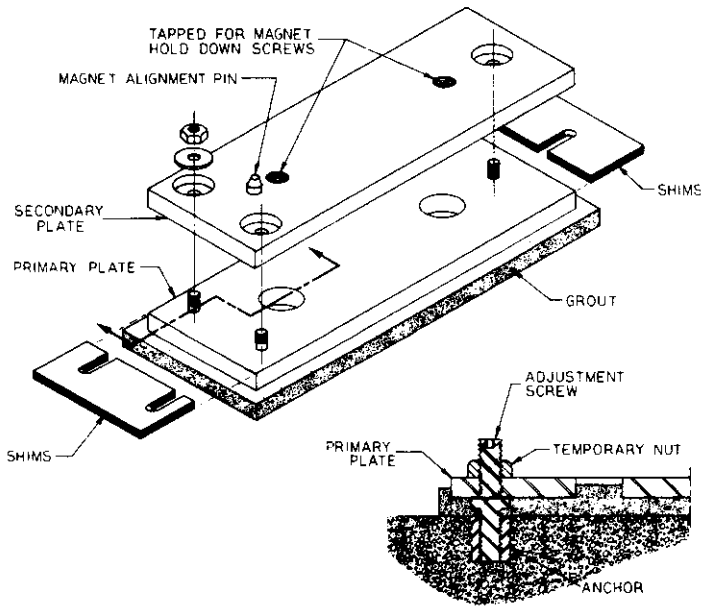

Figure 5.2-24. Mounting plates.

Once the mounting plates are in place, the magnets can be transported and installed. The transport vehicle must be capable of moving magnets within the confines of the tunnel and have the capacity to move the magnet into position onto the mounting plates or atop a lower magnet, and also onto the mounting plates under a magnet already in place in the top ring.

Magnet-to-Magnet Interconnections

With the magnets installed the task remaining is physically to connect magnet to magnet. All systems are connected by welding, thereby eliminating seals and the common problems associated with them. Figure 5.2-12(a) is a cross section at the interconnection area showing the relative position of each system. All systems are assembled from the inside, starting with the beam tube and working outward to the vacuum vessel.

Since all systems are welded, equipment must be employed which can perform within the limited confines of the interconnect region and tunnel, providing high quality welds insensitive to the human operator. The equipment must therefore be compact and utilize power supplies regulated by microprocessor controls programmed for weld optimization of each system. Such equipment is readily available commercially. All welds use the TIG process, with the cold mass containment and vacuum vessels requiring filler material; all other systems are fused using consumable inserts.

Disconnection Procedure

Once connected, the inevitable need to disconnect will occur. This requires the design to allow disassembly as well as assembly. All systems are readily disassembled in the reverse order of assembly using commercially available cutting equipment modified to accommodate the limited space imposed by the interconnect area and tunnel. These devices are analogous to a lathe, but instead of a stationary tool bit cutting a rotating part, the tool bit orbits the part, cutting deeper at each orbit.

Dynamic Analysis and Testing

The effects of seismic, shipping and handling loads on SSC magnets are currently under study. ANSYS, a finite element code with dynamic analysis capabilities, is being used to predict maximum stress and deflections in the magnet system to ensure structural integrity during all phases of installation and operation. Actual dynamic testing of completed magnets and individual supports will provide realistic damping values and verification of predicted results.

5.3 Cryogenic System

The refrigeration requirement for the SSC, though large in aggregate, is well within the scope of current technology. Machinery and techniques that are part of current cryogenic practice are adequate to support SSC operation, and the individual plants proposed for its use are smaller than ones now in service. The experience gained in the operation of the Tevatron [5.3-1], particularly the system experience, gives confidence that the SSC cryogenics will meet expectations for performance and availability. Where new ground is broken is in the extent of the system and in the low levels of heat leak for which it is designed [5.3-2].

The basic concept of magnet cooling and refrigeration distribution is illustrated in Fig. 5.3-1. In this figure a refrigeration plant is on the left, providing and accepting flow. Single-phase helium at 4.15 K and 4 atmospheres is forced out into the magnet string of each ring upstream and downstream from the refrigerator for a distance of 4 km. It flows through the magnets in series and is recooled periodically to maintain the superconducting windings at or below the specified 4.35 K. At the end of the 4 km string, the flow is returned toward the refrigerator. This fluid is flowing at a pressure above its critical pressure, so in all parts of the circuit only a single phase is possible. Along this line small flows are withdrawn and expanded into pool-boiling recoolers spaced at intervals of one cell, 192 meters. The saturated gas from the recoolers is collected and returned to the refrigerator in a third line.

These low-temperature parts of each ring are enclosed in separate vacuum insulated cryostats containing shields at 20 K and at 84 K with multilayer insulation. The helium gas flow cooling the 20 K shield passes out from the local refrigerator in one ring and is returned in the other ring. Heat is removed from the 84 K shield by subcooled liquid nitrogen that is produced at two central air separation plants. It is passed around the accelerator ring through the shield piping and subcooled and circulated by pumps and heat exchangers at each refrigerator location. Liquid helium can also be passed around the ring from refrigerator station to refrigerator station through the cryostat piping. Except for a warm header for the collection of power lead cooling flow, all of the system piping is contained within the magnet cryostats. Figure 5.2-10(a) shows how these various lines are arranged within the cryostat. The figure also shows the folded post for the support of the cold iron of the magnet. This design, with its 20 K and 84 K heat stations, is crucial to achieving the low heat leak while providing accurate alignment. In Fig. 5.2-12(b) a longitudinal section of the cryostat shows the connection region concept. The space between magnets gives room for strain relief of the bus work and helps control pressure rise during quench. A more complete description of the construction of the cryostat can be found in Section 5.2.9.

The principal design issues of the SSC cryogenic system are the production of the refrigeration needed for the operational loads, the transport of the refrigeration to all parts of the system, the provision for redundancy and reparability leading to high availability of the system, and the provision for non-steady state operation such as cooldown and quench recovery in a way that provides a suitable operating schedule for the whole facility. The following sections describe a system layout and operating modes that meet these requirements.

5.3.1 Cryogenic System Description

The layout of the collider facility showing the positions of the various parts of the system is given in Fig. 3.3-2. The system is divided into 10 cryogenic sectors of more or less equal length, 8.06 km, each with a refrigeration plant, helium storage, and four loops of cryostats. There are in the ring eight arc sectors and two IR sectors. Except for liquid nitrogen supply, each of these sectors is capable of independent operation at the rated heat loads. The capability of passing refrigeration from one sector to another and sharing load when required by equipment failure or other non-standard condition is crucial, however, to achieving high system availability. All of the arc sectors are nearly the same size and have

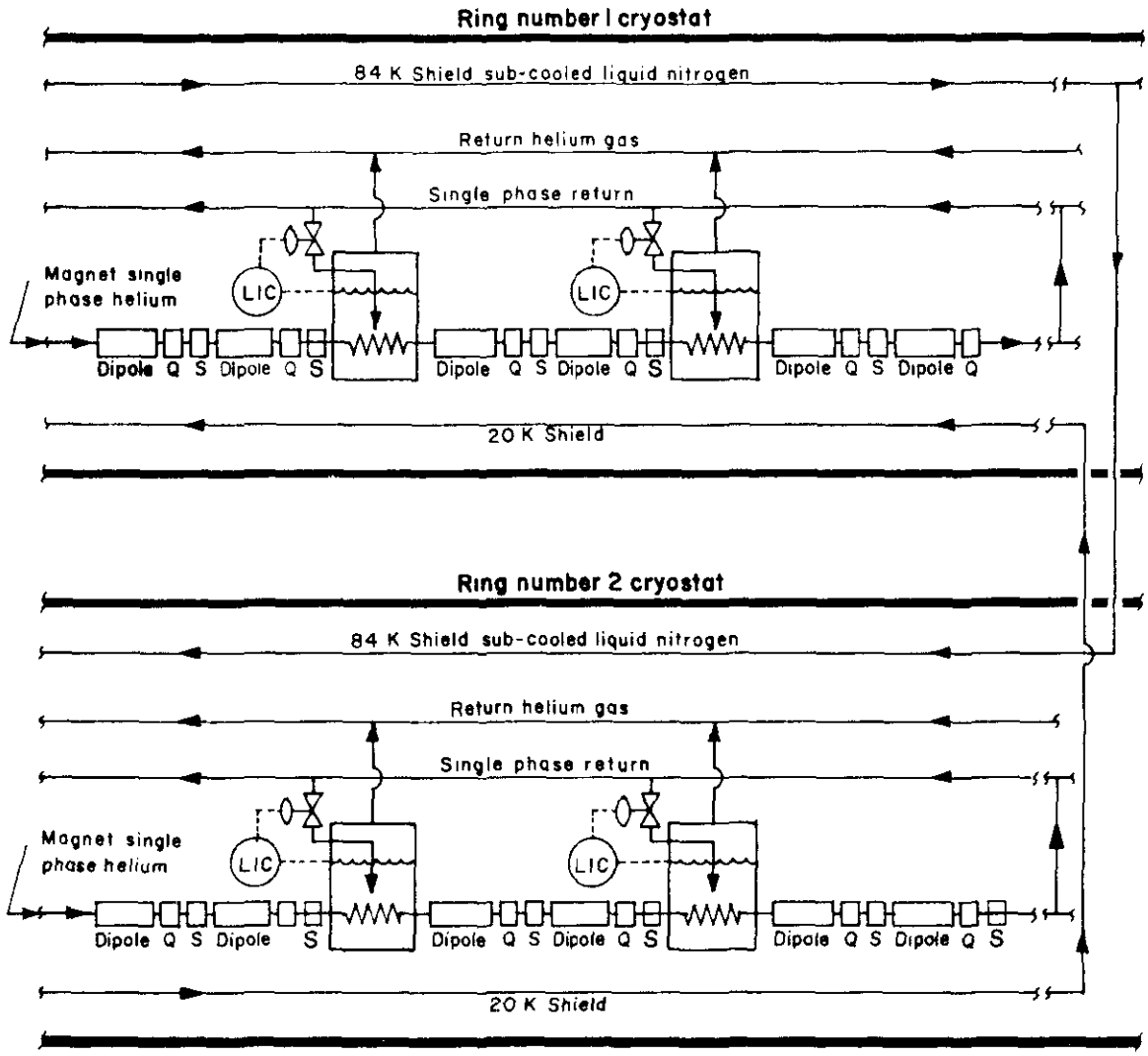

Figure 5.3-1. A conceptual representation of the SSC collider rings cryogenics system. In each of the two rings the collider magnets are cooled in series by a flow of single-phase helium. This stream is recooled at cell intervals by heat exchange with boiling helium. The cryostat of each ring contains cooled shields at 84 K and 20 K.

the same cryogenic loads. The IR sectors have less synchrotron radiation load but more heat leak and a larger liquefication load, resulting in a total refrigeration capacity requirement within 15% of that of each arc sector.

Each of the ten refrigeration plants is sized at 1.5 times the expected heat load. The extra capacity provides for cooldown, for capacity decline during service periods, and most important, for plant maintenance and plant failure. Any one of the plants may be off without affecting the operation of the facility by shifting the load of the affected sector to the adjacent sectors. Refrigeration load can be shared effectively among as many as six plants by opening valves in the "end boxes" at the sector boundaries. Studies have shown that with reasonable models of mean time between failure and repair, availability of greater than 97% can be achieved with this distributed redundancy [5.3-3].

Other boxes with U-tube disconnects allow isolation of parts of the system for warmup and repair. These U-tubes are very important in providing flexibility in the cryogenic system and deserve special mention. They are used extensively in the Tevatron system. At an isolation box the flows of the various cryogens are directed separately upward through vacuum insulated U-shaped tubes that are plugged into the boxes by means of bayonets. These tubes may be withdrawn through seals and valves closed. A removable U-tube not only reliably disconnects and isolates two systems, but it allows the systems to be reconfigured by redirecting flow. It also provides an easily serviced location for instrumentation and valving. Figure 5.3-4 below shows a cross section of an isolation box with U-tube connections. Similar boxes with U-tubes are used to make the connection between the refrigeration plants and the rings, between transfer lines and the rings in the IR regions, and at the sector boundaries (the end boxes mentioned above).

Because of the near independence of the two rings, it is possible to run one ring for beam studies in a large number of situations while the other is not operating. In the arcs, which comprise 75% of the machine circumference, the rings are independent in the 4.35 K parts of the cryogenics, and the shield flows have independent operating modes at some sacrifice of capacity. In the IR clusters the two rings are more interdependent; however, even in these complex regions of the machine considerable operational flexibility is available.

5.3.2 Description of the Arc Region Cryogenics

A block diagram of the cryogenics of a typical arc sector is shown in Fig. 5.3-2. In this figure only the single-phase helium circulation is shown. The refrigeration plant is centrally located in the sector and feeds two strings, one for each ring, in either direction. The strings each consist of 21 machine cells and so are $21 \times 192 = 4032$ m long. The overall length of a sector is thus 8.064 km. Each string is divided into four sections by U-tube disconnects at three isolation spool pieces. In a typical string there are three sections of five cells and one section of six cells. The section, of length 960 or 1152 meters, is the minimum length of the machine that can be isolated and warmed up for service. At each end of each arc there are strings of 20 cells rather than the standard 21. Thus the total length of an arc is $166 \times 192 = 31.872$ km.

Table 5.3-1 lists the important cryogenic components and the structure of an arc sector. This structure follows a hierarchy of size beginning with the half-cell and going to cell, section, string, and sector. Table 5.3-2 gives the heat load budget for the arc sector. Note that

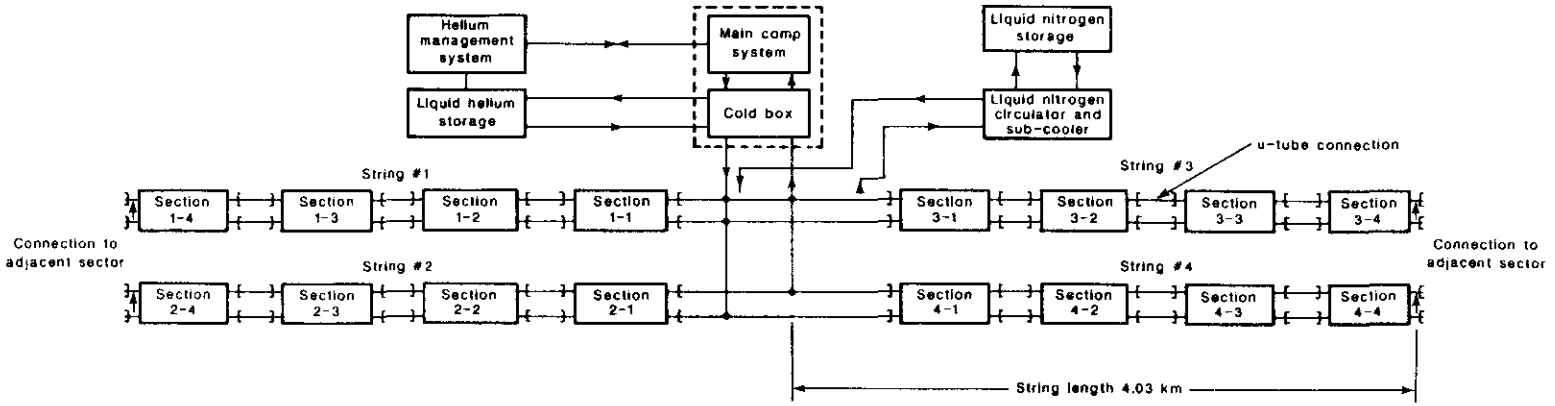

Figure 5.3-2. Block diagram of the major components of a cryogenic sector of the collider ring. The refrigerator at center cools four loops of magnets, one in each ring in either direction from the refrigerator. Blocks for other components of the refrigerator station are shown. A cryogenic sector includes the magnets of 1/10 of the circumference of each ring.

Table 5.3-1
Each of the two arcs is divided into 4 cryogenic sectors.
Each sector has the following structure:

In Each Ring:	
Half-Cell:	96 meters long
5 dipoles with interconnection	
Quadrupole with interconnections	
Spool piece with safety leads and correction coils	
Beam-line connection	
Quench relief valve	
Vacuum barrier	
Instrumentation	
Cell:	192 meters long
Two half cells plus:	
Recooler with auxiliaries	
Safety valves	
Instrumentation	
Section:	960 or 1152 meters long
5 or 6 cells plus:	
Isolation box	
U-tubes	
Warm beam-line valves	
Instrumentation	
String:	4.03 km long
4 sections plus:	
End Box with 6.5 kA lead pair	
Connection to refrigerator with 6.6 kA lead pair	
Instrumentation	
Including Both Rings:	
Cryogenic Sector:	8.06 km long
4 strings in pairs plus:	
Refrigeration plant with compressors	
Helium management system with gas storage	
Liquid helium storage	
Liquid nitrogen circulator and subcooler	
Liquid nitrogen storage	

the total heat load for the arc refrigerator includes contributions from both rings. Also in this table is a listing of the total load expressed as ideal isothermal power. This allows comparison of the different parts of the load, and it is immediately apparent that the synchrotron radiation is a very important fraction.

At the half-cell interval in the spool piece (the multipurpose section of the cryostat system between the quad and the next half-cell dipole) there are several things of particular cryogenic importance. First, there is a pair of safety leads with their quench stoppers, and there is a quench relief valve. This valve connects the single-phase space with the 20 K shield header. Second, there is a vacuum barrier in the insulating vacuum. Thus each half-cell is separate for leak checking and is evacuated separately with a portable pump station. There is no permanent pumping installed for the insulating vacuum.

Also in the spool piece at the cell interval is the recooler, with its control valve and level gauge, and safety and cooldown valves for the single-phase space. At less frequent intervals are safety valves for the other cryogenic circuits and for the beam line. All of the cryogenic system is designed for a maximum working pressure of 20 atm. A diagram of the system showing the relationship of these various parts is given in Fig. 5.3-3. It is clear that from a cryogenic point of view almost all of the critical parts of the system are to be found in the spools. Figure 5.3-4 shows a cross section of a spool piece. The various components include the primary correction package with leads as necessary and some of the components listed above. Also shown in this section are a pair of isolation boxes with their U-tube connections and the warm beam line valve with the cold to warm beam line transitions. In addition to the removable U-tubes connecting the isolation boxes, there is a permanent connection carrying the superconducting bus. This connection is designed so that either side can be warmed up while the other remains cold.

In addition to the eight arc sectors, approximately 50% of the two IR sectors consist of the regular cell structure organized as described here. Thus some 90% of the circumference of the collider is made up of these cells with their cryogenic system.

5.3.3 Description of IR Region Cryogenics

In the IR regions the cryogenic system is considerably more complicated in layout than in the uniform arc regions; however, most of the components are similar. Double cryostats are needed to contain the insertion region magnets in which the beam separation is 35 cm. This is too close together for separate cryogenics to be provided although two sets of helium flows must be carried through these cryostats. A more complete description of these magnets and their cryogenic system can be found in Section 5.2.14. There are approximately 1600 meters of these 2-in-1 cryostats in the four IRs.

There are magnets common to both rings in the IRs. These cryostats must be able to operate from the flows of either ring, and some of them may need to operate at a different temperature from the ring by means of satellite refrigeration. In addition, cryostats near the interaction point intercept especially heavy beam-loss heating. There is a pair of such cryostats in each of the four IRs.

In addition, there are sections with long pieces of room-temperature beam line which must be bypassed by transfer lines carrying the cryogenic flows. Because it is often the case that elements on opposite sides of the interaction region must operate at the same current, these transfer lines carry superconducting bus work with its quench protection as well.

Table 5.3-2
Heat Loads for an Arc Cryogenic Sector

	LHe (g/s)	4.15 K (watts)	20 K (watts)	84 K (watts)
Dipole				
Infrared		0.05	2.16	17.7
Supports		0.12	0.82	7.2
Connections & instrumentation		0.15	0.32	2.1
(Synchrotron radiation)		(2.34)		
Total static		0.32	3.30	27.0
4 km String (in one ring)				
210 dipoles		67.2	693	5670
42 quadrupoles		6.8	65	538
42 beam position detectors		8.4	26	36
42 spool lengths		13.7	133	1075
Piping & valving		7.5	75	359
Vacuum breaks (42)		1.4	47	420
Isolation & end boxes (9)		26.0	96	400
6.6 kA leads (4)	1.58	31.7	2	6
0.1 kA leads (140)	0.84	23.8		
Safety leads (84)	0.42	1.5		
Splices		30.0		
Subtotal	2.84	218.0	1137	8504
Synchrotron radiation		492.0		
Beam-gas loss		25.0		
Beam microwave loss		50.0		
Totals	2.84	785	1137	8540
Heat loads per refrigerator (includes both rings)				
4 strings	11.36	3140	4548	34016
Liquid helium storage	0.64			
Distribution		20	252	2284
Purifier				2500
Totals	12.00	3160	4800	38800
Total load expressed as ideal isothermal power at 300 K				
Helium Refrigeration				
Static loss & shielding				
20 K		67200		(18%)
4.15 K		62160		(16%)
Subtotal Static		129360		(34%)
Current leads		78110		(21%)
Synchrotron radiation & beam loss		161680		(43%)
Miscellaneous		9045		(2%)
Helium refrigeration total		378200		
Liquid nitrogen refrigeration		106700 watts		

There are 8320 meters of these lines in the two clusters, over 40% of the total cluster length of 19,200 meters. The cryogenic flows of both rings must be carried in the line. Figure 5.3-5 shows a cross section that indicates the number and kind of pipes in such a transfer line and their general arrangement. This line is to be constructed from components identical or as similar as possible to those of the dipole cryostat. The modular length is the same, the construction techniques are the same, and the installation tools and procedures are the same. It is economical both in initial cost and in installation and maintenance costs to have this system like the standard cryostat.

It is impractical to maintain the two rings functionally separate in the IR clusters because of the cost in power supply, cryogenic power leads, and system complexity in dealing with the 2-in-1 and other common elements. It would be possible to combine the single-phase and gas flows of the two rings in the transfer line sections. However, the difficulty of dealing with the bus and control problem that would result is not worth the small advantage in number of lines.

In the different IR configurations the various elements are assembled in whatever way is suitable to provide for the operation of the magnets of each ring. This is done by means of U-tube disconnects, which can be shifted to provide for the flow arrangements required. Figure 5.3-6 shows the cryogenic layout of a typical interaction region. The region has cryogenically ordinary sections of cells in each ring at each end and a bridging transfer line around the special cryostats in the center. Note that the two rings exchange position on either side of the interaction point.

The complete cluster consists of four regions of this length and general structure, differing somewhat according to function. The utility regions have very much the same cryogenic arrangement as the IR regions, except that there are no 2-in-1 sections or common elements. Instead, there are quadrupole pairs in each ring. For most of their length the transfer lines will be in the same tunnel with the beam line and only a meter or two from it, so that the many U-tube connections shown in the figure are like those connecting sections in the arcs. It is only in the interaction hall itself, a length of 100–200 meters, that the transfer line is separated from the beam line by any significant distance. Table 5.3-3 lists the components of an IR cluster, and Table 5.3-4 gives the heat load budget. As has already been mentioned, more than half of an IR cluster consists of cells of dipoles, quads, and spools that are the same cryogenically as those in the arcs. From an operating point of view the two types of regions, arcs, and clusters, are very much the same, and the same sequences will be used for cooldown, warmup, and quench recovery.

5.3.4 Refrigeration Station Description

Each of the ten refrigeration stations around the collider ring is shown in Fig. 5.3-2 to consist of a compressor-cold box system connected to the ring cryogenics, a helium management and storage system, and a liquid nitrogen circulator and subcooler with liquid nitrogen storage. Not shown in this figure are the two air separation plants that supply the liquid nitrogen around the ring.

The capacities of the helium refrigeration and the air separation plants proposed for the SSC are listed in Table 5.3-5. The ten helium plants provide refrigeration at 4.15 K, at 20 K, and liquefication at the single-phase circulation conditions for lead cooling. The distinction between a refrigeration load and a liquefication load is the temperature at which

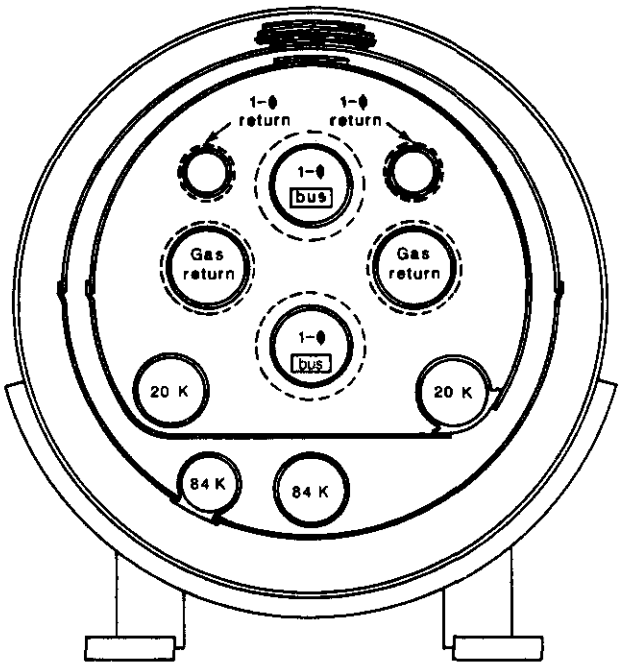

Figure 5.3-5. Interaction region transfer line cross section. Each interaction region and utility region is bypassed by a transfer line approximately 1 km in length. The line carries the flow circuits of both rings and superconducting bus connecting the ring magnets.

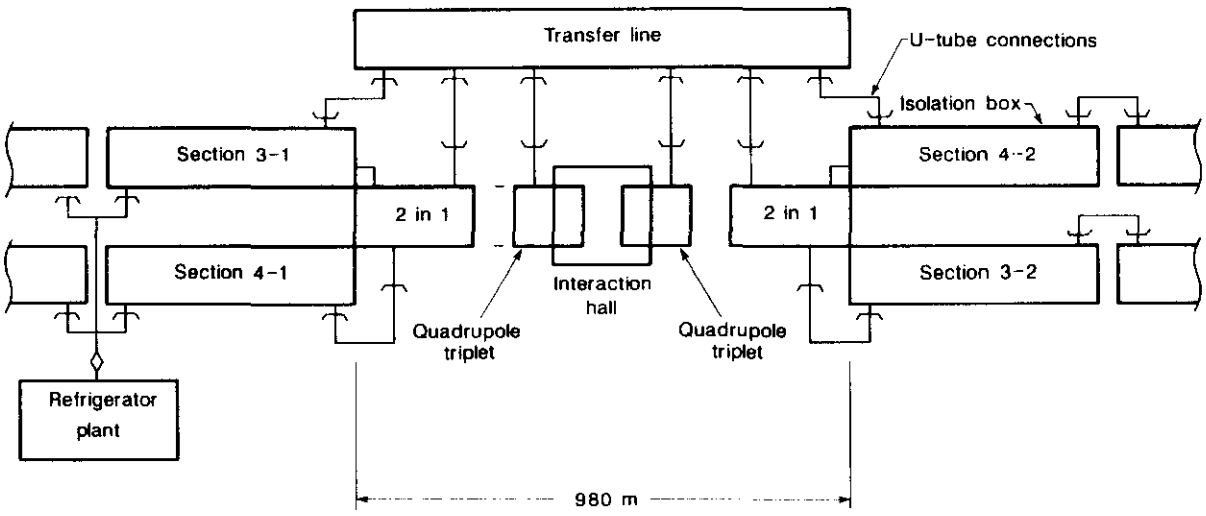

Figure 5.3-6. Block diagram of the cryogenics of a typical interaction region. The refrigeration plant on the left supplies cooling to both rings. Bridging the interaction region itself is a transfer line carrying the circuits of both rings. The line and the special purpose magnets of the region are interconnected by U-tubes.

Table 5.3-3
Cryogenic Components of an IR Cluster

Per Ring:

- 8 sections of regular cryostat, total length 5440 meters
  - 52 half-cells
    - 260 dipoles
    - 52 quadrupoles
    - 52 spool pieces with correction elements
  - 4 quadrupole doublets (utility region, outer doublets)
  - 4 quadrupole doublets with five vertical dipoles (IR regions, outer doublets)
  - 2 end boxes with 6.5 kA lead pair
  - 2 refrigeration connection boxes with 6.6 kA lead pair
  - 4 isolation boxes
  - 8 special end boxes (without 6.6 kA leads, with bus)
- 4 quadrupole doublet cryostats, length 35 meters each (utility inner doublets)
  - 4 double end boxes (7 flows plus bus)

Per Cluster:

- 2 sets of 8 sections and 4 quadrupole doublet cryostats
- as above, plus
  - 4160 meters transfer line in 4 lengths
    - 16 special end boxes
    - 12 double end boxes
  - 4 2-in-1 cryostats, 200 meters long each
    - 14 vertical dipoles, 16 quadrupoles
    - 8 special end boxes
    - 4 bus connections
  - 4 quadrupole triplet cryostats, 90 meters long each
    - 4 quadrupole triplets
    - 2 vertical dipoles
    - 4 double end boxes

Table 5.3-4
Heat Loads for a Cryogenic IR Cluster

	LHe (g/s)	4.15 K (watts)	20 K (watts)	84 K (watts)
Per Ring:				
260 dipoles		83.2	858	7020
52 quadrupoles		8.3	80	666
52 beam position detectors		10.4	32	45
52 spool pieces		17.1	40	1331
Quadrupole doublet cryostats (4)		3.2	31	256
Piping & valving		11.2	114	532
Vacuum breaks (60)		2.0	67	600
Isolation & end boxes (8)		24.0	96	400
Special end boxes (8)		24.0	96	400
Double end boxes (4)		12.0	72	300
6.6 kA leads (8)	3.17	63.4	4	12
0.1 kA leads (250)	1.50	30.0		
Safety leads (120)	0.60	2.2		
Splices		43.0		
Subtotal	5.27	334.0	1490	11562
Synchrotron radiation		652.0		
Beam-gas loss		50.0		
Beam microwave loss		100.0		
Totals	5.27	1136	1490	11562
Per Cluster:				
2 sets as above	10.54	2275	2980	23124
Transfer line (4160 m)		72	720	6138
2-in-1 cryostats (800 m)		32	300	2560
Quadrupole triplet cryostats (320 m)		10	90	758
Double end boxes (16)		48	288	1200
Special end boxes (24)		72	288	1200
6.6 kA leads (20)	7.13	143	6	18
1 kA leads (24)	1.11	22	6	18
Subtotal	18.78	2671	4678	35016
IR beam loss		400		
Liquid helium storage	0.62			
Distribution		29	242	2184
Purifier				2500
Totals	19.40	3100	4920	39700
Total load expressed as ideal isothermal power at 300 K				
Helium refrigeration				
Static loss & shielding				
20 K		68880		(16%)
4.15 K		76006		(18%)
Subtotal Static		144946		(34%)
Current Leads		129582		(30%)
Synchrotron radiation & beam loss		142863		(33%)
Miscellaneous		9509		(3%)
Helium refrigeration total		426900		
Liquid nitrogen refrigeration		109180 watts		

Table 5.3-5
Capacities and Power Needs of Helium Refrigeration and Air Separation Plants

Refrigerator and Storage Capacity		
4.15 K	4700 watts	(150%)
20 K	7200 watts	(150%)
Liquid helium	620 liters/h	(150%)
Power	Nominal Load (100%)	Installed
Compressor: (90% pf)	2.2 MW	3.5 MW
Auxiliaries: (70% pf)	0.5 MW	0.5 MW
Helium Storage Capacity		
Liquid storage		16 × 120,000 liters
Gas storage		100 × 60,000 SCF (at 16 atm)
(Liquid: 89% of inventory, gas: 11% of inventory)		
Air Separation Plant Capacity		
Capacity		200 tons/day (2100 g/s)
Power:		
Compressor: (90% pf)		5.6 MW
Auxiliaries: (70% pf)		1.0 MW
Liquid Nitrogen Storage		
Liquid storage		8 × 20,000 gal 4 × 55,000 gal
(6 days supply at 2000 g/s)		
Total Cryogenic System Power		
Power	Nominal Load (100%)	Installed
10 Helium plants	27.0 MW	40 MW
Air separation plants	6.6 MW	13 MW
Total	33.6 MW	53 MW
Power breakdown		
Static loss & shielding		
84 K	4.95	(15%)
20 K	4.99	(15%)
4.15 K	4.80	(14%)
Subtotal Static	14.74	(44%)
Current Leads	6.53	(19%)
Synchrotron radiation & beam loss	11.66	(35%)
Miscellaneous	0.67	(2%)
Nominal Power Total	33.60 MW	

the refrigerant returns from the load. A refrigeration load is isothermal or very nearly so, and the refrigerant returns to the plant at the load temperature. A liquefication load warms the refrigerant all the way from the operating temperature to room temperature, so heat is removed at all temperatures in between.

In the table also are given estimates of the power consumption for the cryogenic system and a breakdown by load type. It should be noticed that the synchrotron radiation and other beam-loss loads are 35% of the total. The cost of operating current leads also shows up clearly. The importance of the 20 K shield in the system is shown by these figures. If the 20 K load were taken at 4.15 K, the operating power would need to be increased by 15 MW.

To give a perspective on the size of the individual SSC refrigeration plant, a comparison on the basis of ideal isothermal power can be made with similar plants recently successfully completed. The SSC plant capacity is equivalent to 0.58×10^6 ideal watts at 300 K. This is about 0.81 of the size of the CVI plant for the MFTF-B at Lawrence Livermore National Laboratory. It is 0.27 the size of the large refrigerator at Brookhaven National Laboratory and 0.64 of the central helium liquefier at Fermilab. Among refrigerators now under construction, particular mention should be made of the three plants for the storage ring HERA at DESY. Each of these is 1.25 the size needed for the SSC and are noteworthy for being designed for the high efficiency of 24% of Carnot [5.3-4]. The important points in these comparisons are not only that the size of the SSC plant is within current industrial practice, but that an adequate basis of experience exists for specifying and acquiring such systems in a timely and efficient way.

A flow sheet that shows the various parts of a compressor-cold box system appears in Fig. 5.3-7. Here features likely to be part of any final design are shown. This plant operates in a conventional Claude cycle. Two expanders, labeled EX-1 and EX-2, provide precooling for a circuit that is expanded in series to the operating temperature. In this case the series expansion is accomplished in two steps. Four atmosphere, single-phase fluid is produced by an expander, EX-3, and then part of this flow is expanded in a Joule-Thompson process to provide subcooling to the 4.15 K operating temperature. The saturated gas return from the subcooler and from the magnets passes up the heat exchanger to the induction of the first stage compressor.

The cooling for the 20 K shield is produced by expander EX-4 connected in a Brayton cycle. Although refrigeration for intermediate temperature loads is often produced by secondary loops in an integrated cycle, in this case the shield cooling circuit is largely separate.

Although the overall arrangement of this plant is similar to that of most other large systems, there are several features here specific to the requirements of the SSC. The most obvious of these is the use of a separate circuit for the precooling turbo-expanders. This is done for two reasons. First, it isolates the turbomachinery from contamination, and second, it allows the refrigeration power of these machines to be varied in a simple way with little efficiency penalty. This is done by charging the loop with more or less gas from the ballast. Under these conditions the pressure ratio in the loop remains constant while the absolute pressures vary. Scaling in both the compressors and the expanders is such that this adjusts loop output without changing, at least to first order, the efficiencies.

For much the same reasons, expander 3 is pictured here as a reciprocating device. As such it is very resistant to damage by contamination in the helium flow, and its output can

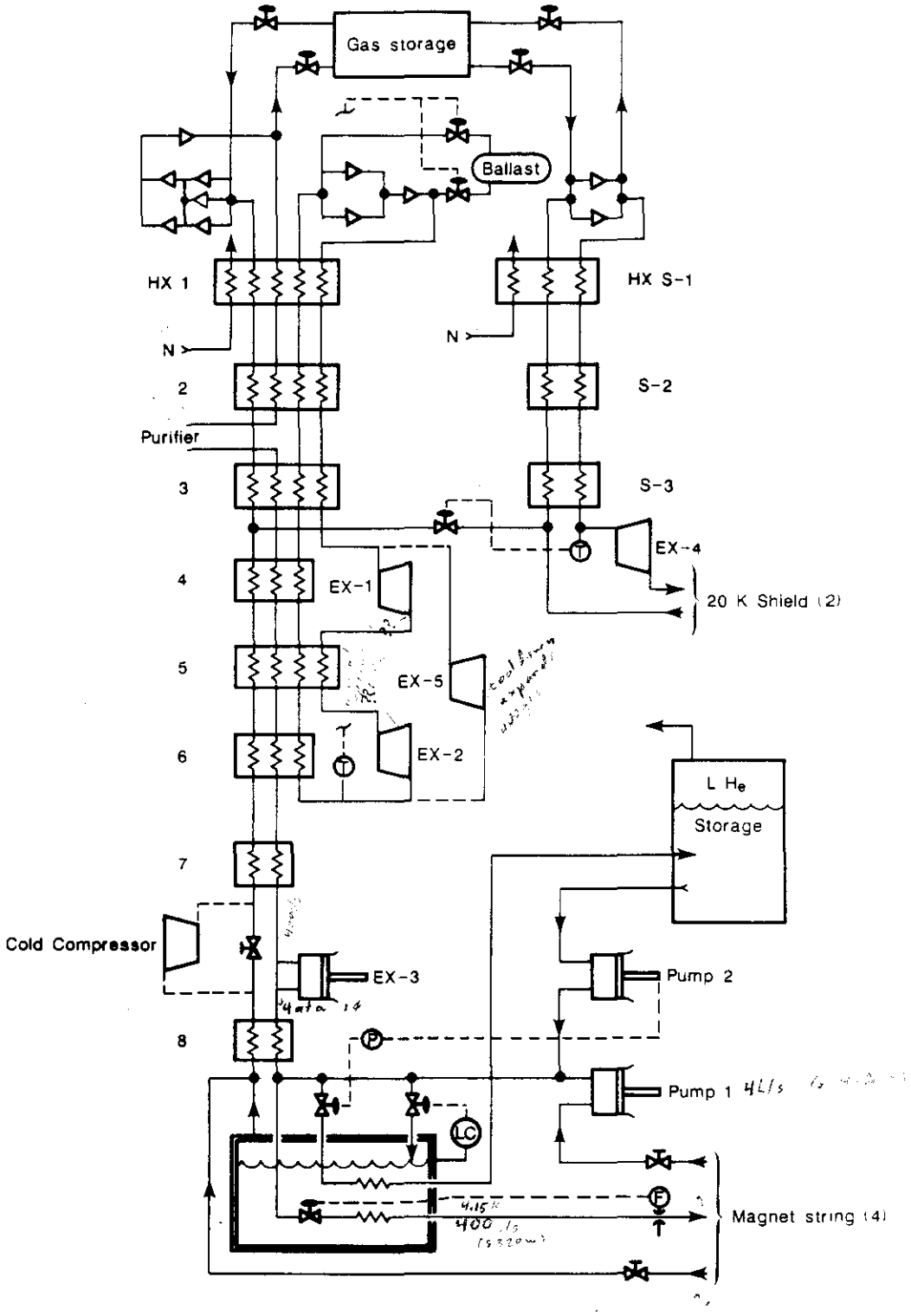

Figure 5.3-7. Schematic flow sheet of a refrigeration plant for the SSC. There are three compressor skids, five expanders, and two liquid helium pumps in the cycle. The four magnet strings connect at right to both the 4.15 K and the 20 K circuits. There are eleven such plants in the SSC cryogenic system.

be varied easily by control of the speed. In fact, as the system is drawn here, this expander speed is the primary determiner of the plant output at 4.15 K.

The separation of the 20 K shield refrigerator has already been remarked on. This is preferred for the SSC for reasons of being able to remove rime and maintain this part of the system separately and because of the use of the shield circuit for returning quench gas. The shield refrigerator acts to buffer the pressure surges associated with quench and to distribute the gas vented both during the quench itself and during the recovery period.

Last among the features of this plant to be mentioned are the liquid helium pumps. There are two in the design. One recirculates the liquid return from the magnets, and the other returns liquid from storage. The pumps each have a displacement of about 4 liters/second and are interchangeable. The need for rapid and independent adjustment of the magnet single-phase flow and for the capability to handle efficiently the very large inventory makes these pumps essential in the SSC system.

In the cycle 200 g/s of nitrogen gas, the boiloff from the 84 K shield cooling, is used in normal operation for precooling. Liquid nitrogen in this heat exchanger is used to produce the large unbalanced flow needed in the first stage of sector cooldown. In addition to the liquid nitrogen, an extra expander, EX-5, is needed for the cooldown process. It can be placed in the cycle in a number of places. Here it is shown in the same loop with the precooling expanders.

The helium compressors in the SSC plant are oil-flooded rotary screw machines. In the past decade, after some initial difficulties, the technology of these machines in helium refrigeration service has been well worked out. It is encouraging that during this period major machine failures have been rare, and most of the reported problems have been attributed to auxiliary systems. Problems of oil removal are understood, and the compressors have demonstrated many thousands of hours of very reliable operation at the Tevatron and in other installations [5.3-5]. The efficiency disadvantage of these machines relative to multi-stage piston compressors is largely offset by their lower maintenance costs and by their slide valve unloader, which permits close matching to load conditions. The recent operation of the compressor plant of the large BNL refrigerator at 57% of isothermal efficiency overall clearly shows the progress in the application of this technology and what can be accomplished by a careful selection process [5.3-6].

In the design presented here, the compressor plant has three separate compressor skids each having several machines, so there are a large number of relatively small compressors. Thus some economy of scale is lost, and the redundancy of multiple, parallel operation is not available. These disadvantages are mitigated, however, by the good record that is developing for the screw compressor. With care in specifying the machinery, with motors sized for overload, and with auxiliaries and instrumentation chosen for reliability, high availability can be achieved with only minimum redundancy in the compressor plant. The advantage of organizing the refrigeration plant along the lines suggested here is considerable, and the design addresses real and important problems that must be effectively solved in the SSC system.

The optimum plant design is the product of many decisions that take the full range of operating conditions into account. Technical considerations of importance include the high single-phase flow required (400 g/s) and its control, upsets associated with relief flows from single and multiple quenches, various cooldown requirements, and very important, the turn-up capability needed for failure-mode operation, and the turn-down capability to deal

efficiently with the load variations. Furthermore, these capacity control functions and other system operations such as load shifting must be able to be accomplished in a way that is consistent with the operating requirements of the rings and in time frames set by beam activities. Also considered are factors of capital and operating cost and enlargement capability. Certainly the refrigeration plant specifications must be developed with great care and complete design studies by vendors required.

Control of the helium inventory for each refrigerator station is accomplished through a combination of liquid and gas storage connected to the compressor-cold box. The size of the inventory is given in Table 5.3-6 and the storage tank capacity necessary to hold it is listed in Table 5.3-5. These tanks are distributed around the ring at each station. The stations that come into operation first have two liquid tanks, the later ones only one. As the collider reaches completion, liquid inventory can be passed around the ring in the cryogenic system. The six inch diameter warm gas header provides ample capacity for distributing gas from a central delivery point.

As final designs for the system are made, it may prove more practical for the site and more economical to plan a partially centralized storage system. One large site-erected liquid helium tank would be the cheapest way to provide the storage. A single location for the gas storage tank farm might be desirable in order to minimize the surface occupation of the site. In this event only relatively small liquid and gas tanks for use as a ballast for the operation of the refrigeration plants need to be distributed around the ring.

The cost of the helium inventory is about $3.5M, but even more costly will be the operating time necessary to accumulate and move it. Steady loss of inventory is not only expensive in itself, but it is accompanied by contamination problems and a consequent loss of machine availability. That the system uses an uncomfortably large amount of refrigerant is further illustrated by the fact that at the single-phase circulation rate of 400 g/s in each sector, it requires 17 hours to circulate the total inventory through the system once. Each plant running purely as a liquefier at full capacity will produce about 1200 liters/hr, so if the gas were available in that quantity, 140 hours would be required to fill all of the liquid storage. Handling the inventory prudently is a major consideration for the SSC, and its systems must be designed with this in mind.

In addition to storage, the helium management systems for each sector station will include a recycling purifier with regenerator, a utility compressor, and other auxiliaries for insulating vacuum and cold box clean-up and servicing.

5.3.5 Liquid Nitrogen Supply

Liquid nitrogen in the SSC cryogenic system is used for several requirements. First, it is used in cooldown of the large cold-iron mass of the ring dipoles, and second, as has been mentioned before, subcooled liquid nitrogen is used as the heat transport medium for the 84 K cryostat shields. Third, the latent heat of the nitrogen provides the 84 K shield refrigeration, and last, the sensible heat is used in the refrigeration process. The choice of nitrogen for the first two purposes is dictated by technical necessity. Liquid nitrogen can be stored and marshalled for rapid cooldown, and for the purposes of heat transport, it is the most practical choice. Stored liquid nitrogen also is important for control of the heat leak and helium inventory loss in the case of utility failure.

Table 5.3-6
Helium Inventory

Dipole and Cryostat	
Dipole body	81.8 liters
Connection	33.5
Single phase return	22.3
Gas return	9.9
20 K shield line	5.7
Total	153.2 liters
Other Components with Cryostats	
Quadrupole with connection	93.4 liters
Average spool piece	118.4
Average isolation box	13.9
Average end box	41.0
IR transfer line	8.4 liters/meter
Cryogenic Sector	
840 dipoles	128,690 liters
168 quads	15,690
144 spools	19,980
Isolation & end boxes	170
Refrigerator working inventory	1,000
Total	165,440 liters
Whole Machine Inventory	
10 cryogenics sectors	1,654,400 liters
Transfer lines (8 km)	67,200
Cold gas in storage tanks	200,000
Margin (10%)	172,160
Total	2,093,760 liters
	2.5×10^5 kg
	52 MSCF

The choice of nitrogen provided by air separation for the third and the last use mentioned above is mainly an economic one. The primary choice is between refrigeration produced by a helium cycle integral with each of the ten refrigeration plants and the use of nitrogen latent heat. A secondary choice exists between air separation and reliquefication if nitrogen is used. It is somewhat lower in capital cost to produce the nitrogen and distribute it than to produce the refrigeration with helium. In addition, if the sensible heat can be used, as it can here, operating cost is lower as well.

Until the final choices can be made, the system illustrated in Fig. 5.3-8 will be taken as representative. Liquid nitrogen is supplied to the SSC site from two 200 ton/day (2100 g/s) air separation plants located near the IR clusters. The ring requirement for LN is about 2000 g/s so there is redundancy. However, the total site usage, including the injector ring and experimental areas is larger than half of this capacity. Located at each air plant are two 55,000 gal (168,000 kg) storage tanks and at each of the other eight refrigerator stations a 20,000 gal tank. The total storage capacity is sufficient for six days consumption. In normal operation both plants are running at partial capacity, perhaps using the storage for electric power load leveling or to take advantage of time-of-day power pricing. The liquid nitrogen is delivered around the ring through the shield piping by unbalancing the flows in the way shown in the figure. Here 900 g/s is being delivered to storage and 500 g/s is being sent in each direction in the ring. The cold gas from the subcooler at each station is used in the refrigeration process and exhausted at room temperature.

In the event that one air plant is not functioning, the ring can be supplied from the other plant by reversing the normal flow in the shield of one ring so that each shield carries 500 g/s. The valving necessary for this operation is not shown in the figure. For failure mode operation there are standby subcoolers at each sector interface. These allow the shield coolant to operate with less than the normal flow or more than the normal heat load without reaching saturated conditions. When the ring cannot be used for transport of the nitrogen, trucks can be used. Each station has storage and can be supplied by road. The consumption of the system as a whole is equivalent to 14 truckloads a day.

5.3.6 Design Operating Conditions

The major refrigerated systems of the SSC are the 84 K shield, the 20 K shield, and the 4.35 K magnet cooling system. Table 5.3-7 lists the important parameters for these three systems. The steady-state operation of each is discussed in the following paragraphs.

The operation of the nitrogen shield has already been described and need only be reviewed here. The heat load on the shield system is 17,000 watts for a complete cooling loop of 8 km length. The nominal flow rate is 750 g/s average, entering at 5 atm and 77.5 K and exiting at 4 atm and 88.5 K. Liquid nitrogen transport through the shield system is accomplished by unbalancing the flow in the two halves of the loop and passing flow from one sector to the next.

The 20 K shield operates in the same 8 km loop as the 84 K shield, 4 km in each of the two rings. The heat load is 2274 watts on this length. The flow rate is 100 g/s, entering at 3.5 atm and 17 K and exiting at 3 atm and 21.2 K. Each refrigerator supplies flow for two such loops, so that the total flow to each sector is 200 g/s. The average pressure chosen depends on the final choice of the refrigerator operating pressures. It needs to be somewhat

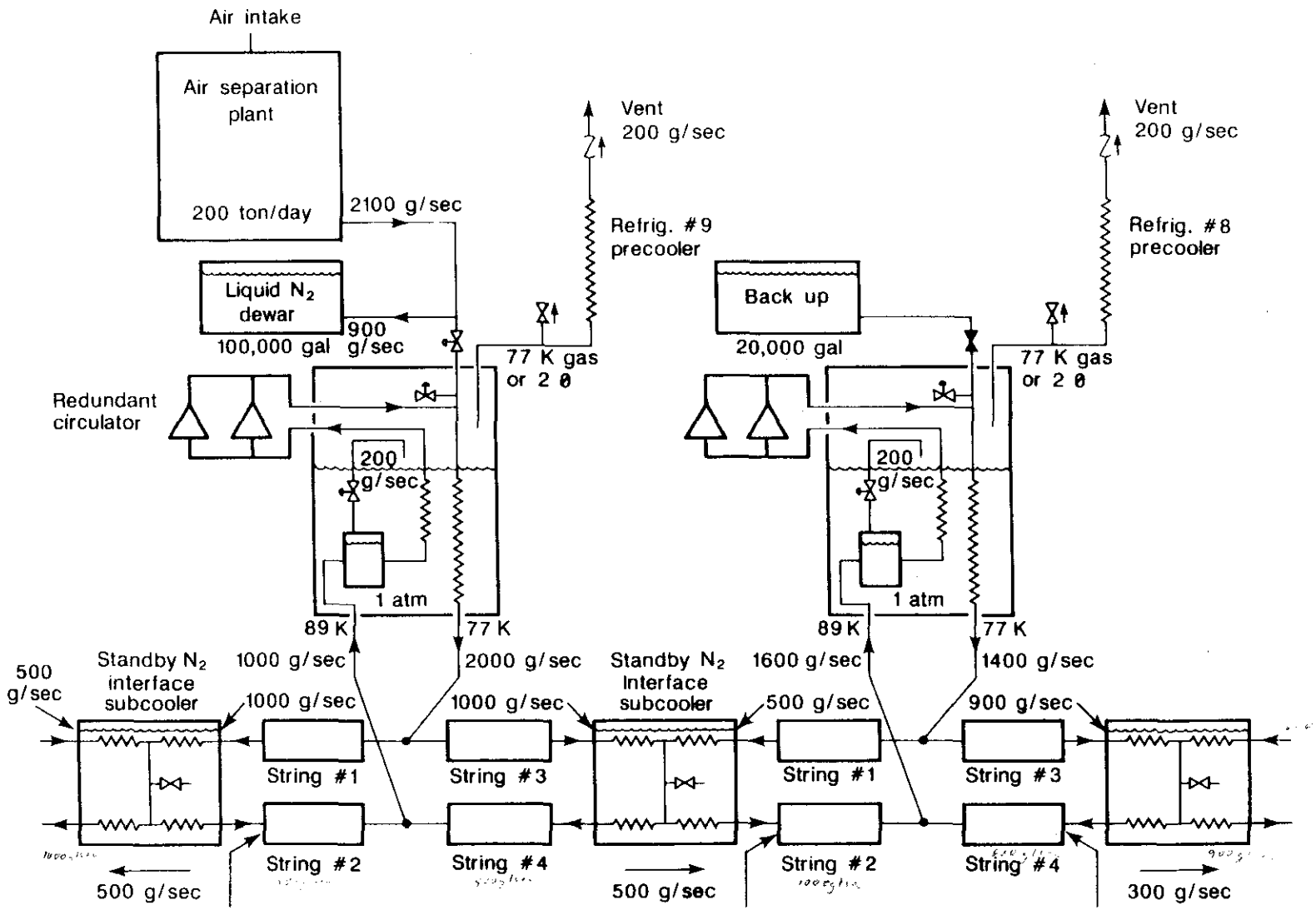

Figure 5.3-8. Schematic of the liquid nitrogen system for the SSC ring. One-fifth of the ring is shown with two refrigerator stations and one air separation plant. The liquid nitrogen shield circuit of both rings is shown with the flow rates characteristic of normal operation. The interface subcoolers are used only under abnormal conditions.

Table 5.3-7
System Steady State Operating Parameters

4.15 K Circuit Parameters	
Synchrotron radiation (dipole) W/m	2×0.142
Synchrotron radiation W	2×9100
Beam microwave load W	2×1000
Beam-gas loss load W	2×500
IR beam loss load W	800
Heat leak, average W/m	2×0.057
Total load for 2 rings kW	31.5
Heat load per refrigerator W	3150
Refrigerator capacity W	4700
Refr. liq. helium cap. g/s	20.67
Number of refrigerators	10
Liquid He volume liters	2.1×10^6
Total lead flow g/s	129
1 phase He flow rate g/s	2×100
1 phase He flow pressure atm	4.5–4.15
1 phase return line (i.d.) inches	1.53
1 phase return line pressure atm	4.15–3.83
Temperature rise between recoolers K	0.090 (typical)
Number of recoolers	836
Distance between 1 phase recoolers m	192
Recooler duty W	32 (typical)
Maximum He temperature at the coil K	4.35
Highest temperature 1 phase (last cell) K	4.295
Lowest temperature 2 phase (first cell) K	4.175
Cold mass kg/m	2×373
20 K Circuit Parameters	
Heat leak W/m	2×0.29
Total for 2 rings kW	48.2
Shield flow rate g/s	100
Temperature in K	17
Temperature out K	21.4
Circuit flow pressure atm	3.0–2.12
Cold mass kg/m	2×12.1
Surface area sq-ft/m	2×12.0
Trace pipe size (i.d.) inches	3.0
84 K Circuit Parameters	
Heat leak W/m	2×2.2
Total for system kW	365
Fluid for shield cooling	LN
Flow rate g/s	500–1000
Temperature in K	77.5
Temperature out K	89
Circuit flow pressure	6.0–4.68
Cold mass kg/m	2×14.3
Surface area sq-ft/m	2×14.6
Trace pipe size (i.d.) inches	2.50
Number of LN plants	2
LN plant capacity tons/day	200

less than the single-phase loop pressure for the proper operation of quench venting and recovery.

The concept of the magnet cooling loop has already been described, as has the operation of the refrigeration station. Heat transport in the 4 km lengths of the strings is of equal importance in the design of the system. Three steps are involved, conduction of heat into the single-phase coolant flow, convection of this helium through intercoolers where heat is exchanged with saturated helium, and flow of the saturated gas to the refrigerator. Each of these steps has temperature drops associated with it which in aggregate are of concern in the management of the system.

The major sources of heat generation in the bore region of the magnet are the ramping loss, consisting of hysteresis in the superconductor, the iron and eddy current loss in the copper of the conductor and the plating on the inside of the beam pipe, and the synchrotron radiation. Of these the synchrotron radiation has the most cryogenic importance. The iron hysteresis loss is about 40 J/m-cycle and the superconductor loss 37 J/m-cycle for 5 micron filament size. For the 1000 second ramp time, the total hysteresis loss is about 40 mW/m and the eddy current losses are quite small. Thus the synchrotron radiation heating of 0.142 W/m dominates the cooling of the windings.

The synchrotron radiation assumes an even larger aspect when the operating cycle of the collider is factored in. The ramping takes 15 minutes. The synchrotron radiation rate is proportional to the fourth power of the energy of the beams, so it is significant above 15 TeV and has the value quoted above at 20 TeV. For the remainder of the 12 hour machine cycle the synchrotron radiation is the single largest heat load at 4.15 K.

Because of the close spacing around the beam tube, most of the the single-phase helium passes through holes in the iron, and there is an estimated flow of only 1 g/s in the central region of the magnet. The heat load in this region is therefore transferred to the bulk of the coolant by conduction through the collars and the iron yoke. Table 5.3-8 lists the temperature differences associated with the conduction. In calculating these figures, heat transport by thermal convection of the helium between and around the laminations of the collar is not considered. This process is very sensitive to the exact configuration of the magnet, especially the ground wrap insulation, and can be significant under some conditions.

Two other distributed heat loads that are smaller than those discussed above, but nonetheless significant for the machine as a whole, are beam image conduction loss and beam-gas interaction loss. The first of these has a low value in the uniform sections of the beam pipe, but can have larger values at discontinuities. The average value of this source of heat is estimated to be about 500 W for each ring. The second source of heating also has a low value in most of the system but can be larger in regions of poor beam-line vacuum. It is the case, however, that if significant levels of beam-loss heating occur in the collider, the beam lifetime is so shortened that the system cannot be operated. For the expected beam-line vacuum and beam lifetime, this heating amounts to 1 kW for both rings, excluding the heating by secondaries from the collision points.

Table 5.3-8
Temperature Drop Budget

Conduction of Heat from Bore Tube Region
Heat Flux of 0.142 W/m

0.04 cm kapton insulation	0.012 K
1.5 cm stainless steel collar	0.027
0.025 cm helium	0.006
Iron laminations	0.009
Helium heat transfer	0.001
Total ΔT	0.055 K

Heat Transport ΔT

	Nominal	Failure Mode*
Conduction	0.055 K	0.055 K
Single-phase temperature rise	0.090	0.090
Intercooler ΔT	0.015	0.015
Gas line ΔP	0.015	0.105
Gas line head (max)	($\pm$0.028)	($\pm$0.056)
Total ΔT	0.175 K	0.265 K

*One plant off, example Site "A".

The heat from within the magnet and the heat leak load in the various parts of the string is picked up by the flowing single-phase helium. Uniformity of heating is assured by mixing that occurs between each dipole, so the total load of 32 watts per cell produces a temperature rise of 0.090 K in the 100 g/s flow. At every other spool piece a heat exchanger recools the flow. Heat transfer in the recooler is governed by the nonlinear effects of the pool boiling, and a minimum practical temperature difference of about 15 mK is needed in the exchanger almost independent of the total heat transfer. The saturated gas from the recoolers is conducted back to the refrigeration plant in the gas return line. There is, of course, a temperature difference associated with the pressure drop in this flow. Table 5.3-8 lists the various temperature differences associated with the heat transport to the refrigerator. Under normal operating conditions these are seen to add up to 0.175 K, so that the nominal superconductor operating temperature of 4.35 K requires that the refrigeration be produced at about 4.15 K. In various parts of the system compensation must be made for the temperature differences produced by head pressure in the gas return line in a tilted ring. A value for this appropriate to site example A is listed in the table. The failure mode referred to in the table is the case in which a refrigerator is off and the heat load of that sector is being shared by the two adjacent plants. This is discussed more fully in the following section.

It is important to recognize that long time constants are associated with some of the temperature differences described above. The inventory of a cell is about 1600 liters or 200 kg of helium. Thus at 100 g/s circulation rate, 2000 seconds are required for this inventory

to pass through a recooler. Some control of the temperature is possible by adjusting the refrigerator, but because the synchrotron radiation heat load is such a large part of the total, there will be temperature changes in some of the dipoles of the order of 0.15 K as the system ramps from injection to 20 TeV. This uniformity is well within that required to produce a tolerable sextupole coefficient due to persistent currents in the superconductor of the dipoles even for filament size as large as 9 microns [5.3-7]. The most stringent requirement on the temperature, therefore, is the 4.35 K maximum superconductor temperature.

Another time constant of importance is the heating rate of the magnet system in the absence of flow. This is just the same as calculated above, namely a temperature change of 0.175 K in 2000 seconds. Therefore the system provides time to make cryogenic changes such as switching loads between refrigerators during collider operation.

5.3.7 Failure Mode Operation

The strategy for dealing with refrigerator scheduled down-time or refrigerator failure is load shifting between adjacent cryogenic sectors. The method by which this is accomplished is illustrated in Figs. 5.3-9 and -10. In the normal mode of operation shown in the first figure, two strings are connected to the circulation of the refrigerator. At the end boxes there are U-tube connections to the strings of the adjacent sector through the auxiliary box, and in this box are valves, normally closed. Likewise, the 20 K shield flow passes between strings through this box with a valve. Reversing these valves shifts to the failure-mode flow patterns shown in the second figure. The temperature transients during the shift are dealt with by purging to the warm header and by the recoolers in the end boxes. In the failure mode the strings of magnets from one sector are placed in series with the flows of the strings of the adjacent sector. Thus this sector refrigerator cools six instead of four strings and its refrigeration load is increased a factor of 1.5. If this amount is not available from the adjacent sector, then it in turn can share the load with its neighbor on the other side. The aim is to be able to do these shifting and sharing operations without disturbing the operation of the rings.

It is assumed that the liquid nitrogen circulator continues to operate. It is clear from the figure, however, that nitrogen circulation can easily be shifted, and with the use of the standby subcooler will continue to operate with any single station circulator out of service.

In the operation described above the circulations and heat loads of two strings are shifted from one refrigerator to an adjacent one in order to provide for refrigerator shutdown. Load sharing may be accomplished in a similar way. Either single strings can be shifted or refrigeration can be shifted by sending single-phase flow from one sector to the next and returning the helium by way of the warm header. Thus several plants can share the shifted load when a failure or a shutdown occurs. Sending inventory and refrigeration around the ring in this way is likely to be a common operation of the SSC cryogenic system, done regularly even when all plants are running. In order to maintain schedule and run reliably, the system must have some immunity from the plague of low-grade problems always encountered in any complex operation, problems such as contamination, local poor cryostat vacuum, and so on. Load shifting is a primary way of providing this immunity for the SSC. A somewhat simplified model of the SSC refrigeration system has been used to estimate availability [5.3-2]. Using nine refrigerators, assuming that each refrigerator can help one adjacent neighbor, and that the mean time between failures is 30 times the mean

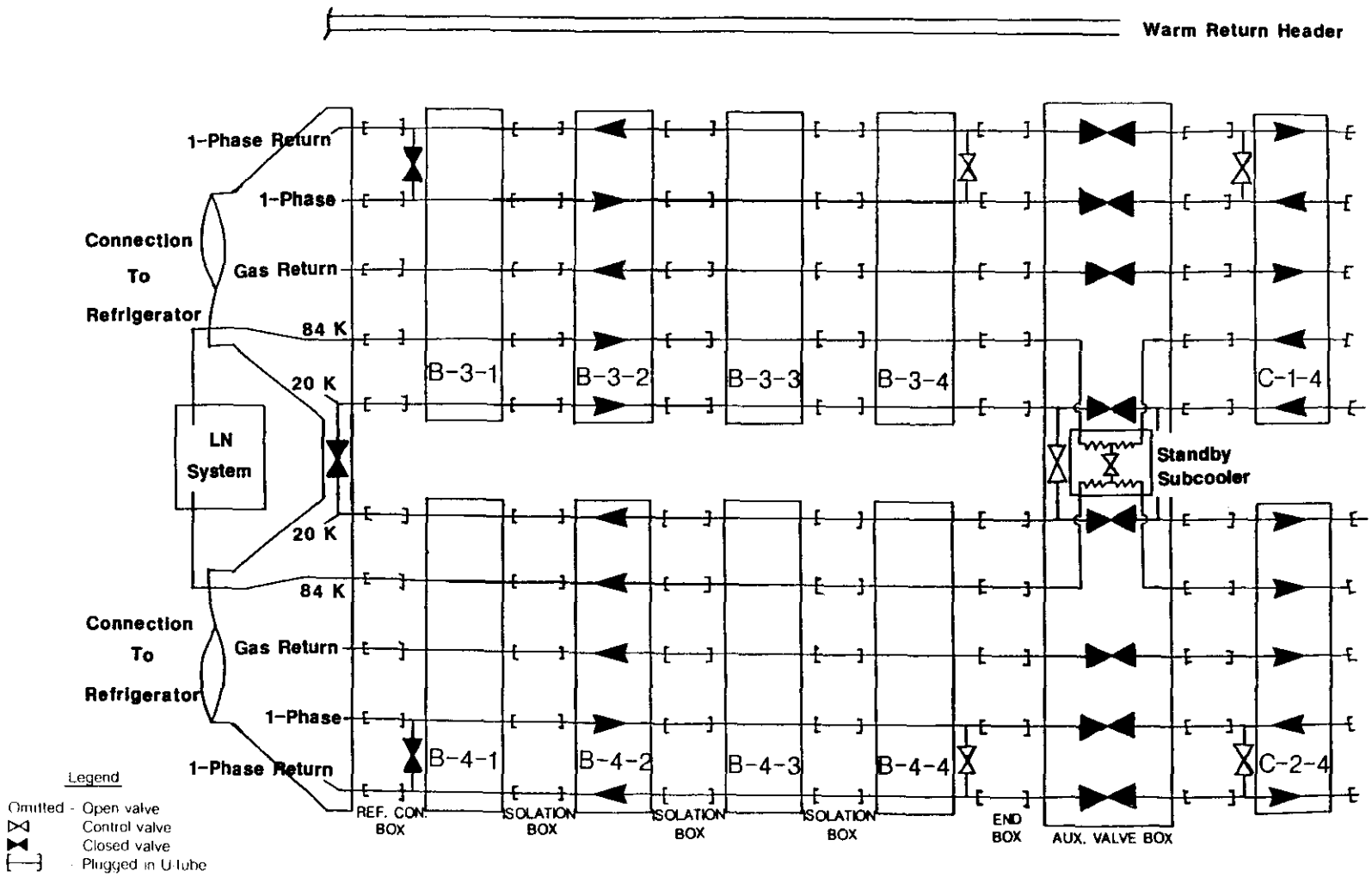

Figure 5.3-9. Block diagram of half of a cryogenic arc sector showing valve status and flow directions for normal operating conditions. In this example sector B is drawn. The refrigeration connection boxes are shown on the left of the four sectors of each string, and the connection through the auxiliary valve box to the strings of the adjacent sector, sector C, is shown on the right. Each numbered box represents a section consisting of 5 or 6 cells and either 960 or 1152 meters in length.

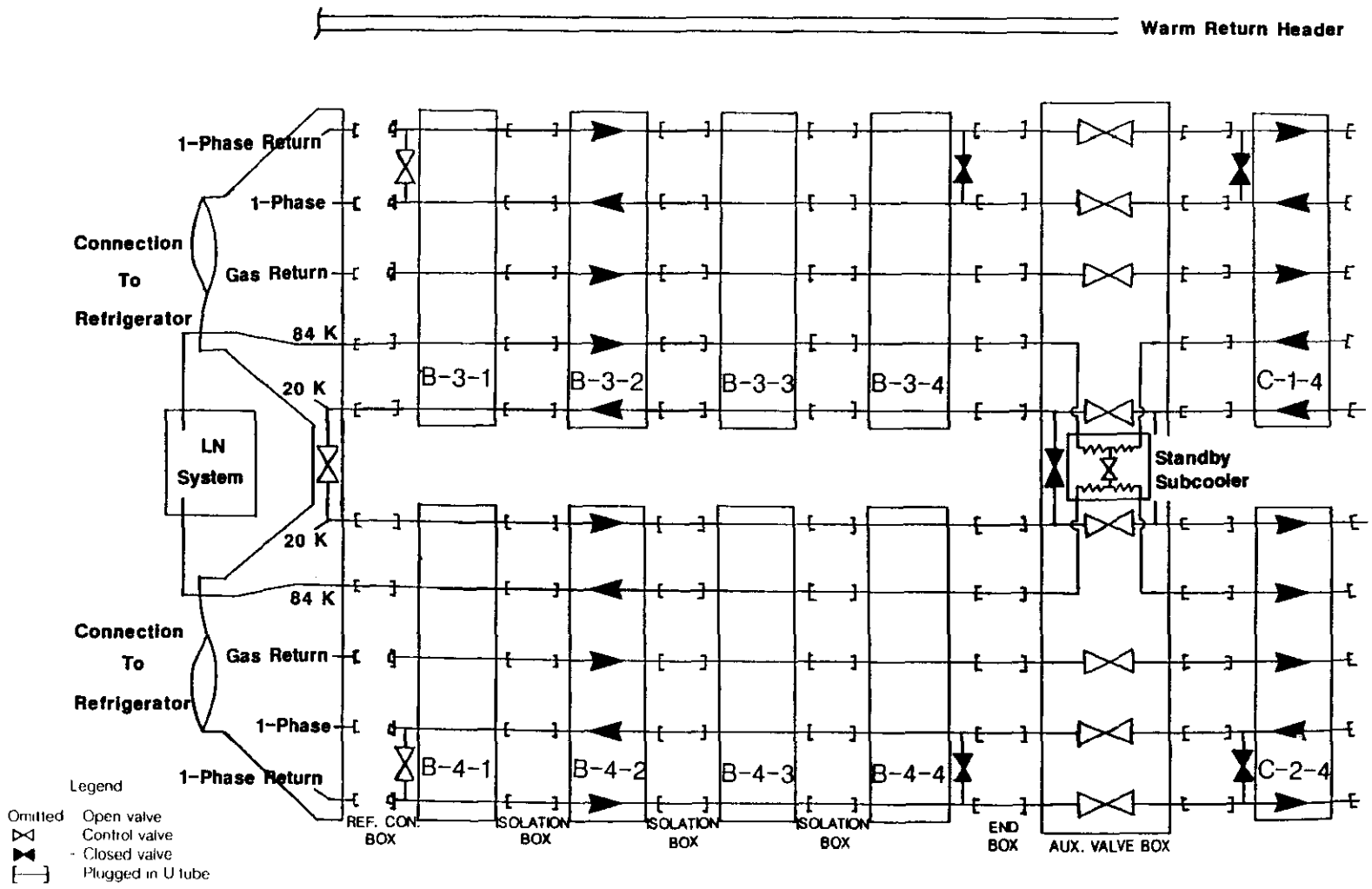

Figure 5.3-10. Block diagram of half of a cryogenic arc sector showing valve status and flow directions for failure mode conditions. In this case the refrigeration plant for the sector, drawn to the left of the picture, is disconnected and the strings of the sector are being cooled from the adjacent sector. Connections from one sector to the next are made through the auxiliary valve box shown on the right.

time to repair (consistent with Fermilab's Central Helium Liquefier experience), the availability of the cryogenic system is calculated to be greater than 97%.

Assuming that the single-phase flow remains at 100 g/s in the shifted string, the various heat transport temperature drops in the failure mode are as shown in Table 5.3-8. In order to maintain the 4.35 K maximum superconductor temperature under these conditions, the refrigerator operating temperature is lowered to 4.1 K.

5.3.8 Cooldown and Warmup Operation

The first situation to consider is the cooldown of a complete cryogenic sector of four strings using only one refrigerator. Before the cooling can be started the system of magnets must be dried and purified by circulating helium gas in series through the nitrogen-cooled charcoal purifier and the magnet strings at room temperature. A flow of 16 g/s can be established in each string with a pressure drop of 3.5 atm. At this rate the gas will circulate 4-1/2 times an hour, and clean-up will be completed in a few hours. At the same time the 84 K shield in at least one of the strings must be cooled down in order to establish the liquid nitrogen supply. It is estimated that this can be done in 12 to 16 hours.

Cooling of the strings is begun by setting up a flow from the refrigeration plant of 100 g/s at about 55 K into each. About 7% of this flow is directed through the 20 K shields and the rest through the single-phase space of the magnets. Because the iron yoke of the magnet and the helium coolant are in good thermal contact, the heat exchange occurs over a flow length of only a few meters. Thus the cooling proceeds as a wave, very short compared to the length of the system, with warm magnets in front and cold magnets behind. The room-temperature gas is removed from the string through cooldown valves located at every cell (see Fig. 5.3-3) and returned to the refrigerator in the warm header. As the cooling progresses down the string, successive valves are closed, and whereas the 300 K helium only flows through one cell of magnets, the 55 K gas passes through the whole cooled length of the string. Thus as the string is cooled the total circulation pressure drop rises. When the cold flow passes down the whole length of the string, the pressure drop is 10 atm. As this point is reached the cooldown valves are closed, and the 55 K gas is returned to the refrigerator in the 20 K shield line.

In this first stage of the cooling the plant is producing about 500 kW of refrigeration. Of this, 90% comes from 1200 g/s of liquid nitrogen fed into the heat exchangers and the rest from the cooldown expander (see Fig. 5.3-7). Although the final specifications of the refrigerator are not now worked out, this performance is reasonable, and 50 kW can be taken as a specification of this expander. The total enthalpy to be removed in cooling the sector to 55 K is 4.8×10^{11} joules, and the time required is 11 days. During this period 1500 tons of liquid nitrogen is used, including the shield cooling.

At 55 K only 1.3% of the room-temperature enthalpy of the magnets remains to be removed. With a gas return at 55 K the cooldown expander will produce 35 kW, and the second wave of cooling, to 40 K, takes 1.6 days. After the third wave, which takes 0.8 days, the magnets are below 15 K, and the remainder of the cooling and filling is accomplished by pumping in liquid helium from storage. This process is limited by the rate at which the refrigeration plant can accept the returning cold gas and takes about 0.6 days. Thus the total time for cooling the four strings of a sector using liquid nitrogen and the one sector refrigerator is 14 days.

If the whole ring is to be cooled starting at room temperature, cooling is limited by the liquid nitrogen production rate. Initially, the 400 ton/day rate allows three sectors to be cooled simultaneously in the way described above. However, as the shield system comes into operation, less liquid nitrogen is available for the magnet cooling. It is estimated that a complete ring cooldown from room temperature takes about 50 days, unless the liquid nitrogen supply is supplemented with a trucked-in product.

If the ring is "stored" at 80 K, and cooldown begins at this level, then all the refrigerators can be started simultaneously. The first wave of cooling to the 55 K level takes 5.2 days, and the rest of the cooldown proceeds as described above. Thus from nitrogen temperature the whole ring can be brought into operation in about 9 days.

In practice, one sector will be the last to be ready for cooling, so the situation likely to arise is the relatively unhurried cooling of nine sectors of the ring followed by a very hurried tenth. Under these conditions cooldown can be assisted by the adjacent refrigeration plants with a reduction in cooldown time from 14 to something like 10 days. Likewise the cooldown of single strings or single sections (960 m) can be considered. The cooling of single sections is a part of the magnet repair procedure and is discussed in paragraph 5.3.11 below. The cooldown rate of single strings is limited not by refrigerator capacity but by the flow rates possible in the magnet passages. Because the three operating strings of a sector can be shifted to the adjacent refrigerators, in effect a whole refrigerator is available for a single string cooldown. It is expected that just under a week is needed for such an operation.

5.3.9 Quench and Quench Recovery

With the active quench protection adopted for the SSC, the minimum unit of the accelerator to undergo quench is a single half-cell. When the voltage threshold is exceeded in any magnet, heaters are used to initiate quench in all of the five dipoles and the quadrupole of that half-cell. At the same time the other magnets of the ring are turned down with a current time constant of 20 seconds, the current being shunted around the quenching half-cell through the safety leads and an SCR switch. The quench process is described in more detail in Section 5.2.8.

The important cryogenic consequence of a single half-cell quench is the heat deposited in the coils as the stored energy of the magnetic field decays. The energy stored in the dipole at 6.6 T is 1.1 MJ per magnet, and the decay time is about 0.5 seconds. If this amount of heat is deposited evenly in the coil, the temperature increases to 70 K. However, the heat distribution in the coil immediately after the field decay is not uniform and is a complication in modeling the quench process.

The simple model described below predicts an estimated quench pressure of 7 atm. Most of the helium will be vented from the half-cell as the heat from the quench diffuses outward from the coils. As has been described in Fig. 5.3-3 this venting occurs through valves located in the spool pieces at each end of the quenching half-cell. These valves open on signal from the quench detection electronics and automatically on pressure rise to vent into the 20 K shield line. In addition, there are safety valves set at the 20 atm maximum working pressure of the cryostat to relieve the pressure into the tunnel. The 20 K shield line is similarly protected with two safety valves per section.

The pressure rise and venting rate on quench is determined in large part by the rate of diffusion of heat from the coils into the bulk of the helium that is in the bypass channels in the iron. The heat, deposited in a fraction of a second, must be conducted through the coil insulation, the stainless steel collars, the gap between collars and iron, and the iron itself. It can be estimated from a highly simplified model that the helium heating profile rises with approximately a 15 second time constant to a maximum of about 20 kW in each dipole, and then remains nearly constant over 20 seconds. Equilibrium is approached after this period.

With the above situation in mind, it is possible to use a simple thermodynamic argument to estimate the peak venting rate from the peak heat flux. This is 2000 g/s for the half-cell of five dipoles. With less confidence, the peak venting rate can be placed at 15–20 seconds after quench initiation. The high rate of venting subsides after about 60 seconds. The peak pressure is estimated to be about 7 atm, and the amount of the quench heat carried away by the helium is on the order of 60%. Under these conditions the equilibrium temperature of the magnet after quench and venting is about 25 K. The vented gas ends up at an average of 9 K and fills 900 meters of the shield line.

As the venting subsides, recooling begins as the single-phase flow is reestablished. First the vented gas at the upstream end of the half-cell falls in temperature and the quench relief valve is closed. The magnets then cool and fill with the single-phase fluid, venting the 25 K gas into the shield line at the downstream relief valve. The single-phase flow is doubled for the recooling period, and after 10 minutes the downstream vent valve cools and is closed. After a further 20 minutes has elapsed, all of the helium in the string has passed through a recooler and recovery is complete. In time the vented cold gas in the shield line returns to the refrigeration plant and is reliquefied into storage.

The above discussion applies to a single half-cell, high-field quench. Quenches at lower field levels produce considerably less heating. A quench at the injection field introduces only 1/400 of the energy of a full-field quench. This raises the temperature of the single-phase coolant only 50 mK and produces only a negligible pressure rise and no venting. At the normal circulation rate the result is an increased heat load of 14 watts for 1000 seconds. Thus even a multiple quench on injection will require only a few minutes of recovery time.

Multiple high field quenches are of more concern. Clearly quenches in adjacent half cells produce higher peak pressures, and although the shield line can hold at equilibrium the quench gas from ten half cells without serious pressure rise, the transient pressures in such an event could reach the 20 atm level at which loss of helium occurs. Also, since recovery is sequential, the loss of operating time from a large quench event will be long.

The investigation of quench behavior is one of the primary goals of the half-cell test now in preparation at Fermilab. The measurement program together with more complete modeling will provide a satisfactory basis of understanding of the various aspects of the quench processes.

5.3.10 Utilities Interruption

Electric power reliability is of great importance for a system with the complex operating procedures and the long time constants of the SSC. For this reason a two-feeder distribution system has been planned for the site, and alternate sectors are powered from the two separate primary systems. Thus even a primary failure will leave half of the refrigeration

plants in operation, and by load shifting the cryogenic system can be kept in equilibrium without loss of refrigerant for a substantial period. However, the consequences to the cryogenic system of a total site power failure, as rare as it might be, must be considered.

It is clear that some emergency power supply for the SSC is necessary, and it is assumed that the computer and control systems in the service buildings will continue to operate in the failure period. The most important additional cryogenic subsystem that will be supplied with emergency power is the liquid nitrogen circulation pumping. There is liquid nitrogen storage capacity sufficient for six days, and so the cryostat shield system will continue to operate also.

Under these conditions the cryogenic system is handled as follows: For each sector the return lead flow is connected with three of the ten available gas storage tanks and the four magnet strings connected with the other seven from the end boxes through the 20 K shield lines. It is assumed that the tank farm begins at one-quarter full with all of the tanks at 4 atm pressure. The helium in the magnets, warming as time passes, flows out to the tanks through the leads and through the 20 K shield intercepting some of the incoming heat. The pressure of the system rises as the tanks fill, and the proper proportion of lead flow is maintained by the ratio of tanks connected to the two outflowing streams. The rate of pressure rise is calculated to be about 0.5 atm/hour, and the system can operate to a pressure within 10% of the safety valve settings of 20 atm. Thus no refrigerant is vented for the first 28 hours after a total power failure. At the end of this period the system is at a pressure of 18 atm, and the temperature of a magnet string has risen to about 5 K at one end and 10 K at the other. At this time the lead flow will be vented to the atmosphere. The strings will either be vented through the shield or blown down through the single-phase return line into the liquid storage tanks. The helium inventory loss after the first 28 hour period is expected to be about 10% in each 24 hours.

If the power outage is expected to last for more than 48 hours, another procedure will be employed to shut down the system with minimum loss of inventory. In this case the liquid helium pumps in each refrigerator will be used to compress cold gas. With an induction at 1.1 atm saturated and a discharge at 4 atm, the pair of machines in each cold box will move 100 g/s. At 80% efficiency the power consumption is 1.6 kW, and the temperature of the discharge is 8 K. This gas is sent to the end boxes in the 20 K shield lines, warming as it goes to 18 K. The gas then goes from the shield to the magnet single-phase space displacing the cold fluid which flows out the other end into the refrigerator where it is expanded to liquid at 1.2 atm, slightly subcooled, and sent to the liquid storage tank. The rate at which the liquid can be stored in this way is about 1000 g/s, and the time required to handle the entire inventory of the magnets is 6 hours. The expansion and subcooling of this stream together with heat leak produces about the 100 g/s of cold gas drawn in by the pumps, so the process produces very little, if any, boil-off. Gas is displaced as the storage tank fills, however, and this is lost. If the tank is stratified to an average temperature of 12 K, this loss is 4%. During transient periods of unbalance more helium will be lost, so at the end of the process about 80% of the helium is recovered into liquid storage, 10% remains in the magnet strings at 15 K and 4 atm, and about 10% is lost. The gas in the strings can all be recovered into the gas storage as it warms up.

Very important to the operation of this process is the high transverse and low longitudinal thermal conductivity of the iron laminations of the magnet which stabilizes the temperature and density gradient in the strings. There will be some mixing in the connection

regions and in the spools, so some heat may have to be added and some gas vented to keep things in balance. However, it is clear that it is possible to shut down the cryogenic system in an orderly way in the event of a complete electric failure, with the recovery of the substantial part of the inventory using only a low level of emergency power.

5.3.11 System Maintenance and Repair

A very important procedure for the SSC is the change of a dipole or other ring component when a failure in service occurs that prevents operation. Clearly the machine down-time under these conditions is very costly, so the repair sequence must take as little time as possible. As has been described previously, each ring of the SSC is divided by means of U-tube disconnects into sections about 1 km long. One of these sections is the unit that is warmed up in a repair sequence.

The normal operating configuration of a cryogenic sector is illustrated in Fig. 5.3-9. In order to take a section of one of the rings out of service and warm it up while keeping its neighbors cold, U-tubes at the isolation boxes are removed and the flow patterns of the string are altered. Shown in Fig. 5.3-11 is the configuration for warmup of a section, here called B-3-2 as an example. At an intermediate stage in reaching this arrangement, the cryogens are removed from the section. This is done for the liquid nitrogen by pushing it back into the adjacent section with gas. For the removal of the single-phase helium, a quench relief valve in one of the isolation boxes is opened, and the dense helium in the magnet is displaced into the adjacent section by 20 K gas from the shield system. During this process the contents of the recoolers in the section boils away and is vented to the warm return header. Thus as the warmup circulations begin, the magnets of the section are at 20 K, and the system contains only a small inventory.

The cold mass of the magnets is warmed by means of electric heaters, 6 kW on each dipole and a proportionate amount on the quadrupoles. At the same time helium gas is circulated through the single-phase space, through the two return lines, and through the 20 K shield. This gas flow spreads the heat applied to the magnets and warms the piping and shield. The 84 K shield is warmed up by nitrogen gas drawn from the shield of the adjacent section and heated. With these arrangements the section takes 24 hours to reach room temperature. Table 5.3-9 lists the tasks and estimated times for the complete magnet change procedure.

The operating mode of the rest of the system is diagrammed in Fig. 5.3-11 as well. The sections B-3-3 and B-3-4 and the shield flows of sections B-4-3 and B-4-4 are shifted to sector C, to the right of the figure, through the valves in the auxiliary box. This is similar to the failure mode configuration described in Section 5.3.7 above. The 84 K shield of section B-4-2 is cooled by the net flow between sectors B and C and the 20 K shield of this section is not cooled. This results in an increase of the heat load on the sector B refrigerator of only 150 watts. The important result of this manipulation is that the lower ring, the one not being repaired in this example, remains operable. Under some circumstances during the 24 hour warmup period and the other periods of the magnet change during which the tunnel can be cleared, one ring can be operated for machine studies. This is a very valuable recovery of useful machine time.

Figure 5.3-12 shows the arrangement for cooldown of the various circuits. The magnets are cooled by drawing a flow of 200 g/s from the refrigerator through the 20 K shield

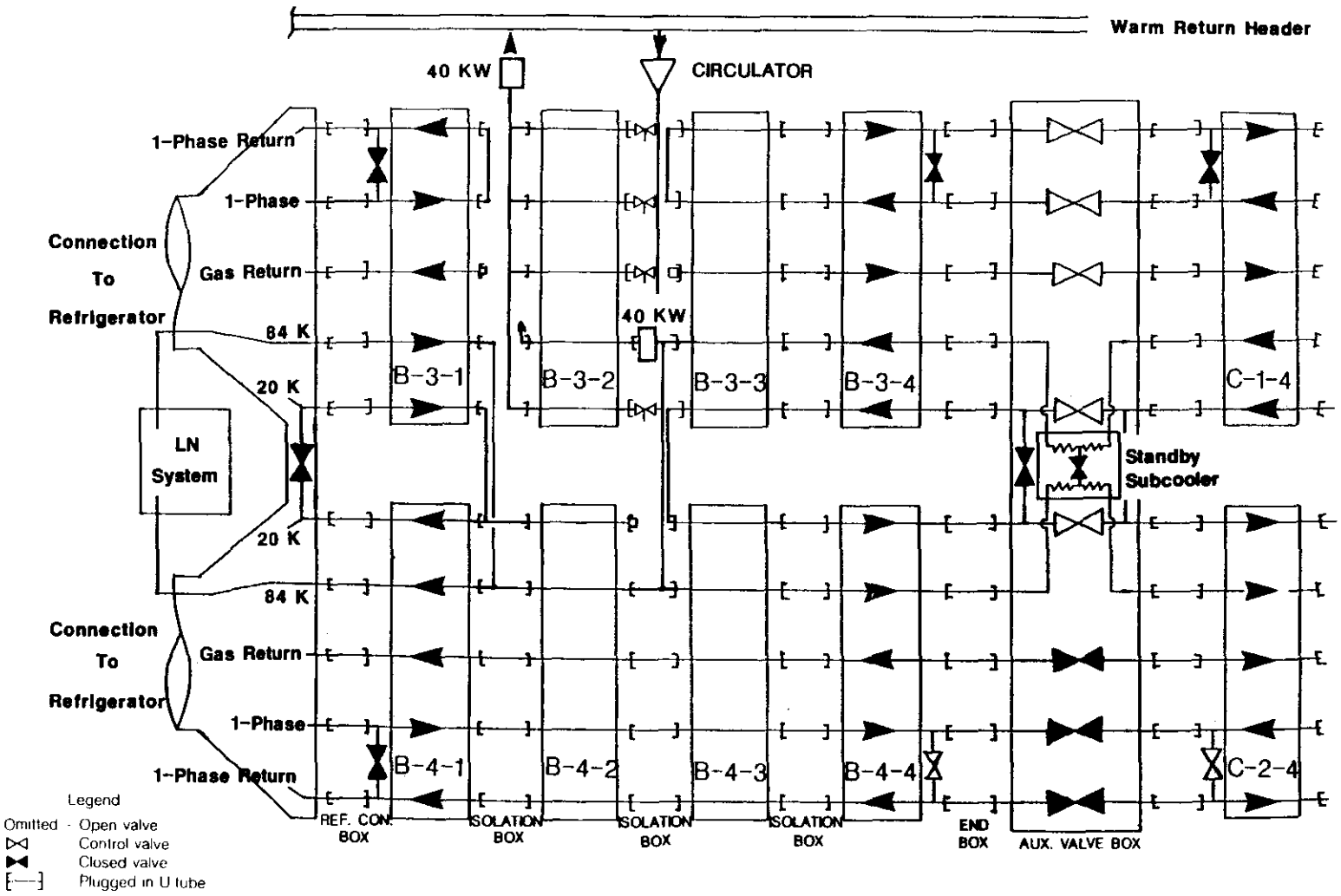

Figure 5.3-11. Block diagram of half of a cryogenic arc sector showing valve status and flow directions for magnet change conditions. The section labeled B-3-2 is out of service and warmed up. The sections B-3-3 and -4 have been shifted to the adjacent sector through the auxiliary valve box on the right. The lower ring in the condition shown can be operated for beam studies.

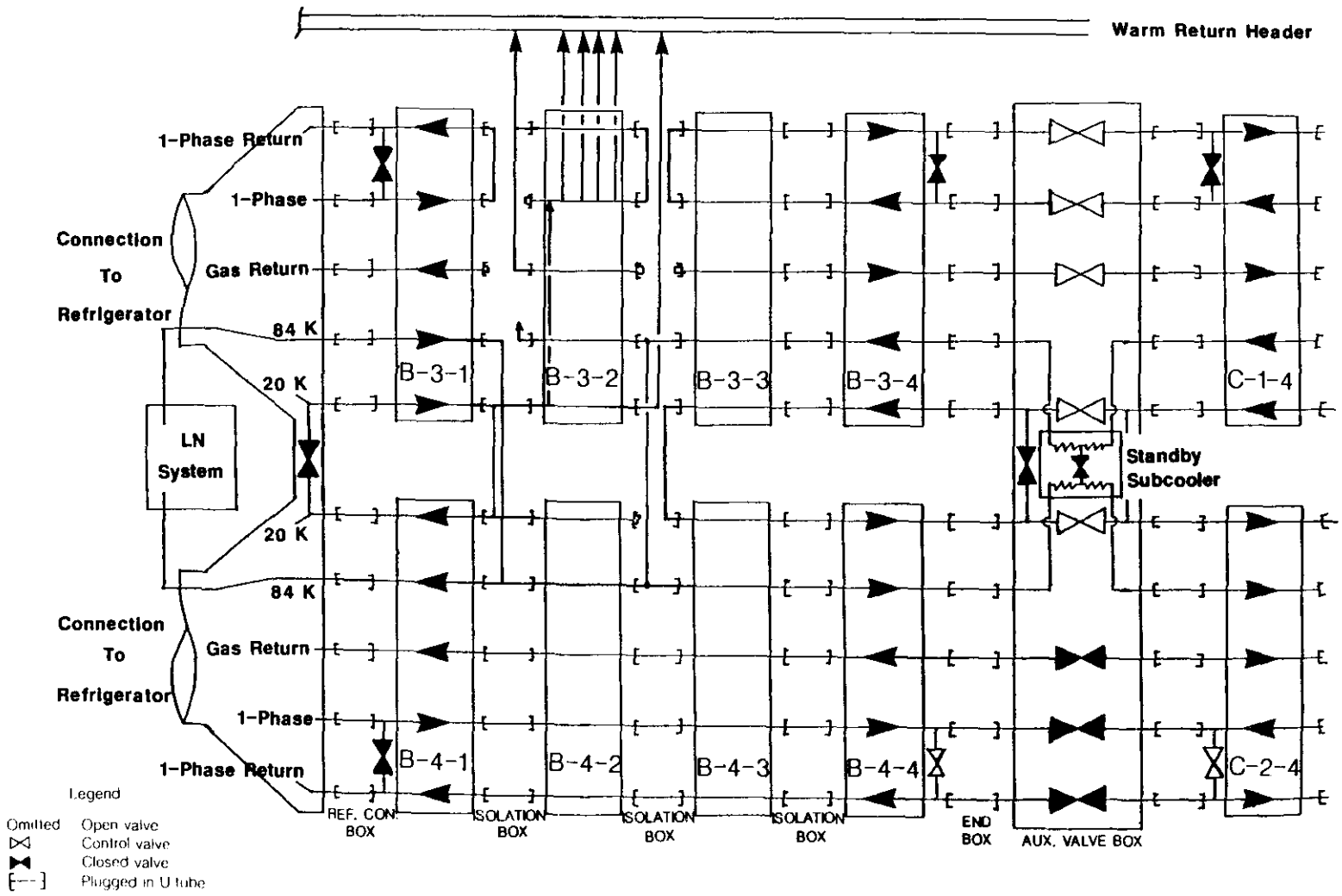

Figure 5.3-12. Block diagram of half of a cryogenic arc sector showing valve status and flow directions for section cooldown after magnet change procedure. The section labeled B-3-2 is cooled by means of a flow of gas from the refrigeration plant at the left of the picture. This flow is delivered through the 20 K shield line, and after passing through the section is vented to the warm return header through the cooldown valves.

line. This passes into the single-phase space through the quench vent valve, passes down the section, and then out through the cooldown valves to the warm return header. There is more information about magnet cooldown in Section 5.3.8. Small flows through the return lines and the 20 K shield cool these circuits. By load sharing among several refrigerators, enough refrigeration is available to provide this cooldown flow and operate one of the rings at low field or current during the 1.5 days necessary for the section to reach 20 K. At this point the U-tubes are reconnected in the normal operating configuration, and the section is cooled the rest of the way and filled by pumping in liquid from storage. Cold gas produced during this process is vented to the 20 K shield system through the quench relief valves. This final cooling and filling takes about 12 hours. The whole magnet change process takes seven days.

Magnet change is a major undertaking that will be necessary in the SSC only infrequently. Much more common will be minor problems with valves, level gauges, or sensors. Such devices are designed to be maintained without warmup of the cryogenic system. Only depressurization of the single-phase volume is necessary. Depressurizing a single string involves releasing 260 kg of helium into storage, about 6% of the inventory of the string. The temperature drops 0.3 K during this process, so at the end, the string is slightly subcooled. These are safe conditions under which to work on the system, and a valve stem or sensor can be replaced in a routine way. With only the heat leak, the string warms up at the rate of 0.1 K per hour. Repressurization with the liquid helium pump takes 11 minutes. After an additional 30 minutes of circulation, the temperatures in the string are back to normal and ring operation can begin.

Table 5.3-9
Magnet Replacement Time Estimate

1.	Diagnose problem	16 hours
2.	Warmup, get organized	24
3.	Spoil vacuum	1
4.	Disconnect bad magnet	4
5.	Remove bad magnet	2
6.	Preparation for new magnet	4
7.	Place new magnet	2
8.	Align	4
9.	Connect and check electrical	6
10.	Connect and check mechanical	6
11.	Pump down and leak check	36
12.	Hi-pot	2
13.	Cooldown	48
14.	Pre-start check out	8
Total		163 hours

5.3.12 Ring Cryogenic Instrumentation

The control system for the SSC is described in Section 5.13. A significant number of the monitoring and control points of the system are concerned with the cryogenics. Of the ring total some 20,000, or about one third, are allotted to cryogenic control of the ring and to refrigeration plant operation. Table 5.3-10 lists in outline the monitoring and control function in a cryogenic sector. In general, cryogenic valves have a temperature measurement, an actuation signal, and a stem status or a stem position measurement associated with them. In the recooler the single-phase helium temperature is measured both into and out of the heat exchanger. There is a liquid level measurement and a control valve in the recooler as well. The flows in the 20 K and 84 K circuits are measured in the end boxes and the temperatures at several points in each string.

Table 5.3-10
Cryogenic Monitoring and Control Functions
for One Sector, Both Rings
(Vacuum System Monitoring Not Included)

Type (number per sector)	Monitor	Control
Quench relief valve (168)	168	336
Cooldown valve		
1-phase (84)	84	168
20 K (32)	32	64
84 K (32)	32	64
Other valves		
end box (8)	8	16
auxiliary box (24)	24	48
lead flow control (48)	48	96
Recooler (88)	264	176
Circuit monitoring (40)	40	
Refrigerator	200	200
TOTAL	900	1168

5.4 Vacuum

The SSC has two major and independent vacuum systems:

1) the beam tube vacuum system,
2) the insulating vacuum system.

The beam tube pressure must be low enough so that it does not effect the luminosity lifetime of the machine. This low pressure is maintained in 93% of the beam tube length by cryopumping on the 4 K walls of the tube. Ion pumps at 192 m intervals provide for gas removal from the cryogenic beam tube and for pressure monitoring. Approximately 7% of the beam tube length is at 300 K and must be pumped at 20 m intervals.

The insulating spaces surrounding the cryogenic components are evacuated to about 10^{-6} Torr (1.3×10^{-4} Pa) to avoid heat conduction by gas molecules from the outer container of the cryostat to the cold components within. After initial pumpdown with portable pumps, self-cryopumping will be the principal means for maintenance of the insulating vacuum. Such a vacuum is very conservative for the purpose. Data from a model cryostat at Fermilab show that the vacuum can be 10^{-4} Torr or worse before any significant heat conduction by the gas occurs (See Attachment B, Section B.09).

Extensive means for continuous pressure monitoring and for leak isolation and detection are provided for both the beam tube and the insulating vacuum systems. Monitoring and isolation devices are linked by the control system to provide equipment-protection interlocking functions and diagnostic information. While the SSC beam tube and insulating vacuum have new features, the existing Tevatron system serves as a useful model in the conceptual design of the SSC vacuum system.

5.4.1 Cold Beam Tube Vacuum Considerations

The reliable performance of the Tevatron has established the basic practicality of a cold beam tube cryogenic pumping system. Primary components of this system are the beam tube itself and its expansion joints, which must accommodate about 5 cm motion in each 17.5 m magnet unit, auxiliary pumps, gas-pressure monitors and associated electronics, in-line isolation gate valves, and secondary valves for pump out and leak detection.

The residual gas pressure in the beam tube must be low enough to ensure adequate beam lifetime as determined by beam-gas scattering and to limit emittance growth from Coulomb scattering. Tevatron experience indicates that desired pressures can be readily achieved in the absence of the beam. However, the intense and energetic SSC beams will initiate a number of mechanisms that can, in principle, increase the residual pressure or partially neutralize the beams, leading to lowered luminosity lifetime and to unwanted changes in the betatron tune. The mechanisms that might increase the pressure are gas desorption by synchrotron radiation, the pressure-bump phenomenon, and beam-induced multipactoring. Cumulative trapping of electrons in the potential well of the beam could, if it were to occur, cause partial neutralization. These topics have received extensive analysis and, especially in the case of synchrotron radiation desorption, experimental testing. None of these phenomena present a fundamental problem for SSC operation.

Gas Desorption by Synchrotron Radiation

The SSC will be the first machine in which synchrotron radiation of significant power will strike a cold beam tube. (See Section 4.7.) Synchrotron radiation desorbs large quantities of gas from even clean and well baked vacuum surfaces. This effect is well known at electron storage rings with room temperature beam tubes. At electron machines this desorbed gas is continuously removed by distributed vacuum pumping. The amount of gas

desorbed decreases with accumulated exposure; thus at electron machines with gas removal, the illuminated surfaces are eventually cleaned of desorbable gases.

Distributed pumping to remove desorbed gases permanently would be expensive for the SSC because of the need to enlarge the dipole coils to accommodate pumps. Hence desorbed gases, although they will be cryopumped by the cold beam tube walls, will largely remain in the SSC bore. As discussed briefly in Section 2.4.5, an experiment was performed at the National Synchrotron Light Source (NSLS) at Brookhaven National Laboratory to determine the pressure within a cold (4.5 K) beam tube irradiated by synchrotron light, [5.4-1]. The experimental apparatus is shown schematically in Fig. 5.4-1. Synchrotron light from the vacuum ultraviolet (VUV) electron storage ring at NSLS illuminated one side of the 4.1 m stainless steel tube and the desorbed gases were detected by quadrupole mass spectrometers, shown in Fig. 2.4-10. More than 90% of the incident light was absorbed by the test tube, thus simulating the SSC, where all the light is eventually absorbed.

The synchrotron radiation from the VUV ring is capable of matching the 284 eV characteristic energy and 0.1 W/m power density of the SSC synchrotron radiation. The vertical divergence of the VUV ring light, however, is a factor of fifteen greater than the SSC light. This results in the preferential exclusion of very low energy ($\sim$ 1 eV) photons from the test beam tube. Fortunately, low energy photons were found during the experiment not to be effective in desorbing gas.

The predominantly desorbed gases were found to be H_2 and CO. The pressures extrapolated to the SSC bore for these gases and the luminosity lifetimes (from residual gas nuclear scattering) they imply are listed in Table 5.4-1. An upper limit only is reported for the H_2 pressure as the extrapolation for this gas is subject to uncertainties due to its non-condensability in the warm ($\sim$ 70 K) housings of the mass spectrometers. An upper limit calculated from known sensitivity is also reported for CO_2 which was expected but not detected. The lifetime limit for H_2 is an order of magnitude greater than the lifetime from collisions in the interaction regions. Thus gas desorption by synchrotron radiation appears to present no problem to SSC operation.

Table 5.4-1
Gas Pressures Resulting from Synchrotron Radiation and Associated Luminosity Lifetimes

Gas	Pressure (Torr)	Lifetime (Hours)
H_2	$<8\times10^{-9}$	>150
CO	1×10^{-10}	2300
CO_2	$<2\times10^{-11}$	>5000

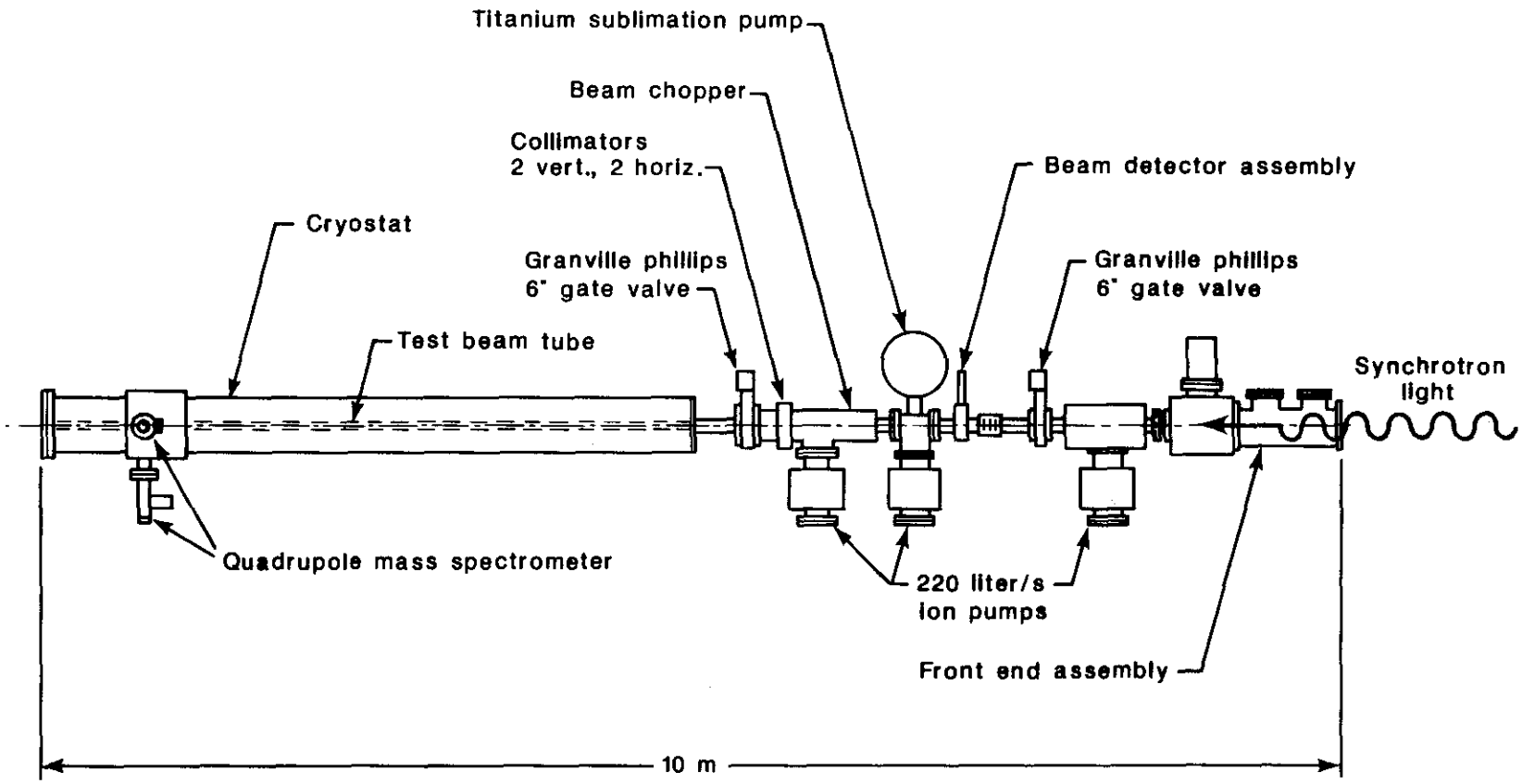

Figure 5.4-1. Schematic of the photodesorption experiment. The synchrotron light is incident from the right. It impinges at a glancing angle at the beam tube at the left. The desorbed gas molecules are detected by the two quadrupole mass spectrometers at the left. Photographs of the apparatus are shown in Fig. 2.4-10.

The effect of a magnetic field, which will be present in the SSC, was not investigated by the experiment. As photodesorption is thought to proceed via photoelectrons, a magnetic field could be a factor. This effect will be investigated in the near future by a U.S.-Japan collaboration at KEK.

Beam-Gas Multiple Coulomb Scattering

Although negligible beam loss occurs from single coulomb scattering of the beam protons by the residual gas nuclei, the random accumulation of a large number of small-angle scatterings causes emittance growth. Using the partial pressures given in Table 5.4-1, one finds that each proton beam takes more than 400 hours to traverse a radiation length of the gas. As discussed in Section 4.6, the corresponding emittance growth does not pose a problem for the SSC.

Pressure-Bump Phenomenon

A pressure rise can occur when positive ions, created by the beam protons, are driven into the wall, desorbing gas molecules lodged there. The process can be regenerative if a certain beam current threshold is exceeded. This threshold increases as the pumping speed increases and is inversely related to the ionization cross section and to the desorption coefficient. It is independent of the initial gas pressure. Formulas for estimating the threshold beam current in a cold beam tube system are given in [5.4-2] and [5.4-3]. Predicted threshold values vary depending on the velocity of the desorbed molecules, but they remain above 1 A, compared with a beam current of about 0.07 A for the SSC. As currents comparable to those for the SSC have already been accelerated in the cold beam tube of the Tevatron, and since many amperes of circulating beam were stored in the ISR with a cold beam tube insert without observing this phenomenon, we conclude that it should not trouble the SSC.

Beam-Induced Multipactoring

Electrons released in beam-gas ionization events can be accelerated by the beam itself. These electrons strike the walls, emitting secondary electrons that can be accelerated by the electric field of subsequent bunches. If the secondary emission coefficient is large enough, a particular relationship between the bunch spacing and acceleration can cause a resonant buildup of the secondary electrons leading, for example, to the multipactoring observed in microwave cavities. Desorption induced by the resonant electrons can cause a pressure rise, as was seen with bunched beams in the ISR during experiments with a cold aluminum vacuum chamber [5.4-4]. This effect was not otherwise seen in the ISR and its occurrence was attributed to the high secondary emission coefficient of the aluminum oxide layer that invariably covers aluminum surfaces, a conclusion verified by laboratory experiments in which the beam was simulated by a coaxial electrically-pulsed wire [5.4-4]. The coefficient of secondary emission for naturally occurring aluminum oxide varies from 2 to 10, whereas for cleaned stainless steel and copper it is typically 1.2 to 1.3. No beam-induced multipactoring has been observed in proton accelerators with stainless steel vacuum chambers, and it is not expected from the copper lining of the SSC.

Partial Neutralization by Trapped Electrons

Some fraction of the electrons produced in ionizing collisions between beam and residual gas can be, in principle, trapped by the potential well of the beam. The consequent partial neutralization of the beam can lead to a shift in the betatron frequency. Requiring that the tune shift be limited to 0.01 limits the fractional trapping neutralization to 0.001 according to calculations based on [5.4-5].

Such a tune-shift effect was observed at the ISR and has been analyzed in detail [5.4-5]. However, the ISR was a continuous-beam machine with a constant beam potential well. In the SSC the trapping potential is pulsed at the bunch frequency and further modulated by abort gaps.

Given the upper limit for the hydrogen pressure determined by the photodesorption experiment and given the ionization rate in hydrogen gas, each proton would produce less than 10 ions/second. If there were no removal of the ionization electrons, a proton bunch of 7×10^9 protons would be neutralized to a fractional level of 0.001 in about 100 μs, a time during which some 6000 bunches traverse each given region. For a cylindrical beam distribution model, less than 2×10^{-5} of the ionization electrons produced by one beam bunch actually remain after the next beam bunch passes. The remaining electrons are moved at least a factor of 20 in radius away from the beam center toward the beam tube wall during each subsequent bunch traversal. Sufficient electron trapping in stable orbits to yield a fractional neutralization approaching 0.001 is therefore unlikely.

The Sp$\bar{p}$S, the FNAL main ring, and the Tevatron have bunched beams with current and spacing comparable to the SSC beam. Time-varying tune shifts of 0.01, easily noticeable during the delicate process of slow extraction, have not been observed and are thus not expected in the SSC.

RF Impedance Considerations

In addition to the requirements mentioned above, the vacuum chamber components must present a low electrical impedance to the beam in order to avoid instabilities as discussed in Chapter 4. As shown there, a beam tube coating of about 0.1 mm thickness of copper with a residual resistance ratio of 30 will suffice in the frequency range defined by potential instabilities from 1 kHz to several GHz. (Relative resistivity ratios in excess of 50 have been measured for test copper plated beam tubes at 6 tesla.) Low impedance is likewise required of the beam tube expansion joints and in-line gate valves. In the conceptual design we have assumed engineering solutions similar to those now applied in electron storage rings where the impedance requirements are more severe. In these accelerators, sliding, low-profile rf liners are used at the expansion joints, and rf liners move into place in the beam tube as valves are opened [5.4-6]. These solutions have proven effective at room temperature, but R&D is needed to apply the techniques to a cryogenic machine.

Helium Leaks Into the Beam Tube

We assume that room temperature helium leaks can be detected with a sensitivity of 10^{-11} Torr·liters/s. Liquid helium can be expected to have a leak rate higher by a factor of 1000 or more than room-temperature gas. If the cold helium leak rate were 10^{-8} Torr·liters/s then, with a beam tube conductance of 2.1 liters/s at 5 K and with 192 meters between ion pumps, the helium would initially plate out to a monolayer over about 1% of the surface. It would then advance in its coverage at a rate of about 12 m/day until it

reached pumps in both directions and finally built up a triangular pressure profile with a peak pressure of 2.2×10^{-7} Torr.

The photodesorption experiment measured the pressure rise resulting from synchrotron light falling on a 1% helium monolayer surface coverage. The measurements imply a pressure rise of 0.5×10^{-7} Torr for 70 mA of SSC beam current. An average helium pressure of approximately 1.6×10^{-7} Torr (corresponding to the above postulated leak plus the desorbed gas) cannot be tolerated around the entire ring; however, a few local pressure bumps of this magnitude will not significantly affect the beam lifetime.

5.4.2 Cold Beam Tube Design

The above considerations have led to a cold beam tube with the following design features:

(a) For rf conduction requirements it has a copper layer of about 0.1 mm thickness.
(b) To keep gas desorption by synchrotron radiation acceptably low, the tube is treated as an ultra high vacuum part.
(c) Penetrations (such as for ion pumps) require an rf grill.
(d) All beam valves require rf liners that move into place when the valve is open.

Pumpdown

There are no permanently installed roughing stations. Instead, roughing is accomplished by the same mobile turbo-molecular pumpcarts that are used for the insulating vacuum system pumpout (see Section 5.4.5).

Pumpdown stations consist of a 40 mm all-metal hand valve backed up by a 40 mm O-ring hand valve at every spool piece, corresponding to one set of valves per half cell per ring. Near interaction regions where there is no cell structure, a similar spacing is used. There is also an extra hand-valve set at each cryogenic break point, i.e., on either side of the beam tube isolation valve at this point. The number of hand-valve sets is then 1792. In 24 hours of pumping at room temperature, a pressure of 10^{-4} Torr can be achieved in the beam tube. Cryo-pumping completes the pumpdown.

Beam Valves

Beam valves occur every 5 cells and at the boundary of each cryogenic loop. Whenever it is necessary to replace a cryogenic element, a section of 5 cells is brought to room temperature. With this spacing, it is possible to have warmup and cooldown times on the order of one day and two days, respectively. There are a total of 160 beam valves in the cold system. (Beam valves in the interaction regions and the utility straights are counted separately in the warm beam tube section below.) In addition, a burst disk is installed at the pumpout port closest to each beam valve to guard against overpressuring the beam tube if accumulated frozen gases in the beam tube are warmed. The beam valves are at room temperature and have an rf sleeve connecting to the beam tube on either side when the valve is open.

Ion Pumps

Ion pumps are used on the beam tube for pressure monitoring, for valve interlocks, and to stop the progress of helium in case of a leak. There is one ion pump at the hand-valve location of every full cell for each ring. For the cold beam tube near the interaction and utility regions the pump spacing approximates the 192 m full cell spacing. As in the case of the pumpout hand valves, there is an ion pump on either side of the warm beam tube valves at cryogenic break points. The total number of ion pumps is 1024.

Electronics

Every pair of ion pumps is served by a printed circuit card that contains two high-frequency high-voltage generators, circuits for monitoring the pump currents, the hard-wired valve interlock for each beam tube, and readout and control circuitry. A separate card controls and monitors the two beam tube isolation valves (one per ring) at each cryogenic break point. The cards reside in the same rack as the electronics for the cryostat vacuum, quench protection, beam position, and beam loss systems.

5.4.3 Warm Beam Tube Vacuum Considerations

About 7% of the complete beam envelope is at room temperature in the utility straight sections and in the interaction regions. Additional warm regions are the injection and abort lines. Requirements for these parts of the system are similar to those for existing accelerators and storage rings having room temperature beam tubes.

To determine the required pressure in the interaction regions, we estimate the background flux for a N_2 pressure of 10^{-9} Torr. Assuming a multiplicity of 50 and a total beam current of 140 mA (sum of both beams), beam-gas interactions from a 100 m length give a background flux of 1.4×10^7 particles/s. This flux should not be a problem for detectors, either at the trigger or the analysis level. However, it is easy to improve the gas pressure in the vicinity of the detectors; pressures of 10^{-10} Torr are feasible. Since the low-beta quadrupoles near the interaction region produce very little synchrotron radiation, the pressure in the quadrupole bores is likely to be better than 10^{-12} Torr. Therefore background particle flux due to beam gas interaction poses no serious problem for the SSC interaction regions.

Pressures of 10^{-9} Torr N_2 equivalent are adequate for utility straight sections. Pressures in the injection and abort lines can be higher as they are one-pass beam lines.

5.4.4 Warm Beam Tube Vacuum Design

The room temperature sections of the beam tube are the regions near the interaction points (approximately ± 200 m), the utility straights (1070 m each), the injection lines (800 m each), and the abort lines (1400 m each). The utility straights contain the injection and abort optics as well as the rf systems. At present there are four interaction regions, two utility regions, and two future interaction regions. The future interaction regions are similar to the utility regions.

Beam Pipe

The room temperature beam pipe is 10 cm diameter stainless steel. A copper inner layer (as used elsewhere for rf impedance reasons) may be required even though this diameter is considerably larger than the rest of the bore. Transitions to smaller diameters are cones having an opening half-angle of 30 degrees or less. All flanges are of a copper knife-edge design, except where size or quick replacement (to avoid radiation exposure of workers) is a concern.

All components are conditioned by a bakeout either prior to or after installation. Near the interaction regions, the system is baked at 400 C after each exposure to atmosphere. Elsewhere, including such delicate devices as Lambertson magnets, the warm system is heated to 130 C after each exposure to atmosphere. Only ultrahigh vacuum compatible materials are used.

The two abort beam lines are special. They flare from approximately 5 cm to 2 m diameter over their 1400 m lengths. A double window of titanium with a trapped gas volume between separates the beam tubes from the beam dumps. The abort beam lines have acoustic baffles to disperse a shock wave if a window rupture were to occur and to aid in matching the relatively poor vacuum of the abort lines to the high vacuum of the ring beam lines. Each abort line also has a fast closing emergency valve in case of a rupture of a window. The material for the larger diameter low vacuum portions of the lines is regular steel, instead of stainless steel.

Pumpdown

No permanent roughing stations are installed. Instead, mobile turbo-molecular pump carts, equipped with cold traps, are used for evacuation. These are the same carts used for the cryostat vacuum system. Pumpdown time takes less than 24 hours.

Pumps

Vacuum in the room temperature beam tubes is maintained primarily by titanium sputter-ion pumps, with specialized pumps, such as non-evaporable getter pumps, used occasionally near interaction regions. Titanium sublimation pumps are also employed where appropriate.

Sputter-ion pumps are required as follows:

(a) There are 5 rf cavities per ring, with three 150 liter/s pump on each one and at the ends, for a total of 34 ion pumps for the two apertures.

(b) There are 66 m of abort Lambertson septum magnets and 25 m of injection Lambertson magnets per ring, for a total length of 181 m. There is one 20 liter/s pump every meter in the Lambertson septa for a total of 181 pumps.

(c) For other straight beam pipe sections (about 12000 m for the total of both rings and the injection lines) there is one 20 liter/s pump every 20 m, or approximately 600 pumps for both rings.

(d) There are five 150 liter/s pumps per abort line for use in the acoustic baffles for a total of ten pumps for both abort lines.

Valves

There is a beam isolation valve at every warm/cold transition. At interaction regions an additional four valves are budgeted for a total of 12 valves at each interaction region. Also four extra valves are assigned to each utility straight per ring above the six that would be there for warm/cold transitions. Each Lambertson magnet string has a valve at each end for a total of eight. The injection and abort lines have five and two valves for each ring respectively. This totals to 150 warm valves. These valves are 10 cm gate valves with rf fingers and O-ring seals, except in the immediate vicinity of the interaction points where the valves have all metal seals to accommodate high bakeout temperatures. Additionally, each abort line has a fast acting valve to seal an abort line in case of rupture of a beam dump window.

Each isolatable section requires a set of hand valves for pumpdown. A set consists of a 40 mm all metal hand valve and a backup 40 mm O-ring sealed hand valve.

Bakeout Equipment

Heaters, thermal insulation, and installed power are necessary to bake the warm beam pipe and Lambertson magnets. For the utility straights including Lambertson magnets, channel heaters and prefabricated insulation jackets are used. The warm beam pipe at the interaction points is heated (to 400 C) by mineral-insulated tubular heaters and prefabricated sleeves. A small number of 3-phase controllers are used on the Lambertson magnets.

Electronics

Each warm ion pump requires a high voltage generator along with circuits for readout and control and for monitoring the pump current. Also, each automatic warm tube beam valve has circuits for valve control and readout of valve status. Circuits for individual pumps or valves are grouped on printed circuit cards as feasible to reduce costs.

5.4.5 Insulating Vacuum

After initial pumpdown by portable units, cryopumping by the cold parts of the cryostat maintains the pressure needed to ensure adequate insulation. This is current practice in most large cryogenic systems.

Pumping: Mobile Turbo-Molecular Pump Carts

Mobile pumping systems will be used for three purposes:

(1) Initial pumpdown during installation and prior to cooldown. Cryostats are concatenated as desired by flexhose jumpers to each cart. Pressures while warm are not expected to drop much below 10^{-2} Torr in most places.

(2) Initial leak checking. The carts when equipped with mass spectrometer heads and electronics become highly sensitive leak detectors. A cold trap increases their pumping speed for condensable gases.

(3) Leak control. Leaks left in the machine because they are too small to be detected when warm can be rendered ineffective by installing one or more mobile turbomolecular pumping carts near the leak. This technique is now in use at several places at the Tevatron.

The mobile turbo-molecular pumping carts consist of a roughing pump, a turbo-molecular pump, a cold trap (for use during leak checking and on ultrahigh vacuum systems), a gate valve with associated interlock controls, and suitable pressure gauges. The gate valve will close upon power failure, turbo-molecular pump failure, and/or roughing pump failure. The cart forms a self-protected system. It is connected through an umbilical cable to the nearest electronics station for monitoring and control. Figure 5.4-2 is a sketch of such a pump cart. There are a total of 200 such carts, a number sufficient to bring one refrigerator sector on line with a 20% contingency.

Cryostat Vacuum System Components

Figure 5.4-3 shows the components of both the cryostat and cold beam tube vacuum systems at the boundary of a full cell. The cryostat for each spool piece has a vacuum barrier to facilitate leak checking and to contain the damage if there is a catastrophic system problem, such as an arc discharge that ruptures the helium vessel wall. The spool piece has a Pirani gauge and cold cathode gauge for the cryostat vacuum. Each dipole cryostat and each spool-piece cryostat has a hand operated O-ring sealed pumpout valve. At alternate spool locations there are electronics racks that are part of the control system and contain printed circuit cards, each with the electronics for two Pirani gauges, two cold cathode gauges, and a turbo-molecular cart interface.

Each spool location also has 480 V 30 A 3-phase power, 110 V ac power, and compressed gas with a local ballast tank. The power is used to run pump carts and on occasion to bakeout room-temperature devices. The compressed gas is used to operate the remotely controlled beam tube isolation valves and the fail safe pump cart valves.

5.5 Magnet Power Supplies and Quench Protection

5.5.1 Magnet Power Supplies

The magnet power supply system energizes the two magnet rings that constrain the colliding proton beams of the SSC to closed orbits. The rings are one above the other and are powered independently to allow separate operation. They are further divided into ten isolated circuits per ring congruent with the cryogenic circuits; four sectors in each of the two arcs, and one in each of the two sections that contain the interaction regions (IRs) (Fig. 3.3-2). Each of these major circuits contains one 300 V, 6.5 kA power supply. This segmentation greatly simplifies installation, commissioning and maintenance, but complicates magnet current regulation because the magnets are not powered in series as a single circuit.

Operating experience with the Sp$\bar{p}$S collider and calculations of allowable tune modulation and emittance growth indicate that the tracking between the quadrupole and dipole magnets, and from one sector to another, have to be a few parts per 10^5. This regulation tolerance limits the tune spread to less than 0.002. Since the dipole magnets are in series with the quadrupole magnets, the tracking in a sector is automatically taken care of except for saturation effects in the dipoles. In the SSC magnets this saturation effect is about 2% at peak field and is compensated by the correction quadrupoles.

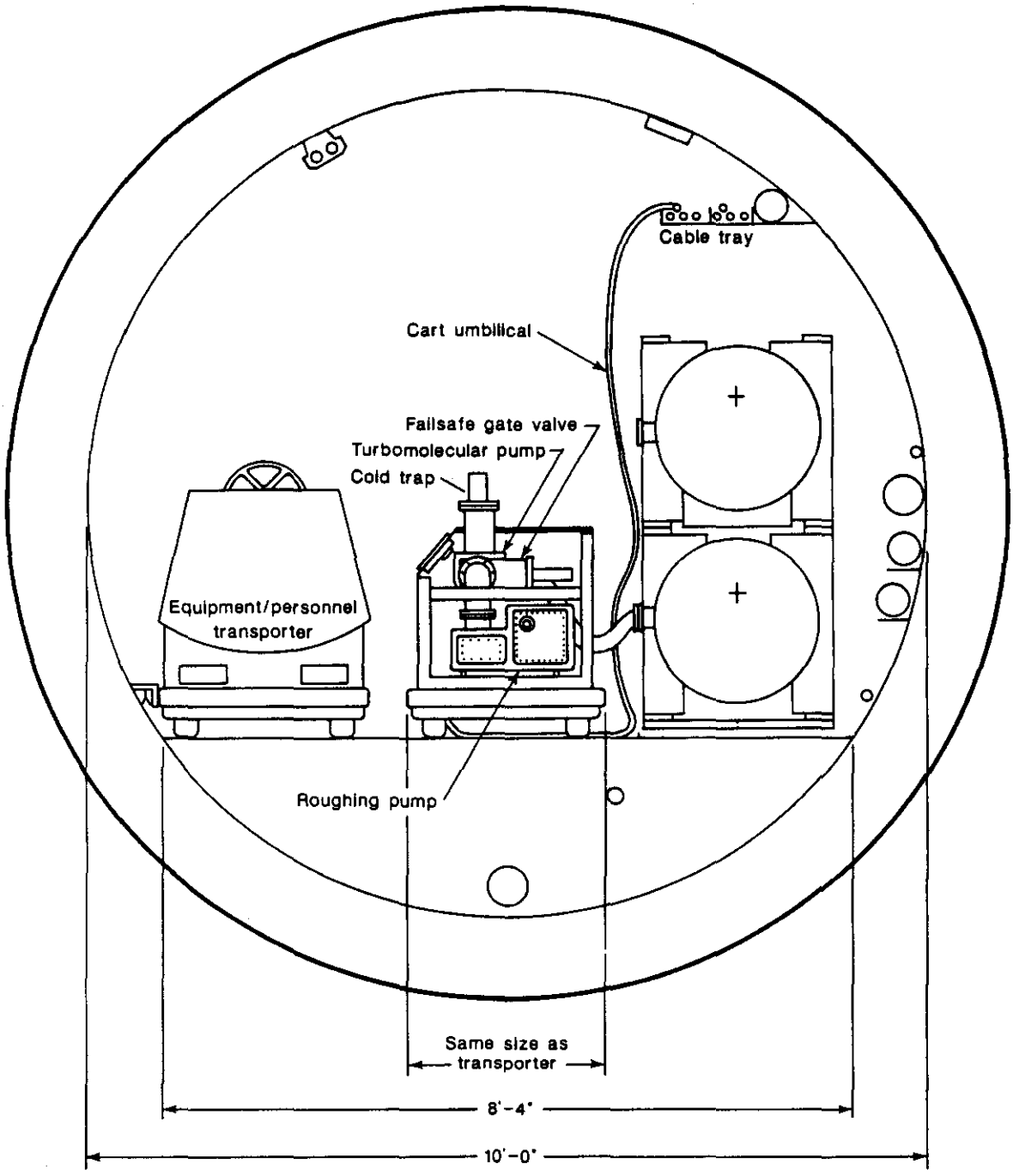

Figure 5.4-2. Sketch of a mobile turbomolecular pump cart consisting of a roughing pump, a turbomolecular pump, a cold trap, and a gate valve with associated interlock controls.

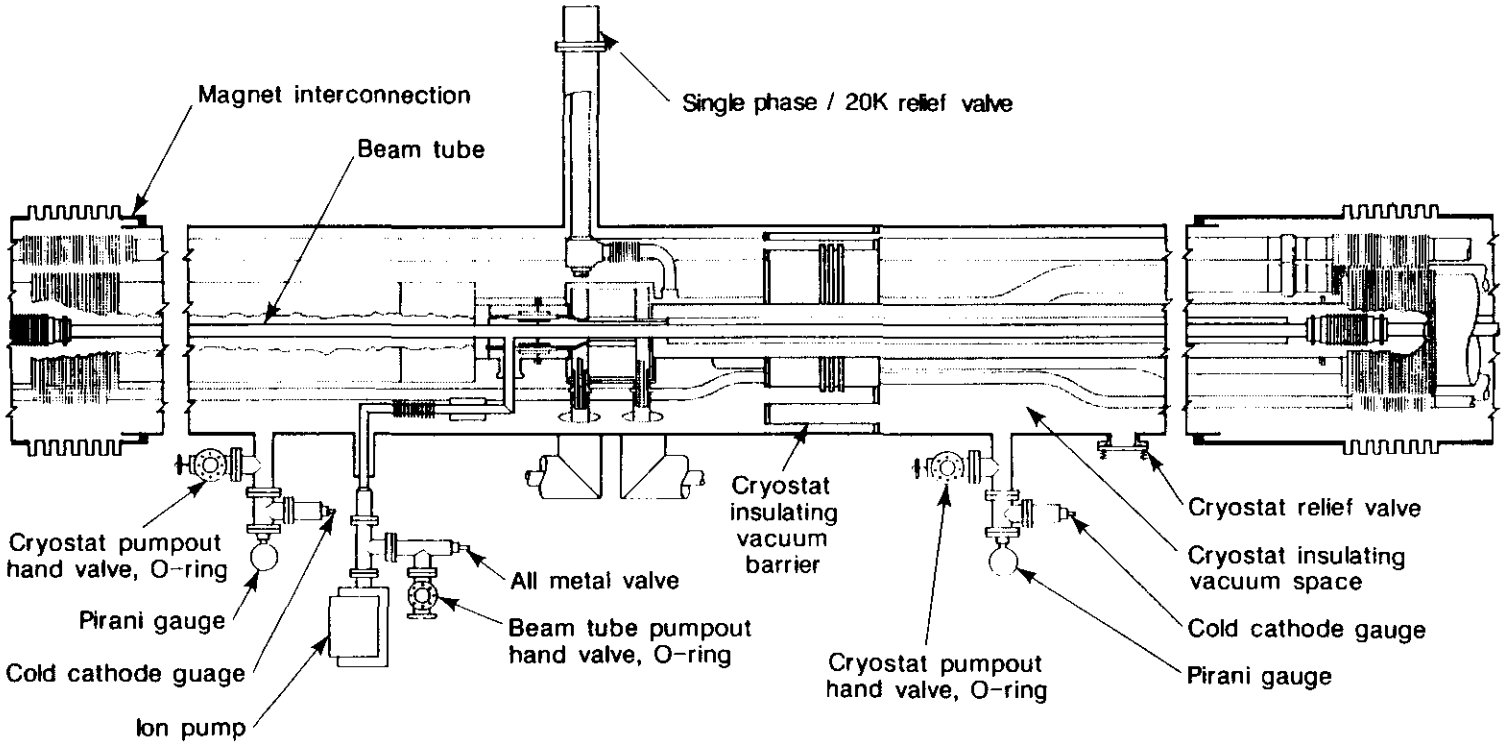

Figure 5.4-3. The valves, instrumentation, and piping for the vacuum at a full cell boundary.

A magnet current regulation tolerance of a few parts in 10^5 presents an interesting design challenge because ten separate power supplies are coupled together by differential transductors to provide the dipole and quadrupole magnet current. Assuming that the current errors of the sectors are random, each power supply must then regulate to a factor of $\sqrt{10}$ better than the overall regulation requirement. One way around these random errors would be to connect the entire ring in series with ten equally spaced power supplies, with all except one operating in the voltage control mode and with the remaining one operating in the current regulation mode, thereby closing the current regulation loop. For the specified ramp rate of 6 A/s, the total power supply voltage requirement of less than 1500 V, including the power lead drops, is easily satisfied. However, the single loop solution requires at least nine high current thyristor switches as used in the Tevatron power supply system. These switches must act reliably during upset conditions to limit voltage to ground by isolating the faulty sector from the circuit. Communication is also required to 40 dump circuits distributed around the ring that need to actuate synchronously. To eliminate these complications, and to obtain the obvious operational advantage that results from separate sectors, the independent power supply option has been adopted. The necessary degree of regulation can be achieved.

Regulation

The ability of the SSC power supply system to provide a current in response to a command value from the control system is limited by four main effects:

1) The transductor that measures the current flowing in the magnet bus has both an offset error and a gain error in its conversion of current to voltage.
2) The regulation loop has finite gain, built-in offsets, and limited bandwidth.
3) Control systems typically provide digital information that must be converted to analog voltages for use by the error amplifiers in the power supply regulation loops. This conversion has a finite error.
4) Because of the scale of the SSC magnet structure, transmission line effects set a lower limit on the current tracking error in a sector during ramping. Because of the large magnet inductance, this transmission line effect sets a lower limit of $\Delta I/I > 1 \times 10^{-5}$ for the expected ramp rate.

A scheme that accomplishes the necessary tracking accuracy is shown in Fig. 5.5-1. One of the circuits is declared to be the master. The current in this circuit is regulated in a conventional manner similar to the regulation method used in the Tevatron. Every sector's power supply receives identical current and voltage program signals from the control system, giving them equal opportunity using identical regulator electronics to run at the desired current. However, every circuit is expected to have its own offset and gain errors, causing the actual current to depart somewhat from the desired program.

This situation, if left alone, would demand extraordinary precision in all of the regulation circuits in order to have the field tracking from sector to sector be acceptable. Therefore, at the ring location where two sectors join, a differential current transductor mounted on the current buses of both sectors will directly measure the difference in sector currents. The two sectors adjacent to the master sector use this difference measurement to make a regulation correction, bringing their currents in much closer agreement with the master sector. A sector-to-sector tracking improvement on the order of 10^2 to 10^3 can be realized by

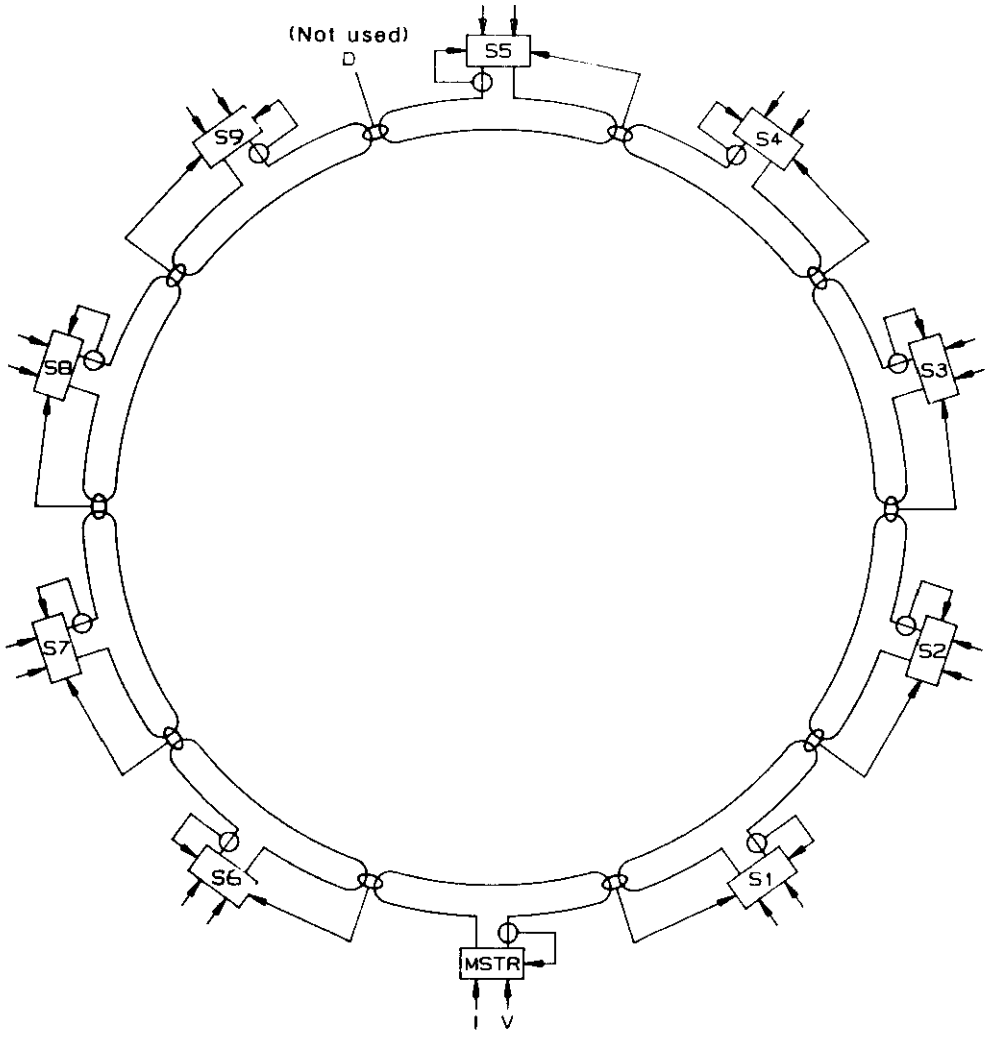

Figure 5.5-1. The layout of the master power supply and nine slave power supplies for the main bus of one ring. Each power supply is current regulated, following the same program as the master, and also receives an error signal from a transductor that measures the difference in current between it and one of its neighbors. The regulation loop is not closed between sectors S5 and S9.

this technique. These two sectors then pass along their secondary current references to the next two sectors, etc., until all of the sectors are coupled. The regulation loop is not closed at the last sector boundary in the ring. However, the current difference is measured to check the overall performance of the system. The remaining tracking errors expected in this system are typified in Fig. 5.5-2 which displays the errors calculated in a SPICE simulation [5.5-1] using realizable regulation systems and the magnet load parameters determined from the prototype SSC magnet. This simulation included a total ring circuit and the transmission line behavior of the magnets with damping resistors.

Preliminary indications are that sensing the currents and providing the digital to analog command voltages in each sector are straightforward at a part in 10^5 level. Using the high gain differential transductors and taking proper account of the delay line characteristics of the magnet, it appears feasible to link the individual power supply loops around the ring to achieve the required overall few parts in 10^5 average tracking tolerance during colliding operation for the 6.6 T design.

Transient Response

Another feature of magnet power supply systems that is often overlooked with painful consequences is the transmission line behavior caused by the magnet inductance and shunt capacitance. The cutoff frequency of these transmission lines can be in excess of several tens of kHz. It was observed during commissioning, that the Sp$\bar{p}$S collider had a dramatic sensitivity to switching noise spikes from the power supply that caused field spikes at the milligauss level and excited the first betatron resonance at 12 kHz. The Sp$\bar{p}$S magnet as a transmission line has a low-pass cutoff at 50 kHz, so these noise spikes were transmitted without adequate attenuation by the magnet system. Installation of a low pass filter on the power supply output eliminated these spikes and improved the luminosity lifetime by 30%. A preliminary analysis of transmission line effects in the SSC magnet shows that propagation of signals by the magnet transmission line can be damped simply by including a shunt resistance across the magnets at each quench protection bypass diode. These resistors may pose a commissioning and operational difficulty when measuring coil leakages unless it is possible to disconnect them. Although it may be simpler to provide well filtered power supplies, the shunt resistors are necessary to improve the transient response of the magnet circuit to assure the necessary current regulation.

To analyze the transient response of the magnet system, the circuit analysis program SPICE has been used with input parameters of inductance and capacitance to ground measured on the 6 T magnet prototype [5.5-2]. That transmission line effects are important is dramatically illustrated in Fig. 5.5-3, which shows the magnet response to a voltage step at the power supply as a function of distance from the power supply. The curves show the instantaneous current as a function of time at different locations along the magnet string with damping resistors in place. The damped oscillation remaining represents a substantial reduction compared to the ringing that is present with no damping resistors. Even more effective damping can be achieved by lowering the value selected for the damping resistor. Since this resistor shunts current around the magnets during ramping, the impact of this effect must be considered in selecting the damping resistor value.

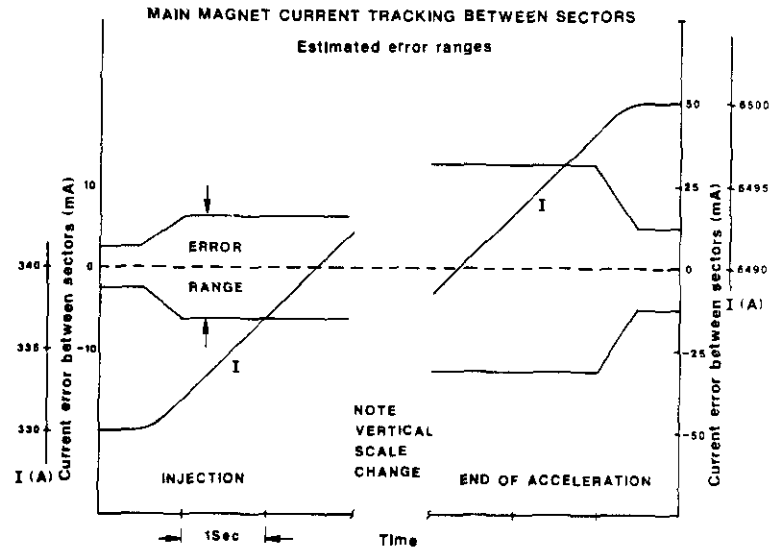

Figure 5.5-2. The range of main magnet bus current errors between sectors during flat-tops for injection and collision, and during ramping, based on the regulation scheme shown in Fig. 5.5-1. This result is from a SPICE simulation and includes transmission line effects. Note that the vertical scales for injection and collision are different.

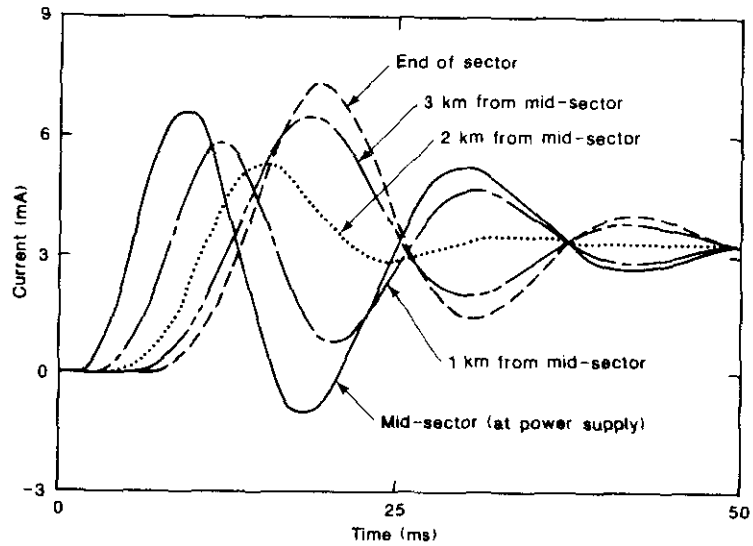

Figure 5.5-3. The effect of the transmission line properties of the magnet string. The curves show the instantaneous current as a function of time at different locations along the magnet string in response to a voltage step of 10 volts at the power supply. The resistance of the damping resistors across each half-cell is 25.5 ohms.

AC Power Requirements

As with any superconducting magnet system, the power dissipation in the magnet power supply system for the SSC is entirely in the room temperature components during steady state operation. This power dissipation is dominated by the voltage drop in the necessary series filter inductance and is typically 12 V for a 800 μH, 6.5 kA inductor. A well designed lead system from the power supply to the magnet will have a total voltage drop of 2 V. In addition, there is a 2 V drop per series switch shunting the dump resistors necessary for the quench protection system. This gives a total voltage drop of 22 V for each power supply circuit. The total power requirement is then given simply by multiplying this 22 V drop by the total current in each circuit and doing the sum. Assuming a power supply efficiency of 90%, this indicates that the main power supply power requirement for the SSC is 3.2 MW for steady operation at 6.5 kA. The reactive power from operating a 300 V SCR-controlled power supply steadily at this 22 V level is excessive, so the detailed design of this power supply system will require a means to reduce this effect to a level tolerable to the power utility. This type of phased-back operation of the power supply can also cause excessive heating in the power components and can subject the power system to high harmonic voltages.

Special Interaction Region Power Supplies

The 20 V, 6.5 kA power supplies used to power the outer quadrupoles on each side of the IRs are conventional twelve phase SCR power supplies with passive filters and a regulation of 1 part in 10^5. One 20 V power supply is used to power four quadrupoles: an element pair in each of the two proton rings. A total of ten 20 V, 6.5 kA power supplies are required for the four IR regions. Eight 6.5 kA superconducting buses span each IR region, four main power supply buses and four buses for the outer quadrupoles. The inner quadrupoles are powered directly by one of the ring buses and six 10 V, 650 A unipolar shunt supplies per IR are used to trim the quadrupole currents.

5.5.2 Quench Detection and Protection

As the magnets are superconducting, some means must be provided to protect them from the consequences of a quench. The coils of the SSC magnets have a relatively high superconductor to copper and electrical insulation ratio in order to achieve high magnetic fields at minimum cost. During a quench, the current transfers from the superconductor to the copper and the now resistive cable has insufficient cross sectional area to prevent the temperature rise that will damage and eventually melt the cable unless the current is rapidly decreased to zero. Care must be taken during the current extraction to assure that the resulting inductive voltage does not exceed the voltage capacity of the electrical insulation.

Similar to the quench protection systems described in Section 5.1.4 of the RDS, the present quench protection design utilizes the combined action of a slow current extraction system and a fast quench bypass system to protect the magnet components. A slow extraction system unit consists of the magnets that comprise the sector, high power electronic and mechanical switches, and resistors which are inserted into the sector magnet circuit after the detection of a quench. The fast quench bypass system consists of warm diodes and external bypass cables which shunt the magnet circuit in increments of a half cell. Heaters imbedded inside the dipole and quadrupole coils are used to distribute and enhance the quench

resistance of a bypass unit. This type of active, heater-assisted quench protection with warm bypass loops is utilized in the Tevatron and has proved very effective and reliable.

Quench Behavior

As discussed in Sections 2.4 and 5.2.3, the availability of superconducting cable with a higher critical current density than has been used in the past allows increasing the operating field of the SSC dipole to 6.6 T without a corresponding increase of the cable cross-sectional areas.

In an active quench protection system, magnets are protected by operating at a low quench detection threshold, with a minimum heater-induced quench delay. By quenching a large enough volume of the magnet coils with the heaters, the time constant of the quench bypass system is small enough to prevent overheating. For the SSC magnets, a reasonable lower limit for the quench detection threshold is probably 0.5 V. This threshold has proved immune to spurious noise in the Tevatron. The heater quench delay and the current bypass rate are in principle limited only by the amount of heater energy storage. However, the space limitation that results from locating the heater power supplies in the tunnel and the desire to increase overall reliability by minimizing the number of electronic components, dictates that the minimum necessary heater system be utilized.

Test data on the spontaneous quench behavior and heater induced quench behavior of a full scale SSC magnet are presently not available. However, calculations have been made using experimental data from 4.5 m models [5.5-3]. Figure 5.5-4 contains the calculated quench voltage (constant current) in a full-length magnet for a quench that starts at the post (top turn) of the inner coil. The behavior for the outer coil is expected to be similar. For magnet currents of 5 kA and higher, a detection threshold of 0.5 V will detect the quench within 32 ms, which is adequate. At lower quench currents, the quench detection delay becomes less critical as the cable heating rate is reduced.

A conservative estimate of the peak quench temperature in a cable as a function of its heating history can be obtained by ignoring heat flow out of the cable (adiabatic approximation). The peak inner and outer cable temperatures for an SSC magnet have been calculated using the adiabatic approximation and are plotted as a function of Miits (1 Miit = 10^6 A^2 s) in Fig. 5.5-5. The curves have a magnetic field dependence because of magnetoresistance.

At a quench current of 6.5 kA, with a 32 ms quench detection delay and a 45 ms heater quench delay, the theoretical maximum temperature that can be reached is 550 K [5.5-3]. An analysis using the expected performance characteristics of the pulsed heaters suggests that the maximum local temperature will be only 350 to 400 K [5.5-4]. A more accurate analysis will require quench velocity data for the outer coil and quench heater performance data.

Quench Detection System

Each sector of the SSC has a separate power supply and refrigeration system. Each of these sectors also has completely independent quench protection. A typical sector contains approximately 80 half-cells of standard lattice elements. The half-cell is considered the fundamental quench protection unit. A pair of half-cells is shown schematically in Fig. 5.5-6. A quench detection unit is located at every other quadrupole in the lattice, monitoring the upper and lower bus circuits of two half-cells in each ring. The twelve analog signals per

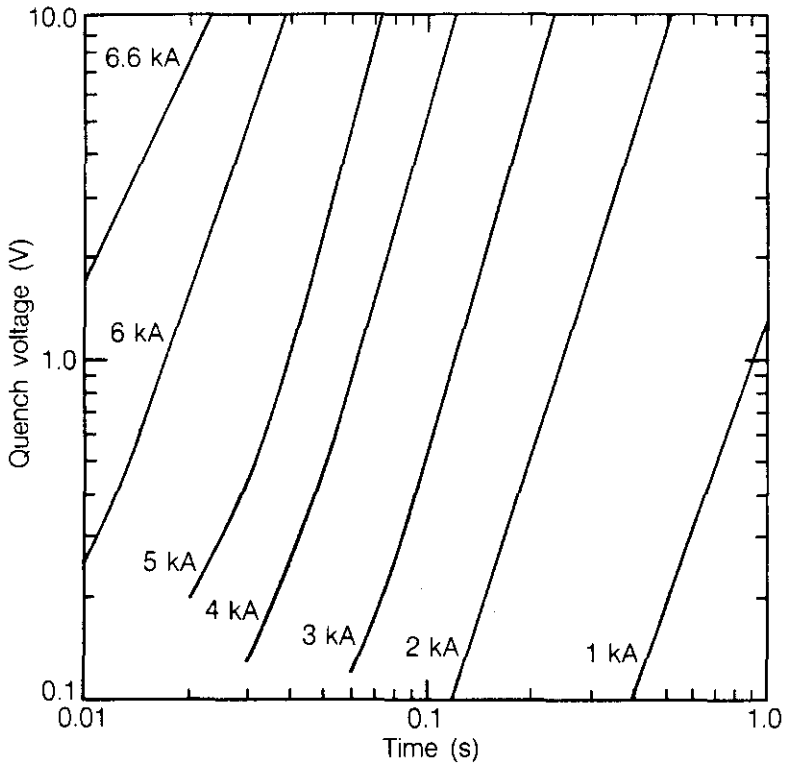

Figure 5.5-4. The calculated quench voltage across a magnet as a function of time for various constant currents. This calculation assumes that the quench started at the top inner coil turn of the magnet.

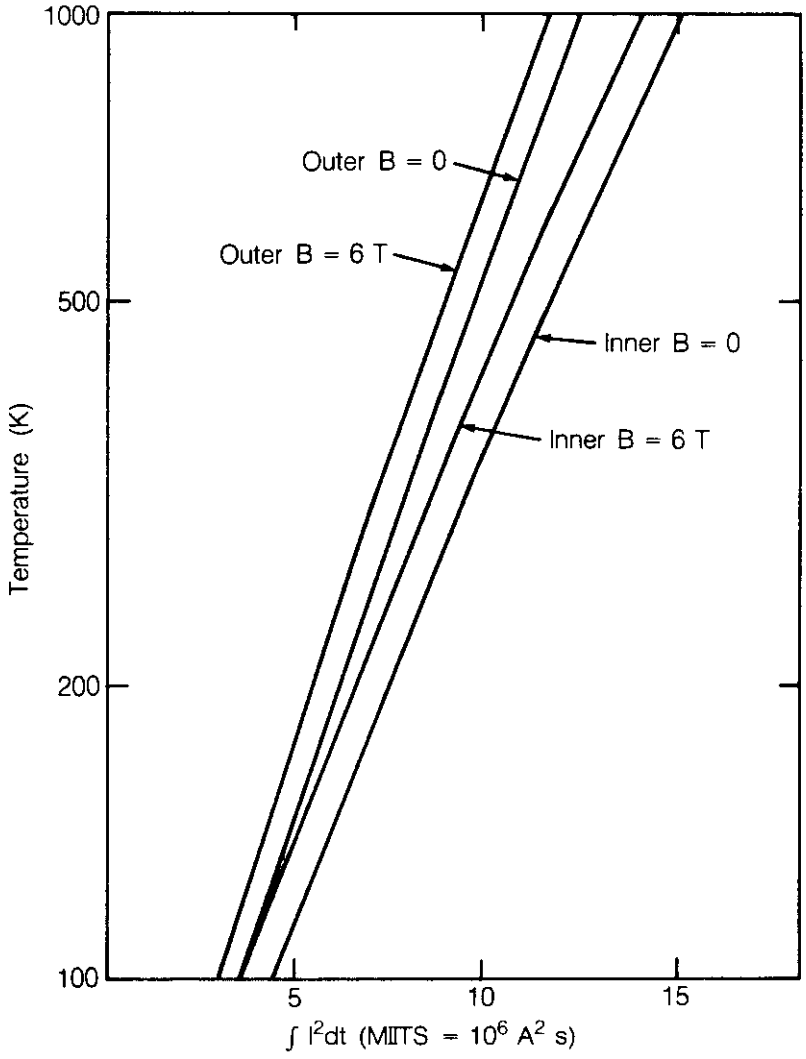

Figure 5.5-5. The peak temperature calculated as a function of Miits (1 Miit = 10^6 A^2s) for the inner and outer cable of the SSC dipole. The temperature has a dependence on magnetic field due to magnetoresistance.

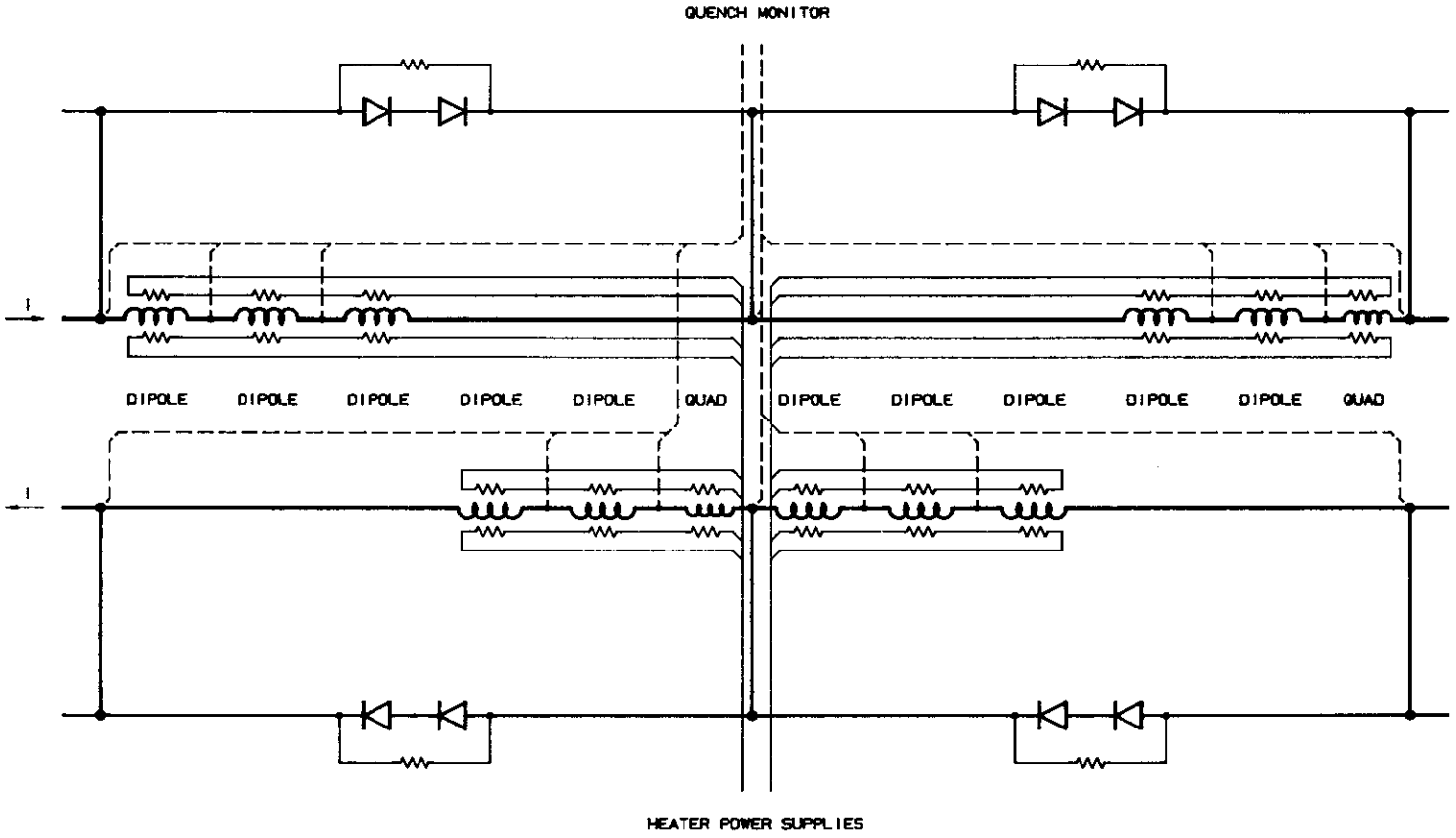

Figure 5.5-6. A schematic of the circuit of a cell of one ring of the SSC showing the alternation of the magnets on the clockwise and counter-clockwise current buses. Also shown are the current bypass diodes and the pulsed quench heater arrangement.

ring, representing the voltage across each of the magnets, are brought out of the cryostat at this quadrupole location, integrated for one 60 Hz power line cycle (17 ms) to eliminate line related noise, and digitized. These twelve signals are compared to each other to determine if any of the magnet sections has a resistive component (i.e., the magnet is quenching) with a detection threshold on the order of 0.5 V. All voltage tap wiring is internal to the magnets; only short cables are needed to connect from the quadrupole to the electronics units mounted overhead in the tunnel ceiling.

A second, backup level of quench detection is accomplished by sending the digitized cell voltages over a serial link to a sector microprocessor where all such signals for the sector are compared with the product of that cell's inductance and the system dI/dt determined from a direct measurement of the magnet current. The comparison allows this processor to guard against symmetrically spreading quenches which might be undetectable in the domain of any single local processor. Determination of a quench by the sector microprocessor results in a message being returned over the serial communications link to the local detection circuit to fire the heaters for the quenching half-cell.

This segmentation allows for more localized heater control than the system described in the RDS and hence minimizes the extent of a spurious quench due to a detection circuit malfunction. A microprocessor located at the power supply controls its response to a quench. Ancillary processors are attached to the serial link at each dump location to provide the correct dump action and to monitor dump readiness. Loss of communication on the link results in system shutdown (power supplies off, dumps activated). The local processors at the alternate quadrupole locations continue to monitor the magnets for quenches. The default response to a failure of a local monitor is to fire the heater power supplies for the two half-cells in its domain. Its failure will interrupt link traffic, resulting in system shutdown.

The serial communication link is a necessary part of the quench protection system. Its existence requires a microprocessor at each of the local protection locations. Any unit capable of serving this function is also easily capable of providing the local monitoring functions for both rings. This unit can also store a limited history of its small number of channels for system trouble-shooting after a quench or other event causing shutdown. The central sector computer stores a more comprehensive set of data for the total sector.

In addition to the serial communications link, a redundant hardwire connection available to all monitors and power supply and dump electronics units provides a "bell-cord" type shutdown capability. All local electronics associated with quench detection or heater power supplies must have battery-backup power with sufficient isolation characteristics to prevent power transients or outages from causing heater activation. The central microprocessor preserves its event history buffer in the event of a power outage.

Energy Extraction

After a quench has been detected in a sector, the sector power supply voltage is reduced to zero, and the sector magnet current is extracted from the unquenched magnets in the sector by inserting four resistors in series with the magnet power bus, as shown in Fig. 5.5-7. These dump circuits are equally spaced along the magnet bus, one each at the ends of the sector and the remaining two in the upper and lower bus at the sector power supply location. Since the load inductance in each of the IR sections is only slightly larger than one-half that in the arc sectors, two dump resistors instead of four can be used in these

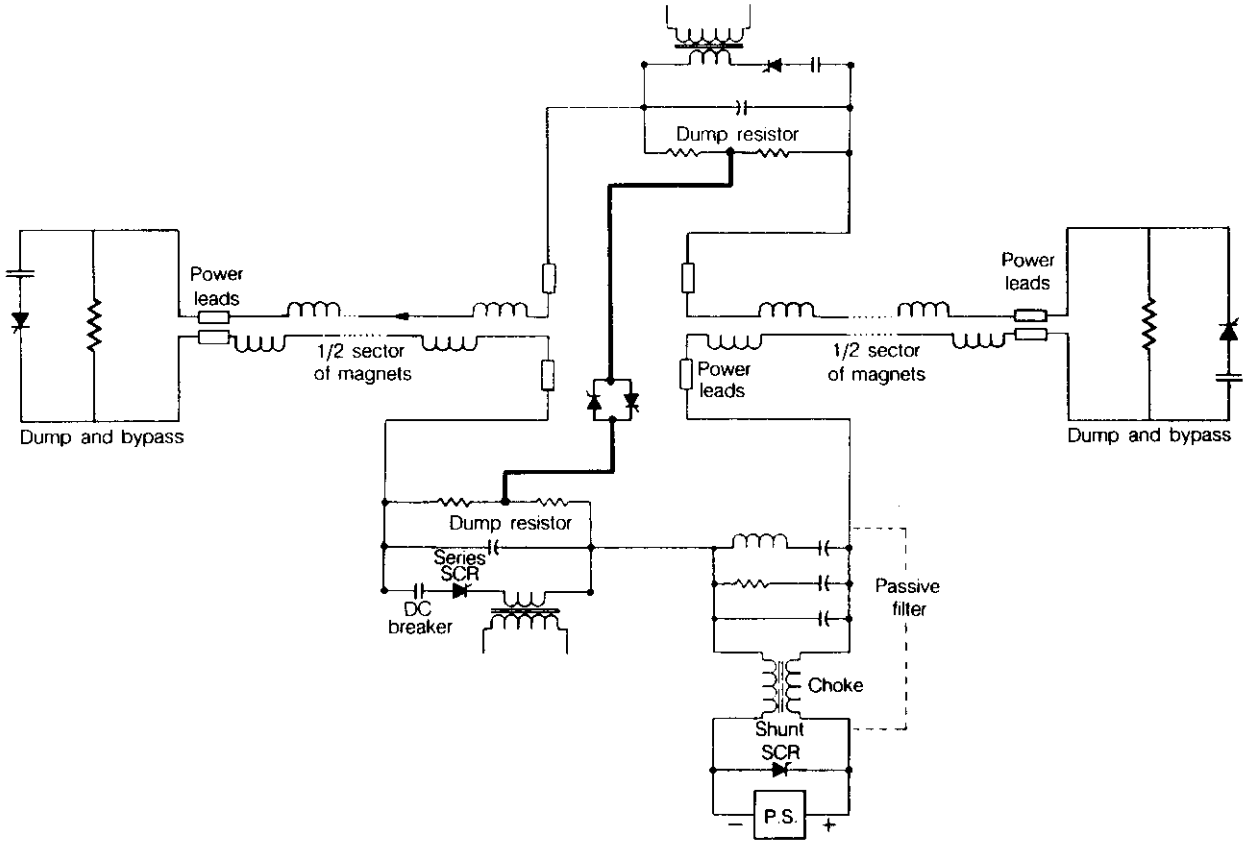

Figure 5.5-7. A schematic of the power supply and energy extraction resistors of a typical arc sector of the SSC. In the event of a quench the four bypass SCRs are opened up, dissipating the energy stored in the magnetic field in the resistors. The bipolar SCR switch connecting the middle of the two center dump resistors shorts the clockwise and counter-clockwise circuits together, effectively isolating the sector into independent left and right halves.

power supply circuits. In addition, a bipolar thyristor switch is used to short the upper and lower magnet bus at the center of the sector. This effectively isolates the two halves of the sector and minimizes the possible voltage redistribution from multiple quenches.

Each of the four dumps has a resistance of 0.28 ohms. With an arc sector inductance of approximately 22 henries, the dump time constant is 20 s. This limits the voltage to ground to 900 V (1800 V with one side of the dump grounded) and results in reasonably sized bypass components. The maximum current decay rate is 330 A/s. The magnets are not expected to quench spontaneously until at least 450 A/s.

The dump resistors and associated electronics reside in the tunnel with each resistor absorbing 116 MJ during a full current dump. A dump failure can double this value. The resistors are directly water cooled or surrounded by a water-filled enclosure. Assuming total heat transfer to the water and a permissible 50 C water temperature rise, a minimum low conductivity water volume of 1100 liters per dump is required. The dump resistor volume is several times larger.

The dump resistors are switched into the magnet power circuit by commutating (turning off) the thyristors that normally short the dump resistors. Direct current contactors that have relatively slow switching times are placed in series with the thyristors in case the thyristors fail to open. The dump switching time is not critical, as the quenching magnets are protected by the local quench bypass circuits. However, the four dumps in a sector must be synchronized to minimize the voltage transients during their activation. The bypass circuit components and dump components are specified to prevent failure even if one of the four dump circuits fails to function.

Quench Bypass System

A schematic representation of a full standard magnet cell is shown in Fig. 5.5-6. The magnets utilize two heavily stabilized buses located outside and extending the whole length of the iron of the magnets to allow the interconnection geometry shown. Connections between magnets are stabilized with additional copper. This geometry eliminates the upper to lower bus magnetic coupling present in a completely symmetric upper-lower coil configuration and places the high upper to lower bus voltages present during a dump on the exterior magnet buses, which are easily insulated.

Independent bypass circuits outside the cryostats are connected to the upper and lower power buses in the magnets and protect each half cell of magnets. Two diodes in series are used as bypass switches as the maximum forward voltage per half cell from the magnet ramp is expected to be approximately 1 V. Such warm diodes are readily replaced in the event of a failure. Every quadrupole location requires two safety leads per ring to connect the warm bypass diodes to the 4 K magnet bus. They are helium-vapor cooled for rapid recovery after a quench and to reduce their heat leak, but of sufficient mass to withstand several bypass cycles without overheating. A single 500 MCM cable is used for each bypass loop. A redundant bypass is not necessary as the diodes are expected to fail in a shorted condition. A dedicated tunnel enclosure located at alternate quadrupole locations contains the bypass diodes for a complete cell of both rings. The diode assemblies have sufficient mass to absorb the energy of the current bypass cycle without overheating. The location of the diodes within the enclosures dedicated to low level electronics would be possible, but would require some means to isolate these electronics from the heat generated within the diodes during a quench.

An alternative bypass system utilizing cold diodes is also feasible. This system was first proposed for CBA and is now planned for implementation at HERA. It could still be adopted for the SSC if present uncertainties concerning the voltage distribution within a quenching magnet and radiation damage to cold diodes are favorably resolved. A cold diode bypass system using one or two diodes per magnet would be attractive if these problems can be solved and if it can be shown that the magnets can be passively protected without quench heaters. This would eliminate the need for quench heaters and heater power supplies. The warm bypass circuit with its safety leads, warm diodes, and bypass cable could then be eliminated or kept as a redundant current path for a failure involving an open magnet bus. The quench detection system and the energy extraction system would be unaffected.

Quench Heaters

Eight heater power supplies are required per magnet cell per ring. Four of the supplies are redundant in case of a power supply or heater malfunction. A power supply delivers 300 J (3 mF charged to 450 V) to three strip heaters distributed within three magnets. The strips are designed to deposit the energy in 12 equidistant locations along the magnet length. The total delay from heater power supply trigger to heater-induced quench is expected to be approximately 45 ms for a 6.5 kA quench, of which 16 ms is from the power supply discharge time constant.

The quench heaters are inserted in the ground insulation contiguous to the outer coils to simplify magnet construction. The inner coil is quenched via heat propagation through the splices and the electrical insulation that separates the inner and outer coils. Each magnet has two heaters on separate power circuits to obtain redundancy. At a 6.5 kA magnet current, the longitudinal quench velocity and turn-to-turn quench delay have terminal values of approximately 50 m/s and 2 ms respectively [5.5-3]. This distributes the quench resistance and reduces the voltage gradient in the magnet through resistive-inductive voltage cancellation. The voltage cancellation will be measured on the prototype magnets. Should it prove inadequate, spot heaters can be inserted in the insulation that isolates the inner and outer coils.

5.6 Correction Element Power Supplies

Correction elements are required in the SSC to provide adjustment of lattice parameters and to correct the effects of systematic and random errors in magnetic field and magnet placement. The types of correction elements and their required strengths are described in Section 4.4. The design and construction details of correction elements and spool pieces are found in Section 5.2.13. This section contains a discussion of the distribution of the various types of correction elements and their associated power supplies and controls.

The SSC divides naturally into two distinct geometries, the main arcs, which are repetitions of the standard cell, and the cluster regions, which contain utility sections and interaction regions, in addition to short sections similar to the arcs. The correction elements also divide along these lines.

5.6.1 Main Arc Correction Elements

Most of the correction elements in each of the main bending arcs are located in the spool piece drift spaces adjacent to each quadrupole, the exceptions being correctors of systematic sextupole and decapole fields that are part of the main dipole construction. There are either 82 or 84 spool pieces per ring in each of the four sectors in an arc. Every spool piece has a 1.5 m long "primary" correction package containing elements that must be located near every arc quadrupole. Twenty of the spool pieces in each sector contain, in addition, 2 m long "secondary" correction packages used for compensating the effects of random multipole errors in the main bending and focusing magnets. Separating the functions that are required at every location from those that are not allows the secondary packages to be placed in the lattice only where they are required. In addition, whenever space is needed for special functions required in the spool pieces, such as cryogenic fluid input, or main 6500 A power leads, the secondary package can be left out of the assembly to provide the necessary space. Table 5.6-1 lists the characteristics and numbers of the various arc correction elements.

Table 5.6-1
Arc Correction Elements

Type	Name	$B\ell$ at I_{max} (T-m @ 1 cm)	I_{max} (A)	Volts (V)	Inductance (mH)	Number of Elements/Circuits
Primary package						
Dipole	H, V	3.18	±100	±5	1400	1328 / 1328
Quadrupole	QF, QD	0.60	±100	±30	850	1328 / 32
Sextupole	SF, SD	0.13	±100	±10	210	1328 / 32
Secondary Packages						
Quadrupole	Q1 - Q4	0.56	±100	±5	160	64 / 64
Skew Quadrupole	SQ1 - SQ4	0.90	±100	±5	180	64 / 64
Sextupole	S1 - S4	0.80	±100	±5	550	64 / 64
Skew Sextupole	SS1 - SS4	0.80	±100	±5	550	64 / 64
Octupole	O1 - O4	0.36	±100	±5	410	64 / 64
Skew Octupole	SO1 - SO4	0.36	±100	±5	410	64 / 64
Persistent current						
Sextupole	PCC	0.04	±5	±10	15	6640 / 16
Decapole	PCC	—	±5	±10	—	6640 / 16

Primary Correction Package

The primary correction package consists of a dipole, a sextupole, and a quadrupole element arranged coaxially as described in Section 5.2.13. This package is located in every spool piece at each of the 332 quadrupoles per ring in each arc, so there is a total of 1328 of these primary packages in the arc sections of the SSC.

Dipole Correctors

Dipole correction magnets are used to compensate for random errors in quadrupole alignment, dipole vertical plane alignment ("roll"), and main dipole field integral. Quadrupole misalignment is the dominant effect and is expected to have a gaussian distribution with an rms width of 0.5 mm. Because of the potentially large orbit distortion that could result from alignment errors, the correction dipoles are individually powered to correct the closed orbit errors locally, resulting in 1328 separate power supplies. The horizontally bending correction dipoles are adjacent to horizontally focusing quadrupoles, and the vertical correctors are adjacent to the defocusing quadrupoles, as shown in Fig. 5.6-1.

The present trim dipole design is capable of a maximum integrated field strength of 3.1 T-m at its peak current of 100 A, sufficient to correct a 6 σ variation from the rms quadrupole placement accuracy.

Series Quadrupole and Sextupole Correctors

The correction quadrupoles and sextupoles in the primary package are connected in series circuits, illustrated in Fig. 5.6-1. The quadrupole circuits are used to vary the tune of the SSC and to compensate for a systematic difference in the saturation of the main dipoles relative to the main quadrupoles. The present design of the correction magnets allows the tune to be changed by ± 2 units, in addition to compensating for a saturation difference between dipoles and quadrupoles of two per cent. The sextupole circuits are used to vary the chromaticity. They are strong enough to change the chromaticity by ± 400 units, almost twice the natural chromaticity of the SSC.

Each sector of each ring contains two correction quadrupole circuits, with elements adjacent to the horizontally focusing main quadrupoles in one circuit, and those at the defocusing locations in the other circuit. The sextupole circuits are divided similarly. Hence, there is a total of 32 series quadrupole circuits and 32 series sextupole circuits in the arc regions of the SSC. Each of the circuits has 41 or 42 correction elements, depending on the sector, with each element connected to its neighbors by superconducting strand.

The series circuits are interrupted at the section boundaries, about every kilometer, by bringing the leads to room temperature and returning them to cryogenic temperature. In normal operation, the circuits are continued across the interruption with short pieces of cable. If it becomes necessary to remove one of the circuits from series operation in a particular section, a power supply can be substituted for the cable. This guarantees that no more than six sequential correction elements would have to be disconnected in case of a ground fault or open circuit.

Secondary Correction Package

There are several additional types of correction elements for the purpose of canceling the effects of random errors. In the present design these consist of quadrupoles, sextupoles, and octupoles, in both normal and skew orientation. Each ring has four elements of each of the six types in every sector. All of these elements are individually powered, requiring 24 power supplies in each sector for each ring, totaling 384 power supplies. The secondary quadrupole and skew quadrupole elements are in a single coaxial package similar to the primary package. The secondary sextupole and octupole elements are packaged individually with the appropriate skew elements created by rotation in the spool piece. Specific designs are described in Section 5.2.13.

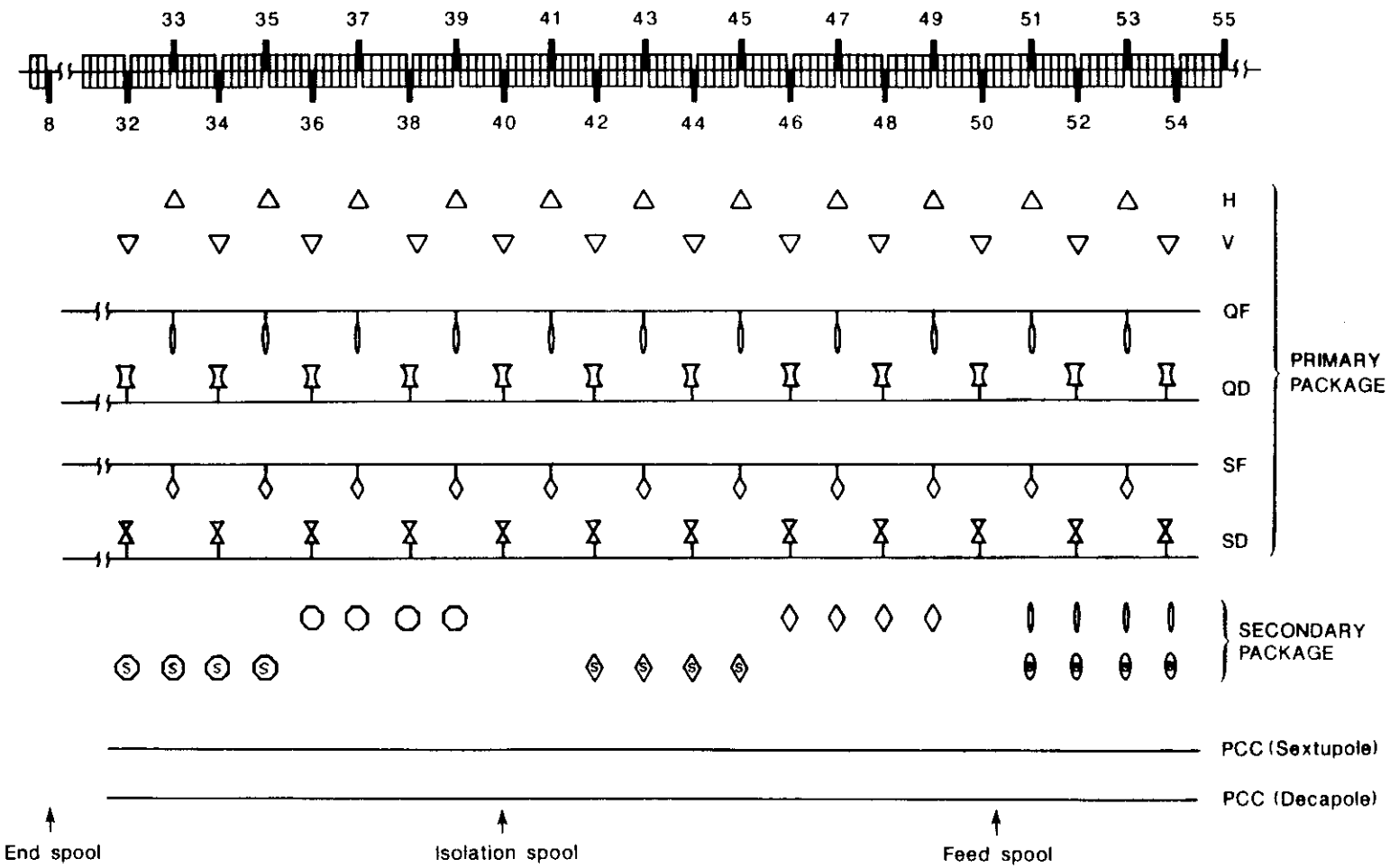

Figure 5.6-1. The standard arc correction arrangement for one of eight arc sectors, for one ring. Each of the secondary package correctors is individually powered, as are the H and V dipoles of the primary packages. The other elements of the primary packages are powered in two quadrupole and two sextupole circuits per ring arc sector. The two persistent current correctors in the main dipoles are powered in one circuit each per ring arc sector.

Persistent Current Correctors

Dipoles containing large amounts of superconductor suffer at low excitation from unwanted multipoles, particularly sextupole and decapole, caused by persistent currents. These fields reduce the effective aperture at injection. In addition, saturation of the steel yoke of the main dipoles gives rise to a significant sextupole field at high excitation. The dipoles have as a part of their internal structure correction coils that are used to cancel these systematic sextupole and decapole moments. These coils are described in Section 5.2.7.

The persistent current correctors are internally connected in series so that one circuit is the length of a sector. This results in 32 power supplies capable of ± 10 A for the arc regions of the SSC. A single circuit provides effective correction of each of the unwanted multipoles even though there is a temperature dependence of the persistent currents. This is because the major temperature fluctuations are repetitive from recooler to recooler (cell to cell), and because the overall temperature rise from one end of the cryogenic loop to the other is very small. Redundancy is provided by allowing the possibility of breaking and reconnecting the circuit at each section boundary, just as in the series circuits described above.

5.6.2 Cluster Region Correction Elements

Table 5.6-2 lists the correction elements for the two cluster regions. The clusters are composed of special areas, four developed interaction regions, two utility sections, and two undeveloped interaction regions, identical to utility sections. These special areas are separated from each other by short arcs of 13 or 14 half-cells, depending on their location, and from the main bending arcs by short arcs of six half-cells. Most of the main quadrupoles in the cluster regions are longer than the quadrupoles in the arcs. To accommodate these longer quadrupoles the spool pieces are made shorter, and the secondary packages are left out. This is true everywhere in the short cluster regions arcs; the only special correctors in the clusters are located in the interaction regions and the utility sections. If independent adjustment of quadrupole or sextupole correctors in the arcs is needed, the correctors in the primary package can be removed from the series circuits and powered independently.

The primary correction package for the cluster arcs is the same as the primary package in the main bending arcs. The dipole correctors are positioned at each quadrupole location, except in the interaction region inner triplet, and are individually powered. There are a total of 208 correction dipole power supplies associated with the cluster region arcs. In addition, there are special correction packages located in the vertical bend and inner triplet regions of the IRs and near the utility straight sections. These consist of vertical and horizontal dipoles, either together or separately. There are 208 power supplies associated with these special correctors.

As in the main arcs, the quadrupole and sextupole correction elements are each connected in series to form two circuits (F and D) per short arc. The number of elements in each series circuit depends on the location in the cluster and varies from 4 to 14. There are a total of 80 series circuits in the cluster regions. Figures 5.6-2 and 5.6-3 are schematic views of the interaction region circuitry and the utility section circuitry, respectively.

The persistent current corrections are also in a single circuit in each short cluster arc, yielding 40 power supplies in all.

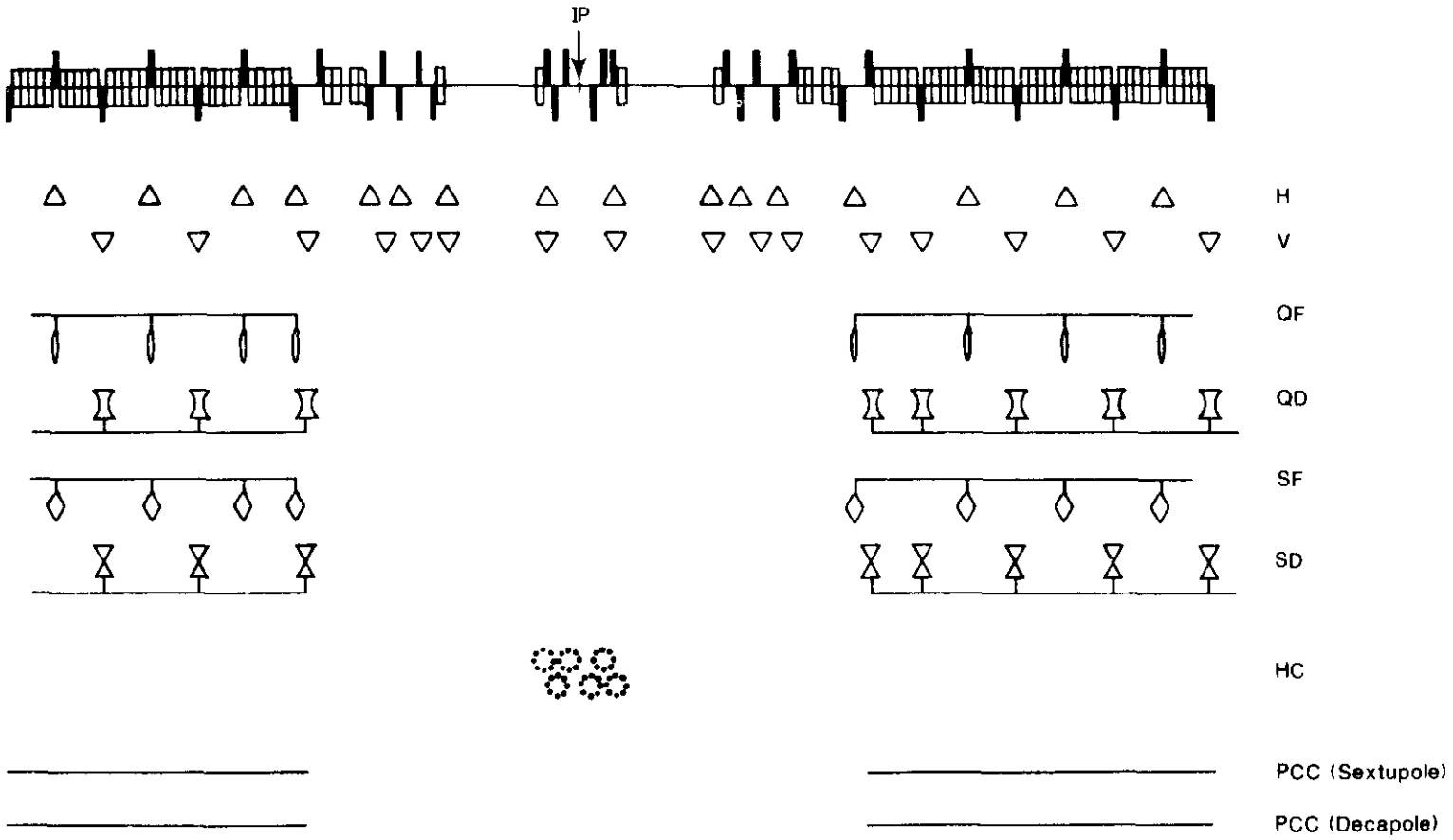

Figure 5.6-2. The correction element arrangement for the interaction regions. The quadrupoles near the interaction point (IP) contain built-in high-order multipole correctors that are individually powered, represented by the circuits labeled HC.

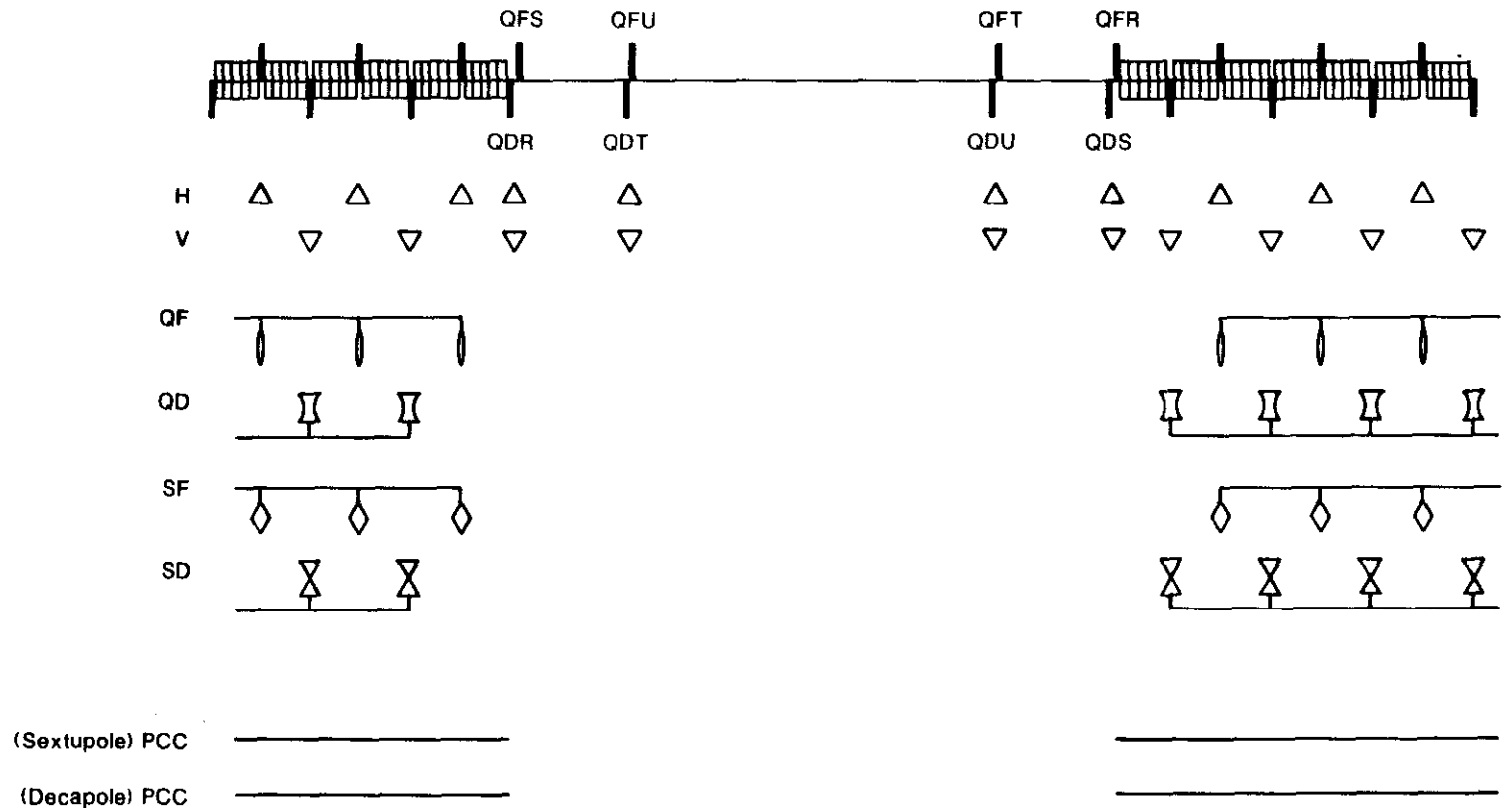

Figure 5.6-3. The correction element arrangement for the utility straight sections. The spool pieces adjacent to the quadrupole doublets have both vertical and horizontal dipole correctors.

Table 5.6-2
Cluster Correction Elements

Type	Name	$B\ell$ at I_{max} (T-m @ 1 cm)	I_{max} (A)	Volts (V)	Inductance (mH)	Number of Elements/Circuits
Primary Package						
Dipole	H, V	3.18	±100	±5	1400	208 / 208
Quadrupole	QF, QD	0.60	±100	±5	850	208 / 40
Sextupole	SF, SD	0.13	±100	±5	210	208 / 40
Special Packages						
Dipoles	H	3.18	±100	±5	1400	48 / 48
Dipoles	V	3.18	±100	±5	1400	48 / 48
Dipoles	H&V	3.18	±100	±5	1400	112 / 112
Skew Quadrupole	SQIR	1.20	±30	±5	—	24 / 24
IR Triplet	High Order	—	±30	±5	—	264 / 264
Persistent Current						
Sextupole	PCC	0.04	±5	±5	15	1040 / 20
Decapole	PCC	—	±5	±5	—	1040 / 20

5.6.3 Special Cluster Region Corrections

In addition to the elements listed above there are also skew quadrupole correction elements placed in the interaction region triplets. These are individually powered and allow corrections of the solenoidal field of experiments and roll misalignment of the high gradient quadrupoles. In addition to the skew quadrupole elements, there are also windings in the high gradient quadrupoles to compensate for the random errors in each. This is necessary because of the very high beta function values at these locations, and because the required high gradient does not permit the quadrupoles to be built with a large diameter bore. Each of the high gradient quadrupoles is corrected with a skew quadrupole and normal and skew sextupole, octupole, and duodecapole, resulting in 168 of these special circuits in the four developed interaction regions. Each of these power supplies has the capability of ±30 A.

5.6.4 Power Supplies and Quench Protection

Each power supply must be regulated to a few parts in 10^4. This is easily achievable using either a series-pass linear or switching regulator. Switching-mode stabilization has been chosen to minimize size and power dissipation. The current program is supplied by a function generator that interpolates between points in a preloaded look-up table. In most cases the correction current is only a function of the main bus current, but it is possible to have time dependent, or even manually entered values.

In order to save cabling costs, the power supplies for the dipole correction elements and the individually powered quadrupole and sextupole correctors are placed near the

magnets that they power, in the shafts that also contain the distributed control system electronics. These sealed shafts are bored into the tunnel ceiling at roughly 192 m intervals near spool pieces, so the average cable length is about 50 m. The shafts have a controlled environment and have ac power available. Most of the shafts contain four power supplies, and the most densely populated shafts have 12 power supplies. The power supplies for the series circuits are installed in service buildings above ground.

The correction dipole power supplies have a self contained quench protection system in which each one compares its output voltage to a measured dI/dt. In the case of imbalance the power supply is shut off. The quench grows fast enough in the closely packed coils of the correction element that no other action is necessary. In fact, because of the limited voltage capability of the supply, failure to turn off the supply will cause no damage.

A fast energy extraction system is required for the series circuits to prevent damage during a quench. The energy extraction system consists of a dump resistor bypassed by a silicon controlled rectifier (SCR) and a backup mechanical switch. A voltage tap in the center of the circuit allows the voltage in each half of the loop to be measured. The existence of a quench can then be detected by comparing the voltage drops across the two halves of the loop. In the event of a quench the power supply is shut off and the dump resistor is inserted into the circuit by the opening of the SCR and the mechanical switch. This decreases the time constant of the energy extraction to the point where no damage is done. The physical extent of the series circuits, the total energy stored in them, the magnet styles, and the quench protection technique are very similar to the proven system of the Tevatron.

5.6.5 Reliability

The large number of power supplies in the SSC correction system requires that considerable attention be paid to reliability. It is possible to operate the machine with a considerable number of the dipole correction supplies not functioning, but the loss of one of the supplies while beam is being stored will likely result in loss of the beam or, at least, dilution of the beam emittance.

The correction dipole power supplies used in the Tevatron, for example, have roughly the same power rating as the ones in the SSC. They are series transistor regulated. Examination of the down-time log of the Tevatron [5.6-1] for the months of April through August, 1985, show that there were 44 failures among the 220 correction dipole power supplies in 2600 hours of scheduled running. This failure rate of $\lambda = 77 \times 10^{-6}\ h^{-1}$ is consistent with information from an available data base [5.6-2]. The failures were about evenly split between failures of the regulators and failures of the control logic circuits, with a small number of operator error or other system malfunctions. The mean time to repair was about 0.5 hours.

Direct translation of the Tevatron system to the SSC, with 2500 similar power supplies, would result in one failure every five hours on the average, an unacceptable situation, particularly since the time to repair the fault and restore the beam is considerably longer than 30 minutes. An improvement by at least an order of magnitude in unit mean life is necessary, unless an alternative solution can be found. One possible approach is to put two power supplies and their associated controls in parallel at each location where one is needed. The circuits can be designed so that the failure of one power supply will

automatically switch in the other "hot spare," without interrupting the current waveform. Furthermore, intelligent design of the dual supply and controls does not increase the testing or installation time, but only the cost of the supplies themselves.

With N doubled units in series, the system can be shown to have a survival probability (with no provision for repair)

$$P(t) \simeq \exp(-N\lambda^2 t^2) \quad ,$$

valid for arbitrary N and $N\,\lambda^3 t^3 << 1$ [5.6-3]. With $N = 2500$ and $\lambda = 8 \times 10^{-5}\ h^{-1}$, the survival reaches 50% at $t = 208$ hours. This time is comparable to a running period. It is therefore plausible that at the beginning of each run both halves of all units can be in working condition and that, although 80 single supplies may fail during the run, the system has only a 50% chance of failure.

Based on the Tevatron failure rate, the doubled supply solution is acceptable, but one would like a better margin. Because of the presence of λ^2 in the probability, improvement in the single-unit lifetime is crucial. For example, a factor of two improvement over the Tevatron experience causes the survival probability to be 84% after 208 hours, with 40 individual supplies failing on the average.

5.7 Radio-Frequency Accelerating System

The radio-frequency system of the main rings of the SSC is required to perform three functions: raise the beam energy from 1 TeV to 20 TeV, maintain the tight bunching of the beams during collisions, and compensate for energy loss by synchrotron radiation. Each ring of the collider has its own rf accelerating system, permitting independent operation.

5.7.1 Choice of RF Frequency

In considering the rf frequency of the SSC a broad range of values from 200 to 420 MHz is found to be adequate. The accelerator issues leading to this range are outlined in Section 4.6.3. Cost, reliability, and life expectancy of klystrons and cavities favor frequencies at the upper end of this range. These factors led both the PEP and the LEP large e^+e^- storage rings to a choice of about 360 MHz for the rf system. Choosing the rf frequency of the SSC close to 360 MHz has the significant advantage that it can be modeled on the existing PEP system. Based on the size of the SSC ring, the number of bunches stored and possible bunch spacing alternatives, an rf frequency of 375 MHz has been chosen (see Section 4.6.3). Here parameters are presented for a system of this frequency.

5.7.2 Description of System

The rf system must be capable of supplying the 5.26 MeV per proton per revolution necessary to accelerate particles from the injection energy of 1 TeV to the operating energy of 20 TeV in 1000 seconds. It must also supply 0.123 MeV per turn at 20 TeV to compensate for the energy loss due to synchrotron radiation. Finally, the rf system must control the beam emittance growth while maintaining a reasonable bucket to beam area. As

described in Section 4.6.3, a cavity capable of producing a peak voltage of 20 MV is adequate.

The power required to attain the necessary peak voltage is supplied by klystron tubes. Somewhat more than 1 MW of rf power fed to PEP style cavities will provide the 20 MV peak voltage. In the design chosen, each klystron is capable of delivering an output power of 1 MW. In order to add adequate safety margin, two klystrons supply a total of 2 MW of rf power for each ring. In the initial installation, each klystron feeds four accelerating sections (each 2.1 meters in length) for a total of eight sections per ring. Power splitters are provided in the klystron shelter; these will divide the output of each klystron twice to energize its four cavities. Each section comprises five coupled π-mode cavities that are very similar in design to the PEP cavities. The klystrons are housed in shelters above ground as shown in Fig. 5.7-1. The klystron power supplies are located on concrete pads outside the buildings. Wave guides running through vertical penetrations connect the klystrons to the accelerating sections in the tunnel below. Typical parameters for the rf system are given in Table 5.7-1.

5.7.3 Accelerating Structure

The two SSC beams, which are vertically separated by 70 cm in the arcs, are also separated by 70 cm in the utility straight sections. This allows cavities similar to the ones used at PEP to be used. These cavities have been optimized for high shunt impedance. They consist of shaped cavities with nose cones, strongly coupled with circumferential slots in their common walls and operating in the π mode. The structure is depicted schematically in Fig. 5.7-2.

Table 5.7-1
Typical SSC Main Ring RF Parameters
(Per Ring)

Frequency (MHz)	375
rf power (MW)	2
Number of klystrons	2
Number of 5-cell cavities	8
Total shunt impedance (MΩ)	400
Peak rf voltage (MV)	20
Coupling factor (β)	3
Synchrotron tune	
at 20 TeV	1.91×10^{-3}
at 1 TeV (capture)	8.54×10^{-3}
at 1 TeV (accelerating)	8.39×10^{-3}
Bucket-to-beam area ratio	15.5
Accelerating voltage per turn (MV)	5.26

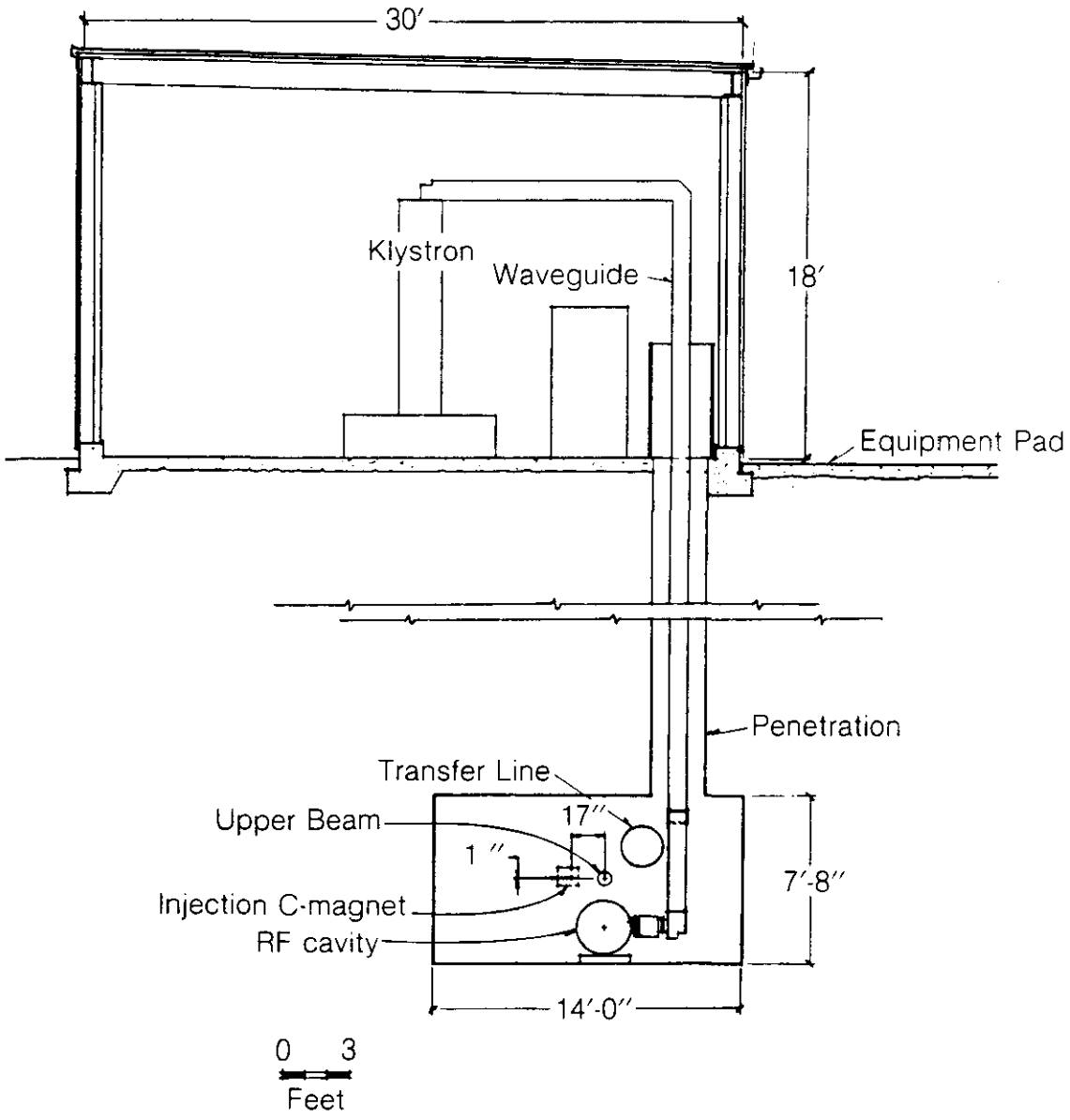

Figure 5.7-1. Schematic diagram indicating the above-ground position of a klystron and the wave-guides that feed power to the rf cavities located in the main ring tunnel.

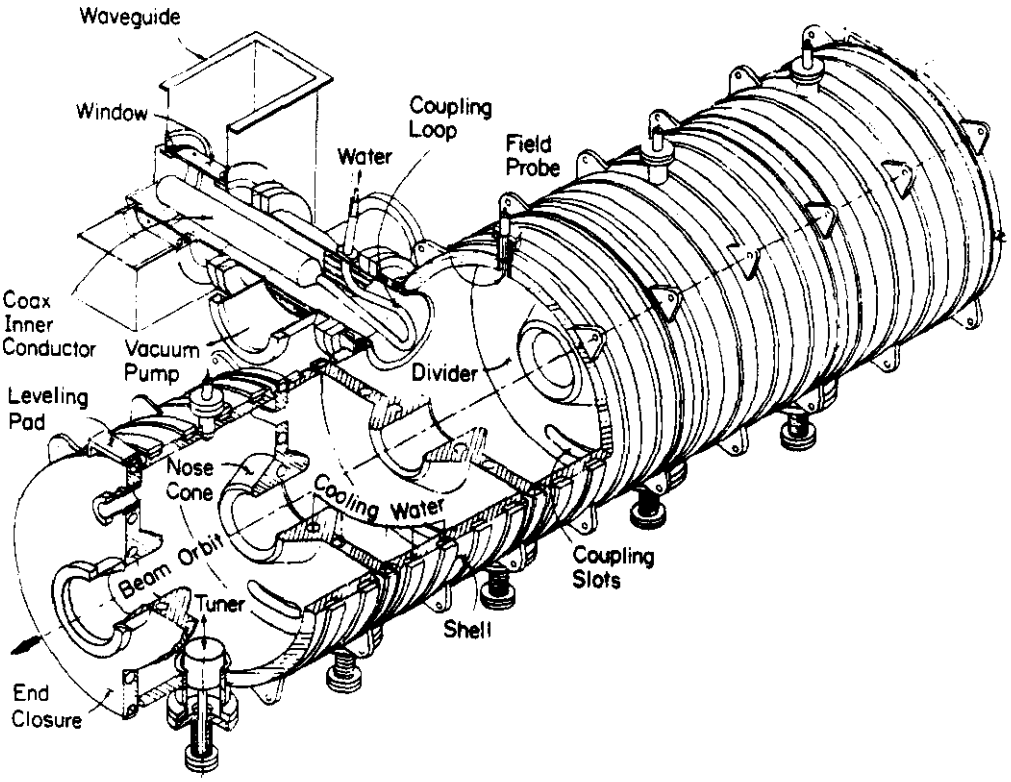

Figure 5.7-2. Design of an rf cavity for the SSC main ring. The diameter is approximately 0.6 m and the length 2.1 m.

The shape of the individual cavities has been adjusted to produce a high shunt impedance that for a perfect copper surface would be in excess of 30 MΩ/m. The coupling slots reduce this figure by about 10%. An additional reduction is caused by the fact that the real surface conductivity falls 5% to 10% below the theoretical prediction. A net shunt impedance per unit length of about 25 MΩ/m is predicted. This value is confirmed by studies of PEP cavity operation in the accelerator. Thus, each five-cell cavity yields 50 MΩ and with the choice of eight cavities per ring, there is a total of 400 MΩ of shunt impedance at the fundamental frequency of the cavities. Approximately 1 MW of rf power fed to the cavities provides the necessary peak rf voltage of 20 MV. During acceleration, an additional 400 kW is needed for increasing the energy of the beam. Some power is required for wave-guide losses, radiation into higher-order modes, and reflections from the cavity, which will be over-coupled, leading to the specification of 2 MW per ring stated above.

5.7.4 Layout of the System

The rf buildings house the power amplifiers and controls for the rf system as well as power and control electronics for the feedback systems. Each 25 m long string of cavities is placed in the upstream drift length of the utility section in the opposite ring from the injection system, as shown in Fig. 5.7-3. The cavities are situated at positions of relatively low beta and zero dispersion. Allowance for the cavities and wave guides is made by providing an enlarged tunnel section at this location. The projected profile of the cavity sections and tunnel is shown in Fig. 5.7-4. Wave-guide runs to the surface are oriented to avoid a direct line of sight for radiation (from beam loss) at the cavities. A wave-guide chase for each of the 8 wave guides in each section connects the tunnel to an rf building above. Each building is 24 m long, spanning the length of the cavity assembly below.

5.7.5 Cavity Coupling

For stability reasons, the cavities will not be detuned to compensate for reactive beam loading. At resonance (tuning angle $\psi = 0$), the power required from the generator P_g is given by [5.7-1]

$$P_g = \frac{1}{4\beta}\left[I_0^2 R + 2(1+\beta)\, vI_0 + (1+\beta)^2 \frac{V^2}{R}\right] \tag{5.7-1}$$

where V is the peak rf voltage (20 MV), β is the cavity coupling parameter, R is the cavity shunt impedance, I_0 is the average beam current (70 mA), and v is the average accelerating voltage (related to the synchronous phase angle ϕ_s by $v = V \sin \phi_s$). We consider two circumstances, acceleration (v = 5.26 MV) and storage (v = 0.123 MV). With V fixed at 20 MV (see Section 4.6.3) and a given beam current, the input power can be minimized by appropriate choice of β (also giving minimum reflected power). The optimum β and P_g values are

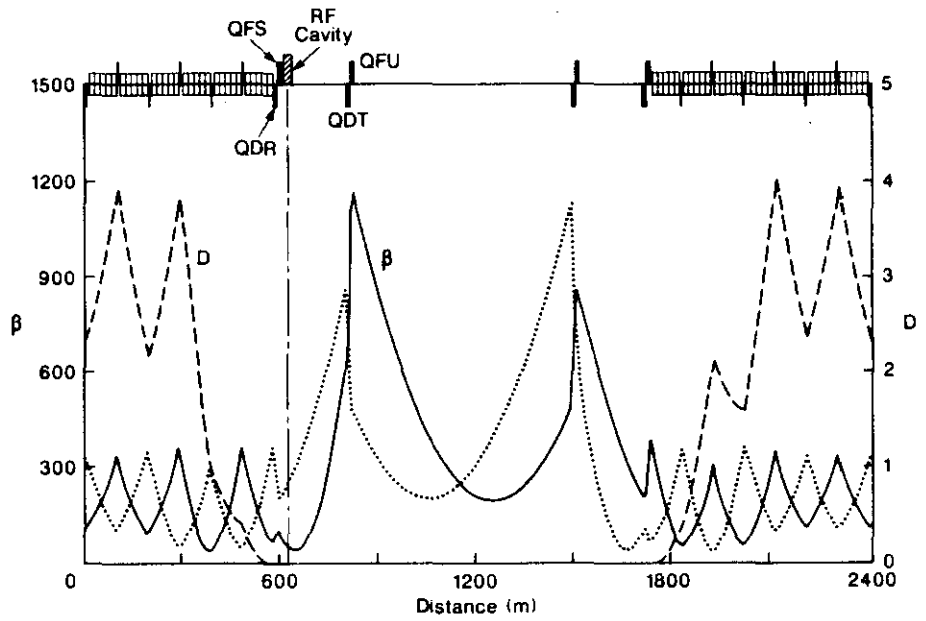

Figure 5.7-3. Layout of a utility straight section showing magnet and cavity positions.

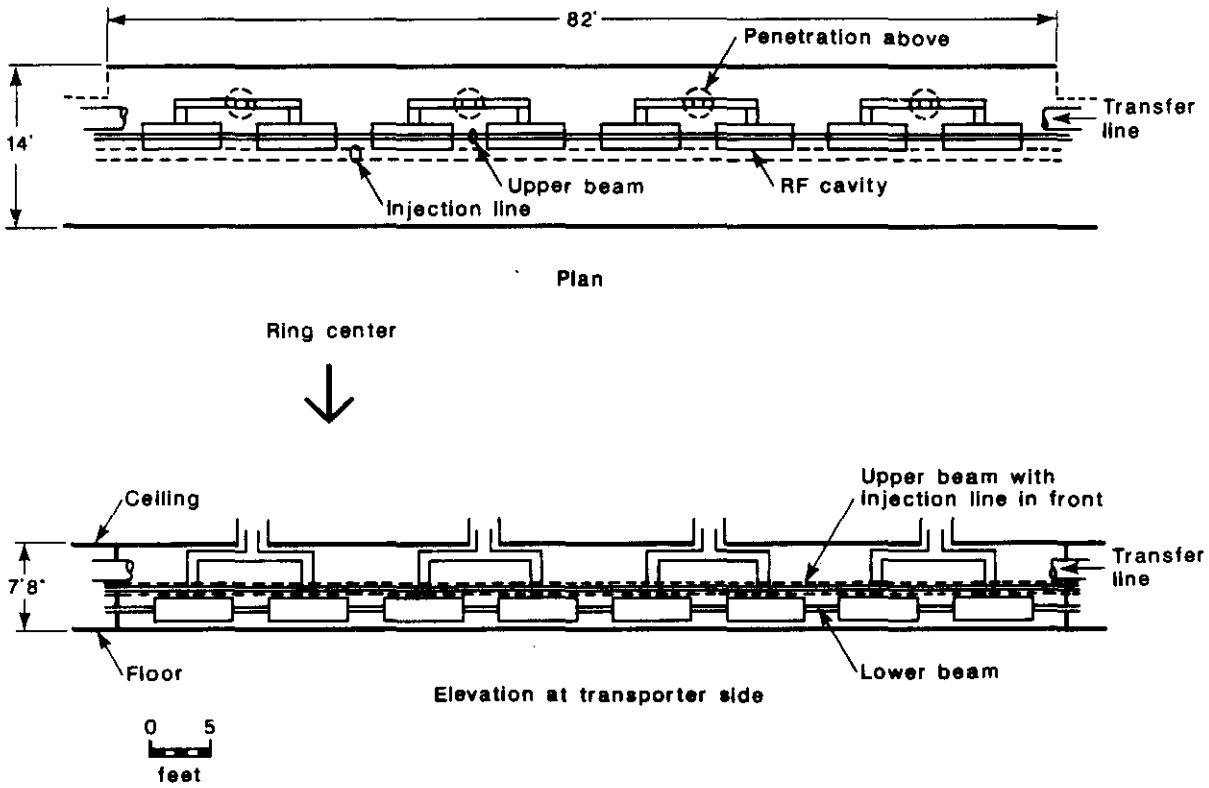

Figure 5.7-4. Projected profile of rf cavities in tunnel.

Acceleration: $\beta = 1.92$, $P_g = 1.65$ MW

Storage: $\beta = 1.73$, $P_g = 1.37$ MW

The minimum is very flat — for β values from 1 to 4 there is less than a 15% change in P_g in the acceleration phase, and only 24% for the storage mode.

In order to minimize the effects of beam loading, a coupling factor $\beta = 3$ is used. This still corresponds to quite a modest-sized coupling loop and reduces the beam-induced voltage from 28 MV to 7 MV, because the impedance seen by the beam at the fundamental frequency is reduced from 400 MΩ to 100 MΩ. The generator power is then calculated to be 1.74 MW for acceleration and 1.50 MW for storage. This power is available from the two klystrons in each ring, so the effects of beam loading are quite modest. The reflected power from the cavities coming back to each klystron is about 250 kW. This power is absorbed in the loads of the "magic-T" combiners and is not seen by the klystrons themselves.

5.7.6 RF Monitoring, Phasing, and Controls

Low level rf drive and feedback circuits deal with the control and stabilization of the amplitude and phase of the cavity fields and the suppression of rf noise. These functions are achieved by four servo-loops shown in Fig. 5.7-5: (i) klystron phase-lock loop; (ii) gap-voltage automatic leveling circuit; (iii) cavity phase control; and (iv) intercell power balance loop. Because suppression of noise density at the synchrotron frequency is necessary, a high-quality rf source is used (e.g., a Hewlett-Packard 8662A synthesized signal generator). In addition, the noise density will be controlled by the rf phase feedback loop (see Section 4.4.10).

5.7.7 Klystrons

Klystrons capable of supplying 1 MW of continuous rf power at 360 MHz are presently being supplied to the LEP project at CERN by two European manufacturers, Valvo and CETH. These tubes will be modified slightly to accommodate the 375 MHz operating frequency. The efficiency of the tubes is about 65%, so the input power per tube would be about 1.54 MW supplied by a 100 kV/20 A power supply.

5.7.8 Power Supplies

In the interests of economy and simplicity, the power supplies that provide the beam voltage and current to the klystrons are unregulated. Slow regulation of voltage and adjustment over a limited range are afforded by variable-voltage transformers in series with the ac input to each power supply. These are capable of varying the voltage over a range of $\pm 15\%$. Fine control of the rf accelerating voltage can be obtained by varying the rf drive to each of the klystrons.

Each supply has a maximum output of approximately 2 MW at 100 kV and 20 A. The supplies are oil-filled units with a solid-state rectifier and a filter choke contained in the same oil tank; they are located outdoors in weatherproof housings. The output of each

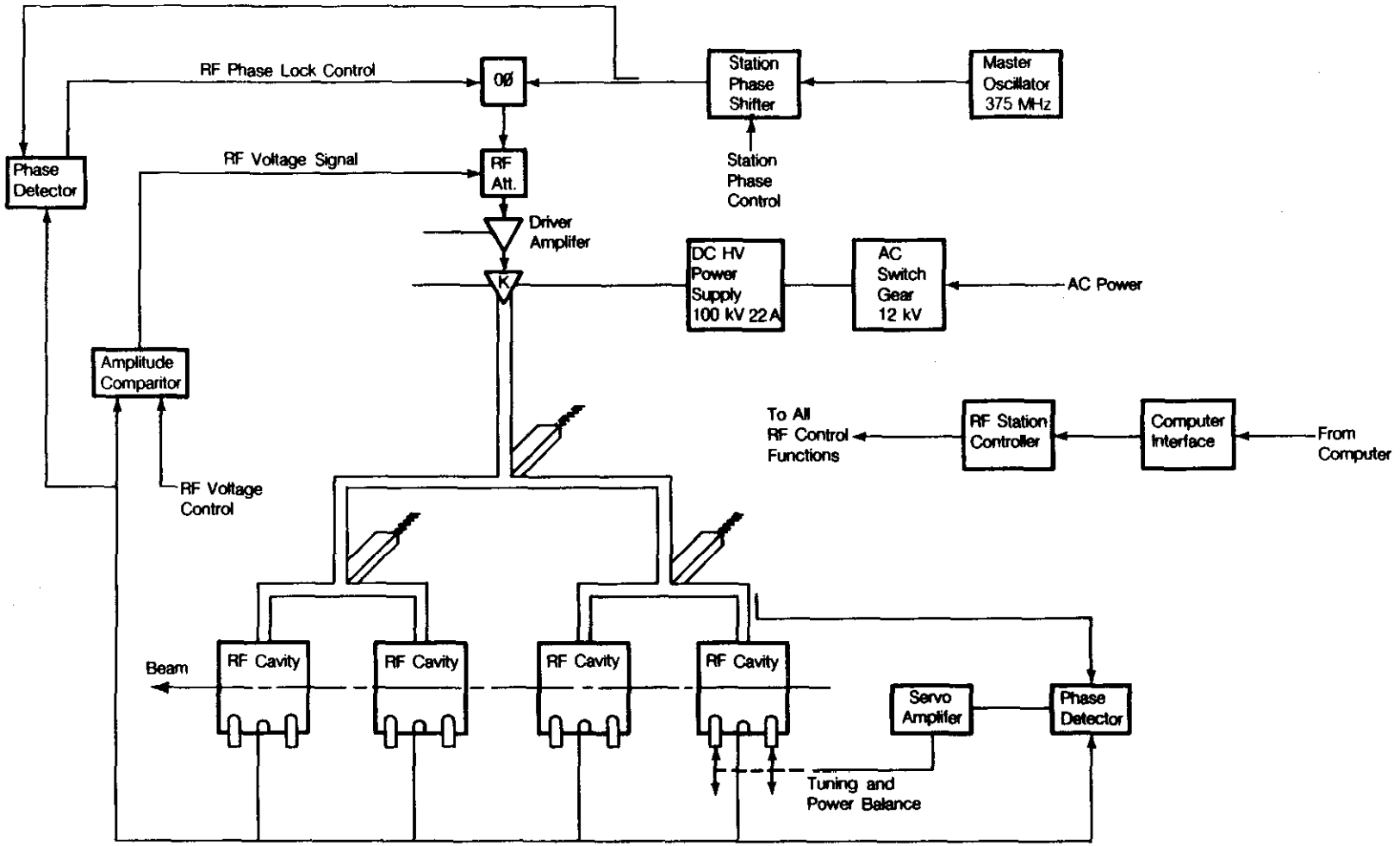

Figure 5.7-5. Master circuit diagram of rf system, indicating servo-loops to stabilize the amplitude and phase of the cavity fields.

supply passes through the wall to an enclosed high-voltage cabinet that contains the filter capacitor, crowbar-interlock circuits, control circuits, and voltage/current metering circuits. In the event of a klystron fault, the energy dissipated in the fault will be held down to a few joules by a spark-gap crowbar. The crowbar circuit is driven by a simple thyratron pulser that is triggered by a current transformer in series with the klystron. A vacuum contactor located at the input to the power supply would simultaneously be tripped. A similar power supply of about half the rating has been in operation for several years at PEP.

5.7.9 System Reliability

The rf system of the SSC is quite similar in design and scale to that already in existence at PEP. The reliability question may thus be answered in terms of scaled PEP reliability. During the 1983–84 PEP run the rf system was inoperative 3.4% of the time, during the 1984–85 run, 2.9%. Of the down time, 35% was due to low-power circuits, which are essentially the same as the SSC, and 65% was caused by the high-power circuits. PEP has twelve 0.5 MW klystrons, compared to four 1.0 MW klystrons for the SSC, and has 24 cavities, in contrast to 16 in the SSC. A reasonable scaling factor for down time of the high-power circuits is therefore 0.66, and one could expect the rf system to be available greater than 97% of the scheduled running time.

5.8 Beam Stabilization

The beam stabilization system provides the damping necessary to limit instability growth rates to small values so that these instabilities do not appreciably affect the stored beam lifetime and luminosity. Transverse emittance growth arising from coherent betatron oscillations produced by injection errors are minimized by the same system. To insure that the collider produces maximum luminosity, a collision assurance feedback loop provides fast feedback to dipole correction magnets near the IRs by maximizing the instantaneous luminosities as measured by the forward neutral beams (see Section 5.11.8).

5.8.1 Low Level Feedback in the Main RF System

If the signal from one of the rf cavities were analyzed with a spectrum analyzer centered on the main rf frequency of 375 MHz, the frequency spectrum, in the presence of coupled-bunch longitudinal modes and higher-order modes, would be as shown in Fig. 5.8-1. The discrete lines of the oscillating modes are clustered around harmonics of the revolution frequency f_0. For mode m,n at harmonic h, the coupled-bunch longitudinal instability is driven by the quantity

$$R_p = Z(hf_0 + mf_0 + nf_s) - Z^*(hf_0 - mf_0 - nf_s) \tag{5.8-1}$$

where $Z(f)$ is the impedance of the ring at frequency f, and f_s is the synchrotron oscillation frequency [5.8-1]. The negative frequency lines are destabilizing and the positive frequency lines are stabilizing for the collider since it is always operating above the transition energy. The main rf power system can be used to provide the required damping for those modes that lie within the bandwidth of the cavities and the control loops. With a

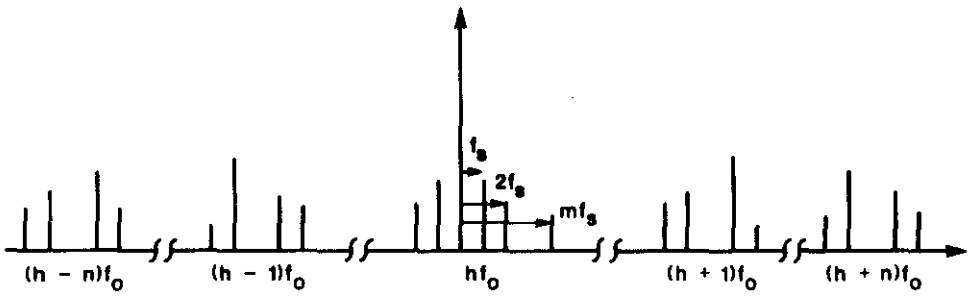

Figure 5.8-1. RF spectrum in the presence of longitudinal coupled-bunch modes and higher-order modes.

Q_L = 5000 and an operating frequency of 375 MHz, this bandwidth is 75 kHz. The fundamental dipole mode (lines that differ from hf_0 by f_s) is damped by the phase-lock loop that locks the main rf phase to the average bunch phase in the ring. This loop, together with the radial control loop that modulates the accelerating frequency as a function of the average beam position, are the main elements of the low level rf system. The phase-lock loop has a limited bandwidth and responds only to the coherent synchrotron oscillation of all the bunches. Its main effect is to reduce the rf noise at the synchrotron frequency, thus minimizing phase space dilution. The fundamental quadrupole mode (lines $2f_s$ away from hf_0) can be damped by a selective feedback system that senses the bunch shape oscillation and modulates the amplitude of the main rf wave. Again, this mode lies within the bandwidth of cavities and the control loops and is damped by the main rf.

5.8.2 Longitudinal Feedback System

If $Z(f)$ were slowly varying with frequency on the scale of the bunch repetition frequency, these stabilizing and destabilizing lines would tend to cancel since R_p would be small and would thereby limit the bandwidth requirement for the longitudinal feedback system. For the higher order resonances of the main rf cavity whose properties are listed in Table 4.5-1 in Section 4.5, the typical unloaded resonance widths are 10 to 20 kHz which are very small compared to one half the bunch repetition frequency of 31 MHz. One half of the bunch repetition frequency corresponds to a mode phase shift of 9 between successive bunches which gives the maximum frequency deviation from the rf fundamental frequency. Unless the Qs of these modes are loaded sufficiently to increase their resonance bandwidths to a substantial fraction of 31 MHz, there is little cancellation between the stabilizing and destabilizing lines, and the feedback system must have the full 31 MHz bandwidth.

The growth rates of the coupled bunch modes have been computed in Section 4.5 by using the calculated average higher mode properties of the main rf cavities as input to the program ZAP [5.8-2]. The averaging process effectively multiplies the impedance of each single cavity-cell resonance by two and then assumes that each cell acts incoherently. Care must be used in the cavity manufacturing process to make sure that the higher mode resonances do not overlap cell to cell. With the widths given in Table 4.5-1, this is not hard to achieve. Compared to the Reference Designs Study, the growth rates calculated in Section 4.5 are approximately a factor of four larger because in the formula for calculating the growth rates [5.8-3], which are used in ZAP, the growth rate is proportional to the square of the number of bunches. The longitudinal coupled bunch mode with the largest growth rate (listed in Table 4.5-4 as the n = 1, m = 7382 mode with a growth rate of 1.6 s^{-1} at 1 TeV) determines the maximum required feedback voltage per turn to damp the instabilities. A growth rate of that size implies a large feedback voltage per turn, generated most economically with a resonant cavity system. Because of the large system bandwidth, a high operating frequency for the cavity is an obvious choice. A full bunch length of 20 to 30 cm at injection places an upper limit on this operating frequency on the order of 1 GHz. A reasonable compromise is to choose a frequency of approximately one half this value and midway between harmonics of Nf_0 in order to cover the instability spectrum efficiently. A frequency of f_{fb} = 531 MHz which corresponds to a harmonic number of 146880 satisfies

these conditions and is chosen as the operating frequency for the longitudinal feedback system.

Feedback Voltage per Turn

The feedback voltage per turn V_{fb}, which is a function of the maximum fractional momentum error Δ_p that can occur in the ring, is given by

$$V_{fb} = 2E\Delta_p/(t_r f_0) \quad .$$

where E is the beam energy and t_r is the shortest (dipole mode) growth time of the instabilities. In the present design, $\Delta_p = 1.5 \times 10^{-4}$. This is the necessary injection energy error to avoid the single-bunch transverse-mode coupling instability driven by the imaginary component of the transverse impedance estimated in Section 4.5. With $f_0 = 3.6$ kHz and $t_r = 0.63$ s, the required voltage is then

$$V_{fb} = 133\ kV \quad .$$

In the center of the dispersion suppressors the momentum dispersion function is $\eta_x = 4.0$ m, which gives a change in position (Δx) of

$$\Delta x = \eta_x \Delta_p = 600\ \mu\text{m} \quad .$$

With modern beam position detectors (resolution of 10 μm), the sensor for the longitudinal feedback system can be a standard beam position monitor.

Power Requirements

Average power requirements can be estimated by considering that the stored energy necessary to create the feedback voltage V_{fb} must be generated in the time interval between bunches. The average power is then given by

$$P_{av} = WNf_0$$

where N is the number of bunches and W is the stored energy in a cavity, given as a function of the cavity parameters, by

$$W = V_{fb}^2/\{(2\pi f_0)(rL/Q)_{fb}\} \quad .$$

For a typical disk loaded cavity $r/Q = 750$ ohm/m so that for a cavity length $L = 2$ m, the stored energy per bunch is $W = 4.7$ mJ, giving $P_{av} = 290$ kW. This substantial power level can be provided either by a klystron with its output cavities stagger-tuned to accommodate the large bandwidth or by a tetrode. The klystron is more efficient and reliable and so is the choice for the feedback cavity power source. The cavity is a ten-cell disk-loaded structure that is heavily overcoupled and will probably require some ferrite inserts to lower the Q to provide the necessary bandwidth.

The system configuration is shown in Fig. 5.8-2. The beam position monitor produces a signal for each bunch passage (every 15 ns). The peak values of successive bunches are digitized alternately by the two "sample and hold and flash" analog-to-digital converter (ADC) units whose outputs are stored in the proper sequence in the 16.6 K, 8 bit word, first in-first out (FIFO) memory. The memory then acts as a digital delay since it is clocked at the bunch passage rate and the position information of the bunch on its last passage is presented to the phase shifter just before the bunch enters the cavity. This gives the appropriate phase in the cavity to provide corrective action on that bunch's position. This scheme only corrects the dipole mode. If the quadrupole and higher multipole modes are shown to be important in subsequent simulation studies, a frequency domain scheme sensing the longitudinal phase of the bunch would have to be implemented. Such a system has been successfully used at CERN [5.8-4].

Since the longitudinal coupled bunch modes are driven by the parasitic higher modes of the main rf cavities, a cavity design that minimizes the unloaded Qs of these modes would substantially reduce the growth rates of these instabilities. This would greatly simplify the longitudinal feedback system by lowering its power requirements.

5.8.3 Transverse Feedback Systems

A feedback system is necessary to control the coherent horizontal and vertical betatron oscillations of the beam bunches. These oscillations are driven by two main sources:

1) The machine impedance drives transverse rigid bunch oscillations that will lead to emittance growth and beam loss if not damped.
2) The process of injection necessarily involves errors that can lead to beam loss and/or substantial emittance growth because of the finite coherence time of the betatron oscillations.

The feedback system can also be used to measure the beam transfer functions and to provide a source of transverse emittance growth if necessary. A typical system has the following principal components:

(a) a pickup electrode array;
(b) preamplifiers;
(c) components for digital data processing;
(d) power amplifiers; and
(e) an array of kicker electrodes.

Common use of pickup electrodes for the various functions mentioned above is foreseen. Kickers and power amplifiers will be different units for the two sources (impedance and injection) because of the substantially different power levels involved.

Based on considerations of instability growth rates and the coherence time for betatron oscillations, a correction rate of 1/50 of the observed error per turn is adequate to damp both types of motion. This analysis is presented in detail in Sections 4.5 and 4.6. A convenient operating frequency for these systems is the first subharmonic of the rf frequency, giving a center frequency of 188 MHz. The system bandwidth required for instability damping is again given by the bunch spacing since rigid bunch oscillations will have to be corrected, but not distortions within a bunch. This results in a required bandwidth of 31 MHz. To correct injection errors, a much smaller bandwidth is required because only

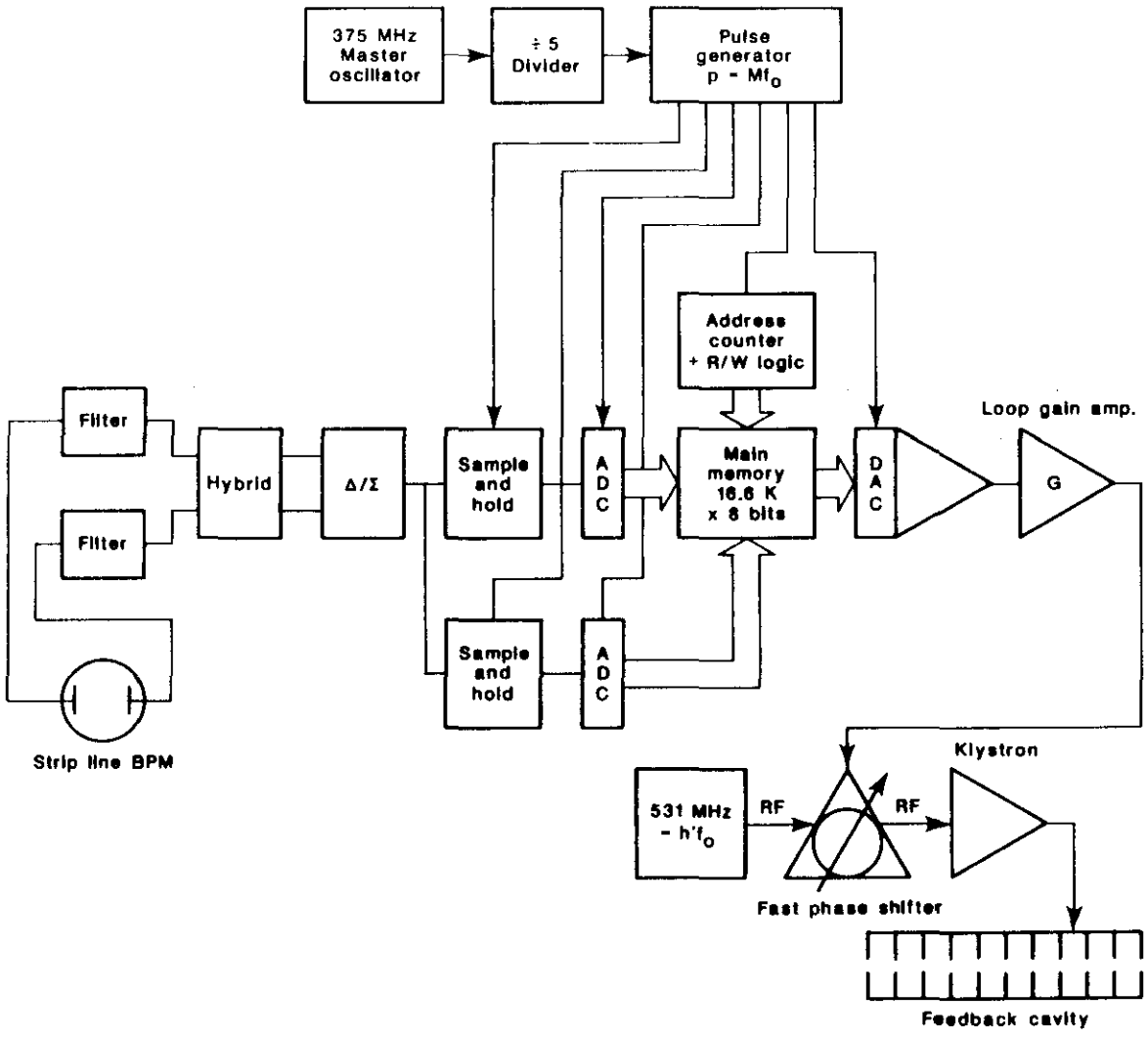

Figure 5.8-2. Block diagram of the longitudinal feedback system for the dipole modes.

minor bunch-to-bunch variations are expected in a single injected booster batch. A bandwidth of 4 MHz, which corresponds to the 150 ns spacing between booster batches, is more than adequate in this higher power system. It is the power level and bandwidth requirement that distinguishes these two systems since a typical injection error is ± 1.5 mm while the displacement in the bunch because of the instability is a fraction of the rms beam size, namely a few tens of microns.

Noise induced emittance heating of the beam is always a concern for the instability damping system, because the system is in continuous operation. For this reason, the higher powered injection error damping system will only operate during injection and then will be smoothly turned off. With a pickup array of adequate sensitivity and low noise preamplifiers, the noise diffusion rates can be kept below those caused by the other major diffusion processes and will not significantly affect the luminosity lifetime.

Pickups consist of a number of stripline electrodes, occupying a total length of 5 m, for the horizontal and vertical planes. Using 2.5 m long 50 ohm terminated stripline kickers results in a power requirement of less than 1 kW for the rigid bunch feedback system. With 5 m long 50 ohm terminated stripline kickers driven by a 30 kW power amplifier, a batch will be given a maximum angular kick of ± 0.25 μrad per passage by the injection error damping system. By locating the kickers in the utility straights where beta is 800 m, a kick of 0.120 μrad damps a ± 1.5 mm amplitude in 50 turns. This kick includes the fact that the error signal is on the average only available for one half of the time as the betatron phase advances through the pickup electrodes. The factor of two larger kick provided by the injection error damping system should provide an adequate safety margin. Figure 5.8-3 is a block diagram showing the two transverse feedback systems.

5.8.4 Collision Assurance System

The very high interaction rate at the SSC makes it possible to monitor luminosity by measuring the current from a multiplate ionization chamber placed in the forward neutral beam dump [5.8-5]. Detailed calculations of the expected beam intensity are given in Section 5.11. It is found that a current measured in tens to hundreds of microamps is produced primarily from the electromagnetic showers of high energy photons. By measuring the phase correlation of the luminosity signal with a small circular motion of one beam about the other, a steering correction is derived and applied to the horizontal and vertical steering magnets on either side of the IRs as shown in Fig. 5.8-4. The tracking has a very rapid response and can be applied continuously with negligible degradation of the nominal luminosity.

5.9 Collider Injection System

The purpose of the injection system is to provide a reliable and accurate method of loading beam from the High Energy Booster (HEB) into the SSC Collider Rings. The overall design is determined by a number of constraints and requirements:

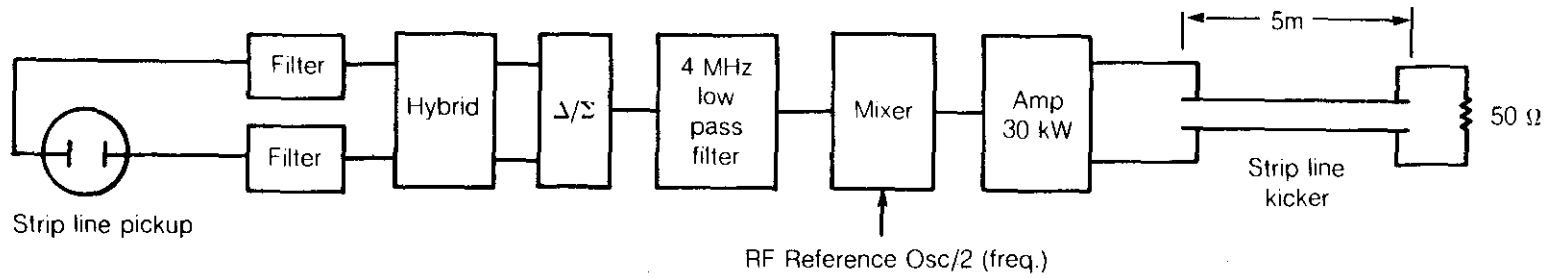

(a) Injection Error Damping System

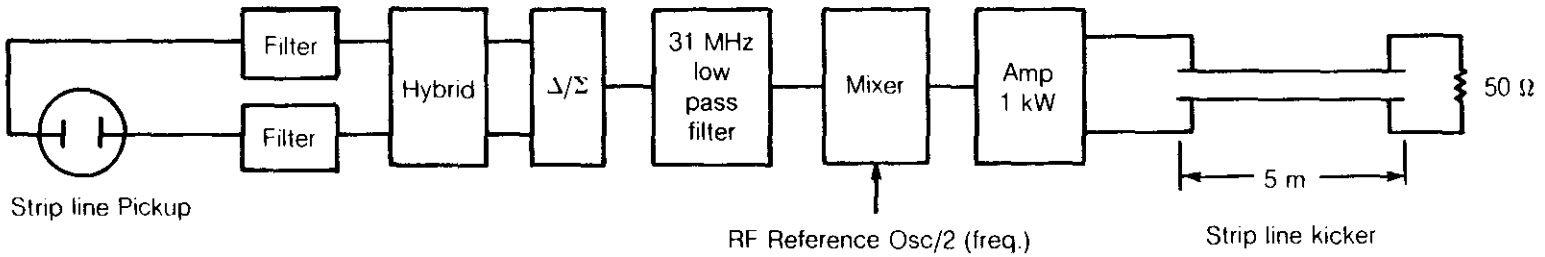

(b) Transverse Instability Feedback System

Figure 5.8-3. Block diagram for the transverse instability feedback system and the injection error damping system.

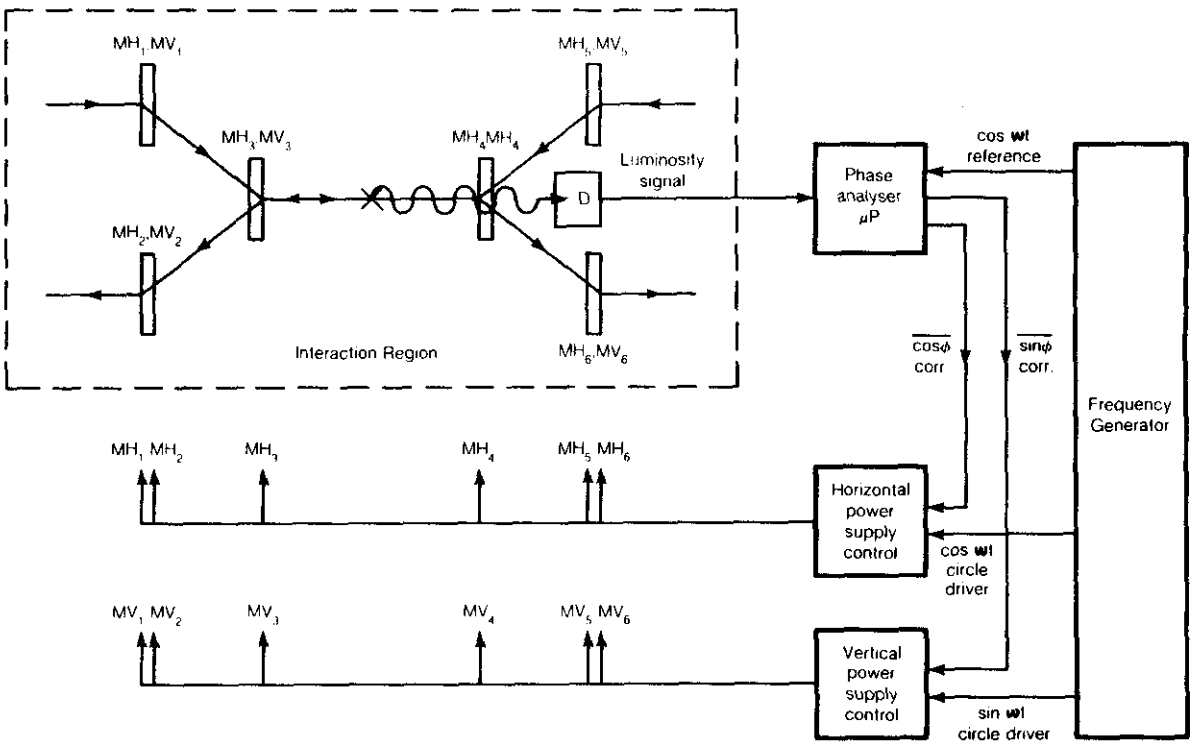

Figure 5.8-4. Block diagram of the collision assurance system. The beams are caused to walk around one another in a circle of one micron diameter. Correlation of the neutral beam dump luminosity D with this motion provides feedback correction signals to the horizontal and vertical steering magnets MH, MV at three locations on either side of the IR.

(a) The relative positions of the collider rings and the HEB;
(b) The lengths of the injection straight sections and the distances between them;
(c) The need to minimize beam losses that might cause superconducting magnets to quench;
(d) The need to have accurate injection orbits to minimize beam emittance dilution;
(e) Redundancy to allow for component malfunction without causing damage to the collider.

Allowing personnel access to the HEB while the collider is operating, and vice versa, imposes a minimum separation between the two of at least six meters [5.9-1]. The injection layout of the present design has a ring separation of nine meters horizontally and seven meters vertically. A significant change in these parameters (for example, a large vertical elevation difference) can be accommodated by straightforward design modifications.

5.9.1 Overall Description

The HEB is centered between the two utility straight sections. Both proton beams are extracted tangentially from the same HEB straight section in opposite directions. There is a slight difference between the two directions because the SSC Collider Rings are displaced 70 cm vertically with respect to each other, requiring different vertical bend angles. This difference is small, and the two injection lines are virtually identical, as shown in Fig. 5.9-1. Henceforth we discuss only one injection line. The length of the utility sections is the same as the interaction region (IR) length, which results in approximately 1150 m region of available drift space divided into a non-cryogenic central region of 670 m and two ends each of 200 m. The centers of the two utility sections are separated by 2400 m.

Within this basic layout the design uses the upstream 200 m region for the injected beam transfer in one ring, followed by the abort system for the same ring in the central region. The injection and abort for the other ring uses the other utility straight section. There are several advantages to this scheme: a) The injected beam does not pass off-axis through any of the lattice quadrupoles, minimizing the aperture requirements in these elements, and simplifying injection tuning. b) The injected beam can be steered directly to the abort dump, allowing a complete checkout of the injector complex and beam transfer system before attempting to circulate beam in the collider. This minimizes the possibility of quenching magnets while tuning up injection. During beam transfer from the HEB to the collider, superconducting magnets are especially vulnerable to beam induced quenches [5.9-2]. In addition, the abort system dog-leg immediately downstream of the injection channel will also sweep out any injection losses occurring in the local region and the injection line.

A detailed layout of the elements in the HEB extraction line, the beam transfer line, and the Collider Rings injection channel is shown in Fig. 5.9-2. The overall length of the beam transfer line is 880 m, determined by the 2.4 km separation of the utility sections.

5.9.2 Injection Process

Beam is extracted from the HEB in a single turn using fast pulsed kicker magnets. These batches are equivalent in length to the circumference of the HEB and are loaded sequentially into the collider rings in boxcar fashion. Fifteen cycles of the HEB are sufficient to fill each collider ring. The minimum separation between batches is 150 ns and is

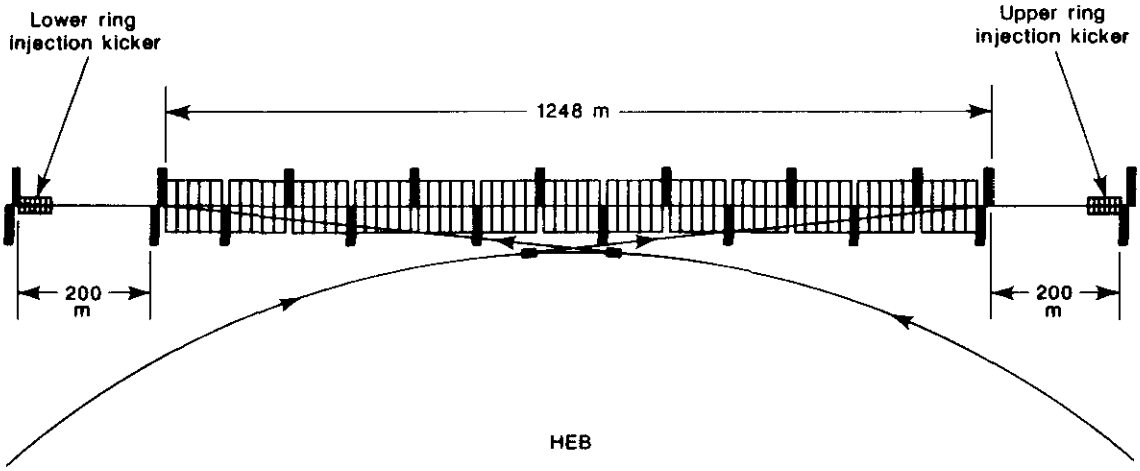

Figure 5.9-1. The relative layout between the High Energy Booster, the injection lines, and the utility regions.

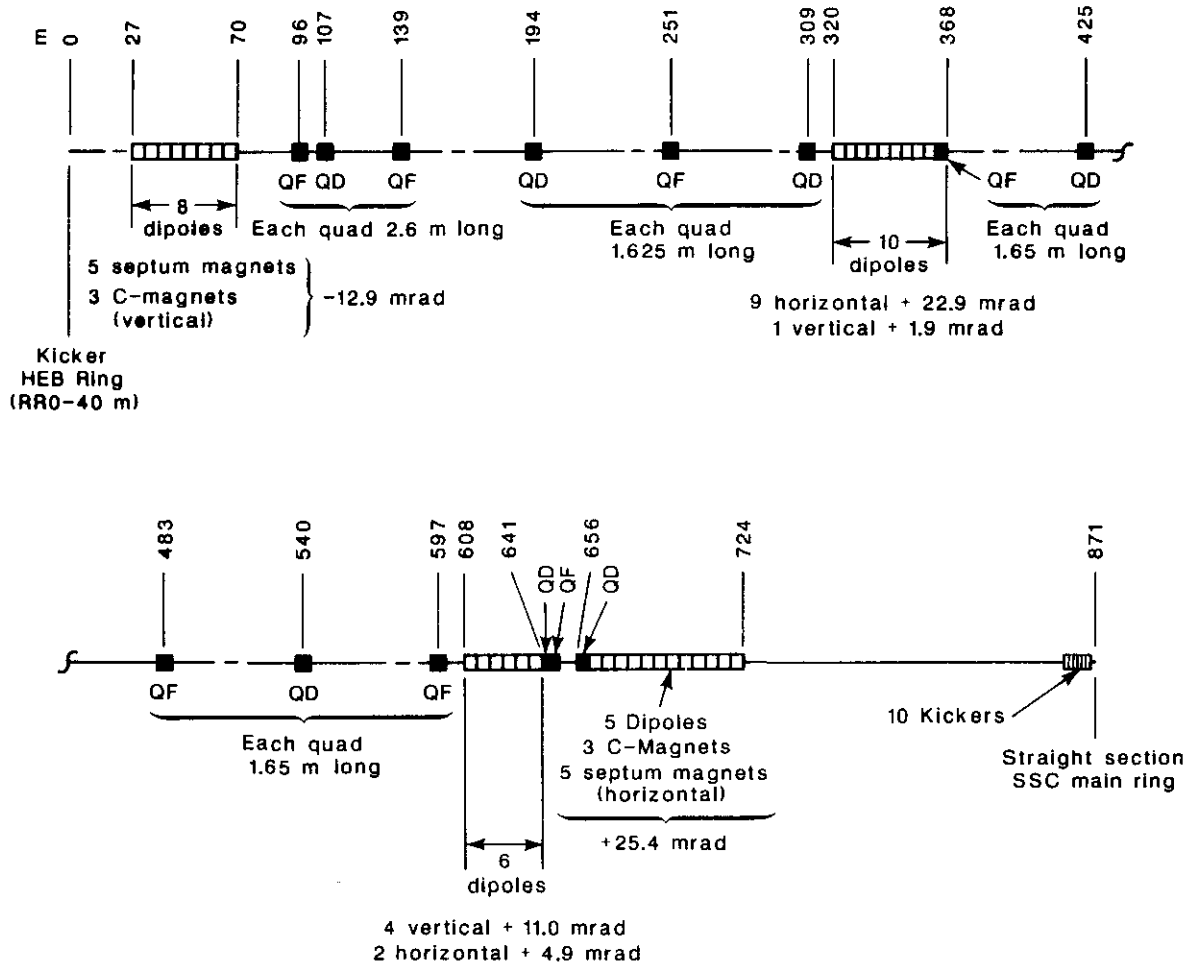

Figure 5.9-2. A detailed layout of a single injection line starting at the HEB extraction channel and ending at the main ring injection channel.

defined by the rise time of the injection kickers. In addition to these short gaps between each batch, a three microsecond beam gap is needed in the collider to allow for the rise time of the abort kickers. This gap is normally established by loading only a partially filled HEB ring into the collider on the last (fifteenth) cycle. The abort gap defines the fall time requirement of the injection kickers. Synchronizing the beam transfer to populate the appropriate rf buckets in the collider is accomplished most naturally by controlling the injection time into the HEB, provided that a phase angle can be maintained during the HEB cycle.

Beam transfers take place at a maximum rate of once per HEB cycle, about 60 s. Allowing for a one second flattop and a two second ramp time for the injection line magnets results in a maximum duty cycle for them of 8.3%. During the time when the beams are colliding the injection system is not needed at all, further reducing the average power needs. Therefore, in order to avoid the complications of non-standard cryogenics and the cost of cooling, conventional magnets are used throughout the injection system.

5.9.3 HEB Extraction Channel

The beam in the HEB is deflected horizontally by a fast kicker into the extraction channel that is in the HEB extraction straight section, 90 degrees in phase advance away. The extraction channel bends the beam vertically downwards through a string of magnetic septa (Lambertson magnets) and C-magnets, as shown in Fig. 5.9-2. The vertical bend angle of 12.9 mrad is chosen so that the beam misses the downstream elements of the HEB extraction straight section. The HEB lattice parameters are such that there is a small vertical beam size and large horizontal beta function at the entrance to the extraction channel. This is suitable for positioning the circulating beam close to the notch in the Lambertson magnets while maximizing the horizontal deflection from the kicker magnets.

5.9.4 Beam Transfer Line

At the downstream end of the extraction channel three quadrupoles match the HEB lattice parameters into a FODO section in the injection line. These quadrupoles provide sufficient phase advance to allow for dispersion cancellation in the injection line. Dispersion cancellation in the injection line is needed since both the HEB and the Collider Rings have zero dispersion in both planes across the straight sections. At the downstream end of the injection line the beam is brought back into the horizontal plane with a set of vertically bending dipoles. The location and relative strength of these magnets is defined by dispersion cancellation.

The utility sections are separated by 6.5 standard cells in a dispersion suppressing arrangement, resulting in a horizontal angle of 106.4 mrad between the injection straight sections. Therefore, each injection line needs a radially inward deflection of half this amount. This bend is provided by a series of horizontal dipoles in the beam transfer lines, plus the bend in the Collider injection channel. The Collider injection channel is identical to the HEB extraction channel, except that it is rotated by 90 degrees, to provide horizontal instead of vertical bending. The location and strength of the injection line horizontal dipoles is dictated by dispersion matching requirements, as was the case for the vertical dipoles. The injection line optics are matched to the Collider Ring lattice with three

quadrupoles located upstream of the injection channel. The lattice parameters of the transfer line are shown in Fig. 5.9-3.

5.9.5 Collider Ring Injection Channel

The choice of horizontal bending in the injection channel avoids complications arising from the fact that the Collider Rings are separated vertically from one another. At the end of the injection channel the injection orbit is positioned on the circulating beam closed orbit horizontally, but displaced vertically. A vertical bend of about 110 μrad positions the beam on the vertical closed orbit at the injection kickers. The injection channel is positioned in the utility straight section as far away from the vertical kickers as possible, in order to minimize the strength of the kickers, while at the same time having the injection beam line not interfere with the cryostat of the closest utility section quadrupole.

The inboard four quadrupoles in the utility section are slightly non-standard since the large beta values of the lattice at these locations would pose dynamic aperture restrictions if the field quality in these magnets were similar to the standard arc quadrupoles (see Section 4.3). The solution to this problem is to increase the coil radius in these elements to the 5 cm value used in the HEB arc quadrupoles. The maximum field gradient is thus reduced to 140 T-m and the element length is increased accordingly. The aperture of these magnets does not effect the beam transfers in this region.

5.9.6 Major Elements of the Injection System

For the purposes of estimating the aperture requirements necessary to avoid beam losses in the injection region, twice the 95% beam size is used to represent the total beam spot size. The critical apertures in the injection system occur in the Lambertson septum magnets, which provide the initial separation between the circulating beam and the kicked beam in both the HEB and the Collider Ring. The beam profiles and separations in these magnets used in defining kicker strengths, nominal orbits, and critical apertures are shown in Fig. 5.9-4. The closest approach of the beam to a physical aperture in the Lambertson septa is 3 mm, which corresponds to a nominal separation of 15 mm between the circulating and injected beam at the downstream end of the septa.

Lambertson Magnets

The first and last series of elements in the injection line are the magnetic septa. A cross section of the magnet is shown in Fig. 5.9-5(a). The magnet is designed to give a maximum field of one tesla at a current of one kiloampere. The pole face dimensions provide a good field region for a beam sagitta (width) of 10 cm and a usable physical aperture (gap) of 25 mm. The magnets are constructed from high-permeability low-carbon steel, stamped into differently shaped inner and outer laminations. This technique allows a vacuum skin to be put around the inner laminations to isolate the coils and the outer lamination from the beam vacuum. The inner laminations are prebaked under vacuum at 800 C before being assembled into the package containing the coils and the outer laminations. A low temperature in situ bake of the whole assembly results in a vacuum of 2×10^{-9} Torr, using five 30 liter/s ion pumps distributed along the length of the magnet.

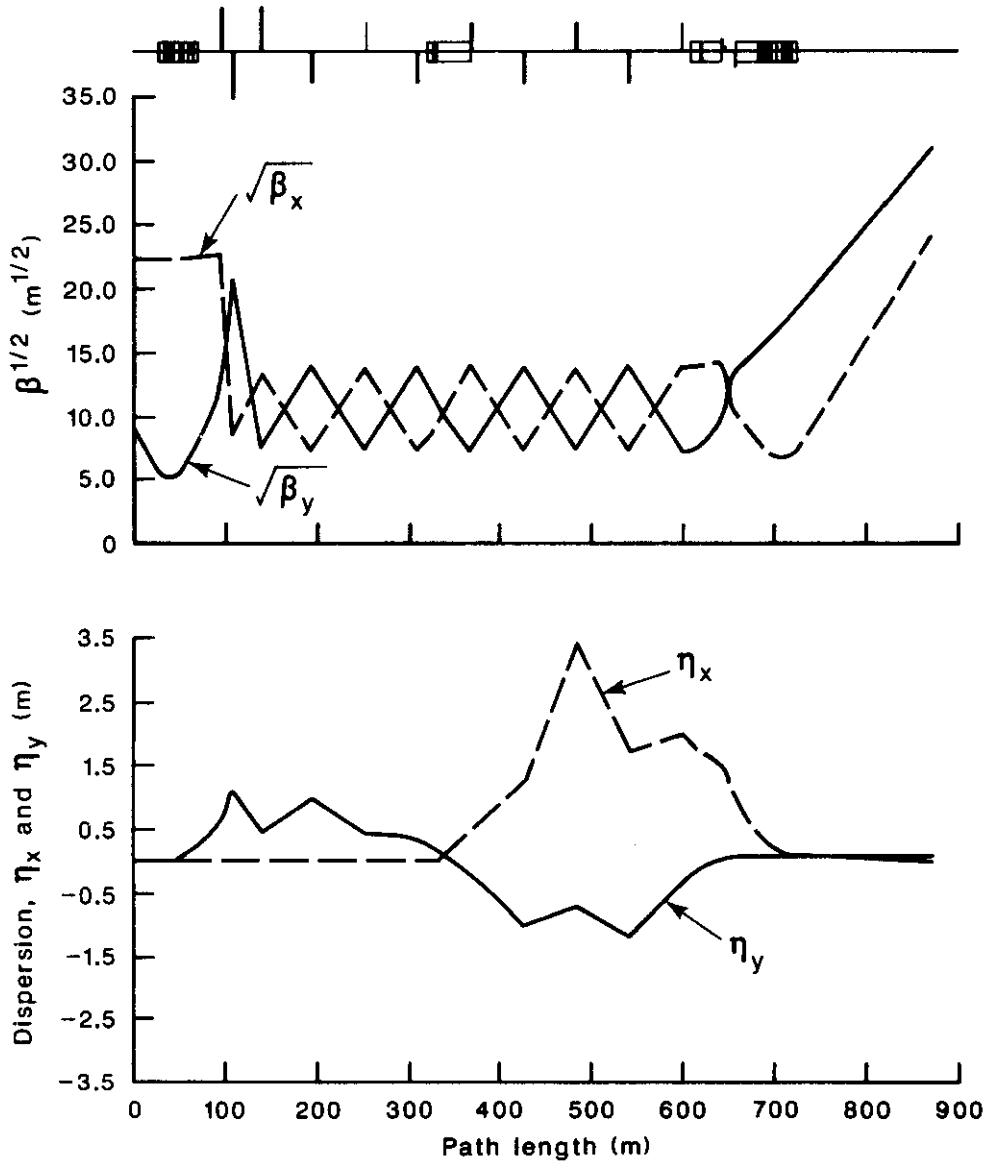

Figure 5.9-3. The injection line lattice parameters. The HEB lattice is matched into a FODO section with three quadrupoles. The matching to the utility region lattice at the downstream end also requires three quadrupoles. The overall phase advance is determined by dispersion cancellation in both planes.

Beam position at HEB
extraction Lambertson septum

Beam size = $\Delta x = \pm 3.0$ mm
$\Delta y = \pm 0.75$ mm

Beam separation = 16 mm

Beam position at collider
injection Lambertson septum

Beam size = $\Delta x = \pm 1.1$ mm
$\Delta y = \pm 1.85$ mm

Beam separation = 15 mm

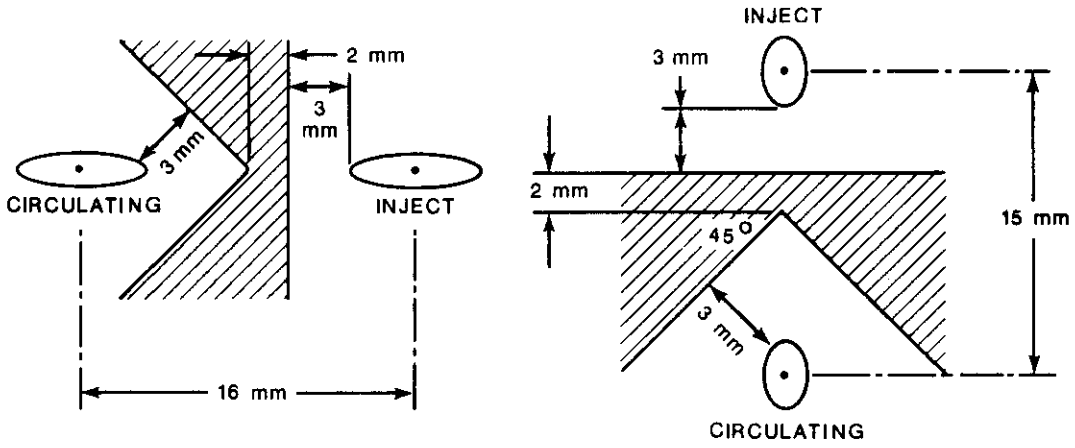

Figure 5.9-4. The beam profiles and separations at the upstream and downstream magnetic septa. These beam positions are used to define the kicker strengths.

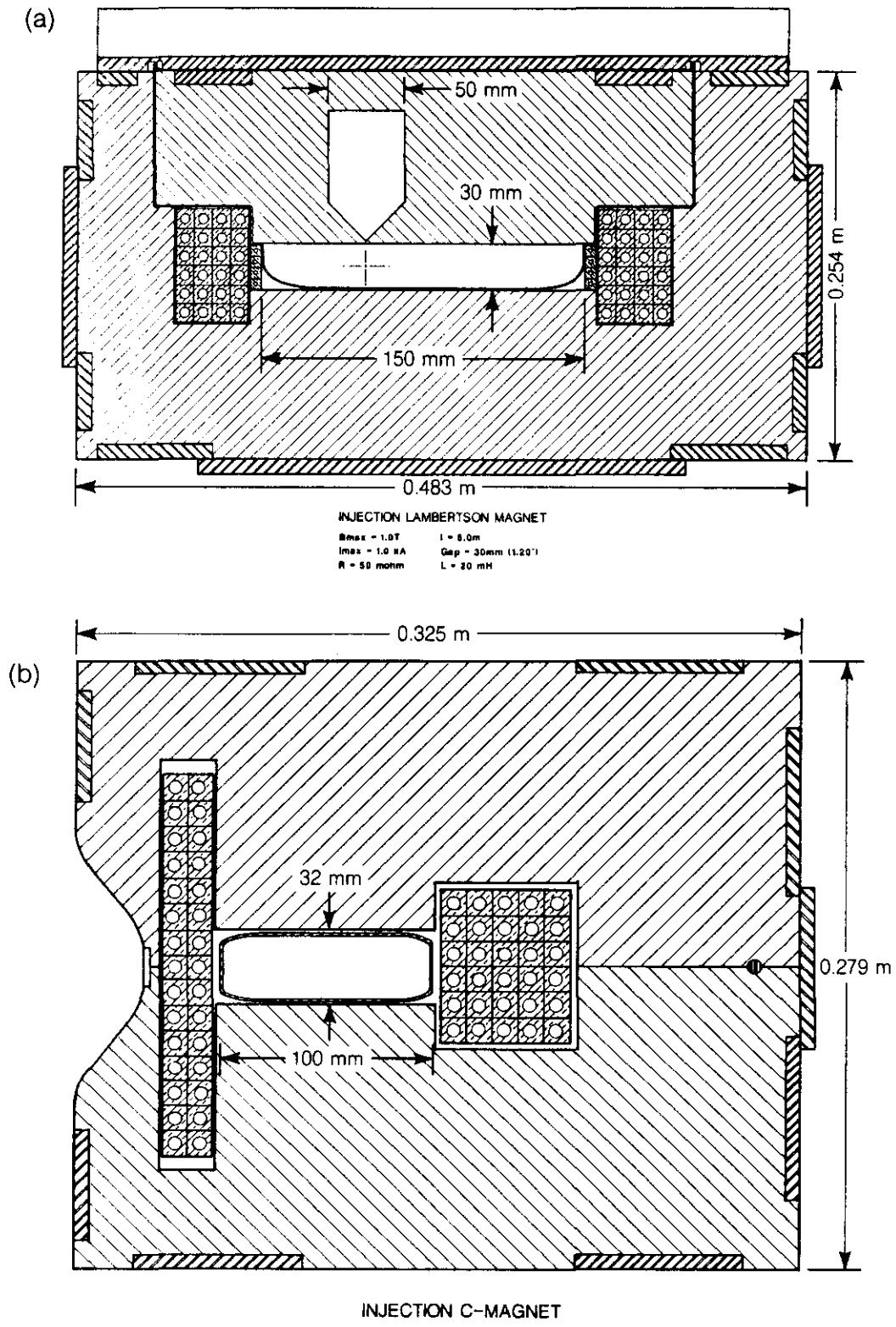

Figure 5.9-5. (a) A cross section of the injection Lambertson magnets. The laminated magnet is built in two halves to minimize the material under vacuum. (b) A cross section of the injection C-magnet. The laminated magnet requires a minimum beam separation of 10 cm.

The stamped laminations have a septum thickness of 1.5 mm, which together with an alignment tolerance of 0.5 mm along the five meter length gives an effective septum thickness of 2.0 mm. The field-free region half angle is 45 degrees, to reduce the leakage field to less than 20 gauss. Fringe fields at the magnet ends are reduced by extending the inner lamination stack beyond the outer stack and the saddle coil turn-around. The field integral in the field free region will be about 200 gauss-meters [5.9-3]. Dipole trim coils are built into the magnets in order to provide small adjustments to the bend angle.

C-Magnets

The transfer line C-magnets, shown in Fig. 5.9-5(b), are designed to match the apertures and beam separation in the Lambertson septa. The five m long magnets are laminated in two identical halves and have a design field of 1.2 T at one kiloampere. Fringe fields around the circulating beam will be less than ten gauss at full excitation and can be reduced further with magnetic shielding.

Quadrupoles

The quadrupoles in the injection line are of varying strengths, ranging from a field integral at 1 cm of 1 T-m down to 0.3 T-m. The different magnets are built with the same cross section but different lengths to achieve the focusing needed. The magnet cross section is shown in Fig. 5.9-6(a). The pole face radius is 26 mm and produces a field gradient of 40 T-m at one kiloampere, which results in a maximum field at the pole tip of 1.0 T.

Dipoles

The bending dipoles, shown in Fig. 5.9-6(b), are standard magnets producing a field of 1.7 T at one kiloampere. In a manner similar to the quadrupoles the lengths and number of elements in a string are varied to produce the required bend angle.

Kicker Magnets and Pulse Forming Networks

The injected beam intercepts the closed orbit at a vertical angle of 110 μrad. The integral field strength of the kicker magnets must remove that angle at the injection energy of 1 TeV and have a 0 to 100% rise time of 150 ns. The system is composed of ten separate modules, each 0.8 m long, and each with an individual pulse forming network (PFN). A magnet module is made from C-shaped ferrite, as shown in Fig. 5.9-7. Electrically, it is a ten-cell lumped delay line with a characteristic impedance of 16.6 Ω. The beam tube is an indium-coated ceramic pipe with image current strips on the outside. The equivalent circuit for the magnet and its PFN is shown in Fig. 5.9-8. The detailed system parameters are given in Table 5.9-1.

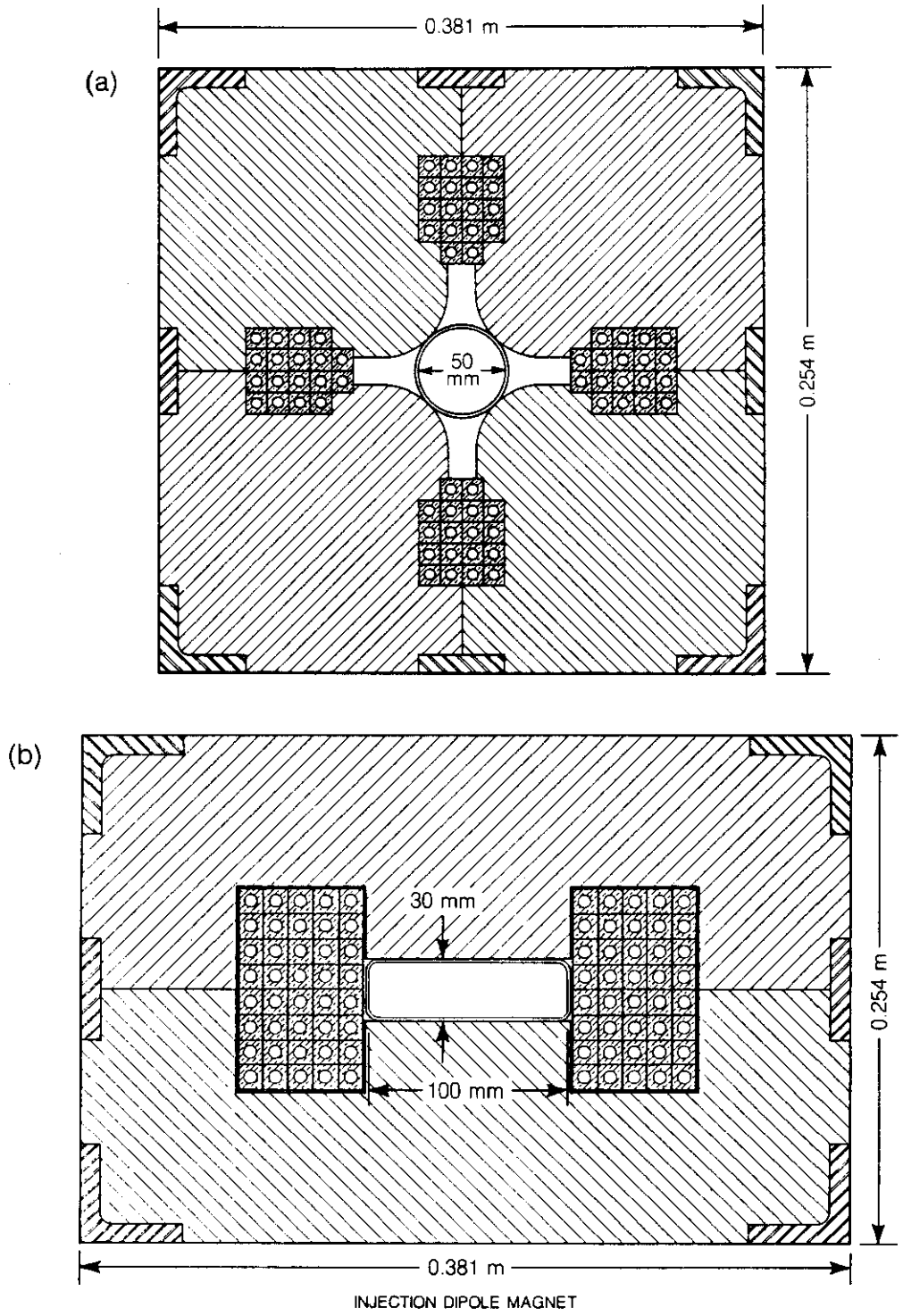

Figure 5.9-6. (a) A cross section of the transfer line quadrupoles. The design gradient is 40 T/m. (b) A cross section of the transfer line dipole.

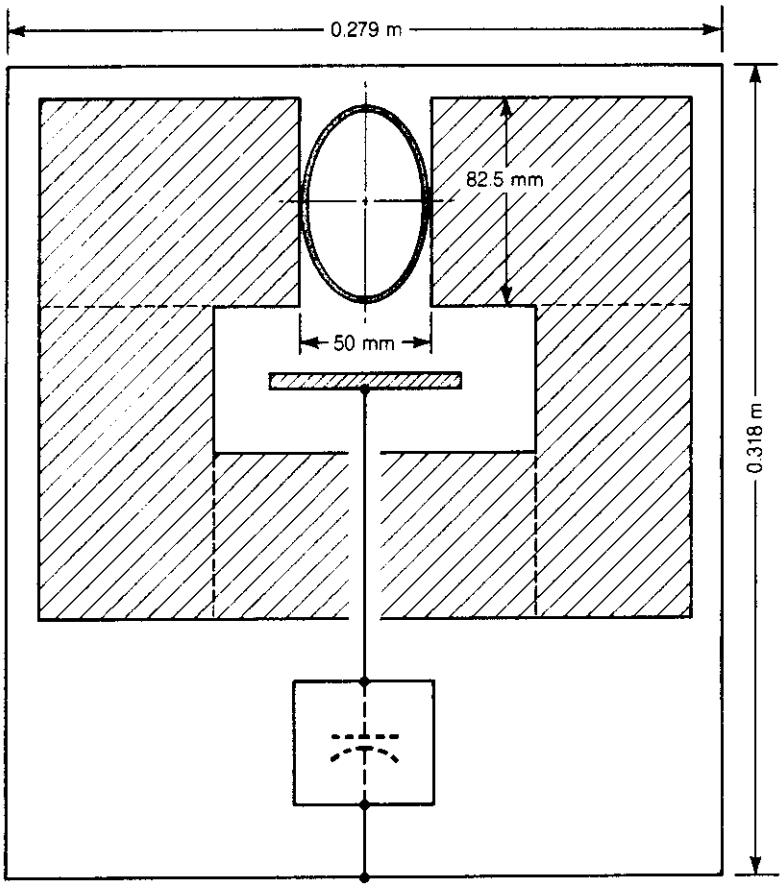

Figure 5.9-7. A cross section of the injection kicker magnet. The C-style ferrite magnet is chosen to facilitate construction as a lumped element delay line.

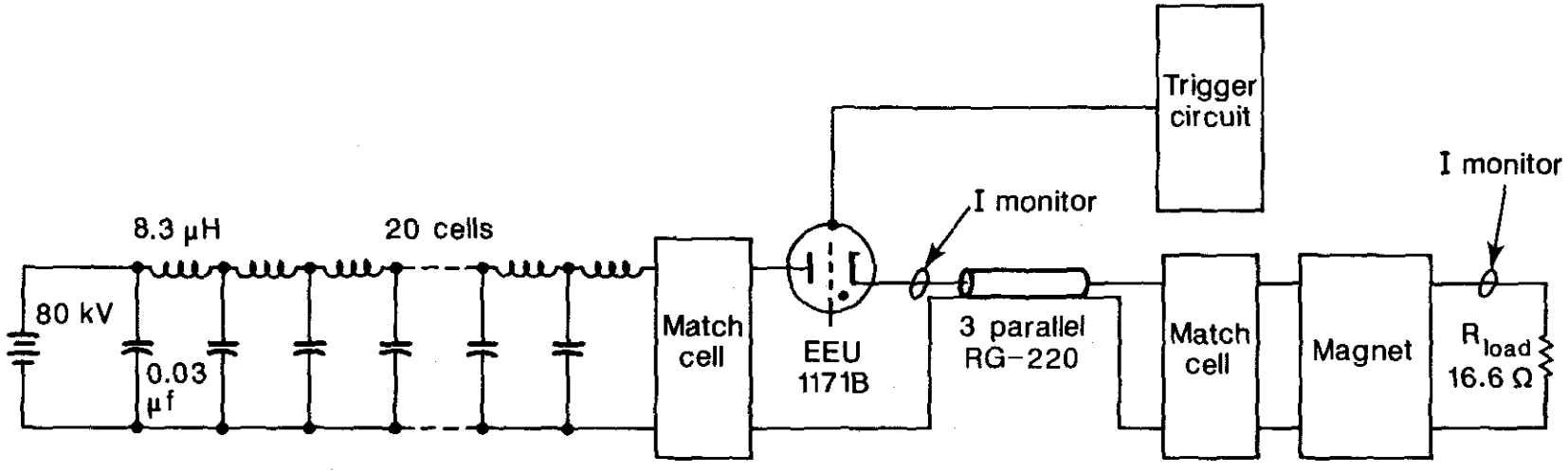

Figure 5.9-8. The PFN/kicker magnet equivalent circuit. The 20 cell PFN delivers a flat (<1%) pulse into a matched load via the 10 cell magnet.

Table 5.9-1.
Injection Kicker System Parameters

Magnet type	Ferrite C-magnet, 10 cell, lumped delay line
Impedance	16.6 Ω
Maximum Field	600 G
Maximum Current	2.1 kA
Maximum Voltage	66 kV
Total Length	8 m
Number of Modules	10
Rise Time (0 to 100%)	150 ns
Fall Time	<3 μs

Power Supplies

All the major magnetic elements in the injection system have been designed to run at one kiloampere, and therefore a single supply could power the whole line in series. In order to reduce the size of the power supplies and create a flexible tuning environment, each line will be split into three main power buses, for the vertical bends, horizontal bends, and quadrupoles. The peak power requirements are 0.9 MW, 1.95 MW, and 0.56 MW respectively. The average power during the injection process is an order of magnitude less. Decoupling the magnets in this way allows straightforward position changes in both planes at the downstream end of the line without varying the transverse phase space matching.

For the major injection elements, see Table 5.9-2.

Table 5.9-2.
Injection System Major Elements (Both Rings)

	Number of units	B_{max}(T)	L(m)
HEB extraction kickers	10	0.06	0.8
HEB extraction magnetic septa	10	1.0	5.0
HEB extraction C-magnets	6	1.2	5.0
Injection line quadrupoles	28	40 (T/m)	0.5→2.5
Injection line horizontal dipoles	32	1.7	5.0
Injection line vertical dipoles	10	1.7	5.0
Main ring injection magnetic septa	10	1.0	5.0
Main ring injection C-magnets	6	1.2	5.0
Main ring injection kickers	20	0.06	0.8

5.9.7 Diagnostics and Tuning

In order to minimize residual beam oscillations we require independent control of position and angle in the horizontal and vertical planes for both the closed orbit and the injected beam at the location of the injection kickers. Beam steering down the injection line is also necessary. Closed orbit control across the utility straight section is provided by standard arc correction dipoles mounted in a spool piece adjacent to the quadrupoles. Each spool piece will contain two dipoles (H and V). The strength of the standard dipole correction element is sufficient to permit orbit adjustment over the full physical aperture in both planes. Horizontal control of the injected beam (in angle) is provided by trim coils in the Lambertson septum magnets, together with trim supplies on the upstream bends and the main bus. Vertical angle adjustment is provided by the kicker strength, while vertical position is adjusted with the main bus, together with trims on the dipoles. Transverse phase space matching can be accomplished by varying the final three quadrupoles in the injection line with shunt supplies.

Injection diagnostics can be considered for the most part to be special operating modes built into the standard beam monitoring systems. The beam position monitor (BPM) system is capable of providing first and second turn instantaneous images of the injected beam batch, as well as turn by turn data from individual BPMs. Beam positions in the injection line are taken in both planes at each quad location with regular BPM pick-ups, allowing verification of the injection line optics, as well as monitoring the beam positions.

The kicker waveforms and relative beam timings are recorded on a pulse by pulse basis in a transient digitizer for display and monitor purposes. Beam profiles are provided in both planes at two locations in the injection line on a request-only basis.

Prior to extracting beam from the HEB, a "prepare-for-beam" timing signal initiates a self checking procedure in the subsystems (kicker voltages, power supply currents, etc.), which will result in an "injection-inhibit" signal to the HEB if the system is not ready.

5.9.8 Failure Modes

During the transfer process and the first several turns, the beam abort system offers little protection against beam loss and subsequent magnet quenching. This was demonstrated during the operation of the Tevatron for fixed target physics in 1985 when 43% of all quenches occurred during injection. Slow-acting faults (power supplies, regulation, etc.) inhibit the beam transfer and thus are unlikely to pose quench problems. The most probable potential quench scenarios are as follows:

Kickers Not Firing

A control system failure to provide the global kicker system trigger results in no kickers firing. The injected beam begins to execute a vertical oscillation around the closed orbit. For the nominal operating conditions this would result in a beam displacement of 50 mm in the arcs. The unkicked beam will pass through the doublet immediately downstream of the kickers with little displacement, but will be about 40 mm low at the upstream end of the abort Lambertson septum string. Installing an internal stainless steel beam dump five meters long at this location will stop the beam, and the secondary spray from this device will be absorbed by the conventional magnets. Particles that manage to enter the good

aperture region of the abort magnets are of low enough energy to be swept out of the machine before reaching the next cryogenic elements.

Kicker Module Not Firing

The failure of a single kicker module would result in a five millimeter vertical oscillation in the arcs. Beam motion of this magnitude lies on the edge of the linear aperture of the machine and would circulate for many turns. The choice of aborting the beam or accepting a certain amount of emittance growth is an operational question, but in any case such a failure should not result in a quench condition.

Loss of Synchronization

Injection kickers might fire at a random time with respect to the injected beam. If the kickers miss the beam pulse totally the analysis is the same if the kickers did not fire. If circulating beam coincides with the kicker pulse, then part of the circulating beam is deposited in the internal dump, but with a positive vertical offset rather than a negative one. Beam that overlaps the rising and falling edge of the kicker pulse will be smeared around the machine and may or may not quench the magnets in various locations. A detailed Monte Carlo calculation is needed to predict the energy deposition resulting from this effect. The calculation would also indicate whether secondary absorbers will be useful.

Radio-Frequency Errors

Various errors in the rf system are difficult to determine without beam in the machine (for example, the synchronous phase) and can result in large amplitude synchrotron oscillations. Errors in the rf system result in beam motion with time constants characterized by the synchrotron frequency, typically hundreds of turns, and so are slow enough that the abort system can be used to remove the beam safely.

5.10 Beam Abort System

The purpose of the beam abort system is to remove beam quickly and safely from the SSC Collider Rings in the event of high beam loss or certain system malfunctions. The abort system also serves to remove beam from the machine during normal operation at the end of a storage or study cycle.

5.10.1 Overall Description

The abort system is a fast acting single turn extraction system capable of removing beam from the machine within three turns of the generation of an abort command. The system is comprised of a series of kicker magnets that directs the beam into a channel which, in turn, deposits the beam onto a beam dump. Because the SSC Collider Rings use superconducting magnets, the abort system has to be 100% reliable, and must be as loss-free as can be realistically achieved. This is a qualitative rather than a quantitative statement, in the sense that the decision to abort the beam can reflect the fact that the beam has already become unstable, and thus nominal beam parameters (position or size, for example) may not apply. The approach taken to deal with this problem is to require the abort

system aperture to be larger than the machine aperture and to use a design that minimizes the beam loss on the superconducting elements in that region.

To provide a loss-free abort there must be a gap in the circulating beam which serves to provide time for the kickers to rise to full field. In the SSC design the gap must be at least 3 μs. In order to extract all of the circulating beam the kickers must maintain full field for at least 300 μs; it is prudent to design for a longer time than this. The magnetic field of the abort system kickers must track the beam energy. Both rings use identical systems; for the purposes of this discussion we shall refer to a single ring only.

The abort system for one ring is located in the central drift region of one of the utility sections, immediately downstream of the injection system for the same ring. The abort for the other ring is located in the other utility section. A schematic view of the arrangement is shown in Fig. 5.10-1. The machine lattice functions in the utility regions have been described in Section 4.2.5, the quadrupoles in Section 5.9.5. The design, which is similar to that employed in the Tevatron, uses a closed orbit bump inside the drift region. The lack of focusing elements in the drift region means that to first order the machine optics are unaffected by the size of this bump. The bump is generated by two 20 m long strings of 1.7 T conventional dipoles at each end of the drift space and a string of Lambertson septum magnets about 66 m long in the center. The beam circulates in the dipole region of the septum magnets and is aborted by kicking the beam (upwards for the lower ring, downwards for the upper ring) into the field free region. The direction of the aborted beam is thus defined by the dog-leg angle, which in turn is defined by the requirement of missing the cryostat of the superconducting quadrupole nearest to the drift region. The kicker magnets are located immediately downstream of the conventional dipoles to maximize the drift length to the septum magnets. The layout of the central region of the utility section is shown schematically in Fig. 5.10-2.

The advantages of using a closed orbit bump for an abort system are twofold. First and most important, the downstream superconducting elements are not in the direct line of the aborted beam and are thus afforded protection from beam losses. Provided the beam clears the magnetic septum, almost complete immunity is expected. Secondaries produced in the dipole region will be charge-selected, with the negatives swept away from the machine, and the neutrals continuing in the general direction of the abort line. Low energy positives will also be swept out of the machine, leaving only high energy positive particles as a potential source of beam loss. A collimator in front of the downstream dipoles will be used to provide additional protection for the superconducting magnets.

The second advantage to this scheme is that the effective horizontal bend point in the abort trajectory is moved as far upstream as possible, allowing the length and strength of the magnetic septa to be reduced, while maximizing the clearance between the downstream quadrupole cryostat and the aborted beam. The abort channel does not rely on a magnetic field to remove the beam, consistent with a fail-safe approach.

The ability to remove a single batch of badly injected beam with a fast abort system that leaves the rest of the circulating beam intact could prove to be an attractive enhancement to the overall design. A system of fast kicker magnets immediately downstream of the slow kickers with specifications similar to the injection kickers (150 ns rise time, 20 μs flattop, 110 μrad bend angle) would satisfy these requirements. A more elegant but less straightforward approach is to recharge the injection kickers themselves to $\sim$60% of their injection voltage and refire. The badly injected batch would have to circulate for the

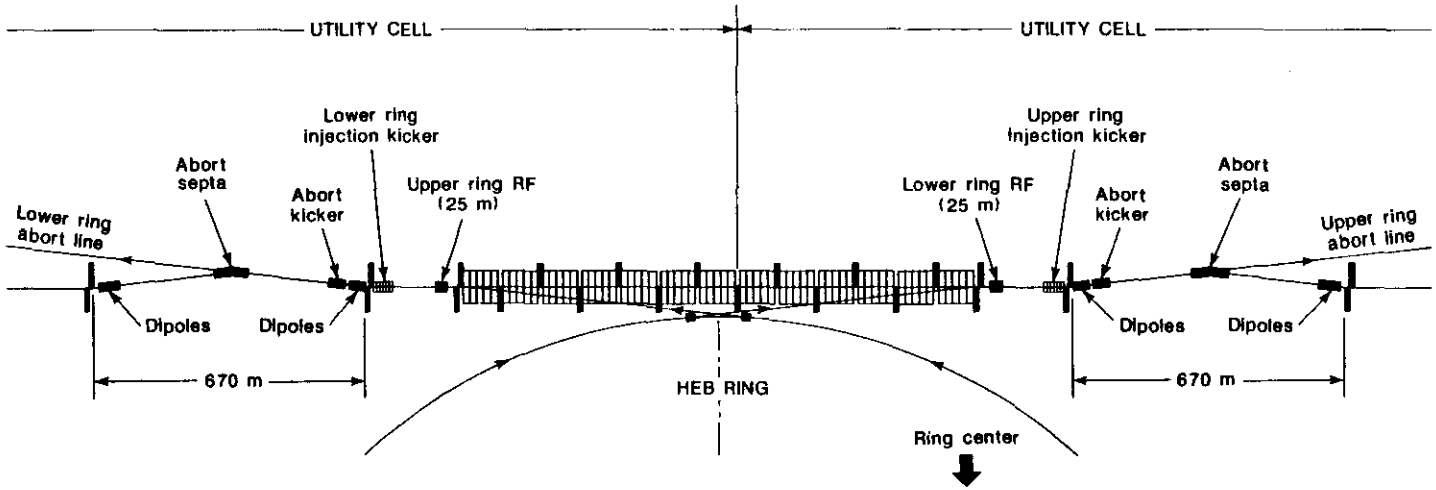

Figure 5.10-1. Collider beam abort systems. The two utility sections are separated by the 6.5 cell dispersion suppressor and reflect the antisymmetry of the machine lattice in their internal layout.

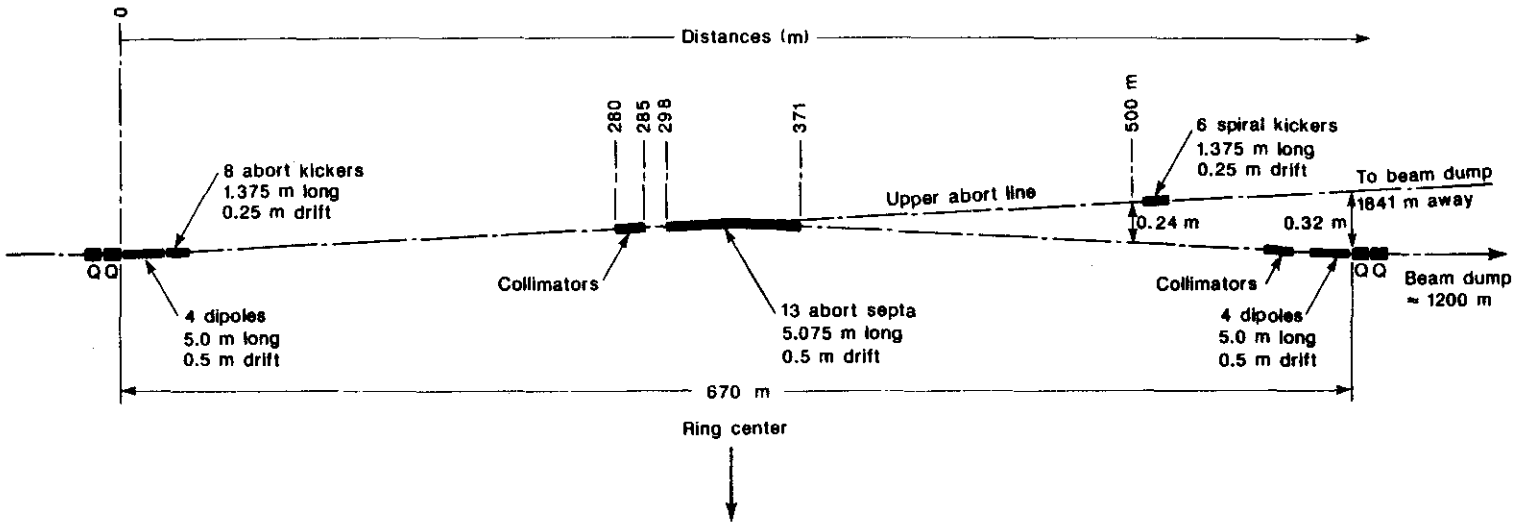

Figure 5.10-2. Utility section central region. The location of the major abort system elements and initial beam trajectory are shown.

several seconds needed to recharge the injection system, but the 40 s cycle time of the HEB allows this operating scenario. The high field orbit stability of the HEB should be as good as that of the Tevatron (<0.3 mm), which leads one to believe that, when tuned up, the pulse to pulse variations of the injected beam ought to be small. We have chosen not to present a fast abort in the machine design but only to comment on the feasibility.

5.10.2 Required Aperture in the Abort System

The design of the individual elements is strongly influenced by the required aperture. An estimate of the necessary abort aperture is obtained by projecting maximum aperture of the standard cell in which particles can circulate, estimated at a 10 mm radius, onto the abort elements. The results, shown in Fig. 5.10-3, yield beam sizes that range from 18 mm by 12 mm in the dipoles, to 8 mm by 8 mm in the magnetic septa. These beam sizes correspond to an emittance growth of a factor of about 225 at 20 TeV. The magnet apertures and kicker strengths are then calculated assuming a beam spot of this size and allowing an approach to a physical aperture of no less than two millimeters. These are deliberately chosen extreme criteria. It is difficult to postulate mechanisms that could produce amplitudes or smeared beam of this magnitude (the unlikely event of two injection kickers misfiring at the same time would produce a vertical oscillation amplitude of about this size). It is worth noting that the Tevatron abort system, which is relatively trouble free, would fail this test. The reason why the Tevatron abort system can work with an effective aperture that is smaller than the standard cells is because beam pathologies are invariably detected before the beam fills the available aperture. The SSC dynamics will, in all likelihood, permit similar early detection of problems.

5.10.3 Elements in the Ring

Kicker Magnets

With the aperture criteria derived above, the nominal separation between the circulating and the aborted beam at the start of the magnetic septa is 26 mm, which corresponds to a vertical bend angle of 95 μrad, or 6.5 T-m integrated field at 20 TeV. Hence, a magnet string with a field of 0.6 T requires an effective length of 11 m to produce the required vertical bend angle. The choice of 0.6 T for the maximum operating field is the result of a trade-off between the current and voltage requirements on the pulsing system, which favor low fields for reliable operation, and the number and length of the magnets that can be reduced by running at higher fields. Ferrite magnets, similar to the injection kickers, are not capable of attaining 0.6 T field; the magnets therefore employ a tape-wound core construction. A cross section of a typical magnet is shown in Fig. 5.10-4.

The pulse shape requirements of the kicker are a rise time less than three microseconds, a flattop length greater than 300 μs, and a flattop stability of five per cent. Because the abort takes the beam out of the machine there is no fall time requirement. The fast rise time together with the long flattop suggest a two-stage pulsing circuit. The system is composed of eight short (1.375 m) elements, each with its own pulser. The pulsing unit is a two-stage device shown schematically in Fig. 5.10-5. The rise time is obtained by discharging a high voltage capacitor bank into the inductive load by closing a thryatron

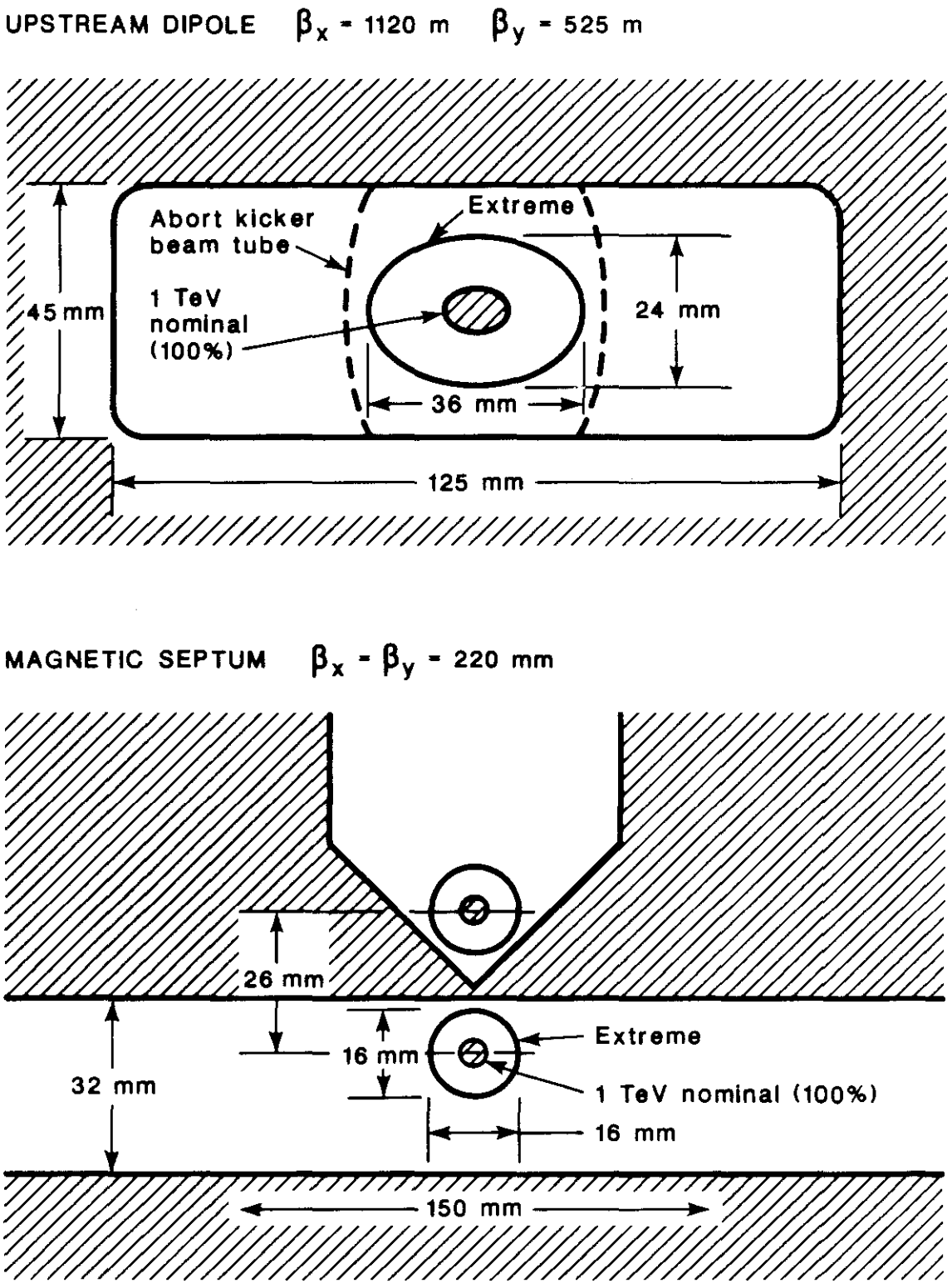

Figure 5.10-3. Abort system aperture requirements. The internal abort system critical apertures are shown together with the relative positions of the circulating and aborted beams. The beam sizes are the nominal injected beam and the maximum possible circulating beam.

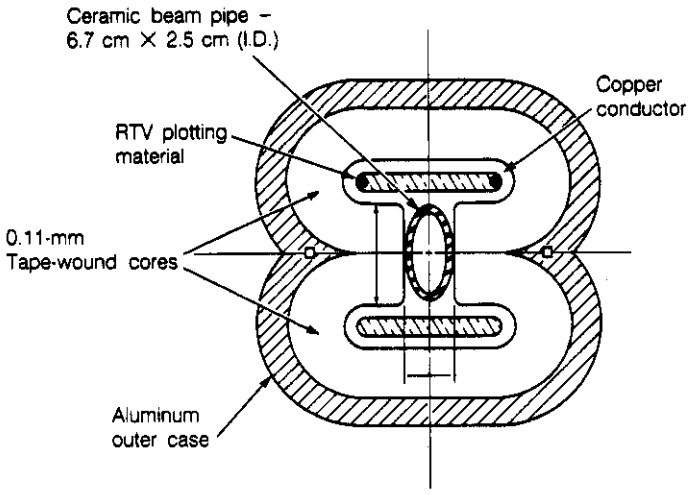

Figure 5.10-4. Cross section of abort system kicker magnet. The magnet is fabricated from tape wound cores to permit the 0.6 T maximum field.

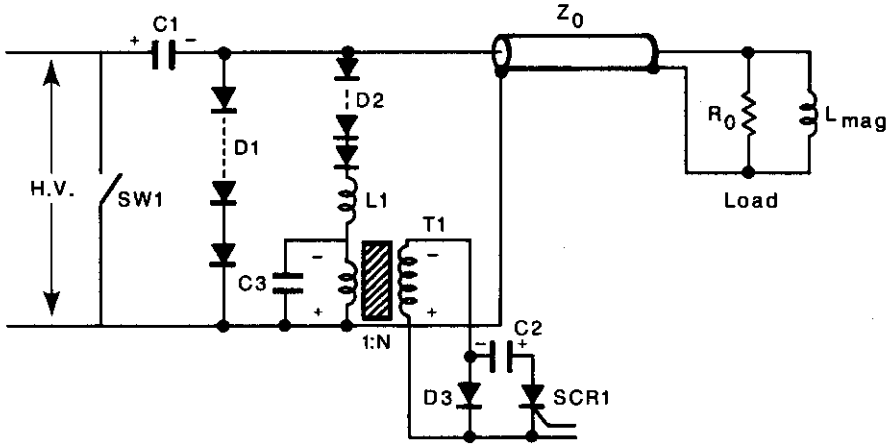

Figure 5.10-5. Schematic of the kicker magnet pulser unit of the abort system. The two stage pulsing system delivers a fast rise time from a capacitor discharge and a long flat pulse from the slower SCR regulating circuit.

switch. When the current reaches its peak value the voltage across the capacitor reverses polarity. The bypass diode starts conducting and the current in the magnet starts to decay with a long L/R time constant. At this point the low voltage circuit is turned on with the silicon controlled rectifier (SCR) switches and the current rise is adjusted so that the composite waveform achieves the required uniformity. The waveform components are shown in Fig. 5.10-6; the kicker and pulser specification are given in Table 5.10-1.

Table 5.10-1
Abort Kicker/Pulser Specifications

Length	1.375 m
Pole Face	40 mm (H) × 75 mm (V)
Inductance	3.25 μH
Resistance	23 mΩ
Magnetic Field	0.056 → 0.6 T
Current	1.07 → 19.0 kA
Voltage	3.0 → 32.0 kV
Rise Time (0 → 100%)	3 μs
Pulse Length	$>$ 300 μs
Flattop Stability	$<$ $\pm$2.5 %

The total high voltage applied to the eight pulsers tracks the beam energy. The minimum voltage across the thyratrons is three kilovolts for reliable triggering, and therefore the twenty to one dynamic range in energy implies a voltage of 60 kV at 20 TeV. To avoid this high voltage, and possible spontaneous triggering, the capacitor banks for particular pulsers and their associated kickers are charged only when required by the increasing beam energy. The choice of eight independent kicker systems ensures that the beam will leave the machine even if two of the abort kickers fail to fire. The aborted beam positions under failure mode conditions are shown in Fig. 5.10-7.

Lambertson Magnets

The magnetic septa, shown in Fig. 5.10-8 (a), are similar in design to those already described in the injection system. The major difference is that these elements are excited in series with the main SSC current bus for reliability reasons. Thus the number of turns and the cross-sectional area of the coils reflect the fact that the magnet must be capable of operating continuously at 6500 A. The beam circulates in the dipole region of the magnets, so the field quality is of some concern. The integrated field strength of the 66 m of septum magnets is less than one arc dipole, so the effect of any harmonic structure in the magnetic

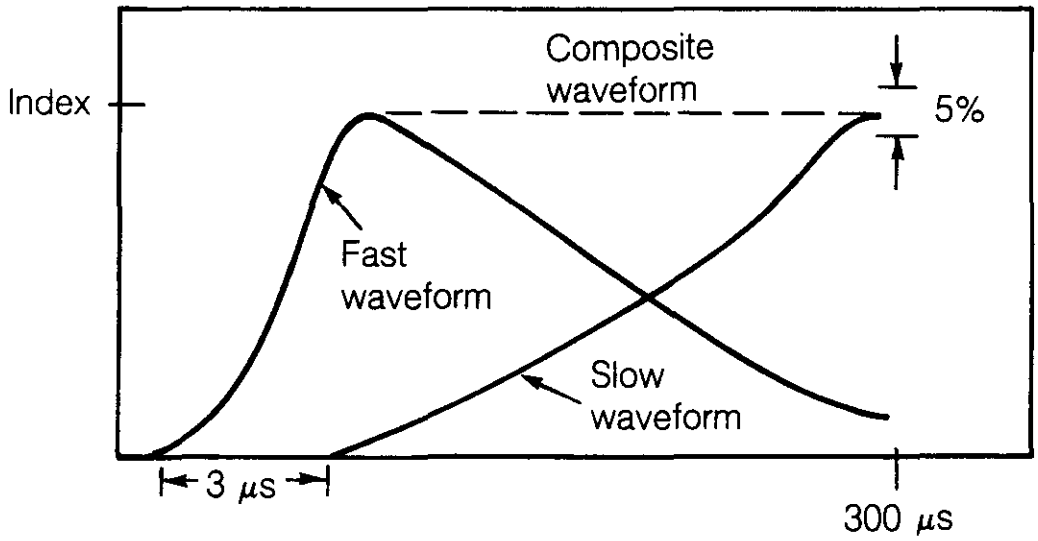

Figure 5.10-6. Output waveform of the abort system pulser unit. The output waveform is the sum of the fast and slow circuits.

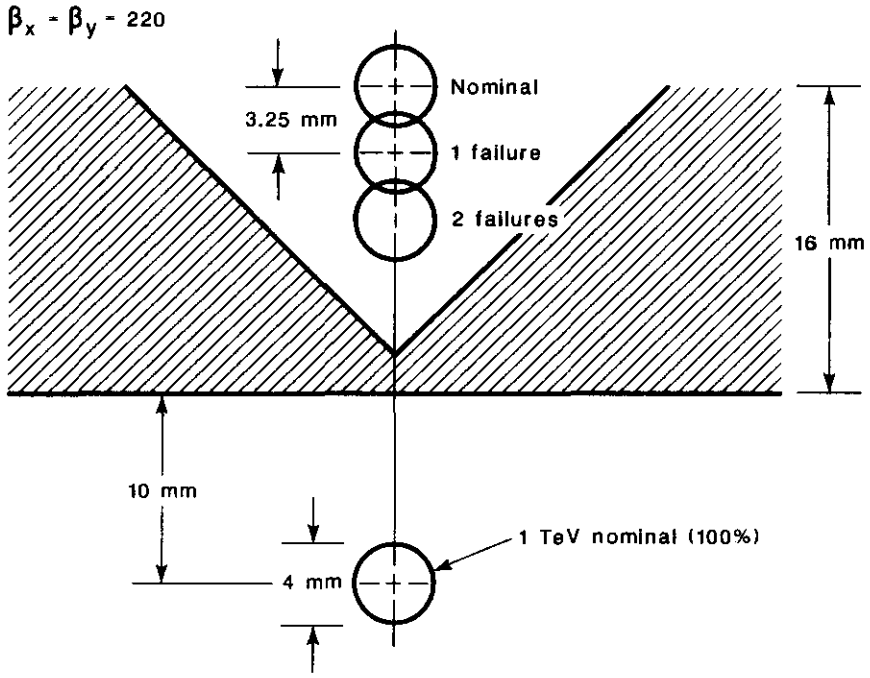

Figure 5.10-7. Internal abort beam positions. The aborted beam position and size are shown at the magnetic septa, which represent the start of the external beam channel, for a nominal beam abort and for one and two kicker magnets failing to fire.

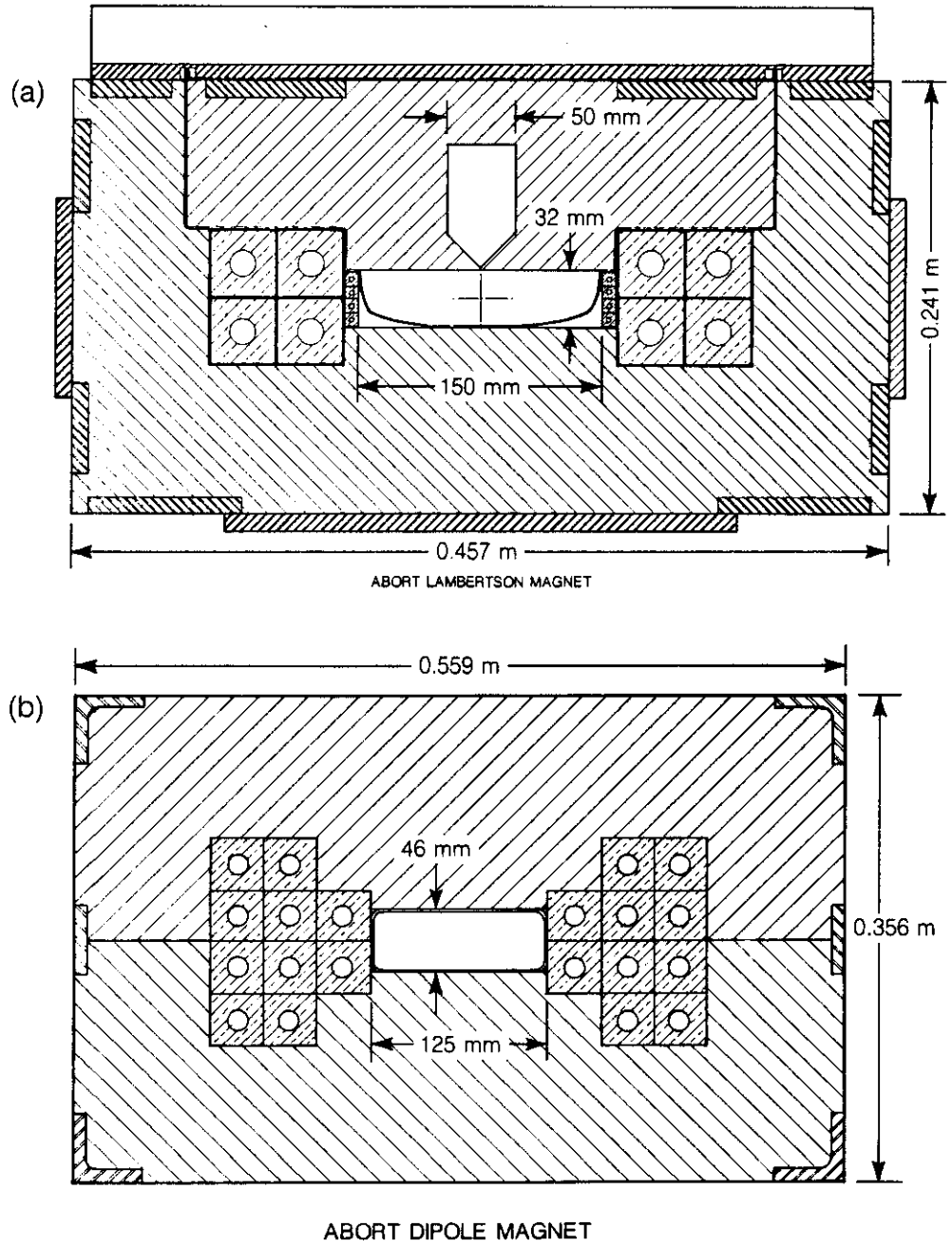

Figure 5.10-8. (a) Cross section of the abort system magnetic septa. The design is determined by the aperture requirements, the geometric layout of the utility region, and the desire to run the magnet in series with the main power bus. (b) Cross section of an abort system dipole. The magnet runs in series with the main power bus, has a maximum field of 1.7 T, and is designed to saturate 3% at full field.

field is small. The magnets produce a maximum field of one tesla, resulting in a separation between the aborted and circulating beam of 44 mm at the downstream end of the septa.

Dipoles

The conventional dipoles [Fig. 5.10-8(b)] at each end of the drift region also run in series with the main SSC current bus. The maximum field is 1.7 T, and the pole face dimensions are defined by the aperture criteria. Both the dipoles and the Lambertson septa are designed to saturate in such a way as to track the main arc magnets.

5.10.4 External Beam Line and Beam Dump

To ensure a clean and safe abort, the external abort system must meet several requirements:

(a) The external beam line should not contain a limiting aperture, in order to avoid creating radiation sources.
(b) The beam dump and beam line elements outside of the tunnel must survive indefinitely, since they are inaccessible.
(c) The beam dump must be able to survive a small number of consecutive failures of devices used to distribute the shower energy.
(d) The beam dump must contain radiation sufficiently well to avoid both personnel exposure at the surface and local ground-water contamination.

The geometry of the external abort line is shown in Fig. 5.10-9. The trajectory of the aborted beam is defined by the machine layout; there are no bending elements in the beam line. The separation between the abort dump and the SSC tunnel is provided by the bending cells in the dispersion suppressing sections of the machine.

Details of the beam dump generally follow the scheme outlined in the RDS [5.10-1]. Two features are used to decrease the energy density in the beam and the shower cascade which could otherwise damage the transport channel or the dump. First, a strong lens is used to enlarge each dimension of the emerging beam. Second, to minimize the local heating of the core of the beam dump at high energies, external kickers, deflecting the beam in both transverse dimensions, are used to distribute the energy at the entrance to the dump. These kickers are not needed at low energy.

For safety reasons the system is designed to be fail-safe. The lack of bending in the line ensures the beam will always hit the dump. It is not required that the external kicker system be perfect. The core of the dump is able to survive a significant number of kicker failures. The defocusing quadrupole string operates in series with the main SSC current bus to ensure energy tracking. The abort line apertures are large enough to transport the beam cleanly in the eventuality of a failure of one of the eight internal kickers.

Beam Line Optics

The beam dimensions and offsets are shown in Table 5.10-2 for nominal operation and also for extreme conditions. The extreme conditions are taken to be a horizontal closed orbit error of up to four millimeters, a single abort kicker not firing, and a beam size that fills the machine aperture. The extreme cases all lie within the apertures if taken individually and are very close to being accommodated simultaneously. A failure of two internal

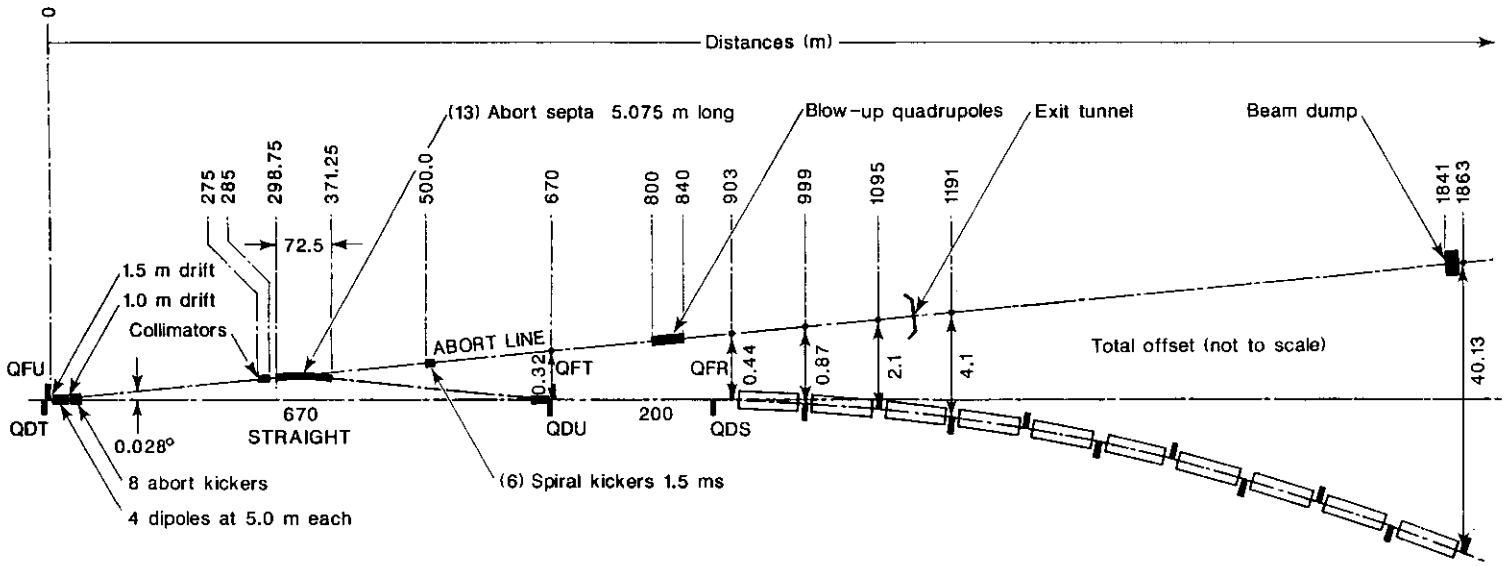

Abort Angle: 0.485 m rad (0.028°)
Half cell bend angle: 8.18 m rad (0.469°)
Beam dump at 1841 m (from 0)

Figure 5.10-9. Geometry of abort system external beam line. There is no steering in the abort line; the separation from the circulating beam is provided by the standard cell bending.

Table 5.10-2
Abort System Beam Sizes, Offsets, and Apertures

Element	Z (m)	β-Values (m)	Nominal			Extreme		Physical aperture (mm)	
			Beam offset (20 TeV) (mm)	Beam Size 1 TeV (95%) (mm)	Beam Size 20 TeV (95%) (mm)	Beam offset (mm)	Beam size (95%) (mm)		
Internal dipoles	0	1.1×10^3	0	4.4	1.02	0	18.2	125	H
		5.4×10^2		3.1	0.71		12.7	47.4	V
Magnetic septum	335	2.2×10^2	0	1.97	0.45	−1.7	8.04	20	H
		2.2×10^2		1.97	0.45	−3.5	8.04	20	V
Spiral kickers	500	2.2×10^2	0	1.97	0.45	−3.0	8.04	40	H
		5.2×10^2		3.02	0.70	−5.95	12.5	75	V
Blow-up lens									
Upstream	800	1.0×10^3	±6.0	4.2	0.97	−4.8	17.35	50	H
		1.8×10^3	±12.0	5.6	1.30	−9.5	23.2	50	V
Downstream	840	4.0×10^3	±12.3	8.41	1.94	−9.3	34.7	50	H
		2.5×10^2	±5.0	2.10	0.5	−3.35	8.9	50	V
Beam dump	1840	3.2×10^6	±349.8	237.9	54.9	−260.8	980	1800	H
		1.5×10^6	±336.2	162.8	37.5	274.0	670	1800	V

kickers to fire will still result in the beam leaving the machine and hitting the dump, but the process will be loss-free only if the beam emittance is within a factor of two of the nominal.

External Beam Line Elements

The beam line elements are as follows:

Blow-up Quadrupole

This lens is a 50 mm aperture vertically focusing conventional magnet with a maximum field gradient of 40 T/m (at 20 TeV), producing a field of 1.0 T at the pole tips. An effective length of 60 m, together with the 1000 m drift length, increases the β-values at the dump from 1.15×10^4 m to 3.2×10^6 m horizontally, and 1.4×10^4 m to 1.51×10^6 vertically, thereby increasing the beam area by a factor of 160. The lens is chosen to be vertically focusing to minimize the beam spot deflection at the dump in the event of an internal kicker failure.

External Kickers

For high intensity and high energy operation, vertical and horizontal kickers with oscillating fields are operated 90 degrees out of phase with one another, so that the beam spot executes a spiral pattern at the face of the dump. The requirements are similar to the internal kickers, but without the slow circuit to produce a current flat top. A rise time of three microseconds ($\pi/2$) will produce a ringing period of 12 μs; hence 25 cycles occur during the 300 μs beam passage. To produce a maximum deflection of 350 mm at the dump we need an offset of 6 mm horizontally and 12 mm vertically at the blow-up lens. This corresponds to angles of 20 μrad (H) and 40 μrad (V), which can be made using six modules identical to the internal abort kickers, with simplified pulse forming networks.

Beam Dump

The beam dump, shown in Fig. 5.10-10, is at the end of a 1000 m pipe and is isolated from the beam line vacuum by a thin window. The pipe is stepped in size, so that it is 75 mm in diameter near the Collider Ring, and two meters in diameter at the end near the dump. Only moderate vacuum is required in the majority of the pipe, to avoid creating radiation sources. The vacuum is improved by differential pumping near the Collider to avoid having to have a window where the beam power density is high. The beam tube is an acoustic delay line, so that if the large window at the dump end breaks, there will be sufficient time to close fast acting valves near the Collider, to avoid a large in-rush of gas.

Between the vacuum window and the dump is a closed atmospheric gas volume. The entrance window of the dump is titanium, a strong refractory material, sealed to a two meter diameter water-cooled steel cylinder that contains the graphite core of the dump. The steel cylinder is surrounded by sufficient concrete to keep both instantaneous and residual radiation away from the surface and out of the local ground water. The closed circuit cooling water system has a peak capacity of one megawatt.

The choice of graphite to absorb the hadronic shower is based primarily on two features, low atomic weight to reduce nuclear fragmentation and power density in the shower, and excellent refractory properties. To avoid a progressive deterioration of the internal structure from thermal shock, the graphite is in the form of pellets. This composition also has the advantage that it will not transmit intense shock waves to the container.

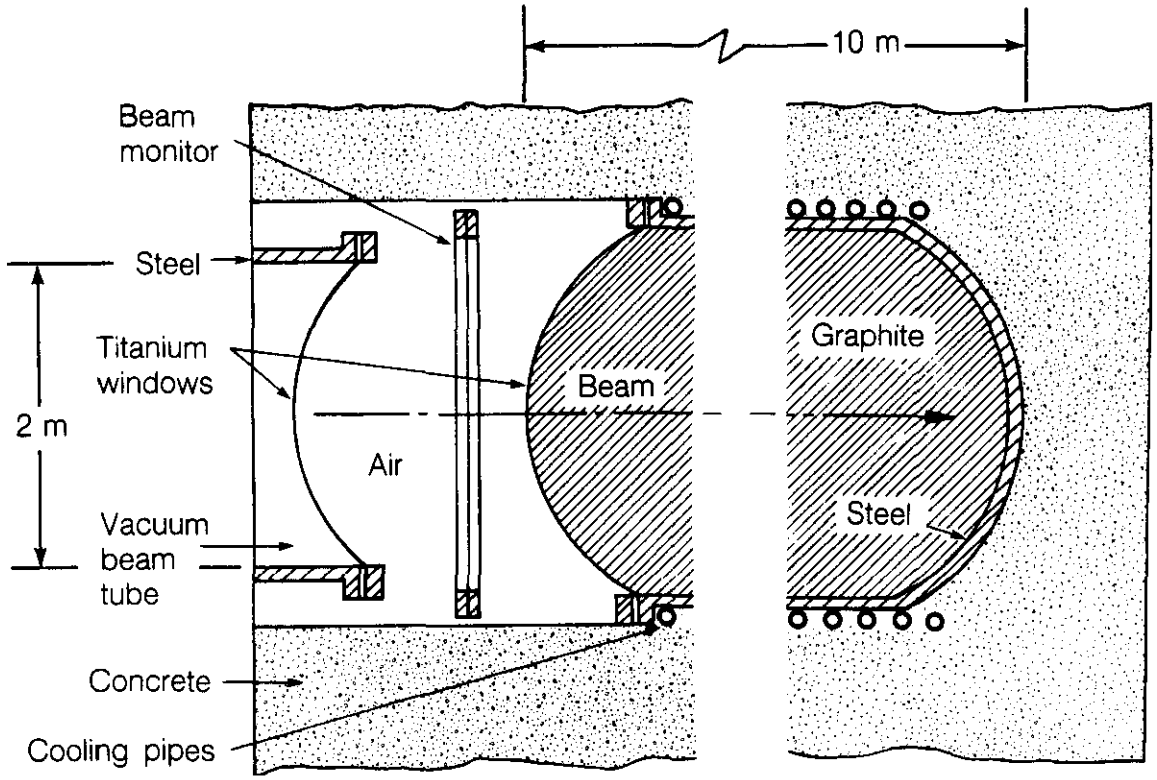

Figure 5.10-10. Abort system external beam dump. The abort dump is a passive sealed unit capable of withstanding indefinitely the 400 MJ of beam energy.

The core must contain the shower sufficiently to prevent excessive heating of the steel container. The longitudinal development of the shower scales logarithmically with energy. For 99% containment, about 20 absorption lengths (10 m at 1.5 g/cm^3) are needed. This provides some insurance in the event that the center of the core loses density because of local overheating.

The intense part of the shower is spread longitudinally over approximately three meters at a depth of about three meters. Assuming that the incident beam has been spread out over an initial area of 0.5 m^2, approximately 1.5 m^3 or 2.4 tons of graphite participate in the initial absorption of energy. Taking 0.7 J/g-C for the heat capacity, this results in an average temperature rise at the center of 600 C/GJ, well below the 4000 C boiling temperature of graphite.

The diffusion of energy to the larger volume of the core takes place in a geometry intermediate between cylindrical and spherical. The volume of graphite contained in a length of five meters is 5π m^3, an order of magnitude more than that in the initial core. Without cooling, this volume will approach an equilibrium temperature of 60 C/GJ; with cooling the temperature rise will be even less. The basic dump design therefore appears to be satisfactory for conditions well beyond the machine specifications.

The container consists of spiral-wound water pipes between thin cylinders and potted in concrete. The forces on the container include the weight of the graphite and the pressure of the confined gas, which is in local thermal equilibrium with the graphite. At the center of the hadronic shower, the instantaneous pressure rise is about two atmospheres per gigajoule. At the container surface it will be much less. For a 10 mm thick steel cylinder, a hoop stress of 1000 atmospheres is produced with an average internal pressure of ten atmospheres. At equilibrium, the five millimeter entrance window with a one meter radius of curvature has the same stress as the cylinder. Any gas that leaks through the seal in the entrance window can be detected and easily removed from the closed gas volume in front of the dump.

5.10.5 Abort Generation

The actual abort command is generated from the various devices and subsystems around the ring. Devices are read individually into the dedicated abort link at their respective locations. If a device signals for an abort, a pulse train traveling around the ring on the dedicated cable is interrupted, causing a trigger to be latched at the abort kickers which fire at the next beam gap. A fail-safe abort link running the entire circumference of the machine will produce a worse-case reaction time of three turns from the generation of an abort signal to the removal of the beam from the machine. While this is probably sufficiently fast for most scenarios, sensitive detectors located in the utility regions next to the abort system can reduce the reaction time to a single turn, if necessary.

An important requirement, which places design criteria on the subsystems, is that of data retrieval for subsequent analysis in the event of an abort. The abort command circuits (concentrator modules) store information about which system requested the abort and at what time, so that the time sequence of abort requests can be reconstructed after the fact. The abort link is a single cable but it must be capable of carrying the information about both rings independently. There are several techniques of multiplexing and decoding independent signals from a common carrier; a time-slice system probably represents the

simplest solution. Another important capability in a collider is the ability to prevent specific devices from generating abort requests at various times in the running cycle to minimize the possibility of dumping the beam erroneously. This requirement argues for a two-tiered abort system which, during the time when the beams are in collision, can report various system errors without automatically removing the beam from the machine.

The decision to abort the beam is based on three main indicators:

(a) equipment malfunction
(b) beam position information
(c) beam loss information

These indicators naturally fall into a hierarchical structure in the sense that it is possible to detect hardware failures before they are translated into pathological beam conditions. Likewise, under certain conditions, beam position information can be used to predict the onset of beam loss before it actually occurs. The use of loss monitors to trigger the abort system should be considered the lowest level of protection; this serves as the system of the last resort. We examine each category of abort generation in more detail below.

Equipment Malfunction

With the advent of microprocessor-based systems, techniques to ensure correct equipment performance are now well established and can be implemented in a relatively straight-forward fashion. Examples of this approach include refrigeration plants where, during the course of normal operation, many input variables are continuously monitored, power supplies that require output waveforms to follow the input reference, and so on. Intelligent subsystems can be made to respond in quite sophisticated ways to possible error conditions, and can thus be made to err on the side of caution if required. The intelligent systems also have continuously updating rotating buffers that freeze when the abort link is interrupted. In this way the system history is always available for analysis post-facto if needed.

Lower level "dumb" systems, e.g., vacuum valves, can be interlocked to the abort system in the normal manner and still leave plenty of time for efficient beam removal. Experience at the Tevatron indicates that equipment failure as a source of beam-induced quenches can be reduced to a very small fraction of the total.

Beam Position Monitoring

The use of beam position information can identify several types of potential beam loss before losses start to occur. This is an important function of the position monitoring system and is an integral part of the design. The ability to set a position threshold at each monitor point is a fundamental requirement—beam positions outside these preset thresholds cause an abort. It is important to recognize that different parts of the machine cycle (injection, start of acceleration, acceleration, collisions) have fundamentally different dynamics. It is possible to vary threshold settings depending on what part of the cycle is in progress. The beam position monitoring (BPM) system also has the ability to record and store information on a turn-by-turn basis in a time-ordered circular buffer holding several thousand turns.

Simple abort threshold levels can be usefully augmented by beam envelope detection schemes. Beam loss during acceleration in the Tevatron is primarily incoherent, and thus

is not revealed by position information. Very often, however, these losses are preceded by some sort of injection mismatch. Energy errors at injection can dilute the longitudinal phase space to the point that, when the bucket area shrinks during acceleration, beam loss occurs. Transverse phase space blow-up can also be revealed later in the cycle. For the SSC, therefore, there are two beam envelope detectors, one with a time constant suitable for synchrotron frequencies, the other for betatron motion.

Beam Loss Monitoring

In principle, given a sufficiently sensitive loss monitor, it is straightforward to establish loss thresholds that allow the beam to be aborted before losses cause magnets to quench. In practice, however, things are not quite that simple. The response of a loss monitor can change by several orders of magnitude depending on the relative position of the loss point and that monitor. The structure of the machine lattice as well as the layout of the aperture restrictions (collimators, beam transfer septa, etc.) will make certain areas of the machine much more sensitive to beam instabilities than others.

While a global system of loss monitors at the standard quadrupoles is necessary for a variety of reasons, a small number of additional monitors strategically placed in the utility regions close to the abort system can provide many advantages. The relatively high beta-values in the area provide good sensitivity, which could be further enhanced by remotely controlled collimators or wires positioned close to the beam. If the area downstream of the abort channel were made the critical machine aperture, then the onset of losses would start there. This is beneficial in two ways: first, the region contains only conventional magnets and is relatively insensitive to beam loss; and second, the transit time for signal propagation is short, allowing the beam to be removed from the machine in a single turn. Detecting beam loss at an early stage also ensures, insofar as possible, that the beam transfer to the dump is clean.

In a similar fashion to the BPM system abort loss thresholds vary, depending on the machine cycle.

It is desirable that the loss monitors in each ring be independent of one another, so that both beams are not automatically dumped in the event of losses in one ring. This is especially important during injection time. Separating the beam transfers to take place in different utility areas naturally fits in to the philosophy. Since one ring will be heavily monitored in a given utility area and the other rather sparsely, beam loss information in these regions will be relatively ring specific and probably represents the best chance to separate the beam behavior. In the interaction regions it may prove difficult dynamically to reduce diagnostic information to point to individual ring components. This presents a interesting design goal.

Besides equipment failures and beam instabilities, the other major causes of magnet quenches are those due to operator error. It is difficult to be specific on these types of occurrences, since human ingenuity can always be expected to rise to the occasion. Software interlocks present the best approach. However, in the final analysis, the magnets must be capable of withstanding high field quenches induced by beam losses, although they should never experience energy deposition levels that are more than a tiny fraction of the total circulating energy.

5.10.6 Diagnostics and Tuning

The diagnostic requirements of the abort system are relatively modest. The trajectory of the aborted beam will be measured in both planes at four locations in the line to ensure it hits the dump. Standard loss monitors at the aperture locations will also be needed. A charge-sensitive toroid in the abort line will monitor the integrated dose on the dump.

The kicker waveforms and trigger timing will be monitored via a transient digitizer system which records the current pulse in the magnets and the beam signal in the abort line as it leaves the machine. Failure to fire on request, shorted magnets, and trigger problems will be detected from these data.

The integrity of the dump itself requires monitoring to ensure environmental controls are maintained. The closed-loop cooling water system and the vacuum system are also monitored.

The aborted beam trajectory is defined by the closed orbit in the utility section and is controlled by the correction dipoles as described in Section 5.6. Beam steering in the line is not needed, but trim elements could be installed beside the spiral kickers if that proved necessary.

5.10.7 Failure Modes

The essentially passive nature of most of the system suggests that problems will be largely confined to the kicker magnets or the control system. The most likely failure modes are as follows:

a) Kicker spontaneously firing: If a single kicker module discharges, a beam deflection of 11 μrad will result, which corresponds to a vertical displacement of five millimeters in the arc cells. The beam will circulate in the machine long enough to be removed by the remaining kickers.

b) Failure to track beam energy: A deviation of the capacitor voltage waveform from the desired value will trigger the abort. The threshold on this trip level can be adjusted to ensure that the beam is still removed from the machine with a less than nominal deflection.

c) Kickers not firing: This is a relatively unlikely occurrence but has the potentially serious consequence of having nowhere to put 400 MJ of beam energy. A bizarre sequence of controls problems produced this situation once (in two years) at the Tevatron, resulting in the largest non-deliberate quench on record (nine quarter sectors). It is difficult to be specific about how to recover operationally from this kind of situation. A total manual override is the safest fallback position, allowing the system to be fired locally by hand if all else fails.

d) Loss of synchronization: In the event of losing the information on the circulating beam gap the system must fire in any case. The three microsecond rise time of the magnetic field will smear about 1% of the beam (10^{12} particles) over the abort aperture. It is likely that this situation will result in a quench in the downstream elements. A detailed Monte Carlo calculation is needed to predict whether a collimation scheme can be developed to provide adequate protection from this situation.

e) Power failure: A loss of power will trigger the kickers causing an abort. Power backup on the local controls will maintain the beam gap signal, so the abort will be normal. If the beam gap information is lost, an unsynchronized abort will occur.

5.11 Interaction Regions

The interaction regions (IRs) are those areas of the machine in which the particle collisions take place. The special design constraints and requirements of these regions can be summarized as follows:

(a) lattice manipulation around the interaction points
(b) radiation tolerance
(c) enhanced sensitivity to alignment and field errors
(d) maximum experimental free space
(e) vertical beam separation

Some of these criteria are mutually exclusive to such an extent that an optimum design choice for one set of lattice parameters (or experimental environment) is not appropriate for a different one. The overall lattice chosen for the SSC has considerable flexibility to accommodate different experiments by local modifications near and at the IRs. In keeping with a philosophy of integrating the IR design with the requirements of an experiment, we examine a high luminosity (low beta) IR and comment on a somewhat lower luminosity one that allows a longer free space for experimental equipment.

The layout of the inner region of a low-beta IR is shown schematically in Fig. 5.11-1. The 20 m drift space between the interaction point (IP) and the first lattice element (Q1) is not totally available for experimental equipment since a certain amount of space (of the order of 3 m) is needed for radiation shielding, cryogenic plumbing, and possibly compensation of detector magnetic fields.

The lattice parameters at the IP are adjusted via the triplet quadrupoles (Q1–Q3) together with quadrupoles Q4, Q5, and Q6. All other quadrupole gradients are the same as in the standard cell. The various focusing requirements have been obtained by scaling the magnet lengths. The details of the machine lattice in the interaction regions have been given in Section 4.2.4. The 70 cm vertical beam separation is accomplished in two equal steps, 180 degrees apart in phase to ensure vertical dispersion cancellation.

5.11.1 Variable Strength Quadrupoles

The β^* values at a low-beta interaction point are variable in the range 0.5–6.0 m, and are controlled by the six quadrupoles (Q1–Q6). This feature together with the 20 m free space on each side of the IP define to a large extent the basic quadrupole parameters. Table 5.11-1 shows the quadrupole gradients as a function of β^*. The maximum field gradient allowed in the inner triplet is 231 T/m, which then in turn defines the length of the elements. The outer quadrupoles, where physical space is not at a premium, have a maximum gradient of 212 T/m.

The change in the triplet quadrupole strength as a function of β^* is sufficiently small that these elements run in series with the main bus and use shunt supplies (10% max) to provide the current variation. During normal operation the shunt supplies are carrying 0.5% of the total current for regulation purposes. Of the other tuning quadrupoles, Q4 and Q5 have a large enough range to require independent excitation; Q6 also uses a 10% shunt across the main bus. A single shunt supply is used to control the magnets in both rings at a given location or a single element in the triplet that is common to both beams. Where

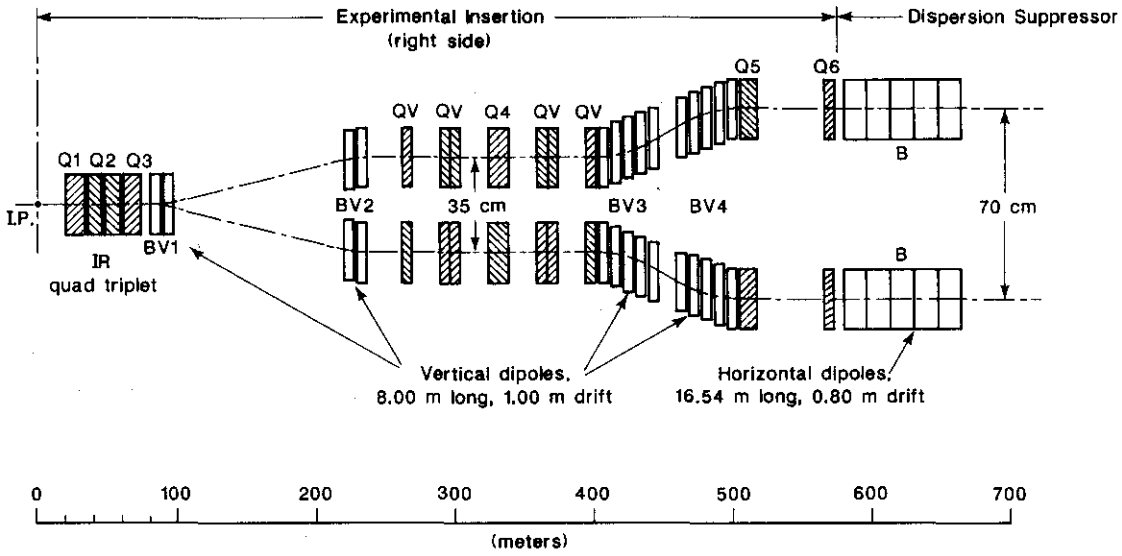

Figure 5.11-1. Low-beta interaction schematic. The IP lattice parameters are adjusted via Q1–Q6. Vertical separation is done in two steps with VB1, VB2, VB3, and VB4. The split into separate cryostats occurs between VB3 and VB4.

Table 5.11-1
Low Beta Quadrupole Excitation versus β^*
(Quadrupole excitation is in T/m at 20 TeV)

β^* (m)	0.5	1.0	2.0	3.0	4.0	5.0	6.0
Q1	223.3	223.1	223.4	230.0	228.0	219.4	231.3
Q2	−213.2	−214.6	−217.1	−230.3	−222.5	−223.9	−228.7
Q3	215.9	217.6	218.2	221.4	223.6	226.1	227.2
Q4	−212.2	−186.0	−161.6	−148.8	−138.8	−130.9	−125.2
Q5	163.8	133.0	110.0	97.8	91.9	89.3	84.0
Q6	−193.9	−189.4	−188.1	−189.7	−193.1	−197.2	−202.9

possible the use of shunt supplies in the IR region, rather than independent 6.5 kA power supplies, greatly reduces the heat load from the power leads, as well as simplifying the power supply regulation. The power supply circuits in the IR region are shown in Fig. 5.11-2 and described in detail in Section 5.5.

The small β^* values at the IP produce a correspondingly large beta in the quadrupoles. These lattice parameters, together with the large focusing strength needed to attain them, have important consequences in terms of alignment, aperture, and field quality. Roughly speaking, the figure of merit for these effects involves the product of the field gradient, the length, and the beta value. For the highest luminosity settings the lattice is approximately 100 times more sensitive to errors in each element of the triplet than a standard arc quadrupole.

The problem of alignment can be separated into x and y offsets and roll angle. A small (0.2 mm) displacement in a single element of the triplet with respect to the beam would result in a closed orbit error of 10 mm in the arcs if uncorrected. The quadrupole misalignment might easily be too large to compensate via correction dipoles. The magnets therefore are individually mounted on motorized supports. The magnets are capable of up-down and side-to-side motion within a range of several mm. Using the beam itself as a diagnostic, quadrupole positioning accuracies of 10^{-2} mm should be achievable.

The flexible bellows, which permit transverse motion, do not allow rotational motion. Quadrupole roll errors are important since they introduce an effective skew quadrupole term that couples horizontal and vertical beam motion when the tunes are close together. The tune separation needed to decouple the motion is a convenient method of parameterizing the skew quadrupole component. In Section 4.4.3 the minimum tune separation was required to be 0.001. If we assume that half this coupling arises from the IRs and there are two identical IRs, then the maximum allowable average coupling from each element in the triplet is 0.0001 in tune units, corresponding to a roll angle error of 0.002 mrad [5.11-1]. This tolerable roll angle is much smaller than that which can be achieved by accurate surveying. We therefore propose to install independent skew quadrupole trim windings with a

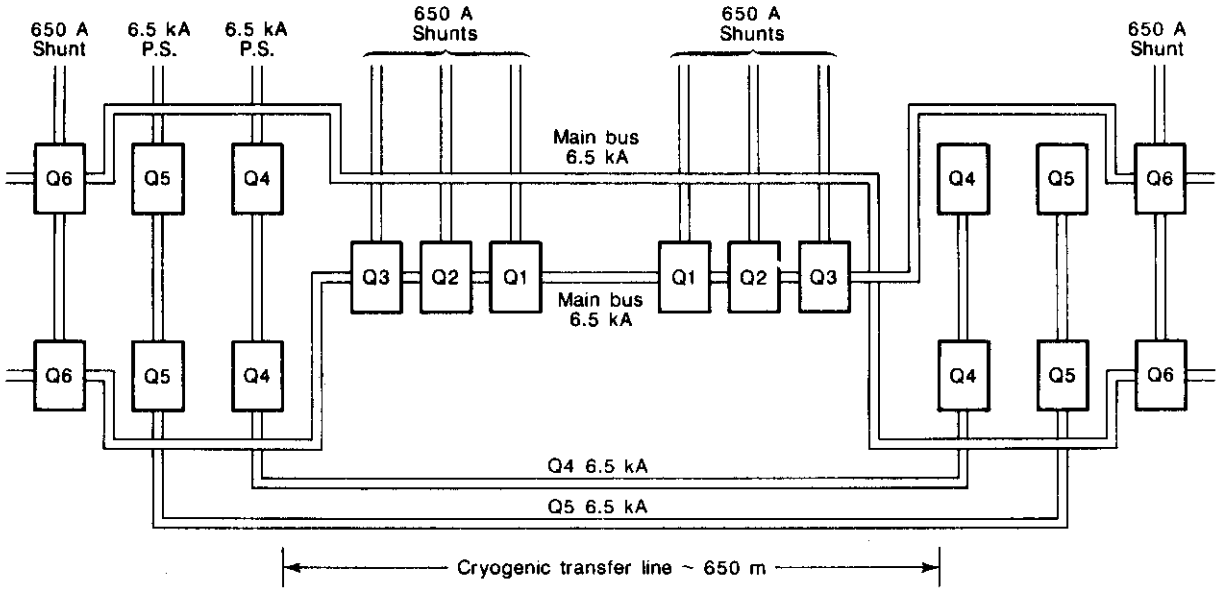

Figure 5.11-2. Low-beta interaction region power supply circuit diagram. The inner triplet (Q1–Q3) is varied by 10% shunt supplies across the main bus, as is Q6. Both Q4 and Q5 require independent 6.5 kA supplies. The rest of the elements run in series with the main bus.

maximum excitation of 10^{-3} of the main coils, equivalent to an angle adjustment range of 1 mrad. The excitation of these trim windings is determined empirically by minimizing the tune separation.

As shown in Section 4.4.8, the lattice sensitivity to the triplet quadrupoles is such that the machine aperture is severely reduced if these elements have a multipole content similar to that of the standard arc quadrupoles. To avoid compromising the machine dynamics, a factor of 10 reduction in the lower-order field components (skew and normal up to 12-pole) is necessary. At present, the most viable technique to achieve this level of field uniformity seems to be individual multipole correction coils around the bore tube in each element. The excitation of each multipole circuit is determined prior to installation during the measuring process. A cross section of these quadrupoles in shown in Section 5.2.14.

The machine tune, as well as the aperture, is strongly coupled to the triplet quadrupoles. A fractional current change of 10^{-4} in a single magnet can change the machine tune in the appropriate plane by 2.5×10^{-3}. The operational tolerance on tune modulation in the machine is set at 10^{-3} (Section 4.4.3). With two low-beta IRs, and allowing half this modulation to arise from these areas, a current regulation capability of 5×10^{-6} is needed for random variations. This is a relatively tight tolerance. Fortunately the situation is helped by the fact that the quadrupoles are powered in series with the main bus. Random current variations are therefore only generated by the shunts across the elements rather than by the main supplies. The maximum current rating of the shunts is 10% of the total; the regulation requirements are thus 5×10^{-5}, or a factor of three less stringent than the main supplies.

5.11.2 Vertical Beam Separation

In a similar way to the IR triplet quadrupoles, the vertical bending dipoles (VB1–VB4) require better field quality than the standard arc dipoles (Section 4.4.8). The most straightforward way to achieve this higher field uniformity is to increase the coil inner diameter from 40 mm. The magnetic field in these dipoles is defined by the geometry of the second step which requires a 35 cm beam separation in the available 103 m drift space. Five 8 m magnets running at 5.2 T (20 TeV) at each end of the drift space will suffice. The 187 m of free space available for the initial separation requires two of these 8 m dipoles at each end. The field strength of 5.2 T with large aperture has been demonstrated by Tevatron dipoles (with coil diameter of 75 mm) wound with improved superconductor.

The fact that the beam separation is only 35 cm for 200 m on each side of the IP means that both sets of magnets must be contained within a single cryostat. The split into two independent cryosystems occurs between BV3 and BV4.

5.11.3 Orbit Control

Orbit manipulations in both planes around the IP are necessary to adjust the IP position and separate the two beams when collisions are not desired. Changes in position and angle of the beam at the downstream end of the IR triplet are shown in Table 5.11-2 for several beam geometries. These data can be converted into correction dipole strengths by imposing the criterion that the beam trajectory is returned to nominal at BV2 with a system of orbit correctors as shown in Fig. 5.11-3.

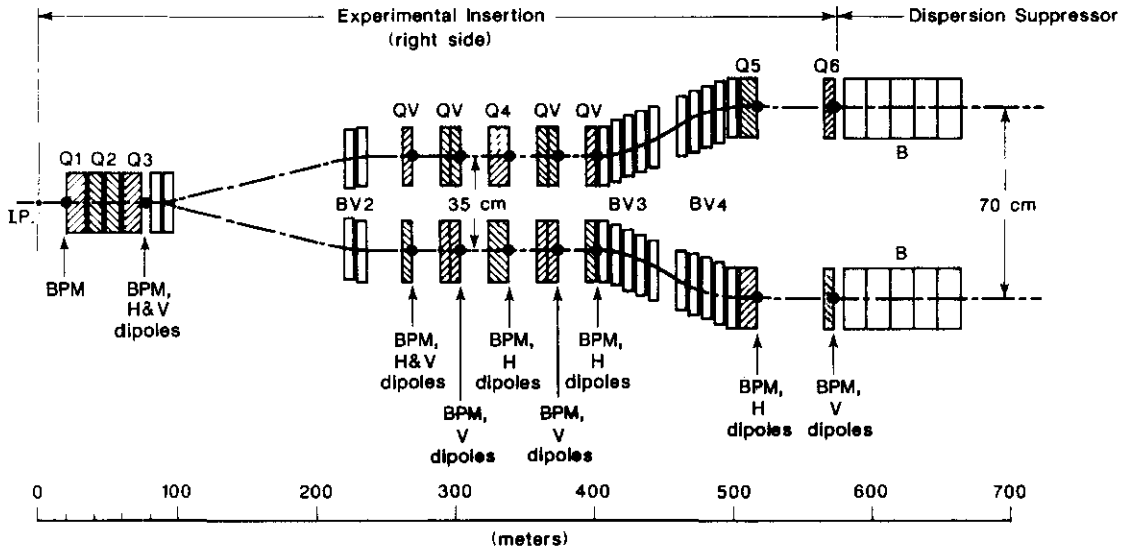

Figure 5.11-3. Low-beta interaction region orbit correctors. Control of the crossing angle and beam separation is provided by a set of 6 correction dipoles in each plane together with a system of position monitors.

Table 5.11-2
Orbit Control Dipole Settings
(Correction Dipole 3 T-m ≡ 45 μrad at 20 TeV)

Case	Crossing Angle (μrad)	Separation (mm)	Dipole 1 (μrad)	Dipole 2 (μrad)
Injection	±75	0	±5.5	±30.6
Injection	0	±2	±36	±8
$\beta^* = 0.5$ m	±75	0	±4.7	±29.3
$\beta^* = 0.5$ m	0	±2	±38.2	±6.6

The strengths of the necessary correctors are shown in Table 5.11-2. The maximum bend angle needed is 38 μrad which corresponds to 2.5 T-m at 20 TeV. The standard arc correction dipole delivers this field integral. We therefore require six non-standard spool packages that contain both horizontal and vertical dipoles at each IR.

Orbit control and corrections in the dispersion suppressors are provided by a standard primary spool package at each quadrupole location.

5.11.4 Dispersion Suppressors

The zero horizontal dispersion in the IR regions is matched to the standard cell via a three-cell section. The quadrupoles in these cells are of different lengths from the standard cell. The cell length is held constant by using a 3.5 m spool piece in this region and installing the quadrupole in a longer cryostat than necessary. This is possible since only the primary correction package is needed in these areas. By using this scheme, only one length of special spool piece and one type of special quadrupole cryostat are needed. The quadrupole effective lengths and drift space lengths in the dispersion suppressors are shown in Table 5.11-3.

Table 5.11-3
Dispersion Quadrupole and Drift Lengths

Name	Effective Length (m)	Drift Length (m)
QG	4.88	1.42
QH	4.80	1.50
QI	4.59	1.71
QJ	4.05	2.25
QK	3.48	2.82

5.11.5 Medium Luminosity Interaction Region

It is clear that the design of the highest luminosity IR is not appropriate for certain classes of experiments that would benefit from a longer free space around the IP, and a somewhat lower luminosity.

An IR that has $\beta^* = 10$ m and 100 m of free space on either side of the IP is representative of a series of possible solutions that require simple modifications to the low-beta case. Figure 5.11-4 shows a layout in which the inner triplet quadrupoles are 100 m from the IP. The first vertical split is shortened by 80 m to compensate, so that the physical layout outside BV2 is essentially unchanged. This reduction in drift length means that the bend angle in BV1 is approximately twice that needed for the low-beta IR. The beam separation in the common elements is thus increased to a maximum of 8.4 cm in the downstream element. To accommodate this aperture with the required field quality the downstream two dipoles have a 16 cm coil diameter.

With this layout the quadrupole gradients needed for injection and collision optics are shown in Table 5.11-4. The strength of the IR triplet quadrupoles has been lowered to 212 T/m. These elements are also fitted with bore tube multipole correctors, as in the low-beta case, to enhance the field quality. Independent 6.5 kA supplies are needed on Q4, Q5, and Q6.

Table 5.11-4
Medium-Beta Quadrupole Excitation versus β^*
(Quadrupole excitation is in T/m at 20 TeV)

β^* (m)	10	13	16	19	31	64
Q1	210.0	208.6	208.4	208.7	201.5	185.7
Q2	−200.6	−198.9	−199.9	−201.5	−200.1	−193.5
Q3	210.0	200.9	200.9	200.9	200.9	200.9
Q4	−212.0	−200.9	−187.6	−174.3	−167.6	−160.9
Q5	19.8	49.2	60.0	70.1	86.1	110.7
Q6	−47.5	−79.1	−85.7	−90.5	−109.6	137.4

The reduced luminosity alleviates the problems with energy deposition in the magnets. Beam monitoring, orbit control, correction elements, and diagnostics will follow the same scheme as the low-beta IRs.

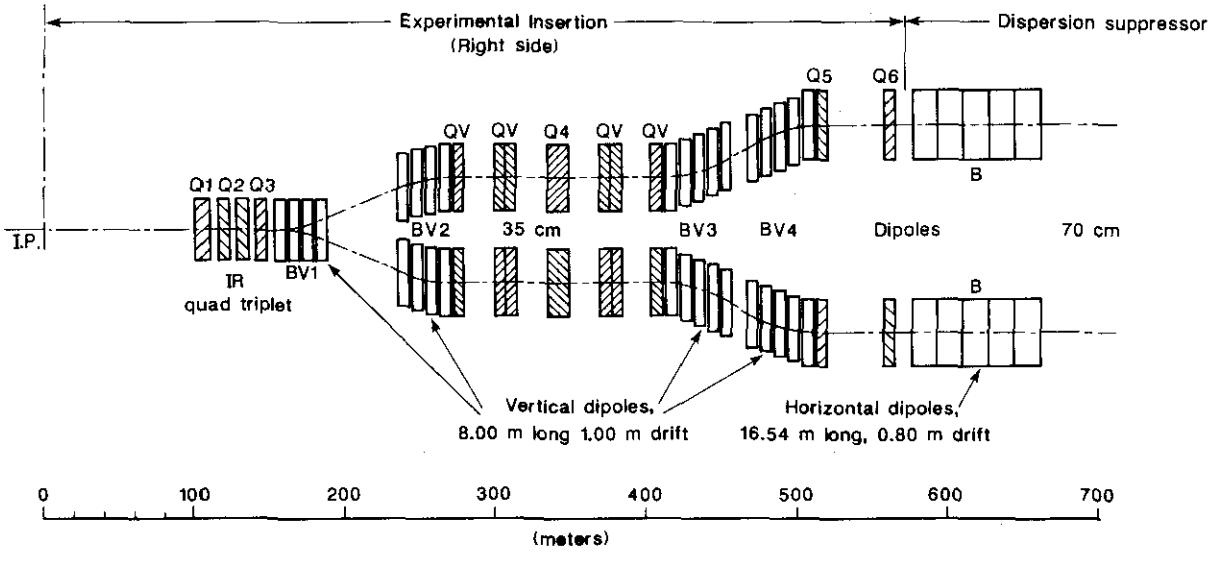

Figure 5.11-4. Medium-beta interaction region schematic. Similar topologically to the low-beta IR, the 200 m experimental drift space is achieved by reducing the luminosity by a factor of 10.

5.11.6 Scattered Beams

Beam-beam scattering is discussed in some detail in Section 4.8, with the conclusion that it has serious impact on the design of IR magnets, beam pipes, etc. For full luminosity operation, it adds about 60 W to the cryogenic load of each final focus triplet, most of which goes into the second half of Q1. The first vertical bend magnet (BV1) acts as a sweeping magnet for inelastically scattered particles that survive the triplet. There also exists a halo of more or less in-aperture particles that have been elastically or quasielastically scattered. In addition, a substantial beam of neutrals (60 W at the nominal luminosity) continues down the magnet bore and must be dealt with at the point the beams are separated. All of this calls for a rather carefully designed beam pipe, shielding around it, a neutral beam dump, and a system of movable collimators.

A schematic drawing of the proposed beam pipe/collimator arrangement is shown in Fig. 5.11-5. A "normal" beam pipe (3.3 cm o.d.) goes through the triplet, then flares to 7.6 cm o.d. in the larger-bore BV1. At the exit of BV1 the beams are 2.0 cm apart, and they continue to separate with a divergence angle of 1.72 mrad. The beams continue to travel in a common pipe until they are sufficiently far apart for (a) separate beam pipes and (b) enough room between these pipes for a thin exit window for the neutral beam. In the example of the transition section shown in Fig.5.11-5, the beams are 10 cm apart in a 14 cm pipe at the transition point, 60 m from the end of BV1 and 140.5 m from the IP. The beam pipe flares to this diameter in two or more steps.

After exit from the thin window in this transition section, the neutrals are escorted through a 100 m long evacuated pipe to the neutrals beam dump discussed in Section 5.11.8. The pipe serves the dual function of preventing shower development in the 4% of a radiation length of air that would otherwise be present, and keeping the path free of accidental obstructions.

Simplistically, one would expect a vertical fan of low-momentum charged particles in the vertical bend direction away from the outgoing beam. This is largely true for the hadrons, which carry most of the energy and are most effective in activating material they strike. Lead shielding over the outbound beam pipe in the vertical bend direction (i.e., top or bottom, depending upon position) serves the dual function of shielding against radiation and minimizing the meson-decay muon flux.

5.11.7 Collimators

A collimator in front of the first triplet element prevents much of the wide-angle scattered beam from depositing its energy in the Q1 cryostat. It has the secondary function of shadowing the thin window about 120 m further downstream, where the forward beam of neutrals produced at the IP exits the machine vacuum system. In the absence of such shadowing, a large flux of neutrals would interact in the thick parts (welds, flanges, etc.) of the beam pipe transition section.

This collimator is of modest radius (0.5 cm) because the incoming beam must not be scraped. During operation with $\beta^* = 0.5$ m, the beta function at this location is about ten times smaller than its maximum value inside the triplet. As a result, the beam envelope is about three times smaller at this collimator than in the quadrupole, so that in principle a fixed-radius collimator three times smaller than the good-field radius in the triplet would suffice. In practice, the maximum beta function is much smaller during injection and

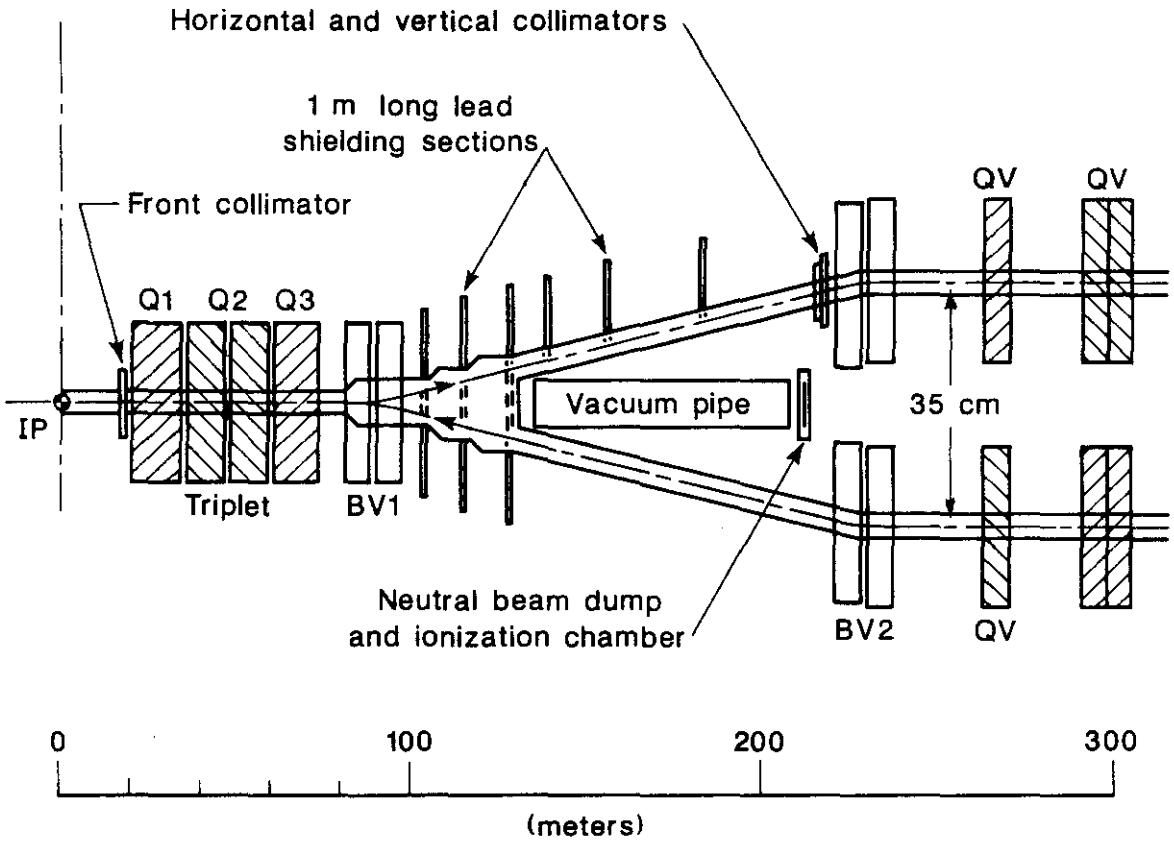

Figure 5.11-5. Beam pipe, shielding, collimator, and neutrals dump arrangements in a typical high-luminosity IR.

ramping, so that a movable collimator is required. Extreme positioning accuracy is not necessary, but because of detector requirements space in all directions is at a premium. The requirements are met by a two-jawed collimator, each half being a half-cylinder with a central hole of the proper radius. The outer radius has yet to be fixed on the basis of detailed shower simulation, but should be about 10 cm. In order to contain at least 90% of the shower, the length should be about 5 $\lambda_{nucl.}$. Depending upon material, it will thus be 80 cm to 100 cm long. Experience at the ISR suggests that molybdenum is superior to tungsten because of its outgassing and thermal properties [5.11-2]. Together, the two jaws weigh about 320 kg. Positioning is done either by moving the jaws longitudinally along wedges, or transversely with screws. In either case the motion is coupled to external stepping motors through bellows.

More severe collimation takes place just before the outgoing beam enters the second vertical bend magnet (BV2), nearly 280 m from the IP. Taking advantage of the large vertical dispersion and moderately high β in this region, one can scrape most of the IP-scattered particles that would strike elsewhere in the ring. On the basis of ISR experience [5.11-2] we would also expect some of the grazing-incidence particles to be reflected via multiple scattering. Such particles are removed by additional collimation at suitable phase advances ($\pi/2,\pi,...$) further downstream.

The requirements for this collimator are very different from those for the one in front of the triplet. Jaws must come very close to the beam, particularly in the vertical direction where the off-momentum particles are most separated. On the other hand, there is no space shortage in either direction. Movable collimators of the sort developed for the ISR provide a basis for the SSC design. These consist of horizontal and vertical pairs of blocks that could be accurately positioned by means of external stepping motors and position transducers. In the SSC case the target positions would be set using beam position information from nearby position monitors.

5.11.8 Beam Monitoring With IR Collisions

IR collisions provide an intense forward beam of secondary particles that can be exploited for purposes of luminosity monitoring and optimization. Charged secondaries might be monitored at a number of points, but present difficulties. Access to detectors in the first collimator would be difficult, and off-center detectors are particularly sensitive to beam steering. Most charged secondaries are dispersed by the triplet and by the first vertical bend. On the other hand, neutral particles carry about 40% of the collision energy, and travel until they interact in the collimators (10%) or in the neutral beam dumps (30%).

Detectors installed in the neutral beam dump will produce accurate and fast signals proportional to the luminosity. After establishing low-beta conditions, a raster-scan algorithm can be used to steer one beam until the correct collision position is found. Beam centering can then be established and maintained by the technique of measuring the amplitude and phase of the detector response for circling beams [5.8-5]. (The longitudinal position of the interaction point can be established by precision timing, using signals from beam position monitors near the IR.)

We describe here a simple but effective means of beam monitoring which will permit rapid diagnostic, tuning, and monitoring by detecting the neutral products of the IR collisions.

Luminosity Monitor

According to ISAJET Monte Carlo calculations, a neutral particle detector of 4 cm radius imbedded in one of the neutral beam dumps 200 meters from the interaction point will intercept 14% of the collision energy [5.11-3]. Figure 5.11-6 shows the fraction of neutral energy within a given angle for photons, K_L^0s, neutrons, lambdas, and various neutral antiparticles. One half of the neutral energy is carried by neutrons with average energy 2 TeV, and another one quarter is carried by photons with $\langle E \rangle$ = 100 GeV, largely from π^0 decay.

Advantage can be taken of the localized electromagnetic showering of the photons by placing a multiplate ionization chamber across the peak of the shower distribution. At design luminosity, the ionization collected in a typical chamber from the 10^9 photons per second will produce a current of 0.3 mA. The ionization chamber can be a rugged, radiation-hard device that produces a fast signal, proportional to luminosity over a wide dynamic range.

Beam Profile, Alignment, and Centering

The beam profile at the interaction point can be accurately measured by the raster-scan steering procedure described above. At design luminosity the signal corresponds to 10^9 photons per second, but even with the beams 5σ out of registry, the signal corresponds to 10^6 100 GeV photons per second. Clearly, detailed mapping of the beam tails is possible with this steering scheme. Beam alignment is then a straightforward process.

When tuned to design β^*, the standard deviation of the projected beam is 5 μm. The beams can be caused to circle each other with a 1 μm incremental separation by a small, properly phased oscillation superimposed on the horizontal and vertical beam steering magnets. When misaligned, the luminosity signal will oscillate, and its amplitude and phase provide a measure of the direction and magnitude of the separation, which can be fed back as a steering correction. For example, the average value of $\cos \theta_x$ determines the x separation as shown in Fig. 5.11-7. The loss in luminosity is less than 1% when centered. Rapidly changing and large misalignments can be tracked with little loss in luminosity by this method.

5.12 Beam Instrumentation

5.12.1 General

The beam instrumentation design satisfies the broad requirements of four different modes of operation:

(a) Commissioning
(b) Normal operation
(c) Fault diagnosis
(d) Advanced accelerator studies

The large scale of the SSC and the varied conditions of operation require the beam instrumentation to cover a large dynamic range. Because of the long time between

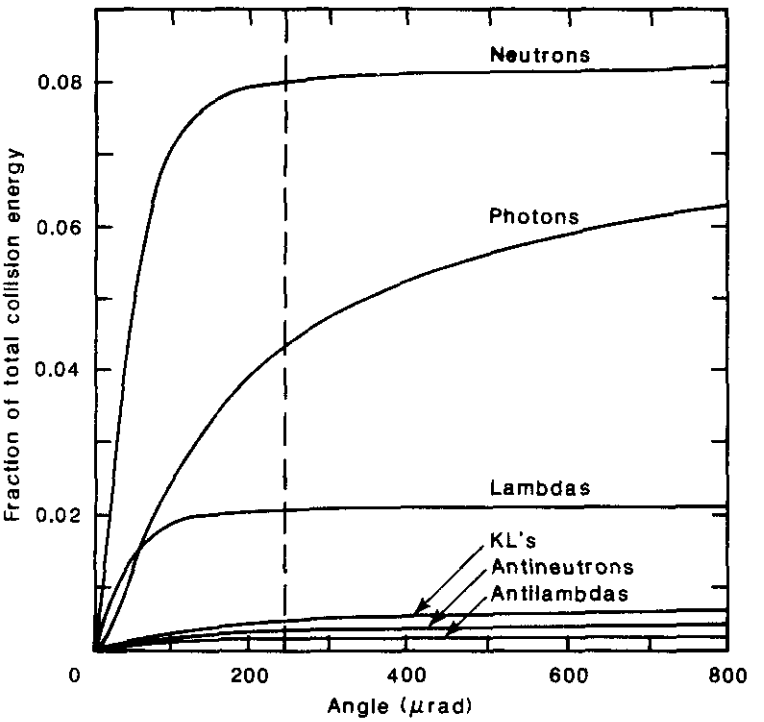

Figure 5.11-6. Fraction of the total IR collision energy appearing within a given angle of one beam direction for several stable neutral particle types. The neutral-particle beam-dump electromagnetic shower ionization chamber is sensitive to particles at angles less than 200 microradians. Angles beyond 240 μrads (dashed line) are in the shadow of the first collimator (0.5 cm radius).

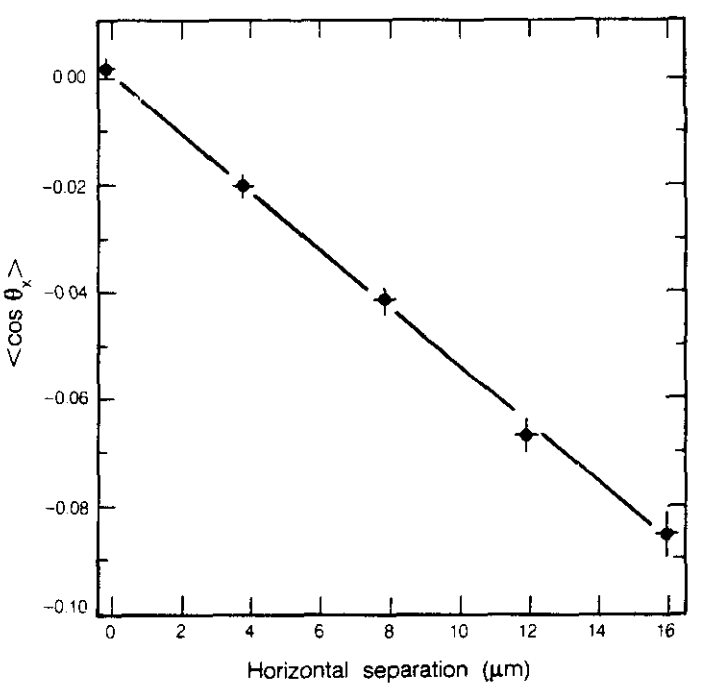

Figure 5.11-7. Mean value of the cosine of the horizontal phase angle for 5 μm beams circling at a separation of 1 μm, as a function of beam separation (from a Monte Carlo study).

injection cycles, maximal data collection is required during injection. The hundreds of megajoules of stored beam energy require extensive protective measures to prevent component damage or radiation-induced quenches. The remoteness of much of the beam instrumentation from the host computers and the large amount of data collected per injection cycle require distributed intelligence and memory in order not to overburden the control system. Each system has sufficient flexibility to allow the development of new measurements that may be found necessary during the commissioning and initial operation.

The beam instrumentation systems described below include:

5.12.2 Beam Position Monitoring System
5.12.3 Beam Loss Monitoring System
5.12.4 Beam Profile Monitoring System
5.12.5 Beam Intensity Monitoring System
5.12.6 Beam Schottky Monitoring System
5.12.7 Other Beam Diagnostic Systems

Much valuable experience has been gained in operating large proton collider rings such as the CERN SPS and the Fermilab Tevatron. The long cycle times and the superconducting nature of the Tevatron required a design philosophy similar to the systems envisioned for the SSC, although on a smaller scale. The relative ease with which the Tevatron was commissioned provides some confidence that such a system can be built for the SSC [5.12-1]. The SSC system specifications are based to a great extent upon the Tevatron design, and upon experience gained during the first three years of Tevatron operation. During initial Tevatron operation, only the beam position and beam loss monitoring systems were operational. The other systems, although necessary to obtain design performance specifications, were not essential for initial commissioning.

5.12.2 Beam Position Monitoring System

The SSC beam position system contains the most important instrumentation for beam control. It consists of almost 900 beam position sensing devices in each ring. Beam position signals are digitized by local electronics in the tunnel and then stored in local memory for readout by the control system. The basic design proposed here follows closely the beam position system used in the Tevatron [5.12-2].

Each sensing device is a pickup detector consisting of four 8 cm, 50 ohm striplines placed above, below, and to both sides of the beam as shown in Fig. 5.12-1. Its physical aperture is 3.3 cm. Passage of the beam through these electrodes induces signals whose relative amplitude is a measure of the beam position [5.12-3]. The detectors are rigidly welded to the quadrupoles in each half-cell for alignment purposes and therefore operate at cryogenic temperatures. This pickup design provides for measurement of both the horizontal and vertical position at each half-cell in contrast to the Tevatron alternating planes.

Signals from the striplines are brought out of the cryostat on eight small coaxial cables, one from each end of each stripline. Four cables go to the electronics and four to back terminations. The back termination is necessary to minimize standing waves in the signal lines and to allow microprocessor-controlled cable continuity tests. Although there is no power dissipation in the back terminations during normal operation, accessibility for their maintenance requires external cabling. The cables are designed to minimize their total cryogenic heat leak, estimated to be about 0.9 watts per half-cell.

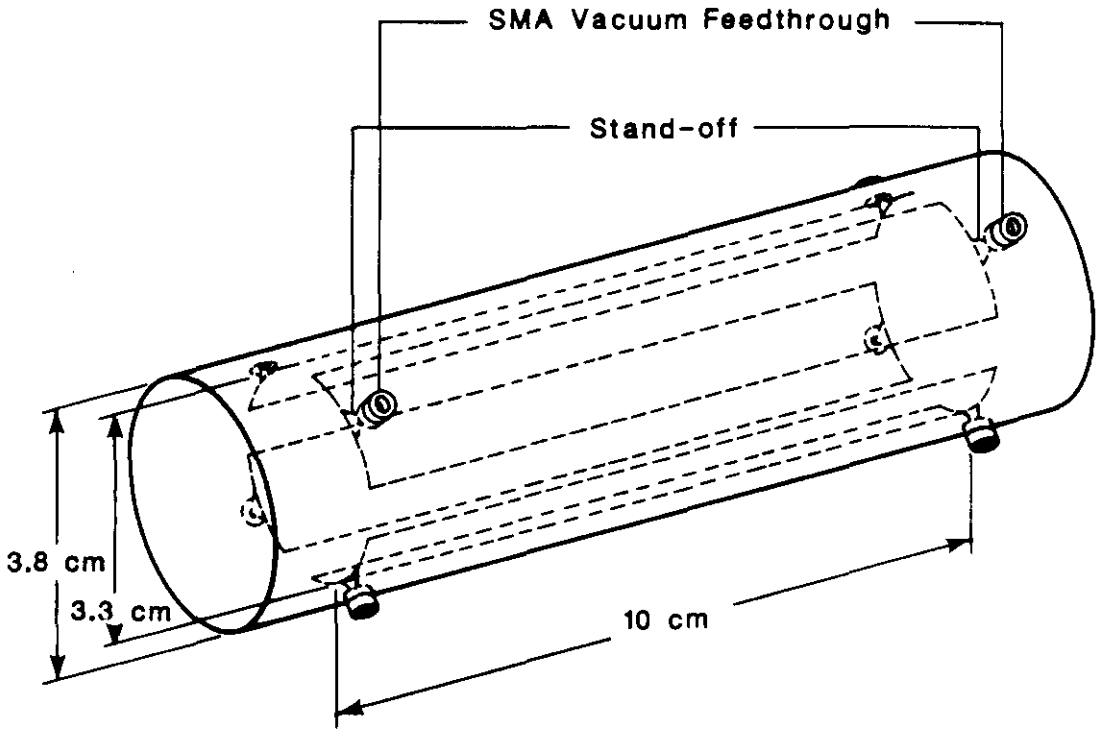

Figure 5.12-1. Arrangement of the four stripline pickup detectors for one of the beam position monitors.

Coupling impedances for the beam position monitors are included in the machine component tabulation of Section 4.5. Impedance-matched striplines are chosen over the more conventional electrostatic electrodes to minimize these beam coupling impedances [5.12-4], as well as to minimize the power dissipation at cryogenic temperatures. The electronics for each cell is located in local alcoves, normally in the tunnel ceiling at every other quadrupole. This space is shared with correction element power supplies, quench protection circuitry, and other controls. Figure 5.12-2 shows a block diagram of the electronics in the tunnel.

Beam position signal processing uses the amplitude-to-phase conversion technique as used in the Tevatron [5.12-5]. This process, which converts signal amplitude ratios to phase shifts, operates over a large amplitude dynamic range (1000:1 in beam intensity), and provides a real-time signal representing beam position without any digital processing. Signal processing is done using only the frequency component near 62.5 MHz, as this Fourier component is least affected by the beam bunch shape. The signal strength is larger near 125 MHz, but the electronics is more costly. As a narrow band filter is used, the circuit measures the position of single isolated proton bunches (shock excitation of the filter) as well as protons spaced at 4.8 m intervals. In addition to the position signal, this circuit also provides a sum signal representing the beam intensity. This signal is necessary for self-triggering the electronics for each ring.

In order not to quench magnets, initial commissioning is carried out with about 5×10^9 protons, corresponding to 2×10^8 protons per bunch in 25 contiguous bunches (4.8 meter spacing). Full beam operation requires about 1.3×10^{14} protons, or 7.4×10^9 protons/bunch in about 17,000 bunches.

The detector position resolution includes both a systematic contribution (about 100 microns rms, due to mechanical tolerances and to imbalances in cables and electronics), and a statistical contribution dependent on beam intensity (about 100 microns rms during commissioning, and 10 microns during operation with full beam). In addition, the analog-to-digital converter (ADC) granularity is about 20 microns (with an 10 bit ADC). The beam intensity is measured to an accuracy of 10 to 20 per cent at each detector. This is the only global measurement of beam intensity in the SSC. It was a very important feature of the Tevatron system during initial commissioning.

The electronics is divided into VME crate circuits (all digital) and non-VME electronics (primarily analog). The non-VME system can be housed in a simpler and cheaper environment than a VME crate and protected better from electromagnetic noise, if necessary. Local intelligence is extensively used in this system. The microprocessor code and the operating parameters are downloaded from the control system prior to injection of beam. Local memory is used to store results of beam position and intensity measurements for later access by the control system.

Once the microprocessor code and the operating parameters are downloaded, the system runs without intervention by the control system. In addition to the normal control system interface (a serial link with a highly structured data encoding format), there is a SSC clock signal (actually two, one in each direction) with encoded timing events to synchronize all the beam position electronics and trigger special processing functions. This cable is shared with all other systems distributed around the ring and allows synchronization to about 100 ns. The beam intensity signal described above will provide the synchronization to the passage of beam. This differs from the design of the Tevatron system only in that

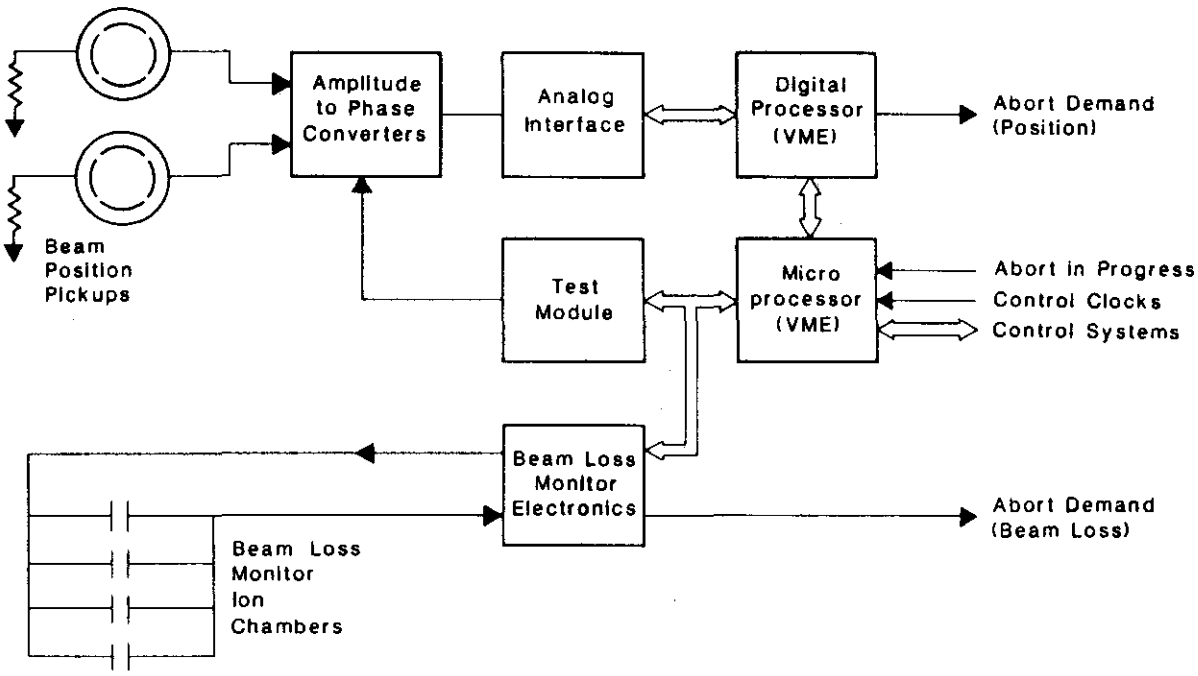

Figure 5.12-2. Block diagram of the electronics for the beam-position and beam-loss monitoring systems.

the microprocessor operating code is downloaded into random access memory (RAM) rather than being in program only memory (PROM). Although there has been no modification to the Tevatron beam position electronics hardware since its initial installation, there have been many revisions to the microprocessor software. Use of PROMs in the SSC would require excessive access time in the tunnels to change.

During normal operation the electronics digitizes the beam position and stores it in local memory. This can be a single turn (single passage of beam) or an average of many turns to obtain a good closed orbit measurement with the betatron oscillations averaged out. These data, if requested by the control system in the downloaded operating parameters and event triggers on the clock signal, are held in memory for later readout. In addition, beam position information is continuously loaded into a first in first out (FIFO) memory that is stopped whenever the electronics has been triggered by a control signal representing the activation of the beam abort system. This allows for off-line analysis to reconstruct the beam orbit prior to the abort. The electronics may in addition request a beam abort if the beam position strays beyond preset limits as determined by downloaded parameters.

One feature that needs to be implemented in the beam position system is the ability to locate the source of orbit distortions, such as ripple on a dipole correction element, which can modulate the luminosity. Due to the high conductivity of the beam pipe in the superconducting magnets, these ripple fields are less than a few Hz. Assuming that orbit distortions of the order of 10% of the rms beam size are important, this leads to the requirement that the beam position system, under special operating conditions, be able to measure orbit distortions of about 10 micron peak amplitude with sufficient accuracy to locate the cusp. This implies an ultimate resolution of the order of 1 micron. In the Tevatron beam position system (which did not have this capability), manually installing low-pass filters on the outputs of the amplitude-to-phase conversion circuits provided an ultimate analog ripple resolution of about 3 microns.

Due to the very large amount of electronics in this system, it will include many self-test features. These self-tests include measurements of dc voltages, tests of cable continuity by measuring the back termination resistance in the pickup, and injection of rf signals into the electronics to emulate the presence of beam. By varying the relative amplitudes of the rf signals, calibration of the electronics can be obtained, and the beam abort feature can be tested. The entire self-test program is stored in RAM and is triggered by a request from the control system. Results of the self-test are stored in local memory for access by the control system.

A host computer (probably the sector computer) is used to linearize the beam position information (the beam position signals are slightly nonlinear in beam centroid displacement from the detector center), changing digitizer counts to engineering units, and to correct for known mechanical offsets. In addition, the central host computer will perform the necessary calculations to determine the settings of the correction dipoles to obtain a closed orbit and to minimize orbit distortions. Any measurements that require comparison of orbits under different operating conditions (such as measurement of momentum dispersion, the effect of beam bumps, etc.) is done at the host level.

A few stations are equipped with additional electronics to record beam position on successive turns. This provides a measurement of betatron and synchrotron oscillations caused by injection errors. In addition, coherent beam oscillations can be induced on the

beam by exciting the beam with a pulsed magnet. This allows measurement of the coherent tune at any time during the acceleration cycle. There are two of these pulsed magnets in each ring (one in each plane). These pulsed magnets are sufficiently strong (about 0.5 T-m) to induce a coherent betatron oscillation of 2 mm peak-to-peak at the full energy of the SSC. These magnets have a rise time about 100 ns and a pulse length of about 0.5 ms; their triggering can be synchronized with the beam position system.

5.12.3 Beam Loss Monitoring System

The beam loss monitoring system uses a network of argon-filled ionization chambers distributed around the rings to detect the radiation associated with beam losses. Ionization chambers with about 100 cc of argon at 1 atm and close electrode geometry have adequate sensitivity and rise time to provide the necessary monitoring functions at the Tevatron [5.12-2]. The use of nickel electrodes in a sealed glass envelope provides a detector of known sensitivity (about 80 nanocoulombs per rad) capable of monitoring instantaneous doses exceeding 10 rads without saturating, requiring minimum maintenance and no gas circulation system. In the Tevatron detectors, the signal rise time is less than 10 μs for electrons and 300 μs for ions.

Detectors are located at each quadrupole and at 2 points between them. This is equivalent to a detector spacing of about 32 m. By comparison, the detector spacing in the Tevatron is 30 m. As the two rings are separated by 0.7 m, only one set of ionization chambers is needed to monitor both rings.

The electronics is adjacent to and coupled with the beam position monitor electronics. Local intelligence (shared with the position monitors) controls the operating parameters, digitization, data buffering, and self-test features. Because of the very large dynamic range, the current amplifier is logarithmic to compress the signal into the range of a 10 bit ADC.

There are two important functions of the beam loss monitoring system that place conflicting design parameters on the system. First and foremost, the beam loss monitor system must provide a high reliability system for protection against radiation damage and component destruction by lost beam. Secondly, the system provides the only way to detect aperture restrictions and semitransparent obstacles that lead to slow emittance blowup or beam intensity losses too small to be seen by the position system. Fast radiation losses resulting in more energy than about 1 mJ/g in the superconductor, and slow loss rates exceeding about 10 mW/g, are likely to induce quenches. In order that the beam loss monitor system measure radiation losses in a manner representing the probability of inducing quenches, this same time constant (about 1/16 s) needs to be included in the signal processing electronics. This represents about 225 revolutions of the beam; such an integration time constant prevents seeing structure on a turn-by-turn basis.

As the beam loss monitoring system provides the primary protection of the SSC from beam loss, it must be highly reliable. Functionally, the protection system works as follows: After the operating parameters are downloaded, the system operates in a stand-alone manner, completely independent of both the control system and the microprocessor in the VME crate. Downloaded parameters include digital-to-analog (DAC) settings controlling the high voltage applied to the ion chambers and the analog voltage controlling the threshold for firing the beam abort system. Whenever a beam-loss signal (either an analog sum

or an analog OR) exceeds this preset threshold, the abort system is triggered. This method avoids digital processing in the abort circuit.

The self-test features must be complete and reliable. The major self-test routine (under microprocessor control) is to ramp the ion chamber high voltage down and up again resulting in an induced signal in the ion chamber electronics. (The interelectrode capacitance is about 2 pF and the high voltage about 2 kV.) The digitized signal is compared to an acceptance window. This test checks the cable continuity, the presence of the ion chambers, the operation of the high voltage, and most of the protection electronics. A more complete test of the electronics includes setting the abort threshold low enough to be triggered by the cable test and testing each station sequentially for a beam abort request. Complete simultaneous testing of all stations is not possible, as the abort loop is a hardwired logical OR circuit.

5.12.4 Beam Profile Monitoring System

The spatial transverse beam size is measured at several locations around each ring to obtain information on relative betatron amplitude functions, emittance, and emittance growth. The two methods planned to make these measurements are flying wire scanners and synchrotron radiation light monitors.

The flying wire scanner is a motor-driven thin fiber or wire a few microns in diameter that is swept through the beam once with a velocity of about 0.1 m/s. Placement of a scintillation detector downstream of the scanner records the temporal radiation loss signal which can be analyzed to provide beam profile information. The wire diameter should be of the order of 0.25 times the rms beam size to provide good spatial resolution. In the normal lattice, the rms beam size is expected to be about 100 microns. Because of the highly directional nature of the radiation, such a unit could be used near intersection points where beams are traveling in both directions to determine their relative spatial overlap. At the CERN SPS [5.12-6] and at the Tevatron, such systems provide the best information on beam profiles. Each intersection point would need about four such systems.

As such a device intercepts the beam, it inevitably leads to emittance growth due to multiple scattering. Such a device placed at a normal lattice point (β = 330 m) could be used about once a minute without causing excessive emittance growth. However, use of these devices is known to create some background problems in the underground experiments at the CERN SPS.

The second method of measuring beam profiles at the SSC is to use the spatial profile of synchrotron radiation. At the injection energy, the wavelengths of the synchrotron radiation from the constant field regions are too long to be useful. Radiation from regions of abrupt field change at the entrance and exit of the dipoles extends into the visible region and can be used to obtain beam profiles with about 100 micron resolution. Such systems have been built and successfully used at the CERN SPS [5.12-7], although undulators have more recently been employed. Even at injection, the higher energy and the stronger exit and entrance field gradients of the SSC will provide much more light. At higher beam energies greater precision is required and, above a few TeV, soft synchrotron-radiation x rays from the constant field region can be used to obtain resolutions of perhaps 25 microns. The synchrotron radiation method is superior to that of the flying wire since it does not cause emittance growth. However, the flying wire can be used in regions free of magnetic

fields and can provide simultaneous relative position measurements of two counter-rotating beams near the interaction points.

Special equipment is needed to monitor the longitudinal bunch profile. The rms longitudinal spread of a bunch is about 7 cm but under certain circumstances can be several times longer. The monitoring is done using a combination of sampling oscilloscopes connected to wide-band gap pickups that have a time resolution in the order of 10 psec.

5.12.5 Beam Intensity Monitoring System

Beam intensity monitoring systems are needed in both rings to monitor the total circulating current. Precise measurements are needed to allow determination of beam current lifetimes of the order of 100 hours in a few minutes. Typically dc beam current transformers have long term stability in the range of 1 microamp [5.12-8]. As the nominal circulating current in each ring is about 70 milliamps, it is possible to measure a 100 hour beam current lifetime in about 10 seconds. At lower circulating currents the measurement time is correspondingly longer. These units, which use a low frequency oscillator (of the order of a kilohertz) to measure the dc flux bias produced by the beam current in a high permeability tape-wound core, are inherently low frequency devices and cannot measure intensities in single bunches or in injector batches. To measure higher frequency components, ac coupled toroids with a variety of rise and fall times will be needed in addition. Their accuracy is probably limited to about 1%.

Measuring the intensity of beam in individual rf buckets is particularly important, as protons in neighboring rf buckets do not contribute to the luminosity but do contribute to the dc current transformer measurements. This measurement, limited to about 1% accuracy, is done using the wideband gap monitor or synchrotron radiation monitor mentioned under beam profile monitors.

5.12.6 Beam Schottky Monitoring System

Schottky signals, i.e., signals due to the quantized nature of the proton charge (shot noise), are used to monitor incoherent tunes, tune shifts, tune spreads, chromaticity, etc. Equally important, this equipment is used to measure coherent effects that are too small to be seen by the other monitoring systems, and that are important to minimize in order to limit emittance growth.

The tune and tune spread are measured by measuring the structure of betatron sidebands between successive harmonics of the frequency of revolution [5.12-9]. These sideband signals are many orders of magnitude below the amplitude of the harmonics in bunched-beam applications. In the SSC, the harmonics are spaced at 3600 Hz intervals, and the sidebands are about 1400 Hz on either side. Both the harmonics and the betatron sidebands will have synchrotron sidebands from coherent longitudinal motion of the bunches in the rf buckets. As this is equivalent to FM or phase modulation, many harmonics of the fundamental synchrotron frequency (about 7 Hz at 20 TeV) may be present. Due to the close spacing of the revolution harmonics, measurements probably will have to be made in the time domain, and a fast Fourier transform used to separate out the sidebands.

5.12.7 Other Beam Diagnostic Systems

Valuable information can be learned about the accelerator structure as seen by the beam, and about beam stability limits, by measuring the beam transfer function. In this measurement the beam is excited by an rf oscillator swept over a range of frequencies, and the beam response is measured with another set of electrodes. The ratio of beam amplitude response to rf drive is the beam transfer function. Such measurements have been done at the CERN ISR in both the transverse and longitudinal planes with unbunched proton beams [5.12-10].

5.13 Control System

A modular design of the control system for a collider complex on the scale of the SSC is the only approach that will lead to a successful and operable collider. A common framework avoids duplication, minimizes capital and maintenance costs, and, because of this simplicity, substantially improves overall system reliability.

The boundary between the control system and the other systems is defined as follows: Each system contains the cost elements for the design, fabrication, procurement, installation, and test of instrumentation, controls, and software pertaining to itself. These are called device-dependent modules. It is both possible and highly desirable to standardize most of the hardware and software in these device-dependent modules. The delineation between controls and subsystems pertains only to cost estimates and not to design. Device-dependent hardware modules are installed or otherwise connected to a crate that contains a network interface which, in turn, connects to the data network. The crate, data network, and all higher level computers and networks are device-independent modules and are part of the control system. The same rules apply to the software. The system, network, and database software are device-independent and are part of the control system. Applications programs, device-specific software resident in dependent modules, and device-dependent analysis program are device-dependent modules and are cost elements of the particular system to which they apply.

5.13.1 Overall Description

The control system for the collider complex is shown in increasing levels of detail in Figures 5.13-1, 5.13-2, and 5.13-3. The system consists of the following device-independent elements:

(a) A host computer cluster;
(b) Operator control consoles and other terminals;
(c) Eight sector computers and two cluster computers;
(d) Five-injector subsystem computers (same as the sector computers);
(e) Approximately 400 distributed front-end processors;
(f) A ring information network and local area networks that connect the system.

The monitoring and control functions below these levels are considered to be device-dependent.

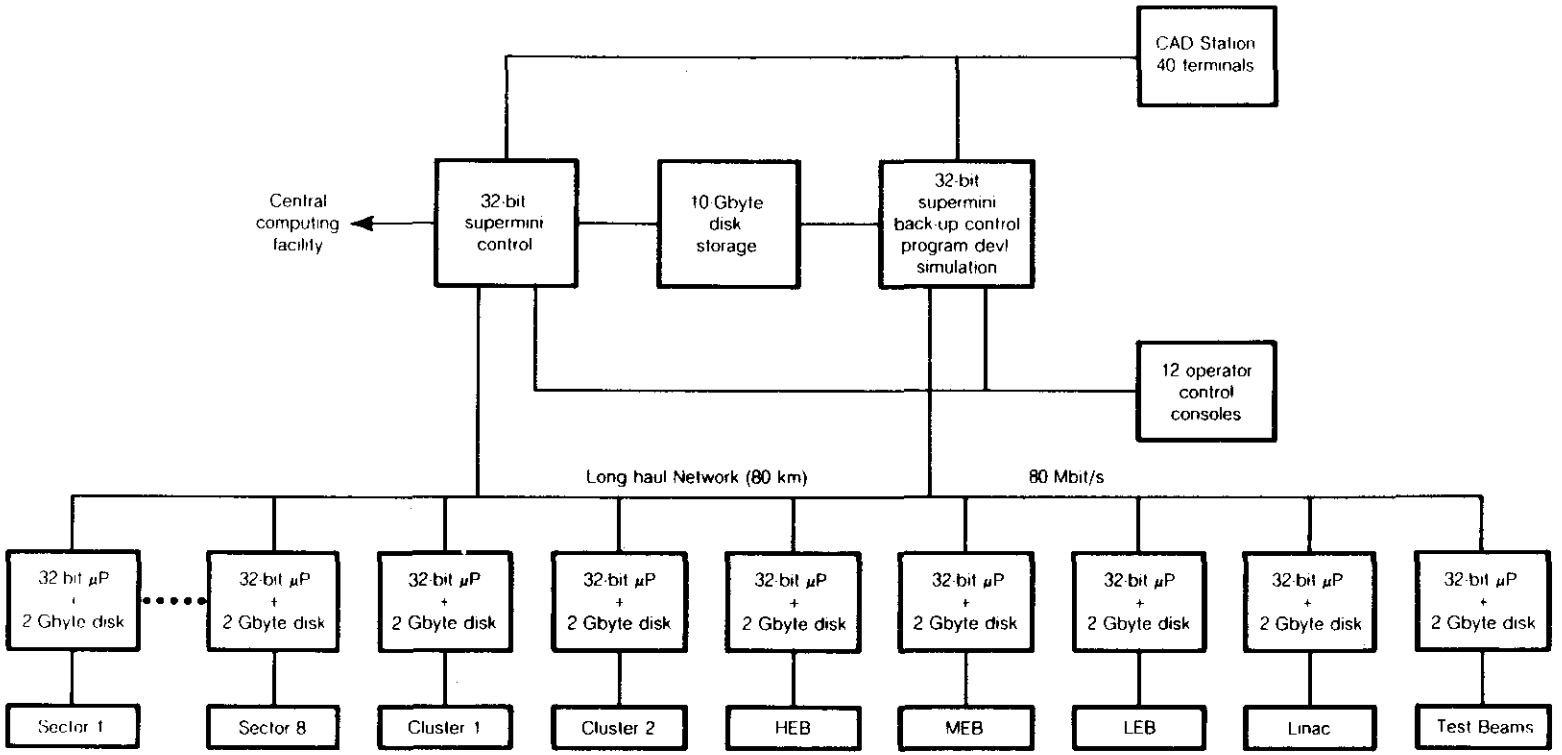

Figure 5.13-1. Host computer block diagram.

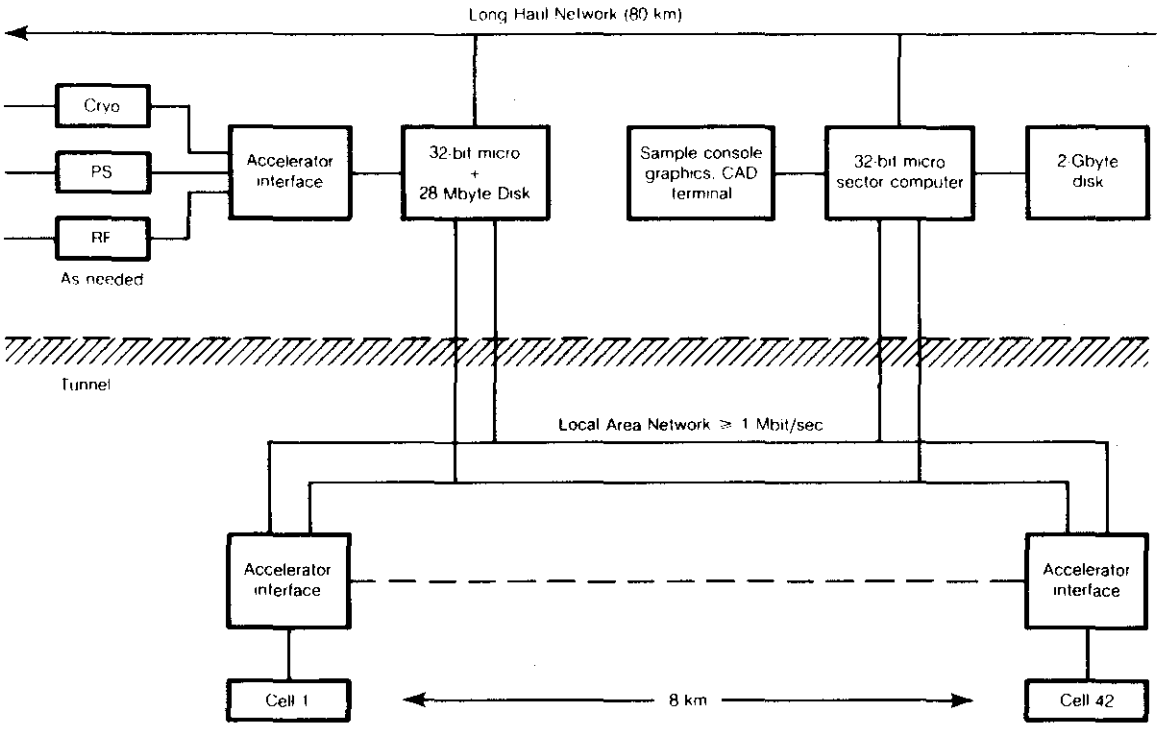

Figure 5.13-2. Sector computer block diagram.

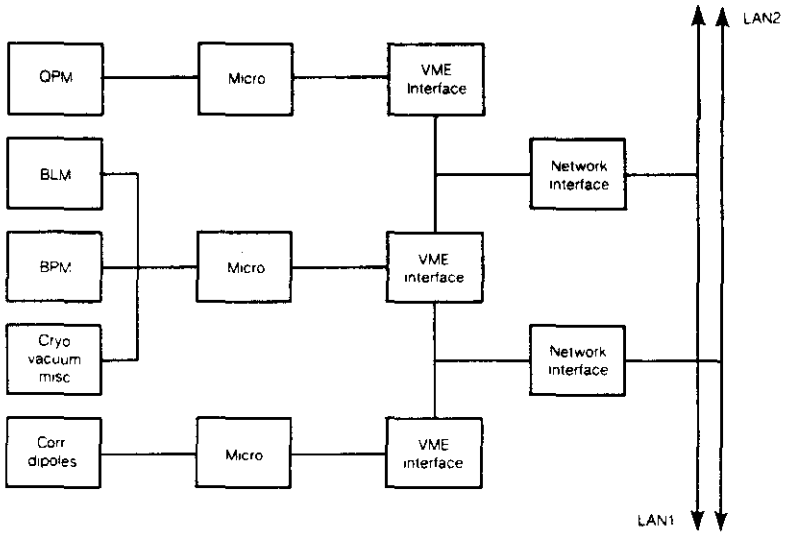

Figure 5.13-3. Block diagram of tunnel interface electronics.

The structure of the collider is such that control functions exist primarily at the main control room area, at the sector service buildings, and at the ends of cells near the spool pieces. The layout of the control system reflects this fact.

The host computer complex resides near the main control room. It contains the complete data base for all of the accelerator complex. It is connected to control consoles and terminals, to the ring network that communicates to the sector computers, and to the computers that control the injector complex. Around the collider ring there are eight sector service buildings and two cluster service buildings separated from one another by roughly eight kilometers. The control functions at these areas are complex, involving the operation of a large refrigerator and two main bus power supplies, in addition to communication with, and data base maintenance for, all of the tunnel devices that are in that sector. The sector computer is a large system (>1 MIPS) 32-bit microprocessor with 6 Mbyte of RAM and 2 Gbyte of disk storage. The eight sector computers and the two cluster area computers are connected to the central host computer and to each other by an 80 Mbit/s bandwidth long haul network.

Each accelerator in the injector complex (and the HEB test beam) is controlled and connected to the ring network via a system identical to the sector computers. This amount of processing power is ~50% greater than that currently in use at the Tevatron. It is assumed that the same interface crates, distributed processors, and system computers used in the collider are used in each of the injector subsystems. This assumption, of course, is not a necessary part of the control system design but does lead to a uniform approach that eases the software development costs and maintenance costs.

In the tunnel, the bulk of the devices that must be monitored and controlled are at the spool pieces. An electronics rack containing an interface crate and numerous device dependent modules is located at every other spool piece (at each cell). In order to protect the electronics from radiation and environmental damage, it is installed into a shaft that is drilled in the tunnel ceiling. The interface crate contains several microprocessors, two transceivers for the two independent local area networks (LANs), and sufficient analog readback and control channels for the variable number of devices at that location. Typical device-dependent modules at the spool pieces or in the interface crate include the control modules for the beam position monitor system, the quench protection system, the waveform generators for controlling the correction element power supplies, and the vacuum and cryogenic controls and sensors. Communication to the network takes place from the individual modules themselves via the network interface. Table 5.13-1 is a listing of the device-dependent control functions that exist in a typical cell control rack.

Table 5.13-1
Control Functions and Signals
at Each Cell (Both Rings)

Beam position monitor	16
Beam loss monitor	6
Vacuum pump status	4
Vacuum pump current	4
Vacuum gauge current	8
Cryogenic monitors (temperature & pressure)	12
Cryogenic valves (positions & actuators)	24
PS & quench voltage taps	24
HFU status	8
Dipole correction (status, readback & reference)	16
Tunnel environment	6
Total	128

The interface crates communicate with their sector computer over two LANs which are both "live" to provide redundancy in this essential link in the control system. The fast real time decisions necessary for the protection of the collider components by the quench protection system are performed at the interface crate level and do not require the LANs except to provide diagnostic information to the control system. Much of the processing for the beam position monitors and the beam loss monitors is also performed at the crate level and thus generates little traffic on the LANs. Either the Ethernet (IEEE standard 802-3) or Pronet protocols can handle the expected traffic between the 42 interface crates and the sector computer.

The data base for the collider is quite large, totalling about 62,000 control and monitor points alone. Each of these elements has some number of words in the data base to describe it and specify its properties. This large data base could overwhelm the data links and decrease the response time of the control system. To avoid this traffic the data base is divided up and stored at the lowest possible level for each device. In particular, the complete data base for each sector resides in the sector computer, so that the long haul network is not burdened by data base transmissions to and from the host. Table 5.13-2 is an approximate listing of the control and monitor points in the data base, showing how they are divided among the various control subsystems. A complete data base exists at the host computer.

The complete data base reflects not only the number of individual elements but also the number of major subsystems. The HEB, while smaller than the main ring, is functionally equivalent in the sense that it is a complete accelerator in its own right and requires

Table 5.13-2
Estimated Monitor/Control Points for the Collider (both rings)

System	Cell	Arc Sector	Cluster	Total
Beam position	16	672	476	6328
Beam loss	6	252	186	2373
Beam profile	—	4	8	48
Vacuum:				
Ion pump (S&I)	8	336	308	3304
Gauge (I)	8	336	308	3304
Gate valve	—	12	28	148
Cryogenics:				
Monitor(T&P)	12	504	412	4856
Relief valve	8	336	258	3184
Cooldown valve	4	168	144	1632
Level control	12	504	412	4856
Refrigerator control	—	400	400	4000
Magnet PS&Q:				
Voltage taps	24	1008	664	9392
HFCU	8	336	248	3184
Dipole corr.	16	672	446	6308
Persistent current	—	8	8	80
Quad. corr.(tune)	—	8	8	80
Sext. corr.(Chrom.)	—	8	8	80
Quad corr.(beta)	—	16	—	128
Skew quad.	—	16	—	128
Sext. (trans.)	—	16	—	128
Skew sext.	—	16	—	128
Oct.	—	16	—	128
Skew oct.	—	16	—	128
Main dipole & quad.	—	2	2	20
IR quad	—	—	56	112
IR dipole corr.	—	—	60	120
Energy dumps	—	8	8	80
Misc.	—	20	200	560
Tunnel environment:				
Helium det.	—	4	8	48
Electronics temp.	2	84	52	776
Smoke detector	1	42	26	388
Water detector	1	42	26	388
Crate voltage	2	84	52	776
Total	128	5946	4812	62004

Arc sector = 42 cells
Cluster = 26 cells + 2 IRs + 2 UTs
Machine = 8 arc sectors + 2 clusters

injection, rf, abort, extraction, and power supply systems that are as complex as the main ring. Because of this fact, the injector complex data base is not significantly smaller than that for the main ring.

5.13.2 Host Computer

The host computer system must provide overall control of the hardware at the collider complex. It receives the relevant data from the hardware, ships it to the appropriate operator console, reacts to operator commands to change data displays, and sends the control information to the accelerator hardware. Because of the complexity of the collider beam dynamics, and the complicated interaction of some of the machine components, substantial computational capacity is necessary to allow the simulation of the collider response to operating point changes. A typical example might be to adjust the dipole correctors to improve the beam orbit, followed by an adjustment of the quadrupole correctors to obtain the desired tune of the machine.

The operator control consoles located in the main control room are connected by a local area network to the host computer. The control consoles should be designed to make them straightforward to use and to transmit large amounts of information quickly. These requirements mean fast, high resolution color graphics, a menu-driven selection system, and disk storage of frequently used programs and display conditions. The consoles should be identical. The existing control consoles at the Tevatron satisfy these requirements and will be used as the model for this aspect of the control system design. Each console will have its own microprocessor and considerable ($>$100 Mbyte) local disk storage.

Recent experience with the Tevatron control system host computer, a VAX 785, shows a 75% utilization during machine studies and 50% during normal operations. This indicates that the estimate for the capacity of the host computer proposed in the Reference Designs Study (RDS) was too small by at least a factor of two. The present generation of 32-bit superminicomputers (produced by a number of manufacturers) can be configured to provide the scale of computing power needed to carry out the beam dynamics simulations. At the same time, computers in this range can provide the control functions necessary to operate the collider complex. Operating systems for computers of this class tend to be robust and user friendly, thus minimizing problems associated with a large variance in computer expertise among the potential users of the system.

A reliable and flexible host computer system is provided by a cluster of CPUs connected to a common large (at least 10 Gbyte) disk storage facility and connected to each other by a high speed bus. Typically one of the CPUs is connected to the collider ring broadband network and the control console local area network and would provide the control and data acquisition necessary to operate the collider. Another CPU serves as a "hot" spare, i.e., it is connected to the broadband network and the control console LAN and is ready to take over in the event of a failure in the primary control CPU. It would be used for machine simulations and program development. The top half of Fig. 5.13-1 shows a block diagram of the proposed configuration; Table 5.13-3 summarizes the characteristics of the host computer system.

Table 5.13-3
Host Computer Characteristics

CPUs	2 4-MIPS class, with floating point hardware
RAM	16 Mbyte per CPU
Disk storage	10 Gbyte, shared by all CPUs
Magnetic tape	4 6250 BPI drives
High speed bus	Star coupler with 10 Mbyte/s transfer rate
Communication	2 local area network ports, 2 long haul network ports
Terminals	40
Floor space	12 m^2 plus access space (computer environment), terminal space, and control space (office environment)
AC power	40 kW

5.13.3 Sector Computers

The sector, cluster region, and injector system computers require substantial computing power, large memories, and large capacity disks for program storage and archival storage of past operating parameters. In addition, they must be able to operate in a stand alone mode during commissioning and during machine maintenance periods.

The present generation of powerful 32-bit microprocessors with the parameters listed in Table 5.13-4 provide a more powerful and convenient computer system at a substantially lower cost than the system used as the model for the sector computers in the RDS. These computers are connected to the host computer by the broadband ring network. The development of computer networking hardware and software now provides a 80 Mbit/s token ring network (Pronet), a factor of 8 faster and a factor of 16 cheaper than the system proposed in the RDS. The sector computer is connected locally to a simple control console for local operator intervention and fault diagnosis, to several terminals for system commissioning and monitoring, and to a computer aided design (CAD) work station for retrieval of schematics, and cryogenic system layouts.

The sector computer connects to the interface crates in the main ring tunnel by two independent and "live" local area networks so that there is a redundant control path to the lowest level of the control system. In addition, at the sector computer, there is a microprocessor with smaller RAM and disk storage that is connected to the long haul network and to the tunnel LANs to serve as a backup to the sector computer. Besides its backup function, it also controls the refrigerator and the accelerator subsystems (rf, main magnet power supplies, etc.). It has stand alone capability to facilitate cryogenic system commissioning and assist during maintenance periods. The layout of a typical sector computer is shown in Fig 5.13-2.

Table 5.13-4
Sector Computer Characteristics

CPU	32-bit microcomputer, with floating point hardware
RAM	6 Mbyte
Disk space	2 Gbyte
Communication	1 local area network port, 1 long haul network port, 8 serial ports, 1 parallel port
Tape	1 6250 BPI tape drive

An 32-bit microprocessor configuration identical to the sector computers is used as the control host computer for each of the injector subsystems, i.e., one for the High Energy Booster, one for the Medium Energy Booster, one for the Low Energy Booster, one for the Linac and ion source, and one for the external test beams. These CPUs are connected to the central host computer via the broadband ring network.

The computers chosen for the "distributed" control functions, i.e., the sector, cluster, and injection complex computers, have a common operating system. This leads to very substantial savings in software development costs, as well as increased reliability of the entire system. Because the eight arc sectors of the machine are essentially identical, the software developed for one sector can be replicated to provide the software for all eight sector computers. The cluster region computers service a more varied set of elements and require special software. They probably represent more than half of the software development effort for the distributed computers used in the collider ring.

The sector computers require only a clean office environment and therefore do not require a air-conditioned computer room. Included in the configuration is a battery backup power source for the memory so that the information in the memory will be protected from power interruptions.

5.13.4 Accelerator Interface Crates in the Tunnel

The interface crate provides the connection to the elements of the collider to be controlled and monitored by the control system, in other words, the interface between independent and dependent hardware modules. In the RDS, the model for this crate was based on Multibus. Since that time, VME, developed primarily by Motorola in Europe, has achieved much wider acceptance than Multibus in industrial control applications. This is primarily because of its 32-bit architecture, the use of the 68000 series microprocessor as the CPU, and a substantially more robust mechanical format. At the moment, the costs of the two systems per function are roughly equivalent. Because of the wide industrial base in automated manufacturing, the cost of the VME system will continue to drop and simultaneously provide a cheaper, more powerful, and more reliable solution for the accelerator interface crate.

Software for the tunnel microprocessors resides on the disk of the sector computer and is downloaded sequentially over the local area network. All microprocessors in the tunnel can be remotely booted.

Figure 5.13-3 is a block diagram of the parts of the control system that reside in the tunnel. The spacing of the interface crates and dependent modules is set by both technical and economic considerations. The maximum distance that signals can be transported before processing is determined by degradation of the signals in cable, a few hundred meters for the beam position signals, longer for other signals. The total cost of the interface station is approximately the same as the overhead incurred by transporting the signals the 96 m from one spool piece to the next. The number of devices and control points (Table 5.13-1) per cell is well matched to a single crate. Reliability considerations (Section 5.13.8) argue for minimizing the number of interfaces by fully utilizing the VME crates at each station. Based on these considerations the interface crates are located in the tunnel with a frequency of one per cell. It is conceivable that as the subsystem designs mature less control functions may be required per cell and the spacing of the tunnel electronics may increase.

There is the question of radiation damage to this electronics and its implication on the reliability of the control system. In Section 4.8.4 an estimate of the integrated neutron fluence in a full luminosity year is given as $2\text{–}8 \times 10^{10}$ cm^{-2}. From these projected dose levels, it is clear that the electronics for the control system needs some shielding to achieve the reliability level necessary for successful SSC operation. A simple 80 cm diameter hole, 2 m deep, drilled into the ceiling of the tunnel, and covered by a shielding plug on the bottom provides a two orders of magnitude reduction in the radiation dose. This level of reduction is sufficient so that the lifetime of the electronic components is not compromised by the radiation background (see Table 4.8-2).

As well as providing shielding the hole and door also provide an environmental enclosure. A water cooled metal surface with an area of one square meter provides sufficient cooling to remove the projected 2–2.5 kW of power consumed by the electronics. The operating temperature should be kept as low as possible since an increase of 10 C decreases the mean time to failure of silicon-based electronics by more than a factor of two. The temperature difference between the enclosure and the tunnel should be positive to ensure that the humidity is kept low. Care should be used in selecting the connectors so that they are relatively insensitive to humidity.

5.13.5 Ring Information Network

The ring information network consists of 12 broadband cables that reside in the tunnel and carry all the necessary communications from the central control facility around the ring. These cables have at least a 300 MHz bandwidth and are either CATV 75-ohm coaxial cables with repeaters or fiber optics cables with repeaters, depending on which is the cheaper and more reliable medium. Given the radiation field in the tunnel, presently available commercial fiber optics cables are probably too radiation sensitive. This is a rapidly evolving field, and there is no strong reason for making a decision between the two media at this time. For purposes of cost estimate, the use of CATV 75-ohm coaxial cable is assumed.

The assignment of the 12 cables is:

(a) Two cables for the ring data network
(b) Two cables for accelerator timing signals (one for each ring)
(c) One cable for voice, television, and security communications;
(d) One cable for fast beam abort;
(e) Two cables for the safety system;
(f) One cable for the quench protection system;
(g) Three cables for future expansion.

The communication cables around the ring are frequency division multiplexed to provide the necessary number of subchannels.

5.13.6 Software Development Effort

The scale of the needed development is roughly the same as developing the control system software for the Tevatron since it is a modern superconducting magnet accelerator and storage ring. The complication of rapid cycling and beam extraction probably compensate for the difference in size compared to the SSC. The uniformity in the proposed control system for the SSC eases the problem of matching software to several different processors and the use of more powerful processors at the lowest levels in the system also reduces the software development effort.

Table 5.13-5
Tevatron Software Effort

	Network (man-years)	Microprocessor (man-years)	Applications (man-years)	Total (man-years)
AD/Controls	48	12	8	68
Other	—	13	36	49
Totals	48	25	44	117

At the Tevatron, the software effort necessary to commission an entirely new control system extended over approximately 45 months. This work included manpower from the Accelerator Division Controls Group (AD/Controls) along with other physicists and engineers. The total effort amounted to 117 man-years, as summarized in Table 5.13-5. The work is categorized as involving the network, including some utility software (database retrieval, etc.), the distributed microprocessors, and applications written for the consoles and host computer. We expect that more work is necessary to commission the SSC network; this effort may well double to 100 man-years. The microprocessor software effort should remain the same, however, because the subsystems are the same, and of a comparable scale. Likewise, the applications software should be comparable to the Tevatron. The total software effort should thus be on the order of 160 to 180 man-years.

5.13.7 Installation Effort

The main computer systems are installed by the vendor and the installation costs except for ac power, air conditioning, and raised flooring, are included in the purchase price. The interface crates are in rack-mounted packages and require installation in a rack, connection to the two local area networks, and post-installation tests. The major installation effort is in connecting the various processors to the ring broadband network and the two local area networks, and in installing the network cables. Each coaxial cable going around the ring requires approximately 0.8 man-years to install, including repeater installation and tests. The other major effort involves the assembly and commissioning of the control consoles attached to the host computer; this effort is included in the cost analysis of the control consoles.

5.13.8 Reliability

The control system is essential to the operation of the SSC. In addition, certain control subsystems, the Quench Protection System and Beam Loss Monitor, are essential for safe operation of the SSC. Finally, a system the size of SSC must be designed to run in spite of inevitable, minor component failures. The control system must identify these failures, reconfigure the accelerator to run without the failed component, and note the nature and site of the failure so that repairs can be made at an appropriate time.

Because the control system plays a large role in the reliable operation of the SSC, much of its design concerns reliability. SSC will have a fourteen day running period, ten days of beam delivery to experimenters followed by four days of accelerator development and maintenance. To insure maximum utilization of the SSC, the control system is designed so that the mean time between failures (where "failure" refers to something that results in loss of the stored beam) is greater than fourteen days and the mean time to repair a failure is less than four days. In addition, the Quench Protection and Beam Loss systems are designed to be "fail-safe" — no combination of component failures will allow the magnets to operate without protection.

A rough calculation illustrates the reliability problem: Typical integrated circuits (ICs) have a mean time to failure (*MTTF*) on the order of 10^6 hours (roughly 100 years). There are approximately 400 instrumentation crates with 100 ICs per crate in the tunnel. Thus one would expect one IC to fail somewhere in the tunnel every 25 hours or 10 IC failures in the 10 day running period.

To design a system with better reliability than its aggregate component reliability, the following steps were taken:

(a) A detailed, "strawman", design of the tunnel instrumentation crates was made (since system failure rate goes as the sum of its component failure rates, the 400 instrumentation crates effectively determine the control system reliability).

(b) Each crate was expanded into its subsystems and each subsystem into its individual components. Industrial and military models were then used to compute component reliabilities.

(c) The subsystem reliability was computed from the reliabilities of its components. The accuracy of these calculations was checked by comparing the predicted reliabilities against actual failure data from equivalent subsystems at the Tevatron.

(d) Areas shown to be "trouble spots" by this modelling were redesigned by adding higher reliability components and/or redundant components to improve subsystem reliability.
(e) The subsystem interconnections were modified so that there were at least two, orthogonal ways to perform each function. The secondary paths cannot only be used to perform the function but also to diagnose completely the original failure so that the eventual repairs can be completed in minimum time.
(f) The final system was reanalyzed.

The remaining sections give some background on system reliability theory and describe the system evolution and final design in more detail.

Component Reliability

The reliability $R(t)$ of a system is the probability that the system will perform its function without failure for a length of time t. The failure density $f(t)$ of a system is the probability density distribution of system failures, $f(t) = dF(t)/dt$ where $F(t) = 1 - R(t)$. The reliability of electronic systems is usually characterized by the ratio of failure density to reliability, a quantity known as the failure rate or hazard rate of the system, denoted $\lambda(t)$. Intuitively, $\lambda(t)dt$ is the probability that the system will fail in the interval dt, given that it has not failed prior to t. For electronic components, $\lambda(t)$ is essentially constant over the useful life of the component. Mathematically, a constant failure rate implies that the reliability is a simple exponential, $R(t) = \exp(-\lambda t)$, and the component's mean time to failure is $1/\lambda$.

A constant component failure rate also implies that λ is a property of a component, much like its gain or power dissipation. Starting in the late 1930s, military and industrial laboratories were established to determine the failure rate constants of all types of electronic components. The most recent compendium of this data, MIL-HDBK-217C [5.6-2] was used to model the reliability of components used in the SSC control system. MIL-HDBK-217C has been shown to predict component failure rates within 1% of observed rates. Several large power reactor and avionics systems, each with a number of components on the order of the number expected in the SSC control system, have been modeled using MIL-HDBK-217C and predicted system failure rates have been within 10% of observed failure rates [5.13-1][5.13-2].

The algorithm of MIL-HDBK-217C for a component's failure rate is

$$\lambda = \pi_L \pi_Q [C_1 \pi_T + (C_2 + C_3)\, \pi_E] \tag{5.13-1}$$

where

π_L is a learning factor that accounts for initial design errors. It is 10 for components that have been on the market less than a year and 1 for components that have been available for more than two years.

π_Q is a quality factor that accounts for the degree of component screening and burn-in. Possible values of π_Q and the military standards that define the required screening level are shown in Table 5.13-6.

Table 5.13-6
MIL-HDBK-217 Quality Levels

Level	Screening Standard	π_Q
S	MIL-M-38510S	0.5
B	MIL-M-38510B	1.0
B-1	MIL-STD-833B	3.0
B-2	(B-1 with some tests waived)	6.5
C	MIL-M-38510C	8.0
C-1	MIL-STD-833C	13.0
D	Commercial, Hermetic Seal	17.5
D-1	Commercial	35.0

π_T is a temperature acceleration factor to account for the in-situ operating temperature of the component. π_T is one at 25 C and increases exponentially with temperature (e.g., for silicon ICs, π_T is 2 at 40 C and 10 at 70 C).

π_E is an environmental factor to account for mechanical or electrical stress in the operating environment. Values for some typical environments are shown in Table 5.13-7.

C_1 and C_2 are device complexity factors. They both depend on the component type (e.g., MOS RAM, TTL MSI) but are usually on the order of $10^{-3}\sqrt{N_g}$ where N_g is the number of gates or transistors on the component. C_3 is a package complexity factor. It depends on the package type (e.g., DIP, surface mount) but is on the order of $10^{-4}(N_p)^{3/2}$ where N_p is the number of pins on the package.

Table 5.13-7
MIL-HDBK-217 Environmental Factors π_E

Computer room	1.0
Factory floor	2.5
Aircraft cockpit	3.5
Aircraft equipment bay	4.0
Ship engine room	5.0
Fighter cockpit	7.0
Fighter equipment bay	8.0

Some general features of this model are:

(a) It is possible to increase reliability an order of magnitude by using MIL-SPEC parts. Unfortunately, MIL-SPEC components are an order of magnitude more expensive than their commercial counterparts.
(b) It is possible to increase reliability an order of magnitude by lowering the operating temperature 40 C and a factor of two by lowering the operating temperature 10 C.
(c) It is possible to increase reliability a factor of two by carefully controlling the environment (i.e., placing the equipment in an air-conditioned computer room).
(d) Linear (analog) devices are about a factor of two less reliable than digital devices.
(e) Replacing N components by a single integrated circuit that performs the same function will improve system reliability by roughly $\sqrt{N}$.

Table 5.13-8 gives the reliabilities for components similar to ones that will be used in the SSC instrumentation crates. The environment was assumed to be "factory floor" (π_E = 2.5); all components were mature (π_L = 1), selected, burned-in, commercial hermetic packages (π_Q = 9) water cooled to run at 25 C. To illustrate the importance of the water cooling, failure rates at 40 C and 70 C were also computed (the in-situ component temperature of air-convection-cooled crates would be between 40 and 70 C).

The next section describes how these component reliabilities are combined to calculate subsystem reliabilities and how the calculated reliabilities compare to field data on equivalent subsystems at the Tevatron.

Subsystem Reliability

Subsystem reliability is computed by applying series and parallel combination rules to the subsystem's component reliabilities. A subsystem that fails when any of its components fails is said to have its components in series. A subsystem that fails only when all of its components have failed is said to have its components in parallel. Any system can be decomposed into a combination of series and parallel subsystems.

Series/parallel reliability subsystems should not be confused with series/parallel elements of the electrical circuit whose reliability is being modeled. For example, Fig. 5.13-4 is a simplified schematic of one input channel to the Quench Protection Monitor. It contains some elements that are electrically in series and some in parallel. However, for a reliability calculation all elements are in series since the failure of any one of them results in a failure of the entire monitor channel. Figure 5.13-5 shows a reliability schematic of the QPM input channel.

The reliability of a series connection is simply the product of its component reliabilities. If the reliability of component i is $R_i(t)$, the subsystem reliability is

$$R(t) = \prod_i R_i(t) \qquad (5.13\text{-}2)$$

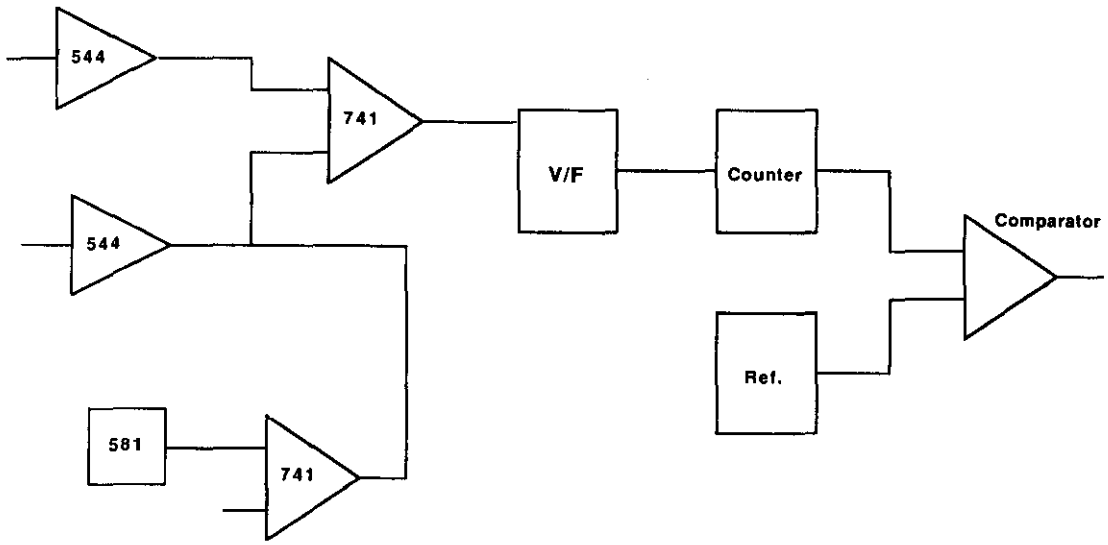

Figure 5.13-4. Block diagram of a quench protection monitor channel (1 of 12).

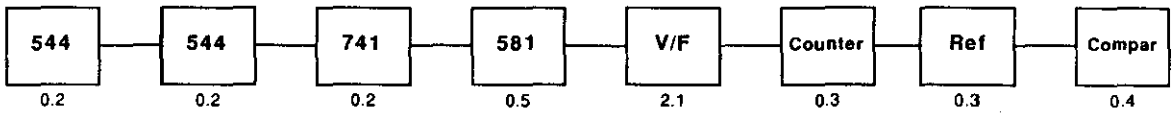

Figure 5.13-5. Quench protection monitor reliability diagram.

Table 5.13-8
Component Reliability for Components Used in SSC Control System
(in Failures Per Million Hours of Operation) Evaluated Using MIL-HDBK-217C

Device	Failure Rate 25 C	40 C	70 C	Qual.	Therm. Resist.	Power Diss.	Pack. Type	Technology	Pins	Gates
MC68000, 10MHz, Plas.	95	26.2	183.9	17.5	30	1.50	P	NMOS	64	12667
MC68000, 12.5MHz, Plas.	15.7	43.4	288.4	17.5	30	1.75	P	NMOS	64	12667
MC68000, 10MHz, Plas.	1.8	3.1	10.4	9.0	30	1.50	C	NMOS	64	12667
MC68000, 12.5MHz	2.3	4.2	14.0	9.0	30	1.75	C	NMOS	64	12667
MC68010, 10MHz	12.0	33.9	240.9	17.5	30	1.50	P	NMOS	64	25000
MC68010, 12.5MHz, Plas.	20.1	56.5	378.0	17.5	30	1.75	P	NMOS	64	25000
MC68010, 10MHz	2.1	3.9	13.5	9.0	30	1.50	C	NMOS	64	25000
MC68010, 12.5MHz	2.8	5.3	18.2	9.0	30	1.75	C	NMOS	64	25000
MC68020, 16.7MHz	4.4	7.6	24.7	9.0	30	1.75	C	NMOS	144	50000
MC68881 FPU	3.6	6.9	23.9	9.0	30	1.75	C	NMOS	68	50000
MC68851 MMU	4.6	10.3	46.6	9.0	30	1.75	C	CMOS	68	25000
AM7990 LANCE	1.5	2.7	8.9	9.0	30	1.75	C	NMOS	48	4000
AM7991 SIA	0.7	1.0	2.3	9.0	30	1.75	C	B LSI	24	1000
MCM6256 256K×1, 120 ns	3.0	6.0	27.2	9.0	30	0.35	C	NMOS DRAM	16	262144
F1600 64K×1 45ns SRAM	2.5	5.0	22.6	9.0	30	0.35	C	NMOS SRAM	22	65536
64K×1 120ns DRAM	1.3	2.5	10.9	9.0	30	0.30	C	NMOS DRAM	16	65536
8K×8 MOS PROM	0.6	0.9	3.6	9.0	30	0.30	C	NMOS ROM	28	65536
32K×8 MOS PROM	0.9	1.5	6.2	9.0	30	0.30	C	NMOS ROM	28	262144
74LS257 quad 3 bit mux	0.1	0.1	0.2	9.0	30	0.10	C	B SSI	16	15
74LS253 dual 4 bit mux	0.1	0.2	0.2	9.0	30	0.10	C	B SSI	16	16
74LS393 dual 4 bit counter	0.1	0.1	0.2	9.0	30	0.13	C	B SSI	14	34
74LS243 quad bus xcvr	0.1	0.1	0.2	9.0	30	0.27	C	B SSI	14	20
68174 VME arbiter	0.9	1.3	3.1	9.0	30	1.75	C	B LSI	20	2000
68172 VME bus controller	0.9	1.4	3.2	9.0	30	1.75	C	B LSI	28	2000
68153 VME Interrupter	1.0	1.5	3.3	9.0	30	1.75	C	B LSI	40	2000
68155 VME Interrupt Handler	1.0	1.5	3.3	9.0	30	1.75	C	B LSI	40	2000
MC74F2960 Err Detect & Corr	1.3	1.9	4.1	9.0	30	2.00	C	B LSI	48	2000
MC74F2968 Dyn. Mem. Ctrl	0.8	1.1	2.1	9.0	30	1.50	C	B LSI	48	1000
MC74F2969 EDAC Mem. Tim.	0.8	1.1	2.1	9.0	30	1.50	C	B LSI	48	1000
MC74F2961 EDAC Bus Buff.	0.8	1.1	2.1	9.0	30	1.50	C	B LSI	48	1000
Power Supply & Chassis	89.5	106.7	654.0	1.0	0	25.00	C	Misc.	0	1
MC1741/AD741 op amp	0.2	0.2	0.9	9.0	150	0.08	C	Linear	8	18
MC3512 12 bit, 200ns D/A	1.0	2.0	8.9	9.0	40	1.00	C	Linear	24	53
MC6890 8 bit, 100ns D/A	0.7	1.3	6.1	9.0	80	0.35	C	Linear	20	73
MC10317L 70ns, 7 bit A/D	5.4	12.8	69.4	9.0	50	0.60	C	Linear	24	1500
AD650 1MHz, 0.01% F/V	2.1	4.6	21.3	9.0	80	0.60	C	Linear	24	100
MC74LS686 8-Bit Comparator	0.2	0.3	0.4	9.0	30	0.40	C	B SSI	24	100
AD581 Voltage Ref.	0.5	0.7	2.7	9.0	30	0.25	C	Linear	24	100

and for exponential component reliabilities

$$R(t) = \prod_i e^{-\lambda_i t} = e^{-\lambda t} \quad \text{where} \quad \lambda = \sum_i \lambda_i \tag{5.13-3}$$

Thus the failure rate of a series exponential system is just the sum of its component failure rates and the *MTTF* of the system is the inverse of its failure rate.

For a parallel system, the probability of failure is the probability that all of the parallel components have failed. The probability of failure of component i is $1 - R_i(t)$. Thus the probability of failure of the system is $\prod_i (1 - R_i(t))$ and the reliability is

$$R(t) = 1 - \prod_i (1 - R_i(t)) \tag{5.13-4}$$

This expression does not have a simple form even if the component reliabilities are exponential, and the failure rate is not constant. Although *MTTF* can be misleading in such circumstances, it is often useful to estimate the *MTTF* of a system of n parallel components as

$$MTTF_{sys} = MTTF_{comp}/n \tag{5.13-5}$$

where $MTTF_{comp}$ is the average component *MTTF*.

Figure 5.13-6 shows the subsystems of an SSC instrumentation crate and their reliability relationship. There are five independent subsystems, Quench Protection, Beam Loss, Beam Position, Cryo/Vacuum, and Correction Dipole. Since these subsystems are independent, they are drawn in parallel. Quench Protection has its own microprocessor and network. Beam Loss, Beam Position, and Cryogenics share a microprocessor and network. Correction Dipoles have their own microprocessor but share one of the other networks. All of the subsystems share a common crate and power supply.

The numbers on Fig. 5.13-6 give the subsystem reliabilities, in failures per million hours of operation, computed using MIL-HDBK-217C for the initial design. For example, the reliability of the Quench Protection system is the sum of the QPM, Micro, Network, VME, Power Supply, and Chassis numbers or 215 failures per million hours of operation. Summing over all crates, this translates into a system wide QPM *MTTF* of 12 hours, well below the target of 336 hours. The next section describes the design modifications necessary to achieve a 336 hour *MTTF*.

Although there is a great deal of literature validating the use of MIL-HDBK-217C models for industrial and military systems, there is very little in the literature on their application to accelerator systems. Since the Tevatron controls are quite similar to the system modeled for SSC, the failure logs of five months of fixed target Tevatron running were analyzed. For the Tevatron QPM system, the model predicts an *MTTF* of 204 hours. The observed *MTTF* of the QPM from April through August, 1985, was 212 hours (17 failures). The model predicts 160 hours for the *MTTF* of the BPM/BLM. The observed *MTTF* of the BPM/BLM system was 144 hours (25 failures). The agreement between the model's predictions and the observed failure rates is remarkably good.

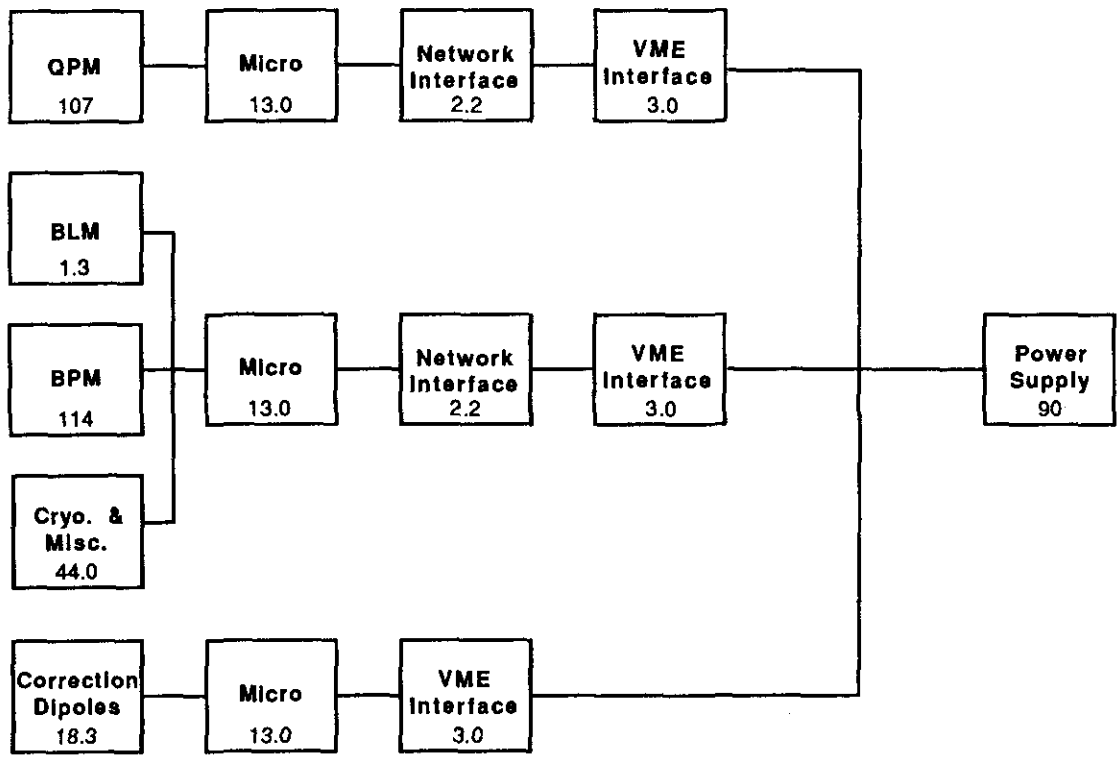

Figure 5.13-6. Reliability diagram for a complete tunnel interface crate. Numbers indicate subsystem failures per million hours of operation.

Design Refinement

The Table 5.13-9 summarizes the reliability of the initial and final SSC control system designs.

Table 5.13-9
Summary of the Reliability of the Initial and Final SSC Control System Designs

Subsystem	Initial λ (10^{-6} h^{-1})	Final λ (10^{-6} h^{-1})	Final *MTTF* (h)
Beam loss monitors	110	0.4	6,250
Beam position monitors	222	0.7	3,571
Cryogenics miscellaneous	152	0.4	6,250
Correction dipoles	130	0.4	6,250
Quench protection monitors	215	7.3	342

The Quench Protection system is the only SSC control subsystem that cannot tolerate a failure in any crate. The other subsystems bring the SSC down only if that subsystem fails in two adjacent crates simultaneously. Taking the worst of these subsystems, Beam Position Monitoring, the per-crate failure rate is 134 failures per 10^6 hours. If any two of the three adjacent BPM systems at some cell are working, that cell can be considered working. The effective failure rate λ_s for k out of n systems where each system has failure rate λ and the average repair time of $1/\mu$ hours is

$$\lambda_s \approx \frac{n!}{(k-1)!}\,\frac{\lambda^{n-k+1}}{\mu^{n-k}}$$

[5.13-3]. This approximation is valid for $\mu << \lambda$ and useful provided $\lambda_s << 3 \times 10^{-3}$ h^{-1} (inverse of 336 h operations cycle). We assume that all repairs in the tunnel will be effected by swapping modules. This implies that the repair times will be dominated by the travel time to the failure site. A conservative estimate for the mean repair time would be four hours (1.5 hour out, 1 hour to replace the board, 1.5 hour back). Thus, taking $k=2$, $n=3$, $\lambda = 114 \times 10^{-6}$ h^{-1} and $\mu = 1/4$ h^{-1} gives a $\lambda_s = 3.12 \times 10^{-7}$ h^{-1}. Thus the *MTTF* for all 400 crates would be 8013 hours or about 1 year (assuming, of course, that all failures are fixed during the four-day accelerator maintenance period). The component reliabilities of the final design give a total of 277 failures per 10^6 hours of operation per crate. For 400 crates, this would imply 37 failures in each 14-day running period. At four hours per repair, repairs would take 148 man-hours. Assuming three shift operation, it would take a staff of three people per shift to effect the necessary repairs in two days.

Although the QPM cannot use adjacent crates as backup systems, there is substantial redundancy within a single crate. Since the VME bus allows different modules in a crate to communicate, either of the other two microprocessors in the crate can run the QPM if the QPM microprocessor fails. Similarly, the other network can be used to communicate QPM

information if the QPM network fails. Figure 5.13-7 shows the QPM system including the redundant, parallel connections. Using an analysis similar to that used in the previous paragraph, it is clear that the microprocessor and network failure rates become negligible and the QPM reliability depends upon the front-end instrumentation reliability and the crate/power supply reliability. Since the crate power supply is a simple logic supply, the easiest way to improve its reliability is to use several power supplies connected by a diode network. With three power supplies, the power system reliability is essentially that of the diode network. For commercial diodes this would be on the order of 0.6 failures per 10^6 hours. MIL-SPEC diodes would give 0.06 failures per 10^6 hours. For all crates this would yield a power system *MTTF* of 33×10^5 hours or 3.8 years.

It is more difficult to add redundancy in the QPM front-end instrumentation but it is simple to use MIL-SPEC parts. Using all MIL-SPEC components, the QPM failure rate becomes 7.3 failures per 10^6 hours for a system wide *MTTF* of 342 hours (14 days). Although this meets the SSC availability criteria, we consider it marginal. Alternative QPM front-end designs that would increase the *MTTF* to a time comparable to the BPM (6 months) are being considered and look quite feasible.

Conclusions

A model of the failure rate of major elements of the SSC control system has been developed. When applied to the Tevatron control system, the model predicts failure rates within a few per cent of the observed rates. The model's predictions for the SSC are that there will be relatively few component failures (<50) during a two week SSC running period. Furthermore, the control system has been designed so that elements in adjacent crates or the same crate can absorb the work of a failed component in the event of a failure. This design also provides pathways that allow a failure to be unambiguously diagnosed so that repairs can be effected easily.

The model pointed up two subsystems that required special attention, the crate logic power system and the Quench Protection Monitor. Using a dual redundant power supply and reliable diode mixer, the crate power system achieves an order of magnitude better reliability than required. Using MIL-SPEC chips, the QPM will meet the required reliability and there appear to be alternative designs that would improve the QPM reliability by a further factor of five or ten.

5.14 Personnel Safety Interlock System and Communications

The safety interlock system described here covers only the safety aspects related to those hazards to accelerator personnel caused by radiation, high voltage, high current, and large amounts of stored electrical energy, in addition to possible suffocation hazards caused by the displacement of oxygen by other gases such as nitrogen and helium. Protection of equipment due to failure of electrical circuits, cryogenic facilities, radiation, and other causes are not discussed. General questions of radiation protection, shielding, and site safety are treated in Sections 3.5 and 6.9.

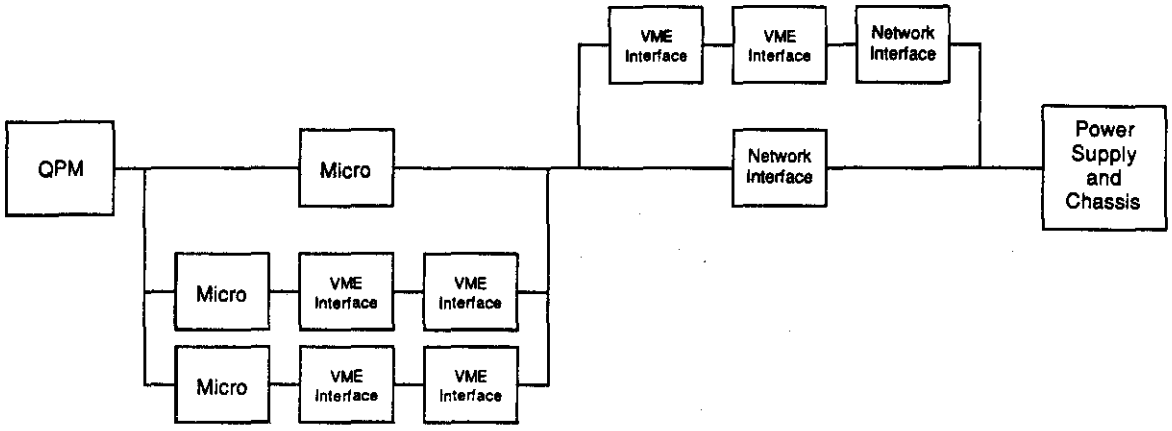

Figure 5.13-7. Quench protection monitor subsystem reliability diagram showing redundancy.

5.14.1 System Description

The personnel safety interlock system contains two continuous hard-wired channels to provide full redundancy. Either channel can fail without compromising the ability of the system to function safely. Every possible effort is made to make a fail-safe system.

The basic electrical and radiation safety system is controlled by two tone-loop channels. If the continuity of either channel should be broken by unauthorized access or failure to lock out a hazardous source, all hazardous equipment will be set to a safe condition with alarms activated in the main control room. In order to activate hazardous equipment, both tone loops must be uninterrupted and must be of the correct frequency and amplitude. One loop operates at about 4 kHz while the other operates at about 5 kHz. These frequencies are well above the 60 Hz power distribution range and well below any rf source so that it is difficult for a foreign signal to compromise the integrity of the system. In addition there are local tone links, configured like the main tone loops, which connect related equipment within a sector.

A "crash-off" system provides the means immediately to turn off hazardous equipment and, in the unlikely event that a person should be trapped inside the enclosure, to prevent beam injection. Crash-off boxes are located about 192 meters apart for this purpose.

To reset the personnel safety interlock system, reset boxes are strategically located within each sector and other enclosed areas. These boxes must be reset in a particular order, and in some cases within a certain period of time, to ensure that the area was searched in the proper order. Only then can local tone interrupt units be reset in order to provide a fail-safe system for search procedures.

Klaxtons are located around the tunnel at intervals of about 192 meters. These will signal an alarm before injection and a different alarm when an oxygen deficiency or fire is sensed.

5.14.2 Modes of Entry

Open Access Entry

In the open access mode keys are not required for entry nor is it necessary to log in or out. This mode applies to a long shut down under non-hazardous conditions when the heavy load of logging personnel in and out exceeds the effort to search the ring.

Controlled Entry

This mode of entry has two access levels. Level one restricts access to only those qualified personnel who are familiar with all equipment hazards. The equipment is in a de-energized state but can be reenergized. At level two the operation of any equipment is prevented and strict control over the personnel working in various parts of the ring is required. A log is kept of each location and time of entry and exit to account for all personnel. Film badges are a part of the badges used to access the ring so that complete records are available in the unlikely event of a radiation exposure.

Access to the ring is gained in the following manner. The employee goes to an entrance and puts his badge in a badge reader. The badge reader transmits the employee data to the main or sector control computer, which verifies the employee data and informs the main control room of the entry request. The main control room can verify by video

link the identity of the employee and then at its option instruct the control computer to release a key and log the relevant access information. If all hazardous equipment is locked out, an alternate form of access operation is to record only the employee information and, with main control room permission, release a key.

Restricted Access Entry

Entry under the restricted access condition is granted only when it has been determined by the appropriate authorities that access at a time when equipment is turned on should be granted. The system does not allow beam to be injected during such access.

No Access

When hazardous systems are on and there is beam or when hazardous systems could be turned on and beam injection started, access will not be allowed under any condition.

5.14.3 System Operation

Safety Interlocks

A block diagram of the tone-loop system is shown in Fig. 5.14-1. Only one of the two tone loops is shown. The following discussion applies to either of the two tone-loop systems.

The tone is broken by a device called a "Tone Interrupt Unit" which opens the input to the tone receiver and shorts the output of the tone transmitter. The tone is no longer received at the main control room tone receiver. This inhibits the tone generator located in the master reset unit and this in turn results in no tone in the rest of the ring. All remote tone receivers (remote from main control room) now remove permissive control from all hazardous equipment.

In the case of the Collider magnet power supplies, the firing pulses to the SCRs will be inhibited. SCRs connected across the output terminals of the power supplies will be discharged and the output current monitored. Only when output current is sensed will the power supply contactor be opened, thereby minimizing stress on the SCRs. Other systems are handled as required for the desired level of safety.

When the main control room tone receiver has no input of the correct amplitude and frequency it will remove the permissive control for beam injection and will abort any stored beam.

The oxygen deficiency hazard system is an "alarm only" system. Control units are placed in shelters at every entrance and the sensing heads are located in the refrigeration buildings and at 400 meter intervals in the tunnel. When a deficiency of oxygen is sensed, an alarm with appropriate coverage is activated. The output of the oxygen level detectors are connected to the control system computer loop and all oxygen levels are recorded so that any trend can be noted by an operator.

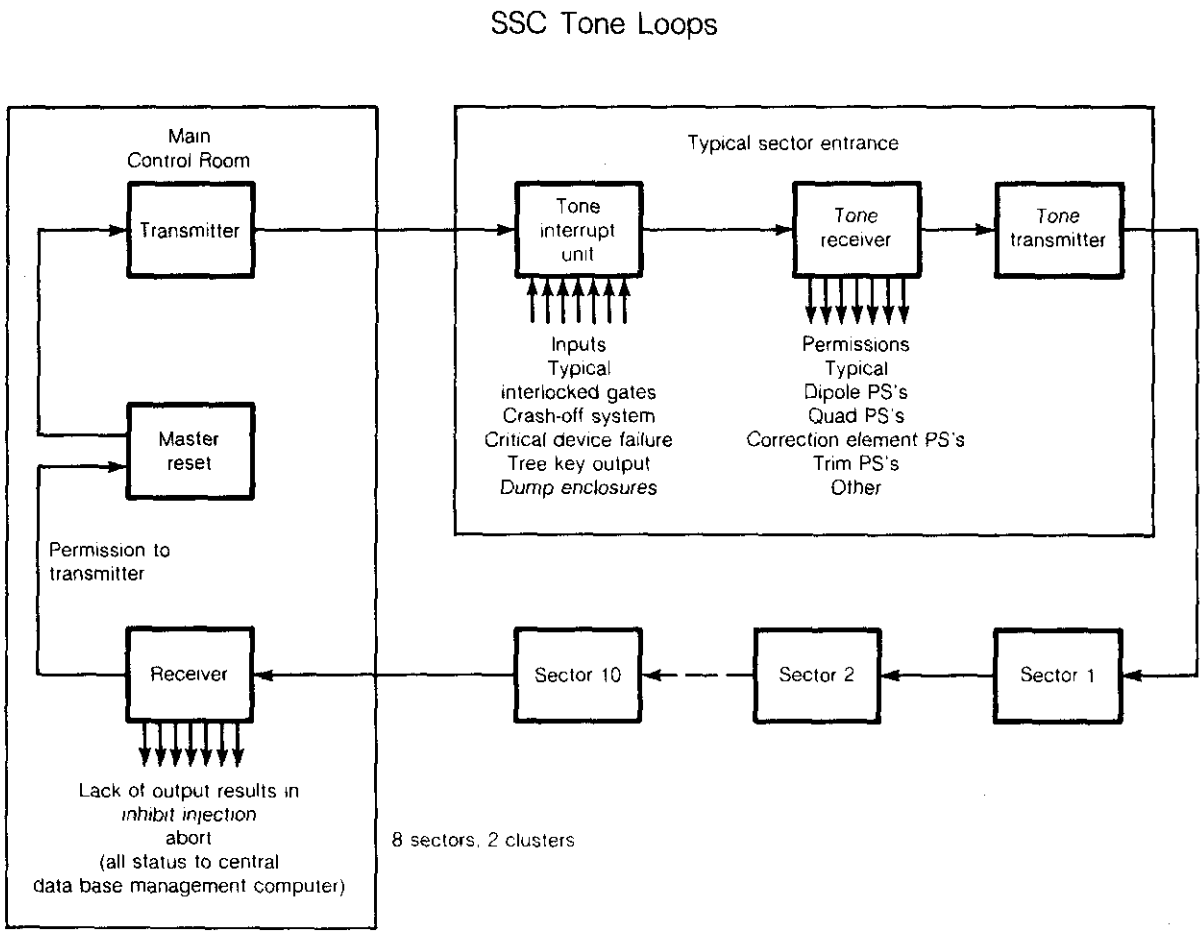

Figure 5.14-1. One of the two ringwide interlock loops. Each of the eight sectors and two clusters has its own loops that can be closed to permit local equipment to be operated even if the loops of other sectors are open. Beam is inhibited unless both loops of all of the sectors are interlocked.

Communications

The communications system is an important adjunct to the personnel safety interlock system. Audio and video loops provide multichannel communications networks through CATV modulators and demodulators that are placed at 192 meter intervals around the tunnel and at strategic locations in the refrigerator and other service buildings. Audio and video units can be plugged in as needed and portable receiver/transmitter units provide necessary communications with the main control room and between personnel engaged in service or repair.

5.15 Injector Complex

The SSC injector system design requirements have been described in Section 4.10. The details of the hardware are presented here with elements common to all the accelerators making up the injector grouped together. Descriptions of the linac, magnets, cryogenics, vacuum, power supplies, rf, beam transfers and aborts, diagnostics, controls, and test beams are included.

5.15.1 600 MeV H^- Linac

The designs of all components of the linac proposed for the SSC are based on those used in past or existing accelerator systems. While these components must be redesigned to be optimized for the SSC, their details and configurations are sufficiently close to permit their use for cost estimating purposes.

Ion Source

The H^- beam is created in an ion source, then formed into a laminar beam by an extractor, and matched to the input acceptance of the radio-frequency quadrupole (RFQ) with magnetic lenses. This assembly establishes the minimum beam emittance and determines the beam current.

A variety of ion sources are potential candidates for the SSC. The Dudnikov-type (Penning) ion source that is used on the Accelerator Test Stand (ATS) of the "White-Horse" program at Los Alamos [5.15-1] has the highest brightness of any known H^- source and has routinely performed at levels much higher than required by the SSC. It is the source chosen for the injector.

The SSC version of the Dudnikov source will deliver 13.8 mA of H^- particles at an energy of 50 keV and a normalized rms emittance of 0.08 mm-mrad. Permanent magnet quadrupoles match the beam to the input acceptance of the RFQ. Ion source operation at 50 kV dramatically simplifies the design, allowing the ion source and associated electronics to be enclosed in a small housing within a single equipment cabinet, as was done for the PIGMI program at Los Alamos. The equipment cabinet is a standard electronics rack ($0.6 \times 1 \times 2$ m high) that is mounted on casters and contains the high voltage power supplies, vacuum pumps, gas bottle, cooling system, and the electronic control modules. The ion source electronic equipment operates at 50 kV and is located on a high voltage deck situated within the cabinet. The necessary electrical operating power is supplied by a small 1 kVA isolation transformer. The hydrogen gas flow and water cooling are provided from ground potential through nonconducting tubes. Local control of the equipment on the high

voltage deck is provided through nonconducting rods extending in from the cabinet face. Remote control and monitoring are provided through a fiber optics link to a microprocessor-based system located at ground potential. A vacuum valve permits an ion source to be changed without letting the accelerator structure up to air.

A second complete and identical ion source system is required for operational backup. A short diagnostic beam line is provided for source testing. Both systems occupy the same room, which may be manned during operation if a shield wall is installed at a convenient location along the low energy portion of the linac. A room of 4 × 5 meters provided with ready equipment access is required.

RFQ and Chopper

The RFQ structure, based on the concepts of Kapchinskii and Teplyakov [5.15-2], is a relatively new structure that is an ideal first accelerator for a linac chain because it can accept a high current, low velocity, dc beam, bunch it with high efficiency, and accelerate it to a velocity suitable for injection into a drift tube linac. RFQ accelerators have been built by the Los Alamos, Lawrence, and Brookhaven National Laboratories in the USA, by the Institute for Nuclear Studies and the National High Energy Physics Laboratory KEK in Japan, AECL in Canada, and by Saclay, GSI, and the University of Frankfurt in Europe.

An RFQ accelerator consists of four symmetrically located vanes (rods) supported by spiral mounts, as shown in Fig. 5.15-1. The vane tips approach each other rather closely and define a channel along the pipe centerline through which the beam travels. The vane tips are machined with a precise wavy shape which, when the pipe is excited properly with rf power, establish electric fields that confine, bunch, and accelerate the beam.

The major cost item is machining the vanes. The options available for vane mounting and cooling, rf feed, and field stabilization, all cost essentially the same. The estimate is based on cost experience with the ATS RFQ in the White Horse Program and the spiral mounted vane RFQ cold model developed in the Heavy Ion Fusion program at Los Alamos. Table 5.15-1 lists the RFQ specifications.

The full width of the output beam longitudinal bucket is 25 degrees at 49.5 MHz, which represents 225 degrees of one out of each nine cycles of the DTL frequency of 445.2 MHz.

To fill two adjacent DTL buckets and leave the next seven empty requires lengthening the pulse from the RFQ to 540 degrees (at 445.2 MHz). This is done by utilizing two 49.5 MHz cavities at the output of the RFQ. The first cavity creates a correlation between phase and energy that allows the beam to debunch rapidly in the following drift space. The second cavity lays the ellipse horizontally over 450 degrees of the $\delta\Phi$ axis. A beam chopper is intertwined amongst the cavities and focusing elements between the RFQ and DTL to remove every-other, two-out-of-three, etc., bunches to provide multiples of 4.8 m bunch spacing in the SSC main ring, if desired.

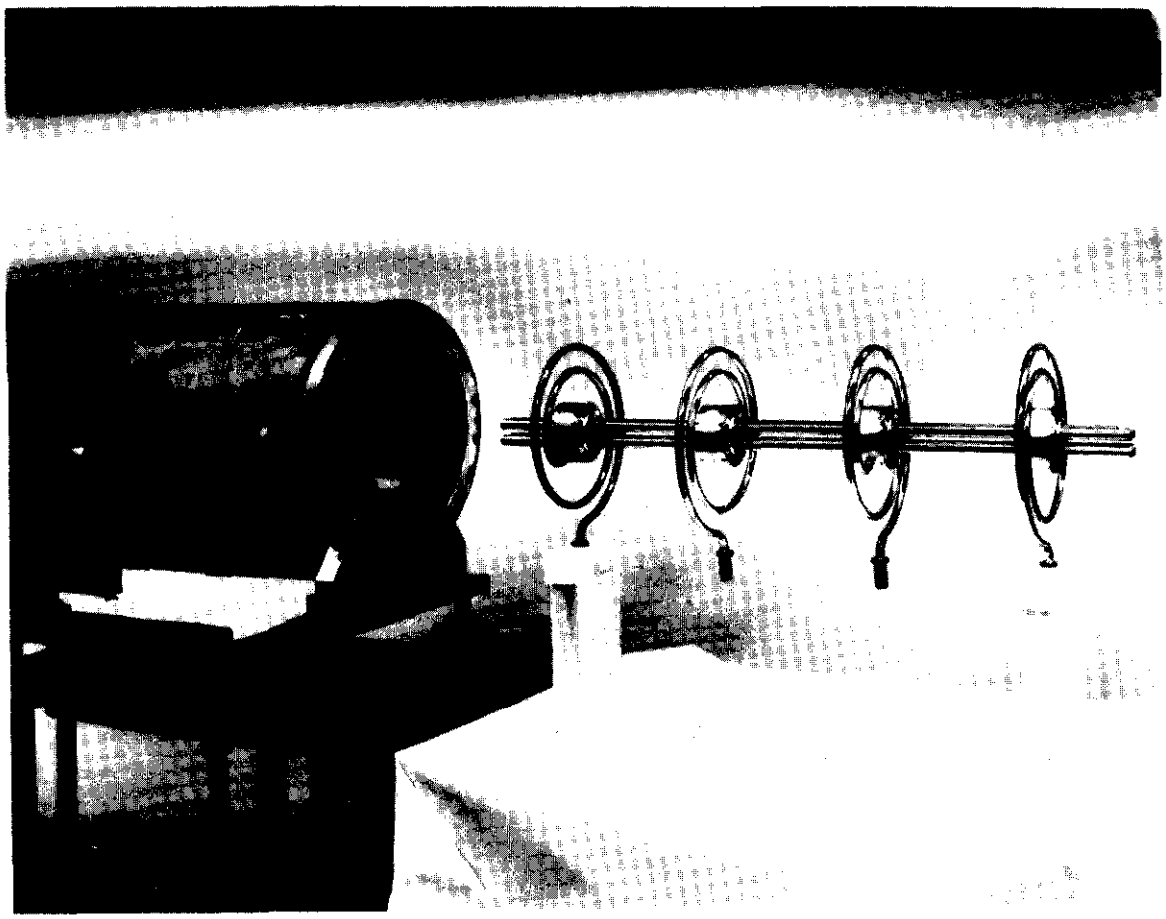

Figure 5.15-1. RFQ structure with spiral-mounted vanes (developed in the Los Alamos heavy ion fusion program).

Table 5.15-1
RFQ Specifications

Energy range (MeV)	0.05–2.5
rf frequency (MHz)	49.5
Power lost in copper (MW)	0.2
Maximum power to beam (MW)	0.04
ac to rf efficiency (%)	45
ac power for rf (kW)	0.39
Number of tanks	1
Total tank length (m)	3.0
Output beam current (mA)	13.0
Output beam emittance	
Normalized transverse (mm-mrad)	0.44
Longitudinal (rms) (MeV deg)	0.50

Drift Tube Linac

The drift tube linac is essentially identical in design to the one recently completed for the ATS at Los Alamos. Since the RFQ provides 2.5 MeV particles and permanent magnet quadrupoles are used in each drift tube, the drift tubes at the low energy end of the drift tube linac (DTL) do not present the spatial design problem traditionally experienced with this type of structure. The particles have sufficient velocity that it is relatively easy to incorporate the necessary focusing quadrupole magnet in the front end drift tubes, even at the 445.2 MHz frequency. The DTL will be contained in six tanks, each powered by a single klystron. Isolation valves, steering magnets, and beam diagnostic stations are placed between the tanks.

For reasons of alignment precision and ease of maintenance, girder-mounted drift tubes are selected over tank wall mounting. This method provides the option of installing the tanks with prealigned girders as subassemblies. If an alignment or drift tube problem arises, the entire girder is removed so that the drift tubes can be easily aligned relative to their nearest neighbors. The girder can be mounted either on the top or the bottom of the tank. Top mounting provides easier removal, permits prealigning the tanks, and ensures alignment of the drift tubes with the tank end walls. Aligning the drift tube girders with respect to each other is easier with bottom mounted girders, as they would be mounted on a common beam. The costs are the same in either case, so the actual method can be based upon experience gleaned from the stable of "White-Horse" Program DTLs which will use both methods.

The rf power requirements of the DTL are so low that rf heating cannot be used for controlling the temperature, and thus the dimensions, and thus the resonant frequency of

the structure. The "cooling" system in this case actually helps the rf to elevate the temperature of the structure enough above ambient to provide a measure of control. The drift tube linac specifications are listed in Table 5.15-2.

Table 5.15-2
Drift Tube Linac Specifications

Energy range (MeV)	2.5–125
rf frequency (MHz)	445.2
Klystron turn-on time (μs)	8
Tank rf fill time (μs)	50
Total HV on time (μs)	79
Power lost in copper (MW)	10.4
Maximum power to beam (MW)	0.48
ac to rf efficiency (%)	45
ac power for rf (kW)	27
Number of tanks/Number of klystrons	6/6
Total length of tanks (m)	39.8
Accelerating gradient (MV/m)	4.52
Number of drift tubes	200
Beam capture (%)	30
Transmission of captured beam (%)	100
Output beam emittance	
Normalized transverse (mm-mrad)	0.45
Longitudinal (rms) (MeV deg)	2.0

Side Coupled Linac

The side coupled linac (SCL) is based upon the structure developed for LAMPF and copied for literally hundreds of other accelerators. This structure is used in essentially all commercially built x-ray machines over 100 keV that are used for radiography and medical therapy. A typical example is shown in Fig. 5.15-2. The dimensions are almost identical to those of the free electron laser accelerator at Los Alamos. The fabrication technique proposed is that used by Los Alamos for the electron microtron accelerators built for the National Bureau of Standards and the University of Illinois. This technique involves fabricating the structure in half-cells, i.e., a forged oxygen-free high-purity copper disk has one half of the accelerating cell machined into one side and one half of the coupling cell

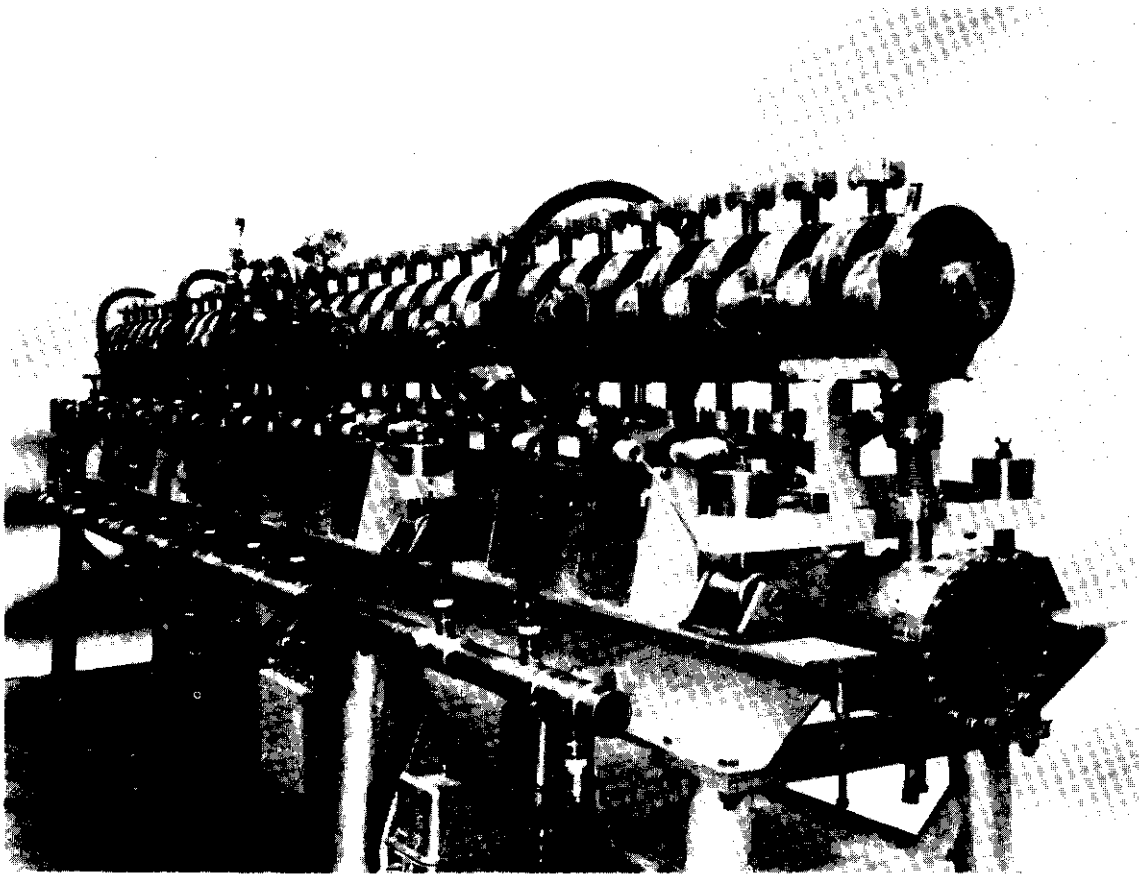

Figure 5.15-2. Typical side-coupled linac.

machined into the other. The two cells are deep enough into the billet faces that they intersect, forming the slot through which rf power flows. Cooling passages, keying, and vacuum ports are also machined in the faces. Most of the forming is done on a numerically controlled milling machine and, with the proper jigging and tooling, is accomplished in only minutes per billet. This technique reduces the total number of pieces that must be made and the number of brazes that must be done; it also reduces the amount of inspection, cleaning, furnace stacking, and leak checking required. The structure might weigh more since the excess copper is usually not all machined away as it has been when utilizing the LAMPF SCL assembly technique.

Eleven accelerating cells, with their ten intermediate coupling cells, are brazed together into a cluster. A permanent magnet quadrupole is inserted into the ends of the cluster and other clusters are bolted on, thereby building up a module, which is powered by one klystron. The vacuum pumpout tube extending from every other coupling cell is welded to a vacuum manifold that runs the length of each module. The vacuum pumps hang from this manifold pipe. The space between modules is occupied by a vacuum valve, a pair of steering magnets, and a diagnostics station.

The SCL "cooling" system functions in the same frequency controlling fashion as that for the DTL. Important parameters for the side coupled linac are called out in Table 5.15-3.

Radio-Frequency Power Systems

The RFQ and beam shaping cavities require one 49.5 MHz rf system. The DTL requires six 445.2 MHz rf systems. Seven of the 445.2 MHz systems will be installed, with the seventh serving as a test stand and spare. A minimum of eight 445.2 MHz klystrons will be procured.

The SCL requires six L-5081, 1336 MHz klystrons. Seven 1336 MHz systems will be installed and a minimum of eight klystrons procured. The seventh system will serve as a test stand. Both test stands are provided with water cooled dummy loads to permit full power tube testing and conditioning.

The klystrons are sized to provide approximately 17% more power than required when accelerating the beam. This extra capacity is required to provide overdrive to excite rapidly the structures to their proper level and to provide a margin of power for control purposes.

Pulse forming networks are utilized to hold the high voltage pulse to the klystrons up for the approximately 100 μs required of the rf systems. A modular arrangement, which includes the klystron, waveguide, modulator tank, pulse forming network, high voltage filter, ac to dc HV power supply and control chassis, is used for each rf system. These modules have a footprint of 3×7 m for the 445.21 MHz systems and 1.5×12 m for the 1336 MHz system. The floor space must be doubled over these equipment footprint sizes to provide code mandated clearances for maintenance and to allow for equipment changes. The traditional arrangement is to provide a basic weatherproof building located above the accelerator structure and site the klystrons directly over the tanks and modules they serve. The waveguides pass from the klystrons downward through pipes embedded in the tunnel backfill to the accelerator. The 445.2 MHz klystrons require a 5 m ceiling height, while the 1336 MHz klystrons require 3.7 m.

Table 5.15-3
Side Coupled Linac Specifications

Energy range (MeV)	125–600
rf frequency (MHz)	1336
Klystron turn on time (μs)	6
Module fill time (μs)	30
Total HV on time (μs)	57
Power lost in copper (MW)	104
Maximum power to beam (MW)	1.8
ac to rf efficiency (%)	31.5
ac power for rf (kW)	295
Number of modules/Number of klystrons	6/6
Total length of modules (m)	75.0
Accelerating gradient (MV/m)	9
Number of cells	913
Focusing quadrupoles	
Placement	1 every 11 cells
Length (cm)	5.08
Gradient (T/m)	60
Beam transmission (%)	100
Output beam emittance	
Normalized transverse (mm-mrad)	0.45
Longitudinal (rms) (MeV deg)	5.9

Transfer Line

Figure 5.15-3 shows the transfer line between the linac and the Low Energy Booster (LEB). The transfer line forms a spectrometer, which, when used with strippers removes any beam halo and off-momentum tails. The quadrupole magnets have a 15 cm bore and the dipole bore is 7.5 cm high by 15 cm wide. A 22.5 degree bend module that is 20 m long, consisting of five quadrupole focusing magnets and two dipole benders, is utilized. The dipoles are two meters long and have 0.46 T fields. Space is provided to add two more of these dipoles between the existing ones so that, by reducing their fields to 0.32 T, this line will transport a 1 GeV beam through the existing components. Four of the 22.5 degree bend modules are used to provide a 90 degree bend for injection tangentially into the LEB.

The transfer line is heavily instrumented to provide complete tailoring and characterization of the beam. Instruments include six current monitors, 14 centroid monitors, 11 profile monitors, and two streak cameras. Five 4-jaw strippers are used to shape the beam, and they require three beam dumps to dispose of the discarded particles. The third beam dump also is used to absorb the total beam when the linac is being tuned up. A beam plug reduces the chances of unwanted beam going beyond the linac during tune up. A debuncher cavity is placed centrally in the transfer line for beam shape control.

Instrumentation, Control, and Safety Systems

The linac instrumentation, control, and safety systems are an integral part of the whole SSC control system. Distributed control modules monitor the outputs of the various components and compare these with the desired set points that reside in computer memory. Most components are capable of being driven by the computer to new positions.

A fast protect system prevents beam from being started down the accelerator, or shuts it off, if conditions are not right for the beam to be properly handled. That is, the rf systems must have the proper fields established in the tanks and all magnets must be at the proper settings. Beam spill monitors trip the fast protect system if their setpoints are exceeded.

A personnel protection system provides barriers, visual indicators, access restriction keying, and manually operated "scram" switches to reduce the probability of accidentally operating the machine with personnel in dangerous locations. Electrical gear will incorporate the normal protective devices mandated by code, as well as power interrupting interlocks used with experimental equipment having dangerous levels of electrical energy.

5.15.2 Magnets

The three circular accelerators in the injector string have in common the need for dipole magnetic fields for bending the protons, quadrupole magnetic fields for focusing, and sextupole magnets for correcting chromaticity. The LEB and Medium Energy Booster (MEB) magnets utilize copper coils and iron yokes, while the High Energy Booster (HEB) requires superconducting magnets. Special magnets, such as kickers, septa, and correction elements are also needed. These magnets are not described here as they are virtually identical to the magnets of this type presently in use at Fermilab. The beam transfer lines between the LEB and MEB, and between the MEB and HEB, use LEB style and MEB style magnets respectively. Magnets used in the HEB to SSC line are described in Section 5.9.

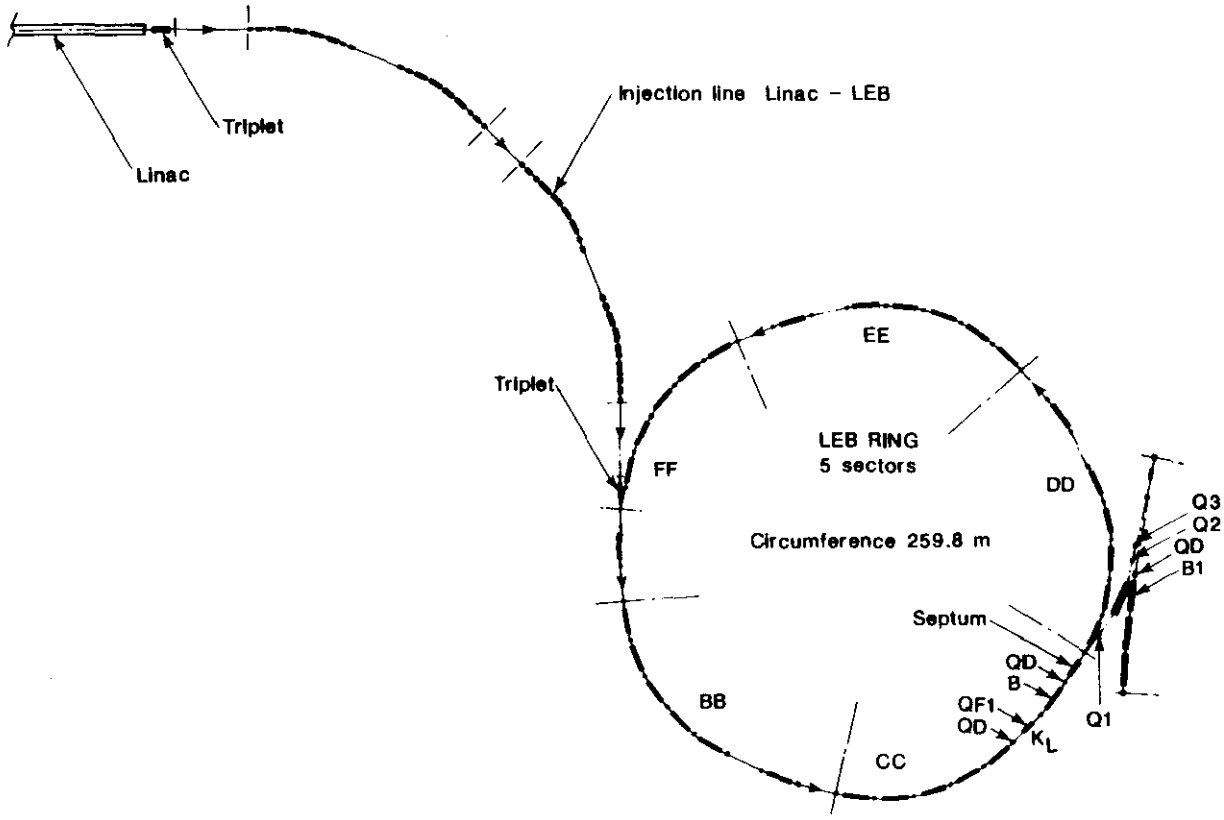

Figure 5.15-3. H^- transport line between the Linac and the Low Energy Booster, the LEB layout, and also the LEB to MEB transfer line..

LEB Magnets

The LEB uses conventional iron core magnets. In order to minimize core losses while cycling at 10 Hz, laminations are made of 0.635 mm (25 mil) thick M-22 steel. In order to avoid saturation effects during acceleration, the peak fields in the magnets are kept low — 1.24 T in the dipole and 0.64 T at the quadrupole pole tip. Cross sections of the dipole and quadrupole are given in Fig. 5.15-4. The fundamental properties of the magnets are described in Table 5.15-4.

Medium Energy Booster Magnets

The MEB also utilizes conventional steel core, copper conductor magnets. Since the cycle time is relatively long it is not necessary to go to the trouble of using very thin laminations. Laminations of thickness 3.2 mm (0.125 in.) will be used. The dipoles are run with a peak excitation of 1.8 tesla.

The properties of the MEB magnets are shown in Table 5.15-5. Cross sections of the dipole and quadrupole magnets are given in Fig. 5.15-5. The horizontal aperture of the magnets is large because of the need to provide a momentum aperture of $\pm 0.3\%$ in the presence of a large dispersion (see Section 4.10.4).

Table 5.15-4
LEB Magnet Parameters

	Dipole	Quadrupole	Sextupole
Strength	1.24 T	18.4 T/m	28.0 T/m^2
Length	4.5 m	0.3 m	0.2 m
Full Aperture	4.0 × 5.0 cm^2	7.0 cm	7.0 cm
Turns/Pole	28	14	8
Maximum Current	705 A	604 A	20 A
Coil Resistance	0.11 Ω	0.014 Ω	0.050 Ω
Coil Inductance	62 mH	1 mH	0.2 mH
Peak Power	54 kW	5 kW	20 W
Average Power	19 kW	2 kW	7 W
Water Cooled	Yes	Yes	No
Number Required	30	40	10

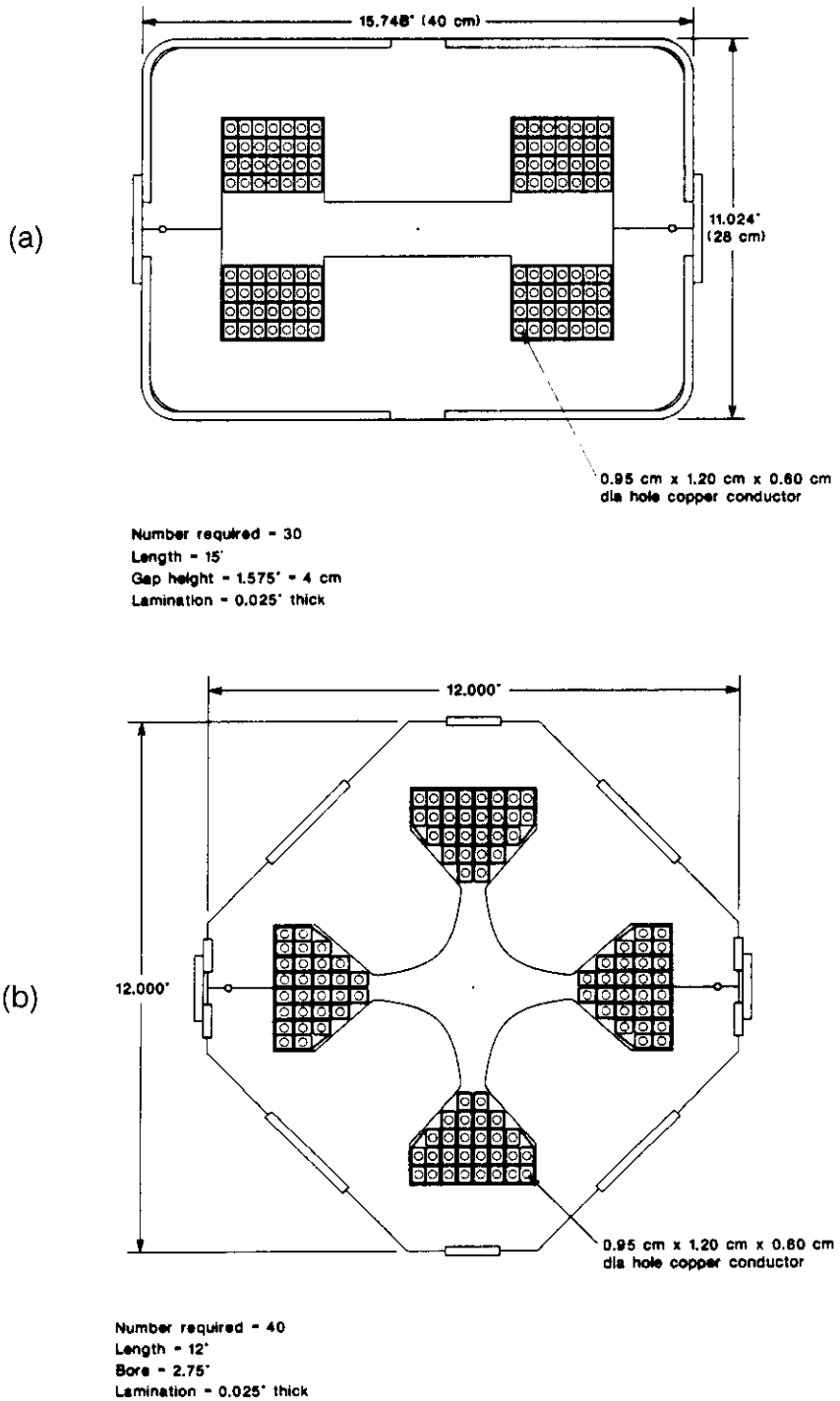

Figure 5.15-4. Cross-sectional view of a) the dipole, and b) the quadrupole magnet used in the LEB.

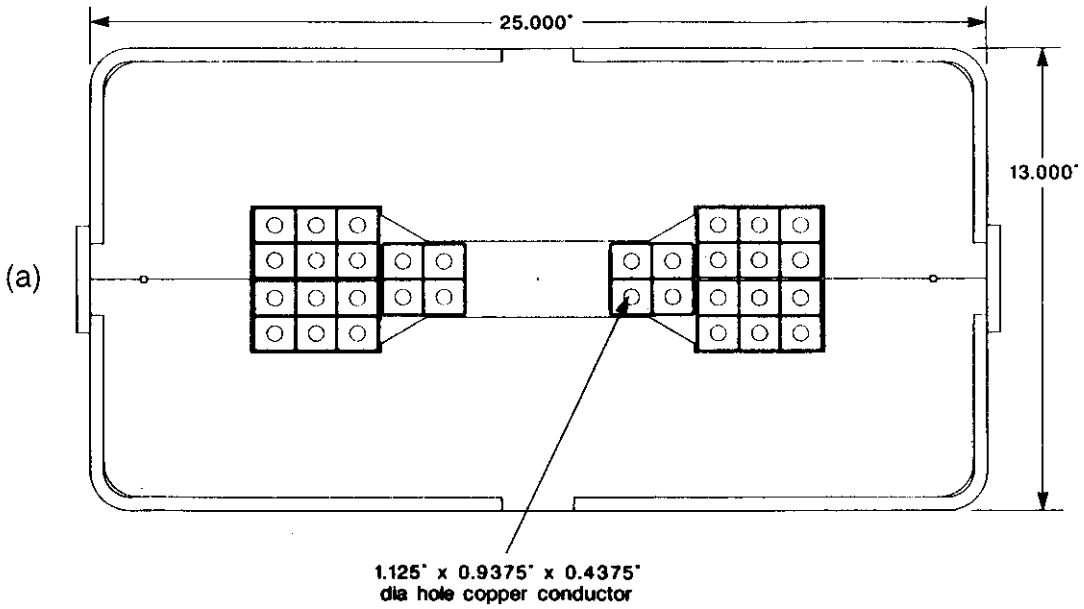

Number required = 216
Length = 18'
Gap height = 2.000"
Lamination = 0.125" thick

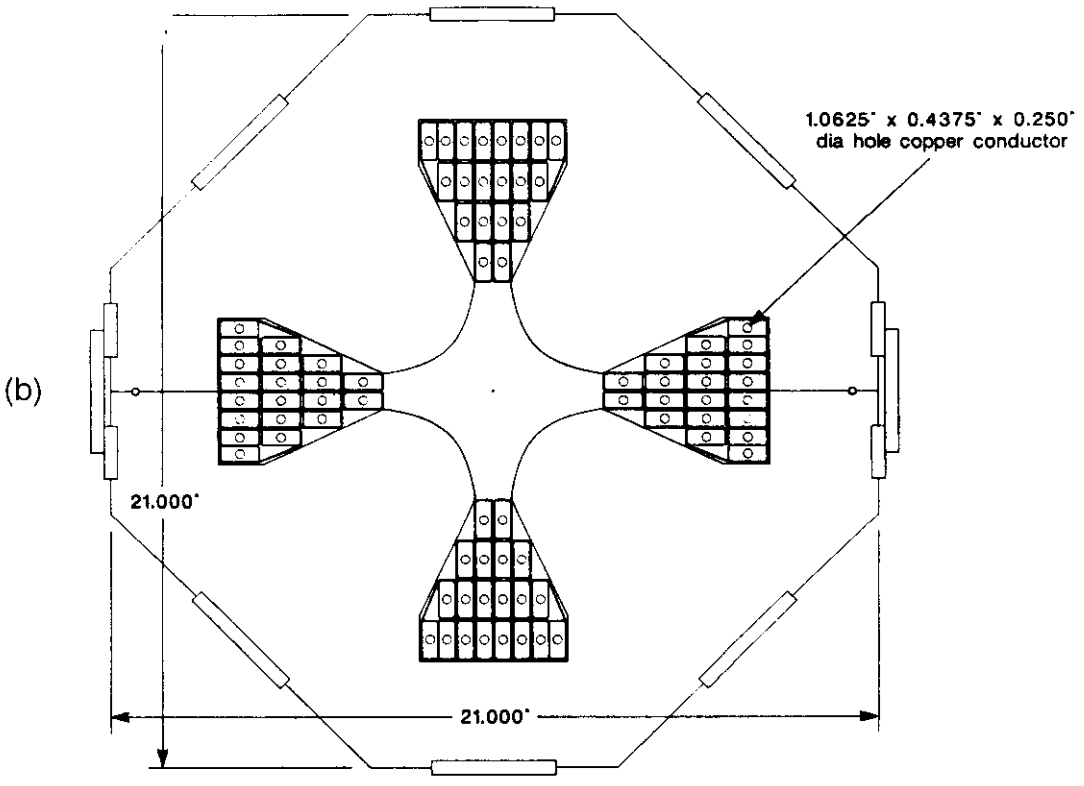

Number required = 96
Length = 30"
Bore = 3.5"
Lamination = 0.125" thick

Figure 5.15-5. Cross-sectional view of a) the dipole, and b) the quadrupole magnet used in the MEB.

Table 5.15-5
MEB Magnet Parameters

	Dipole	Quadrupole	Sextupole
Strength	1.80 T	22.8 T/m	22.0 T/m^2
Length	5.4 m	0.75 m	0.2 m
Full Aperture	10.0×5.0 cm^2	8.4 cm	8.4 cm
Turns/Pole	8	10	10
Maximum Current	4550 A	1756 A	25 A
Coil Resistance	0.006 Ω	0.007 Ω	0.03 Ω
Coil Inductance	3.5 mH	0.6 mH	0.23 mH
Peak Power	118 kW	21 kW	0.02 kW
Average Power	39 kW	7.1 kW	0.008 kW
Water Cooled	Yes	Yes	No
Number Required	216	96	72

High Energy Booster Magnets

The HEB magnets use superconducting wire and are based on a cosine theta design. Parameters for the 5 cm aperture, 7 m long dipole, are given in Table 5.15-6 and the single-phase cross section is shown in Fig. 4.10-6.

The conductor is the same as used in the magnets for the SSC collider rings. The HEB dipole design has 20 inner and 19 outer turns with two copper wedges in the inner and one in the outer for field shaping. Off-centering of the collared coil in the iron has been assumed to allow the cancellation of quadrupole moments that are built into the magnet. A similar procedure was employed in the Tevatron dipole and is also being used in HERA dipoles and SSC prototypes.

The collars surrounding the coil are stainless steel, 1.5 cm thick radially. This provides adequate restraint for the coil and insures survival of the collars under the fatigue stress associated with pulsing the machine during filling of the SSC, or when the HEB is used to provide test beams.

The iron around the collars contributes 24% of the dipole field and its outer diameter is 26.7 cm (10.5 in.), the same dimension as for the SSC design iron. The saturation effects on multipoles are expected to be small; about one unit (at a reference radius of 1 cm) change is expected for b_2 between injection and high field.

Table 5.15-6
HEB Dipole Magnet Parameters

Central field	5.67 T
Nominal central field (without iron yoke)	4.33 T
High field in winding (with yoke)	6.00 T
Nominal current	5614 A
Number of turns	78
Inner coil diameter	0.050 m
Inside yoke diameter	0.122 m
Outside yoke diameter	0.267 m
Magnet length (effective)	7.0 m
Inductance (per dipole)	27 mH
Stored energy at B_{max}	0.43 MJ
Superconducting strand diameter (inner/outer) (with Ebanol)	0.808 mm/0.648 mm
Number of strands in cable (inner/outer)	23/30
Cable dimensions (inner) (outer)	$1.45/1.75 \times 10.63$ mm^2 $1.21/1.421 \times 10.06$ mm^2
Cu/SC ratio (inner/outer)	Cu/SC 1.3:1/1.8:1

The effects of persistent currents on the multipoles are expected to be small enough to make full length correction coils inside the magnet unnecessary.

Energy loss per cycle is an important consideration. Five sources of heat are superconductor hysteresis, eddy current losses in the copper matrix surrounding the NbTi, hysteresis and eddy current losses in the iron, eddy current losses in the copper wedges used for field shaping, and eddy current losses in the beam pipe. The superconductor losses are about 440 J/cycle (dB/dt = 0.2 T/s and filament diameter = 5 μm), and iron and beam pipe losses are 300 J/cycle to make 0.74 kJ/cycle per magnet for the total loss. A 60 second cycle is assumed. The implications of this heat load in terms of cryostat design and the operating temperature of the magnet are discussed in the following subsection.

The standard quadrupole magnet is simply a scaled version of the SSC quadrupole with a 5 cm coil aperture. The increased aperture results in a smaller gradient — the quadrupole has a gradient of 144 T/m and a length of 1.0 m. The 36 special quadrupoles required in the straight sections require a coil aperture of about 7 cm. Detailed designs of these magnets do not exist. The costs have been estimated by scaling from the HEB dipole.

5.15.3 Cryogenics

Introduction

The HEB helium refrigeration system has the same capacity as the ten other collider refrigerators. In addition, a transient response capability has been added in order to increase the peak capacity by a factor of three for a period of three hours. A 30,000 gal helium dewar is used to store excess helium gas and less dense liquid helium during the 60 s cycle time used during filling of the collider rings. After filling the HEB cycle time must be increased to 5 min (e.g., for operation of the test beams) and the majority of the refrigeration capacity is used to return the dewar and the ring to its initial condition. Thermal equilibrium is maintained in the HEB with a cycle time of 3 minutes. A schematic diagram of the refrigeration system is given in Fig. 5.15-6.

The refrigerator is located at straight section NN (Fig. 4.10-1) opposite the extraction straight section RR. At RR the single HEB ring is cross-connected into the collider rings, for redundancy and liquid nitrogen supply.

Magnet Cryogenics

Figure 5.15-7 shows the HEB superconducting dipole magnet cross section, including the dewar and piping. The iron has the same outside diameter as the collider ring magnet, and it is located in an almost standard cryostat. The coil diameter is 5 cm, while the bore tube is the same as the collider magnets. This permits the single-phase liquid helium supply to be in good contact with the coils; the coil flow being 60 g/s compared to 1 g/s in the collider ring magnets.

The magnet cryogenic system is similar to that used in the collider ring. Both the 80 K and 20 K shield use the same pipe sizes. The HEB magnets form a single 6.0 km loop. Liquid nitrogen is drawn from the 80 K shield of the main ring.

The liquid inventory has been reduced by incorporating a small bellows to interconnect the magnet iron; this permitted larger return pipes in order to reduce pressure drops. The liquid return pipe has an inner diameter of 7 cm versus 4 cm in the collider ring magnets. The gas return has an inner diameter of 10 cm compared to 7 cm in the collider magnets.

Transient Response System

The transient response system has to meet two major requirements:

(1) It must deal with the 5% helium mass change in the single-phase coil chamber as the helium warms from 4.4 to 4.8 K. Approximately 2000 liters of liquid is generated. Assuming this occurs over 10 min, we get a return flow of 400 g/s.

(2) During the 45 min of fast ramping, the transient response system must triple the 5 K refrigerator output.

The concept is to use a dewar to store excess helium gas and less dense liquid. The dewar gas return flow is controlled to keep the refrigerator operating at optimum. At the start of the fast ramping the compressors and turbine are adjusted for full capacity. After about three hours they are reduced to 70% of full capacity. The dewar is sized for three beam filling cycles, in case problems cause beam aborts.

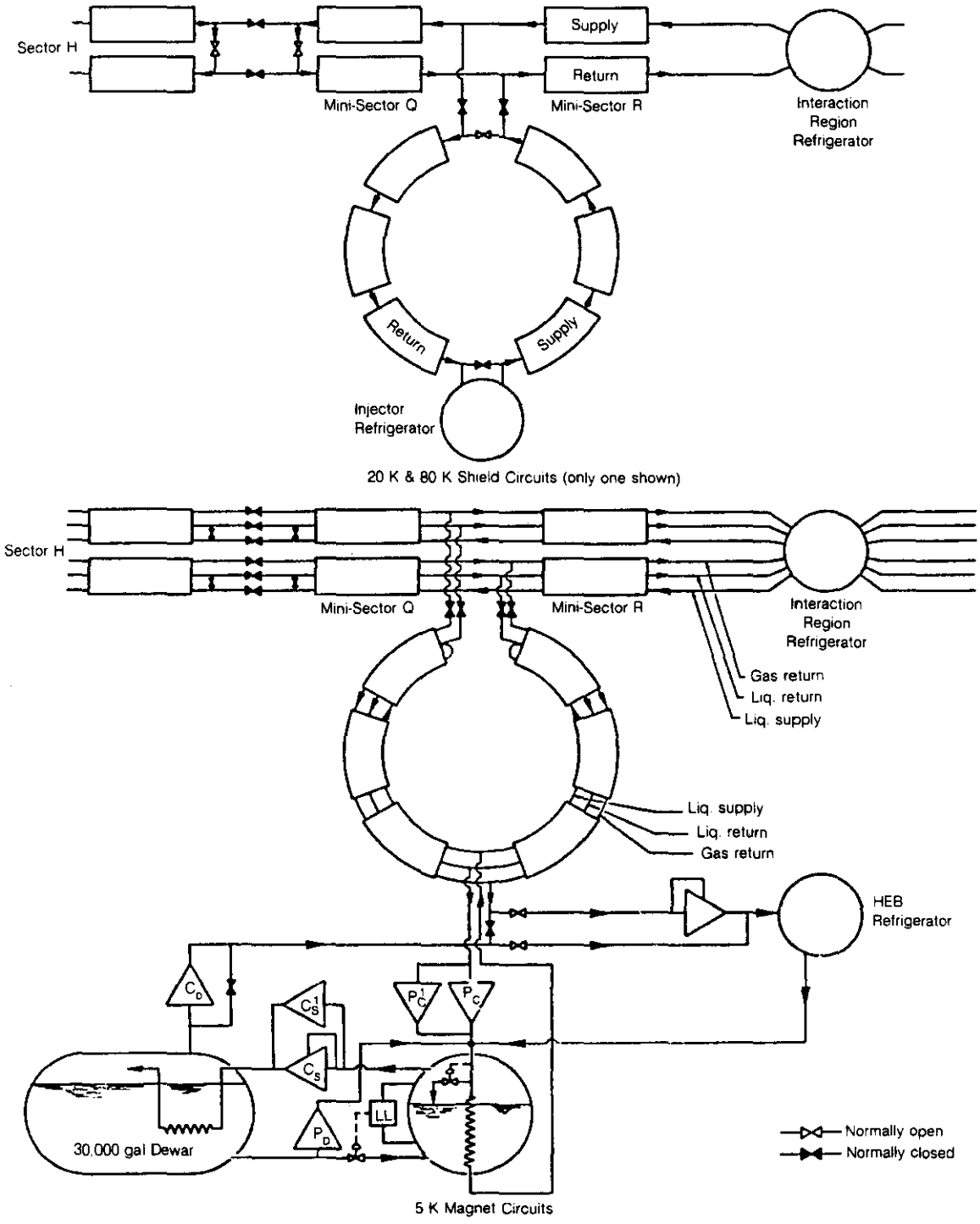

Figure 5.15-6. The HEB refrigeration system. The 30,000 gallon dewar at the lower left is the heart of the transient response system.

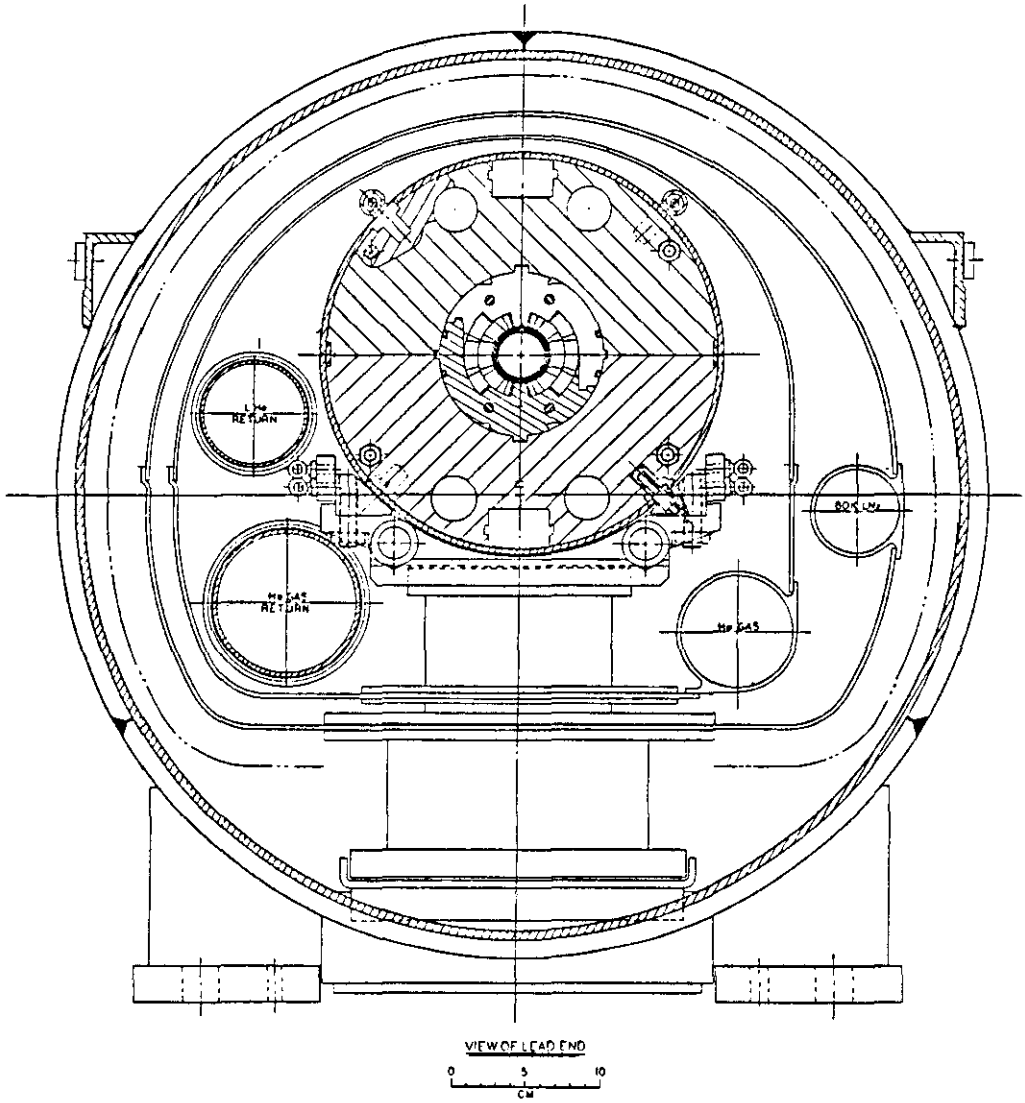

Figure 5.15-7. Cross-sectional view of the HEB dipole magnet and cryostat.

Refrigerator

The HEB refrigerator is similar to the 10 units deployed around the collider rings. In addition 5 K pumps and compressors have been added. The refrigerator is discussed in detail in Section 5.3. The (budgeted) heat loads are given in Table 5.15-7 for operation on a 3 minute cycle. As described above, operation on a sixty second cycle generates a higher ramp load which is handled by the transient response system.

Table 5.15-7
Budgeted Heat Loads for HEB (in watts)

	Liquid	5 K	20 K	84 K
528 dipoles	—	106 W	528 W	5280 W
150 normal quadrupoles	—	23	120	1200
36 special quadrupoles	—	5	29	288
174 spool pieces	130 liters/h	217	348	2958
6 short spool pieces	5	8	9	72
6 80 m bypasses	—	6	42	336
12 15 m bypasses		12	72	192
36 7.5 m bypasses	—	36	180	396
60 7.5 m spacers	—	6	60	600
12 1 m spacers	—	1	3	24
6 end boxes	140 + 12	180	120	360
Miscellaneous	—	120	20	50
Splices	—	10	—	—
Synchrotron radiation	—	0	—	—
Ramp load	—	2328	—	—
TOTAL	287 liters/h	3058 W	1531 W	11755 W
Collider ring load	360 liters/h	3200 W	4810 W	38800 W
Refrigerator capacity	620 liters/h	4700 W	7200 W	NA

5.15.4 Vacuum Systems

Low Energy Booster

Vacuum Chamber

The Low Energy Booster (LEB) cycles at 10 hertz. The vacuum chamber has to meet two electrical requirements: (1) the resistivity must be high enough to keep eddy current effects from affecting the beam, (2) the walls must be sufficiently conductive to transport the beam image currents smoothly and to contain the bunch wake fields. Existing rapid cycling machines have used a variety of solutions, such as coated ceramic pipes, rib-reinforced thin wall chambers, and chamberless magnets totally inside a vacuum enclosure. Recent advances in plastic-fiber composite materials provide the opportunity for another solution, which offers freedom in the choice of resistivity, good vacuum properties, and, potentially low cost. The proposed vacuum chamber is constructed similarly to chambers pioneered by CERN (UA1). It is constructed by wrapping a thin metal foil (stainless steel in this case) around a mandrel of appropriate cross section. The foil also overlaps a thin section of the two end flanges. The foil is wound with carbon-fiber-epoxy material and cured into a single, strong assembly. Figure 5.15-8 shows the proposed vacuum chamber in a cut-away isometric view.

Resistivity Value and Wall Thickness

If we define r to be the horizontal distance from the beam center line, we can write the induced eddy current during the LEB ramp as $\Delta I = \dot{B} t r \Delta w / \rho$, where ΔI is the current carried in a strip of foil of width Δw, t is the foil thickness and ρ the resistivity. A reasonable solution is obtained for

$t = 25.4\ \mu\text{m}$ (0.001 in.)

$\rho = 80 \times 10^{-8}$ ohm-m (80% Ni, 0.1% C, 20% Fe)

$\dot{B} = 2\pi f(B_{\max} - B_{\min}) = 68$ T/s,

and a vacuum chamber of 8 cm × 4 cm. Most of the current flows in the vertical sides of the chamber, and near the outside edge, giving a total peak current of 13.6 A and an average heating power of 190 W for each 4.5 m long dipole chamber. Thinner foils can be used, if the image currents and the beam wake fields allow. Note that the maximum thickness is given not by field distortion from eddy currents, but by the heat input to the vacuum chamber walls.

Outgassing and Pumps

The outgassing rate of such a composite chamber can be calculated, assuming that 1% of the surface area is epoxy, while 99% is unbaked, clean stainless steel. The total gas load per dipole is

$$Q = \text{Area} \cdot |(0.01\, q(SS) + 0.99 * q(\text{epoxy})|$$

With Area = 1.08 m^2/dipole, $q(SS) = 4 \times 10^{-8}$ W/m^2 (from Varian specifications for cleaned, unbaked *SS* after 40 hours), and $q(\text{epoxy}) = 2 \times 10^{-4}$ W/m^2 after 100 hours [5.15-3], we get $Q = 2 \times 10^{-6}$ W per dipole. Assuming one 30 liter/s ion pump per dipole, the pressure will be 5×10^{-7} Torr (6.7×10^{-5} Pa).

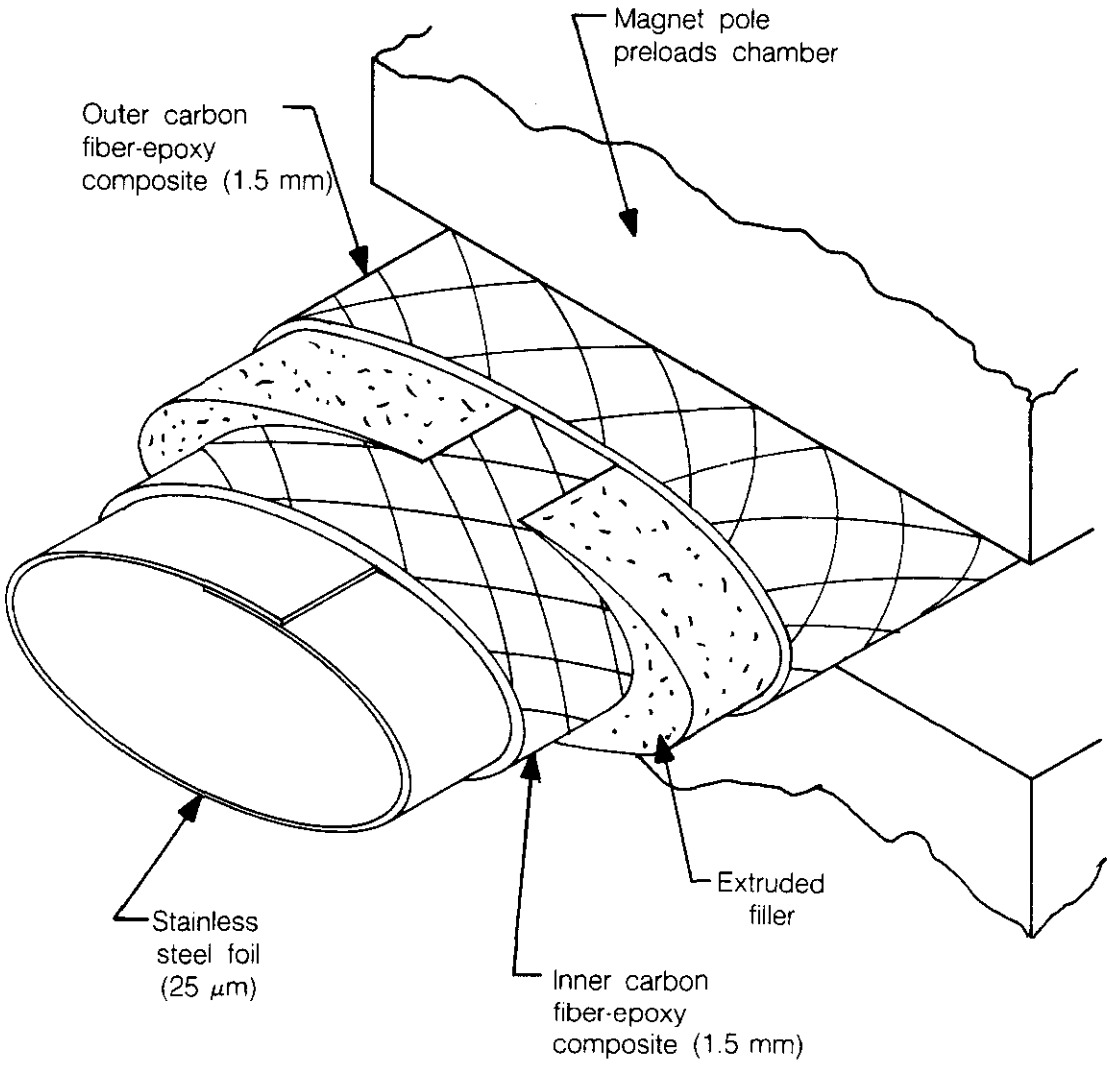

Figure 5.15-8. The LEB foil/carbon composite vacuum chamber.

Flanges, Pumps, and Gauges

The carbon fiber composite vacuum chambers are installed in each magnet under preload in the factory. Each chamber has an integral elliptical bellows on one end and an ion pump port on the other. The chambers are interconnected with sexless flanges and Helicoflex-type seals (soft aluminum cover over an Inconel spring insert). The clamps are of the CERN design, which uses four aluminum blocks to provide adequate compression. Figure 5.15-9(a) shows a layout of the vacuum equipment. Each half-cell has an ion pump, which is also available for pressure gauging and valve interlocks. Beam valves partition the machine into ten sections, as shown. Each of the sections has two all metal, 3.8 cm (1.5 in.) valves for pumpdown and leak checking. There are also two Pirani gauges for each section. The system is rough pumped with mobile turbo stations, similar to the ones in use at the Tevatron. These stations plug into wall outlets for power and compressed air, are fully interlocked, and radiation-hard. The carts have a cryogenic trap with a 24 hour holding capacity. This allows sufficient time for the ion pumps to start. The same type of mobile turbo stations are used on the other two injectors and on the SSC itself. In this way, the cost of fixed pump stations is avoided and maintenance is simplified.

Medium Energy Booster Vacuum System

Vacuum Chamber Design, Outgassing, and Pumps

The Medium Energy Booster is a warm magnet machine with a conventional ultrahigh vacuum (UHV) chamber. In modern practice, large improvements in base pressure and large economies can be realized by building an all metal, clean system, which can provide low outgassing rates even after venting and without subsequent baking. Using an outgassing rate of 4×10^{-8} W/m^2, quoted by Varian for unbaked stainless steel, we obtain for a three dipole string, pumped by one 30 liter/s ion pump, a base pressure of 7×10^{-8} Torr (9×10^{-6} Pa) after 40 hours. Baking all system components prior to assembly may reduce outgassing another factor of ten. To achieve and maintain adequate cleanliness, the chambers must be sealed after their vacuum bake and cannot be exposed to magnetic measurement equipment. Therefore, complete chambers with blank flanges at each end are inserted into the magnets at the factory site after magnetic measurements are completed. The blank flanges are removed in the tunnel just prior to interconnection. The same flange/seal combination as proposed for the LEB can be used for the MEB, i.e., Helicoflex seals in sexless flanges, closed with heavy duty clamps.

Pumps, Valves, and Gauges

Steady state pumping is done by 30 liter/s ion pumps, one for every half-cell (three dipoles). At each end of each six long straight sections there is a beam valve, as shown in Fig. 5.15-9(b). Each long straight section has pump out valves (3.8 cm, all metal), a Pirani gauge, and an ion gauge at each end. The arcs have pumpouts every three half-cells, for a total of five pumpouts in each arc. Rough pumping is again done with mobile pump stations with cold traps. Rough pumping is assumed to be a rare occurrence, and the pump stations can be shared with the other machines. The readout and control system is similar to the one operating at the Tevatron and consists of a crate at six locations in which the various cards are inserted, such as the Pirani card, ion pump interface cards, and ion gauge cards. The crates communicate with the host computer through a link.

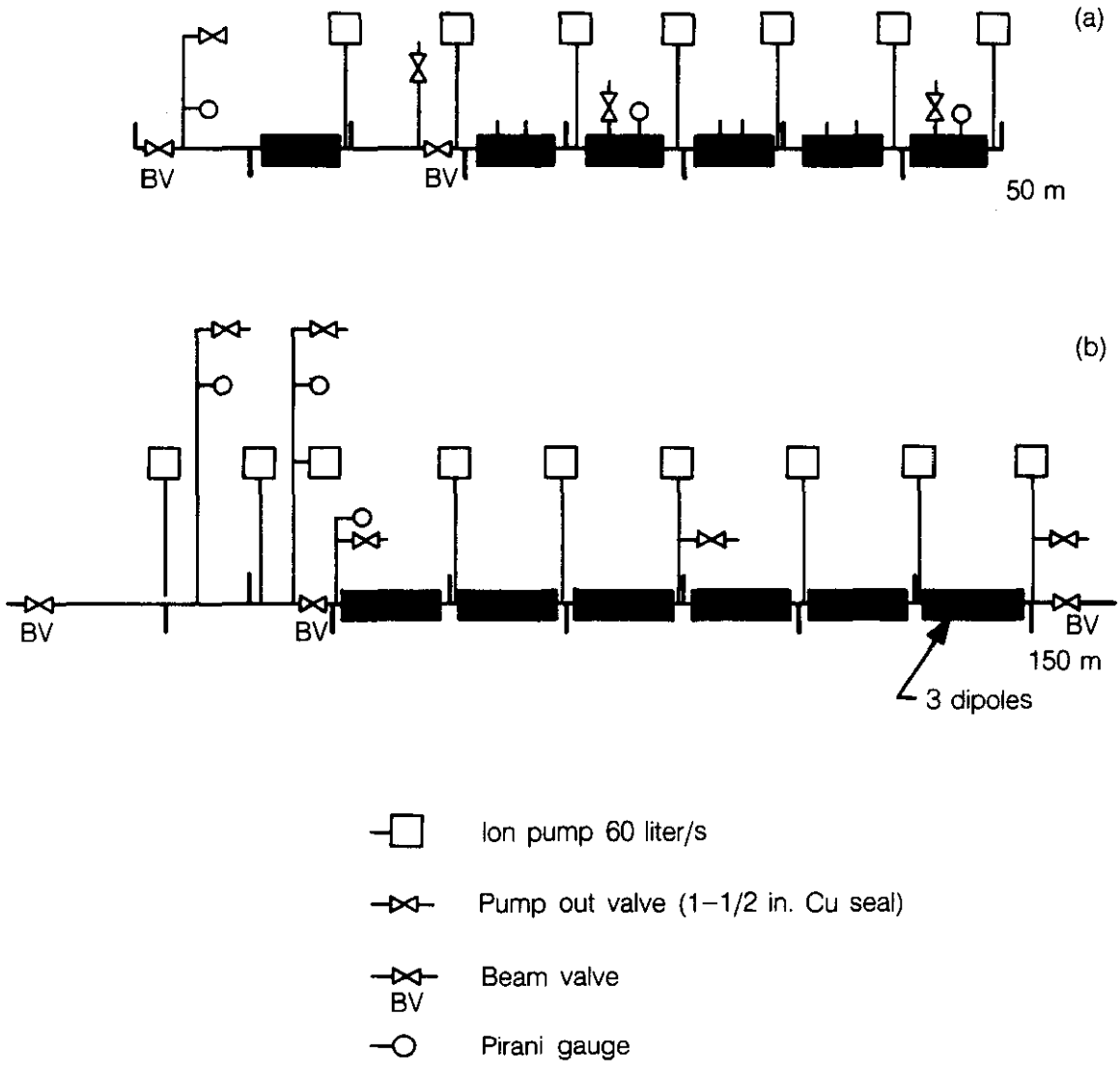

Figure 5.15-9. (a) Schematic view of the LEB vacuum system. (b) Schematic view of the MEB vacuum system.

High Energy Vacuum System

The High Energy Booster (HEB) is a cryogenic machine with some warm straight sections. There are two parts to the cryogenic vacuum, the insulating vacuum and the beam tube vacuum.

Insulating Vacuum System

The insulating vacuum system must maintain a pressure of 10^{-5} Torr or less when cold. It also must be capable of operating in the 10^{-3} Torr range when warm to help clean up the insulating space. Lastly, it must be capable of maintaining a pressure of better than 10^{-2} Torr locally under bad helium leak conditions. Figure 5.15-10(a) shows the proposed system for the HEB insulating vacuum. Such a system is best based entirely on mobile turbo pump stations, monitored through plug-in umbilical cables. During warm operation, a small number of these pumps maintain and eventually clean up the insulating vacuum space to reduce bursts of outgassing under quench conditions. For this task, one pump station per superperiod, for a total of six, is adequate. This same number can be left on the system when cold if there are no leaks. If leaks are found to hinder operation, additional pumps are connected at the leak location. This works better than a system of fixed pumps, which will not normally be at the right place for leak containment.

Cryogenic Beam Tube Vacuum

Operational experience at the Tevatron has not shown any advantage of removing condensable gases from the beam tube beyond a rough vacuum prior to cooldown. Therefore, permanent pumps are not needed. The system will, however, contain a small number of ion pumps to provide reliable valve interlocking and pressure sensing in case of quenches. For this purpose, one 30 liter/s ion pump will be installed every full cell. Connections to the beam tube are of the Tevatron "sniffer" type, with two bends and a nitrogen intercept to reduce the heat leak. These ports are needed in any case for leak checking during installation. There will be four beam valves per superperiod, as shown in Fig. 5.15-10(b). Appropriate locations for pumpout ports, Pirani gauges, and overpressure reliefs are also shown in that figure.

Warm Beam Tube Vacuum

The warm tubes form a conventional UHV system, pumped by a few 30 liter/s ion pumps. These pumps are also used for valve interlocks and vacuum pressure monitoring. The system is roughed by the standard mobile turbo pump station.

5.15.5 Power Supplies

Low Energy Booster (LEB)

The LEB is of a rapid cycling (10 Hz) design. It consists of 30 dipole magnets in series, 40 quadrupole magnets on two busses (20 quadrupoles per bus), and ten sextupole magnets on two busses (five sextupoles per bus). In addition, 40 correction dipoles are distributed around the LEB's 250 m circumference. Also required for the external beam line needed for injection into the MEB are three dipoles, four quadrupoles, and four steering dipoles.

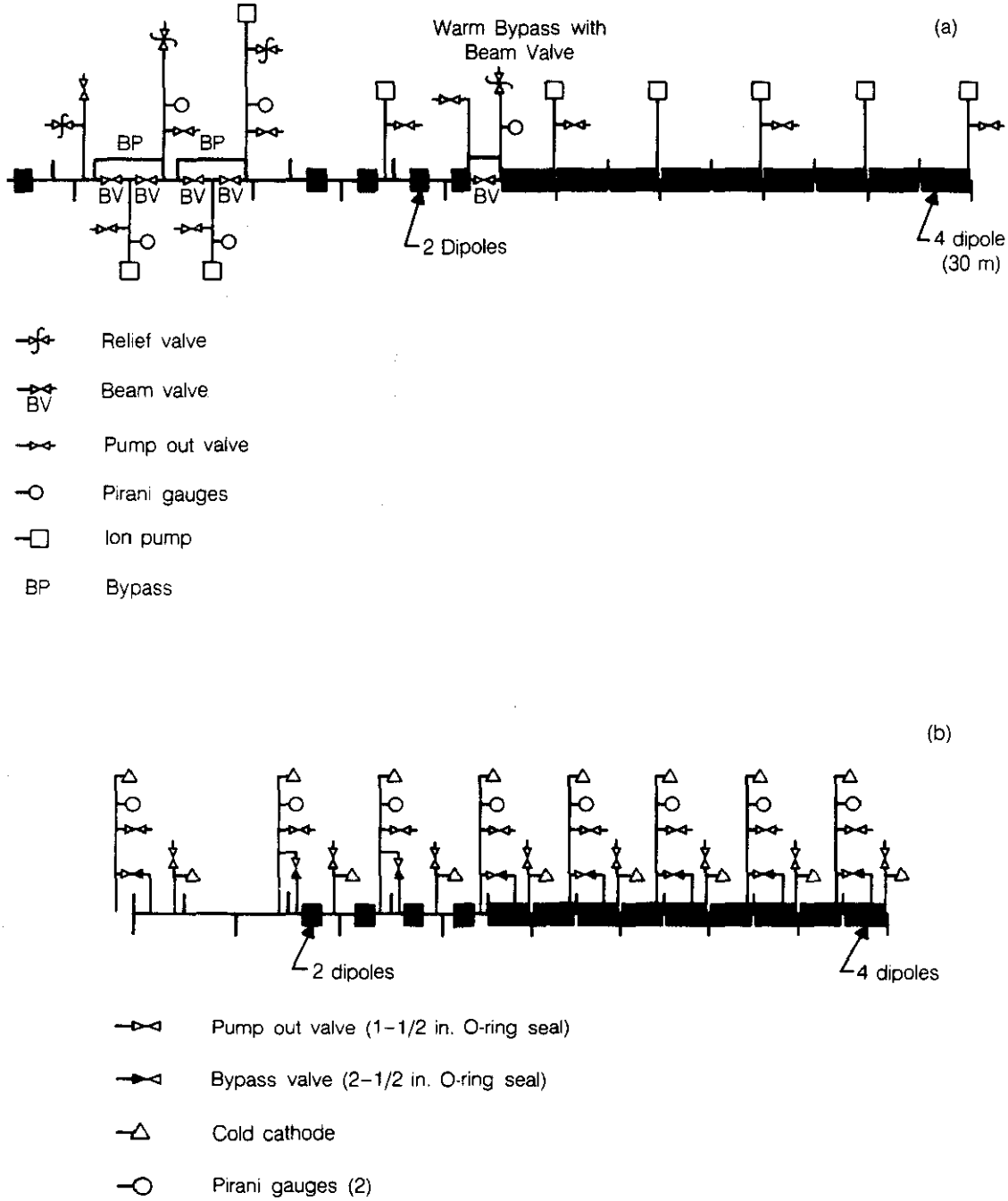

Figure 5.15-10. (a) The HEB insulating vacuum system. (b) The HEB beam vacuum system.

Dipole Power Supplies

Since the LEB is a 10 Hz accelerator, the dipole power supply is designed to resonate at 10 Hz with the dipole inductance tuned by a capacitor bank. It is planned to procure three 750 KVA resonant power supplies connected in series and symmetrically connected to the dipoles, ten dipoles between each power supply. These power supplies deliver the 705 amperes peak required. Located on the mount supporting each dipole is a capacitor bank of nominally 6 mF and a choke of 120 mH in parallel. These components are necessary to provide the proper resonant frequency as well as allow the dc bias for injection into the LEB.

Quadrupole Power Supplies

Two power supplies will be used (one for each bus with 20 magnets) to supply the 604 amperes peak current. Since the inductance of the quadrupoles is quite low, power supplies of conventional design (nonresonant type) will be used.

Sextupole and Correction Dipole Power Supplies

The sextupole and correction dipole magnets have similar current requirements (20 to 25 amperes). Consequently, identical power supplies will be installed, ± 20 volts, and ± 25 amperes.

External Beam Line Power Supplies

Since the external beam lines utilize the same magnets used in the LEB, it is planned to use the quadrupole power supplies for both the dipoles and quadrupoles, and the sextupole power supplies for the steering dipoles.

Medium Energy Booster (MEB)

The MEB consists of 216 dipoles in series, 96 quadrupoles on two busses (48 quads per bus), and 72 sextupoles on two busses (36 per bus). Additionally, there are two external beam lines for the injection of the counter-rotating HEB beams. The long external beam consists of four dipoles and 32 quadrupoles. The short external beam consists of three dipoles and five quadrupoles. These are also conventional magnets of the same type used in the MEB. Also required are 96 correction dipoles distributed around the 1900 m circumference.

Dipole Power Supplies

The 216 dipole magnets are series-operated in a pulsed mode at about 4600 amperes peak and 2450 amperes rms. The peak operating voltage is about 7400 volts. The power supply consists of six identical modules evenly spaced around the ring and alternately connected to 36 dipoles. One midpoint of a power supply module is intentionally connected to ground. This creates a phantom ground throughout the system, resulting in a total operating voltage-to-ground of about ± 650 volts. Power modules are sequentially programmed from zero to 100% output during the injection and acceleration cycles to keep the total power supply ripple low. The power supply must be able to invert. Power factor correction capacitors are installed at each module to reduce line losses, harmonics, and improve line voltage regulation. Specifications of the MEB power supplies are listed in Table 5.15-8.

Table 5.15-8
MEB Dipole Supplies

	Total PS	PS Module
Quantity	1	6
Input	13.8 kV	13.8 kV
Input peak MVA	48.6	8.1
Input peak MW	34	5.7
Input rates	34 MVA	5.7 MVA
Output voltage peak	7400 Vdc	1250 Vdc
Output current peak	4600 Adc	4600 Adc
Operating output current rms	2450 Adc	2450 Adc
Rated output current rms	3200 Adc	3200 Adc

Each power supply module consists of two 2.8 MVA 6-phase secondary transformers feeding indoor mounted watercooled rectifier assemblies. An interphase transformer connects the commutating groups in parallel yielding a 12-phase power supply. It may be more economical to connect the secondary commutating groups in series.

Quadrupole Power Supplies and Beam Line Power Supplies

All magnets for two quadrupole busses and for both the long and short external beam lines operate at various voltage and current levels. The magnets are all energized from two standard power supplies designed with multiple taps and current ratings. This approach reduces complexity, maintenance, and spare inventory.

Sextupole and Correction Power Supplies

The power supplies for the correction dipoles and sextupoles can be identical to those used in the LEB.

High Energy Booster (HEB)

The HEB ring contains 528 superconducting dipoles and 186 superconducting quadrupoles all connected in series. Peak operating dc currents are programmed up to 6000 A with a flattop of 0.2 s, a current rise of about 250 A/s, and a pulse period of 60 s. The equivalent rms current for this current pulse waveform is 3100 Adc. The HEB is required to accelerate protons clockwise and counterclockwise for injection into the SSC ring. This means that the dc output of the power supply must be reversible.

Dipole and Quadrupole Power Supplies

It is proposed to install two sets of silicon controlled rectifiers (SCRs) in the power supply, one set for the clockwise and one set for the counterclockwise operating mode. This type of construction eliminates the need for a reversing switch and results in a reduction of about 100 kW of operating losses for the total power supply. The power supply is connected to the magnets via heavy (low loss) water-cooled bus to the superconducting magnet lead box. The power supply consists of six identical modules evenly spaced around the 6000 m ring circumference and alternately connected in series with 88 dipoles and 31 quadrupoles. One midpoint of a power supply module is intentionally grounded, creating a phantom ground throughout the system. This results in a total operating voltage-to-ground of about ± 700 V. The power supply modules are sequentially programmed on from 0 to 100% during the injection period to keep the total power supply ripple low. The power supply must be able to invert and have special features to work in conjunction with the quench protection system. Power factor correction capacitors are installed at each module to reduce line losses, harmonics, and improve line voltage regulation. Specifications for the HEB power supplies are listed in Table 5.15-9.

Table 5.15-9
HEB Power Supplies

	Total PS	PS Module
Quantity	1	6
Input	13.8 kV	13.8 kV
Input peak MVA	68	11
Input peak MW	48	8
Input rated	48 MVA	8 MVA
Output voltage peak	8000 Vdc	1330 Vdc
Output current peak	6000 Adc	6000 Adc
Operating output current rms	3100 Adc	3100 Adc
Rated output current rms	4200 Adc	4200 Adc

Each of the six power supply modules consists of two 4 MVA 6-phase secondary transformers feeding indoor mounted water-cooled rectifier assemblies. An interphase transformer connects the commutating groups in parallel yielding a 12-phase power supply. It may be more economical to connect the secondary commutating groups in series.

Quench Protection

The 528 superconducting dipoles and 186 superconducting quadrupoles can be divided into 66 quench protection modules. Each module has its own quench protection monitor, antiparallel bypass SCRs, heater firing units, and computer (microprocessor)-based quench decision electronics. Quench detection can be done by forming a "Wheatstone Bridge" from the module magnets and appropriately chosen external resistors. This bridge would be monitored for unbalance voltages caused by local quenches. The monitoring amplifiers can be continuously checked by inserting an offset voltage. Electronics failure or disconnected wires would result in an apparent quench trip. All equipment is designed for failsafe operation. During a quench the stored energy in the magnets must be dumped into external resistors. Appropriate bypass SCRs must be fired, magnet power supplies inverted or clamped off, valves operated, etc., during a dump. The 66 quench protection monitors are connected to a central computer for overall monitoring and control. Solid state quench switches backed up by mechanical switches are probably the most economical means of building the equipment with one level of backup. Backup is critical in a system of this size.

Correction Elements

It is planned to construct the superconducting dipole, quadrupole, sextupole and octupole correction magnets in a common assembly (spool piece). There are two basic power supplies needed for powering these correction elements. The first power unit that supplies current to the superconducting correction dipoles and quadrupoles is a bipolar unit with an output rating of ± 500 A at ± 22 V. In order to supply many different magnet load combinations, the output is fed to a distribution bus where up to 16 regulator units can be connected to supply current to individual or series-connected dipole or quadrupole correction elements. The raw power supply and regulators are housed at required locations around the HEB. The second high precision power supply is for supplying current to the superconducting sextupoles and octupoles. Its major components consist of an SCR power section, transistor regulator, waveform generator, and a transductor for precision monitoring of the current through the correction elements. The output rating is ± 50 A at ± 600 V. Direct current cable runs are very long for some of the element strings. Cable sizes are determined by restrictions in permissible voltage drops and the number of elements in each string. Quench protection is needed only on a few of the strings where inductances become high due to the large number of correction elements.

5.15.6 Radio-Frequency Systems

Radio-Frequency Cavities

The injector rf cavities for the LEB, MEB, and HEB are three variations on a single design. The basic cavity design consists of two quarter-wave resonators connected back to back at their shorted ends. Each quarter-wave resonator is formed from a coaxial transmission line with a characteristic impedance Z_0 of approximately 70 ohm. The resonators operate in the TEM mode. With this geometry, the two accelerating gaps are separated by a drift tube slightly less than a half wavelength long. This foreshortening occurs because of the added gap capacitance of the high voltage corona rolls and results in a cavity length of 2.4 m.

Frequency tuning of the cavities is accomplished by inductively coupling energy from the cavity through a ceramic window into a ferrite-loaded, shorted transmission line tuner. The fraction of energy stored in the tuner is changed by varying the ferrite permeability μ with a dc biasing current. The difference in rf frequency ranges spanned by the LEB, MEB, and HEB requires three separate tuners with decreasing coupling ratios and ferrite volumes. To supply the ferrite biasing current, each rf station must have a programmable, low voltage, high current power supply. The input program to this supply is the sum of a computer generated frequency curve and a phase detector error signal which monitors the relative phase between the rf drive to the cavity and the cavity gap voltage.

The rf drive to the cavities is applied to the drift tube through a ceramic window at the cavity center. To damp the unwanted cavity modes in which the two gaps oscillate 180 degrees out of phase, a mode-damping resistor with an impedance of 5 ohms at 60 MHz is inserted between the two quarter-wave resonator sections. The entire cavity, with the exception of the ferrite tuners, is under high vacuum conditions at $<5 \times 10^{-9}$ Torr. The potential problem of cavity multipactoring at low gap voltages is eliminated by operating the cavities above the multipactoring limit. The voltages of a pair of cavities can then be paraphased to obtain the vector sum of any desired net cavity voltage.

A summary of the injector rf requirements is shown in Table 5.15-10. An additional spare cavity has been added to each of the rings. This will allow uninterrupted operation in the event of a station failure and allow repairs to be made during the next scheduled maintenance period.

Table 5.15-10
Injector RF Parameters

	LEB	MEB	HEB
Harmonic number, h	52	396	1250
Injection frequency (MHz)	49.4930	62.0316	62.4540
Extraction frequency (MHz)	62.0316	62.4540	62.4567
Synchronous phase, ϕ, (deg)	30	30	30
rf voltage (kV)	350	600	1500
Cycle time (s)	0.1	4.0	60
Number of cavities	5	4	6
Peak cavity voltage (kV)	100	250	300
Minimum rf bucket area at V_{rf} (eV-s)	0.147	0.215	1.28
Maximum energy gain/turn (keV)	175	300	750

Power Amplifiers

A common rf power amplifier design is used in the LEB, MEB, and HEB. The final amplifier consists of a cathode-driven power tetrode (Y567B) capable of delivering 150 kW at 60 MHz. The cathode of the final tube is driven by an amplifier consisting of 14 tetrodes (4CW800F) in parallel, which will produce 2 kW when matched into a 50 Ω load. A common −1000 V supply provides the negative voltage for each set of 2 kW drivers. A one-watt low-level rf signal is passed through an rf gate before being amplified by a 200 W solid state amplifier and applied to the 2 kW driver. This rf gate is activated not only by the rf gate program but can also be used to inhibit the cavity rf in the event of poor cavity vacuum, cavity sparking, or insufficient drive current.

The anode voltage of the final tube is controlled by a 0–30 kV series tube, floating-deck modulator with a rise time of less than 10 μs. A Y567B tetrode is again used as the series pass element. The series tube grid is driven by a 4CW800F tetrode whose cathode is driven by a field-effect transistor. The 0–10 V anode program is digitized and transmitted to the modulator deck with a 16-bit serial light link. A 30 kV, 100 A anode supply is needed for the HEB while two 30 kV, 50 A supplies suffice for the LEB and MEB.

Radio-frequency voltage regulation and steady-state beam loading compensation are achieved by measuring the integrated average power-tetrode screen current and generating an error signal to the power-tube control grid. This error signal modulates the anode current, producing a constant rf cavity voltage independent of the average beam current.

Low Level Radio-Frequency

Programmable frequency synthesizers are used throughout the injector to implement the computer generated rf frequency and radial position curves. The synthesizers also accept as input, radial position and frequency error signals obtained from beam pick-ups. To achieve lower rf sum voltages, digitally controlled complex phase modulators are used to shift precisely the phase of the low-level drive signals.

Transient beam loading compensation during the filling of the MEB and HEB is also included. On each machine revolution, the amplitude of the frequency component of the beam current at the fundamental frequency of the rf cavities is measured as a function of time. On the following turn, an rf signal 180 degrees out of phase with respect to the beam and proportional to the measured amplitude of the beam current is added to the low-level radio-frequency drive signal to the cavities. With proper timing, the beam bunch and the compensation signal arrive at the cavity simultaneously, cancelling each other and producing no net effect on the cavity voltage or phase.

Each injector rf station has individual amplitude and phase feedback loops which will force the high voltage output, as measured by the cavity gap monitors, to track the low-level rf drive signal.

5.15.7 Beam Transfers and Aborts

All beam transfers between the LEB, MEB, HEB, and collider occur using single turn injection and extraction. In each ring batches originating in the upstream ring are loaded in a boxcar fashion: three LEB batches are used to fill the MEB, seven MEB batches are used to fill the HEB, and sixteen HEB batches are used to fill each of the collider rings. Beam aborts are provided in the MEB and HEB. There is no abort in the LEB.

Low Energy Booster

The chosen pattern of missing dipoles in the LEB not only makes it possible to raise the transition energy but also facilitates extraction because of the convenient phase advance between adjacent straight sections. A set of three single-turn kicker magnets (one meter long, 80 G, 30 ns rise time) in one straight section displaces the beam about a centimeter at a pulsed septum magnet in the next straight section, which in turn deflects the beam past the lattice quadrupole. To reduce the required kicker strength, the closed orbit is moved toward the septum by a pulsed three-bump just before the kick. If necessary, dc dogleg magnets can also be installed on either side of the septum magnet to displace the low-energy beam around the septum, thereby preventing the septum from reducing the available physical aperture at injection time. The beam transfer line between the LEB and the MEB is shown in both Fig. 5.15-3 and Fig. 5.15-11.

Medium Energy Booster

Injection into the MEB takes place at straight section KK0. The injection system consists of a 2 m long, 6 kG pulsed septum and a 1 m long, 250 G fast kicker. The septum and kicker are both located in the empty cells of the straight section, separated by 60 degrees.

Two extraction systems are provided — one resulting in clockwise circulation, and the other resulting in counterclockwise circulation in the HEB. Extraction is done on a single turn. The extraction geometry is similar to injection but the strength of the elements is necessarily greater. A 6 m long (actually six 1-m long modules), 600 G kicker and two 5.5 m long, 9 kG Lambertson magnets are used. The two transfer lines between the MEB and HEB are shown in Fig. 5.15-12.

The abort is located at LL0 and consists simply of a kicker identical to the extraction kicker followed by a steel dump on the outer wall of the beam pipe 60 degrees downstream.

High Energy Booster

Injection into the HEB from the MEB occurs in the straight section centered at NN0 (clockwise injection) and at TT0 (counterclockwise) injection, as shown in Fig. 4.10-1. As in the MEB, injection occurs boxcar fashion. Both injections are identical and consist of two horizontal Lambertson magnets and a vertical fast kicker. The Lambertson magnets reside in the straight section and are each 5.5 m long with a field of 9 kG. The kicker is 6 m long and resides within the dispersion supressor 270 degrees downstream of the Lambertson magnet. The kickers have a field of 600 G and a rise time of 100 ns.

Extraction to either of the main collider rings is done in the straight section centered at RR0. The geometry is similar to injection — Lambertson magnets located in the long straight section with kickers 270 degrees upstream in the empty spaces of the dispersion suppressors. The two extraction systems are symmetric around RR0. Five Lambertson magnets are required (in each direction). Each Lambertson magnet is 5 m long and has a strength of 10 kG. The kickers each contain four modules of length 1 m. The kickers have have a rise time of 100 ns and a field of 600 G. The transfer line between the HEB and collider is described in Section 5.9.

Two symmetric beam aborts are located in the PP0 straight section. Again a vertical kicker and horizontal Lambertson magnet are used to extract the beam into a dump located within the tunnel.

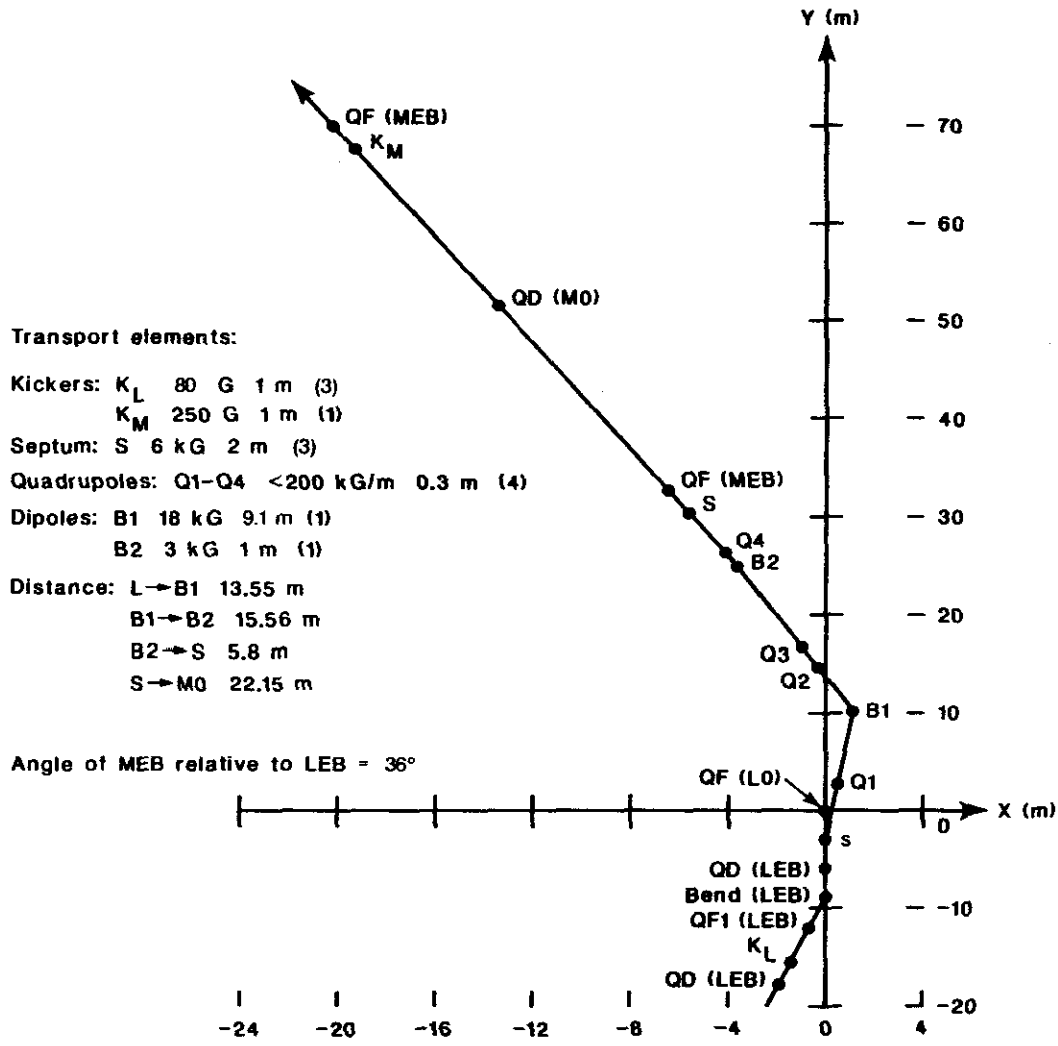

Figure 5.15-11. Schematic view of the LEB to MEB transfer line.

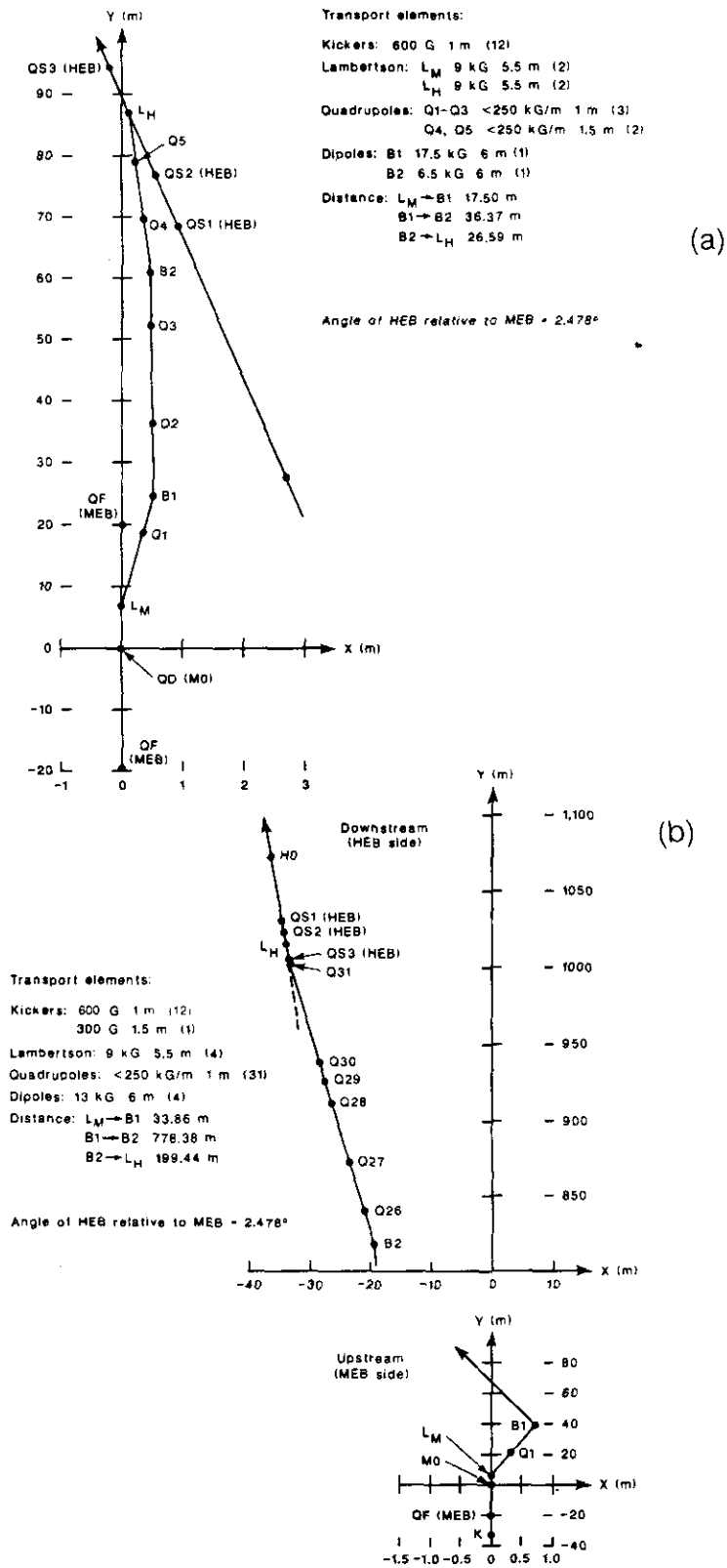

Figure 5.15-12. Schematic view of the two beam lines connecting the MEB to the HEB. The short line (a) is used for counterclockwise and the long line (b) for clockwise injection.

Slow extraction for the test beams is done in the same manner as at the Fermilab Tevatron. The half integer (ν_x = 25.5) resonance driven by the distributed octupole system is used to drive protons across an electrostatic septum located at TT0 where they receive a kick which drives them over the septum of a Lambertson magnet located in NN0. An electrostatic septum displacement of 30 mm results in extraction losses on the septum of a few per cent.

5.15.8 Diagnostics

Beam Position Monitors (BPM)

The BPM system is as similar to the Collider systems as possible, both in requirements and hardware (see Section 5.12). In the case of the HEB and the MEB, the electronics can be identical to the Collider systems. Only the detectors need to be different to meet the unique aperture requirements of each machine. The LEB does pose special problems for a BPM system. It must contend with the injection of 20 turns of H^- ions and their stripping, the frequency swing of the rf (49.5 to 62.0 MHz), and the absence of a gap in the beam, which in the other machines provides a self-triggering mechanism for the rf modules. These problems can be solved in a general way allowing the same rf module in all machines.

The electronics package proposed for the SSC BPM system supports four detectors located in very close proximity. However, the system will be designed to accommodate cable runs of up to 200 m. In the case of the HEB, four electrode pairs are located along 100 m of the accelerator requiring cable runs of up to 60 m. As in the Collider rings, the electronics are located in alcoves in the tunnel. For the BPM system these alcoves are required every other cell. In the MEB the electronics are located in the six service buildings above the ring (longest cable run in this case is around 170 m). In the LEB the electronics is also upstairs.

All of the detectors in this design are 50 ohm directional couplers, or striplines. All are 20 cm long and each electrode covers 110 degrees of the azimuthal angle. The detectors in the HEB are at cryogenic temperature, and, since the HEB is a bi-directional machine, the signal port and back termination port must be reversible via the software and hardware. This is to be a standard feature of the BPM system as a whole, although it is only used in the HEB. The BPM requirements are listed in Table 5.15-11.

Beam Loss Monitors (BLM)

BLMs are the ion chambers used in the Collider rings. There will be one BLM located at each quadrupole in the three rings of the injector.

Other Injector Instrumentation

Since the injector rings are not intended to be storage rings, the demand for additional diagnostics is not as great as in the Collider. However, each ring contains three flying wires for measurement of transverse profiles, (one vertical wire and two horizontal at locations of minimum and maximum dispersion). Transverse and longitudinal Schottky signals are also available for analysis in each ring. Each ring contains a dc beam current transformer for intensity monitoring.

Table 5.15-11
Beam Position Monitor Parameters

	LEB	MEB	HEB
Number of horizontal detectors	20	48	96
Number of vertical detectors	20	48	90
Sets of electronics	10	24	40
Detector diameter	10	10	7 cm
Phase advance between detectors	80	63	90 degrees
BLMs	40	96	186

Transfer Line Instrumentation

Instrumentation for the beam transfer line from LEB to MEB and the two lines from MEB to HEB include BPMs, BLMs, and profile monitors. The profile monitors are secondary emission monitors (SEM grids) of the type found in Fermilab's beam transport lines.

5.15.9 Controls

The injector controls are designed to be a part of the overall SSC system, discussed in Section 5.13. In particular they share with the Collider rings the same operator consoles and host supermini-computers, and have their parameters in the same database. Each of the five major pieces of the injector — the linac, three boosters, and test beams — is driven by its own 32 bit minicomputer and is treated in the control system on the same level with one sector of the SSC main ring.

That part of the control system dealing with the high energy booster, since it interfaces to equipment similar to that found in the main ring, resembles in some detail a main ring sector through all levels of control. There are local area networks in the tunnel of approximately 1 km separation, so that networks longer than this distance are at surface level, not in the tunnel, and are built with optical fibers.

The linac and low- and medium-energy boosters have control systems that are as similar as possible to those of the higher energy machines, but with accommodation made for the inherently different requirements. While these controls do not need to deal with, for example, cryogenics and quench protection, they must collect data from these rapid cycling machines at a high rate to allow pulse-to-pulse stability to be monitored. An attempt is made to keep these essential differences at the lowest level of controls, minimizing software incompatibilities at the higher levels.

The test beam control, as noted above, is also part of the master system. While some of the features of these beams differ significantly from those of the circular accelerators, they do resemble those of the various transfer lines which must also be controlled. One difference is that the test beams have a higher density of hands-on operators than do the

accelerators. Several of the simpler type of controls consoles will be built and devoted to operation of the beam lines.

5.15.10 Layout of the HEB Test Beams

Because the HEB test beams are quite simple from the point of view of intensity requirements (Section 4.10.6), it is possible to produce an economical test beam solution that incorporates cheap target stations and simple straight beam lines with no cryogenic elements. No beam splitting is done anywhere in the system. However, division on the basis of charge allows two beams to be operating at any given time. Figure 5.15-13 shows the layout of four test beam lines.

Resonant extraction is used to produce slow spill from the HEB. The cycle time is 3 minutes (5 minutes if the collider has just been filled — see Section 5.15.3) with a spill length of at least one minute. Protons are extracted in the same straight section used for one of the injection lines from the MEB. The primary proton beam is switched into one of two channels, each of which leads to one individually shielded target station. From each of the two primary targets, a pair of secondary beams is transported to the Test Beam Experimental Hall. To attain 10^7/s requires extraction of a few times 10^{12} protons onto target over the duration of the HEB spill.

Service buildings required include tangent, dipole, and quadrupole enclosures, a target station, and the Test Beam Hall. The amount of power installed in target buildings will be 1 MW total, with an additional 1 MW available in the Hall.

No detailed design of the test beam area has been completed. The layout shown in Fig. 5.15-13 utilizes only elements in use in the external beam lines at Fermilab. Costing has been done on the basis of Fig. 5.15-13 and the experience of building identical or similar devices at Fermilab.

5.16 Survey and Alignment

5.16.1 Introduction

It is essential for the geodetic and alignment engineering to be integrated into the design at a very early stage. A detailed survey plan is described in [5.16-1]. The present section gives a summary of the key elements of the plan. Maintenance of stay-clear regions, and design of alignment fiducials, magnet supports, and mechanical adjusters have a crucial impact on the cost and quality of the final positioning. Since the costs and interferences of survey and re-survey have greatest impact late in the project, it is important to have early organizational means to identify and correct developments that are detrimental to the smooth alignment process. Early completion of the surface network, even though unnecessarily accurate, will have a beneficial impact on all civil construction.

It is essential that the processes of survey and alignment be analyzed and performed separately. Traditionally much of accelerator alignment has been done with optical tooling techniques using spirit or split-bubble levels to determine the elevation of magnets and jig

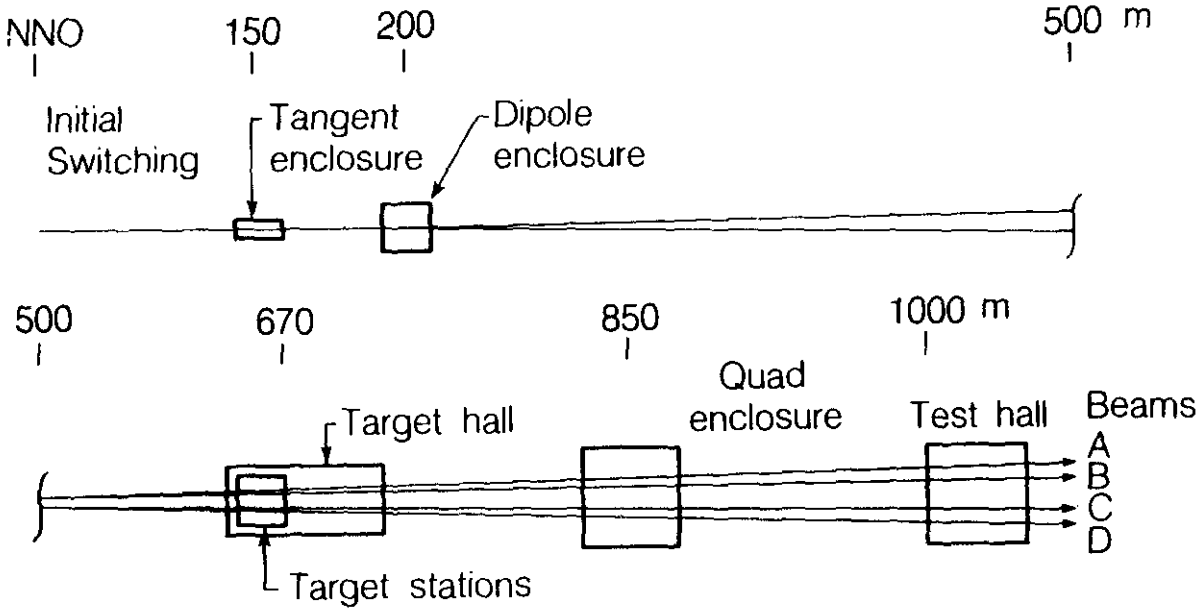

Figure 5.15-13. Layout of the test beam lines.

transits to measure off-sets to a baseline established with a jig transit. Though very flexible, this method is almost entirely avoided in the SSC because of the following disadvantages:

(a) Survey personnel are kept working beyond the survey proper until the alignment is also complete.
(b) Normally, continuous control of the adjustments is impeded by clumsy "shout-and-holler" communication between the surveyor and the adjuster.
(c) The absence of redundant information prevents follow-up or detection of blunders after the setup is torn down.
(d) It is local smoothness rather than absolute location which is essential for satisfactory accelerator operation. Local smoothness is defined only when the survey over an appreciable arc has been completed.

For these reasons the survey and alignment should be conducted separately, though they are described together in the following sections.

Because of the size of the SSC the general reference frame must be spheroidal. To avoid costly errors and multiple coordinate systems, machine lay-out coordinates will be translated into geodetic spheroidal coordinates at a very early stage. For this purpose a model and the necessary software will be developed starting well before construction contracts are let.

To minimize blunders and to improve the logging of data, most operations are monitored by a computer which will, as much as possible, refuse to accept inconsistent data. A single data base will contain all survey information.

A summary of technical data and requirements is given in Table 5.16-1. To simplify the table, software availability is not included. In most cases some software is available, but modifications are needed. The five essential steps are establishment of a surface network, translation down to the tunnel, establishment of the tunnel network, coarse magnet location and magnet smoothing. To a large extent these can proceed independently.

5.16.2 Survey Above Ground

With traditional methods (trilateration and/or triangulation) the surface survey would be a costly and time consuming operation. However, a satellite-based technique has become available, called the global positioning system (GPS). Commercial vendors like Texas Instruments or Macrometrics offer (nearly) turn-key receiver systems. The accuracy has improved recently to the order of 10 mm in 40 km, with the biggest improvement coming from combining the very large baseline interferometry stations, whose separations are known to 1 cm in 10^3 km, with GPS stations in a simultaneous fit to reduce uncertainties in satellite orbits by an order of magnitude. For a project the size of SSC it is more cost effective to acquire the necessary hardware rather than to contract out the job.

The GPS system has to be supplemented for short distances by methods based on electronic distance meters (EDMs, with an accuracy $<10^{-6}$ for distances of a few hundred meters) and theodolites. The EDMs, in conjunction with a permanent SSC baseline, will determine and control the local scale factor for the SSC during the whole of the construction project. Both types of instruments are also needed for work in the tunnels to place and align the components (see below).

The advantages of GPS are: no lines of sight are necessary; monuments can be put on locations which are desirable from a geodetic point of view and do not have to be

determined from the topography of the site; and the measurements are more than an order of magnitude faster than with traditional methods. The GPS output is in the form of three-dimensional coordinates U, V, W in the satellite coordinate system, which must be transformed into global coordinates and further into a local system. Problems of a conceptual and theoretical nature that have to be solved are determination of the transformation parameters needed for transformation of the GPS output into the local spheroidal coordinate system and transformation of the geodetic surface measurements into the same coordinate system. To do the latter, the local geoid has to be determined by measuring the deviation from the vertical with a zenith camera. This determination will be contracted out to a university institute specializing in this type of research.

5.16.3 Transfer from Surface to Tunnel

The surface coordinates are transferred to the tunnel with Invar tapes (vertical) and plumbing (horizontal). For the plumbing, several methods are available: optical plummets with an accuracy of 1:200,000, pendula with oil damping, and inverted pendula. They all have their specific advantages and disadvantages so that a specific choice depends eventually on the accuracy needed and the circumstances of work.

For the SSC any of these methods fulfills the requirements. This is so because the penetrations control only the long wave length deformation of the ring. The more important local smoothness is determined by the network in the tunnel. In the end it is the requirement of local smoothness (0.5 mm over 200 m) which determines the long wave component to be not more than a few cm over 3 to 5 km.

The spacing between surface to tunnel penetrations is determined by the requirement that accumulated survey errors due to optical refraction be limited. Errors of several cm after 3 km are typical. Simulations for the SSC, using the SLC GEONET program [5.16-2], show that, along with gyro theodolite measurements, penetrations spaced 3 to 5 km apart will be satisfactory.

5.16.4 Establishing the Tunnel Net

Once global (surface) coordinates are known in the tunnel, coordinates of the tunnel net can be calculated. Measurements to determine the relative position of tunnel control points (horizontal) and benchmarks (vertical) can be done independently of the transfer, even before the transfer has been made.

The vertical tunnel network is not expected to pose any specific problem, except that some 10,000 marks have to be measured. Non-automatic split bubble levels with Invar rods are used.

The horizontal tunnel net has to be established by traditional methods of measuring distances and angles, albeit with modern technology. It is crucial that distance measurements be fast. This precludes the use of the CERN Distinvar, which exerts a pull of over 30 pounds on the points to be measured, and the cumbersome use of Invar wire. Thus angle measurements are done with electronic theodolites, and the distance measurements

with 2-color electronic distance meters (to be developed). Presently available EMSs are already achieving accuracies just below 1 mm with single-color techniques.

The total error budgets for vertical and horizontal measurements can be kept in limits by measuring short distances in leveling, by using a dispersiometer, and by additional gyro theodolite measurements for the horizontal control.

5.16.5 Installation Alignment

The tunnel network is needed for initial placement of components. It may or may not be needed for the precise alignment, depending on the mechanical construction of magnets (cryostats), and support and adjustment systems. For achieving local smoothness and to avoid a costly and accuracy-limiting translation it is most advantageous to place both instruments and targets for the survey on the magnets.

To place the magnets in their rough (3 to 5 mm) position the same technique used for the tunnel network is employed by measuring angles and distances. For initial installation horizontal and vertical placement can be done in one step by measuring distances and horizontal and vertical angles from a known theodolite position in 3-dimensional space.

5.16.6 Smoothing Alignment

For the more accurate smoothing survey, horizontal and vertical measurements have to be separated. Therefore, precise leveling has to be done here.

The horizontal position could be determined by measuring directions and distances, but because of the long target distances (100 m) the horizontal refraction may make this method too inaccurate. A non-optical off-set measurement is preferred.

CERN has developed a nylon offset technique where a stretched nylon wire is used as a baseline. Offsets from the magnets to this wire determine the location of the magnets. For nylon wire length of up to 90 m, rms deviations of less that 0.1 mm have been determined. It seems possible to use this method for placement of the SSC quadrupoles and bend magnets, but it will require some effort to extend its range from 90 to 200 m. An alternative is to use intermediate points.

Once the position of the ends of the quadrupoles and bend magnets are known they are moved to their desired location under the supervision of computer controlled electronic dial gauges, strictly separating survey and alignment.

5.16.7 Smoothing Algorithms

It is important that all elements be accurately aligned, but, for simplicity, the discussion is limited to the most critical problem, the transverse location of quadrupoles. The effect of horizontal misalignment by Δx of a single quadrupole of strength $2q$ is to give an orbit shift $x_{co}^{(1)}$ at the quadrupole itself which is

$$x_{co}^{(1)} = \left(\frac{\beta_x q \sin 2\pi\nu}{1 - \cos 2\pi\nu} \right) \Delta x \qquad (5.16\text{-}1)$$

where ν is the machine tune and β_x is the local beta function. For regular arc quadrupoles $\langle \beta_x q \rangle \simeq 1$. Special attention must be paid to IR quadrupoles for which this product is much higher, but here they are assumed to be perfectly aligned. Assuming also that the tune is not close to an integer, the expression in parenthesis is close to unity and one can take $x_{co}^{(1)} \approx \Delta x$.

If there is no steering correction and we make the (invalid) assumption that N quadrupoles are randomly misaligned with rms displacement Δx, the resulting closed orbit error would build up to an rms value of

$$x_{co}^{(N)} \approx \sqrt{N}\,\Delta x \quad . \tag{5.16-2}$$

From Table 5.16-1 the absolute quadrupole locations are uncertain by about ± 2 cm. Taking $N = 1000$, the resulting orbit error approaches a meter, which is totally unacceptable. As described in Section 4.5, steering elements in the ring are adjusted to compensate this random build up.

The remaining question concerns local smoothness, assuming the orbit correctors have been adjusted to remove global orbit deformation. The answer depends on the details of the steering correction. Using Fourier analysis it is possible to perform the steering correction with a number of series-wired steering families that is far smaller than the number of elements, but for the SSC it is more economical to have one independently powered steering element per cell. This makes a Fourier analysis unnecessary.

It is still obligatory to ensure by careful survey and alignment that the elements have correct absolute locations over at least a few cells (say 1 km). Arcs of this approximate length will be surveyed, a best smooth curve determined, and then, as described above, the elements will be adjusted onto it. Continuity from arc to arc will be guaranteed by spline techniques (i.e., overlap).

When this is done, it is appropriate to replace the factor $\sqrt{N}$ in Eq. (5.16-2) by a factor of order 1, and to use for Δx a distance of 0.5mm, according to the specifications of Table 5.16-1. This yields a closed orbit rm error less than 1 mm. A more quantitative analysis, described in Section 4.5, obtains an rms orbit error of 0.4 mm.

Table 5.16-1
Summary of Technical Data and Requirements for Survey and Alignment

Step	Parameters to be Determined	Precision°	Apparatus	Availability
1. Surface Network	Scale	2 mm/10 km	Dual-wavelength EDM	Single wavelength: now 2nd wavelength: 1–2 yrs
	Defl. of vert.	0.5 arc second	Zenith camera	Contract: 1–2 yrs
	U,V,W	1 cm/30 km	Dual-wavelength GPS	now
2. Surface-tunnel connection Spacing: 3–5 km Diameter: 80 cm	Surface points	1.5 cm (pos.) 3 cm (hgt.)	Optical plummet (position)	now
	Tunnel points	2 cm (pos.) 3 cm (hgt.)	Invar tape (height)	now
3. Tunnel network Pos.: every 400 m Hgt.: every 40 m	Distance	0.5 mm/400 m	EDM	now (needs modification)
	Direction	0.1 mgon*	electronic theodolite	now
		0.3 mgon*	gyro-theodolite	now (needs automation)
	Height	0.5 mm/1 km	level	now
			electronic fieldbook+	now
4. Magnet alignment (coarse)	Distance (from monument)	2 mm/100 m	EDM (e.g. Kern 503)	now (needs modification)
	Direction (from monument)	Pos.: 2.5 cm (abs), 3 mm(rel)	electronic theodolite	now
		Hgt.: 3.5 cm (abs), 3 mm (rel)	vertical angles/level	now
			electronic fieldbook+	now
5. Smooth alignment (nylon offset)	Differential leveling	0.5 mm/1 km	level	now
	Offset	0.2 mm/200 m	CERN off-set device	needs improvement
		0.1 mm/100 m	electronic fieldbook+	now
	Electronic dial gauges	Pos.: 0.3 mm quad-quad Hgt.: 0.3 mm mag-mag		now (needs jig design)

°All precisions are ±

*2π radians = 400 gon

+ portable computer control

References

5.1-1. Magnet Length Workshop, SSC Central Design Group Report No. SSC-SR-1018 (1985).

5.1-2. J.D. Jackson and P.J. Limon, SSC Central Design Group Internal Report No. SSC-N-17 (1985).

5.1-3. A.F. Greene, D.C. Larbalestier, W.B. Sampson, and R. Scanlan, SSC Central Design Group Internal Report No. SSC-N-64 (June 1985).

5.2-1. SSC Central Design Group Report No. SSC-SR-1011, June 1985.

5.2-2. SSC Magnet Selection Advisory Panel Report to the Director of the Central Design Group, September 9, 1985.

5.2-3. Task Force on SSC Commissioning and Operations, SSC Central Design Group Report No. SSC-SR-1005, July 1985.

5.2-4. P. Dahl et al., Proc. 9th Int. Conf. on Magnet Technology, Zurich (1985), in press.

5.2-5. H.E. Fisk et al., SSC Central Design Group Report SSC-7 (1985).

5.2-6. W.B. Sampson, P.F. Dahl, A.D. McInturff, K.E. Robins, and E.J. Bleser, IEEE Trans. on Magnetics **MAG-15**, 114 (1979).

5.2-7. M.A. Green, Lawrence Berkeley Laboratory Report No. LBL-17249 (1984).

5.2-8. S. Caspi, W.S. Gilbert, M. Helm, and L.J. Laslett, SSC Central Design Group Internal Report No. SSC-Magn-47 (1985).

5.2-9. A.K. Ghosh and W.B. Sampson, Proc. 1985 Cryogenic Engineering/Int. Cryogenic Materials Conf., M.I.T., Cambridge, MA (1985), in press.

5.2-10. J.M. Peterson, private communication.

5.2-11. Design Criteria, Superconducting Super Collider, Design "D", Dipole Magnet Cryostat System, Fermi National Accelerator Laboratory, Batavia, Illinois, 1985 (unpublished).

5.2-12. R.C. Niemann, et al., Adv. Cryo. Engr. **31** (1986) Plenum Press, N.Y. (to be published).

5.2-13. P.O. Mazur, et al., Adv. Cryo. Engr. **31** (1986) Plenum Press, New York (to be published).

5.2-14. R.J. Powers, et al., Adv. Cryo. Engr. **31** (1986) Plenum Press, N.Y. (to be published).

5.2-15. J.D. Gonczy, Adv. Cryo. Engr. **31** (1986) Plenum Press, N.Y. (to be published).

5.2-16. T.H. Nicol, et al., Adv. Cryo. Engr. **31** (1986) Plenum Press, N.Y. (to be published).

5.2-17. M. Kuchnir and T.H. Nicol, Fermilab Memorandum (1980, unpublished).

5.3-1. Helen T. Edwards, Ann. Rev. Nucl. Sci. **35**, 605 (1985).

5.3-2. D.P. Brown, R.I. Louttit, C. Rode, and P.C. VanderArend, Cryogenic Engineering Conference, Boston (1985), Adv. Cry. Eng. **31** (in preparation). D.P. Brown and K.C. Wu, Brookhaven National Laboratory SSC Technical Note No. 28 (1985). Task Force on Commissioning and Operations, SSC Central Design Group Report No. SSC-SR-1005 (1985).

5.3-3. E. Shrauner, SSC Central Design Group Internal Report No. SSC-N-52 (1985).

5.3-4. H.R. Barton, M. Clausen, G. Horlitz, G. Knust, and H. Lierl, Cryogenic Engineering Conference, Boston (1985), Adv. Cry. Eng. **31** (in preparation).

5.3-5. C.H. Rode, et al., IEEE Trans. Nucl. Sci., **NS-32**, 3557 (1985). A.J. Bianchi et al., Paper BC-5, Cryogenic Engineering Conference, Boston (1985), Adv. Cryo. Eng. **Vol. 31** (in preparation). W.E. Cooper et al., Adv. Cry. Eng. **27**, 657 (1982).
5.3-6. D.P. Brown et al., Cryogenic Engineering Conference, Boston (1985), Adv. Cry. Eng. **31** (in preparation).
5.3-7. A.W. Chao and J.M. Peterson, SSC Central Design Group Internal Report No. SSC-N-62 (1985).
5.4-1. H. Jöstlein et al., submitted to J. Vac. Sci. Technol.
5.4-2. J. Bittner and H. Halama, Proc. of Second All Union Conf. on High Energy Accelerators, Moscow, 1972, p. 191.
5.4-3. S. Erents and G. McCracken, J. Appl. Phys. **44**, 3139 (1973).
5.4-4. O. Gröbner, Proc. Xth Intl. Conf. on High Energy Accelerators, Protvino, 2 (1977), p. 277.
5.4-5. E. Keil and B. Zotter, CERN Report No. CERN-ISR-TH/71-58 (1971).
5.4-6. Design Report, Cornell Electron Storage Ring, Cornell University LNS-360 (1977).
5.5-1. SPICE is a general purpose circuit simulation program developed by the Department of Electrical Engineering and Computer Science, University of California, Berkeley.
5.5-2. O. Calvo and G. Tool, Fermilab Internal Report No. TM-1360 (1985).
5.5-3. Peter Wanderer, Brookhaven National Laboratory, private communication.
5.5-4. K. Koepke, Fermilab, private communication.
5.5-5. W.V. Hassenzahl, Lawrence Berkeley Laboratory, private communication.
5.6-1. R. Mau, Tevatron Down Time Log, private communication.
5.6-2. Military Standardization Handbook: Reliability Predictions of Electronic Equipment, MIL-HDBK-217C, U.S. Department of Defense, Washington D.C. (1980).
5.6-3. J.D. Jackson, SSC Central Design Group Internal Report No. SSC-N-137 (1986).
5.7-1. P.B. Wilson, in *Physics of High Energy Particle Accelerators,* A.I.P. Conference Proceedings No. 87, ed. R.A. Carrigan, F.R. Huson, and M. Month, American Institute of Physics, NY, (1982), p. 474.
5.8-1. F. Sacherer, IEEE Trans. Nucl. Sci., **NS-20**, 825 (1973).
5.8-2. M. Zisman, S. Chattopadhyay, and J.J. Bisognano, Lawrence Berkeley Laboratory Report No. 21270 (1986).
5.8-3. B. Zotter, CERN Accelerator School General Accelerator Physics, CERN Report No. 85–19, p. 415.
5.8-4. D. Boussard and Y. Lambert, IEEE Trans. Nucl. Sci., **NS-30**, 2239 (1983).
5.8-5. H. Jöstlein, Fermilab Internal Report No. TM-1253 (1984).
5.9-1. T.E. Toohig, SSC Central Design Group Internal Report No. SSC-N-127 (1985).
5.9-2. M. Harrison, SSC Central Design Group Report No. SSC-27 (1985).
5.9-3. M. Harrison and C. Rad, Nucl. Instr. Methods **227**, 401 (1984).
5.11-1. S. Peggs, SSC Central Design Group Internal Report No. SSC-N-87 (1985).
5.11-2. T. Risselada, R. Jung, D. Neet, H. O'Hanlon, and L. Vos, IEEE Trans. Nucl. Sci. **NS-26**, 4131 (1979).
5.11-3. F. E. Paige and S. D. Protopopescu, Brookhaven National Laboratory Report No. BNL-37271 (1985).
5.12-1. H. Edwards, Annual Review of Nuclear and Particle Science, **35,** 605 (1985).

5.12-2. R. Shafer and R. Gerig, Proceedings of the 12th International Conference on Accelerators (Fermilab, 1983), p. 609.
5.12-3. R. Shafer, IEEE Trans. Nucl. Sci. **NS-32,** 1933 (1985).
5.12-4. R. Shafer, in SSC Central Design Group Report No. SSC-SR-1017, (1985) p. 127.
5.12-5. S. Jachim, R. Webber, and R. Shafer, IEEE Trans. Nucl. Sci. **NS-28,** 2323 (1981).
5.12-6. A. Barisy et al, IEEE Trans. Nucl. Sci. **NS-28,** 2180 (1981).
5.12-7. J. Bosser et al, IEEE Trans. Nucl. Sci. **NS-30,** 2164 (1983).
5.12-8. K. Unser, IEEE Trans. Nucl. Sci. **NS-28,** 2344 (1981).
5.12-9. T. Linnecar and W. Scandale, IEEE Trans. Nucl. Sci. **NS-28,** 2147 (1981); ibid **NS-30,** 2185 (1983).
5.12-10. A. Hofmann and B. Zotter, IEEE Trans. Nucl. Sci. **NS-24,** 1487; ibid **NS-26,** 3405 (1979).
5.13-1. P. Griffin, in Proceedings of the 1985 Annual Reliability and Maintainability Symposium, Jan., 1985.
5.13-2. D. Siewiorek and R. Swarz, *The Theory and Practice of Reliable System Design,* Digital Press, Bedford, MA, 1982.
5.13-3. A. Hevesh, IEEE Trans. on Reliability **R-33**, 324 (1984).
5.15-1. P. Allison and J.D. Sherman in *Production and Neutralization of Negative Ions and Beams*, AIP Conference Proceedings No. 111, ed. K. Prelec, American Institute of Physics NY (1984), p. 511.
5.15-2. I.M. Kapchinskii and V.A. Teplyakov, Prib. Tekh. Eksp. **2**, 19 (1970) [Transl. Instruments and Experimental Techniques, Consultants Bureau, NY, No. 4, 973 (1970)].
5.15-3. J. O'Hanlon, *A User's Guide to Vacuum Technology*, Wiley, NY (1980).
5.16-1. R. Pitthan and R. Ruland, SSC Central Design Group Internal Report No. SSC-N-134 (1986).
5.16-2. R. Ruland, Stanford Linear Accelerator Center, private communication.

6. Conventional Systems

6.1 General Description of Requirements

The SSC is a large facility that presents two separate and distinct site characteristics. First, there is the 52-mile-long Collider Ring and Tunnel. This part of the SSC is located underground and has the linear qualities of a vehicular tunnel or underground pipeline. Periodically along the Collider Ring there are compact surface facilities that make a small visual impact in their immediate vicinity. Over most of its length, however, the tunnel places few constraints on use of the lands over and immediately adjacent to it.

The Campus and Injector Complex has a very different character. In this location, and to a lesser extent at the Interaction Hall Cluster on the other side of the ring, there are groups of laboratory, shop and office buildings with associated grounds, parking lots and utilities yards. The utilities and services for the entire SSC, as well as all of the operating staff, largely are concentrated in these two laboratory areas. As a result, they contain conventional buildings and require support services of significant size. In this respect, the main laboratory area resembles the campus of a medium-size university or a large corporate research center.

The entire facility requires a reliable and stable source of electric power with peak demands up to 200 MW and a water supply of about 1600 gallons per minute. The site's electric power need is comparable to a light industrial town of 30,000 population and the water need to one of about the same size or smaller.

The daytime site population during regular operation will be about 3000 people, of whom 2500 are residents of the surrounding communities and 500 are visiting scientists on short-term stays of days to months. During construction, the population will fluctuate. In addition to the basic buildings, roads and parking areas, appropriate environmental and support systems are needed for this population, including items such as heating and ventilation of buildings and work areas, provision for sewerage and solid waste disposal, provision of police and fire protection, emergency medical aid and other standard considerations.

It is the purpose of this chapter to describe conceptually an SSC site, its buildings, and all the needed conventional facilities and services in sufficient detail to provide a firm basis for planning and cost estimation. It is important, of course, to point out that the design is a

conceptual one and does not make irrevocable choices about the detailed characteristics of the included structures and systems. These decisions can be made only when a specific site has been identified and the detailed engineering design begins. In the conventional facilities area, it is also important to realize that there are certain topics of relatively small dollar cost which nevertheless have special importance where they involve community sensitivities, environmental concerns or federal and state laws and regulations. These topics are noted here, but in the absence of a specific site they can be developed only in a generic sense and will receive further elaboration at the Preliminary Design stage, at which time they can be applied to a specific site with appropriate engineering designs.

In addition to the items noted above, there are also site-related issues that are particularly relevant to a U.S. Government-owned facility used for high energy physics research. These issues include items such as radiation shielding and protection, toxic waste control, site security and equipment safeguards. There are also issues of environmental impact that are unique to a facility of this size and nature. All these items and issues are grouped under the heading of "conventional systems" and are addressed in this chapter, especially as they interact with the conceptual design of the SSC.

The conventional systems described here reflect the practical experience of working high energy physics laboratories in the United States (particularly Fermilab, where the accelerator facilities resemble the SSC injector) and CERN, where a large accelerator tunnel is currently under construction. The existence of these laboratories permits confident modeling of the related conventional facilities needs of the SSC and significantly reduces the uncertainties that might otherwise have been present in specifying and cost estimating them. Table 6.1-1 gives a compilation of the current physical siting parameters of the SSC, developed as in the Siting Parameters Document [6.1-1].

Table 6.1-1
Land and Utility Allowances for Siting the SSC

Campus area and injector	2500 acres
Collider ring areas	$\leq$4000 acres
Cluster expt'l areas	1500 acres
Peak site electrical power	250 MW
Peak site water needs	2000 gal/min

The electrical demands of the facility are quoted in a number of places in this chapter in terms of "peak" demands and "average" demands. These dual specifications are useful because of the pulsed nature of the accelerator systems. As used in this report, "peak" loads mean the maximum power drawn by any system or group of systems in the course of its normal operating cycle. "Average" loads are those which are obtained from averaging the power drawn by a system or group of systems when operating over its cycle. Shutdown periods for the machine are explicitly not included in power averages.

Figures 6.1-1, 6.1-2 and 6.1-3 offer aerial views of the SSC site as it might appear to an airline passenger at 30,000 ft, to a helicopter pilot at 1000 ft and to an arriving visitor on the main campus. A map of the Injector Complex is given as Fig. 6.1-4. The only direct clues to the unique nature of the facility as seen from above are the characteristic circles of the three booster accelerator rings (delineated by their ground-level service buildings and earth shielding berms). The surface manifestations of the large Collider Ring are so slight and on such a large distance scale that they are likely to be apparent only to the trained eye.

The conventional systems described in this chapter of the SSC conceptual design were developed by the RTK Joint Venture, an Architect-Engineer firm engaged by the U.S. Department of Energy to help with conceptual design studies for the SSC. The full report of their design work is included as Attachment C to this report. RTK used as input information for their study current accelerator-related technical design parameters from the SSC Central Design Group together with earlier SSC related documents. Among these are the SSC Reference Designs Study of May 1984; the Parsons, Brinckerhoff, Quade and Douglas Inc. Technical Appendix to that Study (also May 1984); and the SSC Siting Parameters Document issued by the SSC CDG on June 15, 1985 [6.1-1]. The present chapter is intended to be a description of the work done in conjunction with RTK.

6.2 Example SSC Sites

6.2.1 Example Site Concepts

The Conceptual Design Report is non site-specific; the Collider accelerator and its tunnel are 52 miles in circumference and are dominant factors in the cost and schedule of the entire SSC project. The combination of these circumstances, especially the sensitivity to cost and schedule, mandates the need for a careful and sophisticated approach to modeling the geotechnical characteristics of the site or sites on which the conceptual version of the SSC might be placed. It is the purpose of this section to describe how this challenge was addressed and a workable solution obtained.

The process involved the collection of a large geotechnical data base for actual geological and ground water conditions across all parts of the contiguous United States; the reduction of these data into three example sites, each of which is representative of broad physiographic provinces in the U.S.; and finally, the development and use of these three example sites in realistic geotechnical, topographic and stratigraphic models for the study of tunneling and conventional facilities construction. We identify the three example sites in Table 6.2-1.

6.2.2 Geotechnical Data Base

The process by which the three example sites were derived and the degree to which they characterize large regions of the United States is now described in more detail. First, extensive topographic, geological and water distribution data from all parts of the contiguous U.S. were compiled from the appropriate literature. Primary sources of geological

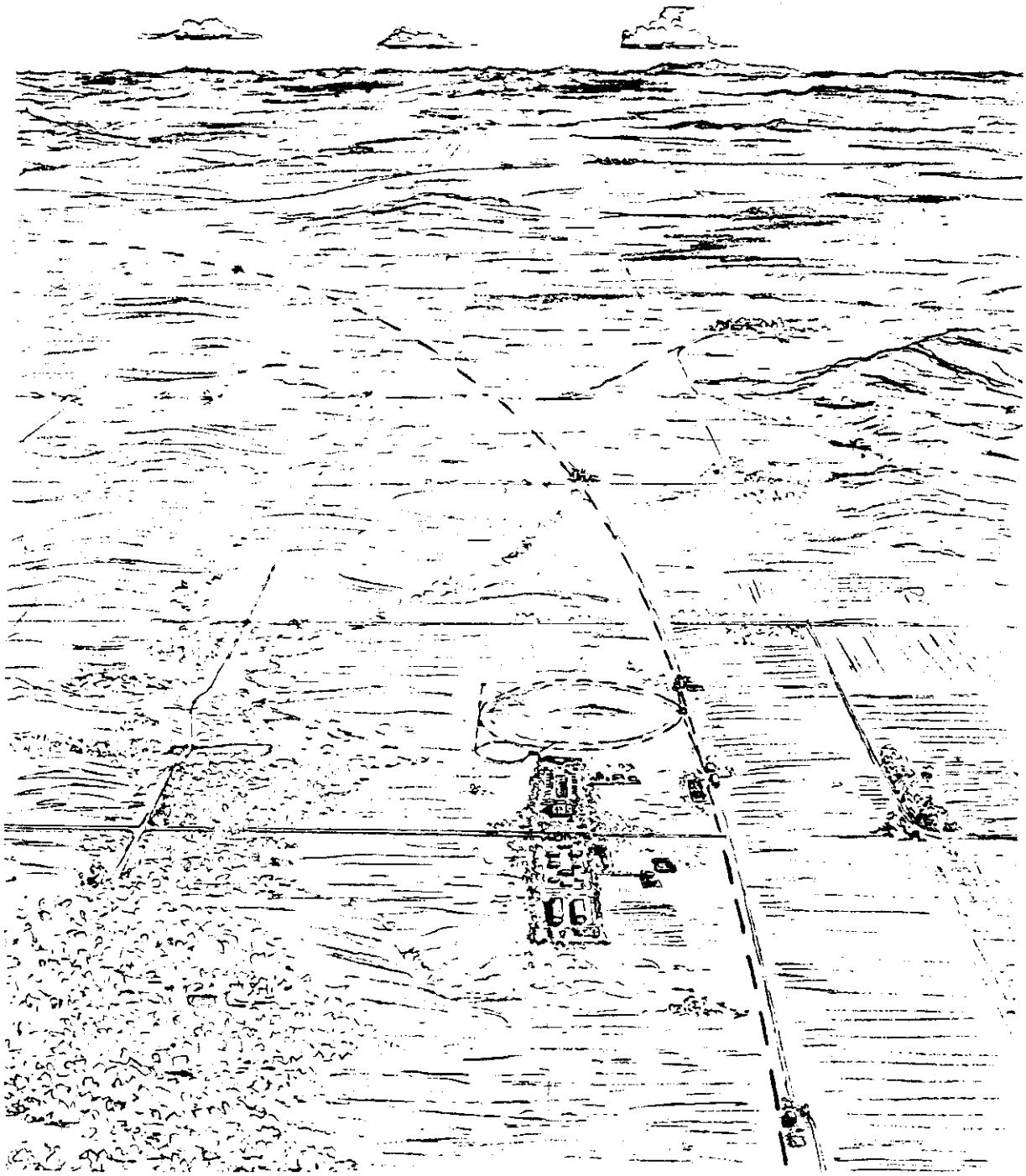

Figure 6.1-1. Aerial view of the SSC site from an altitude of 30,000 ft. The Injector Complex and Main Campus are apparent in the foreground, as are the main features of the booster rings. Very little of the Collider Ring structure is visible from the air. Its path is indicated by the dashed line.

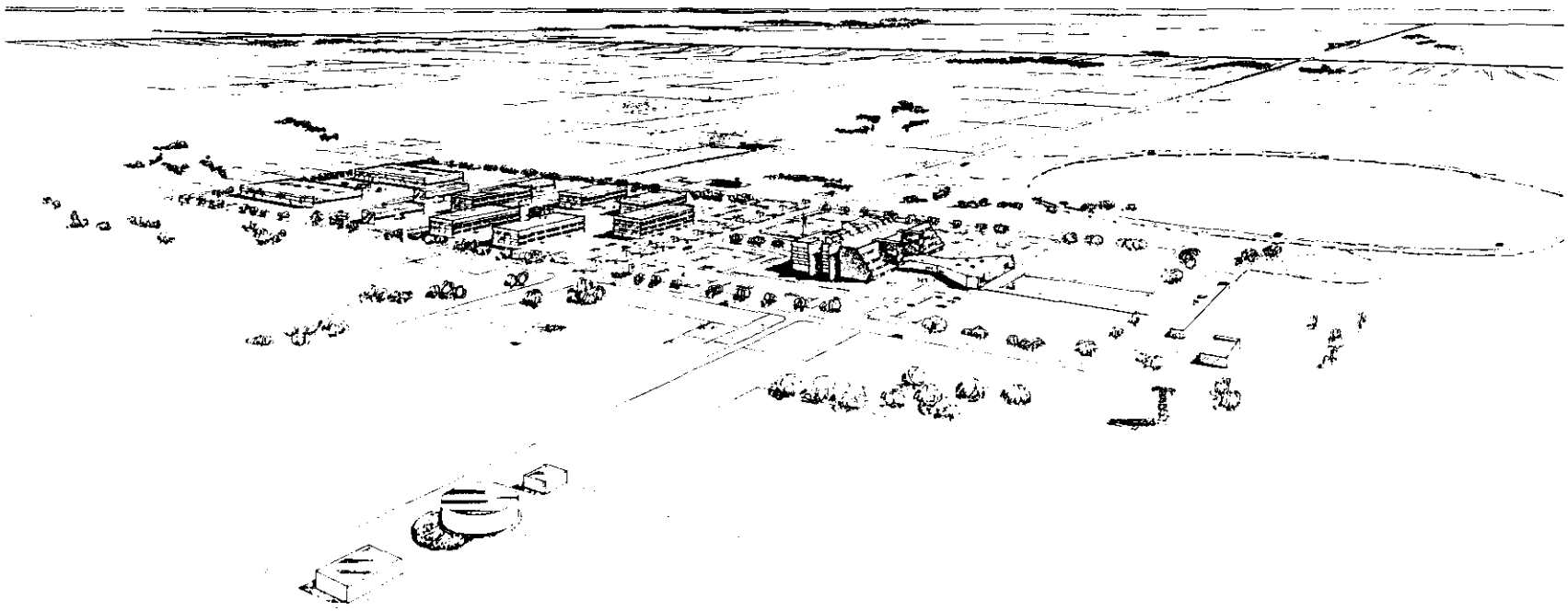

Figure 6.1-2. Aerial view of the Main Campus and Injector Complex from an altitude of 1000 ft. The details of the campus buildings and how they relate to the accelerator elements can be seen in this perspective.

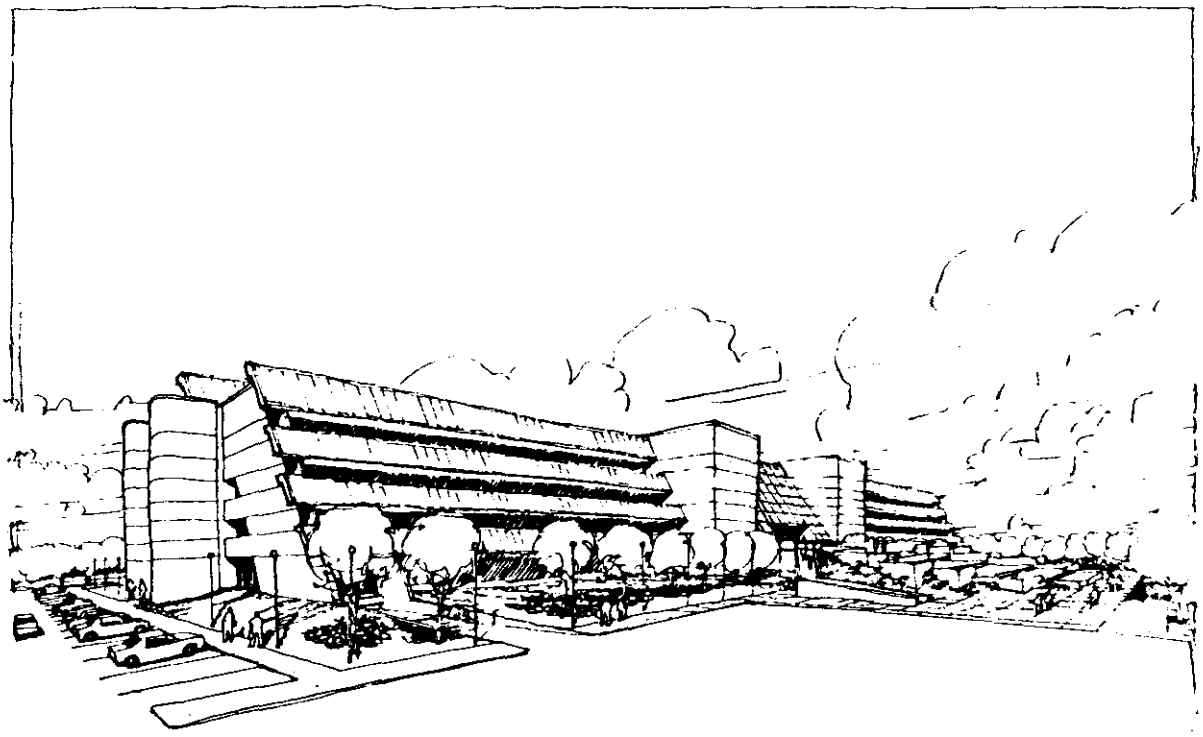

Figure 6.1-3. View of the Central Office Building from the main entrance road. This building houses most of the scientific and clerical personnel and is the main architectural focus of the SSC campus.

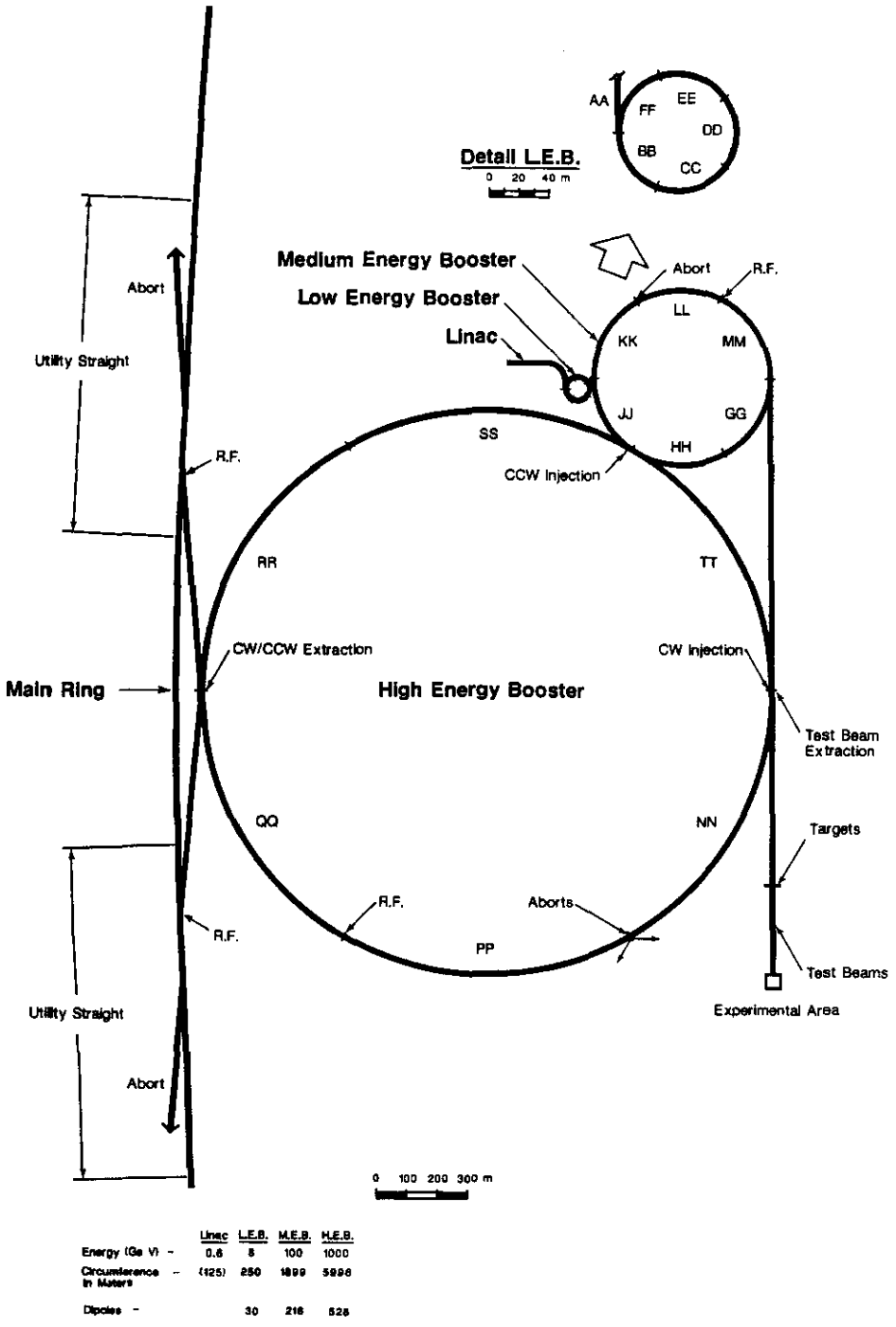

Figure 6.1-4. Map of the Injector Complex, showing the main relations among the accelerators in the injector chain, major equipment access points and service buildings.

Table 6.2-1
Example Sites for SSC Conceptual Design

Site	Characterization
A (soft ground tunnel)	gently rolling topography; geology consisting of various soft soils and sedimentary rocks and a fluctuating water table crossing the tunnel elevation.
B (hard rock tunnel)	rolling topography; geology consisting primarily of hard crystalline rock with small sections of soil and incompetent rock; the water table is above the tunnel elevation.
C (cut-and-cover)	flat topography; geology consisting primarily of soft soils with some rock intrusions and a water table well below the tunnel elevation.

materials data were published papers. These data were significantly reinforced and supplemented by U.S. Geological Survey publications, numerous state publications and various topographic maps. Water distribution data were based on U.S.G.S. Water Supply papers and state-published water resource documents. The RTK Non-Site Specific Conceptual Design Report (Attachment C) describes the gathering and organization of the geological and water data bases; it also details the primary data references.

An important conceptual aid to the compilation of the data base was a 1940 paper by Atwood in which the contiguous U.S. was divided into 20 distinct physiographic provinces. Atwood's map is shown as Fig. 6.2-1. The similarity of lands within each of these provinces allows interpolation of geological characteristics in areas of sketchy or incomplete primary data (across political boundaries, for example). The quality of the resulting data base was adequate for the purpose of creating representative geotechnical models for U.S. topographies, lithologies and geographic variation.

The geological and water distribution data base thus compiled was used to prepare a set of six maps of the U.S. One pair of maps represented geological materials and water distribution conditions at the surface. A second pair of maps reported conditions at a depth of 50 ft. The third set reported conditions 150 ft down. The scale on which detail was reported was of order a few miles in extent. As a supplement to the six maps just described, a seventh map was compiled of the contiguous U.S. dividing it into regions of land (averaged over 10 mile stretches) that have greater than or less than 10% of ground slope. This map essentially differentiates mountainous regions and steep geoclines from other regions in the U.S.

After careful study of these seven maps, it was determined that three example sites (noted above) were adequate to represent the features of possible sites in a realistic manner for non-mountainous areas of the contiguous U.S. The logic flow followed in deriving the three site models is shown in Fig. 6.2-2 and described in Attachment C.

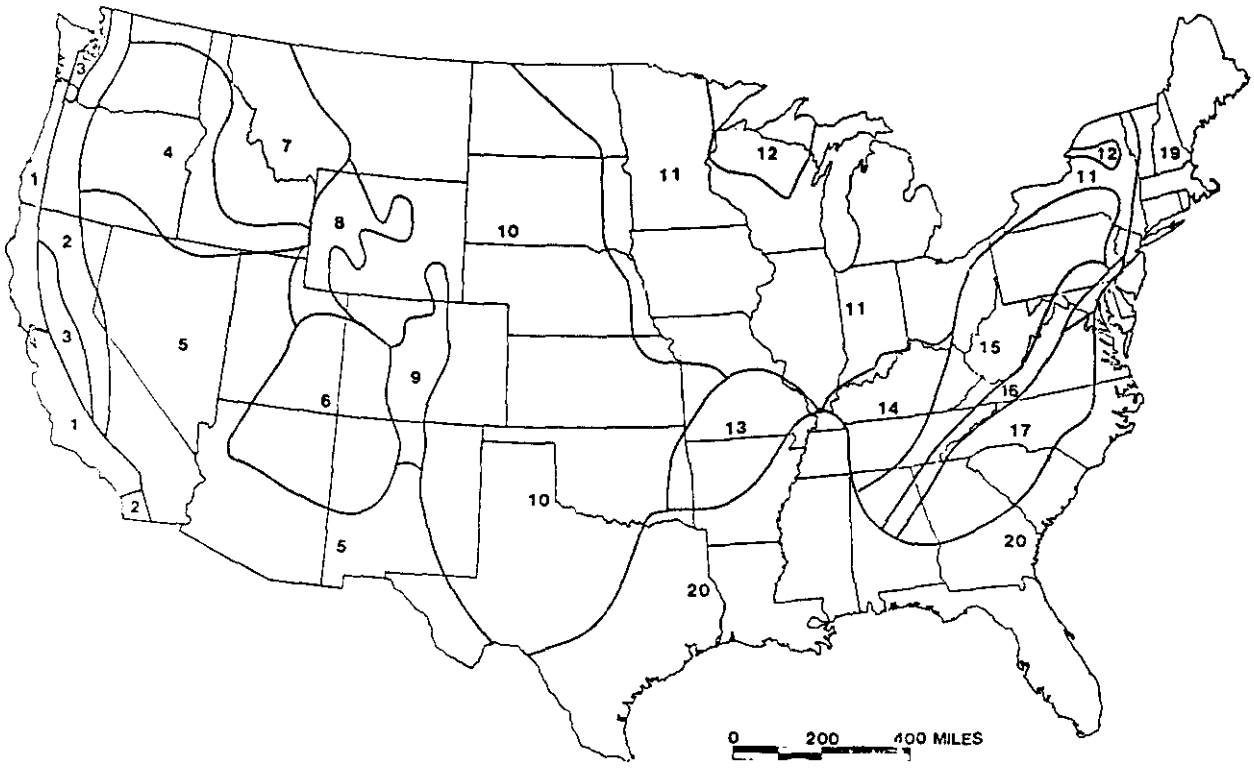

Figure 6.2-1. Map of 20 U.S. Physiographic Provinces (from Attachment C).

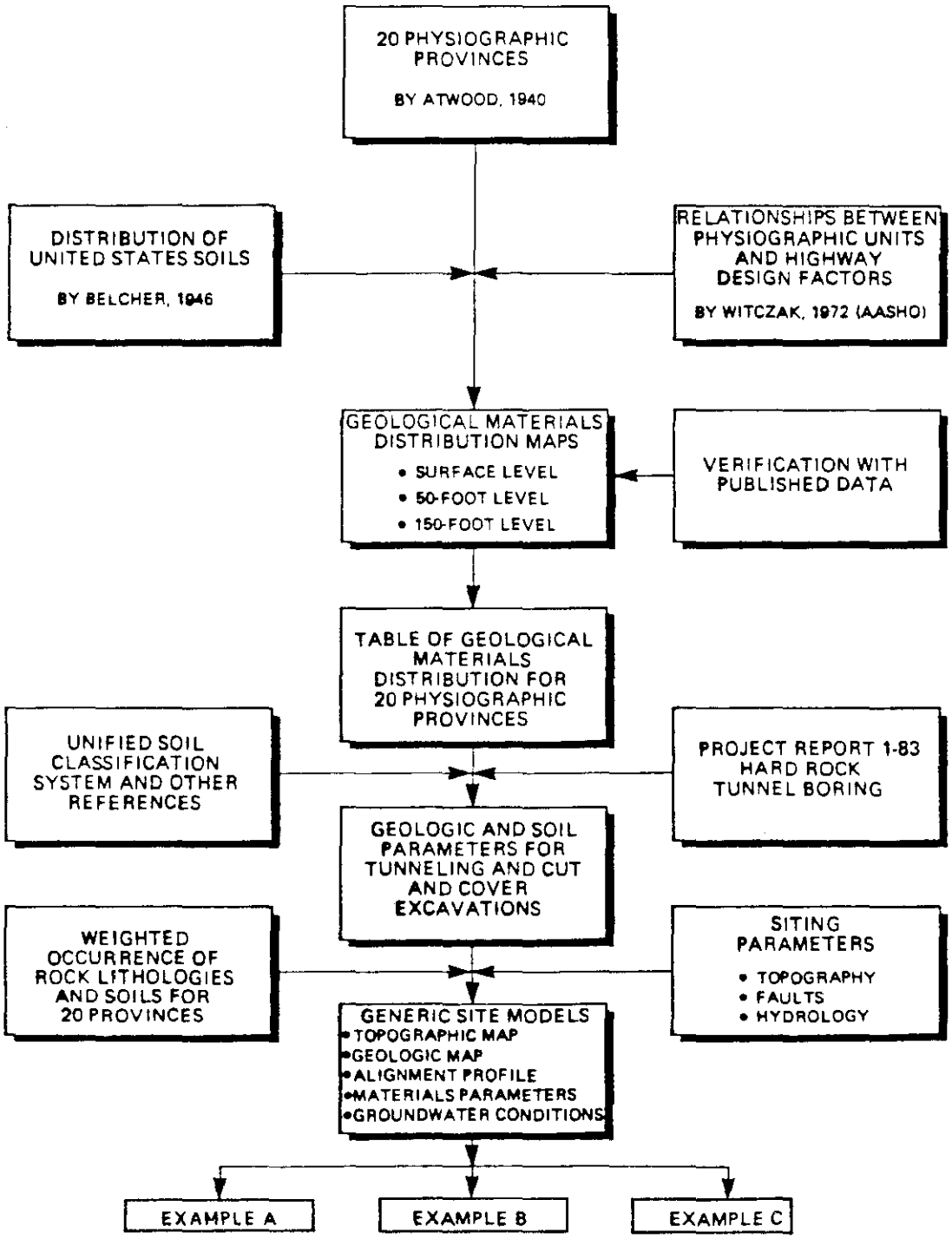

Figure 6.2-2. Flow Chart for Generic Site Models Development (from Attachment C).

6.2.3 Generic Rock and Soil Models

After compiling the geological materials distributions and water distributions, the geological rocks and soils were subjected to analysis and classification into generic classes that were chosen to relate directly to the parameters that are important for tunnel construction. Experimental data for numerous samples of each of sixteen types of naturally occurring rocks, for example, were carefully evaluated and averaged, type by type, to produce good engineering characterizations of each. The sixteen natural rock types were then classified into four generic rock categories, each of which was specifically characterized according to properties important for tunnel boring. These four generic rock types were then informally broken down into two general types, "hard rock" and "soft rock". The first category refers to rock that is "competent" that is, self-supporting and able to be tunneled without further support. The second characterizes rock that must be mechanically supported after being tunneled through.

A similar treatment was made of naturally occurring gravels and soils. Generic varieties relevant to excavation in trench or soft-tunnel environments were developed. Both in the cases of soils and of rocks, the goal of the reduction to generic types was guided by practical engineering considerations without much regard to traditional academic crystallographic or geological categories.

When the process of assay and reduction to generic rock and soil types had been completed, the 20 contiguous U.S. provinces were individually characterized according to the averaged occurrence of the various geological materials as classified into and expressed by the generic rock and soil types just identified. This classification was carried out at each of the three compiled elevations (surface, −50 ft, −150 ft). To appreciate the nature of these classifications, they are reproduced here from Attachment C as Figs. 6.2-3, 6.2-4 and 6.2-5. There is one diagram for each of the three elevations. Also included on each diagram is an area-averaged materials fraction for the entire contiguous United States. The elevation diagram chosen for each example site is, of course, correlated to the chosen optimum tunnel construction method for that type of example site.

6.2.4 Generic Topography and Geological Materials Distributions

The geological materials diagrams are interesting and enlightening, but they are not by themselves directly usable in estimating tunnel costs and schedules. Two more modeling concepts must be added. The first of these is topography. This is a measure of the natural up-and-down contouring that any real area of land will exhibit. Each of the three example sites has a different overall topography. Site A was characterized as "gently rolling," Site B as having a "rolling topography" and Site C as being "flat". In fact, each topographic map was derived from a single, common progenitor by the method of vertical scaling. This means that contour lines on the map of Site A indicate vertical increments of 20 ft, while the same contours on the map of Site B represent increments of 40 ft and those on Site C, 10 ft.

The progenitor map was taken from a real piece of contiguous U.S. land mapped with real contours. The contours were changed just enough to rule out easy identification of the specific area used. This process, accomplished by a draftsman without knowledge of the end purpose, insured against biases in favor of or against extreme topological features. A sensible "average" topography resulted. The resulting model topographic map is shown as

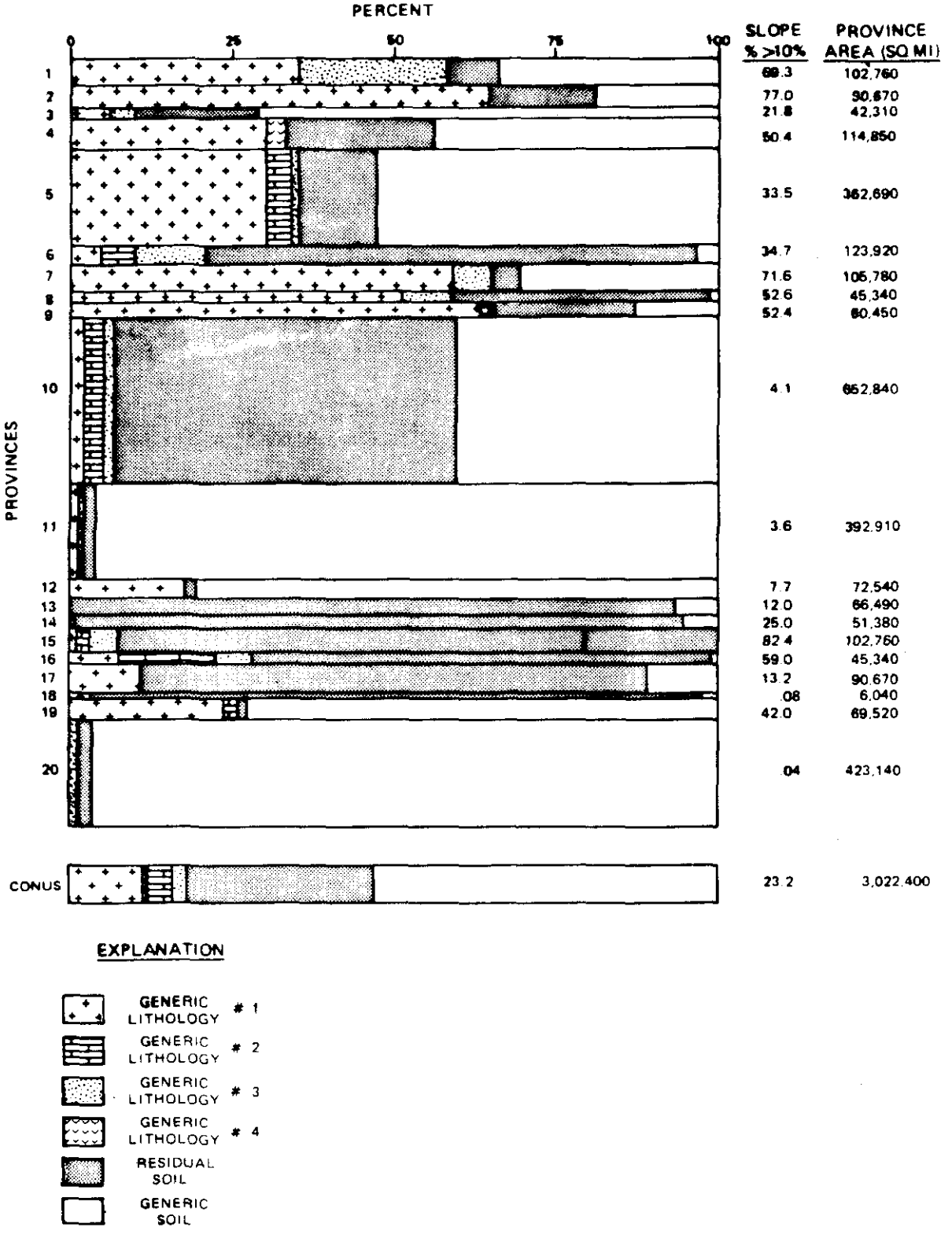

Figure 6.2-3. Surface distributions of generic geological materials in 20 U.S. physiographic provinces.

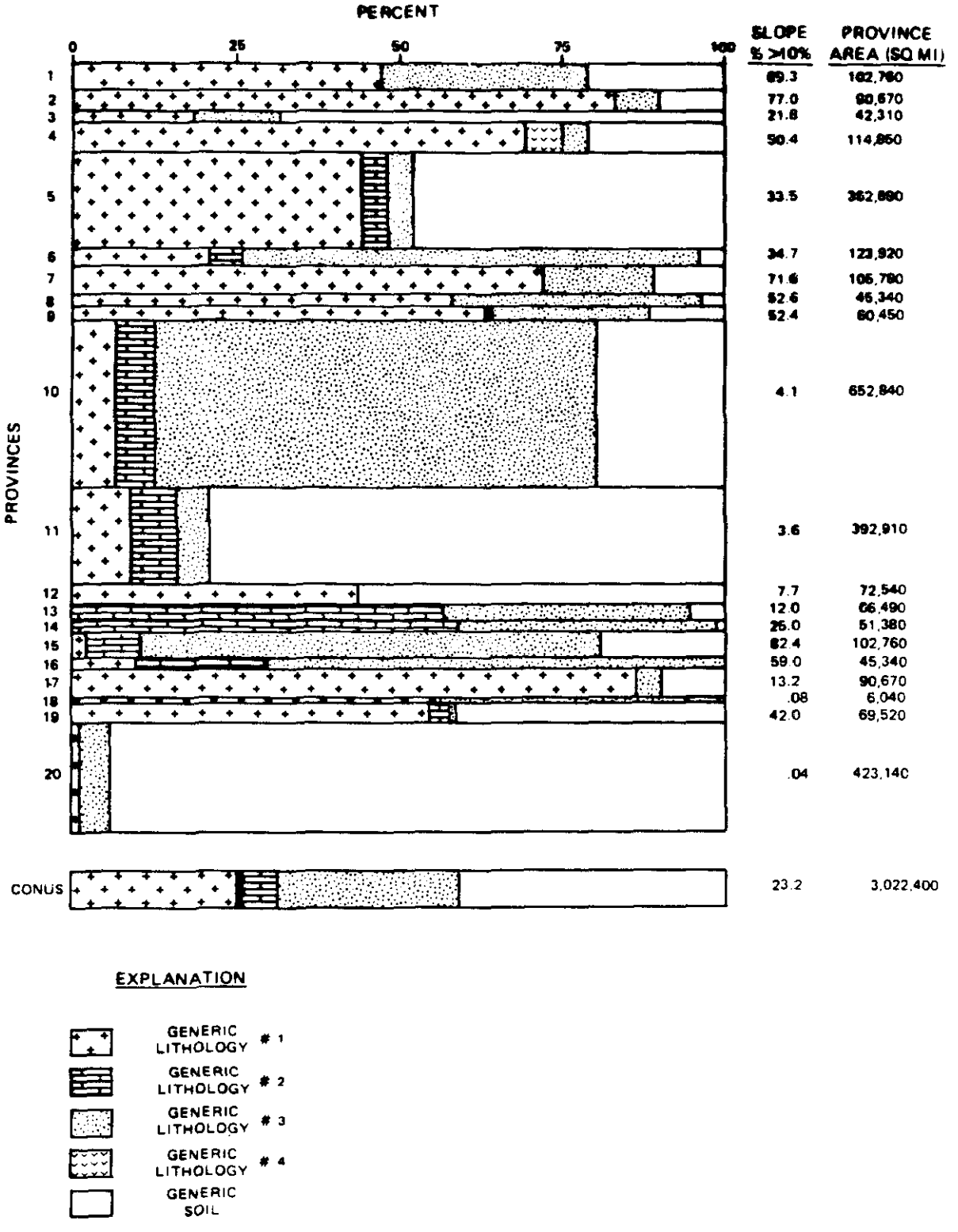

Figure 6.2-4. Distributions at a depth of 50 ft of generic geological materials in 20 U.S. physiographic provinces.

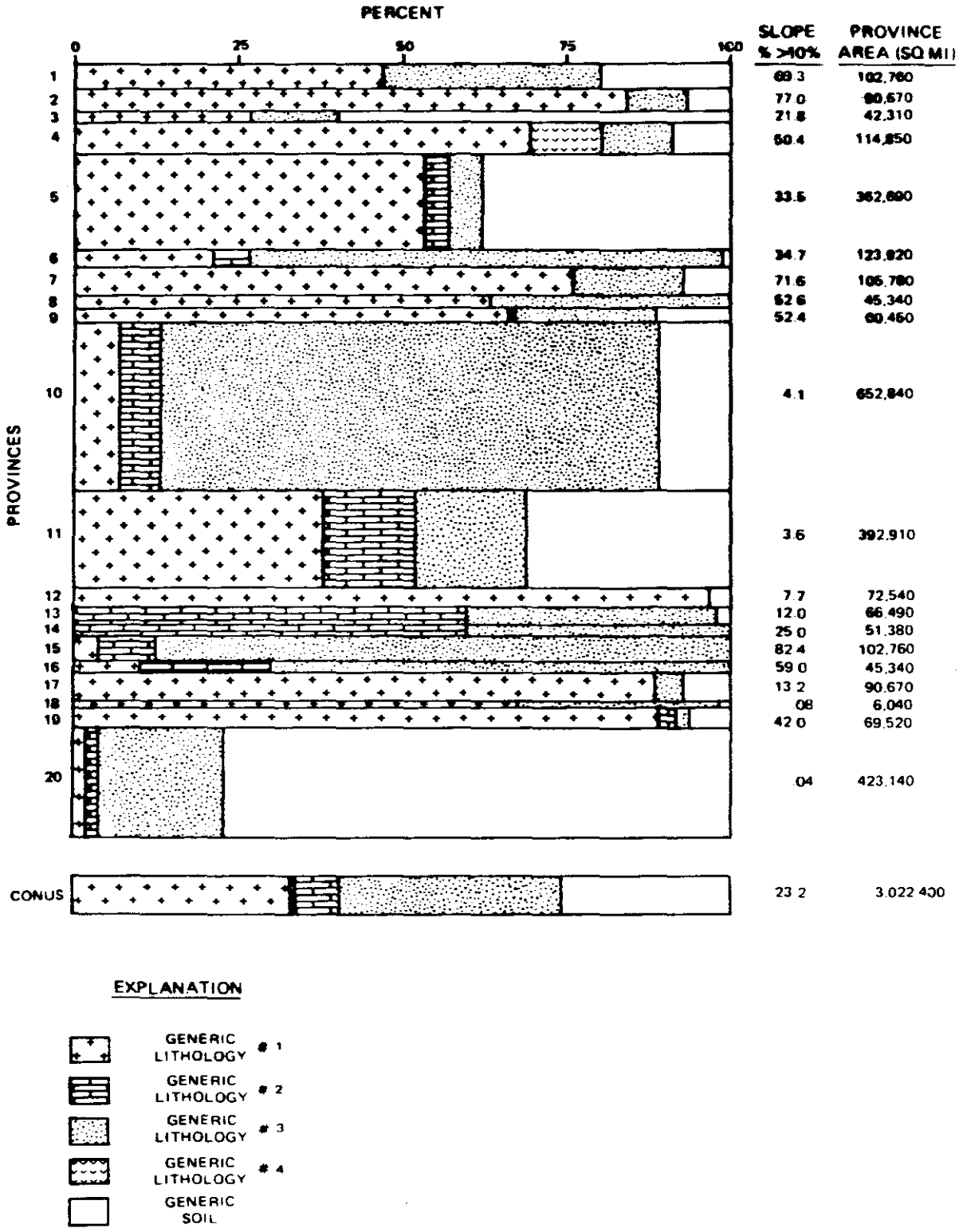

Figure 6.2-5. Distributions at a depth of 150 ft of generic geological materials in 20 U.S. physiographic provinces.

Fig. 6.2-6. The site exhibited in the included figure is that of Example Site A, but the other two differ only in the contour interval.

The last element needed for site modeling is the inclusion of materials variability and scale of distribution for the generic geological materials upon the model topographies. It was possible to characterize the three-dimensional variability of materials mixing and the typical sizes of generic rock and soil elements in a realistic way. The result of this process was a set of three useful stratigraphic lithologies, made up of generic materials and combined with the scaled topographies. These models constitute the three example sites. At each site, two inactive fault lines crossing the site were included so that their influence on tunnel construction could be estimated.

6.2.5 Facility Site-Orientation Models

With the modeled example sites in hand, the remaining conceptual design exercise resembled the process that would be followed with a real site. For each example site, a "best" orientation was found for the collider tunnel relative to the model site, so the tunnel could be constructed at least cost, while meeting all technical constraints of the accelerator design. These constraints included obvious ones such as prescribed vertical and horizontal tunnel-position variations from nominal and freedom of the tunnel from seepage of water. There was also a less obvious constraint on ring tilt. This last relates to specification of the accelerator rings as planar ovals with an allowed overall tilt (or slope) relative to the site-center gravitation vector. This tilt is not allowed to exceed one-half degree. The ring-matching process to the example sites and its relationship to optimum tunneling technology is described in the next section of this chapter.

One idea has been advanced to moderate the difficulty of fitting an acceptable elevation variation to a site with difficult topography for a planar ring. This concept would allow the collider rings to have a "fold" with a half-angle of one-half degree. This idea is discussed in Section 4.2.7, but has not been implemented in any of the three developed example sites.

6.3 Tunneling and Collider Enclosures

6.3.1 Introduction

Three geotechnical example sites for the SSC were developed and described in Section 6.2; the appropriate cost-effective construction methods for providing SSC collider tunnels for each are evaluated in this section. The gently rolling Site A, with its deep layers of soil and soft rock is appropriate for a bored tunnel using a soft-ground Tunnel Boring Machine (TBM). Site B contains hard, competent rock at relatively shallow levels and a rapidly varying surface topography; this site is ideal for a TBM-bored hard-rock tunnel. The flat, level topography of Site C, and the general absence of near-surface rock formations, implies the suitability of a predominantly cut-and-cover excavation with the use of precast-concrete tunnel sections for construction of the tunnel on this site.

The conceptual design by RTK of cost-effective tunnel construction methods for each of these characteristic sites has important ramifications for estimating cost and schedule

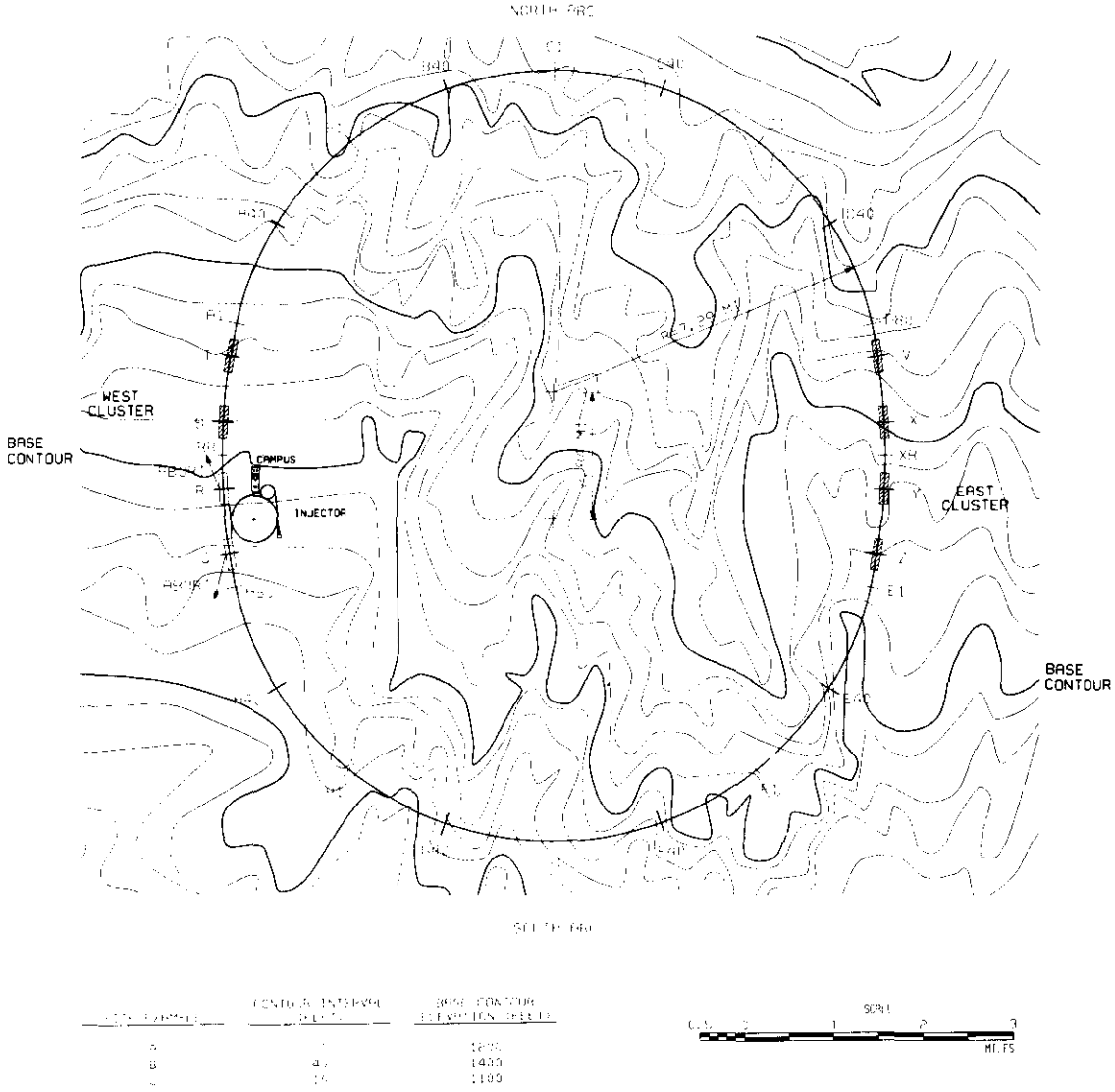

Figure 6.2-6. Topographic map used in the example SSC sites; vertical scaling was used to scale the topography in an appropriate way to each of the three example sites.

parameters (as well as proper contingency values) for the SSC project. The tunneling methods described in this section and documented in Attachment C cover a wide variety of practicable sites for the SSC in the contiguous U.S. and they suggest practical, conceptual plans for constructing the facility on such sites. In particular, the carefully developed parameters given in Section 6.2 provide valuable engineering tools that can be applied to the optimization of construction planning at the chosen real site. We proceed to discuss tunnel construction methods at each of the three example sites.

6.3.2 Site A Tunnel

The unconsolidated soils and soft rock of Example Site A require a bored soft-ground tunnel as noted above. The topography and lithology of Example Site A, along with the chosen tunnel route, is shown graphically in Fig. 6.3-1. This figure is an unrolled "lampshade" diagram of the geological features of Site A along the route of the collider tunnel. Since the ring is oval in shape and is tilted with a 0.26 degree slope to fit it better onto the site, the tunnel path on the diagram appears as a smooth sinelike curve at a nominal depth of 50 ft below the surface. From the materials distribution patterns in the diagram, the geological characteristics of the land are apparent.

The tunnel is bored in phased segments with an array of ten soft-ground and rock tunnel boring machines (TBMs). The soft ground machines have a tooth-cutter working face that is followed by an attached cylindrical steel shield that supports the unexcavated earth immediately behind. As the TBM advances, an earth-retaining structural tunnel liner in the form of segmented concrete sector pieces is installed behind the TBM support shield. The sector liner is typically made of prestressed concrete pieces that form a cylinder of lesser diameter than the cutting head and shield. In this way, the liner can be assembled into its hoop shape within the rear portion of the shield. The space between the tunnel liner and the surrounding soil is packed with pea gravel as the shield moves on. Grout is later forced into the pea gravel to consolidate it and make the tunnel impervious to water. Finally, at a later stage, a concrete invert is poured to create a flat concrete floor at the chosen level in the circular tunnel.

Important characteristics of a soft-ground tunnel-boring machine include its steering and thrust systems, its ability to control a crumbling or water-bearing face and the compatibility of liner placement with continued excavation and muck removal. In contemporary machines, suitable solutions have been found for all these considerations. Steering and thrust are provided through the action of large hydraulic cylinders interposed between the rear-placed gripper arms and the movable cutter head. The shield tracks the cutter head and can execute gradual curves and changes in direction provided by the cutter-head guidance system. The differential force that can be placed across the excavation face by the hydraulic steering cylinders is also used to compensate the external steering forces that result from inhomogeneous materials encountered across the excavated face.

Muck from the excavated face is carried away using a system of conveyors, cars and lifts to the nearest muck-removal shaft. For the SSC tunnels, it is envisioned that these shafts will be at intervals of 4 km (2.5 miles) in the north and south arcs and at closer intervals in the east and west cluster areas. For the arc sections, the starter tunnel areas and muck removal points will coincide with permanent access shafts needed at the Sector Service Areas and at the Sector End Points midway between these buildings.

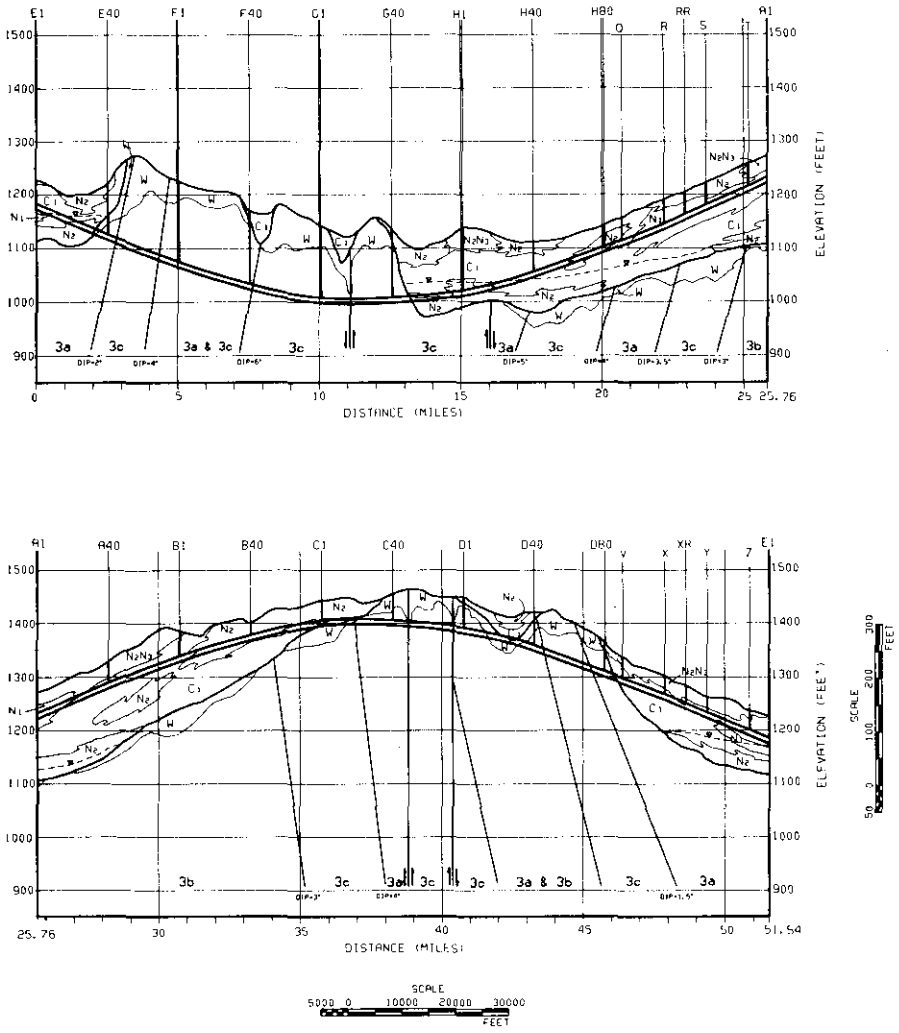

EXPLANATION

ROCK UNITS

3a	SEDIMENTARY SANDSTONE
3b	SEDIMENTARY LIMESTONE
3c	SEDIMENTARY SHALE
3a & 3c	THIN(1/2"-24") INTERBEDDED UNITS
W	WEATHERED ZONE

SOIL UNITS

C_1	SILT
N_1	CLEAN GRAVELS
N_2	GRAVEL WITH FINES
N_3	CLEAN SANDS

SYMBOLS

	CONTACT MARKING SHARP OR GRADED CHANGES FROM ONE UNIT TO ANOTHER
	MAJOR SHEAR ZONE
	TOP OF GROUNDWATER TABLE
•	ALL DIPS ARE CONSIDERED APPARENT DIPS

Figure 6.3-1. Topography and lithology along the route of Example Site A, the soft-ground tunnel exercise.

Disposal of the excavated soil from the tunnel will depend on detailed circumstances that obtain at the actual SSC site. Clean, relatively uniform fill from tunnel excavation in this type of soil is often in demand as fill for related and unrelated construction projects simultaneously underway in the local area. Even if there is no active demand for the spoil, it is not expected to constitute a disposal problem.

Excavation of the access shafts to the tunnel level, creation of the starter tunnels where the TBMs will be assembled and excavation of local side cavities associated with the refrigerator and vent shafts at the Sector Service Areas and Sector End Points will be accomplished by methods best suited to the local materials. For access shafts down to about 15 m (50 ft), surface-based excavation with power shovels and clamshell excavators should be adequate. Starter tunnels for the TBMs, placed off to the side of the collider tunnel, are needed as a result of the fact that the access shafts cannot be located directly on the centerline of the collider tunnel. This constraint comes from the radiation-shielding requirements. Instead, the TBM is started at the bottom of the access shaft. It bores its way toward the collider tunnel at a shallow angle and joins it a hundred meters downstream. The starter tunnels, later equipped with concrete block radiation shielding labyrinths, constitute permanent access paths to the collider ring for personnel and small equipment.

6.3.3 Site B Tunnel

Example Site B, shown in the lampshade diagram of Fig. 6.3-2, has a relatively steep topography underlain by hard, competent rock in near proximity to the surface. Such a site is a good candidate for a TBM-bored hard-rock tunnel. The hard-rock TBMs are equipped with carbide-tipped disk cutter heads. These machines have largely replaced the old drill, blast and muck methods in hard-rock tunneling. As a result, tunnel boring in hard rock has realized significantly increased rates of advance and reduced labor costs. There is reason to believe that even better advance rates can be achieved with new hard rock TBMs.

The optimum collider tunnel placement on Site B resulted in a tunnel at a mean depth of 150 ft below the surface and having an overall slope of 0.48 degrees. The lithology of Site B and the path of the tunnel through it are apparent in the figure. Except for the depth of the access shafts and the different type of TBM used for boring, the hard-rock tunnel follows the same general plan as the soft tunnel of Site A. Again, ten TBMs are used, starting at different points along the collider. Access shafts are sunk and starter tunnels bored at shallow angles to the collider tunnel. Muck-removal systems are essentially the same.

There are, however, some significant differences between the hard-rock and soft tunnels. Most important is the fact that the hard-rock tunnel is bored in mostly (90%) self-supporting rock. There is no need for a structural tunnel liner in most of the tunnel (although such liners may be needed in shear zones where crushed and broken rock is encountered). If water invades the tunnel through such fault zones, shotcrete or tunnel liners can be used locally to control it.

6.3.4 Site C Tunnel

The tunnel for Example Site C is constructed by a distinctly different method from the TBM-bored tunnels discussed for Sites A and B. In this case, the flat topography and the near absence of surface rock outcroppings suggest a cut-and-cover approach for construction

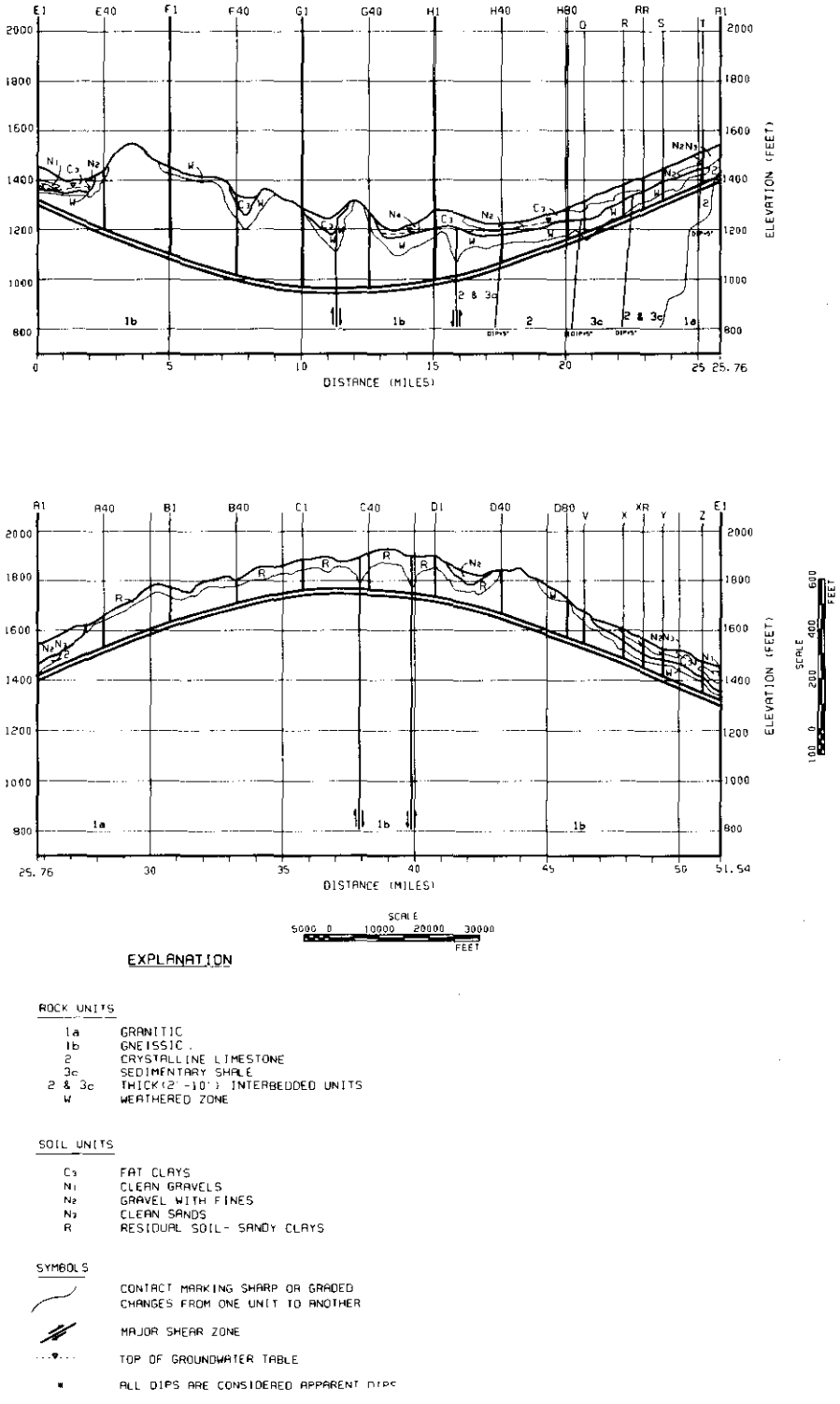

Figure 6.3-2. Topography and lithology along the route of Example Site B, the hard rock tunnel exercise.

of the collider tunnel. The site topography and lithology are exhibited in the lampshade diagram of Fig. 6.3-3.

As can be seen from the figure, most of the collider ring is near the surface. The tunnel is placed just deep enough so that the needed radiation shielding cover of twenty feet of earth can be maintained with a modest earth berm. The tunnel itself consists of a sequence of precast concrete tunnel sections placed in an excavated trench. The precast units are covered over with earth to constitute the radiation shield. After the tunnel is covered with its earthen shield, a concrete invert is poured to achieve a final tunnel cross section with the same size and shape as in the bored tunnels discussed previously. The overall slope of the tunnel is 0.13 degrees, a relatively gentle slope chosen to optimize the cost of excavation and final earth cover for the finished tunnel.

In this construction approach, the tunnel can progress at a very rapid rate compared to underground boring methods. It is the only method, however, that is sensitive to weather conditions at the site. Average rainfall, winter freezing and existing surface water will all play a role in scheduling and carrying out the work. The excavation, on the other hand, can be simultaneously undertaken at a larger number of locations if that is deemed practical. A casting plant or plants to produce and supply the precast concrete tunnel sections will be placed in convenient proximity to the construction work.

The ditch itself is excavated by ordinary earth scrapers which excavate the soil to the required depth. When the excavation is ready, the precast concrete pipe sections are set in place by cranes and sealed together with grout or epoxy. The outer surface of the concrete is damp-proofed with a sprayed-on moisture barrier after which the tunnel is covered, first with granular fill and then with the previously excavated site soil. In the areas with rock outcroppings, explosives are used to shatter the rock before excavation, as in road construction in hilly or mountainous regions. In stretches with significant amounts of preexisting ground water, diversion and dewatering with pumps are used as appropriate.

For the cut-and-cover tunnel construction method, the access shafts and alcoves are particularly simple to construct. They are excavated with power shovels and backhoes and formed with cast-in-place reinforced concrete. The interaction region experimental halls are likewise constructed in open excavations and earth shielded for radiation protection. As described in the Siting Parameters Document, a cut and cover site requires dedicated use of the lands above the tunnel. This is not true for the other two example sites. Because of the muon radiation conditions discussed in Section 6.9, there are important environmental impacts in Site C not encountered in the much deeper sites A and B.

6.4 Central Laboratory Facilities

6.4.1 General Features

The personnel associated with the SSC are concentrated in two areas on the east and west sides of the SSC. The west area is the location of the Central Laboratory Facility and of all the administration, support and technical services for the facility. On a 500-acre campus are located the large Central Laboratory Building, the six Heavy Works Buildings, the three Shops Buildings, the two Warehouse Buildings and several ancillary structures for medical, fire and police protection as well as for other conventional services. This area will

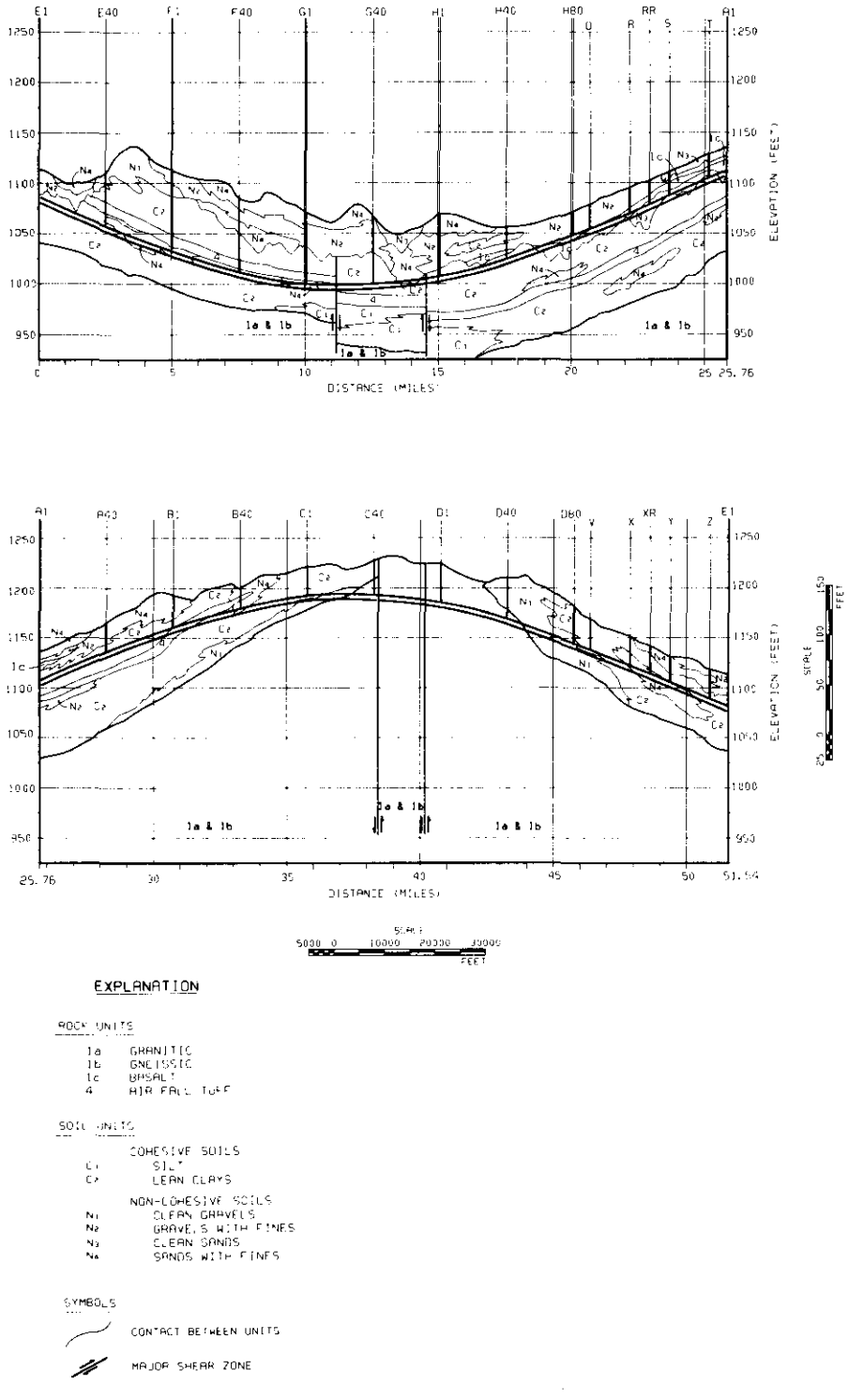

Figure 6.3-3. Topography and lithology along the route of Example Site C, the shallow cut-and-cover trench tunnel example.

typically accommodate about 2000 people associated with the SSC. This section describes the central laboratory facilities in sufficient detail to establish a clear conceptual basis for this part of the SSC facilities.

6.4.2 Site Arrangement and Plan

Figure 6.4-1 shows the arrangement of buildings in the Central Campus and their relationship to the injector facilities. The office and shop buildings are located in the vicinity of the service areas of the injector accelerators and to the injection and extraction areas of the collider ring. Such a location scheme is not only efficient for facility operations but also aids in land utilization and construction phases of the project. The buildings of the Central Office and Laboratory Facilities Area are listed in Table 6.4-1.

Table 6.4-1
Central Facility Buildings

Central office and laboratory	34,100 m^2 (367 K ft^2)
Heavy works buildings (2)	4,000 m^2 (43 K ft^2) ea.
Heavy works buildings (4)	1,800 m^2 (20 K ft^2) ea.
Shop buildings (3)	930 m^2 (10 K ft^2) ea.
Warehouses (2)	3,600 m^2 (40 K ft^2) ea.
Ancillary buildings (5)	2,880 m^2 (31 K ft^2 total
Total floor area	62,200 m^2 (674 K ft^2)

The planned central campus occupies a roughly rectangular area of dimensions 900 m (3000 ft) by 1660 m (5440 ft). The dominating structure on the site is the four story Central Laboratory Building. This building stands at the main entrance to the laboratory and is surrounded by landscaped grassy areas close to the building and parking lots nearby. Near to the Laboratory building are the six heavy works buildings arranged in a cluster with parking lots around the outside and paved loading and hardstand areas inside. Secondary roads pass by on either side of the cluster and allow efficient access by delivery vehicles up to the largest size as well as clear lanes for emergency vehicles such as fire trucks and ambulances.

Beyond the heavy works buildings are the three shops buildings in a linear array that relates directly to the heavy works buildings that they will supply with specialized fabricated parts and components for the detectors and other pieces of experimental apparatus. The shops buildings also have parking lots plus loading and hardstand areas. These are in general smaller than those for the heavy works buildings, reflecting the smaller scale of their operations.

At the end of the central facilities area are two warehouse buildings used for shipping, storage, receiving and inventory control. These two large buildings will have surrounding

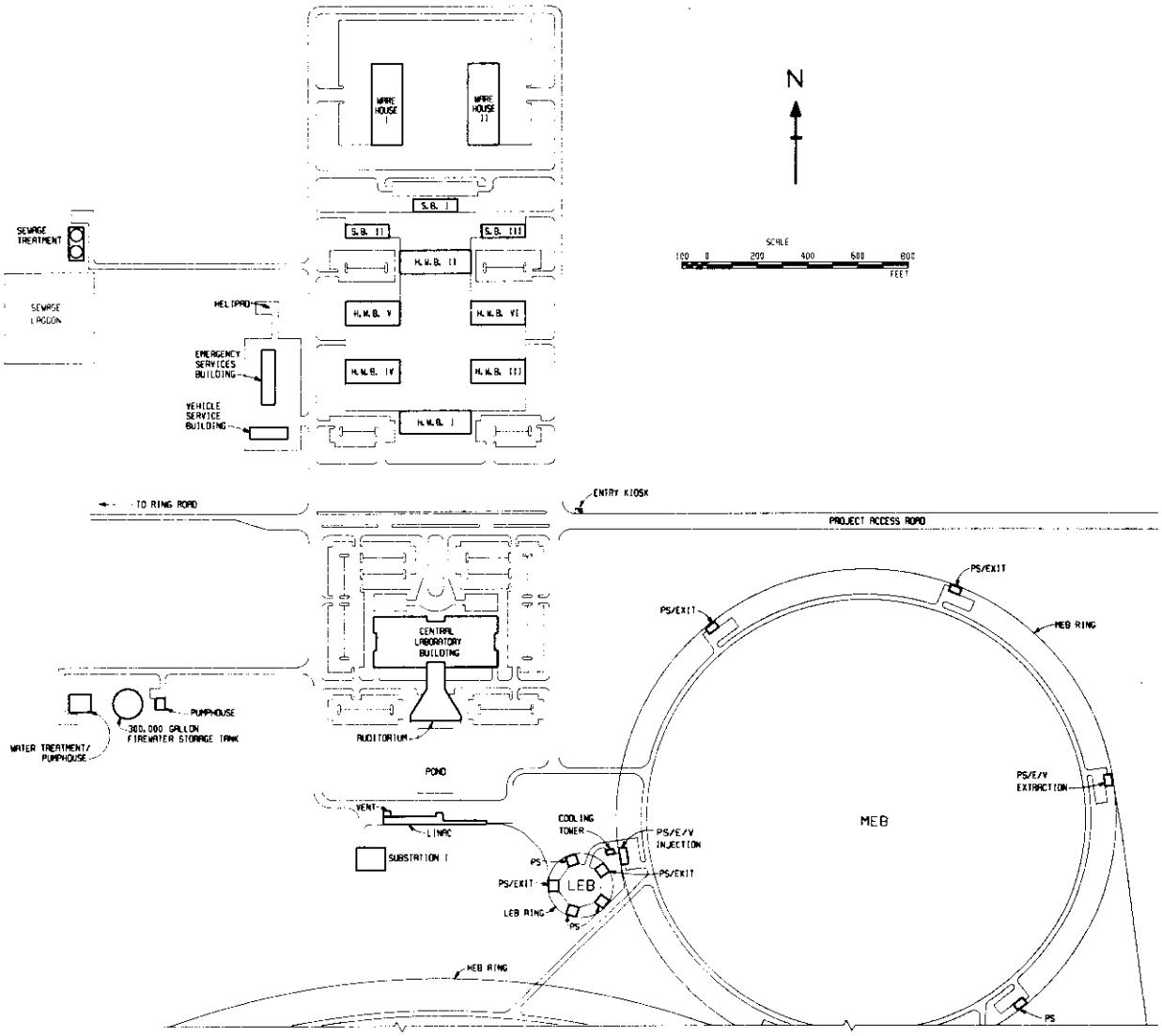

Figure 6.4-1. Layout of central campus relative to injector complex.

hardstand areas, some with security fences for outside temporary storage of large or unwieldy items that do not require inside storage.

Separate from the large building complex but close by are several small, special purpose buildings. The combination fire, rescue and site-control building is one of these. It is located on one of the main site roads to insure easy and rapid access of emergency vehicles to any of the buildings in the central facility, to the service buildings of the injection accelerators and to the west cluster interaction halls. Response time to arrival at the furthest of these buildings following receipt of an alarm is at most a few minutes. Sharing a building with the firemen is a small headquarters of the site-security force. In addition to the site-security office, there is a small kiosk located between the incoming and outgoing traffic lanes at the main entrance to the facility. This will constitute shelter for the security personnel during off-hours periods.

A second ancilliary building houses the vehicle maintenance shop. With a site as large as SSC, a substantial fleet of trucks and vans plus a large number of passenger cars are needed. They are fueled and serviced at the motor pool maintenance service shop. A parking lot and temporary vehicle storage lot stand adjacent to the motor pool building. At the far end of the site is located the water treatment facility that treats makeup water coming onto the site in appropriate ways to meet the needs of site potable, low conductivity, fire-protection, and cooling water use. Also removed from the main building cluster is a sewage-treatment facility with pumphouse and settling ponds. Treated water, meeting all local release standards, is used for irrigation purposes around the site or released to the local creek system.

All site roads are paved. The two main north-south roads that border the central facilities cluster are secondary roads with 7 m (24 ft) wide paving with parking shoulders designed to support arterial traffic. The side and building access roads have 7 m (24 ft) wide paving and narrower shoulders; they are designed for local traffic only. Hardstands are mainly crushed aggregate while parking lots are paved. The paving of all roads and parking lots is asphalt over the appropriate crushed aggregate base.

6.4.3 Central Laboratory Building

Most of the people on site will have occasion to visit the Central Laboratory Building regularly and a majority will have this building as their principal work area. This building will contain the main control room for the entire accelerator complex. The building is envisioned to be four stories high and is arranged in four wings adjacent to a full-length central atrium. A practical floor plan for this building could be as shown in Fig. 6.4-2. Such a building would house a cafeteria and food-preparation area. In the plan, there is a 1000-seat auditorium, several small meeting rooms, and a larger meeting room for up to 200 people. The campus entrance wing of the building is laid out for office space. A typical office is 4 m (13 ft) deep and multiples of 3 m (10 ft) wide (determined by movable partitions). The office space planned will accommodate 1200 people with a mix of professional, clerical and secretarial personnel. In the two wings of the building facing the works buildings are located the technical and laboratory areas on each of the three upper floors. The basic module is 9 m (30 ft) wide by 15 m (50 ft) long, with double-wide access doors at each end opening into access corridors. Provisions are made for routing normal laboratory services (electricity, water, natural gas, compressed air and waste lines) vertically through

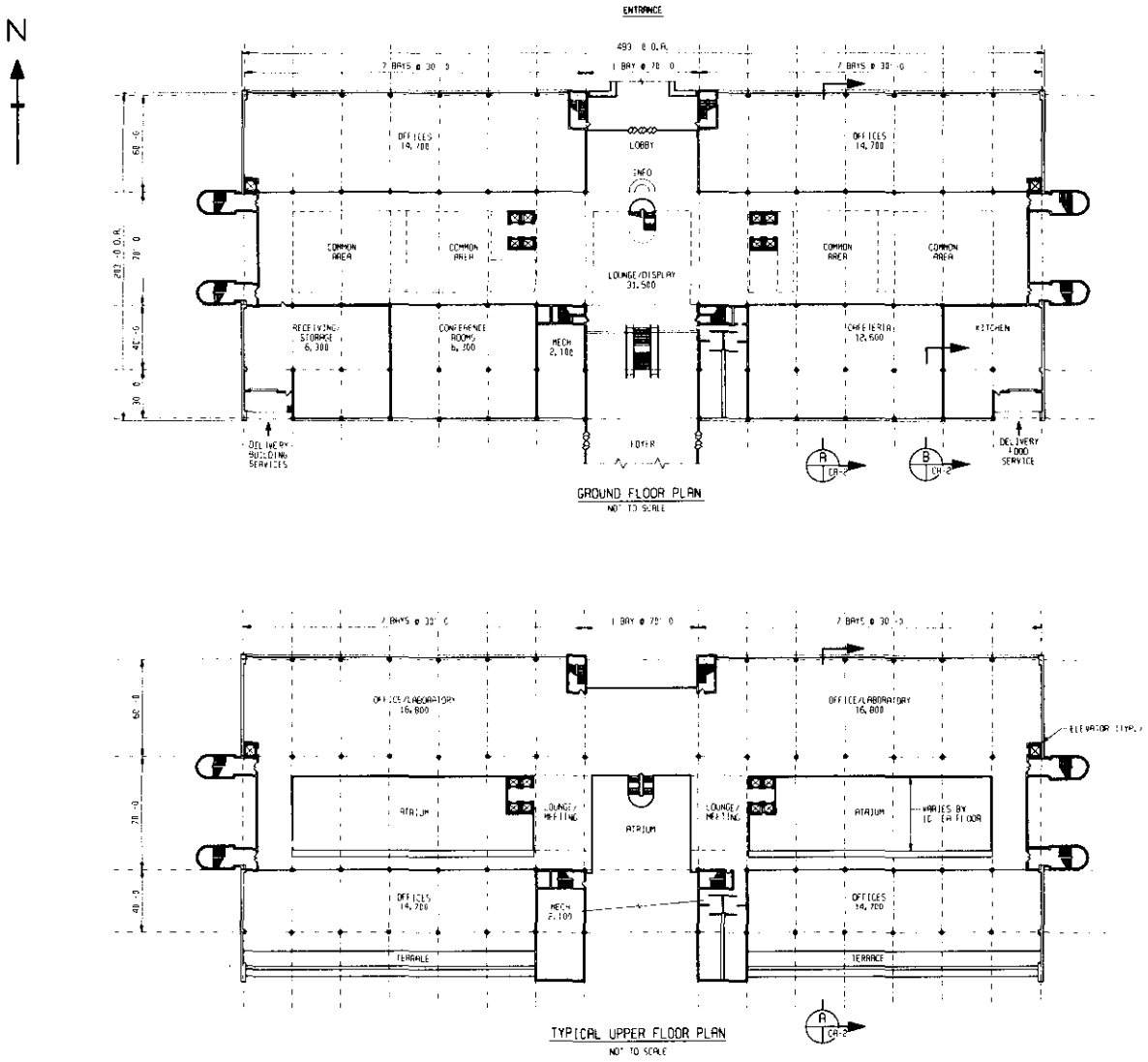

Figure 6.4-2. Floor plan of a typical storey of the Central Laboratory Building.

utility shafts that abut the corridors. These walls will also contain built-in equipment cabinets. Laboratory rooms on the top floor have provision for chemical hoods and fan-equipped exhaust air vents. Floor loading for the laboratory space is 600 kilograms per square meter (150 lbs per sq. ft).

The small conference rooms are located off the atrium on the ground floor of the building. The elevator clusters are centrally located and the fire stairs are placed at the ends of the building wings. The cafeteria is located on the main floor off the atrium; the food-preparation and storage rooms are next to the cafeteria. The main auditorium is separate but attached to the main structure. Building service machinery is located in equipment bays on each floor. In this area are located the building heating and ventilating equipment, pumps and motors.

6.4.4 Heavy Works Buildings

Each of the six heavy works buildings is designed for construction and manipulation of large and heavy objects such as components of the experimental detectors. The two largest feature single high-bay work areas 18 m (60 ft) wide by 85 m (280 ft) long by 15 m (50 ft) high (Fig. 6.4-3). Two thirty-ton cranes ride on rails above the high bay area. In a side bay of the building, is a two story mezzanine area with office and work space. Each level has an office floor area of dimension 9 m (30 ft) by 85 m (280 ft) broken into three sub-areas separated by stairwells and toilet facilities. A concrete block wall between the high-bay work space and the office areas provides appropriate sound insulation. The ground floor under the mezzanine area is devoted to a machine shop, supply rooms, a tool crib and building services rooms. The building services include heating and ventilating equipment, water pumps, air compressors and electrical switchgear. Outside the building is a power transformer and oil switch which transforms primary site power down to the 480 V feeds for the building's main switch-boards. Each of the two heavy works buildings has its own 750 KVA transformer.

The four smaller heavy works buildings are sized to produce smaller and lighter objects, such as conventional beam transport magnets or detector sub-assemblies. Each of the four has a common floor plan with a high-bay work area and an adjacent office/shop area. The shop space is given over to small shop areas, a tool crib and materials storage areas. The high-bay areas are 18 m (60 ft) wide by 66 m (220 ft) long by 12 m (40 ft) high. One thirty-ton crane travels on rails above the high-bay areas. A fifteen-ton crane covers the smaller bays, which have floor dimensions of 9 m (30 ft) wide by 66 m (220 ft) long. Also, following the pattern of the larger heavy works buildings, the building services systems are located in one end of the buildings. Electric power comes from 300 KVA transformers located outside.

All the heavy works buildings are based on steel-framed structures erected on steel-reinforced concrete foundations. Walls are foam-insulated metal sandwich panels and glazing for the office areas is done with energy-conserving double thermopane glass. Roofs are steel decked with insulation board and single-ply moisture membranes. This construction method results in sturdy, cost-effective structures with minimum maintenance costs.

The heavy works buildings and high-bay areas have heating and ventilation systems. The large roll up doors are of the insulated type to aid in energy conservation. Fire protection is accomplished by ceiling-mounted sprinkler heads. There are also smoke detectors

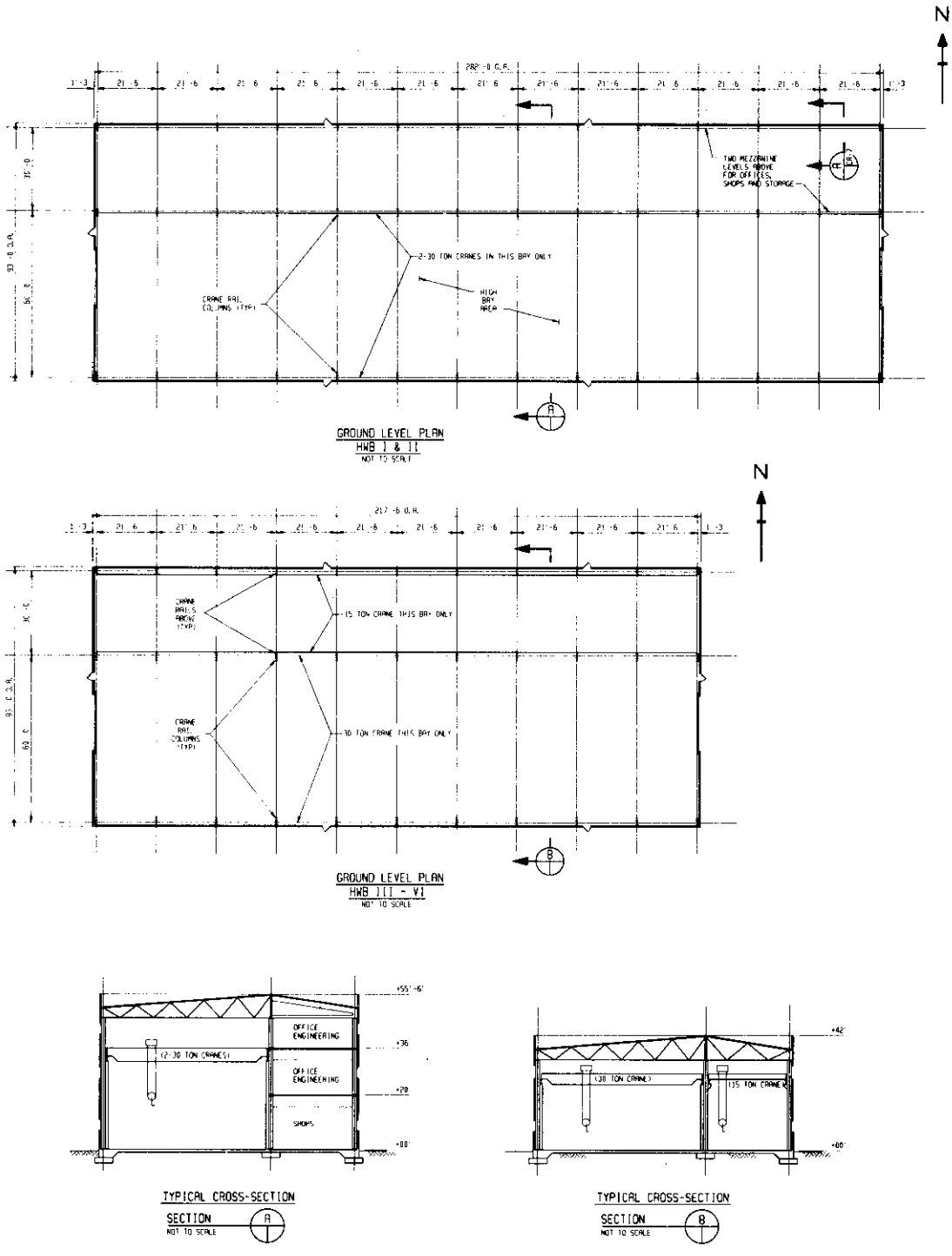

Figure 6.4-3. Floor plan for large Heavy Works Building showing main floor and mezzanine floor plans.

connected to a site-wide fire alarm system. Hand-held small extinguishers are located along area walls in clearly marked accessible locations.

Area lighting in the high-bay areas is done with high-intensity discharge metal-vapor lamps at the ceiling. Office areas have suspended acoustical-tile ceilings for noise control and are lighted with fluorescent tubes. Normal services in the high-bay include periodic electrical outlets for 480 V, 208 V and 115 V applications. Compressed air is available around the outer high-bay periphery, supplied from a local air compressor.

6.4.5 Shop Buildings

There are three single-story shops buildings, one of area 15 m (50 ft) by 66 m (220 ft) and two of area 15 m (50 ft) by 53 m (175 ft); all have a 9 m (30 ft) ceiling height. The two smaller buildings each have one 2-ton and one 5-ton crane mounted to move lengthwise along the entire area (Fig. 6.4-4). The larger shop building has one 5-ton and one 10-ton crane. The space in these buildings is used for various shop and technical fabrication activities. One of the buildings is given over to use as a main machine shop. In this shop are located the largest machine tools belonging to the SSC facility. A tool crib and small office area are also included in this shop.

A second shops building is given over to carpenter shops, sheet metal shop and welding shop work. Each of the three shop sections has its own supply area and tool crib. There is a small office area for job management. Each activity area has its own roll up door and personnel access doors, but all areas share the overhead cranes, which are radio-controlled and can move freely over internal partitions without problems of interference.

The third shop is for technician work, especially the fabrication and repair of cryogenic systems components. This type of activity suggests a single large work bay interrupted only by a small office area for job management and a tool crib. Individual work stations are delineated only by tool chests and metal cabinets which can be moved around on a job-to-job basis as the work demands.

All the shops buildings are constructed of structural steel frames on a reinforced concrete slab at ground level. Siding is a double metal-surface, foam-insulated panel with good insulation characteristics and modular sizing. Double-glazed windows in the shop office areas provide light and energy efficiency. The roofs are of the shallow-sloped metal-deck variety with fiberglass insulation and single-ply membrane. Lighting in the shop areas is from high-intensity discharge metal-vapor lamps near the roof, while fluorescent tubes are used in the office and drafting areas. Fire protection is accomplished by overhead sprinklers and by hand-operated small extinguishers located at clearly marked places along the outside walls.

A 300 KVA transformer supplies electric power to each shop building; each also has its own 480 V switchboard and transformer breakdown to 208 V and 115 V. Compressed air for each building is provided by means of a small compressor in each shop building. The buildings are heated, and roof-mounted fans provide air circulation with outside air exchange. All shop buildings have toilet facilities and are serviced by domestic water and sanitary waste lines.

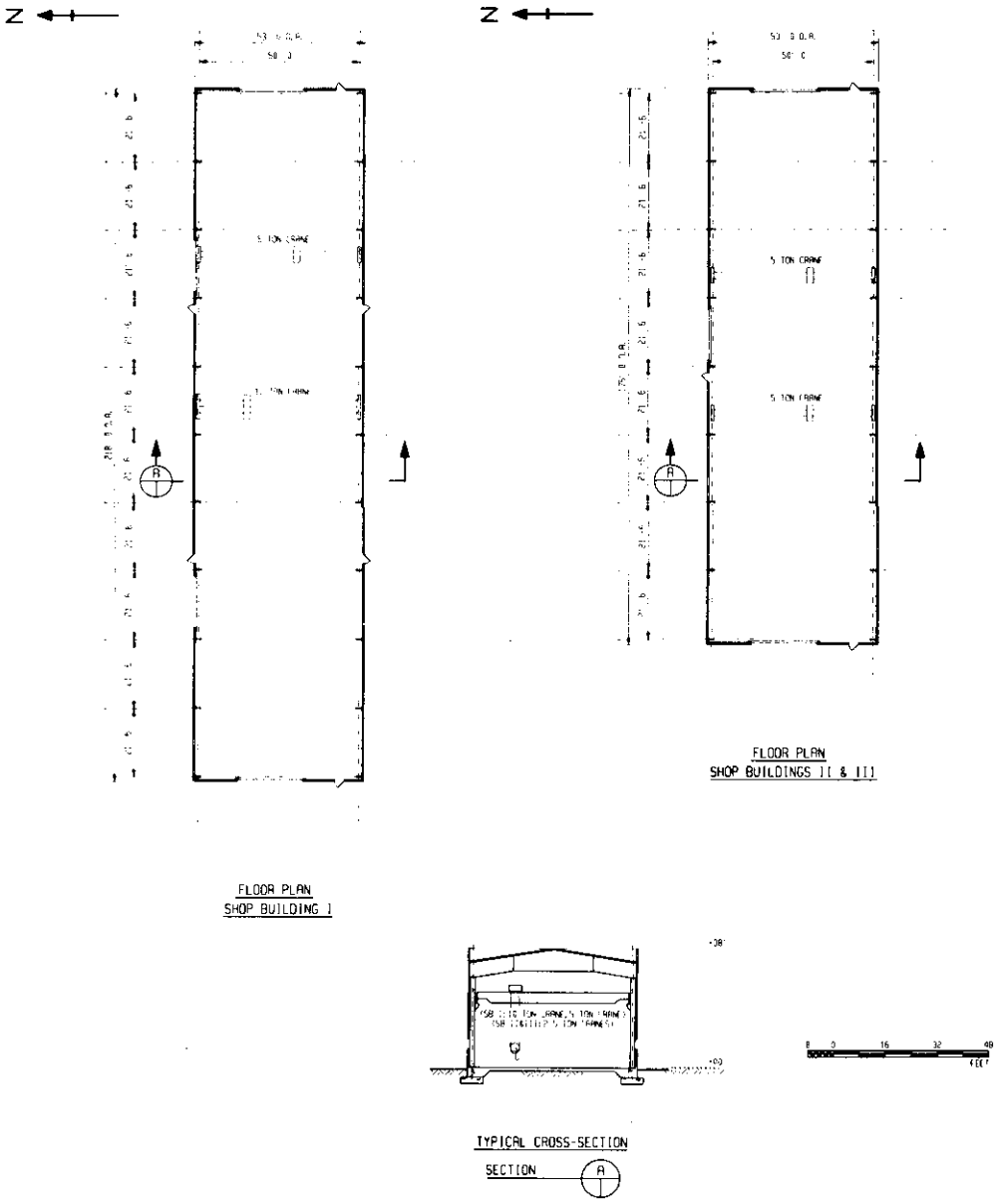

Figure 6.4-4. Floor plan of typical Shop Building showing work bay, office and toilet areas plus access doors.

6.4.6 Ancillary Buildings

The remaining buildings in the central facilities cluster are single-purpose structures of specialized function. They have the general property, however, of being constructed as one-story light steel-framed structures with insulated metal panel siding on concrete slabs at grade level. None of these buildings accommodates large or heavy equipment, so they are built to light commercial rather than industrial standards. Heating is via forced-air furnaces and lighting by fluorescent tubes. All have toilet facilities and are piped for potable water and sanitary waste. These buildings all have shallow-slope trussed roofs and are fiberglass insulated. All have sprinkler systems installed for fire protection and are equipped with clearly-marked hand-operated extinguishers at appropriate locations. The office areas of these buildings have suspended acoustical ceilings for sound control. We comment briefly on the individual structures.

The emergency services building is a 16 m (52 ft) by 66 m (216 ft) structure located just east of the heavy works building group. It has four full-depth vehicle bays for housing the fire equipment, small office and communications areas, a ready room and a domestic area for the fire crew. The site patrol and security operations occupy an area of dimensions 11 m (36 ft) by 15 m (50 ft) at one end of the building. This space includes office and communications areas. Behind this building is a hose tower for storage of fire hoses.

The vehicle and grounds maintenance facility consists of a 15 m (50 ft) by 46 m (150 ft) building, vehicle repair bays and supply areas. There are two repair bays with the capability of servicing passenger cars and small trucks, plus a small office area and a parts and supplies room. The grounds maintenance operations are located in a 13 m (43 ft) by 15 m (50 ft) area at one end of the building. The building has an air compressor to power lifts and tools. Outside the building is a set of fuel dispensing pumps connected to three 10000-gallon underground fuel storage tanks. The building is surrounded by a paved parking lot and a gravel hardstand storage lot.

The water treatment facility is a 11 m (35 ft) by 7 m (24 ft) pump house with room for all the needed water pumps. An electric power transformer stands near the pumphouse and feeds the major switchboards inside. The pumps are fed by 480 V power feeds and small amounts of 208 V and 115 V power are available for utility use. Outside, but near the pump house, is a large tank for water storage and consumption averaging. The tank always has a fire-water reserve adequate to supply water to a four-hour-duration fire in the campus area.

The Sewage Treatment Plant (Fig. 6.4-5) is an advanced treatment plant sized for the needs of the SSC facility. Waste is collected from buildings in the west cluster in a combination of gravity and pumped lines and brought to the treatment facility. The treatment facility is located away from the central building cluster, but close enough to lie on the site. At the plant there are settling tanks, digester tanks and three stages of waste water purification. Released water is of good quality for general surface water standards, but may be retained in a pond for site irrigation if needed. All local and federal water standards for release of the waste water will be met.

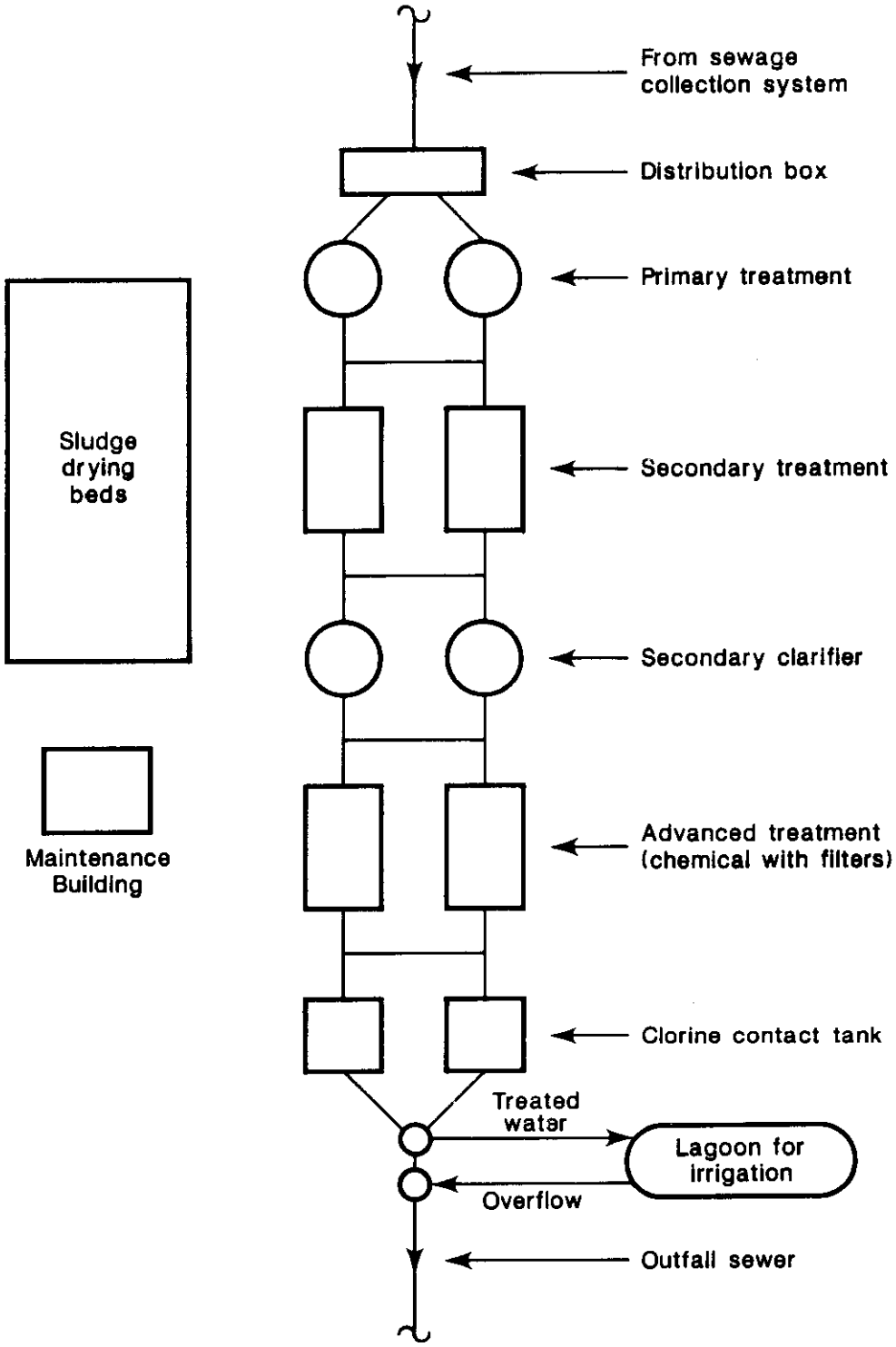

Figure 6.4-5. Facility layout of Sewage Treatment Plant, showing pumping facilities, settling ponds and runoff water scheme.

At the plant there are settling tanks, digester tanks and three stages of waste water purification. Released water is of good quality for general surface water standards, but may be retained in a pond for site irrigation if needed. All local and federal water standards for release of the waste water will be met.

6.5 Injector Facilities

6.5.1 Introduction

The cascade of accelerators, starting with the Linac and ending with the High Energy Booster (HEB), are all variants of existing accelerator designs and systems. Their design profits from knowledge gained in the construction and operation of their predecessors. The near-surface location of the HEB suggests that the injector complex be housed in shallow, cut-and-cover concrete enclosures and that earth-berming be used to maintain appropriate shielding thicknesses around the accelerators of the injector. The test-beam facilities are also located a few meters underground for the same reasons.

It is also clear that, once a specific site has been chosen, the detailed placement of the injector components will be optimized to suit the local topography. Finally, the decision to cluster the interaction enclosures in the east and west areas, and in close association with the injector, results in a strong concentration of utilities and people in the immediate vicinity of the injector complex and its associated campus. This approach to component placement strongly links the construction and operation phases of the injector complex with those of the campus and the interaction regions. The location of the test beam facilities is determined by location of the HEB from which the test beams are derived.

6.5.2 Linac

The first section of the injector chain is the Linac. It is a straight-line device 125 m (410 ft) long with relatively modest radiation-shielding requirements and heavy demands for rf power, cooling water and controls. The basic conventional construction parameters are given in Table 6.5-1.

Table 6.5-1
Linac Conventional Parameters

Enclosure size	3.6 m × 3.6 m (12 ft × 12 ft)
Enclosure length	151 m (494 ft)
Klystron gallery total floor area	1090 m^2 (11750 ft^2)
Electric power demand	
Peak	1.2 MW
Average	1.2 MW

The conceptual design for the Linac enclosure is shown in cross section in Fig. 6.5-1. The rf gallery is located above the linac structure in a configuration that facilitates a desirable close coupling between the rf source and accelerator drift tubes, while accommodating the intervening shielding that separates controls, rf power supplies and klystrons above, from the linac accelerator tube below. This design is based on successful existing machines and presents no unusual challenges.

The Linac itself is housed in a conventional structure of cast-in-place reinforced concrete; the accelerator gallery is shielded partly by earth and partly by a thick concrete wall with appropriate penetrations for rf system links and other needed umbilicals. There are personnel access stairways connecting the Linac enclosure with the klystron gallery and shop areas above. At one location there is a major equipment access point. As can be seen in Fig. 6.5-1, there is room in the gallery to the side of the Linac itself for installation or removal of any piece of the accelerator, as well as for routine maintenance of the installed equipment. The main utilities and services are routed along the wall to the side of the gallery away from the service aisle. Above the concrete accelerator enclosure and separated from it by radiation shielding, is a steel-framed, metal-paneled building housing the rf power supplies and linac associated work areas and offices. This structure is a conventional type.

The Linac accelerator is maintained by a staff whose working space is incorporated in the power supply gallery level of the Linac building. Routine operation of the linac machine, however, like all of the accelerators, is done from a central accelerator control center. Routing of the control cables is accomplished, via cable trays, through the Linac building and Booster Complex to the main control room. Needed conventional and radiation-safety systems constitute part of the overall controls system, and are routed back to the main control room also. In this way, personnel security is monitored and maintained from a single central point, facilitating appropriate area control with a minimum of needed shift personnel. This control pattern is repeated throughout the injector complex.

Fire protection consists of sprinkler lines as appropriate. Clearly marked CO_2 and dry-chemical fire extinguishers are located periodically along the walls in accessible locations for all the technical areas, and smoke detectors and alarms are part of the safety and controls systems.

6.5.3 Low Energy Booster

The Low Energy Booster (LEB) is the first circular accelerator in the sequence. Its magnets are arranged around a ring of circumference 250 m (820 ft). The magnets are non-superconducting and have large electric power requirements. Since the LEB is a resonant, fast-cycling machine, there is also a large rf installation. The basic civil construction parameters of this machine are displayed in Table 6.5-2.

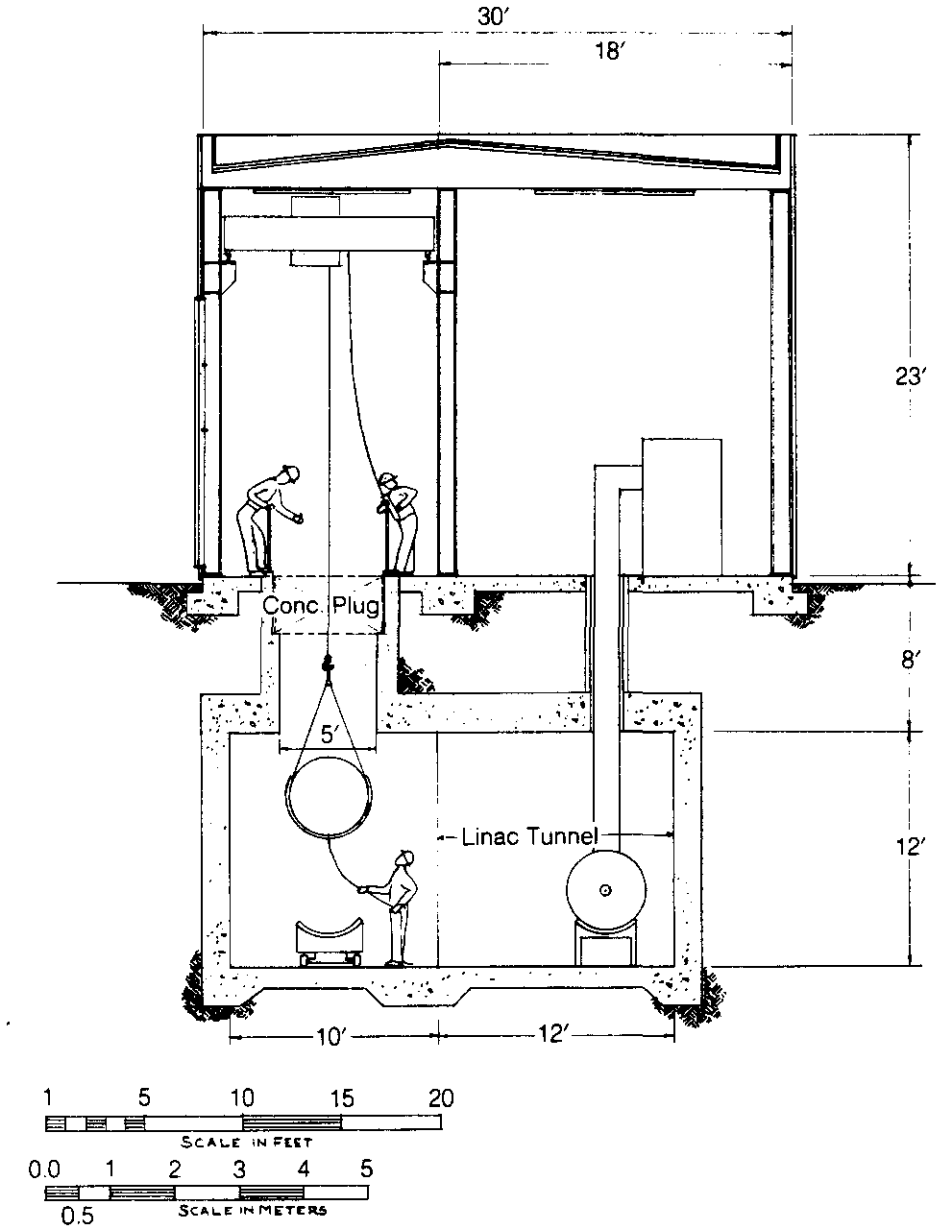

Figure 6.5-1. Linac Accelerator and Power Supply Gallery cross section showing the relationship of accelerator structure, rf klystron power supplies, tech/office areas and access aisles.

Table 6.5-2
LEB Conventional Parameters

Enclosure size	2.4 m × 2.4 m (8 ft × 8 ft)
Enclosure length (circular)	250 m (820 ft)
5 service buildings floor area	845 m^2 (9090 ft^2)
Electric power demand	
Peak	2.5 MW
Average	1.4 MW

The LEB requires five service buildings at ground level. The accelerator magnet ring is housed in a cast-in-place concrete enclosure located below ground, as shown in the cross section view of the LEB magnet enclosure and power supply gallery (Fig. 6.5-2). The needed radiation shielding is provided by earth fill between the accelerator enclosure and the power supply gallery and technical shop areas above.

The magnet power supplies, rf power amplifiers and control electronics are located in the power supply buildings above and offset from the accelerator gallery. There are also technician space and storage areas in these buildings. The gallery structure itself consists of a conventional steel-framed metal-paneled building erected on a reinforced concrete slab.

Personnel access to the accelerator enclosure is via a set of two stairwells, one of which is associated with a major equipment access. It is through this access that the magnets are installed and removed from the accelerator enclosure. The major equipment access is shielded with removable concrete blocks that can be lifted with mobile crane. Within the accelerator enclosure, wheeled carts are used to transport the magnets; hydraulic jacks lift them into place. This is in accord with current practice at existing accelerator installations.

Electric power for the magnets is provided via water-cooled copper busses connecting the DC power supplies in the power supply gallery to the magnet strings below. The copper coils for the magnets themselves are cooled with low conductivity water (LCW). The LCW supply and return mains are wall-mounted copper pipes with ceramic-insulated connections to the individual magnet manifolds. The system water is circulated from a central pumping station. The heat transfer is accomplished using cooling towers.

As in the Linac, the LEB is operated remotely from the main control room with control cables routed in trays along the power supply gallery walls and thence from the LEB through communication ducts to the main control room. Area personnel security plus conventional and radiation safety systems are also routed to, and controlled from the main control room. Fire protection of the LEB-gallery is accomplished by a sprinkler system with overhead lines as appropriate. Fire extinguishers of the correct types are clearly marked and located at appropriate intervals. Smoke detectors are part of the control system.

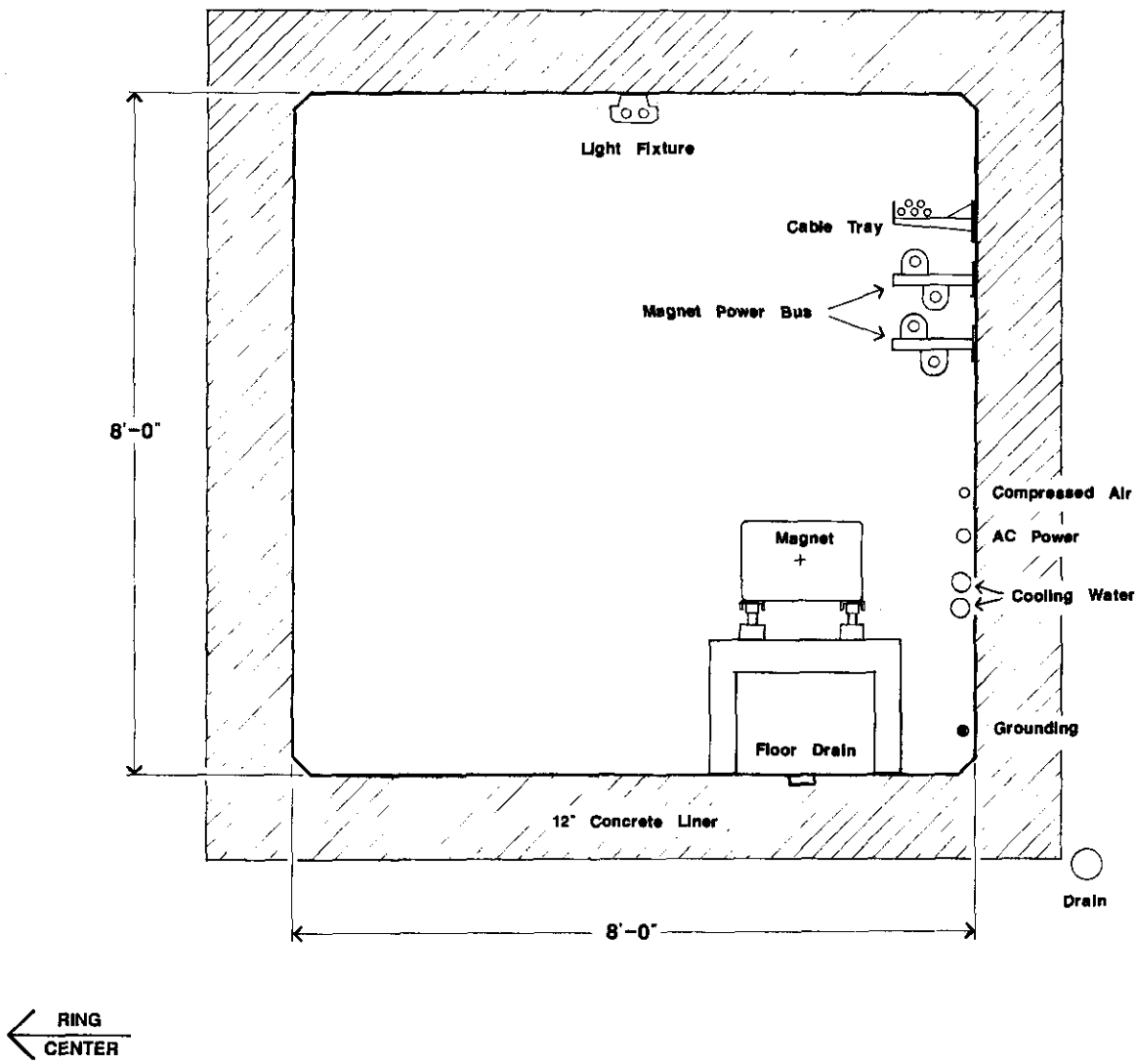

Figure 6.5-2. LEB cross section view, showing the relationship of the magnet ring and access aisle plus the utility and service mains below.

6.5.4 Medium Energy Booster

The Medium Energy Booster (MEB) is the middle-size circular accelerator in the injector chain. It raises the beam momentum from 8 GeV/c to 100 GeV/c and is the second conventional (iron and copper) magnet ring in the accelerator sequence. The MEB tunnel is 1901 m (6236 ft) long. The conventional construction parameters of the MEB are shown in Table 6.5-3.

Table 6.5-3
MEB Conventional Parameters

Enclosure size	3 m (10 ft) diameter
Enclosure length (circular)	1901 m (6236 ft)
6 service buildings, floor area	604 m^2 (6500 ft^2)
Electric power demand	
Peak	28 MW
Average	10 MW

The MEB has six service buildings located around the ring that provide space for the power supplies and accelerator controls system. The accelerator magnet ring and rf cavities are located in an underground tunnel constructed by the cut-and-cover method. Precast concrete sections are used for the normal tunnel areas and cast-in-place sections are used for access points, special alcoves and service building connection areas. The needed radiation shielding is provided by an earth berm of 3 m (11 ft) thickness over the concrete tunnel. A tunnel cross section is shown in Fig. 6.5-3.

Personnel access to the magnet ring enclosure is provided by stairways at each of the service buildings; a heavy equipment access is located at one point on the ring. The service buildings are placed above and slightly offset from the accelerator tunnel in order to accommodate the earth berm that provides the necessary radiation shielding. These service buildings are constructed as steel framed metal paneled structures on a reinforced-concrete slab foundations. Concrete encased conduits connect the service buildings with the accelerator enclosure below. In these conduits are carried the power cables, communications cables and copper buses that supply the accelerator components. The cooling water lines are direct-buried in the ground.

Primary power substations are located in close proximity to the service buildings so that 480V AC runs are short and optimally arranged. The 13.8 KV feeders that supply the substations are run in ducts that constitute part of the 13.8 KV power feeder grid.

As noted for the lower energy accelerators, the MEB is controlled and operated from the main control center. The personnel-access security system, radiation-interlock and fire-alarm systems are transmitted to and monitored from the main control room. The maintenance and upgrade of the MEB is similar in nature to that of the LEB and the maintenance personnel are common between these two machines.

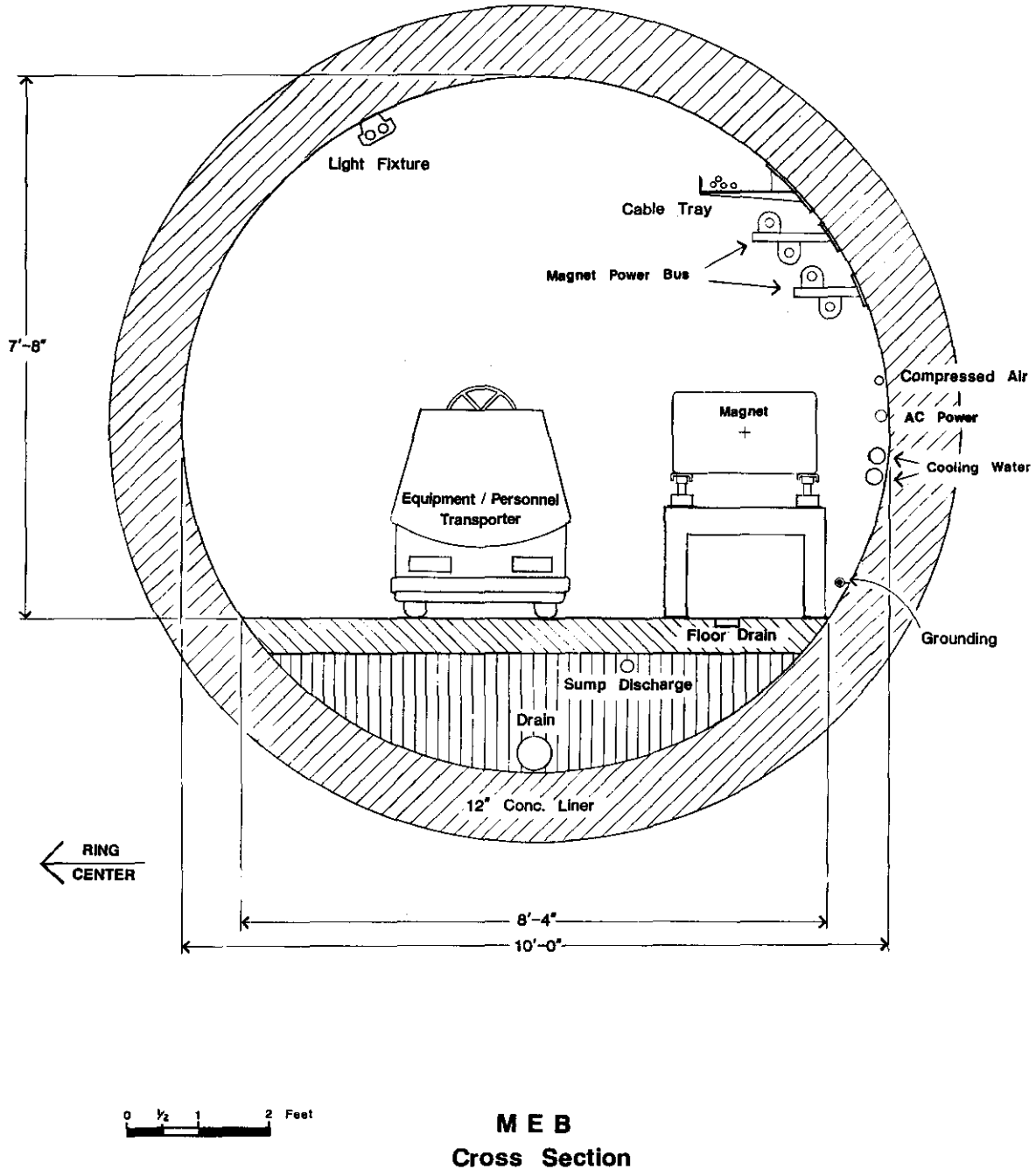

Figure 6.5-3. MEB tunnel cross section. The relationship among the accelerator components, utility and service mains and the access aisles are shown.

6.5.5 High Energy Booster

The High Energy Booster has more in common with the Collider Ring than it does with the lower energy boosters. It is a slow-cycling accelerator with superconducting magnets that increase the beam energy from 100 GeV to 1 TeV. It is also distinguished as the accelerator that supplies test beams for the SSC complex. Its placement in the injector complex and the location of the test beams can be seen on the map in Fig 6.1-4. The conventional construction parameters are given here as Table 6.5-4.

The HEB is over one mile in diameter and begins, therefore, to take on some of the characteristics of the Collider Ring. The planning must include consideration of access roads, utilities supply, land use away from the tunnel right-of-way, and other geographical and topographical considerations. Special technical considerations associated with superconducting magnets and their associated cryogenic systems are introduced in the HEB.

Table 6.5-4
HEB Conventional Parameters

Enclosure size	3 m (10 ft) diameter
Enclosure length (circular)	6000 m (3.7 mi)
Number of service buildings	15
Service building total floor area	2100 m^2 (22,600 ft^2)
Electric power demand (incl. test beams)	
Peak	21 MW
Average	18 MW

In the HEB, the size of the accelerator also introduces the first opportunity for significant economies of scale (there are 528 dipoles in the lattice, for example) and for significant cost savings associated with minor dimensional and technique changes in the methods of conventional construction. It is not practical in a conceptual design study, lacking a specific site, to pursue this in detail.

For purposes of this conceptual design study, the design concept taken with the Fermilab main ring tunnel is followed. A profile of the HEB tunnel and associated earth shielding is shown in Fig. 6.5-4. The cryogenic magnets and their cryostats take up a significant part of the tunnel cross section. Service mains and utilities are positioned in proximity to the magnets on the tunnel walls and ceiling. Space is provided on the inside of the ring for transport of magnets on a motorized vehicle.

The tunnel itself consists mainly of reinforced precast concrete pipe sections placed on a crushed aggregate foundation. As in the MEB, all special tunnel areas such as alcoves, access stairways and utilities penetrations are cast-in-place concrete. Since there are only six access points, the special sections constitute only a small fraction of the tunnel length.

There are three special sections along the HEB ring. These are the straight sections where injection from the MEB takes place and where extraction in both directions to the

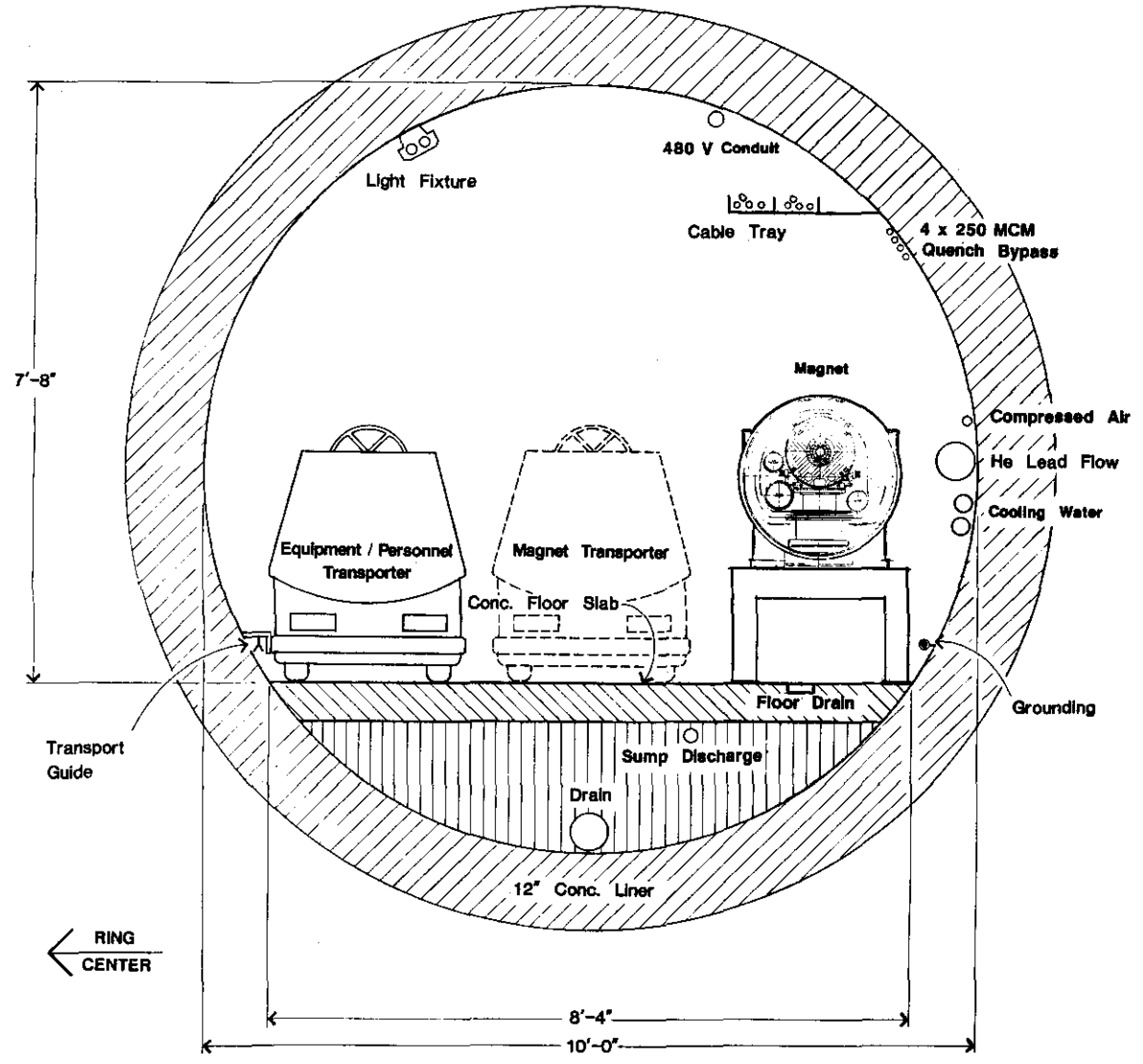

Figure 6.5-4. HEB tunnel cross section. The superconducting magnet ring in its cryostat is shown along with utility and service mains. Cost optimization will tightly constrain the overall tunnel cross section size.

Collider Ring and to the test beam area is done. In these areas, the normal small tunnel cross section gives way to wider tunnel sections that accommodate the added beam transfer and external beam transport components. Major equipment accesses are provided at two points in the ring to allow equipment and magnet carrying vehicles to enter and leave the tunnel. Magnets are raised and lowered from ground level to accelerator level at the far end of the major equipment accesses with twenty-ton cranes at each of the two points. The lifting bays are large enough to install or remove any of the accelerator components including the magnet-transport vehicles themselves.

The accelerator tunnel is shielded with a 4 m (13 ft) thick earth berm along its entire length. As in the MEB, the HEB service buildings are located at ground level and are sufficiently offset to the inside of the accelerator ring to clear the shielding berm. Electrical service mains connect between the service buildings and the tunnel in concrete-encased shafts. All the power supplies and control electronics racks are contained in the six service buildings. All the cryogenic services for the HEB are located in the single cryogenic service complex at NN.

The service buildings themselves are constructed, like those of the MEB, as steel-framed, insulated metal structures on reinforced concrete foundations. A road around the inside of the ring connects the service buildings with the rest of the injector complex. Electric power feeders at 13.8 KV parallel the ring road. The superconducting character of the HEB results in its using less power than the MEB and in a greatly reduced need for 13.8 kV power. Six small transformers for house power are placed around the ring, where they accommodate the service building needs. The main magnet power supplies operate directly from the 13.8 KV feeder.

The HEB control and safety systems are treated as in the MEB and need not be described again here. The new qualitative feature is the added circumstance of potential oxygen-deficiency hazard, a safety condition that enters in the HEB and Collider rings because of the presence of large amounts of cryogenic fluids. The instrumentation for detecting a condition of oxygen deficiency joins the other safety systems and controls in its implementation and maintenance.

6.5.6 Test Beam Facilities

A very important capability needed by the SSC experimental program is the ability to test detector components and subassemblies of the high energy physics detectors in particle beams. Much of what needs to be known can be determined at beam energies much lower than the beam energy of the collider itself (20 TeV). With these ideas in mind, a set of four test beams is included as part of the Injector Accelerator complex, along with a high-bay experimental hall in which to carry out the tests. We now describe the conventional facilities associated with the test beams.

Protons are extracted from the HEB at 1 TeV in the same straight section used for one of the injection lines from the MEB. The primary proton beam is switched into one of two channels, each of which leads to one individually shielded target station. From each of the two primary targets, a pair of secondary beams is transported to apparatus test sites in the Test Beam Experimental Hall farther along the beamline.

The conventional civil facilities are mostly below ground in order to exploit the economical radiation-shielding capabilities of earth. A small concrete enclosure starts off

tangent to the HEB tunnel and then leads away to the test-beam area. At the end of this enclosure, a dipole switch allows the primary beam to enter one of two beamlines.

After the tangent enclosure, the extracted beam is carried in buried vacuum pipes down to a dipole bending enclosure and then, again in buried pipes, on to one of the two primary production target enclosures. The primary targets are located in heavy steel vaults placed at the downstream ends of 80 m (260 ft) long underground concrete enclosures. A small service building at surface level holds power supplies and controls electronics for the two target stations and the associated beamline magnets.

The secondary beams leave the target enclosures in buried vacuum pipes which lead to small underground quadrupole enclosures placed upstream of the test hall. Dipole magnets in these enclosures allow momentum tagging of the beam particles before they enter the Test Beam Hall. The underground test beam enclosures (except the target enclosure) are constructed of precast concrete tunnel sections of dimension 2.4 m (8 ft) wide by 2.4 m (8 ft) high. The target hall itself has dimensions of 3.7 m (12 ft) by 3.7 m (12 ft) and has a 4.6 m (15 ft) high ceiling. Each enclosure has a personnel access labyrinth and stairway. Magnets are placed and removed in the small enclosures through earth buried roof hatches, except for the case of the target halls where a concrete hatch in the roof allows direct access to items below; the concrete access hatches in the target halls are sealed with removable concrete blocks to complete the radiation shielding. This approach to transport of high energy particle beams has been proven cost-effective at existing accelerator installations.

At the end of the test beam transport is the Test Beam Experimental Hall (Fig. 6.5-5). This building has a high-bay floor area of dimensions 30 m (100 ft) by 30 m (100 ft) with a floor to ceiling height of 15 m (50 ft). The high bay area is divided into two side-by-side working bays of 15 m (50 ft) width by a support column row. Each of the two functional bays is served by a pair of 15-ton overhead cranes which are used to maneuver the items to be tested. The four test beam lines enter the building at a depth of 3 m (10 ft) below ground level and are separated horizontally by about 3 m (10 ft) or more. The actual test setups share the building floor space roughly in quadrants, but the exact configurations will vary with the needs of the detector test programs. Heavy equipment access is provided by a pair of large roll up doors at the downstream ends of the large bays. Access ramps leading down from ground level to the roll up doors allow trucks to back their loads under the cranes for easy handling. Outside the high bay workspace, the Test Beam Experimental Hall has a low-bay extension of width 9 m (30 ft) along each side. These side bays run the full length of the building. The side-bays are used for data collection electronics, computers and electronic and mechanical bench space. Power supplies for the final beamline elements and for the needs of powered items under test are located in a small low-bay service building extension attached to the Test Beam Hall at its upstream end. The floor area of the service bay is of dimensions 7.6 m (25 ft) by 13 m (43 ft). In addition to large power supplies it also houses pumps and purification equipment for low-conductivity cooling water for these supplies and test devices. Surrounding the Test Beam Building are appropriate parking and hardstand areas, transformers for the electrical supply to the service building and a cooling tower for dissipation of heat from the electrical leads.

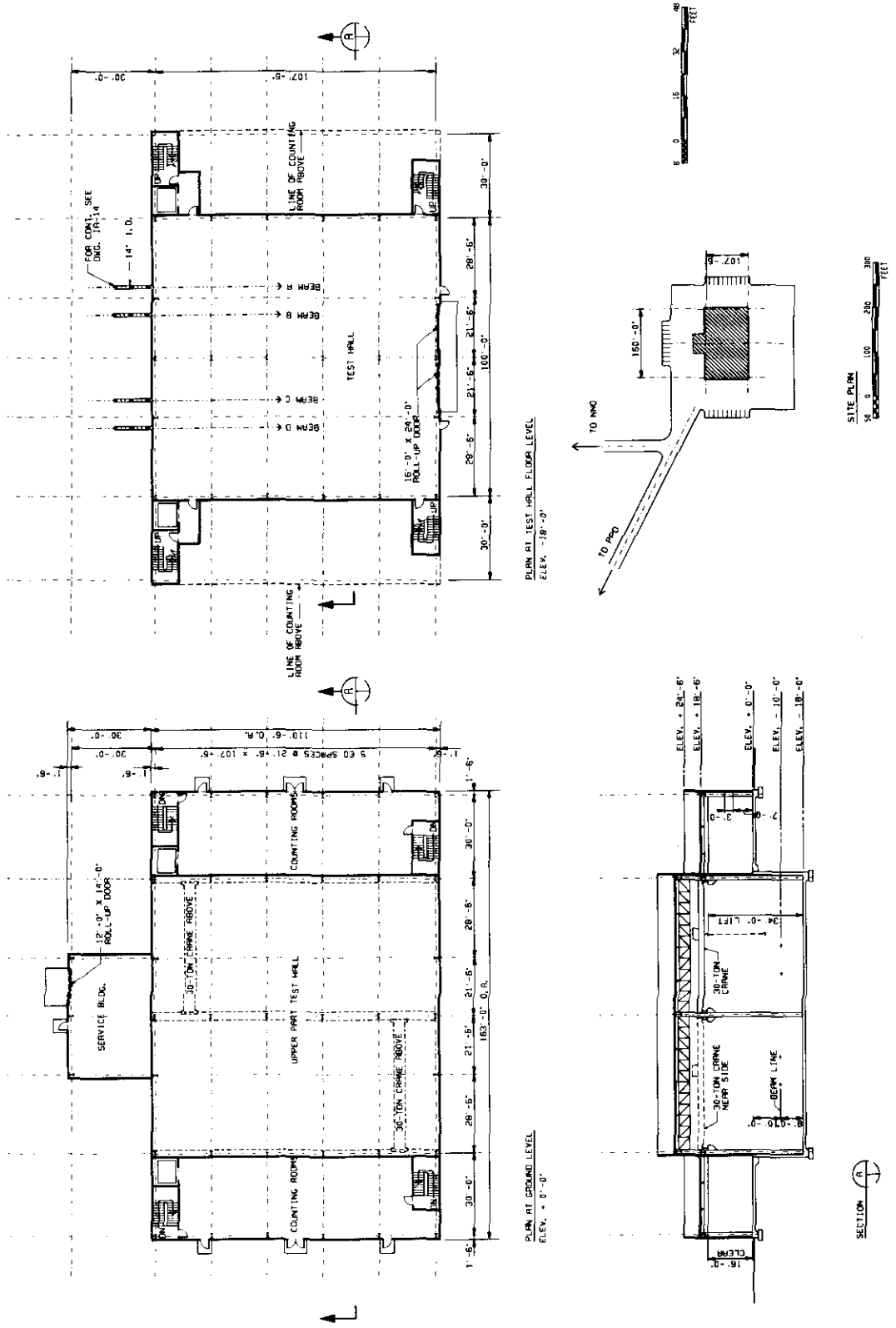

Figure 6.5-5. Test Beam Facilities associated with the HEB accelerator.

6.6 Collider Ring Facilities

6.6.1 Tunnel Configuration

The Collider tunnel over most of its length is very simple; Sections 6.2 and 6.3 describe how appropriate construction methods could be used to provide the needed tunnel in various geological circumstances. The tunnel cross section size and layout relate directly to the technical requirements of the collider and are the same for each of the three tunnel models. This common tunnel cross section is shown in Fig. 6.6-1, where the main features are exhibited.

Basic to the tunnel function is that it contains the rings of superconducting collider magnets, one above the other, around the circumference of the machine. To service these magnets, their cryogenics and associated control systems, the tunnel must also permit access by motorized vehicles of size and power adequate to lift, transport and maneuver the cryogenic dipoles, as well as smaller and lighter items that are needed in the tunnel. There will be ten normal entry exit points to the collider tunnel and another ten emergency exits, so there must also be room for one vehicle to pass another. Finally, the utility mains and lighting for the tunnel must be accommodated. These mains are individually small in cross section and can be distributed around the tunnel periphery in an economical way.

One striking aspect of the SSC Collider tunnel is how few service utilities must be accommodated. This is, of course, due to the simplicity of the accelerator design and its realization in a superconducting magnet lattice with only one high-current bus per ring. This bus is contained, together with the correction-coil buses, in the magnet cryostats, leaving the tunnel walls free of dc power runs.

The two rings of magnets are positioned one above the other with a beam center-to-center offset of 70 cm (27.6 in). As described in Chapter 5, the cold mass of each 17 m (56 ft) long dipole magnet is supported at five internal points. The nine-ton overall weight of the magnet is transferred from these points through the outer vessel to magnet stands on the tunnel floor (Fig. 6.6-1). It is important that the supporting floor be essentially free of vibration and stable against significant distorting motions over time. The tolerable amplitude for vibration when beam is circulating in the rings is of order tens of microns. This condition is easily satisfied in deep tunnels, but for shallow rings the presence of nearby railroad lines or heavy truck traffic on nearby roads are cause for concern. Careful analysis of ambient ground vibration and its coupling into the magnet stands will be done in such cases. Because the magnet vehicles do not operate while beam is in the machine, they are not a source of such vibrations.

Long-term ground motion is also a concern. It is important that the tunnel not cross active geological faults since such faults could displace one part of the ring relative to another. Correction coils in the magnet rings working with beam-position monitors have the capability to correct small, slow changes in the positions of one part of the magnet rings relative to another, but the magnitudes of the relative motions cannot exceed a few millimeters per kilometer. This type of motion can be anticipated to occur at any site on land as a result of "earthtides," a term that describes a diurnal rise and fall of the earth's crust under the gravitational influence of the moon (and sun). On the scale of the collider rings, the tidal flexing is controllable by means of the correction coils as noted above.

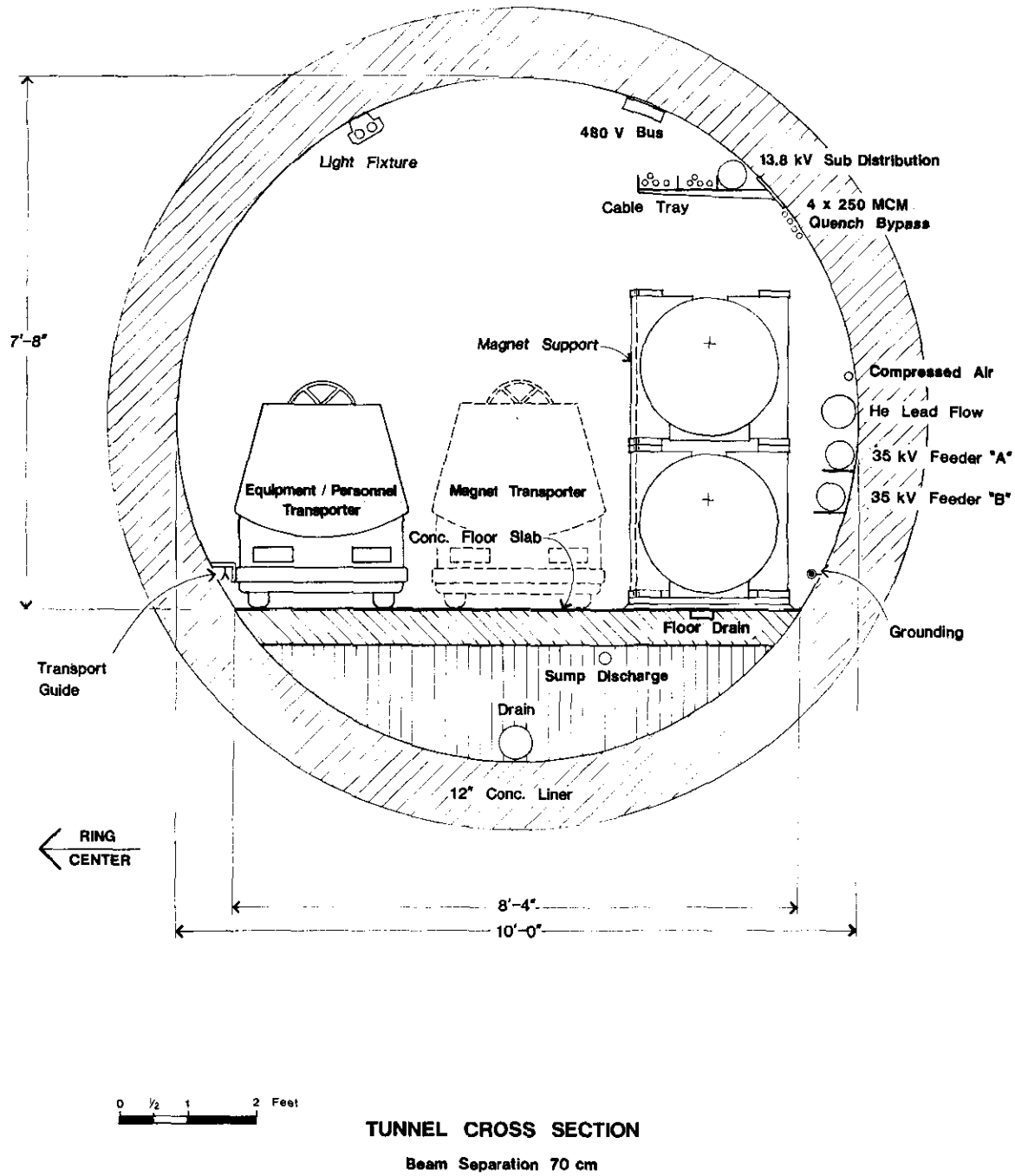

Figure 6.6-1. Collider Ring Tunnel profile showing the position of the two collider rings, the tunnel service vehicle and routing of tunnel utilities service mains.

A final important tunnel property relates directly to the geometry of the collider magnet rings. In the design developed in this report, the two rings lie one above the other, each in a plane; the two planes are parallel to one another. The accelerator-physics issues in this design and departures from planar are addressed in Section 4.2. The plane of the magnet rings may be allowed to tilt by up to one-half degree relative to the gravity vector at the geographical center of the collider rings. Technical considerations related to temperature-control parameters in the liquid helium systems of the collider ring magnets will be used to establish the maximum tilt criterion for acceptable SSC sites. As noted in Section 4.2.7, it would be possible to introduce a "fold" in the plane of the collider rings of maximum angle one degree if this were needed to accommodate a difficult site.

Once the vibration, slope and mechanical stability criteria are met, the remaining conventional systems requirements in the tunnel are straightforward. The water, gas, electrical and controls system mains are seen in Fig. 6.6-1 and detailed in Table 6.6-1.

Table 6.6-1
Collider Tunnel Utilities Mains

35 KV	Electric feeder main 'A'	22 MW
35 KV	Electric feeder main 'B'	22 MW
13.8 KV	Electric power distribution	500 kW/section
	Heater and maintenance power bus	500 A @ 480 V
	Feed rail and transporter guide bus	10 A @ 480 V
	Lighting bus	5 A @ 480 V
15.2 cm (6 in.)	He gas return main	15 psi
5 cm (2.0 in.)	Compressed air supply	100 psi

Electric power to furnish the total power needs of the eight Sector Service Areas (in the north and south arcs of the collider) is transmitted through the two 35 KV feeders in the tunnel. Each feeder is capable of transmitting 22 MW of power and is sized to supply half the operational needs of the collider. Both 35 KV feeders circle the entire collider ring inside the tunnel.

The local power requirements in each tunnel sector are supplied by means of 13.8 KV feeders. Each feeds the primary side of step-down transformers that are spaced uniformly along the 8 km tunnel sector. These transformers, in turn, supply the four 480 V buses that power the magnet heaters; the welding outlets; the correction dipole power supplies; the transporter vehicles; the local electronics crates and the tunnel lighting. The various buses and their locations in the tunnel are labeled in the figure.

The majority of the cryogenic-fluid transport takes place within the magnet cryostats, but there is one return gas main on the tunnel wall. This main is a 15.2 cm (6 in.) diameter stainless-steel helium gas main at 15 psi pressure that returns helium gas from the magnet

leads back to the refrigeration buildings in each sector. There is also a 5 cm (2.0 in.) diameter instrument air line which are used for controlling vacuum gate valves that are located periodically around the rings. Beneath the tunnel floor is a 30 cm (12 in.) water drain line through which water in the tunnel floor reaches a sump from which it is pumped out of the tunnel.

Above the magnets are two 23 cm (9 in.) cable trays for electrical and fibre-optics signal cables of various kinds. The SSC control plan relies heavily on local intelligent control systems, which are clustered in the instrumentation racks in the tunnel, so the number of signal and control cables needed in the trays is very low. There are approximately ten main coaxial serial-data highways that communicate the main control data around the ring. Locally within each sector there are additional coaxial and multiconductor cables that connect magnet and tunnel detector devices with the local signal-processing electronics. Also included are such needed items as lights, smoke-detector heads, oxygen deficiency monitors, radiation monitors and other typical monitoring or warning equipment.

Notice that a large part of the tunnel cross section is made available for the magnet mover vehicles. These electric-powered trucks are a very important part of the SSC installation and maintenance plan. There are entrances to and exits from the tunnel only at 4 km (2.5 mile) intervals and for vehicles and heavy equipment only at 8 km (5 mile) intervals. For this reason, it is necessary to have vehicles in the tunnel that can travel at speeds up to 25 km/h (15 MPH) to insure that repair and maintenance functions can be performed in reasonable periods of time. It is also important to make provision for one vehicle to pass another and for the vehicles to have sufficient on-board battery power to serve as escape means during a tunnel power outage. The vehicles must be strong enough to transport the 9-ton dipoles, hence they are rather large and heavy. Finally, the tunnel vehicles must not be allowed to crash into the collider rings!

The solution to these requirements is a fleet of sturdy rubber-tired electric trucks that run along a guide rail attached to the tunnel wall on the side opposite to the magnets. Inside the C-shaped guide rail are located the protected three-phase 480 V power busses that supply electricity to the trucks. In operation, the guide-grabber attaches to the power bus and the truck is mechanically guided along the tunnel at speeds up to 25 km/h (15 MPH). When it arrives at the work area, it can be uncoupled from the guide and maneuvered locally on battery power. In particular, it is possible to park the vehicle in the center aisle of the tunnel in such a way as to allow another vehicle to pass. There is sufficient battery power on the truck (one hour at normal speeds) to allow it to return to an exit point in the event of a tunnel power failure. The truck has special trailers with equipment-handling devices that allow a magnet to be lifted and removed from either ring in the tunnel or replaced there. The magnet-handling vehicles are used in the initial magnet installation as well.

Not visible in the cross section drawing is another essential feature of the tunnel, namely its air-handling and ventilation system. To maintain a supply of fresh air in the tunnel, fans in the access shafts draw stale air from the tunnel. The air is drawn from both directions; the exit/vent shafts midway between the buildings provide the source of fresh air and also have induction fans to aid the air flow. As noted before, smoke and oxygen-deficiency monitors in the tunnel continuously sample and report air quality. Temperature control is maintained by heating the incoming air in cold weather.

6.6.2 Collider Service Areas

The preceding description summarizes the facilities and conditions along typical stretches of normal collider tunnel. At various intervals, however, there are also niches, alcoves, stairways and hatches. In addition, at the surface and spaced at 8 km (5 mile) intervals, there are the ten Sector Service Areas.

To get a perspective on the collider tunnel and its periodic structural features, it is useful to make reference to Fig. 6.6-2, where a schematic plan view of the collider ring is shown with these main features labeled. The north and south arcs constitute the main accelerator enclosures and are discussed in the next few paragraphs. There are four Sector Service Areas in the north arc, four in the south arc and one at each interaction cluster (IRC). All the electric and cryogenic services needed in the tunnel enter at these ten points. They are also access points for people, equipment, air and water. These services were discussed in the tunnel context, except for the cryogenic fluid transfer lines that connect the cryogenic refrigerators in the refrigeration buildings which are part of the sector service area with the superconducting magnet rings below. These are seen in Fig. 6.6-3, a cross section view of the access-shaft and tunnel intercept.

From Fig. 6.6-4, the general relationship between the collider tunnel and the vertical access shaft can be seen. The 9.1 m (30 ft) diameter access shaft is offset by 6 m (20 ft) to the side of the collider tunnel and has a 12 m (40 ft) by 12 m (40 ft) head house over it. The offset is necessary to permit room for needed radiation shielding between the shaft and the tunnel. The cryogenic transfer lines are routed down the sides of the shaft to a large heat exchanger tank (cold box) at the bottom. Liquid helium and liquid nitrogen lines then connect the cold box to the magnet cryostat system inside the tunnel. The cryogenics pipes are routed beneath the floor of the tunnel so that they do not interfere with tunnel traffic. The access shaft contains a metal stairway and small elevator for personnel and small equipment transport. From the bottom of the shaft, a two-section labyrinth leads to the collider tunnel. In places where a tunnel-boring machine has started, the shaft is longer and the radiation labyrinth is created by concrete shielding blocks. In either case, it is possible for personnel and small pieces of equipment to enter and leave the collider tunnel without compromising the function of the radiation shielding.

The refrigerator components and storage tanks, as well as the power supplies for the collider magnet rings, are located at the surface, as shown in Fig. 6.6-5. Here, at each of the ten locations, there are two service buildings, one of dimensions 14 m (45 ft) by 31 m (102 ft) that houses the compressors and cooling water pumps and the other 14 m (45 ft) by 26 m (86 ft) that contains the power supplies and refrigeration (PS/R) equipment. Surrounding the service buildings are other technical components including two large buffer tanks for liquid helium, one tank for liquid nitrogen and electrical transformers that convert electric power from the 35 KV main feeders to locally required secondary feeds at 13.8 KV, 4160 V and 480 V. There is also a cluster of ten helium gas storage tanks each of diameter 3.7 m (10 ft) and length 20 m (65 ft) located in the Service Area.

Also located at each Service Area cluster are cooling towers to dissipate waste heat generated by the power supplies and compressors. Water in a closed loop system transfers the heat between the heat sources and the cooling towers. There, prevailing winds or fans remove it from the radiator surfaces of the towers by convection. Finally, there are parking and hardstand areas around the buildings and access shafts to facilitate staff service

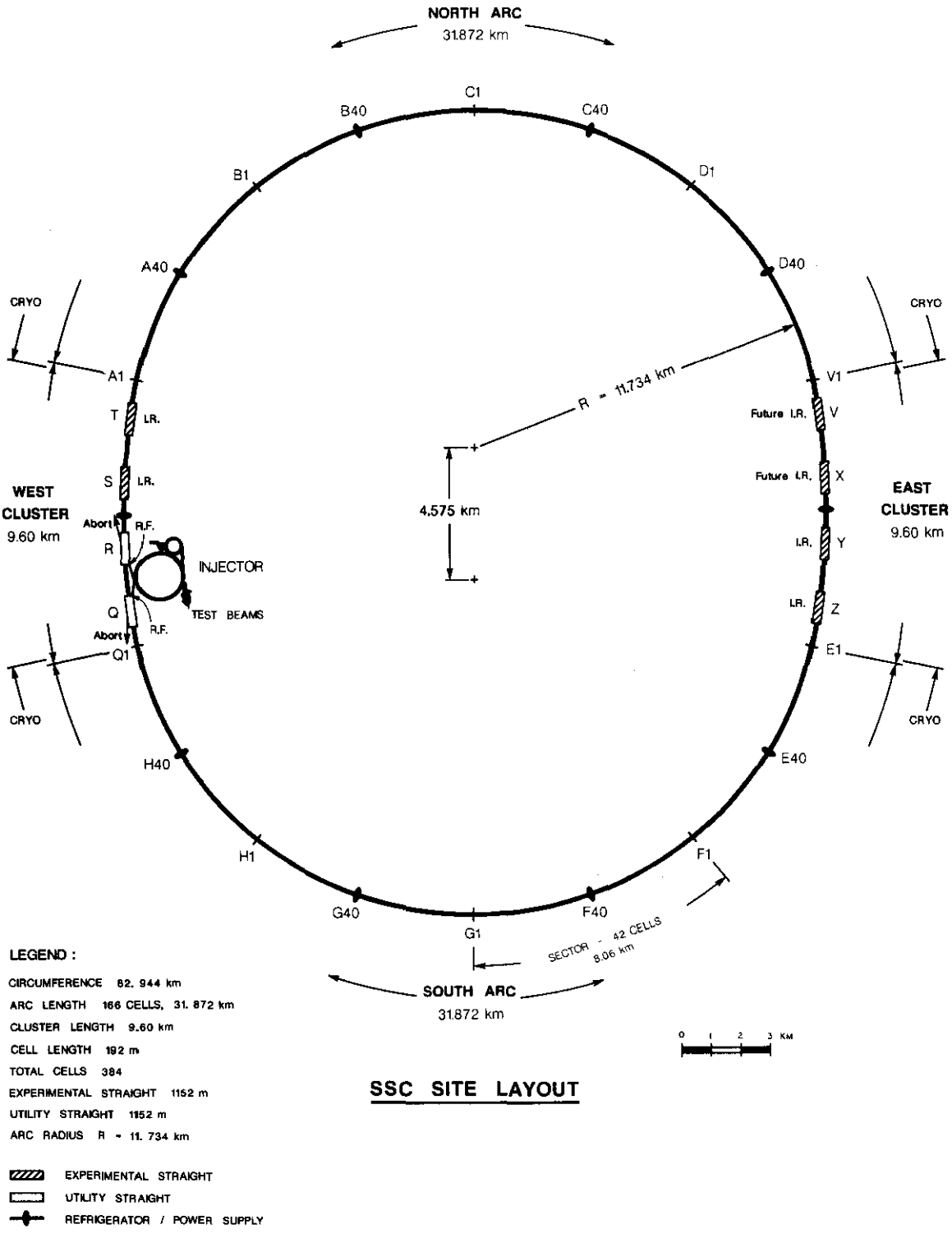

Figure 6.6-2. Schematic Collider Ring plan view showing major features of the conventional facilities and services.

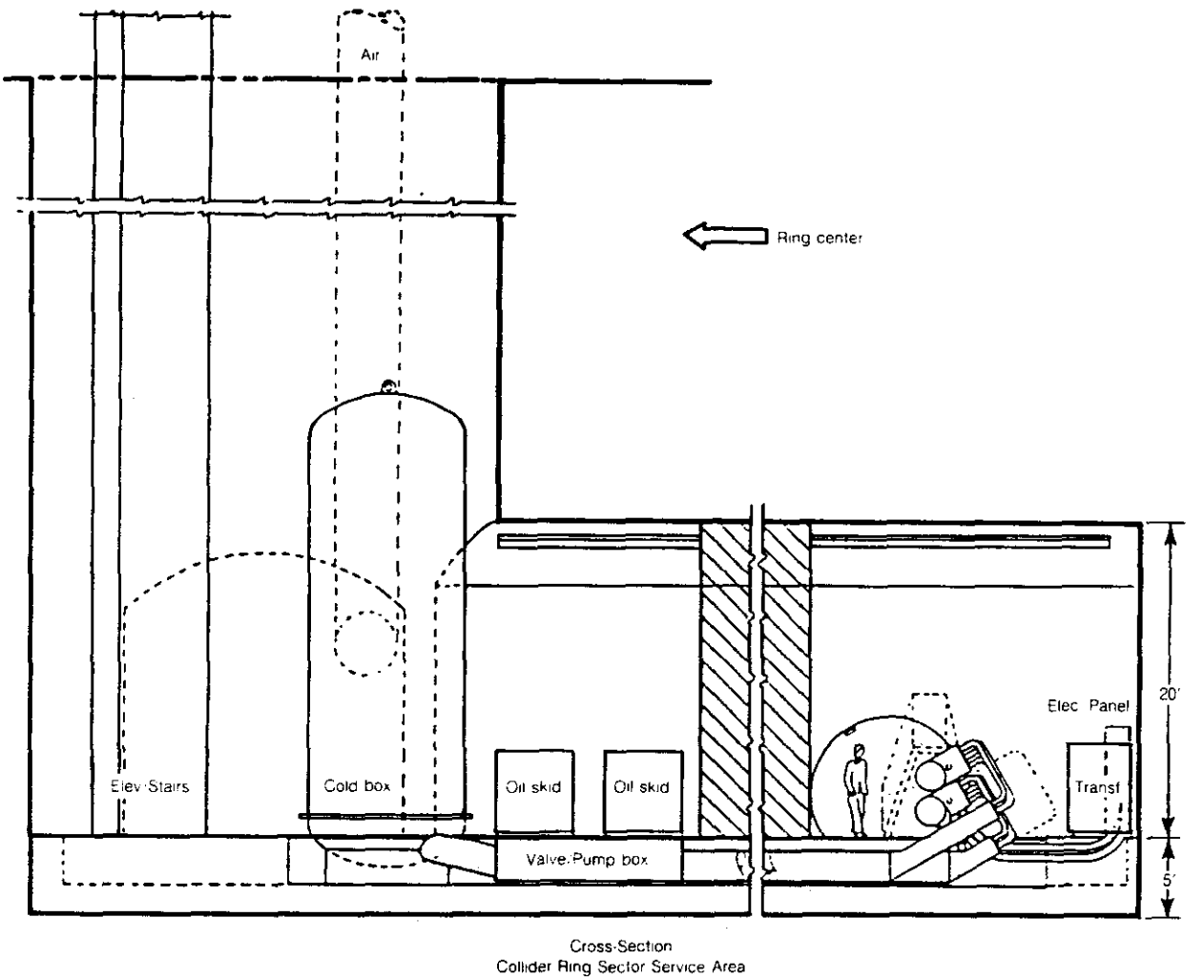

Figure 6.6-3. Collider Ring Sector Service Area, Access-Shaft and Tunnel Intercept seen in cross section.

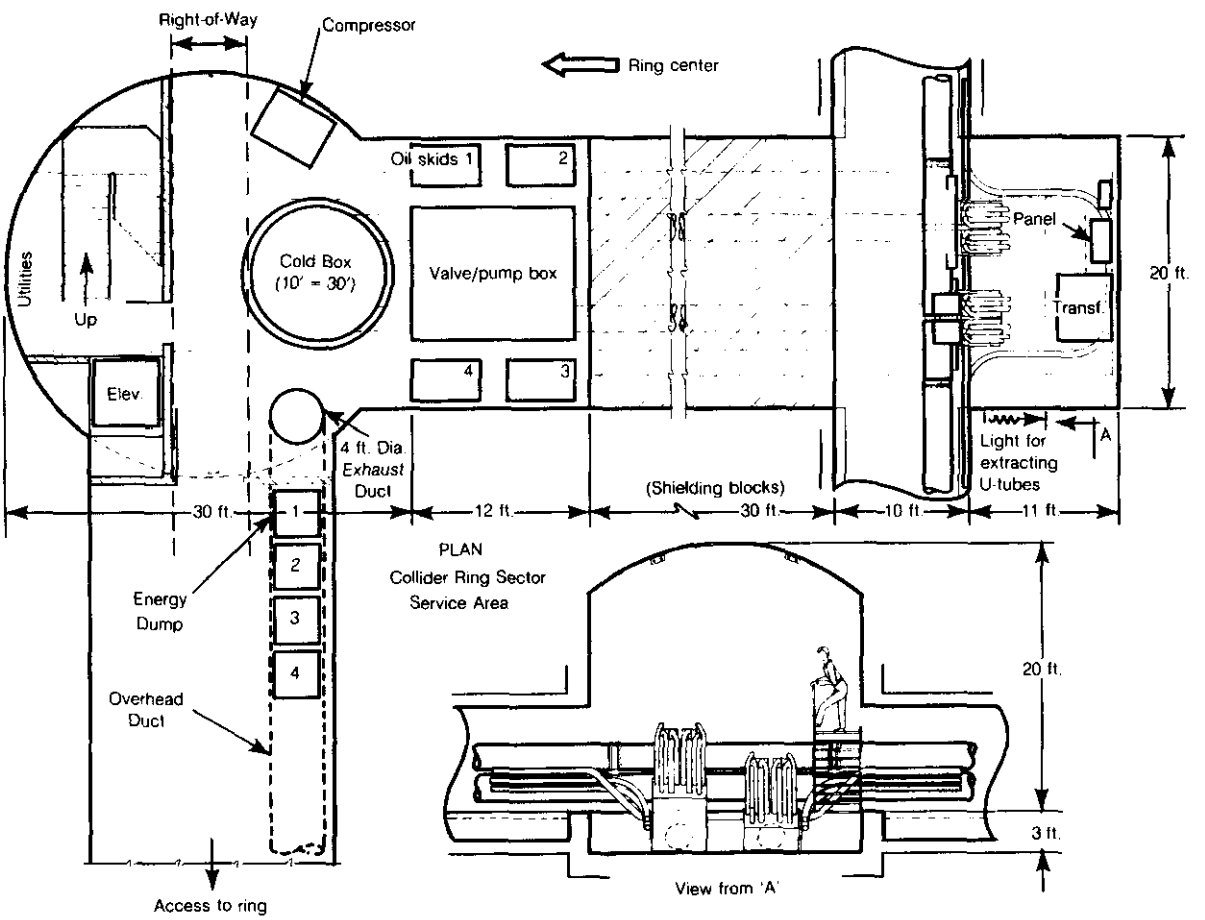

Figure 6.6-4. Collider Ring Access Shaft plan view.

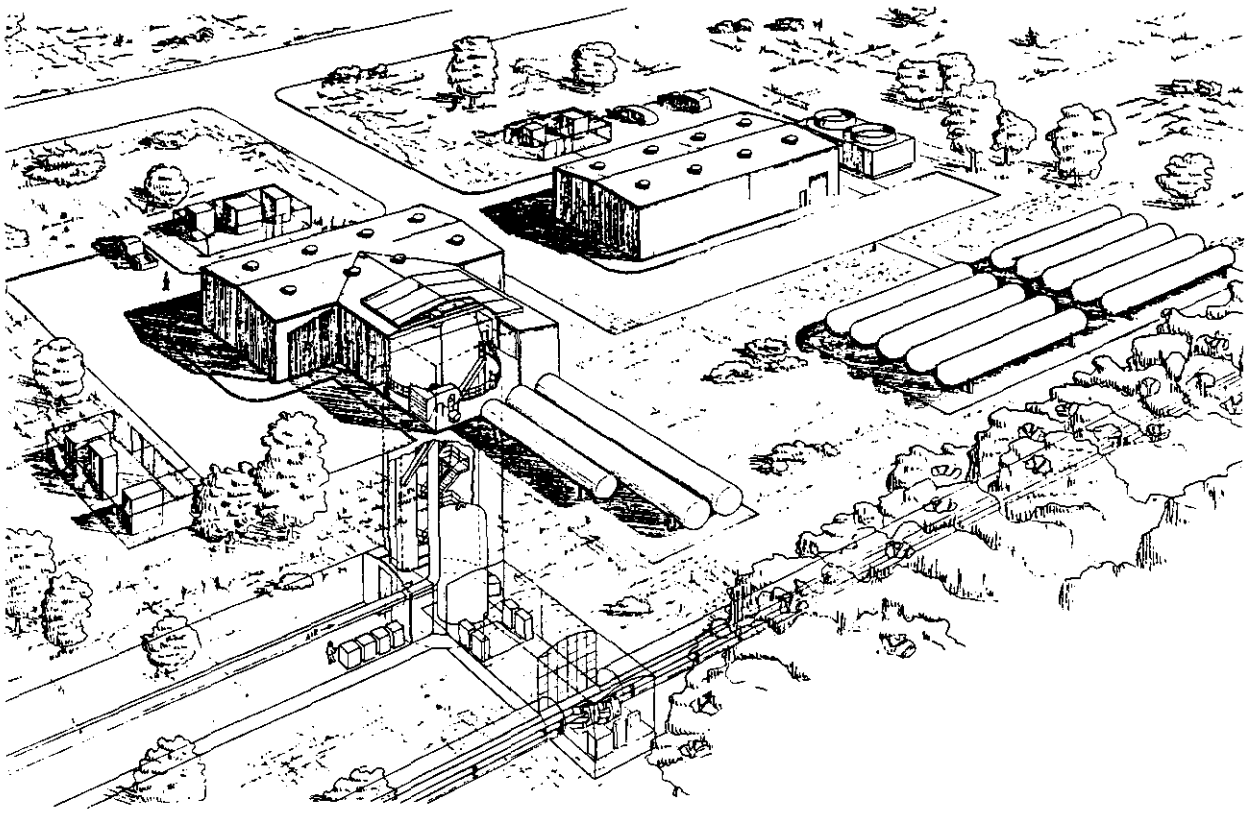

Figure 6.6-5. Perspective view of the Sector Service Area in the Collider ring.

operations. As displayed in Fig. 6.6-4 and 6.6-5, an area of about 6 acres is needed to accommodate each PS/R service building cluster.

Midway between the Service Areas in the north and south arcs are the Sector End Point Areas and associated exits. The distance between two successive End Point Areas around the ring is 8 km (5 miles), a stretch of tunnel that houses a unit of the SSC called a "sector." A sector is divided into two half sectors, each of which contains 21 "cells" of magnets. The cell is a basic unit of the accelerator and consists of ten dipoles, two quadrupoles and two correction magnet units or "spools" all of which are superconducting. This pattern repeats around the arcs for each of the two magnet strings. The Service Areas discussed above are located at the middle of a magnet sector. The magnet pattern is slightly different in the bending regions of the interaction clusters.

From a conventional-systems point of view, the magnet cell is the basic repeating unit in the tunnel; information from the magnets is obtained from each collider magnet cell. Signals from transducers such as beam-position monitors, quench protection monitors, and other devices emerge from the spool packages on wires. The signals pass via cables or twisted-pair buses in trays to shielded, electronic instrumentation clusters that are located at intervals of 192 m (630 ft) (1 cell) along the tunnel. We briefly describe the electronic clusters here.

Contemporary signal-processing electronics is almost totally dependent on solid state devices. The solid-state devices are, in turn, quite sensitive to radiation damage, suffering gradual degradation in their performance with accumulated doses. The main damage is caused by slow neutrons. However, slow neutrons can be readily shielded against. In the SSC collider tunnel, it is anticipated that the expected levels of radiation could cause damage of this sort to the electronics. For this reason, the clustered electronics modules that process signals from each magnet cell are located in rack units that are recessed into small niches in the walls of the collider tunnel. Such niches provide very good neutron shielding.

6.6.3 Injection, Extraction and RF Areas

In order to bring beam into the collider, accelerate it and finally dump it safely, the collider rings have special straight sections where these functions are accomplished. In particular, the two straight sections labeled Q and R in Fig. 6.6-2 are used for these injection and extraction systems. The plane of the HEB lies above that of the collider rings, so the injected 1 TeV protons are sloping down and bending horizontally as they enter the collider ring vicinity. This beam geometry is responsible for a somewhat complicated enclosure structure where these beams enter. The enclosure shapes are further complicated by the need to accommodate the two abort beam transports that are also required in IR areas Q and R.

The injection enclosure geometry can be seen in Figs. 6.6-6, 6.6-7. The goals of this design include both the accommodation of apparatus for beam transport (magnets, etc) and the provision of radiation shielding which allows occupation of the collider tunnels while the HEB accelerator is running. Both primary goals are met in the tunnel design shown in the figures. The combination of the earth shielding (where only the beam pipe itself connects the HEB and collider tunnel systems) and the doubly redundant critical device protection method (see Section 6.9) guarantees that protons cannot enter the collider from the HEB when the collider tunnel is occupied. Likewise, the fact that the magnet rings are at

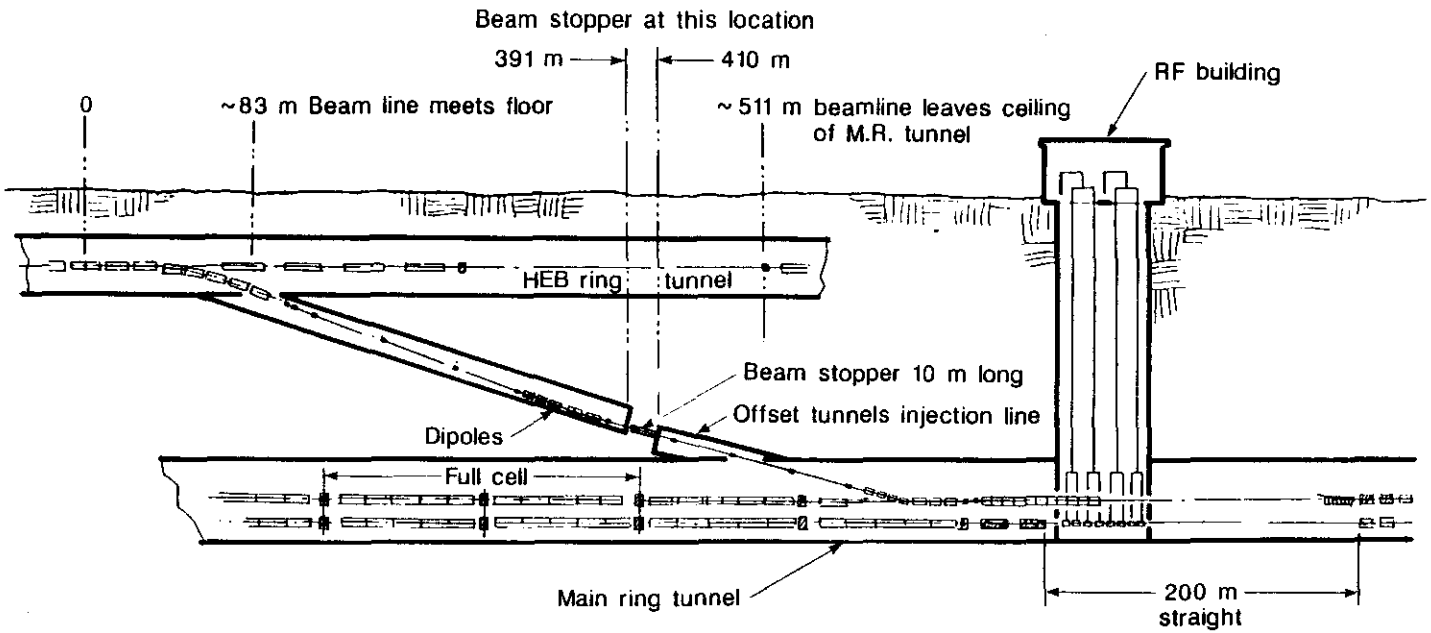

Figure 6.6-6. Injection Tunnels from the HEB to the Collider, Elevation View.

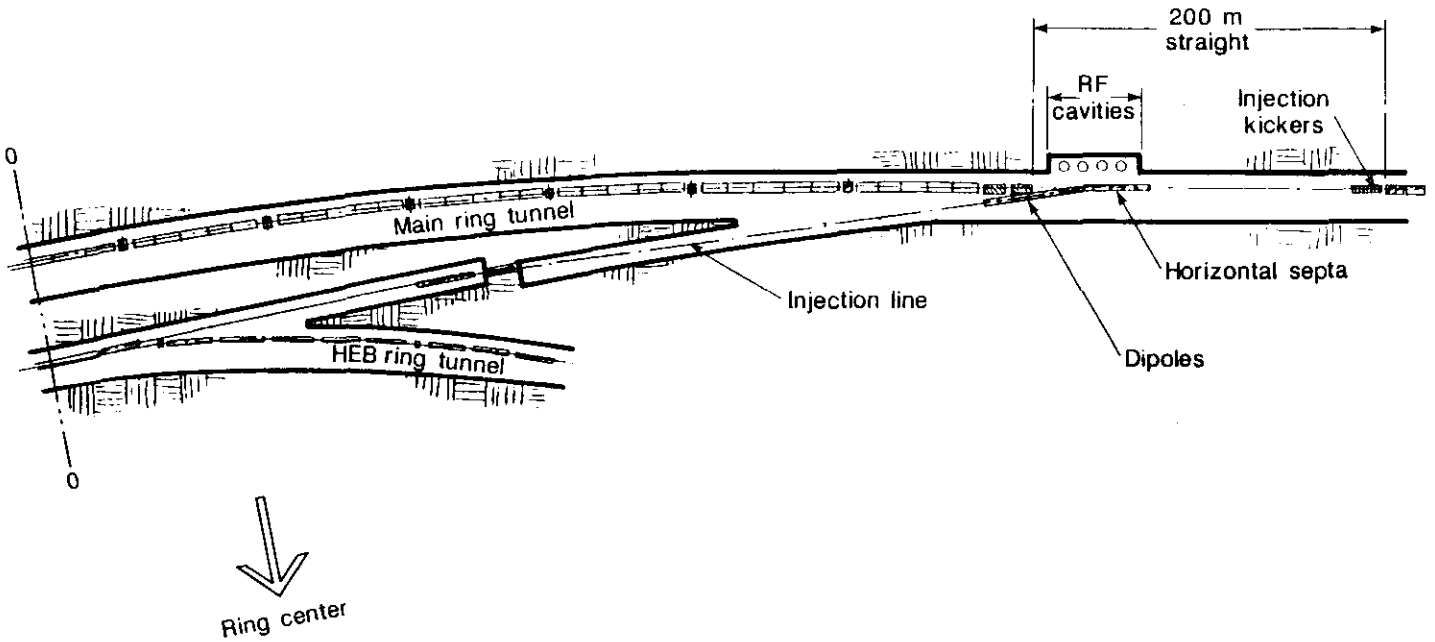

Figure 6.6-7. Injection Tunnels from the HEB to the Collider, Plan View.

different elevations insures that muons from the HEB do not constitute a radiation safety hazard in the collider tunnel.

These tunnels are constructed using a combination of reinforced concrete pipe as used in the HEB tunnel and stretches of cast-in-place concrete for the transition areas where the injection tunnels meet the collider and HEB rings. These tunnels present no unusual problems. The floor slopes shown in Fig. 6.6-6 are exaggerated by the use of different scales in horizontal and vertical dimensions. The true floor slope is about 1%. Services for the magnets in the connection tunnels are provided by the same service systems as the accelerators themselves. Power supplies and controls systems for the injection equipment are located in service buildings located near the intersection of the injection tunnels with the HEB and with the collider tunnel.

The radio-frequency beam accelerator (rf) systems for the two collider rings are housed in two rf service buildings, each of dimensions 8 m (32 ft) by 26 m (86 ft) at ground level above the Q and R straight sections. The waveguides that connect the power amplifiers in the service buildings with the resonant rf cavities in the tunnel pass through pipe conduits in the ground. These are gradually bowed along their length in such a way as to maintain the necessary radiation safety shielding protection. Power and cooling water for the rf system are provided by transformers and cooling towers located outside the rf service buildings.

A final important special aspect of the Q and R straight sections are the beam dump abort systems that are located in these areas. Each collider ring has its own beam abort system. It has been found advantageous for test purposes to locate these systems in such a way that beam injected from the HEB can be kicked directly into an abort line without ever entering the collider lattice. This is indicated schematically in Fig. 6.1-4, where the two abort lines lead off in more or less straight lines from their respective injection lines. Circulating beam can also be diverted to the abort lines at any energy between 1 TeV and 20 TeV, of course. These beam dumps are the primary protection of the collider magnets from damage by beams that try to depart from their intended closed design orbits. Technical details of the functioning of the abort system are given in Chapter 5.

The beam dump abort systems are housed in special concrete vaults located downstream of the Q and R straight sections. The aborted beams reach the dump vaults in vacuum beam pipes of increasing radius that are direct buried alongside the collider tunnel sections. The aborted beams at full collider energy and intensity deliver a great deal of stored energy to the dumps (see Section 6.9) and must therefore be defocused and swept in a spiral pattern over the face of the dump. The energy spreading requirement ends up prescribing a final vacuum pipe diameter of 1.8 m (6 ft), as well as an active dump core of the same size. The vacuum pipe is stepped up from its initial 10 cm (2 in) diameter at the exit of the spiral sweeping magnet string in a series of discrete pipe segments chosen to present a clear path to the emerging beam.

The dump vault itself is of reinforced concrete sized to accommodate the multilayered beam dump. The inner dump consists of graphite pellets which are the primary energy absorbers. These absorbers are cooled by contact with an aluminum box that surrounds the graphite. Water passages in the aluminum shell allow the heat to be carried away by a closed loop cooling system which is heat exchanged with an ordinary cooling water supply. Finally, there is a massive layer of steel blocks that limit neutron escape into the surrounding soil. The concrete vault that encases the beam dump is made watertight so that

groundwater cannot enter to leach radio-nuclides from the steel shield. The groundwater around the dump vaults is monitored for signs of activation. The protection philosophy is elaborated in Section 6.9.

The power supplies, controls and pumps for the abort systems are housed in two small ground level service buildings of dimensions 7.6 m (25 ft) by 13.1 m (43 ft) located at the downstream ends of the Q and R straight sections. The electric power needs of these service buildings are met by small transformers at each building and the cooling water heat transfer needs are met with cooling towers.

As in all the other accelerator associated service buildings, the design of the rf and Abort Kicker Service Buildings is based on a modular steel framed, insulated metal building built on a concrete slab. The service buildings are not normally occupied by personnel, so they have no domestic water or sewerage connections. The buildings are kept locked and security is provided by periodic site patrol. This subject is covered in some detail in Section 6.9.

6.7 Experimental Facilities

6.7.1 Features of Experimental Areas

A striking feature of colliding beams experiments, and one that is especially clear in hadron collider machines, is the growth in the size of experimental detectors with beam energy. For the important subclass of detectors seeking to capture a large fraction of the total 4π center-of-mass solid angle, that growth scales slowly with collider beam energy. This is fortunate when we consider the fact that beam energies have grown from 30 GeV on 30 GeV at the CERN ISR Machine to 20 TeV on 20 TeV at the SSC, a factor of 667 in this parameter!

The experimental halls for the SSC (described in this section), are larger in size than existing ones at other accelerators, but only by a factor of 1.5 or so in linear dimensions. The size scales roughly like the logarithm of the ratio of beam energies, a result that comes from fundamental characteristics of elementary particle interactions, most notably the exponential absorption of hadrons in bulk matter.

Like experimental areas in earlier colliding beams machines, the SSC will have a small number of Interaction Regions (IRs) where experiments can be done. In the conceptual design presented in this report, four IRs are fully developed for experiments. There are provisions for two more IRs that could be developed later as circumstances require them. To complete the symmetry pattern of the collider ring, there are two more straight sections in the machine, for a total of eight. The latter two are used for injection of beams from the High Energy Booster and for the collider beam abort systems. These eight "straight sections" of the accelerator are concentrated in IR Clusters of four each, one cluster on the east side of the SSC and one on the west side. This section describes the developed experimental areas that occupy four of the eight straight sections.

6.7.2 Clustered Interaction Regions

Clustering the straight sections together rather than spacing them uniformly around the machine results in a number of design and operational advantages, some obvious and others less so. An obvious advantage is that of proximity. The designed clustering allows the central laboratory campus, the injector facilities and two of the four experimental areas all to lie within a few kilometers of one another and therefore within a few minutes vehicle travel time. This is helpful both in terms of saving time and of increasing productivity for laboratory and scientific staff; it is very important in terms of response times for emergency services such as ambulance and fire calls.

A second benefit of clustering is the concentration of surface land acquisition and use for the site. If land for each experimental hall had to be separately acquired, the size of the experimental halls and the amount of surrounding land required at each IR could cause additional delays in the project. Less obvious but equally real benefits result from eliminating the costs of electric power and water piping runs that would have to be extended over tens of kilometers, either in the collider tunnel or in expensive near-surface duct banks. A third cost saving from IR clustering is associated with property protection and site security. The IR clusters of the present design are optimized from this point of view.

Finally, there is a consideration related to IR placement that impacts directly the high energy physics experiments. Since the collision points are a sizable source of radiation during normal operations, the particles born at one IR collision point can, in principle, reach other collision points and detectors, either through the collider tunnels (diffracted protons and thermal neutrons) or through the earth (high energy muons). Preliminary studies of these effects have shown that interference could be a concern at the highest luminosities if successive IR's were strung very close together with no intermediate bending of the circulating beam. For this reason, the successive IRs are separated by 2.4 km (1.5 mi) of distance and 106 mrad of bending in the accelerator. With this distance and magnetic decoupling, the successive IRs will not interfere with one another.

6.7.3 Collision Halls

Four of the eight straight sections of the collider are developed as experimental halls with high energy physics detectors. The two experimental IRs in the west area (S and T on Fig. 6.6-2) are of type A and those in the east area (Y and Z on Fig. 6.6-2) are of type B. The two types of collision hall differ essentially only in their dimensions. Type A halls are larger in transverse dimensions and shorter along the beam; Type B halls are smaller in transverse dimensions and longer in the beam direction. Both types are useful, but each is optimized for a certain sub-set of experiments.

The Type A Collision Hall is shown in Fig. 6.7-1. The central detector area has dimensions of 21.3 m (70 ft) long by 21.3 m (70 ft) wide by 18.3 m (60 ft) high. The central detector that surrounds the beam collision point is located here. Immediately upstream of this area, along the beamline, are two smaller areas of dimensions 12.2 m (40 ft) by 12.2 m (40 ft) by 15.2 m (50 ft) high. In these areas are placed the "forward" detectors that measure properties of high energy particles that leave the collision point at small angles to the beam. Finally, there are special tunnel sections of length 32.3 m (106 ft) along the beam that match between the type A Collision Halls and the regular tunnel sections. These are of the same transverse dimensions as the regular collider tunnel, but they incorporate the exit

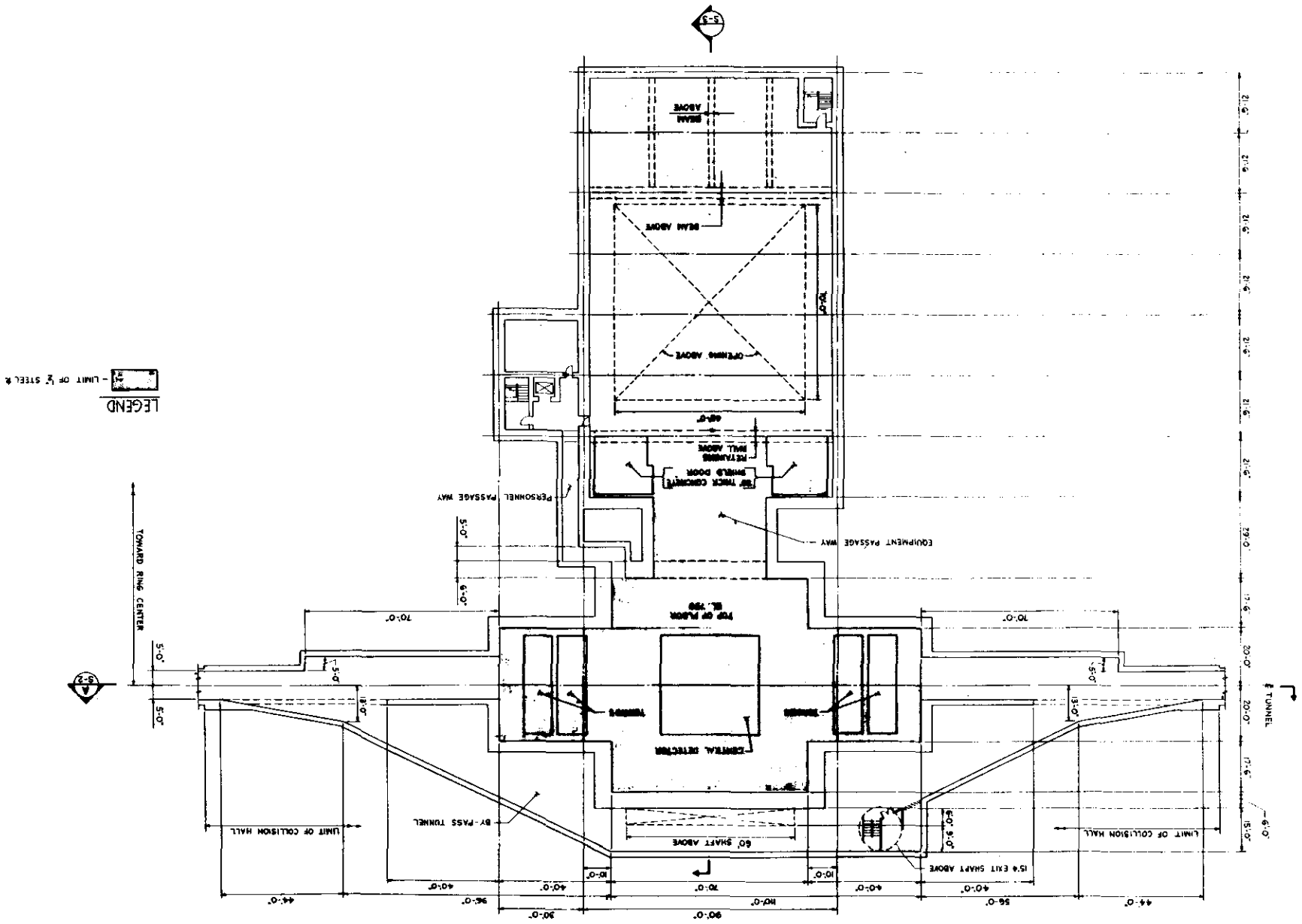

Figure 6.7-1. Plan View of Type A Interaction Region showing collision hall, access way, shield doors, assembly area and Staging Building.

area where a vehicle bypass tunnel (see Fig. 6.7-1) circles around the collision hall. The bypass tunnel allows magnet vehicles to circumnavigate the IRs.

The type B Collision Halls have smaller dimensions in the central detector area than those of Type A. They are also considerably longer in the beam direction than those of Type A. As can be seen in Fig. 6.7-2, the central area of the Type B Hall is of dimensions 15.2 m (50 ft) by 15.2 m (50 ft) by 18.3 m (60 ft) high. this central area is abutted on each side by smaller side bays each of transverse dimensions 7.6 m (25 ft) by 7.6 m (25 ft) by 100 m (328 ft) long. These side bays are used for small angle detectors that are characteristic of a large class of experiments. The side tunnels are equipped with 10 ton cranes and have provision for a magnet vehicle bypass within the 7.6 × 7.6 m (25 ft × 25 ft) tunnel. The vehicle bypass is continued around the central collision area in the same way as in the Type A hall. Both types of collision halls are constructed of reinforced concrete and have a radiation shield cover of earth and rock of minimum thickness 7.2 m (24 ft). Because the collider ring is located at different depths below the surface in each of the example sites, the details of construction of the halls will differ for each of the three sites. The internal details will be the same for all three example sites.

6.7.4 Access Halls and Assembly Areas

For each of the experimental IRs, there is an assembly area at the same elevation as the collision hall in which the experimental detectors are prepared and serviced. The assembly areas are isolated from the collision halls by massive but movable concrete shielding walls that permit the collider to operate at the same time as unrestricted personnel access is allowed in the assembly areas. Above the assembly areas are conventional industrial-type buildings that contain the shops, offices, electronic areas and other support facilities that are required by the detectors. All these features can be seen in Fig. 6.7-3.

The central detector is moved back and forth between the central bay of the collision hall and the assembly area on a rolling support structure that passes through the access way. The access way is the relatively narrow passage that connects the two larger areas. It can be sealed against radiation by two massive concrete shielding doors that are also able to roll into and out of the passage. When the shield doors are in place, there are 7.2 m (24 ft) of shielding between the collider and the assembly area. This is adequate to allow unrestricted personnel access to the assembly area, even with the machine running. This shielding feature means, of course, that the detectors can be constructed and power tested while the machine is first being commissioned and later on, that repairs or upgrades on any of the detectors can be carried out while the remaining detectors run for high energy physics research.

Not apparent from the drawing is the fact that the central detectors that roll in and out of the collision hall typically weigh several thousand tons! For this reason, it is not possible to fabricate such detectors (or even sizable fractions of them) at remote locations for transport to the IRs. It is also not sensible to construct and repair them in the collision halls, since that approach would keep the accelerators off for long periods of time. A workable solution is the one chosen. The detectors are assembled and tested in the lower pit portions of the assembly halls and then rolled into the collision halls when the experiments begin. It takes a few days for the entire movement cycle of opening the shield doors, decabling the

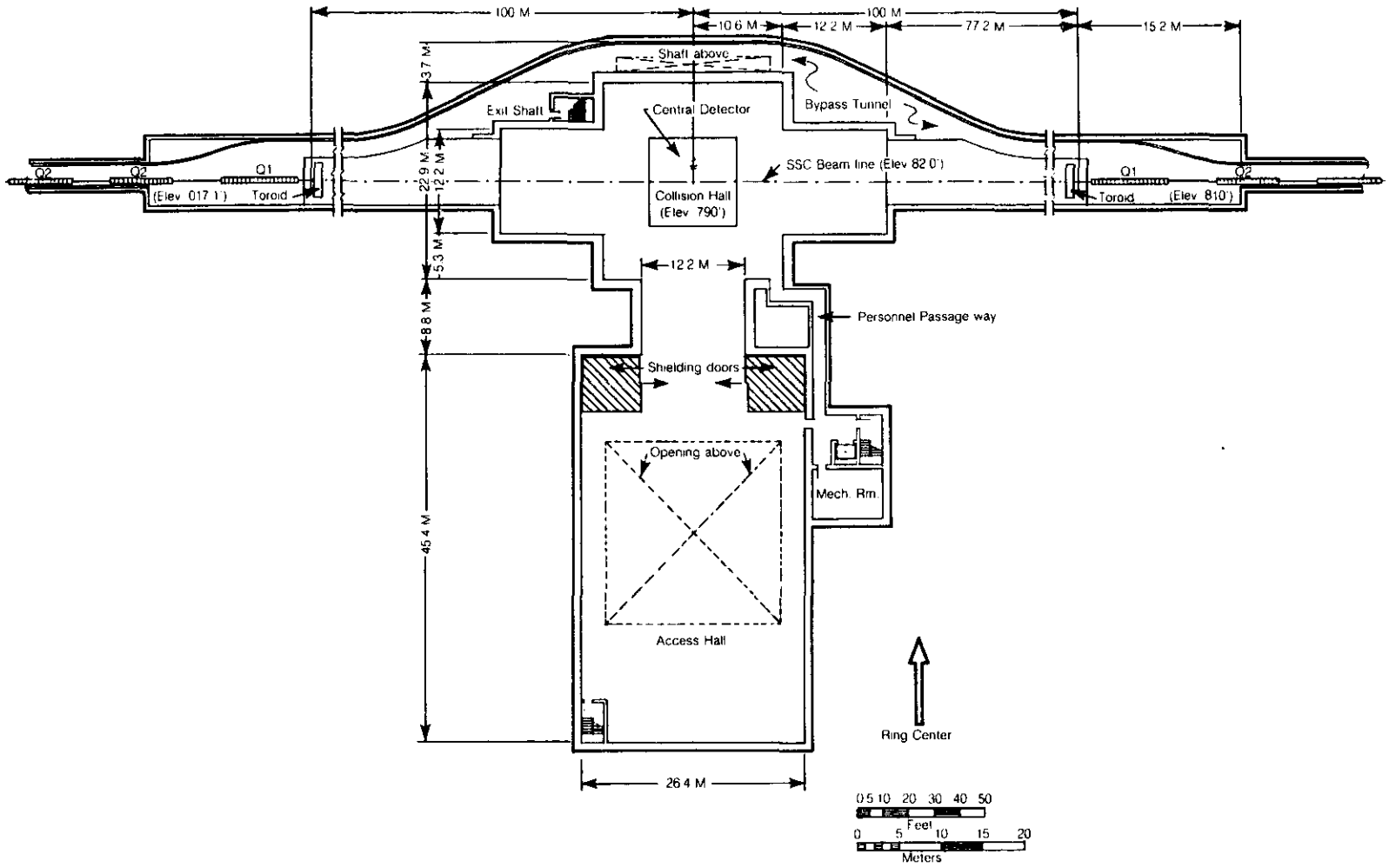

Figure 6.7-2. Plan View of Type B Interaction Region showing collision hall, access way, shield doors, assembly area and Staging Building.

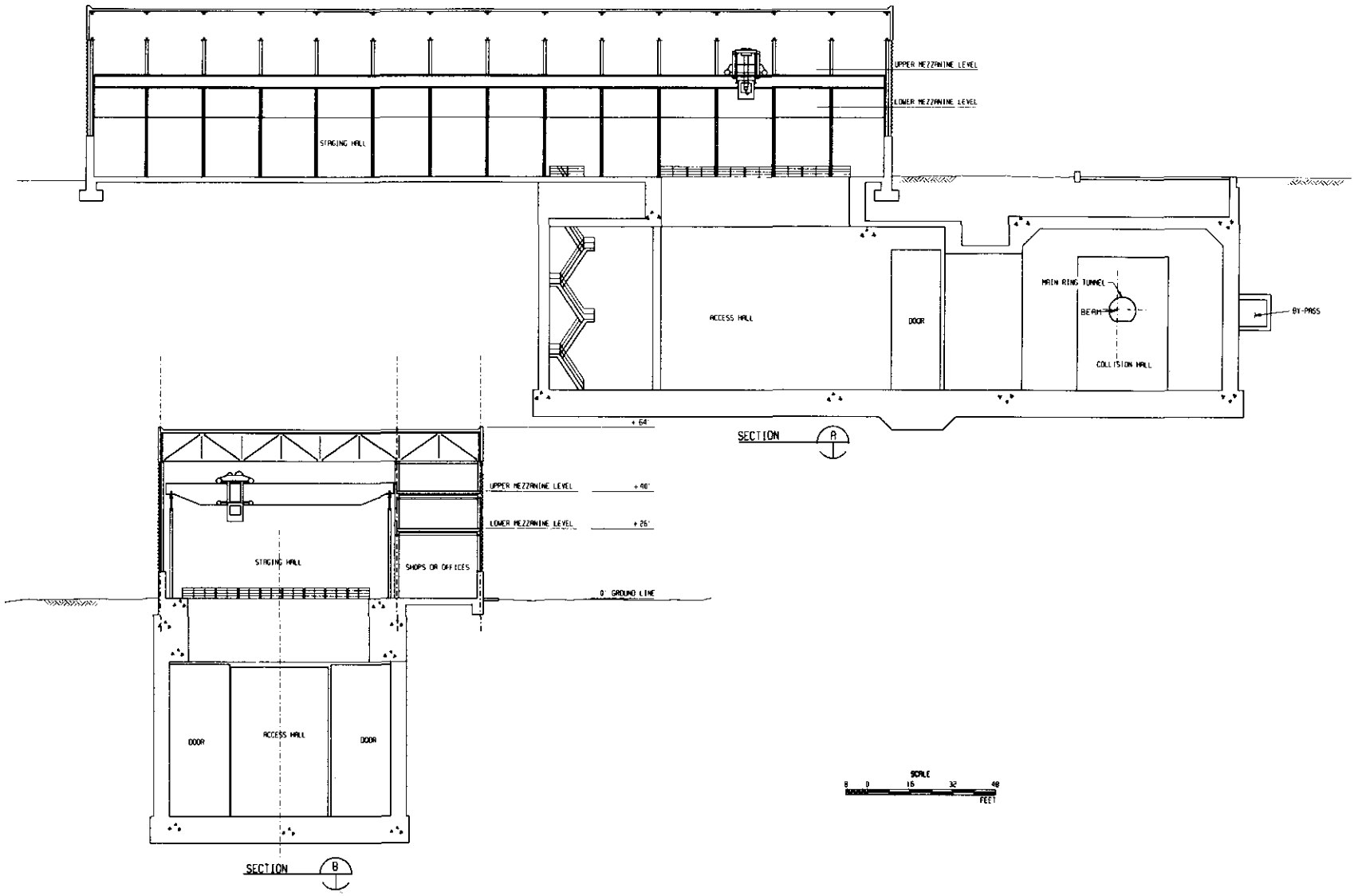

Figure 6.7-3. Cross Section View of Type A Staging Building showing building elements, high-bay area and assembly area; Type B Halls are identical.

detector (to the extent required), rolling it from one location to the other, reconnecting the service wiring and reestablishing the shield.

6.7.5 Detector Staging Buildings

The Detector Staging Buildings are located above the underground assembly areas and extend away from them in a direction perpendicular to the collider tunnels. These buildings are identical for all four IRs; they contain all the support services and facilities for assembling, testing and running their associated detectors. The most dramatic feature of a staging building is the 92 m (300 ft) long by 27 m (90 ft) wide high-bay work space covering the ground level and accelerator level pit areas. In the pit area, the component pieces of the detector can be assembled on the detector carriage. A pair of overhead cranes ride over this high-bay area, one of 50 ton capacity and one of 25 ton capacity. The detector subassemblies are put together in the surface-level workspace and then lowered by crane into the pit area where they are incorporated, piece-by-piece into the final detector.

There are two mezzanine floors incorporating electronic counting rooms, offices and shops in the full-length side-bay of the staging buildings. These bays are 9 m (30 ft) wide. The relationships among the elements of the staging building, the assembly area and the access tunnel can be seen in Fig. 6.7-4.

In terms of building construction and building services, the staging buildings resemble the heavy works buildings in the central laboratory campus. They are steel framed structures with insulated metal panel outer walls and a steel-decked, insulated single-ply membrane roof. Internal partitions are metal-studded drywall or cinder block as appropriate. The buildings are heated and supplied with water for potable, cooling, and fire purposes. A local sewage system is sized to the building occupancy. Fire protection is accomplished by a combination of sprinklers, halon tanks and local extinguishers as appropriate. There are smoke detectors and alarms in each of the areas.

The area surrounding each staging building has a paved parking lot plus various utility elements. Among the latter are power transformers (1.5 MVA), a cooling water tower and a flammable gas storage shed. For detectors that incorporate low temperature or superconducting systems, there is room to accommodate storage tanks for liquid cryogens. The electrical power distribution at 480 V will need to augmented as part of the installation of a specific experimental apparatus.

Utilities that supply the west cluster IRs are part of the central campus system. Those for the east cluster are provided from the East Master Substation. Communications between the IRs and the central control room follow the normal collider tunnel routing. Most of the signal transfer and signal processing associated with HEP experimentation is local and involves only connections between the detector and the electronic counting rooms in its associated staging building.

6.8 Utilities

6.8.1 Electrical

Primary electrical power for the SSC facility is derived from a 230 KV connection to the area power grid at the West Cluster and an independent 138 KV connection at the East Cluster. The capacity of the grid is expected to be more than fifteen times the peak projected load for the SSC and both facility tie points are close enough to the grid sources to

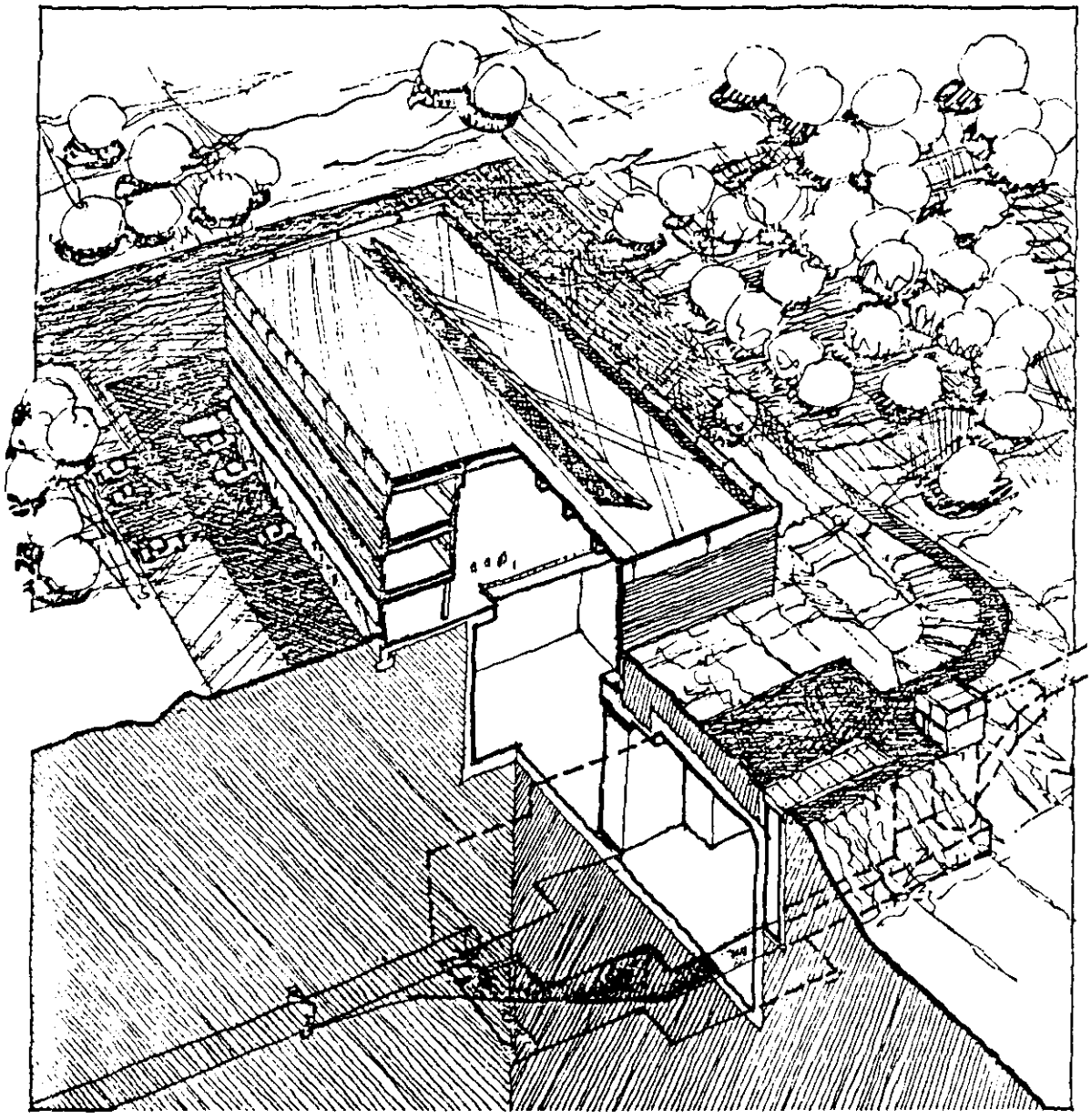

Figure 6.7-4. Perspective view of Experimental Hall.

ensure adequate line voltage stability under transients. The two independent grid ties ensure continuity of site power by preserving sufficient helium refrigeration capacity to prevent any loss of the site helium inventory during maintenance of the primary switchgear or in case of the loss of primary power from one of the two grid connections. This reserve power capability derives from suitable interleaving of power connections from the two sources. In addition there is an interconnection of secondary power feeders at the 13.8 KV stepped voltage level. The 13.8 KV backfeeding connections also obviate the need for emergency generators for most of the site. Additional backup power sources are provided to cover possible life-threatening circumstances occasioned by the collapse of the area grid.

The 230 KV line at the West Cluster terminates in a West Master Substation (WMSS) where it is stepped down by one 30/40/50 MVA, 230 KV/35 KV transformer and four 30/40/50 MVA, 230 KV/13.8 KV transformers. Two of the latter are mechanically braced for pulsed operation. The 138 KV line at the East Cluster terminates in an East Master Substation (EMSS) where it is stepped down by a 30/40/50 MVA, 138 KV/35 KV transformer and a 138 KV/13.8 KV transformer at 30/40/50 MVA. The secondary buses at both substations can be tied together with vacuum connect switches for system backfeed or at the WMSS only for further backup in case of a failed 13.8 KV transformer.

The 35 KV secondary power distribution is a special voltage subfeed for the ten Service Areas around the Collider Ring. This subfeed voltage level was chosen to minimize power distribution costs for the very long distances involved in supplying power to the SSC collider ring facilities. At the East and West cluster service areas power is derived from the 13.8 KV secondary bus for local area power distribution. Figure 6.8-1 illustrates the overall distribution of the electrical power to the site.

Two 500 thousand-circular-mils copper cables comprise the independently fed East and West 35 KV feeders which loop the entire collider ring within the tunnel. One loop is powered from two breakers on the 35 KV bus at the WMSS, and the second from the 35 KV bus at the EMSS. Each 35 KV feeder supplies power to alternate Service Areas, so loss of power on one feeder affects only half of the refrigerators; this type of line failure (or shutoff) leaves sufficient refrigeration capacity on-line to maintain the site helium inventory (though not enough to sustain accelerator operations). At the Service Areas a 35 KV/13.8 KV, 7 MVA substation provides the subdistribution for the normal power requirements of a magnet lattice sector. The 4160 V power for the cryo-compressors and the 480 V technical and conventional power are derived by subtransformation from the 13.8 KV sector secondary bus.

There are two 13.8 KV distributions for the SSC facilities. The first is derived by direct stepdown from the primary feeds at the East and West Master Substations. All the electric power for the East and West Clusters, including the pulsed power for the conventional magnet injector accelerators, is included in this 13.8 KV distribution. The 13.8 KV distribution is accomplished by radial feeders from the Master Substation through underground ducts to transformers at specific end use buildings. The second 13.8 KV distribution is locally distributed at the eight sector Service Areas in the North and South arcs and is derived from the 35 KV buses as described above. All power at the end use points is available at 13.8 KV. This simplifies maintenance and spare parts inventory. The 13.8 KV switchgear is also substantially more economical than would be required for direct transformation from 35 KV.

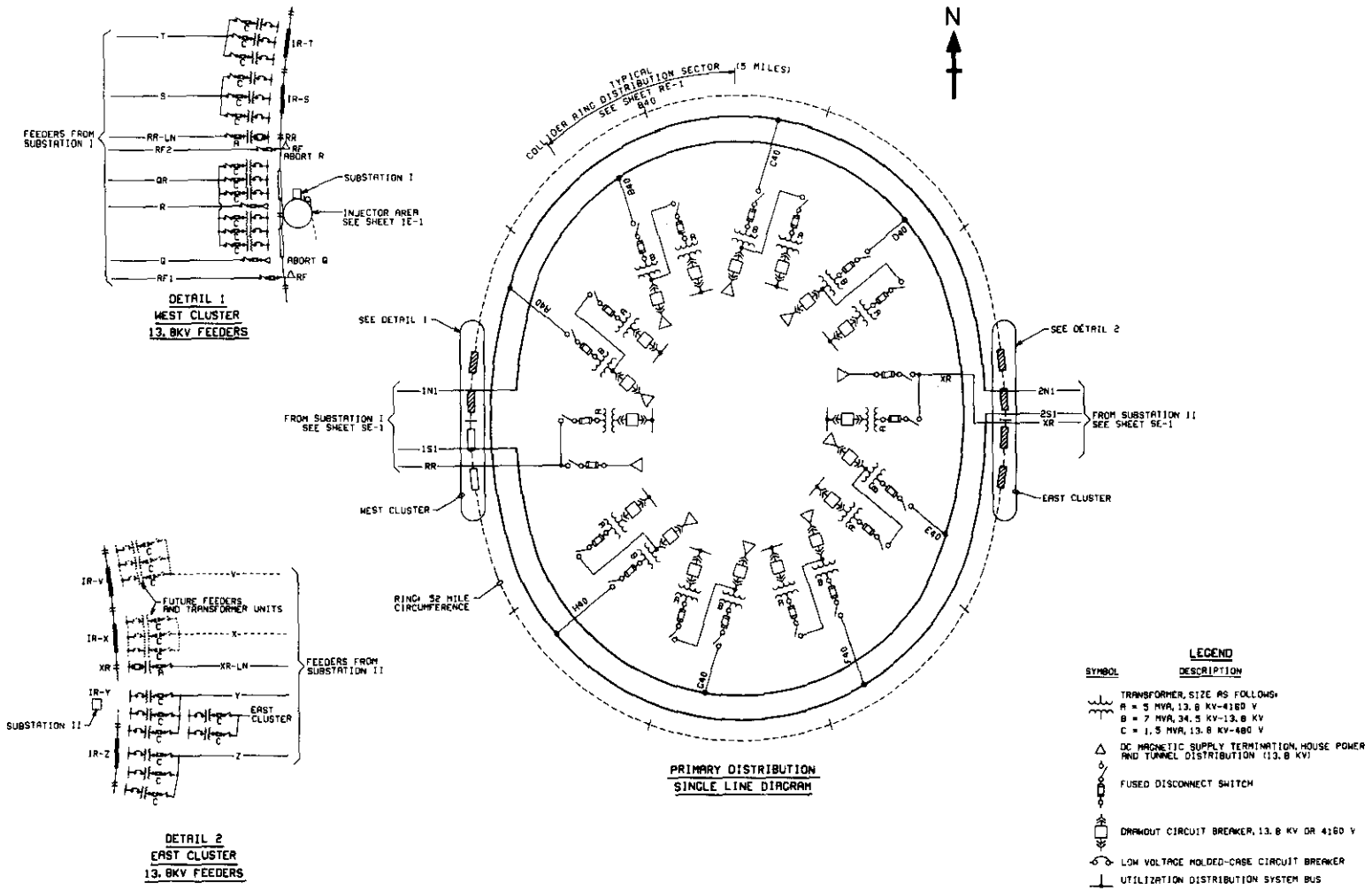

Figure 6.8-1. Schematic drawing of the electric power distribution grid. Main feeder routes and substation locations are indicated.

Distribution of power within each Collider tunnel sector is provided by a 13.8 KV feeder from a mid-sector transformer in the Service Area through the tunnel to the sector end points, 4 km (2.5 miles) in either direction. At five-cell intervals along the tunnel (the cryogenic isolation points), a 500 KVA transformer at 13.8 KV/480 V substation provides the 480 V tunnel utility power subdistribution for approximately 450 m (1475 ft) in either direction. At one end of the sector, the 13.8 KV feeder connects to a 750 KVA transformer that supplies power to that area of the tunnel as well as to special equipment associated with the exit/vent shaft at that location. At the other end of the sector, the feeder connects to a remotely-operable switch capable of connecting the 13.8 KV feeders of two successive sectors together. In case of loss of power at one of the Service Areas, sufficient power for essential systems can be backfed from the adjacent one along their normally separate 13.8 KV lines. This backfeed is accomplished by closing the isolation switch from the main control room.

The 4160 V power for the cryogenic system compressors is provided by a 5 MVA, 13.8 KV/4160 V transformer fed from the 13.8 KV secondary bus of the 35 KV Service Area transformer for the arc sectors. The magnet power supplies for the collider ring are fed directly from the 13.8 KV bus of the Sector Service Area transformers. Pumps and other Service Area equipment operate from the 480 V subfeeds.

6.8.2 Water

A regional water supply source is available at the West side of the SSC laboratory. This will be the major source of makeup water for the laboratory. A 14-inch main supply line connects the water supply source to the West Campus. This serves the potable and fire protection needs of the Campus and the two Interaction Regions constituting the West Cluster. A well field source is provided on the East side of the laboratory. This source is tapped to provide the much smaller potable water needs of the East Cluster.

A substantial amount of industrial cooling water (ICW) is required to carry away the heat generated by the more than 100 MW of projected average power consumption of the laboratory, and to meet fire protection needs at those facilities not included in the East and West Clusters.

At the Sector Service Areas around the Collider Ring, the heat generated by the cryogenic compressors and magnet power supplies will be carried away by the use of evaporative cooling towers. While these operate in a closed loop, a supply of industrial water is needed to make up losses due to evaporation and windage, for periodic blowdown, and for local fire protection. For most of the Service Areas this water will be supplied from local wells. At locations around the Collider where there is a relatively high influx of water into the drainage system of the tunnel, the sump discharge will be retained and used in the heat rejection system to reduce well requirements. At the remote areas that have minimal occupancy, commercial bottled water will be used for drinking water since it is not feasible to guarantee the potability of water in a piped system that is stagnant over extended periods.

The highest volume use of water at the SSC laboratory will be for cooling of technical and heating, ventilating, and air conditioning systems. In these systems, water circulating in a closed loop removes heat from a device or system and releases it to another water system or into the atmosphere. Where the circulating water is subjected to an electrical potential difference (e.g., in water cooled power supplies), it must be deionized to provide water

of low conductivity (LCW). In other applications it is only treated to remove solids (and in extreme cases dissolved chemicals) to meet industrial cooling water standards. Makeup water must be added to the systems periodically to compensate evaporation, leakage and windage. In addition, the systems must be "blown down" (i.e., flushed) periodically to counter the buildup of residual salts.

In the West Cluster, ICW is derived from the west regional water supply. A central utility plant provides treatment, control and monitoring of the water systems for the Linac, LEB and HEB, as well as the Central Laboratory complex. This ICW is distributed to the Linac, LEB and MEB. At the Linac, the LEB, and at each of the six power supply locations on the MEB, closed loop LCW systems of appropriate size are cooled by the process water in water-to-water heat exchangers. The heated ICW then returns to the central plant to discharge its heat in the evaporative cooling towers there.

The HEB has a cryogenic magnet system, so its only requirement for LCW cooling is in the power supplies and the water-cooled copper bus from the power supplies to the magnets. Two LCW systems are provided, each covering three of the six power supplies around the ring. The primary cooling loops for these supplies are at locations QQ and RR with makeup water obtained from the Campus ICW system. The two abort dumps for the HEB are at QQ. To isolate the radiation from the dumps, a secondary closed-loop system is required. The primary loop for this is cooled by a local air heat exchanger. The large cryogenic refrigerator for the HEB, with its severe requirements for compressor cooling, is located at NN. A cooling plant facility identical to those at the Collider Ring Service Areas is provided here with makeup water drawn from its own well.

The collider ring Interaction Regions at S and T are on the same feed of the regional water supply as the Campus and Injector. This source serves potable water, fire protection and ICW needs of the IRs. Cooling towers at each of the IRs provide the required heat removal for the conventional accelerator systems needs. Makeup water for these areas is supplied by the regional water supply. Any additional cooling requirements or LCW requirements of the experiments will be provided as part of the experimental apparatus. The Interaction Regions at V, X, Y, Z in the East Cluster are treated in the same manner as S and T with water being drawn from the east well field. The makeup water for the East Cluster Service Area, which includes the air separation plant at X, is drawn from the same source.

6.8.3 Fuel

As an example for design and cost estimating purposes, it is assumed that heating for the buildings in the East and West Clusters is provided from the high pressure natural gas line postulated to cross to the north of the site. An appropriate main gas line tap and pressure reducers are installed adjacent to the East and West Clusters. From there, the laboratory will distribute gas within the Campus and to the Interaction Regions. This fuel distribution method can provide a very stable, economical and reliable supply.

Heating for the Collider Sector Service Areas will be electrical. These facilities already generate sizable quantities of heat from the installed equipment. Incremental heating will be restricted to those occasions when maintenance personnel are working there. Since the

electrical distribution is configured to ensure reliability of supply to these Areas for technical reasons, the use of electrical heaters for incremental heating needs is sufficiently reliable to protect the systems from freezing even in very cold weather.

6.8.4 Telecommunications

A failure-hardened environmental monitoring system with 9600 baud voice and data capability will be installed throughout the facility to handle fire alarms, building integrity, environmental monitoring, and utility monitoring and control. This non-interruptible system will be supplemented by an FM radio paging system with sufficient range to cover the entire site. A radio repeater system will be designed to allow direct two-way radio communications for technical and emergency personnel who require that capability.

Broadband communication channels, including fiber optics, will connect the Interaction Regions with the West Campus. These, along with the Laboratory phone/data system, will connect into regional communications networks to allow communication of data to home institutions.

6.9 Environment and Safety

6.9.1 Introduction and General Policy

In recent years the issues of environment, safety and pollution have received much consideration during the conceptual and planning stages of projects of all sizes. These issues are particularly in evidence in large federal projects like the SSC where a significant amount of formal control has been put in place in addition to the generally increased sensitivities of project planners and host communities. This section of the Conceptual Design Report addresses these issues in a preliminary way and articulates the principles that will be followed in the course of construction, operation, modification, and decommissioning of the SSC Project [6.9-1]. Underlying all the particular issues that will be discussed is the general position to be followed: All activities in planning, building, operating, modifying, and decommissioning the SSC will be carried out in compliance with applicable federal and state laws and regulations applying to the safety and environmental aspects of this activity. In particular, applicable requirements of the National Environmental Protection Act will be met.

6.9.2 Radiation Shielding and Radioactivity

Before entering into the details of radiation shielding at the SSC and the related issue of residual radioactivity, it is useful to outline some of the basic concepts and issues, particularly for readers who are not technically familiar with them. Radiation at an accelerator is the presence of subnuclear particles moving with sufficient kinetic energy that they are free of their normal atomic binding in atoms. At the SSC, the particles can have very high energies indeed, comparable to the energies of the high energy components of the earth's cosmic ray background, a natural source of radiation that continually bombards the entire globe from deep space.

Most of the particles that constitute radiation in the SSC consist of massive particles that, when brought to rest by collisions with matter, quickly decay into the ordinary particles that make up common materials all around us, that is electrons, neutrons and protons. This is where shielding comes in. When bulk matter (concrete, dirt, water, iron, etc.) is interposed in the path of high energy radiation, the radiation generally suffers rapid degradation of its kinetic energy (by collisions of the particles with the nuclei of the bulk matter atoms of the shielding). The radiation is completely stopped in a few meters to a few tens of meters depending on the energy of the particles in the initial flux, the exact type of radiation and the density of the absorbing material (iron is more effective per meter than dirt, for example).

Once stopped, the energy of the radiation is converted to ordinary heat. The final products of the radiation, electrons, protons and neutrons are absorbed into the matter in which they stop and become a mostly indistinguishable part of it. The heat is removed, as it would be for any other source of internal energy (electrical or chemical, for instance) by a closed cooling water system connected to an outside heat exchanger. In essence, high energy radiation has its source in the accelerated proton beams of the SSC accelerators; it is eventually turned safely into ordinary heat after serving its purpose in the accelerators and experiments of the facility.

Muons

There are a few special circumstances that must be considered beyond this simple picture. One of them is the existence of muons. The other is the subject of residual radioactivity. Muons are a rare (a few tenths per cent) particle component of the radiation ordinarily created in the SSC accelerators, but in contrast to the other particle components, they are not readily absorbed at high energies. Experience at all existing accelerators shows that the high energy muons are very strongly directed along the direction of the proton beams whose interactions create them. For this well-understood reason the shielding problem is quite manageable. The muon radiation, in fact, is only significant in the contexts of the High Energy Booster and the Collider Rings. Since these accelerators are buried in the ground, the radiation exposure from muons will be controlled by restricting human occupancy in below-ground regions located at an elevation of from 6 m above to 6 m below the accelerator level. In the case of the HEB, the restricted zone is a donut shape of width 50 m outward from the HEB. For the Collider, the restricted donut zone is of width 200 m outward from the collider tunnel. In the cases (Example Sites A and B) where the collider tunnel is deeply buried, the restriction will not significantly affect near-surface structures such as ordinary basements of residences and commercial buildings. In the case of Example Site C, the control zone may preclude occupancy with unrestricted access.

Residual Radioactivity

The second special consideration is the issue of residual radioactivity. Radioactive nuclei are produced in the process of stopping high energy particle beams. In the course of stopping, the energetic particles produce numbers of lower energy (shower) particles in the absorber, and these in turn slow down and stop. Low energy (slow) neutrons are produced in the shower and these particles are absorbed by the bulk matter nuclei. Some of the created nuclei are unstable with radioactive half-lives ranging from microseconds to thousands of years. In general, the lighter absorbers (carbon, oxygen, hydrogen) decay

rapidly and exhibit little long-lived radioactivity. A few of the nuclei produced in heavier materials (copper, iron, lead, etc.) can have long lifetimes. These nuclei are the source of the natural radioactivity that we have all about us (and in our own bodies), as well as the artificial radioactivity that is created in the SSC.

The artificially induced radioactivity produced in the SSC accelerator complex is mostly of very low level. The few places where higher activation is produced are mainly the beam abort dumps. These dumps are special facilities designed specifically to discard circulating proton beams when their beam properties have deteriorated to the point that they are no longer useful for high energy physics experiments. The beam dumps are described below, along with the precautions taken to control the radioactivity produced in them.

Shielding Factors

The radiation shielding and radioactive materials handling considerations for the SSC facility are similar to those for existing accelerator facilities, such as those at Brookhaven National Laboratory, CERN, and Fermilab. Four factors that must be taken into account are the prompt radiation from the interaction of beam protons in the collision regions, the accidental scraping of beam protons on elements of the machine, the behavior of penetrating muon radiation, and the residual activation of materials outside the beam by hadron interactions particularly in the beam dumps. Each of these must be considered under normal operating conditions for the facility. The projected facility operations are also reviewed to take into account radiation conditions which might arise from possible accidental loss of beam, even if such accidental losses have very low probability of occurrence.

6.9.3 Collider Ring and Tunnel Shielding

In normal operations, the proton beams are confined in the vacuum chambers of the magnet rings. Radiation normally occurs only at the interaction regions where the two beams cross one another, and at the primary beam-abort dumps where the beams are absorbed at the end of a machine use cycle. A very small amount of radiation, which is absorbed within the walls of the tunnel, is produced uniformly around the ring by the collisions of beam protons with residual gas molecules in the evacuated beam tubes. Approximately 20% of the beam intensity will be reduced over a period of 12 to 24 hours due to interactions; the remaining 80% of the beam will be ejected in a 300 microsecond burst to the beam-abort dumps at the end of the cycle.

Radiation in the transverse direction from the beam interaction points is dominated by hadrons (strongly interacting particles). In the forward direction it is dominated by muons. This is because the forward hadrons are absorbed within the accelerator lattice by special scrapers and absorbers designed to protect the superconducting magnets. Beyond the absorber region and outside the beams enclosure, the radiation is a highly collimated muon cone that is produced in the decay of short-lived particles from the interaction.

The radiation from the primary beam-abort dumps is qualitatively the same as that around the interaction regions, but the shielding presents a different problem. At the interaction points, the shielding must be designed around experimental apparatus; it must also allow access for operations and maintenance. The shielding will usually have to be portable to allow movement of the apparatus into and out of the experimental halls. The

primary beam dumps, on the other hand, have no requirement for access or removal. Because they absorb the energy of most of the accelerated protons (400 MJ) in a very short time (300 μs) the beam dumps must, however, be designed to permit dissipation of the associated thermal and mechanical shocks, in addition to reducing the radiation to permissible levels.

Muons are produced in substantial numbers from the decay of short-lived particles in the colliding beam interactions in the IRs and in the abort dumps. The created muons lose energy mainly through electromagnetic processes as they pass through bulk matter. As a result, muons have a much longer range in bulk matter than the initially much more intense fluxes of strongly-interacting hadrons. Several meters of shielding contain the hadrons, while the energetic muons travel for several kilometers before coming to rest and decaying away. This circumstance results in the need for long shields concentrated along the forward muon beam directions from the interaction areas and from the beam abort dumps and the associated need for personnel access restrictions to the muon shields, as discussed above.

Hadron interactions with bulk matter have been extensively studied for many years and are well understood. This understanding is reflected in the good correspondence between calculated radiation levels and measured levels at operating accelerator laboratories. Several independent computer models for hadron shielding agree quite well with one another and with experiment. The hadron shielding that is needed for the experimental halls and for the primary beam absorbers is seven meters transverse to the beam direction. This shielding thickness will reduce the observed radiation levels to well below that from the naturally-occurring cosmic ray background [6.9-1]. The absorption of muons by bulk matter is also well understood, although there is some uncertainty in the production rate of the most energetic muons at SSC energies. An upper limit to the production can be deduced from known phenomena. Using this upper limit on production and the well understood absorption processes for the muons, it is derived that the muon shield will extend for two kilometers in the forward directions from the experimental halls and from the muon production sources.

As noted above, the shielding around the beam loss locations under normal operation of the machine will be determined by conservative estimates of these well understood phenomena. It is, however, necessary to provide protection against hypothetical worst case accidents in order to ensure that all exposure guidelines are met, even under the most unlikely accident conditions. Sensitive, high-reliability systems of radiation and beam-position detectors, plus appropriate beam-abort devices are incorporated into the machine to sense and prevent accidental loss of beam. This is necessary to protect the machine, since the circulating proton beams of the SSC have the capability to burn a hole in the vacuum chamber and seriously damage the machine if allowed out of their normal orbits. Similar protection systems are incorporated into all major accelerators. A typical operational record is that of Fermilab, where in thirteen years of machine operation, there has not been a single catastrophic loss of beam. An additional characteristic of superconducting machines is the fact that even relatively minor loss of beam will quench the superconducting magnets; this condition requires even tighter control on beam losses than those for earlier machines.

For calculating shielding away from the normal operation loss points, it is assumed (conservatively) that catastrophic loss of beam during normal operations could occur

anywhere on the periphery of the machine with a frequency of once per year. On the basis that such a full energy, full intensity beam loss could occur, the hadron shielding around the tunnel has been specified to be everywhere at least six meters thick around the tunnel. The forward muon cone extends tangentially along the ring for a distance of two kilometers under these circumstances. The sweeping of this cone around the entire periphery delineates a muon radiation zone of 200 m extent measured radially outward from the tunnel. The muon zone lies in the plane of the collider rings. Since muons are far less interactive than hadrons, the muon zone demands less restrictive personnel access conditions than the 6 m radius hadron zone described earlier.

6.9.4 Injector Shielding

The Injector Complex encompasses the same energy and intensity regimes as both Fermilab and the CERN SPS. The operating experience at both of those facilities is directly applicable to the SSC injector and will be used for determining the injector shielding. External beam use (fixed target physics programs) constitutes the most difficult shielding and monitoring aspect of the Fermilab operations; external beams will be present at the SSC only as test beams with operation at low intensities. The maximum repetition rate in this mode will be limited by machine parameters to one beam spill per 3 minute HEB machine cycle. In addition, the design proton beam intensities on the test beam production targets are of order 10^{12} protons per pulse, an order of magnitude below the 10^{13} beam required for the active experimental program at Fermilab.

6.9.5 Other Environmental Issues

Absorbing the energy of SSC beam in the beam dump results in approximately 11% of the energy being dissipated by nuclear breakup and excitation in the absorbing materials. Perhaps half of these encounters lead to radioactive end products, mostly short-lived. A small fraction of the resulting long-lived radionuclides that are soluble in water reach the outside of the beam dump. It is necessary, therefore, to insure that the site ground water is protected from contact with concentrations of these nuclei. In addition, if water is part of the absorber, the oxygen and hydrogen nuclei may also be excited and the resulting radioactivity (mainly tritium) must also be prevented from entering the ground water cycle. The principal sources of radioactive nuclei are the primary beam absorbers and other beam dumps where the beam is disposed of during normal operations. To avoid activation of the ground water either by leaching or by mixing ground water with cooling water, the experience of the high energy accelerators at Fermilab and CERN will be utilized. At these laboratories, concern for protecting the ground water, combined with the experience of operating the accelerators, has led to beam dump designs such as the one shown in Fig. 6.9-1. The core of the absorber consists of carbon pellets which absorb the thermal and mechanical shock after being struck by the 300 microsecond long proton beam pulse. The carbon core is encased in a water cooled aluminum box which diffuses and removes the thermal energy of the beam. Both the carbon and aluminum (which absorb the bulk of the radiation) are of low atomic number; this means that their residual activation is very small. Massive steel blocks surrounding the aluminum and carbon core region reduce the level of prompt hadron radiation so that ground water at the outside of the blocks is not activated,

even under extreme operating conditions. The entire dump is sealed in a reinforced concrete vault. To ensure that ground water cannot penetrate the vault to leach radioactivity from the iron, the whole vault structure is waterproofed. Beam dump designs and construction are closely monitored by an environmental health and safety group. To ensure the integrity of the dump and compliance with the radiation guidelines during operations, an elaborate monitoring system is installed in and around the dump (Fig. 6.9-1). The monitoring system is also the responsibility of the environmental health and safety group. In addition to the direct protection from potential sources of ground-water irradiation just described, a network of wells and surface stations is used to monitor ground water. The function of the monitoring of wells and ground water is to confirm their freedom from radioactive contamination.

Some of the energy absorption in the radiation cascade takes place in the air of the accelerator tunnel. In this case a fraction of the energy absorbed by the air will result in activation of the air nuclei. Since the accelerated beams of the machines are contained in vacuum, the levels produced in air outside are very low. Even in the abort line, the beam is maintained in vacuum right up to the face of the dump to avoid this type of activation [6.9-2]. For the same reasons, the amounts of noxious gases produced by radiation are also negligibly small. To confirm the success of these measures, careful monitoring is maintained to ensure by direct measurement that the laboratory operates well within permissible guidelines.

The SSC laboratory will follow well-established procedures to monitor compliance with all applicable environmental standards set by the U.S. Department of Energy. The thoroughness and sensitivity of these procedures are well documented in the annual Site Environmental Reports submitted to the DOE by each of the presently operating accelerator facilities [6.9-3]. As soon as a site for the SSC is decided, the environmental monitoring systems for the laboratory will be established in order to provide baseline data for natural radioactivity against which the laboratory's operating performance can be compared.

6.9.6 Site Safety

Radiation safety on the SSC Site outside the beam enclosures themselves will be provided by the passive shielding method described above and the results confirmed by active monitoring. The functions of monitoring compliance, keeping of records and preparation of reports will be the responsibility of a laboratory environmental health and safety group that reports to the laboratory director. The policy of separating the line operations safety responsibilities for a facility from the associated responsibility of ensuring compliance, and uniting these responsibilities only at the level of laboratory director, is a well-proven management principle.

Personnel Safety Interlocks

The major radiation problems associated with accelerators occur within the beam enclosures during operation of the beams. Except for residual activation in regions of the accelerators where beam is injected or extracted from the machines, radiation disappears with the shutting down of the beam. For this reason, the primary emphasis in accelerator radiation safety is to ensure that personnel are excluded from beam enclosures during beam operations, and that beam is excluded from enclosures when personnel are present.

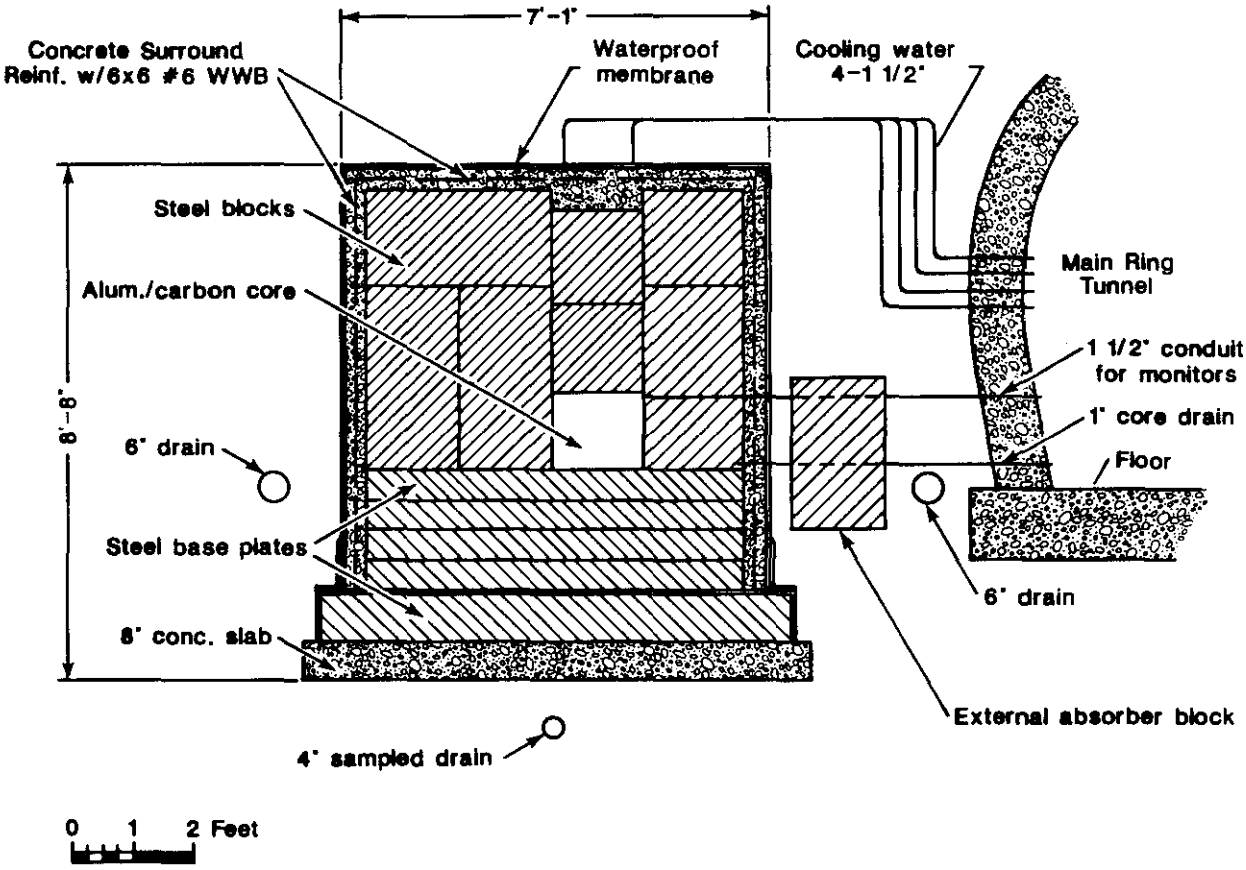

Figure 6.9-1. Cross section view of a typical accelerator beam dump; the graphite absorber, aluminum cooling jacket and outer radiation shielding are apparent.

As described in Section 5.14, the exclusion of personnel during beam operation is insured by carefully regulated levels of access and an interlock-based search-and-secure procedure in all beam enclosures prior to beam operation. For the SSC, this is a complex problem because of the great distances involved. This is particularly true in the Collider Ring Tunnel. The Collider is divided into interlocked segments based on the Sector Service Areas which are located at the center of each machine sector. Each sector is divided into sub-sections (coinciding with the cryogenic sections), which have separate sub-loops summing into the sector loop. Only when all loops have been made up and proper security certification established and sent to the main control room (by the return of all keys to key trees in all of the Service Areas), can beam be brought into the machine. It is not practical in the SSC to demand that all keys be physically returned to the main control room, so the security system is designed to log all personnel in and out by redundant positive identification. When access is required to the ring for inspection or maintenance, only the minimum necessary number of sections and sectors will be opened.

The security system is a two-tier system which remains made up even with personnel in the ring, though the primary level permitting beam is, of course, inhibited. In this way positive control of access is maintained at all times. Because life safety is involved, the security system has secure links to the main control room and multiple back-up power sources [6.9-4]. Once the ring is secured, any personnel access will automatically prevent introduction of beam into the machine.

Enclosure Protection

The second basic security principle is to ensure that no beam is brought into enclosures occupied by personnel. At least two levels of redundant critical devices are required, each of which can absolutely prevent beam from entering such an enclosure. Each of the two critical devices permits beam to pass only while all the interlocks are made up and none of the loops are tripped or open. A minimum physical separation and careful control of the relative orientation of the machines with respect to one another are required between all pairs of adjacent rings (e.g., between the Collider Ring and the HEB). These measures insure that beam loss in one ring will not cause radiation exposure to personnel present in an adjacent ring. The injection lines from one ring to the next are carefully designed with a 10 m long radiation-shield section that is penetrated only by the beam pipe. An accelerator beam pipe emerges from an enclosure only in a location where the beam must be bent by a magnet in order for it to enter that pipe at all. One of the critical devices can now be the magnet that is required to be energized for the beam to enter the channel. The second critical device is usually a beam absorber that physically blocks the channel and prevents beam from reaching the next enclosure.

All personnel entering beam enclosures must be positively identified and equipped with personnel monitoring devices. These devices are routinely monitored and logged by the environmental health and safety group. Detailed exposure records are maintained for each individual. These individuals will be allowed to enter beam enclosures only after attending training classes and receiving proper certification. Preparation and presentation of the training materials for these classes will also be the responsibility of the health and safety group.

Tunnel Safety

The new Federal OSHA tunnel construction regulations currently under consideration will provide guidance beyond the existing regulations. A study of this important issue of tunnel safety during construction is summarized in Attachment C (Section C.10.2). It is based on the California Administrative Code Title 8, considered one of the more stringent of the safety codes, as the primary source. Federal, industry and other codes and regulations were reviewed and cited when they were more stringent than the California Code. Details can be found in Attachment C.

Tunnel safety during installation is monitored by the laboratory safety group, but the primary responsibility for providing and maintaining a safe environment lies with the head of the laboratory section responsible for the installation. Two areas that will require special emphasis during the SSC installation are the provision of adequate fresh air in areas where large groups may be working, and maintaining mechanical tunnel clearance for the magnet and personnel transport systems. Tunnel safety during machine operation is the responsibility of the head of the accelerator section. Within the section there will be a safety group to provide safety training to operations and support personnel. The safety group will monitor the safety of operations and review the safety aspects of equipment, structures and shielding associated with operations.

The SSC tunnel must be monitored for oxygen deficiency (independently of the presence of cryogens in the superconducting magnets) because of the long distances and small air volume between access points. The access control system for the tunnel will prevent personnel access in the absence of a positive signal that circulation fans are on and that oxygen levels are adequate. In addition, personnel entering the tunnel will be required to have a personal rebreather pack with sufficient air capacity to reach an exit in case of an oxygen deficiency alarm. Personnel isolation zones with a positive fresh air supply will be provided in the stair wells at the Sector Service Areas and at the sector-end emergency exits.

Emergency power for lights, communications, sumps, etc. will be provided in several redundant ways. Battery packs and uninterruptible power supplies are provided for immediate backup of the critical systems. The primary provision for emergency power, however, is accomplished by the interconnection of (normally separated) alternate collider sectors via the 13.8 KV subdistribution feeders in the tunnel. This interconnection is accomplished by use of remotely-operable feeder-to-feeder switches at the sector boundaries. The alternate sectors are normally fed from two separate and discrete portions of the site power grid; this dual power source is required to meet the normal operating power needs of the cryogenic system. The half-power emergency connection system provides enough electrical capacity to support the standby power requirements of the collider with a much higher reliability than would a possible alternate emergency power system based on diesel-powered emergency generators at remote locations.

The SSC tunnel is occupied only during installation, maintenance and repair periods. It is empty during regular accelerator operations. In this regard, it resembles a pipe chase more than a tunnel (in the sense of vehicular and transit tunnels or mines). Further to protect personnel in the tunnel from the effects of noxious fumes under accident circumstances (fires, etc.), the procedures established for a similar tunnel at the CERN Laboratory in Geneva, Switzerland will be followed. These procedures carefully specify the safety characteristics of materials to be installed or used in accelerator and beam transport tunnels |page

192 of 6.9-5]. The installed cables are specified to be nonflammable; they must have insulation that does not release toxic gases when heated. Welding equipment for use in the tunnel is also tightly specified for compliance with these needs in mind.

The large distances between access points in the tunnel require that transport vehicles be capable of speeds up to 25 km/h (15 MPH). With distances of 8 km (5 miles) between service areas, this implies an average transit time of 10 minutes at full speed to a tunnel destination. At a lower speed of 8 km/h (5 MPH), it means an average time of 30 minutes to or from a work site. To meet the needed 25 km/h (15 MPH) speeds safely, the transport vehicles are attached to a guide rail on the inner wall of the tunnel. The guide rail is also the vehicle power source. Block system control of the vehicles and obstacle sensors mounted on them will prevent collisions. The system is similar to the "people movers" in use at airports. The vehicles are equipped with backup batteries that are maintained at full charge by the installed vehicle power source. When disengaged from the guide rail power sources, the vehicles may move independently under battery power at slow speed. If all tunnel power is lost, the vehicles are able to move to an exit under battery power. The storage capacity of the on-board batteries is defined by the need to power the vehicle over the full distance between exits in an emergency.

Fire sensor status signals from throughout the SSC facility will be routed to the main control room and to the emergency response center. For the campus areas, the laboratory fire brigade will respond. For both fire and medical alarms at remote areas of the sites, arrangements will be worked out with the nearby communities for rapid response at those sites. Existing vehicular, electrical and cryogenic safety codes will be used as appropriate in all laboratory areas following practice at existing DOE accelerator facilities.

6.9.7 Site Security

Personnel and property security at the main sites (East and West campuses and the Experimental Areas) will be handled appropriately. Since all of the above areas are very active, security personnel are necessary for traffic and parking control as well as for normal site patrol. The patrol function is particularly relevant outside normal daytime working hours when work areas are mostly unoccupied.

The remote sites are mostly unmanned and under the direct control of the main control room. A combination of building locks and TV camera surveillance form the basic security system. The remotely-actuated locked gates will be under TV surveillance by personnel in the main control room. Positive identification of individuals requesting entrance will be provided by coded ID cards to open the locked gates and doors, but only after a visual check of the individuals by means of the TV cameras. This visual check ensures against use of borrowed or stolen ID cards. Infrared emitter/receiver pairs will monitor the secure status of outside doors or other entrance ways to buildings at these sites. Buildings housing specialized equipment, e.g., cryogenic equipment, will be secured by conventional locks. The associated keys will be the responsibility of the laboratory group concerned. For those buildings having multiple functions, ID card access could be required. Site monitoring will be incorporated in the general equipment monitoring and control system along with fire alarms.

6.9.8 Waste Disposal

The solid waste generated at the SSC laboratory will consist of the usual mix of paper, cartons, scrap, etc. that is generated by any university or business community. Based on the comparable experience at Fermilab, a solid waste volume of approximately 30,000 cubic yards per year is generated. This material is collected by the janitorial crews of the laboratory and disposed of under contract by a local waste disposal firm.

By its nature, no high level radioactive wastes are generated in normal operations at an accelerator laboratory. Some low level activity, however, is generated at the places the proton beam impinges on elements of the machine, particularly at the injection and extraction points as was noted above. Since the activated items are mostly machine components, they remain in the tunnels. A small amount of low-level radioactive solid waste is also generated in maintaining and repairing these machine components. This solid waste is disposed of through a licensed waste hauler, who transports it to a radioactive waste disposal facility.

Liquid waste from the SSC facility will consist of sewerage appropriate to a community of 3000 daytime occupants. This will be treated in the laboratory sewage treatment facilities as described as in Section 6.4. There will be no liquid waste of a toxic or radioactive nature resulting from normal laboratory operations. If such a liquid waste should appear as a result of special circumstances, it will be disposed of by proper methods.

6.9.9 Decommissioning

As noted above, there is very little activation of site materials in operation of the SSC. The accelerator will therefore be decommissioned and removed at the end of its useful life. The radioactive materials that are produced in the accelerator itself consist of low level metal components to be disposed of in the manner of similar items at the Zero Gradient Synchrotron at Argonne National Laboratory and the Cosmotron at Brookhaven National Laboratory. The decommissioning will present no unusual or difficult problems.

References

6.1-1. SSC Central Design Group Report No. SSC-15 (1985).

6.9-1. Workshop on Environmental Radiation, SSC Central Design Group Report No. SSC-SR-1016 (1986).

6.9-2. A Fasso et al, CERN Internal Report No. T15-RP/TM/84-16 (1984).

6.9-3. S.I. Baker, Fermilab Report No. 85/32 (1985).

6.9-4. D. Neet, CERN Internal Report No. LEP Note-478 (1983).

6.9-5. CERN Report No. CERN-LEP/84-01, Vol. II (1984).

7. Project Plan

7.1 Laboratory Organization

7.1.1 Overall Structure

The initial Laboratory organizational structure will be geared primarily to encompass all of the project management tasks that are required to accomplish the construction phase of the SSC. At the same time, the organization will be able to accommodate appropriate R&D activities and also maintain the flexibility for a smooth transition to pre-operational and operational phases of the laboratory accelerator systems. A possible organizational structure for the construction period is provided in Fig. 7.1-1. This structure provides a model for project planning and a basis for estimating the cost of the project management functions during the construction period. The actual structure will have to incorporate the detailed conditions under which the Department of Energy (DOE) may arrange the construction program.

The Laboratory Director will be responsible for the full scope of SSC activities, including the external interfaces with DOE and the community, as well as all internal activities including preconstruction R&D, the construction project, preoperations activities phasing into operations, and the integration of the physics program. Within the Directorate, the Project Managers will have full responsibility for the construction project including design, fabrication or construction, assembly, and installation and initial testing of systems. They will utilize the Accelerator and Conventional Systems Divisions as primary operating units and will draw upon the resources of the Support Divisions as required.

The Accelerator Division will oversee and direct the design and construction of all five accelerators that comprise the injector complex and the main collider. A separate group for magnets is projected under this division because of the major role of superconducting magnets in both the high energy booster and the collider ring. The Conventional Systems Division will provide the criteria and oversee the construction of all buildings, enclosures, and utilities that are required by the accelerator systems as well as the laboratory complex. The detailed design and construction activities will be carried out by selected Architectural and Engineering/Construction Management (AE/CM) firms.

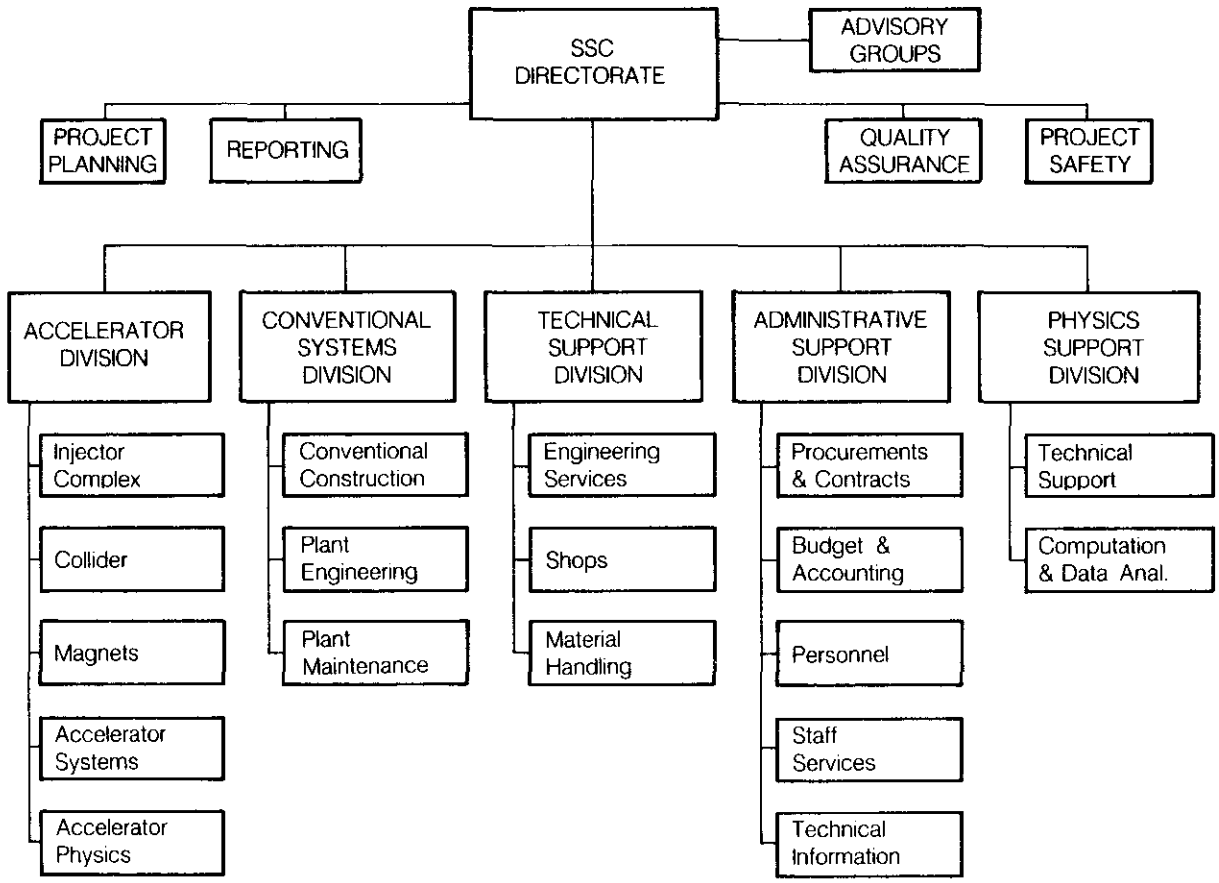

Figure 7.1-1. SSC project management and support organization.

The Technical and Administrative Support Divisions will provide the appropriate services outlined in Fig. 7.1-1 which are required to support the personnel and the construction activities of the Accelerator and Conventional Systems Divisions. The Physics Support Division will provide support to experimenters for the design and development and fabrication of detectors and for the preparations and installation of required experimental area equipment.

It should be emphasized that the Laboratory organization indicated in Fig. 7.1-1 is a model for planning and cost estimating purposes and does not represent a detailed management plan for the SSC.

The SSC Laboratory Organization is projected to interface with the DOE program offices and field offices in the manner displayed in Fig. 7.1-2. This projection is based on prior experience and does not imply that future management relationships will be identical. The technical and programmatic responsibility for the project will reside with the Division of High Energy Physics (DHEP) within the Office of High Energy and Nuclear Physics (OHENP) in the Office of Energy Research (OER). The contract administration and performance monitoring of the construction activities will occur through the DOE Chicago Operations Office (CH). The contracting organization for the current SSC R&D program (Phase I) is the Universities Research Association (URA). The detailed responsibilities of each of the above offices and organizations is described in the SSC Management Plan.

7.1.2 Project Management

The Accelerator Division and the Conventional Systems Division groups will provide the leadership for directing and coordinating the construction activities. The construction plans as well as their execution fall within the responsibilities of these divisions. The directorate and the associated groups for Project Planning, Reporting, Quality Assurance, and Project Safety provide additional project controls for construction activities. These groups would operate in support of the technical activities and at the same time provide the SSC director with appropriate data required for control, management, monitoring, and reporting relative to the total project.

The Conventional Systems Division will provide the criteria and specifications for the design of the conventional facilities and will supervise and monitor the work of the AE/CM firm(s). This division will be the main technical liaison group for conventional systems within the SSC organization. The specific title I, II, III design and construction tasks would be accomplished via an AE/CM organization reporting to the Conventional Systems Division. The AE/CM would have the responsibility for detailed design, construction planning, contracting, and inspection to assure that all construction contracts are carried out according to plan and schedule.

The Accelerator Division leadership would have primary responsibility for the design, planning, and systems integration for each of the injection accelerators (Linac, LEB, MEB, HEB) and the collider technical systems. This Division also provides technical group leadership in the primary area of magnet design and in the area of other accelerator systems such as cryogenics, vacuum, rf, and control systems. The division leadership and the associated group leaders shown in Fig. 7.1-1 will together provide the detailed planning, management, and technical direction for the total engineering, design, and inspection (EDI) and construction effort. The projected staff levels for the above technical management

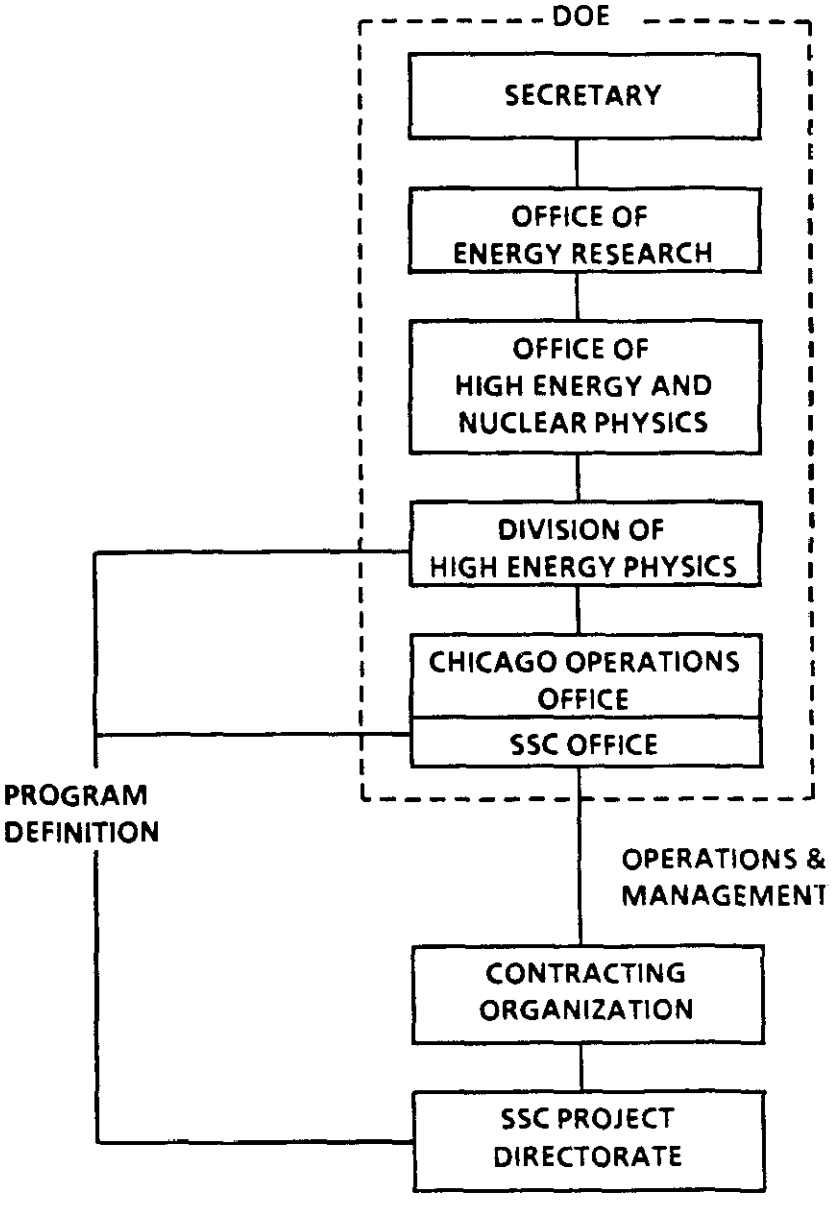

Figure 7.1-2. SSC project management relationships.

groups are provided in Table 7.1-1. A complete summary of all projected laboratory manpower is provided in Section 7.4-5.

7.1.3 Laboratory Support Services

The Accelerator and Conventional Systems Divisions described in the previous section provide the technical leadership for design and construction of the SSC. These divisions require various support functions to operate in an effective and efficient manner. These support functions are to some extent routine at existing laboratories; however, at a new facility such as the SSC the organization for these tasks must be established. While the grouping or arrangement of these functions may vary, the component services are similar to those which are found at existing DOE laboratories.

The Technical Support Division includes the major subgroups of engineering, shops, and material handling. The engineering group will help to provide the appropriate engineers and designers to the technical group staff as required for the overall EDI effort. Consideration must be given to the technical requirements of various tasks, level of effort, and the schedule demands of design and fabrication efforts.

The Shop Group has the major responsibility to insure that fabrication efforts will be achieved with the required specifications and the necessary schedule. While it is expected that most fabrication of SSC accelerator and detector components will be accomplished through "outside" shops, some capability must be maintained on site for special parts and repairs. The Shop Group has the responsibility to establish the necessary facilities and provide direction for their operation. The Material Handling Group will provide and manage warehouse facilities for materials, parts, and systems that are needed for fabrication and testing. In addition this group will provide the necessary transportation facilities at the SSC for materials, components, and equipment that are required for assembly and installations of technical systems.

The Administrative Support Division will support the construction effort via staff groups for procurements and contracts, budget and accounting, and a personnel department for staff management. The Technical Information Group will provide services for producing and distributing all technical reports of the SSC. In addition Tech Information will provide and maintain library facilities for the SSC. Finally the staff services group will maintain a variety of services that are required for an organization of the size projected for the SSC. These include a public information office, travel office, communications office, contract services office, and Health and Safety Department.

The main functions of each of the Technical and Administrative Support groups are summarized in Table 7.1-1 together with the projected staff levels. Initially the activities of these groups will be tailored to meet the needs of the construction project. As the construction nears completion, these functions and associated staff are expected to evolve such that the operational needs of the laboratory can be met.

7.1.4 Research and Development, Pre-Operations, and Physics Support

The R&D areas and pre-operations are outside the scope of the construction program; however, these programs will be part of the Laboratory responsibility and have an impact on total staff at the laboratory. R&D in support of construction as well as pre-operational

Table 7.1-1
Projected Staff Levels for Management and Support Services
(Construction Project)

		FTE*
.4.1†	*Project Management*	
.4.1.1	Director's Office	8
.4.1.2	Project support	38
.4.1.2.1	Planning and budget	
.4.1.2.2	Reporting	
.4.1.2.3	Quality assurance	
.4.1.2.4	Safety	
.4.1.3	Accelerator Division	46
.4.1.3.1	Injector complex	
.4.1.3.2	Collider	
.4.1.3.3	Magnets	
.4.1.3.4	Accelerator systems	
.4.1.3.5	Accelerator physics	
.4.1.4	Conventional Systems Division	57
.4.1.4.1	Conventional construction	
.4.1.4.2	Plant engineering	
.4.1.4.3	Plant Maintenance	
.4.1.5	Technical Support Division	69
.4.1.5.1	Engineering services	
.4.1.5.2	Shops	
.4.1.5.3	Material handling	
.4.1.6	Administration Support Division	99
.4.1.6.1	Procurement & contracts	
.4.1.6.2	Payroll & accounting	
.4.1.6.3	Personnel	
.4.1.6.4	Staff services	
.4.1.6.5	Technical information	
.4.1.7	Physics Support Division	20**
.4.1.7.1	Technical support	
.4.1.7.2	Computation and data analysis	
	Total	337

†Numbers refer to the Work Breakdown Structure.
See Table 8.1-3 and Fig. 8.1-1.
*Average staff during the construction period. Does not include construction, EDI or AE/CM staff.
**Not included as "Construction Project" Staff.

activities will be needed. The staff requirements and associated costs will be treated in a special report. The R&D would include any special engineering developments needed prior to construction of various technical systems. The operation of subsystems for debugging and systems integration would be included in the pre-operations costs after construction is completed. The pre-operational programs as well as SSC related R&D projects are expected to be accommodated within the same organizational structure as shown in Fig. 7.1-1.

The physics research program at the SSC will involve a large group of high energy physicists from throughout the United States. In order to expedite the experimental program the SSC Laboratory will provide appropriate technical support for these research activities in a manner similar to that of other existing high energy research facilities. A Physics Support Division is projected to provide Engineering and Technical Support for outside groups with regard to the development and fabrication of particle detectors and associated apparatus. The support groups will also provide cooperation and assistance during the operations phase of the experiments. A computations group will provide research support in terms of computer and data analysis facilities. The Physics Support Division is expected to keep the SSC Laboratory abreast of overall physics research goals and developments. In particular this group will provide information with regard to the operational requirements of experimental stations. Costs for these activities will be treated in a special report.

7.2 Technical Systems

7.2.1 General Plan for Design and Fabrication

The SSC construction phase is assumed to start at the beginning of FY 1988. The technical design of the SSC and its components will be executed by a highly qualified and experienced staff of physicists, engineers, and designers. The general technical design staff (EDI staff) will report through the supervision and management staff as described in Section 7.1.2 The management group will provide the SSC goals and performance specifications together with detailed schedule plans for both design and fabrication efforts. These efforts are planned and coordinated with the projected schedules for conventional systems as described in Section 7.3.

The EDI staff will involve a variety of design teams. The leadership of a design team for a specific technical system is expected to oversee both the design and fabrication effort through final project installation and testing. The detailed composition of the staff is expected to vary as the system progresses from initial design through detailed engineering design to inspection and testing.

In general the EDI team members are projected to be predominantly SSC Laboratory staff with assistance from other national laboratory staff members and industrial consultants as required. The overall fabrication effort will be undertaken by a combination of resources at the SSC Laboratory, other national laboratories, and industrial facilities as described in the next sections.

7.2.2 Superconducting Magnet Production

The SSC superconducting magnet systems comprise a major fraction of the SSC project costs. As a result pre-construction research and development activities have focused on the development of superconducting dipole magnets appropriate for the SSC collider. Dipole magnet models have been fabricated and successfully tested within the SSC research and development program, and a plan has been formulated to transfer the magnet technology to industrial manufacturers.

The objective of this program is to involve industry in the early stages of research and development in order to facilitate industrially-made superconducting magnets. This will help to provide for a cost-effective process in the mass production of high quality superconducting magnets. These steps will help to provide for early and rapid tooling-up and start of magnet production early in the construction project. The accomplishments of the Phase I R&D work will also provide assurance that the SSC organization will be able to release the major contracts for material purchases and magnet assembly contracts that are implied by the schedule shown in Fig. 7.2-1. The overall magnet production plan summary described by Fig. 7.2-1 shows the main dipole magnet fabrication schedule along with the quadrupole magnet, spool piece, and other special magnet fabrication and installation plans.

The fabrication and installation of the main collider ring magnets have received considerable attention during the planning studies. The magnet production plan is based on the assumption that two or more industrial firms will manufacture the nearly 8000 dipole magnets required and ship them to the SSC site for final testing and installation. The peak production rate of approximately 600 dipole units per quarter requires an efficient and aggressive work plan. Preliminary manufacturing studies, which included tooling development, manufacturing sequences, and assembly and tests have been carried out. The phased steps leading to authorized manufacturing contracts by several qualified vendors in early FY88 are now underway. Figure 7.2-1 shows the major dipole fabrication extending from FY90 (after production tooling is fabricated and installed from June 1988 through December 1989) through approximately December 1993, a period of approximately four years. The fabrication of the quadrupoles and spool pieces starts approximately six months later, March 1990, and the installation of the half-cell units (each comprised of five dipoles, one quadrupole, and one spool) commences near the beginning of FY91.

7.2.3 Technical Systems Fabrication and Procurement

The scale of the SSC project will require fabrication of technical components by a combination of efforts by the SSC Laboratory, other DOE research laboratories, and industry. The exact determination of all production assignments cannot be made at this time; however, a model is used to project a reasonable plan.

It is assumed that the SSC Laboratory management has the prime responsibility for all technical systems. Such responsibility demands that the SSC Laboratory will have the essential technical expertise required to design, fabricate, test, and analyze technical systems. At the same time, it is recognized that considerable expertise as well as production capability for technical systems exists in industry and at the various accelerator laboratories currently in operation. Existing fabrication capabilities at the U.S. accelerator laboratories will be utilized where appropriate. Due consideration must be taken of the cost

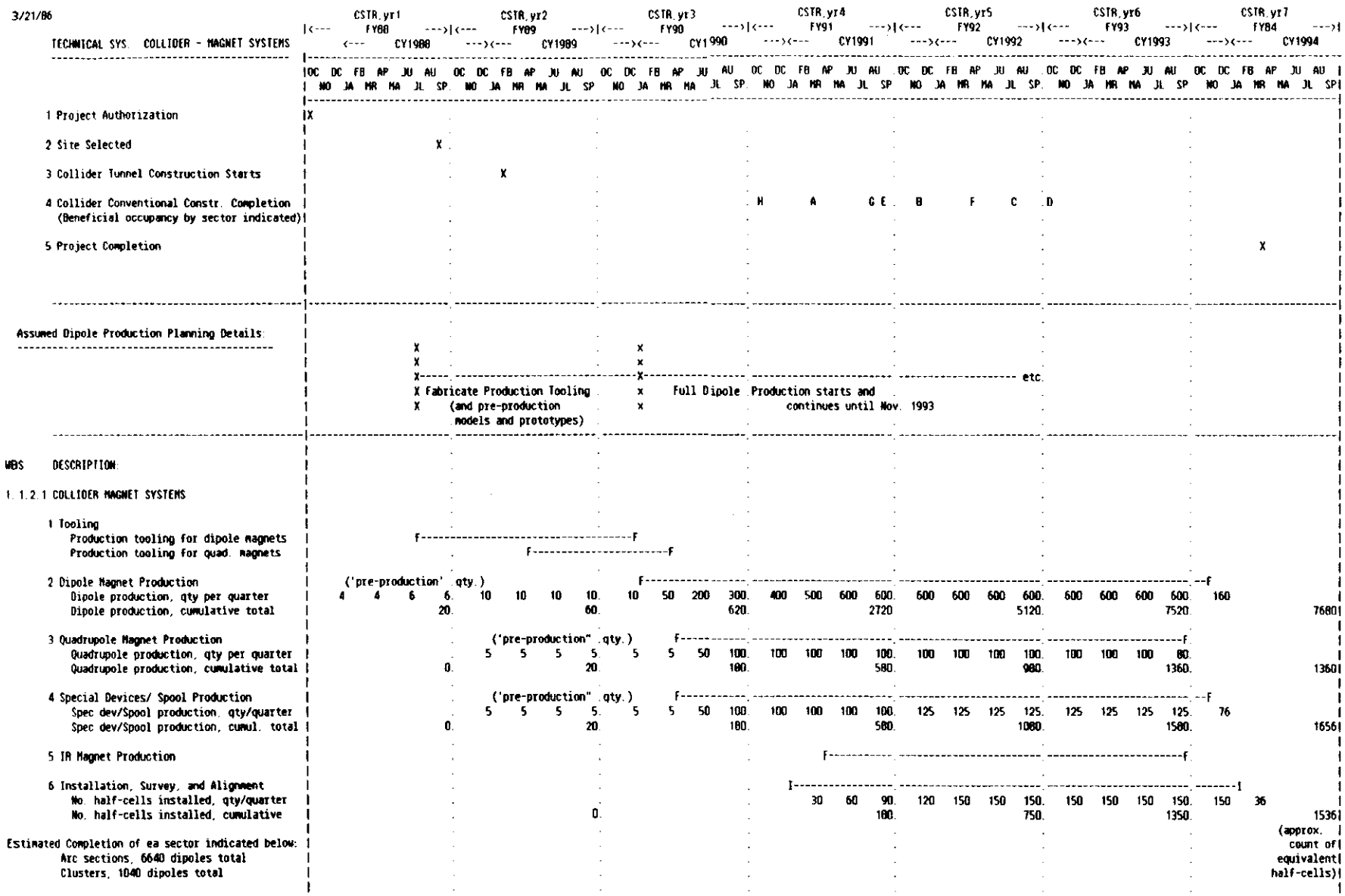

Figure 7.2-1. Collider ring magnet production plan.

effectiveness of such utilization and the availability of other laboratory facilities in view of their ongoing research program needs.

Historically, industry has been progressive and innovative in developing methods and techniques for the mass production of various technical systems and components. It is quite clear that nearly all SSC components and materials (e.g., superconducting cable, magnet components, power supplies, beam tubes, etc.) are dependent on the manufacturing industry. In addition, the industrial assembly of systems, such as superconducting magnets, is assumed herein for planning purposes.

In summary the SSC program is expected to utilize both laboratory and industrial capabilities in completing its mission. The exact plan will depend on the capability, availability, and interest of the possible participants with due consideration to cost effectiveness, quality control and assurance, and schedule requirements. With this flexibility in mind, a general model for the production of technical systems is outlined below.

Within each of the major SSC accelerators (Collider, HEB, MEB, and LEB) the magnet systems represent the major technical system in terms of function, cost, and complexity. The SSC accelerator system will involve some 13,000 magnets of many different types and with varying technical specifications according to their required function. The number of magnets of a given type can vary from a single unit up to nearly 8,000 units for the collider ring dipoles.

For those magnets of a given type where many units ($\geqslant$ 1,000) are required, it is planned that industrial production capabilities be fully utilized. At the same time, the SSC Laboratory will maintain the capability to produce a modest fraction ($\sim$5%) of these units. This SSC capability is vital for the expertise required in the technical evaluation of industrial production methods and potential problems. This laboratory capability is also needed for future developments as well for the expeditious replacement or repair of magnet units if required during future operations.

In the category of magnet types in which the number of units per type is relatively small, large scale production facilities are not a vital requirement. The class of special purpose magnets such as kickers, splitters, vertical dipoles, and a variety of special quadrupoles are examples within this category. It is assumed that the SSC Laboratory together with other existing high energy physics laboratories will have the capability to produce the majority of these magnets.

In addition to the industrial plan for magnet fabrication described above, certain other major systems will be purchased from industry. Such purchases would include, for example, the overall cryogenics plants and associated gas storage systems, a wide variety of power supply systems, computers, and control system electronics. Major rf system components (Klystrons, cavities, and power supplies) are expected to be purchased commercially or fabricated by other laboratories. For example, the entire linear accelerator system which serves as the first injector to the SSC could be assembled by one of the existing accelerator laboratories. In general it is visualized that the majority of technical systems or components will be purchased items with component and systems assembly and test by the SSC technical staff.

7.2.4 Quality Assurance for Technical Systems

The SSC management will be fully committed to achieve quality in all aspects of the construction effort as well as the research and development program. The quality assurance (QA) is being initiated, meeting applicable requirements of ANSI/ASME-NQA-1 [7.2-1] and the applicable elements as prescribed by DOE order 5700.6A [7.2-2]. Quality assurance is defined as all those planned or systematic actions necessary to provide adequate confidence that the SSC will perform satisfactorily in service. Quality control are those QA actions which provide a means to measure and maintain the characteristic of a component or SSC system to established requirements.

In establishing an effective QA program, the following steps shall be accomplished:

a) Preparation of a QA manual that specifies how the QA program will operate.
b) Specification of the procedures and instructions that detail how the QA program is implemented.
c) Definition of the audit that verifies compliance with the manual, the procedures and the instructions and measures the effectiveness of the QA program.

Initial quality planning will determine what areas are critical and require QA. The interfaces between participating organizations will also be analyzed. The overall quality assurance program will include the following elements:

1. Organization
2. QA Program
3. Design Control
4. Procurement Document Control
5. Instruction, Procedures and Drawings
6. Document Control
7. Control of Purchased Items and Services
8. Identification and Control of Items
9. Control of Processes
10. Inspection
11. Test Control
12. Control of Measuring and Test Equipment
13. Handling, Storage and Shipping
14. Inspection, Test and Operating Status
15. Control of Nonconforming Items
16. Corrective Action
17. QA Records
18. Audits

Some of these items are discussed below.

Organization (Element 1)

This calls for specification of the organizational structure, functional responsibilities, level of authority, and channels of communication. Considering the participating laboratories, the numerous subcontractors and complexity of the project, the definition of the organization and the roles of specific individuals are important. The configuration management organization chart will address this aspect.

Design Control (Element 3)

Design inputs must be appropriately specified on a timely basis and correctly translated into design documents. Design interfaces must be identified and controlled. Design adequacy must be verified by persons other than those who design the item. Design change, including field changes, must be governed by control measures and commensurate with those applied to the original design. Design control should be the basis for the QA Program on the SSC.

Procurement Document Control (Element 4)

To the extent necessary, procurement documents will require suppliers to have a quality assurance program consistent with applicable standards. Each Request for Proposal released by the SSC Project will have a QA requirement consistent with NQA-1.

Nonconformance (Element 15), Corrective Action (Element 16), and Audits (Element 18)

The three elements, while separate, are interrelated. Nonconformances will be documented and corrective action recommended. Auditors then ensure by follow-up activities that the corrective action has been taken. Management is informed of all audit activities. The audit activities extend to all subcontractors and to participating laboratories as well as the SSC Laboratory.

7.3 Conventional Systems

7.3.1 General Plan

A considerable number of buildings, enclosures, utility systems, and roads must be provided for the technical systems and experimental uses of the SSC. The design of these units, contracting for their construction, and the supervision of the actual construction of the conventional systems will be accomplished by a firm or a consortium of architectural/engineering and construction/management firms. The possibility of two independent organizations respectively for AE and for CM activities is included here. The individual firms or the consortium, configured into one or more joint ventures, are identified in this document as the AE/CM. The AE/CM will be selected to provide experienced personnel to accomplish the facility objectives under the guidance of the SSC project staff.

The Conventional Systems Division (see Fig. 7.1-1) will supervise the work of the AE/CM as they execute the design and supervise the construction of the conventional facilities. Division personnel will be responsible for interpreting the requirements of the technical systems to the AE/CM, for arranging meetings among concerned parties, and for coordinating the exchange of information on the progress of designs. In addition, technical alternatives must be explored through optimization studies in order to create an efficient and cost effective design. Attention must be paid to the environmental and safety aspects of the design. Administrative tasks will include the establishment of working relations with the appropriate DOE offices to expedite the necessary approval of plans and drawings. The management of funds, the preparation of construction schedules, and the maintenance of a project management system will be among the responsibilities of the Conventional Systems Division.

Since the major direct work load will be handled by the AE/CM, only a modest division staff is necessary. In the early years of the project, division personnel will focus their attention on the construction activities. As construction nears completion, on-site tasks will consist of preparing operating personnel to use the constructed facilities. A preliminary examination of the personnel needed (about half of whom are professionals in physics, engineering, and support disciplines) is provided in Section 7.4.5.

7.3.2 Site Acquisition

The subject of site acquisition is quite important to the entire success of the project. There are numerous steps that must be taken by Federal and State governments in order to initiate the process of finding a site for the SSC. It will be the responsibility of the Department of Energy to orchestrate the process of site selection. In a preparatory step, the CDG was asked to provide technical information concerning site requirements. This was submitted in June 1985 as the SSC Siting Parameters Document. The primary requirements are also described in Section 6.1 of this CDR. Using this and other information, it is projected that a suitable site for the SSC could be selected during FY88.

Early occupancy of critical areas of the site will be important to the overall success of the project. The speed with which significant portions of land can be acquired will be crucially dependent upon existing land ownership and the enabling legislation adopted by the sponsoring state. The cooperation of state and local authorities will be required to expedite the process of land acquisition. The provision of comprehensive maps and surveys by the host state will be required to facilitate the optimum placement of the SSC facilities within the chosen region. Assistance in facilitating on-site geotechnical and environmental investigations will be expected. Information from surveys such as these are important to the positioning studies for the machine and experimental facilities. A precise determination of the eventual placement of the SSC facilities on the chosen site is required in order to locate the parcels of land that need to be acquired by the federal government. It is likely that very little of the land above the collider ring will need to be acquired outright. By determining the placement of the SSC facilities, the few, specific land requirements around the collider ring can be formulated. The lands associated with the campus, injector, and experimental areas must be provided in fee simple to the U.S. government. Lands that are traversed deep underground by the collider ring tunnel will not be directly impacted, and it is expected that subterranean easements will be sufficient.

7.3.3 Mobilization

Mobilization at the site could follow a step-wise process. Arrangements will need to be made with local authorities so that the construction plan for and the mission of the new laboratory can be explained to the population of the surrounding region. The rapid deployment of survey personnel at the site will allow for the gathering of information to supplement that provided by state and local officials. This process will begin with finding temporary housing and work space for the advance teams. Transportation networks must be determined to move people to and from the site. Early attention will focus on the pre-existing environmental conditions in the region in order to provide a baseline of information. Geotechnical investigations, consisting of borings and test penetrations, will be

necessary in order to have basic information for the initiation of detailed design. The location and capacity of the electrical power network must be verified so that arrangements for early electrical service to the site can be made. The AE/CM will then be able to initiate the procurement of long-lead items such as transformers and switch gear.

7.3.4 Design and Construction Approach

The primary objective for construction of the conventional systems is to provide the facilities as needed by the technical groups. In this manner, installation of the technical components can proceed in an orderly manner. Planning to meet such goals is difficult due to the absence of specific site information. Partially to overcome this problem, the A/E firm, RTK, working with the CDG, has developed several alternative schedules in order to understand the issues involved. In their report (Attachment C) they display three schedules for the example sites that they studied. In Case C enclosures are largely constructed by cut and cover methods; the other two cases involve tunneling primarily in soft ground (Case A) and rock (Case B). In the latter two cases the schedule for the civil construction of the 52 mile collider ring tunnel determines the overall SSC conventional facility construction schedule. The above-ground facilities needed for the SSC can all be provided within the time frame determined by the sequence of tunneling construction contracts.

The approach taken in planning the work has been to consider one by one the tunnel segments that must be constructed for the arcs and clusters in each example site. The technical evaluation follows the appropriate ring profile with each segment encountering the rock/soils material postulated by the geological model. From this is calculated the duration of work associated with preparation of the local work site, provision of access and starter tunnels, actual boring of the collider segment, installation of electrical and mechanical systems, and final clean-up. This information, along with allowances for preparatory surveys, development of specific designs and for bid and award of a construction contract are displayed in Table 7.3-1 for a typical segment of collider tunnel.

Table 7.3-1
Overall Construction Times for a Typical Segment of Collider Tunnel of 5 Miles Length – (Site A)

Construction Task	Duration in Calendar Days
Preparatory	
Surveys, preliminary design	90
Detailed design	90
Bid and award	70
Total prepratory	250
Actual Construction	
Mobilization	90
Access, starter tunnels	80
Collider tunnel boring	160
Invert and installation of services	140
Clean-up and vacate site	80
Total actual construction	550
Grand Total	800

The information in Table 7.3-1 is critical to the development of an overall facility construction schedule. If all the tunnel construction were done in series, the overall schedule would be excessively long. Methods of packaging the work into reasonable size contracts were considered and the number of simultaneous efforts that can go forward insuring proper supervision and avoidance of interference were determined. Attention was given to the required year by year funding requirements. The overall durations for the construction of the collider enclosure range from approximately 38 months in the cut and cover case to 48 months in soft ground. In view of the fact that an actual site has not been identified, an average duration for tunnel construction of 44 months was derived. Durations of segment construction consistent with this overall number of months were used in the schedule that is described and shown in Section 7.4.2. Assuming a construction start in FY88, these durations lead to a completion of tunnel construction in November, 1992.

7.4 Construction Plan

7.4.1 Overall Schedule and Milestones

The construction plan presents major tasks and events, and their interrelationships, leading to the completion of the SSC construction. The projected construction period is 6.5 years.

Figures 7.4-1 and 7.4-2 present a summary level construction schedule for the SSC. The construction phase is projected to start at the beginning of FY88 with Congressional approval, authorization, and appropriation of construction funds, and to continue for 6.5 years, until mid-FY94. In order to ensure an efficient construction start, careful and extensive planning during Phase I is essential. The milestones keyed to the start of construction in October 1987 assume submission of site proposals by the states starting in early FY88 with site selection by September 1988.

At the beginning of the construction period (October 1987) the Phase II AE/CM selection process will begin with the expectation that the AE/CM firm(s) selected will be on board pursuing Preliminary Design (Title I) concurrent with the site studies and the announcement of the site selection. The Title I completion and review and the Title II detail designs for certain critical path items in the construction plan (e.g., south arc tunnel sectors for the collider ring tunnels) would then efficiently proceed, and the actual construction on site would be underway by May 1989. The construction plan shows the first complete beneficial occupancy for a tunnel sector in October 1990, and at this point the interrelationships with the first installation of technical systems become apparent. See Fig. 7.4-17 for an overall schedule and the relationships of conventional and technical construction.

The central activities focus on the "Collider Ring Dipole Magnet" production and the "Collider Ring Underground Construction." The scheduling and interrelationships between various sector availabilities in the arc sections and the cluster hall areas are shown in Fig. 7.4-2. The collider construction sequence follows a very closely coupled phased construction approach, and as each tunnel sector becomes available for occupancy, the installation and testing of technical components (magnet systems, cryogenics, vacuum systems, power supplies, etc.) follow in a step-wise fashion such that ultimately each sector can be completed efficiently. As each of these "Collider Ring Sectors" is accepted, the preoperational

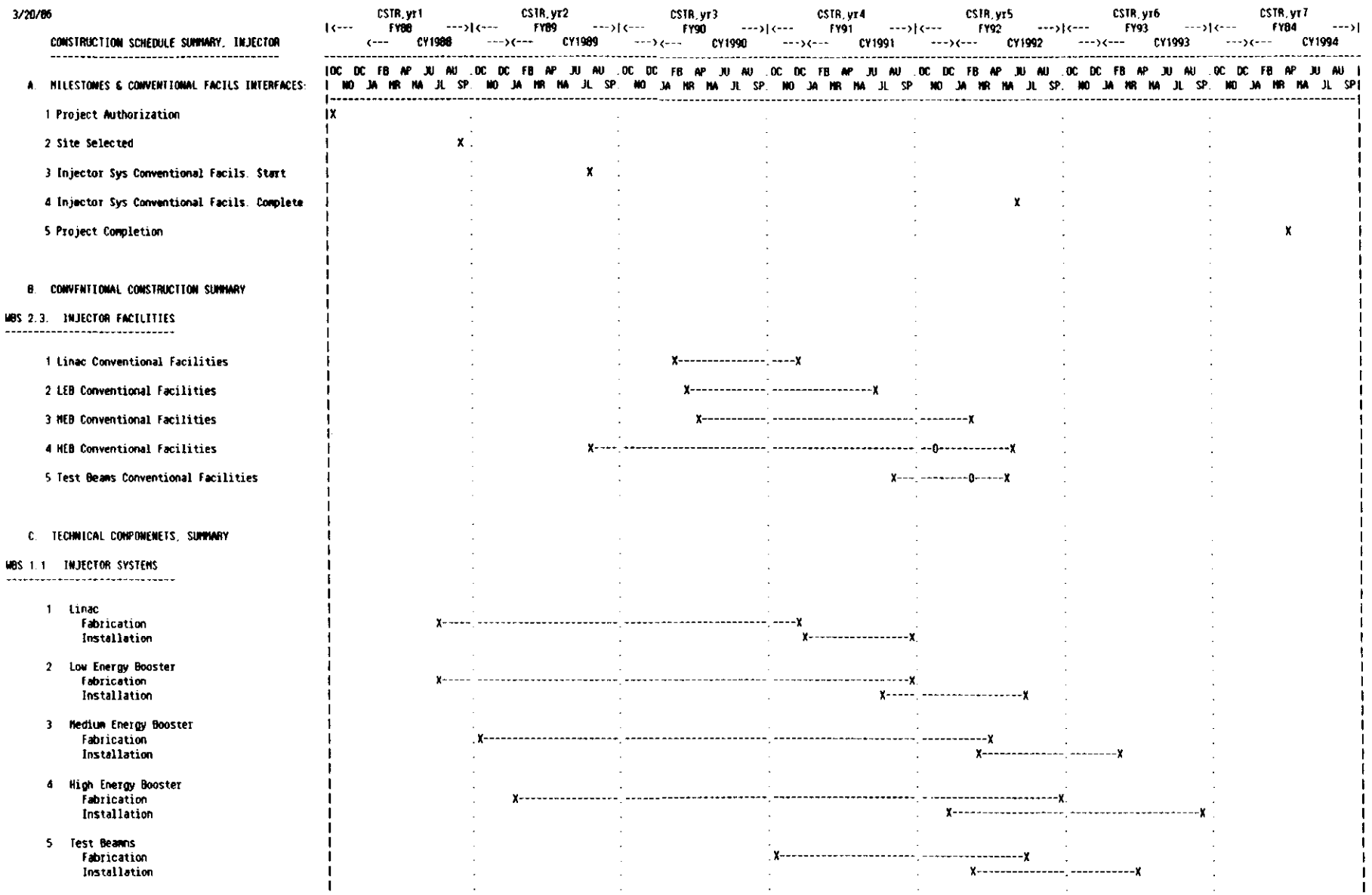

Figure 7.4-1. Construction schedule summary, injector.

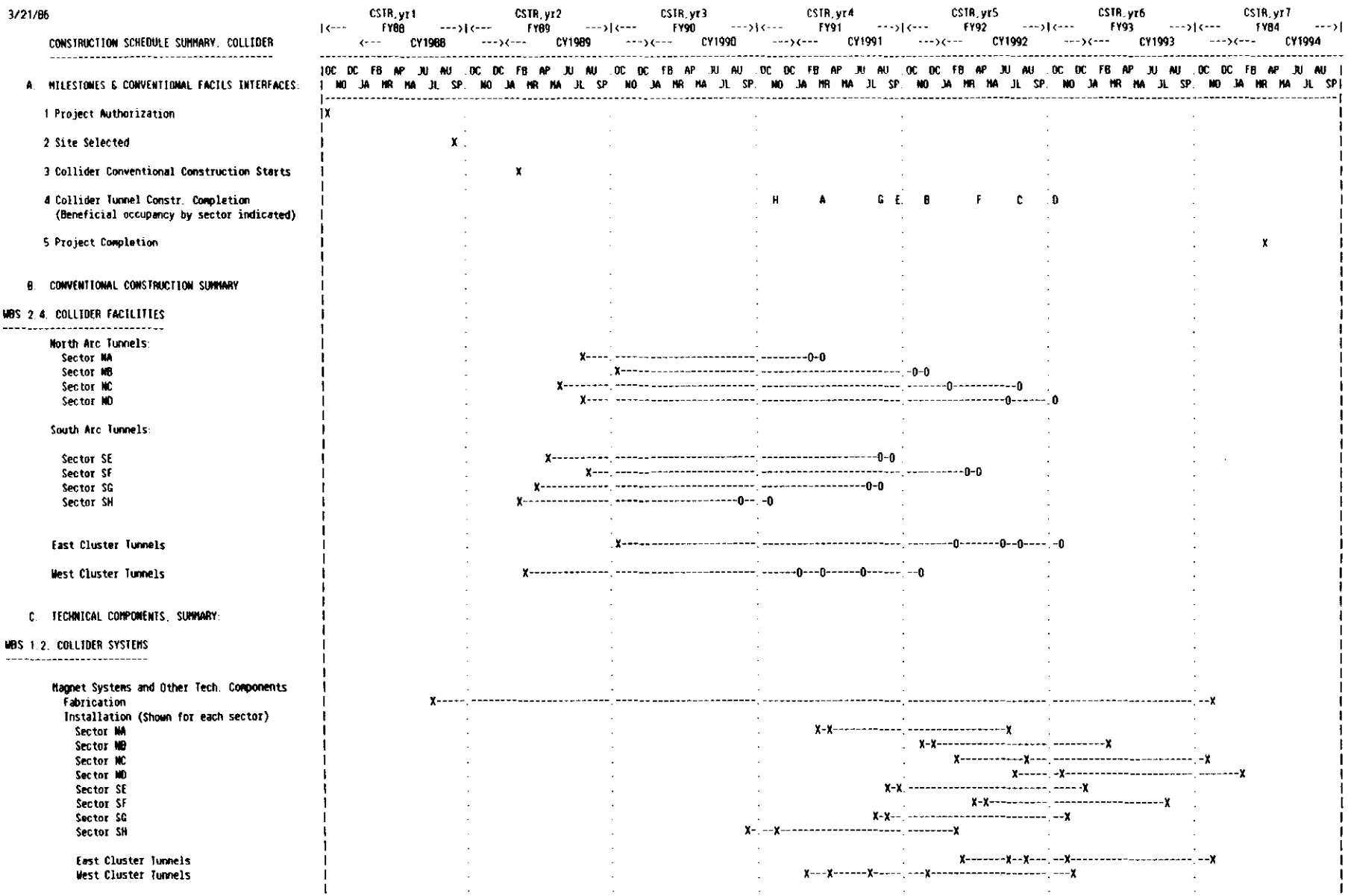

Figure 7.4-2. Construction schedule summary, collider.

testing phase will commence, and the commissioning of each area will proceed sequentially around the ring.

During Phase I, development work on the dipole magnets for the collider rings has been emphasized. Dipole magnet models have been fabricated and tested by the laboratories, prototype units are nearing completion, and the transfer of the magnet tooling and production technology to industrial manufacturers will begin in FY86. These steps will enable the laboratories and industry to plan for a very early and rapid tooling up and start of magnet production early in the construction project. The Phase I program milestones are provided in Table 7.4-1.

Table 7.4-1
SSC Phase I Program Milestones

Date	Item
Oct 1984	Define Selection Criteria and Technical Information needed for Magnet Selection
Nov 1984	Establish Primary SSC Design Features and SSC Phase I Program Plan Objectives
Apr 1985	*Site Parameters Document
Apr 1985	Review Magnet Development Program
Sep 1985	*Magnet Design Type Selection
Dec 1985	Preliminary Conceptual Design
Feb 1986	Start Pre-Production Prototype Magnets
Mar 1986	*Conceptual Design Report (non-site specific) and Other Documentation
June 1986	First Full-Length Magnet Test
Sept 1986	Start Magnet Technology Transfer to Industry
Oct 1986	Start Magnet Systems Test
July 1987	First Full Length Industry-produced Magnet Model
Aug 1987	Recommended SSC Phase II Management Plan
Oct 1987	*SSC Construction Start (NTP)

*Denotes primary milestone

The fabrication and installation plan for the main collider ring magnets has been outlined in Section 7.2.2. The production plan assumes that two or more industrial firms will manufacture the nearly 8000 dipole magnets required and ship them to the SSC for final testing and installation. The schedule for other magnet systems and technical components is provided in Section 7.4.3.

Although the emphasis in the construction plan centers on the Collider Ring (the overall critical path track), an early design start on the Injector Systems is also planned. While the on-site start of the injector construction will necessarily await finalization of the detail siting studies and optimizations for the collider ring specification, an early start on the first injector accelerators is planned such that an efficient step-wise installation-test-acceptance sequence follows for the Linac, Low Energy Booster, Medium Energy Booster, and High Energy Booster accelerators respectively. The overall construction program milestones associated with the schedules of Figs. 7.4-1 and 7.4-2 are presented in Table 7.4-2.

7.4.2 Conventional Systems

A general plan for design and construction of conventional systems, including projections for site acquisition and mobilization, was provided in Section 7.3. A construction approach was described whereby three example sites were used to explore a variety of potential sites in the U.S. The analysis of Section 8.1.2 provides a mechanism by which the information for the example sites is utilized to provide a cost estimate and schedule for the SSC conventional systems. In this section the schedule results from the above analysis are presented in the next five figures. Each figure referenced below corresponds to a Work Breakdown Structure (WBS) level 3 category with summary schedule information at level 4.

Figure 7.4-3 Site and Infrastructure
Figure 7.4-4 Campus Area
Figure 7.4-5 Injector Facilities
Figure 7.5-6 Collider Facilities
Figure 7.5-7 Experimental Facilities

7.4.3 Technical Systems Schedule

The previous Section 7.4.2 has provided the schedules for site preparations and the construction of conventional systems including all buildings, structures, and utilities that are required by the SSC accelerator systems. The top part of Fig. 7.4-8 provides a recap of the Conventional Facilities construction dates and durations for the Linac, LEB, MEB, HEB, and Collider. The lower half of Fig. 7.4-8 provides an overall summary of the schedules for the technical components. The periods for engineering and design, fabrication, and installation are provided for each of the SSC accelerators.

Figure 7.4-8 shows the schedule relationship between the conventional and technical systems. For example, the linac conventional facilities are scheduled for completion December 1990. The installation of Linac technical components starts at that time and proceeds to completion in December 1991. Prior to December 1990, the schedule sequence

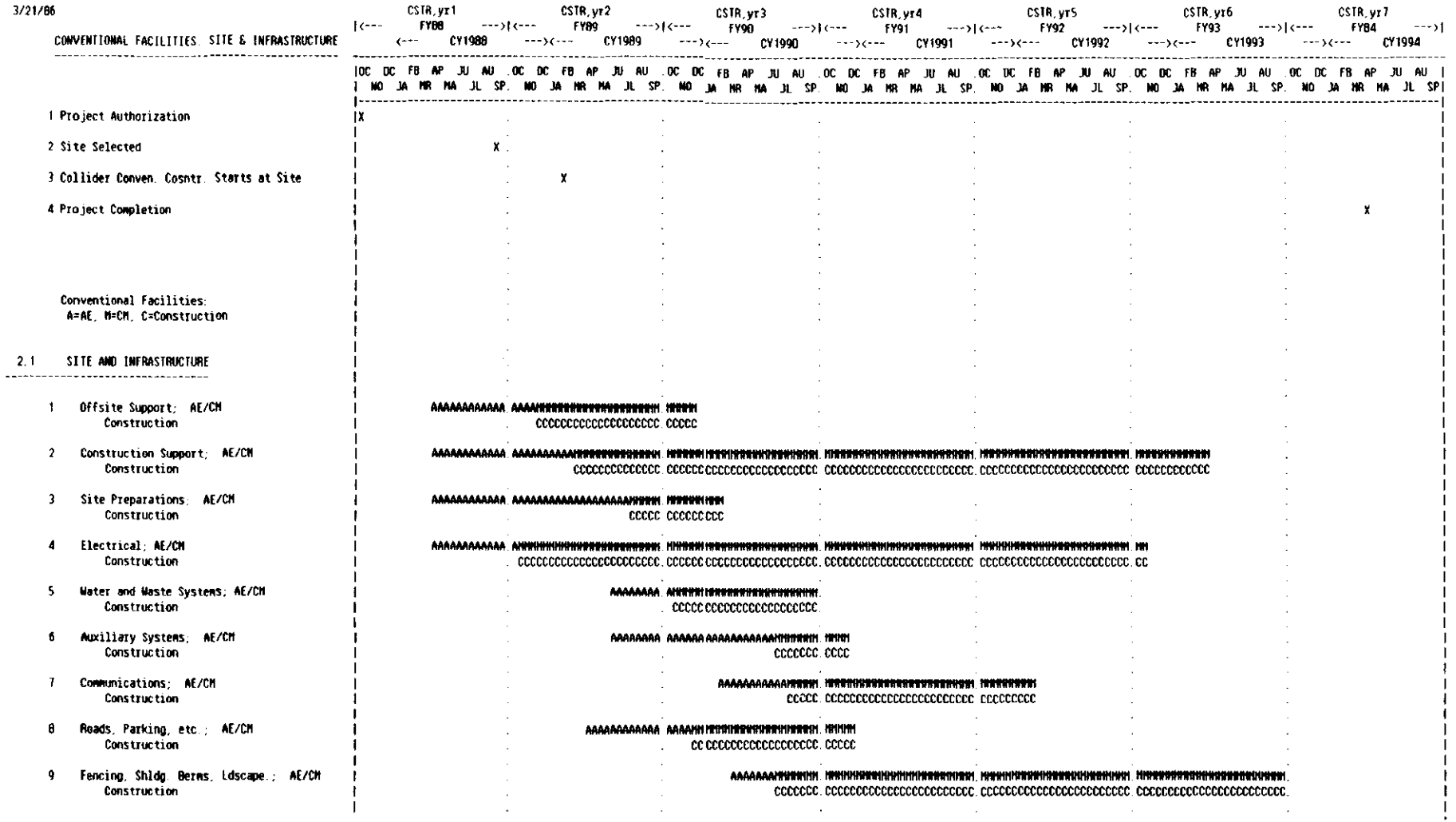

Figure 7.4-3. Conventional facilities summary, site and infrastructure.

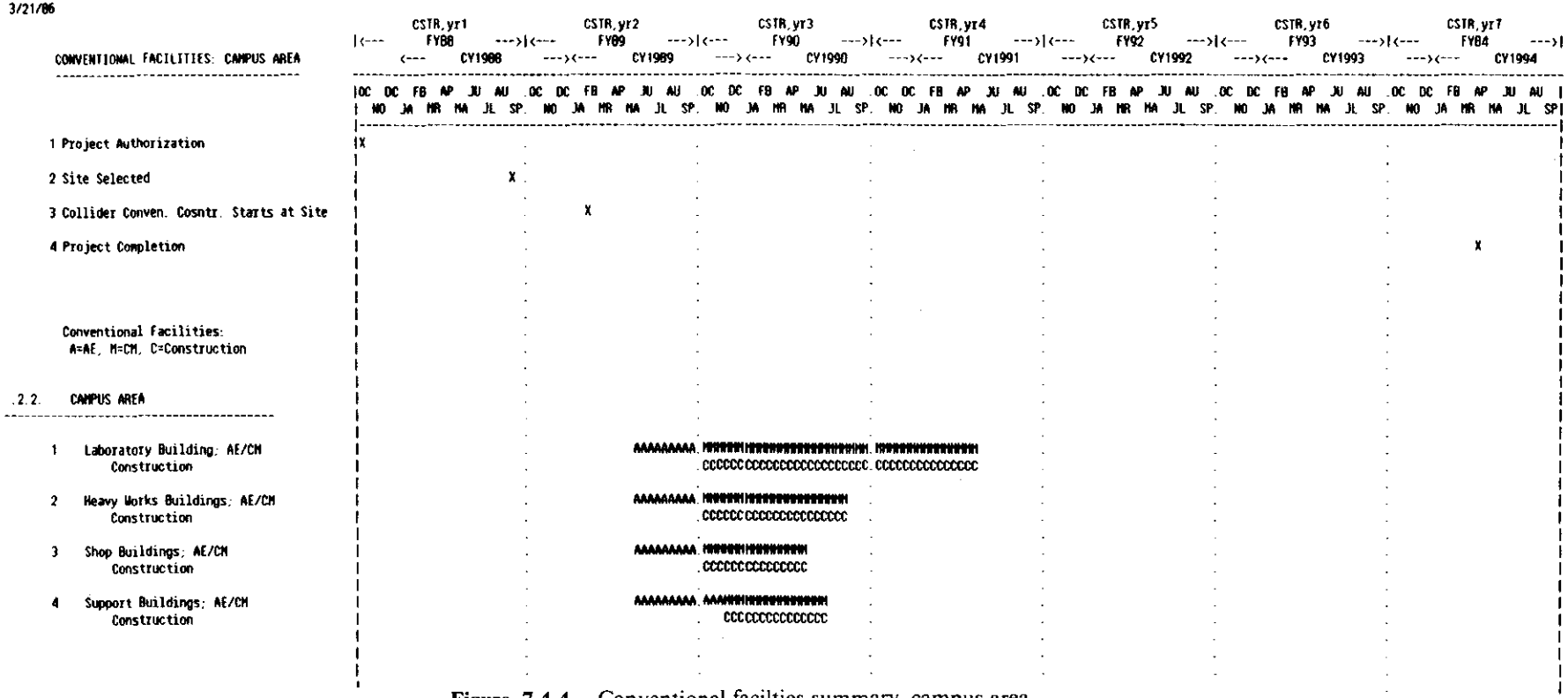

Figure 7.4-4. Conventional facilties summary, campus area.

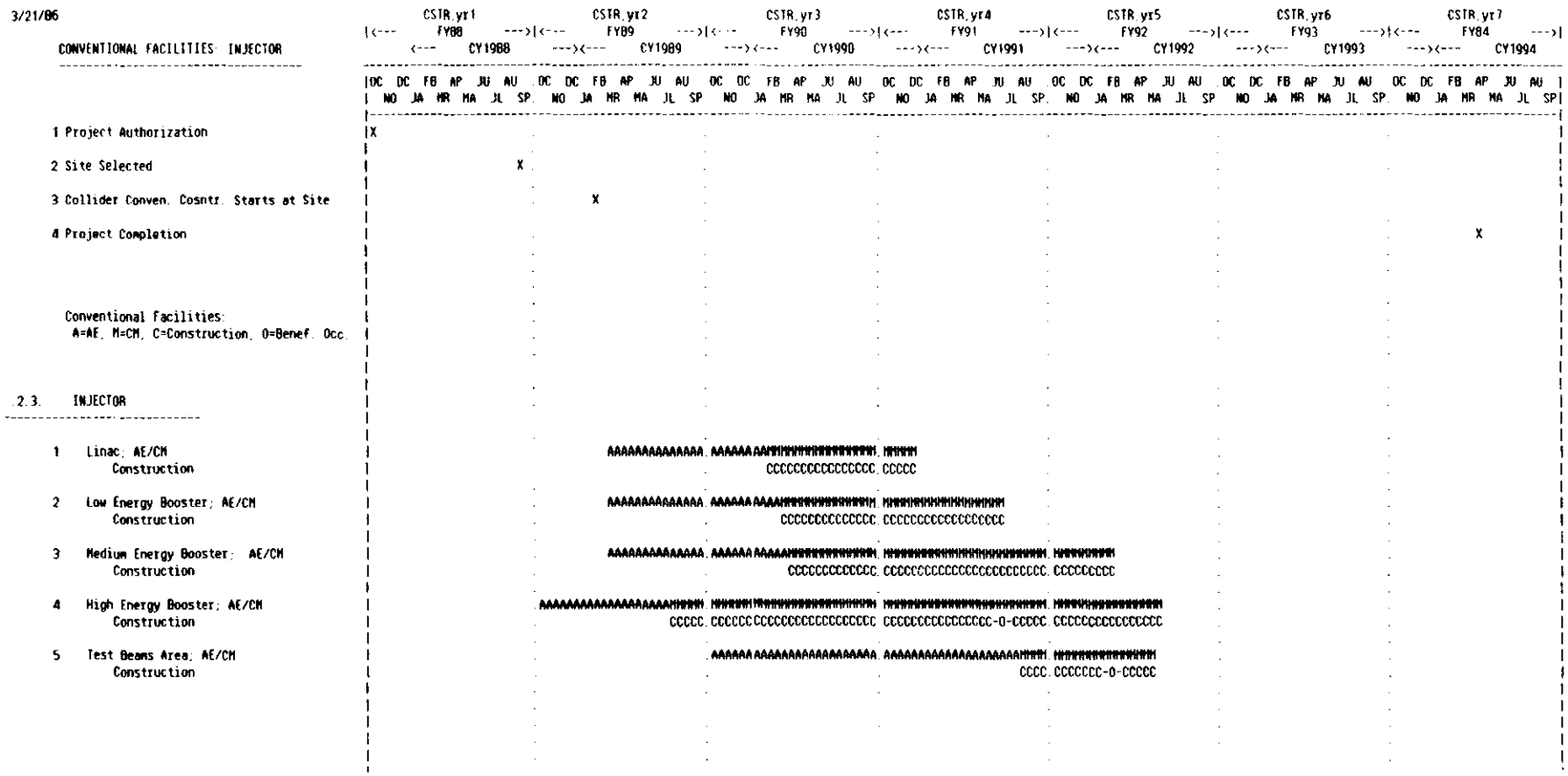

Figure 7.4-5. Conventional facilities summary, injector facilities.

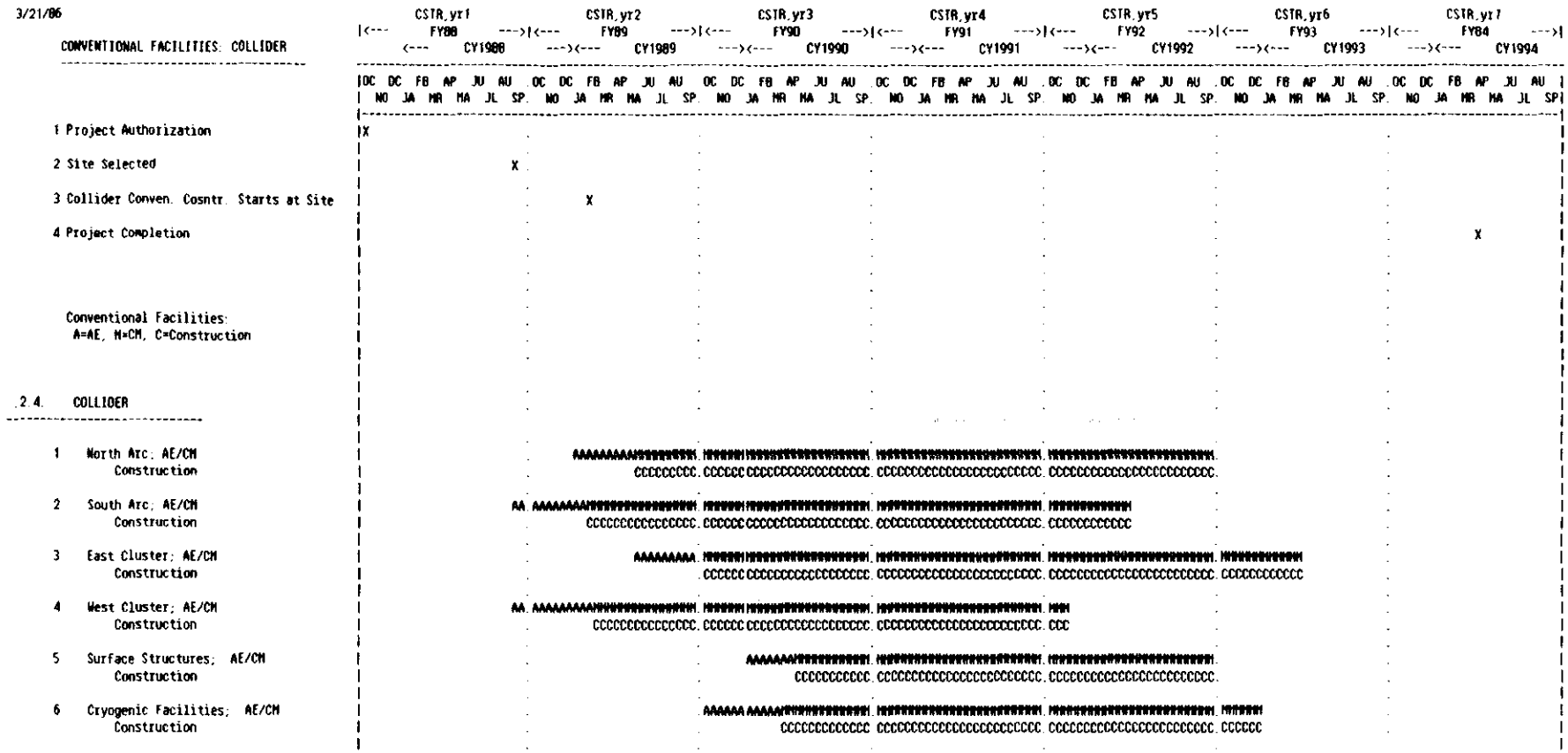

Figure 7.4-6. Conventional facilities summary, collider facilities.

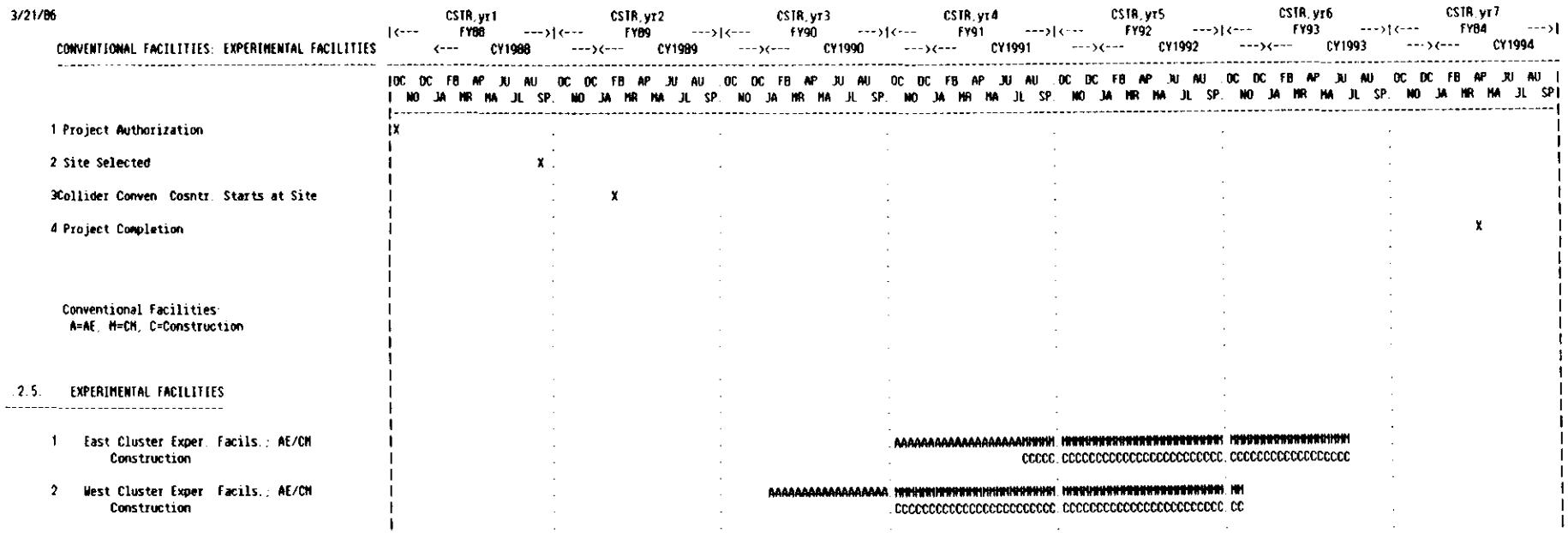

Figure 7.4-7. Conventional facilities summary, experimental facilities.

Table 7.4-2
SSC Construction Milestones

Oct 87	Construction Start
Jun 88	AE/CM Selected
Sep 88	Site Selection Announcement
Feb 89	Ground Breaking
Jan 90	Start Full-Scale Industrial Magnet Production
Oct 90	B.O.* – Sector SH Service Area and Tunnel
Dec 90	B.O. – Linac Conventional Systems
Mar 91	B.O. – Sector NA Service Area and Tunnel
Jul 91	B.O. – LEB Conventional Facilities
Aug 91	B.O. – Sector SG Service Area and Tunnel
Sep 91	B.O. – Sector SE Service Area and Tunnel
Oct 91	Complete Linac Installation
Nov 91	B.O. – West Cluster Area Conventional Systems
Dec 91	B.O. – Sector NB Service Area and Tunnel
Feb 92	B.O. – MEB Conventional Systems
Feb 92	Complete Sector SH Technical Systems Installation
Apr 92	B.O. – Sector SF Service Area and Tunnel
Jun 92	B.O. – HEB Conventional Systems
Jul 92	B.O. – Sector NC Service Area and Tunnel
Jul 92	Complete LEB Installation
Jul 92	Complete Sector NA Technical Systems Installation
Oct 92	B.O. – Sector ND Service Area and Tunnel
Nov 92	B.O. – East Cluster Area Conventional Systems
Dec 92	Complete West Cluster – Technical Systems Installation
Dec 92	Complete Sector SG Technical Systems Installation
Jan 93	Complete Sector SE – Technical Systems Installation
Feb 93	Complete MEB Installation
Apr 93	Complete Sector NB Technical Systems Installation
Aug 93	Complete Sector SF Technical System Installation
Sep 93	Complete HEB Installation
Dec 93	Complete East Cluster – Technical Systems Installation
Dec 93	Complete Sector NC – Technical Systems Installation
Feb 94	Complete Sector ND Technical Systems Installation
Apr 94	Construction Complete

*B.O. = Beneficial Occupancy

for engineering and design and fabrication of linac technical components is indicated. Similar schedules are displayed for the three booster synchrotron accelerators. The schedule interrelations of conventional and technical systems for the collider are more complex. Due to the large size of the collider, the installation of technical components will proceed in phases as various parts of the collider ring conventional systems are completed. The magnet installation details are provided in Fig. 7.4-15. The magnet installation schedule for each sector of the collider ring is indicated following the scheduled completion of conventional construction for that sector. Schedules are provided for each of the eight sectors of the collider arcs as well as the east and west cluster areas. The detailed schedule for production of collider magnets has been provided earlier in Fig. 7.2-1.

Figures 7.4-9 through 7.4-14 provide schedules for the subsystems of each of the SSC injector accelerators and the collider. The schedule information for this section is presented in the following figures as summarized below:

Figure 7.4-8 Technical Components Summary Schedule
Figure 7.4-9 Linac Systems Schedule
Figure 7.4-10 Low Energy Booster Systems Schedule
Figure 7.4-11 Medium Energy Booster Systems Schedule
Figure 7.4-12 High Energy Booster Systems Schedule
Figure 7.4-13 Test Beams (from HEB) Schedule
Figure 7.4-14 Collider Systems Schedule
Figure 7.4-15 Collider Magnet Installation Schedule
Figure 7.4-16 Collider Cryogenics System Installation Schedule

7.4.4 Schedule Analysis

Schedules for the major WBS elements of the conventional facilities were presented in Figs. 7.4-3 to 7.4-7. Similarly, schedules for the injection accelerators and the collider systems were presented in Figs. 7.4-8 to 7.4-16. In this section a simplified integrated schedule network is presented. The major SSC project elements, their schedules, and interrelationships are displayed in Fig. 7.4-17. Site selection, construction of the first collider tunnel sector, and installation of magnet systems constitutes the main critical path.

Site selection remains a critical path process in the first year of construction. A delay in the site selection process would directly delay the start of conventional facilities design and construction completion. The technical designs for the injectors and collider systems can proceed during FY88 independent of the site selection process. This schedule allows for the organizational start-up and reasonable design and fabrication periods for most technical systems.

For the injector complex (Linac, LEB, MEB, and HEB) the conventional construction is projected to be the critical path item through the middle of FY92. In particular the conventional systems for the HEB are of the longest duration. As seen in Fig. 7.4-17, the technical installation and ultimately the injected beam to the collider are directly impacted by the conventional systems schedule. The fabrication of HEB technical components is closely matched to the HEB conventional systems schedule. As a result any delays in the

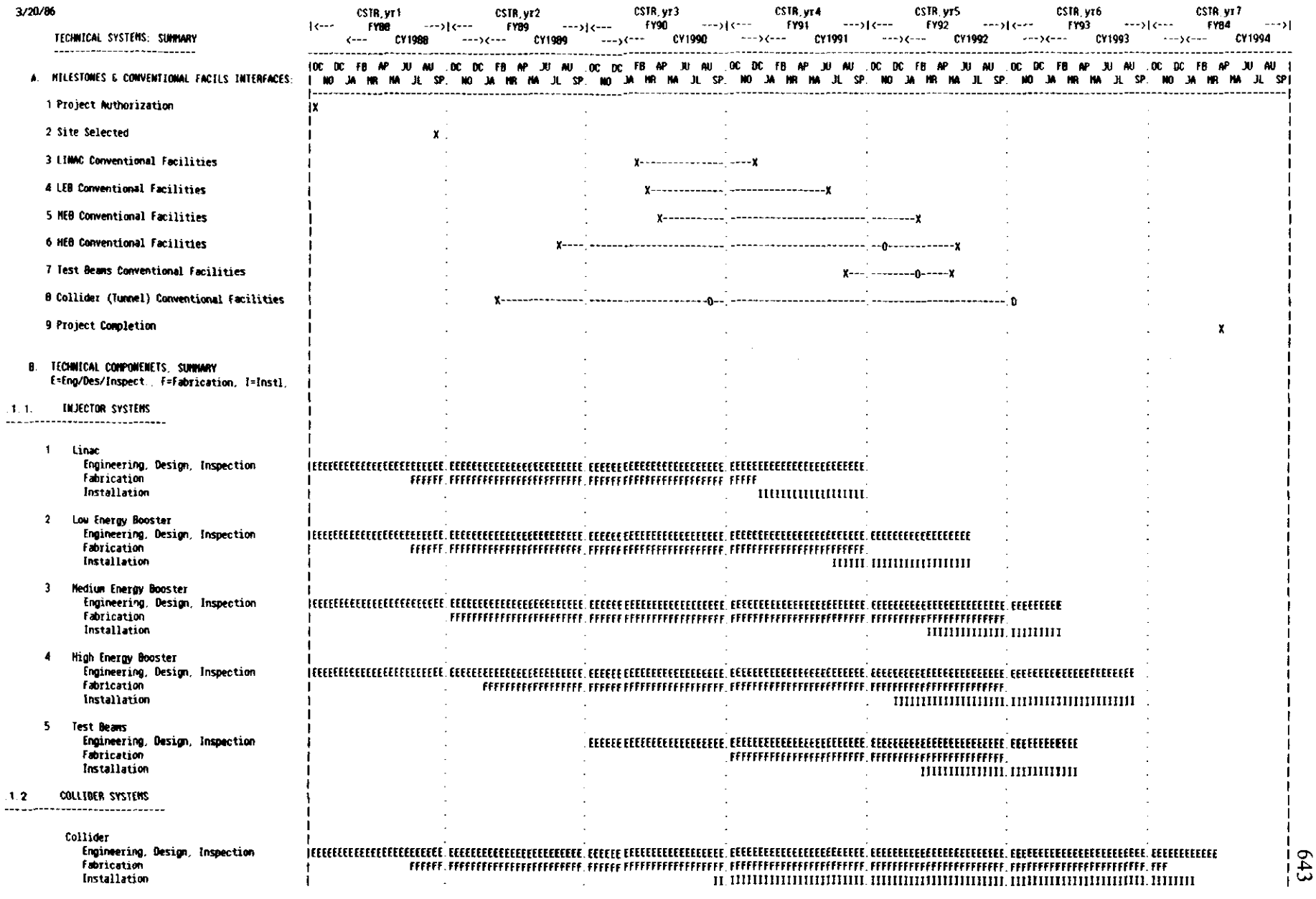

Figure 7.4-8. Technical components summary schedule

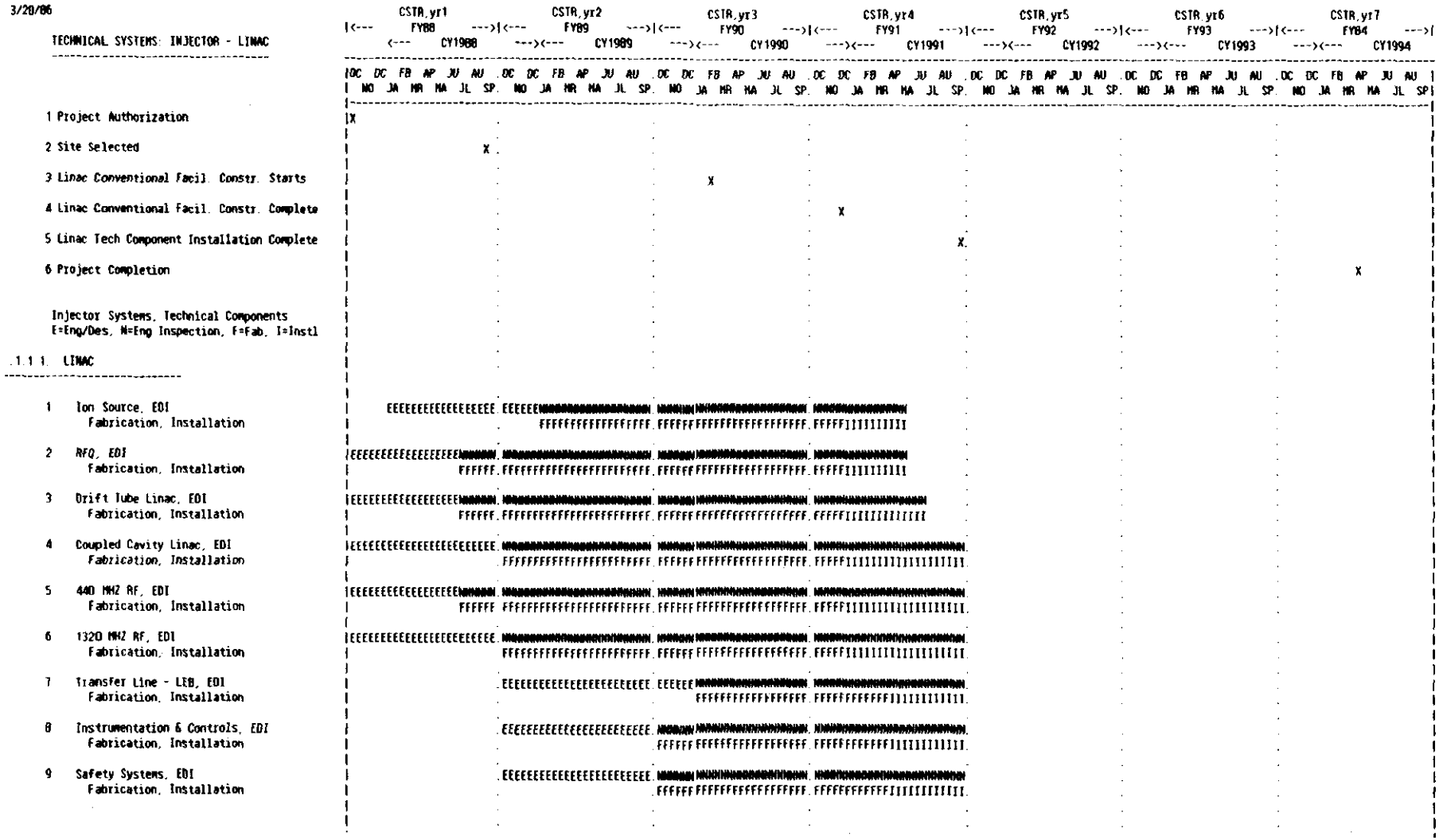

Figure 7.4-9. Linac systems schedule.

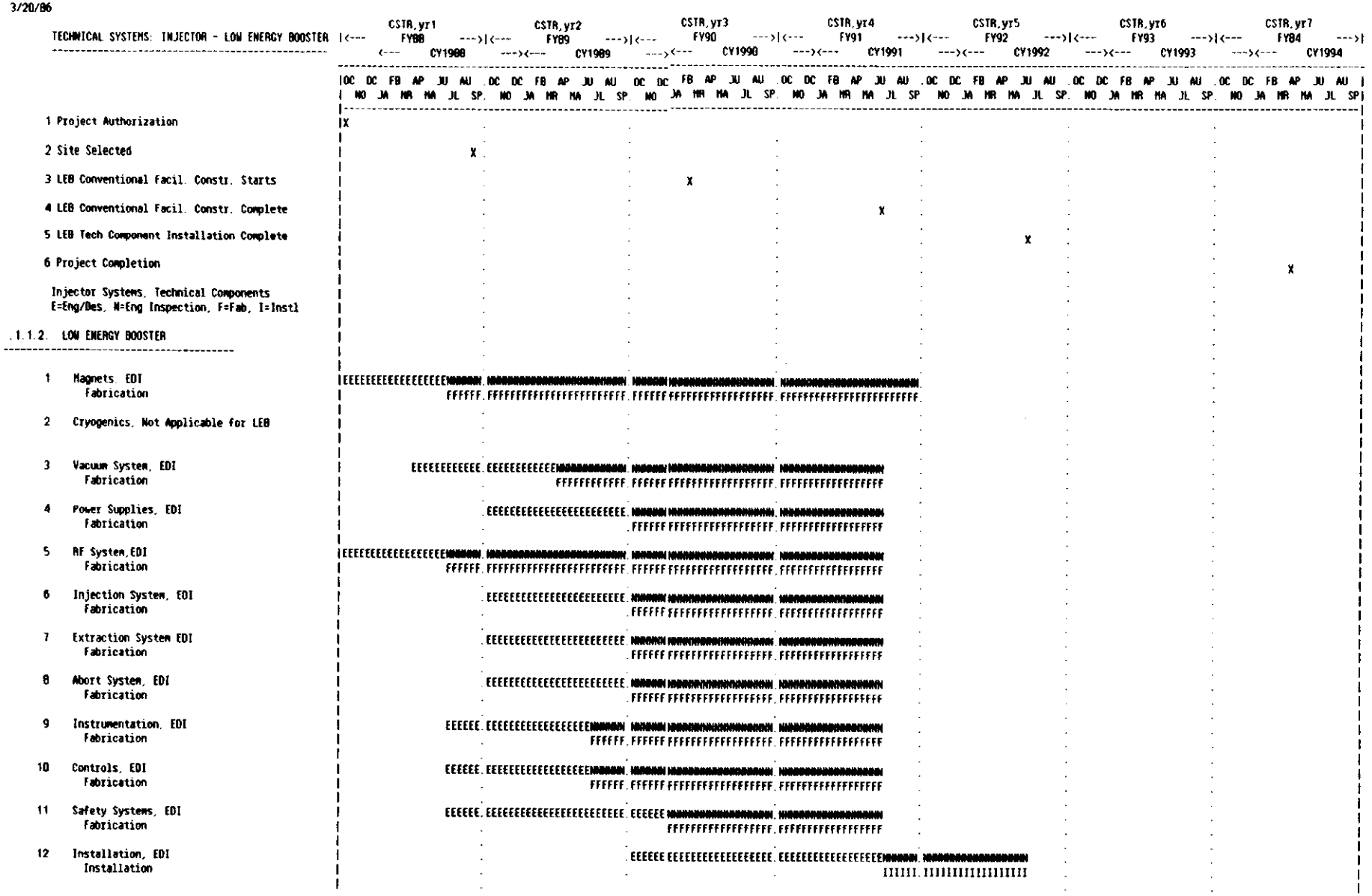

Figure 7.4-10. Low Energy Booster systems schedule.

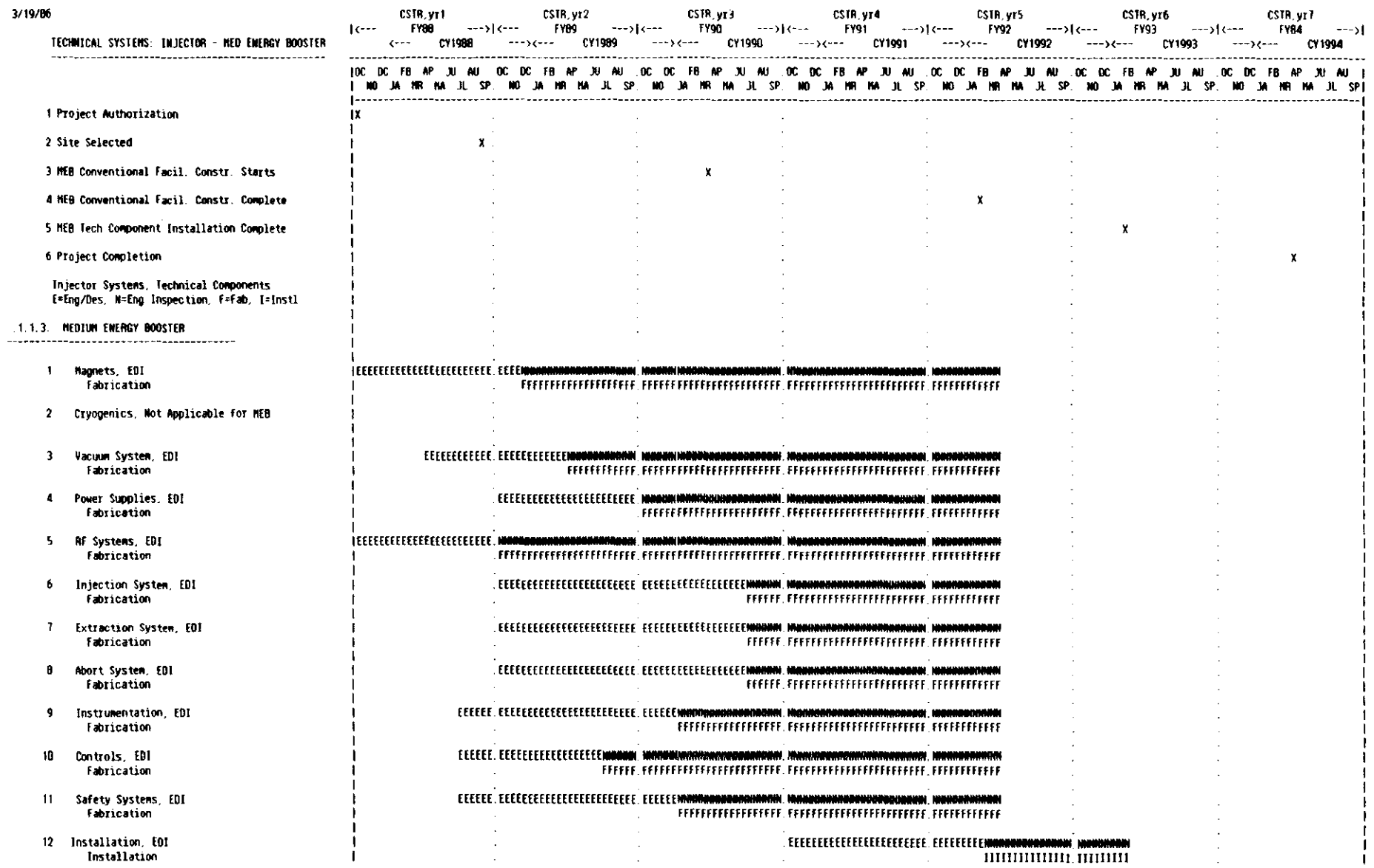

Figure 7.4-11. Medium Energy Booster systems schedule.

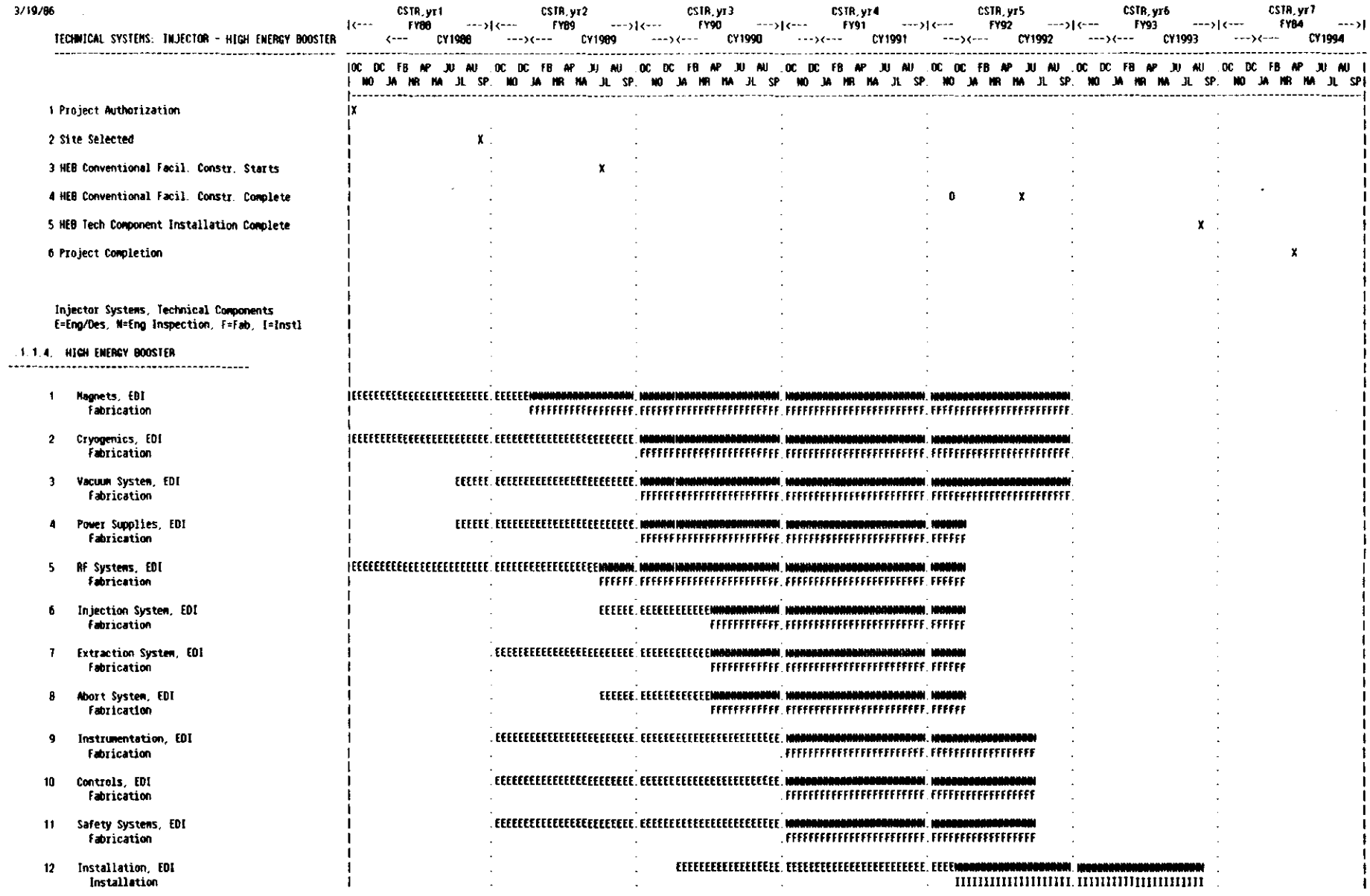

Figure 7.4-12. High Energy Booster systems schedule.

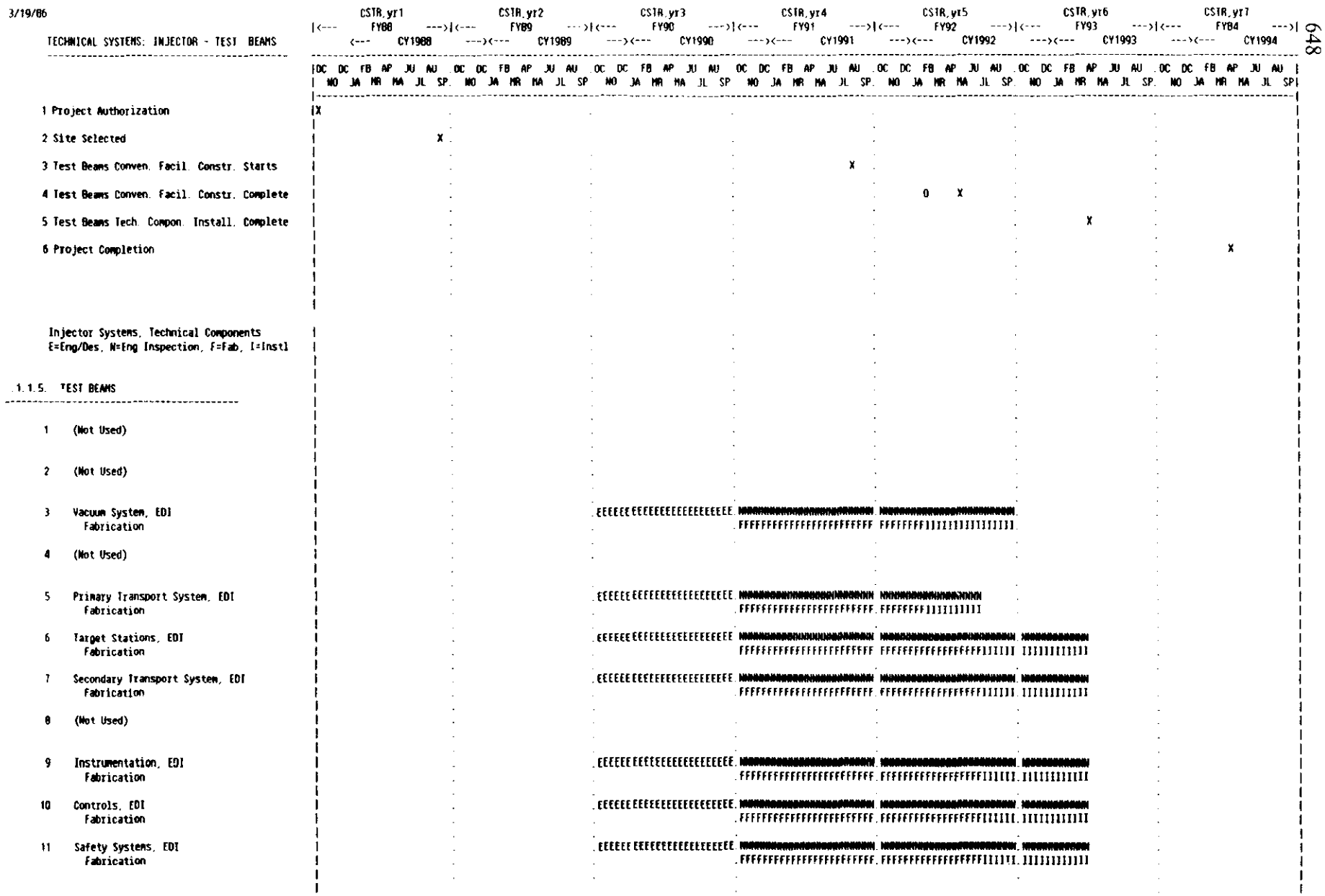

Figure 7.4-13. Test beams (from HEB) schedule.

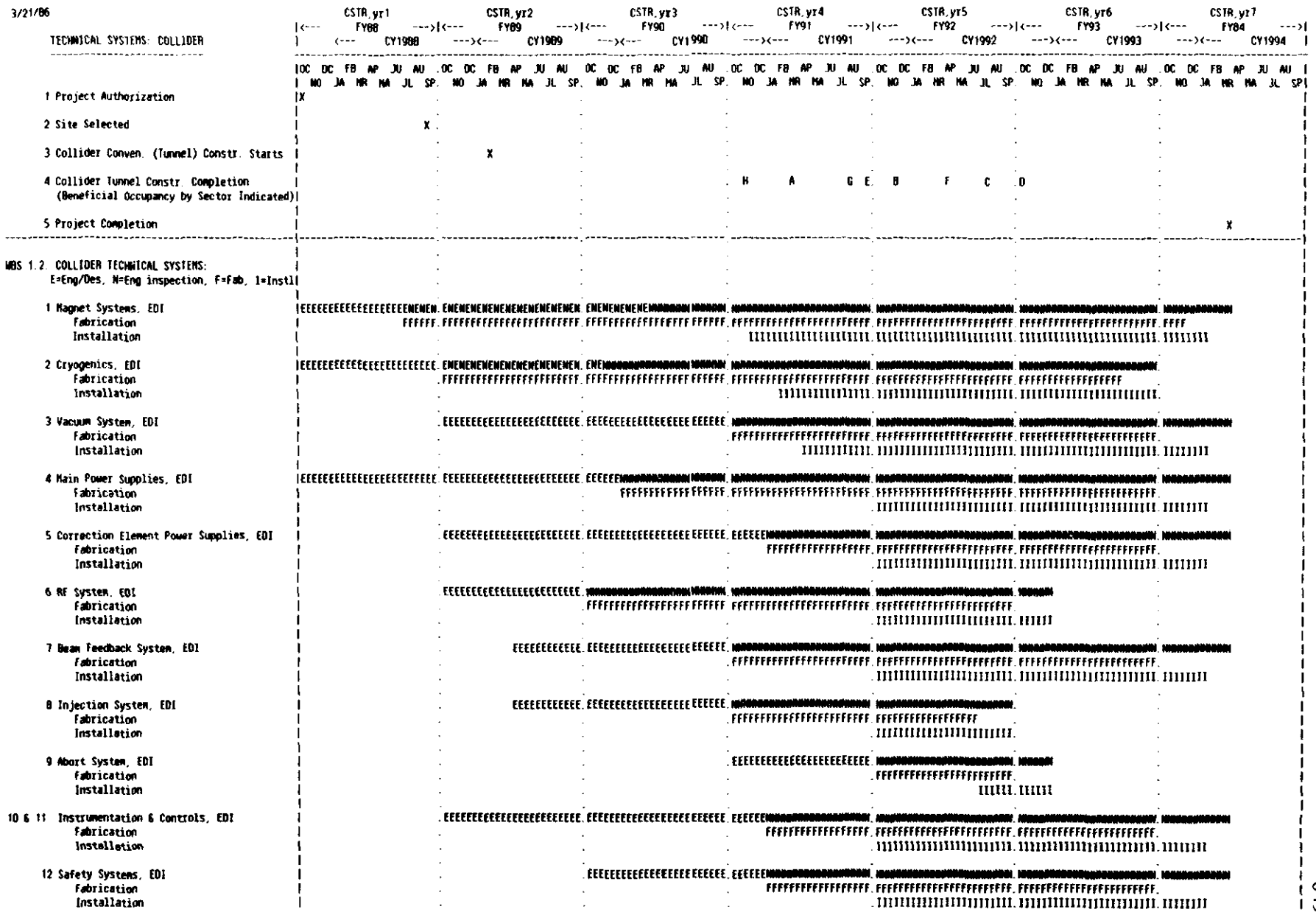

Figure 7.4-14. Collider systems schedule.

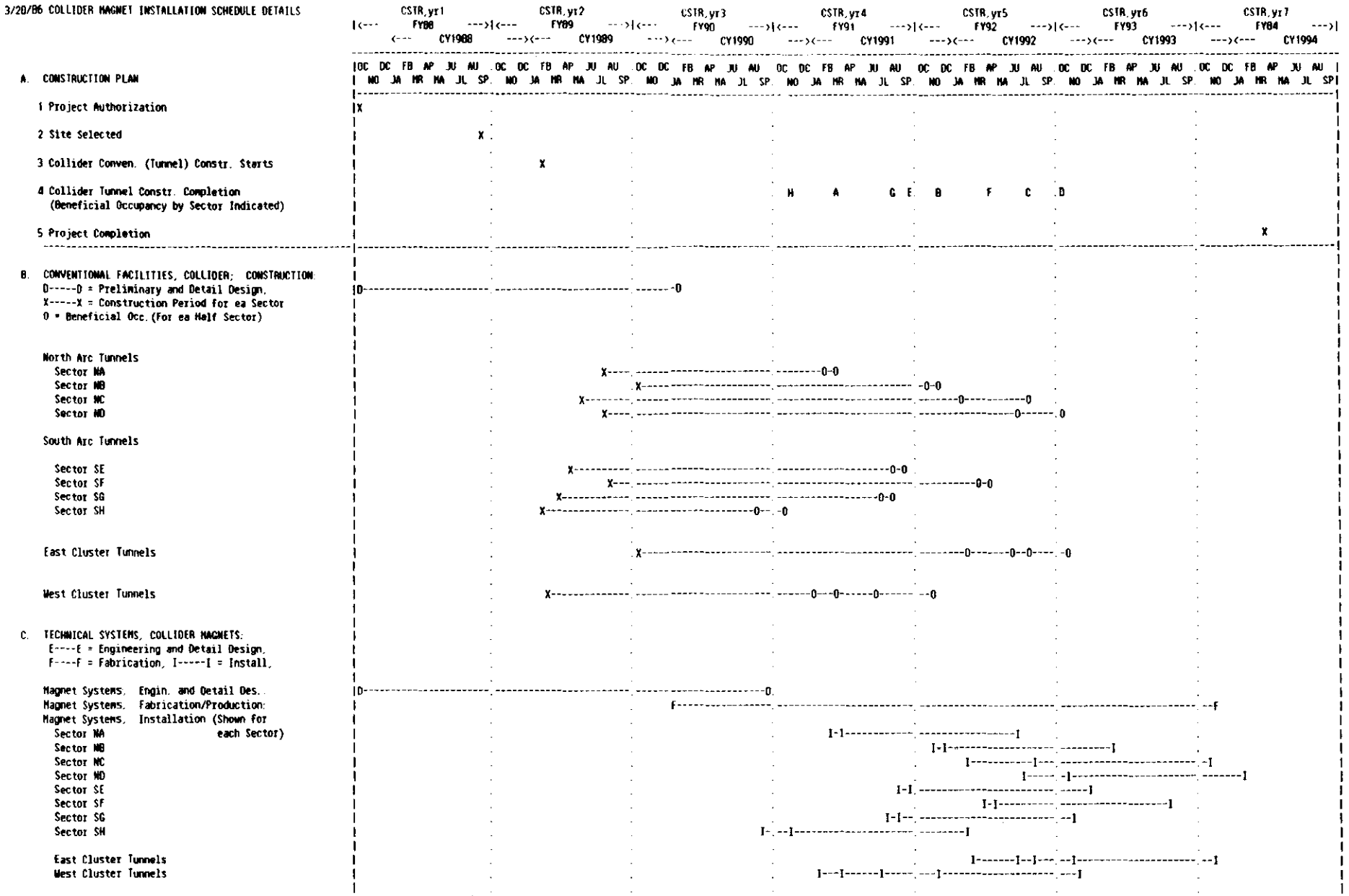

Figure 7.4-15. Collider magnet installation schedule.

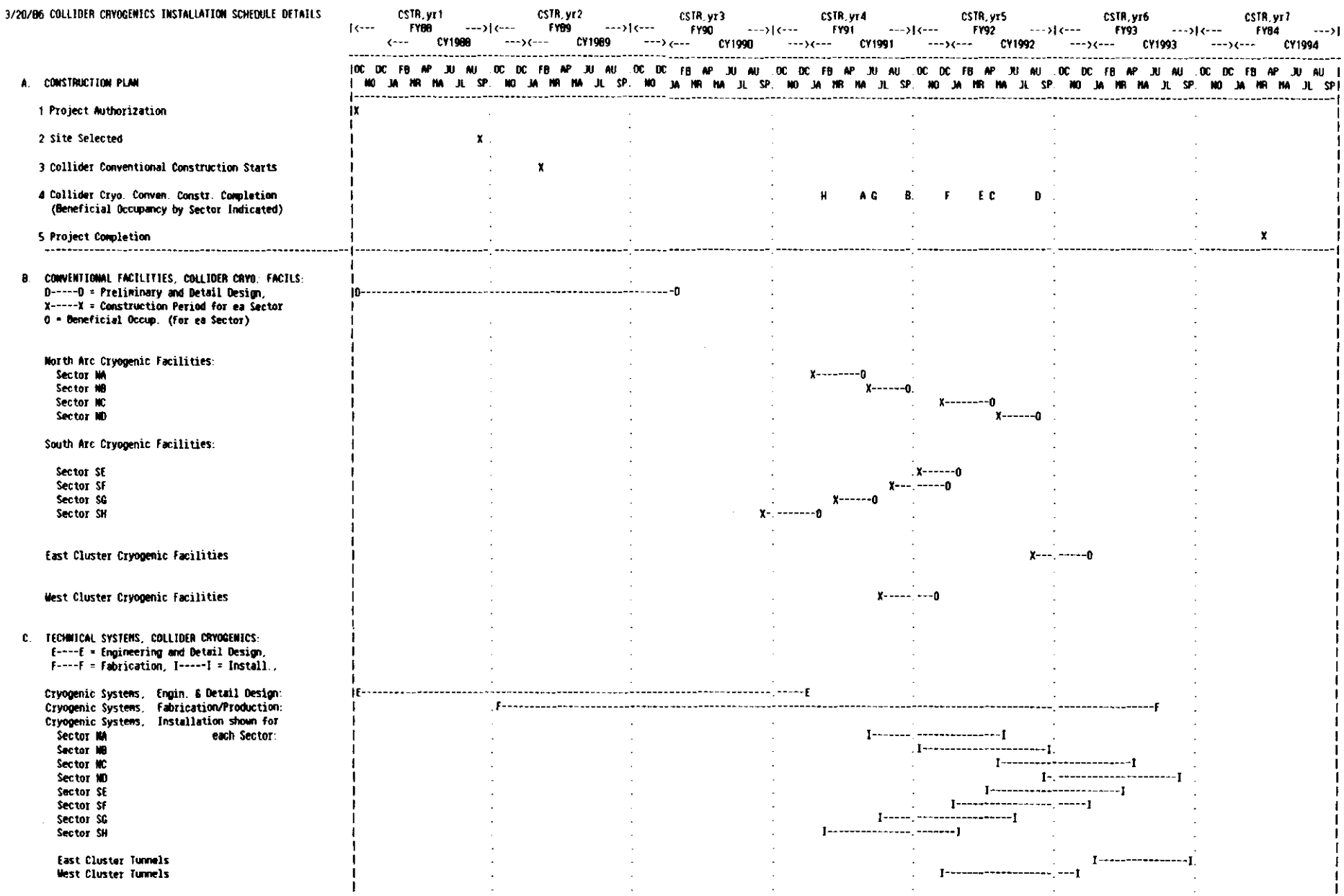

Figure 7.4-16. Collider cryogenics system installation schedule.

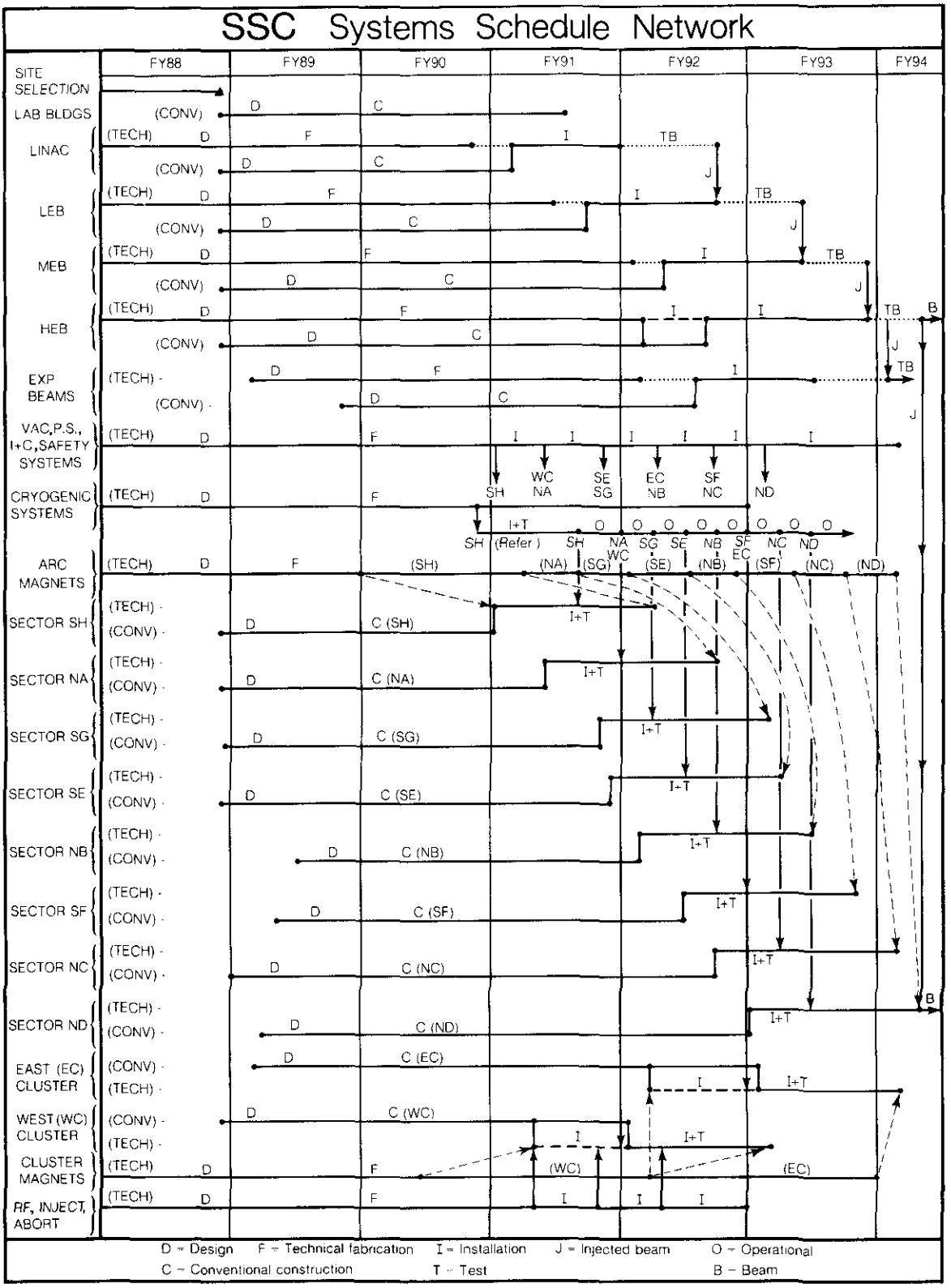

Figure 7.4-17. SSC Systems Schedule Network.

fabrication of HEB technical systems could shift the critical path to technical systems fabrication.

The last two years of the injector schedules are dependent on installation and testing. Barring unreasonable difficulties, the HEB should begin to supply beam to the experimental test beam area near the start of FY94. In addition, it would be expected that low intensity HEB beam would be utilized in the collider at this time to test beam transport through completed sectors of the collider. Circulating beam in the collider is not projected until completion of the final sector (ND) scheduled for February 1994.

With regard to the collider systems, the start of design for the conventional systems is dependent on the site selection date. The first sector (SH) will be somewhat critical as it will lead the way in establishing contractual procedures and verifying construction techniques. While the conventional construction of other sectors will follow in succession with simultaneous construction contracts, the fabrication of technical systems (magnets, power supplies, vacuum, instrumentation and controls) will be geared to the first technical installation start in sector SH in October 1990. The design of technical systems will start immediately in FY88 to establish all necessary interfaces with the conventional systems. The first technical installations in sector SH will pave the way in verifying and refining planned installation methods and techniques.

The schedule of Fig. 7.4-17 indicates completion of conventional systems for sector SH in October 1990; however, the completion of that part of the facilities for the cryogenic plant occurs earlier. This allows for the installation of the refrigerator and cryogenic systems and appropriate testing such that the first refrigeration station for sector SH is ready for operation in June 1991. At this time it is expected that the technical installations for the first half-sector of SH are complete and ready for magnet cooldown and tests. At the same time installation will proceed for the technical systems of the second SH half-sector. A similar schedule for the operations start-up of the refrigeration station for each sector is indicated on the cryogenic systems schedule.

Under the category of "Arc Magnets", the production schedule for magnets is indicated for each sector in a simplified manner to show the adequacy of the production schedule. (In practice the production of magnets of a given time internal would be distributed to several sectors.) If the sequence of conventional construction and technical installation for each sector should proceed faster than indicated, the magnet production schedule would become the critical path item for the collider.

In general, the schedules for the conventional and technical systems for the East and West cluster regions are not critical path items. The West cluster is somewhat more complex with the inclusion of the injection, abort, and rf systems, as well as experimental facilities. This area is scheduled for completion near the end of FY92—well ahead of project completion.

In summary, the schedule projects that all collider systems will be installed and tested by February 1994. The injected beam from the HEB will have been tested into certain completed sectors of the collider several months earlier. Beam tests in the collider are projected in the last two months prior to project completion.

7.4.5 Manpower Analysis

It is of interest to provide a projection for the overall construction staff required by the SSC project. This projection can be used also, for example, to provide an estimate of building and office space that will be needed at or near the SSC site during the construction period. It should be recognized that some parts of the SSC design and fabrication effort may be performed at existing high energy physics laboratory facilities; therefore, the total manpower for EDI and Construction may include personnel at other laboratories for specific "subcontracted" tasks. In particular the construction manpower for fabrication of collider magnets will consist of both SSC laboratory staff and equivalent industrial staff.

An estimate of the SSC project manpower for Management and Support, EDI, and Construction for Technical Systems is provided in Tables 7.4-3 through 7.4-5, with total manpower projection at the summary level in Table 7.4-6. These estimates are based on the schedule data of Sections 7.4.2 and 7.4.3, the construction costs of Section 8.7, and the labor rates of Section 8.1.4. Estimates for AE/CM and Conventional Systems manpower are developed in Attachment C.

Table 7.4-3
Distribution of Management and Support Staff
(Man years)

	Fiscal Year						
Category	88	89	90	91	92	93	94
Directors Office	5	8	11	11	9	6	3
Project Support	18	41	53	53	44	31	12
Accelerator Div.	36	45	59	62	53	31	14
Conv. Systems Div.	16	45	79	110	73	35	14
Tech Support Div.	13	40	105	121	97	55	18
Admin. Support Div.	42	102	150	153	114	58	21
Totals	130	281	457	510	390	216	82

Table 7.4-4
Technical Systems EDI Staff
(Man years)

	Fiscal Year						
Category	88	89	90	91	92	93	94
Injector systems	187	151	93	78	41	9	—
Collider magnets	140	162	289	315	313	313	156
Other collider systems	52	104	105	106	114	95	44
Total	379	417	487	499	468	417	200

Table 7.4-5
Technical Systems Construction Manpower—Fabrication and Installation
(Man years)

	Fiscal Year						
Categories	88	89	90	91	92	93	94
Injector systems (SSC)	4	116	257	299	211	58	—
Collider magnets (SSC)	—	5	44	247	341	330	70
Collider magnets (Industry)	44	165	280	739	835	832	51
Other collider systems (SSC)	—	36	57	162	266	192	14
Total (SSC)	4	157	358	708	818	580	84
Total Project	48	322	638	1447	1653	1412	135

Table 7.4-6
SSC Project—Total Manpower*
(Man years)

	Fiscal Year						
Categories	88	89	90	91	92	93	94
Management and Support	130	281	457	510	390	216	82
EDI (Technical)	379	417	487	499	468	417	200
Construction	48	322	638	1447	1653	1412	135
Total	557	1020	1582	2456	2511	2045	417

*Does not include AE/CM and Conventional Systems Construction manpower.

References

7.2-1. *Quality Assurance Program Requirements for Nuclear Power Plants,* ANSI/ASME-1-1979, American Society of Mechanical Engineers, N.Y. (1983).

7.2-2. DOE Order 5700.6A Quality Assurance, U.S. Department of Energy, Washington, D.C. (8-13-1981).

8. Cost Estimate

8.1 Introduction

8.1.1 General Methodology

The overall responsibility for the SSC Conceptual Design cost estimate rests with the Central Design Group (CDG). The accelerator systems design was directed by technical teams of the CDG, calling on their considerable experience in building and operating major U.S. high energy accelerator facilities. Members of the CDG, assisted by experts from U.S. high energy accelerator laboratories, universities, and industrial consultants, carried out the conceptual designs and then estimated costs for various accelerator systems. Costs for conventional facilities construction have been estimated with the assistance of the architecture—engineering joint venture RTK (Raymond Kaiser Engineers, Tudor Engineering, Keller & Gannon-Knight). The technical systems estimates involved major contributions from Brookhaven National Laboratory (BNL), Fermi National Accelerator Laboratory (FNAL), Los Alamos National Laboratory (LANL), Lawrence Berkeley Laboratory (LBL), Texas Accelerator Center (TAC), Cryogenic Consultants Inc., General Dynamics, and Westinghouse Corp.

The cost estimates for the SSC components and systems are based on previous experience with similar accelerator components and conventional construction practices. This experience is important in assuring that all major technical components have been included in the SSC Design and Cost Estimate. Where the technical systems closely resemble existing systems (for which designs and costs were known through extensive experience), their cost can be more accurately determined; for these, less lower—level cost detail is required. The cost estimate for the collider ring superconducting magnets—a major fraction of the total project cost—represents a considerable extrapolation from previous experience. Accordingly, this area has received considerable attention during the Phase I period, and the details for the magnet design and fabrication as well as the cost estimate material for these magnets is provided in much more detail. In the conventional facilities categories, the underground construction represents the largest portion of the total conventional systems cost. In consequence, complete descriptions of the design and construction conditions

considered, as well as the specific cost estimating models developed for various tunneling practices, are described in detail.

A Work Breakdown Structure (WBS) encompassing all construction cost aspects of the conceptual design has been developed to ensure that all elements of the SSC project are included in the design and costing process. This Conceptual Design Report cost estimate includes all construction costs that are incurred after project approval for the SSC. In particular, we include the construction of the required conventional plant and associated laboratory support facilities. The construction project, as defined here includes associated management and administration, as well as engineering, design, and inspection (EDI) for technical systems and correspondingly architectural, engineering and construction management (AE/CM) services for conventional systems.

The general philosophy for this SSC cost estimate was to include all construction costs incurred after project approval to bring a 20 TeV colliding beam proton accelerator to a state of operational readiness and to create a laboratory environment suitable for conducting high-energy physics experiments at the facility. To accomplish this goal and to insure completeness and uniform procedures in cost estimating, a set of guidelines and assumptions were established. These are listed in Table 8.1-1.

Table 8.1-1
Cost Estimating Guidelines and Assumptions

- All primary technical components are developed to a state of engineering design readiness.
- The facility is constructed at a representative site within the U.S.
- Materials costs and labor rates are national average rates.
- Cost estimates are in FY86 dollars.
- Overall management of construction contracts will be the responsibility of the SSC laboratory administration.
- Engineering Design (EDI) for technical components will be performed by the laboratory staff.
- Design and construction management for conventional systems will be performed by selected AE/CM firms.
- The final installation and testing of technical components and systems will be carried out at the SSC laboratory. The production of the collider ring superconducting magnets will be carried out in an industrial environment. Primary responsibility for technical risk and quality assurance will be borne by the laboratory.

Technical Components

The SSC technical components are estimated based on the premise that all primary technical systems are assumed to be in an advanced state of development at the start of the construction phase. In particular, the collider ring magnet design is presumed to have been developed to the point where industrial technology transfer has begun, and industrial tooling and production studies, as well as model magnet assemblies have been carried out in industry. In addition, during the Phase I R&D, several full scale magnets will have been fabricated and thoroughly tested for magnetic and operational performance, both individually and as assembled into a lattice half-cell module that represents the repeating magnetic structure around the ring. This will ensure adequate knowledge of the performance, reliability, costs, and achievable production schedule for the SSC technical components.

The cost estimate does not include certain preparatory costs that may be incurred prior to project approval in order to ensure an orderly and efficient project start-up. Excluded from the cost estimate are site acquisition costs, primary power distribution to the site substations, geotechnical investigations, preliminary studies for environmental impact and safety analysis reports, and preliminary engineering studies for planning and scheduling. In addition, the SSC conceptual design cost estimate presented here does not include costs for the R&D program for accelerator systems and components, or costs for physics research equipment, particle detectors, and their associated equipment. These programs and their associated costs will be presented in special reports.

Conventional Construction

Conventional construction costs are estimated based on example sites developed in conjunction with RTK. These examples are based on an analysis of the physiographic provinces within the United States. In the Reference Designs Study the conventional facilities were designed in the context of a "median site". That site represented a composite model, developed from characteristics associated with some of the potential sites that were known in 1983. For this conceptual design report, three example sites were developed to provide a more realistic basis for design, schedule and cost studies of an SSC facility. A variety of tunnel enclosure construction methods, appropriate to the three model sites, were also considered in detail. The cost estimating methods were developed in sufficient detail to allow evaluation of the impact in cost of selected technical, and geological variations. Furthermore, the geotechnical models developed, the tunneling methods studied, and the cost estimating procedures could be useful to the Department of Energy during evaluation of proposed sites for the SSC.

The principal differences among the three approaches were in the postulated geotechnical settings for the collider ring and the methods of construction invoked. The examples are described as follows:

Site A: The tunnel is located at a depth below the surface of about 50 feet, and is bored though a mixed medium of soil and sedimentary rock with a varying water table. Soft ground tunneling using a tunnel-boring machine (TBM) with tooth cutters is the appropriate method of construction.

Site B: The tunnel is about 150 feet below the ground surface and is bored through a mixed medium consisting predominately of competent rock below the water table. A TBM with disc cutters is used for construction.

Site C: The collider ring is constructed near the surface using primarily surface construction excavation techniques. The geology consists of a mixed medium made up of soft alluvial soils with some volcanic rock. The tunnel is located above the water table.

In each case, common above-ground facilities were used with changes in the design of the beam transfer lines and experimental halls to account for the variations in depth of the three examples sites around their respective ring profiles.

RTK used the three example sites in exercising their cost development model for tunnels. By determining the duration of tunnel work in conjunction with needed crew sizes, estimates for labor, equipment usage, materials, subcontracts (if any), purchased equipment, overhead and profit were developed for each tunnel segment in all the models. The ancilliary starter tunnels, niches and alcoves were also estimated in appropriate detail. Costs for electrical and mechanical services in the tunnel were then added to produce an overall cost estimate for each tunnel segment. The tunnel costs were summed with their respective above-ground facilities to produce each of the three cost estimates. Each example also includes an estimate of the funds required for the AE/CM services and contingency items. Cost estimates for the three cases are described in Section 8.1.2, and details are found in Attachment C (the RTK report) and associated back-up documentation. In order to provide a single, best estimate for the conventional facilities costs in this CDR prior to the selection of an actual site for the SSC, an average total cost estimate is derived from the specific examples, with consideration being given to cost ranges. The analysis details for the information provided by the example sites are provided in the next Section 8.1.2. The resulting cost estimate for the SSC is used in Section 8.3.

8.1.2 Conventional Systems Analysis

The existence of three cost estimates for the conventional systems is of considerable value in arriving at a perspective on the range of possible costs for the SSC. The work not only addresses the consequences of the different geological settings, facility configurations and depths, and construction techniques, but it provides additional information for the contingency evaluations. The base cost estimates for the three cases are summarized in Table 8.1-2.

Table 8.1-2
Cost Estimates for the Conventional Facilities for the Three Site Examples
(in thousands of dollars)

	Site A	Site B	Site C
Site and infrastructure	85457	85629	85408
Campus	42860	42860	42860
Injector	39758	39758	39758
Collider	385418	360339	308187
Experimental	64358	83497	58466
Total	617851	612083	534679

The starting point for the analysis consists of examining the differences among the costs for the three sites. As expected, there are basically no variations shown for the injector, campus site and infrastructure costs. Attention is focused on the collider and experimental areas. These structures are primarily underground, and are directly affected by the physical and geotechnical assumptions made in the models.

For the collider ring, the cut and cover approach followed for *Site C* results in the lowest construction cost. A majority of the length of the tunnel would be constructed by less expensive surface-excavation techniques. The special sections, as required, are precast, and lowered into position. Even the walls of the experimental halls can be formed in the open, and concrete poured in a routine manner.

In *Site A,* a collider ring orientation is considered that is about 50 feet below the surface. The best technique, considering the depth, is tunneling. However, at this depth one encounters a mixture of materials, and perhaps the occasional presence of groundwater, leading to less than optimum advance rates for the boring machines. Fortunately, the experimental facilities are close enough to the surface that excavation and construction can be undertaken as in the manner for the Site C example.

For *Site B,* located deeper underground, the experimental facilities are considerably more expensive, since access to the deep underground caverns are provided by wide, long shafts to the surface buildings. However, the presence of the better, more competent rock at the lower level makes the tunnel boring move more rapidly. The result of this trend is that the overall cost of Site B is close to that of Site A, indicating only a small dependence upon depth.

It is concluded that the required conventional facilities can be constructed in a wide variety of basic settings for which efficient construction techniques exist and for which the costs will not vary markedly with the basic setting.

Each of the three examples took into account the possibility of encountering difficult conditions which might be found in the particular physiographic setting such as faults, ground water, etc. It is assumed that great care will be used during site selection to avoid sites with large measures of difficult conditions.

These findings have led us to state the Conventional Systems cost estimate as the average of the highest and lowest example cases with contingency sized to encompass reasonable variations of the physiographic setting as well as typical problems that might be encountered during construction.

8.1.3 Work Breakdown Structure

A detailed Work Breakdown Structure (WBS) was developed to ensure that all elements of the SSC project were evaluated for the design and appropriately included in the cost estimate. The WBS extended to the lowest available level appears in Attachment D which also includes the detailed cost estimate for the conceptual design. The WBS is organized into five major sections which are defined below:

.1 **Technical Components** consist of all of the technical systems and equipment required for the accelerator complex. Within category .1 the two next lower level sections are organized as follows: Section .1.1 includes the *Injector System* comprised of the sequence of injection accelerators from the Linac, Low Energy Booster, Medium Energy Booster, and the High Energy Booster, as well as the Test Beam Area fed from the High

Energy Booster. Section .1.2 includes all of the technical components for the *SSC Collider Ring Systems.*

.2 **Conventional Facilities** comprise all of the conventional construction elements grouped into five sub-elements. Section .2.1 addresses the overall *Site and infrastructure* elements that are required throughout the entire site. Section .2.2 is described as a *Campus area* and represents the central laboratory structures including the laboratory building and supporting shops and heavy works buildings. Section .2.3 includes all of the conventional construction specifically identified with the *Injector facilities*, and Section .2.4 includes all of the conventional work identified with the *Collider facilities*—primarily the underground construction for the tunnel, along with the necessary surface buildings and cryogenic facilities. Section .2.5 includes the specific *Experimental conventional facilities* required in each of the cluster areas.

.3 **Systems Engineering and Design** comprises both the technical component engineering, design, and inspection (*EDI*) activities as well as the architect engineering and construction management (*AE/CM*) services for the conventional construction.

.4 **Management and Support** consists of all management, supervision and support functions required for the engineering design and construction phase of the project. Section .4.2 includes all of the project equipment required to carry out the construction phase and to equip the laboratory with necessary standard equipment. Section .4.3 includes the cost for support facilities during construction including leased building space and electrical power.

.5 **Contingency** is described and collected in a separate WBS category for convenience of cost estimating development and assembly. The contingency costs have been developed based on separate assessment of each of the various WBS sections.

The above categories define the major systems required to achieve the SSC technical goals and describe a logical method for providing the WBS at level 2. The expansion of this structure to lower levels 3 and 4 is shown in Fig. 8.1-1. The WBS extended to the lowest practical level was used as the basic structure for organizing the descriptions of the separate systems and facilities as well as for developing and assembling the total estimated project costs. Table 8.1-3 lists the WBS to level 4 (including expansion to level 5 in some areas) and provides the specific WBS numbers for the structure displayed in Fig. 8.1-1.

8.1.4 Labor Rates

Methods for Rate Determination

The labor rates utilized for the SSC cost estimate are in general based upon established rates for the San Francisco Bay area. The basic rates (i.e., direct salary and all benefits) for crafts are Davis-Bacon rates in Alameda County, California. The final craft rates, as explained in the next sections, will vary depending upon the type of work and the specific contractual arrangements that are projected. The conventional systems craft rates are also dependent upon whether the work is above ground or underground.

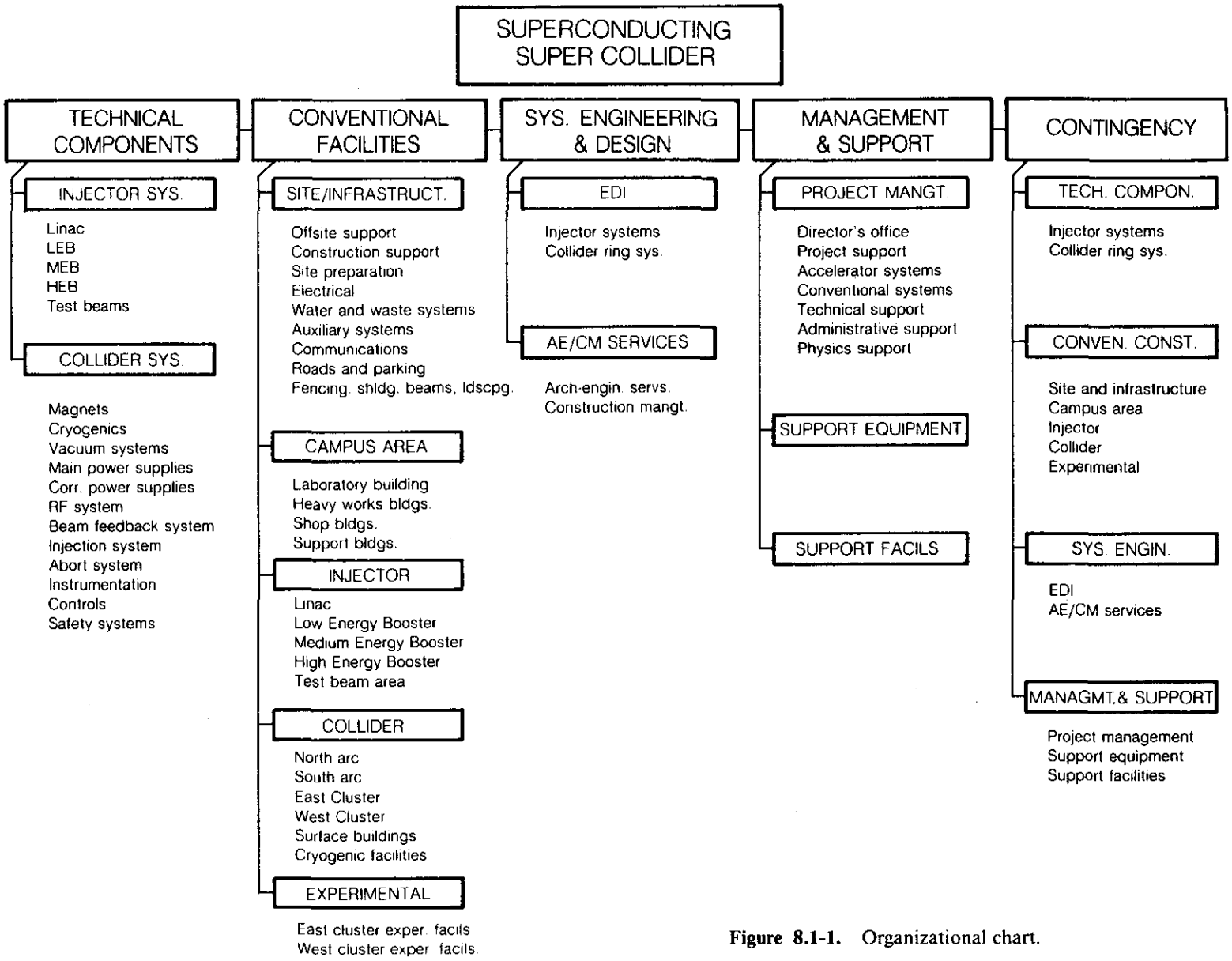

Figure 8.1-1. Organizational chart.

Table 8.1-3
Work Breakdown Structure (WBS)

1.	**Superconducting Super Collider**
.1	**Technical components**
.1.1	*Injector systems*
.1.1.1	Linac
.1.1.1.1	Ion source
.2	RFQ (49.5 MHz)
.3	Drift tube Linac (445 MHz)
.4	Coupled cavity Linac (1336 MHz)
.5	445 MHz rf power system
.6	1336 MHz rf power system
.7	Transfer line (Linac to LEB)
.8	Instrumentation and controls
.9	Safety systems
.1.1.2	Low Energy Booster (LEB)
.1.1.2.1	Magnets
.2	Cryogenics (NA)
.3	Vacuum system
.4	Magnet power supplies
.5	Correction magnet power supply system
.6	rf systems
.7	Injection system
.8	Extraction system
.9	Instrumentation
.10	Controls
.11	Safety system
.12	Installation
.1.1.3	Medium Energy Booster (MEB)
.1.1.3.1	Magnets
.2	Cryogenics (NA)
.3	Vacuum system
.4	Magnet power supplies
.5	Correction magnet power supply system
.6	rf systems
.7	Injection system
.8	Extraction system
.9	Instrumentation
.10	Controls
.11	Safety system
.12	Installation
.1.1.4	High Energy Booster (HEB)
.1.1.4.1	Magnets
.2	Cryogenics
.3	Vacuum system
.4	Magnet power supplies
.5	Correction magnet power supply system
.6	rf systems
.7	Injection system
.8	Extraction system
.9	Instrumentation
.10	Controls
.11	Safety system
.12	Installation
.1.1.5	Test Beams
.1.1.5.1	(Not used)
.2	(Not used)
.3	Vacuum system
.4	(Not used)
.5	Primary transport system
.6	Target stations
.7	Secondary transport system
.8	(Not used)
.9	Instrumentation
.10	Controls
.11	Safety system
.1.2	*Collider Ring Systems*
.1.2.1	Magnets
.1.2.1.1	Tooling
.2	Dipole magnets
.3	Quadrupole magnets
.4	Spools and special devices
.5	IR magnets
.6	Installation, survey, and alignment
.1.2.2	Cryogenics
.1.2.3	Vacuum systems
.1.2.4	Main power supplies
.1.2.5	Correction power supplies
.1.2.6	rf system
.1.2.7	Beam feedback system
.1.2.8	Injection system
.1.2.9	Abort system
.1.2.10	Instrumentation
.1.2.11	Controls
.1.2.12	Safety systems

Table 8.1-3 (continued)

.2	**Conventional facilities**
.2.1	*Site and infrastructure*
.2.1.1	Offsite support
.2.1.2	Construction support
.2.1.3	Site preparation
.2.1.4	Electrical
.2.1.5	Water and waste systems
.2.1.6	Auxiliary systems
.2.1.7	Communications
.2.1.8	Roads and parking
.2.1.9	Fencing, berms, landscaping
.2.2	*Campus area*
.2.2.1	Laboratory buildings
.2.2.2	Heavy works buildings
.2.2.3	Shop buildings
.2.2.4	Support buildings
.2.3	*Injector facilities*
.2.3.1	Linac
.2.3.2	Low Energy Booster
.2.3.3	Medium Energy Booster
.2.3.4	High Energy Booster
.2.3.5	Test beam area
.2.4	*Collider facilities*
.2.4.1	North arc
.2.4.2	South arc
.2.4.3	East cluster
.2.4.4	West cluster
.2.4.5	Surface buildings
.2.4.6	Cryogenic facilities
.2.5	*Experimental facilities*
.2.5.1	East cluster experimental facilities
.2.5.2	West cluster experimental facilities
.3	**Systems Engineering and Design**
.3.1	*EDI*
.3.1.1	Injector systems
.3.1.1.1	Linac
.2	Low Energy Booster
.3	Medium Energy Booster
.4	High Energy Booster
.5	Test beams
.3.1.2	Collider Ring Systems
.3.1.2.1	Magnets
.2	Cryogenics
.3	Vacuum systems
.4	Main power supplies
.5	Correction power supplies
.6	rf system
.7	Beam feedback system
.8	Injection system
.9	Abort system
.10	Instrumentation
.11	Controls
.12	Safety systems
.3.2	*AE/CM Services*
.3.2.1	AE Services
.3.2.1.1	Site and infrastructure
.2	Campus area
.3	Injector facilities
.4	Collider ring facilities
.5	Experimental facilities
.3.2.2	CM Services
.3.2.2.1	Site and infrastructure
.2	Campus area
.3	Injector facilities
.4	Collider ring facilities
.5	Experimental facilities
.4	**Management and Support**
.4.1	*Project management*
.4.2	*Support equipment*
.4.3	*Support facilities*
.5	**Contingency**
.5.1	*Technical components*
.5.1.1	Injector systems
.5.1.1.1	Linac
.2	LEB
.3	MEB
.4	HEB
.5	Test beams
.5.1.2	Collider ring systems
.5.1.2.1	Magnets
.2	Cryogenics
.3	Vacuum systems
.4	Main power supplies
.5	Correction power supplies
.6	rf system
.7	Beam feedback system
.8	Injection system
.9	Abort system
.10	Instrumentation
.11	Controls
.12	Safety systems
.5.2	*Conventional facilities*
.5.2.1	Site and infrastructure
.5.2.2	Campus area
.5.2.3	Injector facilities
.5.2.4	Collider ring facilities
.5.2.5	Experimental facilities
.5.3	*Systems engineering and design*
.5.3.1	EDI
.5.3.2	AE/CM services
.5.4	*Management and support*
.5.4.1	Project management
.5.4.2	Support equipment
.5.4.3	Support facilities

In the technical systems area, labor categories (e.g., engineers and physicists) have been determined from current rates at the National Laboratories. For laboratory support departments, such as Personnel Department, Mechanical Shops, Security, etc., the basic rates have been determined from average rates of equivalent departments at LBL.

In summary, most of the basic labor rates have been determined for the San Francisco area primarily because of the greater access to more detailed data for this area. Adjustments have been made to the basic craft rates depending on the type of contract and the degree of risk. Finally, the above rates are adjusted to National Average Rates by the method described below.

National Average Adjustment

There are a number of national surveys which provide data on the variation of construction costs throughout the United States. These surveys indicate that construction cost factors can vary as much as a factor of two between states or even within regions of a given state. As the site for the SSC is undetermined at this time, it appears appropriate to use a national average for SSC labor rates. Table 8.1-4 shows the construction cost index for the San Francisco area relative to a national average from four sources.

Table 8.1-4
Relative Construction Costs of San Francisco Area

Source	Construction Cost Index*
Engineering News Record	1.2
Lee Saylor (S.F)	1.23
Lee Saylor (Oakland)	1.17
Means	1.23
U.S. Corps of Engineers	1.25

*Relative to a national average of 1.0.

The above construction cost indices are based on a mixture of labor and material costs. Depending on the survey, the labor percentage may vary from approximately 60% to 80%. The detailed analysis of these components would indicate a slightly higher index for labor and a smaller factor for materials. With the above information as a guide, the adjustment factors in Table 8.1-5 have been adopted to determine the SSC rates on a national average basis.

Table 8.1-5
National Average Cost Adjustment Factor

	Management and Support	Technical Systems	Conventional Systems
Labor	1.2	1.2*	1.2
Materials	—	1.0**	1.2
Equipment	—	1.0	1.0

*Except for engineers and physicists where an average for the National Laboratories is used without adjustment.
**As material quotes for technical components come from a wide cross section of the U.S., no adjustment factor is used.

Technical Systems

A summary of the nationally adjusted labor rates used for Technical systems is provided in Table 8.1-6. All labor effort is estimated in hours in association with a particular craft code. The only permitted craft codes were the ones shown in Table 8.1-6. While a greater variety of crafts could be utilized, the simplification to the standard crafts listed here is believed to assure greater uniformity and consistency of the separate cost estimate details that are provided from many sources.

The rates for the installation category are based on Davis-Bacon rates. The base rates before national adjustment are confirmed by actual labor contracts at LBL as of November 1985. These rates include the basic salary, all benefits, and approximately 10% overhead and profit to the labor supplying organization (jobshop).

In the Manufacturing/Fabrication category, the shop rates (before national adjustment) were based on information from shops in the San Francisco area.

The rates for categories under Engineering and Design are determined from an average of the rates at three National Laboratories (LBL, BNL and FNAL). As this determination directly reflects a national average for a closely related scientific laboratory, no further national adjustment factor is applied to these rates.

Conventional Systems

A partial list of craft rates is provided in Table 8.1-7. Rates are provided for the standard above ground crafts as well as for the more specialized underground workers.

Table 8.1-6
Technical Systems
Craft Codes and Nationally Adjusted Rates for FY 1986

	Craft Code	$/h
*Manufacturing / Fabrication / Assembly / Test:		
Technician (assy. tests, etc.), relatively unskilled	T1	22.00
Technician (assy. tests, etc.), experienced/skilled	T2	33.00
Shops (average capability machinists, elect fab, etc.)	S1	38.00
Shops (specialized, precision, high tech, NC, etc.)	S2	44.00
Factory support	F1	33.00
*Installation: (assumes "Davis-Bacon")		
Plumber, steam fitter, sheet metal	IP	36.00
Electrician	IE	33.00
Carpenter	IC	30.00
Painter	IN	28.00
Rigger, crane operator	IG	30.00
Laborer	IL	23.00
Technician	IT	23.00
**Technical Design (and Construction/Installation where applicable):		
Engineering / Design / Inspection:		
Physicist	PH	34.00
Engineer (mechanical and electrical)	EN	32.00
Designer/Coordinator	DC	25.00
Drafter	DR	18.00

*Includes hourly base pay, employee benefits, and overhead & profit for outside vendor or contractor.

**Includes effective hourly base pay and benefits, but does not include laboratory overhead (which is included in a separate WBS category).

Table 8.1-7
Conventional Systems
Labor Rates for FY86 - Partial List*

Craft	($/h)
Above ground	
Iron Worker	33.70
Plumber	38.50
Carpenter	33.30
Laborer	25.60
Electrician	36.40
Teamster	24.00
Bricklayer	30.30
Painter	30.20
Below ground	
Shotcrete	36.50
Blaster	35.80
Bullgang	35.10
Driller	39.30
Mole operator	40.40
Muck operator	40.90

*A more extensive and complete listing of rates is in Attachment C.

For the above-ground crafts, the basic labor rates before national adjustment are the Davis-Bacon rates as used for the same craft under Technical Systems in the previous section. In this case, the crafts are assumed to work for construction contractors. An overhead/profit factor of approximately 20% is applied to reflect such items as management and supervision, field office facilities, etc.

The underground craft rates reflect a higher rate in the base salaries (~12%) with an overhead/profit factor of 40% resulting from increased risk factors in underground construction.

Management and Support

The organizational chart in Section 7.1 provides a model for laboratory construction management and associated support activities. The Director's office and the Technical and Conventional Systems offices are projected to be staffed largely with senior technical management personnel. Salaries commensurate with existing laboratory director's offices are assumed for the key personnel. An average rate for the overall office staff of each of these groups has been developed. In the Technical and Administrative support group categories, the average salary for each group has been based on the average salary of an equivalent group at LBL. These rates have been decreased by an adjustment factor of 1.2 in order to reflect a national average rate.

8.1.5 Data Format and Procedures

The cost data developed for this conceptual design are presented in FY 1986 (current) dollars, and all of the estimates are developed and presented according to the WBS notation. The WBS is used to organize and collect the costs in a systematic way and to ensure that all of the appropriate elements are identified and treated uniformly. This overall framework allows for the technical components and the conventional construction to be treated separately as two major but independent WBS categories. Within this framework, the cost estimating responsibilities were assigned specifically by WBS category to the various technical teams for the injector (.1.1), collider (.1.2), and the conventional (.2) systems. The appropriate EDI, AE/CM, and contingency categories were also developed by the various technical teams and by RTK. The consistency and uniformity of the resulting cost estimating work is ensured by the careful planning and organization of the procedures and data formats that were used.

For the technical component estimating teams, detailed cost estimating guidelines and procedures were developed and provided by the CDG. The individuals responsible for each section are all accelerator scientists, engineers, and designers, as well as experienced project management personnel, who have participated in design, cost estimating, and construction of accelerator systems and subsystems that are very similar to subsystem components of the SSC.

Whenever possible, costing was carried out by a bottoms-up detailed estimate and checked by scaling from known systems. In all cases an attempt was made to cost labor and materials separately. Materials costs included the unit price of "raw" materials or the complete cost of industry supplied components (ISC). For example, ISC includes power supplies, computers, refrigerators and other manufactured parts and subassemblies. Labor estimates for fabrication, assembly, installation, etc. were developed on the basis of labor-hours and labor-type ("craft code"), and the extension to dollars was made utilizing specific labor rates developed to represent a national average. (See Section 8.1.4). The utilization of national average labor rates appears appropriate in view of the range of potential locations for the SSC within the U.S.

Each technical system team was provided with a cost estimating guideline package that included a standard form for estimating to the lowest WBS level, together with other forms for summarizing to higher WBS levels. Information was also provided that tabulated past escalation rates (see Attachment D for a summary of escalation rates) so that construction and labor costs from recently completed accelerator projects or recently purchased similar components could be translated to FY 1986 dollars in the current estimate. The goal of the standardized formats and instructions was to ensure that each estimating group provided information with sufficient detail and accuracy on a uniform basis.

The conventional facilities costs were developed by the CDG Conventional Facilities Division and cost estimating teams within RTK. The direction and coordination of this overall activity was provided by the CDG Conventional Facilities Division to ensure that the data was developed and presented in a similar format and within the same consistent guidelines as specified for the technical component groups. For example, the conventional systems estimates also describe the labor (hours) and materials costs separately, but also include cost items for equipment usage, equipment purchase, and contractor overhead and profit that are unique to the conventional construction area. The RTK estimates were

developed initially in FY 1986 dollars using unit pricing and labor data developed for Northern California; the resulting materials and labor estimates were then also normalized to the national average basis (Table 8.1-5). All of the RTK cost elements are also tied to the integrated WBS identifying number. In addition RTK appends to the first five digits of the SSC WBS identification an additional seven digit code following a decimal separator to denote a link to the "RTK Interactive Estimating" system detail structure used to extract common unit price materials from their comprehensive conventional facilities data base.

The detail estimating worksheets that are presented in the RTK documentation (Attachment C) are very similar in format to the CDG technical component detail spreadsheets. The integration of the two systems was done at WBS level four and five (depending on the subsystem); the summary costs are shown in Section 8.3 and in Attachment D.

8.1.6 Data Assembly and Presentation

All of the detail cost input data provided by the technical and conventional systems estimating teams were reviewed by the appropriate CDG division leaders and the CDG Project Management and Planning Division personnel. Detailed discussions and reviews were held with the estimators to ensure completeness and, where appropriate, to ensure continuity between systems estimates by different groups. Following such reviews, the detailed data were entered into the ARTEMIS computer system which provided the record-keeping function (based on the WBS) along with providing various analysis capabilities.

ARTEMIS, a computerized management information system, is basically a critical path schedule program fully integrated into a modern relational database management system. It offers the capability for storing all elements of the detailed cost estimate as well as for manipulating, summing, printing, and archiving results in a systematic manner. The basic programs were expanded to meet the needs of the SSC cost estimating tasks. The basic system package was used during the Reference Designs Study (RDS) and the overall formats and organization for this conceptual design are basically unchanged.

The calculation of the cost of each WBS element begins at the lowest level using a table of pay rates in the data base. Four quantities are calculated from the detail spreadsheet data for the roll-up by WBS category: total effort labor hours, total cost of effort, total cost of materials, and total overall cost. These values are summed in turn at each higher WBS level until the total project cost is obtained.

8.1.7 Project Cost Summary

The SSC cost estimate derived by the methods outlined above is presented in summary level (WBS level 3) in Table 8.1-8 below. Costs for the separate WBS sections are expanded and are discussed in more detail in the following sections, specifically Technical Components in Section 8.2, Conventional Facilities in Section 8.3, Systems Engineering and Design in Section 8.4, Management and Support in Section 8.5, and Contingency in Section 8.6. A more detailed summary of the total project costs is presented in Section 8.7.

Table 8.1-8
Project Cost Summary

WBS			FY 86 K$
1.	**Superconducting Super Collider**		3,010,318
.1	**Technical components**		1,424,161
.1.1	*Injector systems*	189,252	
.1.2	*Collider ring systems*	1,234,909	
.2	**Conventional facilities**		576,265
.2.1	*Site and infrastructure*	85,433	
.2.2	*Campus area*	42,860	
.2.3	*Injector facilities*	39,758	
.2.4	*Collider facilities*	346,803	
.2.5	*Experimental facilities*	61,412	
.3	**Systems engineering and design**		287,607
.3.1	EDI	195,404	
.3.2	AE/CM services	92,203	
.4	**Management and support**		192,334
.4.1	Project management	114,749	
.4.2	Support equipment	52,635	
.4.3	Support facilities	24,950	
.5	**Contingency**		529,951

8.2 Technical Systems Cost

The two major SSC technical systems are the *Collider Ring* and the associated array of *Injectors*. The summary costs for these two systems is provided below in Table 8.2-1. Detailed costs are provided in the following sections.

Table 8.2-1
Technical Components, Summary

WBS	System Component		FY 86 K$
.1	**Technical components**		1,424,161
.1.1	*Injector systems*	189,252	
.1.2	*Collider ring systems*	1,234,909	

8.2.1 Injector Systems

The overall injection system for the Collider consists of an H^- source, RFQ linac, and three booster synchrotrons, (LEB, MEB, and HEB). The beam kinetic energy range attained by each system is as follows:

H^- Source	0–50 KeV
RFQ	0.05–2.5 MeV
Linac	2.5–600 MeV
LEB	0.6–7.1 GeV
MEB	7.1–100 GeV
HEB	100–1000 GeV

In brief the ion source will provide an H^- beam which is accelerated by a radio-frequency quadrupole (RFQ) to 2.5 MeV. The beam enters a drift tube linac (DTL) for acceleration to 125 MeV. Finally a side-coupled linac system (SCL) accelerates the beam to 600 MeV. A short transport line carries the beam to the Low Energy Booster (LEB).

The LEB is a fast cycling synchrotron with conventional magnets that accelerates the beam from 0.6 GeV to 7.1 GeV. After extraction from the LEB the beam is transported to the medium energy booster (MEB) for acceleration to 100 GeV. The MEB synchrotron (also constructed of conventional magnets) provides the injected beam to the final high energy booster (HEB) system.

The HEB synchrotron provides acceleration from 100 GeV to 1000 GeV for injection into the collider. The bending and focusing magnets of the HEB are superconducting; the overall scale and energy of the HEB is very similar to the Tevatron at FNAL. The extracted beam from the HEB will be used also to provide external test beams for equipment tests and experimental detector calibrations during periods when injection is not required into the collider.

The technical descriptions, specifications, and operational characteristics for each of the above accelerator systems are described in Section 5.15. The resulting conceptual designs for these systems have been translated into a detailed work breakdown structure to define the components of each accelerator. The WBS structure for each accelerator system at its lowest level with associated cost data is provided in Attachment D. Table 8.2-2 provides an overall cost summary for each of the injector accelerators (WBS level 4). The costs for the major systems of each accelerator (WBS level 5) are provided in Tables 8.2-3 to 8.2-7.

Table 8.2-2
Injector Technical Systems Summary Cost

WBS	System Component		FY 86 K$
.1.1	*Injector systems*		189,252
.1.1.1	Linac	25,068	
.1.1.2	LEB	15,585	
.1.1.3	MEB	31,720	
.1.1.4	HEB	107,271	
.1.1.5	Test beams	9,608	

Table 8.2-3
Linac Technical Systems Cost

WBS	System Component		FY 86 K$
.1.1.1	Linac		25,068
.1.1.1.1	Ion source	886	
.1.1.1.2	RFQ (49.5 MHz)	891	
.1.1.1.3	Drift tube linac (445 MHz)	6,235	
.1.1.1.4	Side-coupled linac (1336 MHz)	3,381	
.1.1.1.5	445 MHz rf power system	4,287	
.1.1.1.6	1336 MHz rf power system	3,797	
.1.1.1.7	Transfer line (Linac to LEB)	3,469	
.1.1.1.8	Instrumentation and controls	1,736	
.1.1.1.9	Safety systems	386	

Table 8.2-4
Low Energy Booster Technical Systems Cost

WBS	System Component		FY 86 K$
.1.1.2	Low energy booster		15,585
.1.1.2.1	Magnets	2,671	
.1.1.2.2	Cryogenics (NA)	0	
.1.1.2.3	Vacuum system	371	
.1.1.2.4	Magnet power supplies	4,806	
.1.1.2.5	rf systems	4,224	
.1.1.2.6	Injection system	245	
.1.1.2.7	Extraction system	361	
.1.1.2.8	Abort system	110	
.1.1.2.9	Instrumentation	277	
.1.1.2.10	Controls	1,526	
.1.1.2.11	Safety system	136	
.1.1.2.12	Installation	858	

Table 8.2-5
Medium Energy Booster Technical Systems Cost

WBS	System Component		FY 86 K$
.1.1.3	Medium energy booster		31,720
.1.1.3.1	Magnets	13,492	
.1.1.3.2	Cryogenics (NA)	0	
.1.1.3.3	Vacuum system	919	
.1.1.3.4	Magnet power supplies	7,101	
.1.1.3.5	rf systems	3,759	
.1.1.3.6	Injection system	217	
.1.1.3.7	Extraction system	829	
.1.1.3.8	Abort system	583	
.1.1.3.9	Instrumentation	550	
.1.1.3.10	Controls	1,027	
.1.1.3.11	Safety system	276	
.1.1.3.12	Installation	2,968	

Table 8.2-6
High Energy Booster Technical Systems Cost

WBS	System Component		FY 86 K$
.1.1.4	High energy booster		107,271
.1.1.4.1	Magnets	54,244	
.1.1.4.2	Cryogenics	13,561	
.1.1.4.3	Vacuum system	1,965	
.1.1.4.4	Magnet power supplies	13,108	
.1.1.4.5	rf systems	5,334	
.1.1.4.6	Injection system	1,370	
.1.1.4.7	Extraction system	3,526	
.1.1.4.8	Abort system	1,620	
.1.1.4.9	Instrumentation	958	
.1.1.4.10	Controls	1,767	
.1.1.4.11	Safety system	697	
.1.1.4.12	Installation	9,121	

Table 8.2-7
Test Beams Technical Systems Costs

WBS	System Component		FY 86 K$
.1.1.5	Test beams		9,608
.1.1.5.1	(Not used)	0	
.1.1.5.2	(Not used)	0	
.1.1.5.3	Vacuum system	350	
.1.1.5.4	(Not used)	0	
.1.1.5.5	Primary transport system	2,390	
.1.1.5.6	Target stations	1,200	
.1.1.5.7	Secondary transport system	3,040	
.1.1.5.8	(Not used)	0	
.1.1.5.9	Instrumentation	299	
.1.1.5.10	Controls	2,027	
.1.1.5.11	Safety system	301	

8.2.2 Collider Systems

The chain of accelerators that comprise the injector systems of the last section provide a characteristic beam of protons for injection into the collider rings. After the proper injection sequence in which the protons are stored in both collider rings at 1.0 TeV energy, the two counter rotating beams are accelerated to as high as 20 TeV. Collisions between the beam particles are observed by appropriate detector systems at the prescribed experimental stations.

The technical components of the collider ring are similar to those of other major accelerator facilities such as the existing storage rings at FNAL and CERN. However, the larger scale of the SSC requires considerable care in extrapolating cost information from previous experience. The technical systems of the SSC collider rings have been described in detail in Chapter 5. The corresponding detailed cost information at the lowest WBS levels is provided in Attachment D.

Consideration has been given to manufacturing methods for the major technical elements of the collider. The overall capabilities of industry, existing accelerator laboratories, and the SSC laboratory have been considered. As with past accelerators, almost all of the components are supplied by industrial vendors. Most component costs used for the SSC estimate are based on vendor quotations. In arriving at the costs for complete systems, a detailed analysis of the tooling and the labor required for assembly, test, and installation are combined with the component quotations and estimates.

Table 8.2-8 provides a summary of the collider costs at WBS level 4. Table 8.2-9 expands the costs of the magnet system (.1.2.1) to WBS level 5.

Table 8.2-8
Collider Technical Systems Cost

WBS	System Component		FY 86 K$
.1.2	*Collider ring systems*		1,234,909
.1.2.1	Magnets	1,001,252	
.1.2.2	Cryogenics	121,137	
.1.2.3	Vacuum systems	17,321	
.1.2.4	Main power supplies	26,105	
.1.2.5	Correction power supplies	6,942	
.1.2.6	rf system	7,302	
.1.2.7	Beam feedback system	4,301	
.1.2.8	Injection system	5,201	
.1.2.9	Abort system	9,669	
.1.2.10	Instrumentation	12,871	
.1.2.11	Controls	18,016	
.1.2.12	Safety systems	4,791	

Table 8.2-9
Collider Magnet Systems Cost

WBS	System Component		FY 86 K$
.1.2.1	Magnets		1,001,252
.1.2.1.1	Tooling	56,031	
.1.2.1.2	Dipole magnets	746,120	
.1.2.1.3	Quadrupole magnets	39,262	
.1.2.1.4	Spools and spec devices	78,108	
.1.2.1.5	IR magnets	39,168	
.1.2.1.6	Installation and survey	42,564	

8.3 Conventional Systems Cost

The approach and method used to obtain the cost information for conventional systems has been described in Section 8.1. This basic information was based on a variety of potential site conditions. Different techniques were considered for the construction program in each of three example sites that were studied in detail. The cost data from the three example sites was synthesized to provide the final costs which are summarized in Table 8.3-1. For each of the major categories (WBS level 3), lower level cost details are provided in Tables 8.3-2 through 8.3-6.

Table 8.3-1
Conventional Facilities Cost Summary

WBS	System Component		FY 86 K$
.2	**Conventional facilities**		576,265
.2.1	*Site and infrastructure*	85,433	
.2.2	*Campus area*	42,860	
.2.3	*Injector facilities*	39,758	
.2.4	*Collider facilities*	346,803	
.2.5	*Experimental facilities*	61,412	

Table 8.3-2
Conventional Facilities—Site and Infrastructure Cost

WBS	System Component		FY 86 K$
.2.1	*Site and infrastructure*		85,433
.2.1.1	Offsite support	0	
.2.1.2	Construction support	1,447	
.2.1.3	Site preparation	975	
.2.1.4	Electrical	43,732	
.2.1.5	Water and waste systems	5,913	
.2.1.6	Auxiliary systems	778	
.2.1.7	Communications	11,114	
.2.1.8	Roads and parking	20,530	
.2.1.9	Fencing, berms, landscape	944	

Table 8.3-3
Conventional Facilities—Campus Area Cost

WBS	System Component		FY 86 K$
.2.2	*Campus area*		42,860
.2.2.1	Laboratory building	24,049	
.2.2.2	Heavy works buildings	10,833	
.2.2.3	Shop buildings	2,209	
.2.2.4	Support buildings	5,770	

Table 8.3-4
Conventional Facilities—Injector Facilities Cost

WBS	System Component		FY 86 K$
.2.3	*Injector facilities*		39,758
.2.3.1	Linac	1,743	
.2.3.2	Low energy booster	1,322	
.2.3.3	Medium energy booster	10,953	
.2.3.4	High energy booster	23,618	
.2.3.5	Test beam area	2,122	

Table 8.3-5
Conventional Facilities—Collider Facilities Cost

WBS	System Component		FY 86 K$
.2.4	*Collider facilities*		346,803
.2.4.1	North arc	122,140	
.2.4.2	South arc	137,097	
.2.4.3	East cluster	31,459	
.2.4.4	West cluster	40,688	
.2.4.5	Surface buildings	1,663	
.2.4.6	Cryogenic facilities	13,756	

Table 8.3-6
Conventional Facilities—Experimental Facilities Cost

WBS	System Component		FY 86 K$
.2.5	*Experimental facilities*		61,412
.2.5.1	East cluster experimental facilities	31,136	
.2.5.2	West cluster experimental facilities	30,276	

8.4 Systems Engineering and Design Costs

The costs for the systems engineering, design, and inspection (EDI) for all Technical Systems components are summarized below together with the architectural engineering and construction management (AE/CM) costs for Conventional Systems. These design costs are also expressed respectively as a percentage of construction costs in Table 8.4-1.

Table 8.4-1
Systems Engineering and Design Cost Summary

WBS	Component	Construction (K$)	Systems Engineering (K$)	(%)
.3	**Systems engineering and design**	2,000,426	287,607	14.4
.3.1	*Technical components, EDI*	1,424,161	195,404	13.7
.3.2	*Conventional facilities, AE/CM*	576,265	92,203	16.0

8.4.1 EDI for Technical Systems

In general the engineering, design, and inspection (EDI) costs for the Technical systems are estimated as a percentage of the construction costs. The percentage is based on experience with the design of similar systems together with an evaluation of the variation of the design and/or manufacturing complexity of the current system. Also the degree of replication of each given technical system is folded into the analysis.

As stated in the overall assumptions for the cost estimate, it is planned that the EDI effort for the Technical systems will be undertaken largely by the SSC Laboratory staff.

The EDI costs reflect the effort required to translate the objective of a technical system (in terms of scope and parameters) into a practical design based on detailed engineering calculations and complete detailed drawings suitable for fabrication. Inspection provides the continuous coordination between fabricators and designers required to ensure that the final product meets specifications. Final inspection includes various tests of a system (or its components) to ensure that it meets performance specifications and is ready for pre-operational commissioning.

The general design features of the SSC resemble large accelerator systems now in existence; many of the components and subsystems are already in operation elsewhere. Specifications for these items are well enough understood that EDI can be estimated with confidence based on past experience. Experience from past major accelerator projects indicates that the total EDI for accelerator technical components has been in the range of 20% to 25% of related construction costs. Relevant examples cited in Table 8.4-2 include the Positron Electron Project (PEP), the Fermilab construction project, and the Stanford Linear Collider (SLC).

Table 8.4-2
Engineering Design Costs for Previous Accelerator Projects

Project	Tech Systems Construction (M$)	EDI (M$)	EDI %
Positron Electron Project (1976)	29.612	7.4	25
Fermilab (1968)	89.900	21.6	24
Stanford Linear Collider* (1986)	67.9	13.1	19

*Estimated values at ~80% completion.

The various technical systems for the SSC can be compared in design complexity to particular elements of the accelerator project examples in the table. The ion source, radio-frequency quadrupole, drift-tube linear accelerator, and the side-coupled linear accelerator for the first 0.6 GeV stage of the SSC injector follow similar systems that have been designed, fabricated, and operated at LANL. The 7.1 GeV Low Energy Booster (LEB) and 100 GeV Medium Energy Booster (MEB) both use conventional magnet technology and are similar (smaller in scale) to the Fermilab 400 GeV project, with some of the subsystems being more similar to those of the newer antiproton accumulator rings at Fermilab. The SSC High Energy Booster uses superconducting magnet technology, and relates directly in size and complexity to the Fermilab Tevatron system.

Apart from the injectors, other subsystems of the 20 TeV collider rings of the SSC are comparable in scale and complexity to existing systems as well. The rf system for the collider rings is approximately two-thirds of the size of the PEP rf system and closely follows the PEP design specifications and details.

Using the above similarities with well known projects as a guide, the EDI for the SSC technical systems has been estimated for each WBS level 4 (level 5 for injectors and collider magnet systems) category. With the exception of the main ring magnets and cryogenics categories, most of the EDI percentage factors ranged from 20%–30% depending on the complexity of the particular subsystem. The EDI for the collider ring superconducting magnet system has been developed by analyzing the specific EDI tasks for magnet design and production. The Tevatron magnet design, fabrication, and installation served as the basis model for estimating the EDI costs.

In the RDS, an EDI manpower analysis was made for the Tevatron experience according to the following tasks:

Engineering
Design and Drafting
Inspection, testing, and monitoring
Quality Assurance
Documentation
Office and staff support

Appropriate improvements or modifications were made to the Tevatron manpower levels as suggested by an analysis of that experience. These manpower levels were than extrapolated to the scale of the SSC project. The resulting total level of effort was then represented as a percentage of the total dipole magnet construction cost (10% EDI resulted). For this conceptual design, the same EDI value (10%) is used for the collider ring superconducting dipole and quadrupole construction; values ranging from 15% to 25% are used for other magnet systems categories of magnet tooling, spools, IR magnets, and installation depending on the projected design and fabrication complexity and magnitude of scale. The average percentage resulting for the cryogenic systems (13% overall) is a combination of two components: a lower percentage assigned to the large refrigerator purchase (in which the design costs are included in the approximately 45M$ purchase price), and a higher percentage (25%) assigned to the other portions of the cryogenic system.

A summary of the resulting estimated EDI for all of the technical systems of the SSC is provided in Table 8.4-3.

8.4.2 Architectural Engineering and Construction Management Services for Conventional Systems

The systems engineering, design, and inspection for conventional systems is planned to be accomplished via qualified architectural engineering and construction management firms. This work is defined as AE/CM services for the SSC project. Specifically the AE/CM services include the following tasks:

Project Management and Coordination
Quality Assurance/Control
Site Management
Reporting
Cost and Schedule Control
Contract Administration
Title I Design and Report

Table 8.4-3
Engineering, Design, and Inspection (EDI) Costs

WBS	Component	Construction (K$)	EDI (K$)	EDI (%)
.3.1	*Technical components*	1,424,161	195,404	13.7
.3.1.1	Injector systems	189,252	38,134	20.1
.3.1.1.1	Linac	25,068	5,766	23.0
.3.1.1.2	LEB	15,585	3,896	25.0
.3.1.1.3	MEB	31,720	7,930	25.0
.3.1.1.4	HEB	107,271	19,101	17.8
.3.1.1.5	Test beams	9,608	1,441	15.0
.3.1.2	Collider ring systems	1,234,909	157,271	12.7
.3.1.2.1	Magnets	1,001,252	115,010	11.5
.3.1.2.2	Cryogenics	121,137	15,748	13.0
.3.1.2.3	Vacuum systems	17,321	3,464	20.0
.3.1.2.4	Main power supplies	26,105	5,221	20.0
.3.1.2.5	Correction power supplies	6,942	1,388	20.0
.3.1.2.6	rf system	7,302	1,826	25.0
.3.1.2.7	Beam feedback system	4,301	1,075	25.0
.3.1.2.8	Injection system	5,201	1,300	25.0
.3.1.2.9	Abort system	9,669	2,417	25.0
.3.1.2.10	Instrumentation	12,871	3,218	25.0
.3.1.2.11	Controls	18,016	5,405	30.0
.3.1.2.12	Safety systems	4,791	1,198	25.0

Title II Design
Coordination with Technical Facilities Interface
Inspection and Record Keeping
Construction Management and Administration
Construction Safety and Security
Systems Operational Manuals
Maintenance of As-Built Drawings

The costs for these AE/CM tasks are usually estimated as a percentage of construction costs based on prior experience with similar work. The AE/CM costs will of course depend upon the scope and complexity of a given project. For example the ratio of AE/CM costs to construction costs will be considerably higher for a complex underground project when compared with a standard above ground building structure.

For similar activities, the ratio of AE/CM to construction costs decreases as the magnitude of the construction costs increases. This trend is illustrated by the projects listed in Table 8.4-4. Prior accelerator projects and rapid transit projects are indicated. These

classes of projects are similar in that they involve significant underground tunneling activities which comprise the major fraction of the construction costs. RTK has recommended AE/CM costs at 16% of construction costs. It is recognized that data such as presented in Table 8.4-4 would indicate a lower percentage in the range of 12% to 14%. The higher value of 16% is maintained in view of the lack of detailed site-specific geological data for the SSC.

Table 8.4-4
AE/CM Costs for Previous Projects

Project	Construction (M$)	AE/CM* (M$)	(%)
Accelerator Projects			
Positron Electron Project	28.26	6.64	23.5
Fermilab	95.63	23.14	24.2
Stanford Linear Collider	26.37	3.40**	13.0
Transit Projects			
Boston SW Corridor	593.00	84.80	14.3
Baltimore Rapid Transit	614.00	77.98	12.7
Atlanta Rapid Transit	737.00	88.44	12.0
Washington, D.C. Rapid Transit	2647.00	309.70	11.7

*Design and construction management costs including fees.
**SLC estimated value at 80% completion. Does not include full CM services.

The costs of the AE/CM services have been provided by RTK for the current study of SSC conventional systems of this report. The results are given in Table 8.4-5 for the AE/CM costs at 16% of construction costs in each of the WBS categories. In the 1984 Reference Designs Study the cost of the above services were developed by the AE/CM firm of Parsons Brinckerhoff (PB). They arrived at the same average estimate of AE/CM costs at 16% of construction costs.

Table 8.4-5
SSC Conventional Construction—AE/CM Cost

WBS	Component	Construction (K$)	AE/CM (K$)	AE/CM (%)
.3.2	*Conventional facilities*	576,265	92,203	16.0
.3.2.1	Site and infrastructure	85,433	13,669	16.0
.3.2.2	Campus area	42,860	6,858	16.0
.3.2.3	Injector facilities	39,758	6,361	16.0
.3.2.4	Collider facilities	346,803	55,489	16.0
.3.2.5	Experimental facilities	61,412	9,826	16.0

8.5 Management and Support Costs

The Management and Support costs fall into three categories—project management and support staff, project support equipment, and support facilities. The estimated costs are summarized in Table 8.5-1.

Table 8.5-1
SSC Management and Support Cost Summary

WBS	Component	Cost (FY86 M$)
.4	**Management and support**	192.3
.4.1	*Project management*	114.7
.4.2	*Support equipment*	52.6
.4.3	*Support facilities*	25.0

8.5.1 Project Management

Project management includes all management, supervision, and laboratory support functions that are required to accomplish the SSC design and construction. The specific project management functions have been described in Section 7.1. The costs associated with the management and support services listed in Table 7.1-1 are presented in Table 8.5-2.

Table 8.5-2
SSC Project Management Cost

	FTE* Staff	(FY86 M$) Cost
Director's Office	8	4.0
Project Support	38	12.3
Accelerator Division	46	20.1
Conventional Systems Division	57	14.4
Technical Support Division	69	14.7
Administrative Support Division	98	21.8
Staff Total	317	87.3
Materials and Services	—	17.4
Contractor Fees	—	10.0
Total Costs	—	114.7

*Average staff during construction period.
See Table 7.4-3 for actual distribution.

8.5.2 Project Support Equipment

This category includes certain items of instrumentation and equipment that are required in the SSC construction project. These items are not normally included as part of the technical or conventional facilities costs. The general subcategories are computers, diagnostic instruments, vehicles, shop equipment, and office equipment. The special equipment required for the tunnel transport system is also included in this category.

The computers include general-purpose computers ranging from personal desk computers and CAD systems to super-minicomputers. These computer units are used for calculations and analysis in the engineering and design programs. This category does not include accelerator control system computers which are included separately in the technical systems costs of each accelerator. Also, computers for detector systems are not included here; they are treated in a separate report.

Instrumentation includes a wide variety of diagnostic and monitoring equipment which is required in the testing and evaluation of various accelerator systems and components. Examples are oscilloscopes, meters and monitoring devices, recorders, leak detectors, small power supplies, and survey and measurement instruments.

The SSC collider ring is approximately 52 miles in circumference; hence, transportation is a vital part of the construction program. A wide variety of all types of transport units is required including cars, trucks, fork-lifts, fire trucks, cranes, and heavy equipment movers.

Transportation within the SSC collider tunnel requires special attention. An estimate is provided for an integrated bi-directional transport system within the tunnel enclosure.

Special vehicles are provided for the transportation of manpower as well as magnet transporters with outriggers and cranes for installation. The various vehicles are electric powered and controlled by means of a tunnel guide rail.

The shop equipment category includes the various devices and tools to equip the machine shops, assembly shops, electrical and electronics shops, and other specialized craft shops. The equipment inventories from Fermilab and SLAC were used as a guide in estimating the SSC shop facilities equipment.

Office equipment includes an allowance for office furniture for the scientific, administrative, and technical staff as well as the associated office tools such as typewriters, word processors, and reproduction equipment. The allowances for office equipment and the equipment in the other categories described above are summarized in Table 8.5-3.

Table 8.5-3
SSC Equipment Cost Summary

WBS	Component	Cost (FY86 M$)
.4.2	*Equipment total*	52.6
.4.2.1	Computers	5.0
.4.2.2	Instrumentation	10.0
.4.2.3	Vehicles	11.0
.4.2.4	Tunnel transport system	8.4
.4.2.5	Shop equipment	14.0
.4.2.6	Office equipment	4.2

8.5.3 Project Support Facilities

The two primary items that are included in this category are building rentals and electrical power.

Prior to the construction completion of SSC laboratory buildings on the SSC site, it is planned that a large fraction of the management, support, and ED&I staff will be fully engaged in the design and construction program. This group would be located at or near the SSC Site. Projected manpower estimates have been provided in Section 7.4.5. The estimated office space requirements for the management and design teams are provided in Table 8.5-4. It is expected that the required space will be leased in or near the city closest to the SSC site. As SSC buildings and facilities become available in the fourth year of construction, the need for leased office space will diminish.

In addition to office requirements, significant building space is required for warehousing and production facilities. The production of collider magnets will require approximately 400,000 square feet of industrial space. The collider magnet production facilities are not necessarily located near the SSC site. The production of other technical systems including magnets for the injector accelerators are projected to require as much as 200,000 square feet near the SSC site in addition to available facilities at other Laboratories. For many

components, in particular those of the injection acceleration systems, fabrication efforts will be fully underway in the second and third years of construction. The estimated interim rental space needs prior to construction of the SSC laboratory buildings and the associated rental costs are summarized in Table 8.5-4.

Table 8.5-4
SSC Leased Building and Office Space Projection
(Cost in FY86 K$)

	FY88	FY89	FY90	FY91	FY92	FY93	Totals
Office space (ft^2)	(30,000)	(60,000)	(80,000)	(40,000)	—	—	—
Cost @ $14/$ft^2$/yr	420	840	1120	560	—	—	2940
Collider magnet							
Production Facilities (ft^2)	—	(200,000)	(400,000)	(400,000)	(400,000)	(400,000)	—
Cost @ $3/$ft^2$/yr	—	600	1200	1200	1200	1200	5400
Other tech. production and warehouse facilities (ft^2)	(20,000)	(100,000)	(200,000)	(100,000)	(50,000)	—	—
Cost @ $3/$ft^2$/yr	60	300	600	300	150	—	1410
Preparation of facilities	—	2000	—	—	—	—	2000
Cost Summary	480	3740	2920	2060	1350	1200	11,750 K$

The projected electrical power needs for the SSC are provided in Table 8.5-5. Specifically included are the average electrical power requirements to operate the laboratory buildings and facilities during the construction program. The power to operate the various accelerator systems during test and acceptance periods is also included under construction. After successful completion of acceptance tests and procedures for an accelerator unit, such as the Linac or HEB, it is assumed that the power for that system will be charged to pre-operations. The overall estimates for construction power costs are provided in Table 8.5-5.

Table 8.5-5
Estimated Average Power Utilization (MW)

	FY88	FY89	FY90	FY91	FY92	FY93	FY94*
Linac	—	—	—	0.1	0.3	0.8	0.4
LEB	—	—	—	—	0.3	0.8	0.4
MEB	—	—	—	—	0.2	8.0	5.0
HEB	—	—	—	—	—	2.0	3.0
Collider	—	—	—	3.0	10.0	20.0	25.0
Lab facilities	1.0	2.0	4.0	5.0	5.0	4.0	2.0
Power-Total	1.0	2.0	4.0	8.1	15.8	35.6	35.8
Power – Pre-operations	—	—	—	—	8.4	28.4	33.8
Power – Construction	1.0	2.0	4.0	8.1	7.4	7.2	2.0
Construction Power Costs (M$)**	(0.4)	(0.8)	(1.7)	(3.4)	(3.1)	(3.0)	(0.8)

*6-month period
**Total Construction Power Costs = $13.2 M

8.6 Project Contingency

The estimated contingency for each of the SSC WBS level 3 elements is summarized in Table 8.6-1. The contingency is expressed in dollars and as a percent of construction costs. Additional details are provided in the following sections.

Table 8.6-1
Contingency Costs Summary

WBS	Component	Construction (K$)	Contingency (K$)	(%)
.5	**Contingency**	2,480,367	529,951	21.4
.5.1	*Technical components*	1,424,161	297,056	20.9
.5.2	*Conventional facilities, AE/CM*	576,265	138,734	24.1
.5.3	*Systems engineering and design*	287,607	71,049	24.7
.5.4	*Management and support*	192,334	23,113	12.0

8.6.1 Technical Components

The estimates for contingencies on technical systems and components are based on past experience with similar technical components with appropriate modifications as determined by increased or decreased design and construction complexities of each technical system.

Table 8.6-2 provides a summary of the contingency estimates for the major technical systems for the SSC at WBS level 5. In general, systems such as power supplies, vacuum and RF are similar in design and complexity to previously constructed systems and a nominal contingency of 20% is applied. Systems such as instrumentation and controls tend to be more difficult to estimate because of many details with a greater potential for design changes. A higher contingency of 30% is assigned to these elements.

The superconducting magnets of the collider represent a major cost element of the SSC. For the dipole magnet elements, a more detailed analysis of the contingency has been carried to the WBS level 6 as shown in Table 8.6-3. There has been less design and model experience with quadrupoles and spools relative to dipoles; a higher contingency is therefore assigned. The same is true for special magnets near the interaction regions.

Table 8.6-2
Technical Components—Contingency Cost

WBS	Component	Construction (K$)	Contingency (K$)	Contingency (%)
.5.1	*Technical components*	1,424,161	297,056	20.9
.5.1.1	Injector systems	189,252	43,022	22.7
.5.1.1.1	Linac	25,068	5,014	20.0
.5.1.1.2	LEB	15,585	3,433	22.0
.5.1.1.3	MEB	31,720	6,908	21.8
.5.1.1.4	HEB	107,271	25,746	24.0
.5.1.1.5	Test beams	9,608	1,922	20.0
.5.1.2	Collider ring systems	1,234,909	254,034	20.6
.5.1.2.1	Magnets	1,001,252	202,991	20.3
.5.1.2.2	Cryogenics	121,137	24,227	20.0
.5.1.2.3	Vacuum systems	17,321	3,464	20.0
.5.1.2.4	Main power supplies	26,105	5,221	20.0
.5.1.2.5	Correction power supplies	6,942	1,388	20.0
.5.1.2.6	rf system	7,302	1,460	20.0
.5.1.2.7	Beam feedback system	4,301	860	20.0
.5.1.2.8	Injection system	5,201	1,300	25.0
.5.1.2.9	Abort system	9,669	2,417	25.0
.5.1.2.10	Instrumentation	12,871	3,861	30.0
.5.1.2.11	Controls	18,016	5,405	30.0
.5.1.2.12	Safety systems	4,791	1,437	30.0

Table 8.6-3
Collider Magnets—Contingency Cost

WBS	Component	Construction (K$)	Contingency (K$)	(%)
.5.1.2.1	Magnets	1,001,252	202,991	20.3
.5.1.2.1.1	Tooling	56,031	16,809	30.0
.5.1.2.1.2	Dipoles	746,120	136,241	18.3
.5.1.2.1.3	Quadrupoles	39,262	7,852	20.0
.5.1.2.1.4	Spools	78,108	19,528	25.0
.5.1.2.1.5	IR magnets	39,168	9,792	25.0
.5.1.2.1.6	Installation/Survey	42,564	12,769	30.0

Current R&D efforts have been directed primarily at superconducting dipoles. As a result there is considerable experience in design and model fabrication. This experience allows a contingency analysis at WBS level 8 for the superconducting dipole magnets. Material and labor costs for dipole magnet components are separately analyzed. An individual assessment was made of the general design status and level of detail cost information available for each WBS entry. The lowest contingency values were assigned to the items fairly well developed and costed: superconducting cable unit costs (10%), lamination costs on a dollar per pound of steel and a per piece stamping cost basis, cryostat shield components, and vacuum vessel materials (15%). The highest contingency was assigned to the overall labor (35%) to account for uncertainties in not only the direct labor quantities (hours) but also variable elements such as productivity factors, labor rate variations, etc. The detailed results are presented in Table 8.6-4.

8.6.2 Contingency – Conventional Systems

RTK has made estimates of the contingency for each of the three site examples. The estimate in each case was built up from a detailed evaluation of the potential costs associated with each geological and regional setting, considerations of the specificity of the CDG requirements, the preliminary and conceptual nature of the design for conventional facilities, and the uncertainties associated with construction on a postulated, hypothetical site. The values developed by RTK are shown in Table 8.6-5.

Table 8.6-4
Single Collider Dipole Magnet—Contingency Costs

WBS	Component	Construction Cost Material ($)	Construction Cost Labor ($)	Construction Cost Total ($)	Contingency Material (%)	Contingency Labor (%)	Contingency Total ($)
	Dipole Magnet Coils						
.1.2.1.2.1.1	Cold bore tube	4,897	958	5,855	25.0	35.0	1,560
.1.2.1.2.1.2	Coils	31,212	3,445	34,657	10.0	35.0	4,327
.1.2.1.2.1.3	Coil collaring	6,189	763	6,952	20.0	35.0	1,505
	Dipole Yoke and Helium Contain.						
.1.2.1.2.2.1	Yoke and components	10,716	873	11,589	15.0	35.0	1,913
.1.2.1.2.2.2	Helium containment vessel	3,049	294	3,343	15.0	35.0	560
	Final Assy. into Cryostat						
.1.2.1.2.3.1	Cold mass sub-assembly prep.	583	330	913	20.0	35.0	232
.1.2.1.2.3.2	Cold mass supports	4,676	176	4,852	20.0	35.0	997
.1.2.1.2.3.3	20 K heat shield	1,223	110	1,333	15.0	35.0	222
.1.2.1.2.3.4	80 K heat shield	2,174	165	2,339	15.0	35.0	384
.1.2.1.2.3.5	Vacuum vessel and components	2,600	792	3,392	15.0	35.0	667
.1.2.1.2.3.6	Assembly labor	0	2,062	2,062	25.0	35.0	722
.1.2.1.2.4	Electrical system	1,750	1,988	3,738	25.0	35.0	1,133
.1.2.1.2.5	Magnet interconnections	1,626	83	1,709	25.0	35.0	436
.1.2.1.2.6	Magnetic measurements	297	745	1,042	25.0	35.0	335
	Subtotal	70,992	12,784	83,776			14,992
.1.2.1.2.7	Reject allowance	1,222	534	1,756	20.0	20.0	351
.1.2.1.2.8	Materials usage factor	1,907	0	1,907	20.0		381
.1.2.1.2.9	Factory support labor	0	3,270	3,270		20.0	654
.1.2.1.2.10	Shipping, storage handling	1,300	176	1,476	25.0	25.0	369
.1.2.1.2.11	Materials procurement allow.	930	0	930	20.0		186
.1.2.1.2.12	Industrial fees	4,036	0	4,036	20.0		807
	Total cost per dipole magnet	80,387	16,764	97,151			17,741
	Overall effective contingency:				Per Cent:		18.26

Table 8.6-5
Conventional Facilities—Contingency Cost

WBS	Component	Construction (K$)	Contingency (K$)	(%)
.5.2	*Conventional facilities*	576,265	138,734	24.1
.5.2.1	Site and infrastructure	85,433	17,087	20.0
.5.2.2	Campus area	42,860	8,572	20.0
.5.2.3	Injector facilities	39,758	7,952	20.0
.5.2.4	Collider facilities	346,803	86,701	25.0
.5.2.5	Experimental facilities	61,412	18,424	30.0

In preparation for the distribution of contingency by the CDG, consideration was given by information from the three examples sites to the sensitivity of the costs to regional variations, such as different geological formations, construction techniques, and labor and material rates to name the principal items. In the tunneling area, RTK's study was useful in providing a validation to their models, as well as relating to the information that is available from actual construction projects.

In order to determine the contingency percentage for the conventional systems, the CDG considered, in addition to the base values developed by RTK, an analysis of the range of possible facility costs. An average contingency for the tunnel of 25% has been estimated. Due to additional uncertainties associated with the experimental facilities, 30% was assigned to that area. Surface facilities, including the injector, that are less sensitive to geological variations, were assigned a 20% contingency. The resulting contingencies for the construction costs yield a weighted average contingency of 24.1%.

8.6.3 Contingency – Systems Engineering and Design

Systems Engineering and Design is composed of the Engineering, Design, and Inspection (EDI) for Technical Systems and the Architectural Engineering—Construction Management (AE/CM) services for Conventional Systems. The contingency for EDI has been evaluated at WBS Level 6. This analysis leads to contingency dollar values for the Injector and the Collider Systems as shown in Table 8.6-6. The contingency for AE/CM services results from an overall assessment of contingency in each of the two categories of AE and CM services. The results given in Table 8.6-6 are based on previous experience for the design and construction of similar systems.

Table 8.6-6
Systems Engineering and Design—Contingency Cost

WBS	Component	Construction (K$)	Contingency (K$)	(%)
.5.3	*Systems engineering and design*	287,607	71,049	24.7
.5.3.1	EDI	195,404	48,851	25.0
.5.3.1.1	Injector systems	38,134	9,533	25.0
.5.3.1.2	Collider ring systems	157,270	39,318	25.0
.5.3.2	AE/CM services	92,203	22,198	24.1
.5.3.2.1	AE services	51,864	12,486	24.1
.5.3.2.2	CM services	40,339	9,711	24.1

8.6.4 Contingency – Management and Support

The Management and Support area includes the three categories of project management staff, support equipment, and support facilities. The assigned contingencies for these categories are provided in Table 8.6-7. A detailed analysis has been provided for the project management and support staff in Section 7.4.5. The overall contingency for project management reflects a 10% uncertainty for staff. The costs for support equipment and support facilities, as described in Section 8.5, are extrapolations from past experience and may depend to some degree on the final site location and conditions. A higher contingency of 15% is assigned to these categories.

Table 8.6-7
Management and Support—Contingency Cost

WBS	Component	Construction (K$)	Contingency (K$)	(%)
.5.4	*Management and support*	192,334	23,113	12.0
.5.4.1	Project management	114,749	11,475	10.0
.5.4.3	Support equipment	52,635	7,895	15.0
.5.4.2	Support facilities	24,950	3,742	15.0

8.7 Total Project Cost

8.7.1 Total SSC Systems Cost Roll-up

The cost estimating methods used to arrive at the total SSC project cost are described in Section 8.1. The WBS structure presented in Section 8.1.3 provides five major cost areas (WBS level 2) for the SSC project: Technical Systems, Conventional Systems, Systems Engineering and Design, Management and Support, and Contingency. Cost details for each of these areas have been presented in Sections 8.2 through 8.6 respectively. Table 8.7-1 provides a summary of the resulting costs at WBS level 5. Cost details at lower WBS levels are provided in Attachment D.

Figure 8.7-1 provides a graphical display of the relative project costs for each of the five major cost categories noted above. Similar charts are provided (Figs. 8.7-2 and 8.7-3) for the relative costs of the injector and collider technical systems components. Figure 8.7-4 provides the relative cost picture for the five major categories (WBS level 3) of the conventional systems.

8.7.2 Cost Profile

The schedules for design, fabrication and installation of technical components and conventional systems have been provided in Section 7.4. Manpower estimates have been developed for management and support, system engineering and design, and construction. The cost estimates for manpower levels together with materials costs have been distributed by fiscal year according to the above schedules. The resulting annual costs are summarized in Table 8.7-2. An approximate distribution for the associated obligational requirements is indicated. The exact obligational schedule will depend on details of the actual contractual arrangements.

Table 8.7-1
Superconducting Super Collider Cost Roll-up

WBS Element					Total Cost (FY86 K$)
1.	**Superconducting Super Collider**				3,010,318
.1	**Technical components**				1,424,161
.1.1	*Injector systems*			189,252	
.1.1.1	Linac		25,068		
.1.1.1.1	Ion source	886			
.1.1.1.2	RFQ (49.5 MHz)	891			
.1.1.1.3	Drift tube Linac (445 MHz)	6,235			
.1.1.1.4	Coupled cavity Linac (1336 MHz)	3,381			
.1.1.1.5	445 MHz rf power system	4,287			
.1.1.1.6	1336 MHz rf power system	3,797			
.1.1.1.7	Transfer line (Linac to LEB)	3,469			
.1.1.1.8	Instrumentation and controls	1,736			
.1.1.1.9	Safety systems	386			
.1.1.2	LEB		15,585		
.1.1.2.1	Magnets	2,671			
.1.1.2.2	Cryogenics (NA)	0			
.1.1.2.3	Vacuum system	371			
.1.1.2.4	Magnet power supplies	4,806			
.1.1.2.5	rf systems	4,224			
.1.1.2.6	Injection system	245			
.1.1.2.7	Extraction system	361			
.1.1.2.8	Abort system	110			
.1.1.2.9	Instrumentation	277			
.1.1.2.10	Controls	1,526			
.1.1.2.11	Safety system	136			
.1.1.2.12	Installation	858			
.1.1.3	MEB		31,720		
.1.1.3.1	Magnets	13,492			
.1.1.3.2	Cryogenics (NA)	0			
.1.1.3.3	Vacuum system	919			
.1.1.3.4	Magnet power supplies	7,101			
.1.1.3.5	rf systems	3,759			
.1.1.3.6	Injection system	217			
.1.1.3.7	Extraction system	829			
.1.1.3.8	Abort system	583			
.1.1.3.9	Instrumentation	550			
.1.1.3.10	Controls	1,027			
.1.1.3.11	Safety system	276			
.1.1.3.12	Installation	2,968			
.1.1.4	HEB		107,271		
.1.1.4.1	Magnets	54,244			
.1.1.4.2	Cryogenics	13,561			
.1.1.4.3	Vacuum system	1,965			
.1.1.4.4	Magnet power supplies	13,108			
.1.1.4.5	rf systems	5,334			
.1.1.4.6	Injection system	1,370			
.1.1.4.7	Extraction system	3,526			
.1.1.4.8	Abort system	1,620			
.1.1.4.9	Instrumentation	958			
.1.1.4.10	Controls	1,767			
.1.1.4.11	Safety system	697			
.1.1.4.12	Installation	9,121			

.1.1.5	Test beams		9,608		
.1.1.5.1	(Not used)	0			
.1.1.5.2	(Not used)	0			
.1.1.5.3	Vacuum system	350			
.1.1.5.4	(Not used)	0			
.1.1.5.5	Primary transport system	2,390			
.1.1.5.6	Target stations	1,200			
.1.1.5.7	Secondary transport system	3,040			
.1.1.5.8	(Not used)	0			
.1.1.5.9	Instrumentation	299			
.1.1.5.10	Controls	2,027			
.1.1.5.11	Safety system	301			
.1.2	*Collider ring systems*			1,234,909	
.1.2.1	Magnets		1,001,252		
.1.2.1.1	Tooling	56,031			
.1.2.1.2	Dipole magnets	746,120			
.1.2.1.3	Quadrupole magnets	39,262			
.1.2.1.4	Spools and spec devices	78,108			
.1.2.1.5	IR magnets	39,168			
.1.2.1.6	Installation and survey	42,564			
.1.2.2	Cryogenics		121,137		
.1.2.3	Vacuum systems		17,321		
.1.2.4	Main power supplies		26,105		
.1.2.5	Correction power supplies		6,942		
.1.2.6	rf system		7,302		
.1.2.7	Beam feedback system		4,301		
.1.2.8	Injection system		5,201		
.1.2.9	Abort system		9,669		
.1.2.10	Instrumentation		12,871		
.1.2.11	Controls		18,016		
.1.2.12	Safety systems		4,791		
.2	**Conventional facilities**				576,265
.2.1	*Site and infrastructure*			85,433	
.2.1.1	Offsite support		0		
.2.1.2	Construction support		1,447		
.2.1.3	Site preparation		975		
.2.1.4	Electrical		43,732		
.2.1.5	Water and waste systems		5,913		
.2.1.6	Auxiliary systems		778		
.2.1.7	Communications		11,114		
.2.1.8	Roads and parking		20,530		
.2.1.9	Fencing, berms, landscaping		944		
.2.2	*Campus area*			42,860	
.2.2.1	Laboratory buildings		24,049		
.2.2.2	Heavy works buildings		10,833		
.2.2.3	Shop buildings		2,209		
.2.2.4	Support buildings		5,770		
.2.3	*Injector facilities*			39,758	
.2.3.1	Linac		1,743		
.2.3.2	Low Energy Booster		1,322		
.2.3.3	Medium Energy Booster		10,953		
.2.3.4	High Energy Booster		23,618		
.2.3.5	Test beam area		2,122		

.2.4	*Collider facilities*			346,803	
.2.4.1	North arc		122,140		
.2.4.2	South arc		137,097		
.2.4.3	East cluster		31,459		
.2.4.4	West cluster		40,688		
.2.4.5	Surface buildings		1,663		
.2.4.6	Cryogenic facilities		13,756		
.2.5	*Experimental facilities*			61,412	
.2.5.1	East cluster experimental facilities		31,136		
.2.5.2	West cluster experimental facilities		30,276		
.3	**Systems Engineering and Design**				287,607
.3.1	*EDI*			195,404	
.3.1.1	Injector systems		38,134		
.3.1.1.1	Linac	5,766			
.3.1.1.2	LEB	3,896			
.3.1.1.3	MEB	7,930			
.3.1.1.4	HEB	19,101			
.3.1.1.5	Test beams	1,441			
.3.1.2	Collider Ring Systems		157,270		
.3.1.2.1	Magnets	115,011			
.3.1.2.2	Cryogenics	15,748			
.3.1.2.3	Vacuum systems	3,464			
.3.1.2.4	Main power supplies	5,221			
.3.1.2.5	Correction power supplies	1,388			
.3.1.2.6	rf system	1,825			
.3.1.2.7	Beam feedback system	1,075			
.3.1.2.8	Injection system	1,300			
.3.1.2.9	Abort system	2,417			
.3.1.2.10	Instrumentation	3,218			
.3.1.2.11	Controls	5,405			
.3.1.2.12	Safety systems	1,198			
.3.2	*AE/CM services*			92,203	
.3.2.1	AE services		51,864		
.3.2.1.1	Site and infrastructure	7,689			
.3.2.1.2	Campus area	3,857			
.3.2.1.3	Injector facilities	3,578			
.3.2.1.4	Collider ring facilities	31,212			
.3.2.1.5	Experimental facilities	5,527			
.3.2.2	CM Services		40,339		
.3.2.2.1	Site and infrastructure	5,980			
.3.2.2.2	Campus area	3,000			
.3.2.2.3	Injector facilities	2,783			
.3.2.2.4	Collider ring facilities	24,276			
.3.2.2.5	Experimental facilities	4,299			
.4	**Management and support**				192,334
.4.1	*Project management*			114,749	
.4.2	*Support equipment*			52,635	
.4.3	*Support facilities*			24,950	

.5	**Contingency**			529,951
.5.1	*Technical components*		297,056	
.5.1.1	Injector systems		43,022	
.5.1.1.1	Linac	5,014		
.5.1.1.2	LEB	3,433		
.5.1.1.3	MEB	6,908		
.5.1.1.4	HEB	24,689		
.5.1.1.5	Test beams	1,922		
.5.1.2	Collider ring systems		254,034	
.5.1.1.1	Magnets	202,991		
.5.1.1.2	Cryogenics	24,227		
.5.1.1.3	Vacuum systems	3,464		
.5.1.2.4	Main power supplies	5,221		
.5.1.2.5	Correction power supplies	1,388		
.5.1.2.6	rf system	1,460		
.5.1.2.7	Beam feedback system	860		
.5.1.2.8	Injection system	1,300		
.5.1.2.9	Abort system	2,417		
.5.1.2.10	Instrumentation	3,861		
.5.1.2.11	Controls	5,405		
.5.1.2.12	Safety systems	1,437		
.5.2	*Conventional construction*		138,734	
.5.2.1	Site and infrastructure		17,087	
.5.2.2	Campus area		8,572	
.5.2.3	Injector facilities		7,952	
.5.2.4	Collider ring facilities		86,701	
.5.2.5	Experimental facilities		18,424	
.5.3	*Systems engineering and design*		71,049	
.5.3.1	EDI		48,851	
.5.3.2	AE/CM services		22,198	
.5.4	*Management and support*		23,111	
.5.4.1	Project management		11,475	
.5.4.2	Support equipment		7,895	
.5.4.3	Support facilities		3,742	

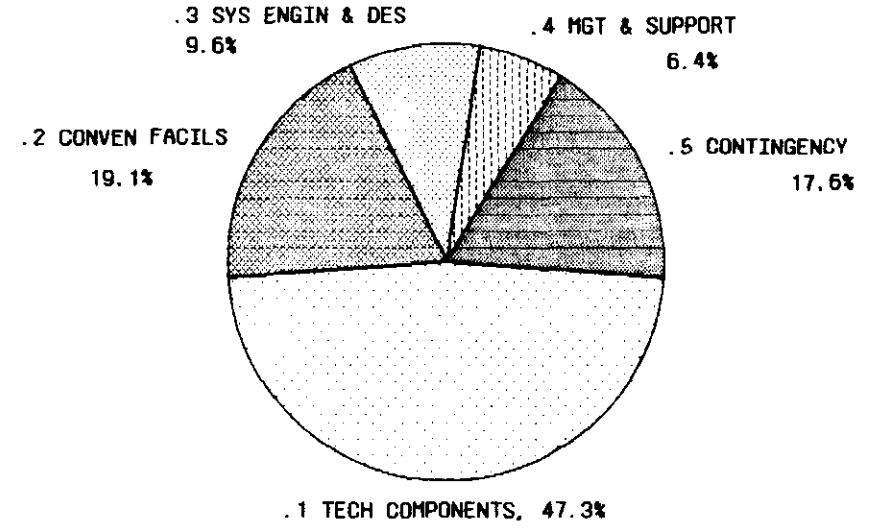

Figure 8.7-1. SSC cost estimate summary: Level 2 WBS categories.

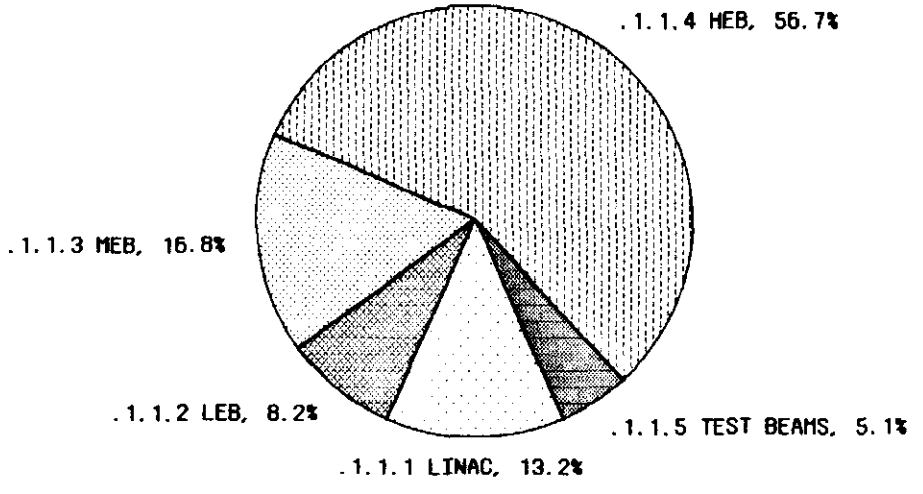

Figure 8.7-2. Injector Systems — Technical Components: Level 4 WBS categories.

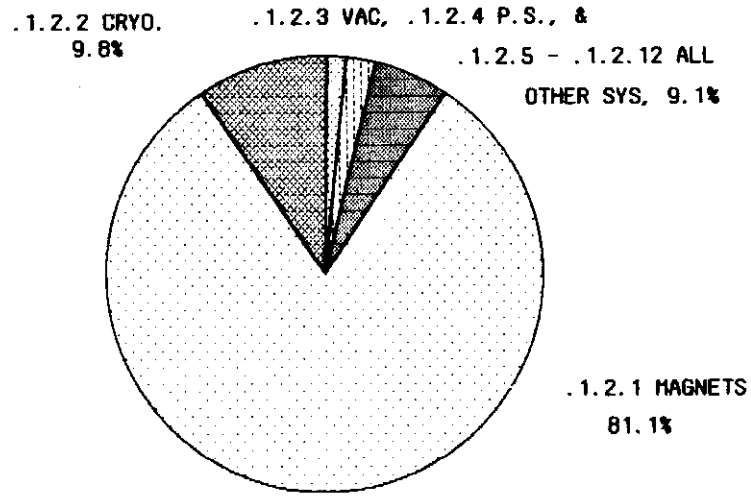

Figure 8.7-3. Collider Systems — Technical Components: Level 4 WBS categories.

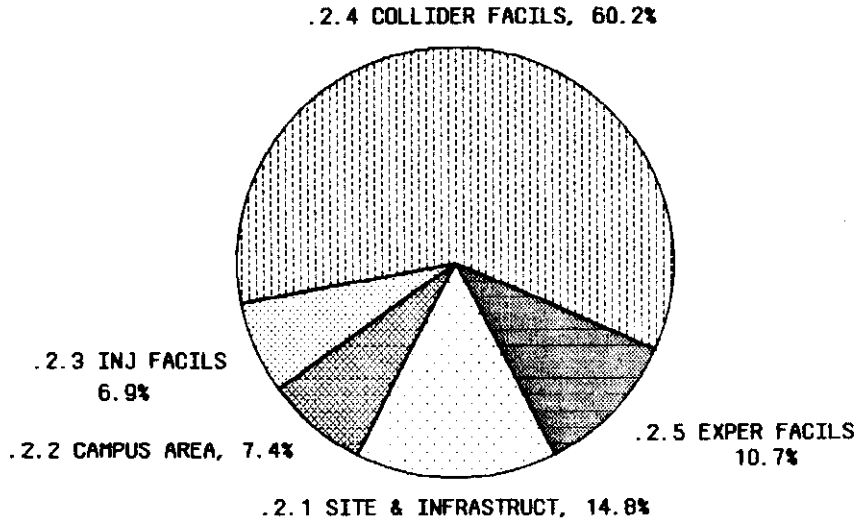

Figure 8.7-4. Conventional Facilities: Level 3 WBS categories.

Table 8.7-2
Projected Annual Funding Distribution

FY	Obligations (M$)	Cost (M$)
88	130	75
89	635	297
90	660	628
91	645	791
92	475	675
93	415	493
94	50.3	51.3
Total	3010.3	3010.3

9. Conclusions

9.1 Physics Opportunities

Current understanding of the fundamental structure of matter envisions quarks and leptons as the basic material constituents with their interactions governed by the electroweak, strong and gravitational forces which are transmitted by force (or gauge) particles. While this picture represents a great stride in synthesizing what is known about the physical universe, there are many fundamental questions that the accompanying theories cannot answer: are quarks and leptons really elementary, what is the origin of mass, is there at root only one force, and many more. Extensive studies of recent years have concluded that the next major step in answering these questions requires a new instrument with capabilities well beyond the limits of existing accelerators.

From the work of the world community of scientists has emerged a consensus concerning the avenues of investigation needed to address the basic issues. Based on this work, estimates have been made of the discovery reach of a new facility presuming various accelerator energies and luminosities. This work has confirmed previous judgements that a proton collider of 20 TeV per beam and 10^{33} $cm^{-2}s^{-1}$ luminosity offers high probability for startling and profound discoveries about the structure and development of the physical universe.

9.2 Design Parameters

This SSC conceptual design, cost estimate and schedule describes a complete accelerator facility having these primary parameters. The eighty-three kilometer circumference collider ring has a racetrack shape and is housed in an underground tunnel. The six collision areas, four initially outfitted, are clustered in the straightaways as shown in Fig. 1.2-1 and Fig. 3.3-2. Within the clusters, collision areas are separated by about two and one-half kilometers. One of the two clusters includes the injector complex (a cascade of a linear accelerator and three synchrotrons) which supplies 1 TeV beams to the collider for acceleration to 20 TeV. The one-hour injection and acceleration process is followed by beam storage and collisions at full energy for one day or more before the need to refill and start

the cycle again. An artist's overview of this part of the facility is displayed in the frontispiece and in Fig. 6.1-1. Near the injector, a campus area includes laboratory, shop, offices and other auxiliary buildings. While all of the ring is underground and not evident from the surface, personnel exits and refrigeration stations alternate so that egress from the tunnel is provided every four kilometers or less. It is expected that normal usage of the land over most of the collider can continue even when the collider is in operation. Most of the circumference is comprised of uniform tunnel segments housing the superconducting magnet rings as shown in Fig. 6.6-1 mounted one over the other, with the beam center lines separated by seventy centimeters. In the clustered interaction regions where the beams are made to collide, specially designed buildings, an example of which is shown in Fig. 6.7-4, house the detectors and provide facilities for their final assembly and operation.

In all it is anticipated that about three thousand workers will be present at the Laboratory, of whom about five hundred will be visiting scientists conducting research with the SSC.

9.3 Technical Feasibility

The conceptual design presented herein is based on studies begun in 1983. It has been shown that the basic accelerator system design principles successfully employed in existing facilities, including the Fermilab Tevatron with its ring of superconducting magnets, can be used directly for the SSC design. Several technically viable approaches to the major accelerator system hardware are known. Optimization studies, including operational considerations and cost analyses, have been used to select the approaches displayed in this report. The results of these studies and the supporting R&D show that the SSC as described in this conceptual design is technically feasible using today's technology.

9.3.1 Accelerator Physics

Analysis of the principal accelerator physics issues has been aided by several previous studies and a number of special workshops and task forces, drawing on the talents and experience of the worldwide accelerator community. The work of those studies has been applied and extended in this report to derive, from the specified end-use parameters, the myriad secondary parameters for the SSC. It is the latter that describe the beam properties and specifications of system performance needed to achieve the desired energy and luminosity with good beam lifetime and sufficient operational flexibility. Primary areas of investigation were luminosity, required aperture, collective effects, lattice and beam confinement design, luminosity lifetime, rf system requirements, synchrotron radiation effects, consequences of lost beam particles, and injector system requirements. In every case the results represent a reasonable extrapolation from current practice.

Energy and Luminosity

The steady increase in accelerator energies of a factor of 10^7 over the past five decades makes us confident that achievement of a 20 TeV beam energy by extension of current methods is practical. The luminosity goal of 10^{33} $cm^{-2}s^{-1}$ is only a factor of ten higher than that achieved in the CERN ISR almost a decade ago. Substantial improvements in accelerator technology have occurred in the meantime. Parameters that directly affect the

luminosity are beam current, beam emittance, focusing strength at the interaction point and the sustainable tune spread due to the nonlinear beam-beam interaction. The SSC beam current of about 73 mA required to achieve the specified luminosity is relatively modest. The design value of the tune spread (because of the beam-beam interaction) resulting from the chosen emittance and beam current is quite conservative, being only about one fourth of that already achieved in $p\bar{p}$ collisions at the Sp$\bar{p}$S. The associated normalized emittance is about one quarter to one third of that commonly achieved in existing large proton rings, and requires care in its achievement.

Although existing proton linacs produce beams with greater brightness (smaller emittance) than are required for the SSC, it has usually been true that emittance dilution occurs in the early stages of acceleration in the booster synchrotron. Calculations indicate that this observed dilution is entirely attributable to space-charge-induced tune shifts and, in some cases, to collective instabilities driven by the relatively high impedance of the vacuum chambers in the older accelerators. These problems are eliminated in the SSC design by utilizing a relatively high energy (600 MeV) linac to reduce the space-charge tune shift, and by taking advantage of modern techniques for greatly reducing vacuum chamber impedances. Because the requisite design calculations are based on well understood principles, achieving the specified SSC emittance should be straightforward.

The focusing strength needed to achieve the target luminosity at the design beam current is characterized by a value of the betatron function at the crossing point of 0.5 m. One meter has already been achieved at the Sp$\bar{p}$S and the Tevatron, and substantially stronger focusing is commonly achieved in electron rings. Development of a small number of superconducting quadrupoles stronger than those now in use at the Tevatron will be required to achieve this strong focusing. Reasonable conceptual designs for quadrupoles with the desired 235 T/m gradient already exist.

Lattice

The lattice is the configuration of bending and focusing magnets used to confine and focus the beams. We have found a flexible, modular arrangement in which two long arc segments are joined by two relatively short segments or clusters, each made up of four units of equal length. The arcs are composed of uniform, repeating cells containing ten dipoles and two quadrupoles each. It is in the cluster regions that the beams are forced to collide and auxiliary functions such as injection, extraction, and acceleration are carried out.

Each cluster unit carries its own matching, dispersion suppression, beam separation and final focus modules, thereby permitting a broad range of individual adjustment within each unit. The flexibility of this design permits continuous evolution of the interaction region layout to optimize experimental usage over the life of the facility. As an example, this conceptual design displays two high luminosity and two intermediate luminosity interaction regions.

Standard lattice design methods suffice to produce a flexible, practical scheme in which the clustered interaction region concept can be employed to advantage.

Aperture

Next to the design energy itself, the physical aperture of the magnets is the single most important collider parameter in determining cost, since it determines the amount of material needed to construct the magnets. Because the magnetic field will not be perfectly uniform throughout the physical aperture, the useful magnetic aperture will be some fraction of the physical aperture, depending in a complex manner on the magnet design and fabrication tolerances, as well as on the design of the lattice.

The needed linear, momentum, and dynamic apertures were determined by examining requirements for injection, acceleration, and collision operation. It was determined that the most stringent requirements are imposed by single particle dynamics during the tune-up and injection processes at low energy. Roughly speaking, a one centimeter magnetic aperture is sufficient. In determining the physical magnet aperture needed to meet this requirement, the expected magnet errors and lattice design are taken into account along with associated costs. The result was that a four centimeter physical aperture of the magnet coil, together with an approximately two hundred meter cell length, are optimum.

Collective Effects

Owing to the high energy and tight focusing that can be achieved at the collision regions, rather modest beam currents are needed. The calculated 73 mA average (2.0 A peak) is only one third that routinely achieved in proton accelerators today. In addition, care is taken in this design to assure that the impedances presented to the beam by its vacuum envelope are low. A high conductivity surface for the beam tube is employed, and special measures are taken at the many expansion joints. As a result the threshold beam currents for instabilities that cannot easily be controlled by feedback are all comfortably above the design operating current.

Luminosity Lifetime

The strongest contributor to beam loss is the interactions of the protons at the collision point. Minor contributions come from inelastic scattering from residual gas and intra-beam scattering. The net lifetime from these effects is more than 100 hours. The luminosity depends not only on the number of particles but also on the emittance, which decreases with time from synchrotron radiation. The net result is that the luminosity actually rises for the first day of collision and begins to fall thereafter. After two days the luminosity is still slightly above its starting value. It seems likely that uninterrupted runs of one to a few days will be practical.

Acceleration System

With a day or more for the useful lifetime of the beams, a combined injection and acceleration time of about one hour suffices to give good utilization. Of this hour, about one quarter is assigned to acceleration from 1 to 20 TeV. Further, as the injected particles are already ultra relativistic, a narrow band rf system can be used. The result is that a modest acceleration system patterned after, but smaller than, those now used for electron colliders can be employed.

Synchrotron Radiation

Each beam radiates 9 kW in the form of soft x rays which impinge on and are absorbed by the cold beam tube. In addition to the obvious consequences for the cryogenic system, the photon flux onto the inner surface of the beam tube increases the residual gas pressure within it. Experiments with a cryogenically pumped tube irradiated by a beam of synchrotron radiation having the spectral characteristics closely approximating that from the SSC beam show that the pressure rise will not impair the beam lifetime significantly.

Lost Beam Particles

An important feature of this conceptual design is the provision of special means to avoid excessive beam loss into superconducting magnets during injection, abort and collision modes of operation. For protection during injection and abort, short lengths of normal magnets are provided close to places where beam might be lost during these operations. At collision, about 800 W is carried away from the high luminosity IRs by lost beam particles. Primary protection of the nearby superconducting quadrupoles is afforded by collimators placed between them and the interaction point for this purpose. Detailed calculations show that the heat generated in the quadrupoles by lost beam particles that get through the collimators can be handled by the cryogenic system while maintaining the superconductor well below the quench threshold.

Some particles are lost in the arcs through inelastic scattering by the residual gas, creating a neutron background in the tunnel while the beam is on. Active electronics components are protected by installing them in special recesses in the tunnel ceiling.

Injector System

The design of the injector system presented herein is based almost entirely on existing accelerators. Careful attention has been paid in the design to preservation of the beam emittance. This objective appears practical with the selected sequence of accelerators and transfer energies.

9.3.2 Accelerator Engineering

Engineering concepts for the primary technical and conventional systems are presented in this report. In each case the engineering concept is based upon well established principles and existing technology. The dominant technical systems are the magnets and the cryogenic system that maintains them at low temperature. The dominant conventional system is the tunnel housing the main collider ring. Practical realization of needed technical and conventional systems requires no new inventions or new technologies.

Magnets

The primary motivation for developing a superconducting magnet design different in detail from those of the Tevatron is economic. Several technically feasible approaches to the needed magnet system are known. As a result of the early phase of the R&D program one of them, the design displayed in this report, was selected as having the best combination of cost and operational characteristics. In developing the design a number of cost saving factors have been exploited:

(a) the relatively small aperture needed for SSC magnets, resulting in reduced materials requirements per unit length;
(b) the steady increase in current carrying capacity of commercially available superconductor;
(c) the improved productivity of automated and simplified manufacturing and assembly methods;
(d) the use of longer magnet units to reduce assembly and handling labor;
(e) the use of improved and more energy-efficient designs to reduce cryogenic requirements.

Comparisons with existing designs show the expected cost savings.

Many models of the selected magnet design have been built, six of them 4.5 meters in length. All have been assembled from industrially supplied components using standard industrial methods. In their cryogenic tests each achieved an operating field above the projected operating field for the SSC. Full length (17 m) models are now in construction and first tests will be carried out this summer. Beyond the obvious tests of each unit for basic performance, extensive system testing will be carried out to demonstrate that this magnet design meets all operational and reliability requirements. Manufacturing plans for the magnets have been worked out by industrial firms expert in manufacturing equipment of this type. The plans show that practical production of the magnets can be carried out on the anticipated time scale.

Cryogenics

The refrigeration requirement for the SSC, though large in aggregate, is well within the scope of current industrial technology. Machinery and techniques that are part of current commercial practice are adequate to support SSC operation, and the individual plants proposed for the SSC are smaller than many now in service. Moreover, the design is such that the SSC can operate when one, or in some cases two, of its eleven plants are under repair. The experience gained in the operation of the Tevatron, particularly the system experience, gives confidence that the SSC cryogenics will meet expectations for performance and reliability. The design heat load that the refrigerators must supply is largely associated with the magnets. Large-scale magnet cryostat heat leak tests conducted as part of the R&D show the design calculations to be reliable.

Other Technical Systems

The other systems of the accelerator—controls, power supplies, rf, injection, abort, beam instrumentation and personnel safety—are all within the range of current engineering practice and pose no outstanding technical challenge. The same can be said of the injector complex since a 1 TeV, superconducting synchrotron capable of producing the required beams has been built and successfully operated. Even for the vacuum system, which must contend with synchrotron radiation in a cryogenic environment, experiments have shown that normal engineering practice suffices.

Conventional Facilities

The standard construction practices and structure types used for past accelerators appear to be entirely adequate for the SSC. Shielding needs of the collider are more modest than for the high-intensity rapid-cycling synchrotron now in existence at Fermilab. Throughout most of the tunnel, critical accelerator components are sealed into the magnet cryostat which provides a uniform and protected environment, independent of external conditions. Thus the tunnel environment can be more austere than has been common practice in the past. As with other strong-focusing accelerators, foundation stability tolerances are not severe. As long as differential settlement occurs on a length scale having a typical dimension of one kilometer and on a time scale of many months or years, experience has shown that a combination of resurvey and orbit-correction settings easily accommodates observed changes. The consequences of constructing the needed tunnel in a variety of geologies and topographies have been examined and it is found that these can be accommodated technically with relative ease.

Considerable attention was given during the conceptual design process to matters of safety and environment. Despite its very high beam energy, the environmental and personnel radiation protection needs of the SSC are comparable with those for other accelerators, such as Fermilab and CERN, now in operation. There, standards considerably more stringent than current federal regulations are achieved. Through extensive study, calculation and measurement over the years the science of accelerator shielding has been put on a sound basis, giving confidence that methods successfully used at other accelerators can be applied to the SSC. Ordinary mechanical, electrical, fire, and atmosphere safety in the tunnel have been carefully considered. It is believed that all standards can be conservatively met. Other safety issues are similar to those dealt with routinely in university and national high energy physics research laboratory environments.

These considerations and others form a firm basis for expectation that the SSC can be built and operated in a safe and environmentally sensitive manner.

9.4 Cost

In support of the cost estimate a complete conceptual design has been created which deals with every needed subsystem. A matching work breakdown structure (WBS) has been constructed all the way to the component, material, and direct labor level where appropriate. As the schematic design of the SSC closely parallels that of existing accelerator complexes, so do the number and variety of subsystems required. Thus considerable practical experience with comparable systems could be brought to bear in helping to assure that all necessary components and processes have been accounted for. The design and cost estimating were directed by personnel having direct, senior level, experience in the design, construction, and operation of existing accelerator facilities. A combination of historical information, detailed estimates based on current vendor quotations, scaling from existing subsystems, and several independent estimates for important subsystems were used in our attempt to place the estimate on the soundest possible footing. Estimates of prudent contingency allowances were also made at the detailed level in an effort to determine the best possible cost envelope. The greatest challenge in the cost estimate is presented by the conventional systems because of the uncertainty of siting. An elaborate system for dealing with

that uncertainty was devised and subsequently improved through criticism by panels of independent experts.

The results of the full cost estimate are displayed in summary form in Table 9.4-1.

Table 9.4-1
Project Cost Summary

		FY 86 K$
Superconducting Super Collider		3,010,318
Technical components		1,424,161
Injector systems	189,252	
Collider ring systems	1,234,909	
Conventional facilities		576,265
Site and infrastructure	85,433	
Campus area	42,860	
Injector facilities	39,758	
Collider facilities	346,803	
Experimental facilities	61,412	
Systems engineering and design		287,607
EDI	195,404	
AE/CM services	92,203	
Management and support		192,334
Project management	114,749	
Support equipment	52,635	
Support facilities	24,950	
Contingency		529,951

Contingency

Contingency estimates were conducted in conjunction with the main cost estimate. For the conventional systems the task is particularly difficult given that the site is unknown. Nevertheless there is a basis for estimating. For each of the three sites studied, detailed conditions appropriate to the particular physiographic region were developed. From these, detailed contingencies were estimated. This array of contingencies and their ranges were then used to estimate probable contingencies, assuming that a reasonably tractable site is chosen. Our study has shown that tractable sites exist in many different geological and topographic settings.

The estimates for contingencies on technical systems and components can be based on past experience with appropriate modifications as determined by increased or decreased design needs and construction complexities. In important cases material and labor cost

contingencies were analyzed separately. In every case an assessment of design status and supplied level of cost detail was taken into account, The overall contingency figure is given in Table 9.4-1.

Potential Cost Savings

In addition to treating possible cost increases, as in done in the contingency analysis, a balanced picture must consider the possibility that some of the assumptions made are overly conservative or that further technical developments can lower costs. While we see no possibility for drastically cutting the costs while maintaining the full energy and luminosity capabilities as described in this report, there are worthwhile cost saving possibilities.

In the area of conventional systems, sites of moderate difficulty were used in the estimates as were national average labor rates. How much the selection of a favorable site in a favorable market location would save cannot be estimated with precision. The contingency estimate for the underground systems, about $100M, might serve as a reasonable guess.

In the area of technical systems, the single largest item is the magnets. If the operating magnetic field were increased by even a small amount, significant savings would accrue as fewer magnets would be required and the circumference of the ring would shrink, this giving significant leverage in cost savings. The design operating field is based on the properties of the superconducting cable available commercially today. There is evidence that even better cable may be available from industry soon. Estimates taking into account possible corresponding operating field increases indicate that overall savings of between $100M and $200M through superconductor improvement are not out of the question.

9.5 Construction Schedule

As an aid to planning and as part of exploration of technical feasibility, a construction schedule has been developed which is consistent with achievable construction rates for both technical and conventional systems. The rates of advance used for the conventional systems were obtained by detailed consideration of possible site conditions and allowance for adequate time for design and preparation and for efficient contracting. The rates of production used for the principal technical components were derived from manufacturing plans made by industrial firms as part of cost estimates. Assuming, among other things, that project authorization precedes site selection by some six to twelve months, the site determination is the principal critical path milestone and forms the anchor point for the developed schedule. Central determinants of the schedule thereafter are collider ring underground construction and collider ring dipole magnet production. The collider ring sequence follows a closely coupled phased construction approach. As each tunnel section becomes available for occupancy, the installation and testing of technical components follow in a stepwise fashion such that acceptance testing of each section can begin as soon as installation is complete. This approach is made possible by the modular nature of the accelerator designs and leads to the most efficient use of time, while serving as a continuous monitor of quality control at the highest level. Analysis shows that the other components of the complete facility can be completed in a time significantly shorter than for the collider ring itself, thus keeping them safely off the critical path. The conclusion of this study is that a six and half year construction duration is technically feasible.

9.6 Summary

In this report and its attachments it is shown that a proton-proton collider of 20 TeV beam energy and 10^{33} $cm^{-2}s^{-1}$ luminosity can be practically realized. This feasibility does not depend on any new invention or development of new technology. A detailed analysis of the technical systems required and of conventional systems in a variety of circumstances shows that the facility, exclusive of research equipment, site acquisition and R&D and pre-operation costs can be provided for three billion dollars (FY 1986). Based on technical considerations cited above, a construction period of six and a half years would bring the facility on stream for physics in the mid 1990s.

☆U.S. GOVERNMENT PRINTING OFFICE:1986—644-459